FLOW SEPARATION

ADVISORY GROUP FOR AEROSPACE RESEARCH AND DEVELOPMENT

PREPARED FOR
NORTH ATLANTIC TREATY ORGANIZATION

NOVEMBER 1975

AGARD-CP-168

AGARD

ADVISORY GROUP FOR AEROSPACE RESEARCH & DEVELOPMENT

7 RUE ANCELLE 92200 NEUILLY SUR SEINE FRANCE

AGARD CONFERENCE PROCEEDINGS No. 168

on

Flow Separation

NORTH ATLANTIC TREATY ORGANIZATION

559

REPORT DOCUMENTATION PAGE			
1. Recipient's Reference	2. Originator's Reference AGARD-CP-168	3. Further Reference	4. Security Classification of Document UNCLASSIFIED
5. Originator	Advisory Group for Aerospace Research and Development North Atlantic Treaty Organization 7 rue Ancelle, 92200 Neuilly sur Seine, France		
6. Title	Flow Separation		
7. Presented at	Göttingen, Germany		
8. Author(s)	Various		9. Date November 1975
10. Author's Address	Various		11. Pages 559
12. Distribution Statement	This document is distributed in accordance with AGARD policies and regulations, which are outlined on the Outside Back Covers of all AGARD publications.		

13. Keywords/Descriptors		14. UDC
Boundary layer separation	Pressure measurement	532.526.5:533.6.011
Laminar flow	Supersonic flow	
Turbulent flow	Transonic flow	
Mathematical prediction	Subsonic flow	

15. Abstract

Proceedings of the Fluid Dynamics Panel Symposium held in Göttingen, Germany 27–30 May, 1975. Forty-two papers and Round Table Discussion dealing with measurements in and prediction of laminar and turbulent two-and-three-dimensional boundary-layer separated flows. Recent results for subsonic, transonic, and supersonic separated flows are evaluated, and directions for future research activity are assessed.

NORTH ATLANTIC TREATY ORGANIZATION

ADVISORY GROUP FOR AEROSPACE RESEARCH AND DEVELOPMENT

(ORGANISATION DU TRAITE DE L'ATLANTIQUE NORD)

AGARD Conference Proceedings No.168

FLOW SEPARATION

Papers and Discussions of the Fluid Dynamics Panel Symposium
held in Göttingen, Germany, 27–30 May 1975

THE MISSION OF AGARD

The mission of AGARD is to bring together the leading personalities of the NATO nations in the fields of science and technology relating to aerospace for the following purposes:

- Exchanging of scientific and technical information;
- Continuously stimulating advances in the aerospace sciences relevant to strengthening the common defence posture;
- Improving the co-operation among member nations in aerospace research and development;
- Providing scientific and technical advice and assistance to the North Atlantic Military Committee in the field of aerospace research and development;
- Rendering scientific and technical assistance, as requested, to other NATO bodies and to member nations in connection with research and development problems in the aerospace field;
- Providing assistance to member nations for the purpose of increasing their scientific and technical potential;
- Recommending effective ways for the member nations to use their research and development capabilities for the common benefit of the NATO community.

The highest authority within AGARD is the National Delegates Board consisting of officially appointed senior representatives from each member nation. The mission of AGARD is carried out through the Panels which are composed of experts appointed by the National Delegates, the Consultant and Exchange Program and the Aerospace Applications Studies Program. The results of AGARD work are reported to the member nations and the NATO Authorities through the AGARD series of publications of which this is one.

Participation in AGARD activities is by invitation only and is normally limited to citizens of the NATO nations.

Published November 1975

532.526.5:533.6.011

Printed by Technical Editing and Reproduction Ltd
Harford House, 7–9 Charlotte St, London W1P 1HD

FOREWORD

The Symposium dealt with recent research results concerning the understanding and prediction of two-dimensional and three-dimensional laminar and turbulent separation phenomena in subsonic, transonic, and supersonic flows. Numerical, analytical, theoretical, and experimental results were discussed.

The Symposium consisted of three Sessions, each of which started with an invited survey paper. The Symposium concluded with a Round Table Discussion, initiated by invited experts, which assessed and evaluated the Meeting papers and suggested directions for future research effort.

The Symposium was held at the Stadthalle, Göttingen, at the invitation of the German National Delegates to AGARD.

CONTENTS

* Not available at time of publication

* Not available at time of publication

Reference

SESSION III – THREE-DIMENSIONAL SEPARATION

OPENING REMARKS

by

D.Küchemann

The Fluid Dynamics Panel held its last Symposium in the eternal city of Rome – now we have come together in the city of Göttingen, known as a city for just a little over one thousand years, with a University which is only some two hundred years old. Yet there is something about this place, which I think is relevant to what we are going to do, and which I should like to recall. My remarks will be partly personal, – after all, I was born here and I grew up here – but I seriously believe that the spirit of this place Göttingen goes beyond personal feelings and concerns us all.

It has been called the "Göttingen spirit", der Göttinger Geist, and I shall try to explain what it means to me and what it can do to people.

On the one hand, the Göttingen spirit means that human endeavours and scientific enquiries to find out about and to understand nature around us and also human nature require and deserve our most strenuous, vigorous, and persevering efforts: we must learn to think clearly and to reason – we must know, and we shall know! On the other hand, it means that our work and thinking, however hard we exert ourselves, cannot be done in exclusive and splendid isolation and be justified as being an end in itself and done for its own sake: whatever we do, we must have some aim in mind, which might benefit the human society in which we live, and we must go far enough in our work to convince ourselves that the outcome of our endeavours can be applied usefully in some way. Many very great men and women have lived and worked here at Göttingen and acted according to these tenets. They taught and set an example to many others, and it is a remarkable characteristic of this Göttingen spirit that quite ordinary people with only modest talents, like myself, could so greatly benefit from it. That is why I take the liberty to use this occasion to speak about it and, at the same time, to offer my own personal tribute to the spirit to which I owe so much.

It may be in order to remind ourselves briefly of some historical facts. The University Georgia Augusta was founded in 1737 by George II, King of England and Elector of Hanover, and the influence of George's adopted country can be felt quite strongly here. Even the Dukes and Princes of Hanover, who used to live in the houses along the Prinzenstrasse, gave their titles in English rather than in German. What concerns us is that Göttingen was one of the first modern Universities, as we know them today, designed by the enlightened Baron Münchhausen (of the same lower-Saxon family as the famous traveller), who from the beginning gathered here some of the most eminent and outstanding teachers and researchers and immediately founded a "Royal Society of Science" according to a pattern already set before in London. One of the many bright people then at Göttingen was Lichtenberg who maintained that "knowledge does not mean all the things we happen to know but only those we have thought about enough to know how they hang together and how they can be applied usefully". This proposition describes the Göttingen spirit very clearly and is still worth thinking about. It sets two aims before us: first, Improving Natural Knowledge, and here I would quote Kant in a passage which Hilbert chose as an epitaph for Gauss: "All human knowledge begins with intuition, then passes to concepts, and ends with ideas". Second, Finding an Application which can be useful to society. I would hope that we can all agree on these two aims, and that we can demonstrate that at this Symposium: that we have found out something and that we can make ourselves useful, realising that nobody owes us a living.

Lichtenberg's proposition differs in a subtle way but nevertheless radically from the demands that are now made on many of us. Nowadays, we are expected to demonstrate the socio-political relevancy (die gesellschaftspolitische Relevanz) of our work before we even start it. Before we obtain any results, we are expected to demonstrate that they will lead to cost-effective products which can be sold in the market place at a profit. This makes no sense to me, and we can but hope that the Göttingen spirit of Lichtenberg will prevail in the end. On the other hand, I am confident that we shall be able to demonstrate at this Symposium that there are people with intuition working in fluid dynamics; that we can come up with new concepts and ideas; and that we can think of useful applications. Our subject already provides an excellent example: how improving our knowledge of flow separations in three dimensions led us to realise the constructive role that flow separation can play in the aerodynamic design of aircraft, which in turn led to the evolution of the design concept of slender wings. This is how we do our work.

To me, the Göttingen spirit means something which came from people who worked here in the 1920s and 30s, such as Felix Klein who brought David Hilbert here exactly one hundred years after Gauss and who inspired the marvellous growth of applied sciences here; Albert Betz, Max Born, Constantin Carathéodory, Richard Courant, Kurt Friedrichs, Werner Heisenberg, Gustav Herglotz, Erich von Holst, Pascual Jordan, Walther Nernst, Emmy Noether, Ludwig Prandtl, Carl Runge, Hermann Weyl. These people worked in the spirit and spread it generously. It proved to be a blessing for life to many who had the fortune to be here in those glorious days. They are deeply in debt to Göttingen and can never repay it. This spirit benefitted even those who only went to school here: the Headmaster of one of your schools was Walther Lietzmann who, as a student, led a successful delegation to dissuade Hilbert from leaving Göttingen for Berlin, and who later transformed the teaching of mathematics in schools; and

one of the science masters was Friedrich Seyfarth, the last personal assistant to Felix Klein. This spirit drew bright young men from all over the world to Göttingen, some of whom Hilbert called his Wunderkinder, and these include Patrick Blackett, Sidney Goldstein, Frederic Lanchester and Herbert Squire. This spirit went further than just mathematics and physics: people like Born or Heisenberg would sit down and play the piano part of Brahms's cello sonata by sight; and Runge's daughter, Nina Courant, was one of the first to revive an interest in learning to play the viola da gamba and thus encouraged others to do the same. If you want to know more about this, then read the book "Hilbert" by Constance Reid (Springer, 1970). There, on page 238, you will find a photograph taken on Hilbert's sixtieth birthday in January 1922, and you will see in the party Richard and Nina Courant, Peter Debye, James Franck, Edmund Landau, Leonard Nelson, Carl Runge, and also Theodore von Kármán and Ludwig Prandtl.

In Ludwig Prandtl the Göttingen spirit abounded. He was one of the engineers invited by Felix Klein to come here to foster the applied sciences. Typically, when he thought out the concept of boundary layers, he immediately went on to consider how this could be applied usefully, and concerned himself with the practical problem of flow separations. We shall hear more about him from Professor Schlichting and more about flow separations during our Symposium.

What does all this mean to us today and what can we do about it? We know that the Göttingen spirit was assaulted here in 1933 in the most brutal and destructive manner, yet it is not dead. It proved to be much stronger than the forces of destruction. These failed completely and ended in disaster; they are dead. But the spirit lives. We can still let ourselves be guided by it. We can apply ourselves as hard as we can in the search for knowledge in our beautiful field of fluid dynamics and then think about our findings enough to know how they hang together, and how they can be applied usefully. In the course of this, we must communicate what we find out to others, and this is what we are going to do this week. In this regard, I would again refer to Hilbert: it has been said that he could produce the most beautiful prose, "the style in the literary sense being the accurate image of the way of thinking". We cannot hope to reach the level of Hilbert or Prandtl in our work and in our communications, but we can at least aspire to reach a decent level so that we can earn our living honestly. Men like Prandtl have set us a standard to go by, and we can at least try to understand it and not rest content too far but to live up to it. I should also like to think that Von Kármán injected a good dose of the Göttingen spirit into AGARD and that this is still alive and will become apparent this week.

Thus I am optimistic, after all, and so our motto should be the words which are engraved on a stone over Hilbert's grave here at Göttingen:

Wir müssen wissen
Wir werden wissen
We must know. We shall know.

AN ACCOUNT OF THE SCIENTIFIC LIFE OF LUDWIG PRANDTL

by H. SCHLICHTING*)

Deutsche Forschungs- und Versuchsanstalt für Luft- und Raumfahrt e. V.
- Aerodynamische Versuchsanstalt Göttingen -

SUMMARY

This Lecture is presented on the occasion of the hundredth anniversary of LUDWIG PRANDTL's birth. It consists of the following three parts:

I) Highlights of PRANDTL's scientific work
II) PRANDTL as a university professor
III) PRANDTL as the head of a large research institute.

After an introduction on PRANDTL's professional career the following subjects accompanied by pictures showing some quantitative results will be dealt with in Part I: boundary layer theory, wing theory at subsonic and supersonic speeds, theory of stability of laminar flow. Furthermore, in this section the following problems will be touched on briefly: Fully developed turbulent flow with application to boundary layers, pipe flow and meteorology. PRANDTL's contributions to development of wind-tunnel techniques will also be mentioned.
In Part II some remarks will be made on the large number (about 80) of doctoral theses which have been supervised by PRANDTL in his capacity as Professor of Applied Mechanics at Goettingen University.
In Part III some remarks will be given on PRANDTL's work as Director of the Aerodynamische Versuchsanstalt Göttingen (AVA) founded in 1907 and of the Kaiser-Wilhelm-Institut für Strömungsforschung (now Max-Planck-Institut), founded in 1925.
At the end we give a few concluding remarks concerning the things that we all should learn from PRANDTL and transmit to future generations of research workers in the field of applied mechanics, and, particularly, of fluid mechanics.

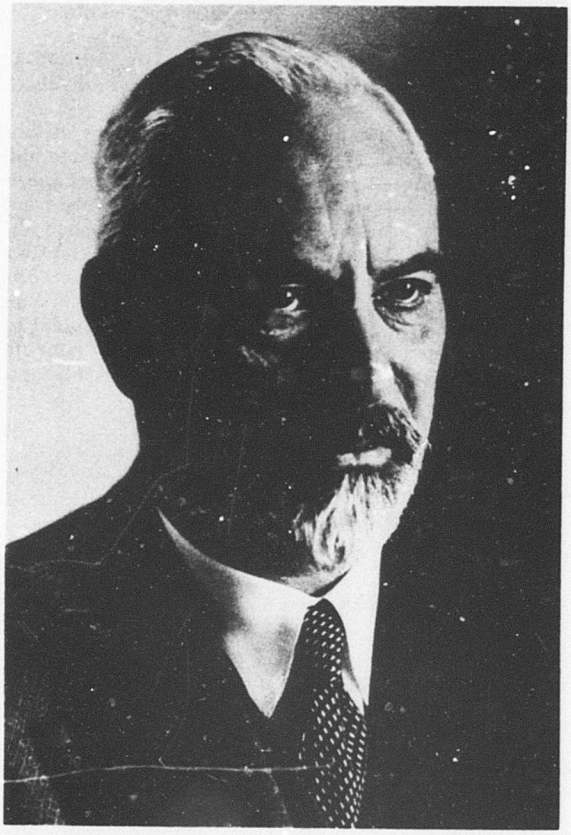

Fig. 1: LUDWIG PRANDTL'S PICTURE TAKEN AT THE AGE OF ABOUT 60

*) Professor, Technical University Braunschweig and Director, Aerodynamische Versuchsanstalt Goettingen.

1) INTRODUCTION

Mr. Chairman, Ladies and Gentlemen,

About one year ago, the Chairman of the Fluid Dynamics Panel asked me to deliver a survey lecture on PRANDTL's work during this year's AGARD Conference on FLOW SEPARATION. The conference has been organized here in Goettingen, Ludwig PRANDTL's work arena for many years on the occasion of the hundredth anniversary of his birth. I accepted this invitation very gladly and for a variety of reasons: In the first place, I feel myself personally very close to PRANDTL because since my student days, that is for almost fifty years, I have worked almost exclusively in the field of the new mechanics of fluids whose foundation was errected by him. Secondly, I believe that I have made some contributions to PRANDTL's heritage in that I have been directing for the last eighteen years the Aerodynamische Versuchsanstalt (AVA) errected by him in the year 1907 in Goettingen. Today this constitutes one of the five research establishments of the German Research Institute for Flight and Space Travel (Deutsche Forschungs- und Versuchsanstalt für Luft- und Raumfahrt, or DFVLR). Last, but not least, I should like to mention that of all members of the AGARD Fluid Dynamics Panel I am the only one, except for our Chairman, Dr. D. KÜCHEMANN, who worked directly under PRANDTL. This I did from 1928 until 1935.

I have organized my lecture under the following headings: After a few introductory remarks concerning the situation of the physics of fluid flow at the time when PRANDTL appeared on the scientific horizon that is at the beginning of this century, I shall present you with reports on

1. Some highlights of PRANDTL's scientific work
2. On PRANDTL's influence as a university professor, and, finally,
3. On PRANDTL's influence as the director of a large research establishment.

At the end, I shall make several remarks on the lessons, which we can learn from PRANDTL's endeavor. I shall illustrate my remarks with many pictures; these will, principally, relate to the first part which deals with PRANDTL's scientific work.

Figure 1 shows a picture of PRANDTL when he was about sixty years old.

Figure 2 reviews the most important dates in PRANDTL's long life. PRANDTL was born on the 4th of February 1875 in the town of Freising in Bavaria; he died on the 15th of August 1953 in Goettingen at the age of 79 years.
He came to Goettingen in the year 1904. Thus he spent almost 50 years of this life (1904-1953) in this city. In the year 1900, when PRANDTL was 25 years old, he was awarded his doctorate (Dr. Phil) at the University of Munich after having completed his studies at the Technical University of Munich under AUGUST FÖPPL; the latter earned him his engineer's degree (Dipl. -Ing.) in machine design. PRANDTL's thesis (1900) contained the solution of a problem of elasticity theory whose absence was then acutely felt in industry. This was the problem of buckling, that is of the lateral instability of a rod subjected to compressions. At first, PRANDTL's subsequent scientific papers were devoted to studies in the theory of elasticity. In the year 1901, after he had worked in industry at M.A.N. in Nuernberg for one year, that is at the age of 26 years, he was invited to join the Faculty of the Technical University at HANOVER as professor of Mechanics. He remained there until 1904. During that time he published the results of his studies on the stress distribution in a bar subjected to torsion; on this occasion he discovered the so-called soap-bubble analogy.

4 Febr. 1875:	Born in FREISING, Bavaria
1900:	Doctorate (Dr. Phil) at the University of MUNICH
1900 - 1901:	Engineer at M.A.N. in NUERNBERG
1901 - 1904:	Professor at Technical University in HANOVER
1904 - 1947:	Professor at University of GOETTINGEN
1907 - 1937:	Director, AERODYNAMISCHE VERSUCHSANSTALT (AVA)
1914:	Elected to the Academy of Sciences in GOETTINGEN
1925 - 1947:	Director, Kaiser-Wilhelm-Institut für Stroemungsforschung (Kaiser-Wilhelm-Institute for Fluid Mechanics)
1947:	Emeritus Professor at GOETTINGEN
15 Aug. 1953:	Died in GOETTINGEN

Fig. 2: PRANDTL's PROFESSIONAL CAREER 1875 - 1953

Along with these studies PRANDTL's attention was already then drawn to a problem in fluid mechanics which he first encountered when he worked for M. A. N. as a young engineer. He was there given the task of improving the design of an air duct for the removal of chips by suction. In a manner typical for his approach to problems, he first measured the energy losses which occurred in the individual elements of the duct. This allowed him to recognize that the largest losses connected with a conical portion which failed to produce the pressure recovery expected on the basis of BERNOULLI's equation. This problem prayed on his mind and led him to his boundary layer theory via the phenomenon of flow separation which, after all, constitutes the framework of our present AGARD Conference.

Allow me, therefore, to dwell a little longer on this topic. In this connection PRANDTL himself later made the following remark: "At that time I was called to the Technical University in Hanover from Nuernberg. As far as the firm itself was concerned, the elusive pressure recovery was of no great importance. However, I could not rid myself of the puzzle posed by the question as to why a stream separated from the wall instead of clinging to it. I did not clear up the conundrum until three years later when boundary layer theory provided the solution." The corresponding paper, read in 1904 at the International Congress of Mathematics, made PRANDTL famous at one stroke. At this point it is useful to recall the level of development attained by theoretical hydrodynamics at the beginning of this century:

The high degree of its completeness was reflected in the standard works by LAMB, LOVE, LORD RAYLEIGH, REYNOLDS, HELMHOLTZ and KIRCHHOFF. Work on EULER's equation for a frictionless fluid led to explicit mathematical solutions for certain characteristic body shapes exposed to an external stream. However, such solutions yielded acceptable agreement with experiment only in rare cases. The complete equations valid in the presence of viscous forces, the NAVIER-STOKES equations, were also well known. Nevertheless the great mathematical difficulties encountered in the solution of these equations led to no practical application of them in engineering. Above all, in the matter of the drag of a body placed in a stream there persisted the insurmountable discrepancy between the solution provided by theoretical hydrodynamics of a frictionsless fluid which yielded the value of zero for it (D'ALEMBERT's paradox), and experiment which showed that all bodies produced a larger or smaller, but finite, drag. As a result, engineering and technology, which were undergoing a period of vigorous development at the beginning of the century, were forced to rely on the purely empirical discipline of contemporary hydraulics when applications of fluid mechanics were required. The science of theoretical hydrodynamics as presented by mathematicians and the empiricism of the engineering discipline of hydraulics stood in glazing contradiction which seemed to be irreconcilable. This hopeless discrepancy between theoretical and experimental fluid mechanics was removed at one stroke by PRANDTL, when he demonstrated the existence of the phenomenon of a boundary layer. Boundary Layer Theory clearly explained how the very small internal friction of fluids-whether water or air - can exert a large effect through the thin boundary layer which develops at the solid surface of the body by sometimes causing it to separate and so to modify completely the velocity field around the body. PRANDTL substantiated his boundary layer theory with the aid of experiments in a small water channel (Fig. 3), which he built with his own hands. The consequences of this discovery are known and familiar to all engineers who work in fluid mechanics and in aeronautics.

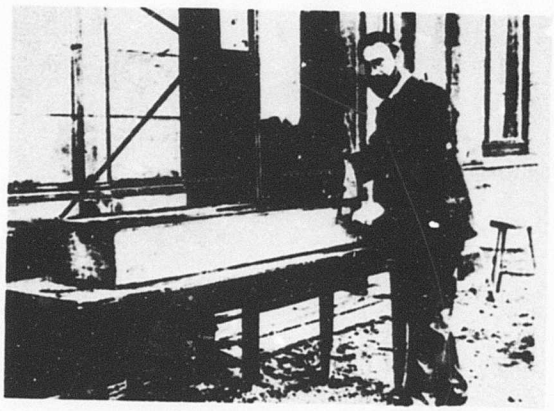

Fig. 3: LUDWIG PRANDTL INVESTIGATING BOUNDARY LAYERS, 1903

The young PRANDTL's achievements were soon recognized by FELIX KLEIN, the great organizer of the mathematical and applied sciences at the University of Goettingen. As a result of his initiative the university founded at the turn of the century several new institutes intended to serve the interests of the applied physical sciences. In 1904, at KLEIN's initiative, Ludwig PRANDTL took over the newly founded Institute for Technical Physics which later became the Institute for Applied Mechanics. Based on this institute and the chair of the same name connected with it, PRANDTL developed a most fruitful activity in research and instruction (education of young scientific cadres). I shall describe these [1, 2] in outline in the remaining part of my lecture. In doing so, it appears to me to be useful to bring to the fore the essentials of his researches rather than their chronology.

2) HIGHLIGHTS OF PRANDTL'S SCIENTIFIC WORK

I now propose to give you a quick review of some of the most important investigations performed by PRANDTL. In doing so, I wish to restrict myself exclusively to a consideration of PRANDTL's papers in the field of fluid mechanics, regardless of the fact that he made fundamental contributions to the other branches of mechanics (elasticity theory, plasticity). PRANDTL's work in the field of fluid mechanics will be reviewed under the following headings:

1) Boundary Layer Theory
2) Turbulent Flow
3) Origin of Turbulence (Stability Theory)
4) Boundary Layer Control
5) Wind Tunnels
6) Airfoil Theory
7) Compressible Flow
8) Meteorological Problems.

In discussing this vast area, I shall endeavor to be brief.

2.1 Boundary Layer Theory

Let me begin with PRANDTL's boundary layer theory mentioned earlier. This is the discipline in which he earned his early fame in the professional, scientific circles [3,4]. At the beginning of this century the view prevailed that it was hopeless to try to solve the NAVIER-STOKES equations for a viscous fluid, especially, as far as the problem of external flow about a body was concerned. For this reason PRANDTL searched for approximate solutions concerning the low-viscosity fluids, such as air and water, which are important in engineering applications. In the case of the two-dimensional steady flow problem involving incompressible flow about a body (Fig. 4), it is necessary to consider the following system of three partial, nonlinear differential equations for the components u and v of the velocity and for the pressure p:

$$\frac{\partial u}{\partial x} + \frac{\partial v}{\partial y} = 0 \tag{1}$$

$$u\frac{\partial u}{\partial x} + v\frac{\partial u}{\partial y} = -\frac{1}{\rho}\frac{\partial p}{\partial x} + \nu\left(\frac{\partial^2 u}{\partial x^2} + \frac{\partial^2 u}{\partial y^2}\right) \tag{2}$$

$$u\frac{\partial v}{\partial x} + v\frac{\partial v}{\partial y} = -\frac{1}{\rho}\frac{\partial p}{\partial y} + \nu\left(\frac{\partial^2 v}{\partial x^2} + \frac{\partial^2 v}{\partial y^2}\right) \tag{3}$$

The boundary conditions are:

$$\left.\begin{aligned} &y = 0 : u = v = 0 \quad \text{(absence of slip at wall)} \\ &y = \infty : u = U_\infty \longrightarrow U(x) \end{aligned}\right\} \tag{4}$$

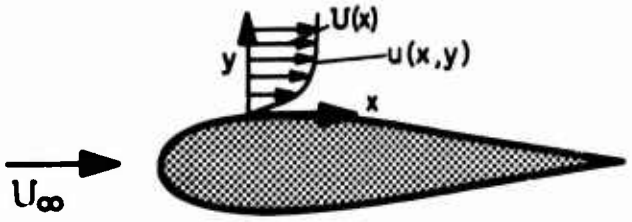

Fig. 4: REDUCTION OF THE NAVIER-STOKES EQUATIONS TO OBTAIN THE BOUNDARY LAYER EQUATIONS, PRANDTL 1904

This is a system of three nonlinear partial differential equations for the unknown functions u, v and p of the position coordinates x and y. Since this system of equations proved to be insoluble even for simple body shapes owing to the attendant mathematical difficulties, PRANDTL sought an approximate solution, which exploited the physical simplifications resulting from the small viscosity. These reduced the mathematical difficulties to such an extent that the simplified system of equations could be solved with the aid of the then existing methods. Thus he was led to the so-called boundary layer equations in which in equation (2) the indicated term was stricken and equation (3) was dropped altogether. From a physical point of view, the simplification consists in the following: PRANDTL divided the complete flow field into two regions; first he considered the thin boundary layer developed very close to the solid wall in which the frictional forces are as important as the inertia forces; secondly, he introduced the external region in which the flow is practically frictionless.
Mathematically speaking, this leads to the following:

The continuity equation (1) remains unaltered. In the equation for momentum conservation in the x-direction, only the larger of the two viscous terms is retained, whereas equation (3) of conservation of y-momentum is completely disregarded. The latter is equivalent to the statement that the fluid particles have zero mass as far as their motion in the direction normal to the wall is concerned. Since the number of equations is reduced from three to two, it is necessary similarly to reduce the number of unknown functions.
This is achieved in that in the reduced system of equations, the pressure $p(x,y)$ ceases to be unknown. Even more, the pressure distribution can be, so to say, determined beforehand from the frictionless external flow $U(x)$; it plays the part of a known force $p(x)$, which is "impressed" on the boundary layer. It is clear that the preceding simplifications (omissions) are "onerous", as far as the equations of motion are concerned. The fact that such "mutilated" equations can, in spite of all this, lead to results which are useful in practice, must be ascribed to PRANDTL's intuitive genius and ability to grasp the essence of physical reality.
What has just been said constitutes the foundation of PRANDTL's boundary layer theory of 1904. For this reason I may be permitted to develop it in a little more detail on the example of a flat plate at zero incidence (Fig. 5). The equations for the flat plate assume the form:

$$\left.\begin{aligned} &\frac{\partial u}{\partial x} + \frac{\partial v}{\partial y} = 0 \\ &u\frac{\partial u}{\partial x} + v\frac{\partial u}{\partial y} = \nu\frac{\partial^2 u}{\partial y^2} \\ &y = 0 : u = v = 0 \quad ; \\ &y = \infty : u = U_\infty \end{aligned}\right\} \qquad (5)$$

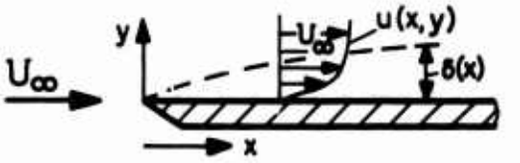

Fig. 5: LAMINAR BOUNDARY LAYER ON FLAT PLATE
PRANDTL 1904 - BLASIUS 1908

The first hint on how to solve these equations was given by PRANDTL himself in his original paper [3] of 1904; the explicit solution was successfully achieved in the 1907 thesis of H. BLASIUS [5].
Here are the most important results:

It is easy to show that the boundary layer thickness, δ, depends on the dimensional variables via the group:

$$\delta \sim \sqrt{\frac{\nu x}{U_\infty}} \quad . \qquad (6)$$

By applying the similarity transformation $\eta \sim y/\delta$, or

$$\eta = y\sqrt{\frac{U_\infty}{\nu x}} \quad , \qquad (7)$$

it becomes possible to reduce the solution of both partial differential equations to the solution of a single ordinary differential equation for the stream function

$$\psi(x,y) = \sqrt{\nu \, x \, U_\infty} \cdot f(\eta) \quad . \tag{8}$$

In this manner we are led to BLASIUS' s differential equation

$$f \cdot f'' + 2 f''' = 0 \tag{9}$$

which is of the third order and which has to satisfy the boundary conditions

$$\eta = 0 : f = f' = 0 ; \quad \eta = \infty : f' = 1 \quad . \tag{10}$$

As the most important result we can now calculate the shearing stress at the wall at position x . We obtain

$$\tau_o(x) = \mu \left(\frac{\partial u}{\partial y}\right)_{y=0} = f''(0) \, \mu \, U_\infty \sqrt{U_\infty / \nu \, x}$$

with $f''(0) = 0,322$.

This leads to the expression for the local skin friction coefficient

$$\frac{\tau_o}{\rho \, U_\infty^2/2} = c_f' = \frac{0,664}{\sqrt{Re_x}} \tag{11}$$

and for the skin friction coefficient of whole plate

$$\frac{D}{F \cdot \rho \, U_\infty^2/2} = c_f = \frac{1,328}{\sqrt{Re_l}} \qquad \text{(BLASIUS, 1907)} \tag{11a}$$

with $Re_x = U_\infty x/\nu$ and $Re_l = U_\infty l/\nu$ and F being the wetted surface of the plate.

Figure 6 compares the former result with measurements; agreement is excellent in the Reynolds-number range $Re_x = 6 \cdot 10^4$ to $6 \cdot 10^5$ over which the boundary layer remains laminar.

Finally Figure 7 compares the theoretical result for the velocity $u/U_\infty = f'(\eta)$ with measurements. These very carefully executed measurements of the velocity distribution in the laminar boundary layer on a flat plate were performed by J. NIKURADSE [6] as late as in the mid-thirties. They confirm in exquisite fashion, first, the existence of similarity of velocity profiles at various distances, x , along the plate demanded by the theory in that they all collapse into a single curve. Beyond that, the actual form of the velocity distribution shows complete agreement between theory and experiment.

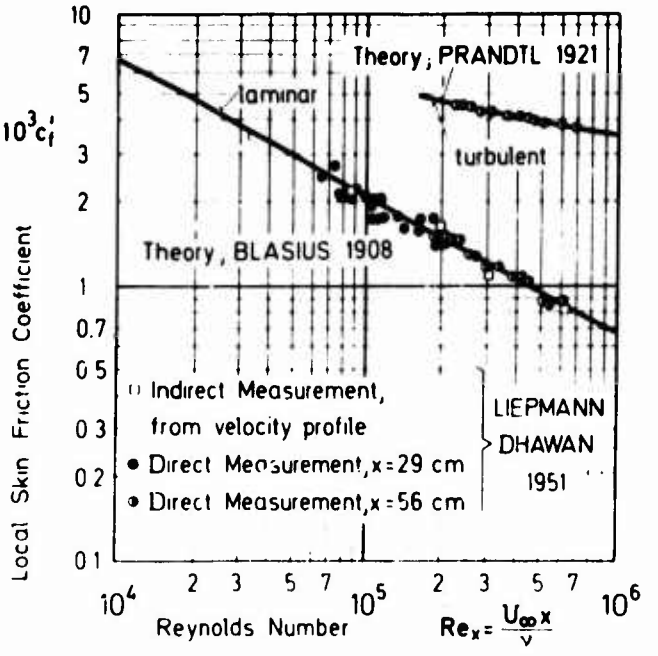

Fig. 6: LAMINAR BOUNDARY LAYER ON FLAT PLATE: LOCAL COEFFICIENT OF SKIN FRICTION

After the achievement of this brilliant confirmation of theory by experiment, it was possible to accept the complete validity of boundary layer theory for laminar flows. The application of boundary layer theory to turbulent flows will be discussed later in this lecture.

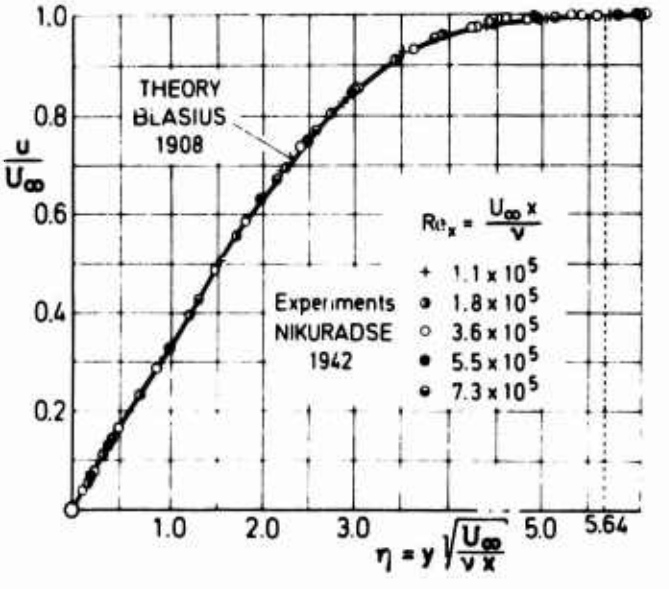

Fig. 7: LAMINAR BOUNDARY LAYER ON FLAT PLATE: VELOCITY PROFILES

2.2 Turbulent flows

Sphere: It was known since Reynolds's time [7] that there existed two fundamentally different flow regimes in pipes-laminar and turbulent. The existence of these two flow regimes in boundary layers was discovered by PRANDTL when EIFFEL [8] published in 1912 his measurements on the drag of spheres which showed large and unexplained mutual deviations. As soon as this became known, PRANDTL charged C. WIESELSBERGER [9a] with the task of remeasuring the drag of spheres in the new wind-tunnel constructed in Goettingen a couple of years earlier. The results of such measurements are represented in Figure 8, which shows the flow pattern made visible with the aid of smoke as well as the plot of drag against the Reynolds number. PRANDTL discovered that the large differences observed in the drag coefficient of spheres can be explained, if it is recognized that the flow in the boundary layer can be either laminar or turbulent. When the flow is laminar, the line of separation places itself far upstream and produces a wide wake thus causing the drag to become large. When the flow becomes turbulent, the separation line moves far downstream.

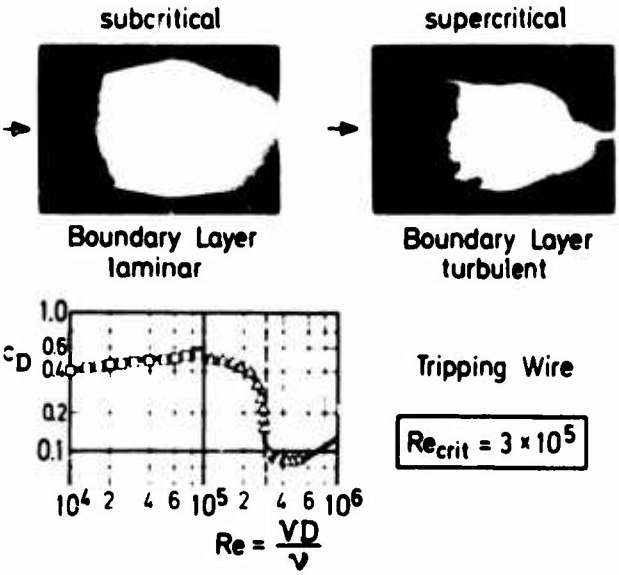

Fig. 8: DRAG COEFFICIENT OF SPHERES AGAINST REYNOLDS NUMBER; PRANDTL 1914

This results in a much narrower wake and a drag which is smaller than that associated with laminar flow. It is in this connection that PRANDTL discovered experimentally the existence of a critical Reynolds number for the boundary layer. The crucial experiment for the clarification of the early results on spheres and for the discovery of the two flow regimes involved the use of a tripping wire. This put on the scientific map the problem of turbulence which occupied Ludwig PRANDTL during the whole of his life. But many years were to pass before a satisfactory theory for it could be created in PRANDTL's institute.

Smooth pipe: Several years later, after the First World War, that is about 1920, PRANDTL reverted to the problem of developed turbulent flows in connection with his study of pipe flow. An analysis of the measurements known at that time led him to the conclusion that the empirical law for turbulent flow in a pipe employed at that time needed to be corrected at high Reynolds numbers. This law asserted that the coefficient of resistance is:

$$\lambda = \frac{0,316}{\sqrt[4]{Re}} \quad , \qquad \text{(BLASIUS, 1913)} \qquad (12)$$

where $Re = \bar{u}d/\nu$, so that the pressure drop was proportional to the 7/4th power of the mean velocity [10]. In the course of this investigation he found that the resistance approaches the quadratic law more and more closely as the Reynolds number is increased. Starting with the very careful measurements of his co-worker J. NIKURADSE [12] and aided by some theoretical considerations, PRANDTL [11] succeeded in deriving the so-called asymptotic resistance law

$$\frac{1}{\sqrt{\lambda}} = 2,0 \log (Re\sqrt{\lambda}) - 0,8 \qquad \text{(PRANDTL, 1933)} \qquad (13)$$

for smooth pipes. Figure 9 compares the two laws one with the other and with the measurements of many authors; the agreement with PRANDTL's law is excellent. In the course of performing these now classical investigations it was possible to discover the relation between the law of friction and the velocity distribution. BLASIUS' s law in equation (12) implies a 1/7 th power in the velocity distribution of the form

$$\frac{u}{U} = \left(\frac{y}{R}\right)^{1/7} \quad , \qquad \text{(PRANDTL, 1921)} \qquad (14)$$

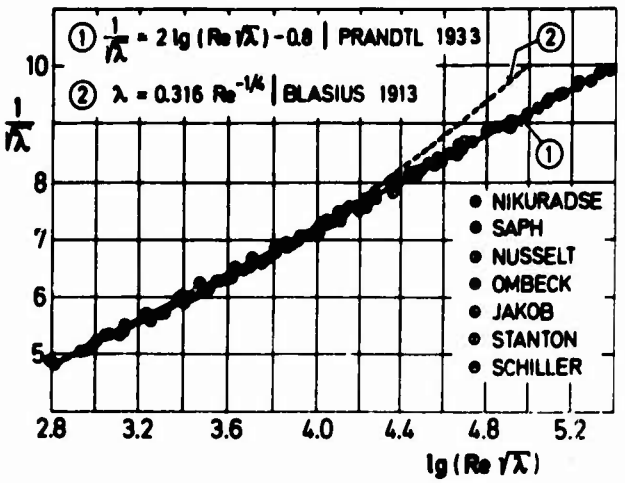

Fig. 9: UNIVERSAL LAW OF DRAG FOR A SMOOTH PIPE IN TURBULENT FLOW; PRANDTL 1932

where u denotes the local and U the maximum velocity, while y is the distance from the wall and R the pipe radius. The diagram in Fig. 10 represents this law of velocity distribution as well as the universal law

$$\frac{u}{v_*} = 5,75 \log \frac{y v_*}{\nu} + 5,5 \quad , \qquad \text{(PRANDTL, 1933)} \qquad (15)$$

where $v_* = \sqrt{\tau_o/\varrho}$ is the friction velocity, based on the shearing stress, τ_o, at the wall. The so-called laminar sublayer played an important role in the derivation which led to this equation. This is the very thin velocity layer adjacent to the wall which always remains laminar, even though the layer may become turbulent at a larger distance. In this layer we have $\varphi = \eta$ with $\eta = y\, v_*/\nu$ and $\varphi = u/v_*$.

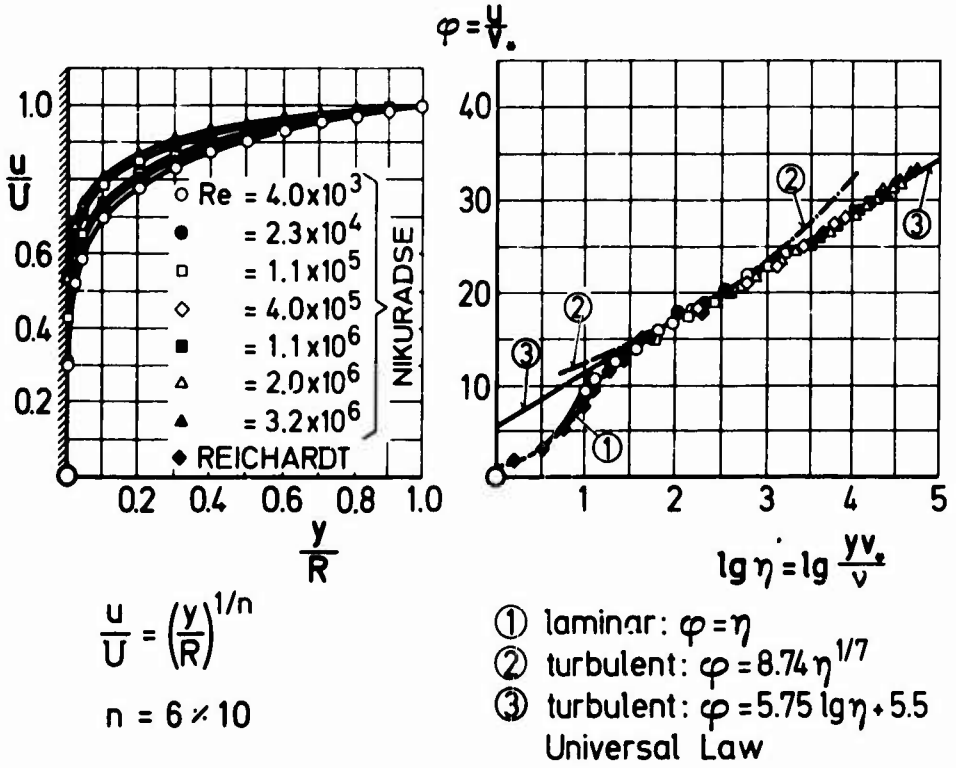

Fig. 10: UNIVERSAL LAW OF VELOCITY DISTRIBUTION IN A SMOOTH PIPE ; PRANDTL 1932

Rough pipe: A knowledge of the resistance of rough pipes is even more important in engineering applications than that of smooth pipes. Recognizing that it is very difficult geometrically to characterize the roughnesses that occur in practice, PRANDTL introduced the concept of a "normal roughness", that is the roughness which is produced by sand of equal grain size, k_s, and closest packing in the pipe. J. NIKURADSE [13] succeeded in obtaining very clear experiments for this case. The diagram in Fig. 11 displays the resistance law for rough pipes obtained in this way. In this case the resistance coefficient, λ, depends on the relative roughness, k_s/R, in addition to the normal dependence on the Reynolds number, $Re = \bar{u}d/\nu$. From the point of view of practical application it is important to determine the limiting or "admissible" value, k_{zul}, of roughness which produces no increase in resistance compared with that of a smooth pipe. This satisfies the relation

$$\left(\frac{k_{zul}U}{\nu}\right) = 100 \quad . \tag{16}$$

When this is the case the roughness element is completely immersed in the laminar sublayer whose thickness is of the order ν/v_*. These results, obtained by PRANDTL and his co-workers in the thirties, can be regarded as in a sense definitive for the understanding of the problem of flow in a pipe which is so immensely important in engineering.

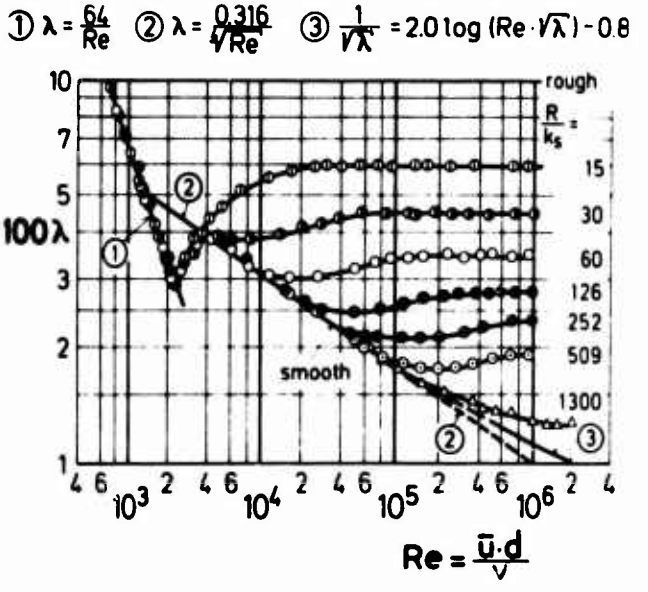

Fig. 11: LOSS COEFFICIENTS FOR ROUGH PIPES; NIKURADSE 1933

Flat Plate: An understanding of the skin friction of a flat plate at zero incidence (determined theoretically for laminar flow by BLASIUS in 1907, see equation (11a) and Figure 7) and at very large values of the Reynolds number which occur in turbulent flow, is of paramount importance for the calculation of the drag of ships, wings and airplane fuselages. As early as 1921, PRANDTL indicated a method, based on the use of the momentum integral theorem, which allowed him to extend the results obtained for pipes to the case of the plate [14]. In the case of a flat plate at moderately large Reynolds numbers, $Re_x = 10^6$ to 10^7, he obtained the equation

$$c_f = \frac{0,074}{\sqrt[5]{Re}} \quad , \quad Re < 10^7 \qquad \text{(PRANDTL, 1921)} \tag{17}$$

with $Re = Vl/\nu$, for the corresponding skin friction of a flat plate. This law is represented in Fig. 12. The extension from the pipe to the plate was successful in this case on the assumption that the velocity profiles along the plate were similar, and on the supposition that the pipe radius corresponded to the boundary layer thickness, the external velocity of the boundary layer being analogous to that in the center of the pipe. In the case of very large Reynolds numbers, that is in the case when the universal resistance law of equation (13) and the universal velocity distribution law from equation (15) become valid, the transposition from pipe to plate becomes considerably more tedious.

The derivation leads to the universal skin friction law for a flat plate [14].

$$c_f = \frac{0,455}{(\log Re)^{2,58}} \quad , \quad Re > 10^7 \quad \text{(PRANDTL, SCHLICHTING, 1932)} \qquad (18)$$

which is also plotted in Fig. 12.

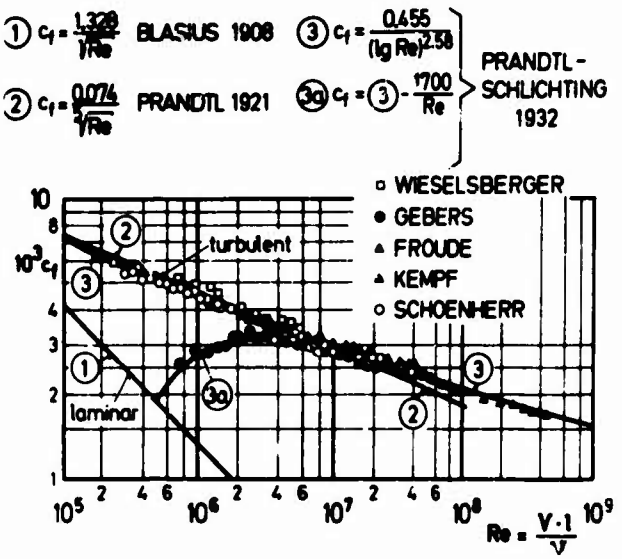

Fig. 12: SKIN FRICTION ON SMOOTH PLATES

The validity of this universal skin friction law extends to Reynolds numbers Re = 10^9 to 10^{10}, that is into the range which is encountered nowadays in the design of ships. The resistance law for rough pipes could also be extended to include rough plates [15]; the latter is seen plotted in Fig. 13. The "relative roughness" is now measured by the ratio k_s/l, that is the ratio of roughness element height to plate length. The limiting, or admissible, height of roughness element satisfies the same equation (16) as does that for a pipe.

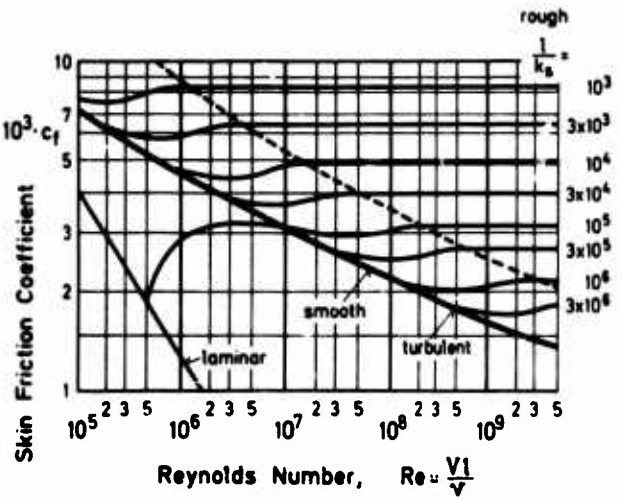

Fig. 13: SKIN FRICTION ON ROUGH PLATES; PRANDTL-SCHLICHTING 1932

Free turbulence: Already REYNOLDS was aware of the fact that the velocity fluctuations u' and v', which are superimposed on the mean velocity components $\bar{u}$, $\bar{v}$, give rise to large mixing motions and, consequently, to considerable "apparent stresses".
The expression

$$\tau_{turb} = -\rho \overline{u'v'} \qquad \text{(REYNOLDS)} \qquad (19)$$

for the "apparent" or Reynolds stress was first indicated by REYNOLDS himself. It is to PRANDTL's credit that he was the first one to make it possible, to calculate developed turbulent flows in that he formulated his "mixing length" theory [16]. The occurrence of strikingly large "apparent stresses" of turbulent flow which are produced inside the fluid as a result of the exchange of momentum between neighbouring regions of different velocities is explained by him intuitively through the introduction of a "mixing length", measured at right angles to the flow, and characterizing the turbulent mixing motion (Fig. 14). Assuming the existence of fluid lumps whose mean velocity is u, PRANDTL assumes that the mean velocity fluctuation in the longitudinal direction is

$$u' = l \frac{du}{dy} \quad . \tag{20}$$

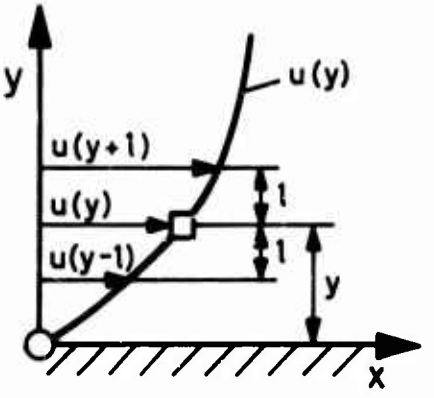

Fig. 14: THEORY OF MIXING LENGTH; PRANDTL 1926

It follows from this representation that the velocity fluctuation in the transverse direction must also be given by

$$v' = l \frac{du}{dy} \quad . \tag{21}$$

With this assumption the shearing stress from equation (19) becomes

$$\tau_{turb} = \rho l^2 \left(\frac{du}{dy}\right)^2 , \qquad \text{(PRANDTL, 1926)} \quad . \tag{22}$$

In subsequent times PRANDTL's students and many other authors solved a large number of special cases of practical importance on the basis of this fundamentally new representation. In the case of the pipe flow, PRANDTL himself made the simple assumption

$$l = \kappa y \tag{23}$$

for the mixing length. Here y denotes the distance from the wall, and $\kappa = 0,4$ according to experiment. This hypotheses led to the derivation of the universal logarithmic velocity - distribution for pipes as given in equation (15). Introducing other hypotheses for the mixing length, W. TOLLMIEN [17] solved the problem of the spreading of a jet, whereas H. SCHLICHTING [18] solved the problem of a two-dimensional wake behind a body in an external stream. Good agreement with experiments was achieved.
I may be interesting to mention that PRANDTL presented his semi-empirical theory of the mixing length at the Second International Congress of Applied Mechanics in Zurich in 1926. Now, half a century later, none of the many "theories of turbulence", conceived by other authors, especially the statistical theory of turbulence, succeeded in replacing it by something substantially superior with regard to the calculation of turbulent flows.

2.3 Origin of Turbulence (Stability Theory)

In addition to his excessive theoretical and experimental studies on the problems of developed turbulence, PRANDTL occupied himself uninterruptedly in the twenties with the problem of the origin of turbulence. This problem had earlier, that is in the eighties of the preceding century, troubled REYNOLDS, after he had obtained his fundamental experimental results. The hypothesis that the appearance of turbulence is the result of an instability developed by the laminar motion can be traced to REYNOLDS (REYNOLDS' s hypothesis). Nevertheless, almost half a century was needed to demonstrate theoretically the truth of this hypothesis and a further twenty years or so elapsed before an experimental verification for this theory was produced. In the course of their theoretical investigations following the formulation of REYNOLDS' s hypothesis the mathematicians active in this field during the first decade of this century derived the ORR SOMMERFELD equation [19, 20] in the framework of a linear theory. They tried to demonstrate the existence of unstable laminar flows by seeking solutions of this equation (Fig. 15). The equation has the form

$$(U-c)\,(\varphi'' - \alpha^2\varphi) - U''\varphi = -\frac{i}{\alpha \mathrm{Re}}\,(\varphi'''' - 2\alpha^2\varphi'' + \alpha^4\varphi) \quad \text{(ORR-SOMMERFELD 1908)} \quad (24)^{*)}$$

where $\mathrm{Re} = U_m \delta/\nu$.

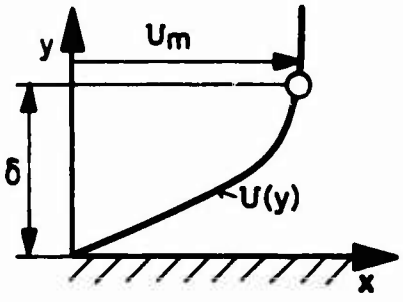

Fig. 15: STABILITY THEORY OF LAMINAR FLOW

The boundary conditions for a boundary layer of thickness δ are

$$y = 0 : \varphi = \varphi' = 0 \; ; \quad y = \delta : \varphi = \varphi' = 0 \qquad (24a)$$

In this homogeneous differential equation U(y) denotes the base flow whose stability is being investigated, $\varphi(y)$ is the amplitude of the disturbance superimposed on it; it is described by the stream function

$$\psi(x, y, t) = \varphi(y)\, e^{i(\alpha x - \beta t)}$$

and represents a wave propagated in the x-direction. The parameter α is a real number, and $\lambda = 2\pi/\alpha$ is the wavelength of the disturbance, whereas $\beta = \beta_r + i\,\beta_i$ represents the circular frequency (real part $-\beta_r$) and the amplification or attenuation factor (imaginary part - β_i).

Whether the motion is amplified or damped depends on the sign, $\beta_i > 0$ signifying amplification, that is instability.

---

*) The dash denotes differentiation with respect to y/δ ; U_m is the velocity at the edge of the boundary layer, $y = \delta$.

The stability analysis of a laminar flow with the aid of equations (24) and (24a) constitutes a very difficult eigenvalue problem for this differential equation. It must be understood that the wavelength, α, and the Reynolds number, Re, are given quantities and that the eigenvalue $\beta = \beta_r + \beta_i$ is the unknown. The efforts of the mathematicians to solve this equation were unsuccessful for a long time. In other words, nobody succeeded to discover unstable disturbances for a given flow U(y) and so to calculate a critical Reynolds number.

When PRANDTL started to work on the problem of transition to turbulence in 1920, he at first showed a certain amount of skepticism with respect to the contemporary considerations of the mathematicians. He started to perform experiments in a six meters long open chanel of rectangular cross section and obtained in it informative pictures illustrating the emergence of vortices. However, these, by themselves, brought no decisive clarification. Thus he induced his students to attack the problem of "instability in boundary layers" with the aid of his own mathematical methods. In doing so he thought that he could take into account his own observations when he provided interpretations for the results of mathematical derivations. At first he discovered that the shape of the velocity profile, U(y), formed on a wall exerts a great influence on the stability of the corresponding laminar boundary layer. However, a theory developed by O. TIETJENS [22] proved to be inadequate for the calculation of a critical Reynolds number to characterize the instability of the boundary layer on a flat plate. It was left to PRANDTL's collaborator W. TOLLMIEN [23] to discover the decisive breakthrough that led to the solution of this problem in the year 1929. TOLLMIEN was able, for the first time, to calculate theoretically a critical Reynolds number for the boundary layer on a flat plate at zero incidence. In the years to follow, H. SCHLICHTING extended the theory in several papers [24, 25] and proved that the critical Reynolds number depended strongly, among others, on the pressure gradient along the wall. In spite of the fact that Ludwig PRANDTL subscribed to the opinion that this problem had now found its complete clarification, it is strange to report that these theoretical results were not for a long time completely accepted by the specialists working outside Germany. Moreover, fourteen years were to elapse until the careful measurements performed by H. L. DRYDEN and his colleagues at the US National Bureau of Standards fully confirmed this theory in the year 1943. The diagram in Fig. 16 presents a comparison between TOLLMIEN's theory and the measurements performed by SCHUBAUER and SCRAMSTAD [26]. All points which represent measured neutral oscillations in a boundary layer on a flat plate position themselves very closely to the theoretical instability curve.

Both, PRANDTL and his collaborators had lost doubts about the theory a long time before. During the Second World War, that is before the time when DRYDEN's confirmation of the theory became known in Germany, the theory, in the form of SCHLICHTING's applications to flows with arbitrary pressure distributions, led to important insights concerning the influence of pressure gradients on the stability of laminar boundary layers and on transition from laminar to turbulent flow. Finally in the forties, this theory was responsible for the success in the development of laminar airfoils.

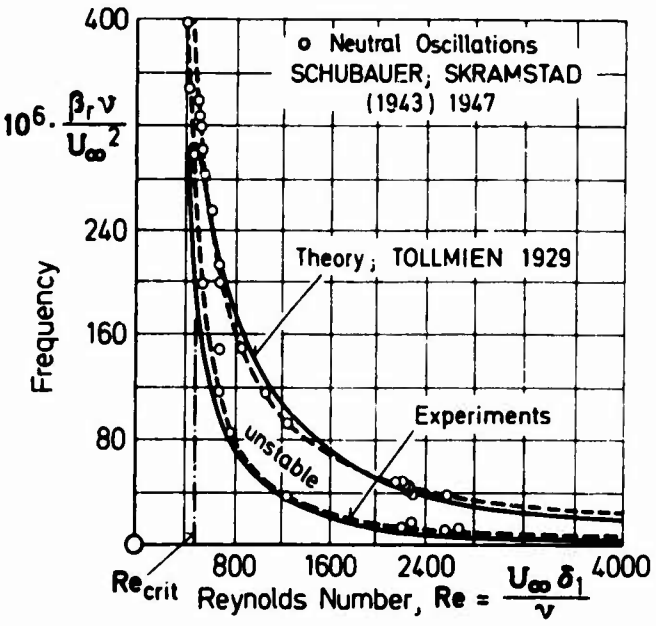

Fig. 16: STABILITY OF LAMINAR BOUNDARY LAYER ON FLAT PLATE

2.4 Boundary-layer control

It is remarkable that the flow in a boundary layer can be very easily influenced in a desired direction by external actions. This can be done, for example, by the blowing of small quantities of fluid at the wetted wall or through the imposition of a suitable pressure distribution. The first experimental result concerning this class of problems was given by PRANDTL in his first paper on boundary layers published in 1904. This illustrated the elimination of separation by suction in the wake of a cylinder.

In the later years there developed a rich literature concerning this set of problems. A comprehensive summary of these endeavors was given in 1961 by G. V. LACHMANN [27] , a former student of PRANDTL's. In this lecture I wish to mention only two results which are illustrated with the aid of Figure 17. The pictures in the left half of this figure illustrate the effect created by suction through slits in a fast diverging channel. Without suction the flow separates completely from both walls. When suction is applied on both walls, there is no separation at all; moreover, the fluid adheres to the two walls in the manner of a frictionless potential flow.

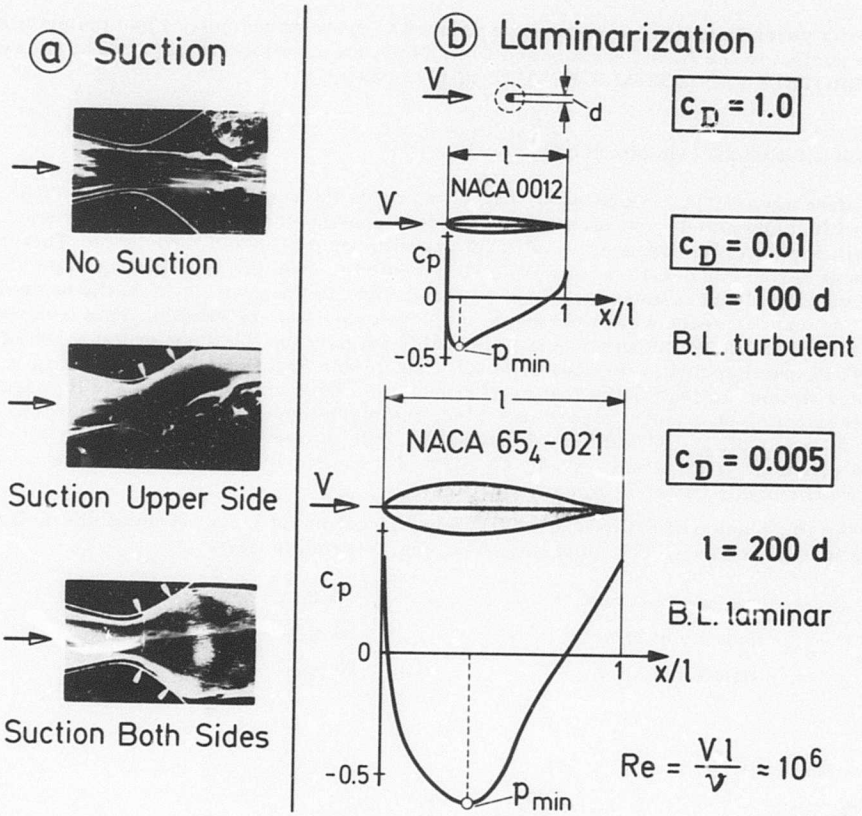

Fig. 17: BOUNDARY LAYER CONTROL

The right-hand side of the same figure illustrates the effect of streamlining (i. e. properly shaping) a body on its drag: the three cylindrical bodies, namely the circular cylinder, the normal airfoil and the laminar airfoil are drawn in such relative sizes that they develop the same drag in streams of equal velocities. The difference between the cylinder with its completely separated boundary layer and the normal airfoil which develops no separation is very large as is well known; equally remarkable is the decrease in drag obtained by a laminar airfoil in comparison with the normal airfoil. The latter is explained by the laminarization of the boundary layer. According to stability theory this effect is achieved by displacing the pressure minimum in the downstream direction as a result of displacing the maximum airfoil thickness in the same direction. In both examples, chanel and airfoil, the effect of modifying the boundary layer is very large.

As I reach the end of my remarks about PRANDTL's work on boundary layers and turbulent flows, I cannot help but recall that it took then a comparatively long time for his ideas to become generally accepted. This circumstance was aptly underlined in 1954 by H. L. DRYDEN on the occasion of the fiftieth anniversary of boundary layer theory by his statement:

The development of BOUNDARY LAYER THEORY during its first fifty years is a fascinating illustration of

- 1) the birth of a new concept,
- 2) its slow growth for many years in the hands of its creator and his associates,
- 3) its belated acceptance by others,
- 4) and the later almost exponential rise in the number of contributors to its further development.

In the last twenty years boundary layer theory continued to grow extensively. I had the privilege to report on this subject to the Heat Transfer and Fluid Mechanics Institute in 1970 [28] , as well as in the WRIGHT BROTHERS MEMORIAL LECTURE of 1973 [29] .

2.5 Experimental technique (wind-tunnels)

A short time after his arrival in Goettingen, namely towards the end of the year 1906, PRANDTL's thoughts turned in a completely new direction. This development was to prove as important for his scientific attainments as his efforts on behalf of flows with separation and turbulence. This was the dawn of the new era of aeronautics. OTTO LILIENTHAL executed in 1896 the first gliding flight. In the United States the brothers WRIGHT achieved the first powered flight in the year 1903. At the beginning of the 20th century German engineers were working on the development of the airship. This task was supported by the MOTOR LUFTSCHIFF STUDIENGESELLSCHAFT (Society for the Study of Research of Airships). Ludwig PRANDTL participated in this development - again with FELIX KLEIN's encouragement - in that he designed an installation for the testing of models in a wind tunnel. This made it possible to determine wind forces acting on a model placed in a wind, the model being at rest with respect to the earth. This wind tunnel was built in 1907 and commissioned in 1908; it operated in competition with another type of wind tunnel constructed simultaneously by G. EIFFEL in Paris and became so successful that other wind tunnels were modelled after it in many countries.

Fig. 18 gives an impression of PRANDTL's first wind-tunnel of 1908; its essential characteristic is that air circulates in a closed duct. The most important characteristics were:

Working section:	2 x 2 m^2
maximum speed:	10 m/s = 36 km/h
power installed:	30 hp.

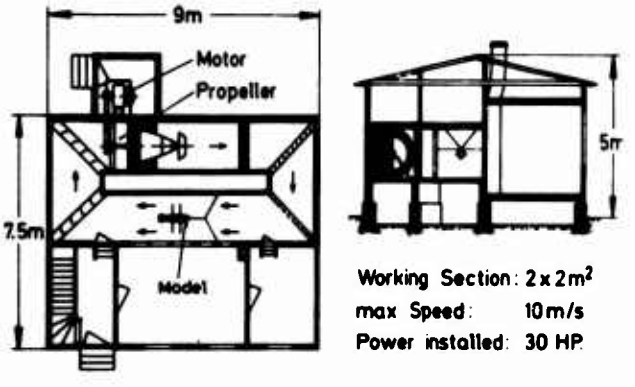

Fig. 18: THE FIRST GOETTINGEN WIND TUNNEL, PRANDTL 1908

This first Goettingen wind tunnel had a closed working section of a relatively large cross section, but the wind velocity was small. The second wind tunnel, built in 1917 was already equipped with a nozzle of large contraction ratio; it also had a closed circuit for the movement of the air, but its working section was open and consisted of a free jet (Fig. 19). The open working section is considerably more convenient for measurements than a closed section owing to the accessibility of the model. The most important characteristics of the second Goettingen tunnel were

Working section:	4 m^2 (D = 2, 25 m)
maximum speed:	50 m/s = 180 km/h
power installed:	400 hp.

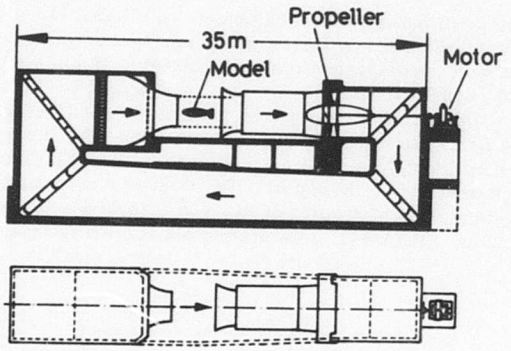

Fig. 19: THE SECOND GOETTINGEN WIND TUNNEL PRANDTL-BETZ, 1917

Working Section: $4\,m^2$ (D = 2.25 m)

max. Speed: 50 m/s

Power installed: 400 HP

This type of wind tunnel (the so-called Goettingen type), conceived by PRANDTL, soon became one of the most important experimental aids for the performance of all manner of experiments on bodies in flow. This tunnel exerted in all countries a large influence on the development of the science of aerodynamics and on the art of aeronautical engineering. During the initial years of the commissioning of the first wind tunnel in 1908, the bulk of the work was performed on airship models. Fig. 20 shows the model of such an airship investigated by G. FUHRMANN. Close by there is a circular disk of a magnitude which produces an identical drag when exposed to a stream at right angles to its plane as does the airship model in axial flow. Soon the wind tunnel was being used for experiments on propellers as well as on flat and curved plates, on airfoils and on lifting surfaces. These experiments delineated the field of endeavor of the new model-testing establishment (Aerodynamische Versuchsanstalt), which proved to be essentially fruitful from the scientific point of view. In the field of engineering this new establishment became the foundation on which the age of flying could be based. I shall have more to say on this topic in the next section.

In this connection I wish to mention that PRANDTL succeeded in persuading ALBERT BETZ to become his collaborator in the year 1911. BETZ played a decisive role in the further development of the experimental installations.

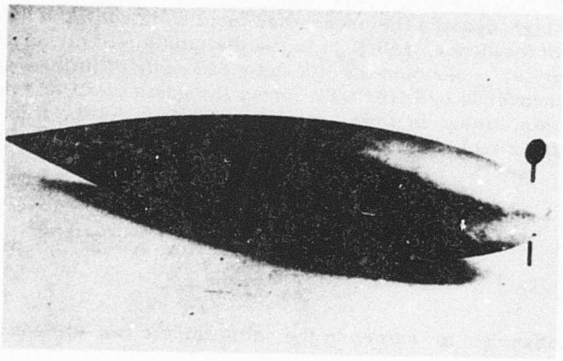

Fig. 20: AIRSHIP MODEL AND DISK OF EQUAL DRAG, FUHRMANN 1910

2.6 Wing theory

As a result of his work in the field of the aerodynamics of wings undertaken during the first decade of this century PRANDTL found himself in competition with F. W. LANCHESTER of England. Both endeavored, at first independently of each other, to determine the effect of finite span of a wing on its aerodynamic properties. In close relation with this problem, they attempted to explain the so-called induced drag created around the edges of the wing. CARL RUNGE, the other important mathematician of Goettingen, deserves to be given credit for having brought together in Goettingen the two aerodynamicists - PRANDTL and LANCHESTER - for a scientific discussion. It was also on RUNGE's initiative that LANCHESTER's book concerning the aerodynamics of flight was translated from the English into the German language [30].

The continuous efforts expended by PRANDTL to understand the observed characteristics of flows, to describe them, as far as possible, theoretically and numerically, and to explore them by the scientific method, characterized all publications which appeared during these pioneering times. In the years 1918 and 1919 PRANDTL submitted two papers to the Goettingen Academy of Sciences [31] on the discoveries concerning wing theory which he made until there. This publication contained PRANDTL's theory of the lifting line for a wing of finite span, the theory of the multiplane, the theory of the wing of minimum induced drag, as well as many other contributions. This is an achievement of the same rank as his boundary layer theory of 1904. I shall now report on a few of the most important - from the practical point of view - results of his work: In order to describe the distribution of lift along the finite span of a wing, PRANDTL established the following integro-differential equation (Fig. 21):

$$\alpha_g(y) = \frac{2\Gamma(y)}{V l(y) \cdot c'_{L\infty}} + \frac{1}{4\pi V} \int_{y'=-s}^{+s} \frac{d\Gamma}{dy'} \frac{dy'}{y-y'} \qquad \text{(PRANDTL, 1918)} \qquad (25)$$

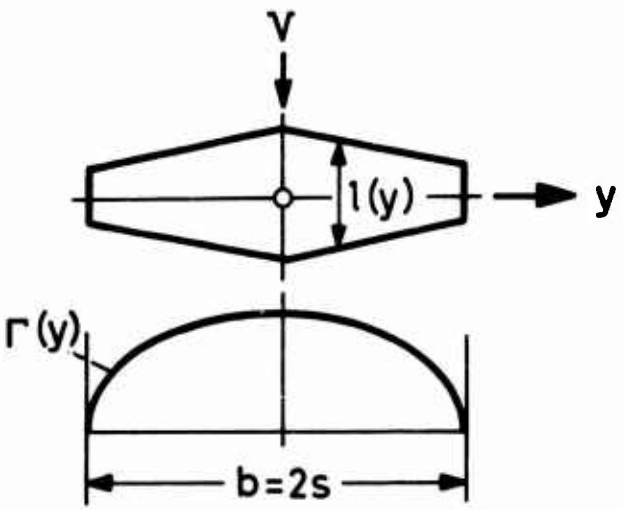

Fig. 21: LIFTING LINE INTEGRAL EQUATION, PRANDTL 1918

Here, $l(y)$ denotes the prescribed local wing chord, $\alpha_g(y)$ is the given distribution of the geometrical angle of incidence, and $\Gamma(y)$ is the distribution of circulation along the span which is to be determined. Further $c'_{L\infty}$ denotes the lift slope of a wing of infinite span. The preceding integro-differential equation discovered by PRANDTL forms the basis of all of wing theory. PRANDTL indicated a method to solve this, linear in $\Gamma(y)$, integral equation. As the first important result, equation (25) leads to the following simple expression for the lift slope in terms of the aspect ratio $A = b^2/F = b/l$:

$$\frac{dc_L}{d\alpha_g} = \left(\frac{dc_L}{d\alpha_g}\right)_\infty \cdot \frac{A}{A+2} = c'_{L\infty} \cdot \frac{A}{A+2} \quad . \qquad (26)$$

The subscript ∞ refers to the value for the two-dimensional problem, that is for the aspect ratio $A = \infty$.

As a second important consequence of this wing theory, PRANDTL derived an expression for the lift and drag as functions of the aspect ratio for arbitrary wings subject to the condition that A is large; these are

a) for the lift coefficient, c_L, in terms of the geometrical angle of incidence, α_g, he found that

$$\alpha_{g2} = \alpha_{g1} + \frac{c_L}{\pi}\left(\frac{1}{A_2} - \frac{1}{A_1}\right) \qquad (27)$$

whereas

b) for the drag coefficient, c_D, in terms of the lift coefficient, c_L, he could prove that

$$c_{D2} = c_{D1} + \frac{c_L^2}{\pi}\left(\frac{1}{A_2} - \frac{1}{A_1}\right) \qquad (28)$$

The experimental verification of this theory is depicted in Fig. 22 which represents a plot of the lift coefficient against the angle of incidence, and in Fig. 23 which plots the same quantity against the drag coefficient. The values measured at five aspect ratios plot directly as five separate curves. However, when they are reduced by calculation to an aspect ratio A = 5 they trace a single curve. Thus, experiment brilliantly confirmed PRANDTL's wing theory.

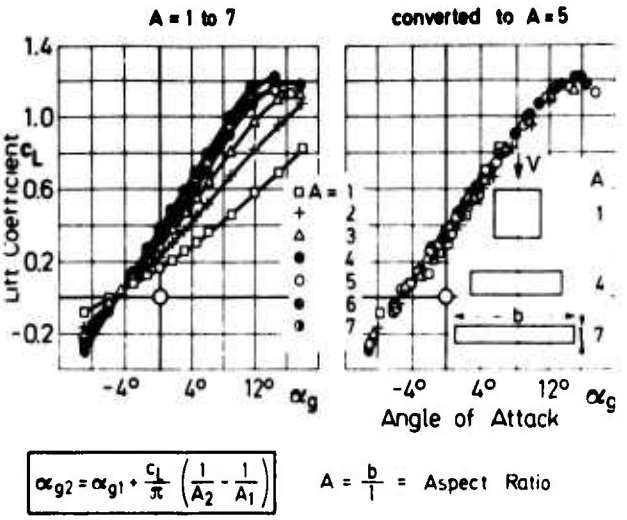

Fig. 22: WING OF FINITE SPAN: PRANDTL-BETZ 1921 - LIFT COEFFICIENT AGAINST ANGLE OF ATTACK FOR DIFFERENT ASPECT RATIOS

The preceding results belong nowadays in the indispensable bag of tools of every aeronautical engineer. In the years following its discovery, PRANDTL's wing theory was extended in many directions [32-35].

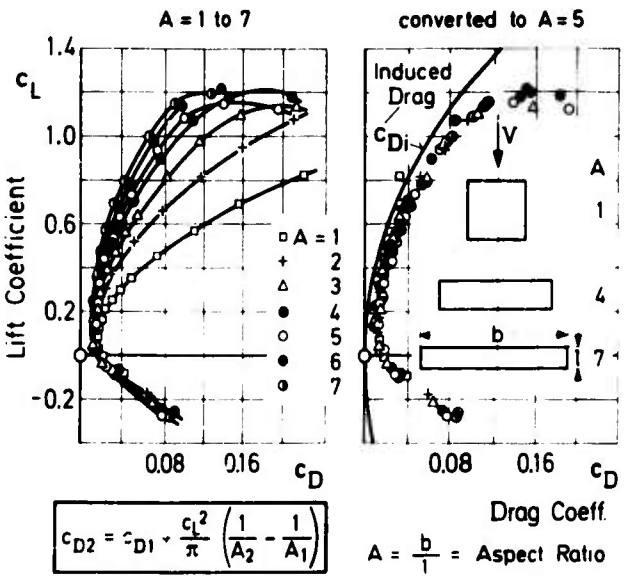

Fig. 23: WING OF FINITE SPAN: PRANDTL-BETZ 1921 ; POLAR CURVES FOR DIFFERENT ASPECT RATIOS

2.7 Compressible flows

Now I wish briefly to touch upon yet another aspect of physics of fluid flow which PRANDTL tackled very early in his career and which also has become very important in modern aerodynamics. Very soon after his arrival in Goettingen, PRANDTL devoted much of his time to the writing of his contribution "On the Flow of Gases and Vapors" to the "Encyclopedia of the Mathematical Sciences" whose publication was taken in hand by FELIX KLEIN in Goettingen at the turn of the century. His contribution became the forerunner of PRANDTL's well-known book "Essentials of Fluid Dynamics" [2]. In this connection he started work on the scientifically novel problem of the flow of compressible gases. In the course of this work he discovered the exact solution of the supersonic flow around a corner (Fig. 24), which entered the literature of the subject under the name of the "PRANDTL-MEYER expansion" [36, 37].

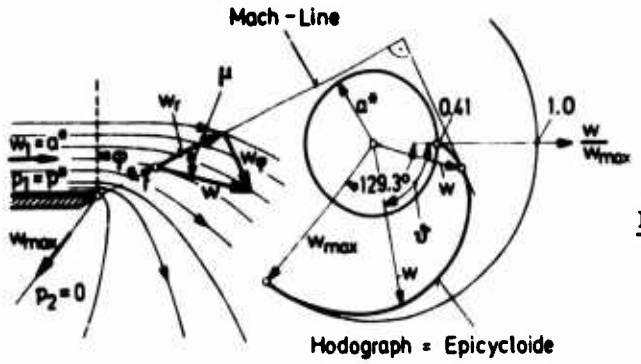

Fig. 24: PRANDTL-MEYER EXPANSION 1908; HODOGRAPH FOR SUPERSONIC FLOW

This solution , too, was confirmed by experiments. Later it turned out that this solution was also very important for a large number of cases of supersonic flow. The flow pattern under consideration is shown in Fig. 24 in the form of a hodograph. Here the velocity vectors along a streamline have been drawn from a single origin, their end-point tracing the hodograph which is an epicycloid.

In a manner similar to the boundary layer paper of 1904 and to the 1918/1919 paper of wing theory, the PRANDTL-MEYER paper dating from the year 1907 also became of fundamental importance, this time for the treatment of compressible flows which acquired a practical importance only many years later. Quite early, around 1905, PRANDTL became interested in flow through convergent-divergent, or LAVAL, nozzles and in the theory of compression shock waves. At that time all these problems were of practical importance only insofar as they applied to steam turbines; at a later time their scope was much extended in cooperation with A. BUSEMANN [38] . BUSEMANN discovered an approximate graphical method for the calculation of two-dimensional supersonic flows. He was able to prove that a two-dimensional steady, potential supersonic flow can be determined approximately with the aid of a system of cross-crossing, stationare acoustic waves. His method has been widely applied to the calculation of flow through supersonic nozzles. In developing the method BUSEMANN succeeded so to determine the nozzle profile as to produce a faultless, homogeneous parallel stream at the exit. His solution has proved indispensible in the design of supersonic wind tunnels.

Another very simple solution became one of utmost importance for flows around bodies at high Mach numbers in the subsonic range in that it associated a simple but related incompressible flow pattern with it. The formula is known in the literature as the PRANDTL-GLAUERT rule [39] . When applied to the lift of a wing at a subsonic Mach number (Ma < 1), it assumes the form

$$\frac{dc_L}{d\alpha} = \left(\frac{dc_L}{d\alpha}\right)_{Ma=0} \frac{1}{\sqrt{1 - Ma^2}} \qquad \text{(PRANDTL-GLAUERT, 1922)} \qquad (29)$$

Fig. 25 illustrates this relation as well as its experimental verification for symmetric airfoils of different thickness ratios; the agreement between theory and experiment is very good until a so-called critical value of the Mach number is attained. The discrepancy beyond that value is caused by the appearance of local shock waves which cause separation. The PRANDTL-GLAUERT rule proved to be of extraordinary importance in the thirties for the development of aircraft capable of flying at increasingly high speeds. PRANDTL' s activities in this field were crowned in 1936 with the formulation of a new theory of lifting surfaces. This constituted an extension [40] of his earlier theory to include wings of large width (small aspect ratio). By introducing the "acceleration potential" PRANDTL succeeded in extending the earlier theory in a very complete way. This created a basis for the calculation of lift distributions on lifting surfaces of finite span at supersonic speeds, too [41] .

2. 8 Meteorological problems

The progress achieved with the solution of problems of developed turbulent flows in pipes and along plates induced LUDWIG PRANDTL quite early to include the investigations of meteorological problems with the aid of his discoveries. As early as 1924 he employed his new hypothesis for the shearing stress at a rough wall in order to calculate the velocity distribution in a wind over the ground including the effect of a pressure gradient and of Coriolis forces. The calculation was performed for various (0, 1 to 100 m) - arbitrary postulated - heights of roughness elements [42] .

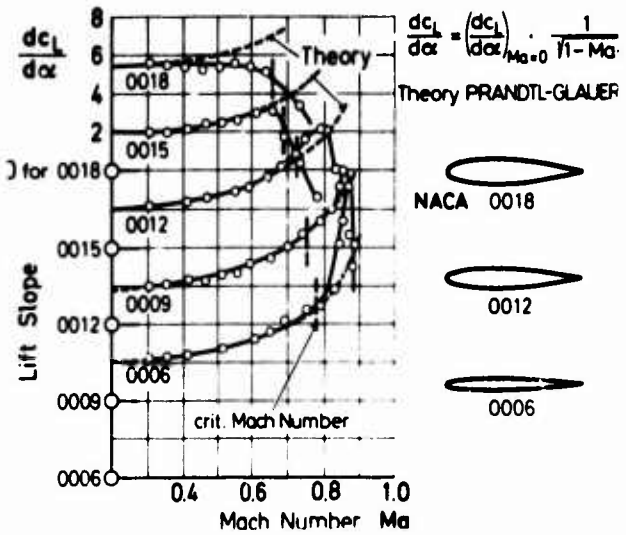

Fig. 25 PRANDTL-GLAUERT RULE FOR LIFT SLOPE AT HIGH SUBSONIC SPEED (1922)

His first publication on meteorological applications of the physics of fluids was followed by numerous others which endeavored "to describe in numerical terms, and hence better to understand" the general circulation in the atmosphere, as he himself neatly expressed it. In this field, too, success crowned his own and his student's endeavors in that they discovered new solutions to the differential equations which govern these complicated phenomena and were able to show that many of the observations which were made purely phenomenologically in meteorology proved to be necessary consequences of the laws of mechanics. Needless to say, in this field too, PRANDTL did not restrict himself to theoretical assumptions and derivations but invented special experiments in support of his hypotheses. Thus there was born a ROTATING LABORATORY in which he could study the effect of Coriolis forces [43]. Among others this installation was employed to render visible by means of a model experiment, the combined effect of terrestical rotation and wind action over the earth [44].

Further problems which he investigated concerned the flow in stratified heavy liquids. And so he treated the effect of the density differences in two contiguous air masses, each of which is homogeneous by itself, the one being denser than the other. This is a configuration which occurs when a cold air mass stagnates at a mountain and penetrates into warm mountain valleys on the other side. Such a confluence of air masses can give rise to a heavy storm in the valley at a time when the sky is otherwise cloudless [45].
The shape of the front of a cold mass of air which breaks into warm air at rest also stimulated his phantasy and prompted him to engage in theoretical considerations on the subject. Afterwards he induced one of his students to check and to confirm these ideas with the aid of experiments with dyed salt solution which moved over the bottom over a water container from one side forward [46].

Further and beyond he was interested in the motion of all manner of waves in stably stratified media in which density varies continuously with height. The special case of waves created in the lee of the crest of a mountain belongs in this category. Such waves were first observed in very high mountains; they become very important for the flight of gliders [47]. In interaction with the ground, it is discovered that the variation of the density in a horizontal direction, and not only that in the vertical direction, plays a very important part. This is due to the fact that the configuration gives rise to horizontal pressure differences and velocity components. Studies of this kind led, for example, to considerations of and statements about the ground winds that occur when a warm front slides over a cold front. Finally, I wish to mention that PRANDTL succeeded in clarifying the fundamental problem of the existence of a general circulation of air above the earth by the use of fluid mechanics. He was able to identify the important forces acting in this connection and to make it possible to perform approximate calculations of such flow processes. He presented a paper "On the Calculation of Weather Pattern" [48] to the Academy of Sciences in Goettingen in his 71st year which can be regarded as a crowning contribution to this series of researches. In it he developed the main outline of a numerical method to calculate the pressure and velocity field in the atmosphere as well as its further evolution when the density distribution is given at a certain instant.

Finally, it is necessary to mention that this investigation was followed by contributions to the theory of jet-streams in the troposphere and in the lower layers of the stratosphere. These were discovered in the forties and fifties, when new meteorological observation methods were introduced, and acquired considerable importance for weather forcasting and air transportation. These jetstreams which blow from west to east with velocities of over 100 m/s, precede extended zones of bad weather (regions of low pressure); they diverge at their eastern end and produce extended zones of precipitation at their right-hand edge, their wind velocity decreasing to the value of the drift velocity of the depression. LUDWIG PRANDTL was able to provide a dynamically justified explanation for these completely new phenomena

which were only discovered in the forties [49] . He was able to do this on the basis of his earlier contributions in meteorology. —

At this point I wish to terminate my account of PRANDTL's scientific works. In doing so, I feel compelled once again to stress that much of importance had to be left out of account. To conclude this section I give a list which contains a summary review of PRANDTL's Publications including those of the doctoral candidates who worked under him. His own publications, including his books and contribution to handbooks, have attained the considerable total of 168; the number of doctorates reached 83.

FIELD OF RESEARCH	PRANDTL Publications	THESES	TOTAL
Viscous Flow: Boundary Layers, Turbulence	33	31	64
Airfoil Theory	25	15	40
Compressible Flow	12	5	17
Wind Tunnels	15	2	17
Meteorology	12	8	20
Elasticity, Plasticity	14	12	26
Miscellaneous Problems	40	10	50
Books, Contribution to Handbooks	17	-	17
Total:	168	83	251

In the succeeding sections I will briefly describe PRANDTL's endeavor as a university professor and as the director of a large research establishment.

3) PRANDTL AS A UNIVERSITY PROFESSOR

PRANDTL's career as an active university professor extended over a period of time of more than 45 years, because he was appointed at the young age of 26 years to an ordinary professorship of mechanics at the Technical University of Hanover in 1901. In 1947 he retired from the professorship at Goettingen at the age of 72. During the whole of this long period of time, PRANDTL applied himself to his lectures with great devotion. At FELIX KLEIN's behest, PRANDTL accepted the invitation extended to him by the University of Goettingen to occupy the newly created chair of applied mechanics. He remained faithful to Goettingen to the end of his life. PRANDTL repeatedly stressed the fact that the link between the pure and the applied science was for him important as well as indispensable and that the cultivation of this spirit was a unique feature of life at Goettingen University.

During the years between the wars PRANDTL followed a four semester cycle of lectures covering "Mechanics of Rigid Bodies", "Graphical Statics", "Aerodynamics" and "Thermodynamics". He lectured for four hours each week and conducted tutorials for two additional hours.

A large number of young students was introduced to the science of mechanics, and, in particular, of fluid mechanics by these lectures. Many of them were induced to continue as doctoral candidates and to work under PRANDTL in one of the institutes directed by him. The fruitful interaction between study and research was achieved under PRANDTL in an ideal fashion. In the year 1909 THEODORE von KARMAN [50] obtained his doctor's degree under PRANDTL in Goettingen; he should be regarded as PRANDTL's most prominent postgraduate student. For this reason I should like to quote von KARMAN's opinion about PRANDTL's lectures as he expressed it in 1925 on the occasion of the latter's fiftieth birthday [51]:

> "The fact that the science of aeronautics has now so far progressed in its development that it has become a fit subject for examinations will forever and inseparably be linked with PRANDTL's name", and: ... "I consider that PRANDTL is one of those men from whom one can learn the most, even though one cannot, after all, apply to him the designation" brilliant teacher". His lectures lack external lustre; for this reason his lectures are less suitable for beginners, regardless of the fact that he does not assume much prior knowledge.

> But he assumes the most difficult thing: a pleasure derived from the process of thinking and an eagerness to follow a trend of thought, particularly one flowing from intuition; for this reason mostly those learn from him who have already spent a longer time in his company and who have come to know his mode of thinking".

I believe that those among us who had the advantage of personally attending his lectures will completely agree with VON KARMAN' s judgement.

The fact that PRANDTL' s Goettingen lectures fell on fertile ground is confirmed by the large number of doctoral candidates who worked under him. I have already mentioned in the previous section that their number reached 83.

W. TOLLMIEN [52] aptly characterized PRANDTL' s peculiar talent to inspire his postgraduate students and co-workers in the Institute and to work fruitfully when he wrote his Introduction to PRANDTL' s "Collected-Works". He said:

> "PRANDTL' s achievement could not have become so brilliant and successful if he did not draw his strength from his own scientific genius, his ability to inspire a large number of students and co-workers to a similar selfdenial and devotion to research. PRANDTL' s goal was not so much to achieve a flash of recognition as to be able to systematically illuminate a whole complex of questions which, precisely, could be achieved only through the creation of a s c h o o l. Goettingen was just the place which made all this possible for him. As the institutes in Goettingen developed with the passage of years, many co-workers arrived and augmented the numbers of candidates who earned their doctorates there. They all experienced his inspiration through personal contacts with him".

I firmly believe that all those who were lucky enough to have worked for some time in one of PRANDTL' s institutes will unhesitatingly agree with this description of PRANDTL' s pedagogical influence.

4) PRANDTL AS THE HEAD OF A LARGE RESEARCH INSTITUTE

During his more than forty years of active service in Goettingen PRANDTL directed three institutes in addition to his university Chair of Applied Mechanics.

These were:

a) The Institute of Applied Mechanics of Goettingen University, 1904 - 1946.

b) The Aerodynamics Research Institute (AVA or Aerodynamische Versuchsanstalt), 1907 to 1937

c) The Kaiser Wilhelm Institute for Fluid Mechanics Research, 1925 - 1946 *)

*) The Institute of Applied Mechanics was not revived after the Second World War. The Kaiser Wilhelm Institute for Fluid Mechanics Research has been in operation since 1947 under a changed name as the Max-Planck-Institute for Fluid Mechanics. After the Second World War, the Aerodynamics Research Establishment was first discontinued and its research installations were dismantled. It was not until 1953, that it was resurrected under its old name and reconstructed. In 1969 the AVA was transferred to the German Research Institute for Flight and Space Travel (Deutsche Forschungs- und Versuchsanstalt für Luft- und Raumfahrt, or DFVLR) as its Goettingen Center.

Thus for a time, i. e. during the years 1925 to 1937 PRANDTL, directed three institutes simultaneously. As the establishment grew considerably, he ceded in 1937 the direction of the AVA to ALBERT BETZ, his faithful co-worker of long years. He did remain, however, a member of the Supervisory board of the AVA until the end of World War II.

I propose to devote the remainder of this section to some remarks on PRANDTL's work as institute director. In doing so, I will confine myself principally to a discussion of PRANDTL's impact on the AVA, because that institute employed the largest number of people and was the eldest of the three.

A very short time after PRANDTL's arrival in Goettingen, namely in 1904, the idea was born that it would be useful to organize a model testing establishment to serve the "Society for the Study of Powered Flight" (Motor-Luftschiff-Studiengesellschaft). The AVA grew out of this establishment quite quickly (in the year 1907). The new testing technique which was developed first for airship models and later for aeroplanes, succeeded under PRANDTL thanks, among others, to the invention of wind tunnels of the Goettingen type (Fig. 18 and Fig. 19). Figure 26 shows the very ancient building which housed the first Goettingen wind tunnel from 1908 to 1919. Towards the end of the First World War, namely in 1917, the AVA completed the second Goettingen wind tunnel on the basis of designs prepared by PRANDTL and BETZ; its free stream had a diameter of 2.25 m; it had a maximum speed of 50 m/s and a motor of 400 hp; see Fig. 19.

Fig. 26: BUILDING FOR THE FIRST GOETTINGEN WIND-TUNNEL, 1908 - 1918

Fig. 27 shows the building in which this wind-tunnel was accommodated. The picture was taken in 1930 on the day the president of the Kaiser-Wilhelm-Society was buried. On that occasion a Zeppelin visited the AVA. Fortunately, PRANDTL succeeded in maintaining the AVA, and hence also this wind-tunnel, through the difficult years, which followed the First World War. In this he was aided by the Kaiser-Wilhelm-Society. Later, towards the end of the twenties, when the German aircraft industry blossomed again, very many tests on models were performed for the German Aircraft industry in this "classical wind tunnel". The companies DORNIER, JUNKERS, HEINKEL, MESSERSCHMITT and FOCKE WULF, among others, were continuously visiting the AVA bringing orders for wind tunnel testing. This very close cooperation between the AVA and the German Aircraft industry proved stimulating and exceedingly fruitful for both sides. It is no exaggeration when I say that pretty well all designs of German aeroplanes completed between the two World Wars passed through this Goettingen wind tunnel. Additional wind tunnels did not get commissioned at the AVA until the middle of the thirties (larger tunnels, and tunnels capable of developing higher speeds).

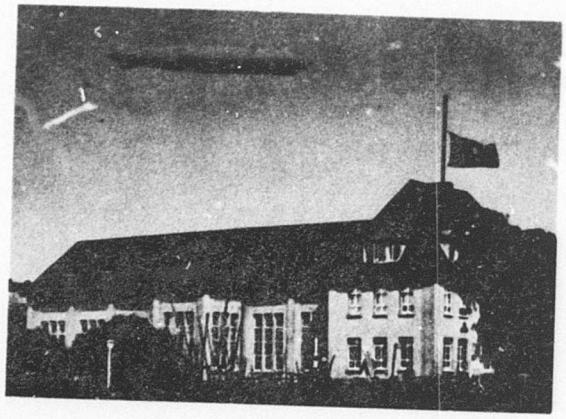

Fig. 27: BUILDING FOR THE SECOND WIND TUNNEL OF THE AVA WITH AIRSHIP 1930

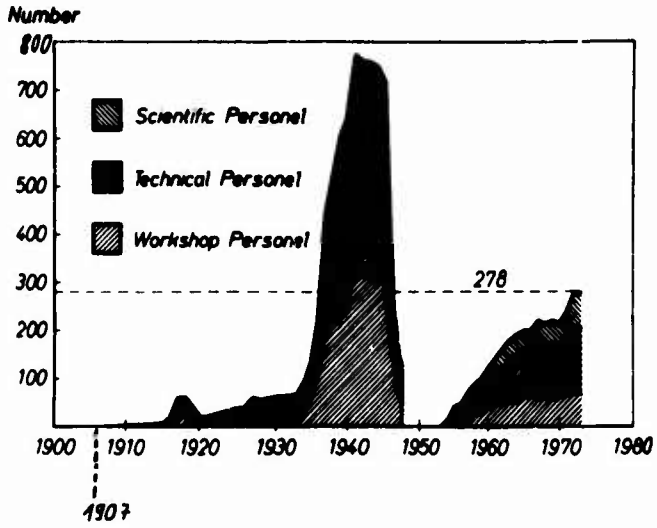

Fig. 28: PERSONNEL OF THE AVA, 1907 - 1973

Fig. 28 illustrates the growth of the personnel of the AVA from 1907 until 1973. Starting as a two man operation in 1907, it became a large research establishment at the end of the Second World War, employing something like a total of 750 workers; it comprised six institutes.

PRANDTL transferred the directorship of the AVA to ALBERT BETZ in the year 1937. A. BETZ gave a detailed account [53] of the development of this institute (during the time preceding the start of the Second World War), which was founded by PRANDTL and which earned world-wide recognition.

For the sake of completeness I wish to put on record the following further details: After it was closed down in 1947 and after its extensive research installations were dismantled, there begun in 1953 a period of slow regeneration. The growth of the personnel of the institute is illustrated in Fig. 29. Starting with about 20 people in 1953, it grew to include about 280 at the end of 1973. The re-created AVA also considers that close cooperation with industry, as initiated by its previous directors PRANDTL and BETZ, constitutes a very essential part of its work. The anniversary Volume "AVA 1945-1969" contains a detailed account of its scientific accomplishments during the period after the Second World War [54].

To conclude, may I be permitted to show two pictures which bring back personal memories and to cite one scientific result taken from the glorious history of the, by PRANDTL and BETZ so successfully directed, AVA. Fig. 30 shows a group photo of the total personnel of the AVA at the end of the First World War in November 1918. In the middle you can see PRANDTL, and in the left up corner I wish to point to BETZ and WIESELSBERGER among others; in the last row you can see K. POHLHAUSEN (in uniform).

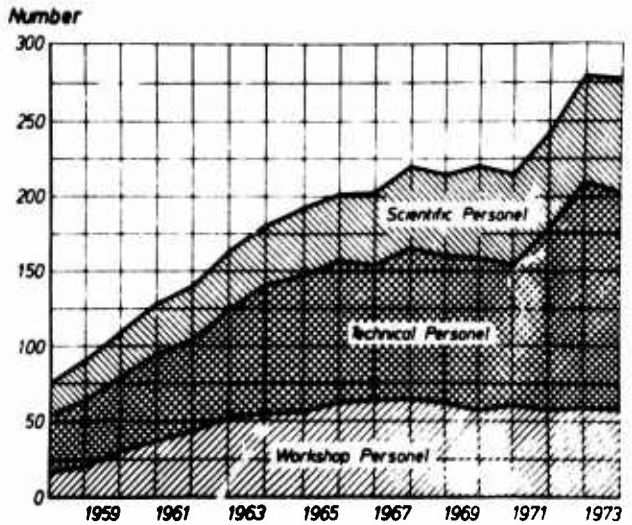

Fig. 29: PERSONNEL OF THE AVA, 1958 - 1973

Fig. 31 contains a group picture of the personnel of the AVA taken in 1925. This picture shows all people from the office, including PRANDTL, BETZ, ACKERET and SEIFERTH, and in the front of the row at the left and ahead, Miss HILDE KREIBOHM, who faithfully served to the AVA as a secretary for a total of 50 years. To this picture there belongs another showing the workshop personnel - exactly 10 people. The AVA consisted at that time, that is in 1925, of the round number of 30 persons, and one cannot help but admire the abundance of results achieved by this small group! Owing to the pressure of time I must stop myself from commenting in greater detail on the differences between now and then; I believe, however, that one should pounder these changes [55].

As my last picture I wish to describe a historic scientific event which dates back to the time shortly before the Second World War. Fig. 32 contains polar diagrams of a swept and an unswept wing in the high-MACH-number subsonic regime (Ma = 0,7 and 0,9). The corresponding measurements were performed by H. LUDWIEG and O. WALCHNER [56] under the direction of A.BETZ in 1939 in a very small high-speed tunnel of the AVA (measuring section 10 x 10 cm). These measurements provided, for the first time, an experimental confirmation of the superiority of swept wings in the high subsonic flow regime. BUSEMANN [57] pointed out as early as 1935 that adopting a swept wing would lead to an improvement in the aerodynamic properties of wings in the supersonic regime.

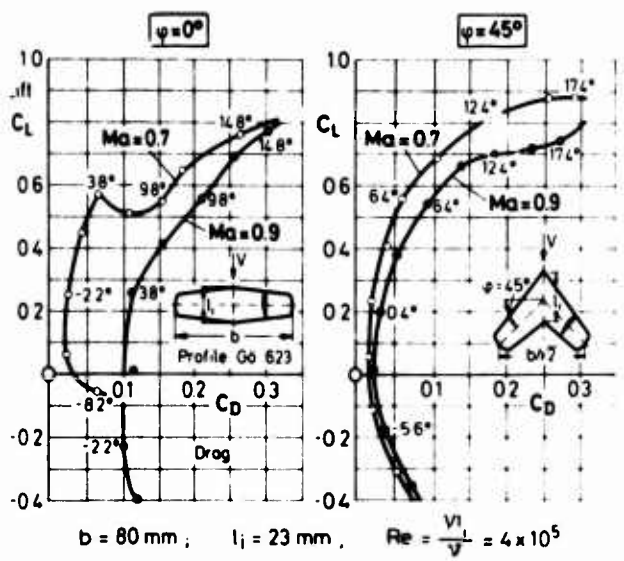

Fig. 32: SWEPT WING AT HIGH SUBSONIC SPEEDS; POLAR DIAGRAMS; BETZ-LUDWIEG 1939

However, the fact that a considerable improvement occurs also at high subsonic MACHnumbers was shown precisely by these AVA measurements of 1939.

To-day, swept wings provide the technical foundation on which we have erected our intercontinental air line network.

It is remarkable that this great and important discovery remained unknown outside Germany until the end of the Second World War. It created a sensation among the members of the first American "Study Commission" which arrived in Goettingen and Braunschweig in the spring of 1945 under the leadership of THEODORE VON KARMAN. GEORGE SCHAIRER, the chief designer of BOEING, who was on the team, cabled SEATTLE saying [58]:

"Stop the bomber design, we have found a new wing planform".

And this then led to the first giant aircraft with swept wings in the United States - the BOEING B 47.

And so I wish to put it on record that in the Institute which was then led by BETZ, and which remained under the general supervision by PRANDTL, a perfectly fundamental contribution to the modern aeronautics was made in the form of the discovery of the swept wing for the transonic velocity range.

Allow me, Ladies and Gentlemen, to conclude these remarks on PRANDTL's effectiveness as a leader of a large research establishment by reading to you a quotation from PRANDTL's essay entitled "My road to hydrodynamic theories" [59].

This dated back to a speach which he delivered in 1947 on the occasion of his election to Honorary Membership of the German Physical Society. This quotation which, according to my mind, is characteristic of PRANDTL's personal and human attitude, reads as follows:

"In his friendly remarks addressed in my direction, Mr. HEISENBERG stated, among other things, that I had the ability to glean from equations, without calculation, what solution they may possess. I feel compelled to answer that even though I do not possess such an ability, I always try to form in my mind I c l e a r c o n c e p t i o n, and as detailed as I can make it, about the things, which lie at the basis of my problems, as well to understand the corresponding processes. The e q u a t i o n s do not intervene until later, when I believe that I understand the phenomenon; on the one hand they serve to arrive at quantitative statements which, evidently, cannot be obtained by

intuition alone; on the other hand the equations constitute a good tool, with the aid of which it becomes possible to produce proofs of my conclusions that other people, too, would be inclined to recognize".

5) CONCLUDING REMARKS

Ladies and Gentlemen!

I believe that the preceding account clearly proves that the science of mechanics, particularly the science of the mechanics of fluids, progressed enormously through LUDWIG PRANDTL. This, so to say, placed our science in a new epoch. For us, who continue to work in this field, thus arises the question: What were PRANDTL's most essential characteristics, which led him to such stunring success and what conclusions would we draw from all this for our own work? I am of the opinion that these reduce, essentially, to the following three points:

a) Real progress in the field of fluid mechanics demands the existence of a very close relationship between experiment and theory; furthermore, theoretical solutions must always be carried to a point where detailed numerical calculations become possible.

b) To secure good progress in science it is necessary continually to introduce able young cadres to the art of conducting important research. In this connection, success is often achieved when the director of a large research institute also assumes teaching duties at a university.

c) In order to safeguard the successful administration of a large research institute it is absolutely necessary to place the top management in the hands of a scientist who has proved himself in his field. The administration of a research institute should always be subordinate to its scientific leadership.

That these principles are right has been convincingly demonstrated by PRANDTL. We, who have adopted as our goal to continue PRANDTL's life's endeavor, ought to take these lessons to heart.

ACKNOWLEDGEMENT:

I express my thanks to my co-worker Dr. F.W. RIEGELS, the Director of the Institute of Fluid Mechanics of the AVA in Goettingen, for the help he gave me during the preparation of this manuscript.

I thank Professor J. KESTIN of Brown University in Providence, Rhode Island, USA, for the English translation of this text.

7) REFERENCES

[1] Ludwig PRANDTL — Gesammelte Abhandlungen zur angewandten Mechanik, Hydro- und Aerodynamik. 3 Vols., Springer Verlag Berlin, Göttingen, Heidelberg, (1961)

[2] Ludwig PRANDTL — Führer durch die Strömungslehre. Braunschweig 1942, 1st. ed. (1965) (6th ed.). English Translation: Essentials of Fluid Dynamics, London and Glasgow (1952)

[3] Ludwig PRANDTL — Ueber Flüssigkeitsbewegung bei sehr kleiner Reibung. Proceedings III. Internat. Math. Congr., Heidelberg (1904), 484-491, see also [1] Vol. II, pp. 575-584

[4] H. SCHLICHTING — Grenzschichttheorie, 1st. ed. Karlsruhe (1951); 5th ed. (1965). English translation "Boundary Layer Theory" by J. KESTIN 6th ed., New York (1968)

[5] H. BLASIUS — Grenzschichten in Flüssigkeiten mit kleiner Reibung. Thesis Goettingen (1907), Z. Math. Phys. 56, S. 1-37 (1908)

[6] J. NIKURADSE — Laminare Reibungsschichten an der längsangeströmten Platte. Monographie Zentrale für wiss. Berichtswesen, Berlin 1942

[7] O. REYNOLDS — An experimental investigation of the circumstances which determine whether the motion of water shall be direct or sinuous, and of the law of resistance in parallel channels. Phil. Trans. Roy. Soc. 174, 935-982 (1883), see also Scientific papers 2, (1951)

[8] G. EIFFEL — Sur la résistance des sphères dans l'air en mouvement. Comptes Rendus 155, 1597 (1912)

[9]	Ludwig PRANDTL	Der Luftwiderstand von Kugeln. Nachr. Ges. Wiss. Goettingen, Math. Phys. Klasse 1914, 177-190, see also "Gesammelte Abhandlungen" (Collected Works) II, 597-608
[9a]	C. WIESELSBERGER	Der Luftwiderstand von Kugeln. ZFM 5 (1914), S. 140- 144
[10]	H. BLASIUS	Das Aehnlichkeitsgesetz bei Reibungsvorgängen in Flüssigkeiten. Forsch. Abt. Ing. -Wesen, Heft 131, Berlin (1913)
[11]	L. PRANDTL	Neuere Ergebnisse der Turbulenzforschung. Z. VDI 77, 105-114 (1933)
[12]	J. NIKURADSE	Gesetzmäßigkeit der turbulenten Strömung in glatten Rohren. Forsch. Arb. Ing. -Wes. Heft 356 (1932)
[13]	J. NIKURADSE	Strömungsgesetze in rauhen Rohren. Forsch. Arb. Ing. -Wes. Heft 361 (1933)
[14]	L. PRANDTL	Ueber den Reibungswiderstand strömender Luft. Reports AVA Goettingen. III. Series (1927) and: Zur turbulenten Strömung in Rohren und längs Platten. Reports AVA Goettingen IV. Series (1932); First mention in I. Series 136 (1921), see also "Gesammelte Abhandlungen" (Collected Works) II, 620-626 and 632-647
[15]	L. PRANDTL, H. SCHLICHTING	Das Widerstandsgesetz rauher Platten. Werft, Reederei, Hafen 1-4 (1934); see also "Gesammelte Abhandlungen" (Collected Works) II, 648-662
[16]	L. PRANDTL	Ueber die ausgebildete Turbulenz, ZAMM 5, 136-139 (1926) and Proceedings II. Intern. Congr. Appl. Mech. Zürich (1926), 62-75; see also "Gesammelte Abhandlungen" (Collected Works) II, 874-888
[17]	W. TOLLMIEN	Berechnung turbulenter Ausbreitungsvorgänge. ZAMM 6, 468-478 (1926); NACA TM 1085 (1945)
[18]	H. SCHLICHTING	Ueber das ebene Windschattenproblem. Thesis Goettingen 1930, Ing. Archiv 1, 533-571 (1930)
[19]	W. M. F. ORR:	The stability or instability of the steady motions of a perfect liquid and of a viscous liquid. Part I: A perfect liquid; Part II: A viscous liquid. Prov. Roy. Irish Acad. 27, 9-68 and 69-138 (1907)
[20]	A. SOMMERFELD	Ein Beitrag zur hydrodynamischen Erklärung der turbulenten Flüssigkeitsbewegungen. Proceedings 4th Intern. Congr. Math. Vol. III, 116-124, Rome 1908
[21]	L. PRANDTL	Bemerkungen über die Entstehung der Turbulenz. ZAMM 1, 431-436 (1921) and Phys. Z. 23, 19-25 (1922) see also "Gesammelte Abhandlungen" (Collected Works) II, 687-696
[22]	O. TIETJENS	Beiträge zur Entstehung der Turbulenz. Thesis Goettingen 1922 and ZAMM 5, 200-217 (1925)
[23]	W. TOLLMIEN	Ueber die Entstehung der Turbulenz. 1. Series, Nachr. Ges. Wiss. Goettingen, Math. Phys. Klasse 21-44 (1929); Engl. translation in NACA TM 609 (1931)
[23a]	W. TOLLMIEN	Ein allgemeines Kriterium der Instabilität laminarer Geschwindigkeitsverteilungen, Nachr. Ges. Wiss. Goettingen, Math. Phys. Klasse, Fachgruppe I, 1, 79-114 (1935), Engl. translation in NACA TM 792 (1936)
[24]	H. SCHLICHTING	Zur Entstehung der Turbulenz bei der Plattenströmung. Nachr. Ges. Goettingen, Math. Phys. Klasse 182-208 (1933); see also: ZAMM 13, 171-174 (1933)
[25]	H. SCHLICHTING	Amplitudenverteilung und Energiebilanz der kleinen Störungen bei der Plattenströmung. Nachr. Ges. Wiss. Goettingen, Math. Phys. Klasse, Fachgruppe I, 1, 47-78 (1935)

[26] G.B. SCHUBAUER, H.K. SKRAMSTAD — Laminar boundary layer oscillations and stability of laminar flow. National Bureau of Standards Research Paper 1772. Reprint of a confidential NACA Report dated April 1943 (later released as NACA War-time Report W-8) and JAS 14, 69-78 (1947): see also NACA Rep. 909

[27] G.V. LACHMANN (Ed.) — Boundary Layer and flow control. Vols I and II: Pergamon Press, London 1961

[28] H. SCHLICHTING — A survey on some recent research investigations on boundary layers and heat transfer. Journ.Appl. Mech. Transaction of the ASME, Vol. 38, Series E, No. 2, June 1971, pp. 289-300

[29] H. SCHLICHTING — Recent Progress in Boundary Layer Research. 37th Wright Brothers Memorial Lecture, 1973; AIAA-Journal 12, 427-440 (1974)

[30] F.W. LANCHESTER — Aerodynamik. Ein Gesamtwerk über das Fliegen (Transl. into German by C. and A. Runge) 2 Bände Leipzig und Berlin 1909/1911

[31] Ludwig PRANDTL — Tragflügeltheorie I und II. Mitteilung. Nachr. der Kgl. Ges. Wiss. Goettingen Math. Phys. Klasse (1918) p. 451-477; (1919) p. 107-137

[32] H. BLENK — Der Eindecker als tragende Wirbelfläche. Thesis Goettingen 1923 ZAMM 5 (1925) p. 290-297

[33] E. TRUCKENBRODT — Tragflächentheorie bei inkompressibler Strömung. - Jahrbuch 1953 WGL, p. 40-65

[34] K. GERSTEN — Nichtlineare Tragflächentheorie, insbesondere für Flügel mit kleinem Seitenverhältnis. Ing. Arch. 30 (1961)p. 431-452

[35] D. HUMMEL — Nichtlineare Tragflügeltheorie in Bodennähe. Thesis for the acquisition of the title of "Dozent", Technical University, Braunschweig 1973. Zeitschr. Flugwiss. 21 (1973), p. 425-442

[36] Ludwig PRANDTL — Neue Untersuchungen über die strömende Bewegung der Gase und Dämpfe. Phys. Z. Bd. 8 (1907), p. 23-30

[37] TH. MEYER — Ueber zweidimensionale Bewegungsvorgänge in einem Gas, das mit Ueberschallgeschwindigkeit strömt. Thesis Goettingen 1907. VDI-Forschungsheft No. 62 (1908)

[38] Ludwig PRANDTL, A. BUSEMANN — Näherungsverfahren zur zeichnerischen Ermittlung von ebenen Strömungen mit Ueberschallgeschwindigkeit. Stodola Anniversary Volume Zürich 1929: p. 499

[39] Ludwig PRANDTL — Ueber Strömungen, deren Geschwindigkeit mit der Schallgeschwindigkeit vergleichbar ist. J. Aeron. Res. Inst. Tokyo Imp. Univ. No 65 (1930), S. 14

[40] Ludwig PRANDTL — Theorie des Flugzeugtragflügels im zusammendrückbaren Medium. Luftf. Forschung 13 (1936), p. 313-319

[41] H. SCHLICHTING — Tragflügeltheorie bei Ueberschallgeschwindigkeit. Luftf. Forschung 13 (1936), p. 320-335

[42] Ludwig PRANDTL (mit W. Tollmien) — Die Windverteilung über dem Erdboden, errechnet aus den Gesetzen der Rohrströmung. Z. Geophys. I. Jahrg. (1924), p. 47-55

[43] H. FETTE — Strömungsversuche im rotierenden Laboratorium. Thesis Goettingen 1934, Z. techn. Phys. 14th Series (1933), p. 257

[44] Ludwig PRANDTL — Betrachtungen zur Mechanik der freien Atmosphäre. Abhandlg. Ges. Wiss. Goettingen. Math.-Phys. Klasse, III. Series, No. 18 (1937), p. 75-84

[45] Ludwig PRANDTL — Neuere Erkenntnisse der meteorologischen Strömungslehre. Schriften der deutschen Akademie der Luftfahrtforschung Vol. 8 (1944), p. 157-179

[46] V.M. GATAGHE — Modellversuche über die gegenseitige Bewegung von Luftmassen verschiedener Temperaturen. Thesis Goettingen 1936

[47] G. LYRA — Theorie der stationären Leewellenströmung in freier Atmosphäre. ZAMM 23(1943), p. 1-28

[48]	Ludwig PRANDTL	Zur Berechnung des Wetterauflaufs. Nachr. Akad. Wiss. Goettingen, Math-phys. Klasse (1946), p. 102-105
[49]	Ludwig PRANDTL	Dynamische Erklärung des Jetstream-Phänomens. Berichte d. deutschen Wetterdienstes US-Zone No. 12 (1950), p. 198-200
[50]	TH. VON KARMAN	Collected Works, 4 Vols., London 1954
[51]	TH. VON KARMAN	Ludwig PRANDTL. Zeitschr. Flugtechnik u. Motorluftschiffahrt (1925), p. 37
[52]	W. TOLLMIEN	Zum Geleit. Foreword in "LUDWIG PRANDTL Gesammelte Abhandlungen" (Collected Works), 3 Vols., Springer Verlag Berlin (1961)
[53]	A. BETZ	Die Aerodynamische Versuchsanstalt Goettingen. Beiträge zur Geschichte der deutschen Luftfahrtwissenschaft- und technik. Vol. I - Published by the "Deutsche Akademie der Luftfahrtforschung", Berlin (1941), p. 1-166
[54]		Die Aerodynamische Versuchsanstalt Göttingen von 1945-1969 Published by the AVA, 1969, 145 pages.
[55]	H. BLENK	Erinnerungen an LUDWIG PRANDTL. Lecture delivered during the 3rd Congress of Bearers of the Prandtl-Ring with young scientists and engineers. 9 May 1972, Bad Godesberg
[56]	H. LUDWIEG H. STRASSL	Verringerung des Widerstandes von Tragflügeln bei hohen Geschwindigkeiten durch Pfeilform. AVA-Report 39 H 18 (1939) see also H. LUDWIEG: Pfeilflügel bei hohen Geschwindigkeiten. Lilienthal-Bericht No. 127 (1940)
[57]	A. BUSEMANN	Aerodynamischer Auftrieb bei Ueberschallgeschwindigkeit. VOLTA Congress, Rome (1935), p. 328-360; see also Luftf.-Forschung 12 (1935), p. 210-220
[58]	TH. VON KARMAN	Aerodynamics; Selected Topics in the Light of their Historical Development, Ithaca, New York 1954
[59]	Ludwig PRANDTL	Mein Weg zu hydrodynamischen Theorien. Phys. Blätter, Vol. 4 (1948), p. 89-92

FIG. 30: GROUP PHOTO OF THE PERSONNEL OF THE AVA, NOVEMBER 1918

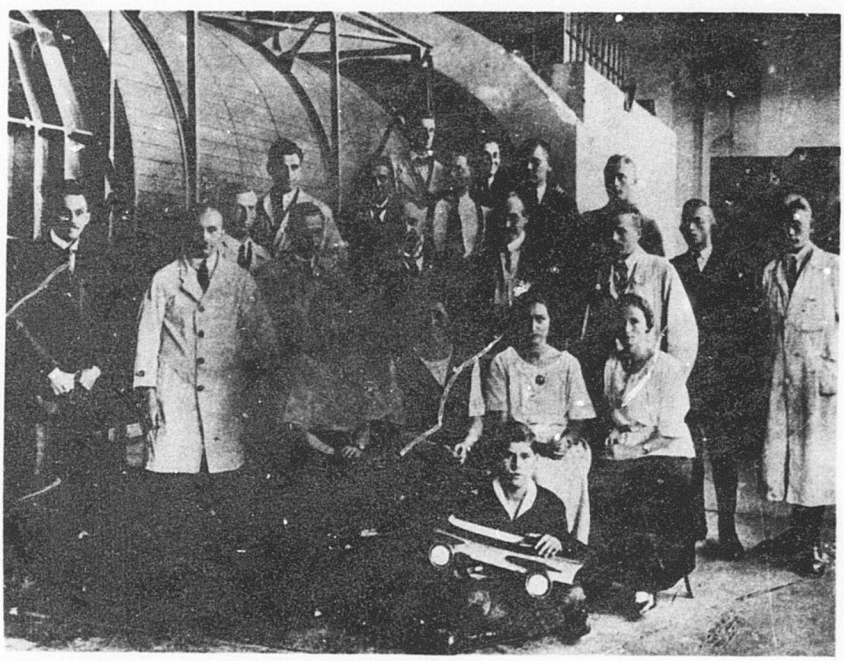

Fig. 31: GROUP PHOTO OF THE PERSONNEL OF THE AVA TAKEN ABOUT 1925

LAMINAR SEPARATION AT A TRAILING EDGE

by Jean-Pierre GUIRAUD* and René SCHMITT

Office National d'Etudes et de Recherches Aérospatiales (ONERA)
92320 CHATILLON (France)

Summary

This work is concerned with a model of incipient separation at the trailing edge of a thin wing in incompressible very high Reynolds number flow. Let ε be the wedge semi-angle at the trailing edge and R be the Reynolds Number. Riley & Stewartson (J.F.M. 44, 2, 347, 1970) showed that, under $\varepsilon \ll 1$ and $R \gg 1$, separation occurs right at the trailing edge if $\varepsilon^{-4} R^{-1/4} = 0$ (1). We show that, under $\varepsilon^{-4} R^{-1/4} \ll 1$, a model of separated flow, with a (small) recirculation zone, of streamwise length $O[\varepsilon^{1/2}(\varepsilon^{-4}R^{-1/4})^{1/2}]$ may be built, which is consistent with a matched asymptotic expansion scheme of solution of the Navier-Stokes equations in the vicinity of the trailing edge. The structure of the flow involves a triple deck of Sytchev's type (Mekh Zhidk Gaz 1972 n°3, p. 47) very close to separation, embedded in another triple deck, of Stewartsons' type, which is relevant to the overall separated flow. Angle of attack effects may be allowed provided the angle of attack α is $\ll \varepsilon^{1/4}$. Ignoring angle of attack effects, the flow depends on two constants: the value of vorticity in the recirculation zone and the precise position of separation, which is known already as far as order of magnitude is concerned $\left(O[\varepsilon^{1/2}(\varepsilon^{-4}R^{-1/4})^{1/2}]\right)$. A solution of the Sytchev's canonical triple deck problem will provide one relation between these two constants. A preliminary step towards such a solution is made through a thorough study of its asymptotic structure both far upstream from separation and far downstream from it.

DECOLLEMENT LAMINAIRE AU BORD DE FUITE

Résumé

Ce travail a pour but de proposer un modèle de la naissance de la séparation au bord de fuite d'une aile mince dans un écoulement incompressible à très grand nombre de Reynolds. Soit ε le demi-angle du dièdre au bord de fuite et R le nombre de Reynolds. Riley et Stewartson (J.F.M. 44, 2, 347, 1970) ont montré que, moyennant $\varepsilon \ll 1$ et $R \gg 1$, la séparation a lieu juste au bord de fuite si $\varepsilon^{-4} R^{-1/4} = 0$ (1). Nous montrons que, pour $\varepsilon^{-4} R^{-1/4} \ll 1$, un modèle d'écoulement décollé avec une (petite) zone de recirculation, d'étendue longitudinale $O\left[\varepsilon^{1/2}(\varepsilon^{-4}R^{-1/4})^{1/2}\right]$, peut être construit, qui est compatible avec une représentation de la solution des équations de Navier-Stokes obtenue, par la méthode des développements asymptotiques raccordés, au voisinage du bord de fuite. La structure de l'écoulement comprend une triple couche de type Sytchev (Mekh. Zhidk. Gaz 1972, n° 3, p.47) très près de la séparation, emboîtée dans une autre triple couche, de type Stewartson, qui s'applique à l'écoulement entièrement séparé. Les effets de l'angle d'attaque peuvent être pris en compte pourvu que l'angle d'attaque α soit $\ll \varepsilon^{1/4}$. En ignorant les effets d'incidence, l'écoulement dépend de deux constantes : la valeur du tourbillon dans la zone de recirculation et la position précise de la séparation, laquelle est connue du moins en ce qui concerne son ordre de grandeur $\left(O[\varepsilon^{1/2}(\varepsilon^{-4}R^{-1/4})^{1/2}]\right)$. Une solution du problème canonique de la triple couche du type Sytchev donnera une relation entre ces deux constantes. Une étape préliminaire à l'établissement d'une telle solution est effectuée à travers l'étude complète de sa structure asymptotique aussi bien loin en amont que loin en aval du point de séparation.

1 - Introduction

We consider a thin wing, at a small angle of attack in a high Reynolds number, steady, incompressible, laminar flow. We set $\varepsilon \ll 1$ for the thickness ratio and $\alpha \ll 1$ for the angle of attack. From inviscid linearized theory and standard boundary layer theory we can compute (numerically) an approximation for velocity and pressure, up to $O(\varepsilon)$ and $O(\varepsilon)$, which is valid except in a three dimensional neighbourhood of the edge of the wing. That this approximation is not uniformly valid is known from the works of Stewartson [7,8] Messiter [3] Van de Vooren and Dijkstra [1] dealing with the flat plate at zero angle of attack and those of Riley and Stewartson [6] Brown and Stewartson [4] for more general trailing edge flows. Our purpose is to extend Riley and Stewartson's work for flows in a vicinity of a trailing edge inclusing a small region of separated flow. Riley and Stewartson have shown that, for a wedge like trailing edge, separation starts at the trailing edge when $\varepsilon = O(R^{-1/4})$, where R is the overall Reynolds number, while Brown and Stewartson have shown that this occurs under pure angle of attack effect when $\alpha = O(R^{-1/4})$. Guiraud [2] deals with the case when $\varepsilon^{-4} R^{-1/4} \ll 1$, $\alpha \ll (\varepsilon^{-4}R^{-1/4})^{1/4}$ shows that a small separation bubble occurs, of extent $\varepsilon^{1/2}(\varepsilon^{-4}R^{-1/4})^{-1/2}$. The bubble is slightly unsymetrical due to angle of attack effect which acts on zero angle of attack trailing edge flow as a small perturbation of order $\alpha(\varepsilon^{-4}R^{-1/4})^{-1/4}$. For pure two dimensional flow or for three-dimensional flow, provided $R^{-1/4} \ll \varepsilon \ll R^{-1/16}$ the flow in

* Also : Université Paris VI -
Laboratoire de Mécanique Théorique
associé au CNRS
Tour 66 - Place Jussieu
75230 PARIS CEDEX 05

the separated region consists in two counter rotating vortices which are locally two dimensional in planes normal to the trailing edge, with constant vorticity.

Here we extend this work by looking at the process of separation, which was just shown to rule the whole trailing edge flow, whithout considering it in any detail. We show that the process of separation is formally identical with the one considered by Sytchev [1] for bluff bodies.

2 - The overall triple deck structure

We use dimensionless coordinates x_4, y_4, z_4 near the (planar) trailing edge Γ, such that ξ_4 is length along Γ while x_4 and z_4 are cartesian coordinates in the plane normal to Γ, oriented in such a way that $z_4 = 0$ coincides with the skeleton of the wing, this last one having, locally, the equation $z_4 = \pm \varepsilon [x_4 m(y_4) + O(x_4^2)]$. We assume that $z_4 > 0$ is leeward, that the speed at infinity is unity and that its projection on the planform of the wing makes an angle φ with the normal to Γ (see figure 1). For the dimensionless components of velocity we use u_4, v_4, w_4 and, for the dimensionless pressure, we use $p = p_\infty + p_4$. The flow near the trailing edge has a triple deck structure with an embedded recirculation zone. Within the outer deck we have:

$$
(1)\quad \begin{cases}
x_4 = \Delta x\ ,\ y_4 = y\ ,\ z_4 = \Delta z\ ,\ \Delta = \varepsilon^{3/8}\mu^{-1}\ ,\ \mu = (\varepsilon^{-1}R^{-1/2})^{1/6} \\
u_4 = \cos\varphi\left(1 + \varepsilon\frac{m}{\pi}\mathrm{Log}\,\Delta\right) + \varepsilon U_e(y) \pm \alpha U_i(y) + \varepsilon u_e + \alpha\Delta^{3/4}u_i + \cdots \\
v_4 = -\sin\varphi + \varepsilon V_e(y) \pm \alpha V_i(y) + \cdots \\
p_4 = \varepsilon w_e + \alpha\Delta^{1/2} w_i + \cdots \\
p_4 = \cos\varphi\left(-\varepsilon\mathrm{Log}\,\Delta\frac{m}{\pi}\cos\varphi - \varepsilon U_e \pm \alpha U_i\right) + \sin\varphi\left(\varepsilon V_e \pm \alpha V_i\right) + \\
\qquad + \varepsilon p_e + \alpha\Delta^{1/2} p_i = P_e + \varepsilon p_e + \alpha\Delta^{1/2} p_i
\end{cases}
$$

where U_e, U_i, V_e and V_i are known functions of y (from a lifting surface theory numerical computation). On the other hand we have:

$$
(2)\quad p_{e,i} + u_{e,i}\cos\varphi = 0\ ,\quad u_{e,i} - i\,w_{e,i} = f_{e,i}(x+iz)
$$

where f is holomorphic within the domain exterior to AIKJB (see figure 2). All along AIKL and BJKL the slip condition holds, while along the free streamlines IK and JK we have

$$
(3)\quad Re(f) = u_3 + (8\cos\varphi)^{-1}\cdot\left(\hat\omega^{\pm}\cdot\hat H^{\pm}(z)\right)^2 .
$$

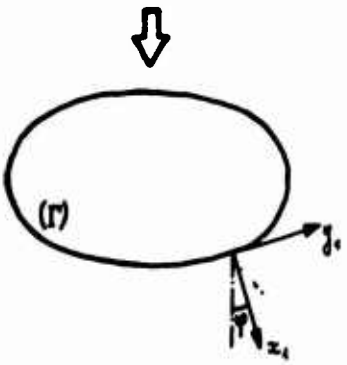

Fig. 1

The upper sign refers to the upper (leeward) free streamline ; $\varepsilon\Delta\hat H^{\pm}$ is the local thickness of the (upper or lower) vortex while $\pm\varepsilon^{-2}\mu^3\hat\omega^{\pm}$ is the corresponding value of the constant voricity.

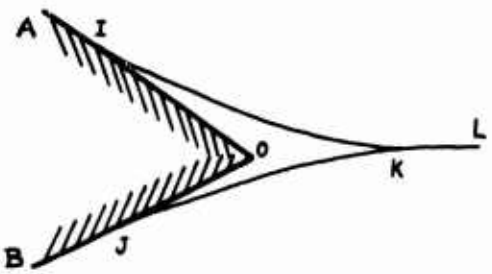

Fig. 2

We refer to [2] for some details concerning this flow and we merely quote here a few results. First we observe that $\alpha\Delta^{1/2} = \varepsilon\alpha\varepsilon^{-1/4}\mu^{-1/2}$ so that the term in $\alpha\Delta^{1/2}$ is a small perturbation due to angle of attack effect superposed on the symmetrical pattern. Second, when $\hat\omega^{+} = \hat\omega^{-} = 0$, the shape of IKL and JKL is given by

$$
(4)\quad x + iz - \alpha\varepsilon^{-1/4}\mu^{-1/2}\frac{i\pi B(y)}{m\cos\varphi}(x+iz)^{3/2} = a\left[\cos\chi + \varepsilon\frac{im}{\pi}\cdot(\sin\chi - \chi\cos\chi)\right]
$$

When $\hat\omega^{+}$ and $\hat\omega^{-}$ are not zero the shapes are changed but the positions of the three points IJK are not. The function B(y) is to be computed from the linearized, inviscid, distribution of lift on the wing. Note the asymmetry associated with the angle of attack. Our third point is that, close to separation, from upstream, we have a square root singularity in the pressure, namely:

$$
(5)\quad \begin{cases}
p = p_s - \left(\frac{z}{a}\right)^{1/2} K\cos\varphi\ \ J^{\pm}(x_s - x)^{1/2} + \cdots \\
J^{\pm} = 1 \pm \alpha\varepsilon^{-1/4}\mu^{-1/2}\frac{3\pi B}{4m\cos\varphi}(-x_s)^{1/2} \\
x_s = -a\left(1 \mp \alpha\varepsilon^{-1/4}\mu^{-1/2}\frac{\pi B}{m\cos\varphi}a^{1/2}\right)
\end{cases}
$$

We observe that the coefficient of the singularity is of a definite sign, corresponding to a pressure rise, as is shown by the following formula :

$$
(6)\quad K = \frac{m\cos\varphi}{\pi} + \frac{1}{8\pi\cos\varphi}\int_{-1}^{+1}\frac{\left[\hat\omega^{\pm}\hat H^{\pm}(\xi)\right]^2}{(1+\xi)\sqrt{1-\xi^2}}\,d\xi
$$

where $\xi = \cos\chi$. Note that K is the same for the leeward and windward sides because of $\hat\omega^{+}\hat H^{+} = \hat\omega^{-}\hat H^{-}$ which is required for continuity of pressure accross OK.

We refer to [2] for the flow within IKJOI and we deal now with the main deck which is a continuation of the slightly perturbed Blasius boundary layer. We have:

$$
(7)\quad \begin{cases}
x_4 = \Delta\tilde x\ ,\ y_4 = \tilde y\ ,\ z_4 = \varepsilon\Delta F(\tilde x,\tilde y) + R^{-1/2}\tilde z\ ,\ p_4 = P_e + \varepsilon\tilde p_e + \alpha\Delta^{1/2}\tilde p_i \\
u_4 = \tilde u\ ,\ v_4 = \tilde v\ ,\quad w_4 = \varepsilon F_{\tilde x}\tilde u + \varepsilon\Delta F_{\tilde y}\tilde v + \Delta^{-1}R^{-1/2}\tilde w
\end{cases}
$$

with

$$
(8)\quad \begin{cases}
\tilde u = U_e(\tilde z) + \varepsilon^{3/8}\mu A_e(\tilde z)\frac{dU_e}{d\tilde z} + \varepsilon^{1/2}\mu\alpha\varepsilon^{-1/4}\mu^{-1/2}\delta^{-1/2}\tilde u_{s0}(\tilde z) + \\
\qquad + \varepsilon^{3/8}\mu\alpha\varepsilon^{-1/4}\mu^{-1/2}A_i(\tilde z)\frac{dU_e}{d\tilde z} + \cdots \\
\tilde v = V_e(\tilde z) - \varepsilon^{3/8}\mu A_e(\tilde z)\frac{dV_e}{d\tilde z} - \varepsilon^{3/8}\mu\alpha\varepsilon^{-1/4}\mu^{-1/2}A_i(\tilde z)\frac{dV_e}{d\tilde z} + \cdots \\
\tilde w = -\varepsilon^{3/8}\mu A_e'(\tilde z)U_e - \varepsilon^{3/8}\mu\alpha\varepsilon^{-1/4}\mu^{-1/2}A_i'(\tilde z)U_e + \cdots
\end{cases}
$$

where $U_o(\tilde{\bar{y}})$ and $V_o(\tilde{\bar{y}})$ may be obtained from the Blasius solution and where Ae and Ai are arbitrary functions. We point out that (8) refers to the leeward side.

Within the lower layer we get :

$$(9)\quad \begin{cases} x_1 = \Delta\bar{x}\ ,\ y_1 = \bar{y}\ ,\ z_1 = \varepsilon\Delta F(\bar{x},\bar{y}) + R^{-1/2}\delta\bar{z} \\ u_1 = \delta\bar{u}\ ,\ v_1 = \delta\bar{v}\ ,\ w_1 = \varepsilon\delta F_{\bar{x}}\bar{u} + \varepsilon\Delta\delta F_{\bar{y}}\bar{v} + \delta\Delta^{-1}R^{-1/2}\bar{w} \\ p_1 = P_o + \varepsilon\bar{p}_e + \alpha\Delta^{1/2}\bar{p}_i \quad \text{with}: \ \delta = \Delta^{1/3} = \varepsilon^{1/2}\mu^{-1} \end{cases}$$

and we have :

$$(10)\quad \begin{cases} \bar{u}\dfrac{\partial\bar{u}}{\partial\bar{x}} + \bar{w}\dfrac{\partial\bar{u}}{\partial\bar{y}} + \mu^2\dfrac{d\bar{p}_e}{d\bar{x}} + \mu^2\alpha\varepsilon^{-1/4}\mu^{-3/2}\dfrac{d\bar{p}_i}{d\bar{x}} - \dfrac{\partial^2\bar{u}}{\partial\bar{y}^2} = O(\Delta) \\ \mu^2\dfrac{\partial\bar{p}_e}{\partial\bar{y}} + \mu^2\alpha\varepsilon^{-1/4}\mu^{-3/2}\dfrac{\partial\bar{p}_i}{\partial\bar{y}} = O(\varepsilon^2) + O(R^{-1/2}) \\ \dfrac{\partial\bar{u}}{\partial\bar{x}} + \dfrac{\partial\bar{w}}{\partial\bar{y}} = O(\Delta) \\ \bar{u}\dfrac{\partial\bar{v}}{\partial\bar{x}} + \bar{w}\dfrac{\partial\bar{v}}{\partial\bar{y}} - \dfrac{\partial^2\bar{v}}{\partial\bar{y}^2} = O(\Delta) \\ \bar{y} = 0\ ,\ \bar{x} < \bar{x}_s \ : \ \bar{u} = \bar{v} = \bar{w} = 0 \\ \bar{x} \to -\infty \ : \ \bar{u} \to K\bar{y}\ ,\ \bar{v} \to L\bar{y} \\ \bar{y} \to +\infty \ : \ \bar{u} \sim K\bar{y} \end{cases}$$

We observe that $\bar{p}_e$ and $\bar{p}_i$ are known from the solution of the outer deck. Consider the symmetrical problem $\alpha = 0$, near separation we have :

$$(11)\quad \bar{p}_e = \bar{p}_{e_s} - \bar{\omega}_e\left(\bar{x}_s - \bar{x}\right)^{1/2} + \cdots\ ,\quad \bar{\omega}_e = \left(\frac{2}{a}\right)^{1/2} K\cos\varphi$$

and may find, near separation, a Goldstein type of expansion :

$$(12)\quad \begin{cases} \bar{u} = K\bar{y} + \mu^2\left[K^{-1}\bar{\omega}_e\xi^{1/2}F_1'(\eta) + \cdots\right] \\ \eta = \left(K\xi^{-1}\right)^{1/3}\bar{y}\ ,\ \xi = \bar{x}_s - \bar{x} \end{cases}$$

with

$$(13)\quad F_1''' - \frac{\eta}{3}F_1'' + \frac{1}{2}\left(\eta F_1' - F_1\right) + \frac{1}{2} = 0\ ,\ F_1(0) = F_1'(0) = 0$$

Near $\eta = \infty$ we get :

$$(14)\quad F_1 \sim \alpha_1\eta^{3/2} + \alpha_2\eta + \alpha_3 + O\left(\eta^{-3/2}\right)$$

and, consequently, we find a second (outer) type of Goldstein's expansion for $\xi \to 0$, $\bar{y}$ fixed,

$$(15)\quad \bar{u} = K\bar{y} + \mu^2\left[\frac{3}{2}\alpha_1 K^{-1/2}\bar{\omega}_e\bar{y}^{1/2} + \alpha_2 K^{-2/3}\bar{\omega}_e\xi^{1/2} + \cdots\right]$$

For the angle of attack effect we have:

$$(16)\quad \bar{p}_i = \bar{p}_{i_s} \mp \bar{\omega}_{i,1}\left(-a - \bar{x}\right)^{-1/2} \mp \bar{\omega}_{i,2}\left(-a - x\right)^{1/2} + \cdots$$

and, consequently we find :

$$(17)\quad \bar{u} = K\bar{y} + \mu^2\bar{u}_1 + \mu^2\alpha\varepsilon^{-1/4}\mu^{-3/2}\left[\pm K^{-2/3}\bar{\omega}_{i,2}\xi^{-1/6}F_2'(\eta) \pm K^{1/3}\bar{\omega}_{i,1}\xi^{1/6}F_1'(\eta) + \cdots\right]$$

with

$$(18)\quad F_2''' - \frac{\eta}{3}F_2'' - \frac{1}{2}\left(\eta F_2' - F_2\right) - \frac{1}{2} = 0\ ,\ F_2(0) = F_2'(0) = 0$$

Near $\eta = \infty$ we obtain :

$$(19)\quad F_2 \sim h_1\eta + h_2 + O\left(\eta^{-1/2}\right)$$

and, consequently we get the outer type of Goldstein's expansion for $\xi \to 0$, $\bar{y}$ fixed :

$$(20)\quad \bar{u} = K\bar{y} + \mu^2\left[\cdots\right] + \mu^2\alpha\varepsilon^{-1/4}\mu^{-3/2}\left[\text{const.}\ \bar{y}^{-1/2} + \text{const.}\ \xi^{-1/6} + \text{const.}\ \xi^{1/6} + \cdots\right]$$

3 - Separation

From no on we assume that the angle of attack is zero. The expansions 2(12) and 2(15) break down when $\bar{y}$, $\mu^2\xi^{1/6}$ and $\mu^2\bar{y}^{1/3}$ are of the same order. This occurs when $\xi = O(D_1)$, $\bar{y} = O(D_2)$ with

$$(1)\quad D_1 = \mu^{12} = \left(\varepsilon^{-1}R^{-1/4}\right)^2\ ,\ D_2 = \mu^4 = \left(\varepsilon^{-1}R^{-1/4}\right)^{4/3}$$

from which we argue that, if separation occurs through a triple deck, this one must have length $\Delta D_1 = R^{-1/3}$ and thicknesses $\delta D_2 R^{-1/3} = R^{-5/12}$, $R^{-1/3}$ and $R^{-1/4}$ respectively. We observe that these are precisely the length scales which occur in the self induced separation model of Neiland [5] and Stewartson and Williams [9] as well as in other free-interaction schemes ar. , for example in the model of separation by a free interaction process as demonstrated by Sytchev [10] and Messiter and Enlow [.]. We point out that the main deck of our embedded triple deck contains, indeed, two layers which are respectively the continuations of the lower and main decks for the overall triple deck. Within the upper layer of the main deck we find, with the notations of 2(7) :

$$(2)\quad \begin{cases} \tilde{u} = U_o(\tilde{\bar{y}}) + \varepsilon^{1/2}\mu\,\tilde{u}_1(\tilde{\bar{y}}) + \varepsilon^{1/2}\mu\,\text{Log}\,\mu\,\tilde{u}_2(\tilde{\bar{y}}) + \\ \qquad + \varepsilon^{1/2}\mu^3\left\{\tilde{u}_3(\tilde{\bar{y}}) + b_1 A\left[\left(\tilde{x} - \tilde{x}_s\right)/aD_1\right]\cdot\dfrac{dU_o}{d\tilde{\bar{y}}}\right\} + \cdots \\ \tilde{w} = -\varepsilon^{1/2}\mu^3 D_1^{-1}b_1 a_1^{-1}A'\left[\left(\tilde{x} - \tilde{x}_s\right)/aD_1\right]\cdot U_o(\tilde{\bar{y}}) + \cdots \end{cases}$$

where a_1 and b_1 are numerical constants which are introduced for further convenience, while $\tilde{u}_n(\tilde{\bar{y}})$ are arbitrary functions. The function $A(X)$ is to be determined when solving the free-interaction problem. The functions $\tilde{u}_n(\tilde{\bar{y}})$ should be determined from matching with the main deck of the overall triple deck.

Within the lower layer of the main deck we have, with the notations of 2 (9):

$$(3)\quad \begin{cases} \bar{u} = K\bar{y} + \mu^2\bar{u}_1(\bar{y}) + \mu^4\,\text{Log}\,\mu\,\bar{u}_{2,0}(\bar{y}) \\ \qquad + \mu^4\left\{\bar{u}_2(\bar{y}) + Kb_1 A\left[\left(\bar{x} - \bar{x}_s\right)/aD_1\right]\right\} + \cdots \\ \bar{w} = -\mu^4 D_1^{-1}b_1 a_1^{-1}A'\left[\left(\bar{x} - \bar{x}_s\right)/aD_1\right]\cdot K\bar{y} + \cdots \end{cases}$$

where $\bar{u}_1$, $\bar{u}_{1,0}$ and $\bar{u}_2$ are arbitrary functions of $\bar{\xi}$ which are to be determined from matching with the lower deck of the overall triple deck. The function A is the same in (2) and (3).

Within the lower deck (of the embedded triple deck) we find*

$$(4)\quad \begin{cases} x_1 = \Delta \bar{x}_0 + a_1 \Delta D_1 X \ , \quad z_1 = \varepsilon \Delta F^* + b_1 \delta D_2 R^{-1/8} Z \\ u_1 = c_1 \delta D_2 U \ , \quad p_1 = P_0 + \varepsilon \bar{p}_2 + \varepsilon D_1^{1/2} d_1 P \\ w_1 = \varepsilon \delta D_2 F_{\bar{x}}^* c_1 U + \varepsilon \Delta F_{\bar{z}}^* v_1 + (\delta D_2)^2 (\Delta D_1)^{-1} R^{-1/8} c_1 b_1 a_1^{-1} W \end{cases}$$

and

$$(5)\quad \begin{cases} U \dfrac{\partial U}{\partial X} + W \dfrac{\partial U}{\partial Z} + \dfrac{dP}{dX} = \dfrac{\partial^2 U}{\partial Z^2} \\ \dfrac{\partial U}{\partial X} + \dfrac{\partial W}{\partial Z} = 0 \end{cases}$$

provided :

$$(6)\quad a_1 = c_1 b_1^2 \ , \quad d_1 = c_1^2 \ , \quad c_1 = K b_1$$

within the upper deck we have :

$$(7)\quad \begin{cases} x_1 = \Delta \bar{x}_0 + a_1 \Delta D \check{x} \\ z_1 = \varepsilon \Delta F + a_1 \Delta D_1 \check{z} \\ u_1 = U_0 + \varepsilon \bar{u}_2 + \varepsilon D_1^{1/2} \check{u} \\ w_1 = \varepsilon F_{\bar{x}} u_1 + \varepsilon \Delta F_{\bar{z}} v_1 + \varepsilon D_1^{1/2} \check{w} \\ p_1 = P_0 + \varepsilon \bar{p}_2 + \varepsilon D_1^{1/2} \check{p} \end{cases}$$

and

$$(8)\quad \begin{cases} \check{p} + \cos\varphi \, \check{u} = 0 \\ \check{u} - i \check{w} = f(\check{x} + i \check{z}) \end{cases}$$

So that, through matching with the upper layer of the main deck, we set :

$$(9)\quad P(X) - i A'(X) = F(X + i0)$$

provided

$$(10)\quad a_1 d_1 = b_1 \cos^2\varphi$$

The relations (6) and (10) fully determine the constants a_1, b_1, c_1, d_1. Matching the pressure with 2(11) we find :

$$(11)\quad X \to -\infty : \ P(X) \sim -\lambda (-X)^{1/2} \ , \quad \lambda = \bar{\omega}_0 a_1^{1/2} d_1^{-1}$$

The behaviour of U and W for $X \to -\infty$ is found through a Goldstein's type of expansion, according to Sytchev [10], namely :

$$(12)\quad U = \frac{\partial \Psi}{\partial y} \ , \quad W = -\frac{\partial \Psi}{\partial X}$$

*We have made a small change from 2(9), F^* now stands for the equation of the upper surface of the wing.

$$(13)\quad \begin{cases} \Psi = \xi^{3/8} \left\{ \frac{1}{2}\eta^2 + \lambda \xi^{-1/4} f_0(\eta) + \lambda^2 \xi^{-1/2} f_1(\eta) + \lambda^3 \xi^{-3/4} f_2(\eta) + \cdots \right\} \\ \xi = -X \ , \quad \eta = Z/(-X)^{3/8} \end{cases}$$

where :

$$(14)\quad \begin{cases} f_1''' - \frac{1}{3}\eta^2 f_1'' + \frac{1}{2}(\eta f_1' - f_1) + \frac{1}{2} = 0 \ , \quad f_1(0) = f_1'(0) = 0 \\ f_2''' - \frac{1}{3}\eta^2 f_2'' + \frac{1}{3}(\eta f_2' - f_2) = \frac{1}{2} f_0 f_0'' - \frac{1}{6} f_1'^2 \ , \quad f_2(0) = f_2'(0) = 0 \\ f_3''' - \frac{1}{3}\eta^2 f_3'' + \frac{1}{6}(\eta f_3' - f_3) = \frac{1}{2} f_0 f_1'' + \frac{1}{2} f_1 f_2'' - \frac{1}{6} f_1' f_2' \\ \qquad \text{with : } f_3(0) = f_3'(0) = 0 \\ f_4''' - \frac{1}{3}\eta^2 f_4'' = \frac{1}{2} f_0 f_3'' + \frac{1}{3} f_1 f_2'' + \frac{1}{6} f_2 f_3'' \ , \quad f_4(0) = f_4'(0) = 0 \end{cases}$$

The behaviour of the f_K for large η is :

$$(15)\quad \begin{cases} f_1 \sim \alpha_1 \eta^{3/2} + \alpha_2 \eta + \alpha_3 + O(\eta^{-3/2}) \\ f_2 \sim \beta_1 \eta \log\eta + \beta_2 \eta + \beta_3 \eta^{1/2} + \beta_4 + O(\eta^{-5/2}) \\ f_3 \sim \gamma_1 \eta + \gamma_2 \eta^{1/2} \log\eta + \gamma_3 \eta^{1/2} + \gamma_4 \log\eta + \gamma_5 + o(1) \\ f_4 \sim \delta_1 \eta + \delta_2 \eta^{1/2} + \delta_3 (\log\eta)^2 + \delta_4 \log\eta + \delta_5 + o(1) \end{cases}$$

As a consequence, for $X \to -\infty$, $Z \to \infty$ in such away that $Z/(-X)^{3/8} \to \infty$ we get

$$(16)\quad \begin{aligned} U = Z &+ \tfrac{3}{2}\lambda \alpha_1 Z^{1/2} + \lambda^2 \beta_1 \log Z + \\ &+ \left(\alpha_2 \lambda \xi^{1/8} - \frac{\beta_1}{3}\lambda^2 \log\xi + \lambda^2 \beta_2 + \lambda^6 \beta_2 + \gamma_1 \lambda^3 \xi^{-1/8} + \cdots \right) \\ &+ \frac{\gamma_2}{2}\lambda^3 Z^{-1/2} \log Z + Z^{-1/2} \left(\frac{\beta_1}{2}\lambda^2 \xi^{1/8} - \frac{\gamma_2 \lambda^3}{6} \log\xi + \gamma_2 \lambda^3 + \frac{\gamma_3 \lambda^3}{2} \right) \\ &+ \cdots \end{aligned}$$

A comparison of (16) with (3) shows, first, that, when $\bar{z} \to 0$, we have

$$(17)\quad \begin{cases} \bar{u}_1 \sim \frac{3}{2} c_1 b_1^{-3/8} \bar{z}^{1/2} \\ \bar{u}_{1,0} \sim -c_1 \beta_1 \lambda^2 \\ \bar{u}_2 \sim c_1 \beta_1 \lambda^2 \log\bar{z} - c_1 \beta_1 \lambda^2 \log b_1 \end{cases}$$

while, for $X \to -\infty$:

$$(18)\quad A(X) \sim \alpha_1 \lambda (-X)^{3/2} - \frac{\beta_1 \lambda^3}{3} \log(-X) + \beta_1 \lambda^2 + \beta_2 \lambda^2 + \gamma_1 \lambda^{1/2} (-X)^{-1/8} + \cdots$$

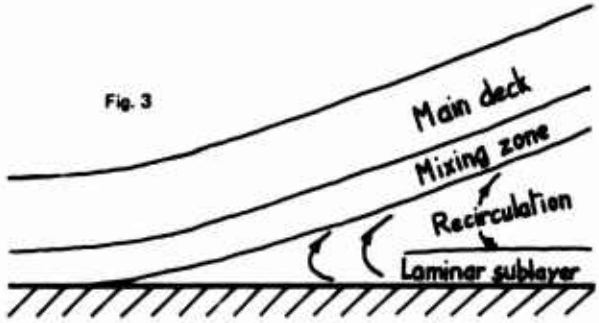

Fig. 3

Near $X = +\infty$, an asymptotic solution of (5) with three layers (see figure 3) like the one of Sytchev [10] is under current study and will be reported later. It appears that :

$$(19)\quad P(X) \sim \pi_0 X^{-3/8} + \pi_1 X^{-7/8} + \pi_2 X^{-5/4} + \cdots$$

with Π_4 probably zero. The outer layer is a mixing layer between the continuation of the main deck and the recirculation zone ; within this mixing layer we have :

$$(20)\quad X = \xi \ , \ Z = G(\xi) + \xi^{3/4}\zeta \ , \ \Psi = \xi^{5/4} g_0(\zeta) + \cdots$$

with

$$(21)\quad \begin{cases} g_0''' + \frac{5}{4} g_0 g_0'' - \frac{1}{2} g_0'^2 = 0 \ , \ g_0(0) = 0 \\ \zeta \to +\infty : \ g_0 \sim \frac{1}{2}\zeta^2 + q_0\zeta + A_0 \ , \ \zeta \to -\infty : g_0 \to -C \end{cases}$$

C and q_0 are two numerical constants which are determined through numerical integration. The value of q_0 depends on the choice $g_0(0) = 0$ which states that $Z = G(X) + o(X^{3/4})$ is asymptotically the equation of the dividing streamline issued from the point of separation.

Within the recirculation zone we find :

$$(22)\quad X = \xi \ , \ Z = \xi^{3/4}\eta \ , \ \Psi = \xi^{11/4} f_0(\eta) + \cdots$$

with :

$$(23)\quad \frac{13}{10} f_0 f_0'' + \frac{1}{2} f_0'^2 + \Pi_0 = 0$$

The solution is easily found and matching with the mixing layer is effected along $\eta = G_0$ such that : $f_0(G_0) = f_0(0) = 0$.

Near $\eta = 0$, we find :

$$f_0 \sim k\eta^{13/7} + O(\eta^{23/7}) \ , \ f_0' \sim \frac{13}{7} k \eta^{6/7} + O(\eta^{16/7})$$

with

$$k = -D^{5/13}\left(\frac{7\sqrt{2\Pi_0}}{13}\right)^{13/7}$$

and it is seen that the no slip condition at the wall does not holds, which shows the necessity of a viscous sublayer. Within this laminar sublayer we find :

$$(24)\quad X = \xi \ , \ Z = \theta \xi^{7/31} \ , \ \Psi = \xi^{11/31} h_0(\theta) + \cdots$$

with :

$$(25)\quad \begin{cases} h_0''' + \frac{13}{31} h_0 h_0'' + \frac{5}{31} h_0'^2 = 0 \\ h_0(0) = h_0'(0) = 0 \ , \ \theta \to \infty : h_0 \sim k\theta^{13/7} \end{cases}$$

We have demonstrated that the problem of incipient separation at a trailing edge is formally identical with the one for separation in the flow around a bluff body as was formulated by Sytchev [10], namely :

$$(26)\quad \begin{cases} U\frac{\partial U}{\partial X} + W\frac{\partial U}{\partial Z} + \frac{dP}{dX} - \frac{\partial^2 U}{\partial Z^2} = 0 \ , \ \frac{\partial U}{\partial X} + \frac{\partial W}{\partial Z} = 0 \\ Z \to +\infty : U \sim Z + \frac{3}{4} a_1 d Z^{3/4} + \beta_1 d^4 \log Z + A(X) \\ X \to -\infty : (11), (12), (13) \text{ hold} \\ X \to +\infty : (12), (19), (20), (22), (24) \text{ hold} \\ P - iA' = F(X + iO) \end{cases}$$

We observe that the definition of (26) contains one undetermined constant λ which enters into the problem through (11). If one tries to find a solution for small λ through linearisation one finds none. There does not exist a continuum of solutions which tend to $U = Z$, $W = 0$ when $\lambda = 0$. We do not know whether there exists any solution to (26) but we may conjecture that there is a smaller value of λ for which there exists a solution. Either the spectrum of values of λ is discrete or it is a continuum. If the first situation holds then this allows to determine the position of separation through the determination of $\bar{\omega}_0$ by (11) and then of a through 2 (11) and 2 (6). The research of a numerical solution of (26) is a formidable problem which has not been explored as yet.

References

1. S.N. Brown and K. Stewartson (1970) - Trailing edge stall - J. Fluid Mech. 42, n°3, p.561-584.
2. J.P. Guiraud (1974) - Ecoulement décollé au voisinage du bord de fuite d'une aile mince tridimensionnelle - Jal de Mécanique 13, 3, p. 1-24.
3. A.F. Messiter (1970) - Boundary layer flow near the trailing edge of a flat plate - SIAM J. Appl.Math. vol. 18, n° 1, p.241-257.
4. A.F. Messiter and R.L. Enlow (1973) - A model for laminar boundary-layer flow near a separation point - SIAM J. Appl.Math. vol.25, n°4, p.653-670.
5. V. Ya. Neiland (1971) - Flow behind the boundary layer separation point in a supersonic stream.- Mekh.Zhidk.gaza 6, n°3, p.19-25.
6. N. Riley and K. Stewartson(1969) - Trailing edge flows - J.Fluid Mech.,vol.39,n°1, p.193-207.
7. K. Stewartson (1968) - On the flow near the trailing edge of a flat plate I - Proc.Roy.Soc. A, vol.306, p.275-290.
8. K. Stewartson (1969) - On the flow near the trailing edge of a flat plate II - Mathematika vol. 16, n°1, p.106-121.
9. K. Stewartson and P.G. Williams (1969) - Self induced separation - Proc.Roy.Soc.A, vol. 312, p.181-206.
10. V.V. Sytchev (1972) - Sur la séparation laminaire - Mekh.Zhidk.Gaza, n°3, p.47-59.
11. A.I. Van de Vooren and D. Dijkstra (1970) - The Navier-Stokes solution for laminar flow past a semi-infinite flat plate - J.Eng. Math., 4, p.9-27.

LAMINAR SEPARATION – A LOCAL ASYMPTOTIC FLOW DESCRIPTION FOR CONSTANT PRESSURE DOWNSTREAM

A.F. Messiter
Professor
Department of Aerospace Engineering
The University of Michigan
Ann Arbor, Michigan 48105
U.S.A.

SUMMARY

A theoretical model is proposed for the description of two-dimensional, steady, incompressible, laminar boundary-layer flow near a separation point. It is assumed that the pressure just downstream of separation is approximately constant, and asymptotic solutions are then sought for large Reynolds number and small distance. The first two terms of the complex perturbation velocity in the external flow are shown to imply a pressure gradient upstream which is generally favorable, and adverse only for a short distance. This representation is no longer valid in a small neighborhood of the separation point where an interaction of the boundary layer with the external flow must be taken into account. Solutions are obtained for the boundary layer just upstream and, with an additional assumption, for the region of backflow just downstream of this region. These results represent a composite of the solutions derived in two earlier studies. A brief review and extension are also given for an asymptotic model of the complete wake behind a circular cylinder, with the assumption of nonzero drag at infinite Reynolds number.

1. INTRODUCTION

The primary difficulty in the development of a theory for steady separated flows at high Reynolds number is that the external potential flow, the flow in the boundary layers and separated shear layers, and the recirculating wake flow must be determined simultaneously. In particular, for incompressible flow past a bluff body such as a circular cylinder, it should be expected that even the flow details close to a separation point can be studied only in terms of an interaction of the boundary layer with the local external flow. It would seem to follow that at least some general information about the wake is needed before a description of separation can be undertaken.

For a prescribed adverse pressure gradient, numerical solutions of the boundary-layer equations have implied the presence of a singularity at separation. Goldstein[1] studied the boundary-layer flow approaching a separation point, assuming a nearly constant local adverse pressure gradient, and showed that the streamline slope may increase as the inverse square root of the distance from separation. His solution was expressed by asymptotic expansions of coordinate type, one in terms of a similarity variable for a thin sublayer and one in terms of the usual boundary-layer coordinate for the remainder of the layer. He also showed that there exists no solution downstream of separation which is consistent with these results for the solution upstream. Goldstein's analysis was later extended by Stewartson[2] and its implications were studied in detail by Kaplun.[3] Stewartson[4] also considered the possibility of a local boundary-layer interaction with the external flow and showed that no local interaction solution exists which is consistent with the Goldstein singularity.

Of the various models proposed for the wake behind a bluff body placed in a uniform stream, those which seem to be quoted most frequently are related in some way to free-streamline theory, with the pressure taken equal to its undisturbed value all along the separation streamlines. For a circular cylinder a family of solutions is available, with differing locations for the separation points (e.g., Thwaites[5]). The most reasonable choice is usually considered to be the one solution having continuous streamline curvature at separation, for which the separation points are located at about 56° from the forward stagnation point. Earlier separation is precluded because the predicted separation streamline would then lie partly inside the body. Separation further downstream would lead to an infinite adverse pressure gradient at separation, and the boundary layer would be expected to separate before that point is reached.

An objection to the free-streamline theory is that measured base pressures at Reynolds numbers of 10^4 or 10^5, such that the boundary layers are laminar at separation, are considerably lower than the undisturbed pressures. Roshko[6] and Woods[7] have attempted to improve the agreement with experiment by introducing modifications permitting variable pressure behind the cylinder. Roshko[8] has also pointed out that unsteadiness in the wake will lower the base pressure, and suggests that a complete theory should take this into account for prediction of the pressures actually observed at these Reynolds numbers.

Another possible objection to the free-streamline theory is that the distance between the separation streamlines grows parabolically as the distance from the body becomes large, and so the wake is not closed. This feature seems unacceptable because a small backflow at infinity would be required to supply the mass required for entrainment in the separated shear layers and because a steady-state closed wake is known to exist at lower Reynolds numbers. One expects instead that the wake length should increase

continuously as the Reynolds number increases (possibly to a finite limiting value as suggested by Batchelor[9]) and that at large distance the flow velocity should approach the undisturbed value. Thus the free-streamline theory taken alone does not seem to provide the correct asymptotic solution of the Navier-Stokes equations for steady flow past a bluff body in the limit as the Reynolds number tends to infinity.

Roshko[10] and Sychev[11] have outlined a possible asymptotic solution for which the wake length grows linearly with Reynolds number. The basic assumption is that the drag of the body is nonzero in the limit, with the wake pressure taken to be approximately constant and equal to the undisturbed pressure. At a distance downstream of the order of the typical body dimension, the separation streamlines are as predicted by free-streamline theory. The velocity just outside these streamlines is approximately the free-stream value, and the fluid between them has much smaller velocity. The viscous shear layers separating these regions will grow in thickness with increasing distance downstream, and will eventually come together at a large distance such that the shear layer thickness calculated according to boundary-layer theory is of the same order as the body thickness. For a proper choice of the wake length, the fluid which continues downstream then has a momentum deficit equal to the body drag. The distance between the separation streamlines is proportional to the square root of the Reynolds number, for matching with the free-streamline solution near the body.

The wake models related to free-streamline theory show a generally favorable pressure gradient upstream of separation, implying that the adverse pressure gradient required for separation might occur only over a distance which decreases to zero as the Reynolds number tends to infinity. If this is true, the velocity profile approaching separation is linear near the wall, rather than quadratic as in the Goldstein theory. A local interaction with the external flow then has the same form as given in other applications by Stewartson and Williams,[12] Stewartson,[13] Messiter,[14] and others. In the limit as the Reynolds number becomes arbitrarily large, viscous forces are important primarily in a thin sublayer adjacent to the wall, and the increase in displacement thickness of this sublayer leads to an outward displacement of the streamlines in the remainder of the boundary layer. The pressure changes associated with the resulting streamline deflections in the external flow must be the same as the pressure changes in the sublayer, since the interaction occurs over a distance somewhat larger than the boundary-layer thickness and the streamline curvature remains small.

The possibility of studying the flow near separation by combining a local-interaction description with the leading terms of a free-streamline solution has been shown by Sychev[15] and by Messiter and Enlow.[16] The idea is that for a circular cylinder the separation point is displaced downstream from the 56° point by an amount which decreases as the Reynolds number increases. There is then a singularity in pressure gradient which decreases in strength as the Reynolds number tends to infinity. A term in the external-flow solution which implies constant pressure downstream and is consistent with the interaction formulation was proposed by Sychev, and its implications were studied in detail both upstream and downstream of separation. The term in the external-flow solution corresponding to smooth separation was studied by Messiter and Enlow, especially with reference to the upstream boundary-layer flow, by expansions analogous to those of Goldstein's theory. These results have been reviewed by Lagerstrom[17] and by Stewartson.[18]

The results to be presented here are primarily a review of work already published, but an attempt has been made to unify the results and to develop a few extensions of earlier work which are needed for this purpose. The next section summarizes the solutions given by Sychev and by Messiter and Enlow, in a combined form. For the assumed pressure gradient it is shown that the velocity profile near the surface must have a specified form for compatibility with the wall boundary conditions. The formulation of a local interaction problem is then reviewed in the present context. A solution for the backflow is derived for the assumption that the mass in the backflow is exactly equal to the mass required for entrainment in the separated shear layer. It is to be emphasized that the assumption of constant pressure just downstream is a local one and does not necessarily imply a free-streamline model for the wake. In the last section the wake model proposed by Roshko and by Sychev is discussed, and the possibility of an infinite sequence of vortices below the separation streamline is considered.

2. THE FLOW MODEL NEAR SEPARATION

The local external flow

It is convenient to begin by considering the family of free-streamline solutions for flow past a circular cylinder. The separation streamline has continuous curvature only if separation occurs at a specific angle θ_0, equal to about 56°, from the forward stagnation point. For separation at any other point, this streamline has infinite curvature at the separation point. If separation were to occur further upstream, the streamline would cut into the body, but if the flow separates further downstream the streamline curves outward from the body. We will assume that separation actually takes place at a small distance downstream from the 56° point, at an angle $\theta_s = \theta_0 + O(\epsilon)$, where ϵ is a function of the Reynolds number Re which tends toward zero as $Re \to \infty$. The pressure gradient is adverse just ahead of separation and is weakly singular at separation, in the sense that the function which becomes large is multiplied by the small parameter ϵ.

Nondimensional variables will be defined in terms of the free-stream velocity U and the cylinder radius a. Thus the Reynolds number is $Re = Ua/\nu$, where ν is the kinematic viscosity. The pressure

and velocity at separation are $\bar{p}_s$ and U_s, where $\bar{p}_s/\bar{p}_\infty = 1 + O(\epsilon)$ and $U_s/U = 1 + O(\epsilon)$, so that $\bar{p}_s$ and U_s are approximately but not exactly equal to the pressure $\bar{p}_\infty$ and velocity U at large distances from the body. We define nondimensional coordinates x and y with origin at the separation point, measured downstream along the surface and outward along a normal to the surface, respectively. The corresponding nondimensional velocity components are u and v. The local static pressure is $\bar{p}$, and the nondimensional perturbation pressure is $p = (\bar{p} - \bar{p}_s)/(\rho U^2)$. The Bernoulli equation then shows that the largest term of the perturbation in the nondimensional complex velocity is $-(p + iv)$.

The local behavior of the free-streamline solution near separation gives

$$p + iv \sim i\epsilon c_0 z^{1/2} + i c_1 z^{3/2} \tag{1}$$

for $Re \to \infty$ and $z = x + iy \to 0$. We take $c_0, c_1 > 0$. As $\arg z \to 0$, $p \to 0$ and $v \sim \epsilon c_0 x^{1/2} + c_1 x^{3/2}$; as $\arg z \to \pi$, $v \to 0$ and $p \sim -\epsilon c_0 |x|^{1/2} + c_1 |x|^{3/2}$. Thus along $y = 0$ the perturbation pressure is zero downstream and the streamline slope is zero upstream; a term iAz, where $A > 0$, could also be added to (1) to account for body curvature. It is seen that $p > 0$ for $x < -\epsilon c_0/c_1$ and $p < 0$ for $-\epsilon c_0/c_1 < x < 0$; $dp/dx < 0$ for $x < -\frac{1}{3}\epsilon c_0/c_1$ and $dp/dx > 0$ for $-\frac{1}{3}\epsilon c_0/c_1 < x < 0$, with $dp/dx \to \infty$ as $x \to 0$; and the minimum value of p is $p \sim -\frac{2}{3}(\epsilon c_0)^{3/2}/(3c_1)^{1/2}$. More terms can be added to (1) to account for higher-order terms in the free-streamline solution and to correct for terms omitted from the approximate Bernoulli equation.

If, as suggested above, a free-streamline solution is assumed, then $\bar{p}_s \equiv \bar{p}_\infty$ and the value of c_1 is determined. A relation between $(\theta_s - \theta_0)/\epsilon$ and c_0 is also obtained. Then one additional condition is needed, and presumably can be found from a suitable boundary-layer solution. Eq. (1), however, is only a local approximation and so does not really require that the pressure remain constant all along the separation streamline. Furthermore it is not essential to assume $\bar{p}_s \sim \bar{p}_\infty$ and $\theta_s \sim \theta_0$. Thus there may be as many as six unknown constants: the first two terms in the expansions of $\bar{p}_s - \bar{p}_\infty$ and of $\theta_s - \theta_0$, plus c_0 and c_1. Again all but one of the needed conditions are presumably to be supplied by a wake solution, with the one remaining condition obtained from a local boundary-layer solution.

The boundary layer just upstream

Since $dp/dx < 0$ just upstream of separation except at small values of -x, the boundary-layer velocity profile remains linear near the wall except at small values of -x. The velocity near separation then is described by a basic profile plus superimposed small changes corresponding to the pressure gradient obtained from (1). The stream function is defined by

$$\frac{\partial\psi}{\partial y} = u \quad , \qquad \frac{\partial\psi}{\partial x} = -v \tag{2}$$

We define a boundary-layer y-coordinate and stream function by

$$\tilde{y} = Re^{1/2} y \quad , \qquad \tilde{\psi} = Re^{1/2}\psi \tag{3}$$

Then $u \sim \partial\tilde{\psi}/\partial\tilde{y}$ and $v \sim -Re^{-1/2}\partial\tilde{\psi}/\partial x$. The basic profile is given by $u \sim \psi_0'(\tilde{y})$, where $\psi_0' \sim a_1\tilde{y}$ as $\tilde{y} \to 0$.

For small values of -x, we anticipate that $\tilde{\psi}$ can be expressed by a series expansion with terms given by powers of x (and perhaps logarithms) multiplied by functions of $\tilde{y}$. For example, the form of the pressure gradient might seem to suggest the series

$$\tilde{\psi} \sim \psi_0(\tilde{y}) + (-x)^{1/2}\epsilon\,\psi_1(\tilde{y}) + (-x)^{3/2}\psi_2(\tilde{y}) + \cdots$$

However, by substituting this series in the boundary-layer momentum equation, and taking the limit for $\epsilon \to 0$ and $-x \to 0$, one easily finds that ψ_1 and ψ_2 satisfy first-order equations and that consequently the no-slip condition cannot be satisfied. If we compare the orders of magnitude of the terms uu_x and $u_{\tilde{y}\tilde{y}}$, recalling that $u = O(\tilde{y})$ as $\tilde{y} \to 0$, we find that viscous forces should be expected to become important when $\tilde{y} = O(|x|^{1/3})$. Thus near the wall we anticipate a series solution in terms of powers of -x multiplied by functions of a similarity variable $\tilde{y}/(-x)^n$, where in this case $n = 1/3$. This is a form of solution introduced by Goldstein, used by him in Ref. 1, as well as elsewhere, and also by many others. Each of the terms in this expansion satisfies the tangency and no-slip conditions at $\tilde{y}/(-x)^{1/3} = 0$ and a matching condition as $\tilde{y}/(-x)^{1/3} \to \infty$. Each term in a solution for the main part of the boundary layer satisfies a matching condition as $\tilde{y} \to 0$.

Combining the results of Sychev and of Messiter and Enlow, we have for the inner solution

$$\tilde{\psi} \sim \tfrac{1}{2}a_1\tilde{y}^2 + (-x)^{3/2} f_{5/2}(\zeta) + \cdots + \epsilon\,(-x)^{1/2} g_{-1/2}(\zeta) + \cdots \tag{4}$$

where $\zeta \equiv \tilde{y}/(-x)^{1/3}$; the notation for a general term is $(-x)^{(2+k)/3} f_k$, $\epsilon(-x)^{(2+k)/3} g_k$. For the outer solution

$$\tilde{\psi} \sim \psi_0(\tilde{y}) + (-x)\psi_1(\tilde{y}) + (-x)^{7/6}\psi_{7/6}(\tilde{y}) + (-x)^{3/2}\psi_{3/2}(\tilde{y}) + \cdots$$
$$+ \epsilon\,\phi_0(\tilde{y}) + \epsilon(-x)^{1/6}\phi_{1/6}(\tilde{y}) + \epsilon(-x)^{1/2}\phi_{1/2}(\tilde{y}) + \cdots \tag{5}$$

Sychev's derivation was carried out in von Mises variables, with $\tilde{\psi}$ replacing $\tilde{y}$ as an independent variable. His results have been rewritten here in rectangular coordinates, and correspond to the terms in (4) and (5) which contain a factor ϵ. The remaining terms in (4) and (5) were obtained by Messiter and Enlow. The functions $f_{5/2}(\zeta)$ and $g_{-1/2}(\zeta)$ satisfy

$$f_{5/2}''' - \frac{1}{3} a_1 \zeta^2 f_{5/2}'' + \frac{3}{2} a_1 \zeta f_{5/2}' - \frac{3}{2} a_1 f_{5/2} = -\frac{3}{2} c_1 \tag{6}$$

$$g_{-1/2}''' - \frac{1}{3} a_1 \zeta^2 g_{-1/2}'' + \frac{1}{2} a_1 \zeta g_{-1/2}' - \frac{1}{2} a_1 g_{-1/2} = \frac{1}{2} c_0 \tag{7}$$

The boundary conditions require that $f_{5/2}$, $f_{5/2}'$, $g_{-1/2}$ and $g_{-1/2}'$ be zero at $\zeta = 0$. It is also required that there be no exponentially large solutions as $\zeta \to \infty$. The solutions can be expressed in terms of confluent hypergeometric functions, and as $\zeta \to \infty$ it is found that

$$\left.\begin{aligned} f_{5/2}(\zeta) &\sim \frac{2}{9} a_{7/2} \zeta^{9/2} - \frac{35}{2a_1} a_{7/2} \zeta^{3/2} + K\zeta + \frac{c_1}{a_1} + \cdots \\ g_{-1/2}(\zeta) &\sim \frac{2}{3} b_{1/2} \zeta^{3/2} + M\zeta - \frac{c_0}{a_1} + \cdots \end{aligned}\right\} \tag{8}$$

The functions in (5) which satisfy appropriate differential equations and match asymptotically as $y \to 0$ with the terms in (4) expanded for $\zeta \to \infty$ in (8) are found to be

$$\left.\begin{aligned} \psi_1 &= -\psi_0' \int_0^{\tilde{y}} \frac{\psi_0'''}{\psi_0'^2} \, d\tilde{y} \\ \psi_{7/6} &= A_{7/6} \psi_0' \\ \psi_{3/2} &= -c_1 \psi_0' \int_0^{\tilde{y}} \left(\frac{1}{\psi_0'^2} - \frac{1}{a_1^2 \tilde{y}^2} \right) d\tilde{y} + \frac{c_1 \psi_0'}{a_1^2 \tilde{y}} \\ \phi_{1/6} &= B_{1/6} \psi_0' \\ \phi_{1/2} &= c_0 \psi_0' \int_0^{\tilde{y}} \left(\frac{1}{\psi_0'^2} - \frac{1}{a_1^2 \tilde{y}^2} \right) d\tilde{y} - \frac{c_0 \psi_0'}{a_1^2 \tilde{y}} \end{aligned}\right\} \tag{9}$$

where $A_{7/6} = K/a_1$ and $B_{1/6} = M/a_1$. Also

$$\phi_0' \sim b_{1/2} \tilde{y}^{1/2}$$

as $\tilde{y} \to 0$, for matching with the solution of (7), and from (7) it is found that $b_{1/2} = (9/a_1)^{1/2} c_0 \Gamma(1/6)/\Gamma(-1/3)$. Messiter and Enlow studied additional terms and in particular showed that for the assumed pressure gradient the form of the basic velocity profile $\psi_0'(\tilde{y})$ which is compatible with the boundary conditions at the wall is

$$\psi_0'(\tilde{y}) \sim a_1 \tilde{y} + a_{7/2} \tilde{y}^{7/2} + a_4 \tilde{y}^4 + a_6 \tilde{y}^6 + a_{13/2} \tilde{y}^{13/2} + a_7 \tilde{y}^7 + \cdots \tag{10}$$

where $a_{7/2} = -(c_1/7) a_1^{1/2} \Gamma(-5/6)/\Gamma(-1/3)$; a_4 and a_7 are arbitrary; and a_6, $a_{13/2}$ could be obtained by numerical integrations.

The local interaction problem

At points very close to separation it is expected that an interaction with the external flow must be taken into account. The pressure then cannot be prescribed but instead must be obtained as part of the solution. Although the local pressure gradient may be large, the interaction occurs over a short distance, such that the magnitude of the local pressure changes is small. The velocity profile is therefore undisturbed throughout most of the boundary layer. In particular $\tilde{\psi} \sim \psi_0(\tilde{y})$; and $u \sim a_1 \tilde{y}$ as $\tilde{y} \to 0$. Perturbations in the viscous forces are therefore small, and so the increased pressure gradient is balanced primarily by an increase in the magnitude of the acceleration, or in this case a deceleration. In a sublayer close to the wall, viscous forces must also be important in order that the no-slip condition may be satisfied.

Thus near separation we postulate a representation of the flow as $Re \to \infty$ in the form given, e.g., in Refs. 12, 13, and 14. For a short interaction distance, we require in a sublayer very close to the wall that mass be conserved; that viscous, pressure, and inertia forces be of the same order of magnitude; that $u = O(\tilde{y})$; and that the streamline slope v/u be of the same order of magnitude as the nondimensional pressure perturbation p. The last condition follows from the result, which we will anticipate, that not only can $\partial p/\partial \tilde{y}$ be neglected but also that the largest term in v/u is independent of $\tilde{y}$ except in the sublayer. Since v/u and p are of the same order in the external flow outside the boundary layer, they are also of the same order in the sublayer.

These conditions are sufficient to show that the interaction occurs over a distance $\Delta x = O(Re^{-3/8})$; the sublayer is characterized by $y = Re^{-1/2} \tilde{y} = O(Re^{-5/8})$; and the perturbations p, $\tilde{y}(u - a_1 \tilde{y})$, and v/u are all of the same order. If we require further that the relative changes in u are not small, as must be true

in the present case, the orders of magnitude of the perturbations are determined. It is found that p, v/u, and $(u - a_1 \tilde{y})^2$ are all of order $Re^{-1/4}$. Finally, to complete the formulation the form of the pressure upstream must be introduced. We have

$$p \sim -\epsilon\, c_0 (-x)^{1/2} \qquad \text{as} \qquad \frac{-x}{\epsilon} \to 0, \qquad \frac{-x}{Re^{-3/8}} \to \infty \tag{11}$$

Rewritten in "inner" variables this becomes $p \sim -\epsilon\, c_0 Re^{-3/16} (-Re^{3/8} x)^{1/2}$, and for matching with a term of order $Re^{-1/4}$ in the interaction solution it becomes necessary that $\epsilon = O(Re^{-1/16})$; we choose

$$\epsilon \equiv Re^{-1/16} \tag{12}$$

Thus in the sublayer $x = O(\epsilon^6)$ and $\tilde{y} = O(\epsilon^2)$.

The sublayer problem, for $\epsilon \to 0$ with x/ϵ^6 and $\tilde{y}/\epsilon^2$ fixed, is formulated in the manner described, for example, in Refs. 12, 13, and 14:

$$\tilde{\psi}(x, \tilde{y}; \epsilon) \sim \epsilon^4 \psi^*(x^*, y^*) + \cdots \tag{13}$$

$$p(x, \tilde{y}; \epsilon) \sim \epsilon^4 p^*(x^*) + \cdots \tag{14}$$

where

$$x^* = \frac{x}{\epsilon^6} \qquad y^* = \frac{\tilde{y}}{\epsilon^2} \tag{15}$$

and

$$\frac{\partial \psi^*}{\partial y^*} \frac{\partial^2 \psi^*}{\partial x^* \partial y^*} - \frac{\partial \psi^*}{\partial x^*} \frac{\partial^2 \psi^*}{\partial y^{*2}} = -\frac{dp^*}{dx^*} + \frac{\partial^3 \psi^*}{\partial y^{*3}} \tag{16}$$

$$\psi^*(x^*, 0) = \frac{\partial \psi^*}{\partial y^*}(x^*, 0) = 0 \tag{17}$$

$$\frac{\partial \psi^*}{\partial y^*}(x^*, y^*) \sim a_1 y^* \qquad x^* \to -\infty \tag{18}$$

$$\frac{\partial \psi^*}{\partial y^*}(x^*, y^*) \sim a_1 y^* + a_1 G(x^*) \qquad y^* \to \infty \tag{19}$$

$$G'(x^*) + H(x^*)\, c_0 x^{*1/2} = -\frac{1}{\pi} \int_{-\infty}^{\infty} \frac{p^*(\xi) + H(-\xi)\, c_0 (-\xi)^{1/2}}{x^* - \xi}\, d\xi \tag{20}$$

where $H(x^*)$ is the step function defined by $H(x^*) = 0$ for $x^* < 0$ and $H(x^*) = 1$ for $x^* > 1$, and

$$p^*(x^*) \sim -c_0 (-x^*)^{1/2}, \quad x^* \to -\infty \qquad ; \qquad G'(x^*) \sim -c_0 x^{*1/2}, \quad x^* \to +\infty \tag{21}$$

Presumably a velocity profile for the backflow as $x^* \to \infty$ is also needed as an initial condition to supplement the initial condition (18). A possible choice for this condition will be discussed below. Assuming that some such condition can be chosen, we expect that the solution to the interaction problem will provide some kind of information which helps toward the determination of a proper choice for the external-flow parameters. The constant c_0 in (21) is the only free parameter appearing in the problem formulation, and should probably be regarded as unknown. Although no proof can be given, one might conjecture that a solution to the interaction problem may exist for only a single value of c_0, and that the solution therefore provides a condition which determines c_0.

A numerical solution of the system given by (16) through (21), with the supplemental initial condition for the backflow, might perhaps be started by guessing a plausible form for the pressure perturbation $p^*(x^*)$. If an initial velocity profile for the backflow is specified at a large positive value of x^*, it should be possible to determine the flow below the line along which $u = \partial \psi^* / \partial y^* = 0$ by integrating in the direction of the backflow, for decreasing values of x^*. The form of the line $u = 0$ would be found from this calculation, and the calculated values of ψ^* along $u = 0$ would provide an assumed boundary condition for the forward-moving flow above this line. One might then integrate in the forward direction from a large negative value of x^* and thus obtain an estimate for the function $G(x^*)$. Eq. (20) can then be inverted to give a new function $p^*(x^*)$, which is to be compared with the assumed $p^*(x^*)$, so that an improved estimate can be made.

The backflow

Downstream of separation the form of the free streamline is obtained by integrating the streamline slope v obtained from (1) for $\arg z \to 0$. One finds $y \sim \frac{2}{3} \epsilon\, c_0 x^{3/2} + \frac{2}{5} c_1 x^{5/2}$. For $Re = \infty$, or $\epsilon = 0$, this is the equation of a vortex sheet across which the velocity is discontinuous. For $Re < \infty$ and $\epsilon > 0$, the vorticity is large but not infinite, and the change in velocity occurs across a free shear layer of small but nonzero thickness. The separation streamline $\tilde{\psi} = 0$ will be defined by $y = Y(x; \epsilon)$, where

$$Y(x; \epsilon) \sim \frac{2}{3} \epsilon\, c_0 x^{3/2} + \frac{2}{5} c_1 x^{5/2} \tag{22}$$

for $\epsilon \to 0$, $x \to 0$, and $x^* \to \infty$. To describe the flow in the free shear layer, we define

$$\hat{y} = Re^{1/2} (y - Y)$$

such that $\tilde{\psi} = 0$ at $\hat{y} = 0$. For most of the layer the velocity of each fluid element is nearly unchanged, so that $\tilde{\psi} \sim \psi_0 (\hat{y})$, with $u \sim a_1 \hat{y}$ as $\hat{y} \to 0$.

As for the flow upstream of separation, viscous forces cannot be neglected very close to $\tilde{\psi} = 0$. Therefore we expect that a solution of the boundary-layer equations is required in a thin sublayer for small values of $\hat{y}$, satisfying the condition $u \sim a_1 \hat{y}$ as the sublayer coordinate becomes large. We take

$$\tilde{\psi} \sim x^{2/3} F(\eta) \quad , \quad \eta = \hat{y}/x^{1/3} \tag{23}$$

where $F(\eta)$ satisfies

$$F''' - \frac{2}{3} F F'' + \frac{1}{3} F'^2 = 0 \tag{24}$$

$$F(0) = 0, \quad F''(\infty) = a_1 , \quad F'(-\infty) = 0 \tag{25}$$

The condition for $\eta \to -\infty$ assumes that in the limit the flow below the free shear layer has velocity which approaches zero faster than $x^{1/3}$.

Since $Re^{-1/2} x^{1/3} << Y(x;\epsilon)$ for $x >> Re^{-3/8}$, the thickness of this viscous sublayer is much smaller than the distance from the wall to the separation streamline. It follows, as can be shown by a more careful asymptotic formulation, that most of the separated flow is described approximately by inviscid-flow equations. The backflow below $\tilde{\psi} = 0$ must supply at least enough mass for entrainment in the separated shear layer, which is equal to $Re^{-1/2} x^{2/3} |F(-\infty)|$. Sychev[15] assumed that the backflow supplies exactly this amount of mass, and explored the consequences of this assumption in detail. Messiter and Enlow[16] briefly suggested the same possibility; this assumption has been used in other separation problems by Stewartson and Williams[19] and by Klemp and Acrivos.[20] Sychev's results for $p + iv \sim i\epsilon c_0 z^{1/2}$ are summarized below and extended to include the effect of the term $i c_1 z^{3/2}$ in $p + iv$.

If $Y(x)$ has the form given in (22), a solution for the backflow which provides exactly the mass required for entrainment is

$$u \sim Re^{-1/2} x^{2/3} F(-\infty) \left\{ \frac{2}{3} \epsilon c_0 x^{3/2} + \frac{2}{5} c_1 x^{5/2} \right\}^{-1} \tag{26}$$

The Bernoulli equation gives the corresponding pressure:

$$p \sim -\frac{1}{2} Re^{-1} x^{4/3} F^2(-\infty) \left\{ \frac{2}{3} \epsilon c_0 x^{3/2} + \frac{2}{5} c_1 x^{5/2} \right\}^{-2} \tag{27}$$

This provides a very small accelerating pressure gradient for the backflow, and for the forward-moving fluid in the separated shear layer the pressure gradient remains adverse. The viscous forces acting on the fluid very close to $\tilde{\psi} = 0$ give an acceleration in the positive x-direction to a small amount of mass which must be supplied from below. A weak pressure field is set up which provides the needed backflow. For $x/\epsilon \to \infty$ and $x \to 0$, (27) gives $p = O(Re^{-1} x^{-11/3})$, implying terms of order Re^{-1} at a distance $x = O(1)$. For $x/\epsilon \to 0$, (27) becomes $p = O(Re^{-1/4} x^{*-5/3})$, and this represents the first term of an expansion of the solution (14) as $x^* \to \infty$.

The solution given by (26) does not satisfy the no-slip condition at $y = 0$, and so a "backward boundary layer" is also required. The "external-flow" velocity seen by this boundary layer is given by (26). The thickness of the layer varies from $O(Re^{-1/4})$ when $x = O(1)$ to $O(Re^{-5/8})$ when $x = O(Re^{-3/8})$. Finally, the perturbations in the shear-layer flow above the sublayer about $\hat{y} = 0$ can be obtained in a form similar to the solutions given by (5) and (9) for the flow upstream of separation. Again the first effect to appear is a displacement effect due to acceleration of fluid in the sublayer.

3. DISCUSSION

In the preceding section it is assumed that for steady two-dimensional laminar flow past a bluff body at high Reynolds number a correct local solution near separation can be obtained if the pressure is taken to be approximately constant just downstream of separation. A sketch summarizing some general features of the asymptotic flow model is shown in Fig. 1. Certain aspects of the proposed model seem quite promising, but the model is clearly far from complete. The results do appear to be self-consistent, in the sense that formal asymptotic matching appears possible among the various parts of the solution. The pressure distribution has the correct general form, in that separation follows after a small pressure rise which occurs over a small distance. Furthermore, the possibility that various quantities may change very slowly with Reynolds number seems to be in agreement with existing experimental and numerical results. On the other hand, the existence of a solution to the interaction problem as posed has not yet been demonstrated, and some other uncertainties arise due to lack of knowledge of the flow in the wake. Several constants are undetermined, and the observed low value of base pressure has not been explained. Finally, the assumption about the nature of the backflow has not been properly justified.

In order to proceed further, it appears necessary to study the complete wake. For a bluff body such as a circular cylinder at a Reynolds number of about 10^4 or 10^5, the boundary layer at the body surface is laminar at separation. The separated thin shear layer is unstable and the flow becomes unsteady somewhat downstream of separation. A realistic attempt at predicting the flow close to the body must take this unsteadiness into account. However, it also seems important to study the flow which would exist at very large Reynolds number in the absence of instability, both for a better general understanding of solutions to the Navier-Stokes equations and as a step toward understanding the actual nonsteady flow.

We will assume that the steady-state solution to the Navier-Stokes equations for flow past a circular cylinder gives a nonzero value for the drag coefficient C_D in the limit as the Reynolds number tends to infinity. Certain consequences then seem to follow rather directly. The assumption that $C_D \to 0$ is based on the belief that in the limit the pressures on the back of the cylinder are not likely to be large enough to cancel the pressures on the front part of the cylinder so as to give $C_D = 0$. The drag can also be expressed in terms of a momentum deficit in the wake at large distances from the body. If we tentatively assume a constant-pressure wake, each of the free shear layers is described by a similarity solution, with the nondimensional thickness of each layer growing as $(x/Re)^{1/2}$. The momentum loss of the fluid entrained from the external potential flow is of order one when $x = O(Re)$; this order of magnitude would remain the same even if the pressure were allowed to vary throughout the wake. Roshko[10] and Sychev[11] therefore postulated a closed wake of length proportional to Reynolds number. A free-streamline solution is presumed to describe the flow for $x \ll Re$, with the distance between the free streamlines taken to grow as $x^{1/2}$ for $1 \ll x \ll Re$. A matching of solutions for $x = O(1)$ and $x = O(Re)$ then implies a maximum wake thickness of order $Re^{1/2}$. The two shear layers therefore merge at a large distance behind the body. The fluid in the inner parts of the layers is turned back toward the body, and the fluid outside the separation streamlines continues downstream in a layer having thickness of order one. The nondimensional momentum deficit in this layer extending downstream along the center line remains constant and equals the drag coefficient of the body.

It is at this stage that the consequences of the assumptions become quite difficult to understand. The fluid which is turned back near the wake stagnation point is acted upon primarily by pressure forces, in a region having dimensions of order one, so that locally the Bernoulli equation can be applied for each fluid element. Since the significant pressure gradients are confined to this region, it follows that the magnitude of the velocity for each element just after the turning is equal to the value just before the turning. This statement can be written more formally as an asymptotic matching condition which provides an initial condition for the backflow within a distance of order one from the center line. In particular, if the pressure is assumed constant everywhere in the wake except near the wake stagnation point, the fluid velocity is small except in the shear layers and near the center line, and the similarity solution for the shear layers gives the velocity at $\psi = 0$ as $u = 0.587$.

If we continue tentatively to assume a constant-pressure wake, we have a jet-like backflow along the center line, with the neighboring fluid at rest. The momentum flux remains constant as the fluid moves from the wake stagnation point toward the body. The mass flux increases and the velocity decreases, but the velocity remains of order one in an asymptotic sense, although it may be numerically small. This fluid must again be turned, in the neighborhood of the body, primarily by pressure forces. The pressure coefficient $c_p = (\bar{p} - \bar{p}_\infty)/(\frac{1}{2}\rho U^2)$ along the back part of the body would remain of order one and positive, although numerically small. For example, if the velocity were to decrease by 50% between the wake stagnation point and the body, its value might be about 0.3, corresponding to a pressure coefficient of about 0.1 as compared with a pressure coefficient 1.0 at the forward stagnation point on the body.

It does not seem that this conclusion is necessarily inconsistent with experimental and numerical results, since these results are not available for really high Reynolds number. For example, Roshko[8] gave one set of data which clearly showed that measured pressures were strongly influenced by wake unsteadiness, and therefore do not at all correspond to a steady-state flow. For a circular cylinder with $2\,Re = 2\,U_a/\nu = 14{,}000$ the pressure coefficients on the back of the body with and without a splitter plate were, respectively, about -0.5 and -1.0.

After the backward-moving fluid in the jet-like layer along the center line is turned so as to move again in the forward direction, it still has velocity of order one and occupies a layer having thickness of order one, adjacent to the assumed thin shear layer along the separation streamline. Thus for the initial development of the free shear layers there appears to be a small but nonzero velocity in the adjacent wake fluid, so that the tentatively assumed similarity solution is not exactly correct.

These considerations of course carry implications for the flow close to the separation point. The fluid moving along the back of the cylinder provides more mass than is needed for entrainment in the thin shear layers, and must encounter an increasing pressure if it is to be turned so as to move again in the forward direction. The boundary layer at the cylinder surface then has an adverse pressure gradient and is expected to separate long before reaching the separation point assumed for the boundary layer on the front of the cylinder. The assumption of nearly constant pressure used in the preceding section can still be correct, provided only that the leading term of the complex velocity is given by (1) for $\epsilon \to 0$ and $z \to 0$. We require only that the perturbation pressure p be of smaller order of magnitude than the streamline slope, so that $|p| \ll \epsilon\, c_0\, x^{1/2} + c_1 x^{3/2}$. The assumption that the backflow provides exactly enough mass leads to the very small downstream pressure given by (27). The actual p could be considerably larger in magnitude and still be consistent with (1).

Several hints can be found in the literature as to what kind of modification might be considered for the flow just downstream of separation. Stewartson[2] suggested a form of solution containing an essential singularity and noted that infinitely many such solutions might exist. For low Reynolds number, Moffatt[21] obtained solutions to the Stokes equations for flow near an interior corner which showed an infinite sequence of vortices. Secondary eddies also appeared in the numerical solutions obtained by Burggraf.[22]

A possibility here is to add an infinite series of terms to the complex velocity in the external flow, with qualitative properties which might correspond to an infinite sequence of vortices in the flow below the separation streamline. These terms should decay in some reasonable way as arg z increases from zero, and should satisfy the condition $v \to 0$ as $\arg z \to \pi$. A function which has the desired properties is

$$w(z) = \alpha e^{-i\pi\beta} z^{\beta} e^{-i\gamma/z^{1/2}} \tag{28}$$

$$= \alpha e^{i\beta(\theta-\pi)} r^{\beta} e^{-\gamma r^{-1/2}\sin(\theta/2)} \times \left\{\cos\left(\gamma r^{-1/2}\cos\frac{\theta}{2}\right) - i\sin\left(\gamma r^{-1/2}\cos\frac{\theta}{2}\right)\right\} \tag{29}$$

where $r = |z|$, $\theta = \arg z$; α, β, γ are real; and $\gamma > 0$. For $\theta = 0$, $w = \alpha e^{-i\beta\pi} x^{\beta} e^{-i\gamma/x^{1/2}}$. A wave length Δx is found by setting $\gamma/x^{1/2} - \gamma/(x+\Delta x)^{1/2} = 2\pi$; it follows that $\Delta x \sim (4\pi/\gamma)x^{3/2}$. If θ increases from 0 to π for a fixed value of r, the exponential factor decreases monotonically, and is very small for $r \ll 1$ and $\sqrt{r} \ll \theta \leq \pi$. For $\theta = \pi$, w is real and so satisfies the condition $v = 0$.

The oscillating form of w(z) for $\theta \to 0$ implies a periodicity in the backflow, with eddies having length $(4\pi/\gamma)x^{3/2}$. If we consider first $\epsilon^6 \ll x \ll \epsilon$, then the separation streamline is given by $Y(x) \sim \frac{2}{3}\epsilon c_0 x^{3/2}$. The height and length of the eddies would be of the same order if $\gamma = O(\epsilon^{-1})$. The stream function for any one of the eddies would be described by Poisson's equation $\psi_{xx} + \psi_{yy} = \omega(\psi)$, where ω = vorticity and possibly would be assumed constant for any particular eddy; the eddy presumably would have irregular shape. The corresponding pressure might be represented in terms of Fourier series, implying also an infinite series of terms in the complex velocity for the local external flow. Thus infinitely many terms of the form (28) might be considered.

For $\epsilon^6 \ll x \ll \epsilon$, $|w(z)|$ remains small compared with $\epsilon|z|^{1/2}$, the largest term in (1), provided that $\alpha|z|^{\beta} \ll \epsilon|z|^{1/2}$. Since $p = O(\alpha x^{\beta})$ for $\arg z \to 0$, the velocity in the eddies is $O(\alpha^{1/2} x^{\beta/2})$. Since $y = O(\epsilon x^{3/2})$, the vorticity is $O(\alpha^{1/2}\epsilon^{-1} x^{(\beta-3)/2})$. If the vorticity were assumed, for example, to be of the same order of magnitude in all of the eddies, we would take $\beta = 3$. For $\alpha = O(1)$, the pressure $p = O(x^3)$ would remain very small in comparison with $\epsilon x^{1/2}$ for $\epsilon^6 \ll x \ll \epsilon$. The same form for w(z) might also be assumed for $\epsilon \ll x \ll 1$, or perhaps different forms should be anticipated for the two ranges of values of x. In any case, the scale and velocity are such that a local Reynolds number for each individual eddy is large, and so each eddy is described by inviscid-flow equations, except at its boundaries where thin shear layers would have to be taken into account. All of these conjectures, of course, refer to possible forms for the limiting steady-state solution. For an actual flow at a Reynolds number of 10^4 or 10^5, it might instead be necessary to study a nonsteady vortex shedding. If, however, the pressure were still to remain nearly constant just downstream of separation, the complex velocity given by (1) would again provide a correct description of the mean flow, with the unsteadiness affecting some of the unknown constants rather than the form of the solution.

The main purpose of the speculation of this section was to suggest that the general form of the local flow description proposed near separation does not seem to imply any specific model for the complete wake. It is only necessary that the pressure be nearly constant, in a suitable asymptotic sense, immediately downstream of separation.

REFERENCES

1. Goldstein, S., On Laminar Boundary-Layer Flow Near a Position of Separation, Quart. J. Mech. Appl. Math. 1 (1948), 43-69.

2. Stewartson, K., On Goldstein's Theory of Laminar Separation, Quart. J. Mech. Appl. Math. 11 (1958), 399-410.

3. Kaplun, S., Fluid Mechanics and Singular Perturbations, P.A. Lagerstrom, L.N. Howard, and C.S. Liu, eds., Academic Press, New York, 1967.

4. Stewartson, K., Is the Singularity at Separation Removable?, J. Fluid Mech. 44 (1970), 347-364.

5. Thwaites, B. (ed.), Incompressible Aerodynamics, Oxford Univ. Press, 1960.

6. Roshko, A., A New Hodograph for Free-Streamline Theory, NACA Tech. Note 3168, 1954.

7. Woods, L.C., Two-Dimensional Flow of a Compressible Fluid Past Given Curved Obstacles with Infinite Wakes, Proc. Roy. Soc. A 227 (1955), 367-386.

8. Roshko, A., On the Drag and Shedding Frequency of Two-Dimensional Bluff Bodies, NACA Tech. Note 3169, 1954.

9. Batchelor, G.K., A Proposal Concerning Laminar Wakes Behind Bluff Bodies at Large Reynolds Number, J. Fluid Mech. 1 (1956), 388-398.

10. Roshko, A., A Review of Concepts in Separated Flow, Canadian Congress of Applied Mechanics, Quebec, Canada, 1967.

11. Sychev, V.V., On Steady Laminar Flow of a Fluid Around a Bluff Body at Large Reynolds Numbers, Symposium on Fluid Mechanics, Tarda, Poland, 1969.

12. Stewartson, K. and Williams, P.G., Self-Induced Separation, Proc. Roy. Soc. A 312 (1969), 181-206.

13. Stewartson, K., On the Flow near the Trailing Edge of a Flat Plate. II, Mathematika 16 (1969), 106-121.

14. Messiter, A.F., Boundary-Layer Flow near the Trailing Edge of a Flat Plate, SIAM J. Appl. Math. 18 (1970), 241-257.

15. Sychev, V.V., On Laminar Separation, Mekh. Zhid. i Gaza 3 (1972), 47-59.

16. Messiter, A.F. and Enlow, R.E., A Model for Laminar Boundary-Layer Flow near a Separation Point, SIAM J. Appl. Math. 25 (1973), 655-670.

17. Lagerstrom, P.A., Solutions of the Navier-Stokes Equation at Large Reynolds Number, International Symposium in Honor of Sydney Goldstein, Haifa, Israel, 1974.

18. Stewartson, K., Multi-Structured Boundary Layers on Flat Plates and Related Bodies, Advances in Applied Mechanics 14, Academic Press, New York, 1974.

19. Stewartson, K. and Williams, P.G., On Self-Induced Separation II, Mathematika 20 (1973), 98-108.

20. Klemp, J.B. and Acrivos, A., High Reynolds Number Steady Separated Flow past a Wedge of Negative Angle, J. Fluid Mech. 56 (1972), 577-590.

21. Moffatt, H.K., Viscous and Resistive Eddies near a Sharp Corner, J. Fluid Mech. 18 (1964), 1-18.

22. Burggraf, O.R., Analytical and Numerical Studies of the Structure of Steady Separated Flows, J. Fluid Mech. 24 (1966), 113-151.

This work was supported by the U.S. Army Research Office - Durham under Contract DAHC 04 68 C0033.

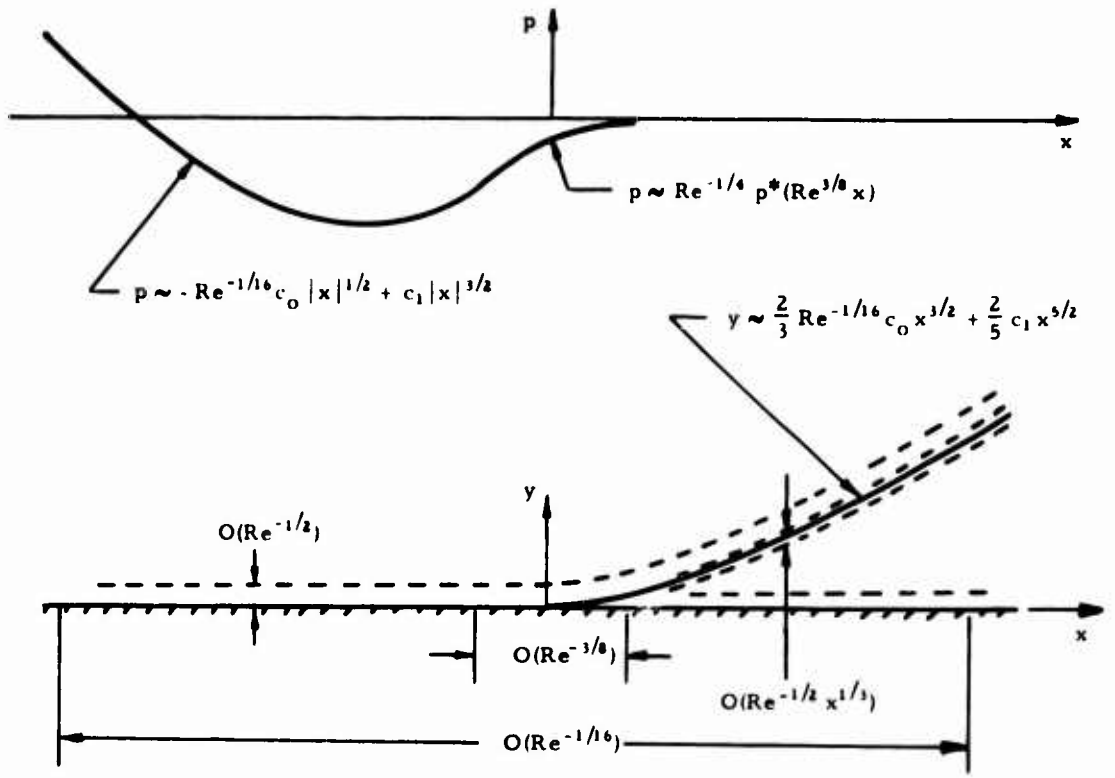

Figure 1. Perturbation pressure and regions of validity for solutions near separation

DEPENDENCE OF LAMINAR SEPARATION ON HIGHER ORDER BOUNDARY LAYER EFFECTS DUE TO TRANSVERSE CURVATURE, DISPLACEMENT, VELOCITY SLIP AND TEMPERATURE JUMP

A. Wehrum
Institut für Thermo- und Fluiddynamik
Ruhr-Universität Bochum, FRG

SUMMARY

The laminar compressible higher order boundary layer along a circular cylinder in axial parallel supersonic flow is studied according to the method of matched asymptotic expansions. A weak constant mass flow is injected into the boundary layer through the surface of the cylinder. The injected fluid is the same as in the outer supersonic flow. As a consequence of the homogeneous mass injection the first order boundary layer solution already leads to separation of the boundary layer within a finite distance from the leading edge, first determined by Catherall, Stewartson and Williams (1965) for the semiinfinite flat plate.

In a second order theory the influence of higher order boundary layer effects, such as transverse curvature, displacement, velocity slip and temperature jump, on the wall shear stress and the location of the separation point is studied. For determining the nonviscous second order solution of the outer flow the operator method of Ward (1955) has been used.

As numerical results show, transverse curvature and low density effects due to velocity slip and temperature jump at the wall increase the wall shear stress and therefore lead to a downstream shifting of the separation point. Displacement effect increases the wall shear stress near the leading edge. But further downstream there will be a decrease of wall shear stress due to the displacement effect, which leads to an upstream shifting of the separation point.

Within these three different effects influencing the location of separation, the displacement effect is the largest one, while the influence of low density effect may be neglected in comparison with the other two effects.

NOMENCLATURE

C	Chapman-Rubesin parameter defined by Eq.(7)
c_f	coefficient of the wall shear stress defined by Eq. (8)
c_p	specific heat capacity
I, K	modified Bessel functions, Eq.(A12)
$\dot{m}_w$	injected mass flow Eq.(6)
p	nondimensional static pressure
Pr	$= \mu_\infty c_p/\kappa_\infty$, Prandtl number
r_o	cylinder radius
Re	Reynolds number defined by Eq.(4)
T	nondimensional temperature based on T_∞
T_b	body temperature
T_∞	free stream temperature
U_∞	axial free stream velocity
u	nondimensional velocity component parallel to the wall based on U_∞
v	nondimensional velocity component normal to the wall based on U_∞
W	function defined by Eq.(A12)
x	nondimensional axial coordinate based on the cylinder radius
y	nondimensional coordinate normal to the wall based on the cylinder radius
α, β	coefficients in Eq.(A8) and (A9)
γ	ratio of heat capacities
ε	perturbation parameter defined by Eq.(4)
η, ξ	nondimensional coordinates defined by Eq.(5)
λ	variable in Eq.(A12)
μ	nondimensional viscosity based on the free stream value
ν_∞	kinematic viscosity of the free stream
ρ	nondimensional density based on the free stream value
τ_w	wall shear stress
φ	potential function Eq.(A10)
κ	nondimensional heat conductivity based on the free stream value

Subscripts

∞	undisturbed free stream
w	fluid quantities at the wall
1	first order
2	second order
s	separation
b	body

Superscripts

o	outer flows
$*$	dimensional quantities

INTRODUCTION

In the following a laminar boundary layer with injection will be investigated. The location of separation is defined as the point of zero skin friction ($\tau_w = 0$). There are two different possibilities to cause separation, one due to adverse pressure gradient and the other one due to injection into a constant main stream. It is well known that in classical boundary layer theory a singularity occurs at the

separation point, but the mathematical character of this singularity is completely different in the two cases. Goldstein (1948) first studied the bahaviour of boundary layer separation due to an adverse pressure gradient. He found the following asymptotic formula for the wall shear stress close to separation

$$\tau_w \sim \bar{x}^{1/2} \qquad \text{(due to pressure gradient)} \tag{1}$$

where $\bar{x}$ is the upstream distance from the separation point.

As a typical example for flow separation caused by injection, Catherall, Stewartson and Williams (1965) investigated the boundary layer flow along a flat plate with constant mass injection. For the asymptotic behaviour of the wall shear stress they found the following formula

$$\tau_w \sim \left(\frac{\bar{x}}{\ln \bar{x}}\right)^2 \qquad \text{(due to injection)} \tag{2}$$

From this equation it follows immediately that the wall shear stress gradient with respect to $\bar{x}$ at the separation point is zero in contrast to the first case, where this gradient is infinite.

It is well known that the location of separation is independent of the Reynolds number within the framework of classical Prandtl's boundary layer theory. But this is only an approximation. The classical boundary layer theory gives only the first term of an asymptotic expansion of the full solution of the Navier-Stokes equations for large Reynolds numbers.

By using the method of matched asymptotic expansions, higher order terms can be calculated which will yield corrections of the boundary layer solutions for lower Reynolds numbers. Within the analysis to obtain asymptotic solutions of the Navier-Stokes equations for high Reynolds numbers the classical boundary layer theory can be considered as the first order theory. The so-called second order boundary layer theory will take into account the next terms of the asymptotic expansion of the solution. From second order boundary layer theory the second order effects can be determined.

As a consequence of the expansion, the differential equations for the second order terms are all linear. This means that the different second order effects can be separated. Important second order effects are due to displacement, due to surface curvature and due to low density effects such as velocity slip and temperature jump at the wall. Further second order effects due to entropy and enthalpy gradients in the outer flow will not be considered here.

ANALYSIS

The purpose of this paper is the investigation of the separation by the second order boundary layer theory with the aim to determine the dependence of the location of separation on the second order effects.

With respect to surface curvature, only the case of pure transverse curvature was of interest. Therefore the supersonic flow along a semi-infinite circular cylinder with homogeneous mass injection has been considered (see fig. 1). Only the flow outside the cylinder is discussed.

Boundary layer calculations are singular perturbation problems. This leads to a division of the solution into two parts, an inner part - the boundary layer or inner solution - and an outer part or outer solution. For both solutions all flow variables are expanded in the same manner as for example the axial velocity component u:

$$u = u_1 + \varepsilon\, u_2 + O(\varepsilon^2) \tag{3}$$

with the perturbation parameter

$$\varepsilon = Re^{-1/2} = \left(\frac{U_\infty\, r_o}{\nu_\infty}\right)^{-1/2} \qquad (r_o = \text{cylinder radius}) \tag{4}$$

These expressions for the dependent variables are substituted into the Navier-Stokes equations and then terms of the same powers of ε are collected. This leads to the differential equations for the first and second order terms of the asymptotic solution of the Navier-Stokes equations. Within the first and second order solution the outer flow is inviscid and irrotational. The first order outer solution is just the constant main flow. The second order outer flow is the solution of the linearized potential equation, which has been solved by using the operator method described by Ward [6] (see A2). From this solution only the pressure, velocity and temperature distribution along the surface are needed for the second order boundary layer calculation as boundary conditions at the outer edge of the boundary layer. Now only the solution of the second order boundary layer will be discussed in detail because it contains the information about the second order wall shear stress and hence about the location of separation.

For calculations of compressible boundary layer it is convenient to use the Howarth transformation which transforms the first order compressible boundary layer equation for the flat plate into an incompressible form. The axial coordinate x can also be

transformed into a more appropriate one. The following transformation formulas have been used:

$$\xi = \dot{m}_{1w}\sqrt{\frac{x}{C}} \quad ; \qquad \eta = \frac{1}{\varepsilon\sqrt{Cx}}\int_0^y \rho_1 \, dy \tag{5}$$

where $\dot{m}_{1w}$ is the injection parameter, defined by

$$\dot{m}_{1w} = \frac{1}{\varepsilon}\dot{m}_w = \frac{1}{\varepsilon}\frac{\rho_w v_w}{\rho_\infty U_\infty} \quad . \tag{6}$$

$$C = \frac{\rho_w \mu_w}{\rho_\infty \mu_\infty} \tag{7}$$

is the so-called Chapman-Rubesin parameter. Because of constant mass flow injection no self-similar solution will exist and therefore the systems of partial differential equations have to be solved numerically even for the first order boundary layer equations. (For the analysis see appendix A)

The wall shear stress is now expanded and written in a nondimensional form:

$$\frac{\tau_w(\xi)}{\rho_\infty U_\infty^2} = c_f(\xi) = c_{f_{10}}(\xi)\,[c_{f_1}(\xi) + \varepsilon c_{f_2}(\xi) + O(\varepsilon^2)] \tag{8}$$

where $c_{f_{10}}$ is the wall shear stress of a flat plate without mass transfer:

$$c_{f_{10}} = \varepsilon\sqrt{\frac{C}{x}}\left(\frac{\partial u_1}{\partial \eta}\right)_{w,\ \dot{m}_{1w}=0} = \varepsilon \cdot 0{,}3321\sqrt{\frac{C}{x}} \tag{9}$$

c_{f_1} is the first order wall shear stress for constant mass injection, normalized by $c_{f_{10}}$.

$$c_{f_1}(\xi) = \frac{\left(\frac{\partial u_1}{\partial \eta}\right)_w}{\left(\frac{\partial u_1}{\partial \eta}\right)_{w,\ \dot{m}_{1w}=0}} \tag{10}$$

This function has been determined by Catherall, Stewartson and Williams [1].

c_{f_2} contains the influence of the second order effects. Because of the expansion of the viscosity and the velocity u in the defining equation for the shear stress, c_{f_2} consists of two terms, one is related to the second order velocity u_2 and the other to the second order viscosity μ_2 which is expressed by the temperature T_2. Therefore c_{f_2} yields

$$c_{f_2} = \frac{\left(\frac{\partial u_2}{\partial \eta}\right)_w + \frac{T_{2w}}{T_{1w}}\left(\frac{\partial u_1}{\partial \eta}\right)_w}{\left(\frac{\partial u_1}{\partial \eta}\right)_{w,\ \dot{m}_{1w}=0}} \tag{11}$$

The first term in the brackets contains all second order effects, which are considered, while the second vanishes if the temperature jump is neglected, because T_{2w} is the difference between the gas temperature at the wall and the body temperature $T_b/T_\infty = T_{1w}$.

Due to the linearity of the differential equations of the second order boundary layer (see A3) c_{f_2} can be split up into a sum of terms representing the individual second order effects, i.e. displacement effect (index D), curvature effect (index C) and low density effect (index L), where velocity slip and temperature jump at the wall are combined. The coordinate ξ_s of the location of vanishing wall shear stress is determined by the condition

$$c_{f_1}(\xi_s) + \varepsilon\,[c_{f_{2D}}(\xi_s) + c_{f_{2C}}(\xi_s) + c_{f_{2L}}(\xi_s)] = 0 \tag{12}$$

As the analysis shows (A2), an interaction term of displacement and transverse curvature occurs, which vanishes if one of both goes to zero. Here this term was included into the curvature term. This means always that $c_{f_{2D}}$ gives the displacement effect of the flat plate and that the term $c_{f_{2C}}$ represents the difference between the flow along the circular cylinder and the flow along the flat plate. The significance of each effect can also be demonstrated by its contribution $\Delta\xi_2$ to the second order location of the separation.

To show the contribution of each second order effect to the location of the second order separation point, $\xi_{s(1+2)}$, the solution of Eq.(12), is split up in the following manner:

$\xi_{s1} + \Delta\xi_{2D}$ is the solution of Eq.(12) without curvature and low density effects, i.e. the solution for the flat plate due to displacement only. (ξ_{s1} is the coordinate of the first order separation point.)

$\xi_{s1} + \Delta\xi_{2D} + \Delta\xi_{2C}$ is the solution of Eq.(12) for the cylinder without low density effects.

$$\xi_{s1} + \Delta\xi_{2D} + \Delta\xi_{2C} + \Delta\xi_{2L} = \xi_{s(1+2)} \qquad (13)$$

is the solution of Eq.(12) containing all second order effects, which are considered.

NUMERICAL RESULTS

For the numerical calculations the following values for the characteristic parameters of the flow problem have been choosen:

Prandtl number: $Pr = 0.72$

ratio of specific heats: $\gamma = 1.4$

ratio of body temperature to free stream temperature: $0.1 \leq \frac{T_b}{T_\infty} \leq 4$

Mach number: $\sqrt{2} \leq Ma_\infty \leq 4$

injection parameter: $0.5 \leq \dot{m}_{1w} \leq 2$

To illustrate the behaviour of the boundary layer near separation some shear stress profiles across the boundary layer are shown from the first order solution close to the separation point (Fig. 2). The curves show that the region of dominating shear stress is drifting away from the wall without thickening itself. For comparison the dotted line is drawn, which represents the shear stress distribution in a free shear layer between a parallel free stream and fluid at rest. The resulting velocity and shearstress profils in the interface havebeen determined by Lock [4]. It is very likely that in the separated free shear layer downstream of the separation point the same shear stress profile as Lock has calculated will occur (fig. 3). This profile is almost fully developed already a bit upstream of the separation point as the comparison of the dotted line with the curve ③ in figure 2 shows.

The results for the second order boundary layer calculations start with Fig.(4). Here the second order pressure distribution along the surface, induced by the first order boundary layer displacement, is shown. The pressure is multiplied by the square root of x because of the singularity at the leading edge. For the flat plate without mass transfer (self-similar solution) the induced pressure at the wall is given by

$$\frac{p_w^* - p_\infty}{\rho_\infty U_\infty^2} \frac{1}{\varepsilon} = 0{,}9755\sqrt{\frac{\zeta}{x}} \qquad (Ma_\infty = \sqrt{2}\ ,\ \frac{T_b}{T_\infty} = 1) \quad .$$

This formula is a horizontal line in the diagram. The deviation from this line is due to curvature as well as due to mass transfer at the wall.

The combined solution of first and second order wall shear stress is given in Fig.(5) for several values of the perturbation parameter ε. The curves are drawn for the cylinder as well as for the flat plate to show the influence of transverse curvature. The influence of the low density effect is so small that it cannot be distinguished in the diagram. A comparison with the dotted line, which corresponds to the first order wall shear stress determined by Catherall, Stewartson and Williams, shows an increase of the wall shear stress near the leading edge and decrease in the neighbourhood of separation. The curvature of the line for the combined first and second order wall shear stress has in the vicinity of separation also another sign as that of the line for the first order wall shear stress. The tendency of the line curvature is the same as in the case of separation caused by an adverse pressure gradient in the first order main flow.

The contribution of the individual second order effects to the location of the separation point according to Eq.(13) is listed in the following table.

$Ma_\infty = \sqrt{2}$; $\frac{T_b}{T_\infty} = 1$

a) $\dot{m}_{1w} = 1$

ε	ξ_{s1}	$\Delta\xi_{2D}$	$\Delta\xi_{2C}$	$\Delta\xi_{2L}$	$\xi_{s(1+2)}$
10^{-3}	0,863	- 0,162	0,007	$0{,}7 \cdot 10^{-4}$	0,708
10^{-2}	0,863	- 0,270	0,023	$10 \cdot 10^{-4}$	0,616

b) $\dot{m}_{1w} = 0.5$

ε	ξ_{s1}	$\Delta\xi_{2D}$	$\Delta\xi_{2C}$	$\Delta\xi_{2L}$	$\xi_{s(1+2)}$
10^{-3}	0,863	- 0,137	0,014	$0,4 \cdot 10^{-4}$	0,740
10^{-2}	0,863	- 0,236	0,039	$5 \cdot 10^{-4}$	0,666

This shows: a) displacement has the largest influence, upstream shifting

b) curvature influence is rather small, downstream shifting

c) low density effects can be neglected

The increase of the curvature effect for decreasing injection parameter $\dot{m}_{1w}$ (table b) is due to the following facts. The physical coordinate x_{s1} of the first order separation point is shifted downstream for decreasing injection parameter ($x_{s1} = \text{const}/\dot{m}_{1w}^2$, see also Eq.(5)). Moreover the entire mass injected from the leading edge down to the separation point decreases for increasing injection parameter. The increase of the boundary layer due to mass injection is weaker for increasing $\dot{m}_{1w}$ and therefore the transverse curvature effect on the wall shear stress decreases.

In Fig. 6 and 7 the ratio of the distances from the leading edge of second order and first order separation point is drawn as a function of the Reynolds number. The upstream shifting is increased for decreasing Reynolds number, increasing wall temperature and decreasing Mach number.

The last two diagrams (Fig. 8 and 9) illustrate the influence of transverse curvature on the location of separation. Due to transverse curvature the separation point is shifted downstream. This shifting is increased for decreasing Reynolds number, decreasing Mach number and increasing body temperature.

The increase of the curvature effect for decreasing Mach number can be explained by the fact, that the curvature term includes the interaction term of curvature and displacement, and this term increases for decreasing Mach number.

REFERENCES

[1] D. Catherall, K. Stewartson and P. G. Williams: Viscous flow past a flat plate with uniform injection. Proc. Roy. Soc. London Ser. A 284, 1965, 370-396.
[2] M. Van Dyke: Perturbation methods in fluid mechanics. New York, Academic Press, 1964.
[3] S. Goldstein: On laminar boundary-layer flow near a position of separation. Quart. J. Mech. Appl. Math. 1, 1948, 43.
[4] R. C. Lock: The velocity distribution in the laminar boundary layer between parallel streams. Quart. J. Mech. Appl. Math. 4, 1951, 42.
[5] H. S. Tsien: Superaerodynamics, mechanics of rarefied gases. J. Aeron. Sci., 13, 1946, 653-664.
[6] G. N. Ward: Linearized theory of steady high-speed flow. Cambridge Univ. Press, 1955.
[7] A. Wehrum: Die laminare Grenzschicht 2. Ordnung längs eines Kreiszylinders mit poröser Oberfläche in einer Überschallströmung. Dissertation, Ruhr-University Bochum, 1975

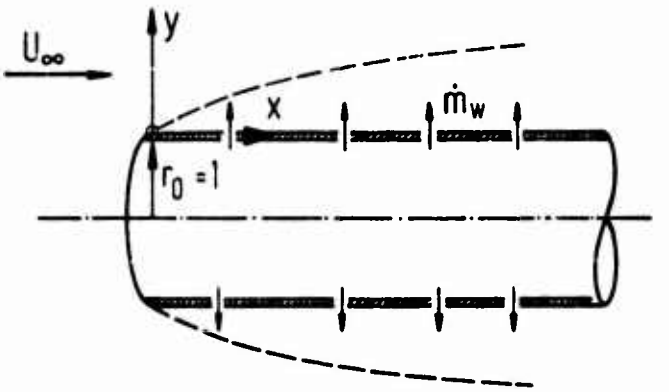

Fig. 1: Geometry of the problem

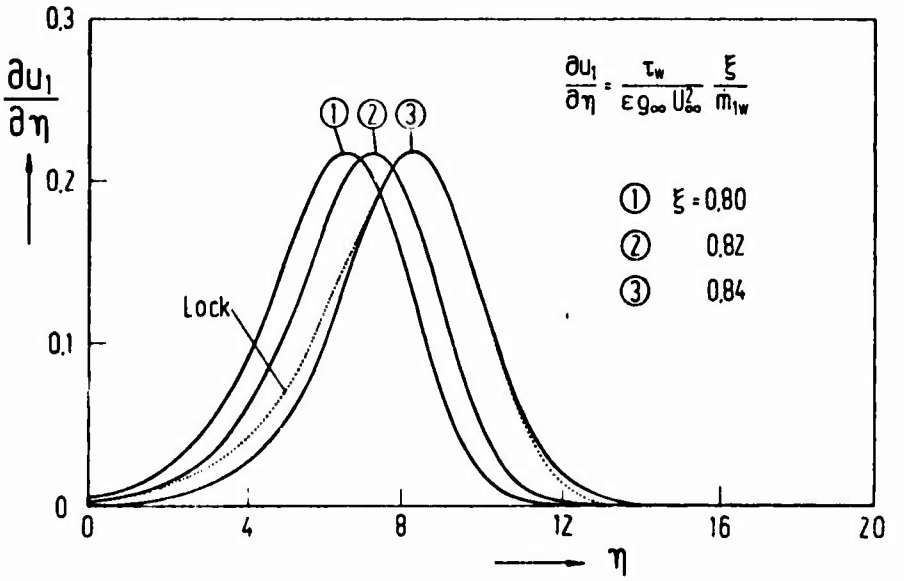

Fig. 2: Shear stress profiles across the boundary layer near the first order separation point
- - - free shear layer shear stress profile

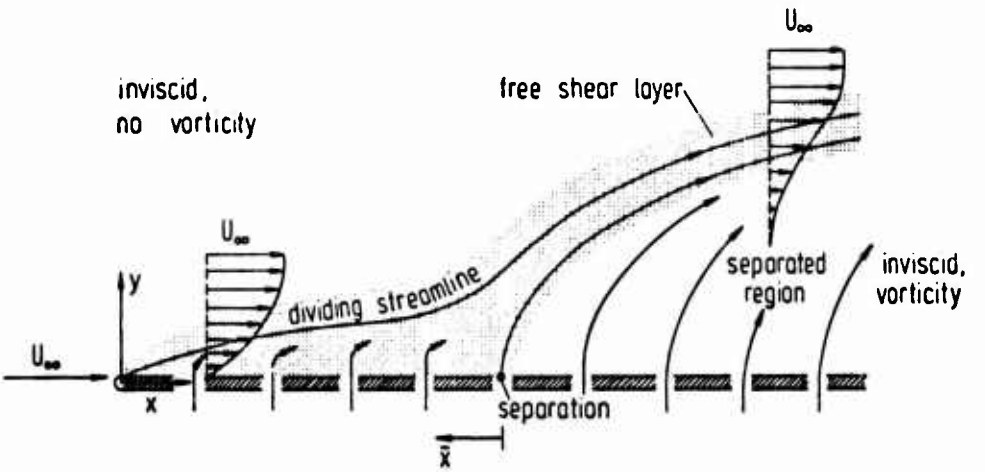

Fig. 3: Boundary layer separation

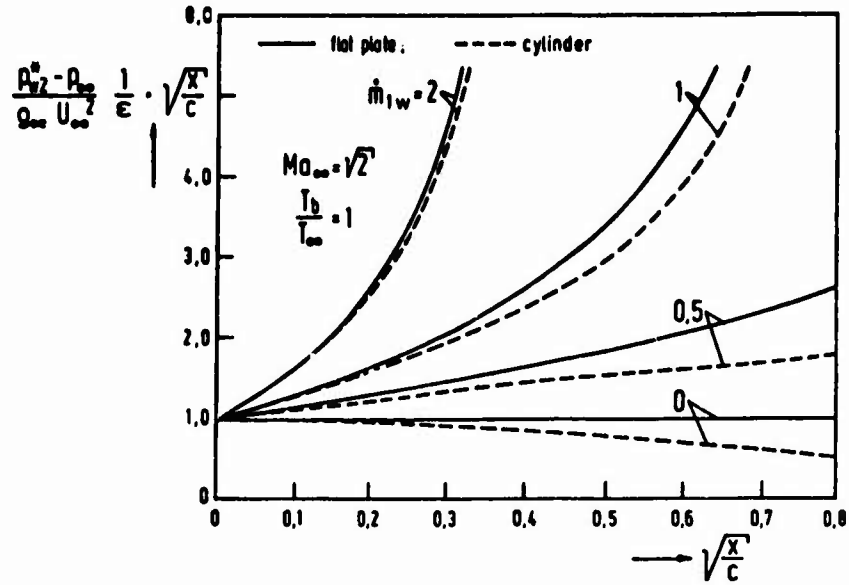

Fig. 4: Second order pressure distribution at the surface

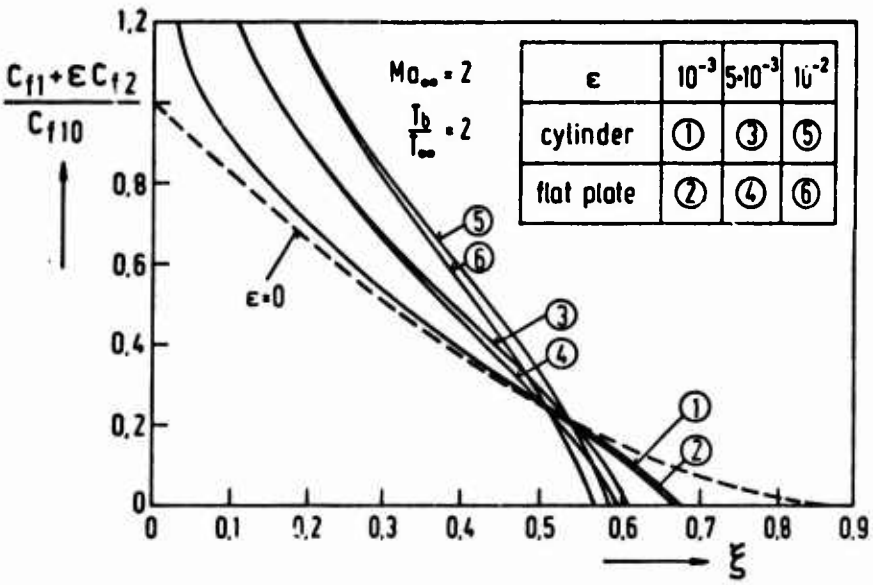

Fig. 5: Combined first and second order wall shear stress
- - - first order solution

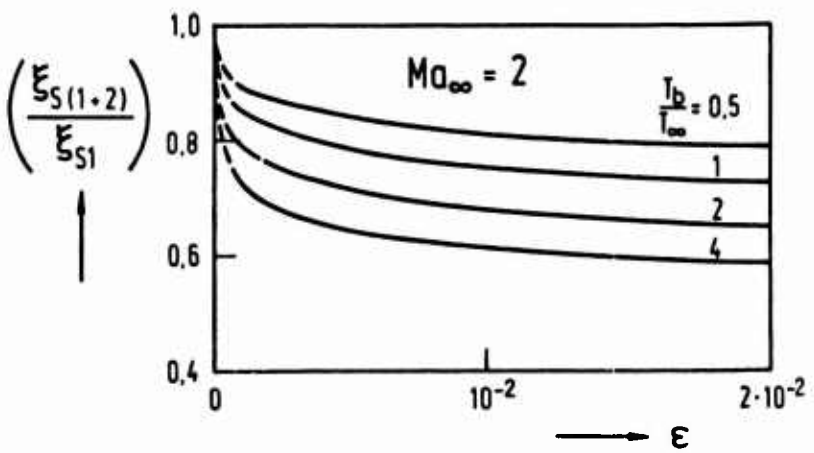

Fig. 6: Ratio of the coordinate lengths of the location of second and first order separation, $\xi_{S1} = 0,863$

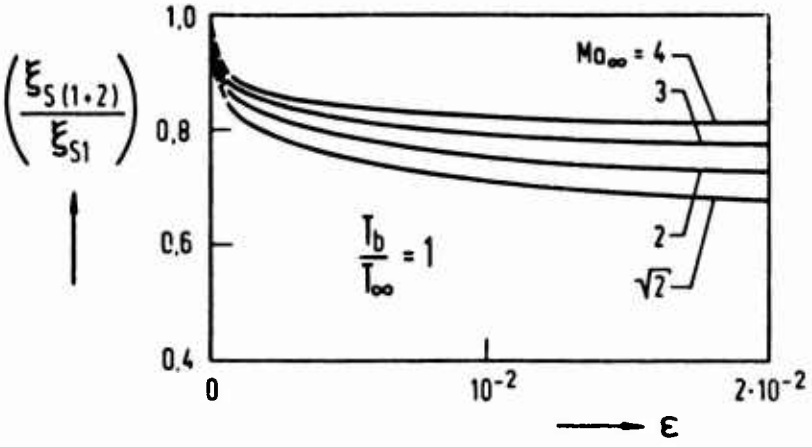

Fig. 7: Ratio of the coordinate lengths of the location of second and first order separation, $\xi_{S1} = 0{,}863$

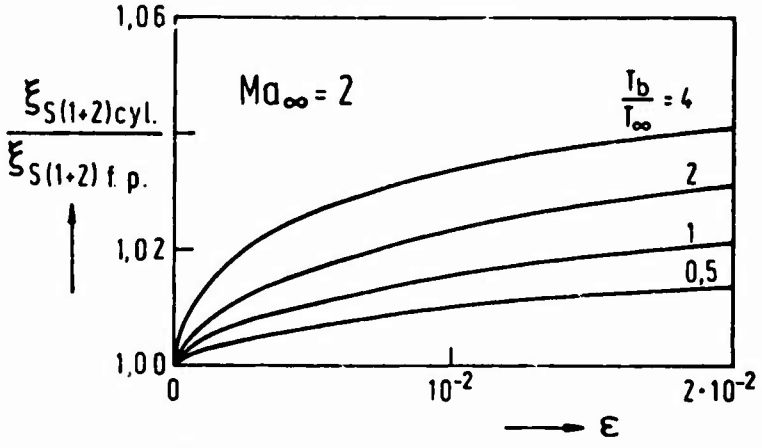

Fig. 8: Influence of transverse curvature on the location of separation

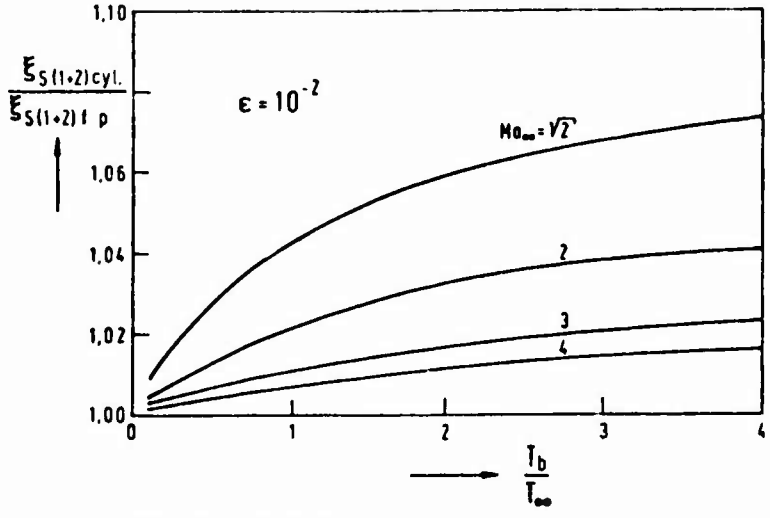

Fig. 9: Influence of transverse curvature on the location of separation

APPENDIX

A1. Basic equations (see also Fig. 1)

x is the coordinate along the surface and y the coordinate perpendicular to the wall. Both are nondimensionlized with the constant radius r_o.

The dimensionless basic equations written in cylindrical coordinates are:
(The reference values of the variables are their corresponding free-stream values except the pressure, which is refered to $\rho_\infty U_\infty^2$. i.e. $p = (p^* - p_\infty)/\rho_\infty U_\infty^2$); $r = y + 1$

equation of continuity:

$$\frac{\partial}{\partial x}(r\,\rho u) + \frac{\partial}{\partial y}(r\rho v) = 0 \tag{A1}$$

equation of motion:

$$x: \quad \rho \frac{Du}{Dt} = -\frac{\partial p}{\partial x} + \frac{1}{Re}\{2\frac{\partial}{\partial x}(\mu \frac{\partial u}{\partial x}) + \frac{1}{r}\frac{\partial}{\partial y}(r\,\mu \frac{\partial u}{\partial y}) + \frac{1}{r}\frac{\partial}{\partial y}(r\,\mu \frac{\partial v}{\partial x}) - \frac{2}{3}\frac{\partial}{\partial x}[\mu(\frac{\partial u}{\partial x} + \frac{\partial v}{\partial y} + \frac{v}{r})]\} \tag{A2}$$

$$y: \quad \rho \frac{Dv}{Dt} = -\frac{\partial p}{\partial y} + \frac{1}{Re}\{\frac{2}{r}\frac{\partial}{\partial y}(r\,\mu \frac{\partial v}{\partial y}) - \frac{2\mu}{r^2}v + \frac{\partial}{\partial x}(\mu \frac{\partial u}{\partial y} + \mu \frac{\partial v}{\partial x}) - \frac{2}{3}\frac{\partial}{\partial y}[\mu(\frac{\partial u}{\partial x} + \frac{\partial v}{\partial y} + \frac{v}{r})]\} \tag{A3}$$

equation of energy:

$$\rho \frac{DT}{Dt} = (\gamma-1)\,Ma_\infty^2\,(u\frac{\partial p}{\partial x} + v\frac{\partial p}{\partial y}) + \frac{1}{Re}\{\frac{1}{Pr}[\frac{\partial}{\partial x}(\kappa \frac{\partial T}{\partial x}) + \frac{1}{r}\frac{\partial}{\partial y}(r\,\kappa \frac{\partial T}{\partial y})] + (\gamma-1)\,Ma_\infty^2\,\mu\,\phi\} \tag{A4}$$

where the dissipation function ϕ is given by

$$\phi = 2[(\frac{\partial u}{\partial x})^2 + (\frac{\partial v}{\partial y})^2 + (\frac{v}{r})^2] + [\frac{\partial v}{\partial x} + \frac{\partial u}{\partial y}]^2 - \frac{2}{3}[\frac{\partial u}{\partial x} + \frac{\partial v}{\partial y} + \frac{v}{r}]^2 \tag{A5}$$

equation of state

$$1 + \gamma\,Ma_\infty^2\,p = \rho\,T \tag{A6}$$

and a linear function for viscosity and heat conductivity

$$\mu = \kappa = C\,T \quad . \tag{A7}$$

The parameters are:

Reynolds number	$Re = \frac{U_\infty\, r_o}{\nu_\infty}$
Prandtl number	$Pr = \frac{\mu_\infty\, c_p}{\kappa_\infty}$
constant specific heat capacity	c_p
ratio of heat capacities	$\gamma = \frac{c_p}{c_v}$
Chapman-Rubesin parameter	$C = \frac{\rho_w \mu_w}{\rho_\infty\, \mu_\infty}$

The boundary conditions are:

at the wall $y = 0$:

$$u = u_w$$
$$(\rho\, v)_w = \text{constant}$$
$$T = T_w$$

in the undisturbed free stream

$x < 0$: $u = 1$; $T = 1$

$v = 0$; $p = 0$

For velocity slip and temperature jump u_w and T_w are given by [5]:

$$u_w = 1{,}255\ \beta\ \sqrt{\gamma}\ \frac{Ma_\infty}{Re}\ \left(\frac{\partial u}{\partial y}\right)_w \qquad (A8)$$

$$T_w = \frac{T_b}{T_\infty} + 2{,}52\ \frac{2-\alpha}{\alpha}\ \frac{\gamma\ \sqrt{\gamma}}{\gamma+1}\ \frac{Ma_\infty}{Pr\ Re}\ \left(\frac{\partial T}{\partial y}\right)_w \qquad (A9)$$

α and β are accomodation coefficients, depending on the surface properties of the material. They are put equal to one here [5].

The equations have to be solved approximately for large Reynolds numbers due to the singular perturbation method of matched asymptotic expansion. The perturbation parameter is $\varepsilon = Re^{-1/2}$.

The Navier-Stokes equations and the dependent variables are expanded in powers series of ε (see Eq.(1)). These expressions are put into the equations (A1)-(A9) and then collected in powers of ε.

A2. Outer solution

Assuming that since the disturbance of the free stream by the boundary layer displacement is weak and therefore no shock wave at the leading edge exists,the linearized supersonic potential equation has been applied for the outer flow. This yields the first order solution after matching with the free stream:

$$u_1^o = 1\ ,\quad v_1^o = 0\ ,\quad T_1^o = 1\ ,\quad p_1^o = 0\ .$$

The second order equations are composed in a potential equation, defined by $\frac{\partial \varphi}{\partial x} = u_2^o$ and $\frac{\partial \varphi}{\partial y} = v_2^o$:

$$-(Ma_\infty^2 - 1)\,\varphi_{xx} + \varphi_{yy} + \frac{1}{1+y}\,\varphi_y = 0 \qquad (A10)$$

This equation has to be solved to get the unknown pressure distribution of the second order outer solution. Using Ward's operator method to solve equation (A10), the pressure at the wall is given by:

$$p_{2w}(x) = p_2(x,\,0) = -\,u_2^o(x,\,0) =$$

$$\frac{1}{\sqrt{Ma_\infty^2 - 1}}\left\{v_2^o(x,\,0) - \frac{1}{\sqrt{Ma_\infty^2 - 1}}\int_0^x W\left(\frac{x-s}{\sqrt{Ma_\infty^2 - 1}}\right)\ v_2^o(s,\,0)\ ds\ \right\} \qquad (A11)$$

In this equation the velocity $v_2^o(x,y=0)$ is given by the first order boundary solution. The function W(z) is given by Ward [6] as:

$$W(z) = \int_0^\infty \frac{e^{-\lambda z}}{K_1^2(\lambda) + \pi^2\ I_1^2(\lambda)}\ \frac{d\lambda}{\lambda} \qquad z \geq 0 \qquad (A12)$$

$K_1(\lambda)$ and $I_1(\lambda)$ are modified Bessel functions. For $0 \leq z < 2$ (that means $\lambda >> 1$) a Taylor expansion for W is possible, and in this paper a something modified power series of sixth order for W has been used. This polynomial represents the function W with sufficient accuracy even for $z \geq 2$.

$$W(z) = \frac{1}{2} - \frac{3}{8}\,z + \frac{3}{16}\,z^2 - \frac{21}{256}\,z^3 + \frac{9}{256}\,z^4 - 0{,}015454\,z^5 + 0{,}003511\,z^6 \qquad (A13)$$

A3. Inner solution

The following coordinates were used:

$$\xi = \dot{m}_{1w}\sqrt{\frac{x}{C}}\ ; \qquad \eta = \frac{1}{\varepsilon\ \sqrt{cx}}\int_0^y \rho_1\ dy$$

(see also page 5-3, eq.(5)).

First order solution:
The first order equations are.
(equation of motion in x-direction combined with continuity eq.)

$$\frac{\partial^2 u_1}{\partial \eta^2} + \left\{\frac{1}{2}\int_0^\eta \frac{\partial}{\partial \xi}\,(\xi\ u_1)\ d\eta - \xi\right\}\frac{\partial u_1}{\partial \eta} - \frac{1}{2}\,\xi\ u_1\ \frac{\partial u_1}{\partial \xi} = 0 \qquad A14)$$

energy equation:

$$\frac{1}{Pr}\frac{\partial^2 T_1}{\partial \eta^2} + \left\{\frac{1}{2}\int_0^\eta \frac{\partial}{\partial \xi}(\xi\, u_1)\, d\eta - \xi\right\}\frac{\partial T_1}{\partial \eta} - \frac{1}{2}\xi\, u_1 \frac{\partial T_1}{\partial \xi} =$$

$$- (\gamma-1)\, Ma_\infty^2 \left(\frac{\partial u_1}{\partial \eta}\right)^2 \qquad \text{(A15)}$$

together with the boundary conditions:

$$\xi \geq 0, \quad \eta = 0: \quad u_1 = 0\,, \quad T_1 = T_{1w} = \frac{T_b}{T_\infty} = \text{const}$$

$$\eta \to \infty: \quad u_1 = u_1^a(\xi, 0) = 1\,, \quad T_1 = T_1^a(\xi, 0) = 1$$

Second order solution:
Concerning the second order equations, a detailed analysis shows that for numerical calculation it is necessary to solve the equations in terms of $\bar{u}_2 = u_2/\rho_{2w}$, $\bar{T} = T_2/\rho_{2w}$ etc., due to difficulties in numerical stability.

One gets for second order equation of motion, combined with first and second order continuity equation: ($f = \rho_{2w}\xi/\dot{m}_{1w}$ and $f' = df/d\xi$)

$$\frac{\partial^2 \bar{u}_2}{\partial \eta^2} + \left(\frac{1}{2}\int_0^\eta \frac{\partial}{\partial \xi}(\xi\, u_1)\, d\eta - \xi\right)\frac{\partial \bar{u}_2}{\partial \eta}\, d\eta + \left(\frac{1}{2}\,\xi\,\frac{f'}{f}\int_0^\eta \bar{u}_2\, d\eta + \frac{1}{2}\,\xi\int_0^\eta \frac{\partial \bar{u}_2}{\partial \xi}\, d\eta\right)\frac{\partial u_1}{\partial \eta} -$$

$$- \frac{1}{2}\,\xi\left(u_1 \frac{\partial \bar{u}_2}{\partial \xi} + \bar{u}_2 \frac{\partial u_1}{\partial \xi}\right) + \frac{1}{2}\left(1 - \xi\,\frac{f'}{f}\right)\bar{u}_2 \cdot u_1 =$$

$$- \frac{1}{2}\left(1 - \xi\,\frac{f'}{f}\right) T_1 - \frac{1}{2}\,\xi\left\{\int_0^\eta \frac{\partial}{\partial \xi}\left(u_1 \frac{\bar{\rho}_2}{\rho_1}\right) d\bar{\eta} + \frac{f'}{f}\int_0^\eta \left(u_1 \frac{\bar{\rho}_2}{\rho_1}\right) d\eta\right\}\frac{\partial u_1}{\partial \eta} +$$

$$+ \frac{1}{2}\,\xi\,\frac{\bar{\rho}_2}{\rho_1}\, u_1 \frac{\partial u_1}{\partial \xi} - \frac{\bar{T}_2}{T_1}\frac{\partial^2 u_1}{\partial \eta^2} - \frac{\partial u_1}{\partial \eta}\frac{\partial}{\partial \eta}\left(\frac{\bar{T}_2}{T_1}\right) -$$

$$- \frac{C^{3/2}}{\dot{m}_{1w}^2}\,\frac{\xi^2}{f}\left\{T_1 + \int_0^\eta \bar{v}_1\, d\eta\right\}\frac{\partial u_1}{\partial \eta} \qquad \text{(A16)}$$

energy equation:

$$\frac{1}{Pr}\frac{\partial^2 \bar{T}_2}{\partial \eta^2} + \left\{\frac{1}{2}\int_0^\eta \frac{\partial}{\partial \xi}(\xi\, u_1)\, d\eta - \xi\right\}\frac{\partial \bar{T}_2}{\partial \eta} - \frac{1}{2}\,\xi\, u_1 \frac{\partial \bar{T}_2}{\partial \xi} + \frac{1}{Pr}\frac{\partial}{\partial \eta}\left(\frac{\bar{T}_2}{T_1}\frac{\partial T_1}{\partial \eta}\right) +$$

$$+ \left\{\frac{1}{2}\left(1 - \xi\,\frac{f'}{f}\right) u_1 + \frac{1}{2}\,\xi\, u_1 \frac{\partial T_1}{\partial \xi} + (\gamma-1)\, Ma_\infty^2 \frac{1}{T_1}\left(\frac{\partial u_1}{\partial \eta}\right)^2\right\}\bar{T}_2 -$$

$$- \frac{1}{2}\,\xi\left\{\int_0^\eta \frac{\partial}{\partial \xi}\left(u_1 \frac{\bar{T}_2}{T_1}\right) d\eta + \frac{f'}{f}\int_0^\eta \left(u_1 \frac{\bar{T}_2}{T_1}\right) d\eta\right\}\frac{\partial T_1}{\partial \eta} = \frac{1}{2}(\gamma-1)\, Ma_\infty^2 \left(1 - \xi\,\frac{f'}{f}\right) u_1\, T_1$$

$$- 2(\gamma-1)\, Ma_\infty^2 \frac{\partial \bar{u}_2}{\partial \eta}\,\frac{\partial u_1}{\partial \eta} + \frac{1}{2}\,\xi\,(\bar{u}_2 + \gamma\, Ma_\infty^2\, u_1)\frac{\partial T_1}{\partial \xi} -$$

$$\frac{1}{2}\,\xi\left\{\int_0^\eta \frac{\partial \bar{u}_2}{\partial \xi}\, d\eta + \frac{f'}{f}\int_0^\eta \bar{u}_2\, d\eta + \gamma\, Ma_\infty^2 \int_0^\eta \frac{\partial u_1}{\partial \xi}\, d\eta + \gamma\, Ma_\infty^2 \frac{f'}{f}\int_0^\eta u_1\, d\eta\right\}\frac{\partial T_1}{\partial \eta} -$$

$$- \frac{C^{3/2}}{\dot{m}_{1w}^2}\,\frac{\xi^2}{f}\left\{\frac{1}{Pr}\, T_1 + \int_0^\eta \bar{v}_1\, d\eta\right\}\frac{\partial T_1}{\partial \eta} \qquad \text{(A17)}$$

Boundary condition
The boundary conditions at the wall are

$$\xi \geq 0\,, \quad \eta = 0: \quad \bar{u}_2 = \bar{u}_{2w}\,, \quad \bar{T}_2 = \bar{T}_{2w}\,.$$

Without velocity slip and temperature jump there is

$$\bar{u}_{2w} = \bar{T}_{2w} = 0$$

whereas in the other case, $\bar{u}_{2w}$ and $\bar{T}_{2w}$ are given by

$$\bar{u}_{2w} = a_1 \frac{Ma_\infty}{C\, f\, T_{1w}}\left(\frac{\partial u_1}{\partial \eta}\right)_w \quad \text{and} \quad \bar{T}_{2w} = a_2 \frac{Ma_\infty}{C\, f\, T_1}\left(\frac{\partial T_1}{\partial \eta}\right)_w$$

where a_1 and a_2 are defined by eq.(A8), (A9). The second order blowing velocity v_{2w}, occuring in the integrated continuity equation, has been determined by the assumption of constant injected mass flow.

$$\varepsilon^{-1}\,\dot{m}_w = \dot{m}_{1w} + \varepsilon\,\dot{m}_{2w} \ldots = \rho_{1w}\,v_{1w} + \varepsilon(\rho_{1w}\,v_{2w} + \rho_{2w}\,v_{1w}) \ldots = \text{const}$$

it yields

$$v_{2w} = -\frac{\rho_{2w}}{\rho_{1w}}\,v_{1w} = -\frac{\rho_{2w}}{\rho_{1w}^2}\,\dot{m}_{1w} \qquad \text{(A18)}$$

At the outer edge of the boundary layer, the conditions are obtained from matching with the outer solution:

$$\xi \geq 0\,, \quad \eta \to \infty: \quad \bar{u}_2(\xi,\,\eta \to \infty) = u_2^a(\xi,\,0)/\,p_{2w}(\xi) = -\,1$$

$$\bar{T}_2(\xi,\,\eta \to \infty) = T_2^a(\xi,\,0)/p_{2w}(\xi) = (\gamma-1)\,Ma_\infty^2$$

The wall shear stress is given by Eq.(8) - (11).

Numerical procedure

The discretisation of the differential equations for the inner solution has been carried out according to the Crank-Nicolson difference-scheme. For solution of the systems of algebraic equations Gaussian algorithm has been used and the nonlinear first order equation of motion was solved by n-dimensional Newton iteration. The meshlengths of the grid were $\Delta\xi = 0.02$ and $\Delta\eta = 0.2$. The iterative process was stopped, when a relative accuracy of 10^{-6} was reached.

The computing time on the computer Telefunken TR 440 of the Ruhr-University Bochum was less than 10 min. for one complete solution.

The values of the parameters which have been kept constant are: $Pr = 0{,}72$; $\gamma = 1{,}4$; $C = 1$. The accomodation coefficients of the slip velocity and temperature jump are $\beta = 1$, $\alpha = 1$ (see Eq.(A8), (A9)). The range of the remaining parameters is

$0.1 \leq T_b/T_\infty \leq 4$; $\sqrt{2} \leq Ma_\infty \leq 4$; $0.5 \leq \dot{m}_{1w} \leq 2$.

EVALUATION OF SEVERAL APPROXIMATE MODELS FOR LAMINAR INCOMPRESSIBLE SEPARATION BY COMPARISON WITH COMPLETE NAVIER-STOKES SOLUTIONS*

by

K.N. Ghia, U. Ghia
University of Cincinnati, Cincinnati, Ohio, U.S.A.

and W.A. Tesch
General Electric Company, Evendale, Ohio, U.S.A.

SUMMARY

Several approximate mathematical models have been analyzed for studying laminar separation for incompressible flow, for which the Navier-Stokes equations comprise an exact mathematical model. Two model flow configurations have been used. The first configuration considered consists of the flow in the boundary layer on a two-dimensional semi-infinite slab with a vertical leading face and shoulders, with varying degree of bluntness, forming an external corner on the body. The second flow configuration represents a class of two-dimensional bodies with an internal corner and a more pronounced separation region; this configuration is used for only one approximate model so far.

Results obtained with the various approximate models are evaluated by comparison with the corresponding Navier-Stokes solutions. All the models considered lead to improved results as the Reynolds number is increased. Of particular significance is one model which yields excellent agreement with Navier-Stokes solutions for separated flow as well as for low Reynolds number flows. The inclusion of displacement effects has been found to be most significant for the proper representation of the separated flow fields.

1. INTRODUCTION

An important characteristic of viscous flow past a solid body is the separation phenomenon. Inspite of considerable success in dealing with laminar flow phenomena, studies of separation for incompressible flows have been limited [Brown and Stewartson[1]]. With the advent of high-speed computers, Navier-Stokes solutions for flows with separation have now become feasible [Briley[2] and Leal[3]]. However, these solutions generally require large computer time even for flat plate geometries. On the other hand, it has been sufficiently demonstrated that, if inviscid-viscid interaction is permitted, it should be possible to remove the Goldstein square-root singularity[4] at the separation point and integrate the boundary-layer equations for separated flow. The present study serves to further confirm this concept by verifying it with respect to some model problems with surface curvature. Inclusion of some second-order curvature terms is found necessary when the surface curvature becomes large.

Recently, U. Ghia and Davis[5] have determined the full Navier-Stokes solutions for the first model problem used in the present study. Their study also provided solutions using a simplified mathematical model which neglected the elliptic terms from the vorticity equation but retained the complete elliptic stream function equation. This simplified model correctly calculates the elliptic external inviscid flow, i.e., accounts for the displacement effects and thereby yields results that agree remarkably well with the Navier-Stokes solutions for cases with small separation bubbles imbedded in the viscous region. This study gave further evidence that it should be possible to obtain solutions using boundary-layer-type equations for a mildly separated flow if viscous-inviscid interaction is considered. Werle and Bernstein[6] considered a further simplification of this approximate model by neglecting, from the parabolized vorticity equation, all terms arising due to the second-order curvature effects while maintaining the tangential pressure gradient term to vary with normal distance. Briley and McDonald[7] considered the interaction for laminar, transitional and turbulent, mildly separated flow by calculating the displacement flow using a source-sink distribution approach. Dancey and Pletcher[8] have recently suggested the inclusion of interaction effects by using the complete Bernoulli equation in the inviscid flow region.

All of these studies constitute approaches wherein the displacement thickness interaction is included by retaining the appropriate terms in the governing differential equations. An alternative approach consists of including this interaction through suitable modification of the boundary conditions. This involves the specification of the boundary values for a flow quantity that is most sensitive to the separation phenomenon, e.g., displacement thickness or surface vorticity.

Catherall and Mangler[9] were the first to overcome the difficulty in the boundary-layer equations at the separation singularity by prescribing the displacement thickness instead of the inviscid pressure, and calculating the latter quantity as a part of the solution. Klineberg and Steger[10] could remove the separation singularity by using a model in which the inviscid-viscid interaction was accounted for by prescribing the wall

---

* This research is supported by the National Science Foundation under Grant No. GK-35514.

shear. Later, Carter[11] extensively studied both these approaches and concluded that, of the two, the problem with prescribed displacement thickness is a better approach for considering the necessary interaction. Carter arrived at this conclusion because the numerical scheme with which he modeled the problem with prescribed wall shear resulted in a discontinuity in the outer-edge velocity for the post-separation region. It appears, however, that this may not necessarily be a direct consequence of using prescribed wall shear, but rather the effect of the numerical scheme employed. It is shown, in the present work, that careful handling of the numerical procedure can eliminate this discontinuity.

The goal of the present study is to appropriately represent and compute the separated flow field which can occur in flow configurations with large curvature of the body surface, as the Reynolds number is increased. The Navier-Stokes equations, of course, comprise an exact mathematical model for these flow problems with separation. But the presentation here discusses several approximate models that can be derived from the full Navier-Stokes equations. If an approximate model is such that it does not take into account the viscous-inviscid interaction in the flow field, then it is obviously not suitable for a separated flow calculation. The viscous-inviscid interaction may be taken into consideration either by retaining in the approximate model those terms that significantly account for this interaction or through suitable modification of the boundary conditions for the problem. Both of these approaches have been investigated in the present work.

The first problem considered consists of the flow past a class of two-dimensional semi-infinite bodies with a vertical leading face and shoulders with varying degree of bluntness [Fig. 1]. In the limit of zero shoulder bluntness, the body reduces to a semi-infinite rectangular slab of specified thickness. For certain values of the problem parameters, the flow encounters a finite region of separation which occurs shortly after the flow negotiates the turn around the body shoulder. Four different approximate models are evaluated and discussed with respect to these separated flow configurations. This model problem also makes it possible to study the limitations on the boundary-layer solutions due to the sharp shoulder that develops on the thick slab of vanishing shoulder bluntness.

The second configuration studied is shown in Fig. 2 and represents the flow over a class of bodies with a cylindrically shaped stagnation surface followed by a concave corner, of varying roundedness, merging into a parabolic surface. Solutions are presented for this flow configuration using the complete Navier-Stokes equations. An approximate model that performs remarkably well for the first flow configuration is shown to, again, almost reproduce the Navier-Stokes solutions for this new configuration. As a limiting case, this second configuration can correspond to the flow past a circular cylinder; some results are presented for this case also.

2. ANALYSIS

The Navier-Stokes equations constitute an exact mathematical model for the separated flow problems of present interest. Therefore, these equations are developed first. The development here is similar to the earlier work of U. Ghia and Davis[5].

The nondimensional Navier-Stokes equations in terms of vorticity and stream function for two-dimensional flow are

$$\omega_t + \psi_y \omega_x - \psi_x \omega_y = \omega_{xx} + \omega_{yy} \tag{1}$$

and

$$\psi_{xx} + \psi_{yy} = -\omega \ . \tag{2}$$

Here, the following nondimensionalization has been used.

$$\psi = \frac{\psi^*}{\nu} \ , \quad \omega = \frac{\omega^*}{U_\infty^2/\nu} \ , \quad u = \frac{u^*}{U_\infty} \ , \quad v = \frac{v^*}{U_\infty}$$

$$p = \frac{p^* - p_\infty}{\rho_\infty U_\infty^2} \ , \quad x = \frac{x^*}{\nu/U_\infty} \ , \quad y = \frac{y^*}{\nu/U_\infty} \ , \quad t = \frac{t^*}{\nu/U_\infty^2} \ . \tag{3}$$

For the problems considered, it is more advantageous to formulate these equations in a coordinate system (ξ,η) obtained from the Cartesian coordinates by conformal transformations. In the new coordinates, the body surface lies along one of the coordinate surfaces, thus facilitating the specification of boundary conditions.

For a conformal transformation of the type

$$z = F(\zeta) \ , \tag{4}$$

where $z = x + iy$ and $\zeta = \xi + i\eta$, the scale factors h_1 and h_2 are given as

$$h_1 = h_2 = \left|\frac{dz}{d\zeta}\right| \ . \tag{5}$$

It is found more convenient to work with a scale factor function H as defined below, rather than with the scale factors themselves, such that

$$H = \frac{1}{h_1} = \frac{1}{h_2} \quad . \tag{6}$$

Therefore, Eqs. (1) and (2) can be written in terms of the conformal coordinates (ξ,η) as

$$\omega_{\eta\eta} + \omega_{\xi\xi} + \psi_\xi \omega_\eta - \psi_\eta \omega_\xi = \frac{1}{H^2}\,\omega_t \tag{7}$$

and

$$\psi_{\eta\eta} + \psi_{\xi\xi} = -\frac{1}{H^2}\,\omega \quad . \tag{8}$$

Similarity forms are now introduced for the stream function and the vorticity. Based on the corresponding inviscid flow in terms of the (ξ,η) coordinates, the suitable form for the stream function of the viscous solution is taken to be

$$\psi = \xi\, f(\xi,\eta) \quad . \tag{9}$$

Substitution of Eq. (9) into the stream function Eq. (8) leads to the following definition for the new vorticity function $g(\xi,\eta)$ as

$$\omega = -\,\xi\, H^2\, g(\xi,\eta) \quad . \tag{10}$$

Using Eq. (10) in the vorticity Eq. (7) yields, after some algebra, the transformed vorticity equation as

$$g_{\eta\eta} + \left[4\,\frac{H_\eta}{H} + f + \xi\, f_\xi\right] g_\eta + \left[\frac{4}{\xi}\,\frac{H_\xi}{H} + 2\left(\frac{H_\eta^2 + H_\xi^2}{H^2} + \frac{H_{\eta\eta} + H_{\xi\xi}}{H}\right) + 2\,\frac{H_\eta}{H}\,(f + \xi\, f_\xi)\right.$$

$$\left. - f_\eta\left(1 + 2\xi\,\frac{H_\xi}{H}\right)\right] g + \left[4\,\frac{H_\xi}{H} - \xi\, f_\xi\right] g_\xi + g_{\xi\xi} + \frac{2}{\xi}\, g_\xi = \frac{1}{H^2}\, g_t \quad . \tag{11}$$

The stream function Eq. (8) can now be written as

$$f_{\eta\eta} + f_{\xi\xi} + \frac{2}{\xi}\, f_\xi = g \quad . \tag{12}$$

In terms of the new stream function $f(\xi,\eta)$, the velocity components u and v along the ξ and η directions, respectively, are obtained as

$$u = \xi H\, f_\eta \qquad \text{and} \qquad v = -\,H[\xi f_\xi + f] \quad . \tag{13}$$

Equations (11) and (12) comprise the Navier-Stokes in terms of the new variables. The boundary conditions needed for a unique solution of these equations are presented next. At the surface of the solid body, the condition of zero slip requires that

$$f(\xi,\eta_w) = 0 \qquad \text{and} \qquad f_\eta(\xi,\eta_w) = 0 \quad . \tag{14}$$

At large normal distances from the body surface, the flow asymptotically approaches the external inviscid flow so that the outer boundary conditions are expressed as

$$f_\eta(\xi,\infty) \to 1 \qquad \text{and} \qquad g(\xi,\infty) \to 0 \quad . \tag{15}$$

The flow is assumed to be symmetric about the line $\xi = 0$; use of this condition in the Navier-Stokes Eqs. (11) and (12) leads to two equations for f and g valid at this symmetry line.

Finally, as $\xi \to \infty$, the Navier-Stokes Eqs. (11) and (12) have been shown to reduce to

$$g'' + fg' - f'\left[1 + \lim_{\xi\to\infty}\left(2\xi\,\frac{H_\xi}{H}\right)\right] g = 0 \quad , \tag{16}$$

and

$$f'' = g \tag{17}$$

where the primes denote differentation with respect to η. Solution of Eqs. (16) and (17) provides the correct downstream boundary condition for the general Navier-Stokes equations (11) and (12).

In the present study, several approximate flow models have also been studied. The governing differential equations for these approximate models will be written first; the boundary conditions given earlier will be stated once, for completeness, only after all the models have been presented.

Mathematical Models For Incompressible Separation

The hierarchy of approximations considered for separated incompressible boundary layers leads to the following mathematical models:

a. Navier-Stokes Model
b. Parabolized-Vorticity Model
c. Parabolic Approximation Model
d. Parabolized-Vorticity Model without Curvature Effects
e. Boundary-Layer Model

Equations (11) and (12) comprise the Navier-Stokes model which is considered to represent the separated flow problem in an exact manner. The approximate models listed above are derived from these equations.

b. Parabolized-Vorticity Model

In this flow model, the stream function equation (12) is retained completely, but the vorticity equation (11) is parabolized by dropping the terms $g_{\xi\xi} + \frac{2}{\xi} g_{\xi}$. Hence, the governing differential equations become

$$g_{\eta\eta} + [4\frac{H_\eta}{H} + f + \xi f_\xi]g_\eta + [\frac{4}{\xi}\frac{H_\xi}{H} + 2(\frac{H_\xi^2 + H_\eta^2}{H^2} + \frac{H_{\eta\eta} + H_{\xi\xi}}{H}) + 2\frac{H_\eta}{H}(f + \xi f_\xi) - f_\eta(1 + 2\xi\frac{H_\xi}{H})]g + [4\frac{H_\xi}{H} - \xi f_\eta]g_\xi = \frac{1}{H^2} g_t \quad (18)$$

and

$$f_{\eta\eta} + f_{\xi\xi} + \frac{2}{\xi} f_\xi = g \quad . \quad (19)$$

c. Parabolic Approximation Model

Both the vorticity and the stream function equations are parabolized by dropping the terms $g_{\xi\xi} + \frac{2}{\xi} g_\xi$ and $f_{\xi\xi} + \frac{2}{\xi} f_\xi$ from Eqs. (11) and (12), respectively. The reduced vorticity equation retains in it the terms corresponding to curvature effects. Thus, the parabolic approximation model is comprised of the following equations:

$$g_{\eta\eta} + [4\frac{H_\eta}{H} + f + \xi f_\xi]g_\eta + [\frac{4}{\xi}\frac{H_\xi}{H} + 2(\frac{H_\xi^2 + H_\eta^2}{H^2} + \frac{H_{\eta\eta} + H_{\xi\xi}}{H}) + 2\frac{H_\eta}{H}(f + \xi f_\xi) - f_\eta(1 + 2\xi\frac{H_\xi}{H})]g + (4\frac{H_\xi}{H} - \xi f_\xi)g_\xi = \frac{g_t}{H^2} \quad (20)$$

and

$$f_{\eta\eta} = g \quad . \quad (21)$$

d. Parabolized-Vorticity Model Without Curvature Effects

If the curvature terms are neglected in the parabolized vorticity equation (18), while retaining the full stream function equation (19), the following mathematical model is obtained:

$$g_{\eta\eta} + [f + \xi f_\xi]g_\eta - f_\eta[1 + 2\xi\frac{H_\xi}{H}]g - \xi f_\eta g_\xi = \frac{g_t}{H^2} \quad (22)$$

and

$$f_{\eta\eta} + f_{\xi\xi} + \frac{2}{\xi} f_\xi = g \quad . \quad (23)$$

As will be seen shortly, Eq. (22) has the form of boundary-layer equations; however, the present dependent and independent variables and the scale factor function H are not boundary-layer type variables. Also, the inviscid pressure gradient term [containing $\xi\frac{H_\xi}{H}$] is not evaluated at the body surface, as in a conventional boundary-layer analysis.

e. Boundary-Layer Model

The nondimensionalization used in Eq. (3) is not suitable for a boundary-layer analysis. For instance, the viscous length ν/U_∞ is not an appropriate reference length for nondimensionalizing the boundary-layer equations. Instead, if some length L is used as the reference length, then the new nondimensional variables, denoted by (~) over them, will be related to the present nondimensional variables as follows:

$$\psi = Re\,\tilde{\psi} \quad , \quad \omega = \tilde{\omega}/Re \quad , \quad u = \tilde{u} \quad , \quad v = \tilde{v} \quad , \quad p = \tilde{p} \quad , \quad H = \frac{1}{\sqrt{Re}}\tilde{H} \quad ,$$

$$\tilde{x} = \tilde{x}\,Re \quad , \quad \xi = \sqrt{Re}\,\tilde{\xi} \quad , \quad \eta = \sqrt{Re}\,\tilde{\eta} \quad , \quad t = Re\,\tilde{t} \quad \text{where} \quad Re = U_\infty L/\nu \quad . \tag{24}$$

The corresponding boundary-layer variables denoted by ($\bar{}$) over them, are obtained from these new dimensionless variables through the following relations:

$$\tilde{\psi} = \epsilon\bar{\psi} \quad , \quad \tilde{\omega} = \bar{\omega}/\epsilon \quad , \quad \tilde{H}(\tilde{\xi},\tilde{\eta}_w) = \bar{H} \quad , \quad \tilde{\xi} = \bar{\xi} \quad , \quad \tilde{\eta} = \tilde{\eta}_w + \epsilon\bar{\eta} \tag{25}$$

where $\epsilon = 1/\sqrt{Re}$.

The boundary-layer assumptions can now be used in the full Navier-Stokes equations written using the new nondimensional variables given in Eq. (24). This will lead to the following boundary-layer vorticity and stream function equations in similarity-type variables in general conformal coordinates:

$$\bar{g}_{\eta\eta} + [\bar{f} + \bar{\xi}\bar{f}_{\bar{\xi}}]\bar{g}_{\eta} - \bar{f}_{\eta}[1 + 2\bar{\xi}\frac{\bar{H}_{\bar{\xi}}}{\bar{H}}]\bar{g} - \bar{\xi}\bar{f}_{\eta}\,\bar{g}_{\bar{\xi}} = \frac{g_t}{\bar{H}^2} \tag{26}$$

and $$\bar{f}_{\eta\eta} = \bar{g} \quad . \tag{27}$$

This form of the boundary-layer equations contains much more information than is first apparent. For instance, substituting Eq. (27) into Eq. (26) leads to an equation that can be analytically integrated once with respect to η. The arbitrary function of integration will be a function of ξ only and can be determined by evaluating the result in the outer inviscid flow region. This reveals that the quantity $[1 + \bar{\xi}\frac{\bar{H}_{\bar{\xi}}}{\bar{H}}]$ is related to the inviscid pressure gradient. Further, if terms containing $\bar{\xi}$-derivatives are ignored, the equation reduces to the Falkner-Skan equation in similarity variables. It is for this reason that the present formulation leads to a self-similar solution along the stagnation line $\bar{\xi} = 0$ and as $\bar{\xi} \to \infty$ where $\bar{f}_{\bar{\xi}}$ and $\bar{g}_{\bar{\xi}}$ are known to vanish.

Boundary Conditions For Approximate Models b through d:

At the surface of the body, the no-slip condition states that,

$$\text{at} \quad \eta = \eta_w \;:\; f = 0 \quad , \quad f_\eta = 0 \quad . \tag{28}$$

Asymptotically far from the body surface, the external inviscid flow prevails and, hence,

$$\text{as} \quad \eta \to \infty \;:\; f_\eta \to 1 \quad , \quad g = 0 \quad . \tag{29}$$

The symmetry of the flow about the line $\xi = 0$ is used to provide the limiting equations for vorticity and stream function valid at the symmetry line. In addition, models b and d require a downstream boundary condition for the stream function variable; this is provided by the solution of the limiting form of the stream function equation:

$$\text{as} \quad \xi \to \infty \;:\; f''' = g \tag{30}$$

where the primes denote differentiation with respect to η. Model c does not require this downstream boundary condition because it consists of totally parabolic equations only.

Boundary Conditions for Boundary-Layer Model e:

At the surface of the body, the no-slip condition states that

$$\text{at} \quad \bar{\eta} = 0 \;:\; \bar{f} = 0 \quad , \quad \bar{f}_{\bar{\eta}} = 0 \quad . \tag{31}$$

At the outer edge of the boundary layer where the vorticity function approaches zero, the following condition holds:

$$\text{as} \quad \bar{\eta} \to \bar{\eta}_e \;:\; \bar{f}_{\bar{\eta}} \to 1 \quad , \quad \bar{g} = 0 \quad . \tag{32}$$

The symmetry of the flow about the line $\xi = 0$ is used to provide self-similar equations for vorticity and stream function at the symmetry line:

$$\bar{g}_{\eta\eta} + \bar{f}\,\bar{g}_{\eta} - \bar{f}_{\eta}\,\bar{g} = 0 \qquad \text{and} \qquad \bar{f}_{\eta\eta} = \bar{g} \quad . \tag{33}$$

3. NUMERICAL ANALYSIS

The numerical method used to solve the flow equations for the various approximate models depends on the nature of the equations in the respective approximate model. Thus, the alternating direction implicit (ADI) method is used if the equation is of the elliptic type in (ξ,η) coordinates and a simple implicit scheme, with a backward difference for the streamwise convective term, is used if the equation is of the parabolic type in (ξ,η) coordinates. The ADI method used in the present work is essentially as formulated by Davis[12] and has been discussed elsewhere [Refs. 5 and 12, among others]. Therefore, only some important points are mentioned here; the variations needed in the method for use with the present work are described thereafter.

Since the inviscid flow conditions have to be matched as $\eta \to \infty$, or, even for the boundary-layer type model where the outer boundary condition is imposed at $\eta = \eta_e$ and η_e is a large number, the accuracy of the calculations can be improved by using the following dependent variable for the stream function

$$h = f - \eta \qquad \text{or} \qquad \bar{h} = \bar{f} - \bar{\eta} \quad . \tag{34}$$

Now, as $\eta \to \infty$, the stream function $f \to \eta$ but the new stream function h approaches a finite value.

Further, the analysis presented so far is for two-dimensional semi-infinite bodies with an axis of symmetry. The region of computation for such bodies is the entire upper half-plane. However, the choice of the orthogonal conformal coordinates (ξ,η) is such that the surface of the body lies along η = constant and, in the (ξ,η) coordinates, the computational domain is reduced to a quarter infinite plane. For the actual numerical calculations, the quarter infinite plane will require a large number of grid points for any meaningful resolution. Hence, based on the asymptotic behavior of the flow variables for large ξ and η, the following transformation is used for the coordinates:

$$S = 1 - \frac{A}{\xi} \ln\left(1 + \frac{\xi}{A}\right) \qquad \text{and} \qquad N = \frac{\eta - \eta_w}{C + (\eta - \eta_w)} \tag{35}$$

where the constants A and C are chosen such that the flow variables are regularly behaved with respect to the S and N directions. In terms of the (S,N) variables, the computational region is reduced to a unit square.

Finally, it is seen that there are three η-boundary conditions for f and only one η-boundary condition for g, even though a second-order differential equation in η is to be solved for g also. A unique solution is therefore obtained using a superposition technique by suitably combining the 'homogeneous' and 'particular' solutions of these linear finite-difference equations.

The above discussion in this section pertains to obtaining numerical solutions for unseparated flow. Certain modifications become necessary when calculations are to be made for separated flow. For instance, in the region of reversed flow, the implicit marching method for parabolic equations needs to be modified in order to properly take into consideration the direction of the flow, thereby requiring a field-sweep iterative procedure. In this procedure, the standard implicit marching technique was used in the region from the stagnation line at $\xi = 0$ up to that location of ξ (denoted as ξ_s) where the coefficient of the streamwise convective term first undergoes a change in its sign. The marching technique iterates upon the calculations performed at a given ξ-line until the solution at that ξ-line is completely converged; only thereafter do the calculations proceed to the next ξ-line. In the region between the ξ-line denoted as ξ_s and the line at $\xi \to \infty$ where the Blasius self-similar flow prevails, only one iteration is performed at each station, till all the stations are computed. The calculations then return to ξ_s and the process is repeated in this sub-field, until a required convergence criterion is satisfied. Also, in order to enhance computational stability in the reversed flow region, the solution of the governing equations was obtained after including a time derivative term in the vorticity equation. Thus, the required converged results were obtained as the asymptotic solution, for large time, using the time-dependent equation.

A final comment about the modifications needed for separated flow computations concerns the case when the viscous-inviscid interaction is considered through specification of proper surface vorticity. For this case, the boundary value problem for g becomes simplified and the superposition technique needed earlier is no longer required. The problem for the stream function becomes an initial value problem with both conditions available at the body surface.

The mathematical analysis and the numerical procedures presented above have been applied to compute solutions for separated flow past some two-dimensional bodies; the results obtained are discussed in the following section.

4. DISCUSSION OF RESULTS FOR FLOW PAST A CLASS OF BODIES WITH A SHOULDER

The presentation so far has been quite general and is useful for a wide class of two-dimensional flow problems. As an application, the model problem corresponding to flow past a class of bodies with a shoulder, shown in Fig. 1, is selected. For this geometry, the new plane of coordinates (ξ,η) using the conformal Schwarz-Christoffel transformation is defined such that

$$\frac{dz}{d\zeta} = [Re - \zeta^2]^{1/2} \qquad \text{where} \qquad Re = \frac{2}{\pi} \frac{U_\infty \ell}{\nu} \quad . \tag{36}$$

This relation is used to provide the transformation function H for all the approximate models considered except for the boundary-layer model for which the corresponding relation is

$$\frac{d\bar{z}}{d\bar{\zeta}} = [1 - \bar{\zeta}^2]^{1/2} \quad . \tag{37}$$

Integration of Eq. (36) yields

$$z = \frac{1}{2} [\zeta(1 - \zeta^2)^{1/2} + Re \sin^{-1}(\zeta/\sqrt{Re})] \quad , \tag{38}$$

while the integration of Eq. (37) leads to

$$\bar{x} = \frac{1}{2}\left[\bar{\zeta}(1 - \bar{\zeta}^2)^{1/2} + \sin^{-1}\bar{\zeta}\right] \quad . \tag{39}$$

Thus, η_w and Re comprise the two parameters of the problem for all the approximate models except the boundary-layer model for which the only parameter is

$$\bar{\eta}_w = \eta_w/\sqrt{Re} \quad .$$

Finally, the scale factor function H can be defined using Eq. (5) for this geometry as

$$H^4 = \frac{1}{(\xi^2 + \eta^2 - Re)^2 + 4\,Re\,\eta^2} \quad . \tag{40}$$

For the boundary-layer model, this becomes

$$\bar{H}^4 = \frac{1}{(\bar{\xi}^2 + \bar{\eta}_w^2 - 1)^2 + 4\,\bar{\eta}_w^2} \quad . \tag{41}$$

First, results were obtained for a non-separated case for which the exact Navier-Stokes solutions were given by U. Ghia and Davis[5]. The parameters for this case are $Re = 161.5$, $\eta_w = 10$ so that $\bar{\eta}_w = 0.786$, and correspond to a blunted body at moderate Reynolds number. Figure 3 shows the surface vorticity function g_w as well as the outer-edge stream function $(f - \eta)_e$ for the Navier-Stokes as well as the approximate models. The parabolized-vorticity model almost reproduces the Navier-Stokes solution for this case. The boundary-layer model leads to a solution that corresponds to the Hiemenz solution at the stagnation point and monotically approaches the flat plate Blasius value at downstream infinity, as it should. Inclusion of the curvature effects is seen to improve the results in the stagnation region; this is seen clearly from the results observed for g_w with the parabolic approximation. Thus, the analysis leads to reasonable results for the non-separated cases; its application to the separated flow cases is discussed next.

The Navier-Stokes model and the parabolized-vorticity model (with or without curvature effects) require no special treatment in the presence of separation because the equations for these models directly include the viscous-inviscid interaction due to displacement thickness effects. This interaction is not included in the equations for the parabolic-approximation model and the boundary-layer model. For these two models, the displacement thickness interaction is accounted for by proper re-definition of the boundary conditions [Eqs. (28-29) or Eqs. (31-32)]. Without this interaction, the solution encounters a singularity at the separation point and fails to converge thereafter. This is clearly seen in Fig. 4 where the curves resulting from the parabolic-approximation model and the boundary-layer model are not continued beyond $\xi/\sqrt{Re} = 1.0$ for both cases presented.

It must first be recalled that, in the conventional boundary-layer approach, the vorticity-stream function formulation involves prescribing $f_\eta = 1$ at the outer edge of the boundary layer where the vorticity function $g = 0$ at all ξ locations. Mathematically, this states that

$$\text{as} \qquad \eta \to \eta_e \quad : \quad f_\eta \to 1 \quad , \quad g = 0 \quad . \tag{42}$$

For the separated flow calculations, the boundary condition $f_\eta \to 1$ as $\eta \to \eta_e$ is not accurate. Even for mildly separated flow, the inviscid-viscous interaction must be accounted for by proper inclusion of displacement effect. It has been observed (Refs. 1, 3, 10) that including this interaction by employing the interacted values of the inviscid pressure gradient does not serve to remove the separation singularity from the boundary-layer equations. To confirm this for the present formulation, the boundary condition that $f_\eta \to 1$ as $\eta \to \eta_e$ was modified to use f_{η_e} prescribed from the results of the Navier-Stokes calculations. The results showed that, with such use of the interacted f_{η_e} values, the separation singularity persists in the flow field and exhibits itself in the form of algebraic decay of vorticity and stream function at various ξ locations in and aft of the separation region. This is because prescribing the interacted f_{η_e} is equivalent to specifying the interacted pressure gradient in the inviscid flow, so that both the parabolic approximation and the boundary layer models lead to a singularity at separation with this approach.

Instead of prescribing the outer edge velocity, it is equally possible to specify the interacted stream function $(f - \eta)_e$ which includes the displacement interaction more effectively. This leads to a computational procedure which will be referred to as the inverse problem of prescribed stream function as described next.

The formulation that follows will pertain to the parabolic-approximation model. It is equally valid for the boundary-layer model, when referred to the appropriate differential equations and boundary conditions, with the proper boundary-layer variables.

Prescribed Interacted Stream Function $(f - \eta)_e$:

The governing differential equations remain unchanged, but the boundary conditions

are now as follows:

$$\text{At} \quad \eta = \eta_w \; : \; f = 0 \; , \; f_\eta = 0 \; ; \; \eta \to \eta_e \; : \; (f - \eta)_e \text{ specified} \; , \; g = 0 \; . \qquad (43)$$

For the separated flow configurations, results are obtained with the boundary-layer model as well as the parabolic approximation model, using $(f - \eta)_e$ from the corresponding Navier-Stokes solutions. The resulting distribution of the wall shear function is shown in Fig. 5 for three typical blunted-shoulder configurations with separation. For all three cases, the parabolized-vorticity model yields results that are undistinguishable from the Navier-Stokes results. When curvature effects are dropped from the parabolized-vorticity model, the resulting model tends to under-predict the extent as well as the severity of the separation region. However, since curvature effects become less significant with increasing Reynolds number, the results obtained with this model lead to some improved agreement as the Reynolds number becomes large. Thus, for Re = 161.5 with $\tilde{\eta}_w = 0.5$ (Fig. 5a) this model shows significant deviation in the stagnation region and up to the shoulder region and indicates that the flow experiences no separation anywhere even though the Navier-Stokes solution shows a separated flow region. As the Reynolds number is increased through 262 to 2000, the results obtained with model d show better agreement in the region upstream of the shoulder; some amount of negative wall shear function is predicted for the case with Re = 2000. For the parabolic approximation model, which contains curvature effects in it, including displacement interaction through prescribing the proper $(f - \eta)_e$ does lead to regularly behaved solutions near separation and reattachment, with no sign of the separation singularity. As seen in Figures 5a-c, the parabolic approximation yields results that are generally in better agreement with the Navier-Stokes solutions in the region upstream of the shoulder, confirming that curvature effects are most important in this region. Also, the parabolic approximation is seen to over-predict the extent of separation but, again, as the Reynolds number is increased, the results of model c show better agreement with the Navier-Stokes solutions. Finally, model e is seen to be unable to yield results for the large curvature configurations of Fig. 5a and b ($\tilde{\eta}_w = 0.039$ and 0.093) but performs reasonably well for $\tilde{\eta}_w = 0.223$.

Thus, these results demonstrate that the behavior of the approximate models can be made regular if the inviscid-viscous interaction is treated appropriately. This is also generally true for another inverse problem formulated by prescribing the interacted value of the surface vorticity function g_w.

Prescribed Interacted Vorticity Function g_w:

In this formulation, the governing equations are again unchanged, but the boundary conditions are now given as follows:

$$\text{At} \quad \eta = \eta_w \; : \; f = 0 \; , \; f_\eta = 0 \; , \; g_w \text{ - specified} \; ; \; \eta \to \eta_e \; : \; g = 0 \; . \qquad (44)$$

These boundary conditions given in Eq. (44) clearly show that the boundary value problem for the vorticity function is simplified and the superposition technique needed earlier is no longer required. The problem for the stream function now becomes an initial value problem with both conditions prescribed at $\eta = \eta_w$.

The results obtained by prescribing the interacted g_w for the separated flow configurations are shown in Figs 6a-c. From the comparison shown for the outer-edge values of the stream function, it is clear that prescribing the interacted wall shear does serve to remove the separation singularity from the calculations. As Figs. 6a-c show, the results for $(f - \eta)_e$ obtained with the parabolic approximation agree well with the Navier-Stokes solutions, the agreement becoming better as the Reynolds number increases from 161.5, through 262, to 2000. Using the boundary-layer model, the cases with extreme shoulder-curvature yielded meaningful solutions only in the region upstream of the shoulder. However, when $\tilde{\eta}_w$ is increased to 0.223, the boundary-layer results for $(f - \eta)_e$ agree well with the Navier-Stokes solutions everywhere, including the separation region. Since the parabolized-vorticity models, with or without curvature effects (i.e., models b and d), account for displacement interaction directly through the equations, the results for these models should not be associated with whether g_w or $(f - \eta)_e$ is prescribed. Whereas the parabolized-vorticity model yields results that are almost identical to the Navier-Stokes solutions, neglecting the curvature effects from this model leads to $(f - \eta)_e$ values that differ significantly from the Navier-Stokes results, even for the largest Reynolds number considered here. The hump in the curves for $(f - \eta)_e$ corresponds to the growth of the displacement thickness in the separated flow region, since $(f - \eta)_e$ is related to displacement thickness.

Before concluding the discussion on this inverse problem for separated flow calculations, it must be pointed out that the use of upwind differencing, for the cases with g_w prescribed, was first seen to cause a discontinuity in outer-edge values of f_η and $(f - \eta)$. Similar observations have also been reported by Carter[11] for separated boundary-layer calculations for a flat plate with adverse pressure gradient. However, it was believed, in the present work, that this difficulty has its origin in the numerical procedure, at least for the case of Re = 2000 which is well within the realm of boundary-layer theory. Indeed, careful choice of the time steps and the solution procedure did eliminate this discontinuity for the high Re cases. The results presented here have been obtained using upwind differencing.

Results for f_{η_e}, Surface Pressure p_w and Streamlines:

The behavior of the velocity function f_{η_e} at the edge of the viscous region is shown in Figs. 7a-c. It may appear, at first, that the f_{η_e} results do not agree with the Navier-Stokes solutions as well as the g_w or the $(f - \eta)_e$ result did. But this is not quite true if one recognizes that the scale used for f_{η_e} is several times larger than that used for g_w or $(f - \eta)_e$ in Figs. 5a-c or 6a-c. As seen in Figs. 7a-c, the function f_{η_e} remains nearly constant, at its stagnation point value, until the shoulder region where it experiences a small decrease, followed by a rather rapid increase in the region where the flow separates. Thereafter, f_{η_e} decreases smoothly to approach its asymptotic value of unity. This is in accordance with what should be expected physically when the flow negotiates the turn around the convex shoulder. Further, the pressure drop in the separation region must be accompanied by some increase in f_{η_e}. These changes in f_{η_e} become more significant as the Reynolds number increases, and are most obvious in Fig. 7c where Re = 2000. Again, the parabolized-vorticity model almost reproduces the Navier-Stokes solutions. The parabolic approximation tends to predict more prominant variations in f_{η_e} in the shoulder region and the separation region, whereas model d predicts rather subdued variations in f_{η_e} as compared to the Navier-Stokes results. All the models perform better at the high Reynolds number of 2000. In fact, the boundary-layer model which fails in the presence of extreme curvatures ($\bar{\eta}_w = 0.039$) actually shows reasonable results for the separated flow case with $\bar{\eta}_w = 0.223$. However, for $\bar{\eta}_w = 0.093$, the boundary-layer model yields fair results when g_w is prescribed although it breaks down in the region downstream of the shoulder when $(f - \eta)_e$ is prescribed. Also, it is observed that the flow in the separation region and the post-separation region is better represented by g_w - prescribed boundary condition than by the $(f - \eta)_e$ - prescribed boundary condition.

Figure 8 shows the pressure distribution on the surface of the blunt-shouldered bodies under consideration. The surface pressure was determined by integrating the tangential component of the momentum equation along the surface $\eta = \eta_w$. For the cases with sharper shoulders (i.e., small $\bar{\eta}_w$), it was also necessary to employ the normal component of the momentum equation along the stagnation line $\xi = 0$. For all three separated flow cases discussed, the pressure experiences a severe drop in the region of the shoulder ($\xi = \sqrt{Re}$). Thereafter, the pressure rises, causing separation of the boundary layer. As the pressure approaches the free stream value further downstream, the boundary layer reattaches to the body surface, resulting in a finite separation bubble. All the models considered appear to yield good agreement with the Navier-Stokes pressure results, except the boundary-layer model for the extreme curvature cases.

A good pictorial representation of the physical flow field is obtainable from the streamline contours shown in Figs. 9a-c. A larger scale has been used along the vertical axis than along the horizontal y-axis. This allows the vertical coordinate x to be stretched in order to make the vertical extent of the separation region more easily visible. It is seen that, the magnitude of the minimum value of ψ occurring inside the separation bubble is larger for $\bar{\eta}_w$=0.039 than for $\bar{\eta}_w$=0.093. Also, as the Reynolds number increases, the separation bubble tends to get convected along the body surface, so that its vertical extent diminishes while the bubble is elongated along the streamwise direction.

5. FURTHER EVALUATION OF PARABOLIZED-VORTICITY MODEL FOR LOW REYNOLDS NUMBER FLOWS

The parabolized-vorticity model of U. Ghia and Davis[5] (represented as model b in the present work) is seen to almost exactly reproduce the Navier-Stokes solutions for the flow configurations considered thus far. This is recognized as being due to proper inclusion of the displacement thickness effects in the flow. However, one may be also inclined to partially attribute the success of this model to the high (and moderate) Reynolds number flows discussed in the preceding sections. On the other hand, certain geometrical configurations can lead to the occurrence of flow separation even at fairly low Reynolds numbers; a familiar example is the flow past a circular cylinder. Therefore, the parabolized-vorticity model was further tested with respect to the class of bodies with a shoulder (Fig. 1) at low Reynolds number. These results serve to ascertain the role of the flow Reynolds number in the success of this model which takes due account of displacement effects.

Figure 10 shows a comparison of some typical results for the surface vorticity function as determined from the Navier-Stokes solutions and the parabolized-vorticity model. The cases presented include body configurations with sharp shoulders ($\eta_w = 0.5$) as well as rounded shoulders ($\eta_w = 10.0$). It is found that, even for these low Reynolds numbers, the parabolized vorticity model leads to excellent agreement with the Navier-Stokes results.

For the values of η_w shown, the stagnation point vorticity function, determined from the two solutions, differs by a maximum of 3.5 percent for a range of Reynolds numbers between 2.22 and 2000.0. This has the very significant implication that it is not necessary to solve the complete Navier-Stokes equations in these studies; it is possible to use a considerably simplified form, of the boundary-layer type, for the vorticity equation. It is important to emphasize, however, that the success of the simplified model depends greatly on the use of proper variables and suitable coordinates for formulating the model. The parabolized-vorticity equation model is given some further consideration in the next section by testing it with respect to a flow configuration

that can encounter separation at fairly low Reynolds number and exhibits rather severe separation for increasing value of the Reynolds number.

6. FLOW PAST A CLASS OF SEMI-INFINITE BODIES WITH CYLINDRICAL-SHAPED LEADING SURFACE

Next, the class of two-dimensional bodies shown typically by the curves of constant η in Fig. 2 are considered. In the limit of $\eta_w = 0$, the body consists of a cylinder with a semi-infinite flat plate at the rear. A sequence of simple conformal transformations is used to provide the final form of the conformal transformation which transforms the corresponding inviscid flow problem to the stagnation flow problem. Thus, the complete Navier-Stokes equations are solved using the transformed coordinate system (ξ,η) defined by the equation

$$z = \frac{1}{2}\left[\left(\frac{\zeta^2}{2} - 2Re\right) + \zeta\left(\frac{\zeta^2}{4} - 2Re\right)^{1/2}\right] \tag{45}$$

where Re is the Reynolds number based on the radius of surface curvature at the nose of the corresponding body with $\eta_w = 0$. For the coordinate transformation given by Eq. (45), the scale factor function H, defined in Eqs. (5-6), can be determined as

$$H^2 = \frac{4(p^2+q^2)}{(\xi^2+\eta^2)(p^2+q^2) + T} \tag{46}$$

where
$$p^2 = \frac{1}{2}\left(\frac{\xi^2-\eta^2}{4} - 2Re\right) + \frac{1}{2}\left[\left(\frac{\xi^2-\eta^2}{4} - 2Re\right)^2 + \frac{\xi^2\eta^2}{4}\right]^{1/2}$$

$$q^2 = -\frac{1}{2}\left(\frac{\xi^2-\eta^2}{4} - 2Re\right) + \frac{1}{2}\left[\left(\frac{\xi^2-\eta^2}{4} - 2Re\right)^2 + \frac{\xi^2\eta^2}{4}\right]^{1/2}$$

and
$$T = (\xi^2+\eta^2)(\xi p+\eta q) - 4Re(\xi p-\eta q) + \frac{1}{4}(\xi^2+\eta^2)^2 - 2Re(\xi^2-\eta^2) + 4Re^2 \quad . \tag{47}$$

The transformation maps the body surface onto a coordinate surface, denoted as η_w, in the transformed plane. Also, the semi-infinite region in the Cartesian plane maps to a quarter-infinite region in the (ξ,η) plane. In these new coordinates, it becomes possible to accurately formulate all the boundary conditions for this flow problem, including the condition at downstream infinity. The asymptotic solution at $\xi \to \infty$ is, again, the Blasius solution. The problem is characterized by two parameters - the Reynolds number Re and the quantity η_w which is related to the bluntness of the corner on the body. The flow past the thin flat plate (Re = 0, $\eta_w = 0$), the parabolic cylinders (Re = 0, $\eta_w \neq 0$) and the vertical wall ($\eta_w \to \infty$) can be obtained as special cases of this flow problem; these were used as check cases for ascertaining the accuracy of the formulation and the numerical calculations.

Figure 11 shows the surface vorticity function distribution $g(\xi,\eta_w)$ for some typical cases of this class of bodies. In Fig. 11a, the case with $\eta_w = 5$, Re = 100 shows that the flow remains attached to the body surface everywhere. But as η_w is reduced to 1, i.e., the corner in the body is made considerably sharper, the flow separates in the vicinity of the corner and exhibits a finite region of reversed flow even for a Reynolds number of 50. The parabolized-vorticity equation model is seen to reproduce the Navier-Stokes results for both cases of the new configuration also. This flow configuration experiences a more enhanced separation as compared to the body configuration with a shoulder, described earlier in the paper; the shouldered configuration had experienced no separation at these low Reynolds numbers even for $\eta_w = 0$. The use of fine resolution in certain critical regions of the flow field is appearing to be a significant factor in obtaining numerical solutions for these severely separated flows.

The behavior of $g(\xi,\eta_w)$ for typical configurations with a sharp corner ($\eta_w = 0$) is shown in Fig. 11b. The parabolized-vorticity model appears to experience no difficulty due to the presence of the sharp corner located at $\xi = 2\sqrt{2Re}$ along $\eta_w = 0$ in the present coordinates.

Flow Past Cylinders

Finally, it is recognized that, in the limit of $\eta_w = 0$, the body shapes represented in Fig. 2, for $Re \neq 0$, consist of a cylinder with a semi-infinite flat plate emanating from the rear-stagnation point on the cylinder. The downstream asymptotic boundary condition for the Navier-Stokes equations corresponds, therefore, to the Blasius solution for the flat plate flow. Clearly, removing the entire plate from the rear of the cylinder, and appropriately modifying the downstream asymptotic boundary condition to now correspond to the wake flow solution, yields the problem of symmetric flow past a cylinder. Thus, the symmetric flow past a cylinder can be obtained in the present (ξ,η) coordinates [Eq. (45)] by considering the geometries with $\eta_w = 0$, $Re \neq 0$, and setting to zero the vorticity function along the line of symmetry at the rear of the cylinder, i.e.,

$$g(\xi,0) = 0 \qquad \text{for} \qquad \xi > 2\sqrt{2Re} \quad . \tag{48}$$

This is an important flow problem that has been studied by a number of investigators [for example, Refs. 13 and 14] using different approaches. It is believed that application of the present general formulation of the analysis, the alternating direction implicit numerical method and the parabolized-vorticity model for this flow problem

provides a good test of the present techniques for separated flows with wakes. Some preliminary results have been obtained and appear quite promising. Figure 12a shows a computer-generated contour plot of the streamlines for the flow past a cylinder at Re = 3. No separation is observed at this value of the Reynolds number. This result is in general agreement with that obtained in Ref. 13, that, for flow past a cylinder, separation first occurs at about Re = 2.875. Therefore, at Re = 3, even if separation has occurred, it is confined to an extremely small region near the rear of the cylinder and is being missed in the finite difference calculations. It would be necessary to use a further refined grid in the region near the rear of the cylinder in order to obtain finer resolution of the numerical results. Figure 12b shows the corresponding streamline pattern, at Re = 3, when the plate is re-inserted at the rear of the cylinder and the downstream asymptotic boundary condition is restored to correspond to the Blasius solution. As expected in unseparated flow, the streamlines at the rear of the cylinder are now displaced outward, owing to the displacement thickness effects of the flat plate in the viscous flow. Also, no separation is observed for this case because the presence of the plate will tend to suppress the degree of separation.

7. CONCLUSION

It seems clear, from the results obtained, that boundary-layer-type models can successfully predict separated flows if they take account of the interaction between the boundary layer and the external inviscid flow. The displacement thickness effects appear to be of greatest significance in treating the separation singularity. In the several models studied, this interaction has been taken into consideration either directly through the differential equations or indirectly by appropriate modification of the boundary conditions for the viscous solutions.

Another useful direct approach to the problem would consist of simultaneous solution of the boundary-layer flow and the inviscid flow, with suitable matching of the two flow solutions. This would avoid solving the viscous flow equations in the outer flow region. That such a procedure is possible is indicated by the success of the parabolized-vorticity model with or without curvature effects. Efforts are presently being made to pursue this concept further.

REFERENCES

1. Brown, S.N. and Stewartson, K. (1969), "Laminar Separation," Annual Review of Fluid Mechanics, Annual Review Inc., Vol. 1, pp. 45-72.
2. Briley, R. (1971), "The Numerical Study of Laminar Separation Bubbles using the Navier-Stokes Equations," Journal of Fluid Mechanics, Vol. 47, Part 4, pp. 713-736.
3. Leal, L.G. (1973), "Steady Separated Flow in a Linearly Decelerated Free Stream," Journal of Fluid Mechanics, Vol. 59, Part 3, pp. 513-535.
4. Goldstein, S. (1948), "On Laminar Boundary-Layer Flow Near a Position of Separation," Quarterly Journal of Mech. Appl. Math., Vol. 1, pp. 43-69.
5. Ghia, U. and Davis, R.T. (1974), "Navier-Stokes Solutions for Flow Past a Class of Two-Dimensional Semi-Infinite Bodies," AIAA Journal, Vol. 12, No. 12, pp. 1659-1665.
6. Werle, M.J. and Bernstein, J.M. (1975), "A Comparative Numerical Study of Models to the Navier-Stokes Equations for Incompressible Separated Flows," AIAA Paper No. 75-48.
7. Briley, W.R. and McDonald, H. (1974), "Numerical Prediction of Incompressible Separation Bubbles," United Aircraft Research Laboratories Report No. N110887-3.
8. Dancey, C.L. and Pletcher, R.H. (1974), "A Boundary Layer Finite Difference Method for Calculating Through the Separation Point into the Region of Recirculation in Incompressible Laminar Flow," Technical Report HTL-2, ISU-ERI-Ames-74103.
9. Catherall, D. and Mangler, K.W. (1966), "The Integration of the Two-Dimensional Laminar Boundary-Layer Equations Past the Point of Vanishing Skin Friction," Journal of Fluid Mechanics, Vol. 26, Part 1, pp. 163-182.
10. Klineberg, J.M. and Steger, J.L. (1974), "On Laminar Boundary-Layer Separation," AIAA Paper No. 74-94.
11. Carter, J.E. (1974), "Solutions for Laminar Boundary Layers with Separation and Reattachment," AIAA Paper No. 74-583.
12. Davis, R.T. (1972), "Numerical Solution of the Navier-Stokes Equations for Symmetric Laminar Incompressible Flow Past a Parabola," Journal of Fluid Mechanics, Vol. 51, Part 3, pp. 417-433.
13. Underwood, R.L. (1969), "Calculation of Incompressible Flow Past a Circular Cylinder at Moderate Reynolds Numbers," Journal of Fluid Mechanics, Vol. 37, Part 1, pp. 95-114.
14. Dennis, S.C.R. and Chang, G.Z. (1970), "Numerical Solutions for Steady Flow Past a Circular Cylinder at Reynolds Numbers upto 100," Journal of Fluid Mechanics, Vol. 42, Part 3, pp. 471-489.

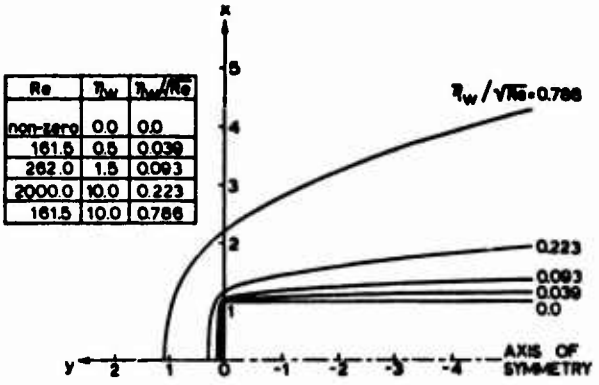

FIGURE 1. CONFIGURATIONS FOR BODIES WITH BLUNTED SHOULDERS.

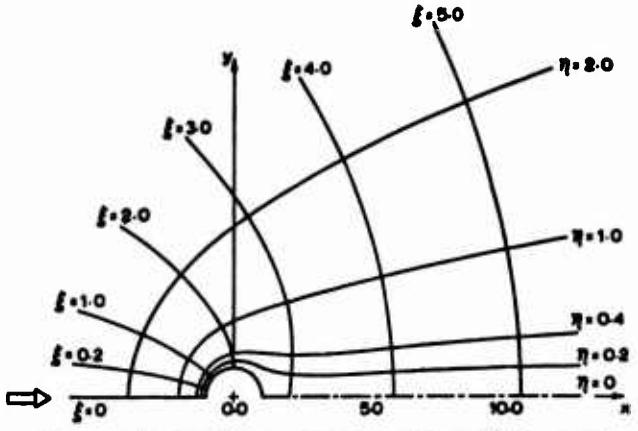

FIGURE 2. TRANSFORMED COORDINATES FOR CYLINDER - PLATE CONFIGURATIONS.

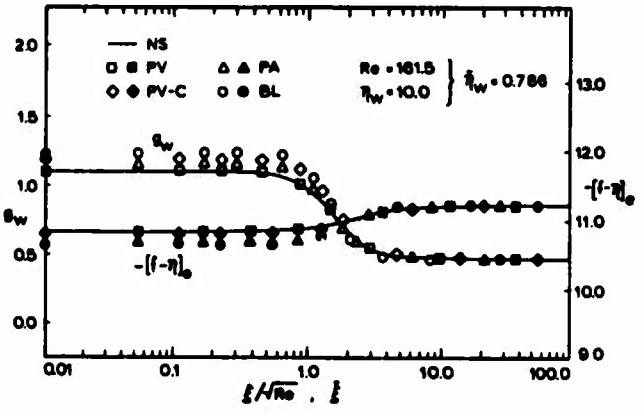

FIGURE 3. SURFACE VORTICITY AND OUTER-EDGE STREAM FUNCTION DISTRIBUTIONS FOR UNSEPARATED FLOW.

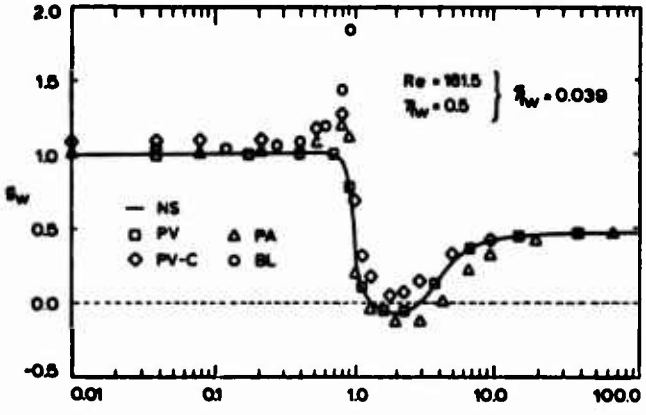

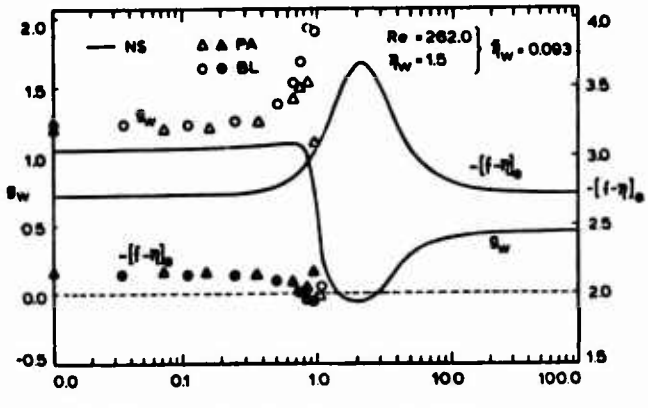

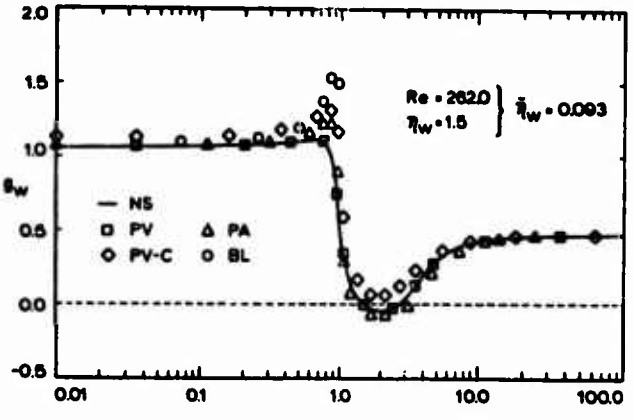

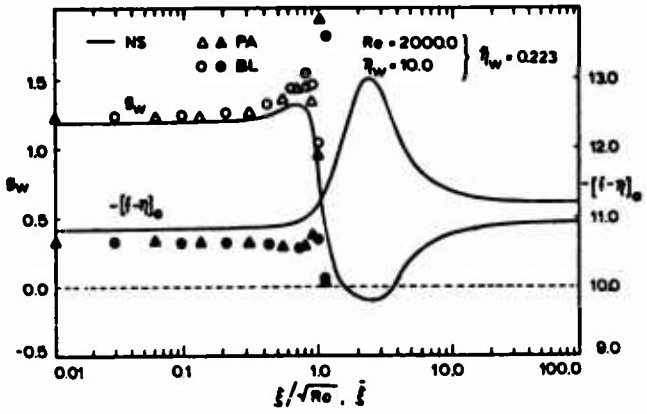

FIGURE 4. SURFACE VORTICITY AND OUTER-EDGE STREAM FUNCTION DISTRIBUTIONS FOR SEPARATED FLOW - $\bar{\eta}_w$ = 1

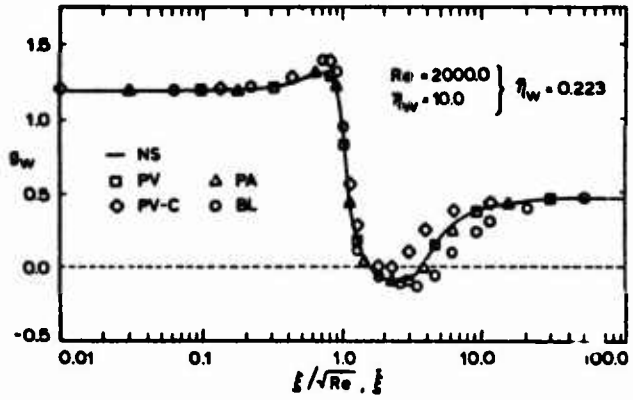

FIGURE 5. VORTICITY FUNCTION DISTRIBUTION ON THE SURFACE - PRESCRIBED OUTER-EDGE STREAM FUNCTION.

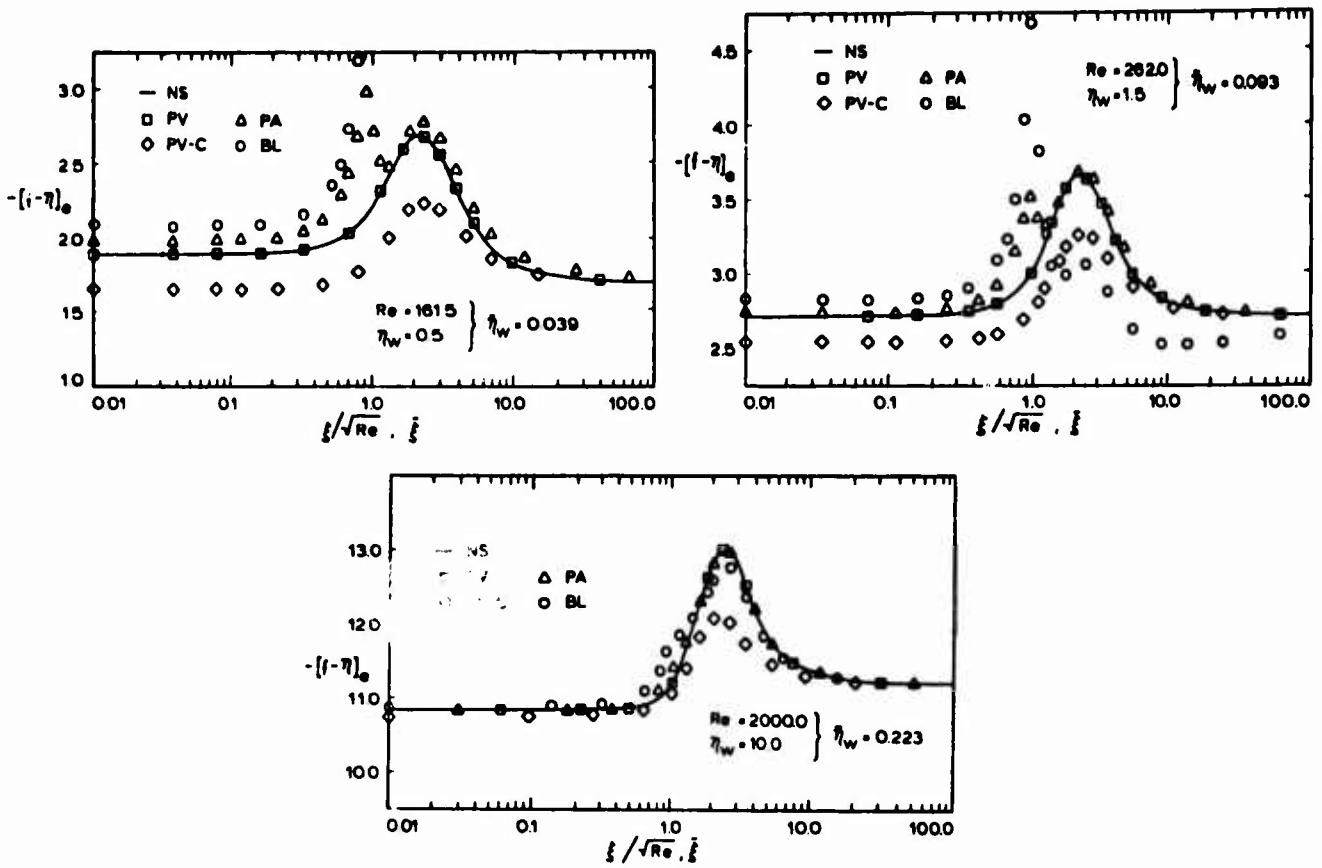

FIGURE 6. OUTER-EDGE STREAM FUNCTION DISTRIBUTION-PRESCRIBED WALL SHEAR FUNCTION.

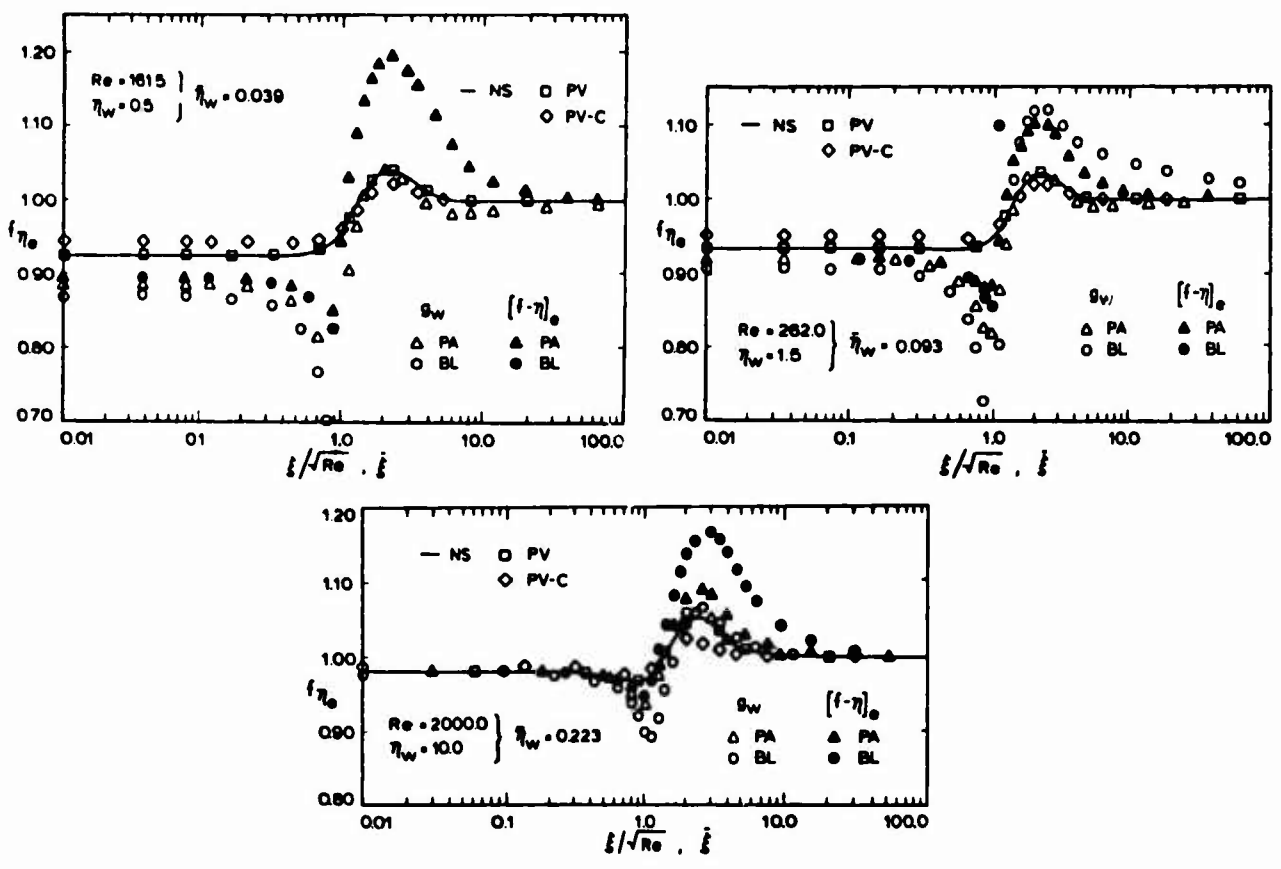

FIGURE 7. OUTER-EDGE VELOCITY FUNCTION DISTRIBUTION-PRESCRIBED OUTER-EDGE STREAM FUNCTION OR WALL SHEAR FUNCTION.

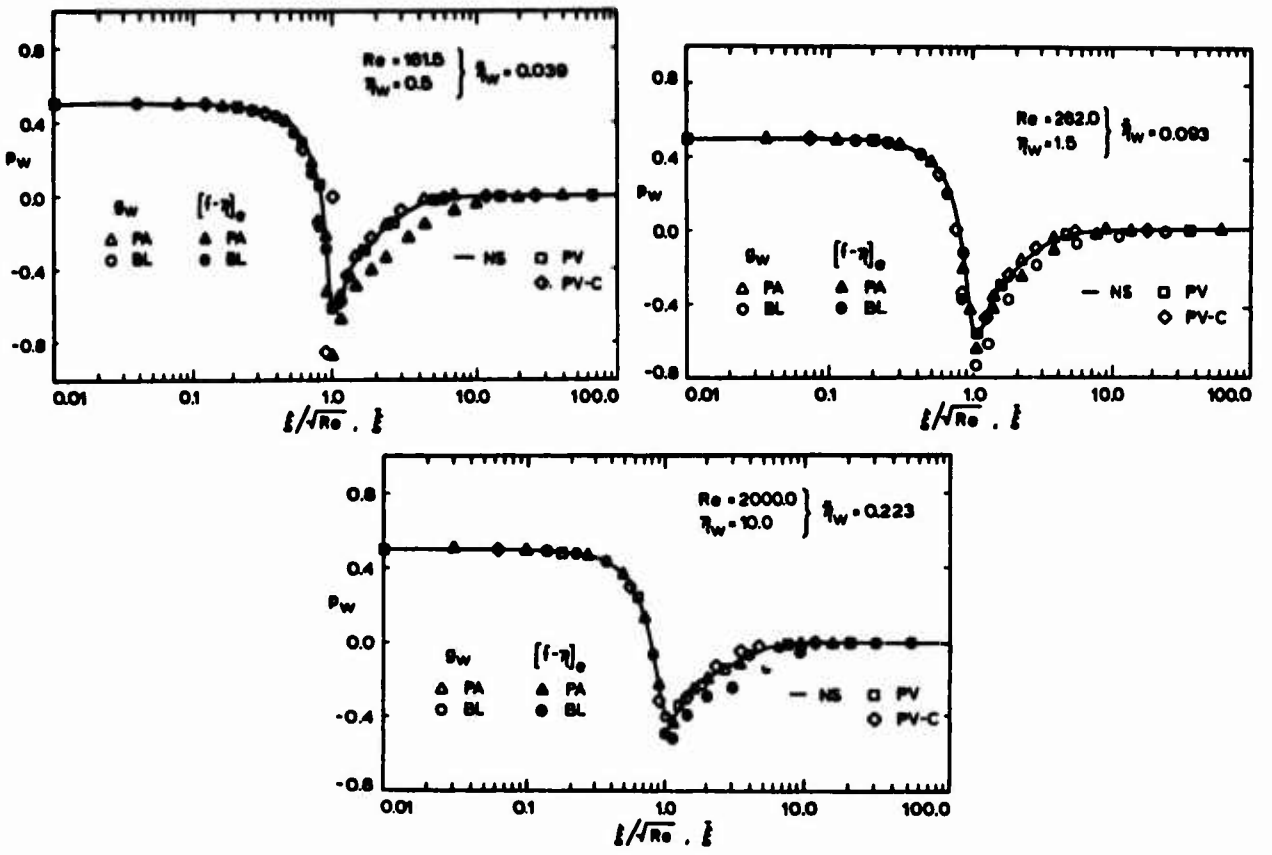

FIGURE 8. SURFACE PRESSURE DISTRIBUTION - PRESCRIBED OUTER-EDGE STREAM FUNCTION OR WALL SHEAR FUNCTION.

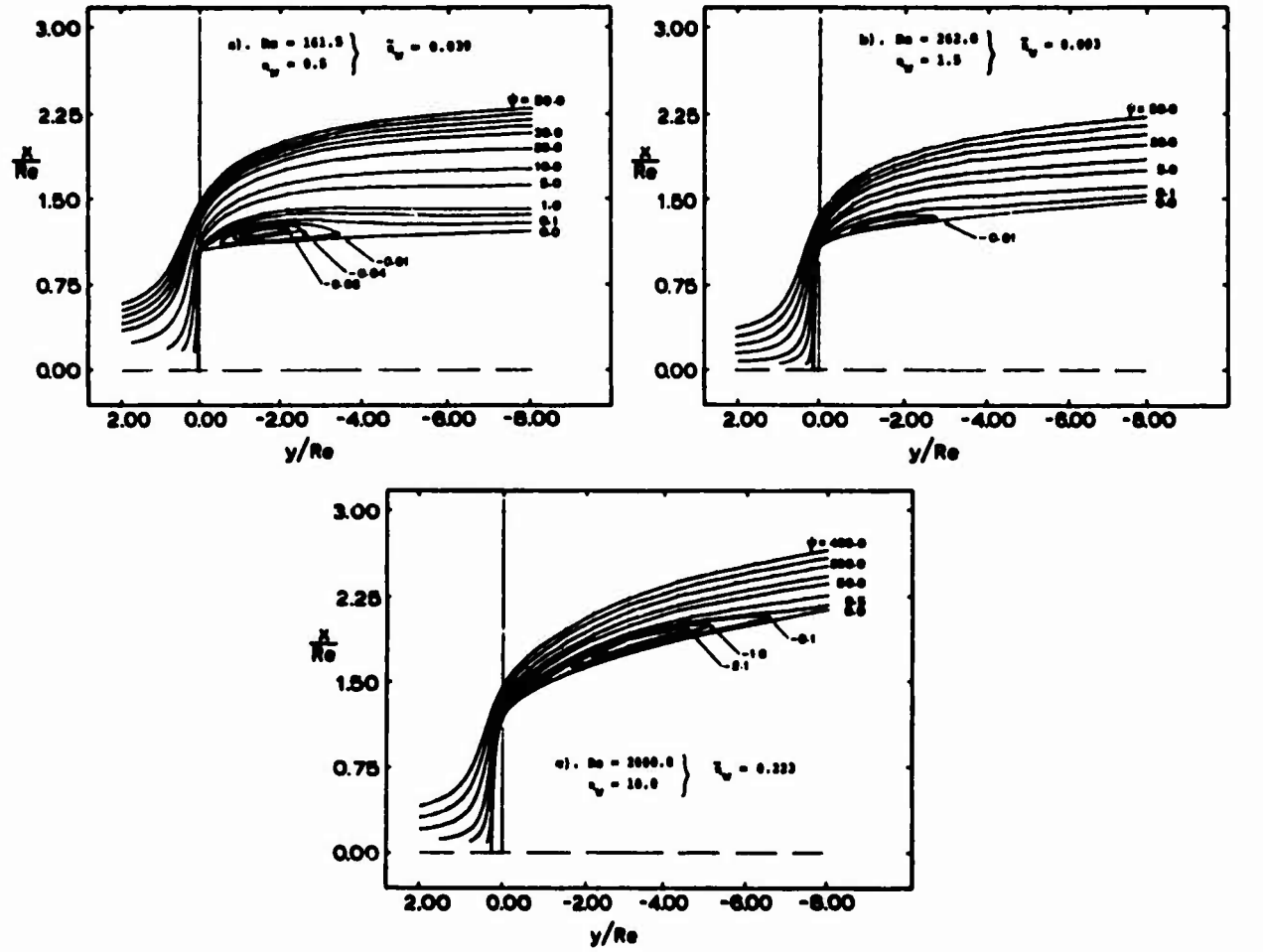

FIGURE 9. STREAMLINES FOR SEPARATED FLOW.

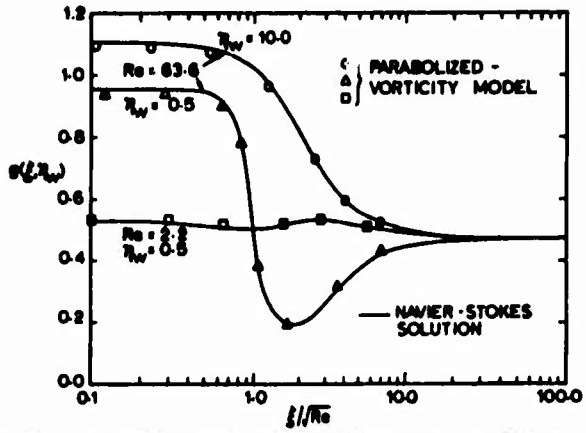

FIGURE 10. COMPARISON OF VORTICITY FUNCTION ON SURFACE OF BLUNT-SHOULDERED BODIES FOR LOW REYNOLDS NUMBERS.

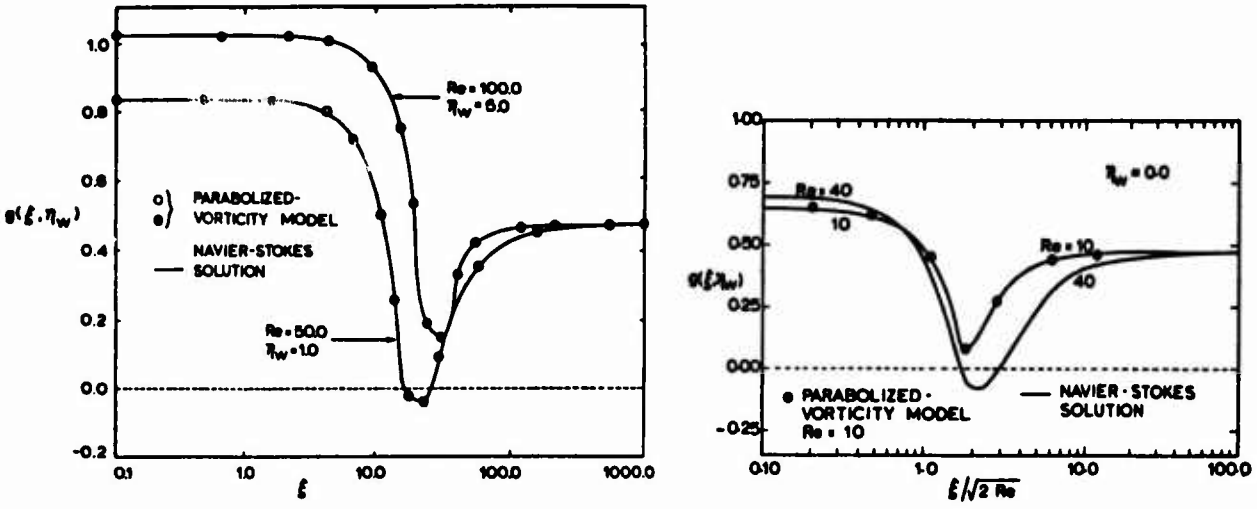

FIGURE 11. COMPARISON OF VORTICITY FUNCTION ON SURFACE OF CYLINDER-PLATE CONFIGURATIONS

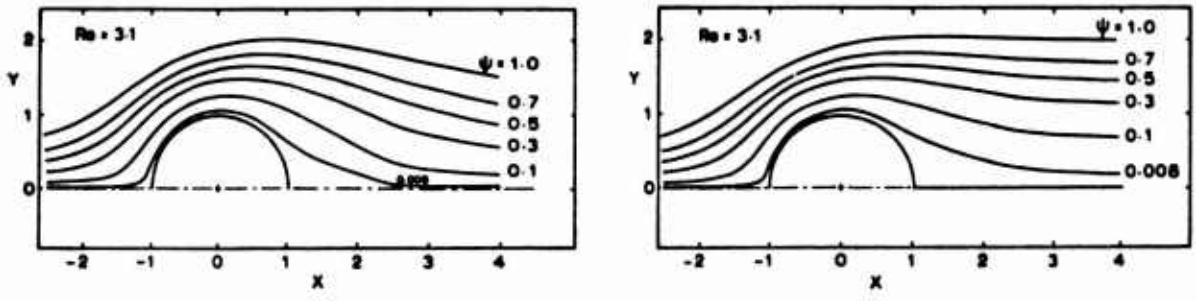

a. CYLINDER ONLY b. CYLINDER WITH THIN FLAT PLATE

FIGURE 12. STREAMLINES FOR FLOW PAST CYLINDER-PLATE CONFIGURATIONS

ABBREVIATIONS USED IN FIGURES			
NS NAVIER STOKES	PV	PARABOLIZED-VORTICITY	PA PARABOLIC-APPROXIMATION
	PV-C	PARABOLIXED-VORTICITY WITHOUT CURVATURE EFFECTS	BL BOUNDARY LAYER

NUMERICAL INVESTIGATION OF REGULAR LAMINAR BOUNDARY LAYER SEPARATION

H. P. Horton*

Queen Mary College, University of London, Mile End Road, London E1 4NS.

SUMMARY

An accurate numerical procedure of the differential-difference type for the solution of the incompressible laminar boundary layer equations is presented. The procedure is applicable to both direct problems, in which the pressure distribution is prescribed, and inverse problems of the type in which the wall shear is prescribed.

Some examples computed by this procedure show that, by prescribing the wall shear to be regular in the vicinity of separation, the usual singularity at separation is avoided. Results are also presented in which downstream marching with prescribed wall shear has been continued to considerable distances beyond separation, including an example in which both regular separation and re-attachment occur. In other cases no solution to the inverse problem can be found beyond a short distance after separation, but by smoothly joining a prescribed pressure distribution to that calculated in the inverse problem upstream, it has been found possible to continue the computation as a direct problem. Questions of stability and uniqueness of the solutions are discussed.

The accuracy of the approximate integral method of Lees and Reeves is assessed on the basis of comparisons with results computed by the present method.

PRINCIPAL NOTATION

f = non-dimensional stream function (Eq.4)

H = δ^*/θ, shape parameter

L = characteristic length

R_e = $u_o L/\nu$, characteristic Reynolds number

S = $(\partial^2 f/\partial \eta^2)_w$, wall shear parameter

u_o = characteristic velocity

u_e = velocity at outer edge of boundary layer

u, v = velocity components along x, y

x, y = Cartesian co-ordinates along and normal to the body surface

β = pressure gradient parameter (Eq.7)

δ^* = displacement thickness (Eq.A4)

η = scaled normal ordinate (Eq.3)

θ = momentum thickness (Eq.A4)

ν = kinematic viscosity

ξ = scaled streamwise ordinate (Eq.3)

τ = shear stress

Subscripts and Superscripts

w conditions at the wall

$'$ differentiation with respect to η

1. INTRODUCTION

It is well known[1,2] that solutions of the equations governing the laminar, incompressible flow in a two-dimensional boundary layer exhibit singular behaviour at the point of separation, where the wall shear stress τ_w vanishes, when the problem is posed in the conventional way, such that streamwise distribution of pressure is prescribed (the 'direct problem'). The singularity is such that τ_w varies as $(x_s - x)^{\frac{1}{2}}$ near separation, where x is distance along the surface and suffix 's' denotes conditions at separation. The resulting infinity in $d\tau_w/dx$ is accompanied by an infinity in the slope $d\delta^*/dx$ of the displacement surface. It has been found impossible to integrate the boundary layer equations through, and downstream of, such a singular separation point.

Catherall and Mangler[3] showed numerically that regular separation, with no singularity, occurs when the displacement thickness is prescribed to be a regular function of x, and it was furthermore shown that the solution could be continued beyond separation by the usual downstream marching procedure. However, in the reversed flow region there was evidence of non-uniqueness of the solution, although it appeared that all possible solutions lay within quite small numerical limits of each other. It was suggested that this non-uniqueness arose because the region of reversed flow should strictly be integrated in the negative x-direction, with boundary conditions provided from downstream.

The problem solved by Catherall and Mangler is an example of what may be termed an 'inverse problem', in which the distribution of some quantity other than the pressure is prescribed, whilst the pressure distribution is treated as unknown. If the prescribed quantity is one which would become singular at separation in a direct problem, then it may be expected that a regular distribution of this quantity in an inverse problem may result in regular behaviour of all other quantities.

In addition to their fundamental interest, accurate solutions of inverse problems involving separation are of importance in providing a basis for comparison with approximate methods of solution of separated flow problems. Also, it may be possible to use an inverse procedure locally near separation when solving complete problems involving interaction between a boundary layer with limited separation and an outer potential flow.

* Lecturer

This paper is concerned mainly with obtaining accurate solutions of inverse problems in which the wall shear is the prescribed quantity. This type of inverse problem is of particular convenience since the points of separation and re-attachment are fixed by the chosen distribution of τ_w. Problems of this type have been previously considered by Keller and Cebeci[4], whose solutions did not, however, extend beyond the point of separation, and by the present author[5].

It will be assumed that the boundary layer equations provide a valid description of separated flows of boundary layer type, in which the thickness of the viscous layer remains of $O(R_e^{-\frac{1}{2}})$, where R_e is a characteristic Reynolds number.

Section 2 describes an accurate numerical method, of the differential-difference type, for solving the incompressible boundary layer equations, applicable to both direct and inverse problems for attached and separated flow. (This method was briefly described, and some early results presented, in Ref.5.)

Section 3 presents and discusses results computed by this method for a variety of examples involving regular separation. These include cases with prescribed wall shear, some of which have been continued into the separated region, and a case in which, after passing through regular separation with prescribed wall shear, the calculation was continued with prescribed pressure gradient. Additionally, a more detailed study of separation is made for one case.

For comparison, results have been calculated for some of the examples by the approximate integral method of Lees and Reeves[6], as modified by Klineberg and Lees[7]. The required re-formulation of this method is given in the Appendix.

2. ANALYSIS

2.1 Governing Equations

The equations to be solved are the usual laminar boundary layer equations, namely

$$u\frac{\partial u}{\partial x} + v\frac{\partial u}{\partial y} = u_e\frac{du_e}{dx} + \nu\frac{\partial^2 u}{\partial y^2} \quad , \tag{1a}$$

$$\frac{\partial u}{\partial x} + \frac{\partial v}{\partial y} = 0. \tag{1b}$$

The boundary conditions for flow over a fixed, impermeable surface are:-

$$\begin{aligned} &u = v = 0 \quad \text{when } y = 0 \ ; \\ &u \to u_e \qquad \text{as } y \to \infty \ . \end{aligned} \tag{2}$$

The equations are now put into a form more suitable for numerical solution, by the application of the Görtler[8] transformation. This has the advantages that the scaled boundary layer thickness is generally almost constant, that the leading-edge singularity is suppressed, and that accurate series solutions are available for comparative purposes.

New independent variables (ξ,η) are introduced, defined by

$$\xi = \frac{1}{u_0 L}\int_0^x u_e(x')dx' \quad , \quad \eta = \frac{u_e\, y}{(2\nu u_0 L\xi)^{\frac{1}{2}}} \quad , \tag{3}$$

where u_0 and L are respectively a reference velocity and length.

Additionally a non-dimensional stream function f is introduced, defined by

$$f(\xi,\eta) = \psi(x,y)/(2\nu u_0 L\xi)^{\frac{1}{2}} \quad , \tag{4}$$

where ψ is the usual stream function, such that

$$u = \partial\psi/\partial y \quad , \quad v = -\partial\psi/\partial x.$$

Equations (1a) and (1b) now become:-

$$\frac{\partial^3 f}{\partial\eta^3} + f\frac{\partial^2 f}{\partial\eta^2} + \beta(\xi)\left[1 - \left(\frac{\partial f}{\partial\eta}\right)^2\right] = 2\xi\left[\frac{\partial f}{\partial\eta}\frac{\partial^2 f}{\partial\eta\partial\xi} - \frac{\partial^2 f}{\partial\eta^2}\frac{\partial f}{\partial\xi}\right] \quad , \tag{5}$$

with boundary conditions

$$f(\xi,0) = \frac{\partial f}{\partial\eta}(\xi,0) = 0 \quad ; \quad \frac{\partial f}{\partial\eta}(\xi,\infty) \to 1 \ . \tag{6}$$

Here β is the pressure gradient parameter defined by

$$\beta(\xi) = 2\frac{\xi}{u_e}\frac{du_e}{d\xi} = 2\frac{\xi u_0 L}{u_e^2}\frac{du_e}{dx} \quad , \tag{7}$$

and the velocity components u and v are given by

$$\frac{u}{u_e} = \frac{\partial f}{\partial\eta} \quad , \quad \frac{v}{u_e} = -\left(\frac{\nu}{2u_0 L\xi}\right)^{\frac{1}{2}}\left[f + 2\xi\frac{\partial f}{\partial\xi} + (\beta-1)\eta\frac{\partial f}{\partial\eta}\right] . \tag{8}$$

When the right side of Eq.(5) vanishes, either at the boundary layer origin $\xi = 0$ or when f is independent of ξ, this equation reduces to the well-known Falkner-Skan[9] equation for the 'similar solutions'.

In direct problems, $\beta(\xi)$ is given while the scaled wall shear stress $S(\xi) \equiv \partial^2 f/\partial\eta^2(\xi,0)$ is one of the important results of the calculation. On the other hand in inverse problems for which $S(\xi)$ is given, the pressure gradient parameter $\beta(\xi)$ is an unknown function whose value is determined to satisfy the boundary conditions given by Eq.(6), together with

$$\frac{\partial^2 f}{\partial\eta^2}(\xi,0) = S(\xi) \ . \tag{9}$$

These four boundary conditions correctly determine the third-order equation, Eq.(5), when $\beta(\xi)$ is treated as unknown.

2.2 Accurate Numerical Solution by the Differential-Difference Method

The method used here to obtain numerical solutions to Eq.(5) is of the differential-difference type originally devised by Hartree[10], and subsequently modified by Smith and Clutter[11]. The present method is closely related to that of the latter authors, but an improved shooting procedure is used, and the extension to the treatment of inverse problems is made.

The range of integration with respect to ξ is divided into a suitable number of intervals, and derivatives with respect to ξ at each ξ-station are replaced by backward difference formulae. Then at each station, marching downstream, the resulting third-order non-linear ordinary differential equation is solved subject to the appropriate boundary conditions.

2.2.1 The Difference Scheme

The first derivatives, with respect to ξ, of f and $\partial f/\partial\eta$ appearing in Eq.(5) are approximated by either 3- or 4-point Lagrange backward difference formulae. For example, taking a constant spacing $\delta\xi$ between successive ξ-stations, the derivative of a function g at the streamwise position $\xi_n = n.\delta\xi$ may be approximated in terms of $g(\xi_n)$, $g(\xi_{n-1})$ etc. by the 3-point formula

$$\frac{\partial g}{\partial\xi}(\xi_n) = \frac{3g(\xi_n) - 4g(\xi_{n-1}) + g(\xi_{n-2})}{2\delta\xi} + O(\delta\xi^2). \tag{10}$$

(More general 3- and 4-point formulae for variable step length, used in the present program, may be found in standard works.)

Making replacements of this type for both $\partial f/\partial\xi$ and $\partial/\partial\xi(\partial f/\partial\eta)$ in Eq.(5) leads to the third-order ordinary equation for f_n :-

$$f_n''' + f_n f_n'' + \beta_n(1 - f_n'^2) + \frac{2\xi_n}{\delta\xi}\left[f_n''\left(\frac{3}{2} f_n - 2f_{n-1} + \frac{1}{2} f_{n-2}\right) - f_n'\left(\frac{3}{2} f_n' - 2f_{n-1}' + \frac{1}{2} f_{n-2}'\right)\right] = 0 , \tag{11}$$

where primes denote differentiation with respect to η.

Putting $E = \frac{3}{2}\frac{\xi_n}{\delta\xi}$, $D = 1 + 2E$,

$$\phi_1 = \frac{\xi_n}{\delta\xi}\left(-2f_{n-1} + \frac{1}{2} f_{n-2}\right) , \quad \phi_2 = \frac{\xi_n}{\delta\xi}\left(2f_{n-1}' - \frac{1}{2} f_{n-2}'\right) ,$$

then Eq.(11) becomes

$$f''' + Dff'' + \beta(1 - f'^2) - 2Ef'^2 + 2\phi_1 f'' + 2\phi_2 f' = 0 , \tag{11a}$$

the suffix 'n' being henceforth omitted.

Finally, for solution by the fourth-order Runge-Kutta method, Eq.(11a) is re-written as a system of 3 first-order equations, viz.

$$\begin{aligned} f' &= U , \\ (f'' =)\ U' &= V , \\ (f''' =)\ V' &= -D.fV - \beta(1 - U^2) + 2EU^2 - 2\phi_1 V - 2\phi_2 U . \end{aligned} \tag{12}$$

Eqs.(12) are solved at each successive ξ-station, using the values of ϕ_1 and ϕ_2 obtained from the solutions at previous stations.

At the origin $\xi = 0$, the terms depending upon ξ vanish and the equation for similar solutions remains. For a sharp leading-edge, the calculation is started with $\beta = 0$ (giving the Blasius solution). If the origin is a stagnation point, the calculation is started with $\beta = 1$ (giving the Hiemenz solution).

The first ξ-step is made using a 2-point difference scheme in place of the 3-point scheme, which is then used for subsequent steps. Alternatively, the 4-point scheme may be used for the third and subsequent steps.

2.2.2 Numerical Solution of Eqs.(12) - Direct Problems

When $\beta(\xi)$ is given, Eqs.(12) have to be solved at each ξ-station subject to the boundary conditions.

Inner: $f(0) = U(0) = 0$;

Outer: $U \to 1$ as $\eta \to \infty$.

A shooting method is used, in which integration is carried out starting at $\eta = 0$ with an estimated value for $V(0) \equiv S$. The integration is then repeated iteratively until the outer boundary condition is satisfied to suitable accuracy, using successively improved values for S obtained as follows.

Let S_i be the i^{th} iterate, and let suffix '∞' denote values at a suitably large value of η, say η_∞. Then, to first order,

$$U_\infty(S_{i+1}) = U_\infty(S_i) + (S_{i+1} - S_i)\left(\frac{\partial U_\infty}{\partial S}\right)_i .$$

We require $U_\infty(S_{i+1}) = 1$, so

$$S_{i+1} = S_i + \frac{1-U_\infty(S_i)}{(\partial U_\infty/\partial S)_i} .$$

To find $\partial U_\infty/\partial S$, a set of equations, obtained by differentiating Eqs.(12) with respect to S, is solved simultaneously with Eqs.(12).

Putting $F_1 = \partial f/\partial S$, $U_1 = \partial U/\partial S$, $V_1 = \partial V/\partial S$, we get

$$\begin{aligned} F_1' &= U_1 , \\ U_1' &= V_1 , \\ V_1' &= - D(fV_1 + F_1 V) + 2(\beta + 2E)UU_1 - 2\phi_1 V_1 - 2\phi_2 U_1 . \end{aligned} \tag{13}$$

The relevant initial conditions are

$$F_1(0) = U_1(0) = 0 \;\; ; \;\; V_1(0) = 1 \;\; . \tag{13a}$$

2.2.3 Numerical Solution of Eqs.(12) - Inverse Problems

When $S(\xi)$ is given, Eqs.(12) have to be solved at each ξ-station subject to the over-determined boundary conditions

$$\begin{aligned} &\text{Inner:} \;\; f(0) = U(0) = 0 \, , \; V(0) = S \; ; \\ &\text{Outer:} \;\; U \to 1 \;\; \text{as} \;\; \eta \to \infty \, . \end{aligned}$$

Again, a shooting method is used, integration being started at $\eta = 0$ with an estimated value for β. In this case, β is improved iteratively until a solution satisfying the outer boundary condition is found. Proceeding in a similar manner to that above, we find

$$\beta_{i+1} = \beta_i + \frac{1-U_\infty(\beta_i)}{(\partial U_\infty/\partial \beta)_i} .$$

Putting $F_2 = \partial f/\partial \beta$, $U_2 = \partial U/\partial \beta$, $V_2 = \partial V/\partial \beta$, we have

$$\begin{aligned} F_2' &= U_2 , \\ U_2' &= V_2 , \\ V_2' &= - D(fV_2 + F_2 V) + 2(\beta + 2E)UU_2 - 2\phi_1 V_2 - 2\phi_2 U_2 - (1 - U^2) , \end{aligned} \tag{14}$$

with

$$F_2(0) = U_2(0) = V_2(0) = 0 \, . \tag{14a}$$

2.2.4 Further Remarks on the Numerical Procedure

The Newton iteration procedure described in the previous sections was originally used by Reshotko and Beckwith[12], and later by Klineberg[13], to obtain similar solutions of the boundary layer equations. In the present application it is found that Eqs.(12) are inherently unstable when solved as an initial value problem starting at $\eta = 0$, in the sense that a small change in either S or β causes a very large change in the value of U_∞. This instability becomes stronger as the length of the ξ-step is reduced, and at some stage it becomes necessary to use double-precision arithmetic in order to obtain the required solution. For values of $\delta\xi < \xi/25$, it becomes impossible to obtain the required solution, as also found by Smith & Clutter[11].

The asymptotic outer boundary condition $U \to 1$ as $\eta \to \infty$ is approximated by the conditions that $|1 - U_\infty| < 10^{-4}$ and $U_\infty' < 10^{-3.5}$. For attached flow, a value of $\eta_\infty = 6$ is generally sufficiently large to ensure that both these conditions can be satisfied. For separated flow, η_∞ is increased if necessary.

The Fortran computer program used to obtain the solutions was based on the program developed by Klineberg[13] for the calculation of similar solutions.

3. COMPUTED EXAMPLES INVOLVING REGULAR SEPARATION

This section presents a selection of results computed by the present differential-difference method. The integration step in the η-direction was 0.2 in all cases, the discretisation error in u/u_e resulting from these integrations then being of order 10^{-4}. The ξ-intervals used are indicated on the figures, the corresponding discretisation errors being more difficult to establish, although applications of h^2-extrapolation, in addition to comparisons of results using both 3-point and 4-point difference schemes, indicate that such errors are generally less than 10^{-3}.

Calculations by the approximate method of Lees, Reeves and Klineberg[6,7] (LRK method) as re-formulated for application to problems with prescribed pressure or wall shear in the Appendix, are also presented for most of the examples, for comparative purposes.

In addition, the series solution of Görtler[8], which is easily inverted for application to problems with prescribed wall shear, has been computed for some of the cases. This provides a check on the

accuracy of the difference calculations, in the initial part of the boundary layer, but because the series is truncated at the fifth power of ξ, and because it has a finite radius of convergence, the series solution generally diverges away from the difference method solution at some distance from the origin.

The distributions of wall shear have been chosen so that separation occurs at $\xi = 1$ (i.e. $S = 0$ at $\xi = 1$), except for Case III in which separation is approached asymptotically as $\xi \to \infty$. Also the value of wall shear at $\xi = 0$ has been taken to be such that $\beta = 0$ there in all cases.

3.1 Boundary Layers Approaching a Regular Separation Point

The three examples in this category as defined by

$$\text{Case I} \quad : \quad S = S_B.(1 - \xi) ;$$
$$\text{Case II} \quad : \quad S = S_B.(1 - \xi)^8 ;$$
$$\text{Case III} \quad : \quad S = S_B.\exp(-\xi) ,$$

where $S_B = 0.4696$, the value of the scaled wall shear S for constant pressure (Blasius) flow.

Case I, with linearly-decreasing wall shear, has already been computed by Keller and Cebeci[4] by a finite-difference method, these results having already been compared with those of the present method in a previous paper[5]. As shown in Fig.1a, there is initially good agreement between the distributions of β computed using the present method, the LRK method and the series solution, but there is quite rapid divergence of the latter as separation is approached. The distribution of shape parameter H computed by the LRK method is however in good agreement with the present method, as shown in Fig.1b.

Similar remarks apply to the results for Case II, also shown in Figs. 1a and 1b, which has incipient separation at $\xi = 1$, and for Case III, shown in Figs. 2a and 2b, which tends exponentially towards separation as $\xi \to \infty$. The Görtler series gives poor results near separation in the latter case, as might be expected since ξ tends to infinity there.

One feature common to these cases and all other cases with regular separation so far computed is that $d\beta/d\xi > 0$ at separation according to the present method, so that separation occurs in a weakening adverse pressure gradient. This condition implies that $d^2u_e/dx^2 > 0$, which has been given by Prandtl (quoted by Smith and Clutter[11]) as a requirement for the avoidance of the singularity at separation. Although this appears to be a necessary condition for regular separation, we shall later show that it is not sufficient.

3.2 Cases Continued Beyond Separation with Prescribed Wall Shear

It was not originally expected that calculations by the present method could be continued beyond the separation point, even in inverse problems with regular separation, and it was indeed found that Case I could not be so continued.

However, some calculations with prescribed distributions of S in which the rate of decrease of S beyond separation is smaller than in Case I, and in which S does not take large negative values, have been continued well beyond the separation point. Three examples are presented here:-

$$\text{Case IV} \quad : \quad S = S_B(1 - \xi)(1 - .52649\xi) ;$$
$$\text{Cases V and VI} \quad : \quad S = S_B.\left[1 - (1 - e^{-k\xi})/(1 - e^{-k})\right],$$
$$\text{with } k = 1.98256 \text{ for Case V ;}$$
$$k = 1.73976 \text{ for Case VI.}$$

The parabolic distribution of S prescribed in Case IV has zeros at $\xi = 1$ and $\xi = 1.9$, corresponding to separation and re-attachment respectively, with a minimum value of $S = -.05$ at $\xi = 1.45$, as shown in Fig.3a. This figure also shows the distribution of β computed by the present method, the LRK method and the Görtler series. The calculated distributions of H are shown in Fig.3b, and a comparison is made in Fig.3c of the computed variation of S with β, compared with that for the Falkner-Skan similar solutions. The computation by the present method passed smoothly through both points of zero wall shear. The Görtler series agrees very well with the present method up to separation, but thereafter diverges rapidly, whilst the LRK method predicts both H and β quite satisfactorily. The degree of departure from local similarity is clearly shown in Fig.3c.

Cases V and VI have prescribed distributions of S which tend exponentially to $S = -.075$ and -0.100 respectively for large ξ. The boundary layers thus tend to the similar solutions corresponding to these values of S, as $\xi \to \infty$. Now, as shown in Fig.3c, there are a pair of values of β for each such value of S, suggesting that the solution to the non-similar problem may also not be unique. This lack of uniqueness is not apparent in the results for Case V, shown in Figs. 4a and 4b, and there is good agreement between the present and LRK methods. The solution tends to the similar solution with $\beta = -.189$, with a shallow reversed flow region ($H = 5$).

However, in Case VI the lack of uniqueness becomes evident. The calculation by the present method tends apparently towards the similar solution with $\beta = -.043$, with a deep reversed flow region, although the calculation was terminated well before this asymptotic condition was reached. On the other hand, the LRK results diverge rapidly away from those of the present method for $\xi > 1.5$, tending towards the other similar solution with $\beta = -.178$, with a shallow reversed flow region, as shown in Figs. 5a and 5b.

It is shown in the Appendix that the LRK method has a singular point at $H = 8.8$ when used, as here, to solve inverse problems, and therefore it would not be possible with that method to compute a case in which H rises above this value, as it would have to in order to follow a solution of the type given by the present method. Thus, in inverse problems the LRK method appears to be limited to cases with fairly shallow reversed flow regions.

The solution obtained by the present method is smooth and apparently free from singularities. However, it was found that at $\xi = 1.7$, the iteration process failed unless a good initial estimate for β was provided. At the same time, it was found that at this position the variation in velocity ratio at the boundary layer edge caused by unit change in the value of β, i.e. $\partial U_e/\partial\beta$, suddenly changed sign from that at the previous station, whilst the magnitude was very large in both cases. This suggests the existence of either a zero or an infinity in $\partial U_e/\partial\beta$ in this vicinity. The implication of this is not clear, although the existence of a branch point may be indicated.

3.3 Continuation beyond Separation with Prescribed Pressure

In some cases no solution to the inverse problem can be found beyond a short distance after separation. By smoothly joining a prescribed distribution of β to that calculated upstream, it has been found possible to continue the computation as a direct problem.

As an example, results are presented in Fig.6 for a case defined by :-

Case VII : $S = S_\beta.(1 - \xi).(1 - 0.4\xi)$ for $\xi < 1.16$,

with β prescribed numerically for $\xi > 1.16$ as shown in Fig.6b.

($\beta = -0.1$ for $\xi > 2.0$)

There was no evidence of instability in this case, and it appears that, if continued sufficiently far, the solution would tend towards the similar solution for $\beta = -0.1$. However, another example became numerically unstable for large ξ, and the question of stability requires investigation.

3.4 Detailed Study of Separation

The question is now examined of whether a distribution of β which has been calculated to correspond to a regular prescribed distribution of S leads to singular behaviour at separation, if it is then used as the prescribed β distribution in a direct problem.

The distribution of β calculated in an inverse problem, Case IV above, was used as input (to 5 significant figures) in a direct calculation. The result, as shown as Curve B of Fig.7a, was a distribution of S which was identical to the original input, Curve A, up to the last ξ-station before separation, but which then followed an entirely different, attached-flow path. Other calculations with changes in the 5th significant figure in the input value of β at $\xi = 1$ produced entirely different results thereafter. But if β was treated as unknown at the separation point only, with S put to zero there, one of two branches was subsequently followed depending upon the sign of the original estimate for S at $\xi = 1$. The lower branch follows the original input, Curve A, whilst the upper branch, Curve C, corresponds to attached flow. These two branches are directly analogous to the upper and lower branches of the similar solutions; however, the upper branch has a discontinuity in the slope of the displacement surface at $\xi = 1$, as shown in Fig. 7b.

The separation point thus appears to be a critical, branch point in these circumstances. It appears that the separation singularity will always occur, even if weakly, for cases with prescribed pressure, and it is evident that the previously-mentioned condition that $d^2u_e/dx^2 > 0$ for regular separation is not sufficient.

4. CONCLUSIONS

The above computations by the differential-difference method show clearly that a regular prescribed distribution of wall shear leads to regular behaviour of all other variables, the usual singularity at separation being suppressed.

The possibility of continuation of the integration beyond regular separation by downstream marching has been demonstrated, using either prescribed wall shear or prescribed pressure. However, questions of uniqueness and existence of the solutions require further investigation, particularly in view of the use of a downstream marching procedure in a region containing reversed flow.

The integral method of Lees, Reeves and Klineberg has been shown to predict the integral properties of the boundary layer to good accuracy, for attached flow and moderately-separated flow. However, the occurrence of a singularity in the LRK method with prescribed wall shear has prevented evaluation of the method for well-separated flow.

REFERENCES

1. Goldstein, S — "On laminar boundary-layer flow near a position of separation", Quart.J.Mech.Appl.Math., 1, pp.43-69 (1948).

2. Brown, S.N. and Stewartson, K. — "Laminar Separation", Annual Review of Fluid Mechanics, Annual Reviews Inc., pp.45-72, (1969).

3. Catherall, D. and Mangler, K.W. — "The Integration of the Two-Dimensional Laminar Boundary Layer Equations Past the Point of Vanishing Skin Friction", J. Fluid Mech., 26, pp.163-182, (1966).

4. Keller, H.B. and Cebeci, T. — "An Inverse Problem in Boundary-Layer Flows", J. Computational Phys., 10, pp.151-161 (1972).

5. Horton, H.P. — "Separating Laminar Boundary Layers with Prescribed Wall Shear", AIAA Journal, Vol.12, No.12, pp.1772-1774, (Dec.1974).

6. Lees, L. and Reeves, B.L. "Supersonic Separated and Reattaching Laminar Flows", AIAA Journal, 2, No.11, pp.1907-1920 (1964).

7. Klineberg, J.M., and Lees, L. "Theory of Laminar Viscous-Inviscid Interactions in Supersonic Flow", AIAA Journal, 7, No.12, pp.2211-2221 (1969).

8. Görtler, H. "A New Series for the Calculation of Steady Laminar Boundary Layer Flows", J. Math. Mech., 6, pp.1-66 (1957).

9. Falkner, V.M. and Skan, S.W. "Some approximate solutions of the Boundary-Layer Equations", Aero. Research Counc. R. & M. 1314 (1930).

10. Hartree, D.R. "A Solution of the Laminar Boundary-Layer Equation for Retarded Flow", Aero. Research Counc. R. & M. 2426 (1939).

11. Smith, A.M.O. and Clutter, D.W. "Solution of the Incompressible Laminar Boundary-Layer Equations", AIAA Journal, 1, No.9, pp.2062-2071 (1963).

12. Reshotko, E. and Beckwith, I.E. "Compressible Laminar Boundary Layer over a Yawed Infinite Cylinder with Heat Transfer and Arbitrary Prandtl Number", N.A.C.A. Tech. Rept. 1379 (1957).

13. Klineberg, J.M. "Theory of Laminar Viscous-Inviscid Interactions in Supersonic Flow", Ph.D. Thesis, California Inst. of Technology, Pasadena, Calif. (1968).

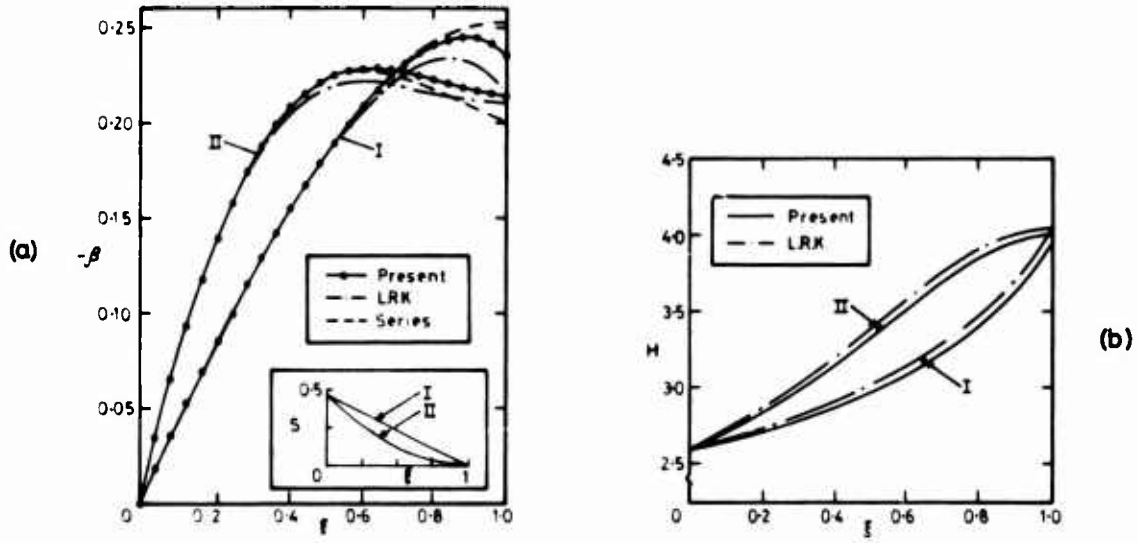

Fig. 1 Computed results for Cases I and II.
Inset: the prescribed wall shear distributions.

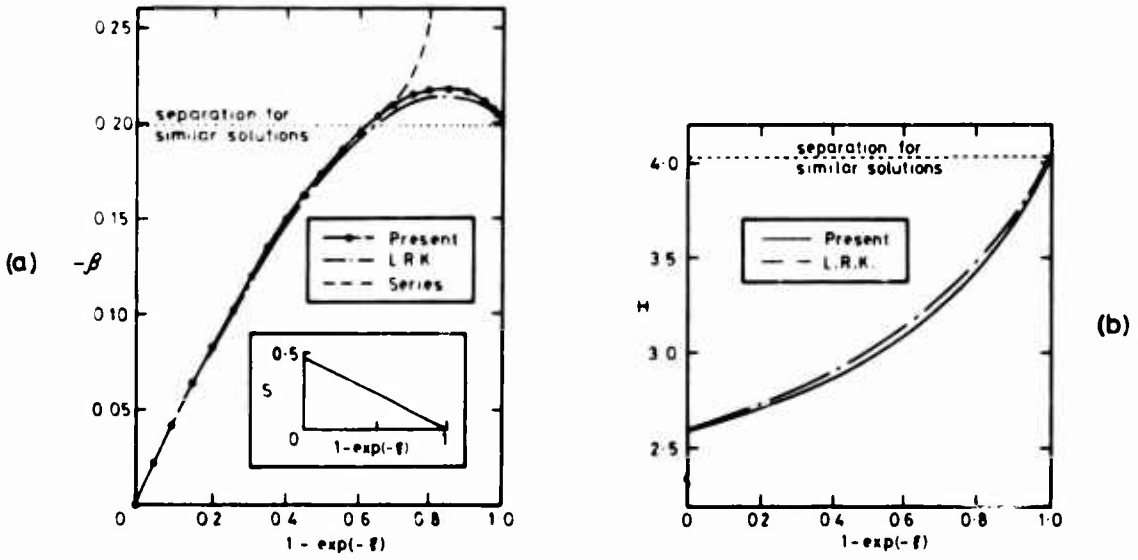

Fig. 2 Computed results for Case III.

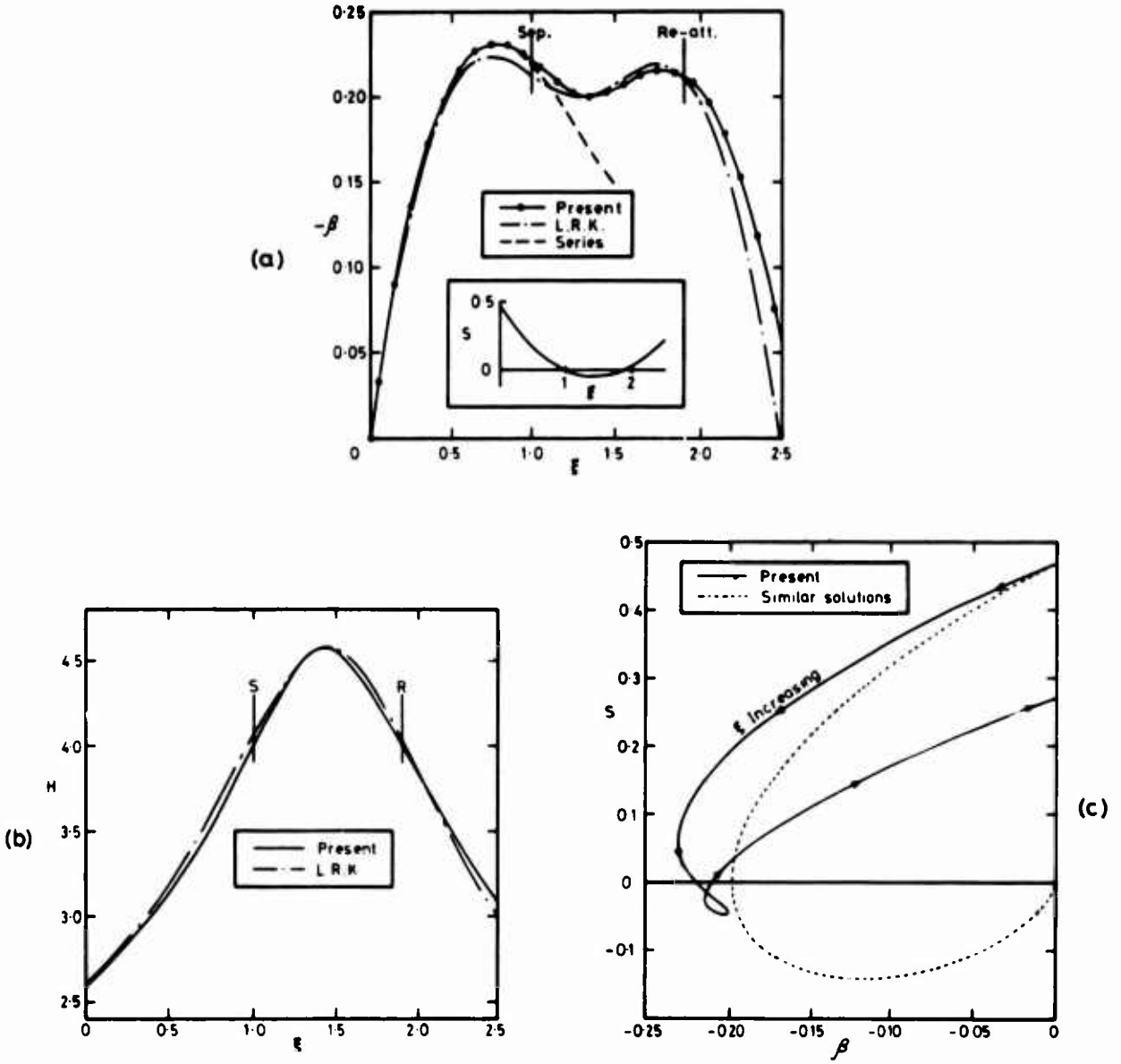

Fig. 3 Computed results for Case IV.

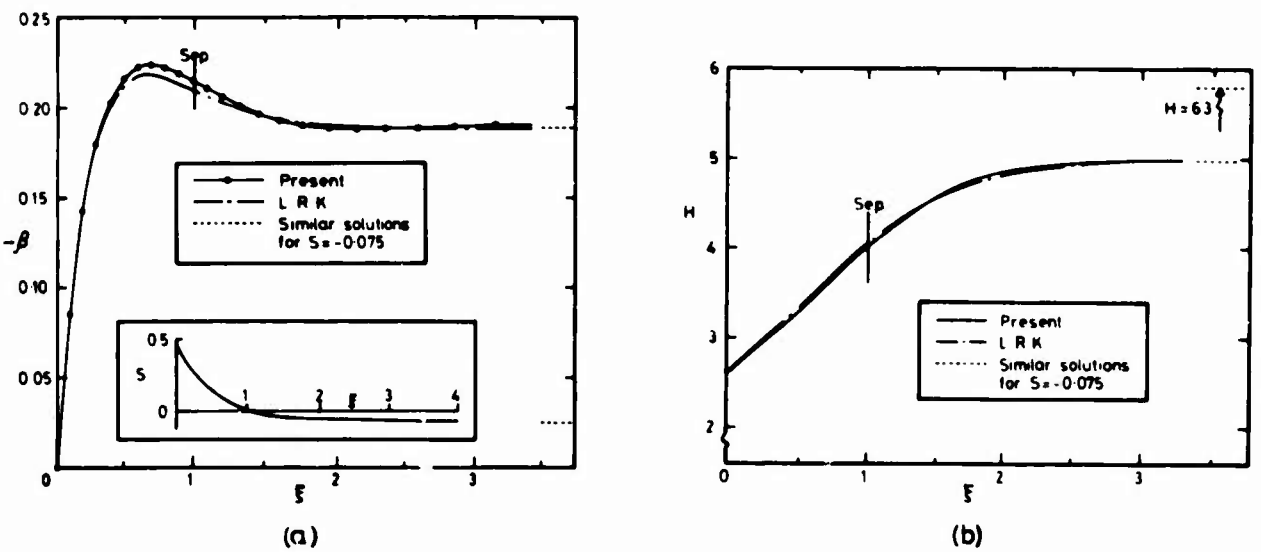

Fig. 4 Computed results for Case V.

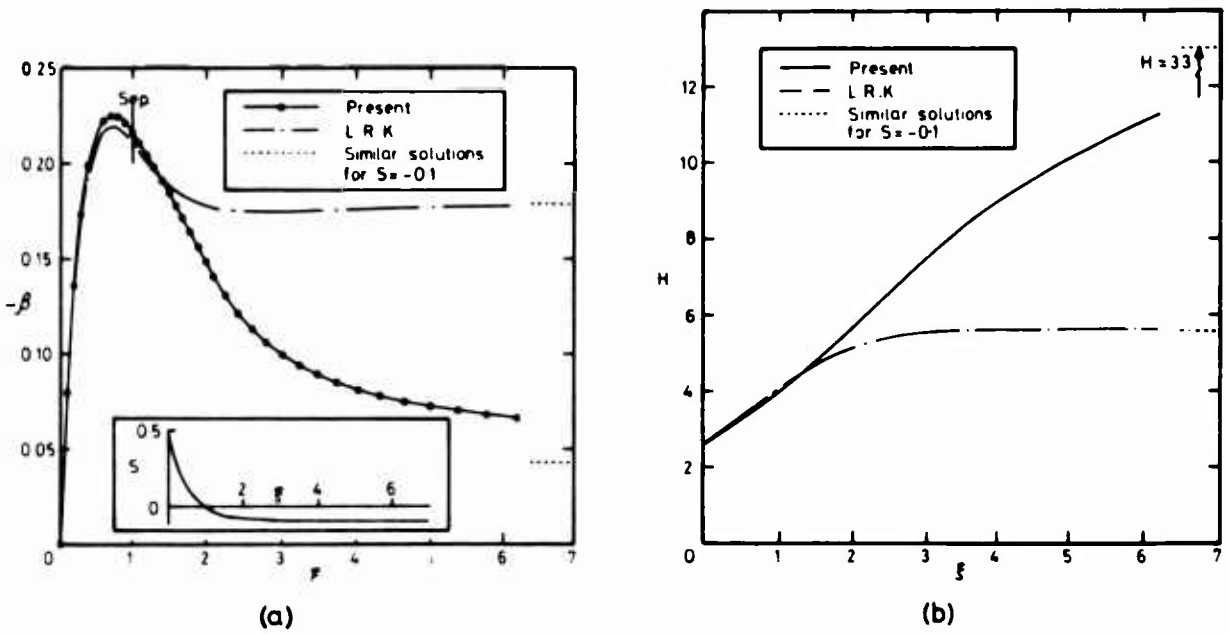

Fig. 5 Computed results for Case VI.

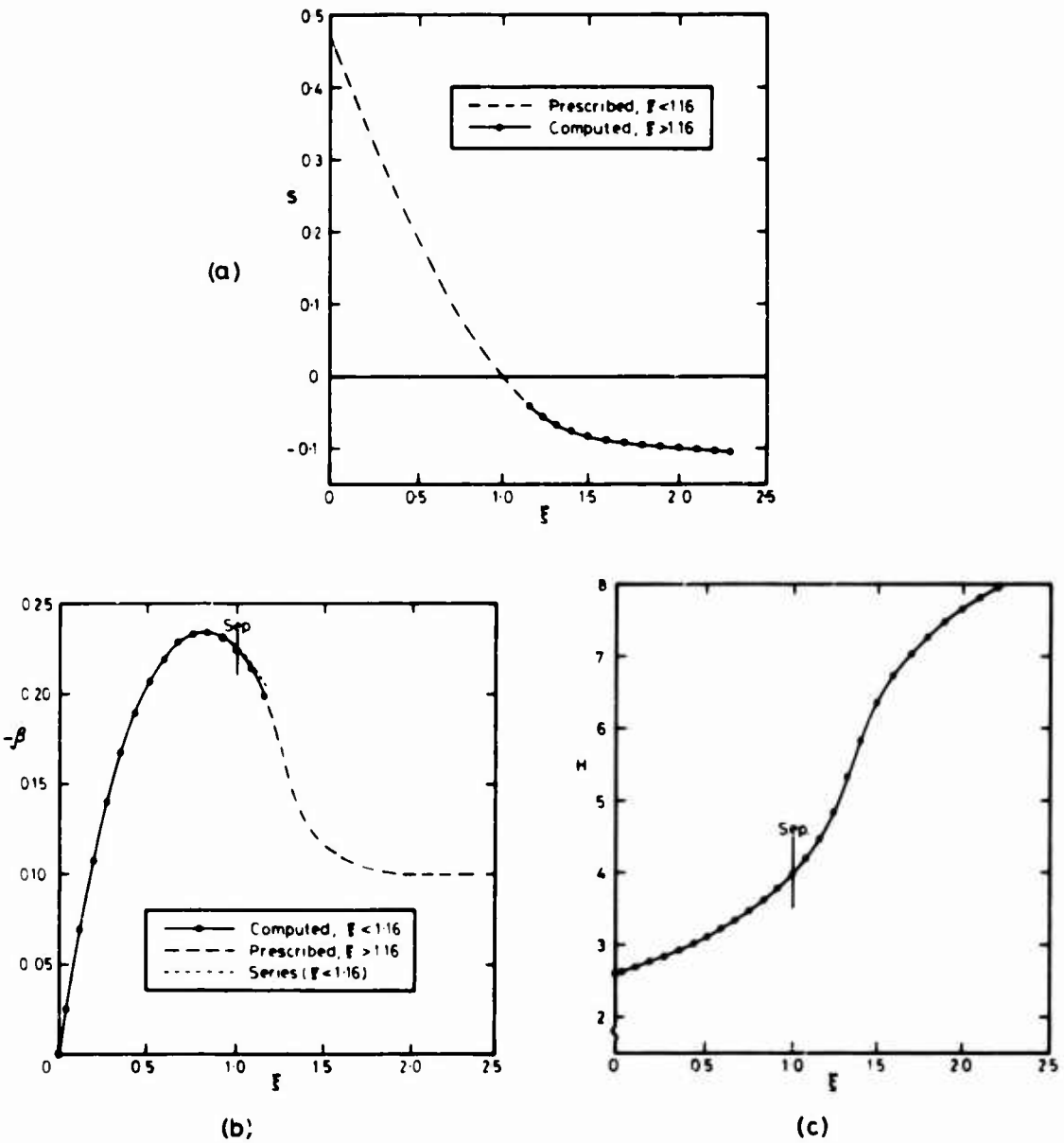

Fig. 6 Computed results for Case VII.

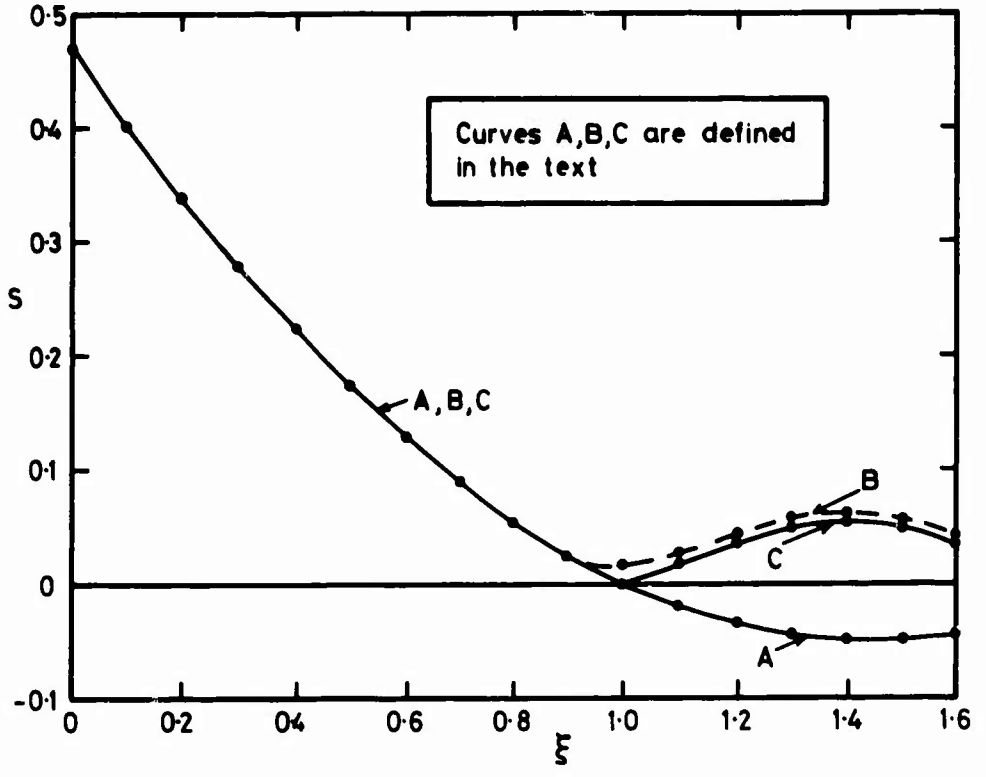

(a)

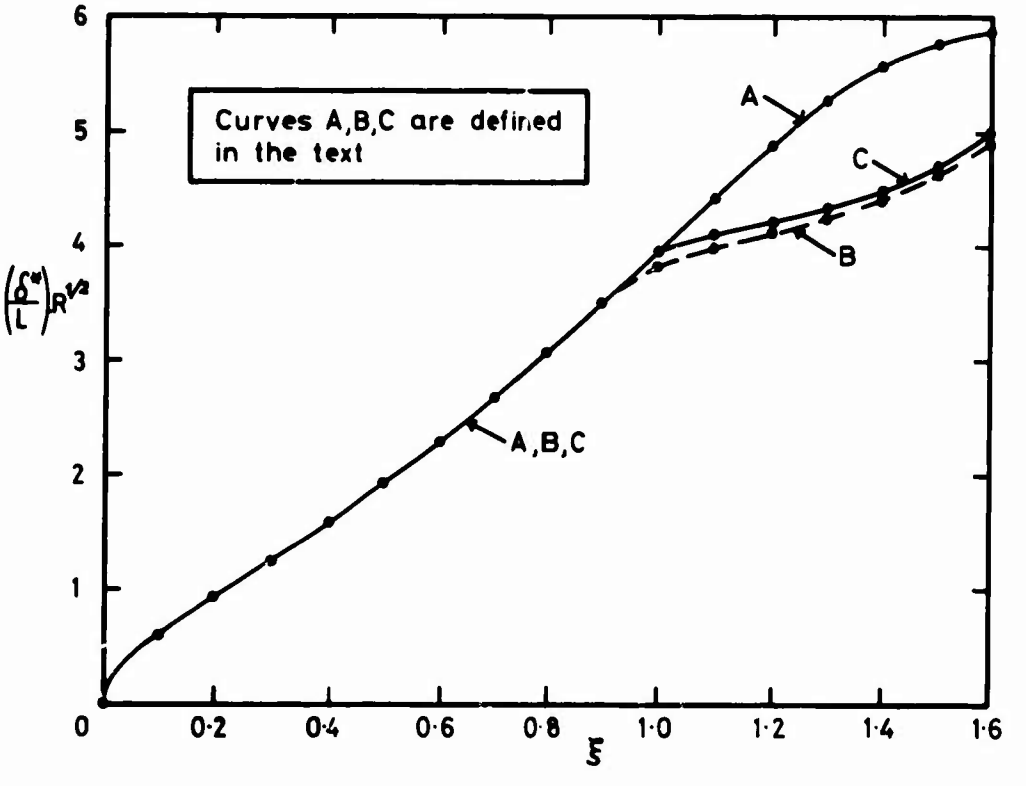

(b)

Fig. 7 Computed results for Case IV treated as both an inverse and a direct problem (see text).

APPENDIX

Approximate Solution by the Integral Method of Lees-Rees-Klineberg

This integral method for the approximate solution of the boundary layer equations, for both attached and separated flow, was originally used by Lees and Reeves[6] for the solution of shock wave/boundary layer interactions in adiabatic flow. In that case, the momentum integral and moment-of-momentum integral equations were solved together with a coupling equation linking the external, inviscid flow with the boundary layer growth. This coupling equation is not required here, and instead either the pressure gradient or the wall shear is specified. Since the method was applied in the transformed, incompressible plane, the basic relations are directly applicable to incompressible problems.

Here, we show how the method may be applied in Görtler co-ordinates.

A.1 Integral Equations

The momentum integral and moment-of-momentum integral equations are obtained by multiplying Eq.(5) by unity and $f'(\equiv u/u_e)$ respectively, and then integrating with respect to η from $\eta = 0$ to a suitably large value, η_∞ say. This leads to

$$2\xi \frac{d\theta}{d\xi} + \theta + \beta(\theta + \Delta^*) = S \,, \tag{A1}$$

$$2\xi \frac{d\theta^*}{d\xi} + \theta^* + 2\beta\theta = I_1 \,, \tag{A2}$$

where
$$\Delta^* = \int_0^{\eta_\infty}(1-f')d\eta, \quad \theta = \int_0^{\eta_\infty} f'(1-f')d\eta, \quad \theta^* = \int_0^{\eta_\infty} f'(1-f'^2)d\eta,$$
$$f' = u/u_e \,, \quad S = (f'')_{\eta=0}, \quad I_1 = 2\int_0^{\eta_\infty}(f'')^2\, d\eta. \tag{A3}$$

Now we may relate these quantities to those used in the method of Lees and Reeves, viz.

$$\mathcal{H} = \frac{\theta}{\delta^*} = \frac{\theta}{\Delta^*} \,, \quad \text{where } \delta^* = \int_0^\delta (1-\frac{u}{u_e})dy, \quad \theta = \int_0^\delta \frac{u}{u_e}(1-\frac{u}{u_e})dy \;;$$

$$J = \frac{\theta^*}{\delta^*} = \frac{\theta^*}{\Delta^*} \,, \quad \text{where } \theta^* = \int_0^\delta \frac{u}{u_e}(1-\frac{u^2}{u_e^2})dy \;;$$

$$P = \delta^* \left[\frac{d}{dy}(\frac{u}{u_e})\right]_w = \Delta^* S \;; \tag{A4}$$

$$R = \frac{2\delta^*}{u_e^2}\int_0^\delta (\frac{du}{dy})^2\, dy = \Delta^* I_1 \,.$$

The integral quantities $\mathcal{H}$, J, P and R are then taken to be functions of a single profile parameter 'a', these functions being polynomial curve-fits calculated from similar solutions of the boundary layer equations. We use here the revised polynomials calculated by Klineberg[13,7] for adiabatic flow. Eqns. (A1) and (A2) now become:-

$$2\xi(\Delta^*\frac{d\mathcal{H}}{d\xi} + \mathcal{H}\frac{d\Delta^*}{d\xi}) + \left[\mathcal{H} + \beta(1+\mathcal{H})\right]\Delta^* = P/\Delta^* \,, \tag{A5}$$

$$2\xi(\Delta^*\frac{dJ}{d\xi} + J\frac{d\Delta^*}{d\xi}) + \left[1 + 2\beta\right]J\Delta^* = R/\Delta^* \,, \tag{A6}$$

$$\text{with } \mathcal{H} = \mathcal{H}(a), \quad J = J(a), \quad P = P(a) \text{ and } R = R(a). \tag{A7}$$

A.2 Solution of Direct Problems by the Integral Method

When $\beta(\xi)$ is given, Eqs.(A5) and (A6) may be re-arranged for step-by-step integration by, for example, the Runge-Kutta method, to give:-

$$\frac{\xi}{\Delta^*}\frac{d\Delta^*}{d\xi} = \frac{(P\frac{dJ}{d\mathcal{H}} - R)\,\Delta^{*-2} - \beta\left[(1+\mathcal{H})\frac{dJ}{d\mathcal{H}} - 2J\right]}{2(\mathcal{H}\frac{dJ}{d\mathcal{H}} - J)} - \frac{1}{2} \,, \tag{A8}$$

$$\xi\frac{da}{d\xi} = \frac{\beta J(1-\mathcal{H}) - (PJ - \mathcal{H}R)\,\Delta^{*-2}}{2(\mathcal{H}\frac{dJ}{d\mathcal{H}} - J)\frac{d\mathcal{H}}{da}} \,. \tag{A9}$$

A series expansion is used to start the downstream integration from $\xi = 0$.

Note that $(\mathcal{H}dJ/d\mathcal{H} - J)$ vanishes at the separation point (a = 0). This leads to singular behaviour at separation when $\beta(\xi)$ is prescribed.

A.3 Solution of Inverse Problems by the Integral Method

When $S(\xi)$ is given, the solution may be obtained by eliminating β between Eqs.(A5) and (A6), to give

$$2\xi \frac{d\mathcal{H}}{d\xi}\left[2J - (1+\mathcal{H})\frac{dJ}{d\mathcal{H}}\right] + 2J(\mathcal{H}-1)\frac{\xi}{\Delta^*}\frac{d\Delta^*}{d\xi} = \left[2PJ - (1+\mathcal{H})R\right]\Delta^{*-2} - J(\mathcal{H}-1) \quad . \tag{A10}$$

This equation is then integrated in conjunction with the relation between P,Δ^* and the given wall shear distribution, Eq.(A4), viz.

$$P = \Delta^* S \quad . \tag{A11}$$

The most convenient method of solution is to firstly differentiate Eq.(A11) with respect to ξ, and to then solve the resulting differential equation simultaneously with Eq.(A10). The equations to be solved are then:-

$$\xi \frac{da}{d\xi} = \frac{2J(\mathcal{H}-1)\xi\frac{d\xi}{d\xi}\Delta^* + P\left[\{2PJ - (1+\mathcal{H})R\}\Delta^{*-2} - J(\mathcal{H}-1)\right]}{2\left[J(\mathcal{H}-1)\frac{dP}{d\mathcal{H}} + P\{2J - (1+\mathcal{H})\frac{dJ}{d\mathcal{H}}\}\right]\frac{d\mathcal{H}}{da}} \quad , \tag{A12}$$

$$\frac{\xi}{\Delta^*}\frac{d\Delta^*}{d\xi} = \left[\{2PJ - (1+\mathcal{H})R\}\Delta^{*-2} - J(\mathcal{H}-1) - 2\xi\frac{da}{d\xi}\cdot\frac{d\mathcal{H}}{da}\{2J - (1+\mathcal{H})\frac{dJ}{d\mathcal{H}}\}\right]\cdot\frac{1}{(\mathcal{H}-1)} \quad . \tag{A13}$$

As before, a series expansion is used to initiate the integration from $\xi = 0$.

The distribution of $\beta(\xi)$ may be obtained from the calculated distributions of a and Δ^* using either Eq.(A8) or Eq.(A9).

Eqs.(A12) and (A13) do not exhibit singular behaviour at the separation point, so the integration can be continued through separation. However the denominator of Eq.(A12), which is a function of 'a' alone, vanishes in the separated region when a = 0.327, corresponding to a value of $H(=\delta^*/\theta) = 8.8$. Hence, for prescribed $S(\xi)$, a singularity occurs when H rises to this value, effectively terminating the solution.

It may also be shown that, as a result of the vanishing of $(\mathcal{H}dJ/d\mathcal{H} - J)$ at separation, the value of the local pressure gradient parameter λ has the unique value of -0.068 at a point of regular separation, where

$$\lambda = \frac{\theta^2}{\nu}\frac{du_e}{dx} \equiv \beta\theta^2.$$

FINITE DIFFERENCE SOLUTIONS FOR SUPERSONIC SEPARATED FLOWS

by

M.J. Werle, A. Polak, V.N. Vatsa, S.D. Bertke
Department of Aerospace Engineering
University of Cincinnati
Cincinnati, Ohio U.S.A. 45221

SUMMARY

Laminar and turbulent separation bubbles are addressed for a wide range of geometries using an implicit finite difference technique to solve the interacting boundary layer equations. Solutions are presented for laminar compression ramps at M_∞ = 4 and 6, wall temperature ranges, T_w/T_o of 0.2 to 1.0 and angles of sweep (yaw) relative to the mainstream of up to 60°. In addition, solutions for laminar flow over wavy walls with multiple separation bubbles are given here for M_∞ = 3. Application of the approach to turbulent separated flows ahead of a compression ramp at M_∞ = 3 is also considered.

SYMBOLS

A	eddy viscosity damping factor
C_f	skin friction coefficient
$\bar{C}_f$	modified skin friction coefficient
C_p	specific heat
d	scale length for transition process
F	normalized longitudinal velocity in cross plane
G	normalized spanwise velocity component
h	time term multiplication factor
K_1, K_2	eddy viscosity constants
ℓ	normalized viscosity coefficient
L	reference length
M	Mach number
n	distance normal to surface
N	stretched normal distance
p	pressure
Q_w	surface heat transfer
$\bar{Q}_w$	normalized surface heat transfer
r_o	transverse radius of curvature
Re_∞	Reynolds number based on free stream viscosity
Re	Reynolds number based on reference viscosity
s	surface distance in cross plane
t	time
T	static temperature
u	viscous longitudinal velocity in cross plane
U	inviscid longitudinal velocity in cross plane
V	transformed normal velocity
w	viscous spanwise velocity
W	inviscid spanwise velocity
$\alpha_{1,2}$	dissipation coefficients of energy equation
β	pressure gradient parameter
γ	ratio of specific heats
$\bar{\gamma}$	transverse intermittency function
Γ	longitudinal intermittency function
μ	viscosity
δ	displacement thickness
δ_{inc}	incompressible displacement thickness
ε	eddy viscosity
$\bar{\varepsilon}$	momentum equation eddy viscosity function
ε	energy equation eddy viscosity function
η	transformed normal coordinate
θ	static temperature ratio
θ_T	angle of deflection of inviscid streamlines
θ_s	slope of surface
θ_R	ramp angle
λ	sweep (yaw) angle
ξ	transformed longitudinal coordinate in cross plane
ρ	density
σ	Prandtl number
σ_T	turbulent Prandtl number

Subscripts

e	inviscid edge values
∞	free stream values
o	previous time values
w	wall values
ref	reference values

Superscripts

*	time level t^*
n	time level t^n

1. INTRODUCTION

The problem studied here is that of a laminar or turbulent supersonic boundary layer separating and reattaching along an aerodynamic surface. In the cases studied, separation is induced by the surface geometry itself when the boundary layer is forced to negotiate a region of severe adverse pressure gradient, a situation typified by the flow over a simple compression corner. In such a case the boundary layer strongly interacts with the local mainstream to establish a surface pressure level significantly different than that predicted from inviscid considerations alone. Thus, to obtain meaningful solutions to this problem requires that one consider simultaneous solution of the viscous and inviscid flow equations taking account of their coupling through a representation of the interaction effect of one on the other.

The approach taken here employs the interacting boundary layer concept. The governing equations for the viscous region are taken to be the classical boundary layer equations except that the local inviscid properties driving these equations are determined through the deflection of inviscid streamlines passing over the displacement body. This approach is not new, and in one form or another, has been employed by a large number of investigators (see Ref. 1 for a review of the history of this problem) and has been reasonably successful in providing quantitative estimates to the influence of separation on the local surface properties. Recent asymptotic studies of the laminar supersonic problem by Stewartson and Williams (Ref. 2) and Jenson, Burggraf and Rizzetta (Ref. 3) has put this approach on a firmer analytical basis so that it now appears that the "interacting boundary layer model" can be considered exact, at least in the sense that for large Reynolds number it retains all the principle contributors from the compressible counterpart of the Navier Stokes equations.

It only remains then to seek an equally exact (but efficient) numerical method of solving these governing equations and to demonstrate the applicability of such. The ground work for such an effort has been laid by many previous investigators (see Refs. 4 through 8) who employed finite difference techniques for solving these types of problems and the present paper reports on continued progress in this area. In the work presented here, the numerical approach laid down by Werle and Vatsa (Ref. 9) and Bertke, S.D., Werle, M.J. and Polak, A. (Ref. 10) is applied to a broad range of separated flow situations to demonstrate the applicability of the solution technique.

The main feature of the numerical technique is its treatment of boundary conditions, more specifically the downstream compatibility condition. Heretofore, the requirement that the surface pressure level asymptotically approach the inviscid downstream pressure level was satisfied through iteration on the flow state at the upstream extent of the interaction region. In the new algorithm, the downstream conditions are imposed directly and solutions obtained using an implicit alternating direction finite difference scheme, leading to rapid accurate solutions of the separation problem.

In the present work, this numerical algorithm has been applied to both the laminar and turbulent cases for supersonic flow (Mach numbers of 3-6) over the ramp geometry given in Figure 1 for a wide range of wall temperature levels. Solution to the laminar quasi-three dimensional case obtained by sweeping (yawing) the ramp geometry relative to the mainstream direction is also presented. In addition, solutions for the case of laminar flow over a wavy wall with multiple separation bubbles are also shown here.

2. GOVERNING EQUATIONS

2.1 General

In the present approach, the flow field is divided into two distinct regions. The viscous region is taken to be governed by the boundary layer equations as driven by the properties of the inviscid flow as it passes over the displacement body (the original surface thickened by the displacement thickness). The inviscid properties can be determined in any convenient and appropriate manner and for present purposes approximate methods were found to be sufficient. Since such approximate inviscid models necessarily depend on the geometry involved, it is difficult to present them in any generalized statement. For this reason only the viscous equations are presented in detail in this section and the presentation of the inviscid model is only discussed in general, the details being deferred to that section dealing with application of the present study to a particular goemetry.

2.2 Viscous Equations

To anticipate application to laminar or turbulent compressible flow over two dimensional, axisymmetric, or swept (yawed) configurations, the boundary layer equations are presented here in a somewhat generalized form. Once the governing equations have been nondimensionalized using a characteristic length, L, the free stream velocity, U_∞, the free stream density, ρ_∞, and a reference temperature, $T_{ref} = U_\infty^2/C_p$, they are scaled to remove the explicit Reynolds number dependence by stretching the velocity and distance normal to the surface using

$$\varepsilon = Re^{-1/2} = \left[\frac{\mu(T_{ref})}{\rho_\infty U_\infty L}\right]^{1/2} \qquad (1)$$

The principle dependent variables are then normalized according to the scheme

$$F = u/U_e \quad , \quad \theta = T/T_e \quad , \quad G = w/W_e \quad , \quad \ell = \rho\mu/\rho_e\mu_e \qquad (2)$$

where the subscript e refers to the inviscid flow values at the current location on the surface and u represents the velocity along the surface in the normal plane depicted in Figure 1, T is the static temperature, w is the velocity component normal to the cross plane of Figure 1 and is non-zero only for swept (yawed) configurations, ρ is the density, and μ is the viscosity coefficient here calculated from Sutherlands law.

The independent variables used in the cross plane are Levy-Lees type (see Ref. 11) and are given as

$$\xi = \int_0^s \rho_e \mu_e U_e r_o^{2j} ds \tag{3}$$

and $$\eta = \frac{U_e r_o^j}{\sqrt{2\xi}} \int_0^N \rho \, dN$$

where N is the stretched coordinate given as

$$N = n\sqrt{Re} \tag{4}$$

and s and n are the longitudinal and normal surface coordinates respectively. Note that the superscript j is non zero here only for axisymmetric flows where j = 1 recovers the correct relations. With these transformations the governing equations become

Continuity:

$$V_\eta + F + 2\xi F_\xi = 0 \tag{4a}$$

Normal Plane Momentum Equation:

$$(\bar{\varepsilon}\ell F_\eta)_\eta - VF_\eta + \beta(\theta - F^2) - 2\xi FF_\xi = 0 \tag{4b}$$

Energy Equation:

$$\left(\frac{\hat{\varepsilon}\ell}{\sigma}\theta_\eta\right)_\eta - V\theta_\eta + \alpha_1 \ell\bar{\varepsilon}F_\eta^2 + \alpha_2 \ell G_\eta^2 - 2\xi F \theta_\xi = 0 \tag{4c}$$

where σ is the Prandtl number

Yaw Plane Momentum Equation:

$$(\ell G_\eta)_\eta - VG_\eta - 2\xi FG_\xi = 0 \tag{4d}$$

Note that the turbulent effects are completely contained in the eddy viscosity coefficients $\bar{\varepsilon}$ and $\hat{\varepsilon}$ which are included here only in the normal plane equations because these effects will only be considered for the two dimensional case (zero yaw) in the present study.

The additional inviscid parameters appearing in these relations are given as

$$\beta = \frac{2\xi}{U_e}\frac{dU_e}{d\xi} \tag{5a}$$

$$\alpha_1 = U_e^2/T_e \tag{5b}$$

$$\alpha_2 = W_e^2/T_e = \alpha_1 \tan^2\lambda \tag{5c}$$

Following the now rather standard approach (see Ref. 12) the turbulent eddy viscosity parameters are defined here as

$$\bar{\varepsilon} = \left[1 + \left(\frac{\varepsilon}{\mu}\right)\Gamma\right] \tag{6a}$$

and $$\hat{\varepsilon} = \left[1 + \frac{\sigma}{\sigma_T}\left(\frac{\varepsilon}{\mu}\right)\Gamma\right] \tag{6b}$$

where σ_T is the turbulent Prandtl number here taken as 0.9, Γ is the longitudinal intermittency function used to model the transition process, and $\left(\frac{\varepsilon}{\mu}\right)$ is the eddy viscosity term. The longitudinal intermittency is taken as a function of surface distance only and serves to describe the probability of turbulence at a given distance, s, assuming a value of 0 for laminar flow and 1 for fully turbulent flow. For $0 < \Gamma < 1$, the flow is transitional and Γ has the form

$$\Gamma = 1 - \exp(-0.412\,\bar{s}^2) \tag{7a}$$

where

$$\bar{s} = (s - s_{ti})/d \tag{7b}$$

with s_{ti} taken as the position where transition begins and d provides the length scale for the transition process as

$$d = (s)_{\Gamma=3/4} - (s)_{\Gamma=1/4} \tag{7c}$$

In practice the value of d is determined such that $\Gamma = 0.995$ at $s = s_{tf}$, the end of the transition zone.

The eddy viscosity, ε, was modeled using the now standard two layer description wherein an inner region is described in which

$$\left(\frac{\varepsilon}{\mu}\right) = Re\,\frac{\rho \ell^2}{\mu}\left|\frac{\partial u}{\partial n}\right| \tag{8a}$$

where $$\ell = K_1\, n\left[1 - \exp\left(-\frac{n}{A}\right)\right] \tag{8b}$$

with $K_1 = 0.4$ and the damping constant A is given as

$$A = \frac{26}{Re^{1/2}}\,\frac{\mu}{\rho}\left\{\frac{\mu_w}{\rho}\left(\frac{\partial u}{\partial n}\right)_w\right\}^{-1/2} \tag{8c}$$

In the outer region, the eddy viscosity is taken as

$$\left(\frac{\varepsilon}{\mu}\right) = K_2\, Re\,\frac{\rho_e U_e}{\mu_e}\,\frac{\bar{\gamma}\,\delta_{inc}}{\ell\theta^2} \tag{9a}$$

where $$\delta_{inc} = \int_0^\infty \left(1 - \frac{u}{U_e}\right) dn \tag{9b}$$

and $\bar{\gamma}$ is the transverse intermittency function given as

$$\bar{\gamma} = \frac{1}{2}\left[1 - \mathrm{erf}\left[5(n/n_e - 0.78)\right]\right] \tag{9c}$$

and n_e is defined as that position where $F = u/U_e = 0.995$.

Although the application of this eddy viscosity in regions of severe pressure gradient still causes some controversy (see Ref. 13 for example), space will not be taken here to address this point. Rather, this point will be considered in detail in the later section where direct application of the method is considered.

The boundary conditions to be applied to this governing set of equations are

(a) the no slip condition

$$F(\xi,0) = G(\xi,0) = 0 \tag{10a}$$

(b) the wall temperature condition, either a specified temperature

$$\theta(\xi,0) = \theta_w = T_w/T_e \tag{10b}$$

or the adiabatic condition

$$\frac{\partial\theta(\xi,0)}{\partial\eta} = 0 \tag{10c}$$

(c) the zero injection condition

$$V(\xi,0) = 0 \tag{10d}$$

and the edge conditions

$$\begin{aligned} F &\to 1 \\ \theta &\to 1 \quad \text{as } \eta \to \infty \\ G &\to 1 \end{aligned} \tag{10e}$$

Finally, the only remaining points of concern are the boundary layer properties themselves. These are given as

(a) the displacement thickness (in the normal plane)

$$\delta = \int_0^\infty \left(1 - \frac{\rho\, u}{\rho_e\, U_e}\right) dn = \frac{\varepsilon\sqrt{2\xi}}{\rho_e\, U_e}\int_0^\infty (\theta - F)\, d\eta \tag{11a}$$

(b) the skin friction coefficient (in the normal plane)

$$C_f\sqrt{Re_\infty} = \bar{C}_f\sqrt{Re_\infty/Re} = \rho_e\mu_e U_e^2 r_o^j\, \ell_w f_{\eta_w}/\sqrt{2\mu_\infty\xi} \tag{11b}$$

(c) the surface heat transfer

$$Q_w \sqrt{Re_\infty} = \bar{Q}\sqrt{Re_\infty/Re} = \rho_e \mu_e U_e r_o^j T_e \ell_w \theta \eta_w / \sigma\sqrt{2\mu_\infty \xi} \tag{11c}$$

2.3 Inviscid-Viscous Interaction Equations

As discussed above, the influence of the viscous flow on the inviscid flow properties will be accounted for here through the displacement body concept. In all cases considered, the inviscid fluid will be assumed to be flowing past that surface formed by adding the displacement thickness to the original body contour.

For estimating the inviscid flow properties over an arbitrary body shape in supersonic flow, simple and well tested approximate methods seem appropriate. For two dimensional flows, such models as linear theory, tangent wedge, or the unified tangent wedge laws (see Ref. 14) all provide reasonable estimates of surface pressures on a body in the form $p_e = f(\theta_T)$ where θ_T is the slope of the displacement body at a given station given as

$$\theta_T = \theta_s + \frac{d\delta}{ds} \tag{12}$$

The remainder of the edge flow properties along this displacement body streamline can be reasonably estimated from isentropic flow theory. The more significant point is that the local pressure gradient, dp_e/ds, is given as

$$\frac{dp_e}{ds} = f' \frac{d\theta_T}{ds} \tag{13a}$$

which influences the governing viscous flow equations through the parameter β according to the relation

$$\beta = \frac{-2\xi}{\rho_e^2 \mu_e U_e^3 r_o^{2j}} \frac{dp_e}{ds} \tag{13b}$$

For the case of yawed (swept) bodies, the extension of linear theory or unified tangent wedge theory is straightforward (see Ref. 15) and again leads to a relation of the same form as that given in Eq. (13).

2.4 Upstream and Downstream Boundary Conditions

It is important to realize the nature of the problem at hand since it involves the coupled solution of the viscous and inviscid equations. Based on the work of Neiland (as discussed in Ref. 17), Garvine (Ref. 18), and Werle et al (Ref. 19) it is now clear that the interaction problem (even without separation) is ill posed as an initial value problem and should be addressed directly as a boundary value problem in the surface coordinate direction. This calls for the direct specification of flow conditions at both the upstream boundary and the downstream extent of the interaction zone.

Conditions at the upstream boundary cause no problems and are conceptually quite straightforward for the problems of interest here, all of which involve a flat surface of significant length, ahead of the interaction zone. Thus it appears that all the flow properties can be specified in detail at the initial station. This only remains true so long as there is no region of strong interaction because as shown by Neiland (Ref. 17), Garvine (Ref. 18), Werle et al (Ref. 19) and Hankey et al (Ref 20) such a region has an impact to some degree on the solution at all stations preceeding it. It is this property that is usually invoked (perhaps only tacitly) by most investigators to initialize supersonic strong interaction solutions, for by slightly perturbing the boundary layer equations off of the weak interaction solution, they are then found to automatically proceed into a strong interaction type behavior (referred to as the branching behavior of the boundary layer equations). Closure on this approach is achieved by iteration on the initial perturbation until a downstream compatibility condition is achieved, this usually being a statement that at some point reasonably far aft of the strong interaction zone, the weak interaction solution be recovered.

There is however a weakness in such an initial value approach. Garvine (Ref. 18) followed by Werle and Vatsa (Ref. 21) clearly showed that the interaction equations are ill posed as initial value problems in the sense that any error encountered at the initial station - no matter how small - will grow exponentially in the s direction (i.e. will cause a branch) and thus produce a solution unrelated to the correct initial conditions.

To overcome this weakness, it is necessary to specify directly the downstream condition in terms of some constraint on the displacement thickness distributions. This is most easily handled by specifying that the downstream pressure return to its weak interaction level at some point. To do this however requires that some condition be given-up at the upstream extent of the strong interaction zone. The most reasonable approach is to free the second derivative of displacement thickness at the initial station and letting this be determined from the solution itself. Rigorously, this approach requires that the initial station solutions be obtained by invoking the family of branching solutions identified by Werle et al (Ref. 19) and Hankey et al (Ref. 20) by relating them to an unspecified constant that in turn is determined by imposition of the new downstream boundary condition. The complexity of this approach seems unwarranted at

this time and it is replaced here by an approach that follows the concept of this requirement if not the exact detail. At the initial station, the profile quantities are completely specified from the weak interaction solution. However, for the purpose of determining the downstream interaction effect on the displacement thickness distribution, the weak interaction condition is used only to specify the value of the displacement thickness at the initial point.

3. NUMERICAL METHOD

The numerical method invoked here is essentially that presented by Werle and Vatsa (Ref. 9) with some modifications recently introduced for computational efficiency purposes. Due to space limitations, only the general approach will be outlined here. For more details the reader will be referred to those publications that consider the particular geometries as they are presented in the later sections.

The essence of the present approach can be delineated quite clearly by first re-writing the governing momentum equation using the pressure gradient equations (12) and (13) to explicitly display the influence of the displacement thickness. This leads to a relation of the form

$$F_{\eta\eta} + B_1(\xi,\eta)\delta_{\xi\xi} = B_2(\xi,\eta) \tag{14}$$

Numerical solution of this equation is accomplished using alternating direction implicit concepts and proceeds in artificial time from level t^n to $t^* = t^n + \Delta t/2$ with the relation

$$F^*_{\eta\eta} + B^*_1\left[\delta^n_{\xi\xi} - \frac{\delta^* - \delta^n}{\Delta t/2}\right] = B^*_2 \tag{15a}$$

and then from time t^* to $t^{n+1} = t^* + \Delta t/2$ with the relations

$$F^*_{\eta\eta} + B^*_1\left[\delta^{n+1}_{\xi\xi} - \frac{\delta^{n+1} - \delta^*}{\Delta t/2}\right] = B^*_2 \tag{15b}$$

In the first step, the viscous properties are determined, while the second step serves to update the displacement thickness contribution to the inviscid pressure gradient parameter. This time like march is allowed to proceed until a steady state is achieved and the time like terms of Equations (15a) and (15b) thus becomes negligible.

Note that the first step involves solution of a boundary layer like equation and can proceed in a marching fashion from the initial station using an implicit finite difference scheme similar to that endorsed by Blottner (Ref. 11). Boundary conditions at the edge and wall are imposed at each station according to Equations (10a) through (10e).

The second sweep equations only involve the displacement thickness as an unknown and must satisfy imposed initial and final conditions. At the initial station, the displacement thickness is held fixed at its self similar level. At the downstream boundary, the displacement thickness derivative is taken so as to assure that the weak interaction solution is recovered. This second sweep equation is quite easily solved using central differences leading to a tridiagonal set of difference equations easily inverted using the Thomas algorithm.

There are two general areas of concern that should be discussed in some detail at this point. The first of these involves computation in regions of reverse flow where a numerical stability analysis would indicate that an instability should be encountered when a marching technique is applied here. This problem is quite easily handled in the present time like approach using the concept of upwind derivatives on the convective terms of Equation (4).

An alternate approach employs the concept of "artificial convection" introduced by Reyhner and Flugge-Lotz (Ref. 7) to gain numerical stability in the reverse flow direction. The basis for this approach is found in the usual low levels of longitudinal velocity, F, in reverse flow regions such that this convection term is consistently quite small. With this in mind, it has been found useful to simply reverse the sign of the convection term and weight it to some convenient degree to achieve numerical stability. While such an approach seems less palatable than the upwind differencing scheme, it requires considerably less computer storage and has not yet proven to be a problem quantitatively. Both approaches have been used by the present authors in several studies (Refs. 9 and 10 for example) and only minor differences have been observed. It appears to be more a matter of convenience than rigor that produces a final decision on this matter.

The second area of concern that should be discussed in detail here is that of the solution behavior at the separation point. While it is now generally understood that the interacting boundary layer equations have a regular behavior at separation (see Ref. 2, for more discussion), the now classical Goldstein singularity can still plague the numerical solution unless care is taken to assure its absence. Recall that if one attempts to pass through the zero skin friction point with the pressure gradient specified, a singularity results and the solution necessarily must terminate. Allowing interaction of the viscous and inviscid flow through this term [see Equations (12) and (13)] does not allow the singular solution to emerge. However, it must be realized

that the present approach will experience difficulty in this regard. To see this attention is directed to the first sweep equation (15a) wherein the solution algorithm proceeds to march along the surface with the displacement thickness derivatives contribution to the pressure gradient term specified at its earlier time value. Since this very term is the one that removes the separation singularity, lagging this term in time is tantamount to specifying the total pressure gradient value. It is not surprising then to reencounter the separation singularity using this form of the algorithm and action must be taken to cure the problem.

As noted in Ref. (9), the procedure used to remove this singularity is not at all obvious or unique. The present author's initial attempts involved a modification of the artificial time like terms of Equation (15(to remove the singularity. That approach was successful and has been given in detail in Ref. (9) so that it need not be presented here. It was employed to obtain all the laminar solutions presented in the later sections of this paper and can be recommended as one successful means of avoiding the occurrence of an unnecessary singularity in the difference equations.

For some of the turbulent boundary layer solutions presented later, an alternate approach was used to remove the artificial singularity. The approach being now used in these high Reynolds number cases is based on the concept that the singular behavior being observed in the numerical solutions is completely seated in the nonlinear nature of the convective term. If this term were absent or linear, no singularity should occur. Arguments supporting this contention can be easily made by simply differentiating the momentum equations twice with respect to the normal coordinate η and evaluating the resulting equation at the wall, $\eta = 0$. Without the nonlinearity in the convective term, these results indicate that no singular behavior in the skin friction should be anticipated. This approach has proven quite useful in the study of turbulent flows and should be considered in any future studies of separation effects.

4. RESULTS AND DISCUSSION

Attention will be directed in this section to the application of the above algorithm to a wide class of geometries in order to demonstrate its flexibility. No attempt will be made here to perform a thorough parameter study of any particular problem, although the related reference works do address this issue and the reader is referred to those works for such detail.

4.1 Two Dimensional Ramps - Laminar

The most straightforward example of supersonic separated flow is that encountered ahead of a two dimensional compression corner - here modeled with the smooth ramp geometry of Figure 2. The inviscid pressure distribution for this geometry was obtained here from the unified supersonic-hypersonic tangent wedge law (see Ref. 14 for example). The geometrical constant for the ramp was set at $C = 0.05$ producing the resulting inviscid pressure distribution of Figure 3a. Comparison of this distribution with the oblique shock theory distribution shows that the present pressure law reasonably well handles the geometry of interest.

Use of this geometry to study the influence of the wall temperature ratio on separation at $M_\infty = 6$ is shown in Figures (3a)-(3c). Comparison of the cold wall experimental surface pressure distribution of Lewis et al (Ref. 22) shows excellent comparison while the increase in wall temperature is seen to cause a large increase in the extent of the interaction zone. This is better reflected in the skin friction distributions of Figure (3b) showing a rather rapid drop from the weak interaction zone as the separation point creeps forward with increasing wall temperature. Simultaneously, the reattachment point moves aft causing a delay in return to the necessary weak interaction zone on the ramp face.

4.2 Swept (Yawed) Ramps - Laminar

The most obvious extension of this method to the study of three dimensional effects on separation characteristics is to apply it to the swept (yawed) ramp configuration. Holding all flow and geometry details fixed, the sweep (yaw) angle of the ramp shown in Figure 2 was increased systematically in 20° increments and the resulting surface pressure distribution determined from a swept leading edge version of the unified supersonic hypersonic tangent wedge law. This is determined by first considering sweep effects on the hypersonic small disturbance theory to obtain the tangent wedge law (see Ref. 15 for discussion of this approach) and then adjusting the final relation such that it recovers the supersonic linear theory (with sweep) relation as $M_\infty > 1$. The resulting equation is

$$p/p_\infty = \frac{1}{\gamma M_\infty^2} + \frac{\gamma+1}{4}\,\theta_T^2\cos^2\lambda\left[1+\sqrt{\frac{1}{\left(\frac{\gamma+1}{4}\right)^2\theta_T^2\left(M_\infty^2\cos^2\lambda-1\right)}}\right] \qquad (16)$$

and application of such to the present ramp geometry produced the inviscid pressure distributions of Figure 4a.

Results of application of the present method to solution of this problem for an adiabatic wall condition is shown in Figures (4b) and (4c). It was most surprising to find that as the sweep (yaw) increased the separation bubble extent increased very rapidly apparently due to the combined effect of a reduction in the normal flow Mach number and effective normal flow Reynolds number.

An equally interesting case for study is that of a cold swept (yawed) ramp - here one area of concern being the influence of cross flow on peak heating levels. The inviscid pressure distributions of Figure (4a) still hold for these cases and the resulting separation pressure distributions are given in Figure (4d). The resulting skin friction distributions of Figure (4e) again show a rapid increase in the size of the separation region as λ increases.

4.3 Two Dimensional Wavy Wall Flow - Laminar

The purpose of this study was to test the generality of the present method to cases with multiple separation bubbles. The geometry chosen for this effort is depicted in Figure (5a) and consists of a train of sine wave shaped protuberances located on a flat plate in a supersonic stream. No theoretical studies of this kind have been made in the past although solutions for attached boundary-layer flow over a wave shaped wall by an inverse method were obtained before by Pannelop and Flugge-Lotz (Ref. 23) using the implicit finite difference procedure of Blottner and Flugge-Lotz (Ref. 6).

Although a variety of flow conditions were studied here, a base case was identified for extensive parametric studies. The flow conditions for this study are given as $M_\infty = 3$, $Re_\infty = 2 \times 10^5$, $T_w/T_o = 0.45$, and T_∞ 390°R. The interaction of the boundary layer with the isentropic inviscid flow was modeled using a Prandtl-Meyer relation here approximated to second order in terms of θ_T.

The effect of wave amplitude on the separation characteristics is shown in Figures (5b) and (5c). For small single bumps with height $h < 0.09/\pi$ it is seen that no separation occurs, and for $h = 0.12/\pi$ a very disruptive separation bubble appears both fore and aft of the protuberance. It is interesting to note that the peak heating and maximum skin friction do not increase after separation has occured.

The effect of the number of waves on surface shear and pressure is shown in Figures (5d) and (5e) for $h = 0.06/\pi$ and standard flow conditions. No separation occurs over the single wave (curve 1). Adding a second wave of the same amplitude and wavelength behind the first wave is seen to produce separation between the two waves (curve 2). When additional waves, one ahead of the first one and one behind the second one are added two more separation bubbles appear with the middle one increasing in extent.

Figure (5e) shows the pressure and displacement thickness solutions produced by the train of four waves shown in Figure (5d). Over the first wave, where the boundary-layer is still attached, the pressure variation resembles a sinusoidal curve and the averaged displacement thickness grows as the displacement thickness over the flat plate. However, after separation has occured (as observed from the C_f distributions of Figure 5) both the surface pressure and the displacement thickness are significantly distorted. The distortion of the displacement thickness serves to fill the valleys of the protuberances and the pressure levels reflect this in a smoothing of the extremes of pressure observed.

More extensive studies of this geometry have been conducted and the reader is referred to Ref. (24) for detailed results.

4.4 Two Dimensional Ramps - Turbulent

The two dimensional turbulent flow over the ramp geometry depicted in Figure 2 has also been studied with the present approach. Initial efforts aimed at testing the use of the present algorithm for such a case centered on the base line test conditions of $M_\infty = 3$, $T_w/T_o = 0.5$, $Re_\infty = 10^5$ and $T_\infty = 100°F$, using simple linear theory to model the inviscid pressure law. More recent studies have used the tangent wedge law but the earlier results still serve to demonstrate the results. These initial turbulent studies were conducted using the same method of removing the singularity at separation in the difference equations as that employed in the laminar cases discussed above.

Results of application of the present algorithm to the case of a 15° compression ramp are depicted in Figures (6a) and (6b). Note that sharp discontinuous behavior was observed in the numerical results around the ramp juncture point ($s = 1.30$) when the pressure gradient parameter of Equation (13) was not handled carefully. The appearance of these discontinuities was traced to manner in which the derivatives in Equation (13) were written. It can easily be shown that if finite differences are used to represent the derivatives of δ while a differential representation of θ_s is used, large truncation should occur in regions of rapid change in surface curvature, as in the ramp juncture region. These can very effectively be removed by writing both terms of θ_T using a finite difference representation of both terms. Subsequent calculations performed with this approach have completely removed this discontinuous behavior and the use of the same can be recommended for all future studies.

Returning to Figures (6a) and (6b) it is seen that the position of the transition zone from laminar to turbulent flow has a marked influence on all surface properties. Early transition delays separation.

Figure (6c) and (6d) give the surface properties for early transition occuring ahead of a 30° ramp (with its effective corner at s = 1.55) showing an extremely short separation bubble accompanied by rapid variations in pressure and skin-friction (see Ref. 10 for more details of this study). Viewing these results, it is difficult to see how any of the earlier shooting techniques for solving these equations could have been successful on flows with such large excursions of the flow variables.

Consideration of higher Reynolds turbulent flows has proceeded and found need to make use of the second method described earlier to remove the difference equation singularity. In addition, the tangent wedge pressure law was incorporated into the solutions and a 30° compression ramp again considered. Here interest was in assessing the applicability of the rather standard eddy viscosity laws to such severe adverse pressure gradient regions. Comparison of the present results with the experimental data of Pate (Ref. 25) is shown in Figure (6e) to be unsatisfactory. Efforts to improve the eddy viscosity model are now underway with initial interest being in the relaxation approach successfully employed by Shang and Hankey (Ref. 13). Hopefully such an approach will produce better correlation with data and allow meaningful study of turbulent separated flows with the present approach.

5. CONCLUSIONS

It seems clear now that proper modeling of separated flow should be done by directly accounting for the downstream boundary condition. This approach has given the finite difference technique significant flexibility and allowed attack of separation problems that would have been otherwise out of reach. Even the approximate integral methods should benefit from this concept and should not have to be concerned with overcoming saddle point like singularities to proceed with interaction solutions.

Further study of separated flows should be concerned with achieving higher levels of numerical efficiency, better modeling of turbulence, removal of sharp corner singularities, and true three dimensional effects.

6. ACKNOWLEDGEMENTS

The authors wish to express their appreciation to the U.S. Air Force Aerospace Research Labs for partial support of this effort through contract F 33615-73-C-4014 and the U.S. Naval Air Systems Commands partial support through contracts N00019-73-C-0223 and N 60921-74-C-0203.

7. REFERENCES

1. Brown, S.N. and Stewartson, K., "Laminar Separation," Annual Review of Fluid Mechanics, Vol. 1, 1969, pp. 45-72.
2. Stewartson, K. and Williams, P.G., "Self-Induced Separation," Proceedings of the Royal Society of London, Ser. A. Vol. 312, September 1969, pp. 181-206.
3. Jenson, R., Burggraf, O., and Rizzetta, D., "Asymptotic Solution for Supersonic Viscous Flow Past a Compression Corner," presented at the Fourth International Conference on Numerical Methods in Fluid Dynamics, Boulder, Colorado , June 24-28, 1974.
4. Baum, E., "An Interaction Model of a Supersonic Laminar Layer on Sharp and Rounded Backward Facing Steps," AIAA Journal, Vol. 6, No. 3, March 1968, pp. 440-447.
5. Lees, L. and Reeves, B.L., "Supersonic Separated and Reattaching Laminar Flows: I - General Theory and Application to Adiabatic Boundary-Layer/Shock-Wave Interaction," AIAA Journal, Vol. 2, No. 11, November 1964, pp. 1907-1920.
6. Flugge-Lotz, I. and Blottner, F.G., "Computation of the Compressible Laminar Boundary Layer Flow Including Displacement Thickness Interaction Using Finite Difference Methods," TR131, 1962, Division of Engineering Mechanics, Stanford University, Stanford, California.
7. Reyhner, T.A. and Flugge-Lotz, I., "The Interaction of a Shock Wave with a Laminar Boundary Layer," Rept. 163, November 1966, Div. of Engineering Mechanics, Stanford University, Stanford, California.
8. Orenberger, J.T., and Baum, E., "A Theoretical Model of the Near Wake of a Slender Body in Supersonic Flow," AIAA Paper No. 70-792, presented at the Third Fluid and Plasma Dynamics Conference, Los Angeles, California, June 27 - July 1, 1970.
9. Werle, M.J., and Vatsa, V.N., "New Method for Supersonic Boundary Layer Separations," AIAA Journal, Vol. 12, No. 11, November 1974, pp. 1491-1497.
10. Bertke, S.D., Werle, M.J., Polak, A., "Finite Difference Solutions to the Interacting Supersonic Turbulent Boundary Layer Equations, Including Separation Effects," Report No. AFL-74-4-9, January 1974, Department of Aerospace Engineering, University of Cincinnati, Cincinnati, Ohio.
11. Blottner, F.G., "Finite Difference Methods of Solution of the Boundary Layer Equations," AIAA Journal, Vol. 8, pp. 193-205, 1970.
12. Harris, J. E., "Numerical Solution of the Equations for Compressible Laminar, Transitional, and Turbulent Boundary Layers and Comparisons with Experimental Data," NASA TR-2-368, August 1971.

13. Sheng, J.S. and Hankey, W.L., Jr., "Numerical Solution of the Navier Stokes Equations for Supersonic Turbulent Flow over a Compression Corner," AIAA Paper No. 75-3, presented at the AIAA 13th Aerospace Sciences Meeting, Pasadena, California, January 20-22, 1975.
14. Cox, R.N. and Crabtree, L.F., ELEMENTS OF HYPERSONIC AERODYNAMICS, The English Universities Press Ltd., London, 1965.
15. Cole, J.D., "Sweepback Theory For Shock Waves at Hypersonic Speeds," Report P-1337, Rand Corporation, Santa Monica, California, 1958.
16. Syvertson, C.A. and Dennis, D.H., "A Second-Order Shock-Expansion Method Applicable to Bodies of Revolution Near Zero Lift," NACA Report 1328, 1957.
17. Mikhailov, V.V., Neiland, V.Ya., Sychev., V.V., "The Theory of Viscous Hypersonic Flow," Annual Review of Fluid Mechanics, Vol. 3, 1971, pp. 371-396.
18. Garvine, R.W., "Upstream Influence in Viscous Interaction Problems," The Physics of Fluids, Vol. 11, July 1968, pp. 1413-23.
19. Werle, M.J., Hankey, W.L., and Dwoyer, D.L., "Initial Conditions for the Hypersonic Shock/Boundary-Layer Interaction Problem," AIAA Journal, Vol. 11, No. 4, April 1973, pp. 525-530.
20. Hankey, W.L., Dwoyer, D.L. and Werle, M.J., "Branching Solutions for Supersonic Interacting Boundary Layers," AIAA Journal, Vol. 11, September 1973, pp. 1349-1351.
21. Werle, M.J. and Vatsa, V.N., "Numerical Solution of Interacting Supersonic Boundary Layer Flows Including Separation Effects," Aerospace Research Laboratory Report ARL-73-0162, December 1973.
22. Lewis, J.E., Kubota, T. and Lees, L., "Experimental Investigation of Supersonic Laminar Two Dimensional Boundary Layer Separation in a Compression Corner With and Without Cooling," AIAA Journal, Vol. 6, January 1968, pp. 7-14.
23. Fannelop, T. and Flugge-Lotz, I., "The Laminar Compressible Boundary Layer Along a Wave-Shaped Wall," Ingenieur-Archiv, Vol. 33, 1963, pp. 24-35.
24. Polak, A., Werle, M.J., Vatsa, V.N. and Bertke, S.D., "Supersonic Laminar Boundary-Layer Flow Past a Wavy-Wall with Multiple Separation Regions," Rept. AFL 74-12-15, Department of Aerospace Engineering, Univ. of Cincinnati, Cincinnati, Ohio, Dec. 1974.
25. Pate, S.R., "Investigation of Flow Separation on a Two-Dimensional Flat Plate Having a Variable Span Trailing Edge Flat at M_∞ = 3 and 5," Rept. No. AEDC-TDR-64-14, ARO Inc., March 1964.

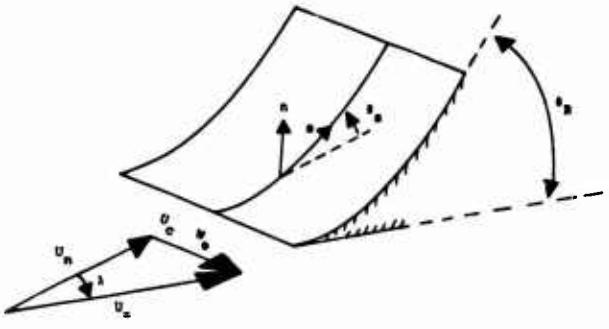

FIGURE 1 NOMENCLATURE

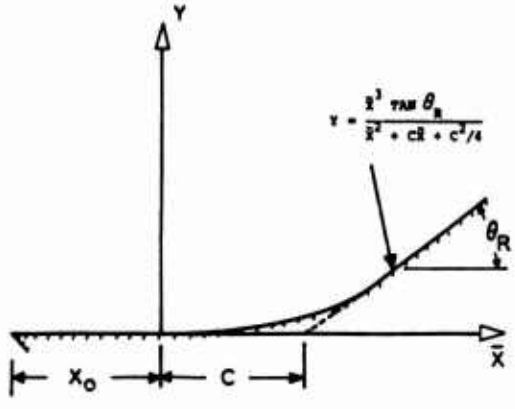

FIGURE 2 RAMP GEOMETRY

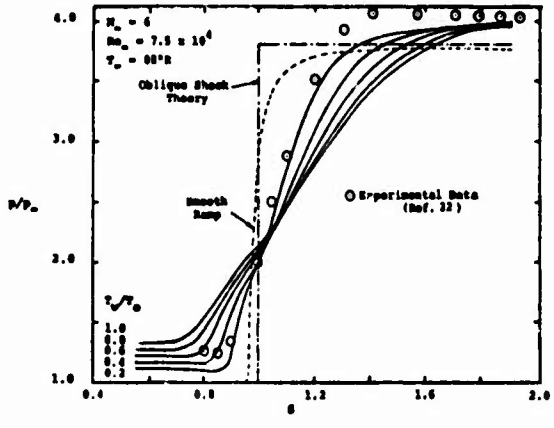

(A) PRESSURE DISTRIBUTIONS

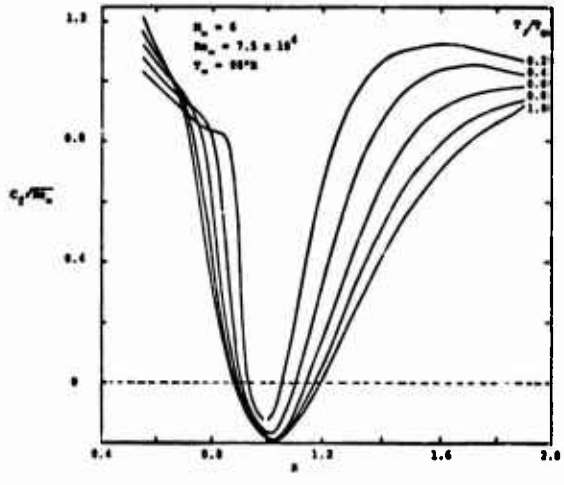

(B) SKIN FRICTION DISTRIBUTIONS

FIGURE 3 COOLING EFFECTS ON LAMINAR, 2-D RAMPS

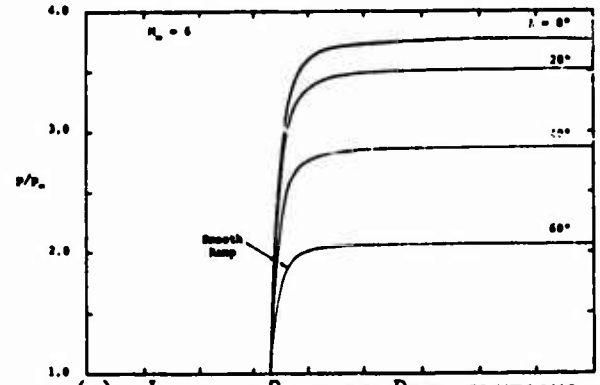

(A) INVISCID PRESSURE DISTRIBUTIONS

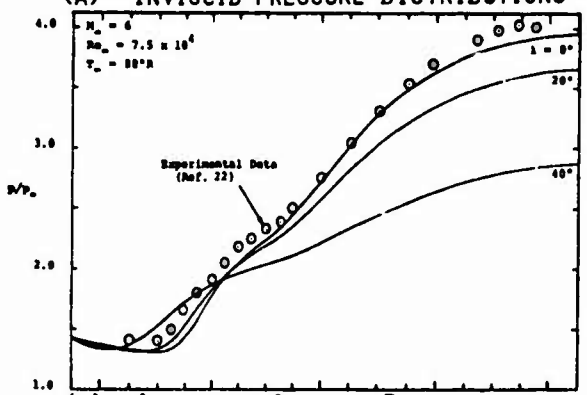

(B) ADIABATIC SURFACE PRESSURES

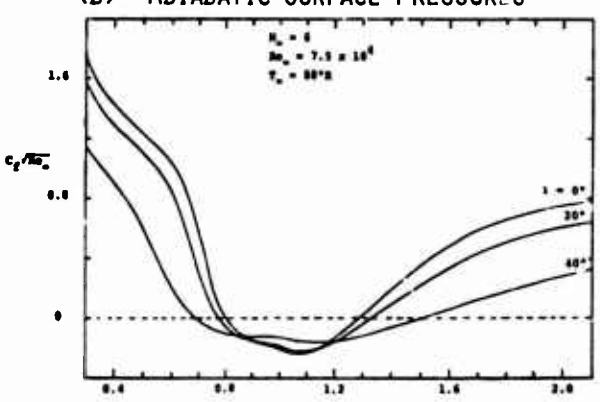

(C) ADIABATIC SKIN FRICTION

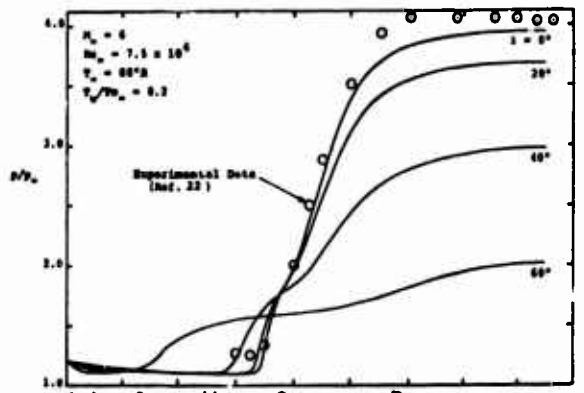

(D) COLD WALL SURFACE PRESSURES

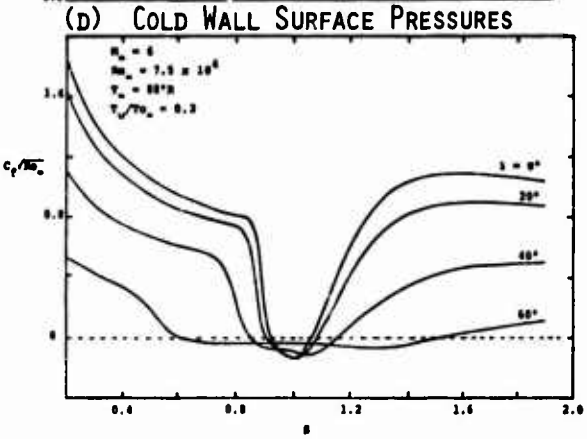

(E) COLD WALL SKIN FRICTION

FIGURE 4 SWEEP EFFECTS ON RAMP SEPARATIONS

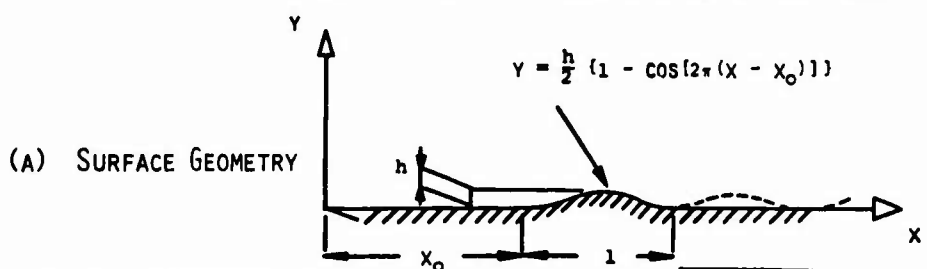

(A) SURFACE GEOMETRY

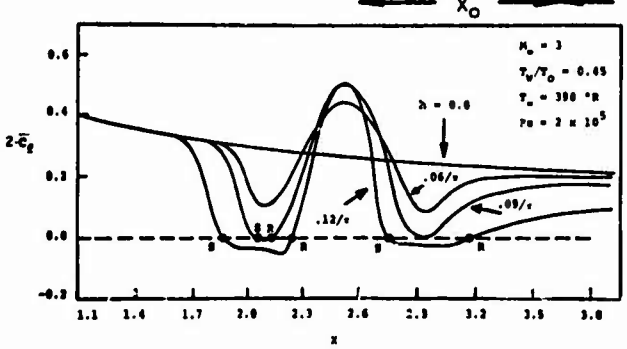

(B) EFFECT OF PROTUBERANCE HEIGHT ON SHEAR

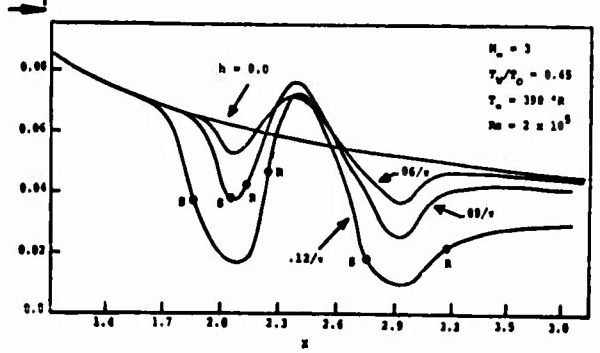

(C) EFFECT OF PROTUBERANCE HEIGHT ON HEATING

FIGURE 5 WAVY WALL SEPARATIONS

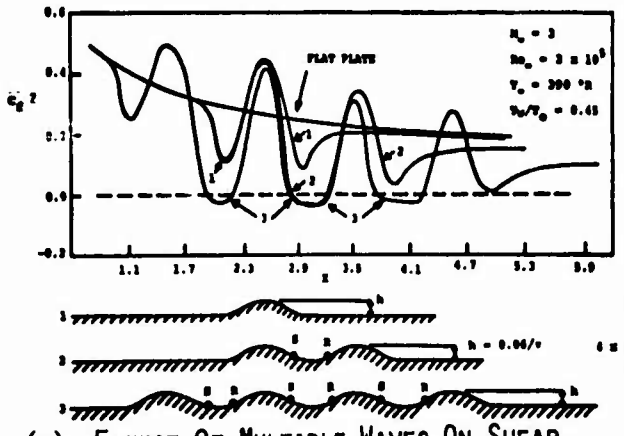

(D) EFFECT OF MULTIPLE WAVES ON SHEAR

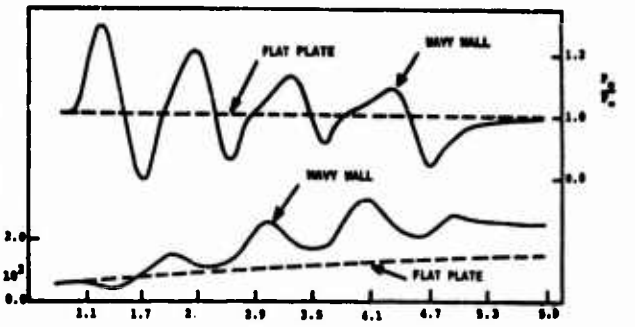

(E) EFFECT OF MULTIPLE WAVES ON PRESSURE

FIGURE 5 WAVY WALL SEPARATIONS

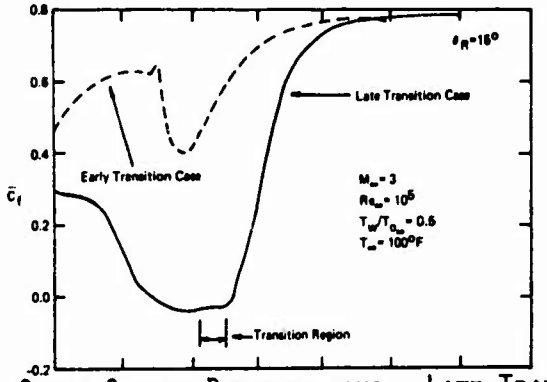

(A) SHEAR STRESS DISTRIBUTIONS - LATE TRANSITION

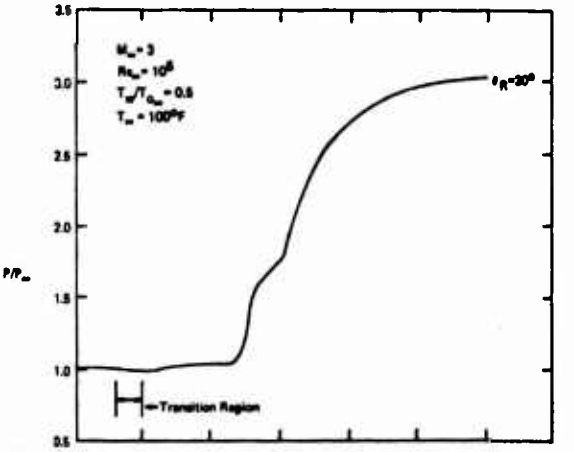

(C) PRESSURE DISTRIBUTIONS - EARLY TRANSITION

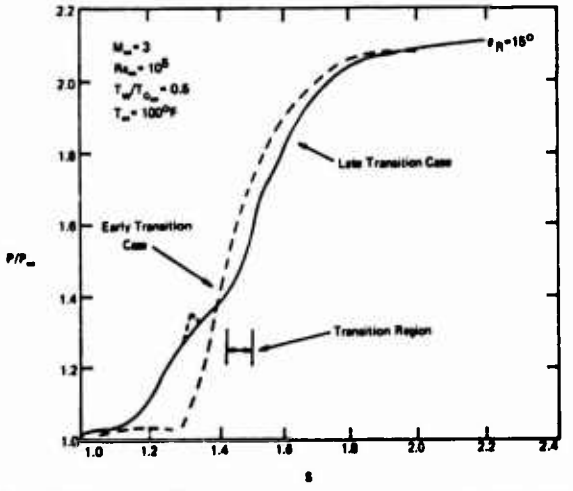

(B) PRESSURE DISTRIBUTIONS - LATE TRANSITION

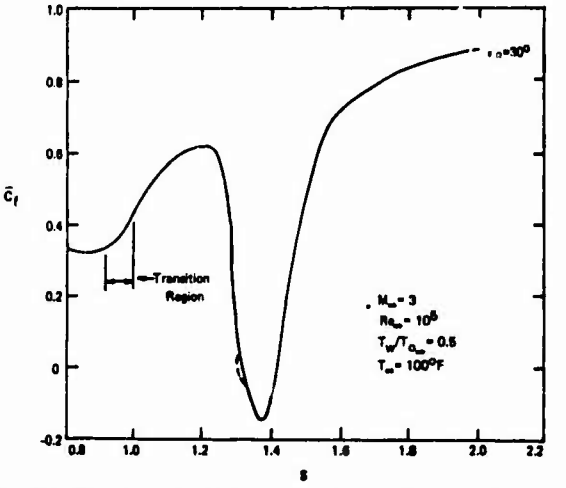

(D) SHEAR STRESS DISTRIBUTIONS - EARLY TRANSITION

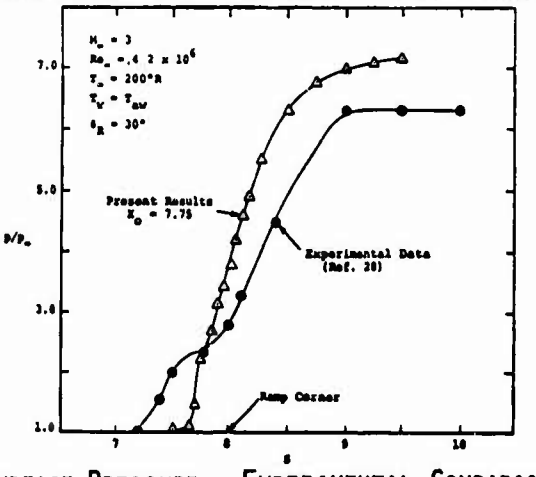

(E) SURFACE PRESSURE - EXPERIMENTAL COMPARISON

FIGURE 6 SEPARATED TURBULENT BOUNDARY LAYERS

BULBE DE DECOLLEMENT PRODUIT PAR UNE FAIBLE DEPRESSION DE PAROI EN ECOULEMENT LAMINAIRE SUPERSONIQUE

par

B. PRUNET-FOCH, Mme F. LEGAY-DESESQUELLES, G.B. DIEP
Laboratoire d'Aérothermique du C.N.R.S.
4 ter, route des Gardes, 92190-MEUDON (France)

RESUME

En écoulement supersonique, un creux de faible amplitude aménagé à la surface d'une plaque plane est, en général, la source d'un bulbe de décollement au sein de la couche limite. Le travail porte essentiellement sur la prévision du décollement et du recollement laminaires en présence de transferts de chaleur à la paroi.

L'analyse théorique des phénomènes est faite à partir de la méthode intégrale de Dorodnitsyn en adoptant le concept d'interaction libre et, pour la répartition des vitesses et des températures dans la couche limite, les expressions proposées par Nielsen. Cette méthode permet de poursuivre le calcul dans toute la zone décollée jusqu'au recollement. Dans la zone de détente de l'écoulement où cette théorie ne peut s'appliquer, le calcul est effectué par différences finies. Les caractéristiques des champs dynamique et thermique de l'écoulement sont ainsi calculées tout le long de la surface considérée.

Parallèlement, des expériences ont été effectuées en soufflerie. Une exploration de la couche limite a permis d'obtenir les profils de vitesse et de température pour plusieurs configurations de paroi, chauffées ou non, et d'en déduire les évolutions des coefficients de pression et de transfert de chaleur à la surface.

La comparaison des résultats expérimentaux et théoriques ne laisse apparaître que de très faibles écarts. Ceci a permis d'énoncer des lois de comportement du bulbe en fonction des paramètres physiques du creux et de l'écoulement principal.

SUMMARY

In supersonic flow, a shallow deformation on a flat plate induces a small separated bubble in the boundary layer. In order to predict this laminar separation and reattachment process including heat transfer phenomena at the wall, a theoretical study was built up, using Dorodnitsyn integral's method as well as expressions suggested by Nielsen for the velocity and temperature profiles.

Thereby the calculation can be carried out up to the reattachment point. Simultaneously experiments were made in a wind tunnel. Experimental and predicted results are in good agreement.

NOTATIONS

a	amplitude
c_i, E_i	fonctions de ξ intervenant dans les profils de vitesse et de température "extérieurs"
K_f, K_p	coefficients locaux de frottement et de pression à la paroi
ℓ	longueur de référence
M	nombre de Mach
Nu	nombre de Nusselt
Pr	nombre de Prandtl
P_t	pression génératrice
Re	nombre de Reynolds
$S = T_t/T_{te} - 1$	
T_t	température totale locale
u	composante horizontale de la vitesse
$\bar{u} = u/u_e$	
$U_o = u_o$	
x, y	coordonnées dans le plan réel
x_s	abscisse du début du creux sinusoïdal
x_{DEC}, x_{REC}	abscisses de décollement et de recollement
X, Y	coordonnées dans le plan de Stewartson
α_p	valeur de $\partial\bar{u}/\partial\eta$ à la paroi
β	angle en degrés permettant de repérer un point sur la sinusoïde. $\beta = (x-x_s)\ 360/\lambda$
δ_1	épaisseur de déplacement
λ	longueur d'onde
ν	viscosité cinématique du fluide
ξ, η	coordonnées dans le plan de Dorodnitsyn

INDICES

e	valeur à l'extérieur de la couche limite
G	valeur à la frontière des deux domaines
o	valeur au départ du calcul
P	valeur à la paroi
S	valeur sur la frontière $\mathcal{S}(x)$
∞	valeur à l'infini amont

INTRODUCTION

La présence de petites déformations locales sur les parois de véhicules aériens peut avoir des effets importants sur les comportements dynamique et thermique de ces appareils. Les paramètres qui gouvernent ces effets sont nombreux et leurs interactions souvent complexes, ce qui rend indispensable l'analyse fine de configurations aussi simples que possible /1/.

Sur une plaque plane présentant, à une abscisse donnée, une faible déformation sinusoïdale, il peut se produire un décollement suivi d'un recollement laminaires. Une étude préliminaire /2/ avait permis de déceler la présence de tels décollements en écoulement subsonique incompressible, elle pourrait d'ailleurs être utilement complétée et précisée maintenant à partir des travaux tout récents de Inger /3/. Cette première série de résultats nous a amenés à poursuivre nos recherches et à envisager le cas d'un écoulement supersonique. Une seule déformation en creux a été retenue ; dans ces conditions, le phénomène complet peut être prévu à l'aide d'un calcul reposant sur la méthode de Dorodnitsyn /4/. L'adoption du concept d'interaction libre et, pour la répartition des vitesses et des températures dans la couche limite, des expressions de Nielsen /5,6/ permet de poursuivre le calcul dans toute la zone décollée jusqu'au recol-

lement /7/. Cette méthode a été proposée par Nielsen pour le cas d'écoulements en compression, le nombre de Prandtl étant supposé égal à l'unité ; son emploi ici a donné l'occasion d'en préciser certains passages et de l'étendre au cas d'écoulements dont le nombre de Prandtl est quelconque.

Dans la zone de détente que constitue le début du creux, le traitement des équations de la couche limite par différences finies fournit les caractéristiques de l'écoulement et, par là, les profils de vitesse et de température pour le départ de la méthode de Nielsen.

L'application numérique de ces méthodes a abouti à des résultats très voisins de ceux obtenus à partir des mesures qui ont pu être réalisées en soufflerie.

1 - ETUDE DYNAMIQUE ET THERMIQUE

1.1 Equations générales

L'écoulement le long d'une plaque plane lisse présentant, à une certaine distance du bord d'attaque, un creux sinusoïdal de faible amplitude peut être considéré, en première approximation, comme un écoulement plan stationnaire, la couche limite vérifiant les équations de Navier-Stokes.

Les amplitudes des déformations prévues sont suffisamment faibles pour que le rayon de courbure de la paroi demeure assez grand. Ceci permet de supposer que, pour une abscisse donnée, la pression statique reste constante dans toute la couche limite.

De plus, dans le cas d'une plaque chauffée, il n'est envisagé que des élévations de température modérées, l'écart entre la température de l'écoulement et celle de la paroi permettant de faire l'hypothèse que le nombre de Prandtl (Pr) et la chaleur spécifique à pression constante du fluide sont constants dans tout l'écoulement. Enfin, l'écoulement libre est supposé isentropique.

Le traitement du problème complet, zone décollée comprise, amène à distinguer dans l'écoulement deux domaines (I et II) dans lesquels les équations de la couche limite sont résolues de manière différente :

- dans le domaine I, constitué par la partie de l'écoulement située au-dessus de la partie plane et du début du creux de la plaque, les équations de la couche limite sont résolues par différences finies. Ceci fournit plus particulièrement les profils de vitesse et de température qui sont indispensables pour commencer, à l'abscisse x_c, le calcul dans le domaine II ;
- dans le domaine II, la méthode de Nielsen permet d'obtenir les champs dynamique et thermique dans la zone proche du décollement et dans toute la zone décollée.

1.2 Calcul dans le domaine I

La transformation de Stewartson /8/ ramène les équations générales de la couche limite, pour un écoulement compressible, à la forme de celles obtenues pour un écoulement incompressible.

Le traitement de ces équations par différences finies permet de calculer de proche en proche la solution. Il suffit pour cela de connaître dans le plan de Stewartson :

- l'expression de l'écoulement potentiel le long de la paroi ; elle est fournie par la théorie des petites perturbations pour une surface sinusoïdale /9/,
- les répartitions des vitesses et des températures dans la couche limite à deux abscisses distantes de ΔX précédant le début du calcul (§ 1.5).

Le couplage entre les deux équations de la quantité de mouvement et de l'énergie se fait par itérations de la solution à chaque pas de calcul.

Dans les cas retenus, il est possible d'améliorer le résultat en procédant à une "correction de couche limite" qui aura pour effet de placer le décollement en un point plus avancé et, par là, plus proche de celui trouvé par l'expérience. En effet, à l'approche immédiate de ce décollement une forte augmentation de l'épaisseur de la couche limite se produit, par suite l'épaisseur de déplacement δ_1 croît rapidement. Cette correction est fondée sur l'hypothèse suivante : l'écoulement réel à l'extérieur de la couche limite se comporte comme celui qui se produirait sur la surface correspondant à la frontière de δ_1 évaluée à partir du premier calcul sans correction. La loi de la détente de Prandtl-Meyer est à nouveau appliquée pour obtenir l'évolution de l'écoulement le long de cette surface.

1.3 Calcul dans le domaine II. Méthode de Nielsen

Dans le domaine II, les caractéristiques de l'écoulement sont obtenues en utilisant la méthode de Nielsen. Les expressions servant à déterminer les profils de vitesse et de température avant le décollement sont respectivement :

$$(1) \qquad \frac{\partial \bar{u}}{\partial \eta} = \frac{(1-\bar{u})\sqrt{\bar{u}+c_4}}{c_1+c_2\bar{u}+c_3\bar{u}^2+\ldots} \qquad \text{et} \qquad S(\bar{u}) = (1-\bar{u})(S_p+E_1\sqrt{c_4}-E_1\sqrt{\bar{u}+c_4}+E_2\bar{u}+E_3\bar{u}^2+E_4\bar{u}^3+\ldots)$$

Appliquant la méthode de Dorodnitsyn, Nielsen ramène les équations de la couche limite, obtenues après la transformation de Stewartson, à deux relations intégro-différentielles en introduisant des fonctions de pondération de la forme $f(\bar{u}) = (1-\bar{u})^n$ ou $f(\bar{u}) = \bar{u}^n(1-\bar{u})$. Ces relations fournissent ensuite, avec celle de l'interaction libre /4/, les équations du système différentiel permettant de calculer pas à pas les valeurs des fonctions c_i et E_i à chaque abscisse. Le décollement et le recollement s'obtiennent lorsque c_4 s'annule.

Après le décollement, un écoulement de retour apparaît, Nielsen distingue alors dans la couche limite deux régions séparées par la ligne $\delta(x)$ où la composante horizontale de la vitesse est nulle. Dans la région "intérieure", comprise entre la paroi et $\delta(x)$, un polynôme de degré quelconque en η est retenu pour chaque profil. Dans la région "extérieure" par contre, les expressions adoptées avant le décol-

lement sont reprises.

1.4 Passage du domaine I au domaine II

La méthode de calcul des champs dynamique et thermique dans le domaine II ainsi adoptée, il ne reste qu'à définir les valeurs des fonctions c_i et E_i sur la frontière (G) de départ de cette région. Ces dernières sont calculées à partir des profils de vitesse et de température obtenus à la fin du calcul par différences finies dans le domaine I, c'est-à-dire à l'abscisse x_G.

- D'une part, les valeurs des c_i sont déterminées à partir du dernier profil de vitesse calculé dans le domaine I. En choisissant quatre valeurs particulières η_i de η, ce profil fournit les valeurs des vitesses $\bar{u}_i$ et des pentes $(\partial\bar{u}/\partial\eta)_i$ en ces points. Ces quantités sont reportées dans l'expression donnant le profil de vitesse (1) et il reste à résoudre un système de quatre équations aux quatre inconnues c_1, c_2 c_3 et c_4.

La solution de ce système non linéaire s'obtient facilement si l'une des équations retenue correspond à la valeur $\eta=0$, ce qui permet d'ailleurs de garder la même valeur du frottement à la paroi. En effet, dans ce cas, l'équation correspondante se simplifie et il vient :

$$(2) \qquad \left.\frac{\partial\bar{u}}{\partial\eta}\right|_P = \frac{\sqrt{c_4}}{c_1} = \left(\frac{U_o}{U_e}\right)^2 \ell \sqrt{\frac{U_o\ell}{\nu_o}} \left.\frac{dU}{dY}\right|_P$$

Dans ces conditions, on aboutit à une équation implicite en c_1 qui se résoud par itérations. Les coefficients c_2, c_3 et c_4 s'obtiennent ensuite directement.

- D'autre part, la coïncidence des profils de température exige notamment l'égalité des températures pour i valeurs particulières de η ; le calcul des valeurs des E_i s'effectue par la résolution d'un système linéaire formé à partir des relations déduites directement de (1) :

$$(3) \qquad (\sqrt{c_4} - \sqrt{\bar{u}_i + c_4})\, E_1 + \bar{u}_i E_2 + \bar{u}_i^2 E_3 + \bar{u}_i^3 E_4 = \frac{S_i}{1-\bar{u}_i} - S_P \qquad (i = 1 \text{ à } 4)$$

A la paroi, la valeur du flux de chaleur doit aussi être la même, qu'elle soit obtenue à partir du calcul par différences finies ou à partir de la méthode de Nielsen ; par conséquent, une des relations précédentes peut être remplacée par cette égalité.

D'après le changement de variables de Dorodnitsyn, nous avons :

$$(4) \qquad \frac{\partial S}{\partial\eta} = \frac{\partial S}{\partial Y}\frac{\partial Y}{\partial\eta} = \frac{U_o\ell}{U_e}\sqrt{\frac{\nu_o}{U_o\ell}}\frac{\partial S}{\partial Y}$$

L'expression de $\partial S/\partial\eta$ est obtenue directement à partir de (1), il en résulte que, le passage d'un domaine à l'autre sera assuré correctement si :

$$(5) \qquad E_1 - 2\sqrt{c_4}\, E_2 = -2\sqrt{c_4}\, S_P - 2c_1 \frac{U_o\ell}{U_e}\sqrt{\frac{\nu_o}{U_o\ell}} \left.\frac{\partial S}{\partial Y}\right|_P$$

Ainsi, les valeurs des fonctions E_i définissant le premier profil de température dans le calcul par la méthode de Nielsen, sont obtenues en résolvant le système d'équations linéaires constitué par la relation (5) et autant d'équations (3) qu'il est nécessaire suivant le nombre des E_i retenu dans le développement de S.

Un tel procédé permet d'obtenir, dans le cas général, un très bon recouvrement des profils.

Cas où seul E_1 est non nul

Dans le cas où seul le coefficient (E_1) est retenu dans le développement de S, la marche à suivre doit être différente. En effet, la relation (1) conduit à une valeur de E_1 qui correspond à un profil de température assez éloigné du profil d'origine, et la poursuite du calcul dans tout le domaine II laisse apparaître de grosses fluctuations dans les températures. Ces fluctuations entraînent à leur tour de fortes instabilités.

Le procédé suivant a finalement été retenu. Il consiste à reprendre, comme dans le cas général, les deux relations exprimant à la frontière des deux domaines l'égalité à la paroi du frottement (2) et celle du flux de chaleur ((5) dans laquelle $E_2=0$). A ces deux relations, il faut ajouter celle fournie par la valeur S_2 de S en un point d'ordonnée quelconque η_2. Ces trois équations permettent de calculer c_1, c_4 et E_1. Pour évaluer c_2 et c_3, il suffit d'écrire l'égalité des pentes des profils de vitesse en deux points arbitraires de la couche limite.

La position respective des trois points retenus dans la couche limite est fixée de manière à obtenir le meilleur recouvrement possible pour les profils de vitesse et de température. Il faut toutefois remarquer que, avec un seul paramètre (E_1), les deux profils de température ne se superposent pas bien.

1.5 Profils de vitesse et de température initiaux

Après l'exposé des méthodes adoptées, pour le calcul dans les deux régions de l'écoulement et le passage de l'une à l'autre, il reste encore à préciser la manière dont sont obtenus les profils de départ.

Ces profils, nécessaires à la résolution des équations par différences finies, auraient pu être fournis, comme tout profil sur plaque plane, à partir d'une quelconque méthode classique, celle de Chapman et Rubesin par exemple /10/. Pour l'unité du calcul, il a été jugé préférable de retenir ceux obtenus à

partir des expressions de Nielsen. La manière dont sont calculés les profils de vitesse a été exposée en détails par Nielsen /5/. Pour les températures, si le nombre de Prandtl du fluide dans l'écoulement est égal à l'unité, les profils se déduisent immédiatement de ceux des vitesses par la relation de Crocco : $S = S_p(1-\bar{u})$. Par contre, dans le cas où le nombre de Prandtl est différent de l'unité, la relation de Crocco modifiée (1) conduit à des coefficients E_1°, E_2°, E_3°, E_4° qui sont fonction du nombre de Prandtl et du nombre de Mach à l'infini amont. En outre, pour un nombre de Prandtl et un nombre de Mach donnés, ces coefficients sont des fonctions linéaires de la température de paroi /7/.

En effet, la relation de similitude pour les profils de vitesse permet de simplifier le système différentiel et la recherche de la solution se ramène au calcul d'un simple système linéaire.

1.6 Température de frottement

Dans le cadre de l'étude d'une couche limite avec échange de chaleur, la température que prend la paroi lorsqu'elle est soumise aux seuls échauffements aérodynamiques, constitue une grandeur de référence pour l'évaluation du coefficient de transfert de chaleur. La valeur de cette température de frottement, pour laquelle le flux de chaleur à la paroi est nul, s'obtient de la manière suivante.

- Dans le domaine I, supposant connus en deux points de la plaque distants de ΔX, d'une part, les deux valeurs des températures de frottement et d'autre part, les profils de vitesse et de température au droit de ces points, on détermine par itération sur la valeur de la température de paroi, celle qui donne, à l'abscisse suivante, un flux nul. Ce procédé est alors employé de proche en proche le long de toute la surface correspondante.

- Dans le domaine II, un calcul sans itération peut être effectué.

Pour la zone où l'écoulement n'est pas décollé, les températures dans la couche limite sont calculées à partir de la relation définissant S. La condition "flux nul à la paroi" entraîne :

$$S_f = S_p = -\frac{E_1}{2\sqrt{c_4}} + E_2 \qquad (6)$$

Pour la zone décollée :

- si la température dans l'écoulement "intérieur" est supposée constante et égale à T_p, la définition de S dans l'écoulement "extérieur" demeure la même qu'avant le décollement et S_f devra vérifier la relation ci-dessus,
- si la répartition des températures de l'écoulement "intérieur" est une fonction linéaire de η, il vient :

$$S = S_p - \frac{\frac{1}{2}E_1 + S_p\sqrt{c_4} - E_2\sqrt{c_4}}{c_1 + \eta_S\sqrt{c_4}}\,\eta \qquad (7)$$

ce qui conduit encore à la même relation.

Dans ces conditions, pour le calcul de l'évolution de la température de frottement le long de la plaque, quelle que soit la région envisagée, la seule équation (6) vient s'ajouter à celles du système différentiel général.

Cas particulier de la plaque plane

Dans le cas d'une plaque plane, les relations linéaires (§ 1.5) qui ont servi dans le cas d'une plaque chauffée ou refroidie peuvent être reprises pour évaluer la température de frottement, seule la condition de flux nul à la paroi est à ajouter. Cette condition se traduisant par la relation (6) qui est aussi linéaire, la valeur de S_f ainsi obtenue n'est bien fonction que du nombre de Prandtl et du nombre de Mach de l'écoulement. Cette valeur dépend évidemment du nombre de coefficients retenus dans le développement de l'expression de S.

2 - EXPERIENCES, CALCULS, COMPARAISON DES RESULTATS

2.1 Dispositifs expérimentaux

Les mesures ont été effectuées dans la soufflerie supersonique du laboratoire d'Aérothermique ; le nombre de Mach (M_∞) y est fixé à 1,92 ou 2,41, les nombres de Reynolds (Re) étant respectivement égaux à 13.10^6 ou $9,7.10^6$ par mètre. Les maquettes sont des plaques planes sur la surface desquelles a été aménagé un creux sinusoïdal (amplitude a = 0,3 ou 0,4 mm, longueur d'onde λ = 30 ou 40 mm) situé à x_s = 20 ou 30 mm du bord d'attaque. Elles sont munies, soit de plusieurs prises de pression statique pour mesurer l'évolution de la pression statique sur la plaque, soit d'un dispositif électrique de chauffage.

La faible épaisseur de couche limite dont nous disposions imposait l'emploi d'une technique expérimentale minutieuse et par suite la réalisation de dispositifs de mesure spécialement élaborés. La couche limite a été explorée au moyen de sondes doubles miniaturisées comprenant une prise de pression totale et un thermocouple. Les fils du thermocouple sont tendus de part et d'autre de la soudure perpendiculairement à l'écoulement pour réduire au maximum les pertes par conduction. Ils sont fixés à l'extrémité d'un support en plastique pour éviter les pertes de chaleur dans le sillage. Ceci permet d'obtenir une bonne estimation de la température locale. Placées dans l'écoulement libre, ces sondes donnent une température qui ne s'écarte pas de plus de 1,5°C de la valeur réelle, ce qui correspond à un facteur de récupération de 0,99.

L'écoulement peut également être visualisé soit au niveau de la surface de la plaque par le dépot d'un film de pétrole, soit dans son ensemble à l'aide d'un banc strioscopique. Ces deux procédés fournissent une valeur approchée de l'abscisse de décollement.

La faible dimension des maquettes imposait l'emploi de méthodes indirectes pour évaluer les flux

de chaleur à la paroi. Le procédé retenu consiste à calculer le flux à partir des pentes des profils de température. Ceci explique l'attention qui a été apportée à la mesure de ces profils.

2.2 Déroulement des calculs

L'étude théorique dont les grandes lignes ont été exposées ci-dessus, exige le recours à un ordinateur de grande puissance pour sa résolution numérique.

Le programme général du calcul comprend environ 2500 à 3000 ordres Fortran, la place occupée en mémoire étant de l'ordre de 300 K-octets ; il permet d'obtenir les caractéristiques d'un bulbe de décollement se produisant dans un creux de forme sinusoïdale situé sur une plaque plane. Les données sont :

a) à l'infini amont, le nombre de Mach, la pression et la température,

b) sur la plaque, l'abscisse du début du creux sinusoïdal, l'amplitude et la longueur d'onde de ce creux,

c) la température de la paroi, dans le cas où l'on envisage une couche limite avec échange de chaleur, cette température pouvant être uniforme ou non.

Le calcul pourrait être aisément adapté à des configurations différentes, il suffirait pour cela de modifier l'équation de la paroi et l'expression de l'écoulement potentiel.

Ayant précisé les données du problème, la solution est recherchée de la manière suivante : l'abscisse de décollement s'obtient en appliquant uniquement la méthode par différences finies. Ensuite, la valeur de x_G est ajustée par évaluations successives pour faire aboutir le calcul dans le domaine II à une abscisse de décollement égale à celle trouvée précédemment. Un autre ajustage portant sur les η_i est également fait pour obtenir un bon recouvrement des profils au passage d'un domaine à l'autre.

Le calcul peut ensuite se poursuivre dans toute la zone décollée jusqu'au recollement. Dans tout ce domaine, sont ainsi évaluées, à chaque abscisse, les valeurs de c_1, c_2, c_3, c_4, U_e, η_S, α_D et, dans le cas où l'on tient compte de l'échange thermique au sein de la couche limite, celles de E_1, E_2, E_3 et E_4.

Remarque

De nombreuses difficultés ont été rencontrées dans l'application de ces calculs, notamment des instabilités qui apparaissent souvent dans l'application de la méthode de Nielsen. Elles se produisent principalement au début du domaine II et au début de la zone décollée.

2.3 Comparaison des résultats

De nombreuses expériences ont été réalisées et les résultats auxquels elles ont abouti ont été comparés à ceux obtenus par le calcul effectué pour les mêmes conditions d'écoulement et de température de paroi.

2.3.1 Abscisses de décollement et de recollement

Il résulte de la comparaison que la méthode par différences finies, après correction de couche limite, prévoit une abscisse de décollement très voisine de celle évaluée par l'expérience. Les faibles écarts trouvés peuvent s'expliquer par le fait que l'épaisseur du bord d'attaque, aussi fin soit-il, introduit une onde de choc dans l'écoulement, onde qui, par la perturbation qu'elle apporte, influence le déclenchement du décollement.

La prise en compte ou non des échanges de chaleur qui se produisent au sein de la couche limite, dans le cas d'une plaque non chauffée, modifie peu les résultats relatifs à l'abscisse de décollement. De même, l'influence de la valeur du nombre de Prandtl du fluide est négligeable du moins entre 1 et 0,72. Pour la plaque P2 (x_s = 30 mm, e = 0,4 mm, λ = 40 mm) par exemple, placée dans l'écoulement Ec2 (M_∞ = 2,41, Re/m = 9,7.10^6) sa température s'équilibre aux environs de 289°K ($T_p/T_{t\infty}$ = 0,96) et le calcul donne dans ces conditions :

x_{DEC} = 43,5 mm soit β_D = 121,5° en faisant l'hypothèse : couche limite isenthalpique
x_{DEC} = 43,18 mm soit β_D = 118,6° pour Pr = 1
x_{DEC} = 43,25 mm soit β_D = 119,2° pour Pr = 0,72

(l'expérience fournissait une valeur de x_{DEC} voisine de 42,5 mm).

Par contre, lorsque la surface de la plaque est chauffée, le calcul montre que l'épaisseur de la couche limite augmente et il prévoit un décollement plus rapproché. Dans ce cas, les mesures ont été faites avec une température de plaque égale à environ 358°K ($T_p/T_{t\infty}$ = 1,16) ; le calcul aboutit, toujours après correction de couche limite, à :

x_{DEC} = 42,70 mm, soit β_D = 114,4° pour Pr = 1,
x_{DEC} = 42,73 mm, soit β_D = 114,6° pour Pr = 0,72

Ces résultats confirment ce que révèle l'expérience : la valeur de l'abscisse de décollement est peu influencée par les variations de température de paroi. Un écart d'une centaine de degrés ne provoque pas un changement de cette abscisse mesurable expérimentalement. Les différences, en effet, sont inférieures aux marges de précision qui nous sont imposées pour son évaluation.

L'écoulement ainsi décollé se poursuit au-dessus du creux. Il vient ensuite se recoller, vers la fin de la déformation, à une abscisse x_{REC} (ou β_R). D'une manière générale, les résultats montrent que plus le décollement se produit tôt sur la surface, plus la zone décollée est importante et plus l'écoulement a tendance à recoller loin.

2.3.2 Configuration dynamique et thermique de l'écoulement.

Les mesures de pression statique à la paroi conduisent à une évolution du coefficient de pression

(K_p) en fonction de la distance au bord d'attaque, très voisine de celle trouvée par le calcul (fig.1).

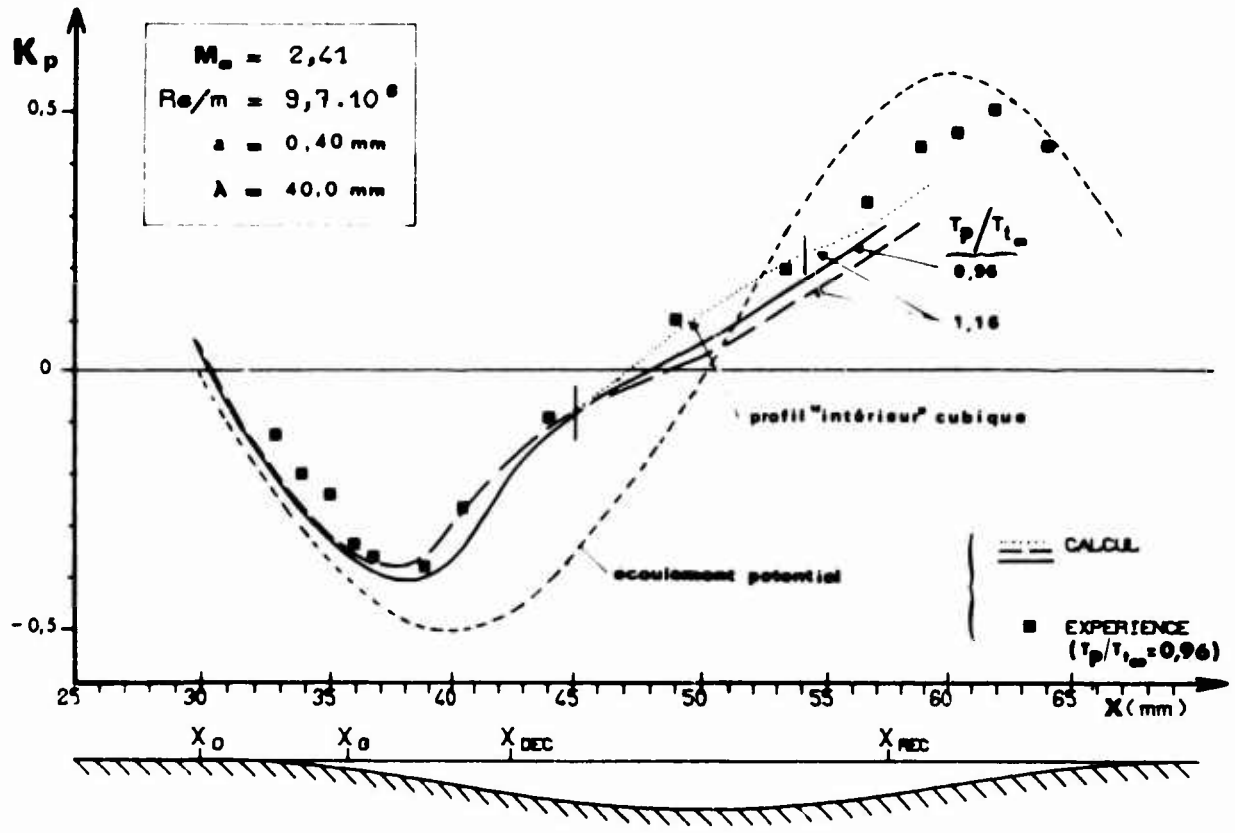

Fig. 1 - Evolution du coefficient de pression

Le très léger décalage qui apparaît, s'explique toujours par l'onde de choc produite par le bord d'attaque. Les différentes courbes obtenues par le calcul montrent qu'un chauffage modéré de la paroi ne perturbe que très peu les résultats.

Les profils de vitesse mesurés et calculés se recouvrent également bien (fig.2) ; par suite, le coefficient de frottement trouvé numériquement est considéré comme correct.

En ce qui concerne la température, sur la partie plane de la plaque, le profil s'obtient, pour un nombre de Prandtl différent de l'unité, à partir de la solution du système d'équations évoqué au paragraphe 1.5. Ce profil est d'autant plus proche de celui de Chapman-Rubesin que le nombre de coefficients retenu dans la relation générale de Nielsen entre la température et la vitesse est plus grand.

Le calcul complet a été effectué en ne retenant que deux coefficients : E_1 et E_2. Néanmoins, les profils de température mesurés et calculés sont très proches comme le montre la figure 3. Dès lors, les valeurs des flux de chaleur à la paroi fournies par le calcul sont, elles aussi, considérées comme très correctes.

Le programme de calcul permettant d'envisager aussi une variation de la température de paroi, l'évolution de la température de frottement peut être obtenue et, par suite, celle du facteur thermique pariétal. Ce dernier, caractéristique du régime de l'écoulement, demeure sensiblement constant.

L'évolution du nombre de Nusselt (Nu) se déduit de celle de la température de frottement et du flux de chaleur à la paroi pour différentes valeurs de T_p (fig.4). En outre, les courbes relatives à un nombre de Prandtl égal à 1 ou à 0,72 se trouvent être très peu éloignées.

3 - APPLICATION DU CALCUL A DES CAS PLUS GENERAUX

La bonne correspondance entre les résultats des expériences et du calcul a permis finalement d'étendre l'application de ce dernier à des cas différents.

Ainsi, pour une même distance du début du creux au bord d'attaque, des lois de comportement du bulbe peuvent être proposées sous la forme suivante :

1) l'écoulement étant fixé :

- pour une longueur d'onde donnée, l'abscisse de décollement rapportée à la longueur d'onde est d'autant plus grande que l'amplitude du creux est plus faible (fig.5),

- pour chaque valeur de la longueur d'onde, il existe une valeur de l'amplitude en-dessous de laquelle le calcul ne prévoit plus de décollement. Cette valeur est elle-même d'autant plus importante que

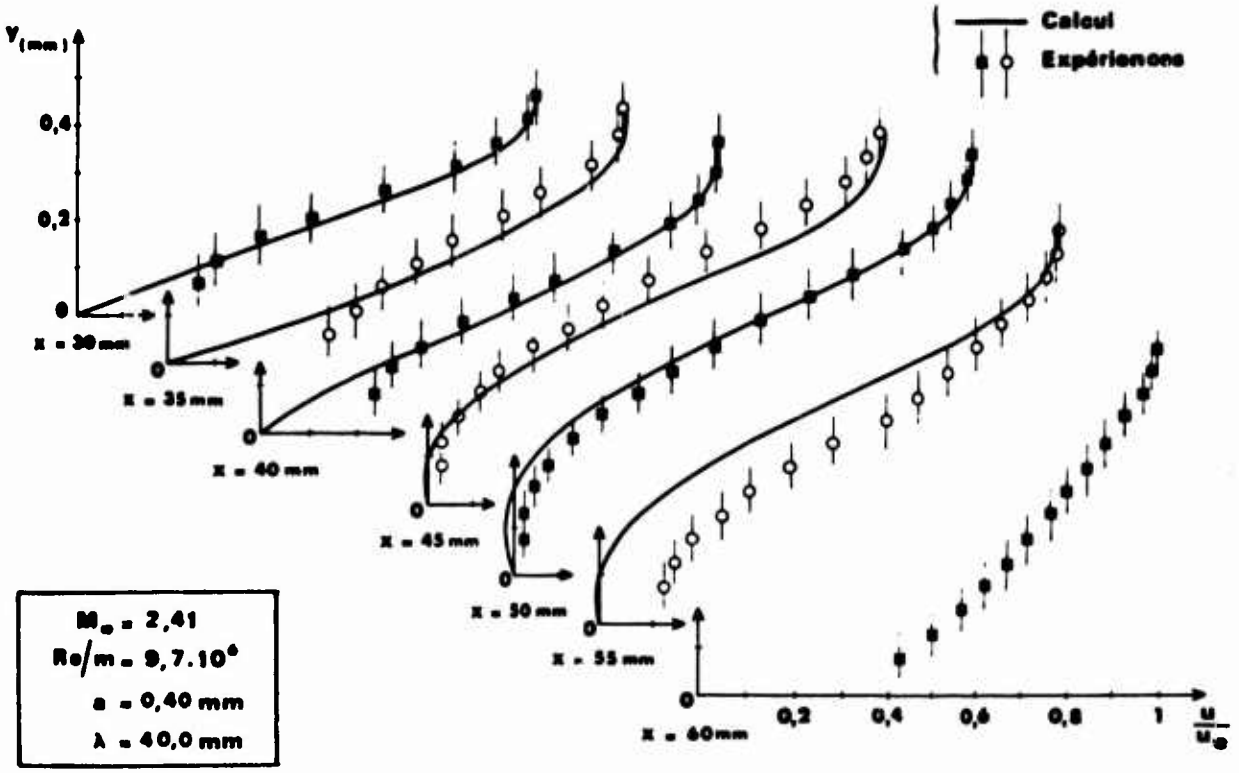

Fig. 2 - Détails des profils de vitesse sur la plaque P2

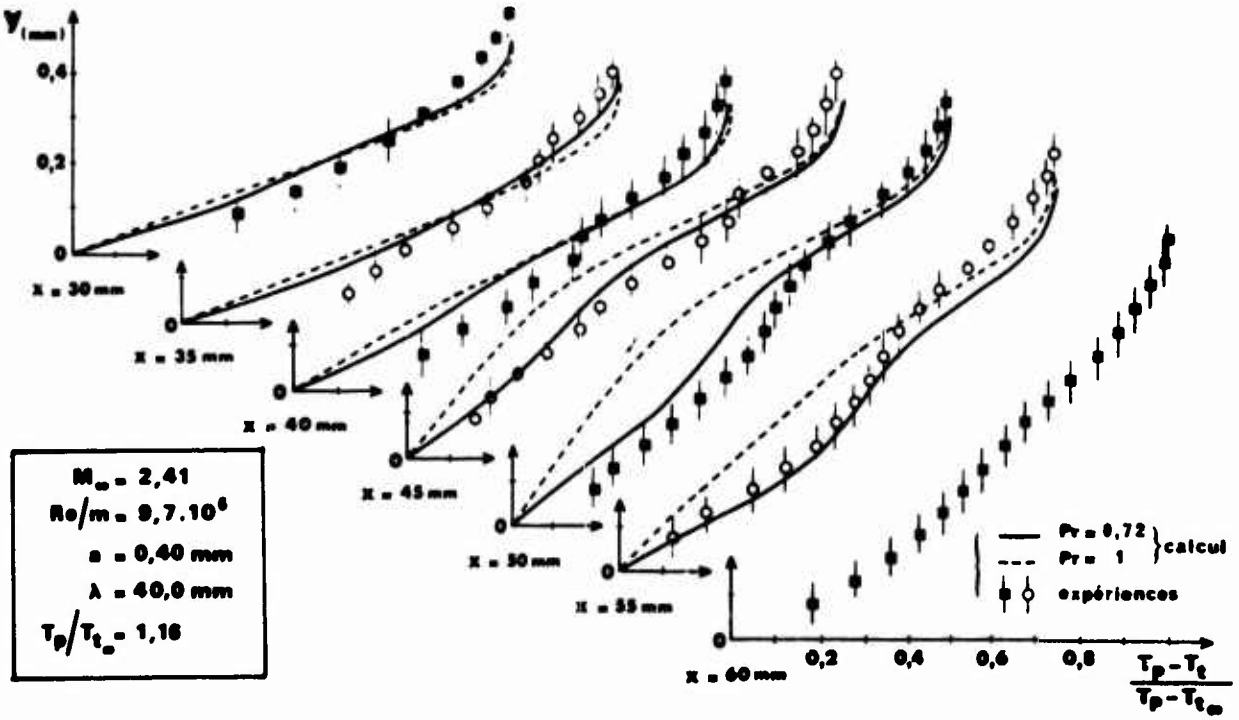

Fig. 3 - Détails des profils de température sur la plaque P2

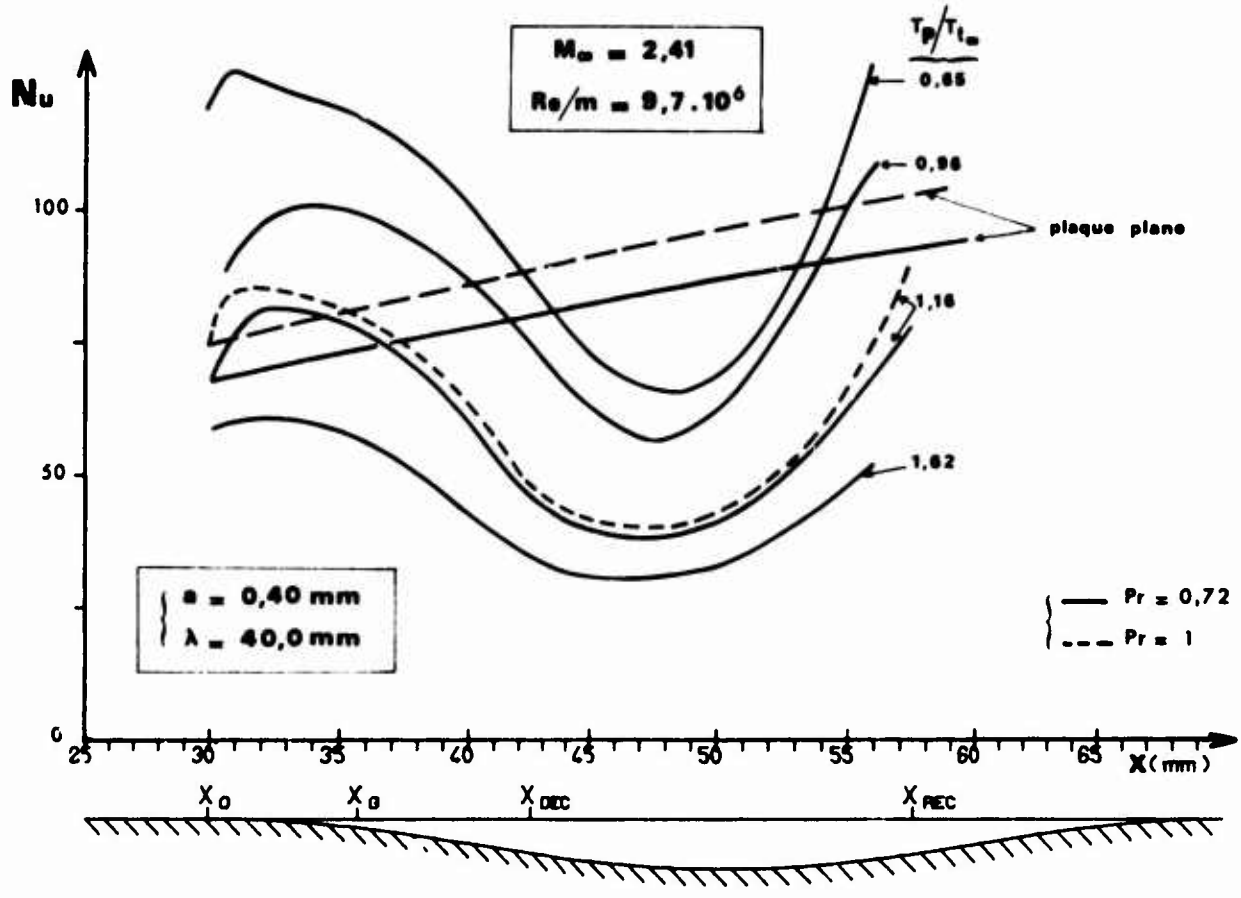

Fig. 4 - Evolution du nombre de Nusselt local

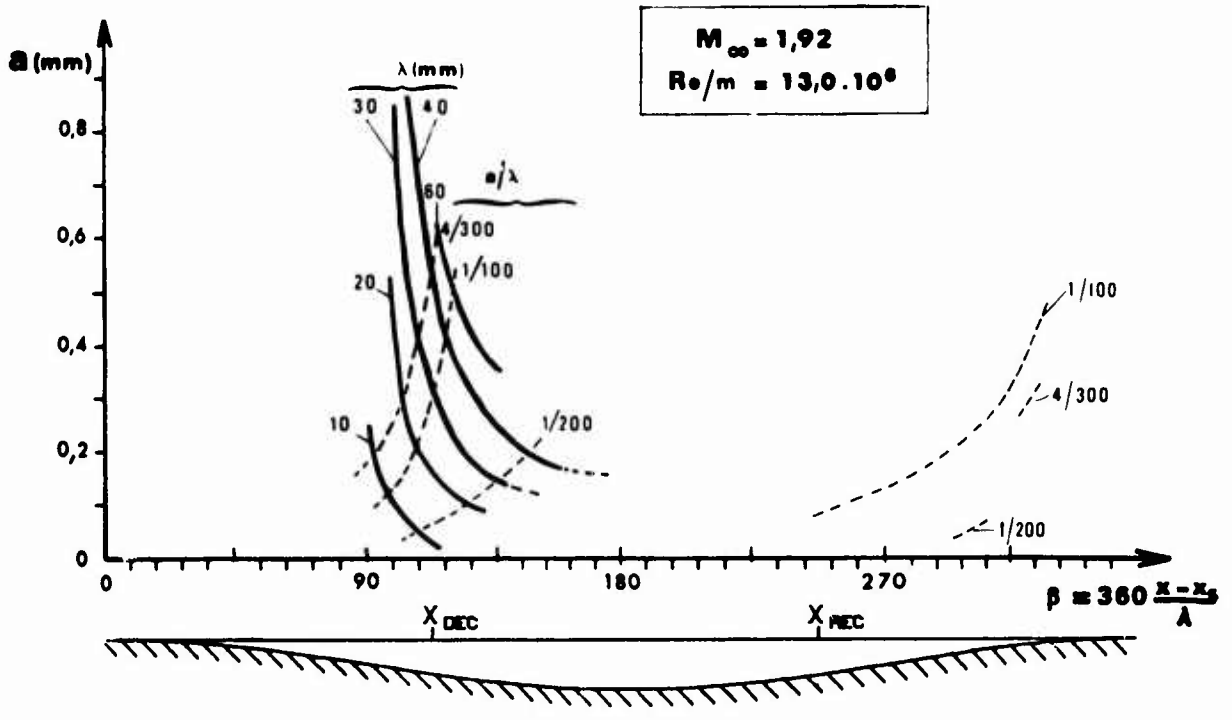

Fig. 5 - Variation des abscisses de décollement et de recollement en fonction de a et λ

la longueur d'onde est plus grande,

- pour une amplitude donnée, plus la longueur d'onde est grande, plus l'abscisse de décollement rapportée à cette dernière est éloignée du début du creux.

2) La configuration de paroi étant fixée :

- pour une température de paroi donnée, l'abscisse de décollement passe par un minimum lorsque le nombre de Reynolds de l'écoulement varie d'une valeur faible à une valeur très grande,

- pour des conditions de l'écoulement amont données, l'évolution du nombre de Nusselt conserve la même allure générale, sa valeur étant d'autant plus importante à une même abscisse que la paroi est plus froide (fig. 4).

CONCLUSION

L'étude présentée ici nous permet de conclure que, dans un écoulement supersonique, la présence, sur une plaque plane, d'une déformation en creux, de profil sinusoïdal, provoque en général, même pour de faibles rapports "amplitude/longueur d'onde", un décollement : un bulbe de faible épaisseur mais allongé se forme dans le creux et l'écoulement vient ensuite recoller à la paroi avant la fin de ce dernier.

L'application d'une méthode par différences finies dans la zone de détente que constitue le début du creux, puis de la méthode de Nielsen conduit à une prévision des champs dynamique et thermique de l'écoulement en bon accord avec ceux qui existent effectivement en soufflerie.

Le léger écart trouvé dans la répartition du coefficient local de pression, s'explique par la présence d'un bord d'attaque réel qui ne peut être parfait, comme le suppose la théorie. Ce bord d'attaque, aussi fin soit-il, a pour effet d'augmenter faiblement l'épaisseur de la couche limite. Si ce phénomène tend à avancer légèrement le décollement, les méthodes appliquées ici conduisent néanmoins à une bonne estimation de l'écoulement, tant au point de vue dynamique que thermique. Par suite, le calcul fournit des valeurs du coefficient local de frottement et du flux de chaleur à la paroi qui peuvent être considérées comme correctes.

Ainsi a été mise en évidence la faible influence de la température de paroi sur la configuration dynamique de la zone décollée, du moins pour des écarts de température modérés. Par ailleurs, les résultats du calcul montrent que, pour des nombres de Prandtl égaux à 1 ou 0,72, l'évolution du nombre de Nusselt le long de la déformation de paroi reste sensiblement la même, y compris dans la zone décollée.

Diverses améliorations peuvent être envisagées :

- la méthode utilisée ici dans la zone décollée peut être perfectionnée en prenant, pour profils de vitesse et de température, des développements d'ordre plus élevé, mais le calcul nécessiterait autant d'équations supplémentaires que de paramètres nouveaux,

- le programme de calcul peut être adapté au cas de déformations de paroi autres que sinusoïdales,

- le calcul peut également être poursuivi pour obtenir les caractéristiques de l'écoulement après le recollement.

REFERENCES

/1/ J.J. BERNARD - Problèmes aérodynamiques et thermiques liés aux déformations de paroi. A.A.A.F. 9ème Colloque d'Aérodynamique Appliquée (8-10 nov. 1972)

/2/ S. BURNEL, G.B. DIEP, P. GOUGAT, B. PRUNET-FOCH - Recherches théoriques et expérimentales sur les décollements liés à une déformation locale de surface. AGARD Conf. Proc. on Fluid Dynamics of Aircraft Stalling. AGARD CP 102 (25-28 avr. 1972)

/3/ G.R. INGER - Subsonic Laminar Boundary Layer Separation and Reattachment with Viscous-Inviscid Interaction. AIAA Paper 74-582. AIAA 7th Fluid Plasma Dynamics Conference, Palo Alto, California (17-19 juin 1974)

/4/ A.A. DORODNITSYN - General Method of Integral Relations and its Application to Boundary Layer Theory. Advances Aeronautical Sciences, 3, p. 207, Perg. Press (1962)

/5/ J.N. NIELSEN, L.L. LYNES, F.K. GOODWIN - Calculation of Laminar Separation with Free Interaction by the Method of Integral Relations. AIAA Paper 65-50 (jan. 1965)

/6/ J.N. NIELSEN, L.L. LYNES, F.K. GOODWIN - Theory of Laminar Separated Flows on Flared Surfaces Including Supersonic Flow with Heating and Cooling. AGARD Conf. on Separated Flows. AGARD CP 4, I (mai 1966)

/7/ B. PRUNET-FOCH - Etude dynamique et thermique du décollement produit par la dépression d'une paroi plane en écoulement laminaire supersonique. Thèse de Doctorat d'Etat, Paris VI, (17 juin 1974)

/8/ K. STEWARTSON - Correlated Incompressible and Compressible Boundary Layers. Proc. Roy. Soc., A, 200, 1060, 84-100 (1949)

/9/ I. SHAMES - Mechanics of Fluids, Mac Graw Hill Cy (1962)

/10/ D.R. CHAPMAN, M.W. RUBESIN - Temperature and Velocity Profiles in the Compressible Laminar Boundary Layer with Arbitrary Distribution of Surface Temperature. J.A.S. (sept. 1949)

ASYMPTOTIC THEORY OF SEPARATION AND REATTACHMENT OF A LAMINAR BOUNDARY LAYER ON A COMPRESSION RAMP*

by
Odus R. Burggraf
Dept. of Aeronautical Engineering
The Ohio State University
2036 Neil Ave.
Columbus, Ohio 43210

SUMMARY

Laminar boundary layer separation and reattachment is here considered for adiabatic flow over a compression ramp with supersonic mainstream. For large ramp angle, calculations based on the Stewartson-Williams "triple deck" theory show that the regions of separation and reattachment become distinct, with an intervening (plateau) region of nearly constant pressure. The mathematical description of each of these distinct regions is given, and simple formulas derived for a number of quantities of interest, including the plateau pressure, conditions at separation and reattachment, and the geometry of the separated region. Detailed comparisons of the theoretical results with available experimental data show favorable agreement, suggesting that the theory can provide a useful tool for engineering analysis.

1. INTRODUCTION

The boundary-layer concept has often been useful as a basis for calculating separated flows in supersonic main streams. When combined with a viscous interaction condition coupling the pressure to the displacement thickness, the boundary-layer equations appear to be an accurate model for certain types of separated flows at moderate Reynolds numbers of practical interest. Examples of the success of these methods are given by the work of Lees and Reeves[1] and of Nielsen.[2] At high Reynolds number R, the boundary layer with viscous interaction has been shown to develop a substructure,[3-5] which Stewartson has named the triple-deck. Computations have been carried out on the basis of triple-deck theory by Jenson, Burggraf and Rizzetta,[6] for the case of a compression ramp with supersonic mainstream. These results show that separation first occurs when the ramp angle α is of order $R^{-1/4}$. As α increases above those values reported in Ref. 6 (but still of order $R^{-1/4}$), a prominent pressure plateau develops between the distinct regions of separation and reattachment (see Fig. 1). Each of these regions has a distinct mathematical description for R large and relatively simple formulas have been derived for a number of quantities of interest. The purpose of this paper is to describe the mathematical structure of the separation, plateau, and reattachment regions and to compare the theoretical results with available experimental data, as outlined below.

2. SEPARATION AND PLATEAU REGIONS

The mathematical structure of the separation region has been given by Stewartson and Williams.[5] Briefly, the boundary layer is disturbed by some downstream obstacle, in this case a ramp. For large enough disturbance, the boundary layer will separate in a distance of order $R^{-3/8}$ ahead of the obstacle. Because of the short streamwise distance, viscous effects are restricted to a sublayer with thickness of order $R^{-5/8}$, while the main portion of the flow in the boundary layer continues as an inviscid rotational flow on the $R^{-1/4}$ length scale. Outside the boundary layer, the pressure disturbance is felt over a distance of order $R^{-3/8}$ in both transverse and longitudinal directions. If the separation point is far enough in front of the obstacle, as for the ramp of Fig. 1, the pressure asymptotes the plateau pressure downstream. This constant pressure region corresponds to an equivalent wedge surface running from separation point S to reattachment point R (see Fig. 2).

The asymptotic structure of the flow leaving the separation region has been described by Neiland[4] as a separated shear layer (centered on the equivalent wedge surface), an inviscid reversed flow which eds the fluid entrained by the shear layer, and a reversed-flow boundary layer. The latter two flows decay with increasing x and are of no further concern to us. However, the velocity in the free shear layer grows with x.

For definiteness, let x, y, u, v, p, α be the physical coordinates, velocity, pressure, and ramp angle, and let X, Z, U, V, P, $\bar{\alpha}$ be the corresponding nondimensional quantities in the sublayer. Following Stewartson and Williams,[5] these are related as

$$\begin{aligned} x &= x_0 + \epsilon^3 aX \quad , \quad y = \epsilon^5 bZ \\ p &= p_0 + \epsilon^2 cP(X) \quad , \quad \alpha = \epsilon^2 (b/a)\bar{\alpha} \\ u &= \epsilon (d/b)U(X,Z) \quad , \quad v = \epsilon^4 (d/a)V(X,Z) \end{aligned} \tag{1}$$

Here $\epsilon = R_*^{-1/8}$, where R is the Reynolds number, and the asterisk subscript refers to a convenient reference state of the external flow in the interaction region. x_0 is a convenient reference length measured to some point in the interaction region, and p_0 is the pressure at the beginning of interaction. The parameters are defined as

$$\begin{aligned} a &= x_0 C^{3/8} \lambda^{-5/4} (M_*^2-1)^{-3/8} (T_w/T_\infty)^{3/8} \\ b &= x_0 C^{5/8} \lambda^{-3/4} (M_*^2-1)^{-1/8} (T_w/T_\infty)^{3/2} \\ c &= \rho_\infty u_\infty^2 C^{1/4} \lambda^{1/2} (M_*^2-1)^{-1/4} \\ d &= x_0 u_\infty C^{3/4} \lambda^{-1/2} (M_*^2-1)^{-1/4} (T_w/T_\infty)^{3/2} \end{aligned} \tag{2}$$

*The research reported here was sponsored by the Office of Naval Research, United States Navy, under Contract No. N00014-07-A-0232-0014

λ takes the familiar value 0.332 when the undisturbed boundary layer is of the compressible Blasius type. C is the Chapman-Rubesin constant and the other variables have their usual meaning.

The flow in the sublayer is governed to first order by the classical incompressible boundary layer equations

$$U_X + V_Z = 0 \tag{4a}$$

$$UU_X + VU_Z = -P_X + U_{ZZ} \tag{4b}$$

subject to the usual no-slip condition on the wall streamline. However, the outer boundary condition is unconventional; it is an expression of the viscous interaction condition obtained by matching to the disturbed main boundary-layer flow, as described by Stewartson and Williams:[5]

$$P(X) = -A'(X) \quad , \quad A(X) = \lim_{Z \to \infty} (U-Z) \tag{5}$$

and A(X) approaches zero as $X \to -\infty$.

Jenson, Burggraf, and Rizzetta[6] have presented numerical solutions of the inner layer problem for the compression ramp, showing that separation first occurs for $\bar{\alpha} \approx 1.65$. The first indications of a pressure plateau appear for $\alpha \approx 2.5$, and a fully developed plateau exists for $\bar{\alpha} = 3.5$ as shown by Fig. 1. The length of the plateau grows rapidly with increasing $\bar{\alpha}$, and for large $\bar{\alpha}$ the separation region appears to be pushed far ahead of the corner (on the $R^{-3/8}$ interaction scale). Hence the asymptotic structure described by Neiland is appropriate to the plateau shear layer when $\bar{\alpha}$ is large.

The shear layer leaving the separation region is described by Neiland,[4] and more fully by Stewartson and Williams,[7] in the form of an asymptotic series:

$$U = X^{1/3} f_0'(\eta) + X^{-1/3} f_2'(\eta) + \cdots \tag{6a}$$

$$P = P_0 + P_2 X^{-2/3} + \cdots \tag{6b}$$

where

$$\eta = [Z - A(X)]/X^{1/3} \tag{6c}$$

The functions f_0 and f_2 satisfy the usual type of third-order ordinary differential equation. It suffices here to note that

$$f_0' = 0.9341 \quad , \quad f_2' = -0.2711 \quad \text{when} \quad f_0 = f_2 = 0. \tag{7}$$

The plateau pressure P_0 has been evaluated by Williams[7] by numerically solving the full inner-layer equations of the triple-deck, requiring that the reversed flow downstream of separation have the asymptotic form given by Neiland. P_0 was found to have the value 1.800, which is seen to agree very well with the plateau pressure of Fig. 1. This suggests that 3.5 is a sufficiently large value of $\bar{\alpha}$ for the asymptotic theory to apply.

Figure 3 is a comparison of the separation-region pressure predicted by the triple-deck theory with experimental data of Chapman, Kuehn and Larsen[8] for a forward-facing step. The reference state has been taken as conditions at the separation point (X = 0). The theory is seen to anticipate the initial pressure rise, but the agreement is quite good following separation. Another case is shown in Figure 4, corresponding to a curved ramp whose foot is tangent to the upstream plate. Two choices of reference state are shown here: (1) the solid symbols are for M_* equal initial freestream conditions, R_* equal to separation conditions, as was chosen in Ref. 5: (2) the open circles are for M_*, R_* both equal to separation point conditions. The latter choice makes the agreement better, although not of the quality of Fig. 3. This dependence on reference state is an effect of finite Reynolds number since the distance between the points is of order $R^{-3/8}$ and the pressure rise of order $R^{-1/4}$ according to the theory.

3. REATTACHMENT REGION

The flow in this region is fed by the separated shear layer, which is described by Neiland's asymptotic expression given above. Hence it is possible to estimate the orders of magnitude of the various terms in the Navier-Stokes equations for the reattachment region from the shear-layer scaling.

From Eqs. (6) and (1), the flow in the shear layer entering the reattachment region scales as follows:

$$u \sim L_p^{1/3} \quad , \quad y \sim L_p^{1/3} R^{-1/2}$$

where L_p is the length of the pressure plateau. Thus the inertia terms in the equations of motion scale as

$$u \frac{\partial u}{\partial x} \sim L_p^{2/3}/L_R$$

where L_R is the length scale of the reattachment region. The viscous term scales as

$$R^{-1} \frac{\partial^2 u}{\partial y^2} \sim L_p^{-1/3}$$

and from linear theory for supersonic flow $\Delta p \sim \alpha$ so that the pressure term scales as

$$\frac{\partial p}{\partial x} \sim \alpha/L_R$$

From continuity,

$$v \sim L_p^{2/3}/(L_R R^{1/2})$$

and requiring $v \sim \alpha u$ yields

$$L_R \sim L_p^{1/3}/(\alpha R^{1/2})$$

We now make the assumption that for large $\bar{\alpha}$ the pressure rise in reattachment is of the order of the dynamic pressure of the flow entering the reattachment region; i.e.

$$u^2 \sim \alpha$$

Hence

$$\begin{aligned} L_p &\sim \alpha^{3/2} \\ L_R &\sim \alpha^{1/2} R^{-1/2} \end{aligned} \tag{8}$$

Summarizing, we find in the x-momentum equation

$$\text{Inertia Terms:} \qquad u \frac{\partial u}{\partial x} \sim \alpha^{3/2} R^{1/2} \tag{9a}$$

$$\text{Viscous Term:} \qquad \frac{1}{R} \frac{\partial^2 u}{\partial y^2} \sim \alpha^{1/2} \tag{9b}$$

$$\text{Pressure Gradient:} \qquad \frac{\partial p}{\partial x} \sim \alpha^{3/2} R^{1/2} \tag{9c}$$

A similar treatment of the y-momentum equation yields

$$\text{Inertia Terms:} \qquad u \frac{\partial v}{\partial x} \sim \alpha^{5/2} R^{1/2} \tag{9d}$$

$$\text{Viscous Term:} \qquad R^{-1} \frac{\partial^2 v}{\partial y^2} \sim \alpha^{1/2} \tag{9e}$$

$$\text{Pressure Gradient:} \qquad \frac{\partial p}{\partial y} \sim \alpha^{1/2} R^{1/2} \tag{9f}$$

For $\alpha \sim R^{-1/4}$ ($\bar{\alpha} \sim 1$) as in the inner layer scaling of Eq. (1), all three terms in the x-momentum equation are of the same order, while the y-momentum equation reduces to

$$\frac{\partial p}{\partial y} = 0 \tag{10}$$

so that the conventional boundary-layer equations apply, as in Eq. (4). This scaling corresponds to $\bar{\alpha}$ less than about 3 (according to Ref. 6) where separation and reattachment both take place on the same length scale and the pressure plateau has not fully developed.

Alternatively if we require $\alpha \sim R^{-1/4}$ but regard $\bar{\alpha}$ large, the viscous term (9b) becomes negligible in the x-momentum equation, while the pressure gradient (9f) still dominates the y-momentum equation. Hence for large $\bar{\alpha}$, the reattachment process is inviscid, confirming Chapman's[8] early ideas.

It is also instructive to consider $\alpha \sim R^{-n}$ with $n \leq 1/4$. The results are as follows: (i) for $n = 1/4$, the reattachment process is viscous; (ii) for $0 < n < 1/4$ but not of order one, the reattachment process is inviscid and the pressure gradient $\partial p/\partial y$ transverse to the wall vanishes; (iii) for $n = 0$ ($\alpha \sim 1$), the reattachment process is inviscid and $\partial p/\partial y$ is important.

For case (i) the complete separated flow region is contained within the triple-deck and a well-developed plateau appears only in the limit $\alpha R^{1/4} \to \infty$, which overlaps case (ii). Case (iii) includes case (ii) and was treated earlier by Burggraf.[3] Numerical results for this case were presented based on Chapman's similarity solution for the free shear layer entering the reattachment zone, corresponding to a long plateau between separation and reattachment. For a short plateau, the appropriate profile is that of Neiland given above, corresponding to case (ii).

We now formulate a calculation procedure for the reattachment zone following a short plateau. For convenience, we assume $\alpha \sim R^{-1/4}$, but regard $\bar{\alpha}$ as large so that case (ii) applies. We introduce new variables for the reattachment zone, indicated by a tilde, as $\tilde{X}$. The initial conditions entering the reattachment zone are provided by Eq. (6), and these together with the scaling of Eq. (8) imply the following relationships between new and old variables:

$$\tilde{U} = U\bar{L}_p^{-1/3} \quad , \quad \tilde{Z} = Z\bar{L}_p^{-1/3} \quad , \quad \tilde{X} = (X - X_R)\bar{L}_p^{1/3} \tag{11}$$

Here $\bar{L}_p$ is the nondimensional form of L_p, scaled as in Eq. (1), and X_R is an arbitrary origin within the reattachment zone, selected below. In addition, the stream function and vorticity are defined as

$$\tilde{\Psi} = \int_{\tilde{Z}_d}^{\tilde{Z}} \tilde{U} d\tilde{Z} \quad , \quad \tilde{\Omega} = \frac{\partial \tilde{U}}{\partial \tilde{Z}} \tag{12}$$

The subscript d refers to the dividing streamline; i.e., that which ultimately reattaches to the wall. Far upstream on the $\tilde{X}$ scale, $\tilde{\Omega}$ is given by Neiland's shear layer as $f_0''(\tilde{Z} - \tilde{Z}_d)$.

With these definitions, the principles of conservation of vorticity and total pressure yield

$$\tilde{U}^2 = 2 \int_{\tilde{\Psi}_m}^{\tilde{\Psi}} \tilde{\Omega} d\tilde{\Psi} \quad , \quad \tilde{P} = \frac{1}{2} (\tilde{U}_d^2 - \tilde{U}^2) \tag{13}$$

where $\tilde{\Psi}_m$ is the minimum value for $\tilde{\Psi}$ at the local $\tilde{X}$ station. Since $\alpha \sim R^{-1/4}$, the outer matching condition (5) applies, and the $\tilde{X}$ location is determined from the pressure:

$$\tilde{X} = \int \frac{d\tilde{A}}{\tilde{P}_f - \tilde{P}} \tag{14}$$

The origin of $\tilde{X}$ is obtained by extrapolating the dividing streamline of the free shear layer linearly to the wall, thus defining X_R above.

Equation (14) defines a unique relation for the pressure distribution in the reattachment zone. This relation is shown by the curve in Fig. 5. The plotted points shown for comparison are experimental data for a 10° compression ramp taken from Fig. 20a of Ref. 2. Since the experimental reattachment point was not defined, it was arbitrarily chosen to match the theoretical pressure at $\tilde{X} = 0$. The comparison shown is reasonably good, and might be improved by accounting for the evolution of the shear layer-velocity profile over the finite plateau length.

Now consider the case of a long plateau. According to Eq. (8), L_p of order one corresponds to α of order one, and thence L_R of order $R^{-1/2}$. More explicitly, the scaling of Eq. (11) for the short plateau suggests that when $L_p \sim 1$, the physical length scale in the reattachment zone is

$$x - x_R = x_0 (L_p/x_0)^{-1/3} C^{1/2} \lambda^{-5/3} (M_*^2 - 1)^{-1/2} (T_w/T_\infty)^2 R_*^{-1/2} \tilde{X} \tag{15}$$

where Eqs. (1) and (2) have been invoked. The appearance of the λ and x_0 factors indicate the history of the upstream Blasius boundary layer; these would be expected to disappear for a truly long plateau. The Mach number and Reynolds number scaling here are exactly those deduced in Ref. 9 on the basis of physical arguments. The curves shown in Fig. 6, reproduced from Ref. 9, were calculated for inviscid reattachment of a Chapman shear layer (Ref. 11), corresponding to a long plateau with vanishingly short upstream boundary layer. Even though plotted in the Mach number scaling of Eq. (15), a residual Mach number dependence is evident. One reason is that Eq. (15) is based on Neiland's shear layer in which the velocity is small and the flow is essentially incompressible. For the long plateau with Chapman's shear layer, the flow is compressible. In addition, the flow turning angle in the latter case is large enough for nonlinear effects to be important in the pressure-angle flow relation.

Also shown in Fig. 6 are experimental data for a 25° compression ramp taken from Fig. 14a of Ref. 8. In this case, the origin was estimated by extrapolating the free shear layer visible in the schlieren photograph, an uncertain procedure. If an origin shift is allowed the comparison with theory is not bad. In general, the effect of the upstream boundary-layer history on the shear layer initiating the reattachment zone should be accounted for. This may be accomplished by calculating the shear layer as it develops downstream from Neiland's profile over the length of the pressure plateau, as demonstrated by Denison and Baum.[10]

4. GEOMETRY OF THE SEPARATED FLOW REGION

According to Neiland[1]'s asymptotic structure for the separation region, the plateau region exhibits only small fluid motion, except for the free shear layer which may be calculated independently. The length of this region can be estimated from Chapman's[11] hypothesis of the reattachment pressure rise: the total pressure on the dividing streamline entering the reattachment zone equals the final pressure recovered when the external flow has been turned parallel to the wall. Using the velocity and thickness scalings given by Neiland's asymptotic shear layer as an estimate for conditions entering the reattachment zone, we have shown already that Chapman's hypothesis implies the length of the free shear layer in the plateau region to be of order $\alpha^{3/2}$. More explicitly, utilizing the linear pressure-angle relation for the external flow and Chapman's hypothesis, we have on the dividing streamline

$$P + U^2/2 = \bar{\alpha}$$

For the short plateau, the left side can be evaluated from Eq. (6). Truncating the series at the first order term in X (which we now interpret as the plateau length $\bar{L}_p$) we find

$$\bar{L}_p \sim [2[\bar{\alpha} - P_0 - f_0'(0) f_0'(0)]/[f_0'(0)]^2]^{3/2} \tag{16a}$$

Substituting the numerical values given earlier yields

$$\bar{L}_p \sim 3.47(\bar{\alpha} - 1.55)^{3/2} \tag{16b}$$

Since this is an asymptotic formula, it is valid only for $\bar{\alpha} \gg 1.55$. While we have no numerical solutions of the type shown in Fig. 1 for such large $\bar{\alpha}$, it is possible to compare with experimental data for at least one of the cases in Ref. 8, the 25° ramp. Converting the ramp angle to the nondimensional form gives $\bar{\alpha} = 6.89$ for that case. According to the above formula, $\bar{L}_p = 42.7$, while an approximate value of about 47 is found by measuring the length of the free shear on the photograph (Fig. 14a of Ref. 8). This agreement lends credence that the above asymptotic formula is useful for practical application, although additional comparison with experiment is essential.

The complete geometry of the separated region is now available. From Williams' solution,[7] the plateau shear layer is inclined at an angle α relative to the wall:

$$\bar{\alpha} - P_0 = 1.800$$

Hence from Fig. 2 and the law of sines, the distance between the ramp leading edge and the separation point is

$$X_c - X_s = \left(1 - \frac{1.8}{\bar{\alpha}}\right) \bar{L}_p \tag{17}$$

A complete pressure distribution for a 10° ramp has been calculated from the above theory and is shown in Fig. 7. The conditions correspond to those of Fig. 20a of Ref. 2, already referenced in Fig. 5. In making these calculations, it was necessary to account for an inconsistency between Eqs. (16) and the reattachment calculation outlined in Eqs. (11) through (14). Equation (16) is based on two terms of the asymptotic expansion for Neiland's shear layer, whereas the reattachment solution shown in Fig. 5 was based on only the leading term. The analysis was made consistent by dropping the term $f_2'(0)$ in (16a), or equivalently, replacing the value 1.55 in (16b) by $P_0 = 1.80$, and requiring the final pressure at the end of the reattachment zone to agree with the inviscid wedge pressure. The agreement with the experimental data in Fig. 7 is fairly good, and could be improved if the freedom of the origin shift in the asymptotic formulas is exploited to shift the theoretical reattachment zone a short distance downstream.

To compare the accuracy available with integral methods, Fig. 8 is taken from Fig. 21 of Nielsen, et al.[2] In their method, the interaction is started at a particular point which is usually chosen to make the resulting solution agree well with experiment. In Fig. 8 the four integral curves correspond to initial points of 0.0525 to 0.0700 feet from the leading edge. If the experimental data were not available, there would be no reason to prefer any of the four integral curves. Comparing Figs. 7 and 8, we conclude that the accuracy of the asymptotic theory is of the same order as that of the integral method.

5. CONCLUSIONS

The evidence presented above supports the view that the asymptotic theory of laminar separation and reattachment is an acceptable formulation for practical purposes. By combining the results of the structure of the three regions (separation, plateau, and reattachment) the complete structure of the flow field can be predicted independent of experimental inputs, although there is some room for adjustment in the theory through optimum choice of reference conditions and origin shifts in the asymptotic expansions. Further development of the Stewartson-Williams free-interaction theory is underway, with promising results both from higher-order analyses and from inclusion of hypersonic effects. Similar improvements in the reattachment theory are also necessary. Nevertheless, even in its present state, the theory can serve as a useful tool for engineering analysis.

6. REFERENCES

1. Lees, L., and Reeves, B., AIAA J. 2, 1907-1920(1964).

2. Nielsen, J., Lynes, L., and Goodwin, F., USAF FDL TR-65-107 (1965).

3. Messiter, A., Hough, G., and Feo, A., J. Fluid Mech. 60, 605-624 (1973).

4. Neiland, V., Izv. Akad. Nauk SSSR No. 3, 19-24 (1971).

5. Stewartson K., and Williams, P., Proc. Roy. Soc. A. 312, 181-206 (1969).

6. Jenson, R., Burggraf, O., and Rizzetta, D., Paper presented at 4th Int. Conf. on Numerical Methods in Fluid Mechanics, held at Boulder Colo., June 1974. To be published in conference proceedings, Springer-Verlag (1974).

7. Stewartson, K., and Williams, P., Mathematika 20, 98-108 (1973).

8. Chapman, D., Kuehn, D., and Larsen, H., NACA Rpt. No. 1356 (1958).

9. Burggraf, O., Proc. 3rd Int. Conf. on Numerical Methods in Fluid Mech., Lecture Notes in Physics, Vol. 18, Springer-Verlag (1973).

10. Denison, M., and Baum, E., AIAA J. 1, 342 (1963).

11. Chapman, D., NACA TN 3792 (1956).

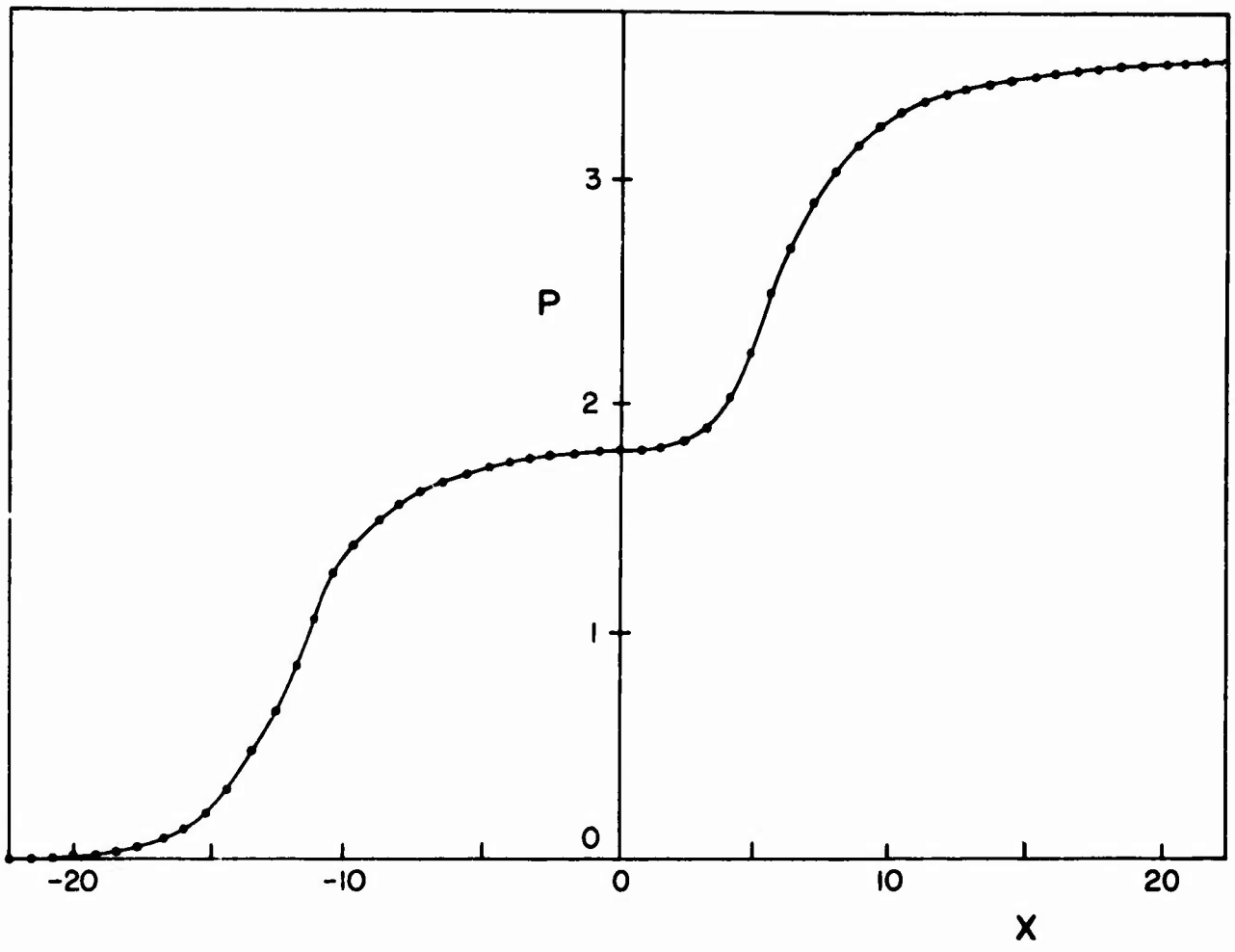

Figure 1. Wall pressure distribution for $\bar{\alpha}$ = 3.5, plotted in inner layer variables. Mesh size: ΔX = 0.8, ΔY = 0.8.

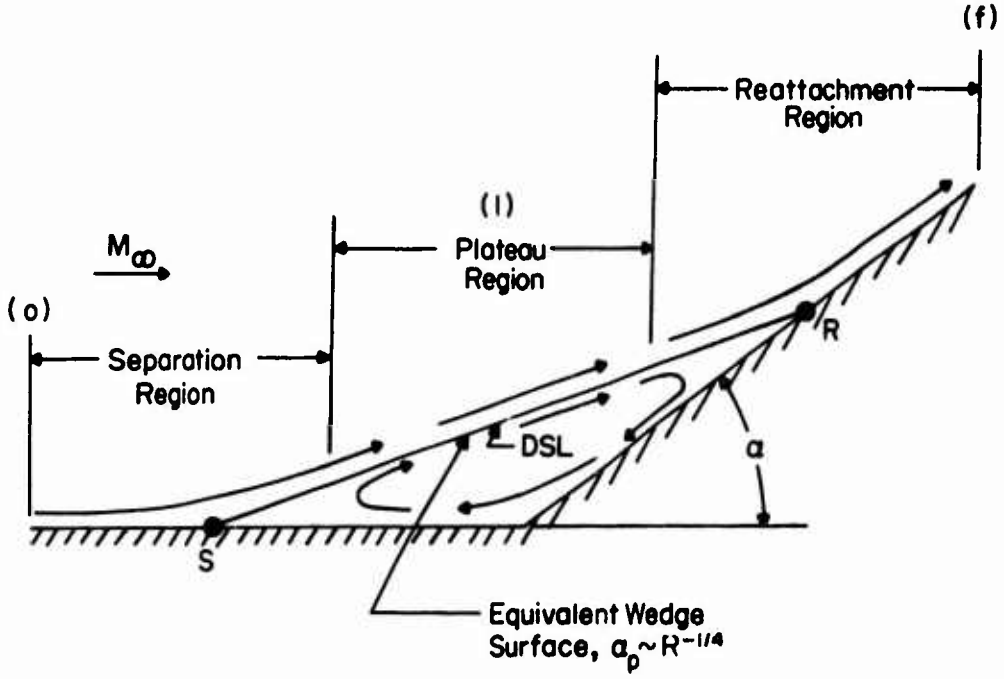

Figure 2. Geometry of the separated flow for α = O(1).

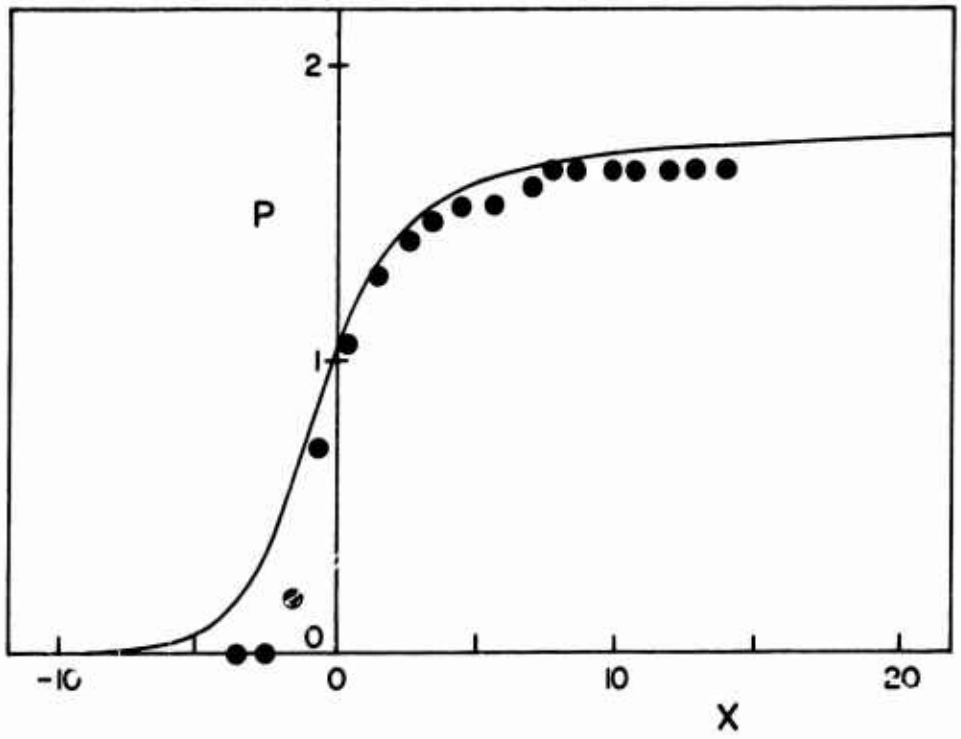

Figure 3. Pressure distribution in separation region for a forward-facing step; $M_* = M_s = 2.21$, $R_* = u_\infty x_s/\nu_\infty = 92{,}000$, $T_w/T_\infty = 1.90$. Asymptotic Theory: ———; experimental data from Ref. 8, Fig. 11a: ●.

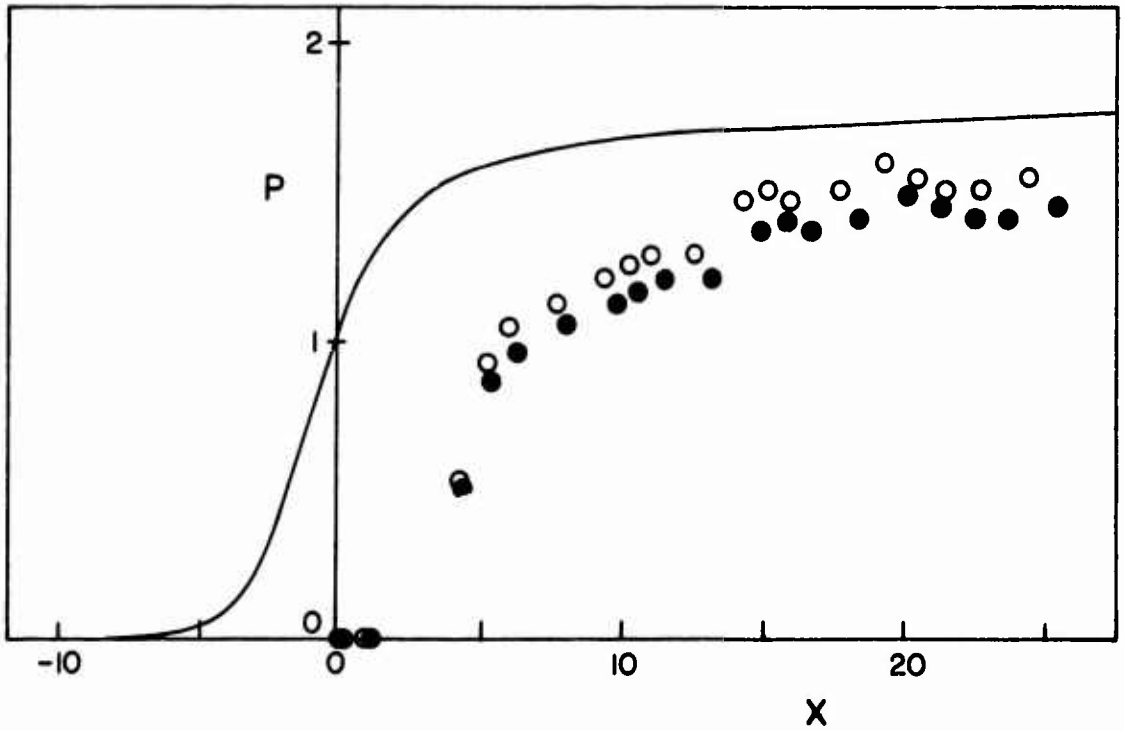

Figure 4. Pressure distribution in separation region for a curved ramp. Asymptotic theory: ———. Experimental data from Ref. 8, Fig. 17a: $M_* = M_O = 2.7$, ●; $M_* = M_s = 2.56$, ○. $R_* = u_\infty x_s/\nu_\infty = 39{,}000$ and $T_w/T_\infty = 2.4$ for both cases.

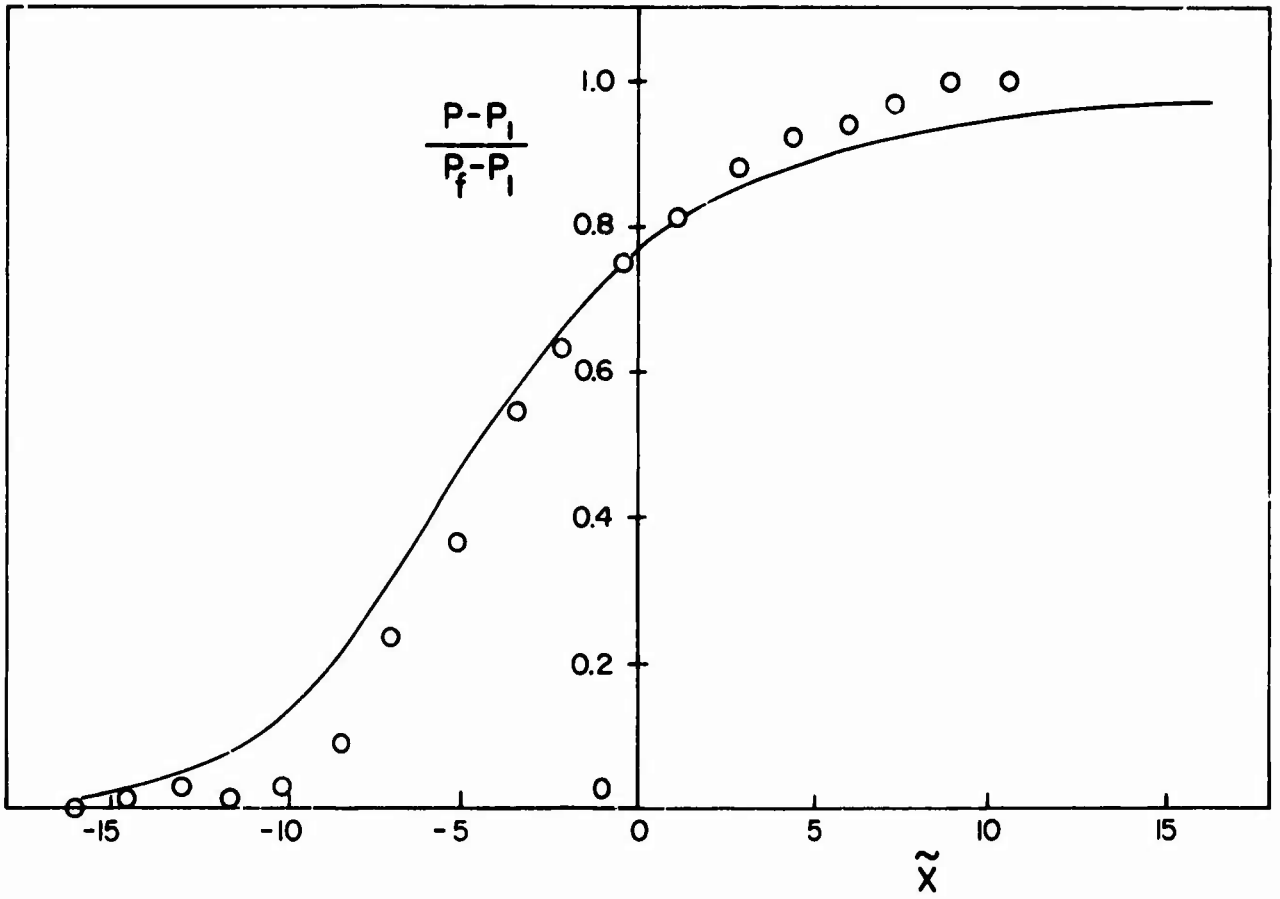

Figure 5. Pressure distribution in reattachment region with a short plateau. Theory: ——— ; experimental data from Ref. 2, Fig. 20a: ○ , $\alpha = 10^{\circ}$, $M_* = 2.55$, $R_* = 206{,}000$, $T_w/T_\infty = 2.11$.

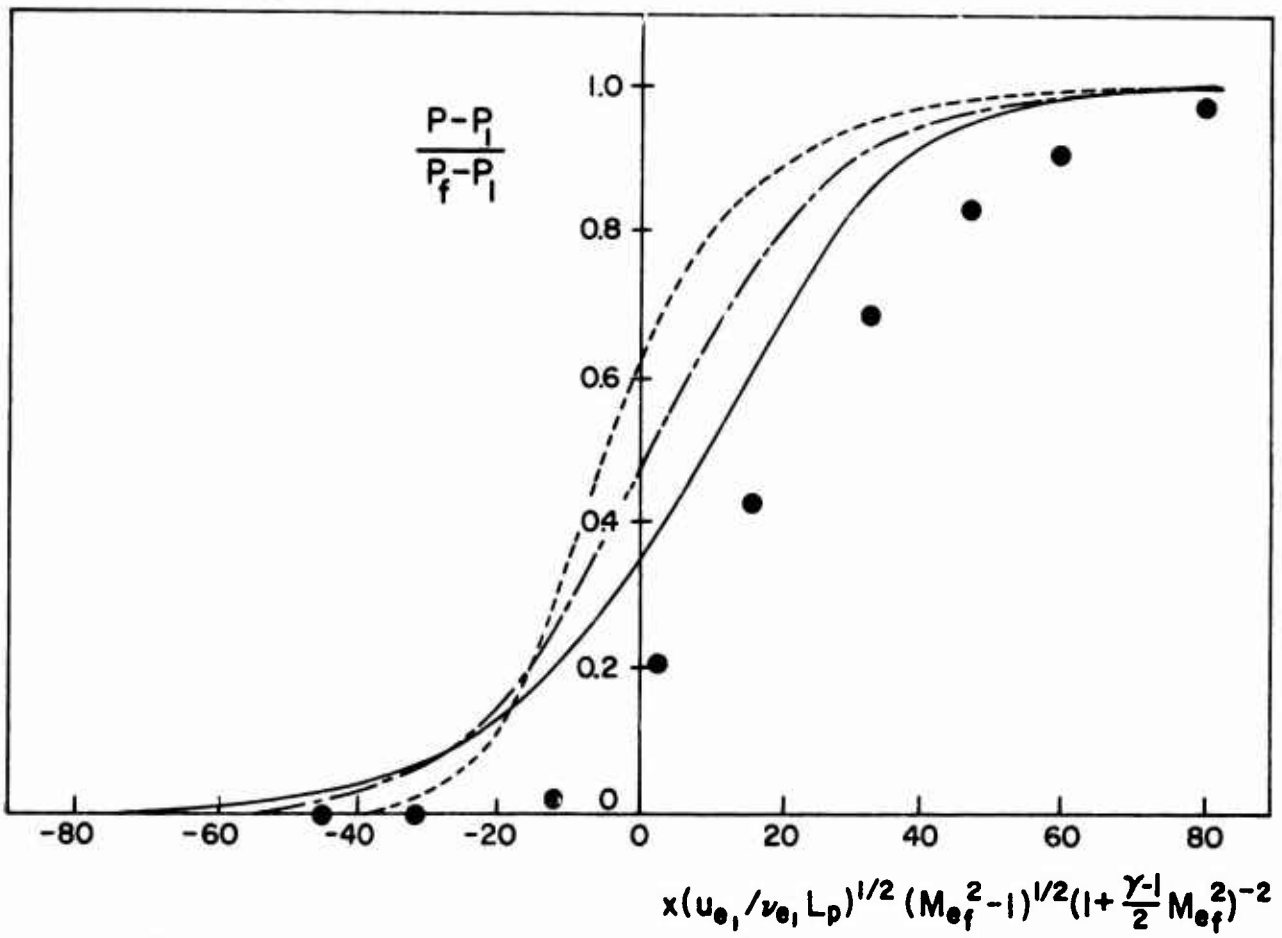

Figure 6. Pressure distribution in reattachment region with a long plateau. Theory from Ref. 9: ----, $M_{e_1} = 1.4$; - - - -, $M_{e_1} = 3$; ———, $M_{e_1} = 7$. Experimental data from Ref. 8, Fig. 14a: ● , $\alpha = 25^{\circ}$, $M_* = 2.7$, $R_* = 33{,}000$, $T_w/T_\infty = 2.24$.

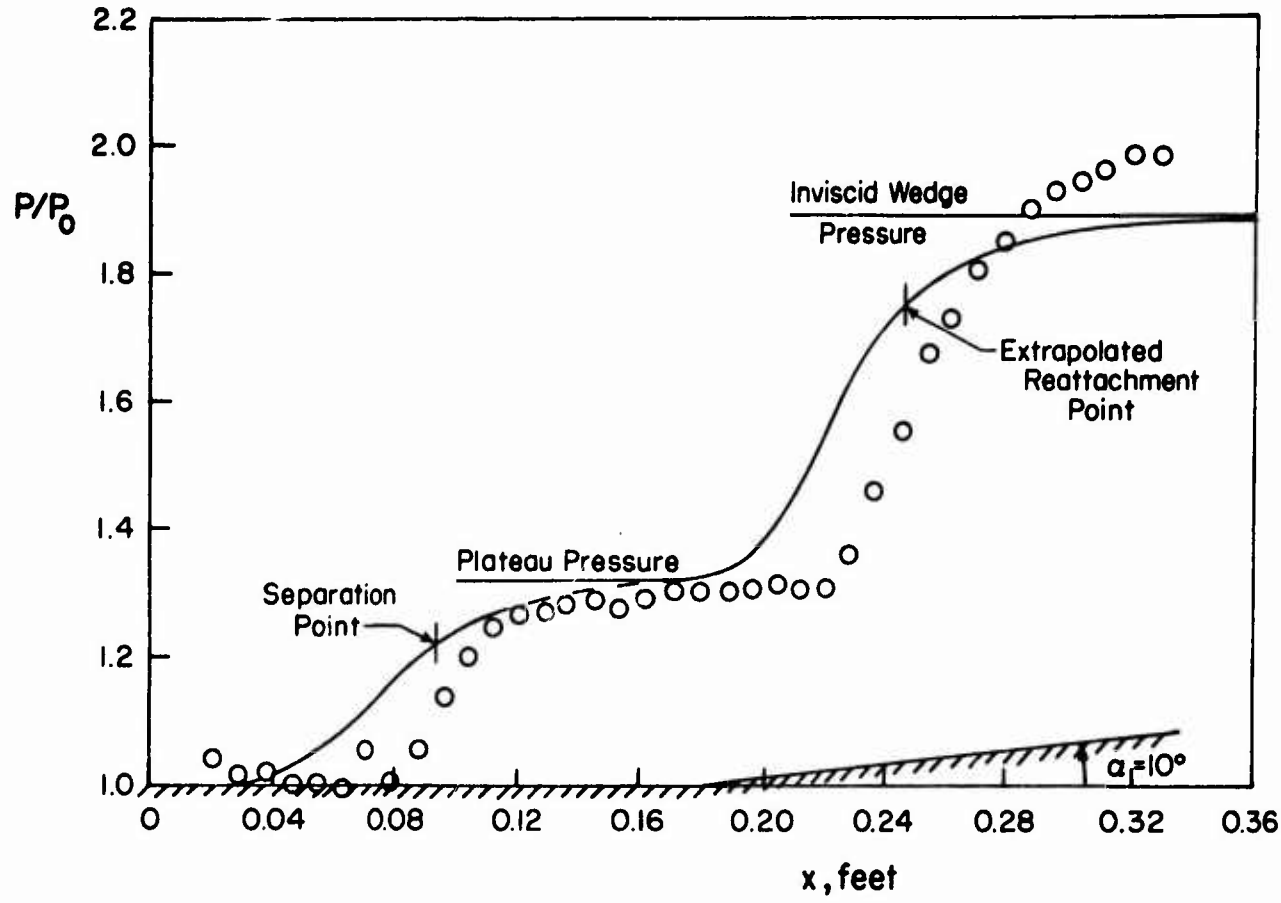

Figure 7. Overall pressure distribution for 10° ramp. Theory: _____ ; experimental data from Ref. 2, Fig. 20a: ○ , M_o = 2.55, R/ℓ = 1.143 x 10^6/ft.

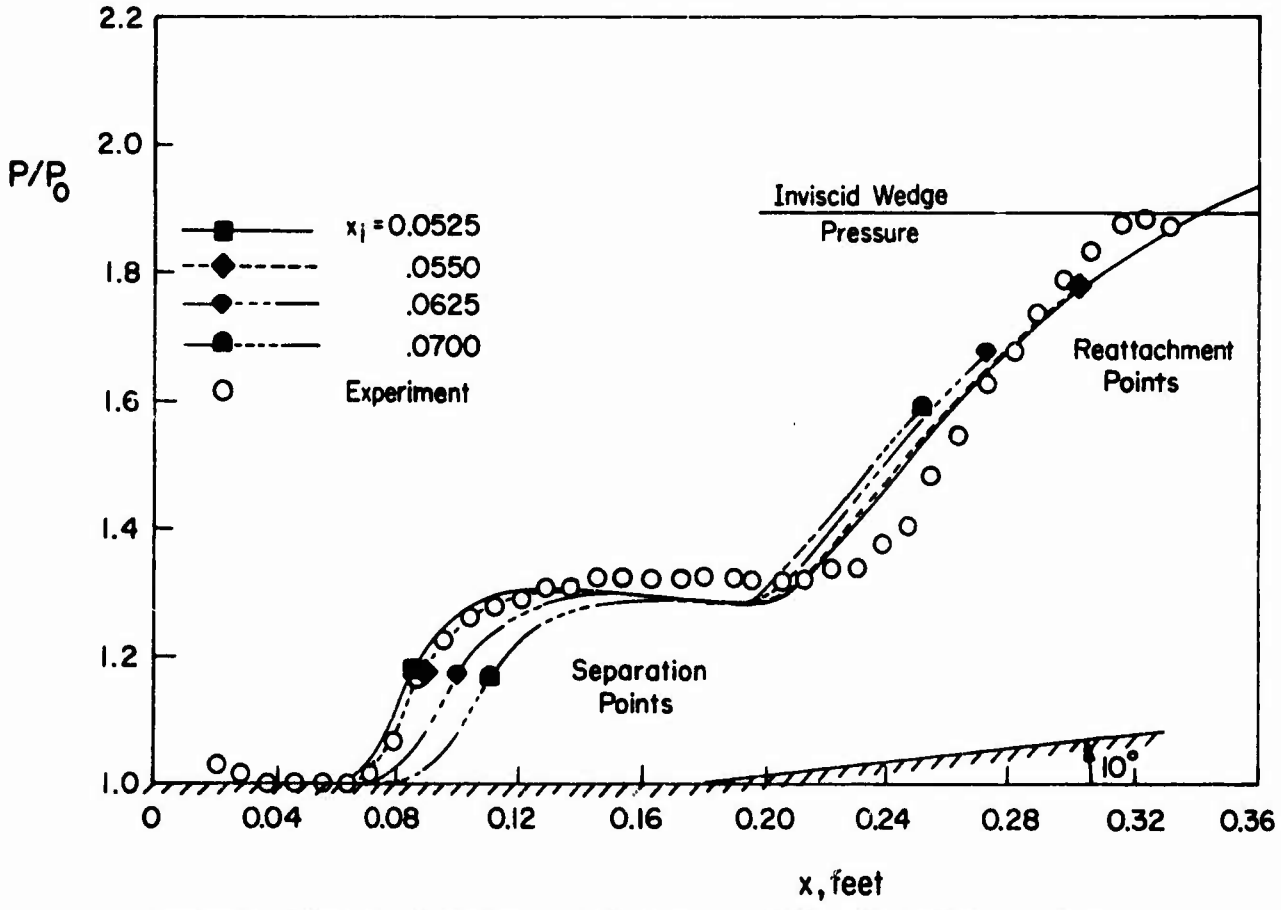

Figure 8. Nielsen integral theory - effect on calculated pressure distribution of variation in beginning of interaction x_i. Theory and experimental data from Ref. 2, Fig. 21: M_o = 2.55, R/ℓ = 85,000/ft.

ON THE CALCULATION OF LAMINAR SEPARATION BUBBLES IN TWO-DIMENSIONAL INCOMPRESSIBLE FLOW

J.L. van Ingen

Department of Aeronautical Engineering, Delft University of Technology, Kluyverweg 1, Delft, The Netherlands

SUMMARY.

The following topics are discussed in the paper.
- A new laminar boundary layer calculation method is presented which combines the simplicity of Thwaites' method for the prediction of the momentum loss thickness θ with the accuracy of Stratford's two-layer method for the prediction of the position of laminar separation.
- Calculated boundary layer characteristics for arbitrarily prescribed pressure distributions in general show a singular behaviour at separation. It is shown that a real separating flow tends to adjust itself in such a way that the resulting pressure distribution prevents a singular behaviour of the boundary layer to occur. It appears that $m = -\frac{\theta^2}{\nu}\frac{dU}{dx}$ shows a maximum value at separation.
- A simple calculation method for the laminar part of the separation bubble is presented. The pressure distribution is not prescribed but it is determined from the calculation such that the separation streamline assumes a prescribed shape.
- An earlier method for the prediction of transition in attached boundary layers, based on linear stability theory, is extended to the case of separated flows.
- Two methods are discussed which might be used to predict whether reattachment of the turbulent shear layer will occur, thus leading to a closed separation bubble.
- Finally some results will be discussed of windtunnel experiments on two different models. The first model is the FX 66-S-196-V1 Wortmann airfoil; the second model consists of a circular cylinder with a tapered tail.

NOTATION

a	constant in Eq. (2)
b	constant in Eq. (2)
B	constant in Eq. (16)
c	reference length, equal to chord for airfoil; equal to radius for cylinder
g	profile parameter for velocity profiles with reversed flow, Eq. (12)
H	δ^*/θ
ℓ	$\frac{\tau_o\theta}{\mu U} = \{\frac{\partial(u/U)}{\partial(y/\theta)}\}_o$
L	$2\ell + 2m(2+H)$
m	$-\frac{\theta^2}{\nu}\frac{dU}{dx} = \{\frac{\partial^2 u/U}{\partial(y/\theta)^2}\}_o$
p	static pressure
P	$\frac{\theta^2_{sep}}{\nu}\frac{\Delta U}{\Delta x}$
r	m/m_{sep}
R_c	$\frac{U_{ref}\, c}{\nu}$
R_θ	$\frac{U\theta}{\nu}$
u	velocity component in boundary layer parallel to wall
U	velocity component at edge of boundary layer
U_{ref}	reference speed
$\bar{U}$	U/U_{ref}
ΔU	change in edge-velocity over length of separation bubble; Fig. 1
x	distance along the wall
$\bar{x}$	$\frac{x}{c}$
Δx	length of separation bubble, Fig. 1
y	distance normal to wall
z	$g = m_{sep}$
$-\alpha_i$	spatial amplification rate, Eq. (23)
β	Falkner-Skan pressure gradient parameter, Eq. (13)
γ	angle at which the separation streamline leaves the wall; Fig. 1
δ^*	$\int_o^\infty (1 - \frac{u}{U})dy$ displacement thickness
θ	$\int_o^\infty \frac{u}{U}(1 - \frac{u}{U})dy$ momentum loss thickness
φ	angular distance around circular cylinder, measured from leading edge
ψ	streamfunction
σ_a	amplification factor, Eq. (23)
ν	coefficient of kinematic viscosity
τ_o	wall shear stress
ω	disturbance frequency, Eq. (22)

Subscripts

$B\ell$	Blasius value
r	reattachment
sep	separation
tr	transition
0	at surface

1. INTRODUCTION

Although quite a number of important references is available on the subject of the laminar separation bubble in two-dimensional incompressible flow (see for instance refs. 1 through 6) a fully satisfactory engineering method for the prediction of the characteristics of these bubbles does not yet exist. The present paper tries to fill some of the gaps in our knowledge; it appears that a complete prediction of the bubble is now within our reach. Some of the problems in this field are illustrated by the well known picture of the

pressure distribution(*) in the separation region (Fig. 1). First we have to determine the separation point S; downstream of S we usually find experimentally a flattening of the pressure distribution. This part of the pressure distribution is not known a priori but it should follow from the calculation. Most of the existing calculation methods assume a constant wall pressure within the bubble but this is only a good approximation at low Reynoldsnumbers. The next problem is to predict the position of transition T in the separated shear layer. Downstream of T we may find a rather steep pressure recovery curve, leading to reattachment at R. Often R is assumed to lie on the dotted pressure distribution curve which would occur without the presence of the bubble. Sometimes reattachment does not occur; the bubble "bursts" and of course a calculation method should be able also to predict this bursting.
In the following chapters the different problems, mentioned above will be discussed in turn.

2. PREDICTION OF THE SEPARATION POINT USING ENGINEERING METHODS.

A well known engineering method for the calculation of the laminar boundary layer is that due to Thwaites (ref. 7). The accuracy of the method is quite good for the prediction of the momentum loss thickness θ; it is less accurate for the prediction of the separation position. The idea behind this method is to use the von Kármán momentum integral relation and the first compatibility condition of the boundary layer in the form:

$$\frac{d}{dx}\left(\frac{\theta^2}{\nu}\right) = \frac{2\ell+2m(2+H)}{U} = \frac{L}{U} \text{ and } m = -\frac{\theta^2}{\nu}\frac{dU}{dx} = \left\{\frac{\partial^2 u/U}{\partial(y/\theta)^2}\right\}_o . \tag{1}$$

Thwaites assumed that ℓ and H and hence L are unique functions of m which allows us to calculate ℓ, m, H, L and θ as functions of x. The required functions $\ell(m)$, H(m) and L(m) were deduced by Thwaites from a number of exact solutions of the laminar boundary layer equations which were available to him at that time. The momentum integral equation can be integrated easily between two points x_1 and x_2 if a linear relation

$$L = a + bm \tag{2}$$

is assumed between L and m (Thwaites took a=0.45; b=6). The result is

$$\left(\frac{U^b\theta^2}{\nu}\right)_{x=x_2} - \left(\frac{U^b\theta^2}{\nu}\right)_{x=x_1} = a\int_{x_1}^{x_2} U^{b-1}\,dx \tag{3}$$

As soon as $\theta(x)$ is known, m(x), $\ell(x)$ and H(x) follow from the compatibility condition and the relations $\ell(m)$ and H(m). This allows us to find the separation point and an approximation to the boundary layer velocity profile. As was remarked already the predicted values of θ are sufficiently accurate for engineering use. For the favourable pressure gradient case (m<0) also the velocity profile is rather accurate. For adverse pressure gradients (m>0) the profile is less accurate and hence the separation position is not predicted accurately enough for the present purpose. This is due to the fact that Thwaites' method belongs to the class where a fixed relation exists between ℓ and m so that separation (ℓ=0) is found at a fixed value of m.
An improved method has been obtained in which $\ell(m)$, H(m) and hence L(m) are allowed to depend on an extra parameter. This parameter is taken as m_{sep}, the value of $m = -\frac{\theta^2}{\nu}\frac{dU}{dx}$ at separation.
To introduce this improved method we refer to figs. 2 through 4 where $\ell(m)$, H(m) and L(m) have been plotted in the same way as Thwaites did for some special accurate solutions of the boundary layer equations. The selected solutions have in common that for zero pressure gradient (m=0) they all reduce to the Blasius flat plate boundary layer. The separation values for H and L fall neatly on curves which coincide with the curves representing the separation points in Head's two-parameter method (ref. 8).
For the range of values of m_{sep} which is of practical interest (m_{sep}>.068) it follows that a good approximation for L_{sep} is:

$$L_{sep} = .14026+10\, m_{sep} \text{ and hence } H_{sep} = 3 + \frac{.07103}{m_{sep}} \tag{4}$$

It follows that ℓ, H and L can be very nearly made unique functions of $r=m/m_{sep}$ when properly scaled (see fig. 5). In what follows Hartree's similar solutions of the Falkner-Skan equation have been used to define these functions.
Introducing m_{sep} as an extra parameter, to be determined later, the new method may now be defined as follows.
For favourable pressure gradients (m<0) use $\ell(m)$, H(m) and $\ell(m)$ as for the Hartree flows for which m_{sep}=.06815.
For adverse pressure gradients (m>0) use the scaled functions

---

(*) In the present paper we will by "pressure distribution" not only denote p(x) but also U(x).

$$\ell = \ell(r) \; ; \; \frac{L-.44105}{L_{sep}-.44105} = L^{m}(r) \; ; \; \frac{H-2.5911}{H_{sep}-2.5911} = H^{m}(r) \qquad (5)$$

as determined from the results for the Hartree flows. The momentum integral equation can then be integrated once a starting value for θ is available. As in Thwaites' method the integration can be performed in the form (3) when using the linear approximation (2). Of course b now depends on the parameter m_{sep}; with (4) it follows that for $m_{sep}>.068$:

$$b = 10 - \frac{.30079}{m_{sep}} \quad \text{or} \quad m_{sep} = \frac{.30079}{10-b} \qquad (6)$$

For favourable pressure gradients we use b=5.16, corresponding to the straight line connecting the stagnation point and the Blasius point in fig. 4; for all values of b we have a=.44105. For each value of b (or m_{sep}) a Thwaites type method is obtained. For large values of b the method gives late separation, for small values of b early separation is obtained.

Of course some additional information is needed to determine b. When analysing experimental results b may be chosen such that the experimentally determined separation point is reproduced. In cases where the separation point is not known a priori we use Stratford's two-layer method (ref. 9) in the version of Curle and Skan (ref. 10) to provide the separation position. Lack of space does not permit to give a more detailed account of the present method; details will be given in a forthcoming report by the present author (ref. 11). A few results to illustrate the method may be found in figs. 6 through 8. Fig. 6 gives some results for the potential flow pressure distribution around a circular cylinder where $\bar{U}=\sin \bar{x}$; a comparison has been made with the accurate numerical results due to Terrill (ref. 12). Fig. 7 gives some results for the measured pressure distribution on a Wortmann airfoil (see section 8).

The free-stream speed for this particular case was such that a closed laminar separation bubble occured. Using the surface oil film technique the separation point was found at a distance of 48% of the chord downstream of the leading-edge(x). It should be noted that the curve of $\bar{U}$ vs.$\bar{x}$ becomes rather flat downstream of the separation point leading to a point of inflexion shortly upstream of the separation point. This appears to be characteristic for all measured pressure distributions in the vicinity of separation.

It follows from fig. 7 that the present method does not predict separation for b>7.23; in fact the calculation tends to the flat plate boundary layer far downstream. For b<7.23 we do find separation while ℓ tends to zero like $\ell \sim \sqrt{\bar{x}_{sep}-\bar{x}}$. This is the type of singularity discussed by Goldstein (ref. 13) which always seems to occur when boundary layer calculations are performed for arbitrarily prescribed pressure distributions. For b=7.23 separation is predicted at $\bar{x}$=47.2% with a finite value of $\frac{d\ell}{d\bar{x}}$ at separation. Apparently the real flow adjusts itself such that the Goldstein singularity can be prevented. It should be remarked that the behaviour for b>7.23 is very similar to what Schubauer found when applying Pohlhausen's method to the measured pressure distribution for an elliptic cylinder with observed laminar separation. Later, Hartree (ref. 14) using an accurate numerical method could only find separation when slightly modifying the observed pressure distribution. It is still an open question whether indeed a small experimental error in Schubauer's experimental results is responsible for the failure to predict separation or that small errors inherent in the boundary layer approximation and the neglect of the longitudinal surface curvature are responsible for it.

It is instructive to invert the present calculation method to find out to what extent the pressure distribution should be modified to produce a noticeable shift in the separation position. The full curves in fig. 8 give the values of ℓ (for b=7.23) and the values of $\bar{U}$ and $\frac{d\bar{U}}{d\bar{x}}$ in the neighbourhood of the separation point for the same case as was shown in fig. 7. The dotted curve for ℓ represents an arbitrarily modified shear stress distribution for x>45% producing separation at 46%. The dotted curves for $\bar{U}$ and $\frac{d\bar{U}}{d\bar{x}}$ indicate the modifications which have to be made to the pressure distribution to produce the changed wall shear stress. These modifications are certainly within experimental error. Hence an important conclusion must be that the accuracy to be obtained in the prediction of laminar separation may depend more on the accuracy of the pressure distribution data than on the level of sophistication of the calculation method.

3. SOME OBSERVATIONS ON THE CHARACTERISTICS OF THE SEPARATING LAMINAR BOUNDARY LAYER.

Laminar boundary layer calculations for arbitrarily prescribed pressure distributions in general show a singular behaviour at separation, such that τ_o and ℓ tend to zero as the square root of the distance to separation (Goldstein, ref. 13). It was shown in section 2 that this singular behaviour is reproduced by the present method. It was also observed that for a measured pressure distribution the singularity may be pre-

(x) note that x is measured along the surface; hence at the trailing edge we have x>100% c.

vented by a proper choice of b. Therefore it seems possible that the boundary layer equations may remain applicable through separation if only the proper pressure distribution is used. It should be remembered however that very small deviations from this pressure distribution will restore the singular behaviour. Therefore we must refrain from prescribing the pressure distribution in the separation region. But we should prescribe a regular behaviour of some other quantity like τ_o, ℓ or the displacement thickness. A recent example of such a method is given by Carter in ref. 15. It is of course very easy to invert the present method and prescribe a quantity other than the pressure. In fact fig. 8 gave a first example of this procedure where $\ell(x)$ was prescribed rather arbitrarily.

In order to be able to proceed in this direction we should first gather more information about the exact behaviour of the viscous flow near separation. Therefore it is useful to recall here an analytical solution of the Navier-Stokes equations which is valid in a small neighbourhood of the separation point where the inertial forces can be neglected. (See Legendre, ref. 16; Oswatitsch, ref. 17; Batchelor, ref. 18, page 226). It follows that the separation streamline leaves the wall at an angle γ (fig. 1) which is determined by:

$$\tan(\gamma) = -3 \left\{ \frac{\frac{d\tau_o}{dx}}{\frac{\partial p}{\partial x}} \right\}_{sep} \tag{7}$$

The streamlines can easily be calculated once γ is known; they follow from:

$$y^2(x \tan(\gamma) - y) = \text{constant} \tag{8}$$

where x is the distance downstream of separation. For points at which the u-component of the velocity is zero we find $\frac{y}{x} = \frac{2}{3}\tan(\gamma)$ and hence

$$\frac{y_{u=0}}{y_{\psi=0}} = \frac{2}{3} \tag{9}$$

The pressure gradient vector is at an angle $\frac{1}{3}\gamma$ with the wall and hence for shallow bubbles where γ is small the pressure gradient normal to the wall is small so that the boundary layer equations might still give a reasonable result.

If we start from the boundary layer equations and assume small values of u and v we can also arrive at the results (7) and (9). Here it is assumed a priori that $\frac{\partial p}{\partial x}$ is independent of y. The result (9) also follows from the expression for the velocity profile in the form:

$$\frac{u}{U} = \ell \frac{y}{\theta} + \tfrac{1}{2} m \left(\frac{y}{\theta}\right)^2 \tag{10}$$

which is valid for a sufficiently small neighbourhood of the wall, not necessarily near the separation point. From (10) it follows that:

$$\frac{\psi}{U\theta} = \tfrac{1}{2}\ell \left(\frac{y}{\theta}\right)^2 + \frac{1}{6} m \left(\frac{y}{\theta}\right)^3 \tag{11}$$

and hence

$$g = \frac{y_{\psi=0}}{\theta} = \frac{-3\ell}{m}\ ;\ \frac{y_{u=0}}{\theta} = \frac{-2\ell}{m}\ ;\ \frac{y_{u=0}}{y_{\psi=0}} = \frac{2}{3} \tag{12}$$

An analogous behaviour is shown for solutions with reversed flow of the Falkner-Skan equation

$$F''' + FF'' + \beta(1 - F'^2) = 0 \tag{13}$$

This equation describes the similar solutions corresponding to the pressure distribution

$$U = u_1 x^{m_1} \tag{14}$$

where u_1 and m_1 are constants.

In (13) F is the non-dimensional streamfunction, primes denote differentiation w.r.t. non-dimensional y; β is the pressure gradient parameter related to m_1 by

$$\beta = \frac{2 m_1}{m_1 + 1} \tag{15}$$

For $\beta > 0$ equation (13) only allows solutions with positive skin friction; for $0 > \beta > -.198838$ solutions with positive and negative skin friction are possible; $\beta = -0.198838$ represents the separation solution.

Extensive tables of solutions with positive skin friction may be found in ref. 19. Some of the reversed flow solutions have been calculated first by Stewartson (ref. 20). Table 1 gives some of the author's own improved results.

It follows from this table that with a good approximation $\frac{y_{u=0}}{y_{\psi=0}} = 2/3$ and $g = \frac{y_{\psi=0}}{\theta} = -\frac{3\ell}{m}$ as for the velocity profile (10). It should be noted that at the end of the table, corresponding to velocity profiles which are found far downstream in a separation bubble, extremely large values of the shape factor H occur. This is due to the strong increase in δ^* which in turn follows from the thick region with reversed flow. Because

the velocities in the separated region remain very small it may be expected that Eq. (8) remains valid within a separation bubble at appreciable distances downstream of separation. This is illustrated by fig. 9 in which a smoke picture of a separation bubble is compared to results of a calculation using Eq. (8). It should be noted that the streamlines can only be calculated when γ is known. In this case the value of γ was taken from the smoke picture.

In ref. 21 it was shown from an extensive empirical investigation that for a wide variety of separated flows it was possible to represent γ by the following simple empirical relation:

$$\tan(\gamma) = \frac{B}{\left(\frac{U\theta}{\nu}\right)_{sep}} \tag{16}$$

where B assumed values between 15 and 20. Later, Wortmann used the relation:

$$B = 64\,|P| \tag{17}$$

where P is Gasters pressure gradient parameter for separation bubbles. It should be mentioned here already that our own new series of measurements to be discusse in section 8 is in agreement with (16) for B=15 to 20 but it does not confirm Wortmann's relation (17). Therefore, in the present paper, we will stick to (16) awaiting clarification of the discrepancy.

Comparing the theoretical result (7) and the empirical result (16) it follows that separating flows apparently adjust itself such that at separation the following relation is satisfied

$$\tan(\gamma) = \frac{B}{\left(\frac{U\theta}{\nu}\right)_{sep}} = \frac{-3\left(\frac{d\tau_o}{dx}\right)_{sep}}{\left(\frac{\partial p}{\partial x}\right)_{sep}} \tag{18}$$

Assuming $\frac{\partial p}{\partial y} = 0$ and using Bernoulli's law and the definitions of ℓ and m it follows that

$$\left(\frac{d\ell}{d\bar{x}}\right)_{sep} = \frac{B\,\frac{d\bar{U}}{d\bar{x}}}{3\,\bar{U}} = \frac{-B\,m_{sep}}{3(\bar{U}\,\bar{\theta}^2)_{sep}} \tag{19}$$

We have seen already that slight modifications of the pressure distribution near separation may correspond to rather drastic changes of the boundary layer characteristics. Hence boundary layer calculations, even when based on a measured pressure distribution, may easily fail to reproduce Eq. (19). However, the calculation method described in section 2 may be inverted to find a corrected pressure distribution which does reproduce Eq. (19). For further details on this method the reader should be referred to ref. 11.

5. CALCULATION OF THE LAMINAR PART OF THE SEPARATED FLOW.

In reference 21 an approximate method for the calculation of the laminar part of the separated flow was introduced. Essential in this method is that the shape of the separation streamline is prescribed instead of the pressure distribution.The pressure distribution then follows from the calculation.In the earlier version of the method m_{sep} was constant and equal to the Hartree value. In order to maintain compatibility with the present method for attached flows, described in section 2, we should make m_{sep} variabel for the separated flow as well.

To introduce this calculation method for separated flow, reference is made to fig. 10 where ℓ and L have been plotted vs. m for the attached as well as the reversed flow solutions of the Falkner-Skan equation. If it is assumed that the curves in fig. 10 would also apply to a non-similar boundary layer developing from a stagnation point (m=-.08547, L=0) via the pressure minimum (m=0, L=.44105) and separation (m=.06815, ℓ=0) downstream into the separated region toward the situation where m=0, ℓ=0, L=0, then it follows that $m = -\frac{\theta^2}{\nu}\frac{dU}{dx}$ shows a maximum at separation. Since at separation L is still positive, it follows from the momentum integral equation that θ^2 is still increasing at separation so that $-\frac{dU}{dx}$ should be decreasing through separation. This leads to an inflexion point in the U vs.x curve slightly upstream of separation. As soon as it is known that there is separation, it is possible to find the separation position by looking for a maximum of m. It can easily be shown from Eqns. (1) and (4) that the condition that m has a maximum at separation leads to:

$$\frac{\bar{U}\,\frac{d^2\bar{U}}{d\bar{x}^2}}{\left(\frac{d\bar{U}}{d\bar{x}}\right)^2} = \frac{.14026+10\,m_{sep}}{m_{sep}} \tag{20}$$

Now, the right hand side of Eq. (20) is only slowly varying with m_{sep} and assumes values between 11 and 12 for the values of b and m_{sep} which are of practical interest ($6<b<8$; $.075<m_{sep}<.15$). Hence the separation

position can be found from $\bar{U}(\bar{x})$ by looking for the value of $\bar{x}$ where the left hand side of Eq. (20) assumes values between 11 and 12. For a number of experiments this gave a very good indication of the separation point. A calculation method for the reversed flow region, which is comparable to that for attached flow described in section 2, could now be developed if also for reversed flows the characteristic parameters L, ℓ and H would be given functions of m/m_{sep}. Since, except for the Stewartson profiles, no exact results for separated flows were available to the author these functions have been "guessed" as follows. For ℓ it was assumed that ℓ is a universal function of m/m_{sep} given by the Stewartson profiles, where m_{sep} follows from the calculation up to the separation point. For L(m) a curve was assumed which is very similar to that for the Stewartson flows namely: tangent to L=a+bm at separation, tangent to the vertical axis at m=0, L=0 (fig. 10) and super-elliptic in between. This leads to:

$$\left(\frac{m_{sep}-m}{m_{sep}}\right)^n + \left(\frac{L-bm}{a}\right)^n = 1 \text{ or } L = bm+a\left\{1-\left(1-\frac{m}{m_{sep}}\right)^n\right\}^{\frac{1}{n}} \qquad (21)$$

where the exponent n was taken equal to the value 1.65 which was found to give a good representation of the Stewartson results. If necessary H can be found from m, ℓ, L and the definition of L.

Since in the separated region the shape of the separation streamline will be prescribed it appears that the proper velocity profile shape parameter is $g = \frac{y_{\psi=0}}{\theta}$. Using the approximation $g = -3\ell/m$ (Eq. 12) and observing that ℓ is assumed to be a universal function of m/m_{sep} it follows that we should use $z=g \times m_{sep}$ where m/m_{sep} is a universal function of z.

The shape of the separation streamline can be prescribed in a number of different ways. In many applications we used a straight separation streamline, leaving the wall at an angle γ given by Eq. (16) with B=15 to 20. Since in most cases the separation streamline is slightly curved upwards in the laminar region (see for instance fig. 9) a better approximation may be obtained by assuming a linear variation of g with x downstream of separation. Since θ is still increasing in the bubble it follows that this leads, together with the linear variation of g, to a separation streamline which is slightly curved upwards. In general the results do not differ much for both cases. It should be remarked that any shape of the separation streamline could be prescribed without difficulty. Summarising, the separated flow can be calculated as follows once m_{sep} and proper starting values for θ and U are given (for instance at separation).

1. Find g from θ and the prescribed shape of the separation streamline.
2. Find m/m_{sep} from the universal relation between $z=g\times m_{sep}$ and m/m_{sep}.
3. Find $\frac{dU}{dx}$ from the first compatibility condition in the form $\frac{dU}{dx} = -m\nu/\theta^2$
4. Find $\frac{d}{dx}\left(\frac{\theta^2}{\nu}\right)$ from the momentum integral relation.
5. Advance a step in x-direction and find new starting values for U and θ, etc.

Full details of the method will be presented in ref. 11; some examples will be given in section 8.

6. PREDICTION OF THE LOCATION OF TRANSITION IN THE SEPARATED FLOW.

For attached flows the position of transition can be predicted by means of a semi-empirical method which is based on the calculation of the amplification of small disturbances in the laminar boundary layer. This method was developed independently by Smith and Gamberoni (ref. 22) and the present author (ref. 23 and 24). In ref. 24 it was shown that the method is also applicable to boundary layers with suction. The idea behind the method is that the calculated amplification ratio of the most critical disturbance at the measured transition position attains nearly always the same value.

At present we are investigating whether this method is also valid for separated flows. This investigation is based on the stability diagrams for some of the Stewartson velocity profiles with reversed flow which have been published recently by Taghavi and Wazzan (ref. 25).

Since these calculations have been restricted to rather low values of R_θ the results have been supplemented by calculating the limiting stability characteristics for $R_\theta \to \infty$ using the inviscid stability equation (Rayleigh equation). These calculations have been performed on one of the hybrid computers of the Delft University Computing Centre.

Both Wazzan's and our own computations were made for the linear stability theory in the spatial mode. This means that in the expression for the streamfunction of the disturbance

$$\psi(x,y,t) = \varphi(y)\, e^{i(\alpha x-\omega t)} \qquad (22)$$

α is complex $= \alpha_r + i\,\alpha_i$ and ω is real. This leads to a factor $e^{-\alpha_i x}$ in the amplitude of the disturbance. Hence the logarithm of the total amplification of a disturbance follows from:

$$\sigma_a = \ln \frac{a}{a_{neutral}} = \int -\alpha_i \, dx \tag{23}$$

Application of the semi-empirical method for the prediction of transition requires the evaluation of Eq. (23) for a range of reduced frequencies $\frac{\omega\nu}{U^2}$ to select the most dangerous frequencies. The available time for the preparation of the present paper did not permit to perform these detailed amplification calculations for the experimentally determined pressure distributions. However, we developed a short-cut method which is thought to provide a reasonably accurate first estimate of the transition position in the separated flow at rather low values of the Reynoldsnumber, where no appreciable amplification occurs prior to separation. This short-cut method will be described in the remainder of the present section. Some examples will be discussed in section 8.

It may be assumed with reasonable accuracy that in the laminar part of the separation bubble θ, U and R_θ are constant and equal to their values at separation. Then constant values of

$\frac{\omega\nu}{U^2} = \frac{\frac{\omega\theta}{U}}{\frac{U\theta}{\nu}}$ also mean constant values of $\frac{\omega\theta}{U}$.

Furthermore it may be assumed that downstream of separation g is proportional to $x-x_{sep}$ with:

$$g = \frac{y_{\psi=0}}{\theta} = \frac{(x-x_{sep})\tan(\gamma)}{\theta} = \frac{(x-x_{sep})}{\theta} \frac{B}{(R_\theta)_{sep}} \tag{24}$$

Hence Eq. (23) may be written as:

$$\sigma_a = \frac{(R_\theta)_{sep}}{B\, m_{sep}} \int (-\alpha_i\theta)\, d(g * m_{sep}) = \frac{(R_\theta)_{sep}}{B\, m_{sep}} \int (-\alpha_i\theta) dz \tag{25}$$

so that the integration with respect to x has been replaced by an integration w.r.t. g. Similarly we can over a short interval upstream of separation, assuming ℓ to be proportional to $x_{sep}-x$, perform the integration w.r.t. ℓ instead of x. Now we make the further assumption that the Reynoldsnumber is so high that the stability characteristics are given with sufficient accuracy by the limiting values determined from the inviscid stability equation. Then $-\alpha_i\theta$ only depends on the value of $\frac{\omega\theta}{U}$ and the profile parameter β or z. Hence the integration w.r.t. z in Eq. (25) can be performed once for all independently of $(R_\theta)_{sep}$ or the pressure distribution for different values of $\frac{\omega\theta}{U}$. A similar result holds for the integration w.r.t. ℓ upstream of separation.

The inviscid instability for different values of β is shown in figs. 11a and 11b. Values of $10^4 \int(-\alpha_i\theta)dz$ are shown in fig. 12 for different values of $\frac{\omega\theta}{U}$ together with the envelope giving the maximum value I of the integral as a function of z. Hence the maximum amplification factor σ_a follows from (25) in the form:

$$\sigma_a = 10^{-4} \frac{(R_\theta)_{sep} I}{B.m_{sep}} \tag{26}$$

Values of z and I for reversed flows may also be found in table 2. According to previous experience with the transition prediction method it may be expected that transition will occur in practice as soon as the calculated value of σ_a exceeds a critical value which is of the order of 10. Assuming a critical value of σ_a (see the last lines of section 8) the transition position may be found as follows. From the known values of $(R_\theta)_{sep}$, m_{sep}, B and the critical value of σ_a we find from Eq. (26) the value of I at which transition will occur. Then table 2 gives the corresponding value of $z=g * m_{sep}$; then Eq. (24) determines the distance between the separation and transition points. A further simplification results when I(z) is replaced by the approximation (see fig. 13):

$$I = 650\sqrt{z} \tag{27}$$

Eq. (27) completely neglects the amplification upstream of separation but is rather accurate for large values of z. Combining Eqs. (26), (27) and (24) it follows that the position of transition x_{tr} follows from:

$$\frac{x_{tr}-x_{sep}}{\theta_{sep}} = \frac{\sigma_a^2\, 10^8\, B\, m_{sep}}{650^2\, (R_\theta)_{sep}} = \frac{237\, \sigma_a^2\, B\, m_{sep}}{(R_\theta)_{sep}} \tag{28}$$

Using as mean values B=17.5; m_{sep}=0.10 and σ_a=14.4 (see section 8) we find:

$$\frac{x_{tr}-x_{sep}}{\theta_{sep}} = \frac{8.6*10^4}{(R_\theta)_{sep}} \tag{29}$$

Equation (29) should only be used instead of (26) for rough calculations; it should be noted that the approximation (27) leads to the unrealistic result that according to Eq. (29) the bubble will only disappear at infinite Reynolds numbers.

7. POSSIBLE METHODS TO PREDICT BURSTING OF THE BUBBLE.

A number of methods may be used to predict whether reattachment of the shear layer will occur downstream of transition. A few of these methods will be briefly described in this section; some experimental checks will be given in section 8.

In ref. 6 Crabtree observed that there seems to be a maximum limit to the pressure rise which a reattaching turbulent shear layer may overcome. From a number of experiments he deduced that the pressure coefficient

$$\sigma = 1 - \left(\frac{U_r}{U_{sep}}\right)^2 \tag{30}$$

is nearly constant for short bubbles about to burst; the constant value he suggested was 0.35. Since it seems better to correlate different experimental results on the pressure rise between transition and reattachment we will use a slightly different coefficient σ_{cr} defined by:

$$\sigma_{cr} = 1 - \left(\frac{U_r}{U_{tr}}\right)^2 \tag{31}$$

If Eq. (30) or (31) is to be used to predict whether reattachment will occur, the value of U_r at the possible reattachment point has to be known. In a first approximation this may be taken from the pressure distribution which would occur without the bubble being present at the position x_{tr}, (the "inviscid pressure distribution").

In ref. 26 Horton gave a method to predict whether and where reattachment may occur. This method is based on the simple criterion that $\left(\frac{\theta}{U}\frac{dU}{dx}\right)_r$ = constant = -.0082 for all reattaching turbulent shear layers.

A simple criterion for bursting was found to be provided by Stratford's zero skin friction limiting pressure distribution, (ref. 27). This is the adverse pressure distribution which a turbulent boundary layer can just negotiate without separation. This limiting pressure distribution curve, starting at the measured transition point T (fig. 1) can at low Reynoldsnumber fail to cross the "inviscid pressure distribution curve". This means that the requested pressure rise is more than the Stratford pressure recovery can provide and hence bursting occurs. For our experimental results on the Wortmann airfoil (section 8) this gave a very good prediction of the bursting Reynoldsnumber.

8. SOME EXPERIMENTAL RESULTS.

Two series of experiments were performed. The first one was on the FX 66-S-196-V1 Wortmann airfoil at an angle of attack of 1 degree in a small 400 x 400 mm windtunnel. The chordlength of the airfoil was 360 mm. The second investigation concerned a 400 mm dia. circular cylinder with a tail (to suppress a fluctuating wake) in the large 1810 x 1250 mm low turbulence windtunnel (model configuration c, ref. 21).

Fig. 14 shows some of the pressure distributions for the airfoil at different Reynoldsnumbers; bursting occurs between R_c=.118 and .099 x 10^6. An extensive series of flow pictures, similar to that shown in fig. 9, was made using the special camera described in ref. 21. Fig. 15 shows a plot of tan(γ)vs.$(R_\theta)_{sep}$; the region of $(R_\theta)_{sep}$ at which bursting occurs is indicated in the figure. It follows that before and after bursting B lies always between 15 and 20.

Gaster's pressure gradient parameter P is shown in the lower half of fig. 16 for the closed bubbles. Extrapolation of this curve to the first value of $(R_\theta)_{sep}$ measured after bursting would give a point beyond Gasters bursting line. It follows that $-.185<P<-.120$ so that Wortmann's relation (Eq. 17) would give $7.7<B<11.8$ which is not in agreement with fig. 15.

The upper half of fig. 16 shows the pressure recovery coefficient between transition and reattachment. It follows that the maximum value of σ_{cr} which is obtained just prior to bursting (0.36) is in good agreement with Crabtree's suggested maximum of 0.35.

Figs. 17 and 18 show the pressure distributions in the region of the bubble for the highest and lowest Reynoldsnumber at which a closed bubble was observed. The curve labelled B=15 is the result of a calculation using the method discussed in section 5 with a straight separation streamline. Results for a linear variation of g and/or B=20 are only slightly different. It is seen that the best fit is obtained at the highest Reynoldsnumber; results for 6 intermediate values of R_c show a gradual change from the results shown in fig. 17 to those of fig. 18. The curves labelled "Horton" indicate the locus of possible reattachment points according to Horton's method. Where this curve crosses the "inviscid pressure distribution" indicated by a dotted curve, a closed bubble is obtained. It follows that Horton's method indicated bursting already in fig. 18. Results for the intermediate Reynoldsnumbers show that bursting is indicated too early by this method. It is possible that a modification of the constants in Horton's method would lead to a better result; this has not been attempted however. The curves labelled Stratford indicate Stratfords limiting pressure

distribution starting from the measured transition point. It follows from fig. 18 that according to this method the bubble is about to burst at $R_c = .118 \times 10^6$; this is in agreement with experimental observation. The length of the laminar part of the bubble is shown in fig. 19 as a function of R_c. The broken curve indicates the predicted length for $\sigma_a = 12.5$ and B=15 using the method of section 6 where I(z) is taken from table 2.

Results similar to those for the Wortmann airfoil have been obtained for the cylindrical model. In this case only closed bubbles have been measured on the cylindrical part. Fig. 20 shows the length of the laminar part of the bubble; included in the figure are calculated curves for B=15 and 20, using the value $\sigma_a = 12.5$ which was found to correlate well the measurements for the airfoil at B=15. It follows that in general the bubble is longer on the cylinder than on the airfoil. From some further calculations, the results of which are not shown in the figures, it follows that for a mean value B=17.5 the value of σ_a is about 11.7 for the airfoil and 14.4 for the cylinder.

Figure 21 shows a comparison of both series of results in the form of $\frac{\Delta x}{\theta}$ vs. $(R_\theta)_{sep}$ where Δx is the length of the laminar part of the bubble and $\theta = \theta_{sep}$. Besides the measured points some calculated curves are shown together with an empirical correlation curve which was given by Vincent de Paul in ref. 28. It follows that the different measurements do not correlate very well so that some other parameter should be of importance. An important difference between our own two series of measurements is that they have been obtained in two different windtunnels. The airfoil was tested in a small tunnel where the noise level, the amount of vibration and possibly the free stream turbulence intensity are much higher than in the large low turbulence tunnel. The large tunnel was very quiet at the low speeds used, while at these low speeds the turbulence level is of the order of .02%. To check whether the noise in the small tunnel could have caused earlier transition, the noise at different speeds was recorded on a tape recorder and reproduced in front of an open window in the test section of the large tunnel. This had a marked effect on transition; the length of the separated region decreased by about 1 degree at high speeds and by about 3 degrees at the lowest speed. The corresponding decrease in $\frac{\Delta x}{\theta}$ ranged from 35 to 50; the value of σ_a which correlates the measurements at B=17.5 decreased from 14.4 for the quiet situation to 13.1 with the noise. (see also fig. 21).

In a further experiment the cylindrical model was subjected to tones recorded from an electronic organ; it proved possible to obtain the same reductions of the distance to transition if only at each speed the proper frequency was used. These frequencies correlated rather well with the dangerous frequencies which can be obtained from fig. 12. Of course there may be other variables like longitudinal surface curvature, mechanical vibrations, free stream turbulence level, etc. which have to be taken into account.

For the time being it is suggested that transition in the bubble can be calculated for "quiet" flows using Eq. (26) and table 2 (section 6) with mean values B=17.5; $\sigma_a = 14.4$; $m_{sep} = 0.10$.

9. REFERENCES.

1. Tani, I.: Low speed flows involving bubble separation. Progr. in Aeron. Sc., Vol 5, p 70-103, Pergamon Press, 1964.
2. Chang, P.K.: Separation of Flow, Pergamon Press, 1970.
3. Young, A.D. and Horton, H.P.: Some results of investigations of separation bubbles. In: AGARD CP4 Separated Flows, 1966, part 2, p 779-811.
4. Gaster, M.: The structure and behaviour of laminar separation bubbles. In: AGARD CP4, Separated Flows, 1966, part 2, p 813-854.
5. Brown, S.N. and Stewartson, K.: Laminar separation. In: Annual Review of Fluid Mechanics, vol 1, Palo Alto, Annual Reviews Inc., 1969, p 45-72.
6. Crabtree, L.F.: The formation of regions of separated flow on wing surfaces. R and M 3122, 1959.
7. Thwaites, B.: Approximate calculation of the laminar boundary layer. Aeron. Quart, 1, p 245-280, 1949.
8. Head, M.R. An approximate method of calculating the laminar boundary layer in two-dimensional incompressible flow. R and M 3123, 1959.
9. Stratford, B.S.: Flow in the laminar boundary layer near separation. R and M 3002, 1957.
10. Curle, N. and Skan, S.W.: Approximate methods for predicting separation properties of laminar boundary layers. Aeron. Quart, 8, p 257-268, 1957. See also: Curle, N.: The estimation of laminar skin friction, including the effects of distributed suction. Aeron. Quart, 11, p 1-21, 1960.
11. Ingen, J.L. van: (a report on the method for calculating the separating laminar boundary layer, discussed in the present paper). To be published in the series of VTH-reports of the Dept. of Aeron.-Eng., Delft University of Technology.
12. Terrill, R.M.: Laminar boundary layer flow near separation with and without suction. Phil. Trans. A 253, 1960, p 55-100.
13. Goldstein, S.: On laminar boundary layer flow near a position of separation. Quart. J. Mech. Appl. Math. Vol 1, 1948, p 43-69.
14. Hartree, D.R.: The solution of the equations of the laminar boundary layer for Schubauer's observed pressure distribution for an elliptic cylinder. R and M 2427, 1939.
15. Carter, J.E.: Solutions for laminar boundary layers with separation and reattachment. AIAA Paper 74-583, 1974.

16. Legendre, R.: Décollement laminaire régulier. Comptes Rendus 241, 1955, p 732-734.
17. Oswatitsch, K.: Die Ablösungsbedingung von Grenzschichten. In: Grenzschichtforschung/Boundary layer research. IUTAM Symposium, Freiburg / Br. 1957, Springer Verlag 1958, p. 357-367.
18. Batchelor, G.K.: An introduction to fluid dynamics, Cambridge Univ. Press, 1970.
19. Smith, A.M.O.: Improved solutions of the Falkner-Skan boundary layer equation. Sherman M. Fairchild Fund Paper FF-10, Inst. Aero. Sci. 1954.
20. Stewartson, K.: Further solutions of the Falkner-Skan equation. Proc. Cambr. Phil. Soc, 50, p 454-465, 1954.
21. Dobbinga, E., Ingen, J.L. van, Kooi, J.W.: Some research on two-dimensional laminar separation bubbles. AGARD CP-102, paper nr. 2, Lisbon 1972.
22. Smith, A.M.O. and Gamberoni, N.: Transition, pressure gradient and stability theory. Report ES 26388, Douglas Aircraft Co., 1956.
23. Ingen, J.L. van: A suggested semi-empirical method for the calculation of the boundary layer transition region. Report VTH-74, Dept. of Aeron. Eng., University of Technology Delft, 1956.
24. Ingen, J.L. van: Theoretical and experimental investigations of incompressible laminar boundary layers with and without suction. Report VTH-124, Dept. of Aeron. Eng., University of Technology Delft, 1965.
25. Taghavi, H. and Wazzan, A.R.: Spatial stability of some Falkner-Skan profiles with reversed flow. Physics of Fluids, Vol. 17, no 12, Dec. 1974, p 2181-2183.
26. Horton, H.P.: A semi-empirical theory for the growth of laminar separation bubbles. A.R.C.-CP 1073, 1967.
27. Stratford, B.S.: The prediction of separation of the turbulent boundary layer. Journal of Fluid Mechanics, Vol 5, pt 1, January 1959, p 1-16.
28. Vincent de Paul, M.: Prevision du decrochage d'un profil d'aile en écoulement incompressible. Paper nr. 5 in AGARD, CP-102, Lisbon 1972.
29. Wortmann, F.X.: Ueber den Ablösewinkel laminarer Ablöseblasen,. DLR-FB-74-62, 1974.
30. Wortmann, F.X.: The quest for high lift. AIAA paper 74-1018, 1974.

ACKNOWLEDGEMENT.

The author is indebted to many persons who in one way or another assisted in the investigations reported in this paper.
The technical staff of the Department of Aeronautical Engineering gave their able assistance during the preparation and execution of the experimental stages of the work. Especially Mr. P. Smit should be thanked for his continuous technical support.
Ir. J.J.H. Blom gave his expertness in obtaining and interpreting surface oil film patterns to determine positions of separation and reattachment. Ir. E. Dobbinga should be thanked for his perseverance to obtain smoke pictures of the highest quality.
Mr. R. Llurba of the Delft University Computing Centre performed the hybrid computations leading to figs. 11a and 11b.
Finally prof. A.R. Wazzan should be thanked for sending an advance copy of ref. 25 and some tabular material related to his paper.

TABLES

β	ℓ	m	H	L	$\frac{y_{u=0}}{y_{\psi=0}}$	$g=\frac{y_{\psi=0}}{\theta}$	$-\frac{3\ell}{m}$
-.198838	0	.06815	4.029	.8218	.667	0	0
-.18	-.0545	.05601	5.529	.7343	.667	2.917	2.920
-.10	-.0545	.01503	12.625	.3308	.678	10.665	10.000
-.05	-.0258	.00283	28.096	.1190	.698	25.748	27.350
-.025	-.0106	.00051	59.821	.0418	.721	56.478	62.353

Table 1: Some results for reversed flow solutions of Eq. (13)

β	$z=g_{sep}$	I
-.198838	0	127
-.198	.042	145
-.197	.061	154
-.195	.088	167
-.190	.134	190
-.180	.199	225
-.160	.307	285
-.150	.360	315
-.140	.420	348
-.120	.556	422
-.100	.682	483
-.075	1.107	659
-.050	1.864	883
-.025	4.249	1331

Table 2: z and I as a function of β for reversed flows.

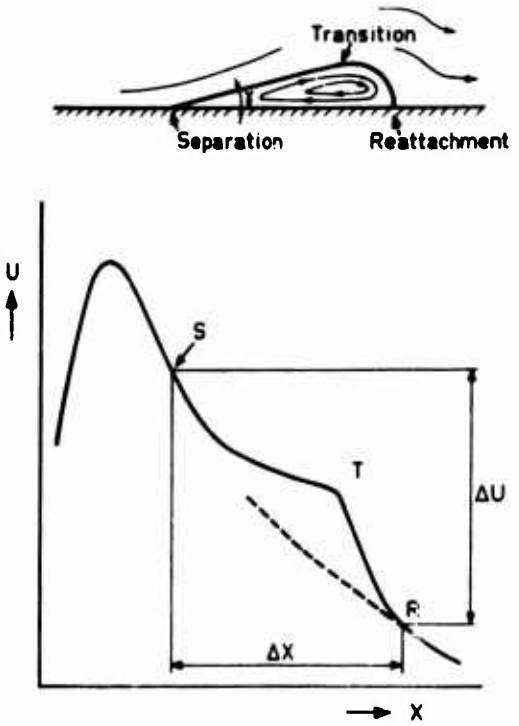

Fig. 1: Schematic diagram of flow field and pressure distribution in a laminar separation bubble.

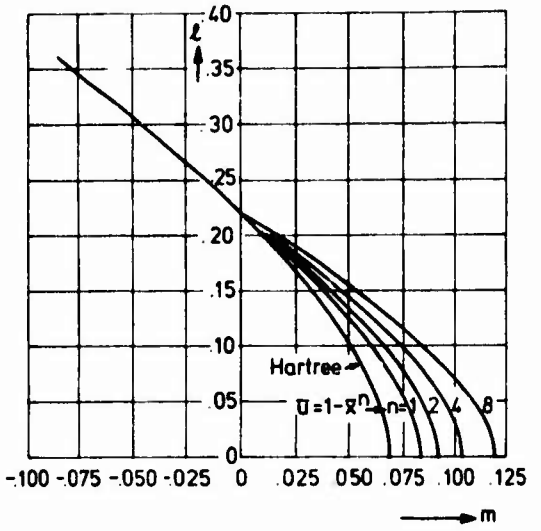

Fig. 2: ℓ(m) for some special exact solutions of the boundary layer equations.

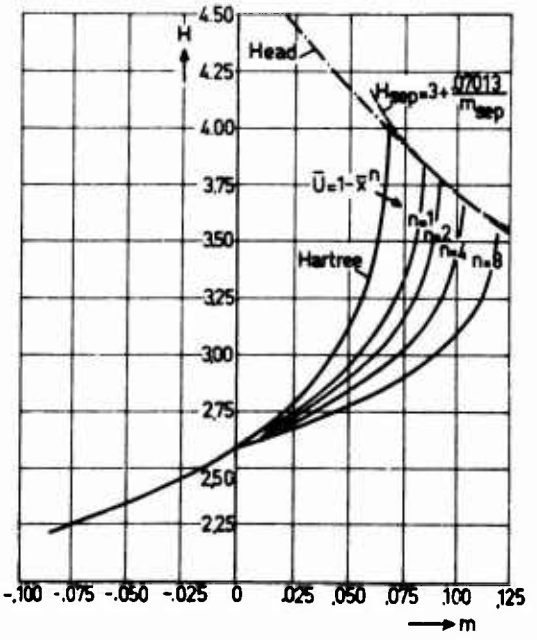

Fig. 3: H(m) for some special exact solutions of the boundary layer equations.

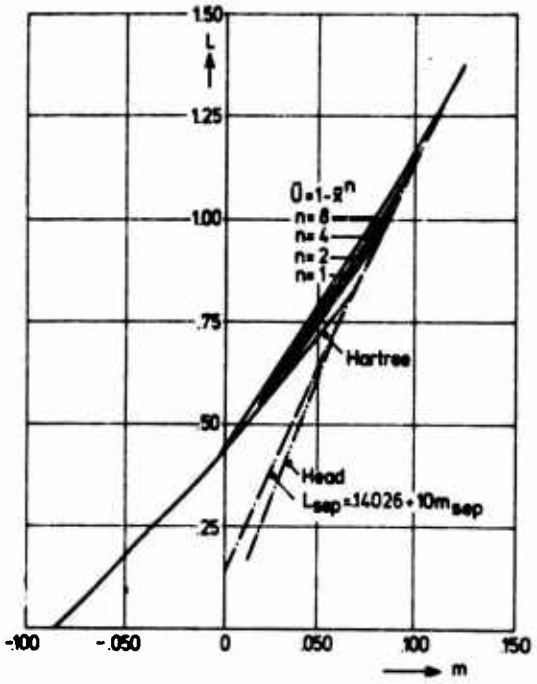

Fig. 4: L(m) for some special exact solutions of the boundary layer equations.

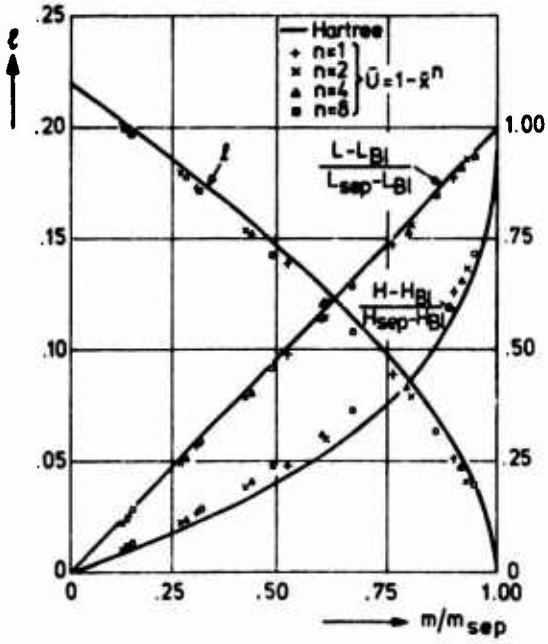

Fig. 5: ℓ(m), H(m) and L(m) in normalised form for some special exact solutions of the boundary layer equations (m>0).

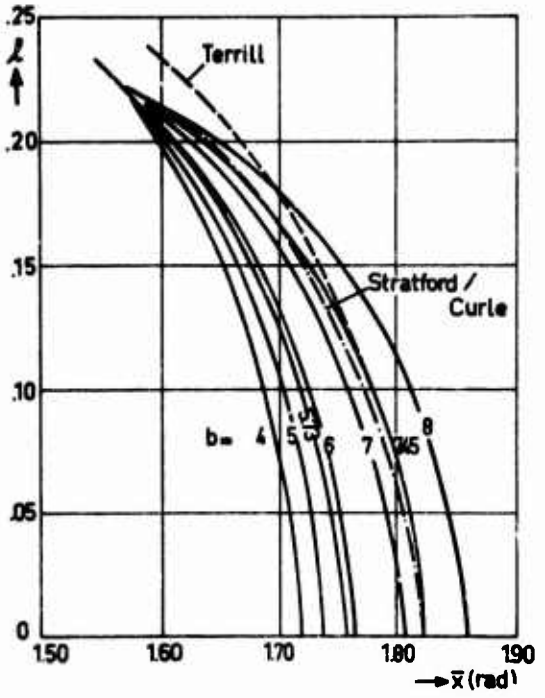

Fig. 6: Some results of the present method for the potential flow pressure distribution for a circular cylinder $\bar{U}=\sin(\bar{x})$ compared to the results according to Terrill (ref. 12) and Curle/Skan (ref. 10).

Fig. 7: $\bar{U}$ (uppercurve) and ℓ (lower curves) for the Wortmann airfoil; $R_c=.638 \times 10^6$, $\alpha=1^o$.

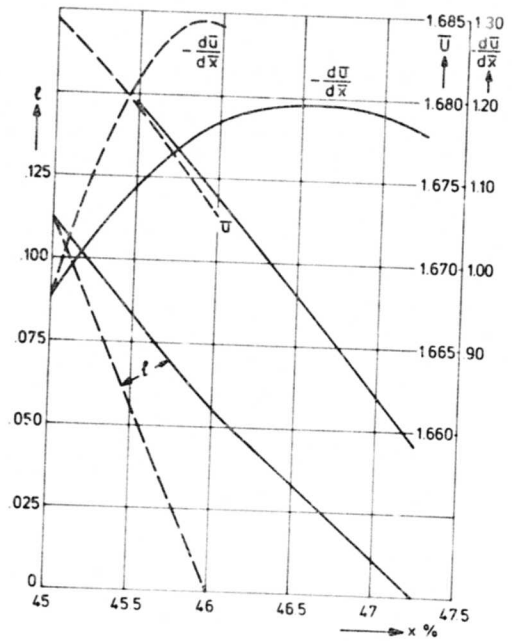

Fig. 8: Modification of the pressure distribution which is required to produce a given change in $\ell(x)$. Wortmann airfoil: b=7.23; $R_c = .638 \times 10^6$; $\alpha = 1^o$; for x<45% same $\bar{U}$ and ℓ as in fig. 7.

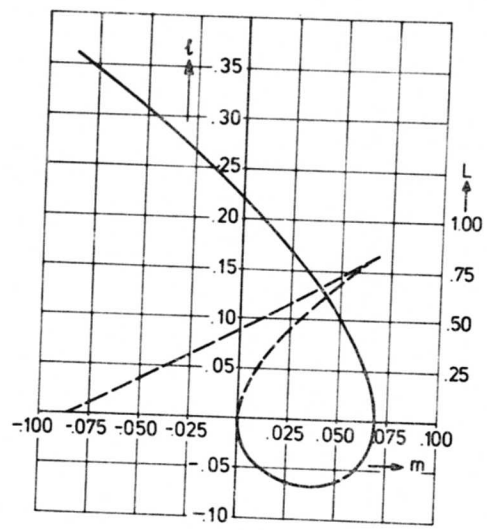

Fig. 10: $\ell(m)$ ——— and L(m)----- for Hartree's and Stewartson's solutions of the Falkner-Skan equation.

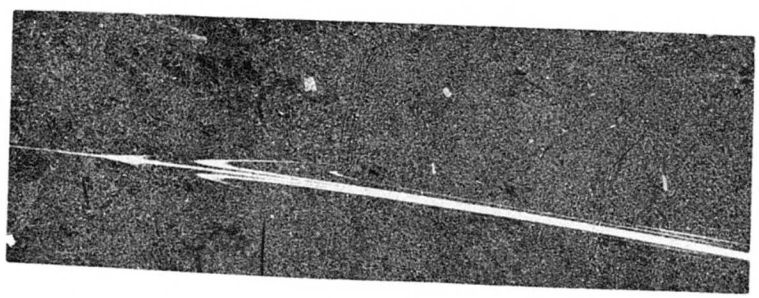

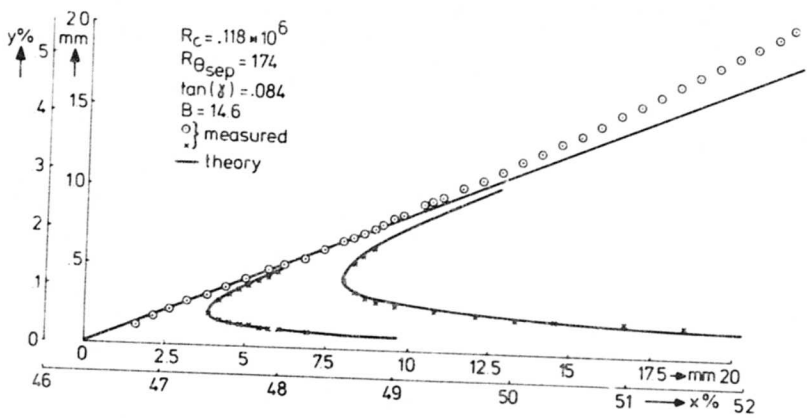

Fig. 9: One of the smoke pictures obtained for the Wortmann airfoil and comparison with Eq. (8).

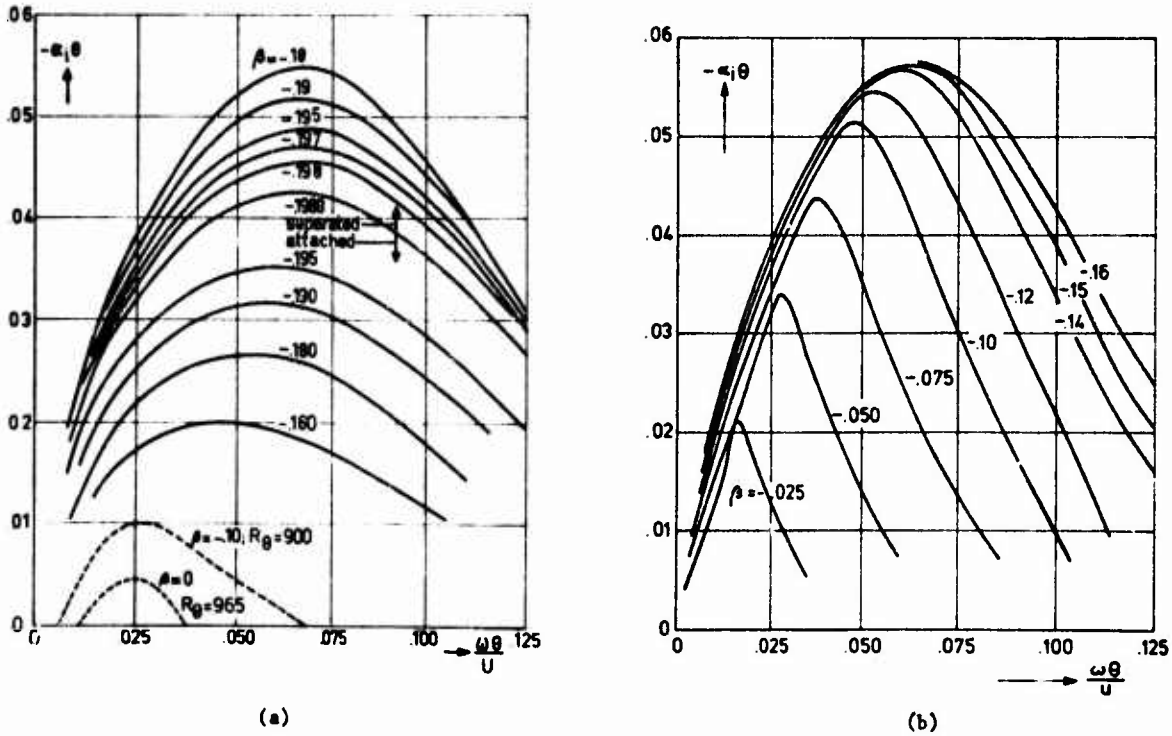

(a) (b)

Fig. 11 a and b: Inviscid instability for Hartree's and Stewartson's velocity profiles. For β=0 and -.10 the inviscid instability becomes very small. For comparison the viscid instability is shown for R_θ of the order of 1000.
(a) attached and separated flows.
(b) separated flows.

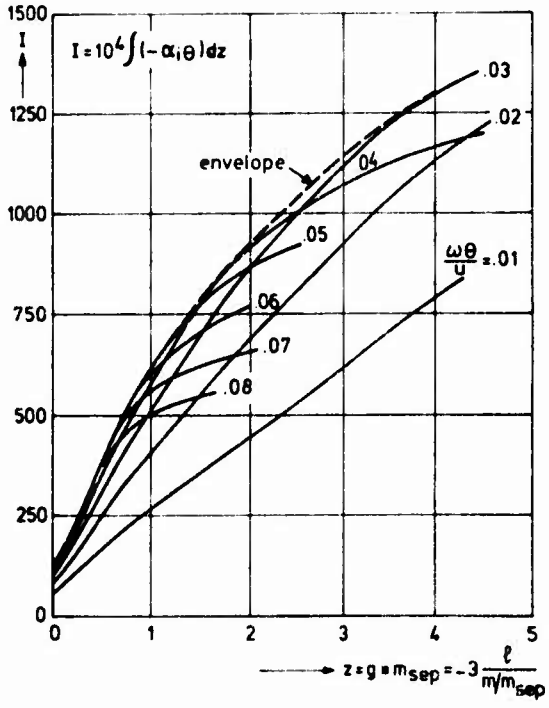

Fig. 12: Normalised amplification integral; see Eq. (25).

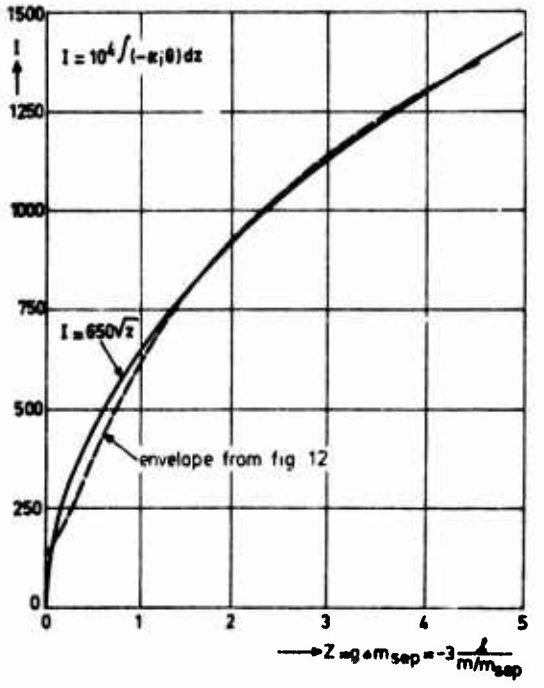

Fig. 13: Approximation to the amplification integral.

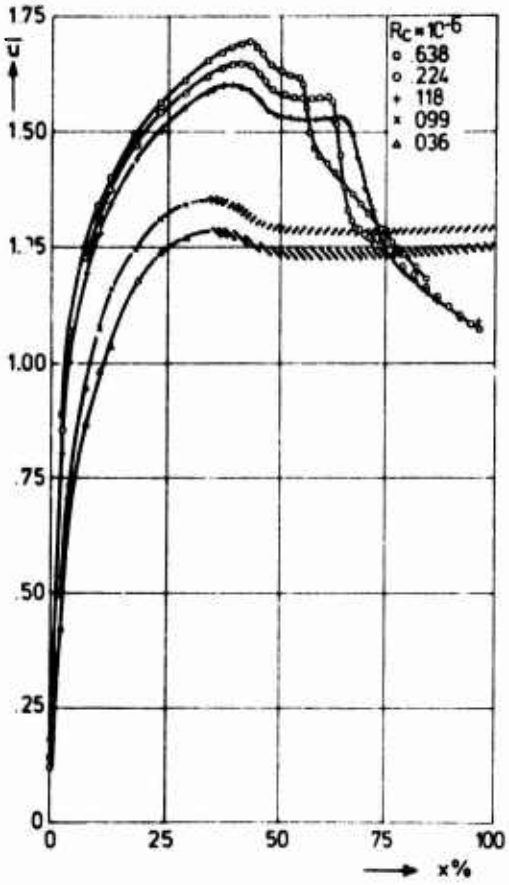

Fig. 14: Some of the measured pressure distributions for the Wortmann airfoil (for $R_c \leq .099 \times 10^6$ the bubble bursts).

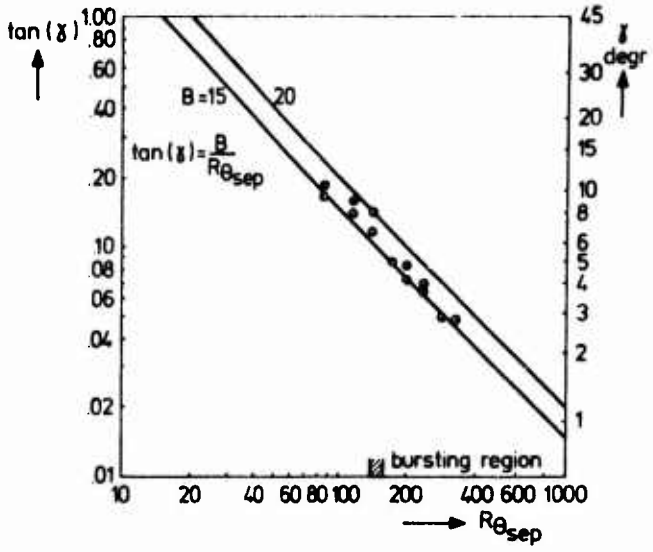

Fig. 15: $\tan(\gamma)$ vs. $R\theta_{sep}$ for the Wortmann airfoil.

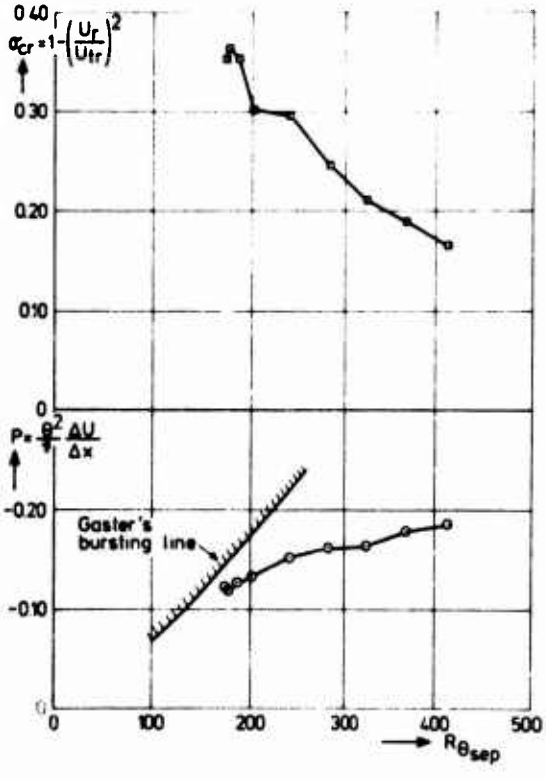

Fig. 16: Pressure recovery coefficient σ_{cr} (Eq. 31) and Gasters pressure gradient parameter for closed separation bubbles on the Wortmann airfoil.

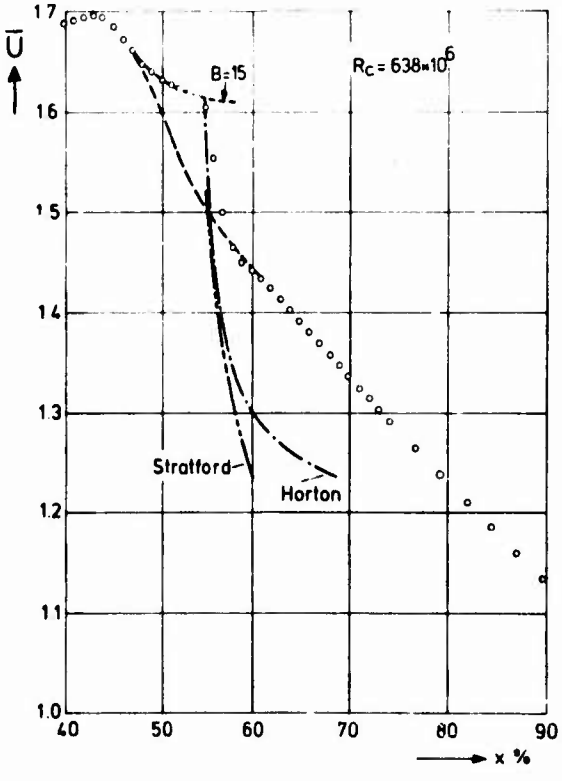

Fig. 17: Some results for the Wortmann airfoil at $R_c = .638 \times 10^6$.

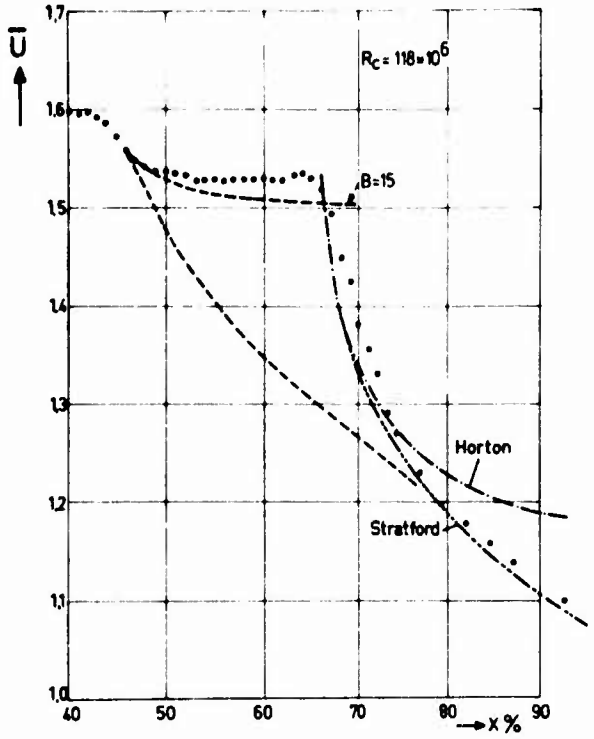

Fig. 18: Some results for the Wortmann airfoil at $R_c = .118 \times 10^6$.

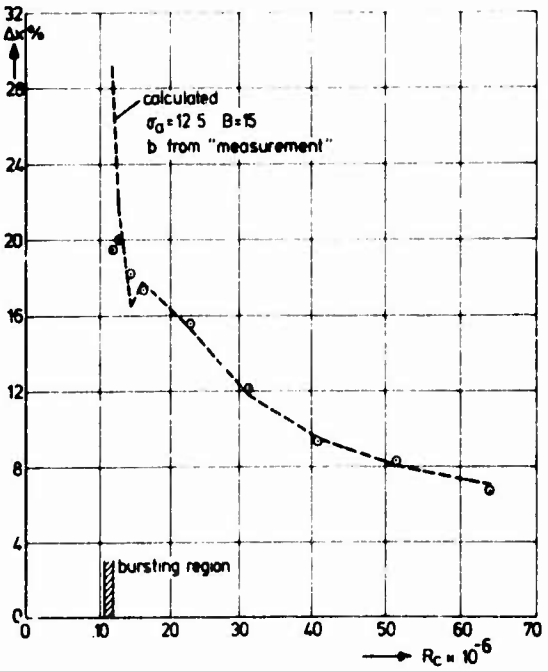

Fig. 19: Length of the laminar part of the separation bubble on the Wortmann airfoil.

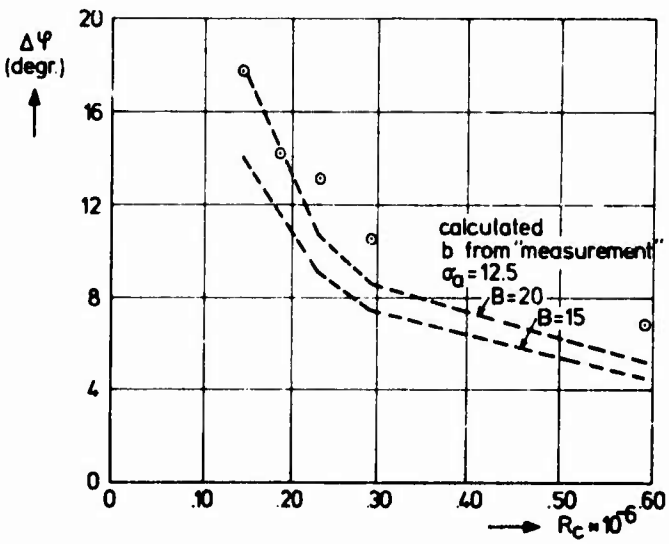

Fig. 20: Length of the laminar part of the separation bubble on the circular cylinder with tail.

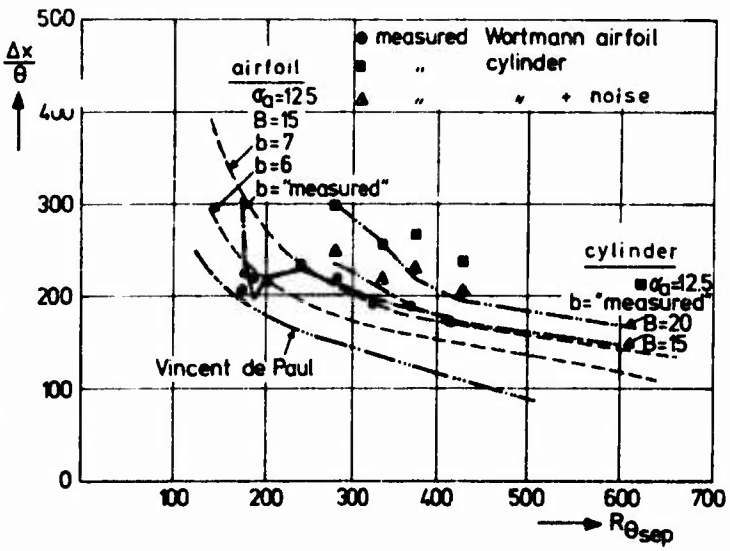

Fig. 21: $\Delta x/\theta_{sep}$ as function of $(R_\theta)_{sep}$ Measured points for the Wortmann airfoil (●) and the cylinder with (▲) and without (■) extra noise. Curve labelled "Vincent de Paul" denotes the correlation curve used in ref. (28).

DÉCOLLEMENT TURBULENT EN ÉCOULEMENT BIDIMENSIONNEL

par Maurice SIRIEIX

Office National d'Etudes et de Recherches Aérospatiales (ONERA)
92320 CHATILLON - France

- RESUME -

Après avoir défini les caractères généraux des zones décollées turbulentes et discuté notamment la réalité physique d'écoulements strictement bidimensionnels, les trois problèmes fondamentaux qui apparaissent lors de l'analyse expérimentale détaillée d'une zone décollée : décollement, recollement, couplage sont successivement abordés de manière à mettre en évidence les principaux facteurs d'influence qui régissent ces phénomènes et dépendent de la nature subsonique, transsonique ou supersonique de l'écoulement.

Une revue rapide des méthodes de prévision actuellement disponibles termine cet exposé.

TURBULENT TWO-DIMENSIONAL SEPARATION -

- ABSTRACT -

The general features of separated turbulent flow regions are defined and in particular a discussion is made on the physical reality of strictly two-dimensional turbulent flows.

The three fundamental problems which occur in the detailed experimental analysis of a separated zone, i.e : separation, reattachment and coupling, are considered successively and the main factors of influence which rule these phenomena according to the subsonic-transonic-supersonic nature of the flow are presented.

Lastly, a rapid review of the methods of prediction currently available is made.

NOTATIONS.

b	: épaisseur du bulbe de décollement.
C_f	: coefficient de frottement pariétal.
C_p	: " pression.
C_q	: " débit généralisé.
Fc	: fonction correctrice de paroi.
$\mathcal{F}$	: " de corrélation pour le décollement libre.
h	: hauteur d'une excroissance de paroi.
H	: rapport d'épaisseurs ($H = \delta^*/\delta^{**}$).
H_{inc}	: paramètre de forme incompressible.
H_i	: $= i / H_{inc}$
i	: quantité de mouvement injectée.
L	: longueur de développement du mélange et échelle caractéristique du décollement.
ℓ	: longueur de mélange et étendue du domaine d'interaction.
M	: nombre de Mach.
M_p	: " à la paroi.
p	: pression.
$\langle p \rangle$	: valeur efficace de la fluctuation de pression.
p_d	: pression au décollement.
p_R	: pression au recollement.
P	: nombre de pression de Busemann.
q	: débit massique injecté dans l'eau morte et pression dynamique.
R	: distance à l'axe en écoulement de révolution et rayon de courbure d'une ligne de courant.
R_δ, R_x	: nombre de Reynolds.
T_p	: température de paroi.
T_f	: température de frottement.
T_r	: " référence.
u	: composante longitudinale de la vitesse moyenne.
u'	: fluctuation de vitesse.
$\hat{u}$	: vitesse à la frontière de la sous-couche limite.
u_1, u_e	: vitesse à la frontière de la zone dissipative.
V	: module du vecteur vitesse.
x	: abscisse.
x_0	: abscisse de l'origine fictive du mélange
x_1	: " " de l'interaction.
X_R	: longueur du bulbe décollé.
y	: ordonnée.
α	: inclinaison de la paroi.
β	: angle de la rampe.
δ	: épaisseur de la couche dissipative.
δ^*	: " déplacement.
δ^{**}	: " quantité de mouvement.
$\hat{\delta}$	: " la sous couche limite.
$\delta_1, \delta_1^*, \delta_1^{**}$	: valeurs de δ, δ^* et δ^{**} à l'origine de l'interaction.
Φ	: fonction de dissipation.
λ	: allongement du bulbe décollé.
τ_t	: frottement turbulent apparent.
ρ	: masse spécifique.
σ	: paramètre de mélange turbulent.
ψ	: angle de recollement.
θ	: direction du vecteur vitesse.

- INTRODUCTION -

L'intérêt qui est porté au décollement d'une couche limite turbulente peut être motivé soit par des considérations utilitaires liées à la réduction des performances que cette circonstance peut entrainer, soit encore, d'un point de vue plus fondamental par la recherche des phénomènes qui caractérisent les écoulements séparés.

Ces deux points de vue se rejoignent d'ailleurs lorsque le constructeur prend conscience que pour maitriser les problèmes de décollement, il est nécessaire d'entreprendre des expériences de base permettant de préciser ces phénomènes et de définir les facteurs qui conditionnent l'apparition et le développement des zones décollées.

C'est dans cette perspective que nous nous efforcerons de placer cet exposé en mettant l'accent non seulement sur les résultats de ces recherches mais également sur les difficultés de nature expérimentale rencontrées.

L'intérêt des expériences de qualité ne nous parait pas compromis mais renforcé par le développement récent et très rapide des méthodes de calcul numériques. L'avènement d'ordinateurs puissants, assurant une réduction considérable des temps de calcul est à l'origine de ce développement, la résolution des équations convenablement modélisées du mouvement turbulent étant actuellement à notre portée dans le cas bidimensionnel. Cette démarche ne peut être menée à bien que par une coopération étroite entre le calcul et l'expérience le rôle de cette dernière étant de fournir, par une analyse fine, des moyens de contrôle très détaillés en même temps que les informations nécessaires à la mise en oeuvre du calcul, notamment en ce qui concerne la structure de la turbulence et sa modélisation.

1 - CARACTERES GENERAUX DES ZONES DECOLLEES TURBULENTES PSEUDO-BIDIMENSIONNELLES -

1.1 - Ecoulements bidimensionnels : réalité ou fiction ?

L'existence physique de tels écoulements est loin d'être confirmées dans de nombreuses circonstances, aussi bien par l'analyse de la structure intime des phénomènes dissipatifs que par l'examen des effets résultants de la nécessaire limitation transversale de l'écoulement en soufflerie.

Dans le cas d'un montage intéressant toute la largeur de la veine d'essai et soumis sans précautions particulières à l'influence des couches limites se développant sur les parois latérales de cette veine, des effets tridimensionnels marqués apparaissent comme le montrent les exemples suivants :

Le premier emprunté à Green concerne l'étude de l'interaction couche limite - onde de choc [1].

La visualisation pariétale met en évidence, dans le cas de décollements étendus, une structure tridimensionnelle complexe dont l'interprétation extraite de [1] est donnée figure 1. On observe une ligne de recollement très incurvée associée à deux tourbillons séparés par une distance égale aux 2/3 environ de l'envergure du montage.

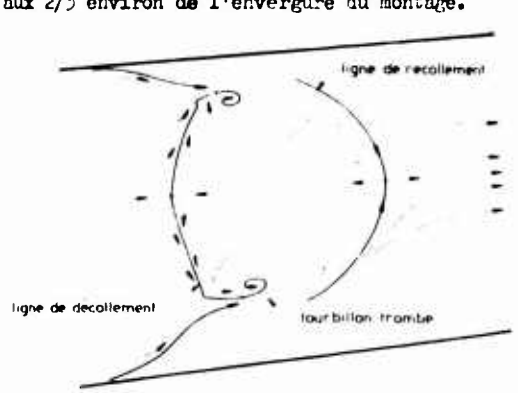

Fig. 1 — Interaction couche limite - onde de choc Visualisation pariétale (Green).

Une observation analogue est présentée par Reda et Murphy [2], qui ont de surcroit montré que l'apparition et le développement initial d'une zone décollée, sous l'effet d'un choc incident d'intensité croissante, est un phénomène de nature typiquement tridimensionnelle, malgré la présence d'un écoulement raisonnablement uniforme en amont de la réflexion tant en ce qui concerne l'épaisseur que le profil de vitesse moyenne de la couche limite. Ces mêmes auteurs, ont tenté de minimiser ces effets par une diminution importante de l'épaisseur des couches limites latérales, en aménageant une fausse paroi, mince, dégagée de la couche limite naturelle, dont le bord était situé à une distance faible du domaine étudié mais suffisante pour que soient établies des couches limites turbulentes.

Les résultats obtenus ont été décevants, les effets tridimensionnels demeurant extrêmement importants [3].

Le second exemple choisi concerne le recollement turbulent d'un écoulement incompressible en aval d'une marche descendante [4]. Dans ce cas, la ligne de séparation est géométriquement fixée et l'écoulement est bidimensionnel à l'extérieur des couches limites latérales.

Le recollement se produit sur une paroi d'inclinaison α variable, en présence d'un écoulement général accéléré ($\alpha > 0$) ou ralenti ($\alpha < 0$).

On observe une variation sensible en envergure de l'étendue longitudinale X_R du bulbe décollé, spécialement pour les valeurs négatives de α, lorsque l'allongement $\lambda = b/X_{R_0}$ de ce bulbe diminue (fig. 2).

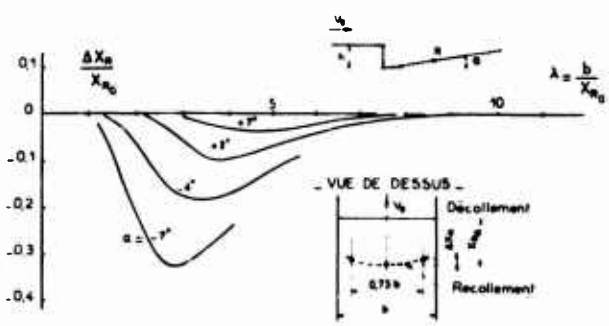

Fig. 2 — Influence de l'allongement sur l'uniformité transversale du recollement.

L'écart maximal $\Delta X_R / X_{R_0}$ enregistré peut atteindre 30 % pour un allongement λ de l'ordre de 3 et dans le cas le plus défavorable ($\alpha = -7°$).

Bien que l'incurvation de la ligne de recollement décroisse rapidement lorsque λ devient très faible, cette circonstance ne constitue plus un critère suffisant de validité. Les résultats obtenus dans ce cas sont très différents de ceux qui sont enregistrés lorsque λ est important, spécialement en ce qui concerne l'évolution longitudinale des pressions dans l'axe du montage ; l'intérêt de réaliser des configurations de zones décollées de grand allongement apparait ici de façon très claire.

Ces différents exemples n'ont pas été donnés dans l'intention de nier l'existence de zones décollées à caractère essentiellement bidimensionnel mais d'attirer l'attention sur la nécessité d'un examen très approfondi des conditions d'essais.

Parmi les remèdes proposés pour diminuer les effets dus à la limitation transversale de l'écoulement, nous signalerons le contrôle des couches limites latérales, en particulier par aspiration, qui conduit à des résultats spectaculaires [31].

Toutefois la méthode probablement la plus satisfai-

sante est celle qui consiste à étudier des configurations axisymétriques pour lesquelles la distance à l'axe R est très grande devant l'épaisseur moyenne δ^* des couches décollées.

C'est cette voie qui a été notamment explorée par Roshko [5 - 6], Bogdonoff [7] et Rose [8].

L'analyse détaillée de telles configurations ne fait pas apparaître d'effets tridimensionnels marqués analogues à ceux que nous avons présentés, l'uniformité transversale étant bien respectée. Cependant, même dans les cas les plus favorables, il n'en demeure pas moins, d'un point de vue très fondamental, que des effets tridimensionnels plus subtils existent dans les zones décollées.

C'est ce que montre par exemple la visualisation pariétale au voisinage d'une ligne moyenne de recollement effectuée par Roshko [6], visualisation qui met en évidence (fig. 3) une structure fine et périodique de nature tridimensionnelle.

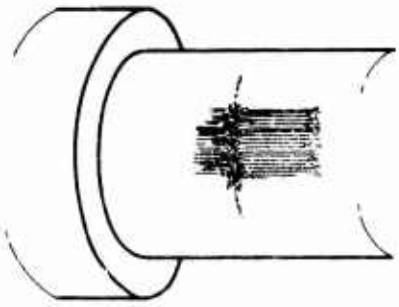

Fig. 3 – Visualisation pariétale dans un recollement turbulent axisymétrique.

Sans pour autant remettre en cause l'existence d'un schéma bidimensionnel moyen, une analyse détaillée de ces phénomènes tant sur le plan théorique qu'expérimental parait souhaitable.

1.2 – Caractères instationnaires propres aux zones décollées –

Le second point que nous aborderons maintenant concerne les aspects instationnaires liés à la formation de zones turbulentes décollées. Nous exclurons toutefois les problèmes spécifiques du décollement instationnaire.

Deux effets peuvent en gros être détectés :

a) d'une part ceux qui découlent de la nature turbulente des couches dissipatives ;

b) d'autre part ceux qui peuvent être attribués aux instabilités existant au niveau du décollement et du recollement et au couplage qu'elles entraînent par suite de l'étroite dépendance de ces deux phénomènes.

Dans le cas où l'écoulement est subsonique l'analyse effectuée par Mabey [9] permet de définir l'importance de ces effets à partir d'un examen détaillé des fluctuations des pressions pariétales.

Dans tous les cas traités qui couvrent une grande variété de configurations, l'évolution longitudinale du niveau des fluctuations $\langle p \rangle / q$ présente une allure triangulaire caractéristique dont le sommet est situé sensiblement au niveau du recollement (fig. 4).

Cette intensité maximale évolue avec la configuration étudiée ; elle se situe en moyenne entre 0,04 et 0,06 et atteint une valeur maximale très importante de l'ordre de 0,1 dans le cas du décollement

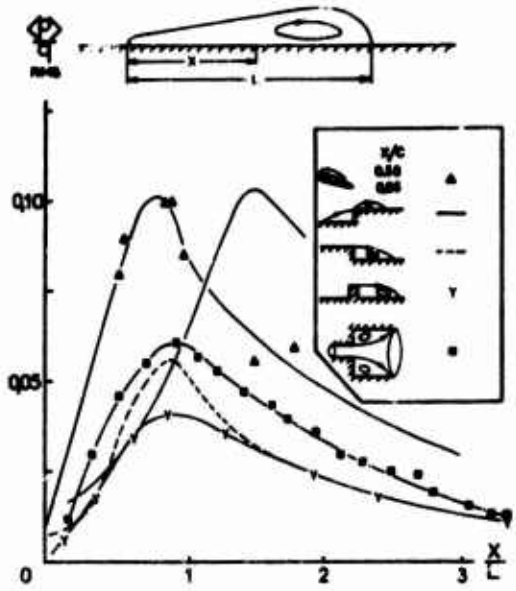

Fig. 4 – Fluctuations de pression dans un décollement subsonique (Mabey).

en amont d'une marche. On remarquera que cette configuration est particulière dans la mesure où elle comporte un couplage de deux bulbes de décollement voisins (fig. 13) $|\langle p \rangle / q|_{max}$ étant situé naturellement au voisinage du recollement le plus aval.

L'analyse du spectre au voisinage du recollement présente l'allure indiquée figure 5 avec un maximum faiblement marqué et une bande assez large, ce maximum correspondant à l'effet de couplage souligné en b)

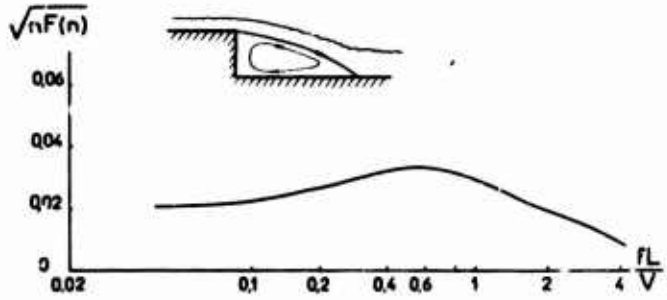

Fig. 5 – Spectre des fluctuations de pression au recollement (Mabey).

Les résultats présentés dans [9] mettent également en évidence une influence très faible du nombre de Mach.

Dans le cas d'un décollement de culot, les phénomènes observés sont caractérisés par un niveau de fluctuation élevé, supérieur aux précédents, et par l'existence d'une fréquence privilégiée liée à la formation de grosses structures turbulentes associées à l'instabilité du sillage.

La nature fondamentalement instationnaire de ces configurations est alors un des aspects essentiels du décollement. Elle conduit notamment à des valeurs moyennes de la pression de culot très différentes dans le cas d'un obstacle symétrique, lorsque ces instabilités ont été supprimées en matérialisant le plan de symétrie par une plaque (fig. 6).

Lorsque l'écoulement est supersonique la visualisation optique constitue un moyen très puissant d'analyse et de contrôle de la stabilité des décol-

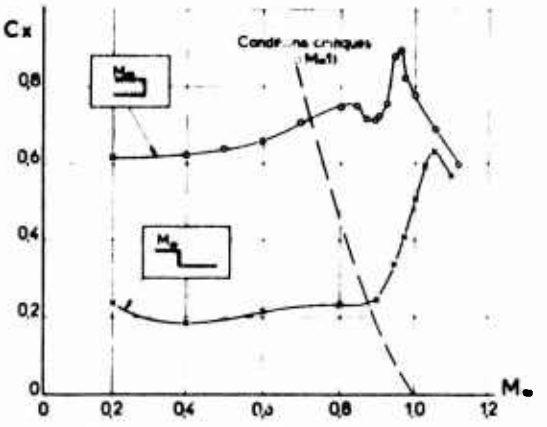

Fig. 6 – Traînée de culot en subsonique – Influence des conditions de recollement.

lements, en particulier l'enregistrement cinématographique. Les observations en temps très bref (fig. 7c) mettent clairement en évidence la structure tourbillonnaire et le caractère instationnaire des couches dissipatives turbulentes dont on perçoit les répercussions par l'analyse des pressions instantanées [10 - 11].

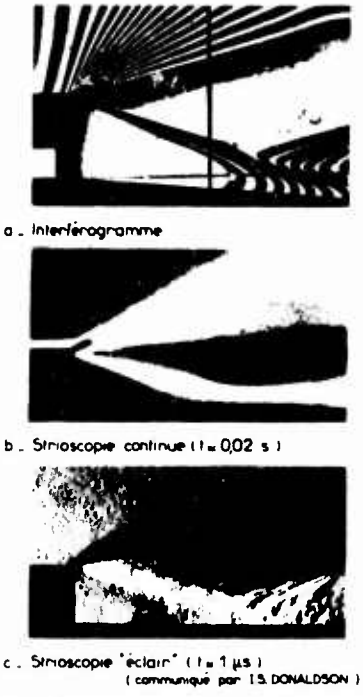

a - Interférogramme

b - Strioscopie continue ($\tau \simeq 0{,}02$ s)

c - Strioscopie "éclair" ($\tau \simeq 1\ \mu$s)
(communiqué par I.S. DONALDSON)

Fig. 7 – Visualisations du recollement turbulent en aval d'une marche.

Le niveau moyen des fluctuations observées est de l'ordre de $\langle p \rangle / q \simeq 0{,}10$ dans la région de recollement comme le montre la figure 8 extraite de [10].

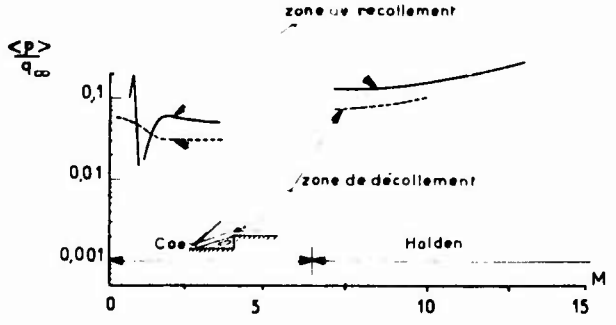

Fig. 8 – Intensité des fluctuations de pression dans une zone décollée supersonique (Holden).

Etroitement associés à ces fluctuations et les entretenant se produisent des déplacements des lignes moyennes de séparation et de recollement qui ont été analysés notamment par Holden [10] à partir de mesures du frottement pariétal. Ces déplacements peuvent atteindre des amplitudes de l'ordre de $\delta/3$.

En revanche, la description de l'écoulement qu'offre l'observation pendant un temps plus long (0,02 s) est celle d'un phénomène permanent en moyenne dans la plupart des cas et reproductible (fig. 7a et b). Ce double caractère est significatif de deux types de démarche qui doivent être étroitement associées sur le plan expérimental : d'une part l'analyse détaillée de la structure du champ moyen, d'autre part celle de la turbulence et de ses effets.

1.3 - Différents types de décollement -

L'examen des aspects instationnaires nous a permis de distinguer parmi les zones décollées :

- celles qui sont organisées sous la forme d'un bulbe accolé à une paroi sur laquelle se situe le point de décollement et de recollement,
- celles qui s'établissent à l'extrémité d'un corps et sont formées par la confluence de deux nappes de courant distinctes qui après avoir quitté la paroi le long d'une ligne de séparation se rejoignent en aval du bord de fuite.

Selon une conception quelque peu idéalisée, le bulbe apparait comme un domaine fermé, au sein duquel l'écoulement moyen s'organise autour d'un tourbillon principal, les points de séparation et de recollement qui le limitent étant fixés ou libres comme le montrent les exemples de la figure 9.

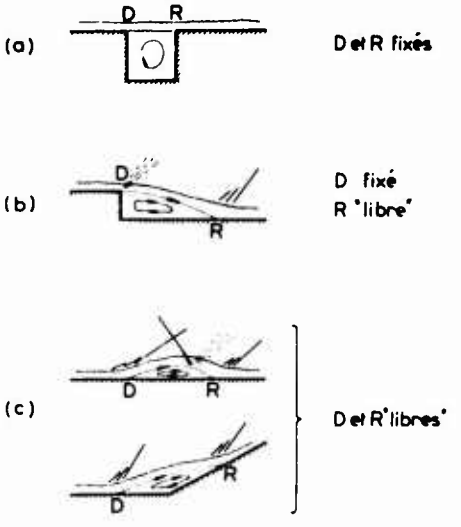

Fig. 9 – Exemples de décollement turbulent.

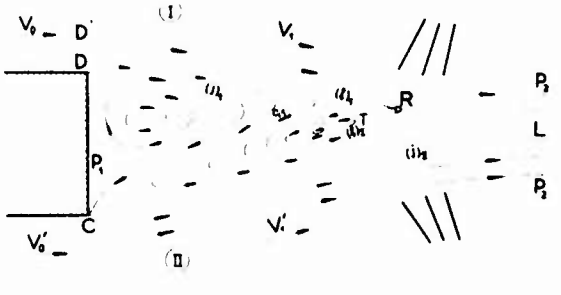

Fig. 10 – Schématisation de la confluence en aval d'un culot.

Par contre, la confluence de deux écoulements en général différents ne peut être imaginée en régime supposé stationnaire que selon le schéma représenté figure 10. Deux zones tourbillonnaires de recirculation apparaissent, contribuant à l'établissement d'un processus permanent d'échange turbulent entre les deux écoulements. Toutefois, comme nous l'avons vu, la stabilité d'un tel schéma est hautement improbable et explique la nécessité des fluctuations de ce bulbe décollé.

D'autre part, nous distinguerons avec Bradshaw [12] 3 types de perturbations induites par le décollement, selon que le bulbe :

a) est noyé au sein de la couche limite : c'est le cas par exemple d'une excroissance de paroi dont la hauteur h est très petite devant δ ; cet aspect particulier ne sera pas envisagé dans notre exposé ;

b) possède une extension longitudinale de quelques épaisseurs δ .

c) atteint des dimensions grandes devant δ .

A cette classification correspondent des effets du nombre de Reynolds R_δ très différents. Importants pour des configurations telles que a) et b), ces effets peuvent être sensiblement réduits dans le cas c), le développement à la frontière du décollement d'une couche de mélange sur une étendue $L/\delta \gg 1$ étant pratiquement indépendant de R_δ .

Ces propriétés sont valables quelle que soit la configuration du décollement. Lorsque les points D et R ne sont pas fixés (fig. 9c), cas le plus fréquemment rencontré, la solution d'un problème de décollement nécessite leur localisation, ceci nous conduira tout naturellement à examiner en premier lieu sur le plan de la connaissance actuelle des phénomènes physiques, les 3 problèmes fondamentaux qui sont associés à cette démarche:

- formation du décollement,
- conditions de recollement,
- problèmes de couplage décollement et recollement.

Après quoi nous tenterons de dresser le bilan des progrès réalisés dans le domaine des méthodes de prévision.

Mais au préalable, avant de clore cette revue générale, nous allons procéder à une évaluation rapide tant des moyens dont nous disposons actuellement pour l'étude expérimentale des zones décollées, que des difficultés spécifiques de ces problèmes.

1.4 - Analyse expérimentale des zones décollées -

Une analyse détaillée de la structure des zones décollées est rendue particulièrement difficile par l'extrême susceptibilité de ce type d'écoulement vis-à-vis des obstacles que constituent les sondes d'exploration matérielles.

Une altération sensible de la forme et de l'étendue d'un décollement peut être enregistrée, au cours du déplacement transversal d'un pitot par exemple, conduisant à une évolution continue des mesures, mais à une description erronée des phénomènes. En second lieu, la présence d'un courant de retour nécessite une adaptation des sondes usuelles à des variations extrêmement importantes et rapides de l'inclinaison du vecteur vitesse moyenne V .

Enfin, l'existence de fluctuations de vitesse du même ordre de grandeur que V local peut être une source d'erreurs importantes pour le fil chaud notamment.

Toutes ces raisons expliquent que les expériences comportant une analyse fine de la structure de tels domaines sont relativement peu nombreuses et parfois sujettes à caution.

Pour surmonter en partie ces difficultés on est conduit à une miniaturisation des instruments de mesure qui ne permet pas toutefois de diminuer l'encombrement local au-dessous d'un certain seuil dont l'ordre de grandeur est $\Phi \sim 1$ mm pour les sondes à fil chaud et une épaisseur d'environ 0,15 mm pour les sondes Pitot aplaties.

Une analyse précise et détaillée des couches dissipatives nécessite des dimensions transversales de ces couches significativement grandes devant ces valeurs, ce qui exclut pratiquement des essais effectués à trop faible échelle.

Heureusement, la vélocimétrie laser ouvre une voie d'analyse nouvelle particulièrement bien adaptée à cette catégorie de problèmes, car elle permet d'effectuer les mesures de vitesse, en grandeur et direction, sans perturber le phénomène et de définir, en outre, les principales caractéristiques de la turbulence.

Les recherches actuellement en cours [13 - 14 - 15 - 16] conduisent à des résultats extrêmement prometteurs comme le montre par exemple la figure 11.

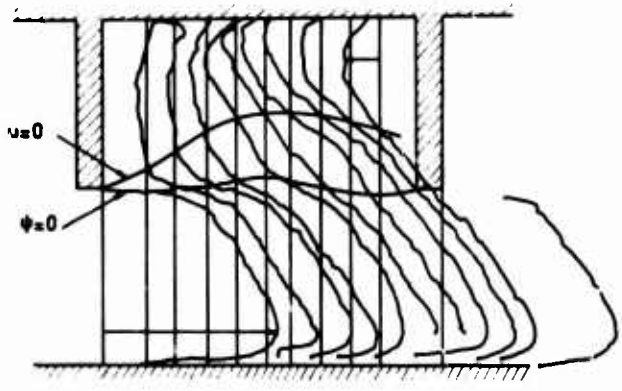

Fig. 11 – Analyse de l'écoulement incompressible dans une cavité par anémométrie laser.

Parmi les moyens de mesure exempts d'interaction de support, il faut également mentionner l'interférométrie dont l'utilisation peut s'avérer très précieuse pour l'étude des décollements bidimensionnels en transsonique et supersonique.

Relativement peu utilisée jusqu'à présent, en raison de son coût et de ses difficultés d'exploitation, cette technique a fait l'objet depuis peu d'un regain d'intérêt, comme le montrent les travaux récents auxquels elle fut associée [17 - 18].

Un des avantages de l'interférométrie est de pouvoir figer, en un seul cliché et au même instant, l'ensemble des informations permettant d'analyser la structure d'un décollement et d'associer son évolution à celle de l'écoulement extérieur. En contre-partie cette technique de mesure qui ne permet pas d'accéder directement aux vitesses ne peut notamment être utilisée pour les faibles valeurs de celle-ci.

2 - PROBLEMES SPECIFIQUES DU DECOLLEMENT -

2.1 - Apparition du décollement en écoulement subsonique -

2.1.1 - Nous examinerons ce problème dans le cas général où le décollement est provoqué par un gradient de pression positif important qui

entraine une destabilisation plus ou moins rapide de la couche limite et la formation d'un courant de retour, apparaissant lorsque le frottement pariétal s'annule.

Comme nous l'avons déjà indiqué, le processus de décollement, révélé par un trop petit nombre d'expériences détaillées, présente un caractère instationnaire mis en évidence notamment par Kline [20] et Sandborn [21].

Ces études ont montré qu'il existe une région dont l'étendue est de l'ordre de δ , assurant la transition entre un état de couche limite non séparée et celui de décollement établi. L'origine de la séparation oscille largement en fonction du temps dans ce domaine comme le montre la figure 12 extraite de [21]. Si τ représente la fraction du temps d'observation T correspondant à un décollement établi, la position moyenne du décollement est ici définie par la condition que τ/T soit égal à 50 %. En général, la localisation expérimentale du point moyen de séparation pourra dépendre largement de la méthode utilisée (mesure du frottement, visualisation pariétale, sondages, etc...).

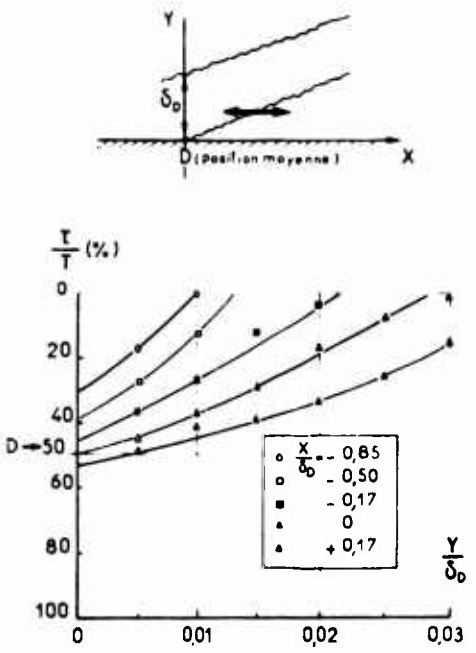

Fig. 12 – Fluctuation de la frontière du courant de retour en incompressible.

Un second aspect important de ce problème est la grande diversité des situations qui apparaissent au voisinage du décollement (D) et se traduisent notamment par des variations sensibles de la forme du profil de vitesse en D.

C'est ainsi que le paramètre de forme $H = \delta^*/\delta^{**}$ évolue entre 1,8 et plus de 3 tandis que le comportement de l'écoulement au voisinage de la paroi tend à s'écarter des lois usuelles.

Dans ces conditions, le concept de couche limite d'équilibre au voisinage du décollement ne peut être en général envisagé. En fait l'état de la couche dissipative en D résulte de son histoire antérieure et des influences diverses qu'elle a subies, parmi lesquelles celle du gradient de pression est la plus marquée.

Pourtant on ne saurait minimiser d'autres facteurs dont l'action sur les circonstances du décollement a une grande importance et qui n'ont reçu que depuis peu l'attention qu'ils méritent.

En premier lieu nous signalerons les effets de courbure, soit de la paroi, soit plus généralement des lignes de courant moyennes de l'écoulement dissipatif au voisinage du décollement.

A titre d'exemple, la visualisation du décollement turbulent obtenue au tunnel hydrodynamique de l'ONERA, à l'aide d'un ressaut est instructive (fig. 13).

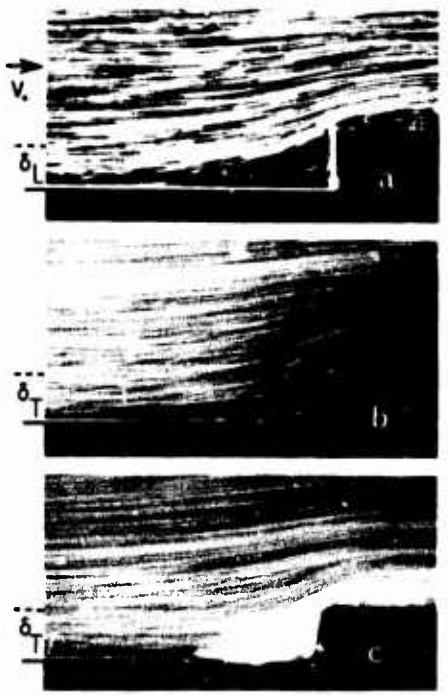

Fig. 13 – Visualisation du décollement incompressible provoqué par une marche.

Cette configuration particulière met en évidence deux décollements successifs, le premier situé en amont du ressaut, le second se développant sur la paroi supérieure de la marche, immédiatement en aval de l'arête.

Le cliché (13a) présente une visualisation par bulle d'air du décollement laminaire obtenu à faible Reynolds, faisant apparaître une influence amont très marquée et une évolution régulière et progressive de la frontière du domaine de recirculation.

Dans le cas où la couche limite est turbulente (13b), l'étendue de la zone décollée est beaucoup plus réduite, ce qui entraîne une forte courbure des lignes de courant moyennes, au voisinage de la séparation (D), imagée sur le cliché (13c) par une injection pariétale pratiquée immédiatement en amont de D.

Cette évolution, spécialement brutale dans le cas considéré, existe toutefois dans la plupart des configurations de décollement étendu et s'accompagne de forts gradients de pression transversaux.

Le second effet spécifique des facteurs de courbure concerne l'évolution de la structure turbulente des couches dissipatives qui y sont soumises (Bradshaw [22], Mathieu [23], Michel [24]).

A titre d'exemple, nous avons représenté figure 14 un résultat de Michel et al. [24], concernant l'évolution des couches limites à l'approche du décollement dans le cas des essais effectués par Schubauer et Klebanoff [25], qui met clairement en évidence l'importance de la prise en compte des facteurs de courbure.

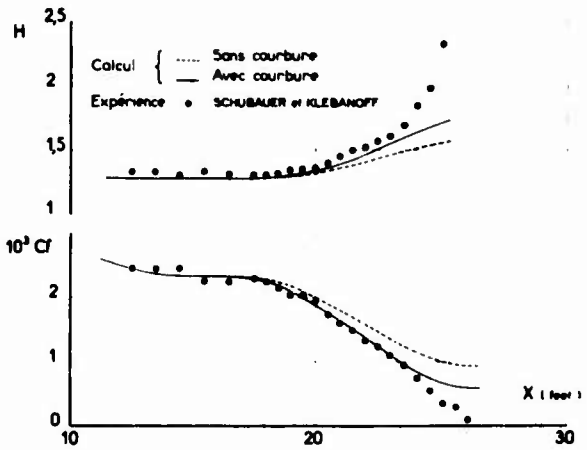

Fig. 14 – Prise en compte des facteurs de courbure.

Dans la méthode utilisée par Michel, le frottement turbulent apparent τ_t est exprimé, à l'aide du concept de longueur de mélange, selon un expression modifiée pour tenir compte de ces facteurs :

$$\tau_t = \rho \ell^2 \left(\frac{\partial u}{\partial y}\right)^2 F_c$$

F_c étant une fonction correctrice empirique dépendant du paramètre $\frac{u/R}{\partial u/\partial y}$, ou R est le rayon de courbure d'une ligne de courant de référence (paroi engraissée de l'effet de déplacement) et u la vitesse locale dans la couche limite.

La turbulence de l'écoulement extérieur, agit également de façon significative sur la position du décollement, comme le montre l'exemple suivant :

- la figure 15 donne l'évolution en fonction de la distance longitudinale x, des grandeurs C_f et H, mesurées au cours d'expériences effectuées par Michel et al. [26], pour deux niveaux de la turbulence extérieure $\sqrt{u'^2}/u = 0{,}3\ \%$ (configuration B_1) et $\sqrt{u'^2}/u = 5\ \%$ (configuration B_2), sur une plaque plane soumise à un même gradient de pression positif intense.

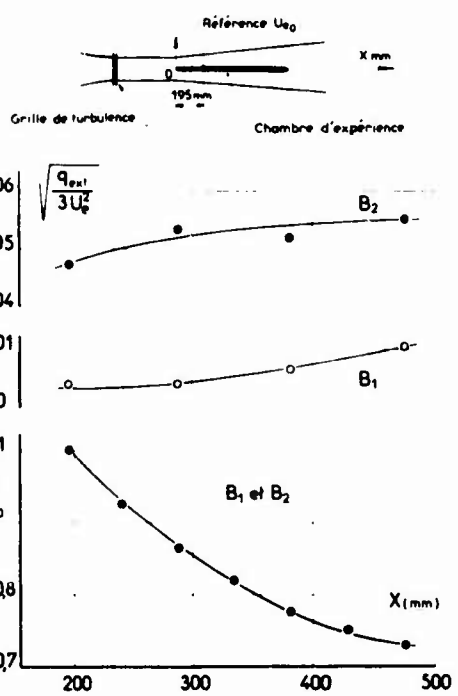

Fig. 15a – Effet de turbulence extérieure – Conditions d'essai.

Alors que dans le premier cas (B_1, turbulence faible) la couche limite à l'extrémité du domaine de mesure ($x = 450$ mm) est dans une situation voisine du décollement (C_f très faible, paramètre de forme de l'ordre de 2,2), dans le second (B_2, intensité de turbulence élevée) H demeure pratiquement constant ($H \sim 1{,}6$) ; l'évolution du C_f n'est que lentement décroissante, la valeur obtenue en $x = 450$ mm étant de l'ordre de $1{,}2.10^{-3}$ c'est-à-dire loin des conditions de séparation.

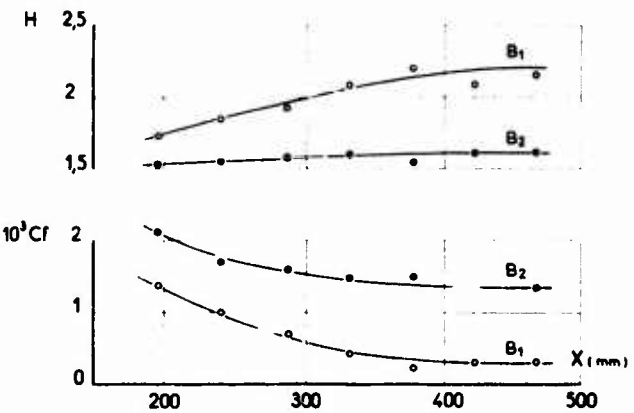

Fig. 15b – Effet de turbulence extérieure – Résultats

Des niveaux de turbulence extérieure aussi importants sont loin d'être irréalistes ; ils se rencontrent par exemple dans les roues de turbomachines mais également lors de l'écoulement autour d'une aile à volets multiples, lorsque l'un d'eux est soumis à l'effet du sillage de l'élément disposé en amont.

2.1.2 – Prévision du décollement par les méthodes classiques –

Avant d'aborder le problème du calcul complet d'une zone décollée il est intéressant d'examiner dans quelle mesure les méthodes de calcul classiques des couches limites permettent de localiser le décollement, l'évolution des pressions sur le contour de l'obstacle étant supposée connue, à partir de l'expérience par exemple.

D'une façon générale nous incluerons dans ces méthodes les critères de décollement plus ou moins empiriques ce qui permet de les classer en deux catégories :

- d'une part celles qui requièrent une solution détaillée des équations de la couche limite obtenue soit par résolution numérique (méthodes de différences finies) soit à l'aide de techniques intégrales ;
- d'autre part des méthodes plus simples basées sur l'existence d'une relation caractéristique du décollement, les grandeurs intervenant dans cette relation ne nécessitant pas en général un calcul complet de couche limite. Un exemple typique est le critère de Stratford [27, 28] qui, pour un écoulement incompressible est défini par la relation suivante :

$$C_p \left(x \frac{dC_p}{dx} \right)^{1/2} \left(10^{-6} R_x \right)^{-1/10} = 0{,}4$$

où x est la distance comptée à partir du maximum de vitesse. En fait, il ne nécessite pour être appliqué que la connaissance de la loi $C_p(x)$ et peut être étendu au cas d'écoulements compressibles [29].

Une étude critique assez complète des performances

de ces diverses méthodes a été effectuée par Cébéci et al. [28] en écoulement incompressible.

Se référant à des expériences existantes où la distribution de pression ainsi que la position du point de décollement D étaient connues, le calcul de D a été effectué en utilisant trois méthodes typiques, assez représentatives des moyens de prévision courants, sans être cependant les plus raffinées :

- la méthode de Cébéci et Smith (Différences finies)
- la méthode de Head (méthode intégrale)
- le critère de Stratford.

Sur les exemples traités qui comprennent une grande variété de configurations (profils d'ailes, cylindre circulaire, cylindre elliptique), ces trois méthodes conduisent à un recoupement assez satisfaisant avec l'expérience, le meilleur résultat étant fourni par la méthode de Cébéci et Smith.

A titre indicatif la figure 16 extraite de [19] représente une statistique effectuée par ces derniers auteurs portant sur 67 configurations, comparant la prévision et l'expérience, l'erreur moyenne sur la position du décollement étant égale à 7,18 %.

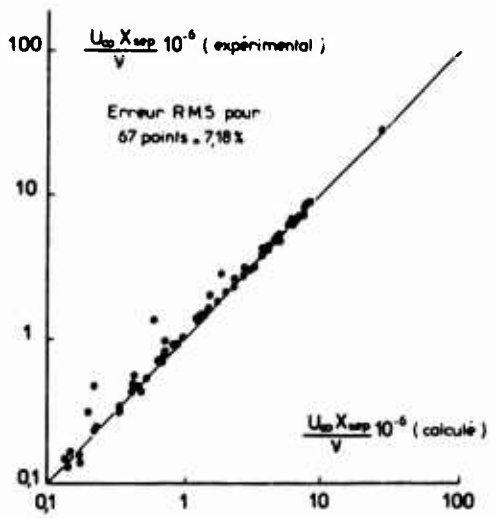

Fig. 16 – Prévision du décollement incompressible (Cebeci et Smith).

Une si faible dispersion pourrait a priori paraître étonnante compte tenu des incertitudes inévitables liées à la localisation expérimentale du point de séparation comme à la mise en place précise de la transition laminaire turbulent.

Elle est l'indice tout d'abord de la fiabilité remarquable de la méthode de calcul, mais aussi d'une interprétation intelligente des distributions de vitesse au voisinage du point de séparation dans les cas difficiles.

Une analyse de même nature, étendue au cas d'écoulements subsoniques compressibles a été effectuée par Gerhart et al. [30].

Huit méthodes de calcul ont été testées en prenant comme référence les résultats expérimentaux obtenus par Alber et al. [31] ; par conséquent cette comparaison porte sur un nombre d'essais limités appartenant à une même configuration expérimentale.

Un examen superficiel des résultats conduit à des conclusions assez décevantes, aucune des méthodes de calcul de couche limite ne permettant une prévision réelle du décollement. Par contre le critère de Stratford définit un point de séparation assez proche de l'expérience.

Toutefois, une interprétation raisonnée des résultats de calculs de couche limite permet d'établir une estimation qui dans certains cas, comme le montre la figure 17 peut être considérée comme satisfaisante, la méthode proposée par Bradshaw et Ferris fournissant le meilleur résultat d'ensemble.

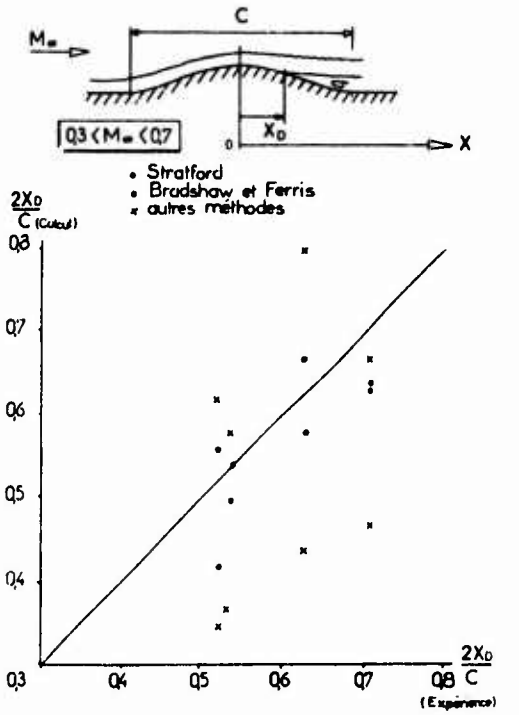

Fig. 17 – Prévision du décollement en subsonique compressible.

Ces deux exemples ont été donnés à dessein pour illustrer deux tendances plutôt contradictoires qui reflètent la situation actuelle.

Si la prévision du décollement dans la plupart des cas "classiques" est correctement effectuée par les méthodes de calcul de couche limite les plus élaborées, il n'en demeure pas moins certains cas rebelles qui nécessitent soit une interprétation "raisonnable" des résultats ou des données, soit la prise en compte des facteurs d'influence évoqués précédemment (courbure, turbulence extérieure ...).

Il convient également de noter qu'une prévision convenable de la position du décollement n'entraine pas nécessairement un calcul précis d'autres éléments tels que facteurs de forme, épaisseurs caractéristiques etc...

Cette carence est spécialement ressentie lorsqu'une évolution réaliste des pressions autour de l'obstacle ne peut être obtenue à partir d'un calcul de fluide parfait, sans tenir compte du couplage entre le développement des couches dissipatives et celui de l'écoulement extérieur.

2.2 – Formation du décollement en écoulement supersonique –

2.2.1 – Phénomènes généraux –

Nous n'examinerons ici que les configurations de décollement se produisant sur une paroi continue. Un des caractères essentiels de telles configurations réside dans le passage extrêmement brutal sur une étendue dont l'ordre de grandeur est comparable à l'épaisseur δ^* de la couche limite amont, d'une situation définie par un profil de vitesse du type plaque plane par exemple à celle d'un écoulement décollé avec courant de retour, ce phénomène brutal s'accompagnant d'une onde de choc intense prenant

naissance au sein de la couche dissipative lorsque le nombre de Mach est important et se propageant dans l'écoulement extérieur.

L'analyse expérimentale détaillée de ce processus faite notamment par Délery et al. [34] et Rose [35] met en évidence qu'au cours de cette compression brusque le rôle joué par la viscosité et la tension de Reynolds devient négligeable dans la majeure partie de la couche limite, confirmant ainsi de nombreuses constatations antérieures concernant les phénomènes d'interaction rapide [6 - 32 - 33]. Les principales observations effectuées au cours de ces analyses sont données sur les figures 18 à 21 extraites de [36].

Dans l'expérience présentée ici, l'écoulement amont non perturbé est plan et uniforme, de nombre de Mach $M_\infty = 1{,}92$.

Les mesures ont comporté un relevé soigné de la pression pariétale ainsi que des explorations détaillées de la couche dissipative. Le calcul de l'écoulement supposé non visqueux dans la zone supersonique a été effectué par la méthode des caractéristiques rotationnelles. Ce calcul part d'une distribution initiale déduite d'un sondage de la couche limite en amont de l'interaction. La progression se fait ensuite vers l'aval en affichant sur la frontière $\hat{\delta}$ (courbe iso-Mach à M = 1,05) la répartition des pressions mesurées à la paroi corrigée si besoin est d'un effet de non uniformité résiduel dans la sous-couche $y < \hat{\delta}$. Comme le montre la figure 18, ce calcul prédit avec une très bonne précision la position de l'iso-Mach M = 1,05 expérimentale, sur une distance dépassant 5 fois l'épaisseur initiale de la couche limite.

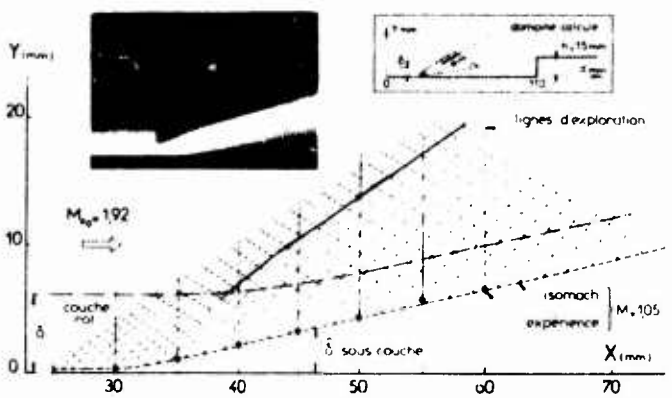

Fig. 18 – Concept de double couche – Structure du champ supersonique supposé non visqueux (résultats ONERA).

Sur la figure 19 sont tracées les répartitions transversales de pression statique qui font apparaître une forte variation de $p(y)$ jusqu'à la station x = 45 mm, voisine du décollement.

L'évolution expérimentale des profils de vitesse moyenne est représentée figures 20 et 21. Elle met en évidence tout d'abord la bonne prévision du champ supersonique des couches dissipatives par les équations d'Euler (fig. 20) et renseigne ensuite sur le comportement de l'écoulement entre la frontière $\hat{\delta}$ et la paroi (fig. 21).

La vitesse $\hat{u}$ constante sur $\hat{\delta}$ a été utilisée pour normaliser cette évolution sous forme de profils réduits $u/\hat{u} = f(y/\hat{\delta})$. On observe une très rapide destabilisation de ces profils bien représentés par une loi en puissance $u/\hat{u} = (y/\hat{\delta})^{1/n}$ l'exposant n tendant vers 1 au décollement.

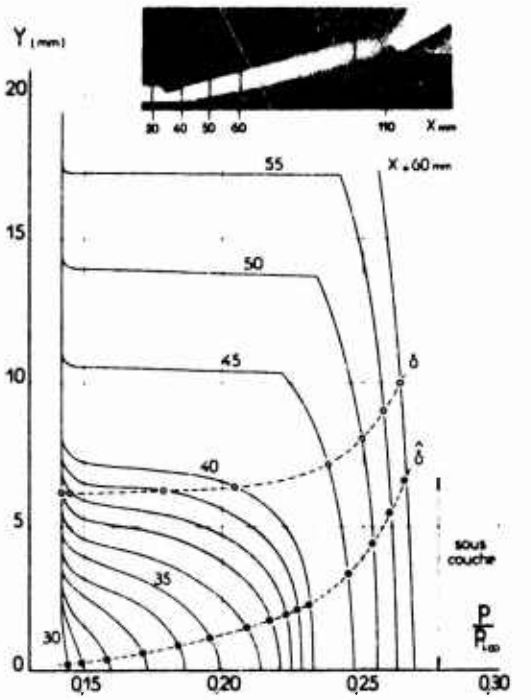

Fig. 19 – Concept de double couche – Répartitions transversales de pression dans un décollement à $M_{e_0} = 1{,}92$.

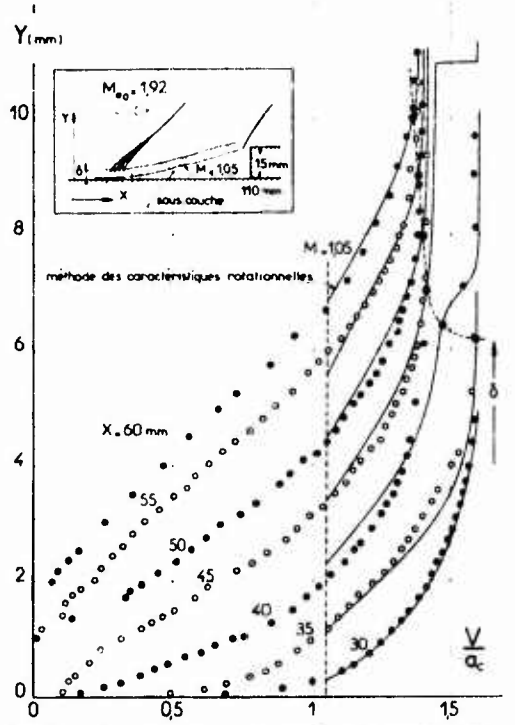

Fig. 20 – Concept de double couche – Profils de vitesse dans un décollement (ONERA).

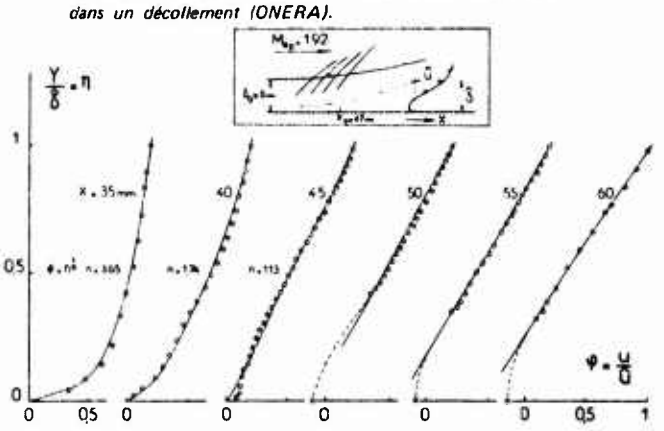

Fig. 21 – Concept de double couche – Profils de vitesse dans la sous-couche (résultats ONERA).

Nous ferons 2 remarques :

- le choix de la frontière $\hat{\mathcal{F}}$ a été imposé ici par la méthode de calcul retenue (méthode des caractéristiques). La seule signification physique apparaissant a posteriori est que $\hat{\mathcal{F}}$ sépare grosso modo la couche dissipative en deux régions dans lesquelles l'évolution $p(y)$ est différente, $p(y)$ étant sensiblement constant pour $y < \hat{\delta}$ et évoluant par contre fortement lorsque $y > \hat{\delta}$;
- $\hat{\mathcal{F}}$ n'assure donc pas nécessairement la séparation entre un domaine extérieur où l'évolution des pressions et des vitesses est régie par un comportement essentiellement non visqueux et un domaine proche de la paroi où sont concentrés les effets liés à la viscosité et à la turbulence.

Le mécanisme du décollement turbulent supersonique apparaît au vu de ces expériences comme le résultat du couplage qui s'établit entre ces deux domaines. L'épaississement rapide de la couche visqueuse voisine de la paroi entraîne une déviation importante de l'écoulement rotationnel extérieur de nature essentiellement supersonique, induisant ainsi des gradients de pression importants qui ont pour effet d'entretenir la destabilisation de la couche pariétale. Les perturbations ainsi créées sont transmises à l'écoulement extérieur, à travers la couche rotationnelle sous forme d'ondes convergentes focalisant rapidement pour créer une onde de choc.

Cette procédure d'auto-induction évidente à l'examen de la figure 22 permet d'expliquer un certain nombre de résultats et notamment le concept d'interaction libre proposé par Chapman [37] dans le cas de décollements étendus.

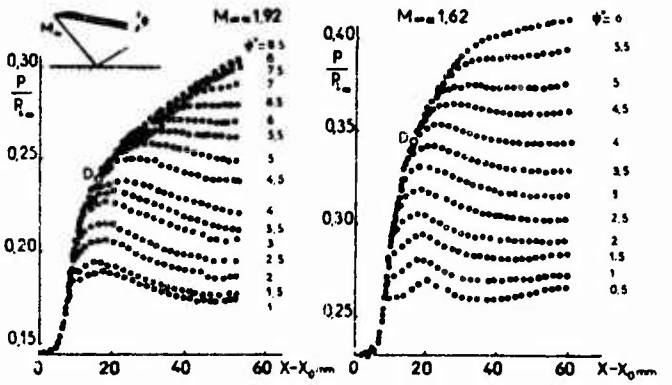

Fig. 22 – Réflexion d'un choc – Evolution des pressions dans le domaine d'interaction.

2.2.2 – Corrélation des pressions dans le domaine de décollement ; critères de décollement –

C'est à partir de ce concept, bien vérifié par l'expérience, qu'a été tentée il y a près de 20 ans, la première démarche aboutissant à la formulation d'un critère de décollement dans le cas d'un écoulement uniforme en amont du domaine d'interaction (Chapman - 37). Ces idées ont été reprises tout d'abord par Erdos et Pallone [38] puis par Carrière [39 - 40] qui les a généralisées et étendues au cas où le décollement se produit dans un écoulement non uniforme.

Cette formulation conduit à représenter la loi d'évolution de pressions dans le domaine d'interaction par l'expression suivante :

$$(1)\quad \frac{p - p_1}{q_1}\,\frac{P(M) - P(\bar{M})}{C_{f_1}} = \mathcal{F}\left(\frac{x - x_1}{l}\right)$$

dans laquelle :

- l'indice 1 caractérise l'origine de l'interaction,
- $\bar{M}$ représente le nombre de Mach qui existerait à l'abscisse x, en l'absence de décollement,
- P est le nombre de pression local de Busemann,
- $\mathcal{F}$ est une fonction empirique universelle ne dépendant que de l'abscisse réduite $(x-x_1)/l$, l étant l'étendue du domaine d'interaction jusqu'au point de séparation.

La détermination de $\mathcal{F}$ a été faite par le regroupement d'expériences diverses, couvrant un assez large domaine de nombre de Mach comme le montre la figure 23, mais correspondant en général à des valeurs modérées de R_{δ}.

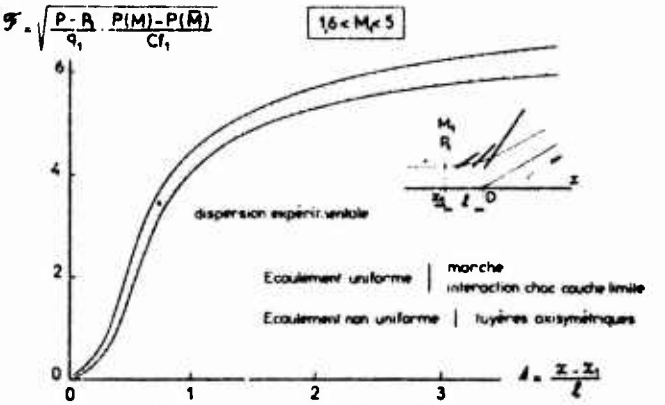

Fig. 23 – Définition expérimentale de la fonction $\mathcal{F}$.

Pour cette gamme de valeurs R_{δ}, les écarts sur C_f, sont malgré tout suffisamment importants pour justifier une dépendance de l'évolution des pressions vis-à-vis du nombre de Reynolds.

A partir de la fonction $\mathcal{F}$, il est possible de définir la pression au point de décollement qui correspond à une valeur de $\mathcal{F} = 4{,}22$ et la pression dite de plateau qui est spécifique d'un décollement étendu et isobare. Cette condition n'est pas toujours assurée, ce qui justifie une dispersion plus grande des points expérimentaux en aval du point de séparation.

On remarquera :

- tout d'abord que cette corrélation qui regroupe des résultats d'origines très diverses (décollement devant une marche ou un coin, interaction choc couche limite, décollement dans une tuyère au point fixe etc...) est une justification évidente du concept d'interaction libre dont la validité est assurée jusqu'au décollement.
- que la relation (1) fait apparaître un effet du nombre de Reynolds R_{δ_1}, de la couche limite en x_1, par l'intermédiaire du coefficient de frottement C_{f_1}.

Une remise en cause de ce dernier résultat est apparue lorsque des essais effectués à des valeurs de R_{δ_1} beaucoup plus importantes ont été disponibles ($R_{\delta_1} \geq 10^6$). Pour cet ensemble de mesures on observe une quasi indépendance vis-à-vis du nombre de Reynolds du saut de pression caractérisant, soit le décollement $[(p_p - p_1)/p_1]$, soit le plateau dans le cas de décollements étendus et isobares $[(p_p - p_1)/p_1]$. Lorsque l'écoulement est uniforme en amont de l'interaction, ce qui est le cas de la plupart des résultats disponibles, le seul paramètre régissant l'évolution de ces grandeurs est alors le nombre de Mach M_1. Un exemple typique (extrait de [5]) des variations de $(p_p - p_1)/p_1$ en fonction de M_1 est donné figure 24.

Sur celle-ci sont regroupées les mesures faites par Roshko [5] sur une configuration du type rampe et les courbes moyennes définies à partir d'expériences collectées par Zukowski [42] et Werlé [43] sur le décollement devant une marche, le recoupement de l'ensemble étant assez satisfaisant.

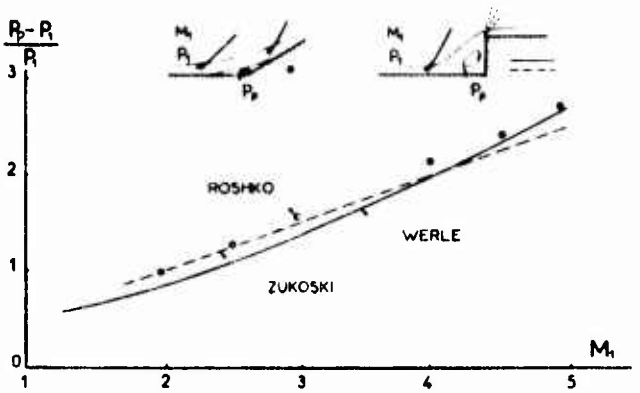

Fig. 24 – Evolution avec le nombre de Mach du saut de pression au plateau.

Ces résultats ne remettent pas en cause un certain caractère d'universalité et d'indépendance vis-à-vis du nombre de Mach que présente l'évolution des pressions et qui apparait, comme l'a montré Zukowski [42], par le choix des variables réduites suivantes :

$$\frac{p - p_1}{p_2 - p_1} = f\left(\frac{x - x_1}{x_2 - x_1}\right)$$

qui n'est autre qu'une certaine normalisation de la fonction $\mathcal{F}$; en effet :

$$\frac{p - p_1}{p_2 - p_1} \simeq \frac{\mathcal{F}}{\mathcal{F}_2}$$

Pour concilier ces deux séries de résultats contradictoires on doit admettre qu'aux faibles valeurs de $R\,\delta_1$, l'évolution des pressions dans le domaine d'interaction peut être représentée par la relation (1) ce qui entraine lorsque $R\,\delta_1$ augmente une décroissance faible de la pression de plateau, par exemple, qui cesse dès que sont atteintes les valeurs correspondant aux résultats de la figure 24.

Les limitations que l'on peut trouver à la validité des critères de décollement ne concernent pas seulement l'influence du nombre de Reynolds, mais surtout le domaine d'application envisageable. Ce domaine est restreint tout d'abord au cas de décollements étendus et isobares conduisant à une pression de plateau bien définie. Ensuite, la plupart des résultats disponibles ont été obtenus dans le cas d'écoulements amont uniformes ou modérément accélérés de telle sorte que le profil des vitesses de la couche limite à l'origine de l'interaction est toujours très voisin d'une configuration du type plaque plane.

Lorsqu'il n'en est plus ainsi, par exemple dans le cas d'une compression continue suffisamment importante, on peut s'attendre compte tenu du mécanisme de formation du décollement, à un effet sensible de la forme du profil des vitesses en amont de l'interaction, susceptible de remettre en cause la généralité des lois présentées.

2.2.3 – Problèmes spécifiques du décollement en écoulement hypersonique, effets thermiques –

Nous examinerons maintenant brièvement l'incidence sur le décollement des effets thermiques, spécialement importants dans le domaine hypersonique où l'étude des phénomènes de forte interaction visqueuse pour une couche limite turbulente a fait l'objet de récentes contributions [44 – 45 – 46 – 47].

Pour de tels écoulements on observe deux particularités typiques :

- tout d'abord la pénétration profonde du choc, lié au décollement, au sein de la couche rotationnelle, [44] qui est une conséquence naturelle d'un nombre de Mach extérieur élevé,
- ensuite l'importance accrue des effets visqueux au voisinage de la paroi.

En ce qui concerne l'évolution des pressions au voisinage du décollement, une large variation du rapport T_p/T_f de la température de paroi à la température de frottement n'entraine que des effets négligeables comme le montre la figure 25 extraite de [43]

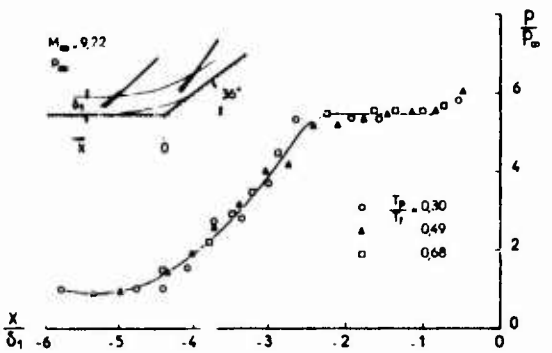

Fig. 25 – Effet de la température de paroi sur l'évolution des pressions au décollement.

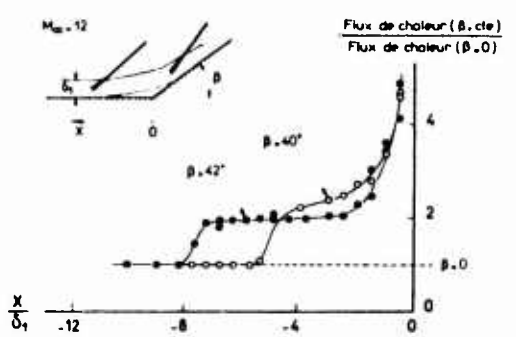

Fig. 26 – Distribution du flux de chaleur dans un décollement.

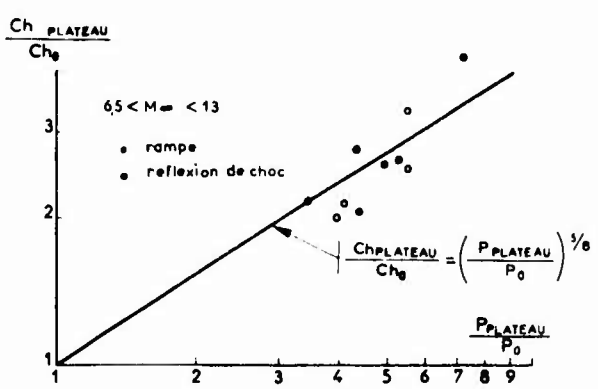

Fig. 27 – Corrélation entre les plateaux de flux de chaleur et de pression.

L'évolution des flux de chaleur dans une zone décollée turbulente présente un aspect caractéristique très différent de celui qui est observé dans le cas laminaire et qui se traduit par un accroissement du flux dans le domaine d'interaction voisin du décollement suivi d'un plateau très marqué dans la zone décollée (fig. 26).

Diverses corrélations associant pression plateau et flux de chaleur correspondant ont été proposées. A titre d'exemple nous donnons figure 27 celle de Holden [44].

3 - CONDITIONS DE RECOLLEMENT -

3.1 - Structure du recollement -

Que l'écoulement soit subsonique ou supersonique, la plupart des résultats utilisés pour caractériser les conditions de recollement proviennent d'études effectuées sur une configuration de marche descendante. L'organisation générale de l'écoulement moyen fait apparaître des caractères communs dans les deux cas.

L'exemple de nature supersonique présenté figure 28, où le nombre de Mach amont est voisin de 2, a fait l'objet d'une analyse expérimentale très détaillée par Taguirov.

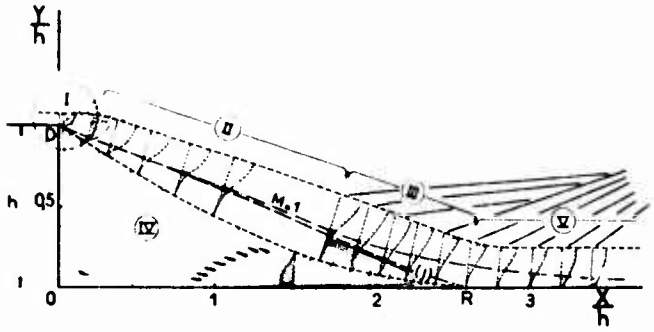

Fig. 28 – Recollement turbulent en aval d'une marche - Différents domaines de l'écoulement.

Lorsque l'écoulement est subsonique, les résultats sont analogues exceptées les circonstances du décollement (la forte déviation initiale apparaissant en supersonique par suite de la détente de l'écoulement extérieur disparait en subsonique).

Nous nous sommes volontairement placés dans le cas d'une couche limite mince en D , condition nécessaire comme nous le verrons pour définir des propriétés très générales concernant le phénomène du recollement turbulent.

Comme le montre la figure 28, l'écoulement dissipatif peut être divisé en 5 régions. La première située au voisinage de D correspond au décollement de la couche limite.

En aval se développe une zone de mélange quasi-isobare (II) qui est suivie jusqu'au point de recollement R (III) par la 1ère partie d'une recompression continue se poursuivant et s'achevant en aval de R (V). Parallèlement s'opère une restructuration de la couche limite jusqu'à un nouvel état d'équilibre.

Au sein de la zone décollée, délimitée par I, II, III, nous avons distingué le domaine de recirculation IV à l'intérieur duquel reflue le courant alimentant la couche de mélange, l'existence d'un tourbillon secondaire contrarotatif situé au pied de la marche, ne jouant pas un rôle important dans l'évolution du courant de retour.

Nous nous intéresserons essentiellement dans ce qui suit aux domaines III, IV, et V qui sont plus spécifiques des conditions de recollement. Tout d'abord l'état initial du domaine III est défini notamment par un profil de vitesse dont la forme est pratiquement indépendante de celle de la couche limite initiale turbulente, lorsque δ_o est faible devant l'étendue de la zone décollée.

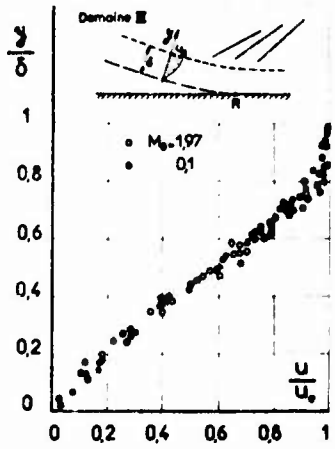

Fig. 29 – Profils de vitesse dans la recompression en amont du point de recollement.

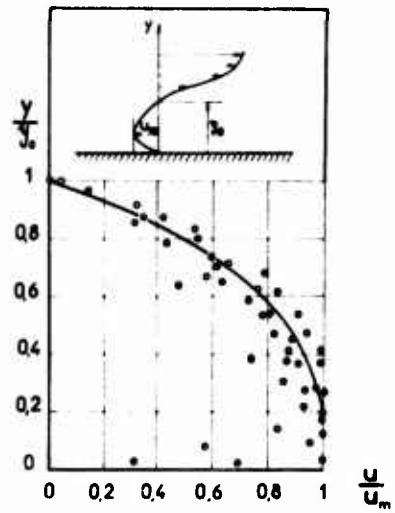

Fig. 30 – Corrélation des profils de vitesse dans le domaine de recirculation.

Dans ce cas, on constate que les profils de vitesse dans les domaines III, IV, V obéissent à des propriétés de similitude que l'on peut définir de la manière suivante :

- quasi invariance des profils réduits dans le domaine III et la partie du domaine IV adjacente, comme le montrent les figures 29 et 30, la couche pariétale du courant de retour étant de faible épaisseur,
- évolution typique dans le domaine V (fig. 31), faisant apparaître une restructuration de la couche limite, caractérisée par une diminution du paramètre de forme H_{inc} lorsque x croît, qui traduit l'accélération progressive de l'écoulement au voisinage de la paroi.

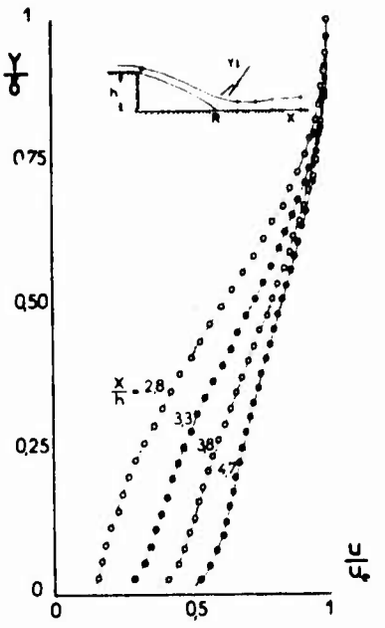

Fig. 31 – Profils de vitesse dans la recompression en aval du point de recollement.

Des lois simples permettent de représenter avec une excellente approximation l'ensemble de ces profils de vitesse ; en particulier Délery et Mirande [36] ont défini une famille à un paramètre principal assurant comme le montre la figure 32 une très bonne représentation de l'expérience. Nous renvoyons à la référence [36] pour l'expression détaillée de ces profils dont la formulation en aval du recollement est très proche de celle de Coles.

On remarquera à l'examen de la figure 32 que cette représentation n'est valable que sur l'étendue des domaines III et V et ne saurait convenir dans le domaine II et dans la partie de IV qui lui est adjacente.

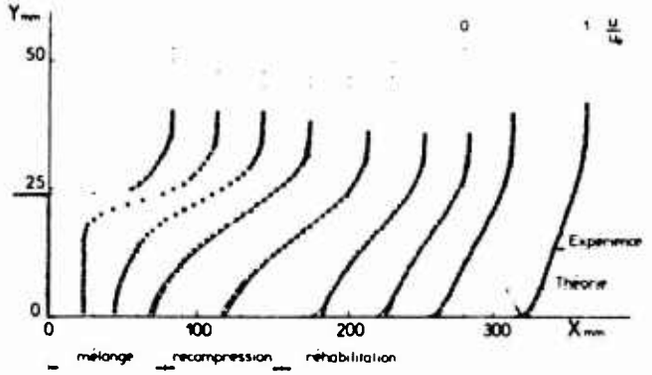

Fig. 32 – Profils de vitesse dans un recollement incompressible turbulent.

Cette transformation rapide des profils de vitesse dans le domaine de recollement, associée à la présence de gradients de pression longitudinaux intenses a pour conséquence deux effets importants :

On constate :

- tout d'abord l'existence de gradients de pression normaux significatifs qui sont liés à la forte courbure des lignes de courant et entrainent dans le cas supersonique la formation d'un choc pénètrant plus ou moins, selon le nombre de Mach extérieur, au sein des couches dissipatives ;
- ensuite, comme l'ont notamment observé Tani [48] et Bradshaw [12], la structure de la turbulence interne subit de profondes modifications entre deux états distincts dont l'un est défini par le processus de mélange et l'autre par une configuration de couche limite pariétale d'équilibre atteinte loin en aval, comme le montre la figure 33.

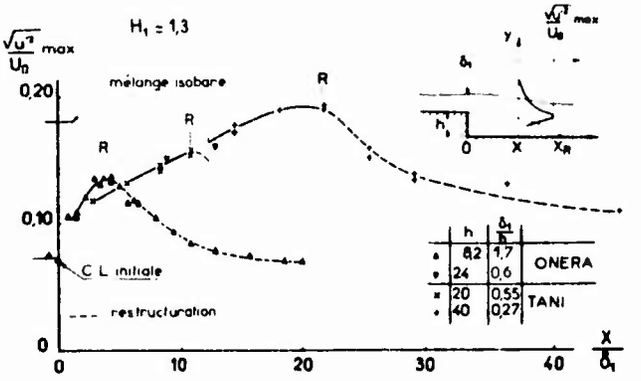

Fig. 33 – Evolution de l'intensité maximale de turbulence dans une zone décollée.

La prise en compte de ces effets est nécessaire lors de l'établissement d'une méthode de calcul précise et les informations détaillées que nous possédons sur ces phénomènes notamment en écoulement supersonique sont rares.

3.2 – Facteurs d'influence du recollement –

3.2.1 – Les facteurs susceptibles d'agir sur les conditions de recollement ont été discutés par de nombreux auteurs (on trouvera une revue de ces travaux dans [36] et [50]). Ils peuvent être classés en deux catégories :

a) des facteurs intrinsèques intervenant au niveau du processus de mélange turbulent et modifiant la structure de l'écoulement qui aborde le domaine III ;

b) des facteurs extérieurs agissant sur l'état de l'écoulement non visqueux à la frontière des couches dissipatives, et notamment sur la relation existant entre la direction locale du vecteur vitesse et la pression.

3.2.2 – Facteurs intrinsèques –

Dans cette catégorie, interviennent essentiellement les effets liés à la compressibilité (Nombre de Mach, température et flux thermique etc...), ceux que provoquent un soufflage ou une aspiration à faible débit et vitesse dans le décollement et enfin la couche limite initiale.

Tant que ces effets demeurent modérés, la forme du profil des vitesses au début de III est pratiquement inchangée.

Moyennant cette hypothèse, on peut montrer [51] que l'état de l'écoulement sur la ligne de courant aboutissant en R (fig. 28) peut être défini à l'aide d'un seul paramètre caractéristique :

$$(2) \qquad C_q = \frac{q}{\rho_1 u_1 L} - \frac{i}{\rho_1 u_1^2 L} + \frac{\delta_1^{**}}{L}$$

dans cette expression interviennent :

- l'épaisseur de quantité de mouvement δ_1^{**} à l'origine de la zone isobare,
- le débit q injecté dans l'eau morte,
- la quantité de mouvement i introduite par cette injection,
- une échelle caractéristique du décollement L ,
- l'état ρ_1 , u_1 de l'écoulement à l'extérieur du domaine II.

En particulier la recompression jusqu'au point de recollement est étroitement dépendante de C_q . En l'absence de soufflage (2) s'écrit :

$$C_q = \frac{\delta_1^{**}}{L} = \frac{\delta_1^{**}}{X_R + x_0}$$

où X_R représente l'étendue de la zone décollée et x_0 un décalage de l'origine du mélange défini dans le cadre du concept d'origine fictive [50] par une relation de la forme :

$$x_0 = K \delta_1^{**}$$

K étant une fonction du paramètre de forme de la couche limite initiale [36].

Une analyse expérimentale détaillée effectuée à l'ONERA en écoulement incompressible plan [49] a permis d'établir la loi empirique reliant la recompression obtenue en R :

$$(p_R - p_1) / q_1$$

au paramètre C_q en l'absence d'effets d'injection de masse dans l'eau morte.
Cette loi est représentée figure 34. Elle regroupe des expériences réalisées pour des conditions de recollement extrêmement diversifiées, en présence d'écoulements extérieurs ralentis ou accélérés et de couches limites initiales d'épaisseur variable.

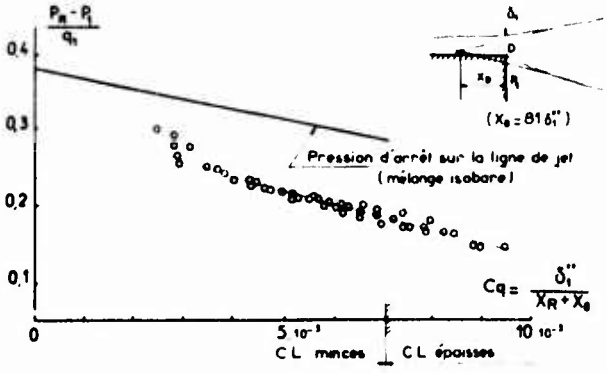

Fig. 34 – Saut de pression au recollement en incompressible.

On constate que le niveau de recompression obtenu ne correspond pas à l'hypothèse généralement admise d'une recompression quasi isentropique sur ($\mathcal{J}$), les écarts étant dûs aux effets dissipatifs rencontrés lors du processus de recompression.

Une loi comparable n'a pas été établie à notre connaissance dans le cas supersonique. Toutefois l'exploitation de quelques expériences effectuées à l'ONERA a permis de montrer que dans le domaine $M > 1$, les effets dissipatifs restent faibles devant les niveaux de recompression obtenus, de telle sorte qu'ils peuvent être négligés en première approximation.

Lorsque la couche limite épaissit fortement, on enregistre non seulement une diminution sensible de la recompression en R , mais également une modification profonde de la structure de l'écoulement dissipatif à l'extrémité du domaine II de la figure 28 (cf. § 1.3). De ce fait, l'évolution ultérieure des profils de vitesse n'obéit plus aux lois de comportement simples, définies § 3.1 (fig. 32). En particulier la valeur de H au point de recollement varie fortement (fig. 35) de même que les relations de dépendance entre les divers paramètres de forme.

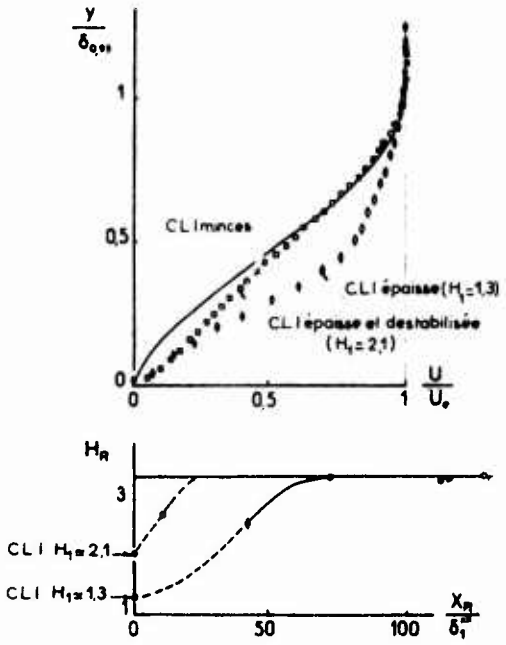

Fig. 35 – Profils de vitesse au recollement – Influence de la couche limite initiale (C L I).

3.2.3 – Facteurs extérieurs –

L'influence des facteurs extérieurs (non uniformité de l'écoulement, courbure de parois) en l'absence de discontinuités marquées telles que des ondes de choc, intervient essentiellement au niveau du couplage entre le développement des couches dissipatives et celui de l'écoulement non visqueux. Cette action prépondérante en ce qui concerne l'évolution des pressions, n'altère cependant pas la structure des profils de vitesse au voisinage du recollement, du moins tant que la couche limite initiale est mince et tant que les facteurs extérieurs demeurent modérés. C'est ce qu'a notamment montré l'étude expérimentale du recollement subsonique en présence d'un écoulement extérieur accéléré ou ralenti, effectuée par Mirande [49]

Un problème particulier est celui rencontré dans le cas du recollement supersonique lorsque sont mises en jeu de fortes perturbations en aval du recollement. Ce problème sera examiné § 5.

3.3 – Lois empiriques de recollement en supersonique –

La plupart des lois de recollement utilisées en écoulement supersonique en vue de prédire notamment la pression de culot ont été établies à partir de critères empiriques plus ou moins inspirés de l'expérience et dont les plus connus sont ceux de Chapman – Korst et de Nash [50]. Très différente est la démarche développée à l'ONERA depuis 1960 [52], qui est fondée sur l'utilisation directe de données expérimentales et repose sur le concept de critère angulaire de recollement. Celui-ci retient comme idée de base que ce phénomène

est entièrement déterminé par l'état de la couche dissipative en fin de la zone II (fig. 28), état qui peut être caractérisé par les éléments suivants :

- la direction Ψ de l'écoulement extérieur non visqueux relativement à la paroi,
- le nombre de Mach extérieur M_1,
- la loi de distribution des vitesses et densités dans la couche dissipative.

Dans ces conditions et compte tenu de ce qui a été exposé précédemment § 3.1 et 3.2, la loi angulaire recherchée doit nécessairement être de la forme :

$$\Psi = \Psi(M_1, C_q)$$

qui s'écrit, C_q pouvant généralement être considéré comme un petit paramètre :

$$\Psi = \bar{\Psi}(M_1) + C_q \frac{\partial \Psi}{\partial C_q}(M_1)$$

On est ainsi amené à déterminer 2 fonctions :
$\bar{\Psi}(M_1)$ et $\frac{\partial \Psi}{\partial C_q}(M_1)$.

A cet effet, la procédure suivante a été adoptée :

la fonction $\bar{\Psi}(M_1)$ a été déduite d'un certain nombre d'expériences systématiques, pour lesquelles les conditions d'essais ont été choisies aussi voisines que possible du cas idéal $C_q = 0$, où la couche limite initiale est négligeable, les corrections dues aux C_q résiduels ayant toutefois été effectuées.

La fonction $\partial\Psi/\partial C_q$ est calculée selon la méthode décrite en (52) et (36). Les fonctions $\bar{\Psi}(M_1)$ et $\partial\Psi/\partial C_q(M_1)$ ainsi obtenues sont représentées figure 36.

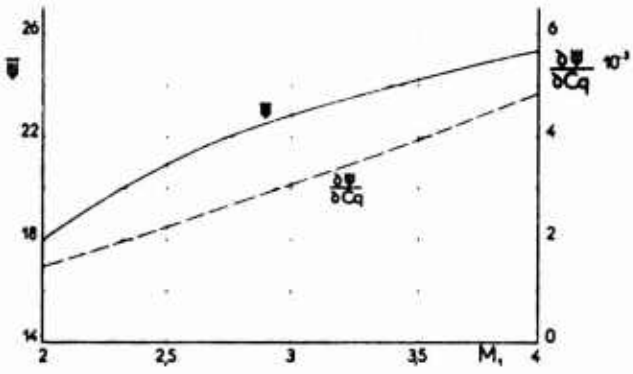

Fig. 36 – Critère angulaire de recollement – Fonctions $\bar{\Psi}$ et $\frac{\partial \Psi}{\partial C_q}$ dans le cas de l'air ($\gamma = 1,4$) (Ψ en degrés sexagésimaux).

Un effort de généralisation et d'extension de cette loi pour traiter des configurations d'obstacles présentant une symétrie axiale a été également entrepris [54].

La corrélation proposée (fig. 37) exprime dans le cas idéal non perturbé, l'écart sur les angles de recollement

$$\bar{\Psi}(M_1)_{révolution} - \bar{\Psi}(M_1)_{plan}$$

en fonction du paramètre F défini figure 37, qui caractérise l'évolution du coefficient de mélange σ avec la géométrie de la frontière isobare. Comme le montre cette figure, la dispersion résiduelle des données expérimentales de $\bar{\Psi}$ est inférieure à 1°, ce qui correspond dans un domaine de nombre de Mach compris entre 1,6 et 6 à une erreur maximale sur la pression p_1 de l'ordre de 5 %.

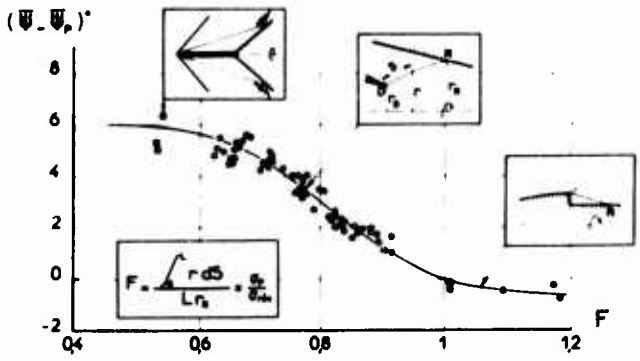

Fig. 37 – Loi angulaire de recollement généralisée.

Parmi les méthodes dérivées du concept de loi angulaire de recollement, nous signalerons celle de Page et al. [53] qui conduit à des résultats voisins.

3.4 – Flux thermiques au voisinage du recollement –

L'intérêt que revêt la prévision des flux de chaleur importants qui apparaissent dans le domaine de recollement d'un écoulement supersonique décollé se manifeste dans des domaines d'application très divers (tuyères propulsives à faible débit secondaire, gouvernes en hypersonique etc...).

D'une façon générale on observe que l'évolution des coefficients de flux de chaleur suit en gros celle des courbes de pression, en particulier dans le domaine hypersonique [44]. Toutefois à des nombres de Mach plus modéré et dans le cas du décollement étendus, le maximum de flux de chaleur se situe près du recollement et légèrement en aval [55]. La corrélation proposée par Holden [44] entre les maxima de flux de chaleur et de pression est représentée figure 38. Elle regroupe un nombre important de résultats obtenus dans un large domaine de nombre de Mach compris entre 2,5 et 13.

Même lorsqu'ils sont élevés ces flux n'ont qu'une faible incidence sur la distribution des pressions dans le domaine de recollement.

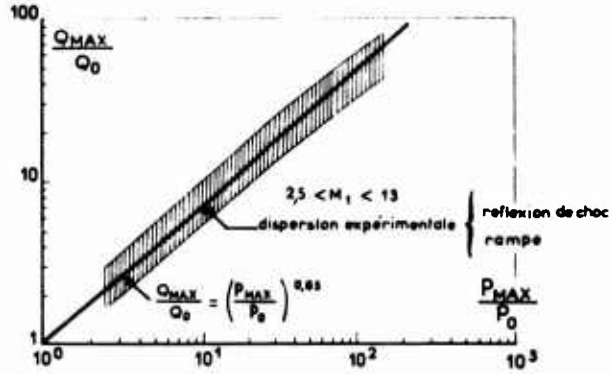

Fig. 38 – Corrélation des maxima de flux de chaleur et de pression.

3.5 – Généralisation de la notion de recollement – Problèmes de confluence –

Les exemples analysés jusqu'à présent concernent le problème du recollement turbulent sur une paroi solide. La parenté étroite qui relie ce phénomène à celui de la confluence de deux écoulements symétriques a été observée depuis longtemps ; les exemples présentés figure 39 montrent que la pression de culot n'est pas affectée de façon sensible par la présence d'une plaque matérialisant

le plan de symétrie qu'il y ait ou non injection de masse à faible vitesse.

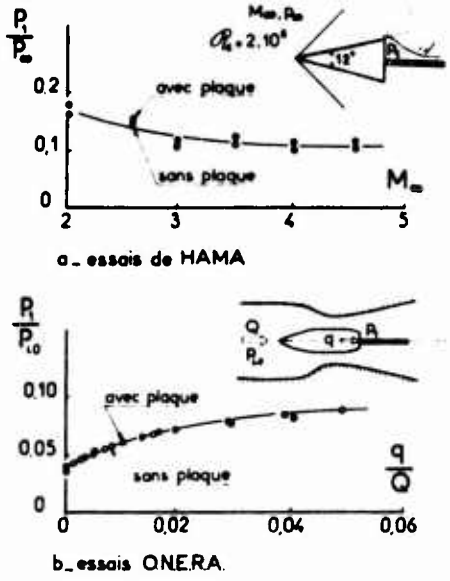

a_ essais de HAMA

b_ essais ONERA.

Fig. 39 – Recollement sur paroi et recollement sur une nappe fluide.

Ces résultats ont conduit à utiliser les lois de recollement sur paroi pour traiter les problèmes de confluence même dans le cas d'écoulements issus de conditions génératrices différentes (fig. 10).

On remarquera que par suite de la ventilation naturelle qui s'organise alors, l'écoulement extérieur (I) se trouve sur cet exemple, dans une situation de recollement avec aspiration d'un débit q_r alors que l'écoulement interne (II) à l'inverse subira les effets d'une injection de masse de même débit.

4 – PHENOMENES DE COUPLAGE DECOLLEMENT-RECOLLEMENT EN TRANSSONIQUE ET SUPERSONIQUE –

4.1 – En dépit de nombreuses expériences accumulées depuis 20 ans, dont beaucoup malheureusement n'offrent pas toutes les garanties de pureté désirables pour les raisons évoquées § 1.1, les mécanismes fondamentaux qui régissent l'apparition et le développement initial d'une zone décollée sous l'influence d'une perturbation d'intensité croissante sont encore insuffisamment connus. En particulier les informations recueillies sur les effets de très larges variations du nombre de Reynolds, présentent des aspects contradictoires, qui ne peuvent pas toujours être expliqués d'une manière rationnelle.

Nous analyserons deux exemples qui nous paraissent assez significatifs des préoccupations actuelles:

- tout d'abord le problème de la rampe en supersonique pour lequel on dispose de nombreux résultats,
- ensuite celui de l'interaction couche limite turbulente – onde de choc en transsonique.

4.2 – Problème de la rampe –

4.2.1 – Aspects généraux –

Nous nous référerons à des essais où l'on ne peut suspecter a priori l'existence d'effets parasites liés à la limitation transversale de l'écoulement. Il s'agit des expériences effectuées par Roshko et al. [6], sur une configuration axisymétrique dont la distance à l'axe est grande devant l'épaisseur de la couche limite (fig. 40), dans le domaine de nombre de Reynolds et de Mach suivant :

$$10^5 < \mathcal{R}\delta_1 < 10^6$$

$$1{,}98 \leq M_1 \leq 4{,}93$$

A titre indicatif, les distributions des pressions mesurées à la paroi pour différentes valeurs de β, M_1 et $\mathcal{R}\delta_1$ étant respectivement égaux à 3,96 et 30.10^6, sont présentées figure 41.

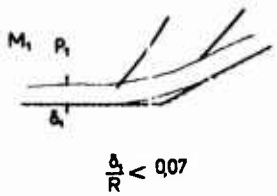

$\frac{\delta_1}{R} < 0{,}07$

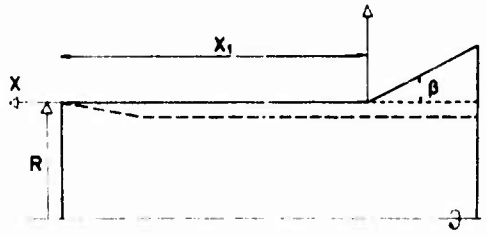

Fig. 40 – Montage expérimental (Roshko).

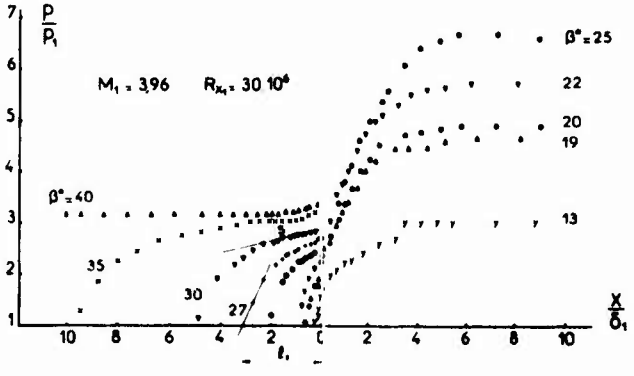

Fig. 41 – Evolution des pressions à la paroi.

Elles mettent en évidence trois types d'évolution bien caractérisés :

- le premier correspond à une compression brutale et monotone ;
- le second est marqué par la présence d'une triple inflexion (de la courbe des pressions) qui est l'indice d'un décollement déjà établi ;
- enfin le dernier est spécifique d'un décollement étendu avec un plateau bien défini (dans ce cas d'ailleurs, l'origine du décollement est situé en dehors du domaine analysé).
  On remarquera que la pression au point d'inflexion médian S, ne tend que lentement vers la pression du plateau. Celle-ci n'est réellement atteinte que lorsque l'origine du décollement est située très en amont de la rampe.

L'évolution en fonction de β de la longueur d'interaction ℓ_1 définie figure 41 et normalisée par l'épaisseur δ_1 de la couche limite initiale est donnée figure 42.

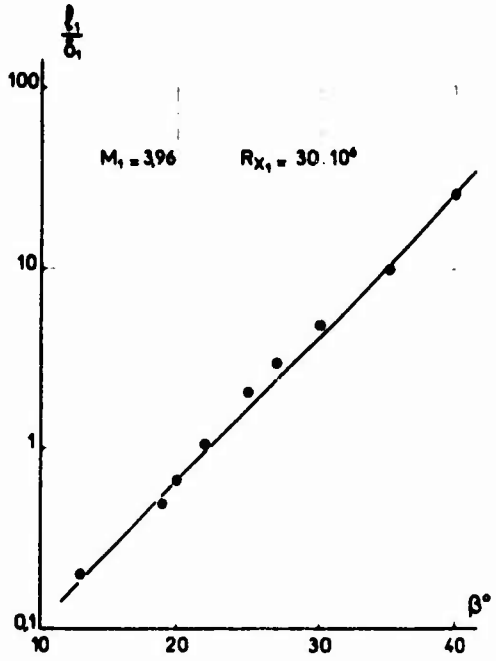

Fig. 42 – Evolution avec β des longueurs d'interaction.

La forme exponentielle de cette évolution explique que lorsque β atteint des valeurs élevées, de petites variations $\Delta\beta$ entrainent un accroissement important de ℓ_1/δ_1.

L'influence du nombre de Reynolds sur l'étendue du décollement (ℓ_1/δ_1) apparait figure 43 ; cette grandeur décroit d'une manière d'autant plus marquée que le nombre de Mach M_1 et l'angle β sont plus grands.

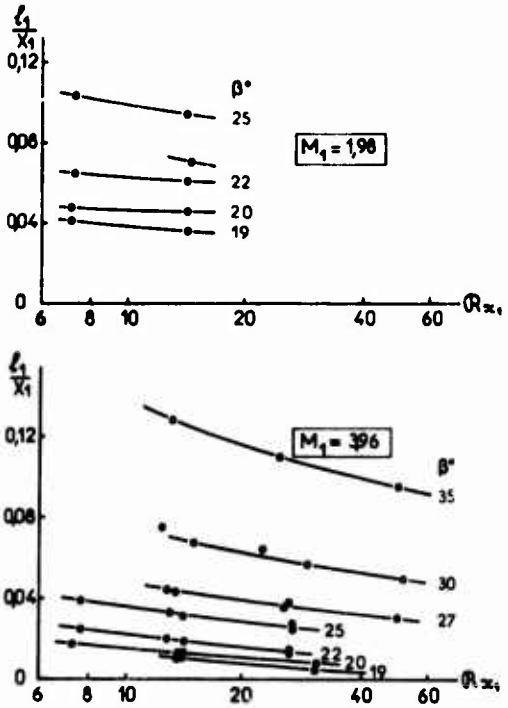

Fig. 43 – Effet du nombre de Reynolds sur la longueur d'interaction.

Cet ensemble de résultats est parfaitement cohérent et explicable à partir des connaissances acquises sur les phénomènes de décollement et de recollement étudiés isolément.

Dans le cas de décollement étendus $(\ell_1/\delta_1 \gg 1)$ et de nombre de Reynolds $R\delta_1$ assez grands, l'utilisation des lois de décollement et de recollement (§ 2 et 3) permet de justifier les traits essentiels observés et notamment :

- les fortes variations que subit ℓ_1/δ_1 lorsque β tend vers une valeur critique qui est la limite des conditions de recollement régulières*.
- la décroissance plus ou moins rapide de ℓ_1/δ_1 lorsque Rx_1 augmente.

Lors de l'exploitation de ces essais, au cours de la recherche d'une forme de présentation commode pour l'utilisateur, Roshko et al. ont observé la particularité suivante qui n'est assortie d'aucune justification : pour une valeur de β fixée, les longueurs réduites d'interaction ℓ_1/δ_1, exprimées en fonction du coefficient de frottement pariétal C_{f_1} à l'origine de l'interaction se regroupent sur une courbe unique indépendante de M_1 (fig. 44).

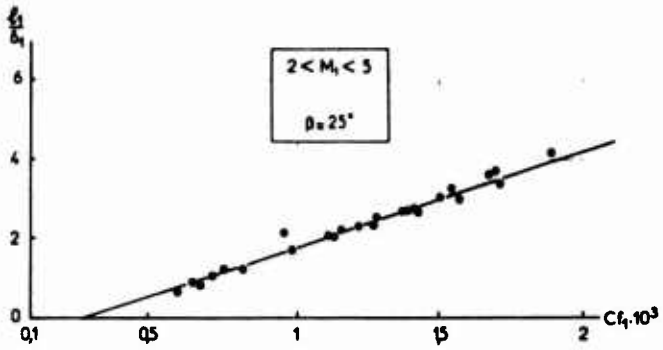

Fig. 44 – Influence amont – Corrélation de Roshko.

Interprétés de cette manière les résultats obtenus dans d'autres séries d'expériences [7 – 56] ne conduisent pas à un recoupement entièrement satisfaisant.

D'une façon générale, les tendances observées dans les essais de Roshko et al. sont sensiblement vérifiées tant que le nombre de Mach reste modéré ($M_1 < 5$) et pour des valeurs de $R\delta_1$, supérieures à 10^5.

Par contre des résultats assez différents en ce qui concerne l'évolution de ℓ_1/δ_1 en fonction de Rx_1 apparaissent soit en hypersonique pour des valeurs $R\delta_1$ assez élevées, soit pour certains essais supersoniques, notamment ceux de Kuehn et al., pour lesquels les valeurs de $R\delta_1$ étaient comprises entre 10^4 et 10^5.

La particularité essentielle de ces résultats est l'inversion de l'effet du Reynolds, ℓ_1/δ_1 croissant lorsque Rx_1 augmente.

Cet effet se manifeste de façon spécialement marquée lorsque $\ell_1/\delta_1 \sim 1$ et plus particulièrement au voisinage des conditions d'apparition du décollement $\ell_1/\delta_1 \ll 1$.

---

* si φ est l'angle de décollement (indépendant de R_e pour ces valeurs $R\delta_1$) la condition géométrique $\beta = \varphi + \Psi$ définit une valeur limite du recollement régulier.

4.2.2 - Décollement naissant -

Il correspond au cas limite d'une configuration associant décollement et recollement lorsque l'étendue L de la zone décollée tend vers 0, c'est donc une des plus compliquées qui soient tant du point de vue de la prévision que de la définition expérimentale. Celle-ci est pour le moins très délicate et dépend fortement de la méthode expérimentale utilisée comme le montre la figure 45 extraite de [57].

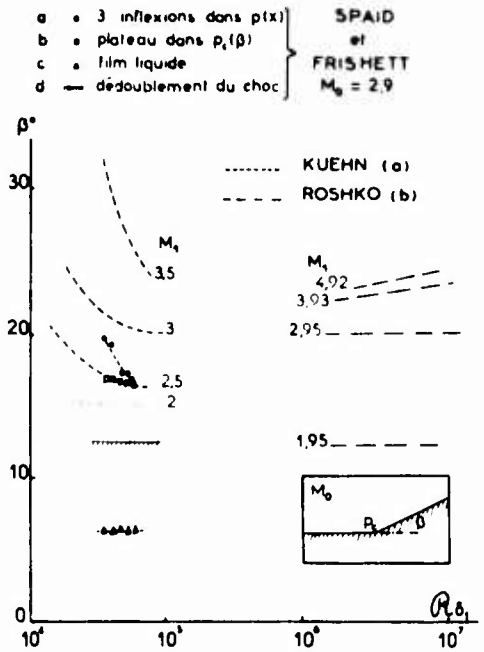

Fig. 45 – Détection du décollement naissant.

Les techniques de détection développées sont extrêmement variées :

- visualisation pariétale par film liquide, observations strioscopiques des couches dissipatives, dédoublement du choc provoqué par la rampe, analyse fine des courbes de pression, perturbation locale (orifice dam), mesure du frottement pariétal. Chacune d'entre elles comporte sa propre part d'incertitude et dans certains cas d'erreur - (film pariétal).

Il n'en demeure pas moins que, malgré cette dispersion et mis à part certains résultats "douteux" obtenus à partir de la technique du film liquide, une tendance générale se manifeste qui corrobore l'effet d'inversion signalé précédemment.

On observe en effet (fig. 46), que le nombre de Mach M_1 étant fixé, lorsque le nombre de Reynolds R_{δ_1} varie, le décollement apparait pour une valeur β de l'angle de la rampe, qui décroit d'abord aux faibles valeurs de R_{δ_1} et croit ensuite lorsque R_{δ_1} augmente, la limite du domaine d'inversion variant de façon assez sensible avec M_1.

Elfstrom a proposé une explication de ce phénomène (s'accordant parfaitement avec les considérations développées § 2.2.1) à partir de laquelle il a pu développer une méthode de prévision du décollement naissant. Celle-ci est basée sur le concept de structure à double couche de l'écoulement dissipatif, une représentation approchée de cette structure étant fournie par la loi de Coles étendue au cas compressible. A partir de cette représentation il est aisé d'extrapoler à la paroi une vitesse limite fictive et par suite un nombre de Mach M_ρ.

Le critère du décollement naissant est fixé pour une valeur de β donnée par la condition d'apparition d'une solution de choc fort.

Comme le montrent la figure 46, l'allure des courbes calculées dans le cas d'écoulements adiabatiques et de parois refroidies traduit bien l'évolution expérimentale et explique notamment les variations en fonction de M_1 et de T_p/T_r du nombre de Reynolds R_{δ_1} définissant la frontière de l'effet d'inversion.

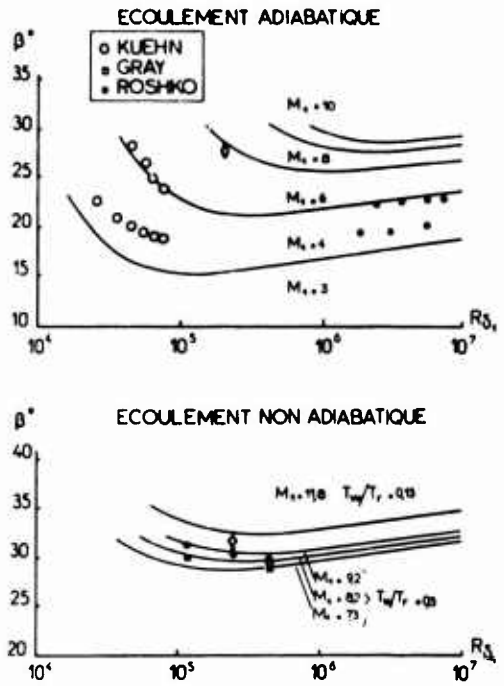

Fig. 46 – Prévision du décollement naissant par Elfstrom.

4.3 - Interaction couche limite onde de choc en transsonique -

4.3.3 - Structure de l'écoulement -

Plus généralement les phénomènes que nous étudierons apparaissent lorsqu'une compression brutale assurant le passage d'un écoulement supersonique à un écoulement subsonique, se produit en présence de la couche limite turbulente établie sur une paroi. Cette situation se rencontre sur le profil d'aile en écoulement transsonique mais également dans les grilles d'aubes de turbomachines, les prises d'air, les tuyères etc....

La configuration de base, que l'on imagine la plus simple est celle de l'onde choc droite qui a été analysée en premier lieu par Seddon [58] et plus récemment par Le Blanc et Goethals [59]. Le petit nombre d'expériences détaillées concernant cette configuration s'explique par la très grande difficulté de réaliser des écoulements stables et bidimensionnels.

La figure 47 définit les caractères spécifiques de ce type d'interaction fournis par l'expérience [58].

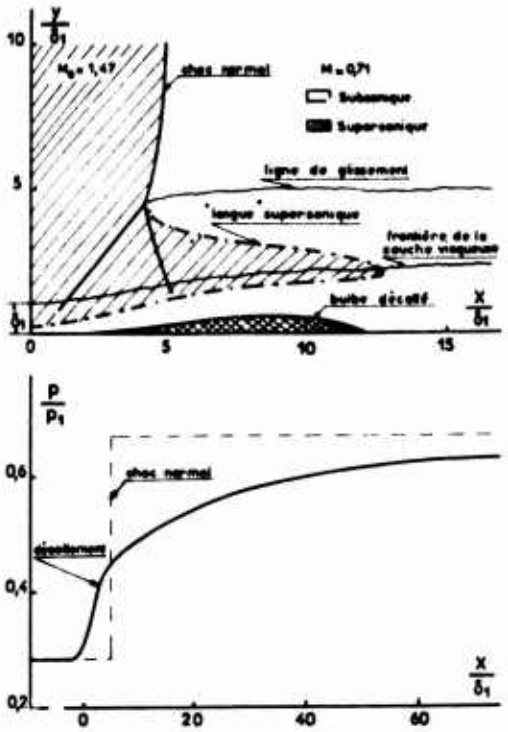

Fig. 47 – Interaction couche limite · onde de choc quasi normale (d'après Seddon).

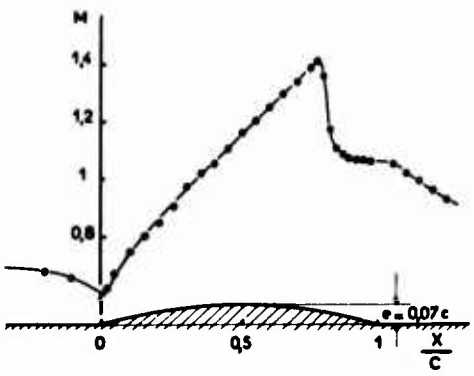

Fig. 48 – Interaction choc · couche limite en écoulement transsonique (essais ONERA).

$M_\infty \simeq 0{,}7$

e = 0,07 c

Fig. 49 – Interaction choc · couche limite en écoulement transsonique : essais ONERA. Visualisation par strioscopie éclair (t = 1 µs).

Le premier et le plus apparent est la nature essentiellement supersonique du décollement, dont le mécanisme de formation est en tout point semblable à celui qui a été décrit § 2.2. Il se caractérise par la présence d'une onde de choc oblique provoquant un accroissement de pression extrêmement brutal jusqu'au point de séparation ; la recompression se poursuit en aval d'une manière beaucoup plus modérée, monotone, d'abord jusqu'au point de recollement et ensuite au-delà sur une étendue importante, supérieure à 50 δ_1 , l'écoulement étant alors entièrement subsonique.

Entre les points de séparation et de recollement, la structure de l'écoulement à l'extérieur des couches dissipatives présente un caractère complexe qui est lié à la présence, tout d'abord d'une configuration de choc en λ résultant de la rencontre du choc oblique de décollement avec le choc principal extérieur, ensuite, d'un étroit domaine faiblement supersonique s'étendant jusqu'au point de recollement.

Dans le cas du profil d'aile, les phénomènes observés sont de même nature, comme le montre l'exemple présenté figure 48 et extrait de [60]. L'interférogramme pris en teinte plate, met bien en évidence la structure des chocs et la déviation brutale que subit l'écoulement lors du décollement.
Dans ce cas particulier l'écoulement est entièrement subsonique à l'aval de la 2ème branche du λ .

Un autre aspect caractéristique de cette forme d'interaction choc couche limite est l'existence d'effets instationnaires marqués au voisinage du recollement qui sont mis en évidence figure 49 par une visualisation ombroscopique à faible temps d'exposition (1 µs). Ces effets se répercutent directement sur la zone décollée, mais aussi peuvent affecter la structure des chocs principaux.

4.3.2 – Influence de la non uniformité de l'écoulement extérieur et du nombre de Reynolds – Apparition du décollement –

Une discussion très complète des phénomènes liés notamment à la présence de gradients de pression adverses qui peuvent être importants en aval de la configuration de choc a été effectuée par Pearcey [61]. On lui doit en particulier une analyse des phénomènes d'interférence entre le décollement créé par l'interaction couche limite onde de choc et celui qui peut se produire au voisinage du bord de fuite d'une aile sous l'effet de ces gradients.

Un exemple typique de ces effets extrait d'une étude de Stanewsky [62] est présenté figure 50. Il montre l'évolution avec le nombre de Mach de la position de l'onde de choc et de l'étendue des zones décollées sur un profil d'aile en écoulement transsonique. Lorsque le nombre de Mach M_∞ augmente, le développement rapide des deux zones décollées existant l'une derrière l'onde de choc, l'autre au voisinage du bord de fuite conduit à la création d'un décollement unique et étendu, entrainant passagèrement une inversion du déplacement du choc en fonction de M_∞.

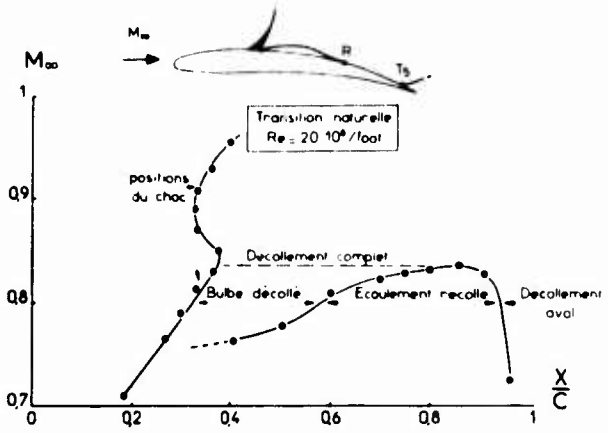

Fig. 50 – Exemple d'évolution du décollement sur un profil d'aile en transsonique.

Les effets spécifiques du nombre de Reynolds défini par l'échelle du profil sont de même nature que ceux rencontrés en supersonique, la diminution de l'épaisseur relative de la couche limite entrainant lorsque R_δ est suffisamment élevé une diminution de l'étendue longitudinale du décollement.

Dans l'état actuel des choses nous ne disposons pas de moyens simples permettant de définir l'apparition du décollement en fonction des circonstances de l'écoulement et de l'état de la couche limite immédiatement en amont de l'interaction, les progrès dans ce domaine étant liés au développement de méthodes de calcul de l'interaction couche limite onde de choc en transsonique.

5 – METHODES DE CALCUL DES ECOULEMENTS SEPARES ET APPLICATIONS –

5.1 – Généralités –

Nous terminerons cet exposé essentiellement consacré à l'analyse expérimentale de la structure des écoulements turbulents décollés par une brève revue des moyens de prévision dont nous disposons, en essayant de préciser dans quelle mesure l'expérience peut aider à leur développement.

Les progrès rapides enregistrés ces dernières années dans le calcul des phénomènes de forte interaction visqueuse en écoulement laminaire se sont répercutés d'une manière très directe sur le développement de méthodes similaires pour traiter le cas turbulent.

Nous classerons les moyens de prévision en trois grandes catégories qui correspondent à trois démarches différentes sur le plan de la connaissance des phénomènes :

- les méthodes globales,
- les méthodes dérivées des techniques intégrales de calcul des couches limites,
- enfin les méthodes purement numériques utilisant des approches du type différence finie ou éléments finis pour résoudre les équations plus ou moins simplifiées du mouvement moyen ;

5.2 – Méthodes globales –

Ces méthodes très rapides de mise en oeuvre, sont essentiellement basées sur l'application à un modèle de fluide parfait représentant schématiquement les frontières d'une zone décollée et indéterminé a priori, des critères de décollement et de recollement permettant de lever cette indétermination.

Les applications les plus connues concernent les calculs de pression de culot et plus généralement les problèmes de confluence écoulements interne-externe traités dans le cadre d'une optimisation des systèmes propulsifs. La qualité des résultats obtenus dépend bien entendu largement de la validité des lois ou critère retenus, le domaine d'application étant en principe restreint au cas des couches limites initiales d'épaisseur modérée (§ 3). Ainsi que le montre la réf. [36] qui présente une revue de ces méthodes de très bons résultats peuvent être enregistrés, notamment lorsqu'il s'agit d'effectuer une analyse paramétrique dans le voisinage d'un cas expérimental connu. Le faible coût en temps de calcul est un des éléments essentiels du succès de tels programmes.

On peut également inclure dans la même catégorie de méthodes, celles qui ont été développées en écoulement incompressible pour prévoir l'effet d'un décollement de bord de fuite sur la portance d'un profil, en simulant le décollement par un écoulement de sources satisfaisant à des conditions particulières aux points de séparation et de confluence [65].

L'amélioration de ces diverses méthodes se poursuit dans l'espoir de traiter avec plus de précision un nombre de configuration plus étendu. Toutefois les progrès que l'on peut envisager à terme demeurent faibles.

5.3 – Méthodes intégrales –

5.3.1 – Ecoulement extérieur supersonique –

Le principe de base défini dès 1952 par Crocco et Lees repose sur la description de la zone dissipative décollée au moyen des équations de Prandtl résolues par une technique intégrale. La loi de pression ou de vitesse imposée à la frontière n'est plus une donnée mais résulte du couplage entre le champ externe et la couche visqueuse.

Dans le cas d'un écoulement extérieur supersonique cette loi peut être déterminée au fur et à mesure de la progression du calcul, dès que la condition de couplage est fixée.

Dans les méthodes les plus récentes développées depuis 1967 [64] les 2 équations retenues pour décrire les couches dissipatives sont celles de Karman et de l'énergie cinétique du mouvement moyen. Leur mise en oeuvre nécessite :

- tout d'abord le choix d'une famille de profils de vitesse à un paramètre principal $\mathcal{H}_1$ à partir duquel sont exprimés les différents paramètres de forme intervenant dans ces équations,
- ensuite une expression de frottement turbulent apparent. Celle-ci intervient essentiellement pour définir l'intégrale de dissipation supposée fonction universelle de $\mathcal{H}_1$.

Une discussion très complète des variations auxquelles conduisent les choix effectués par différents auteurs est présentée dans [36].

Les conclusions sont les suivantes :

En ce qui concerne l'expression des divers paramètres de forme les différentes solutions proposées conduisent à des résultats pratiquement identiques bien recoupés par l'expérience comme le montre l'exemple de la figure 51.

Par contre des écarts importants apparaissent au niveau de la relation $\phi(H, \lambda)$ (fig. 52), selon la modélisation de la turbulence adoptée.

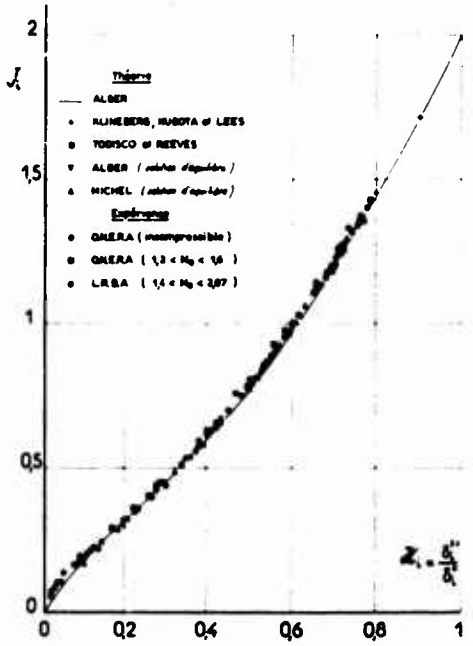

Fig. 51 – Fonction auxiliaire $J_i = \frac{\delta_i^{**}}{\delta_i^*}$

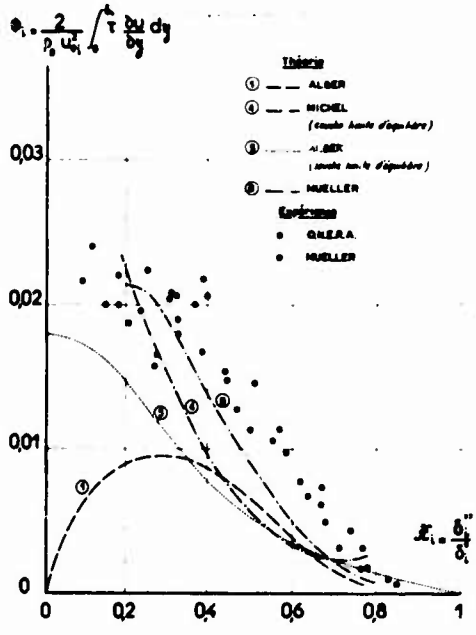

Fig. 52 – Fonction de dissipation en écoulement incompressible – Comparaison avec l'expérience.

On remarquera que l'existence de telles relations n'est justifiée comme nous l'avons vu § 3 que lorsque la couche limite en amont du décollement est d'épaisseur modérée devant l'étendue de la zone décollée.

Le second problème posé par la mise en oeuvre des méthodes intégrales concerne l'intégration du système différentiel (A) formé par les 2 équations de la couche limite auquel on adjoint la relation de couplage.

Une première difficulté apparait lors de l'initialisation du calcul. Lorsque le nombre de Mach n'est pas très faible l'intégration du système (A) conduit à une évolution décroissante de la pression incompatible avec la formation d'un décollement. Cette situation résulte de l'état "supercritique" de l'écoulement en amont de la zone décollée. Pour obtenir une solution de décollement il est alors nécessaire d'avoir recours à l'artifice du saut supercritique - subcritique dont l'effet sur la distribution des pressions est analogue à celui d'un choc [36].

D'autre part, la solution de (A) est en général astreinte à passer par un point critique K du type col, imposé par la nécessité d'un retour à l'état supercritique qui ne conduise pas à une évolution irréaliste des pressions et du paramètre de forme. C'est cette condition critique qui détermine la solution du problème.

La réalité physique du point K a été l'objet de nombreuses controverses. Les détracteurs font remarquer que les valeurs critiques ainsi obtenues (position en x, nombre de Mach local, paramètre de forme etc...) varient de façon sensible selon la loi de couplage retenue. Les tenants par contre se réfèrent à l'expérience qui démontre l'existence en aval du point de recollement d'un point particulier possédant l'essentiel des propriétés de K [36].

Les premières tentatives d'application des méthodes intégrales ont été effectuées en vue de prédire la pression de culot [Alber 1967].

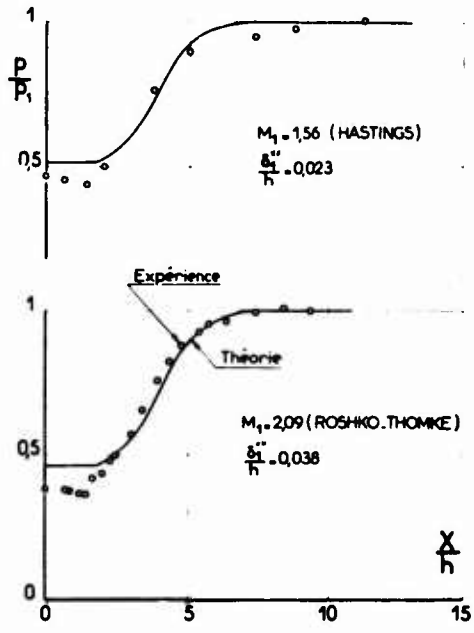

Fig. 53 – Exemples d'application de la théorie d'Alber.

La comparaison avec l'expérience présentée figure 53 et extraite de [64] est assez satisfaisante dans des cas toutefois où l'épaisseur de la couche limite initiale est grande. Une comparaison effectuée sur une configuration comportant une couche limite initiale négligeable (fig. 54) est beaucoup

moins bonne. Sur cette figure sont également présentés deux calculs effectués selon la même technique mais en utilisant un modèle de turbulence basé sur le concept de longueur de mélange proposé par Michel, pour deux lois de couplage différentes : tout d'abord celle proposée par Alber où le couplage est effectué à la frontière δ de la couche limite, ensuite la loi de déplacement classique $d\delta^*/dx = tg\,\theta$, plus exacte comme l'a montré Hankey [73].

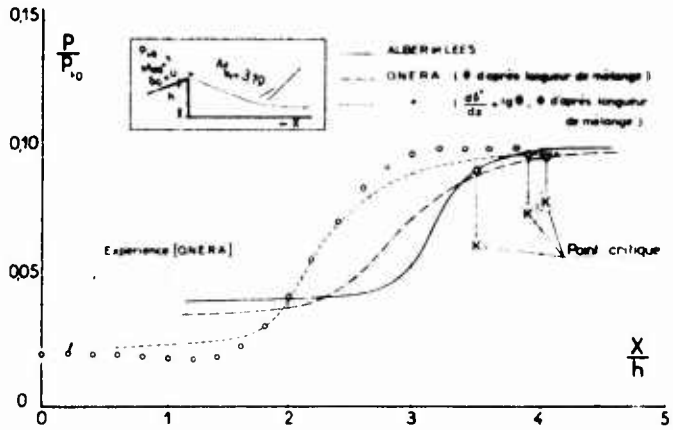

Fig. 54 – Exemple d'application – Couche limite initiale négligeable. $M_{e_1} = 3{,}19$.

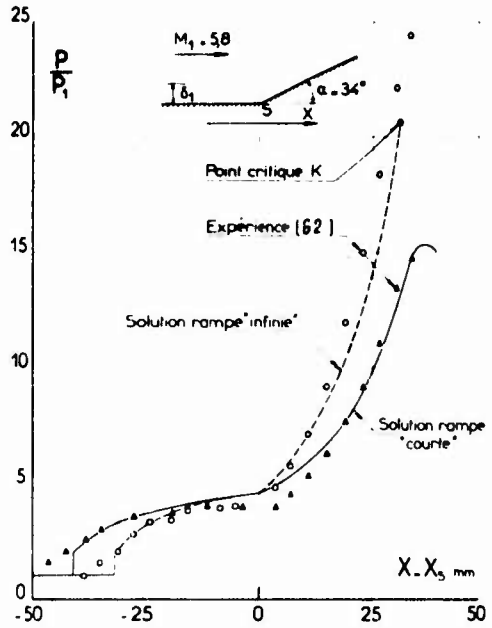

Fig. 55 – Décollement turbulent dans un dièdre – Influence de la longueur de rampe – Théorie de Hunter et Reeves.

On constate que les résultats varient d'une façon très importante selon le choix effectué. Il faut se garder toutefois de tirer des conclusions définitives d'expériences numériques destinées à mettre en évidence la sensibilité de la méthode à deux quantités dont la connaissance est mal établie à savoir le frottement turbulent et l'épaisseur physique δ de la couche dissipative.

Parmi les extensions de cette méthode successivement réalisées on notera :

- le traitement du problème de la rampe par Hunter et Reeves en 1971 [62],
- celui de la confluence de deux écoulements avec décollement de bord de fuite par Klineberg Kubota et Lees en 1972.

L'exemple présenté figure 55 (problème de la rampe), bien recoupé par l'expérience excepté au décollement, met en évidence les principaux caractères de la solution théorique : saut supercritique - subcritique, point critique etc...

La configuration dite rampe infinie correspond à des conditions de recollement régulières, le point K se trouvant en amont du bord de fuite .

Par contre la solution "rampe courte" est relative à une configuration singulière qui est perturbée par la présence d'une détente de l'écoulement au point F en amont du point critique K entraînant une modification profonde des conditions de recollement.

Le calcul d'une telle configuration est mené à bien, en imposant que les dérivées $\frac{d\delta^*}{dx}$, $\frac{dMe}{dx}$, $\frac{d\mathcal{H}_i}{dx}$ tendent simultanément vers l'infini en F .

D'une façon générale, la présence de fortes perturbations dans le domaine de recollement examinée notamment dans [36] et [78] pose un problème qui n'a été résolu par les méthodes intégrales que pour les détentes centrées. Le cas de l'onde de choc n'a pas été traité.

Insuffisances des méthodes intégrales classiques

Outre son inadaptation au traitement des zones décollées peu étendues signalée précédemment, un des points le plus discutable des méthodes intégrales est certainement l'hypothèse d'une pression constante selon y découlant des hypothèses de Prandtl.

Un certain nombre de tentatives ont été faites afin d'introduire les gradients de pression normaux notamment par Shamroth et Mac Donald [69], Hoffman, Myring [70] ces derniers auteurs ayant montré que la solution devient subcritique lorsque l'on tient compte d'une variation de la pression selon y .

Une amélioration important des méthodes intégrales spécialement dans le cas de décollements peu étendus, est celle proposée notamment par Rose [35], en introduisant le concept de "double couche" dont nous avons déjà discuté le bien fondé § 2.

Cette technique permet tout d'abord de prendre en compte d'une manière rigoureuse les effets de gradients de pression normaux et d'obtenir en principe une meilleure description des phénomènes dissipatifs.

Parmi les améliorations possibles de ces méthodes nous signalerons également l'extension au cas turbulent des travaux actuellement entrepris par Crocco en laminaire.

5.3.2 - Ecoulement extérieur subsonique ou transsonique -

Dans ce cas, le caractère elliptique ou mixte des équations régissant l'écoulement extérieur impose le recours à une procédure itérative pour satisfaire les conditions de couplage, consistant à calculer successivement les effets de déplacement de la couche limite pour un gradient de pression connu et l'écoulement extérieur en tenant compte de ces effets ; la procédure est par exemple initiée à partir de la solution de fluide parfait éventuellement aménagée.

Une telle méthode devient impraticable dès qu'un décollement étendu se produit par suite de difficultés numériques liées à l'existence de singularités au voisinage du décollement ; ces difficultés ne peuvent être surmontées qu'à l'aide d'artifices, et les erreurs ainsi commises sont souvent importantes.

Un des progrès marquants enregistrés récemment a été de montrer que les difficultés rencontrées sont inhérentes à la contrainte non réaliste d'un gradient de pression arbitrairement fixé à l'approche du décollement et disparaissent lorsque les données nécessaires au calcul de couche limite sont soit la distribution de frottement pariétal, soit l'évolution de l'épaisseur de déplacement. On obtient alors une procédure de calcul de couches dissipatives dite "inverse" dans laquelle $p(x)$ devient le résultat de calcul et qui permet de traiter les zones décollées sans difficulté numérique. De ce fait, ces méthodes sont susceptibles de bénéficier de toutes les améliorations provenant d'une modélisation plus raffinée de la turbulence et de ses effets.

Les principaux travaux effectués dans cette voie sont ceux de Klineberg et Steger [74] et de Kuehn et Nielsen [75].

L'application de ces procédures au calcul d'écoulements transsoniques présente un intérêt indiscutable.

5.4 - Méthodes numériques -

C'est finalement dans ce domaine que les résultats les plus spectaculaires ont été obtenus. Ce succès est dû à la conjonction de trois effets favorables :

a) la diminution très importante de la durée des calculs liée aux progrès technologiques des ordinateurs,

b) le développement de nouvelles techniques numériques accroissant la stabilité et la convergence de ces calculs,

c) enfin les progrès accomplis dans la modélisation de la turbulence.

Nous ne nous étendrons pas sur les techniques de calcul développées qui seront abondamment commentées au cours de cette session, nous contentant de faire quelques remarques :

En ce qui concerne a), la progression réalisée depuis une décade laisse penser que les calculs basés sur la résolution numérique des équations complètes du mouvement moyen pourront être étendus dans un futur relativement proche à des configurations tridimensionnelles.

Une réduction substantielle des temps de calcul peut également être attendue de b) grâce à la mise en oeuvre de schémas plus élaborés et plus performants.

C'est ainsi que les résultats remarquables publiés notamment par Baldwin et Deiwert [76] ont été obtenus à l'aide du schéma explicite de MacCormack qui s'est révélé particulièrement bien adapté au traitement d'écoulements visqueux, compressibles, comportant des ondes de choc. L'utilisation de schémas implicites, actuellement en cours d'étude, devrait entrainer un accroissement sensible des pas de temps et par suite une plus grande rapidité des calculs.

Mais l'élément déterminant qui conditionne largement la qualité des résultats demeure la modélisation de la turbulence (c), comme le montre l'exemple donné figure 56 et extrait de [77].

Il concerne le décollement se produisant en écoulement incompressible au niveau de l'élargissement brusque d'une conduite cylindrique. Cette configuration a fait l'objet d'une étude expérimentale et théorique très détaillée à l'Institut de Mécanique des fluides de Toulouse.

Sur la figure 56a est présentée une comparaison, portant sur les vitesses moyennes et le frottement apparent turbulent, entre les mesures et des résultats fournis par deux types de calcul. Le premier est basé sur une modélisation ne nécessitant qu'une seule équation de transport, celle de l'énergie cinétique turbulente, l'échelle spatiale caractéristique de la Turbulence étant fournie par une relation algébrique ajustée sur l'expérience.

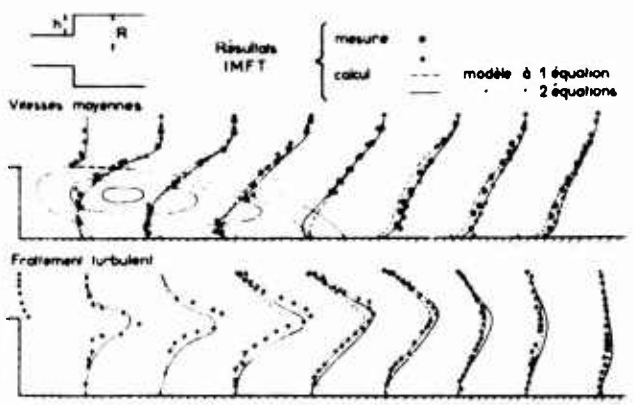

Fig. 56a – Ecoulement incompressible axisymétrique en aval d'un décrochement de paroi h/R = 0,6.

Le second plus élaboré comporte deux équations de transport relatives à l'énergie cinétique turbulente et à la dissipation. Ces deux modèles retiennent le concept de viscosité turbulente.

On constate que le second conduit à des résultats beaucoup plus proches des mesures spécialement en ce qui concerne l'étendue de la zone décollée et la prévision du frottement apparent turbulent.

La distribution des pressions axiales (fig. 56b) est assez correctement prévue par le second calcul, alors que des écarts importants avec l'expérience apparaissent dans les résultats issus du premier. Cependant le modèle le plus élaboré, n'est pas en mesure de fournir une évolution précise des vitesses et du frottement au sein des couches dissipatives dans le domaine de restructuration en aval du point de recollement moyen où se produisent comme nous l'avons vu (§ 3) de fortes variations longitudinales des caractéristiques de la turbulence.

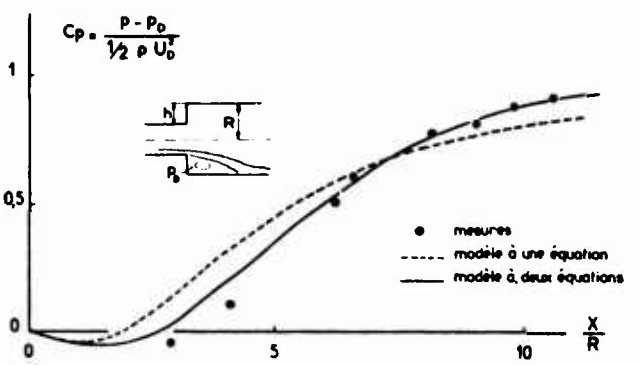

Fig. 56b – Distribution des pressions axiales.

Cet exemple qui concerne le cas relativement simple d'un écoulement incompressible avec point de séparation fixé met en évidence, pour une modélisation de la turbulence déjà élaborée, des écarts modérés mais non négligeables entre le calcul et les mesures, dans certains domaines de l'écoulement.

Il nous parait instructif dans la mesure où il montre :

- qu'une critique expérimentale très détaillée de configurations de calcul-test est nécessaire,
- qu'une modélisation de la turbulence très raffinée peut seule permettre d'obtenir une représentation exacte des phénomènes physiques. Cette condition est impérative lorsqu'il est demandé au calcul de simuler certains effets tels que ceux du nombre de Reynolds par exemple.

Pour obtenir ces résultats des expériences à caractère très fondamental sur des configurations de décollement, comportent notamment une analyse très complète de la structure de la turbulence sont indispensables aussi bien dans le cas incompressible que dans le cas compressible où les informations de cette nature sont rares.

L'association étroite entre théorie et expérience nécessite en particulier la connaissance précise des conditions initiales du calcul ce qui requiert un nombre de données expérimentales d'autant plus grand que le modèle de turbulence est plus élaboré.

6 - CONCLUSION -

Pour conclure cette revue des problèmes posés par l'étude des écoulements décollés bidimensionnels et turbulents, après avoir résumé la situation présente telle qu'elle a été décrite, nous indiquerons les orientations de recherches qui nous paraissent souhaitables.

Sur le plan expérimental, l'état des connaissances actuelles est le fruit de recherches patientes dont les progrès bien que lents ont permis tout d'abord d'obtenir une vue assez complète des aspects phénoménologiques, ensuite de définir les principaux facteurs d'influence régissant la formation et le développement des zones décollées. Toutefois par suite de difficultés importantes spécifiques des mesures dans de telles zones, l'analyse de la structure intime des phénomènes turbulents dans ces domaines ainsi que celle des effets instationnaires associés n'a pas progressé de façon très marquée.

Sur le plan théorique, l'absence jusqu'à ces dernières années d'un support suffisant a été durement ressentie au niveau de l'exploitation et de l'interprétation des expériences et a longtemps limité les possibilités de calcul à quelques configurations susceptibles d'une schématisation relativement simple, imposant malgré tout un large recours à l'empirisme (écoulement de culot en supersonique par exemple). Les progrès réalisés récemment dans le domaine théorique en laminaire ont pu être rapidement étendus au cas turbulent grâce à l'évolution enregistrée dans la modélisation de la turbulence. En particulier, la mise en oeuvre de méthodes numériques susceptible de résoudre des équations complètes du mouvement constitue un tournant dans la maîtrise des écoulements décollés.

La solution de la plupart des problèmes de décollement turbulent bidimensionnels peut être envisagée à condition d'entreprendre une action comportant le développement conjoint de recherches concernant :

- l'élaboration de schémas numériques performants adaptés à des conditions aux limites variées, permettant d'assurer une description fine des phénomènes dissipatifs mais aussi d'obtenir une réduction des temps de calcul ;
- l'analyse expérimentale détaillée dans un large domaine de nombre de Reynolds et sur des configurations de base particulièrement pures, du champ moyen et de la structure de la turbulence dans les zones décollées, en particulier des facteurs agissant sur sa production et son développement.

Cette action pour laquelle l'utilisation de techniques nouvelles telles que l'anémométrie laser peut se révéler décisive comportera un double caractère : aboutir en premier lieu à une modélisation raffinée des phénomènes turbulents, fournir ensuite des éléments de contrôle précis pour les études numériques.

Parmi les aspects fondamentaux liés à l'analyse des structures turbulentes et nécessitant une étude approfondie, il convient de signaler les problèmes concernant :

- les ondes de choc (en particulier dans le domaine transsonique) et leur rôle sur la formation et le développement de ces structures,
- la confluence, notamment en écoulement subsonique, et les instabilités de sillage associées.

REFERENCES

[1] - Green J.E., "Interactions between shock waves and turbulent boundary layers"
Progress in Aerospace Sciences, Vol. 11 - Pergamon Press 1970.

[2] - Reda D.C., Murphy J.D., "Shock wave - turbulent boundary layer interactions in rectangular channels"
AIAA Paper 72-715 - 1972.

[3] - Reda D.C., Murphy J.D., "Shock wave - turbulent boundary layer interactions in rectangular channels, Part II : The influence of sidewall boundary layers on incipient separation and scale of the interaction"
AIAA Paper 73-234 - 1973.

[4] - Le Balleur J.C., Miranda J., "Etude expérimentale et théorique du recollement bidimensionnel turbulent incompressible"
Agard Symposium on Flow separation - Göttingen - Mai 1975.

[5] - Roshko A., Thomke G.J., "Flow separation and reattachment behind a downstream - facing step"
Douglas Report S.M. - 43 056-1 - Janvier 1964.

[6] - Roshko A., Thomke G.J., "Flare induced separation lengths in supersonic turbulent boundary layers"
AIAA Paper 75-6 - 1975.

[7] - Settles G.S., Bogdonoff S.M., "Separation of a supersonic turbulent boundary layer at moderate to high Reynolds Numbers"
AIAA Paper 73-666 - 1973.

[8] - Rose W.C., "The behaviour of a compressible turbulent boundary layer in a shock-wave-induced adverse pressure gradient"
NASA TN D 7092.

[9] - Mabey D.G., "Analysis and correlation of data on pressure fluctuations in separated flow"
Journal of Aircraft - Vol. 9 N° 9 - Septembre 1972.

[10] - Holden M.S., "Shock wave - turbulent boundary layer interaction in hypersonic flow"
AIAA Paper 72-74 - 1972.

[11] - Coe C.F., Chyu W.J., "Pressure-fluctuation inputs and response of panels underlying attached and separated supersonic turbulent boundary layers"
AGARD C.P. 113 - Septembre 1972.

[12] - Bradshaw P., Wong F.Y.F., "The reattachment and relaxation of a turbulent shear layer"
Journal of Fluid Mechanics - Volume 52 Part 1 - Mars 1972.

[13] - Caspersen C., Kristensen H.S., "Laser doppler anemometer measurements in a low velocity windtunnel on a fin-plate model"
DISA Information N° 17 - Février 1975.

[14] - Rose W.C., Johnson D.A., "A study of shock wave - turbulent boundary layer interaction using laser velocimeter and hot wire anemometer techniques"
AIAA Paper 74-95 - 1974.

[15] - Sullivan J.P. et al., "Study of vortex ring using a laser doppler velocimeter"
AIAA Journal Vol. 11 - Octobre 1973.

[16] - Boutier A., "Etude et réalisation d'un vélocimètre compact. Application à des mesures de vitesses en écoulements supersonique et transsonique turbulents"
Thèse - Université Paris-Sud - 1974.

[17] - Délery J, Laval P., Chattot J.J., "Etude expérimentale et théorique de l'écoulement transsonique autour d'un demi-profil"
A.A.A.F. 10ème Colloque d'Aérodynamique Appliquée - Novembre 1973.

[18] - Havener A.G., Radley R.J., "Turbulent boundary layer flow separation measurements using holographic interferometry"
AIAA Journal Vol. 12 N° 8 - Août 1974.

[19] - Smith A.M.O., "Remarks on fluid mechanics of the stall"
AGARD Lecture series n° 74 - 1975.

[20] - Kline S.J. et al., "The structure of turbulent boundary layers"
Journal of Fluid Mechanics Vol. 30 Part 4 - Décembre 1967.

[21] - Sandborn V.A., Liu C.Y., "On turbulent boundary layer separation"
Journal of Fluid Mechanics Vol. 32 part 2 - Mai 1968.

[22] - Bradshaw P., "Effects of streamline curvature on turbulent flow"
Agardograph n° 169 - 1973.

[23] - Mathieu, Jeandel, "Méthode de calcul de la couche limite turbulente utilisant une équation de comportement du coefficient de Boussinesq"
Journal de Mécanique Vol. 12 N° 4 - 1973.

[24] - Michel R., Houdeville R., Cousteix J.
Communication privée.

[25] - Schubauer G.B., Klebanoff P., "Investigation of separation of the turbulent boundary layer"
NACA TN 2133 - 1950.

[26] - Michel R., Cousteix J., Arnal D.
Article à paraître dans la Recherche Aérospatiale.

[27] - Stratford B.S., "The prediction of separation of the turbulent boundary layer"
Journal of Fluid Mechanics Vol. 5 - 1959.

[28] - Cébéci J. et Al., "Calculation of separation points in incompressible turbulent flows"
Journal of Aircraft Vol. 9 - Septembre 1972.

[29] - Townsend A.A., "The development of turbulent boundary layers with negligible wall stress"
Journal of Fluid Mechanics Vol. 8 - Mai 1960.

[30] - Gerhart P.M., Gober L.J., "Comparison of several methods for predicting separation in a compressible turbulent boundary layer"
NASA T.M. X-3102 - Août 1974.

[31] - Alber I.E. et al., "An experimental investigation of turbulent transonic viscous - Inviscid interactions"
AIAA Journal Vol. 11 - Mai 1973.

[32] - Carrière P., "Analyse théorique du décollement et du recollement turbulent au bord de fuite d'un aubage aux vitesses supersoniques"
Symposium "Flow research on blading" Baden - 1969.

[33] - Délery J, Masure B., "Action d'une variation brusque de pression sur une couche limite turbulente ; application aux prises d'air hypersoniques"
La recherche Aérospatiale N° 129.

[34] - Délery J., Le Balleur J.C. et Sirieix M., "Etude expérimentale de l'interaction choc - couche limite turbulente en écoulement supersonique"
Communication au 13ème Congrès I.U.T.A.M. - Moscou 1972.

[35] - Rose W.C. et al., "Interaction of an oblique shock wave with a turbulent boundary layer"
AIAA Journal Vol. 6 N° 9 - 1968.

[36] - Carrière P., Sirieix M., Délery J., "Méthodes de calcul des écoulements turbulents décollés en supersonique"
A paraître dans Progress in Aerospace Sciences.

[37] - Chapman D.R. et al., "Investigation on separated flows in supersonic and subsonic streams with emphasis on the effect of transition"
NASA TR 1356.

[38] - Erdos J., Pallone A., "Shock boundary layer interaction and flow separations"
AVCO Technical Report AD ... 61 2... - Août 1963.

[39] - Carrière P., "Recherches sur les décollements dans les tuyères propulsives"
Revue Roumaine des Sciences Tech. Tome 13 N° 3 - 1968.

[40] - Carrière P., Sirieix M., Solignac J.L., "Propriétés de similitude des phénomènes de décollement laminaire ou turbulent en écoulement supersonique non uniforme"
XIIème Congrès Mécanique Appliquée - Stanford 1968.

[42] - Zukoski E.E., "Turbulent boundary layer separation in front of a forward - facing step"
AIAA Journal Vol. 5 - Octobre 1967.

[43] - Merlé M.J., "A critical review of analytical methods for estimating control forces produced by secondary injection"
NOL T.R. 68-5 - Janvier 1968.

[44] - Holden M..., "Experimental studies of shock wave boundary layer interaction"
Lecture Series 66 - V.K.I. - Janvier 1974.

[45] - Elfstrom G.M., "Turbulent supersonic flow at a wedge compression Corner"
Journal of Fluid Mechanics Vol. ... Part 1 - 1972.

[46] - Stollery J.L., "Laminar and turbulent boundary layer studies at hypersonic speeds"
Paper 72-09 - 8th ICAS Congress - Août 1972.

[47] - Appels C., "Turbulent boundary layer separation at Mach 12"
V.K.I. Technical note 90 - Septembre 1973.

[48] - Tani I., "Experimental investigation of flow separation over a step"
IUTAM Symposium - Fribourg 1957.

[50] - Tanner M., "Theoretical prediction of base pressure for steady base flow"
Progress in Aerospace Sciences Vol. 14.

[51] - Carrière P., "Effet d'une injection de fluide dans l'eau morte sur les conditions de recollement d'un écoulement plan supersonique"
C.R.Académie des Sciences - Paris t. 251 - 1960.

[52] - Carrière P. et Sirieix M., "Facteurs d'influence du recollement d'un écoulement supersonique"
10ème Congrès de Mécanique Appliquée - Stresa 1960.

[53] - Page R.H. et al., "Reattachment of two-dimensional supersonic turbulent flow"
ASME Paper 67-FE-20 - 1967.

[54] - Délery J., Solignac J.L., "Contribution à l'étude aérodynamique des systèmes propulsifs à double flux"
Israel Journal of Technology Vol. 10 N° 1 - 2 - 1972.

[55] - Rougier P., "Etude expérimentale des phénomènes dynamiques et thermiques liés au recollement d'un jet supersonique"
Application à l'étude des éjecteurs supersoniques
Thèse de Docteur Ingénieur - Lyon 1970.

[56] - Law C.H., "Supersonic turbulent boundary layer separation measurements at Reynolds Number of 10^7 to 10^8"
AIAA Journal Vol. 12 - Juin 1974.

[57] - Spaid F.W., Frishett J.C., "Incipient separation of a supersonic turbulent boundary layer, including effects of heat transfer"
AIAA Journal Vol. 19 - Juillet 1972.

[58] - Seddon J., "The flow produced by interaction of a turbulent boundary layer with a normal shock wave of strenght sufficient to cause separation"
Aero. Res. Council - R. et M. 3502 - 1967.

[59] - Leblanc R., Goethals R., "Etude de phénomènes d'interaction onde de choc normale - couche limite turbulente en vue des applications aux turbomachines transsoniques"
A.A.A.F. 11ème Colloque d'Aérodynamique Appliquée - Novembre 1974.

[60] - Délery J, Chattot J., Le Balleur J.C., "Interaction visqueuse avec décollement en écoulement transsonique"
Agard Symposium on Flow separation - Göttingen - Mai 1975.

[61] - Pearcey H.H. et al., "The interaction between local effects at the shock and rear separation"
AGARD Conf. Proc. n° 35 - 1968.

[62] - Stanewsky E., "Shock boundary layer interaction in transonic and supersonic flow - Transonic Flow in Turbomachinery"
V.K.I. L.S. 59 - Mai 1973.

[63] - Jacob K., Steinbach D., "A method for prediction of lift for multi-element airfoil systems with separation"
AGARD C.P.P. 143 - Avril 1974.

[64] - Alber I.E., Lees L., "Integral theory for supersonic turbulent base flow"
AIAA Journal Vol. 6 N° 7 - 1968

[65] - Alber I.E., "Similar solutions for a family of separated turbulent boundary layers"
AIAA Paper n° 71-203 - 1971.

[66] - Michel R., Quémard C., Durand R., "Application d'un schéma de longueur de mélange à l'étude des couches limites d'équilibre"
ONERA N.T. N° 154 - 1969.

[67] - Hunter L.G., Reeves B.L., "Results of a strong interaction wake like model of supersonic separated and reattaching turbulent flow"
AIAA Journal VOL. 9 N° 4 - 1971.

[68] - Klineberg J.M., Kubota T., Lees L., "Theory of exhaust plume/boundary layer interaction at supersonic speeds"
AIAA Journal Vol. 10 N° 5 - 1972.

[69] - Shamroth S.J., Mac Donald H., "A new solution of the turbulent near wake recompression problem"
AIAA Paper 70-228 - 1970.

[70] - Myring D.F., "The interaction of a turbulent boundary layer and a shock at hypersonic Mach numbers"
AGARD C.P. N° 30 - 1968.

[71] - Rose W.C., Page R.J., Childs M.E., "Incipient separation pressure rise for a Mach 3,8 turbulent boundary layer"
AIAA Journal Vol. 11 N° 5 - 1975.

[72] - Rose W.C., Nielsen H.L., Watson E.C., "Shock wave turbulent boundary layer interaction on a blunted compression surface"
Journal of Spacecraft Vol. 9 N° 4 - 1972.

[73] - Hankey Jr W.L., "Theoretical developments in supersonic separated flows"
V.K.I. Lecture Series 62 - 1974.

[74] - Klineberg J.M., Steger J.L., "Calculation of separated flows at subsonic and transsonic speeds"
3rd Int. Conf. on Numerical methods in Fluid Mechanics Vol. 2 - Université de Paris - 1972.

[75] - Kuhn G.D., Nielsen J.N., "Prediction of turbulent separated boundary layers"
AIAA Paper 73-663 - 1973.

[76] - Baldwin B.S., Mac Cormack R.W., Deiwert G.S., "Numerical techniques for the solution of the compressible Navier-Stokes equations and implementation of turbulence models"
AGARD Lecture Series 73 - 1975.

[77] - Ha Minh Hieu, Sananes F., Résultats non publiés.
Institut de Mécanique des Fluides de Toulouse.

[78] - de Richemont G., Délery J., "Effet des conditions extérieures sur le fonctionnement d'une tuyère supersonique double flux"
AGARD CP 150 (1974) "Airframe/propulsion interference".

Measurements in separating two dimensional turbulent boundary layers

by

J. Chu & A.D. Young

Queen Mary College, London University.
Mile End Road, London, E1 4NS, England.

SUMMARY

Two different types of pressure distribution resulting in separation were induced in the flow over a flat plate at zero incidence. Measurements were made of velocity distributions, skin friction (Preston tubes and Clauser plots), turbulence components and shear stress distributions at various stations both prior to and just after separation. The results have been compared with the predictions of various theories. Of these only those of Bradshaw and of Kuhn and Nielsen showed good agreement for integral quantities with the measurements right up to the separation point, the predictions of the remaining methods tended to depart radically from the measurements some little distance ahead of separation. Significant differences were found, however, between the measured shear stress distributions near separation and the predictions of Bradshaw's method, these differences indicate where improvements to the method may be made. With certain important provisos the methods of Stratford and Townsend for predicting the separation position are shown to be fairly reliable.

NOTATION

c_f	local skin friction coefficient $2\tau_w/\rho U_1^2$
u	mean velocity component parallel to plate
U_1	local free stream velocity at edge of boundary layer
U_∞	undisturbed stream velocity
u_τ	friction velocity $(\sqrt{\tau_w/\rho})$
u',v',w'	turbulent velocity components in x, y (normal) and z (lateral) directions
R_x	Reynolds number in terms of max. value of U_1 and x i.e. $U_{1max}.x/\nu$
R_θ	Reynolds number in terms of U_1 and θ
C_p	pressure coefficient
C_{pe}	effective pressure coefficient (see text)
X	distance along plate measured from transition trip in inches
x	distance along plate measured from virtual origin of a zero pressure gradient boundary layer having same momentum thickness as actual boundary layer at beginning of adverse pressure gradient.
y	distance normal to plate
Δ	pressure gradient parameter $\frac{\nu}{\rho u_\tau^3} \cdot \frac{dp}{dx}$
δ^*	displacement thickness
θ	momentum thickness
τ_w	frictional stress

1. INTRODUCTION

The main objects of the investigation were to provide detailed experimental data on two dimensional turbulent boundary layers in the process of separation and to compare the data with the predictions of various available theories.

Two different types of pressure distribution leading to separation were induced towards the rear of a flat plate at zero incidence. For the first (called Series I) an initial region of favourable (negative) pressure gradient was followed by a region of strongly unfavourable (positive) pressure gradient provoking separation in a relatively short distance aft of the peak suction position. For the second (called Series II) a less intense and practically monotonic unfavourable pressure gradient was imposed and the approach to the separation condition was therefore more gradual.

The measurements included pressure distributions, velocity profiles, Preston tube readings, turbulent velocity components and shear stress distributions. The available theories with which some of the salient results were compared were those due to Stratford[2], Townsend[3], Bradshaw[4], Ng and Spalding[5], Head and Patel[6], Horton[7], Kuhn and Nielsen[8].

2. SOME EXPERIMENTAL DETAILS

The plate was about 2½ m long, ½ m wide and 2.5 cm thick, and it had a rounded nose and a flap at the trailing edge to ensure that the front stagnation point was located on the nose without the formation of a separation bubble and the subsequent basic pressure distribution was nearly uniform. The plate had closely spaced pressure tappings (1½ cm apart over the main region of interest) staggered close to the centre-line, and 4 parallel rows of tappings (spaced 2½ cm apart) at about 15 cm and 30 cm from the centre line and on either side of it in the region where significantly non-zero pressure gradients were induced. A transition trip was fixed 5 cm aft of the nose position. For convenience chordwise stations are labelled by the number of inches aft of the trip (X). The plate was set at zero incidence in the working section of a wind tunnel between false walls. The wind speed used for the tests was about 20 m/s giving a Reynolds number in terms of the plate length of about 3×10^6.

The method used to induce the Series I pressure distribution is illustrated in Fig.1. For these tests a cylinder of diameter about 7.5 cm with a porous surface was fixed with its axis parallel to the plate at about 11 cm from it and normal to the wind stream direction at about 1.7 m (X = 65) behind the trip wire.

Air was sucked through the porous surface of the cylinder by means of a suction pump connected to both ends of the cylinder. A small Thwaites flap was fitted to the rear of the cylinder and by adjusting

its position and the suction a strong and steady circulation could be induced about the cylinder with the tunnel running and with only a very thin wake behind the cylinder. In consequence a pressure distribution that was initially favourable and then unfavourable was produced on the flat plate. The intensity of the pressure gradients could be controlled by varying the position of the Thwaites flap as well as the distance between the cylinder and the plate. This arrangement had been previously used for experiments on laminar separation bubbles[1], but was found equally effective in producing turbulent boundary layer separation by inducing a sufficiently strong adverse pressure gradient. Porous panels were also fitted to the side-walls through which the porous cylinder passed, suction through these panels eliminated any tendency for the wall boundary layers to separate due to the pressure field of the cylinder and also helped to ensure a high degree of spanwise uniformity. The streamwise pressure distribution on the plate tested is illustrated in Fig.2. For the Series II tests a spoiler flap of chord 10 cm was fixed near the rear of the plate at X = 75 (i.e. 75 in. behind the transition trip) at an angle of 90° to the plane of the plate. This produced the pressure distribution shown in Fig.3. The slight initial favourable pressure gradient ahead of X = 40 is probably due to the circulation round the plate induced by the spoiler.

The two dimensionality of the flow was investigated by observing the degree of spanwise uniformity of the pressure distributions and by visualising the separation front across the span of the plate as revealed by a thin film of suitably coloured oil that was painted on to the plate. In both Series of tests the pressure distributions showed an acceptable degree of uniformity over the part of the span to which they refer (i.e. the central 2/3 of the span). In the Series I arrangement the flow visualisation showed the separation line to be remarkably straight over the whole span, for the Series II tests there was some curvature of the separation line near the walls associated with an inflow into the wall boundary layers there. It was concluded that the flow upstream of separation could be tentatively assumed to be two dimensional over the central part of the span in which the measurements were made. Downstream of separation the flow visualisation tests revealed no significant flow patterns and the surface pressures remained acceptably uniform, but there can be no doubt that the flow if relatively slow moving was complex and not two-dimensional in any detailed sense of the term although overall there was no well-defined spanwise variation.

The mean velocity profiles at various stations were mainly derived from measurements made with flattened pitot tubes (0.2 mm x 0.75 mm) but some measurements ahead of and at separation were also made with hot wires. Near separation and aft of it the poor accuracy of the hot wire for determining small mean velocities in the presence of large turbulent velocity components as well as its lack of directionality left its reliability there in strong doubt, and the hot wire was not used aft of separation. The main measurements of mean velocity were therefore made with a double headed pitot tube, i.e. one with two pitot tubes facing opposite directions. Such a device after calibration can give both the mean velocity magnitude and direction sense, although it too lacks sensitivity where the mean velocity is small and there are relatively large fluctuating velocities, and there are always doubts about the interpretation of pitot tube measurements in a highly turbulent flow. The Preston tube measurements were made with round tubes, 0.7 mm in diameter.

The measurements of the turbulent velocity components, as well as of the shear stress distributions, were made with single and crossed hot wires.

3. THE MAIN RESULTS

3.1 Overall Data

The integral quantities, i.e. displacement and momentum thicknesses, as well as the skin friction coefficients given by the Preston tube measurements and Clauser plots and the Reynolds number based on the momentum thickness and the local free stream velocity U_1 (R_θ) for the various stations X are given in Table I for the Series I tests and Table II for the Series II tests. In addition these Tables show the corresponding values of the non-dimensional pressure gradient parameter $\Delta = \frac{\nu}{\rho u_\tau^3} \cdot \frac{dp}{dx}$.

It will be seen that tne skin friction distributions are consistent with separation at about X = 69.5 for the Series I tests and at about X = 67.5 for the Series II tests. These positions are also those indicated by the mean velocity profiles as measured by pitot tubes.

3.2 Velocity Profiles

Some representative mean velocity profiles are shown in Fig.4(a) and (b) for the Series I tests and in Fig.5 for the Series II tests. Where measurements were made with hot wires as well as pitot tubes, both sets of measurements are indicated. It will be seen that in general agreement between the two different methods of measurement is good except in the immediate region of the separation point particularly close to the surface. For the reasons already referred to the pitot tube measurements were regarded as the more reliable in that region, although their accuracy there cannot be regarded as high. The kinks in the shape of the velocity distributions aft of separation near the zero velocity point can be plausibly explained as arising from the poor accuracy of the pitot probe in regions where the velocity is low and relatively large fluctuations in velocity are present due to turbulence and local flow unsteadiness.

3.3 Skin friction measurements

As already noted, in addition to inferring the skin friction distributions from Preston tube measurements, they were also determined from Clauser type plots of the velocity distribution. For the former the calibration of Patel[9] was used, and the pitot tube diameter d was chosen so that $u_\tau d/\nu$ was less than about 40 where u_τ is the friction velocity (τ_w/ρ). This ensured that as long as the profile exhibited an identifiable 'log law' region the tube centre was located in and near the lower boundary of that region. For the Clauser type plots the process of identifying the 'log law' portion which determined the skin friction presented no difficulty in regions of small to moderate pressure gradients but they did present some difficulty in the regions of large pressure gradients. This is illustrated in

Fig. 6 and 7 for the Series I and II results, respectively, in the regions near separation. In Fig.6 it will be seen that the profile changed rapidly from that of station 66 which exhibited the characteristic convexity above the sub layer region, due to the preceding large favourable pressure gradient, to that of station 69, just prior to separation, showing above the sub layer region the concavity characteristic of a strongly unfavourable pressure gradient. The arrows mark the position y = d where d is the diameter of the Preston tube and it will be seen that the arrows lie near the lower bound of regions which can be plausibly, if not conclusively, identified as regions where the plots of u/U_1 against log $y U_1/\nu$ are most nearly straight. The values of c_f have therefore been inferred from the slopes of the tangents to the plots in the region of the arrows. For the Series II results as illustrated in Fig.7 the straight line portions of the plots were somewhat easier to identify but the arrows again provided a useful guide as to where to measure the slope.

The resulting distributions of the skin friction coefficient are shown in Fig.8 and 9 for the Series I and II tests respectively. It will be seen that in general the two methods agree fairly well; surprisingly enough the largest differences (about 8%) occur in the upstream region for the Series II experiments where the pressure gradients are very small, elsewhere the differences are less than 5%.

The two methods are not entirely independent since both depend on the existence of a 'log law' region, and the method used for determining the appropriate slope from the Clauser plots makes the link between the two methods somewhat stronger. Nevertheless, the agreement between the two sets of results encourages a degree of confidence in the results shown in Fig. 8 and 9 and in general in the use of the Preston tube method even close to separation.

The corresponding Law of the Wall plots (i.e. u/u_τ against log (yu_τ/ν) are shown in Fig. 10 and 11 for the Series I and II tests respectively. The overall consistency and agreement over the straight portions with the generally accepted relation

$$\frac{u}{u_\tau} = 5.5 \log_{10} \frac{yu_\tau}{\nu} + 5.45$$

provide additional support for the skin friction distributions of Fig. 8 and 9.

3.4 Turbulence Measurements

We denote the turbulent velocity components by (u',v',w'). Lines of constant $\sqrt{\overline{u'^2}}/U_1$ are shown in Fig.12 (Series I) and Fig.13 (Series II). In the former case the reduction in the boundary layer thickness as well as in the overall intensity of turbulence in the region of favourable pressure gradient (X = 55 to X = 65) is very marked as is the subsequent rapid growth of the thickness and turbulence intensity in the region of adverse pressure gradient. It will be seen that at separation the maximum turbulence intensity is of the order of 25%. For the Series II tests the changes are on the whole more gradual, as might be expected, and the maximum turbulence intensity is considerably less than for Series I being of the order of 13%. The plots for v' and w' are similar to those of u' and are not therefore separately shown.

In general the Series II separated flow was much steadier than that of Series I, presumably because of the constraint imposed by the spoiler flap since reattachment had to occur at the flap tip. The unsteadiness of the Series I flow was mainly of a low frequency associated with small oscillatory movements of the separation position and a related oscillation of the separated shear layer. This was reflected in pressure transducer measurements made at the plate surface in the separated region.

In both Series of tests the measurements were taken down into the outer region of the viscous sub-layer at each station as conventionally described by $yu_\tau/\nu = 10$. It was noted however that a high level of turbulence was present in that region and the associated mean velocity gradient was not such as to lead to a viscous stress consistent with the local skin friction coefficient. This implied that the thickness of the viscous sub-layer is significantly smaller than is suggested by $yu_\tau/\nu = 10$.

3.5 Turbulent eddy shear stress distributions

Some representative turbulent shear stress distributions for the Series I and II tests are illustrated in Fig. 14 and 15 respectively. The effect of the initial favourable pressure gradient in the Series I tests in reducing the strength of the shear stress is evident and is consistent with the reduction in turbulence intensity noted above. Further downstream where the pressure gradient is unfavourable the shear stress strength grows rapidly over the outer part of the boundary layer but the position of the maximum shear stress moves characteristically away from the surface. In the region of separation we note that the shear stress does not reduce to zero at the outer edge of the boundary layer. No clear cut explanation can be offered for this except to recall the degree of relatively low frequency unsteadiness in velocity magnitude and direction that was present in the region of separation in the Series I tests, this was evident in the flow outside the boundary layer and may have given rise to an effective $\overline{u'v'}$ correlation there as measured by the crossed hot wires.

For the Series II tests we observe in Fig.15 the steady change of the shear stress distributions from the initial characteristic form for a near-zero pressure gradient at X = 24 with the maximum stress practically at the surface to the separated flow shape beyond X = 67.5 We see that the maximum stress position moves monotonically away from the surface with distance downstream as the effect of the adverse pressure gradient grows.

We note that for the Series II tests the shear stress tends to zero at the boundary layer edge even where the flow was separated. There the flow was markedly steadier in the region of separation than for the Series I tests, and this supports the above suggestion that the unsteadiness of the separated flow in the latter tests contributed to the apparent non-zero shear stress measured outside the boundary layer.

In both Series of tests the measured shear stress distributions close to the surface in the region of separation are unreliable for the reasons already stated.

4 COMPARISONS WITH THEORY

4.1 Separation position theories

Stratford[2] developed a theory based on his two layer concept of the boundary layer for predicting the position of separation. His theory results in the following formula to be satisfied at separation:-

$$C_{pv}\left(x.\frac{d\,C_{pv}}{dx}\right)^{\frac{1}{2}} = K\left(10^{-6}\,R_x\right)^{1/10}$$

Here x is the distance from a virtual origin of the boundary layer derived for an equivalent uniform flow preceding the adverse pressure gradient region and resulting in the same value of the momentum thickness at the beginning of that region as the actual one. Thus, for the Series I tests the velocity of the equivalent uniform flow was equal to that at the maximum suction point, for the Series II tests it was the same as the undisturbed stream velocity. The pressure coefficient C_{pv} is measured relative to the static pressure of the equivalent uniform flow and is in terms of the dynamic pressure of that flow, R_x is a Reynolds number based on x and the velocity of the equivalent uniform flow.

K is an empirical constant which was subject to a change from 0.39 to 0.35 in the course of the development of the theory. With the latter value of K and the measured pressure distribution, the separation point for the Series I tests was predicted to occur at X = 69.3 which is very close to the measured value of 69.5. The earlier value of K of 0.39 leads to X = 69.25 for separation. However, the likely problem in practice would be one in which the theoretical inviscid flow pressure distribution is known and not the actual one which could be very different. Stratford's derivation suggests the value of 0.5 for K if the theoretical inviscid flow pressure distribution is used and this produced a predicted separation position of 68.9.

For the Series II tests x was taken as the distance from the plate leading edge and the predicted separation positions when the measured pressure distribution was used were 67.8 with K = 0.35 and 67.4 with K = 0.39 as compared with the measured value of 67.6.

Townsend's method[3] which can be regarded as a development of Stratford's method results in a formula for the pressure coefficient at separation which involves the skin friction coefficient at the beginning of the region of adverse pressure gradient. The latter is required with a high degree of accuracy as the resulting value of C_p at separation and hence the separation positions are very sensitive to the value of the skin friction coefficient. With the experimental pressure and skin friction values the predicted positions of separation were 68.9 for the Series I tests and 67.5 for the Series II tests.

It seems that both methods can be regarded as fairly reliable in predicting the separation position provided one has a good knowledge of the actual pressure distribution. For Stratford's method one must be able to make a reasonable assessment of the effective origin of the boundary layer in cases where the adverse pressure gradient region is preceded by a favourable pressure gradient region culminating in a maximum suction position. For Townsend's method one must similarly be able to determine the skin friction fairly accurately at the beginning of the region of adverse pressure gradient.

4.2 Detailed development of the turbulent boundary layer

The predictions of the methods of a number of workers were compared with the results of the present experiments, namely, the methods of Bradshaw et al[4], Ng and Spalding[5], Head and Patel[6], Horton[7], Kuhn and Nielsen[8]. The last three are integral methods in which some allowance is made for non-equilibrium effects; the first two are differential methods in which these effects are more directly taken into account.

The predicted values of the integral quantities c_f, R_θ and H for the Series I tests are compared with the values derived from the Preston tube and pitot tube measurements in Fig. 16, 17 and 18, whilst in Fig.19, 20 and 21 the corresponding comparisons are made for the Series II tests.

It will be seen that all the methods lead to results in acceptable agreement with the measured values of c_f for the regions of small to moderate pressure gradient. However, for the Series I tests only Bradshaw's method and that of Kuhn and Nielsen give results in acceptable agreement right up to separation (although the latter method shows a significant departure from the measurements in the region of maximum suction). None of the other methods predicts separation in the sense of leading to a point of zero c_f. Again, in the Series II tests, Bradshaw's method and Kuhn and Nielsen's method show very good agreement with the measurements right up to separation with the other methods tending to fail in the region of strong adverse pressure gradient. Here the methods of Horton and Head and Patel show up rather worse than for the Series I measurements. The same general picture of the marked superiority of Bradshaw's method and Kuhn and Nielsen's method over the other methods considered in the region approaching separation is evident in the R_θ and H distributions shown in Fig. 17, 18, 20 and 21. Kuhn and Nielsen's method can be used beyond separation and although it shows results in good agreement with the measurements there for R_θ and H in the Series I tests, the rapid reduction in R_θ after separation measured in the Series II tests is not reflected in their prediction. However, the accuracy of the measurements there and their interpretation are subject to some doubt.

In view of the generally consistent good agreement between Bradshaw's method and the measured results for integral quantities up to separation it was thought of interest to compare the predictions of this method for the shear stress distributions in detail with those measured. Some comparisons are shown in Fig. 22 and 23 for Series I and these reflect the fact that over much of the streamwise development of the boundary layer the agreement is reasonable. Although the predicted shear stress near the surface is generally a little higher than the measured value there is good agreement at the wall itself. However, near the separation point the predicted values are significantly less than the measured values in the outer half of the boundary layer in contrast to what happens near the surface. Similar comparisons for the Series II measurements are shown in Fig. 24 and 25. Here the differences between the predicted and

measured distributions in the region of separation are even more marked, but again the differences change sign at a little more than half the boundary layer thickness from the surface with the predicted values being considerably greater than the measured values near the surface. One may infer from this that the assumption of the Bradshaw method that the shear stress and the turbulence kinetic energy are linearly related is a reasonable overall assumption for the prediction of integral quantities but in detail it appears to lead to errors of one sign near the surface and of the opposite sign in the outer part of the boundary layer, and these errors can become large in regions of strong adverse pressure gradient.

The observed degree of overall agreement between the measurements and the predictions of the various methods considered, differing as the methods do in their assumptions and structure, lends additional support to the initial inference drawn from the experimental evidence referred to in §2 that the flows tested could be regarded as two dimensional. Checks of the overall consistency of the results in satisfying the two dimensional momentum integral equation were equally encouraging, but it must be noted that this is not a very precise test where the pressure gradients are large.

5. CONCLUSIONS

It is concluded that

(a) Subject to care being taken in interpreting the effective origin of the boundary layer where the pressure gradient is not monotonic, the Stratford method is reasonably reliable for predicting separation positions if the measured pressure distribution is used.

(b) The Townsend method is also reliable if the measured pressure distribution is used and if the skin friction at the beginning of the region of adverse pressure gradient can be accurately determined.

(c) Of the various methods examined for predicting the development of turbulent boundary layers, only the Bradshaw and Kuhn and Nielsen methods give acceptable agreement with measurements of integral quantities (e.g. c_f, R_θ and H) in the region of separation. All the methods showed more or less reasonable agreement elsewhere in regions of small to moderate pressure gradient. Surprisingly enough, it seems that the Series II conditions (monotonic adverse pressure gradient) provided a somewhat more severe test than the Series I conditions (initially favourable pressure gradient followed by an adverse pressure gradient).

(d) Comparison of the predictions of turbulent shear stress distribution by the Bradshaw method with the measured distributions indicate significant differences near separation, with the predicted values being larger than the measured values near the surface, but they are smaller than the measured values away from the surface. This suggests that the assumption of linearity between the turbulent shear stress and the turbulence kinetic energy can in detail lead to errors of one sign in the lower half of the boundary layer and of the opposite sign in the upper half and these errors can be of significant magnitude in regions of strong adverse pressure gradient.

ACKNOWLEDGEMENT

This work has been carried out with the support of the Procurement Executive, Ministry of Defence.

TABLE I Series I

X	δ^* (cm)	θ (cm)	$c_f \times 10^3$ Preston tube	$c_f \times 10^3$ Clauser plot	$\Delta \times 10^2$	R_θ
24	0.213	0.152	3.75	3.70	-	1911
26	0.225	0.160	3.70	3.63	-	2008
28	0.239	0.171	3.65	3.50	-	2146
30	0.252	0.179	3.59	3.35	-	2268
32	0.261	0.186	3.53	3.45	-	2363
36	0.282	0.203	3.43	3.40	-	2589
40	0.301	0.217	3.33	3.33	-	2779
44	0.318	0.229	3.30	3.25	-	2982
50	0.334	0.244	3.30	3.25	-	3227
54	0.322	0.237	3.43	3.37	-	3219
58	0.272	0.208	3.65	3.83	-0.88	3070
60	0.214	0.167	4.10	4.25	-1.21	2613
61	0.181	0.145	4.50	4.50	-1.45	2396
62	0.144	0.116	4.90	4.90	-1.47	2058
63	0.111	0.090	5.10	5.22	-1.30	1750
64	-	-	-	-	-1.11	-
64.5	0.075	0.059	5.28	5.50	-0.84	-
65	-	-	-	-	-0.54	1347
65.5	0.072	0.057	5.23	5.40	0.00	1364
66	0.079	0.063	5.00	5.00	0.73	1533
66.5	0.092	0.072	4.85	4.50	1.68	1692
67	0.116	0.089	4.00	3.95	2.40	1981
67.5	0.146	0.106	3.20	3.18	4.02	2223
68	0.210	0.138	2.45	1.90	8.62	2690
68.5	0.334	0.190	1.50	0.95	22.00	3414
69	0.520	0.245	0.35	0.40	45.6	4147
69.5	0.699	0.292	0	0	0	4896

TABLE II Series II

X	δ^* (cm)	θ (cm)	$c_f \times 10^3$ Preston tube	$c_f \times 10^3$ Clauser plot	$\Delta \times 10^2$	R_θ
24	0.170	0.124	3.93	4.00	-	1562
28	0.194	0.142	3.70	3.88	-	1797
32	0.217	0.159	3.55	3.78	-	2028
36	0.241	0.178	3.42	3.65	-	2253
40	0.264	0.184	3.30	3.50	-	2463
46	0.329	0.231	3.20	3.25	-	2939
50	0.352	0.252	3.10	3.20	-	3194
55	0.413	0.292	2.91	3.00	0.30	3614
58	0.471	0.319	2.70	2.78	0.65	3860
60	0.521	0.356	2.80	2.50	0.95	4205
62	0.616	0.408	2.09	2.21	2.07	4658
64	0.836	0.506	1.50	1.60	5.24	5467
65	1.002	0.570	1.18	1.15	10.00	5952
66	1.29	0.653	0.76	0.65	16.4	6623
67	1.72	0.741	0.25	0.25	57.0	7321
67.5	2.07	0.776	0.02	0.02	-	7541
68	2.43	0.779	-	-	-	7567
68.5	2.79	0.800	-	-	-	7688
69	3.37	0.684	-	-	-	6570
69.5	3.97	0.620	-	-	-	5970
70.5	5.49	0.313	-	-	-	2992

REFERENCES

1. Young A.D. & Horton H.P. — Some results of investigations of separation bubbles, A.G.A.R.D. Conf. Proc. No.4 Separated Flows, p.779, May 1966.

2. Stratford B.S. — The prediction of separation of the turbulent boundary layer, J.F.M. Vol.5, p.1, 1959.

3. Townsend A.A. — The behaviour of the turbulent boundary layer near separation, J.F.M. Vol.12, p.536, 1962.

4. Bradshaw P, Ferriss D.H., & Atwell N.P. — Calculation of boundary layer development using the turbulent energy equation, J.F.M. Vol.28, p.593, 1967.

5. Spalding D.B. & Ng K.H. — Predictions of two dimensional boundary layers on smooth walls with a two equation model of turbulence, Imperial College, Mech. Eng. Dept., Rep. BL/TN/A/25, 1970.

6. Head M.R. & Patel V.C. — Improved entrainment method for calculating boundary layer development, ARC 31043, FM 4035, 1969.

7. Horton H.P. — Entrainment in equilibrium and non-equilibrium turbulent boundary layers, Research Rep. 1094, Hawker Siddeley Aviation, 1969.

8. Kuhn G.D. & Nielsen J.N. — An analytical method for calculating turbulent separated flows due to adverse pressure gradients, Project - Squid TR NEAR - 1 - PU, Oct.1971.

9. Patel V.C. — Calibration of the Preston tube and limitation on its use in pressure gradients, J.F.M. Vol.23, I, p.185, 1965.

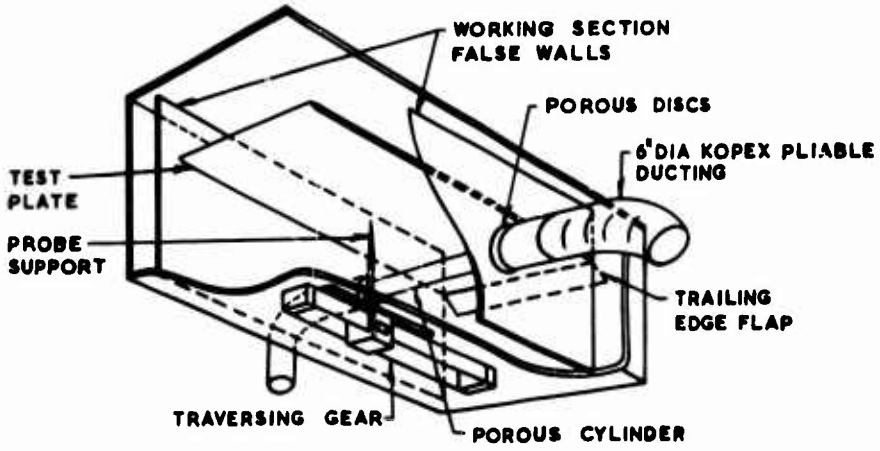

Figure 1. PERSPECTIVE CUTAWAY VIEW OF WORKING SECTION

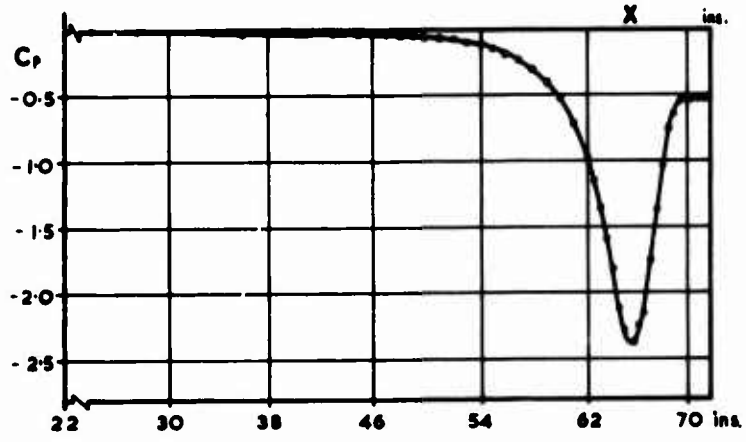

Figure 2. PRESSURE DISTRIBUTION ALONG PLATE. SERIES I

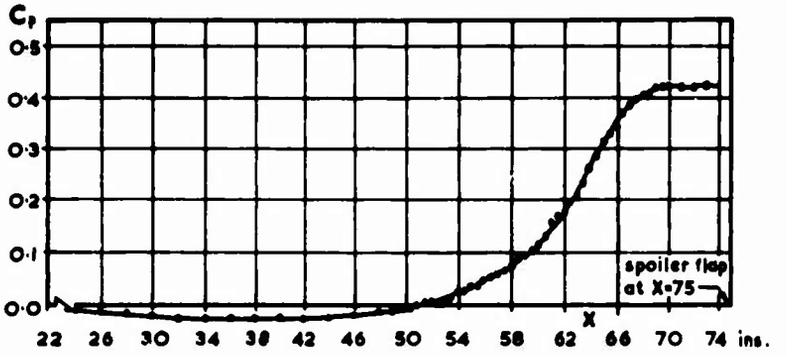

Figure 3. PRESSURE DISTRIBUTION ALONG PLATE SERIES II

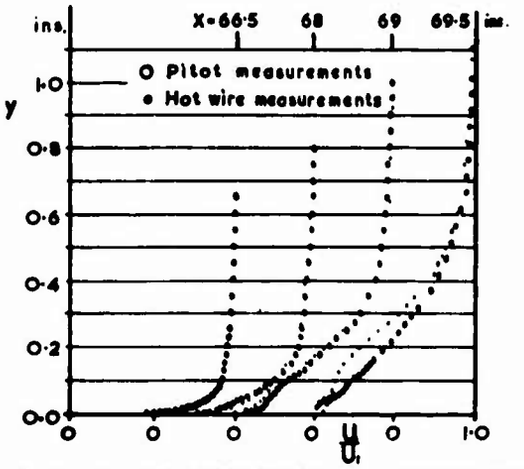

Figure 4a. VELOCITY PROFILES, ATTACHED FLOW. SERIES I

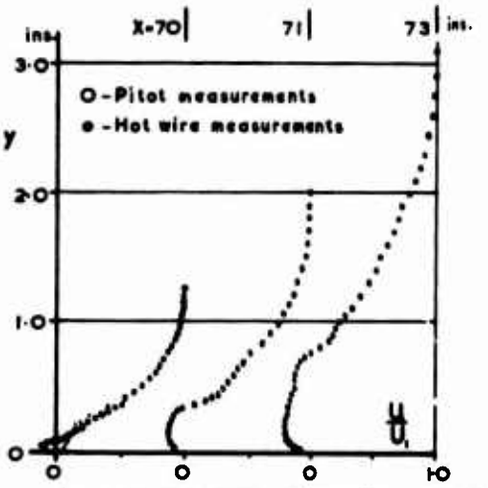

Figure 4b. VELOCITY PROFILES, SEPARATED FLOW. SERIES I

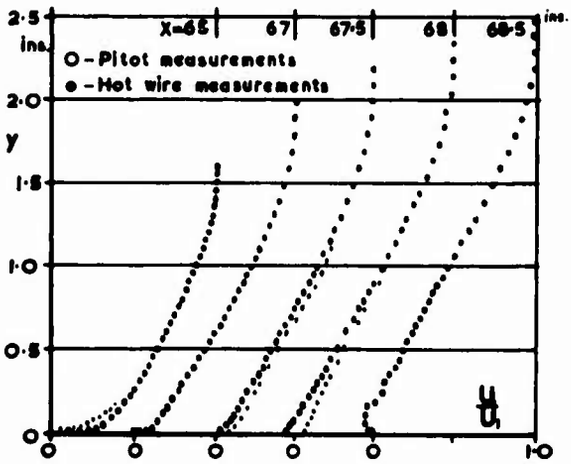

Figure 5. VELOCITY PROFILES. SERIES II

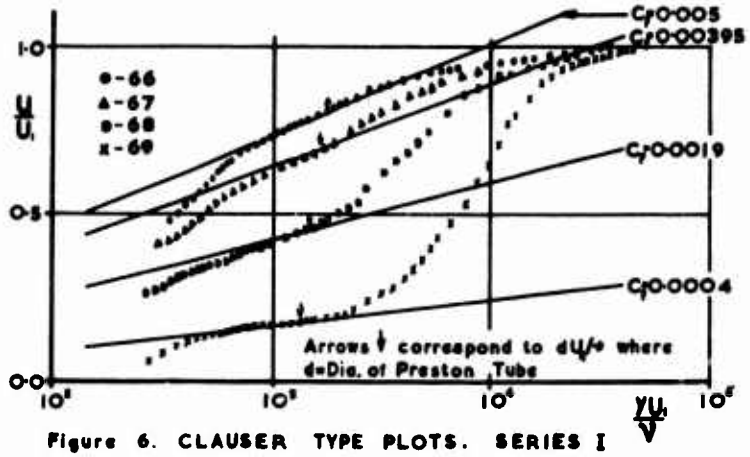

Figure 6. CLAUSER TYPE PLOTS. SERIES I

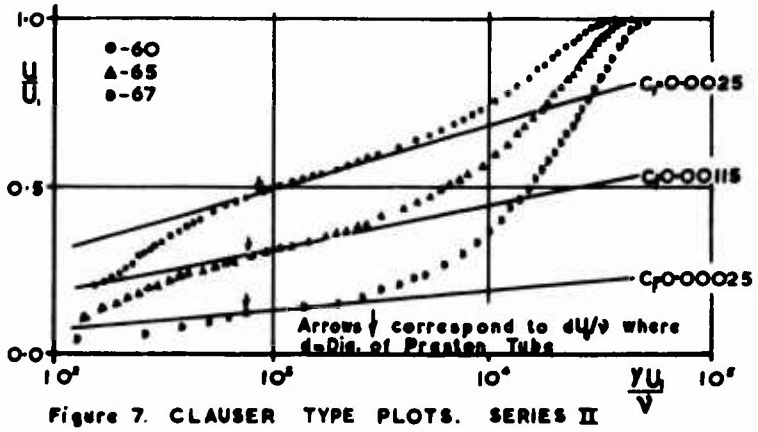

Figure 7. CLAUSER TYPE PLOTS. SERIES II

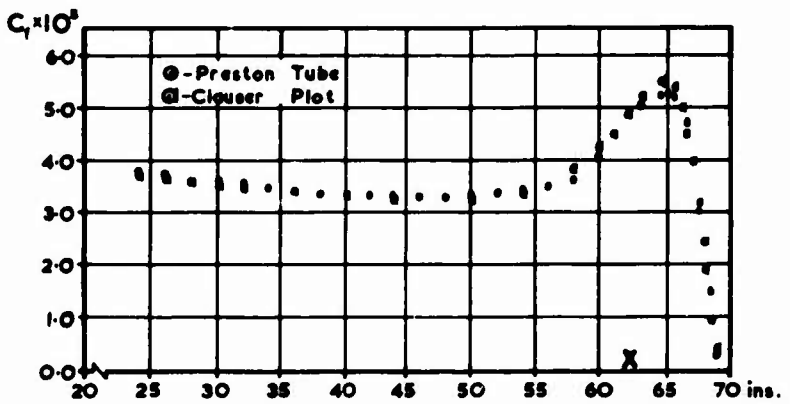

Figure 8. SKIN FRICTION DISTRIBUTION. SERIES I

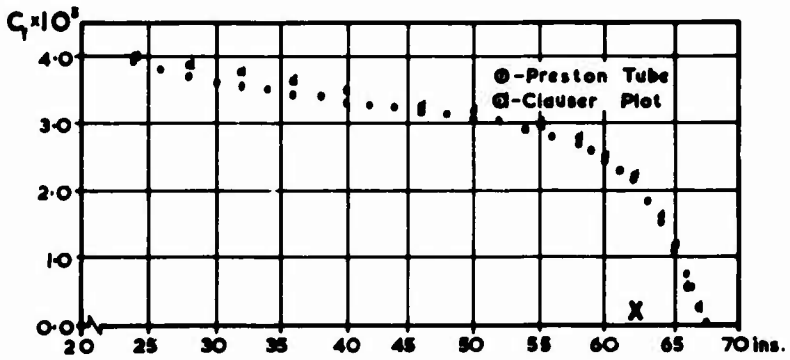

Figure 9. SKIN FRICTION DISTRIBUTION SERIES II

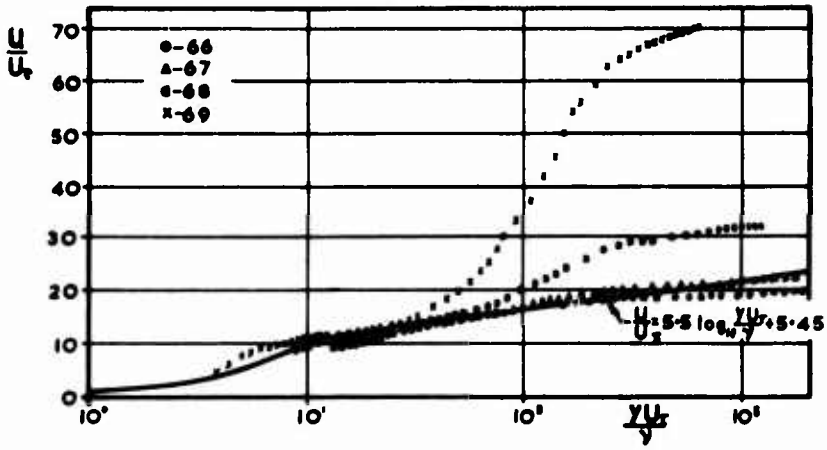

Figure 10. LAW OF THE WALL PLOT NEAR SEPARATION. SERIES I

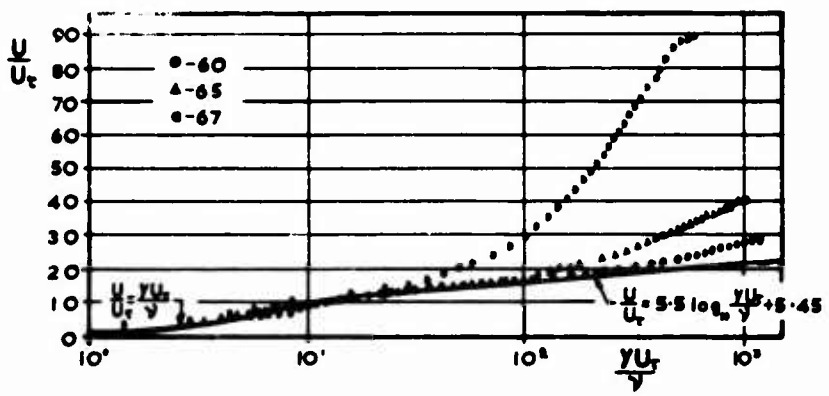

Figure 11. LAW OF THE WALL PLOT NEAR SEPARATION. SERIES II

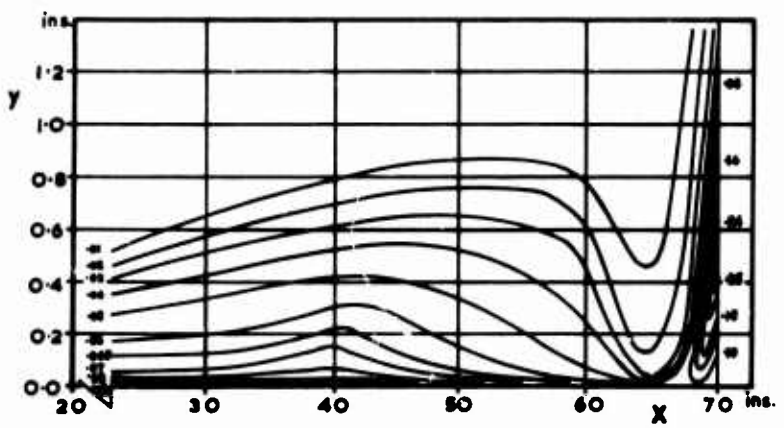

Figure 12. LINES OF CONSTANT $\sqrt{\overline{u^2}}/U_1$. SERIES I

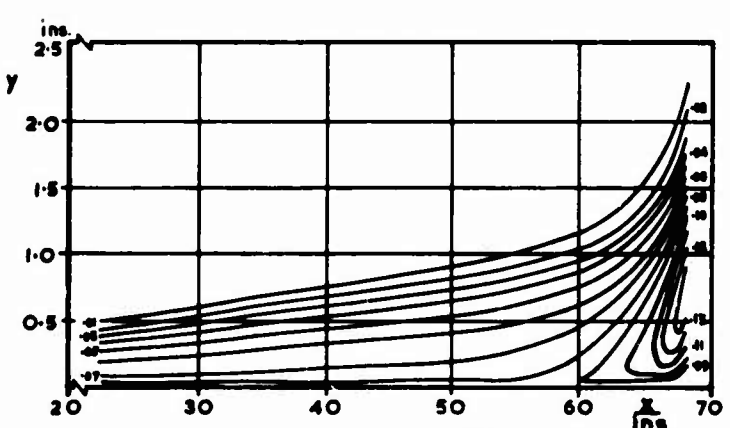

Figure 13. LINES OF CONSTANT $\sqrt{\overline{u^2}}/U_1$. SERIES II

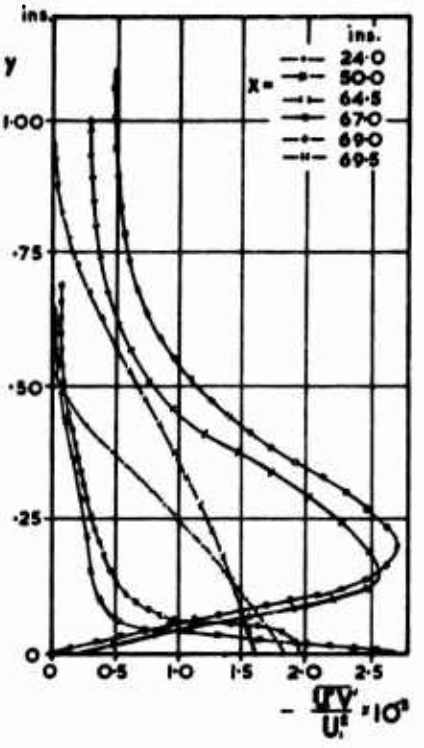

Figure 14. NON-DIMENSIONAL TURBULENT SHEAR STRESS DISTRIBUTIONS. SERIES I

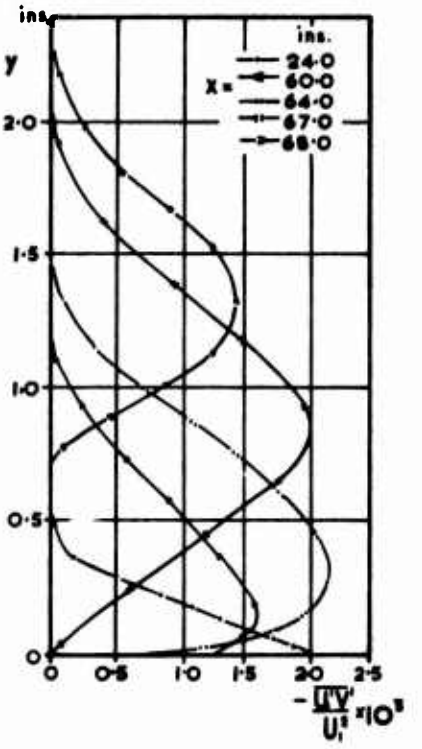

Figure 15. NON-DIMENSIONAL TURBULENT SHEAR STRESS DISTRIBUTIONS. SERIES II

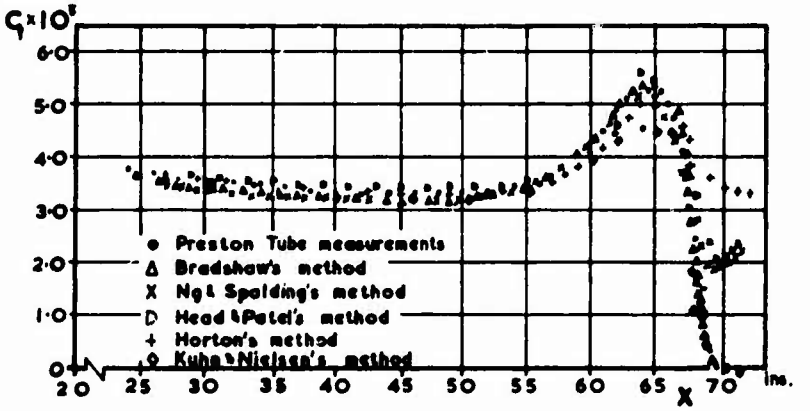

Figure 16. COMPARISON OF MEASURED VALUES OF C_f WITH BOUNDARY LAYER PREDICTION METHODS. SERIES I

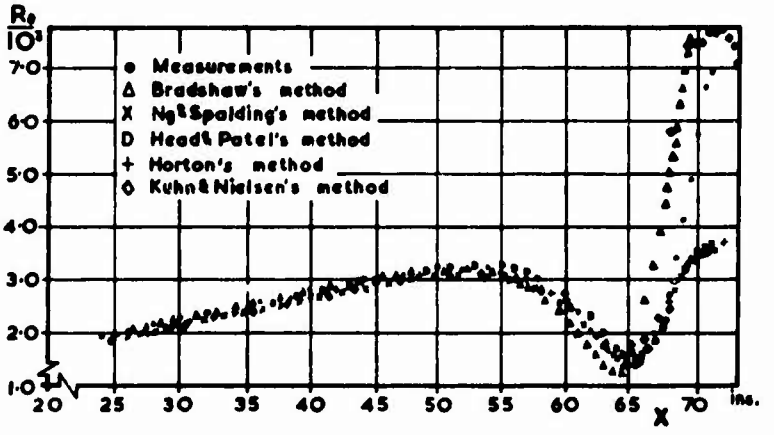

Figure 17. COMPARISON OF MEASURED VALUES OF R_θ WITH PREDICTED VALUES. SERIES I

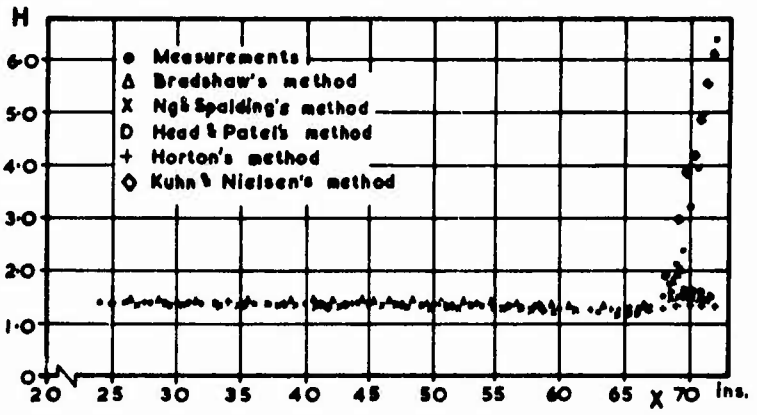

Figure. 18 COMPARISON OF MEASURED VALUES OF H WITH PREDICTED VALUES. SERIES I

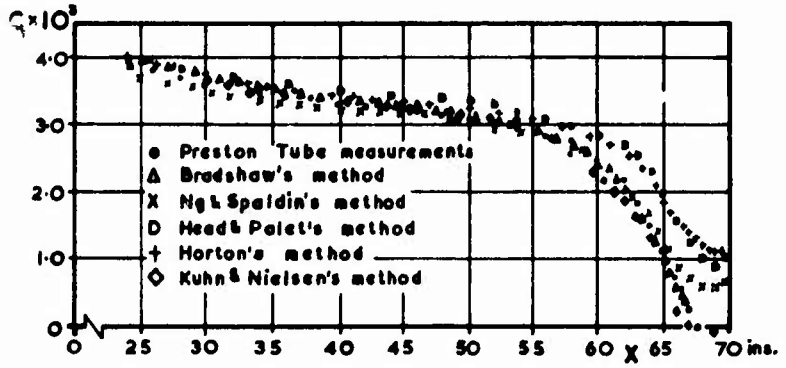

Figure 19. COMPARISON OF MEASURED VALUES OF C_f WITH BOUNDARY LAYER PREDICTION METHODS. SERIES II

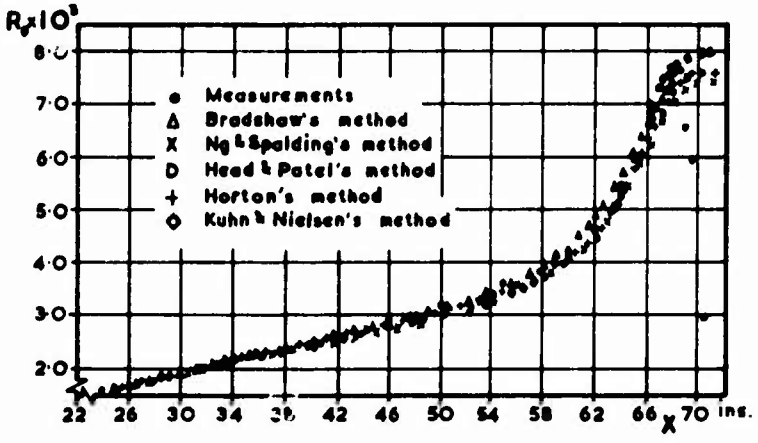

Figure 20. COMPARISON OF MEASURED VALUES OF R_θ WITH PREDICTED VALUES. SERIES II

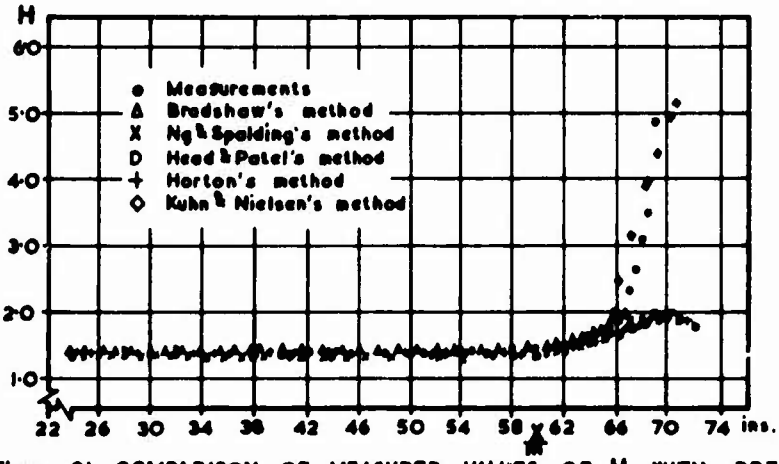

Figure 21. COMPARISON OF MEASURED VALUES OF H WITH PREDICTED VALUES. SERIES II

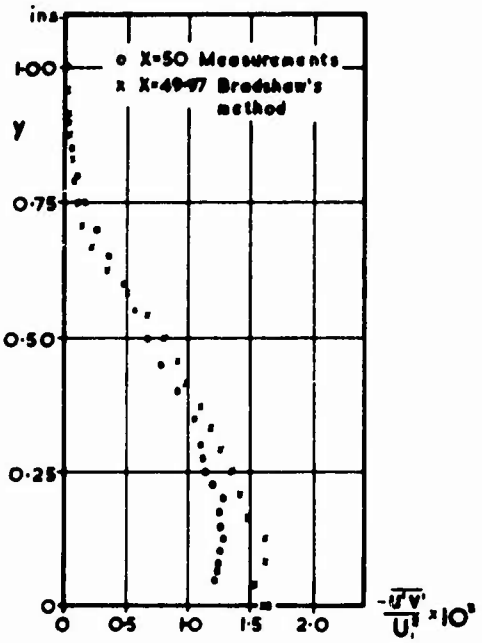

Figure 22. COMPARISON OF MEASURED SHEAR STRESS PROFILE WITH PREDICTION SERIES I

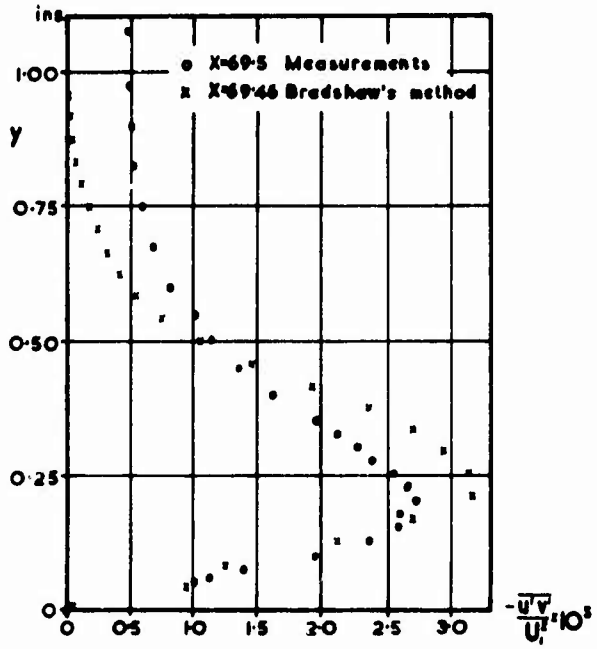

Figure 23. COMPARISON OF MEASURED SHEAR STRESS PROFILE WITH PREDICTION SERIES I

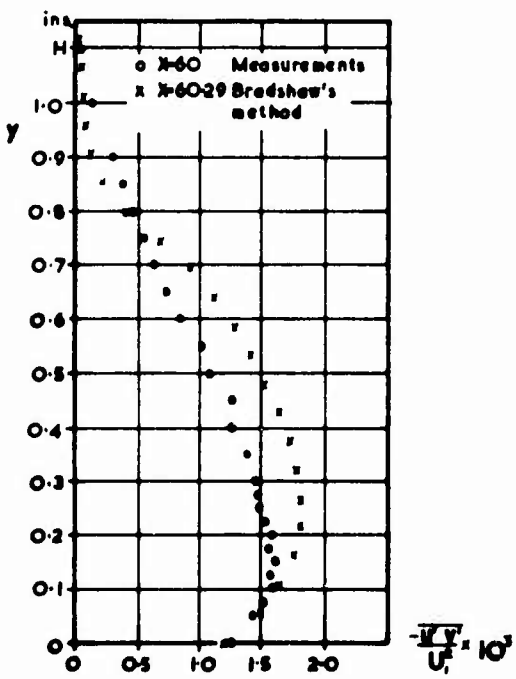

Figure 24. COMPARISON OF MEASURED SHEAR STRESS PROFILES WITH PREDICTION SERIES II

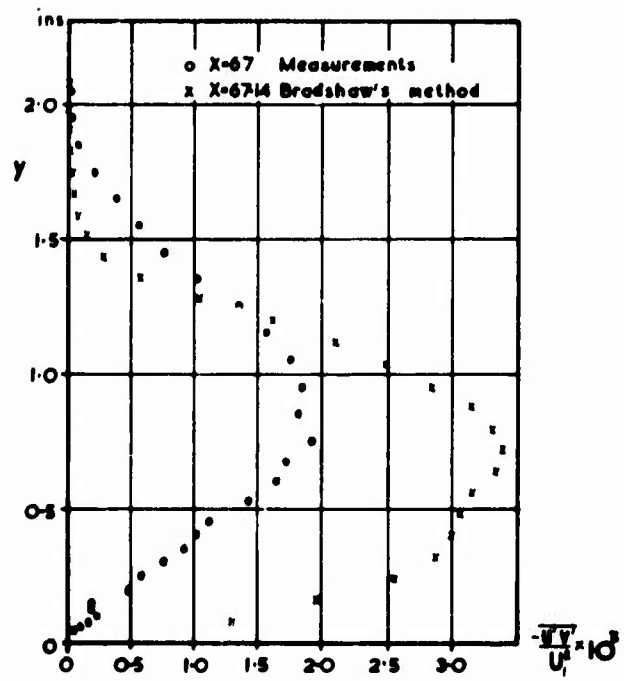

Figure 25. COMPARISON OF MEASURED SHEAR STRESS PROFILES WITH PREDICTION SERIES II

CHARACTERISTICS OF A SEPARATING INCOMPRESSIBLE TURBULENT BOUNDARY LAYER

by

Roger L. Simpson
Associate Professor, Department of Civil and Mechanical Engineering
Southern Methodist University
Dallas, Texas 75275

ABSTRACT

Laser and hot-film anemometer measurements upstream and downstream of the separation zone are presented for a nominally two-dimensional incompressible turbulent boundary layer for an airfoil type flow. The directionally sensitive laser anemometer measurements indicate that the location of intermittent separation as defined by Sandborn is the proper location of where the flow first deflects from the wall to relieve the imposed pressure gradient. Upstream of separation the correlations of Perry and Schofield (1973) for mean velocity profiles are supported within the uncertainty of the data. The separated flow field shows some profile similarity for all measured quantities. The low velocity backflow in the region next to the wall apparently just serves to satisfy continuity requirements.

The normal stress terms in the momentum and turbulence energy equations are shown to be important near separation and cannot be neglected for the close prediction of the separation location. The boundary layer prediction method of Bradshaw, et al. (1974) is modified to include these normal stress effects. Preliminary results show considerable improvement in predictions of $C_f/2$ and H near separation and the location of separation.

NOMENCLATURE

a_1	$\equiv -\overline{uv}/\overline{q^2}$
C_1	constant in eqn. (19)
$C_f/2$	$\tau_o/\rho U_\infty^2$
e	defined by eqn. (3)
f_1, f_2	defined in eqns. (3) and (1)
F	ratio of total turbulence energy production to shear production, eqn. (15)
G	Bradshaw large eddy diffusion function
h	constant in eqn. (3)
H	$\equiv \delta^*/\theta$ shape factor
L	distance from wall of shear maximum
L_ϵ	dissipation length, eqn. (16)
M	distance from wall of $\overline{u^2}$ maximum
$\overline{q^2}$	$\equiv \overline{u^2} + \overline{v^2} + \overline{w^2}$
U	streamwise mean velocity
U^2_{M-}	$\equiv (-\overline{uv})_{max}$
U^2_{Mp}	max pseudo-shear stress, defined by eqn. (8)
U_s	defined by eqn. (1) and $f_2(0) = 1$
U_τ	τ_o/ρ
U_∞	free-stream velocity
U^+	U/U_τ
$\overline{u^2}$, $\overline{v^2}$, $\overline{w^2}$	mean square streamwise, normal and spanwise velocity fluctuations
$-\overline{uv}$	kinematic Reynolds shear stress
V_e	entrainment velocity
x	streamwise distance
y	distance normal to the wall
y_c	defined in eqn. (7)
y^+	yU_τ/ν

Greek Symbols

α	angle of real characteristic with x-axis
γ_p	fraction of time the flow moves downstream
δ	y where $U = 0.99U_\infty$
$\delta_{0.995}$	y where $U = 0.995U_\infty$
δ^*	displacement thickness
Δ	length defined by eqn. (2)
η_1, η_2	defined by eqns. (3) and (1)
θ	momentum thickness
ν	kinematic viscosity
ρ	density
σ_α (β)	defined in eqn. (24)
τ	shear stress
ψ	defined in eqn. (24)

Subscripts

max	denotes maximum value
0	denotes wall value

1. INTRODUCTION

The results from experiments described in this paper are concerned with a nominally two-dimensional incompressible turbulent boundary layer on a flat surface which separates due to an adverse pressure gradient. Many experimental investigations have been made of this classical problem, but none have employed a directionally sensitive laser anemometer to determine quantitatively the flow structure downstream of separation. It is well recognized that this separated flow strongly influences the free-stream potential flow, which in turn influences the upstream flow behavior. The primary objective of this research program is to provide needed experimental information about this type flow.

In addition to laser anemometer measurements, hot-film anemometer measurements were also obtained in regions where the flow did not change direction. Many different types of measurements have been made, including: skin friction, mean velocity profiles, turbulent shearing stress and intensities, downstream-upstream flow intermittency, dissipation rate, and separation zone location, which are all discussed here; and spectra, wall bursting frequencies and spanwise structure, turbulent-non-turbulent interface intermittency and frequency, eddy celerities, and downstream-upstream flow reversal frequency. All of these

measurements are discussed at more length by Simpson, et al. (1974).

One of the most important results deduced from these experiments is that the normal stress terms of the momentum and turbulence energy equations play a significant role in the flow behavior in the vicinity of separation. A model that accounts for these terms is presented, which when incorporated into the Bradshaw, et al. (1967, 1974) turbulent boundary layer prediction program shows close agreement with the experimental results presented here.

2. EXPERIMENTAL EQUIPMENT

Figure 1 is a side view schematic of the 16 foot long, three foot wide test section of the blown wind tunnel. The detailed features of this tunnel as used in the current experiments are given by Strickland and Simpson (1973). The test boundary layer on the wind tunnel floor was an airfoil type with first flow acceleration and then deceleration as shown in figure 2. To eliminate preferential separation of the curved top wall boundary layer, this layer was removed prior to the last eight feet of test section. To provide the necessary backpressure to blow out this flow, a perforated metal plate was located at the exit. Under these conditions, this tunnel produced a free-stream flow uniform within 0.05% in the spanwise direction and within 1% in the vertical direction with a turbulence intensity level of 0.1% at 60 fps.

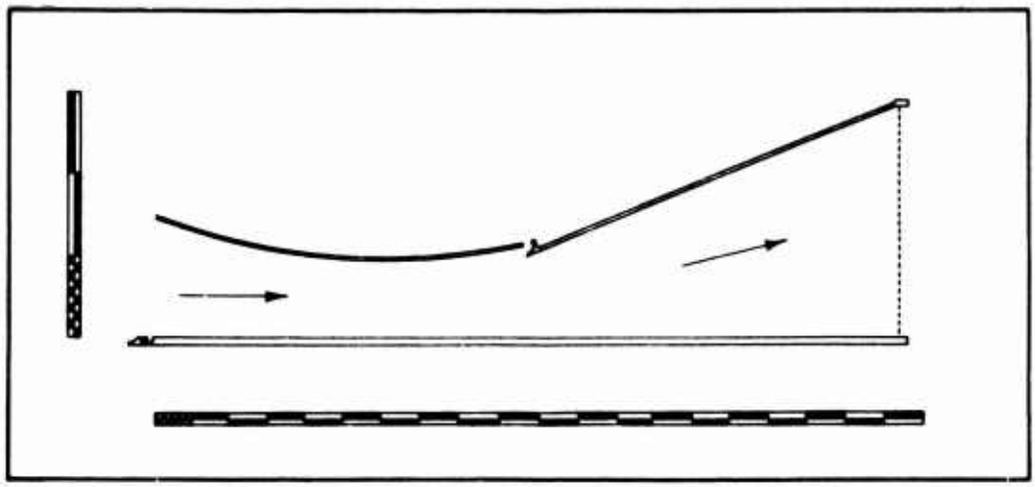

Figure 1. Sideview schematic of the test section. Major divisions on scales: 10 inches. Note baffle plate upstream of blunt leading edge on bottom test wall, upper wall boundary layer scoop, and perforated metal exit plate.

Just upstream of the blunt leading edge of the test wall, 33 smoke ports are located spanwise across the wind tunnel contraction. A baffle plate deflects the smoke in the free-stream direction and tends to produce a uniform spanwise distribution of smoke. The room temperature smoke used for laser anemometer measurements is dioctal phthalate atomized by the shearing action of compressed air jets to approximately 1 micron particles.

The laser anemometer system used a backscattering fringe-type arrangement and is discussed in some detail by Simpson, et al. (1974) and Simpson and Barr (1974a). The argon-ion laser beam (4880Å)passed through an ultrasonic Bragg cell. The horizontal first-order diffracted beam, which was shifted 25 MHz, and the unshifted beam were focused to form real moving fringes in a volume 0.0125 inches diameter and 0.140 inches long. Signals greater than 25 MHz were obtained from flow moving downstream while signals less than 25 MHz were obtained from flow moving upstream. Received signals from this volume were focused onto the plane of a variable aperture diaphragm and passed through a narrow window (~5A°) interference filter to the face of a photomultiplier tube. All the optics were mounted on a single mobile cart which allowed movement along the wind tunnel test section and provided for adjustment in all three directions.

Sampling spectrum analysis of the signals was used because of the high signal drop-out level encountered in this flow with the low particle seeding level and the high signal frequencies produced by frequency shifting one incident beam. Most frequency trackers cannot handle either of these signal conditions. The basic principles of this signal processing method are explained here while more details are given by Simpson and Barr (1974b). The signal from the photomultiplier tube is input to a swept filter spectrum analyzer. For each sweep of the analyzer when a particle is in the focal volume, a vertical voltage distribution proportional to the filter output is displayed. The simultaneous horizontal sweeping voltage is linearly proportional to the signal frequency. The peak of the vertical voltage distribution marks the frequency of the passing particle signal and is used as a gating signal to allow the instantaneous value of the horizontal sweep voltage to be sampled.

Prior to gating the horizontal sweep voltage the vertical voltage distribution is fed into a pulse-shaping circuit which produces a pulse simultaneously with the occurrence of the peak value. This output pulse is used to trigger a sample-and-hold circuit, into which the horizontal sweep voltage has been input. The sampled sweep voltage is held by the sample-and-hold circuit until a new signal from another particle is detected. The output of the sample-and-hold circuit is input to a SAICOR model 41 digital probability

analyzer to obtain a somewhat gaussian-like histogram of output voltages which are related to particle velocities. From a histogram obtained for a given location in the flow, the mean streamwise velocity U, the mean square streamwise fluctuation velocity $\overline{u^2}$, and the fraction of time that the flow moves downstream γ_p (downstream flow intermittency) were obtained from the relations

$$U = \sum_i U_i \left(\frac{\Delta A}{A}\right)_i; \quad \overline{u^2} = \sum_i (U_i - U)^2 \left(\frac{\Delta A}{A}\right)_i; \quad \gamma_p = \sum_{ip} \left(\frac{\Delta A}{A}\right)_{ip}$$

where $(\Delta A/A)_i$ is the fraction of the total histogram area for a given probability analyzer bin corresponding to velocity U and the subscript p denotes positive velocity quantities.

Standard Thermo-Systems, Inc. constant temperature anemometers, linearizers, signal conditioners, and correlator were used in the measurements reported here. Standard Thermo-Systems, Inc. 0.001 inches diameter platinum-coated quartz rod hot-film sensors were used in the normal sensor, the 45° slanted sensor, and the dual cross-film probes used here. The flush surface mounted hot-film sensors used for wall shear stress measurements were fabricated at SMU and are described in detail by Strickland and Simpson (1973). A double hot-film sensor was constructed for measuring the fraction of time the flow was downstream. The probe consists of two 0.02 diameter platinum hot-film sensing spots 180° apart on the side of a 2 mm diameter quartz rod near one end. The probe was inserted through the test wall with one sensor facing upstream and one downstream. The sensing spots were approximately 0.75 inches from the wall.

3. DESCRIPTION OF THE TEST FLOW

The test boundary layer flow on the wind tunnel floor was an airfoil type with first flow acceleration and then deceleration. All experimental data were obtained with the temperature and stagnation pressure being maintained essentially constant at 77°F and 1.310 inches of water.

In the bottom wall boundary layer the static pressure at the wall is essentially equal to that at the boundary layer edge except at the last station measured (183.6). However, in the center portion of the boundary layer the static pressure tends to be less than that at the wall or freestream. Spangenberg, et al. (1967) also noted such a phenomenon in their separating flow. This can first be noticed in the present flow at station 103.8, although the variation is only on the order of .003 inches of water with the uncertainty being about 0.002 inches of water. At station 157.1 the variation is approximately .020 inches of water. Rotta (1962) shows by use of the y momentum equation that the static pressure in the boundary layer is less by an amount equal to ρv^2 from that of the freestream. This appears to account for the variation for stations up through station 139.1. At stations 157.1 and 183.6 the factor ρv^2 accounts for only about 1/3 to 1/2 of the variation. The existence of a significant pressure gradient normal to the wall near station 183.6 is produced by exit screen effects and is responsible for the lack of agreement at that station as discussed by Strickland and Simpson (1973).

Figure 2 shows the free-stream velocity distributions along the tunnel center line obtained using the stagnation pressure and these several static pressure measurements. The agreement of these results indicate a rather uniform pressure across the freestream. Near the exit, the velocity calculated from the wall tap data is seen to be about 5% higher than that obtained using free-stream static pressures. This is due to the wall static pressure being lower than that in the freestream. This effect is primarily produced by the curvature of the free-stream flow toward the bottom wall as the perforated sheet metal exit cover with its associated high pressure drop is approached.

Figure 3 shows the pressure gradient measured along the centerline of the bottom wall. Just downstream of the location of the upper wall scoop (96 inches), the slope of the static pressure gradient changes sign. Near station 128 inches the pressure gradient abruptly drops to an approximately constant value downstream.

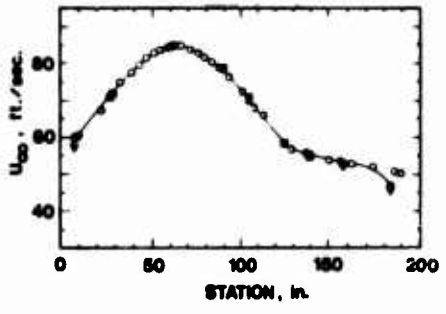

Figure 2. Freestream velocity distribution
○ From bottom wall static taps
□ From bottom B.L. probe (pitot)
▽ From top B.L. probe (pitot)

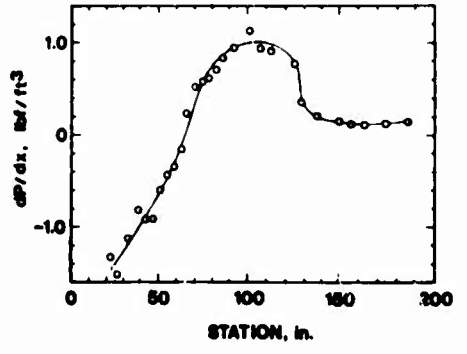

Figure 3. Pressure gradient along bottom wall

Three-dimensionality of the mean flow is often thought to dominate separating boundary layers. Consequently, several types of measurements and observations were made to assess this condition. Boundary layer velocity profiles using impact probes were obtained to examine the upper wall and bottom wall flow behavior (Strickland and Simpson, 1973). Mean streamwise velocity profiles taken across the center 12 inches of the bottom wall indicate that the flow was two-dimensional within about 1 fps. Wall static pressures measured in the same region are within 1% of the dynamic pressure of being uniform across the flow. Mass flow balance considerations indicate that the effective convergence of the flow due to side

wall boundary layer growth introduces some small three-dimensionality. The maximum value of this convergence occurs near station 120 inches and is approximately 0.07 inches/inch of flow length. Prediction of this flow up to separation by the Bradshaw et al. (1967) method, with and without the measured convergence effect, indicates that there was a negligible effect of convergence.

Data obtained with the sensor slanted with 45° angle to the stem was also used to obtain an estimate of the crossflow velocity along the tunnel centerline. By obtaining mean voltage signals at different stem orientations, the W and U components could be deduced at a given spatial location. Results obtained upstream of station 124.8 inches indicate negligible crossflow within the small uncertainty of aligning the probe with the tunnel centerline. Downstream the peak values of W appear in regions near the wall where the mean velocity U is small. The value of W indicated in these regions is less than 1.5 fps or about 3% of the free-stream velocity. However, as discussed below, incipient flow separation and backflow occur in these regions so these latter results from the directionally insensitive hot-film sensor are suspicious.

Some asbestos particles were introduced at the downstream portion of the separation zone and migrated upstream until a dune, straight within about 2 inches, was formed perpendicular to the streamwise direction across the tunnel floor. Thus, within the uncertainty of the instrumentation and techniques employed, the apparent mean three-dimensionality uncovered by all of these measurements appears to be minimal upstream of station 124.8 inches and small downstream.

4. EXPERIMENTAL RESULTS

4.1 Mean velocity and downstream flow intermittency

Figures 4 and 5 present laser anemometer results for the mean velocity along with downstream flow results from the normal hot-film and impact probes. Table 1 presents characterizing parameters for this flow. The laser anemometer results were obtained from two different optical setups at different times. Turbulence intensity measurements from the earlier work (Simpson, et al. 1973) were known to be in error due to dispersion bandwidth limitations of the spectrum analyzer used at that time. The signal processing technique described above and by Simpson, et al. (1974) seems to have alleviated that problem. Good agreement between these two sets of results is observed. Simpson, et al.(1973) have noted good agreement between the impact probe and hot-film mean velocity profiles for the downstream flow, accounting for turbulence intensity effects.

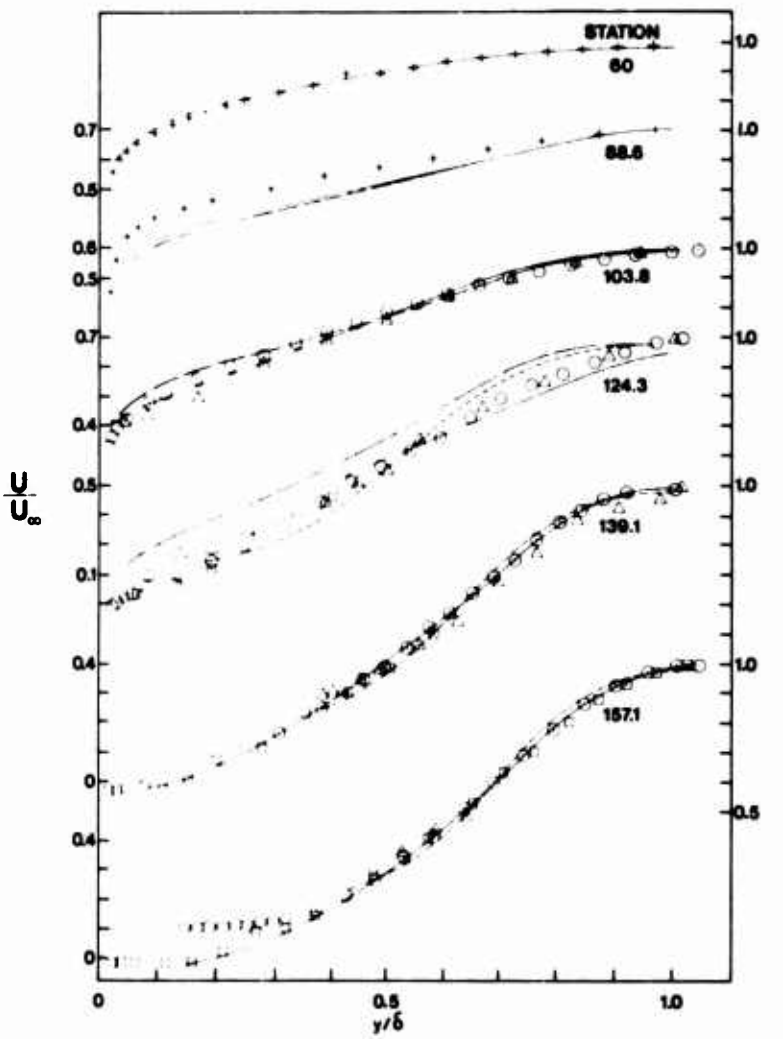

Figure 4. Mean velocity profiles: + impact probe, O normal hot film, △ laser anemometer (Simpson, et al. 1973), □ present laser anemometer. Solid lines: stations 60 and 88.6, predictions of Bradshaw, et al. method; stations 103.8 and 124.3, correlation of Perry and Schofield; stations 139.1 and 157.1, visual aid only. Dashed line: equation (11). —·— : predictions with normal stress effects.

Figure 6 shows γ_p measured 0.010 inches from the test wall while figure 7 shows γ_p at the several streamwise locations. For $\gamma_p \leq 0.8$, we can see from figure 4 that the normal hot-film data agree with the laser anemometer results, even though some signal rectification effect is present.

As mentioned in section 2 above, the double hot-film sensor was constructed for measuring γ_p and the frequency of flow reversal. The original intent was to subtract the signals from the two sensors, thus producing a positive signal when the flow was in one direction. However, thermal coupling and other problems (Strickland and Simpson, 1973) prevented this. Instead, mean voltage signals from each sensing spot were obtained with each spot oriented both upstream and downstream. Using the non-linear cooling relationship for film sensors, it was determined (Strickland and Simpson, 1973) that $\gamma_p = 1/2$ when the mean voltage signals from a sensor facing upstream and downstream were equal. This condition was satisfied at station 132, in agreement with the laser anemometer result shown on figure 6.

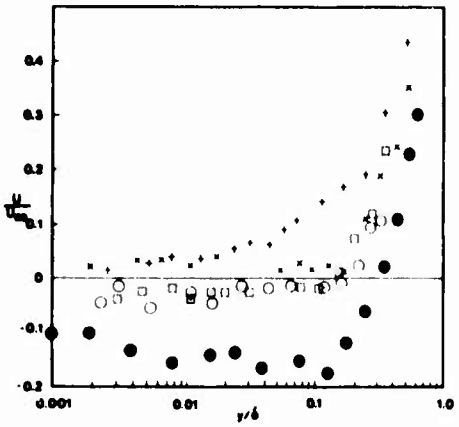

Figure 5. Mean velocity profiles near the wall in the separation region: + 124.6, x 132.2, □ 139.1, ○ 156.0, ● 165.8.

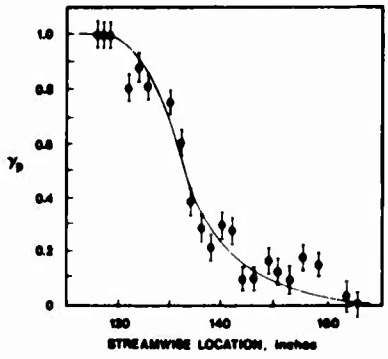

Figure 6. Fraction of time that the flow 0.010 inches from the wall is in the downstream direction. Solid line for visual aid only.

Station (inches)	Re_θ	U_∞ (fps)	$\frac{dU_\infty}{dx}$ $(\frac{1}{sec})$	$(\frac{Cf}{2} \times 10^3)^c$	$\delta_{0.99}$ (inches)	H
28.2	2240	71.6	8.1	2.06[a]	0.69	1.29
60.0	3520	85.0	0.60	1.73	0.82	1.33
88.6	6020	78.0	-5.2	1.30[a]	1.25	1.39
103.8	9220	70.8	-6.15	0.83[a]	1.82[b]	1.63
108.8	10100	67.6	-6.6	0.74	2.13[b]	-
117.8	13600	62.8	-6.9	0.20	2.89[b]	-
124.3	17700	58.9	-5.9	0.113	3.71[b]	2.62
126.8	18400	57.6	-4.6	0.08	3.90[b]	-
136.0	21100	56.0	-2.0	-0.06	5.34[b]	-
139.1	21400	55.5	-1.75	-0.06	6.54	4.63
148.0	22600	54.2	-1.5	-0.3	7.3[b]	-
157.1	24000	53.3	-1.0	-0.1	9.38	5.36
165.8	25700	52.7	-1.0	-0.14	10.2[b]	-
175.7	30000	51.6	-1.1	-0.14	11.4[b]	-
184.5	38000	50.7	-1.2	-0.15	12.23	-

(a) solid line, figure 10. (b) interpolated value. (c) interpolated value from hot surface film results (Simpson, et al. 1973).

Table 1. Values of parameters along the flow. $\nu = 1.68 \times 10^{-4}$ ft^2/sec.

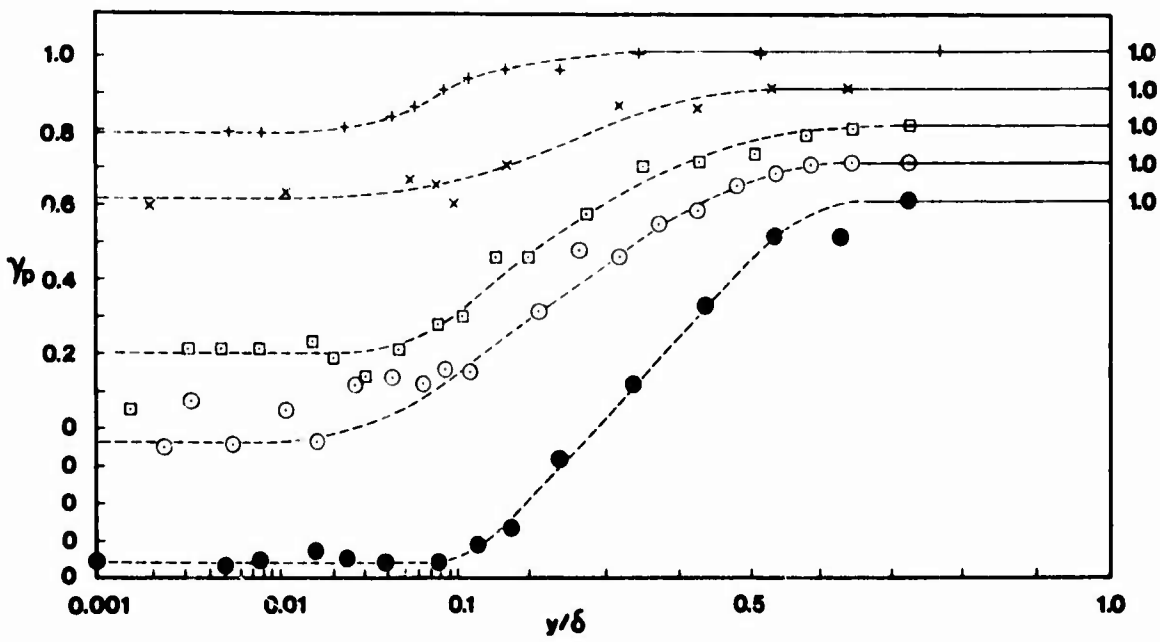

Figure 7. Fraction of time γ_p that the flow is in the downstream direction. Note abscissa scale change and displaced ordinate. Legend same as figure 5. Lines for visual aid only.

4.2 Turbulence

Laser anemometer signal effects on the turbulence intensity $\overline{u^2}$ were found to be negligible for the data presented here (Simpson, et al., 1974). The effects examined were transit-time broadening, velocity-gradient broadening, and low velocity particle biasing. Simpson, et al. (1974) reported good agreement of these data with $\overline{u^2}$ obtained from the cross-film probe for $\gamma_p > 0.95$. Velocity probability diagrams obtained using the normal hot-film indicated a doubled-peaked distribution for $\gamma_p < 0.95$, which evidently indicates some rectification effect. For $\gamma_p < 1$, the hot-film measured $\overline{u^2}$ was drastically lower than the laser anemometer value.

Figure 8 shows $\overline{u^2}/\overline{u^2}_{max}$ vs. y/M for the downstream separated flow stations, where $\overline{u^2}_{max}$ and M are the maximum mean square fluctuation and its location for that profile. The observed similarity is fairly good for $y/M < 1$ even at station 124.6 where $\gamma_p \geq 0.8$. At all other stations shown in that figure, similarity throughout the profiles is shown. It is interesting to note γ_p appears to approach unity for each profile in the vicinity of the maximum observed $\overline{u^2}$ value. A plot of $\overline{u^2}/U^2$ vs. x for 0.010 inches off the wall shows that the maximum value occurs near station 132, which is consistent with the location of $\gamma_p = 0.5$ shown in figure 5, the location of zero mean wall shearing stress shown in figure 10, and the maximum surface hot-film fluctuation signals presented by Simpson, et al. (1973).

Hot-film measurements of $\overline{u^2}$, $\overline{w^2}$, and $-\overline{uv}$ were also reported by Simpson, et al. (1974) for $\gamma_p > 0.8$. Figure 9 presents $-\overline{uv}/U_\infty^2$ results for the several stations for $\gamma_p > 0.95$ obtained by cross-film and slant-film probes. Agreement between measurements made at the same station by both probes is within 20% while the uncertainty of each measurement was estimated to be about 11%.

Spectral data for $\overline{u^2}$ were obtained for $\gamma_p = 1$ using the normal hot-film probe and were used together with the -5/3 law of the inertial subrange to determine the turbulence energy dissipation rate. The dissipation rate was also estimated using the assumptions of local isotropy and Taylor's hypothesis for convection velocities. Agreement of results between these two methods was within 20% at stations upstream of 193.8 inches but was somewhat poorer at the downstream stations near separation. Details about these measurements and the results are presented by Simpson, et al. (1974).

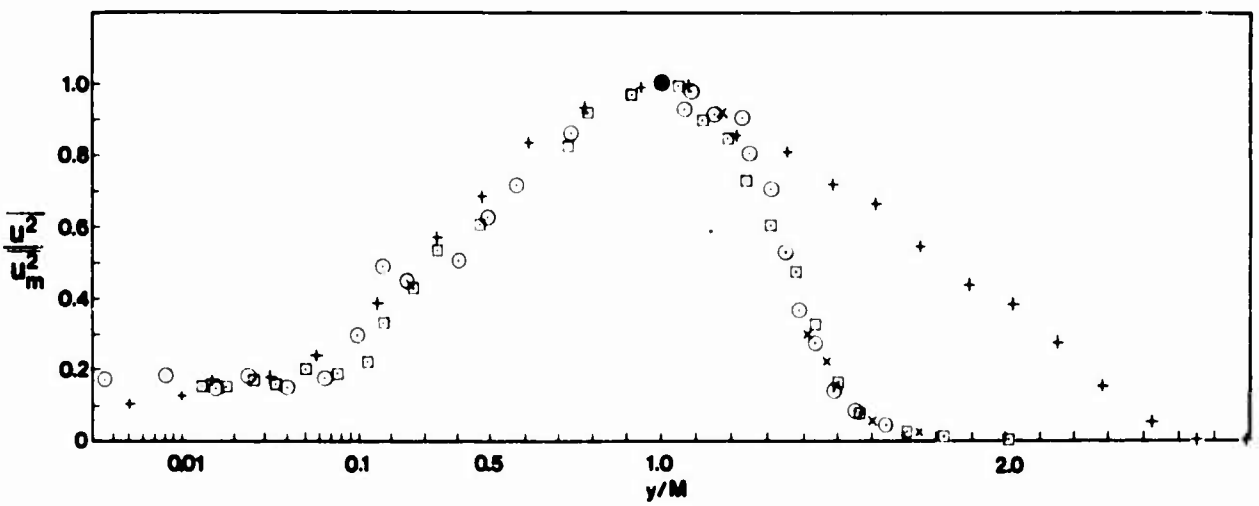

Figure 8. Streamwise normal stress in the separated region normalized on the maximum stress and the distance from the wall to the maximum.

	location	M/δ	$(\overline{u^2}/U_\infty^2)_{MAX}$	$(U/U_\infty)_{M/\delta}$
+	124.6	0.40	17.6 x 10^{-3}	0.47
□	139.6	0.58	27 x 10^{-3}	0.52
○	157.1	0.65	36 x 10^{-3}	0.52
X	183.6	0.66	58 x 10^{-3}	0.59

4.3 Wall shearing stress results

Four different ways of deducing the mean wall shearing stress distribution were used and the results reported in some detail by Simpson, et al. (1973): the velocity profile crossplot used by Coles and Hirst (1968), the Preston tube technique, flush surface mounted hot-film sensors, and the Ludwieg and Tillmann skin friction correlation. The flush surface-mounted hot-film sensors were also used to deduce shearing stress fluctuations. The crossplot, Preston tube, and Ludwieg and Tillmann methods require the existence of a universal logarithmic law-of-the-wall. All velocity profiles obtained upstream of about station 124.3 inches indicated similar logarithmic regions.

The agreement of the mean wall shearing stress values obtained by the several methods is reasonably good. Estimated uncertainties for each type of result were computed with the largest uncertainties occurring at station 124.3 inches. The Coles crossplot and Ludwieg-Tillmann methods using hot-film velocity profile data, the flush hot film, and the Preston tube produce results within ± 16% at this station. Considering the small value of $C_f/2$ being measured, this agreement is gratifying. These results are shown in figure 10. The data obtained by the flush-mounted hot-film sensors are not dependent on the notion of a logarithmic wall region. This would tend to suggest that the law-of-the-wall holds until near where $\gamma_p < 1$ first at the wall, since there appears to be reasonable agreement between flush-mounted hot-film data and the methods which utilize the law of the wall.

The fact that only absolute shearing stresses are detected explains in part why a mean value of shearing stress equal to zero was never observed from the flush-mounted hot-film data in the region of separation. Since time-averaged backflow was observed downstream of station 132 by laser anemometer measurements near the wall, those shearing stresses are presented as negative values. No attempts to correct the mean shearing stresses in the separation region for the rectification effect were made.

The apparent mean wall friction coefficient was also evaluated from the laser anemometer data using the relation $C_f/2 = (\nu/U_\infty^2)(\Delta U/\Delta y)$, where $\Delta y = 0.010$ inches and ΔU the velocity at 0.010 inches. This method gave values of $C_f/2$ about 100% too high as compared with the estimates given by the surface hot-film results. However, these results did indicate that the mean wall shear changed sign at about 132 inches position where $\gamma_p \approx 0.5$.

5. DISCUSSION

The Bradshaw, et al. (1974) computer program was used to predict the behavior of this boundary layer. Velocity and shear stress profiles at station 28 inches were input. The side wall boundary layer effects on the convergence were accounted for, but there was much less than 1% difference when this effect was ignored. The surface shear stress distribution shown in figure 10 indicates good agreement up to about station 108 with the flush surface sensor results while the mean velocity profiles were in good agreement only up to about station 70. Because of this good agreement up to this streamwise location, the discussion here will be limited to the downstream region.

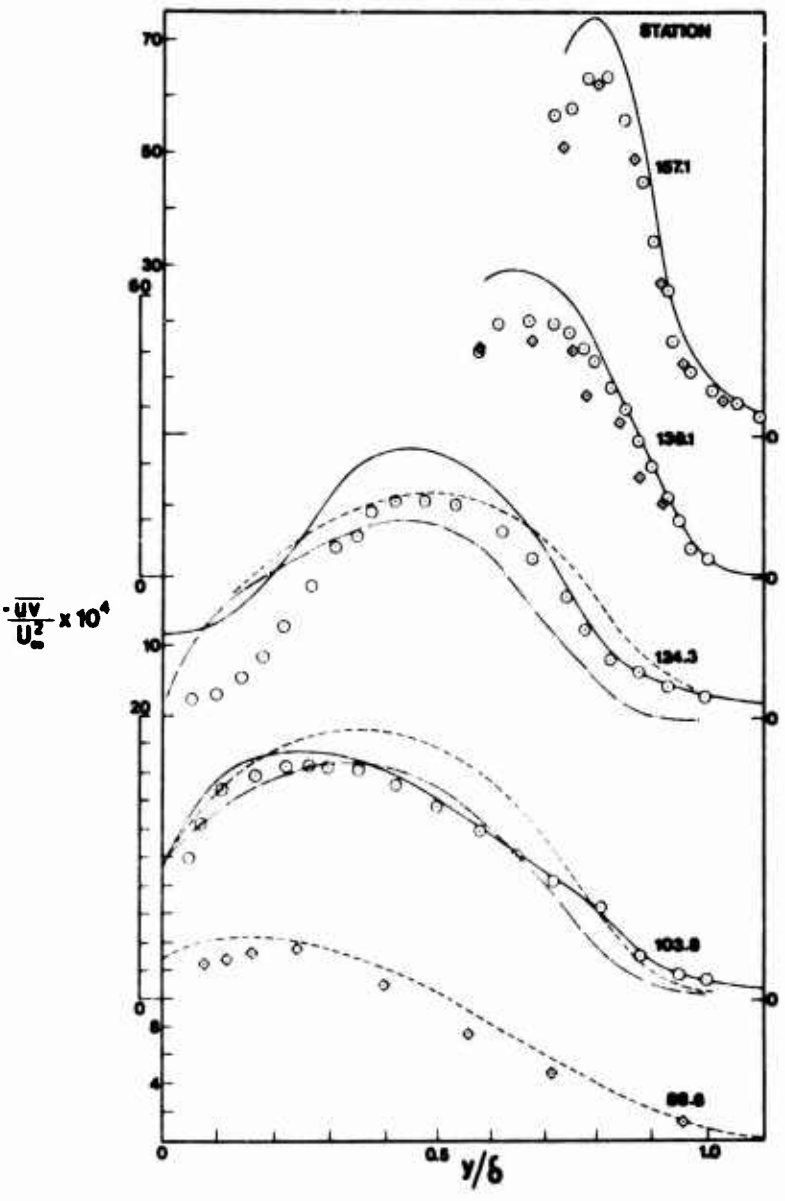

Figure 9. $-\overline{uv}/U_\infty^2$ distributions: ○ cross film, ◇ slant hot-film. Solid lines: pseudo-shearing stress distributions; dashed line: prediction of Bradshaw, et al. method, no normal stresses; —·— : current prediction with normal stress effects. Note displaced ordinates.

Perry and Schofield (1973) have recently proposed a correlation for unseparated flow mean velocity profiles in the presence of strong adverse pressure gradients, based upon 145 mean velocity profiles from flows on flat or slightly curved surfaces taken from Coles and Hirst (1968) and including both equilibrium and non-equilibrium profiles. This correlation only applies when the maximum shearing stress $U_M^2 = (-\overline{uv})_{max}$ exceeds $3/2U_\tau^2$, where U_τ is the wall shear velocity. In the present results, only stations 103.8 and 124.3 meet this requirement.

They proposed that the outer flow be described by

$$\frac{U_\infty - U}{U_s} = f_2(\eta_2) \qquad , \eta_2 = y/\Delta \tag{1}$$

where $f_2(\eta_2)$ is a universal function, $f_2(0) = 1$ defines the velocity scale U_s, and Δ is determined through the displacement thickness δ^* integral

$$\Delta = 2.86 \quad \delta^* \frac{U_\infty}{U_s} \tag{2}$$

Near the wall

$$\frac{U}{U_\tau} - h = f_1(\eta_1), \quad \eta_1 = \frac{y}{e}, \quad e = \frac{LU_\tau^2}{U_M^2} \tag{3}$$

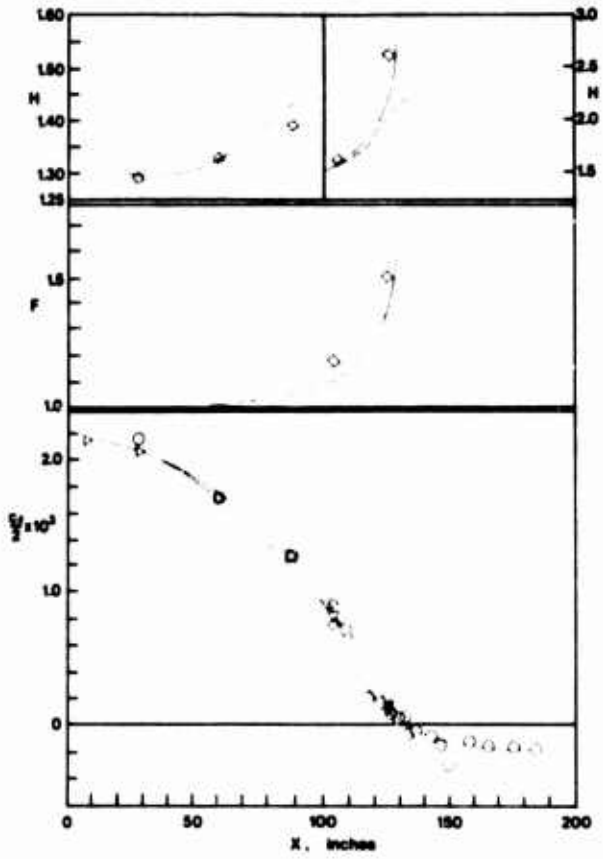

Figure 10. Friction factor distributions: ○ flush hot film, ▷ Preston tube, ◇ crossplot of hot-film data, ▽ from Ludwieg and Tillmann relation (Simpson, et al. 1973). Solid line - visual aid only; dashed line - prediction of Bradshaw, et al. (1967) method; —·— : current prediction with normal stress effects. Experimental F and H, ◇.

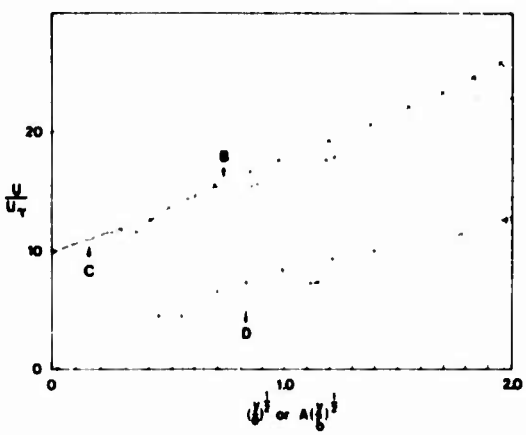

Figure 11. Half-power mean velocity profile relationship near the wall upstream of separation. Station 103.8: x hot-film; ○ laser anemometer; A = 2.96; point B - predicted point of tangency y_c; point C - $y^+ = 32$. Station 124.3: + hot-film; △ laser anemometer; A = 8.56; point D - $y^+ = 10$. Solid lines - 6.4 slope; dashed line - 8.05 slope.

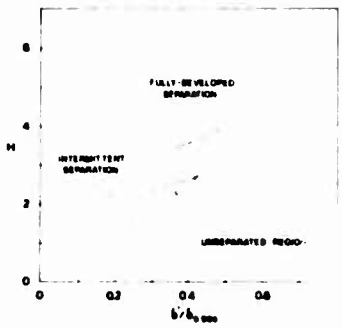

Figure 12. H vs. $\delta^*/\delta_{0.995}$. △ present data: stations 88.2, 103.8, 124.3, 139.1 and 157.1, respectively, for increasing H. Shaded areas - data for intermittent and fully-developed separation (Sandborn and Kline, 1961). Path predicted from Perry and Schofield velocity profiles ---. Solid line —— intermittent separation; —·— fully developed separation (Sandborn); —··— data of Sandborn and Liu (1968).

where h is a constant and L is the distance from the wall to the maximum in the local shear stress profile. The proposed relation for e was empirically determined. The existence of an overlap region between f_1 and f_2 requires that in that region

$$f(\eta_1) = 6.4\eta_1^{1/2} \tag{4}$$

and that

$$\frac{U_s}{U_M} = 8.0\left[\frac{\Delta}{L}\right]^{1/2} \tag{5}$$

where the constants were empirically determined.

Within the inner flow nearest the wall equation (3) takes the usual logarithmic form for $y^+ > 30$

$$U^+ = \frac{1}{0.41}\ln|y^+| + 5.0 \tag{6}$$

and $U^+ = y^+$ in the viscous sublayer. The point of tangency between equations (3) and (6) occurs at

$$y_c = 0.58e \quad \text{or} \quad y_c/\Lambda = 37.1\ U_\tau^2/U_M^2 \tag{7}$$

For the data presented here U_s/U_∞ was determined from a U/U_∞ vs. $(y/\delta)^{1/2}$ plot with the slope of the half-power region extrapolated to the wall, as suggested by Perry and Schofield. This and other parameters are shown in Table 2. In terms of U/U_∞ vs. y/δ, the center of the band of data presented in figure 6(a) by Perry and Schofield for $f_2(\eta_2)$ is plotted on figure 4. For station 103.8 there is very good agreement with the measurements and the scatter is well within the scatter of their correlation. For station 124.3, there is more deviation but the present results fall along the edge of the scatter in their correlation.

Nearer the wall there is some scatter in the present results, as shown in figure 11, but equations (3) and (4) seem to be roughly satisfied. At station 103.8 the slope of equation (4) seems to be satisfied by the laser results while the hot-film results require about a 8.05 slope. The predicted point of tangency y_c is substantially further out in the boundary layer than the inner edge of the logarithmic region. At station 124.3 the predicted point of tangency occurs in the sublayer, so supposedly no logarithmic region remains. However, it should be recalled from section 4.3 that good agreement between wall shear stress measurements that do and do not require the assumption of a logarithmic law of the wall seems to support the existence of some logarithmic region at this station. Plots of U^+ vs. y^+ (Simpson, et al., 1973) also support equation (6) near the wall at these two locations. Figure 5 shows a logarithmic-like region for station 124.3 for $y/\delta < 0.01$. When $U_\tau \to 0$, $h \to 0$ and equations (3) and (4) should become independent of U_τ. Evidently this condition is being approached at station 124.3

The experimentally determined values of U_s/U_M and Δ/L fall within the scatter of the plot from which Perry and Schofield obtained equation (5). However, better agreement with equation (5) is obtained if the "pseudo-shearing stress" is used

$$U_{Mp}^2 = \left[-\overline{uv} + \int_y^\infty \frac{\partial(\overline{u^2} - \overline{v^2})}{\partial x}\, dy \right]_{max} \qquad (6)$$

for the maximum shear. (x-direction derivatives were estimated using the $(\overline{u^2} - \overline{v^2})$ profile similarity along the flow. For more details see Simpson, et al. (1974).) Curves showing U_{Mp}^2/U_∞^2 are given in figure 9. The reason for using this is that Perry and Schofield neglected the normal stresses term in the differential momentum equation (Rotta, 1962)

$$U \frac{\partial U}{\partial x} + V \frac{\partial U}{\partial y} + \frac{1}{\rho} \frac{dP_\infty}{dx} = \frac{\partial}{\partial y} \left[\frac{\tau}{\rho} + \int_y^\infty \frac{\partial(\overline{u^2} - \overline{v^2})}{\partial x}\, dy \right] \qquad (9)$$

when they produced shear stress profiles from mean velocity profiles and this equation. Consequently, they were effectively calculating U_{Mp}^2.

	103.8	124.3
U_s/U_∞	0.7	0.96
U_s/U_M	17.64	17.38
U_s/U_{Mp}	16.7	15.74
y_c/Δ	0.0606	0.00453
Δ/δ	1.01	1.29
L/δ	0.25	0.45

Table 2. Perry and Schofield correlation parameters from the present experimental data.

The data analysis of Perry and Schofield did not support the mixing length theories (Townsend, 1962; McDonald, 1969) which predict a significant departure from equation (6) under strong adverse pressure gradients. The present resul s do not support those theories either. These theories are predicated on a linear shearing stress distribution near the wall being a function of pressure gradient while ignoring the normal stress terms. For station 124.3, the present data suggest that at $y/\delta \approx 0.05$

$$\frac{\partial(-\overline{uv}/U_\infty^2)}{\partial(y/\delta)} \approx 2 \times 10^{-3} \quad \text{while} \quad \frac{\delta \partial(\overline{u^2} - \overline{v^2})}{U_\infty^2 \quad \partial x} \approx 5 \times 10^{-4}$$

so that near separation near the wall, normal stress terms are quite significant in the momentum equation as compared to the shear term. Also note that while the -uv measurements near the wall are relatively uncertain, it seems to be fairly constant and agrees with the wall value, an observation consistent with other measured -uv data (Newman, 1951).

The description of turbulent boundary layer separation is not clear cut as in a steady laminar flow, where separation is presumed to occur at a location along the flow where the wall shear vanishes. Turbulent separation, or intermittent separation according to Sandborn and Kline (1961), occurs at the upstream point at the wall where backflow begins on an intermittent basis. This point is the intermittent separation point or the turbulent separation point. Downstream of this location γ_p decreases along the wall in the intermittent separation region where flow moves both upstream and downstream on an intermittent basis. The so-called fully-developed separation point or time-averaged separation point is where the average wall shear stress is zero.

It is clear from figure 6 that intermittent separation begins somewhere downstream of station 120. At station 124, $\gamma_p \approx 0.8$ near the wall, which as pointed out in section 4.1, appears to be about the lowest value of γ_p for which the hot-film mean velocity values are not appreciably affected by signal rectification. This would appear to be a good criterion for the beginning of intermittent separation, considering also the uncertainty in measuring γ_p as noted in figure 6. Figures 2 and 3 indicate that the pressure gradient drops off rapidly after intermittent separation.

Figure 12 presents the separation criteria of Sandborn as discussed by Sandborn and Kline (1961), which are based on examination of many laminar and turbulent separation velocity profiles. For intermittent separation the following relation was proposed

$$H = 1 + (1 - \delta^*/\delta_{0.995})^{-1} \qquad (10)$$

while the laminar velocity profile at zero wall shear was proposed to predict the H vs $\delta^*/\delta_{0.995}$ at which fully-developed separation was located. The present data are in good agreement with these criteria. Although no velocity profile data were taken at station 132, interpolating between the 124.3 and the 139.1 data points on figure 12 places 132 somewhere near the fully-developed separation curve. The data of Sandborn and Liu (1968), which agree with these criteria, indicated that $\gamma_p \approx 0.7$ near the wall at intermittent separation, somewhat agreeing with the above proposal that $\gamma_p \approx 0.8$ at intermittent separation.

Use of the Perry and Schofield correlation implies that there is only one H vs. $\delta^*/\delta_{0.995}$ path that a flow can follow to separation. This is implied through equation (1), which can be manipulated using their $f_2(\eta_2)$ correlation plot to produce the curve shown on figure 12 for this path. If one allows $U_s \to U_\infty$ which implies that the half-power relation approaches the wall, then $U_\tau \to 0$ and separation is predicted at H = 2.28. Which separation? Judging from all these data and figure 12 it can only be the intermittent separation, although this prediction is only fair. The data used by Perry and Schofield were obtained from flows over low-curvature faired surfaces such as the data presented here. The data of Sandborn and Liu was obtained after a moderately large change in curvature. The H vs. $\delta^*/\delta_{0.995}$ path for those data was at considerably lower $\delta^*/\delta_{0.995}$ than the data presented here or the Perry and Schofield path. Evidently the curvature effect is important in determining this path, and the Sandborn criteria for separation are thus more general.

Downstream of separation the outer mean velocity profiles behave similarly to a two-dimensional mixing layer. For $U/U_\infty > 0.3$ the equation presented by Strickland and Simpson (1973)

$$\frac{U - U_0}{U_\infty - U_0} = \frac{1}{2}\left\{1 + \operatorname{erf}\left[\frac{\delta' y'}{x'}\right]\right\} \tag{11}$$

was found to fit the mean velocity profiles, where $\delta' = 35$, $U_0/U_\infty = 0.2$, y' is measured from $U/U_\infty = 0.6$ near the maximum shear locations, and x' is measured from 88 inches. As shown on figure 4 this relation does not fit the data at 124.3 very well. The value of δ' is about twice the value obtained for mixing layers with zero pressure gradient and with $U_0/U_\infty = 0.2$ (Halleen, 1964).

Rather flat mean velocity profiles are observed for $y/\delta < 0.15$ downstream of the beginning of intermittent separation. This low velocity region evidently just serves the function of providing just the small amount of net backflow required to satisfy the continuity requirement after the energetic flow near the freestream has deflected away from the wall upon separation. In the same region γ_p, U, and the average positive velocity also remain fairly flat, as seen in figures 5 and 7, also indicating that the average negative velocity is also about constant.

Figure 8 strongly suggests that there is some flow field similarity downstream of separation, with the maximum streamwise rms fluctuation $\overline{u^2}_{max}$ and the distance M from the wall to the location of this maximum being the velocity and length scales, respectively. Figure 4 indicates that the location of maximum $\overline{u^2}$ occurs at $U/U_\infty \approx 0.5$ for stations 139.1 and 157.1 while the mean velocity changes direction at $y/M \approx 0.25$. The velocity profile similarity equation (11) also indicates mean velocity profile similarity, at least in the outer region. γ_p also provides further evidence of similarity.

The data shown on figure 7 were replotted to test the proposed similarity relation

$$\frac{\gamma_p - \gamma_{p_0}}{1 - \gamma_{p_0}} = g(y/M) \tag{12}$$

where γ_{p_0} is the near wall value shown in figure 6. For stations downstream of intermittent separation, equation (12) was satisfied within about ±0.05 at a given y/M. An empirical curve fit, accounting for the linear portion and the tail near y/M = 1, produces

$$g(y/M) = 1.58\left[\frac{y}{M} - 0.08\right] - 0.453\exp\left[-27.1(1 - y/M)^2\right] \qquad 0.1 < y/M \leq 1 \tag{13}$$

Thus the separated flow field similarity is supported by all the data presented here.

The turbulence structure seems representative of previous adverse pressure gradient work, although the effects of the normal stress terms have not previously been emphasized (Simpson, et al., 1974). The parameter $-\overline{uv}/q^2 = a_1$, which is fairly constant across the middle of a boundary layer, represents the fact that in most flows the turbulence energy is a direct result of shear production. Bradshaw (1967) obtained values of a_1 around 0.15 for two equilibrium type adverse pressure gradient flows, with values as low as 0.1 for small values of y/δ. Upstream at stations 88.2 and 103.8, a_1 has a value of about 0.13 near the outer boundary layer edge and smaller values closer to the wall, in fair agreement with Bradshaw's result. At station 124.3 a_1 is substantially smaller near the wall, indicating either too low -uv measurements or some other source of turbulence production.

The normal stress production term is not negligible in the turbulence energy equation

$$\left[\frac{U}{2}\frac{\partial \overline{q^2}}{\partial x} + \frac{V}{2}\frac{\partial \overline{q^2}}{\partial y}\right] + \frac{\partial}{\partial y}\left[\frac{\overline{pv}}{\rho} + \frac{1}{2}\overline{q^2 v}\right] + \varepsilon = -\overline{uv}\frac{\partial U}{\partial y} - (\overline{u^2} - \overline{v^2})\frac{\partial U}{\partial x} \tag{14}$$

where the terms are advection, diffusion, dissipation, shear production, and normal stress production, respectively. Figure 13 shows estimates of the ratio of normal stress to shear production for the several stations, along with the results of Schubauer and Klebanoff (1951) near separation. If we multiply a_1 by the factor

$$F = 1 - \frac{(\overline{u^2} - \overline{v^2})\,\partial U/\partial x}{-\overline{uv}\,\partial U/\partial y} \tag{15}$$

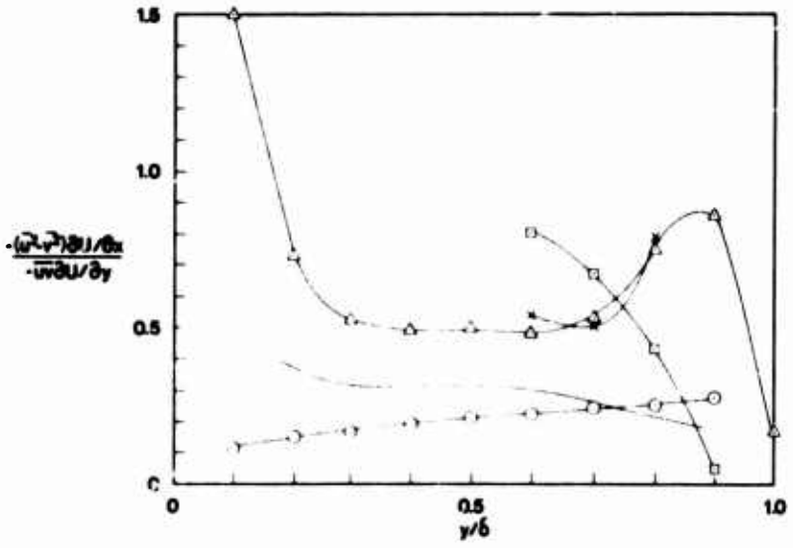

Figure 13. Ratio of normal stress production to shear stress production at the several streamwise locations: O 103.8, Δ 124.3, □ 139.1, x 157.1. Solid line shows results of Schubauer and Klebanoff flow near separation, 24.5 feet.

which is the ratio of total production to shear production, then a_1F should represent the ratio of of the total turbulence production mechanism to the turbulence energy produced. As separation is approached F takes on values of the order of 1.5 or 2, although uncertainties in estimating $\partial U/\partial x$ make the values in figure 13 also uncertain, especially at high and low y/δ. Clearly though, the large value of F near the wall at station 124.3 is needed to at least partially account for the small a_1 observed. In general a_1F takes on values closer to 0.15 than a_1. This suggests that $a_1F \simeq 0.15$ is the more general correlation. The curvature turbulence production term $-uv\ \partial V/\partial x$ (Bradshaw, 1973) has been neglected from the right side of equation (14), since in this flow the largest value of $(\partial V/\partial x)/(\partial U/\partial y)$ is crudely estimated to be less than 0.03. Thus the effect of curvature attributable production is negligibly small as compared to shear production.

Figure 30 of Simpson, et al. (1974) shows that the dissipation length L defined with $-\overline{uv}$ is also quite a bit lower than Bradshaw's (1967) distribution. It should be noted that the data seem to depart from the $L_\epsilon/\delta = 0.4(y/\delta)$ relation in the vicinity of the predicted y_c/δ of the Perry and Schofield correlation at $y/\delta \approx 0.06$ at station 103.8. Again, $-\overline{uv}$ F should be used to represent the amount of energy available for dissipation since we have found that $a_1F \simeq 0.15$, i.e., it seems we should use

$$\frac{L_\epsilon}{\delta} = \frac{(-\overline{uv})^{3/2} F^{3/2}}{\epsilon\delta} \tag{16}$$

with Bradshaw's L_ϵ/δ vs. y/δ distribution for the left side. As shown in figure 30 of Simpson, et al. (1974), the level of L_ϵ/δ using $-\overline{uv}$ F at station 124.3 is about double the result using only $-\overline{uv}$, but is still quite a bit lower than Bradshaw's distribution. At station 103.8 the result is about 30% higher over that obtained not using F. For $y/\delta > 0.4$, the L_ϵ/δ results using $-\overline{uv}$ F at these latter two stations agree with the results at station 88.2, where F is close to unity.

The entrainment velocity V_e, which is proportional to the diffusion of turbulence energy at the outer edge of the flow, was computed using the relation

$$V_e = \frac{d}{dx}\left[U_\infty(\delta_{0.995} - \delta^*)\right] \tag{17}$$

Bradshaw, et al. (1967) found that V_e could be correlated by the maximum Reynolds shearing stress intensity in equilibrium as well as non-equilibrium boundary layers and the high velocity edge of mixing layers:

$$\frac{V_e}{U_\infty} = 10\left(\frac{-\overline{uv}_{max}}{U_\infty^2}\right) \tag{18}$$

Results using equation (18) were in general about 15% higher than those computed from equation (17) (Simpson, et al., 1974). The deviations are within the scatter of data originally used to obtain equation (18). Apparently the normal stress production of turbulence energy does not appreciably affect the entrainment process.

6. PREDICTION MODEL FOR NORMAL STRESS EFFECTS

From our discussion in section 5 above, it is clear that normal stress effects are important in both the momentum equation (9) and the turbulence energy equation (14). Here a simple model is presented for inclusion of these effects. This model was inserted into the Bradshaw, et al. (1974) computer prediction method, which utilizes equations (9) and (14) and forms a hyperbolic set of differential equations since large-eddy diffusion is used.

The normal stress effects in the turbulence energy equation are easily modeled using the approximation that F is constant across the boundary layer, which is about true for the mid-region of the boundary layer for the data shown in figure 13. Thus the total turbulence production term becomes $F(-\overline{uv}\partial U/\partial y)$. One way to specify $(\overline{u^2} - \overline{v^2})$ for the normal stresses in the momentum and F equations is to relate $(\overline{u^2} - \overline{v^2})$ to q^2 $(q^2 = \overline{u^2} + \overline{v^2} + \overline{w^2})$ or to $-\overline{uv}$. For example let us use the model equation

$$\overline{u^2} - \overline{v^2} = C_1 \overline{q^2} \tag{19}$$

where C_1 is a constant, which is approximately true near the region of maximum normal stresses in zero and adverse pressure gradient boundary layers. A brief survey of available data indicates the following values for C_1 in the region of maximum normal stresses: zero pressure gradient, 0.32 (Klebanoff, 1954); $U_\infty \sim x^{-0.15}$ and $U_\infty \sim x^{-0.25}$ equilibrium flows, 0.28 and 0.23, respectively (Bradshaw, 1967); present data: station 88, 0.33; station 103.8, 0.42; station 124.3, 0.38.

With equation (19) inserted into equation (15), it is advantageous to use the relation

$$\overline{q^2} = F(-\overline{uv})/a_1, \quad a_1 = 0.15 \tag{20}$$

suggested in section 5 above for the center portion of the boundary layer. Thus, equation (15) can be rearranged into

$$F = \frac{1}{1 + \frac{C_1}{a_1} \frac{\partial U/\partial x}{\partial U/\partial y}} \tag{21}$$

Since F has already been assumed constant across the boundary layer, equation (21) need only be evaluated at one location in the region of maximum normal stresses, say at the location of the maximum shearing stress, where one also has a finite non-zero value for $(\partial U/\partial x)/(\partial U/\partial y)$.

Since the Bradshaw, et al. program expresses all turbulence quantities in terms of $-\overline{uv}$, it is also advantageous to use equation (20) in equation (19) to produce

$$(\overline{u^2} - \overline{v^2}) = \frac{C_1(-\overline{uv})F}{a_1} \tag{22}$$

for use in the momentum equation (9). For the results presented here, C_1 was selected at 0.30, which is fairly representative of the experimental values presented above. An added benefit of equation (22) is that just as $(\overline{u^2} - \overline{v^2})$ approaches zero near the outer edge of the boundary layer, $-\overline{uv}$ approaches zero, in agreement with experimental results.

The inclusion of normal stress effects into equations (9) and (14) requires a rederivation of the governing differential equations along the three real characteristics of the hyperbolic set of momentum, continuity, and turbulence energy equations (Simpson and Collins, 1975). The angle between a characteristic and the x-axis, α, is given by the three values

$$\tan \alpha = \infty, \quad \frac{V + \left\{ \frac{\psi}{U} + \underset{(\beta)}{\sigma_\alpha} \right\} a_1}{U} \tag{23}$$

where

$$\underset{(\beta)}{\sigma_\alpha} = GU_M \pm \left[\left(\frac{\psi}{U}\right)^2 + \frac{2\psi}{Ua_1}(V + a_1 GU_M) + (GU_M)^2 + \frac{2\tau F}{\rho a_1} \right]^{1/2} \quad \text{and} \quad \psi = \frac{C_1 \tau F^2}{a_1 \rho} \tag{24}$$

By substituting the continuity equation into the momentum equation, the equation along the vertical characteristic is

$$-U \frac{dV}{dy} + V \frac{dU}{dy} = U_\infty \frac{dU_\infty}{dx} + \frac{d\tau}{dy} \tag{25}$$

The equations along the inclined characteristics are

$$\tau F dU \pm \frac{1}{2} \left\{ \underset{(\beta)}{\sigma_\alpha} - \frac{\psi}{U} \right\} d\tau = \frac{\tau dx}{U} \left\{ FU_\infty \frac{dU_\infty}{dx} - \frac{C_1 F \tau dF}{a_1 \rho dx} + a_1 \left\{ \frac{\sqrt{\tau}}{L_\epsilon} + U_M \frac{dG}{dy} \right\} \left\{ \underset{(\beta)}{\sigma_\alpha} + \frac{\psi}{U} \right\} \right\} \tag{26}$$

When C_1 is set equal to zero, equations (24-26) reduce to those derived by Bradshaw, et al. (1967).

Figure 10 shows predictions using the Bradshaw, et al. program with and without normal stress effects. Upstream of the vicinity of separation, there is no detectable effect of normal stresses on $C_f/2$ and H predictions, although F is slowly increasing. Downstream of about station 108, the inclusion of normal stresses more closely predicts $C_f/2$ and H. Note that the predicted F factors agree with the experimentally determined values from figure 13 evaluated at the maximum shear location. Separation is predicted at about station 127.5 which is about midway between the locations of intermittent and fully-developed separation. No separation is predicted when normal stresses are not included. The mean velocity profile predictions are not particularly improved with inclusion of normal stress effects although figure 9 shows some improvement in the shearing stress in the mid-region of the boundary layer.

This model is currently being refined and tested against the strong adverse pressure gradient flows presented by Coles and Hirst (1968). One refinement is the use of the Perry and Schofield wall similarity relations discussed above instead of the McDonald (1969) type law of the wall used by Bradshaw, et al. The results presented here show the small but significant effect normal stresses can have on a turbulent boundary layer near separation.

7. CONCLUSIONS

The following major conclusions may be drawn from the present experiments:

(a) Laser anemometer measurements of $\overline{u^2}$, U, and the fraction of time the flow moves downstream γ_p obtained using a directionally sensitive system are presented for an airfoil type flow in the vicinity of separation.

(b) The correlations of Perry and Schofield (1973) for mean velocity profiles subjected to adverse pressure gradients are supported within the uncertainty of the data.

(c) The separation criteria of Sandborn are supported, with intermittent separation apparently beginning when $\gamma_p = 0.8$ and the free-stream pressure gradient drops rapidly.

(d) Near separation the neglect of the normal stress terms in the momentum and turbulence energy equations is not justified. As much as one-third of turbulence energy production is attributable to these stresses. The correlation factor F, given by equation (15) can be used to account for these normal stress effects on $-\overline{uv}/\overline{q^2}$ and L_ε. There is no apparent effect on the entrainment rate.

(e) The separated flow field shows some similarity in $\overline{u^2}$, U, and γ_p, with the maximum fluctuation $\overline{u^2}$ and M, the distance from the wall to the maximum fluctuation, being the velocity and length scales. The low velocity backflow apparently just serves to satisfy continuity requirements. The inclusion of normal stress effects in the Bradshaw, et al. (1974) prediction method indicate a significant improvement in $C_f/2$ and H predictions, good prediction of F, and slightly improved shearing stress distributions in the vicinity of separation.

REFERENCES

Bradshaw, P. (1967), "The Turbulence Structure of Equilibrium Boundary Layers", J. Fluid Mech., 29, Part 4, pp. 625-645.

Bradshaw, P. (1973), "Effects on Streamline Curvature on Turbulent Flow", AGARD-AG-169.

Bradshaw, P., Ferris, D. H. and Atwell, N. P. (1967), "Calculation of Boundary-Layer Development Using the Turbulent Energy Equation," J. Fluid Mech., 28, Part 3, pp. 593-616; (1974) revised version, Imperial College Aero. Rept. 74-02.

Coles, D. and Hirst, E. (1968), Computation of Turbulent Boundary Layers - 1968 AFOSR IFP Stanford Conference, Vol. II, Data Compilation, Department of Mechanical Engineering, Stanford University.

Halleen, R. M. (1964), "A Literature Review on Subsonic Free Turbulent Shear Flow", Report No. MD-11 Thermosciences Division, Dep. of Mech. Engrg. Stanford University.

Klebanoff, P. (1954), "Characteristics of Turbulence in a Boundary Layer with Zero Pressure Gradient", NACA Rep. No. 1247.

McDonald, H. (1969), "The Effect of Pressure Gradient on the Law of the Wall in Turbulent Flow", J. Fluid Mech., 35, pp. 311-336.

Newman, B. G. (1951), "Some Contributions to the Study of the Turbulent Boundary-Layer Near Separation", Report ACA-53, Dept. of Supply Aeronautical Research Consultative Committee, Univ. of Sydney, Australia.

Perry, A. E. and Schofield, W. H. (1973), "Mean Velocity and Shear Stress Distributions in Turbulent Boundary Layers", Phys. Fluids, 16, pp. 2068-2074.

Rotta, J. C. (1962), "Turbulent Boundary Layers in Incompressible Flow", Progress in Aeronautical Sciences, Vol. 2, Pergamon Press.

Sandborn, V. A. and Liu, C. Y. (1968), "On Turbulent Boundary-Layer Separation", J. Fluid Mech., 32, pp. 293-304.

Sandforn, V. A. and Kline, S. J. (1961), "Flow Models in Boundary-Layer Stall Inception", Journal of Basic Engineering, Trans. ASME, 83, pp. 317-327.

Schubauer, G. B. and Kelbanoff, P. S. (1951), "Investigation of Separation of the Turbulent Boundary Layer", NACA Report 1030.

Simpson, R. L. and Barr, P. W. (1974a), "Velocity Measurements in a Separating Turbulent Boundary Layer Using Sampling Spectrum Analysis," to appear in the Proceedings of the Purdue University Laser Anemometry Workshop, March 27-29, 1974.

Simpson, R. L. and Barr, P. W. (1974b), "Laser Doppler Velocimeter Signal Processing Using Sampling Spectrum Analysis", Rev. Sci. Inst., Dec. 1974.

Simpson, R. L. and Collins, M. A. (1975) "Calculation of Turbulent Boundary Layers with Strong Adverse Pressure Gradients and Separation",(in preparation).

Simpson, R. L., Strickland, J. H., and Barr, P. W. (1973), "Features of a Separating Turbulent Boundary Layer as Revealed by Laser and Hot-Film Anemometry", Third Biennial Symposium in Turbulence in Liquids, University of Missouri-Rolla.

Simpson, R. L., Strickland, J. H., and Barr, P. W. (1974) "Laser and Hot-film Anemometer Measurements in a Separating Turbulent Boundary Layer," Thermal and Fluid Sciences Center, Southern Methodist University, Report WT-3; will appear in NTIS AD series.

Spangenberg, W. G., Rowland, W. R. and Mease, N. E. (1967), "Measurements in a Turbulent Boundary Layer in a Nearly Separating Condition", Fluid Mechanics of Internal Flow, Edited by G. Sovran, Elsevier Publishing Co., New York.

Strickland, J. H. and Simpson, R. L. (1973), "The Separating Turbulent Boundary Layer: An Experimental Study of an Airfoil Type Flow", Thermal and Fluid Sciences Center, Southern Methodist University, Report WT-2; also AD-771170/8GA.

Townsend, A. A. (1962), "The Behaviour of a Turbulent Boundary Layer Near Separation", J. Fluid Mech., 12, pp. 536-554.

ACKNOWLEDGMENTS

The U. S. Army Research Office - Durham supported the experimental work under Grants DA-AKO-D-31-124-72-G31 and DAH CO4-74-G-0024 and is supporting the prediction method work under Grant DAH CO4-75-G-0051.

THE PREVENTION OF SEPARATION BY BLOWING IN TWO-DIMENSIONAL FLOW

by

B.G. Newman* and H.P.A.H. Irwin†
*Professor of Aerodynamics, McGill University
†Research Officer, National Research Council of Canada
Department of Mechanical Engineering
McGill University, P.O. Box 6070, Stn. A, Montreal H3C 3G1

SUMMARY

Two methods have been developed at McGill University for calculating the jet momentum required to prevent the separation of the two-dimensional incompressible turbulent boundary layer in adverse pressure gradients. The first was a strip integral method for plane walls the shear stress at each limit being based on measurements in self-preserving wall jets. It was extended by Kind for curved walls and for cases in which the boundary layer upstream of the blowing slot has a deficit of momentum which is not small compared with the added jet momentum so that the developing wall jet contains a significant outer wake. The second method is an extension of the differential methods pioneered by Spalding, Launder and their associates which uses four model equations for the individual Reynolds stresses and one equation for the rate of turbulence dissipation. The extension consists of systematically accounting for the presence of the wall in certain pressure, velocity-gradient, correlations and also for slight curvature of the wall.

These two methods are compared with measurements of blown boundary layers, curved wall jets in still surroundings and two conventional boundary layers. In general, the differential method is more accurate particularly when the outer wake is large. However, as used, this method required more input data and was about three times more expensive to run. The integral method is therefore still useful and is not limited to low curvature.

NOTATION

a_{mijj}	fourth-order tensor occurring in the expression for the pressure, velocity-gradient correlations (eqn (11))
b	blowing slot width
c	reference length, often aerofoil chord
C_1, C_2, C_w, C_s, C_{ε_1}, C_{ε_2}, C_ε	constants in the model equations of the differential method (eqns.)
C_f	local skin friction coefficient = $\frac{\tau_w}{\frac{1}{2}\rho U_e^2}$
C_μ	blowing momentum coefficient = $\frac{\rho U_J^2 b}{\frac{1}{2}\rho U_\infty^2 c}$
$C_{\mu'}$	excess-momentum coefficient = $\frac{\rho U_J (U_J - U_{es}) b}{\frac{1}{2}\rho U_\infty^2 c}$
$\frac{D}{Dt}$	substantial derivative for the mean flow
H	shape factor $\frac{\delta^*}{\theta}$, of the upstream boundary layer at the slot
k	kinetic energy of the turbulence per unit mass = 1/2 $\overline{u_i u_i}$
K	Kind's curvature factors, (eqn (5))
ℓ_ε	dissipation length scale = $\frac{k^{3/2}}{\varepsilon}$
n	exponent for the shape of the inner boundary layer in the integral method
p	fluctuating static pressure anywhere in the flow
P	time-average static pressure at the wall
R	longitudinal radius of curvature of the surface
R_T	eddy viscosity Reynolds number $\frac{(U_m - U_\delta)(y_{m/2} - y_m)}{\varepsilon_1}$
R_{T_0}	value of R_T when $\xi = 0$
t	time
u,v,w	velocity fluctuations in the x,y and z directions
u_i	velocity fluctuation in the x_i direction
U	mean velocity in the x direction
U_i	mean velocity in the x_i direction
U_e	local mean velocity in the free stream
U_{es}	value of U_e at the slot
U_J	jet velocity at the slot
U_m	value of U at the velocity maximum

U_δ value of U at the velocity minimum

U_θ value of U at $y = \theta$

U_τ skin friction velocity $= \left(\tau_w/\rho\right)^{\frac{1}{2}}$

U_∞ reference velocity, often the velocity far upstream

V mean velocity in the y direction

W_{ij} wall correction to the expression for pressure, velocity-gradient, correlation (eqns (12))

x,y coordinates along and normal to the surface respectively

x_i coordinates in cartesian tensor form $x_1 = x$, $x_2 = y$, $x_3 = z$

y_m value of y at $U = U_m$

$y_{m/2}$ value of y at $U = \frac{1}{2}(U_m + U_\delta)$ where $\frac{\partial U}{\partial y}$ is negative (see fig. 1)

z third orthogonal coordinate perpendicular to x and y

α $\frac{(4C_2+10)}{11}$

β $-\frac{(2+3C_2)}{11}$

δ value of y at $U = U_\delta$ (fig. 1)

δ^* boundary-layer displacement thickness

δ_{ij} Kronecker delta

Δ value of y where U first equals U_e (fig. 1)

ε rate of dissipation of turbulence energy per unit mass

ε_1 eddy viscosity in the outer half-jet

ε_2 eddy viscosity at $y = 1/2\ y_m$

γ $-\frac{(50C_2+4)}{55}$

θ boundary-layer momentum thickness

ν kinematic viscosity

ρ density

τ_1 shear stress at $y_{m/2}$

τ_2 shear stress at $y = \frac{1}{2}y_m$

τ_m shear stress at $y = y_m$

τ_w skin friction

ω $\frac{(20C_2+6)}{55}$

ξ rate of strain ratio $\dfrac{\frac{\partial U}{\partial x} + \frac{V}{R}}{\frac{\partial U}{\partial y} - \frac{U}{R+y}}$

SUBSCRIPTS

i,j,ℓ,m cartesian tensor subscripts; summation convention is used.

p denotes a plane wall, $R \to \infty$

ACKNOWLEDGEMENT

The authors are indebted to Dr. R.J. Kind for providing a copy of the program for his method.

The work on blown boundary layers has been supported over the years by the Defence Research Board under grant number 9551-12 and by the National Research Council of Canada under grant number A7096.

1. INTRODUCTION

Streamwise blowing along a boundary is an effective way of delaying the separation of a turbulent boundary layer in an adverse pressure gradient. In practice it has been used to improve the efficiency of a wide-angle diffuser and to increase the maximum lift of an aerofoil. The momentum of the jet in two-dimensional flow is $\rho U_J^2 b$ per unit length of slot and is usually expressed non-dimensionally as $C_\mu = \dfrac{\rho U_J^2 b}{\frac{1}{2}\rho U_\infty^2 c}$ for an aerofoil of chord c in flow with velocity U_∞. Values of C_μ as low as 0.05 have doubled the maximum lift[1]. Full scale applications are usually designed from model tests at sufficiently high Reynolds number, and such work has been correlated in terms of C_μ or more precisely in terms of the excess momentum coefficient $C_\mu' = \dfrac{\rho U_J (U_J - U_{es}) b}{\frac{1}{2}\rho U_\infty^2 c}$ where U_{es} is the streaming flow velocity at the slot[2].

Analytical methods have also been developed for two-dimensional flow and are becoming increasingly useful. The method of Gartshore and Newman[3] was limited to cases in which the momentum deficit of the boundary layer which forms upstream of the blowing slot is small

compared with the momentum of the jet itself so that a simple wall jet is formed downstream of the slot. In practical applications however the upstream boundary layer frequently persists as a significant wake in the outer part of the wall jet and the flow is more complicated. Kind[4] has extended the Gartshore-Newman method empirically to deal with this complication and also the effect of having a boundary wall which is curved in the flow direction. It is probably the most sophisticated of the integral methods which began with the work of Carriere, Eichelbrenner and Poisson Quinton[5], Thomas[6] and McGahan[7]. However the degree of empiricism necessary to calculate such a complicated flow is high and therefore differential methods based on economical numerical procedures, such as those of Spalding and Patankar[8], become attractive. Early attempts modelled the turbulence using simple mixing-length theory or modelled the downstream variation of turbulence energy dissipation and turbulence energy. In the most sophisticated of these methods the representation of the turbulence energy is replaced by model equations for each component of the Reynolds stress tensor[9,10] (Manjelić and Launder; Launder, Reece and Rodi). Irwin[11,12] has recently modified this latter method to account for the effect of the wall on pressure, velocity-gradient correlations, and also for slight longitudinal curvature of the wall.

The purpose of the present paper is to compare the integral method of Kind and the differential method of Irwin for two-dimensional plane, incompressible, flow. The methods have been compared with experimental data for curved wall jets with still surroundings, several blown boundary layers on plane walls and two-conventional boundary layers. The relative merits of the two methods is discussed.

2. THEORY

2.1 Integral Method

Kind's extension of the Gartshore-Newman method is capable of handling a blown boundary layer in which an outer wake persists, and moreover can treat flow over a longitudinally curved surface for which the radius of curvature is not particularly large compared with the width of the flow.

For the purpose of setting up four integral equations, suitable mean velocity profiles are assumed for the various portions of the flow. Referring to figure 1

Fig 1 Mean velocity in blown boundary layer

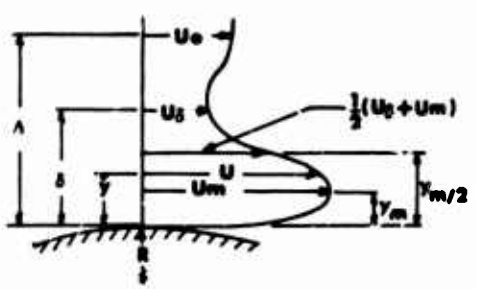

$$\text{For } y \le y_m,\ \frac{U}{U_m} = \left(\frac{y}{y_m}\right)^n \tag{1}$$

$$\text{For } y_m \le y \le \delta,\ \frac{U-U_\delta}{U_m-U_\delta} = \exp\left[-\ln(2)\left(\frac{y-y_m}{y_{m/2}-y_m}\right)^2\right] \tag{2}$$

where $\dfrac{\delta-y_m}{y_{m/2}-y_m}$ is taken to be 2.3.

For $\delta < y$ the profile shape, represented by a power law, is the same as that of the outer part of the upstream boundary layer at the slot.

The total pressure is assumed to be constant along the streamlines in this region and hence the volume flux for $y < \Delta$ is constant unless all the boundary-layer wake becomes entrained by the jet.

Integral angular momentum equations are used with the following limits (see fig. 1)

1) $y = 0$, $y = 1/2y_m$: half the inner boundary layer

2) $y = 0$, $y = y_m$: the whole of the inner boundary layer

3) $y = y_m$, $y = y_{m/2}$: half the outer jet

4) $y = y_m$, $y = \delta$: the whole of the outer jet

The pressure across the flow is calculated in mean streamline coordinates and for convenience an average pressure is assumed between adjacent limits.

The various shearing stresses at each limit must be known: the following forms are assumed:

i) At $y = 0$ $\dfrac{\tau_w}{\frac{1}{2}\rho U_m^2} = 0.0257\left(\dfrac{U_\theta}{U_m}\right)^{11/6}\left(\dfrac{U_m\theta}{\nu}\right)^{-1/6}$ (3)

where U_θ is the velocity at $y = \theta$, the momentum thickness of the inner boundary

$$\theta/y_m = \int_0^1 U/U_m(1-U/U_m)d(y/y_m) = \frac{n}{(2n+1)(n+1)}$$

This is the Ludwieg-Tillmann law with constants adjusted to conform to data for plane wall jets in still surroundings[3]. The effect of curvature on τ_w is considered to be small[13] and is neglected.

ii) At $y = y_{m/2}$. The shearing stress there, τ_1, is calculated assuming a constant eddy constant ε_1 for the half jet which is determined using Townsend's large eddy-equilibrium hypothesis[3]. Kind's theory takes account of the effect of flow curvature on the turbulence structure by incorporating results for curved wall jets in still surroundings. The hypothesis, which also uses experimental self-preserving wall jets in streaming flow, ultimately gives the eddy viscosity Reynolds number

$$R_T = R_{T_0}\left(1 + 295\xi^3 - 20{,}000\xi^4\right) \text{ for } \xi < 0.086 \qquad (4)$$

ξ is defined as the ratio of the rate of lateral strain $\frac{\partial u}{\partial x} + \frac{v}{R}$ to the rate of shear strain $\frac{\partial u}{\partial y} - \frac{u}{R+y}$ where R is the radius of the surface.

$$R_{T_0} = 3^4 \Big/ K_1(0.677+0.369K_3^2 - 0.046K_3^4)$$

where $K_3 = K_1\left(1 + 0.15\,\frac{y_{m/2}}{R}\right)$ and $K_1 = \frac{\tau_1}{\tau_{1p}} = \frac{\left[1+4.48\left(\frac{y_{m/2}}{R}\right) - 1.34\left(\frac{y_{m/2}}{R}\right)^2\right]^2}{\left[1+1.34\left(\frac{y_{m/2}}{R}\right)^2\right]\left[1+0.3\,\frac{y_{m/2}}{R}\right]}$ (5)

where τ_{1p} is the shearing stress for a plane wall.

iii) At $y = y_m$, although $\frac{\partial U}{\partial y}$ is zero here, measurements indicate that the shearing stress τ_m is non-zero and of opposite sign to τ_w because of the relative dominance of the outer turbulence, particularly when y_m is not so inhibited by the presence of the wall. τ_1 is a good measure of the outer turbulence level and once again an empirical expression based on measurements in self-preserving wall jets, is adopted.

$$\frac{\tau_m}{\tau_1} = \left[0.15+0.30\left(\frac{y_m}{y_{m/2}-y_m}\right)^2\right]\left[\frac{2.43K_1\left(1+0.55\,\frac{y_{m/2}}{R}\right) - 1.43}{K_1}\right] \qquad (6)$$

iv) At $y = 1/2y_m$, $\tau = \tau_2$. A constant eddy viscosity is again assumed for the outer part of the inner boundary layer because such an assumption has been established as appropriate for conventional boundary layers. Thus for plane walls

$$\tau_{2p} = \rho\varepsilon_2\left(\frac{\partial U}{\partial y}\right)_{y=\frac{1}{2}y_m} \qquad (7)$$

where $\frac{U_m^{\delta^*}}{\varepsilon_2} = 15 + 35\exp\left[-\left(\frac{\tau_{1p}}{\tau_w}\right)^2\right]$ and $\tau_{1p} = \frac{\tau_1}{K_1}$

If $y_{m/2}-y_m$ becomes very small downstream, the method reverts to the calculation of a conventional boundary layer, $U_m = U_e$ and $\frac{U_m^{\delta^*}}{\varepsilon_2}$ is set equal to 50.

To correct equation (7) for curvature, the curvature effect is assumed to decrease linearly to zero within the boundary layer as the wall is approached. Thus

$$\tau_2 = \tau_{2p} + \frac{\tau_m - \tau_{mp}}{2} \qquad (8)$$

where τ_{mp} is the value of τ_m for a plane wall obtained by putting $\frac{y_{m/2}}{R} = 0$ and $K_1 = 1$. Note that there is no curvature correction if the flow becomes a conventional boundary layer and this is known to be incorrect (e.g. Bradshaw[14]). The exponential part of the expression for ε_2 is an empirical representation of the effect of outer turbulence on the eddy viscosity, and $\frac{\tau_{1p}}{\tau_w}$ is chosen as a suitable non-dimensional measure of this turbulence.

v) For $y > \delta$ the shearing stress (and gradient of stress) is taken as zero so that the velocity U along mean flow streamlines is related to the pressure by Bernoulli's equation. This assumption is similar to that made by Jones when determining the drag of aerofoils from near traverses of the wake[15]. The four integral equations are sufficient to determine the four primary unknowns U_m, $y_{m/2}$, y_m and n. The calculations are usually started at the blowing slot and the flow of figure 1 is assumed to occur at the end of the potential core

about 10 slot widths from the slot. Thus the peak velocity in the initial wall-jet profile is the slot velocity in the potential core. Excess momentum is assumed to be conserved during this process and skin friction is neglected. The stagnation pressure is assumed constant for streamlines outside the wall jet. The initial value of n is taken as 1/11 and $y_m/y_{m/2} = 0.25$, but the the method is relatively insensitive to these particular choices[4].

The prediction of U_δ is unreliable when U_δ becomes small compared with U_e because the neglected shear stress in the outer flow would tend to increase U_δ. However the assumed shape for the outer part of the wake (a piece of power law) is inaccurate in a sense which tends to give too high a value of U_δ. The two errors therefore oppose each other.

Separation is assumed to occur when n becomes $\geq 1/2$.

2.2 Differential Method

The mean momentum equation is written

$$\frac{DU_1}{Dt} = -\frac{1}{\rho}\frac{dP}{dx} - \frac{\partial \overline{u_1 u_2}}{\partial x_2} \tag{9}$$

where P is the pressure at the wall. The normal stresses and viscous terms have been omitted. In cartesian tensors the Reynolds-stress equations can be written

$$\begin{aligned} U_\ell \frac{\partial \overline{u_i u_j}}{\partial x_\ell} = &-\left(\overline{u_i u_\ell}\frac{\partial U_j}{\partial x_\ell} + \overline{u_j u_\ell}\frac{\partial U_i}{\partial x_\ell}\right) \\ &+ \overline{\frac{p}{\rho}\left(\frac{\partial u_i}{\partial x_j} + \frac{\partial u_j}{\partial x_i}\right)} - \frac{1}{\rho}\left(\overline{\frac{\partial p u_j}{\partial x_i}} + \overline{\frac{\partial p u_i}{\partial x_j}}\right) \\ &- \frac{\partial \overline{u_\ell u_i u_j}}{\partial x_\ell} + \nu\left(\overline{u_i \frac{\partial^2 u_j}{\partial x_\ell^2}} + \overline{u_j \frac{\partial^2 u_i}{\partial x_\ell^2}}\right) \end{aligned} \tag{10}$$

In order to express the third order correlations in terms of the Reynolds stresses and mean velocity the turbulence model of Launder, Reece and Rodi [10], with modifications by Irwin[12], is used. The turbulence model uses the approximations given below.

$$\overline{\frac{p}{\rho}\frac{\partial u_i}{\partial x_j}} = -c_1 \frac{\varepsilon}{k}\left(\overline{u_i u_j} - \frac{2}{3}\delta_{ij}k\right) + \frac{\partial U_\ell}{\partial x_m} a_{mi\ell j} + W_{ij} \tag{11}$$

where $a_{mi\ell j} = \alpha\delta_{\ell j}\overline{u_m u_i} + \beta\left(\delta_{m\ell}\overline{u_i u_j} + \delta_{mj}\overline{u_i u_\ell} + \delta_{i\ell}\overline{u_m u_j} + \delta_{ij}\overline{u_m u_\ell}\right) + C_2\delta_{mi}\overline{u_\ell u_j} + \left[\eta\delta_{mi}\delta_{\ell j} + \upsilon\left(\delta_{m\ell}\delta_{ij} + \delta_{mj}\delta_{i\ell}\right)\right]k$

$\varepsilon = \overline{\frac{\nu}{2}\left(\frac{\partial u_i}{\partial x_\ell} + \frac{\partial u_\ell}{\partial x_i}\right)^2}$ = dissipation rate,

$k = \frac{1}{2}\overline{u_\ell u_\ell}$

$\alpha = (4C_2 + 10)/11,$

$\beta = -(2 + 3C_2)/11,$

$\eta = -(50C_2 + 4)/55,$

$\upsilon = (20C_2 + 6)/55,$

and C_1 and C_2 are constants.

The term W_{ij} is the correction in the presence of a wall. The fluctuating pressure is related to the velocity everywhere in the flow by a Poisson equation; the solution, using a simple Green's function, the reciprocal of distance, enables an exact expression for $\overline{\frac{p}{\rho}\frac{\partial u_i}{\partial x_j}}$ to be obtained containing a volume and a surface integral (Chou[16]). The form of equation (11) is, in fact, based on this expression. Irwin[12] eliminated the surface integral by a suitable choice of Green's function which can be interpreted as adding the effect of the image in the wall of the complete turbulent-flow field. For boundary-layer flows this led him to propose

$$W_{11} = -\frac{2}{11} C_w \frac{\ell_\varepsilon}{x_2} \overline{u_1 u_2} \frac{\partial U_1}{\partial x_2}$$

$$W_{22} = \frac{5}{11} C_w \frac{\ell_\varepsilon}{x_2} \overline{u_1 u_2} \frac{\partial U_1}{\partial x_2} \qquad (12)$$

$$W_{33} = -\frac{3}{11} C_w \frac{\ell_\varepsilon}{x_2} \overline{u_1 u_2} \frac{\partial U_1}{\partial x_2}$$

$$W_{12} + W_{21} = (8\overline{u_1^2} + \overline{u_2^2} - 6k) \frac{C_w}{11} \frac{\ell_\varepsilon}{x_2} \frac{\partial U_1}{\partial x_2}$$

where $\ell_\varepsilon = \frac{k^{3/2}}{\varepsilon}$. The values of the empirical constants C_1 and C_2 in equation (11) are obtained directly from experimental data for homogeneous shear flow and anistropic grid turbulence yielding[10]. $C_1 = 1.5$ and $C_2 = 0.4$. A value of C_w which gives good results in computations of both wall jets and boundary layers is 0.095[12]. Very near to the wall the turbulence model becomes inaccurate and unrealistic computed values of $\frac{\ell_\varepsilon}{x_2}$ are possible. For this reason the ratio $\frac{\ell_\varepsilon}{x_2}$ in equations (12) has a prescribed upper limit of 3.8 as the wall is approached, which is consistent with established values in the wall-law region.

Following Launder et al $\overline{pu_j}/\rho$ is assumed to be negligible and $\overline{u_k u_i u_j}$ is expressed as

$$\overline{u_k u_i u_j} = -C_s \frac{k}{\varepsilon} \left(\overline{u_i u_\ell} \frac{\partial \overline{u_j u_k}}{\partial x_\ell} + \overline{u_j u_\ell} \frac{\partial \overline{u_k u_i}}{\partial x_\ell} + \overline{u_k u_\ell} \frac{\partial \overline{u_i u_j}}{\partial x_\ell} \right) \qquad (13)$$

where C_s is a constant. This expression can be considered as a generalization of the gradient-diffusion hypothesis as applied to diffusion of the Reynolds stresses. C_s is set equal to 0.11, originally on the basis computer optimization[10], but a value near to this is also suggested by a direct comparison of equation (13) with measurements of the triple velocity products $\overline{u_\ell u_i u_j}$ in a wall jet by Irwin[12]. The term $\frac{\partial \overline{u_\ell u_i u_j}}{\partial x_\ell}$ is often fairly small compared with others in equation (10) and thus C_s is a relatively uncritical parameter.

The viscous term $\nu\left(\overline{u_i \frac{\partial^2 u_j}{\partial x_\ell^2}} + \overline{u_j \frac{\partial^2 u_i}{\partial x_\ell^2}}\right)$ is first simplified using the assumption of local isotropy. For $i = j$ it then becomes simply $-\frac{2}{3}\varepsilon$, where ε is the rate of dissipation of turbulence energy defined earlier, and for $i \neq j$ it becomes zero. The dissipation rate is a difficult quantity to model because even though an exact transport equation for it can be derived only the advective terms are at all amenable to measurement. The following approximate form of the equation, due to Hanjalić and Launder[9] and resembling in some respects that of Daly and Harlow[17], is therefore one of the least certain elements of the turbulence model

$$U_\ell \frac{\partial \varepsilon}{\partial x_\ell} = -C_{\varepsilon_1} \varepsilon \frac{\overline{u_i u_k}}{k} \frac{\partial U_\ell}{\partial x_i} - C_{\varepsilon_2} \frac{\varepsilon^2}{k} + C_\varepsilon \frac{\partial}{\partial x_k}\left(\frac{k}{\varepsilon} \overline{u_k u_\ell} \frac{\partial \varepsilon}{\partial x_\ell}\right) \qquad (14)$$

where in the present work $C_{\varepsilon_1} = 1.5$, $C_{\varepsilon_2} = 1.9$ and $C_\varepsilon = 0.15$. The value of C_{ε_2} is derived from the observed decay of kinetic energy in grid turbulence[10]. In near wall turbulence (14) reduces to a simple expression which relates C_ε to C_{ε_1} and C_{ε_2}. Thus only C_{ε_1} need be fixed by computer optimization and then C_ε follows from the known properties of near-wall turbulence.

No correction is made to $\overline{u_\ell u_i u_j}$ or ε for the presence of a wall. In the case of $\overline{u_\ell u_i u_j}$ this is because in many flows $\frac{\partial \overline{u_\ell u_i u_j}}{\partial x_\ell}$ is relatively small compared to other terms in (10). In the case of ε it is because viscous dissipation occurs only in the very small eddies which it seems reasonable to assume are unaffected by the wall except within the viscous sublayer.

For flows on flat surfaces this completes the set of equations used in the computations. For curved surfaces a similar set of equations can be derived which contain extra terms due to curvature. For small curvature it is possible to neglect all except first order curvature terms and the resulting simplified equations, which for brevity are not repeated here, are given by Irwin and Arnot Smith[19]. The mean momentum equation is the same as that for flat surfaces but the equations for the Reynolds stresses and dissipation rate contain extra terms involving $\frac{U_1}{R}$.

To solve the above set of equations the finite difference scheme of Spalding and Patankar[8] is used. Since the turbulence model is not applicable to the viscous sublayer the boundary conditions are applied in the form of slip values. The slip values used were $\overline{u_1 u_2} = -U_\tau^2$, $\overline{u_1^2} = 5.2\,\overline{U_\tau^2}$, $\overline{u_2^2} = 0.6\,U_\tau^2$ and $\overline{u_3^2} = 2.9\,U_\tau^2$ where $U_\tau = \left(\frac{\tau_w}{\rho}\right)^{\frac{1}{2}}$. The slip value of U_1 is obtained by matching the velocity to the logarithmic law of the wall (with the constants of Patel[18]) at a point outside the viscous sublayer, and that of ε by equating production and dissipation of turbulence energy near to the wall. At the free stream

boundary the conditions follow directly from the known (or assumed) mean velocity and turbulence properties of the external flow. In the present work the computations were usually started from measured profiles of mean velocity and turbulence properties. However, the program contains an option whereby the starting profiles can be estimated from integral parameters if these are all that are available. For such cases it assumes a power law velocity profile for the upstream boundary layer which is merged into the jet by a thin mixing layer for which a cosine velocity profile is adopted. The inner boundary layer within the slot is neglected and the width of the irrotational region below the mixing layer is assumed to be 0.6 b. In the outer boundary layer $\overline{uv}$ is calculated on the basis of an eddy-viscosity Reynolds number based on displacement thickness of 60 and the three normal stresses are taken to be equal to $\frac{\overline{uv}}{0.45}$. In the mixing layer the same procedure is used except that an eddy viscosity Reynolds number of $\frac{(U_J - U_\delta)}{\varepsilon_2}$ x (thickness of mixing layer) = 160 is assumed. The turbulence in the irrotational region of jet is 0.03 U_J r.m.s. and dissipation is $4\frac{k^{3/2}}{y}$ Elsewhere dissipation is set equal to production.

At each output station the complete profiles of mean velocity, Reynolds stresses and dissipation rate are printed but, for the purposes of the present comparison, only the integral parameters are presented. Complete comparisons of computed and experimental profiles have been given by Irwin[12]. The skin friction is also computed and separation is assumed to occur if C_f falls below about 0.0003.

3. DISCUSSION OF THE TWO METHODS OF PREDICTION AND COMPARISON WITH EXPERIMENT

The flows being considered here are two-dimensional wall jets with or without an outer wake on flat or longitudinally-curved surfaces. The integral method was specifically developed to handle these flows and contains some ad hoc assumptions which are probably not valid in other situations. It can however be used to compute conventional boundary layers for which it assumes a power-law velocity profile and uses a constant eddy-viscosity Reynolds number to obtain the shear stress at $y = \delta/^{\wedge}$. The differential method is a much more general method of computing turbulent shear flows and the empirical assumptions tend to be less restrictive. It has the property common to differential methods of not being limited to particular forms of velocity profile so that most of the empiricism is contained in the representation of the turbulence itself. The present turbulence model has been shown to have moderately wide validity by tests on a large number of different shear flows (Irwin and Arnot Smith[12,19]) but there are some situations where it is demonstrably inaccurate such as plane jets and wakes with small excess or deficit in velocity. An additional limitation of the differential method in its present state is that, in accounting for longitudinal curvature, it assumes the curvature is small. Unlike the integral method, it therefore neglects the variation of pressure across the flow.

Although the integral method is not specifically designed for boundary-layer calculation the two methods are compared with the data of Newman[20] and of Schubauer and Klebanoff[21] for conventional boundary layers approaching separation in figures 2 and 3. In the latter case the surface was slightly curved which is taken into account by the differential method but is left out of the integral method when it reverts to a boundary-layer calculation. The overall level of agreement with experiment for the methods is similar except that C_f tends to be high for the integral method near separation. Considering the simplicity of the assumptions in the integral method its performance is surprisingly good.

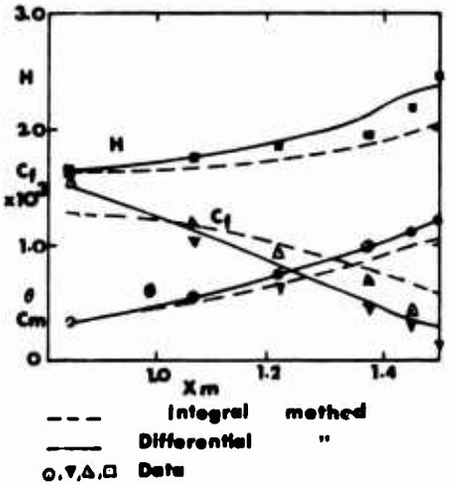

Fig 2 Boundary-layer: Newman

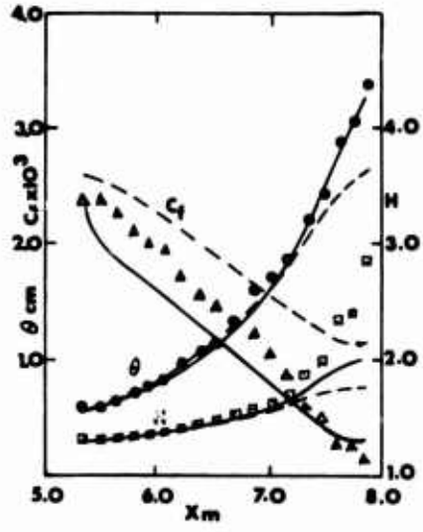

Fig 3 Boundary-Layer: Schubauer & Klebanoff

The next case, shown in figure 4, is the self-preserving wall jet of Irwin[11]. flowing into a positive pressure gradient on a flat wall, the upstream boundary layer being negligible. Agreement with experiment is good for both methods. In the case of the integral method this is largely to be expected since it draws extensively on other self-preserving wall jet data in its empirical assumptions.

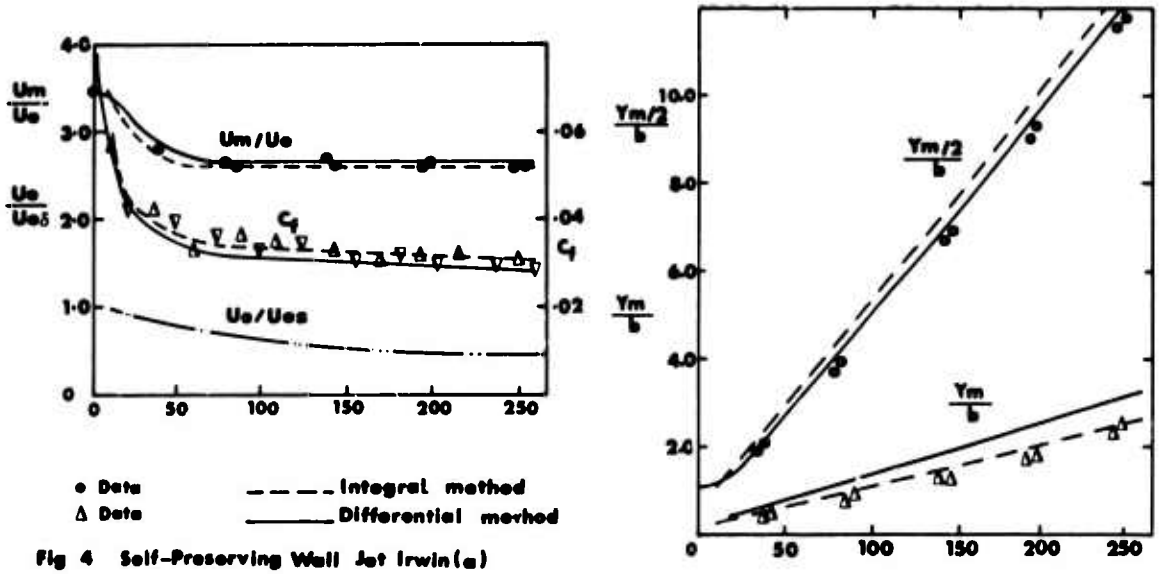

Fig 4 Self-Preserving Wall Jet Irwin(a)

The next four cases, figures 5,6,7 and 8 are uncurved wall jets with outer wakes[12]. in pressure gradients similar to those on blown flaps. A thick upstream boundary layer was artificially generated by placing a rod of rectangular cross-section near to the surface upstream of the slot. The differential method was started just downstream of the slot using measured profiles of mean velocity and turbulence properties. The first of these cases, shown in figure 5, had a relatively small outer wake which was completely absorbed by the wall jet within about 200 slot widths. It is evident that U_δ is not well predicted by the integral method but this is attributed to the initial velocity profile being different to that assumed by the method. The wake from the rectangular bar had not fully merged with the upstream boundary layer at the slot.

Using the empirical starting procedure with profiles generated from integral parameters gives results which are generally closer to the integral method.

In the case in figure 6 the outer wake is larger and the jet momentum less than in figure 5. It can be seen that experimentally the value of $\frac{U_m}{U_e}$ decreased to a value less that 0.5 towards the end of the working section. The initial velocity profile was considerably closer to that assumed by the integral method than for the case of figure 5 but the upstream boundary layer had still not quite evolved into the conventional shape. The differential method is in generally better agreement with experiment. Its prediction of reverse flow in the wake at $\frac{x}{b} \approx 190$ does not agree with the data but, in view of the very low velocities reached in the region of velocity minimum, this may well be due either to experimental inaccuracy or to failure of the boundary layer assumption. For $x/b > 200$ the outer edge of the wake was obstructed by the roof of the working section: thus data points beyond $x/b = 200$ have been given a prime to indicate unreliability. Similar primes are used in figures 7 and 8.

In figure 7 the jet momentum is larger than in figure 6, the upstream boundary layer is virtually identical and the pressure gradient is greater. The value of U_m/U_e remained above 1.0. Two sets of computed curves are shown for the differential method in order to show the effect of making a correction for flow convergence and divergence. Because of the high pressure gradient which caused rapid growth of side-wall boundary layers it was difficult to maintain two-dimensional conditions in the experiments. Slots in side-walls were used to bleed away the boundary layers but there still remained a residue of lateral flow convergence or divergence depending on whether too little or too much was being bled. Figure 9 shows the difference between the measured rate of growth of overall momentum thickness and that calculated from the two-dimensional momentum-integral equation for the flows of figures 6, 7 and 8. It seems highly likely that, because of the low velocity in the outer wake compared to that in the jet, the wake suffered much more from lateral convergence than did the jet in the same pressure gradient. Thus, in applying the convergence correction it was assumed, somewhat crudely, that the jet region was unaffected and that in the wake the local convergence angle was independent of height y. The correction had little effect on computations of the flow in figure 6 but it is evident that in figure 7 it does have an effect, tending to improve agreement of $\frac{U_\delta}{U_e}$, $\frac{\delta}{b}$ and $\frac{y_{m/2}}{b}$ with the data. Thus, in figure 7 it seems probable that for both methods a significant part of the difference from experiment is due to lateral convergence or divergence.

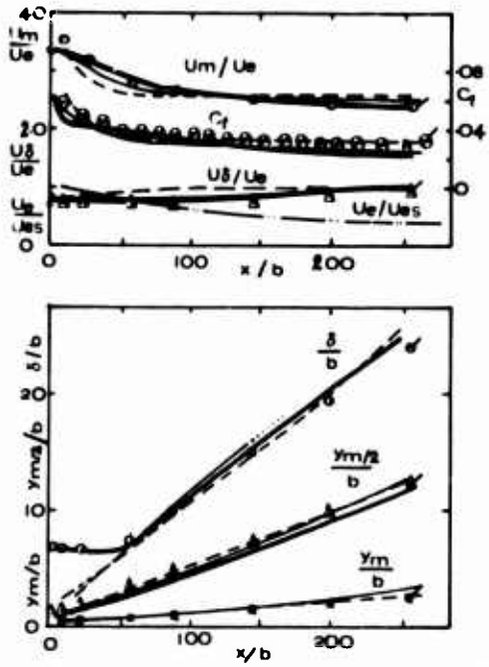

θ,o , Δ , □ Data — Differential method
— With "Synthetic" starting - - - Integral method

Fig 5 Blown boundary-layer: Irwin (b)

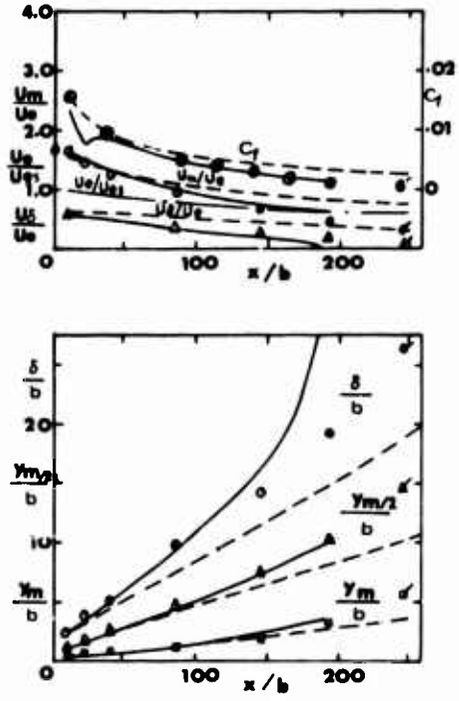

- - - - Integral method
——— Differential "
o,Δ,□,o Data

Fig 6 Blown Boundary-Layer: Irwin (c)

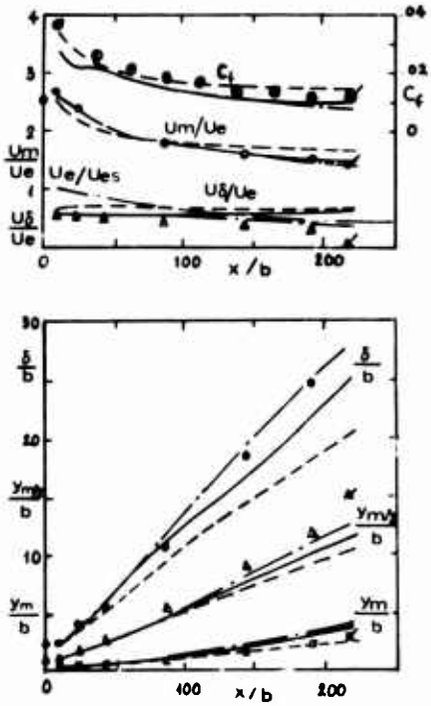

- - - - Integral method
——— Differential "
— · — Diff. method with convergence correction
o,Δ,θ,□ Data

Fig 7 Blown boundary-Layer: Irwin (d)

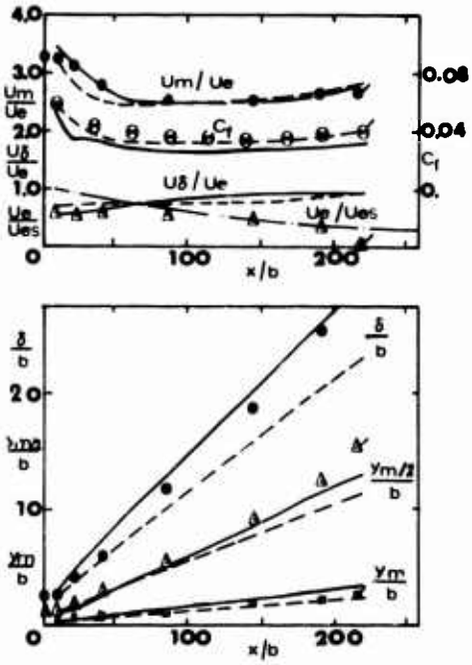

- - - - Integral method
——— Differential "
θ,□ ,Δ , o Data

Fig 8 Blown boundary-layer: Irwin(e)

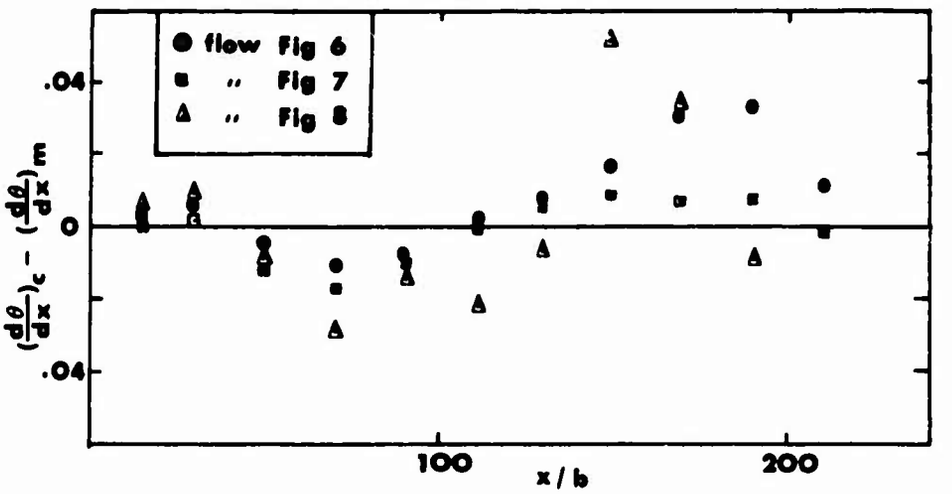

Fig 9 Comparison of calculated & measured gradient of momentum thickness

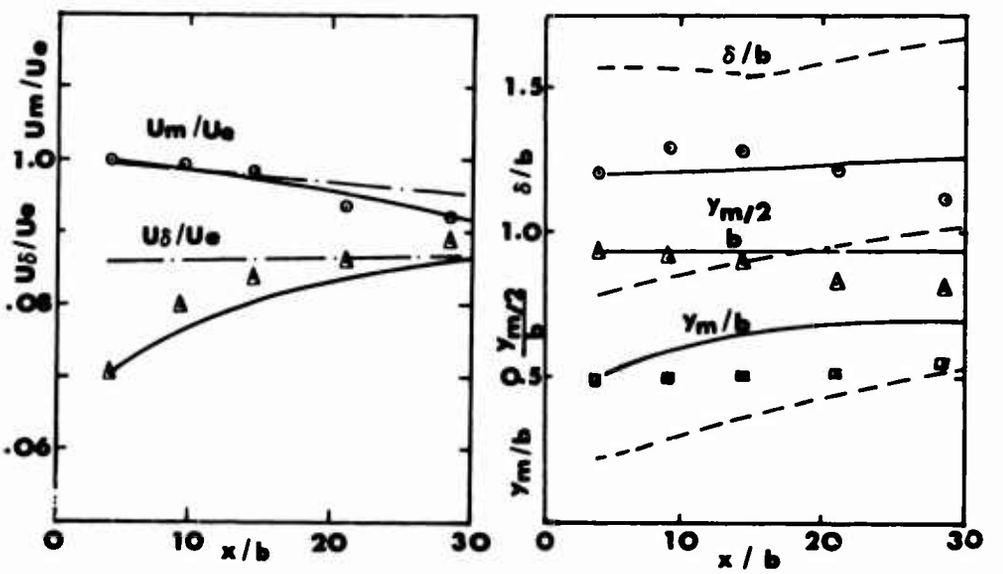

Fig 10 "Slotted Flap" at constant pressure: English[22]

— — — Integral method
——— Differential method
o, Δ, a Data

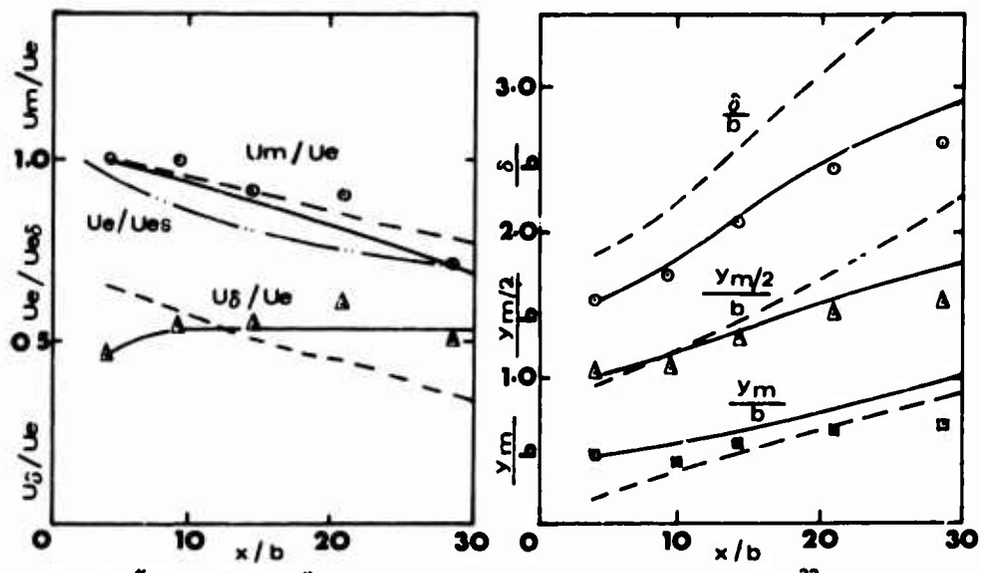

Fig 11 "Slotted Flap", adverse pressure gradient: English[22]

Δ,o,□. Data — — — Integral method ——— Differential method

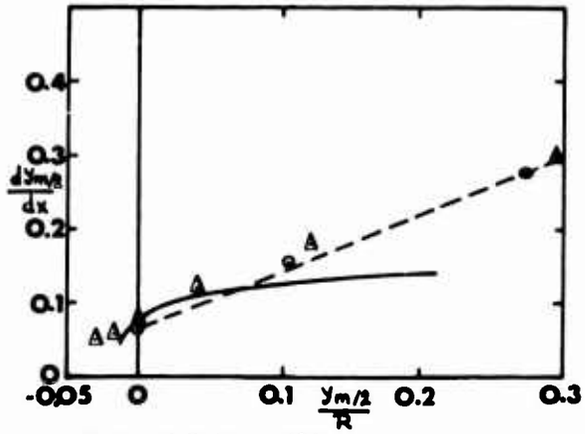

o Data of Guitton (13)

Δ " Giles et al (21)

— — — Integral method (4)

——— Differential " (12)

Fig 12 Wall jet on logarithmic spirals

In figure 8 the jet is stronger, the upstream boundary layer is again the same and the pressure gradient greater than in figure 7. A convergence correction was attempted but it was large and this, combined with the discontinuity in the assumed correction at the junction of the wake and jet regions, caused the computations to become unstable, eventually breaking down. Thus, no corrected results are shown. The level of agreement with experiment of the two methods is about the same, their high prediction of U_δ/U_e being attributed, at least in part, to flow convergence.

The next two cases in figures 10 and 11 are similar to the flow over a slotted flap in that the total pressure in the flow from the slot is equal to that of the free stream. The data is that of English[22], and the surface was flat. Figure 10 shows results for zero pressure gradient whereas figure 11 is for a positive pressure gradient. The maximum value of x/b in these experiments was only about 30, covering the typical range of interest for slotted flaps. Since the empirical assumptions of the integral method are essentially for x/b greater than about 10 it cannot be expected to be very accurate in this situation and thus it is evident that in figures 10 and 11 the differential method is superior.

Finally, in figure 12, a comparison is shown with experimental data for wall jets in still air on logarithmic spirals for which the radius R of longitudinal curvature is proportional to distance x along the surface. For a spiral of given x/R it is expected and found that $dy_{m/2}/dx$ is sensibly constant. Thus, in figure 13, which has $y_{m/2}/R$ as abscissa, each point represents a complete set of data for a particular wall jet. The integral method is in good agreement with the data, particularly Guitton's for which the flow was more accurately two-dimensional. However it should be noted that the method was built

on similar measurements of wall jets on circular cylinders. The differential method, gives a reasonable variation of $dy_{m/2}/dx$ at small $y_{m/2}/R$ but tends to diverge from the data outside the range $-.01 < y_{m/2}/R < .05$. As described in section 2.3, the differential method assumes small curvature in its present form, neglecting amongst other things the pressure gradient normal to the surface. Thus, the poor agreement for high curvature is not altogether surprising. However, in contrast to the integral method the differential method contains no empirical constants especially introduced to account for curvature.

From the foregoing comparisons some general conclusions can be drawn. Both methods are capable of predicting the main features of blown boundary layers, the differential method emerging as generally the more accurate particularly for cases in which the mean velocity profiles are significantly different from those assumed in the integral method. However, the starting conditions for the differential method were considerably more detailed than those for the integral method and part of its advantage in accuracy may well be lost in practice because such information is often unavailable.

It is difficult to compare the cost of running the methods because it depends on chosen step size. Irwin, case (b), was therefore run with various step sizes, using synthetic starting for the differential method, the results indicated that the minimum acceptable step size was approximately one slot width for the integral method, and approximately 0.05 δ for the differential method. The time for both compiling and running the integral method on an IBM 360/75 computer was 20 seconds which is 1/3 to 1/4 of that for the differential method. It might also be remembered that the integral method can be applied to more highly curved flows than the differential method.

It is interesting to note that in shear flows of the complexity of blown layers the integral approach begins to become somewhat cumbersome and possibly involves as much development work as does the differential approach. Extension of the integral method to even more complicated velocity profiles, such as occur on multi-slotted aerofoils, would therefore be inadvisable. More complicated velocity profiles can be handled by the differential method as it stands. However, for such flows it is likely that modifications will be necessary in order to account for significant pressure variations across the flow when its width is not small compared with the radius of curvature.

4. CONCLUSIONS

i) Both the integral and differential methods are capable of predicting the growth of two-dimensional blown boundary layers to useful accuracy. Indeed the accuracy of prediction may be better than that of a corresponding experiment if spurious, three-dimensional, effects are not sufficiently eliminated from the experiment.

ii) When the methods are started using integral parameters their accuracy is similar. If however detailed mean flow and turbulence data is used to start the differential method it is generally more accurate.

iii) The differential method is about three times as expensive to compile and run.

iv) The integral method is not well suited to situations where the starting profiles differ significantly from the flow sketched in figure 1.

v) Starting procedures using integral parameters are important and might usefully be improved in both methods.

vi) The integral method incorporates a good deal of empiricism particularly for curvature effects, and it would probably be unwise to try to extend it to more complicated situations (e.g. multi-slotted flaps). The differential method, on the other hand, is versatile and capable of further development.

vii) When either method must be cycled many times to determine the minimum amount of blowing required to suppress separation in a given situation, the cost may be unacceptable. There is therefore need for an approximate method corresponding to, say, Stratford's method for turbulent boundary layers, which can give quick, if somewhat less accurate, predictions, preferably without the aid of a large computer.

5. REFERENCES

1. Williams, J. Alexander, A.J. -Pressure plotting measurements on an 8 per cent thick aerofoil with trailing edge flap blowing, A.R.C., R&M 3087, 1958.
2. Attinello, J.S. -Boundary layer and flow control Vol. I, ed. G.V. Lachmann, Pergamon 1961, pp. 463-515.
3. Gartshore, I.S. Newman, B.G. -The turbulent wall jet in an arbitrary pressure gradient, Aero. Q. Vol. XX, 25, 1969.
4. Kind, R.J. -A calculation method for boundary layer control by tangential blowing, C.A.S.I. Trans. 4, 88, 1971.
5. Carriere, P. Eichelbrenner, E. Poisson-Quinton, Ph. -Contribution theoretique et experimentale a l'etude du controle de la couche limite par soufflage, Advances in Aeronautical Sciences, Vol. 2, MacMillan, New York, 195[illegible]
6. Thomas, F. -Boundary-la[illegible] control for increased lift by blowing, A.I.A.A. J [illegible], 967, 1965.

7. McGahan, W.A. -The incompressible turbulent wall jet in an adverse pressure gradient, Gas Turbine Lab., Rep. No. 82, Mass. Inst. of Technology, 1965.

8. Spalding, D.B.
Patankar, S.V. -Heat and mass transfer in boundary layers, Parts I and II, Morgan-Grampian, London 1967.
Part III, Imperial College, Dept. of Mechanical Engineering, Report BL/TN/G/15, 1969.

9. Hanjalić, K.
Launder, B.E., -A Reynolds stress model of turbulence and its applications to thin shear flows, J. Fluid Mech. 52, 609, 1972(b).

10. Launder, B.E.
Reece, G.
Rodi, W. -Development and application of a Reynolds stress turbulence closure, Imperial College, Mech. Eng. Dept. HTS/73/31, 1973.

11. Irwin, H.P.A.H. -Measurements in a self-preserving plane wall jet in a positive pressure gradient, J. Fluid Mech. 61, 33. (see also M.E.R.L. Rep. 73-2, McGill University), 1973.

12. Irwin, H.P.A.H. -Measurements in blown boundary layers and their prediction by Reynolds stress modelling, Ph.D. Thesis, McGill University, 1974.

13. Guitton, D.E. -Some contributions to the study of equilibrium and non-equilibrium turbulent wall jets over curved surfaces, Ph.D. Thesis, McGill University, 1970.

14. Bradshaw, P. -Effects of streamline curvature in turbulent flow, AGARDOgraph No. 169, 1973.

15. Schlichting, H. -Boundary layer theory, 6th. ed., McGraw-Hill, pp. 711-714, 1968.

16. Chou, P.Y. -On velocity correlations and the solutions of the equations of turbulent fluctuation, Quart. Appl. Math. 3, 38, 1945.

17. Daly, B.J.
Harlow, F.H. -Transport equations in turbulence, Phys. of Fluids, 13, 2634, 1970.

18. Patel, V.C. -Calibration of the Preston tube and limitations on its use in pressure gradients, J. Fluid Mech. 23, 185, 1965.

19. Irwin, H.P.A.H.
Arnot Smith, P. -Prediction of the effect of streamline curvature on turbulence, Phys. of Fluids, to be published, 1975. (see also Rep. No. 74-2, M.E.R.L. McGill University).

20. Newman, B.G. -Some contributions to the study of the turbulent boundary layer near separation, Australian Department of Supply, Rept. ACA-53, 1951.

21. Schubauer, G.
Klebanoff, P. -Investigation of separation of the turbulent boundary layer, NACA, TN 2133, 1950, TR 1030, 1951.

22. English, E.C. -Ph.D. Thesis, Cambridge University,1970.

THE ANALYSIS OF FLOW FIELDS WITH SEPARATION BY NUMERICAL MATCHING*

by

G. W. Brune and P. E. Rubbert
Aerodynamics Research Unit

and

C. K. Forester
Propulsion Research Unit

Boeing Commercial Airplane Company
Seattle, Washington 98124

SUMMARY

This paper presents a method of computing flow fields characterized by the presence of viscous, separated regions interacting strongly with a surrounding inviscid flow. The procedure is to divide the flow field into several regions, each dominated by a particular type of fluid physics (i.e., boundary layer flow, separated flow, and outer inviscid flow), and to analyze each region by using the numerical solution technique that is computationally optimum for the dominant type of flow. The paper specifically addresses the problem of matching a numerical solution of the Navier-Stokes equations for a region containing separated flow with another numerical solution appropriate for an adjacent region of inviscid flow. A key feature of the method presented is the placement of the matching boundary in space occupied by purely inviscid flow and remote from local areas of strong viscous/inviscid interactions. A detailed study and numerical substantiation of the method are presented for axisymmetric flow over an ellipsoid of revolution with laminar separation.

INTRODUCTION

In the past, complex flow fields with regions of separated flow interacting strongly with the surrounding inviscid flow have been difficult to treat analytically. The classical approach to the problem of describing the complete flow field about bodies exhibiting a variety of flow phenomena has been to divide the flow field into regions of inviscid flow, boundary layer flow, and viscous separated flow, and to employ numerical methods that are computationally optimum to solve the type of flow in each region. The problem of matching the various types of numerical solution procedures across common boundaries in the flow has been the subject of many investigations. These studies have centered about the use of displacement thickness concepts in the formulation of a boundary value problem describing the inviscid parts of the flow (ref. 1).

Matching has usually been applied at the edge of the viscous layer. In cases where a strong interaction exists between the viscous and inviscid regions, however, the commonly used iteration schemes and displacement thickness shapes frequently have failed to converge to a matched solution.

The central idea of the present work is to position the matching boundary some distance into the inviscid field, remote from the edge of the viscous region where strong interactions occur. A numerical method that solves the Navier-Stokes equations is used to calculate the flow interior to this boundary, and a purely inviscid method is used for the exterior flow. By this means, the powerful Navier-Stokes method deals with the strong local interactions at the edge of the viscous region but the interactions along the dividing boundaries of the flow regions are sufficiently weak so that rapid convergence to matched solutions across these boundaries can be achieved.

An alternative approach to predict flow fields with regions of separated flow is described in reference 2. The procedure avoids matching altogether, but it has been applied only to problems wherein the entire flow field is amenable to an integro-differential formulation, as in the case of laminar, incompressible flow.

An approach in which the Navier-Stokes equations are solved in the entire flow field has been employed for the study of viscous transonic flow past airfoils (ref. 3). However, the procedure is unnecessarily powerful and its use computationally expensive in regions of inviscid flow and in regions where the flow can be described adequately by attached boundary layer methods.

A NUMERICAL MATCHING PROCEDURE

Consider first a conceptual division of the flow field about an arbitrary body into two regions, as shown in figure 1. The dividing surface is termed the matching boundary. The spatial position of the matching boundary is arbitrary, except that all viscous phenomena anticipated to occur must be enveloped. The region between the matching boundary and the body surface and encompassing all viscous phenomena is referred to as the inner region. The flow in the outer region is entirely inviscid. All flow properties are continuous across the matching boundary.

Now let the matching boundary be identified as a surface that truly divides the inner and outer flows. This can be done by imposing a set of boundary conditions along the inner and outer surfaces of the matching boundary, properly posed so as to define separate and unique boundary value problems describing the flows in the inner and outer regions. The inner and outer flows thus become amenable to analysis by separate computational means; however, the two flows are related by the boundary conditions and resulting flow properties along the matching boundary.

---

*This research was supported in part by the Flight Dynamics Laboratory/FXM, United States Air Force, Wright Patterson Air Force Base, Ohio, under contract F33615-73-C-3037. The results of the contractual work were published in Technical Report AFFDL-TR-73-153, February 1974.

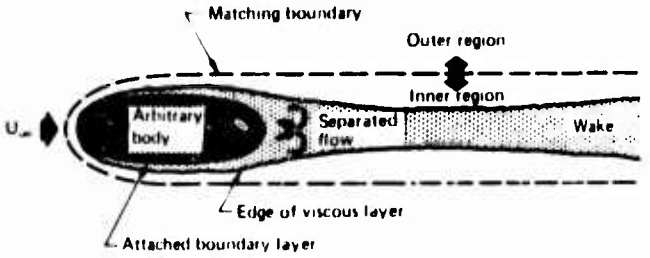

Figure 1. –Matching Boundary Dividing the Flow Field

There exists, in general, a particular set of boundary conditions along the matching boundary for which all velocity components will turn out to be continuous across the boundary everywhere along the boundary. When these boundary conditions are determined, the outer flow becomes an analytic continuation of the inner flow, and the two flows exactly match. The objective is thus to determine that particular set of boundary conditions along the matching boundary that provides an exact matching of the two flows.

Separate outer and inner boundary value problems are depicted in figures 2(a) and 2(b), respectively. Neumann boundary conditions along the matching boundary, together with the onset flow at infinity, govern the outer flow. The equations governing the outer flow are Euler's equations, since the flow in this region is assumed to be entirely inviscid.

a) Boundary Value Problem for Outer Flow

b) Boundary Value Problem for Inner Flow

Figure 2. –Decomposition of Flow Field into Inner and Outer Flow Problems

The governing equations for the inner flow are taken to be the Navier-Stokes equations in anticipation of the appearance of regions of separated flow. The following boundary conditions govern the inner flow. Along the impermeable body surface the normal and tangential velocity components v_n and v_t, respectively, are zero (no slip). Along the matching boundary, the normal velocity component is specified to be continuous with that of the outer flow, and the tangential velocity component is subjected to the free-slip condition in anticipation of the inviscid character of the flow adjacent to the matching boundary.

The inner and outer flows are dependent on the specified distribution of the normal velocity component v_n along the matching boundary. Matching of the two flows is achieved when a distribution of v_n is found that results in continuity of v_t, the tangential velocity component, across the boundary at every point.

Figure 3 illustrates the physical characteristics of a mismatched flow field that results from specification of an incorrect distribution of the normal velocity component along the matching boundary. Mismatch appears as a discontinuity in the tangential velocity component. Physically, this represents a flow that contains a thin free-shear layer or vortex sheet along the matching boundary, and that supports a pressure differential. The flows are perfectly matched only when the strength of this free-shear layer is zero.

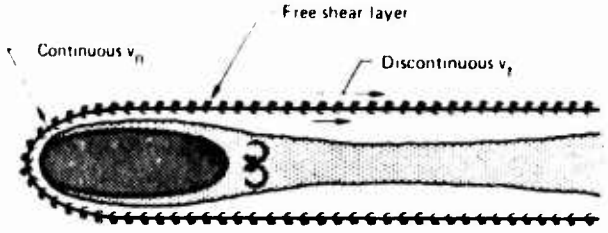

Figure 3. –Physical Characteristics of Mismatched Inner and Outer Flows

The question now is how to determine the distribution of v_n along the matching boundary that will correspond to a matched flow condition. The computation is started with some assumed distribution of v_n, and the perfectly matched solution is arrived at by iteration of the v_n boundary condition. An incremental value of v_n is computed during each cycle of the iteration, leading the procedure closer to a matched solution. The objective of the iteration is to update the specified distribution of normal velocity along the matching boundary by the increment needed to erase the free vortex sheet and obtain a perfect match of the computed tangential velocities across the boundary. This incremental update can be computed directly as the normal velocity component induced by an incremental free vortex sheet positioned along the matching boundary and of a strength equal in magnitude and opposite in sign to the existing velocity discontinuity. In effect, a free vortex sheet that cancels the existing one is added to the inviscid flow, and the subsequent change in the normal velocity through the matching boundary is computed. In practice, this procedure has been accompanied by an inviscid displacement body representation for the inner flow, described later in this paper for a particular example.

Figure 4 illustrates the entire solution process. A spatial position of the matching boundary is selected and an initial guess established for the normal velocity boundary condition along the matching boundary. The initial guess can be obtained conveniently from an inviscid flow solution about the configuration, which also provides the first cycle solution for the outer flow. The inner flow is computed and examined for any viscous regions of high shear extending to the matching boundary. If necessary, the boundary position is changed and the process restarted; if not, the tangential velocity discontinuity across the matching boundary is computed as the difference in velocities provided by the inner and outer solutions. This computed tangential velocity discontinuity is a measure of the

mismatch between inner and outer flows. The discontinuity is compared with an assigned tolerance. If it is less than the tolerance, the iteration has converged and the solution is complete; if it is more, the computational flow returns along a loop in which the incremental change to be applied to the v_n boundary condition is computed. The main computational flow is then reentered with a recomputation of the inner and outer flows based on the updated v_n boundary conditions.

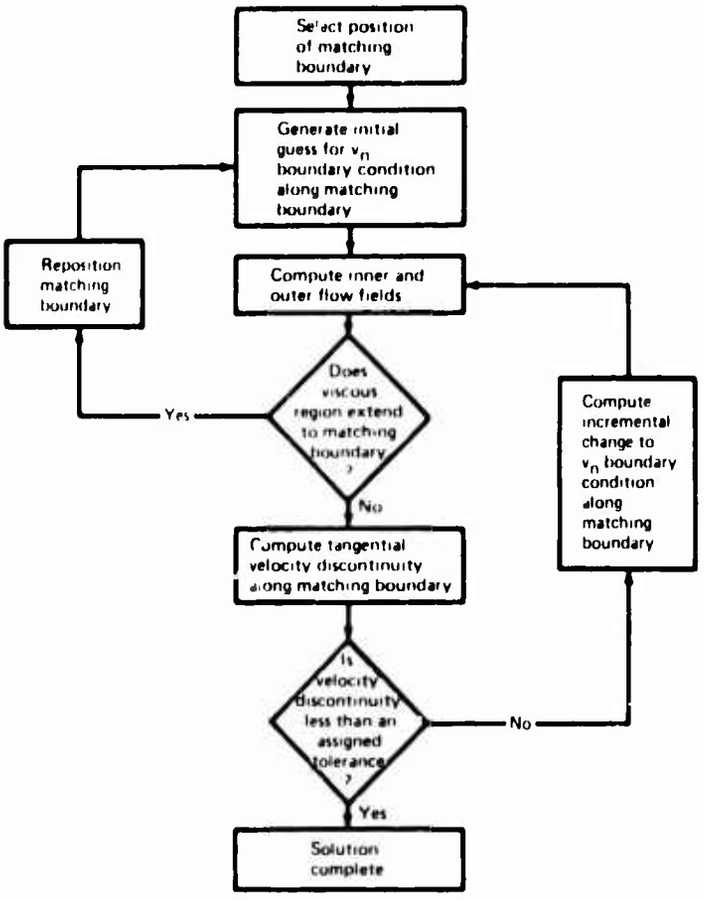

Figure 4.–Solution Flow Chart

APPLICATION TO AXISYMMETRIC SEPARATED FLOW

The problem of predicting laminar flow with separation about a prolate ellipsoid was used to explore and demonstrate the matching procedure just discussed. The shape of the prolate ellipsoid was obtained by rotating an ellipse (a/b = 4) about its major axis a. All calculations were performed for incompressible flow and a Reynolds number of 10^3 based on maximum body diameter (d = 2b). The undisturbed freestream was assumed to be parallel to the major axis of the ellipsoid. In addition, the assumption was made that the separation phenomenon produces an entirely steady and axisymmetric flow field at the chosen Reynolds number.

The flow field about the ellipsoid was subdivided into three different flow regions comprising an upstream boundary layer, an inner region enveloping the region of anticipated separation, and an outer region of potential flow. The boundaries of the inner region which contains part of the boundary layer, viscous separated flow, and some inviscid flow in the vicinity of the matching boundary are shown in figure 5. The matching boundary is a circular cylinder of radius y/L = 0.225 extending from x/L = 0.5 to x/L = 1.26 in the axial direction. Physically, the viscous wake extends far downstream. Computationally, the wake downstream of the aft end of the matching boundary was modeled as a displacement body in the inviscid outer flow.

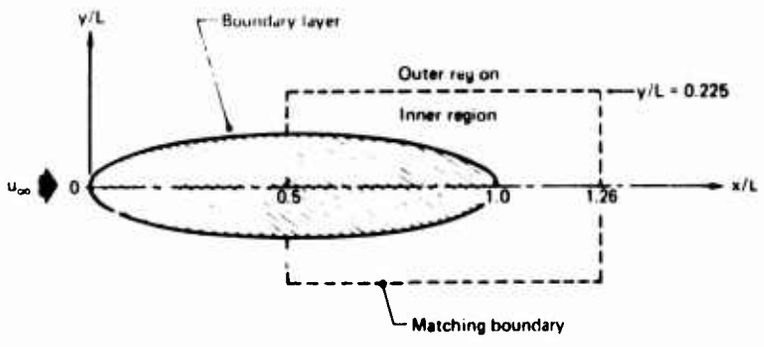

Figure 5.–Computational Flow Regions of Ellipsoid

The flows in the various regions are governed by separate and well-known differential equations. The methods employed for their solution are presented first; then the subject of matching is discussed.

Boundary Layer

Laminar boundary layer growth upstream of the inner region was predicted by an implicit finite difference method of the Crank-Nicholson type (ref. 4). The method solves the axisymmetric form of the boundary layer equations (ref. 5), in which the effect of transverse curvature is not accounted for, subject to the no-slip boundary condition at the body surface and a known tangential velocity at the outer edge of the boundary layer.

Inner Region

The flow in the inner region was determined by solving the time-dependent Navier-Stokes equations (ref. 6). For this purpose, the inner region is divided into a network of rectangular or Cartesian computational cells. Cells at the surface of the ellipsoid are partly bounded by the surface contour, as shown in figure 6. The velocity field is discretized so that the axial velocity component u resides at midpoints of x cell faces and the normal velocity component v is defined at midpoints of the y cell faces. This selection is based on the notion that the divergence of these discrete velocities satisfies mass conservation exactly for each computational cell. All scalar flow variables, such as static pressure, are defined at the center of a computational cell. The momentum equations are formed by centered finite difference expressions for the convective, viscous, and pressure gradient terms. A Poisson equation is formulated for the pressure terms, which provides a simultaneous solution between mass and momentum difference equations. The convective and viscous terms are written implicitly, and an iteration procedure is used during a time cycle to compute a nearly time-centered solution of the discrete equations.

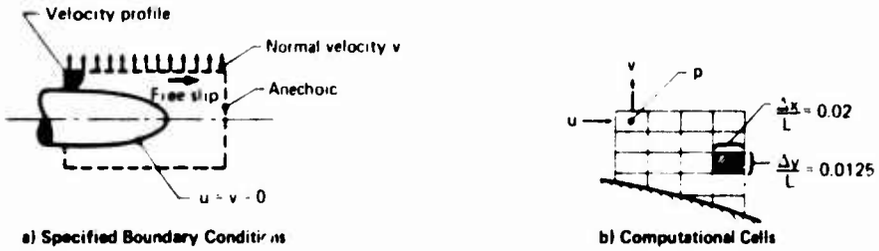

Figure 6.- Inner Flow Calculation

Curved wall boundaries are accounted for in the algorithm by conservative first-order difference expressions. At the surface of the ellipsoid, the no-slip condition was satisfied. Along the matching boundary, the normal velocity component v_n was required to be continuous with that of the outer flow, and the axial velocity component u was provided by application of the reflection principle or free-slip condition. At the inlet plane of the inner region (x/L = 0.5), the normal velocity component and the axial velocity component were specified. A special algorithm (i.e., an anechoic boundary condition) was needed at the exit plane of the inner region (x/L = 1.26) to prevent disturbances at that boundary from traveling upstream. Numerical experiments revealed that this could be achieved by satisfying conservation of mass while using only a first-order approximation to the momentum equation. The principal assumption in the approximation to the conservation of momentum involves the convection terms in which the gradient in the x direction of the v velocity component is neglected.

Potential Flow

An influence coefficient method was used that employs vorticity of linearly varying strength along piecewise conical segments representing the body surface and matching boundary. The particular theoretical model employed a displacement body interior to the matching boundary, as shown in figure 7. (This was done primarily to provide a convenient means for extrapolating the downstream wake.) In the upstream boundary layer region ($0 \le x/L \le 0.5$), the displacement thickness was computed with the familiar definition for two-dimensional flow (ref. 5), and added to the surface of the ellipsoid. In the inner region ($0.5 \le x/L \le 1.26$), displacement thickness was defined by

$$\int_{y_S}^{y_S + \delta^*} u_p\, y\, dy \overset{\text{def.}}{=} \int_{y_S}^{y_M} (u_p - u) y\, dy \quad (L = 1)$$

where y_S denotes the surface of the ellipsoid ($y_S \equiv 0$ in the wake) and y_M denotes the location of the matching boundary. The radius of the displacement body in the inner region is $y_S + \delta^*$. The symbol u_p denotes the axial velocity component of the potential flow about the ellipsoid, whereas u is the axial velocity component furnished by the solution of the Navier-Stokes equations in the inner region. The shape of the displacement body downstream of the inner region (x/L > 1.26) was specified by extrapolation.

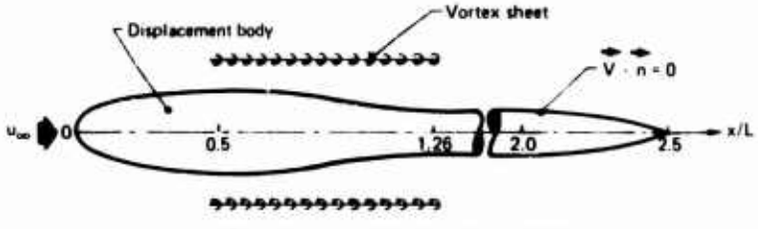

Figure 7.–Potential Flow Calculation

Interface of Flow Regions

The potential flow velocity components u_p, v_p were computed at the midpoints of the x cell faces along the matching boundary. The normal velocity served directly as the boundary condition for the inner region. The axial component u of the inner flow along the matching boundary was calculated using the free-slip condition. The strength γ of the vortex sheet (indication of mismatch) at the corner points of the computational cells along the matching boundary was computed as the difference between the inner flow velocity u and the potential flow velocity u_p.

At the upstream boundary of the inner flow region, both velocity components, u and v, were specified to be continuous across that boundary. With the addition of an auxiliary column of computational cells, the flow field could be discretized in a manner consistent with the algorithm of the Navier-Stokes equation solver.

Matching Procedure

The general course of the matching procedure was outlined earlier. The numerical explorations reported here were conducted using the iteration sequence shown in figure 8. The numbers correspond to the following steps of the matching procedure:

Step 1 An initial guess for the normal velocity component along the matching boundary and for the inviscid part of the velocity profile at the inlet plane of the inner region was furnished by calculating the potential flow about the bare ellipsoid.

Step 2 A boundary layer analysis, with the surface velocity from step 1 as input data, provided δ^* and the viscous part of the velocity profile at the inlet plane of the inner region.

Step 3 The Navier-Stokes equations were solved in the inner region subject to the boundary conditions obtained from steps 1 and 2. Initial values of the time-dependent solution procedure were taken to be those of a uniform stream.

Step 4 The shape of a displacement body was determined as explained earlier under "Potential Flow." The strength γ_1 of a vortex sheet along the matching boundary was calculated as the difference of the axial velocities across the matching boundary between the potential flow solution of step 1 and the Navier-Stokes solution of step 3. The potential flow about the displacement body was then computed in the presence of a vortex sheet of strength $-\gamma_1$ along the matching boundary. The result was a complete and updated flow solution of the outer region and a new set of boundary conditions for the inner region.

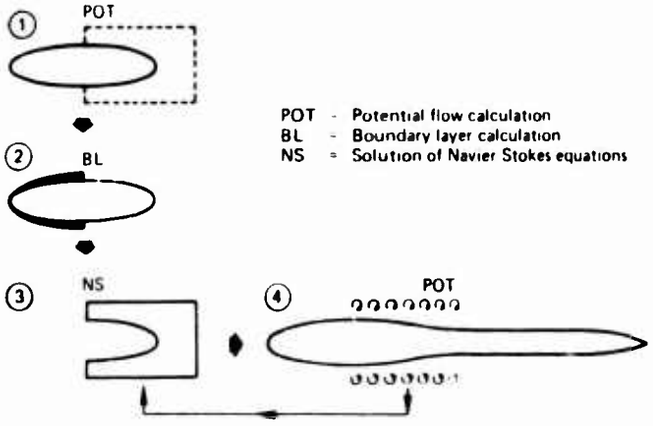

Figure 8.–Picture Flow Chart of Matching Procedure

The next cycle of the iteration procedure was entered at step 3. The properties of the upstream boundary layer were not updated, however, because the subsequent changes in the upstream flow were negligible. Steps 3 and 4 represent a complete cycle of the iteration and were repeated as follows:

Step 3 repeated The Navier-Stokes equations were solved in the inner region subject to the boundary conditions obtained from step 2 and the previous step 4. Initial values of the time-dependent solution procedure were provided by the last steady-state flow solution of the inner region.

Step 4 repeated The shape of the displacement body was updated. The strength γ_i of an incremental vortex sheet along the matching boundary was computed using the most recent solutions of inner and outer flow from steps 3 and 4. The potential flow about the new displacement body was computed with a vortex sheet of strength $-\gamma_1-\gamma_2-\ldots-\gamma_i$ along the matching boundary during the i-th iteration cycle.

The computation was terminated when γ_i was less than a certain prescribed tolerance and when the shape of the displacement body had converged.

Convergence Characteristics

During the iteration, several flow parameters were monitored to determine the convergence characteristics. The strength γ_i of each incremental vortex sheet along the matching boundary is plotted in figure 9. It is shown that the initial mismatch in axial velocities across the matching boundary, of up to 7% of the freestream value, had practically disappeared after the first cycle. The velocity mismatch increased after the second cycle and then decreased in subsequent cycles until, after five iterations, it was everywhere within 1/2% of the freestream speed. It was not possible to erase the vortex sheet completely in a sixth iteration cycle; the iteration procedure slowly oscillated about a solution.

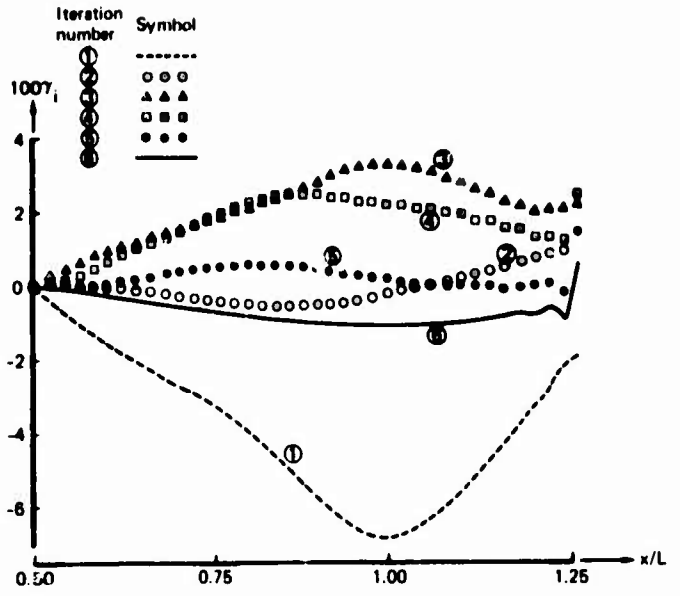

Figure 9.—Strength of Vortex Sheet During Iteration

Figure 10 illustrates how the shape of the displacement body changed. A converged solution was obtained after four iteration cycles. Only minor variations of the displacement shape took place in the upstream part of the inner region, results that seem to justify, a posteriori, the freezing of δ^* in the boundary layer region after the first cycle.

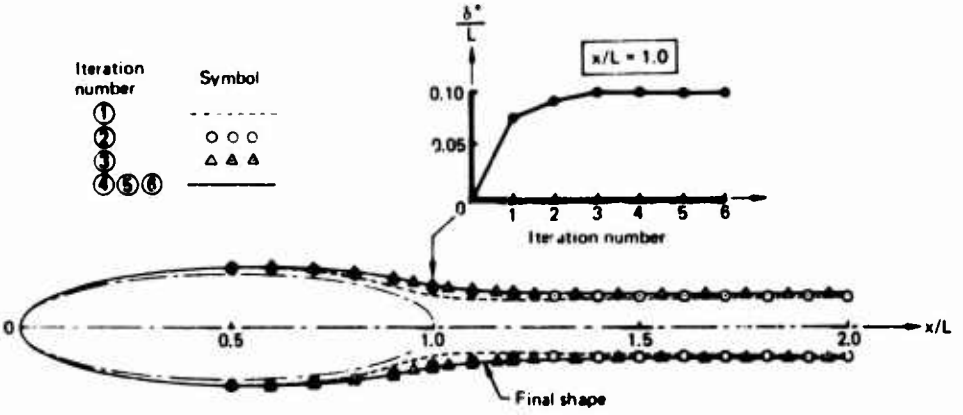

Figure 10.—Shape of Displacement Body During Iteration

The accumulated strength of the vortex sheet along the matching boundary is shown in figure 11. The sum of γ_i decreased during the iteration, but a strong vortex sheet remained, indicating that a simple displacement body is inadequate to simulate the true influence of the viscous, separated region on the outer flow.

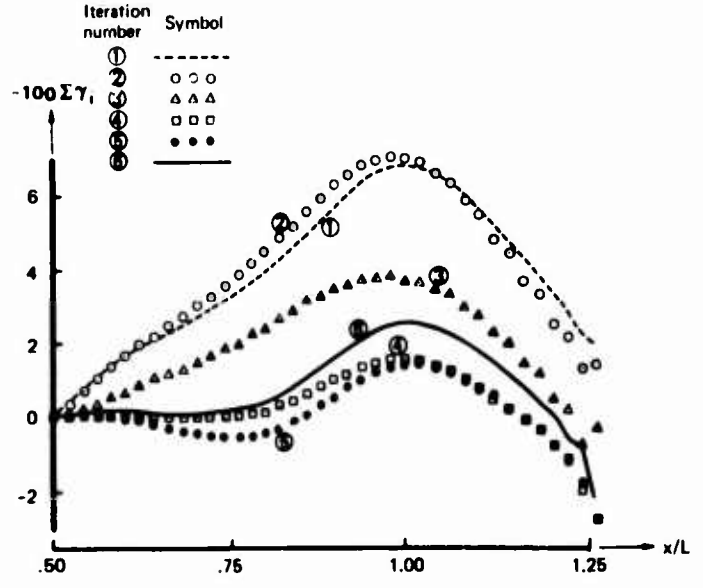

Figure 11.—Accumulated Strength of Vortex Sheet During Iteration

Figure 12 shows the variation of the normal velocity along the matching boundary for each iteration. Again, five cycles were required to obtain a solution that essentially had converged. As expected, there was almost no change in the velocity at the inlet plane of the inner region during the iteration

The surface pressure distribution is shown in figure 13. For clarity, only the results of the first two cycles and the final solution after six iteration cycles are shown. The results display a distribution typical of a separated flow.

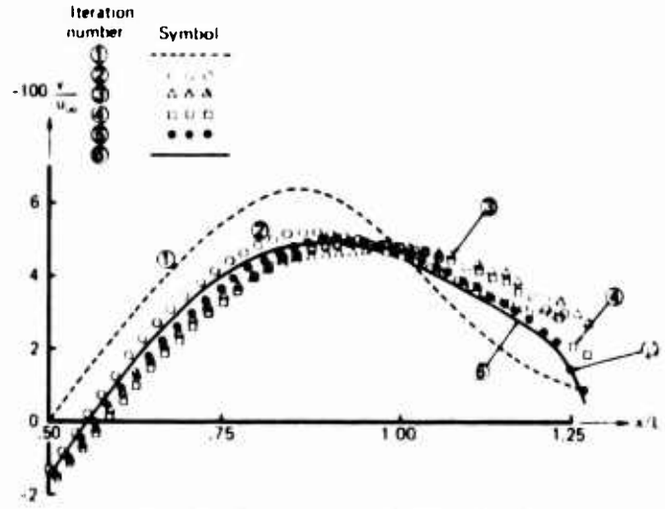

Figure 12. – Behavior of Normal Velocity Along Matching Boundary During Iteration

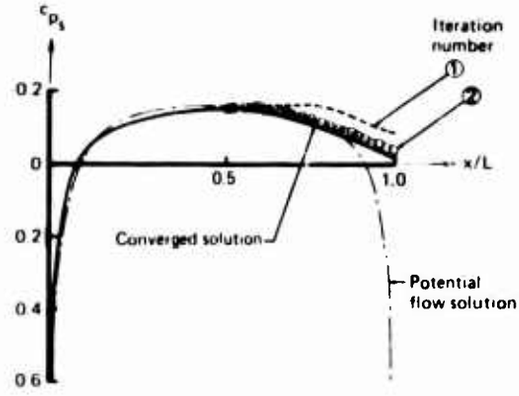

Figure 13. – Surface Pressure of Ellipsoid

The final solution for the distribution of axial velocity is shown in figure 14, illustrating once more that a virtually continuous velocity field across the matching boundary has been obtained. The recirculating flow in the inner flow region can be better visualized with the aid of streamline plots, shown in figure 15. Both figures indicate that separation takes place relatively far downstream, estimated at about x/L = 0.94. For purposes of comparison, note that the boundary layer analysis with the zero skin friction criterion predicted separation further upstream, i.e., at x/L = 0.83 using the potential flow pressures, and at x/L = 0.85 using the final solution of figure 13 as input data.

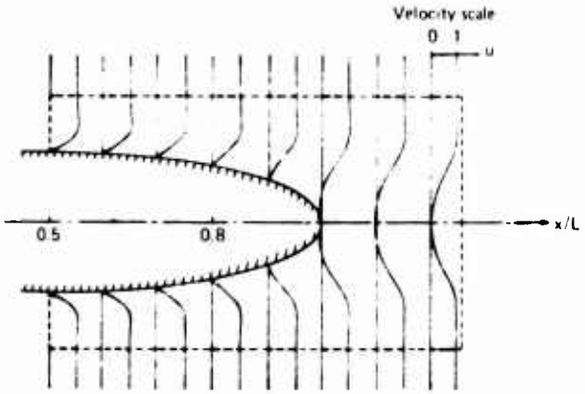

Figure 14. – Matched Axial Velocities

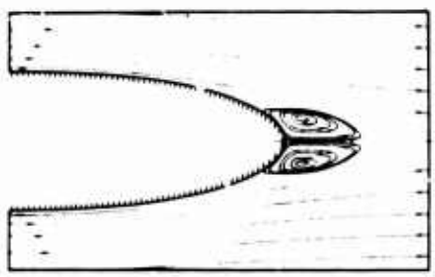

Figure 15. – Streamlines in Inner Region

The drag of the ellipsoid was calculated from the final solution by two different methods. The momentum deficit method, using the computed wake velocity profile at x/L = 1.2, yielded a total drag coefficient of 0.37, referred to maximum cross-sectional area. Computation of friction drag by the boundary layer program for 83% of the body length and pressure drag from figure 13 resulted in friction drag and pressure drag coefficients of 0.28 and 0.09, respectively. The sum of both coefficients is the same as the total drag coefficient calculated through the momentum deficit method. The authors were not able to find measured drag coefficients, but comparing the calculated drag coefficient with the measured drag coefficient, $C_D = 0.50$, of a sphere at the same Reynolds number (ref. 5) adds credibility to the result.

Practical Aspects of the Method

All programs were coded for the CDC-6600 digital computer. The boundary layer and potential flow codes occupied 60K of central memory each and required approximately 20 seconds of central processor time per iteration. The Navier-Stokes equation solver required 140K of central memory for the cases run with 590 computational cells and used 3 input/output units. Its execution time was approximately 4 seconds per time step. An excessive number of time steps was run to ensure a steady-state solution of the Navier-Stokes equations during each iteration cycle of the matching procedure. It is estimated that the final converged solution can be computed with a total of 600 time steps, requiring approximately 40 minutes of execution time. It should be noted that the Navier-Stokes code was not optimized and could be improved to further reduce execution time and core requirement.

A few visual aids were employed, of which the streamline plot of figure 15 is an example. The development of the flow in the inner region was observed on film, where each picture represented an automatically plotted pattern of particle positions at a fixed instant of time. The fluid particles were continuously fed into computational cells located along the upstream boundary and in the wake region.

CONCLUSIONS

A method has been presented for computing flow fields with regions of viscous, separated flow by numerical matching. An apparently new technique has been outlined to match a numerical solution of the complete Navier-Stokes equations with another numerical solution appropriate for an adjacent region of dominant inviscid flow. The method has been successfully applied to a model problem of axisymmetric incompressible flow with laminar separation. The iteration procedure hovered about convergence, and modifications of the described basic procedure—such as scaling the strength of the incremental vortex sheet and scaling the changes in the shape of the displacement body (i.e., improvements typically added to Newton-type iteration schemes)—might be desirable to hasten convergence.

The matching technique presented ultimately can be expected to lead to an economical solution procedure for many problems of interest in fluid dynamics, such as viscous transonic flow, turbulent jets spreading in the vicinity of lifting surfaces, and the problem of predicting the drag of upswept afterbodies.

REFERENCES

1. H. Thwaites, ed., *Incompressible Aerodynamics*, Oxford University Press (Clarendon Press), 1960.

2. J. F. Thompson, S. P. Shanks, and J. C. Wu, "Numerical Solution of Three-Dimensional Navier-Stokes Equations Showing Trailing Tip Vortices," *AIAA Journal*, Vol. 12, No. 6, June 1974, pp. 787-794.

3. G. S. Deiwert, "Numerical Simulation of High Reynolds Number Transonic Flows," AIAA Paper No. 74-603, presented at AIAA 7th Fluid and Plasma Dynamics Conference, Palo Alto, California, June 1974.

4. T. A. Reyhner, The Boeing Company, *A Computer Program for Finite Difference Calculation of Compressible Turbulent Boundary Layers*, 1970, Document D6-23236.

5. H. Schlichting, *Boundary Layer Theory*, 6th ed., New York, McGraw-Hill, 1968.

6. C. K. Forester and A. F. Emery, "A Computational Method for Low Mach Number Unsteady Compressible Free Convective Flows," *Journal of Computational Physics*, Vol. 10, 1972, pp. 487-502.

ÉTUDE EXPÉRIMENTALE ET THÉORIQUE DU RECOLLEMENT BIDIMENSIONNEL TURBULENT INCOMPRESSIBLE

par Jean-Claude Le Balleur et Jean Mirande

Office National d'Études et de Recherches Aérospatiales (ONERA)
92320 Châtillon (France)

RÉSUMÉ.

Une étude expérimentale approfondie du recollement turbulent en aval d'une marche a été conduite en écoulement incompressible bidimensionnel plan, le champ potentiel au voisinage du recollement étant à volonté ralenti ou accéléré. L'analyse détaillée des distributions de pression et de vitesse dans cette zone a permis de dégager des lois empiriques générales en cas de coucne limite initiale mince au décollement.

Le calcul est réalisé en tant qu'interaction auto-induite d'une couche dissipative pariétale et d'un écoulement externe de fluide parfait irrotationnel. Excepté dans les régions où l'interaction est faible, on adopte un mode de calcul inverse qui évite les singularités, selon la technique de Klineberg pour les profils transsoniques. La pression pariétale devient ainsi le résultat d'une méthode intégrale de couche limite, dont l'insuffisance dans les zones fortement décollées peut être facilement surmontée par la substitution d'une loi de pression empirique.

EXPERIMENTAL AND THEORETICAL STUDY OF TWO-DIMENSIONAL, TURBULENT, INCOMPRESSIBLE REATTACHMENT.

SUMMARY :

Turbulent reattaching flow downstream of a backward facing step has been experimented using a two-dimensional plane incompressible configuration, with possibility to induce favourable or adverse pressure gradients in the potential flow near reattachment. Detailed pressure and velocity measurements in this region makes it possible to suggest general empirical rules whose efficiency relies on a thin initial separating boundary layer.

A whole calculation has been performed by obtaining a self-induced interaction in matching a wall dissipative layer with an inviscid and irrotational external flow. Except for weak viscous interaction regions, an inverse calculation process is used to avoid singularities following the Klineberg's method for transonic aerofoils. Wall pressure distribution then results of an integral boundary layer calculation, whose failure for strongly separated regions is easily overcome by substitution of an empirical pressure law.

NOTATIONS.

α : incidence du plancher de recollement par rapport à la paroi en amont du décollement.

δ : épaisseur de la couche dissipative.

$\delta_{0,99}$: épaisseur définie par l'ordonnée du point où la perte de pression totale = 0,02 q_e

δ^* : épaisseur de déplacement = $\int_0^\delta (1-\frac{U}{U_e})\,dy$

δ^{**} : épaisseur de quantité de mouvement = $\int_0^\delta \frac{U}{U_e}(1-\frac{U}{U_e})\,dy$

δ^{***} : épaisseur d'énergie cinétique = $\int_0^\delta \frac{U}{U_e}(1-\frac{U^2}{U_e^2})\,dy$

ϕ : fonction de dissipation.

b : envergure de la marche (largeur de la veine).

D : hauteur du canal amont.

F : fonction d'entraînement.

h : hauteur de la marche.

H : paramètre de forme $= \frac{\delta^*}{\delta^{**}}$

$\bar{H}$: " " $= \frac{\delta^{***}}{\delta^{**}}$

$\tilde{H}$: " " $= \frac{\delta-\delta^*}{\delta^{**}}$

K_p : coefficient de pression $= \frac{P-P_0}{q_0}$

K'_p : coefficient de pression relatif $= \frac{P-P_1}{q_1}$

p : pression statique

P_t : pression totale

q : pression dynamique $= P_t - P = \frac{\rho}{2} V^2$

U : composante moyenne de la vitesse parallèle à la paroi.

U_p : vitesse "extérieure" de la couche dissipative calculée avec la pression statique mesurée à la paroi (hypothèse $\frac{dP}{dy} = 0$)

u' : vitesse de fluctuation.

u_{eff} : valeur efficace de la vitesse de fluctuation $= \sqrt{\overline{u'^2}}$

V : module de la vitesse.

X : abscisse suivant la direction de la paroi de recollement.

$\mathcal{R}_{\delta^{**}}$: nombre de Reynolds construit avec δ^{**}

y : ordonnée normale à la paroi de recollement.

INDICES.

0 : condition à l'∞

1 : au point de décollement.

e : extérieur à la couche visqueuse (en $y = \delta$).

i : début de la recompression.

j : sur la ligne de jet.

R : au point de recollement.

1 - INTRODUCTION.

Cette étude a eu pour objet l'analyse de configurations d'écoulement décollé présentant un point de séparation fixé par un décrochement de paroi. De cette manière l'effort a pu être concentré sur les phénomènes liés au recollement turbulent, restreints dans une première étape au cas d'un écoulement incompressible bidimensionnel plan.

L'essentiel des recherches consacrées à ce sujet [3-9-11-12] se rapporte à des configurations pour lesquelles le recollement se produit sur une paroi parallèle à la direction de la vitesse amont. Il a paru nécessaire de généraliser ces travaux et de les étendre à des cas où une modification du champ potentiel se produit au voisinage et en aval du recollement, induisant des gradients de pression positifs ou négatifs dont les effets peuvent se superposer à ceux qui sont spécifiques du phénomène de recollement.

Les principaux éléments acquis ont été résumés en deux parties :

La première expose l'essentiel des résultats expérimentaux obtenus par l'analyse détaillée du champ de pression et de vitesse au sein du domaine décollé et de son voisinage. Des lois empiriques de portée assez générale ont pu être dégagées.

A partir de ces résultats, une méthode pratique de calcul d'écoulements présentant des zones décollées étendues a été établie. Elle est examinée dans la seconde partie. Le calcul prend en compte les effets de couplage entre couches dissipatives et écoulement extérieur, et met en oeuvre une technique proche de celle développée par Klineberg et Steger pour les écoulements transsoniques.

2 - ETUDE EXPERIMENTALE.

2.1 - Conditions d'essai : Le montage bidimensionnel plan utilisé a été aménagé dans une petite soufflerie subsonique de type Eiffel (fig. 1a). Il est constitué d'amont en aval (fig. 1b) par un canal de section constante débouchant en D sur un décrochement de paroi de hauteur h variable suivi d'un plancher de recollement R d'inclinaison α réglable.

En cours d'essai, la vitesse Vo de référence mesurée en amont de D (fig. 1b) a été maintenue à une valeur sensiblement constante (50m/s), le niveau général de la turbulence de l'écoulement hors couche limite étant caractérisé dans ce domaine par un taux réduit $\sqrt{\overline{u^2}}/V_0$ de l'ordre de 0,4%.

En l'absence de décollement ($h = 0, \alpha \simeq 0$) la couche limite est turbulente en D et possède les caractéristiques suivantes :

$$\delta_1 \simeq 14 \text{ mm} \qquad \delta_1^{**} \simeq 1{,}4 \text{ mm} \qquad H_1 \simeq 1{,}34$$

ces grandeurs ne subissant que de très faibles variations sous l'effet du gradient de pression induit par le décollement lorsqu'il se produit ($h \neq 0$).

En agissant sur les paramètres géométriques α et h ($-7 \leqslant \alpha \leqslant 10$; $8 \leqslant h \leqslant 31{,}5$) il a donc été possible d'étudier de façon systématique les circonstances du recollement en présence d'un écoulement général accéléré ($\alpha > 0$) ou ralenti ($\alpha < 0$) et d'une couche limite initiale d'épaisseur relative δ_1/h variable.

Les mesures ont porté en premier lieu sur la détermination des pressions pariétales au moyen de prises disposées sur la paroi inférieure (fig. 1) suivant l'axe du montage, 4 rangées transversales placées en aval de D permettant un contrôle de la bidimensionnalité de l'écoulement.

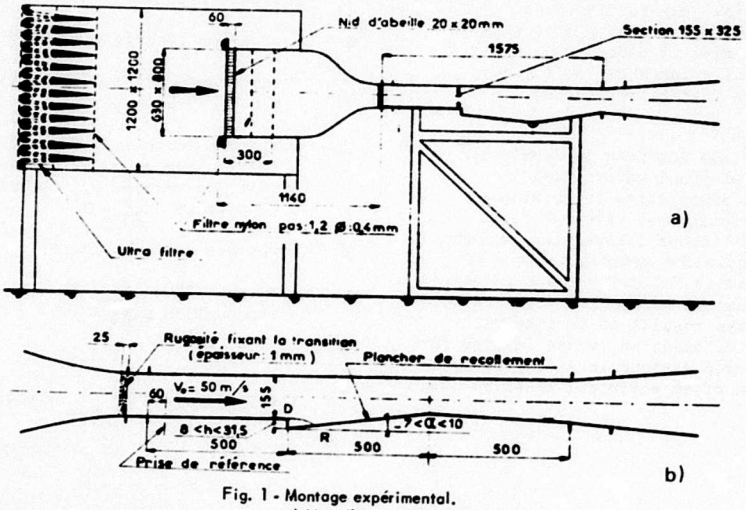

Fig. 1 - Montage expérimental.
a) Vue d'ensemble de l'installation
b) Schéma du dispositif d'étude.

Les profils de vitesse moyenne dans les couches dissipatives ont été obtenus à partir d'explorations de pression statique et d'arrêt au moyen de sondes adaptées à l'étude d'un écoulement comportant un courant de retour [1]. Ces mesures ont été complétées par une analyse au fil chaud des fluctuations de vitesse et par la localisation des lignes de recollement, la visualisation pariétale mettant en jeu une technique exposée également en [1].

Pour toutes les configurations expérimentées le caractère bidimensionnel de l'écoulement a été contrôlé à l'aide des distributions transversales de pression mais surtout par l'observation de la ligne de recollement.

Comme le montre la fig. 2, une variation sensible en envergure de l'étendue longitudinale X_R du bulbe de décollement apparaît, spécialement pour les valeurs négatives de α (écoulement général ralenti), lorsque l'allongement $\lambda = \frac{b}{X_R}$ de ce bulbe diminue. L'écart maximum enregistré $\frac{\Delta X_R}{X_R}$ peut atteindre 30% pour une valeur voisine de 3.

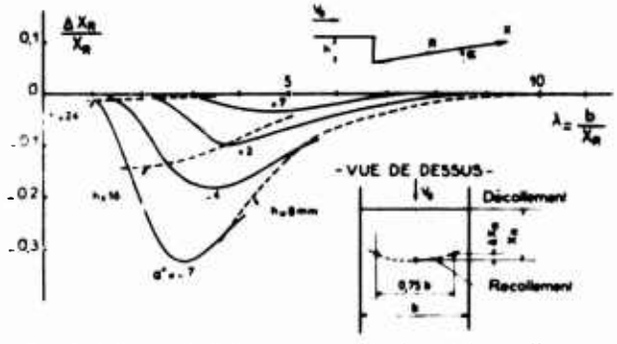

Fig. 2 - Influence de l'allongement sur l'uniformité du recollement en envergure.

On observe également, ce qui peut sembler paradoxal, que pour des allongements plus faibles ($\lambda < 3$) la tendance s'inverse, les écarts ΔX_R s'atténuant, bien que l'importance relative des couches limites latérales augmente.

Faute de pouvoir assurer en toute circonstance des conditions d'essais absolument pures, il a été convenu à la suite d'une étude critique de la cohérence des résultats de n'utiliser que les mesures effectuées dans le plan de symétrie du montage et de ne retenir que des configurations pour lesquelles $\frac{\Delta X_R}{X_R}$ était inférieur à 15%.

2.2 - Analyse des pressions pariétales.

Les fig. 3 fournissent quelques exemples de répartitions de pression obtenues pour des conditions de recollement variées correspondant à un écoulement accéléré (fig. 3a), uniforme (fig. 3b) ou ralenti (fig. 3c).

La position X_R du point de recollement est également portée sur ces diagrammes. On observe que l'étendue $\frac{X_R}{h}$ de la zone décollée augmente sensiblement lorsque la paroi de recollement devient divergente (fig. 3c), cette étendue étant pratiquement indépendante de l'épaisseur relative $\frac{\delta_1}{h}$ de la couche limite initiale pour des parois convergentes ou très faiblement divergentes (fig. 3a et 3b).

L'ensemble de ces répartitions présente entre les points de décollement et de recollement une similitude d'évolution caractérisée par une région initiale quasi isobare suivie d'une recompression rapide jusqu'au point de recollement R . Par contre en aval de R . la forme des distributions dépend de l'inclinaison α du plancher.

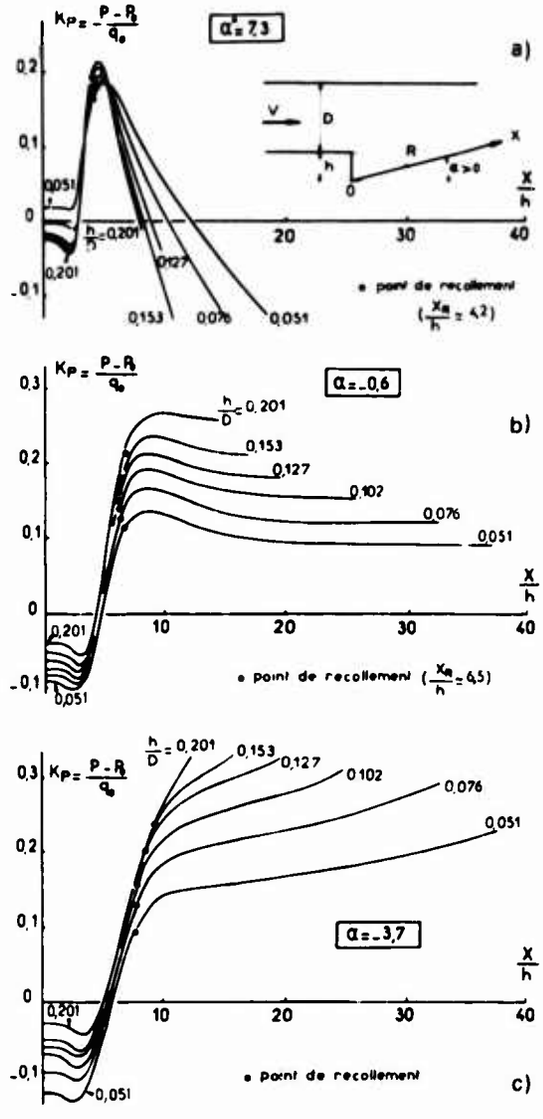

Fig. 3 - Evolution des pressions pariétales en aval du décollement (influence de la hauteur de marche).
a) $\alpha = 7,3°$ b) $\alpha = -0,6°$ c) $\alpha = -3,7°$

Roshko, le premier [3], tirant parti de cette propriété, a proposé une normalisation de l'évolution des pressions dans le décollement sous forme d'une loi empirique

$$\frac{P - P_1}{q_1} = f\left(\frac{X}{X_R}\right)$$

P_1 étant la pression de culot et q_1 la pression dynamique correspondante ($q_1 = P_1 - P_1$)

Dans cette représentation, il subsiste une dispersion assez importante notamment au voisinage du point de recollement, conduisant à des écarts maximaux sur l'ensemble de nos essais pouvant atteindre $\left|\Delta\left(\frac{P_R - P_1}{q_1}\right)\right| \simeq 0,15$

Ces écarts peuvent être interprétés de la même manière qu'en écoulement supersonique [2] [4] en tenant compte des effets de la couche limite initiale à l'origine du décollement sur le développement de la couche de mélange établie à la frontière extérieure du bulbe de décollement.

L'étude théorique simplifiée de ce phénomène [4-5-6] montre en effet que la ligne de courant limite (1) aboutissant au point de

recollement et fixant le niveau de pression par une condition d'arrêt est définie par le paramètre $Cq = \frac{\delta_1''}{X_R + X_0}$

ou X_0 représente une origine fictive du mélange [5-6] donnée par une relation de la forme $X_0 = K\,\delta_1''$, K étant égal à 81 pour un écoulement incompressible [5].

Portant en fonction de Cq l'évolution du saut de pression au recollement $\frac{P_R - P_1}{q_1}$, on obtient alors une relation "universelle" propre à l'effet de couche limite initiale et indépendante de la configuration étudiée, comme le montre la fig. 4.

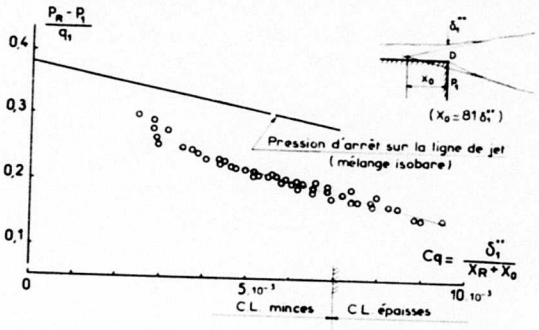

Fig. 4 - Saut de pression au recollement (influence de la couche limite initiale).

Ce résultat appelle 2 remarques ;

Tout d'abord cette évolution est différente de celle à laquelle conduirait l'hypothèse d'une recompression isentropique de l'écoulement sur (1), appliquée à un profil de mélange pleinement établi.

Ensuite le concept d'origine fictive n'est parfaitement justifié que lorsque l'étendue étant suffisante, le profil des vitesses dans la couche de mélange est proche de l'état asymptotique, cette situation étant réalisée pour des valeurs de Cq inférieur à $0,7.10^{-2}$ qui correspondent à $\frac{\delta_1}{X_R} \leqslant 1/6$

Disposant d'une relation permettant de calculer le saut de pression au recollement nous avons été tout naturellement conduits à rechercher une normalisation des répartitions de pression dans la zone décollée plus raffinée que celle proposée par Roshko.

Une loi d'évolution de la forme $\frac{P - P_1}{P_R - P_1} = f\left(\frac{X}{X_R}\right)$ permet d'éliminer les effets de couche limite initiale comme le montre l'exemple présenté fig. 5a dans le cas $\alpha \simeq -0,6$.

Par contre, la longueur relative $\frac{X_i}{X_R}$ de la partie isobare du décollement évolue de façon sensible avec α comme le montre la fig. 5b.

Une représentation commode de cette évolution sous une forme plus générale a été recherchée. Elle est obtenue, en portant $\frac{X_i}{X_R}$ en fonction de l'angle local θ_R de la frontière de déplacement au niveau du point de recollement fig. 5c.

Ce choix qui assure un bon recoupement de l'ensemble de nos expériences permet de rattacher la loi $\bar{\omega}\left(\frac{X}{X_R}\right)$ à une propriété locale de l'écoulement au point de recollement. On définit ainsi une règle d'interpolation des résultats de la fig. 5b, éliminant le paramètre géométrique α au bénéfice d'un paramètre mieux adapté au traitement de configurations de recollement variées.

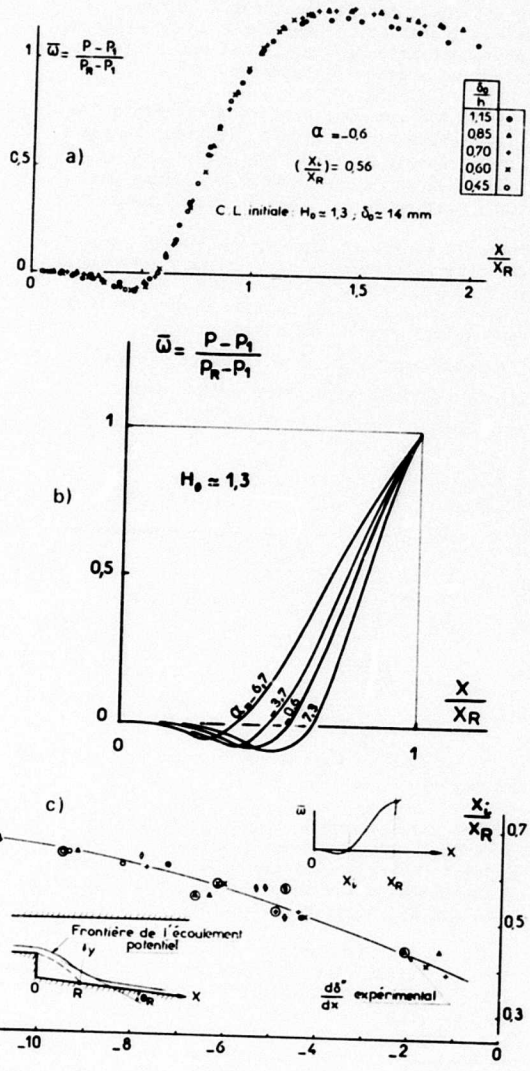

Fig. 5 - Normalisation des pressions pariétales.
a) $\alpha = -0,6°$
b) Influence de l'angle α
c) Loi d'évolution de l'étendue du domaine isobare.

2.3 - Analyse des couches dissipatives.

L'analyse détaillée de ces couches a été effectuée sur 4 configurations géométriques (α = 4,3, -0,6, -3,7, -6,7°) et pour 2 valeurs de $\frac{\delta_1}{h}$ (0,9 et 0,6). Dans tous les cas considérés la longueur X_R du décollement est suffisante pour que le concept d'origine fictive soit applicable (couches limites initiales minces $\frac{\delta_1}{X_R} \leqslant 1/6$).

L'observation des profils de vitesse moyenne pour 3 configurations typiques (fig. 6) met en évidence une analogie d'évolution que nous analyserons en séparant les domaines situés en amont et en aval du point de recollement.

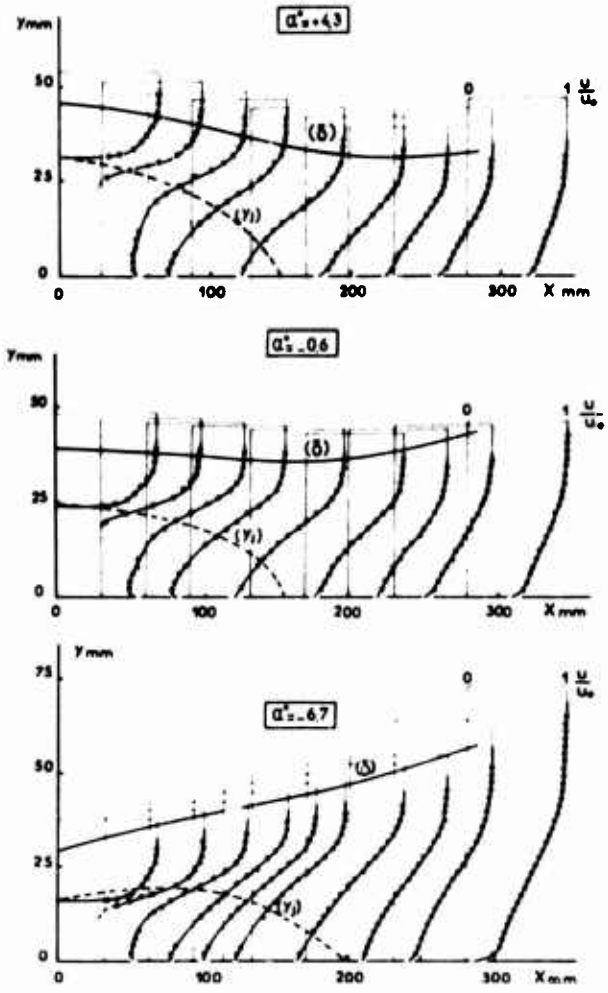

Fig. 6 - Evolution des profils de vitesse en aval du décollement.
a) α = 4,3° b) α = -0,6° c) α = -6,7°

2.3.1 - Profils des vitesses :

Comme le suggère l'analyse des répartitions pariétales de pression nous distinguerons 2 régions dans la zone décollée.

a) la région initiale isobare ($0 \leqslant X \leqslant X_i$) caractérisée essentiellement par le développement d'un processus de mélange le long de la frontière du bulbe de recirculation.

b) la recompression proprement dite ($X_i < X \leqslant X_R$)

Dans la première région la déformation des profils de vitesse mesurés à différentes abscisses (fig. 7) illustre la propagation transversale du mélange qui absorbe progressivement la couche limite initiale et atteint l'écoulement extérieur non dissipatif lorsque $\frac{X_i}{\delta_1} \simeq 6$.

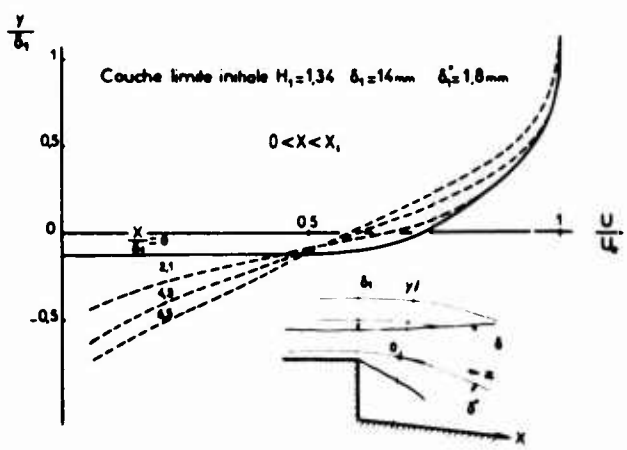

Fig. 7 - Profils de vitesse dans la zone isobare.

La vitesse maximale du courant de retour (fig. 6), située au voisinage de la paroi, croit avec X pour atteindre en fin de zone isobare une valeur significative $\frac{U_{r\,max}}{U_e} \simeq 0,25$

D'une façon plus générale les profils de vitesse dans cette région sont marqués par une double influence, celle de la couche limite initiale, et celle du courant de retour. De ce fait leur structure complexe ne permet pas d'envisager une représentation simple de leurs propriétés mêmes globales (paramètres de forme, épaisseurs caractéristiques etc...).

Dans la zone de recompression, les profils de vitesse sont fortement influencés par l'approche du recollement, le courant de retour diminuant en intensité et étendue transversale lorsque X tend vers X_R . L'évolution de la vitesse maximale de retour est soumise à des effets visqueux importants. C'est ainsi qu'une détente isentropique de l'écoulement de recirculation depuis le point de recollement conduirait à une vitesse environ 2 fois supérieure à celle qui est mesurée (fig. 8).

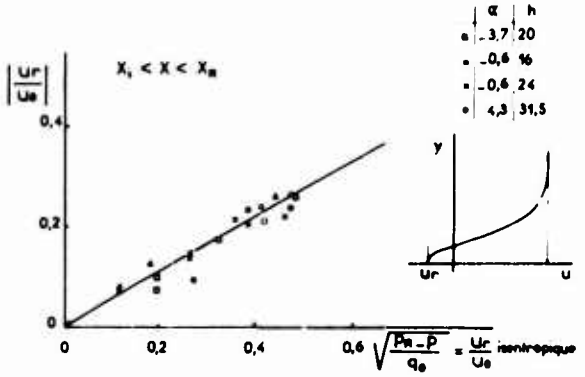

Fig. 8 - Evolution de la vitesse maximale de retour dans la zone de recirculation.

Comme le montre la fig.9 une normalisation des profils de vitesse entre X_i et X_R peut être réalisée sous la forme d'une loi déficitaire :

(1) $$\varphi = \frac{U - U_r}{U_e - U_r} = f\left(\frac{y}{\delta}\right)$$

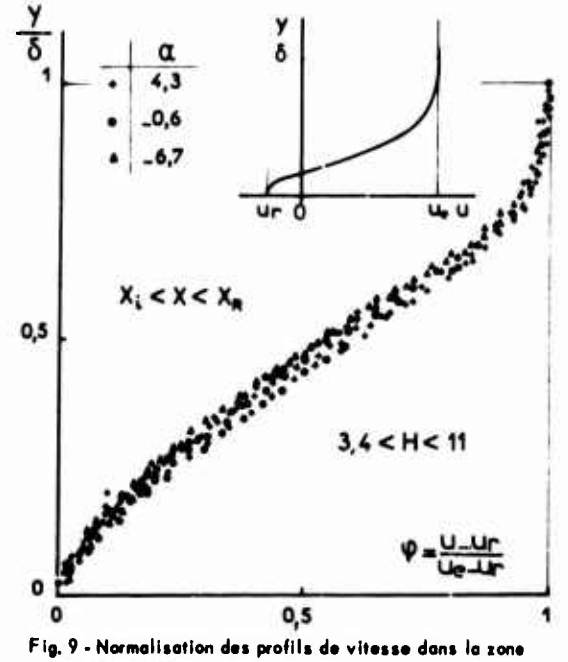

Fig. 9 - Normalisation des profils de vitesse dans la zone de recompression.

Bien que le recoupement auquel cette représentation conduit soit imparfait, il est toutefois l'indice que dans ce domaine les profils de vitesse peuvent être représentés par une famille à 1 paramètre P dont une représentation déduite de (1) est de la forme

$$\frac{u}{u_e} = P + (1-P)\,\varphi\left(\frac{y}{\delta}\right)$$

Cette propriété rappelons le n'est valable que dans le cadre de l'hypothèse de couches limites initiales minces.

En aval du point de recollement ($X > X_R$) domaine que nous appellerons zone de restructuration, on observe une croissance des vitesses longitudinales au voisinage de la paroi (fig. 6), plus ou moins rapide selon que le champ extérieur est accéléré ou ralenti ($\alpha > 0$, $\alpha < 0$).

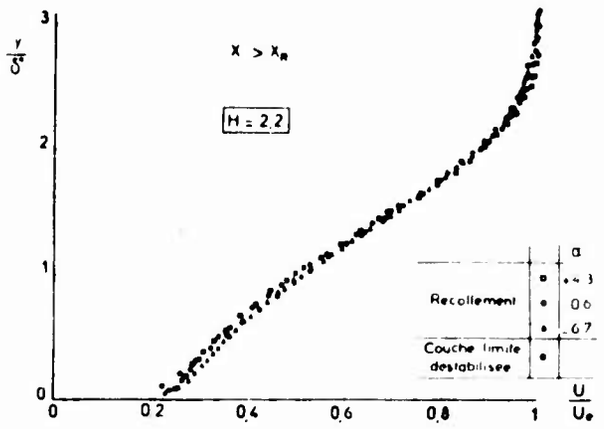

Fig. 10 - Exemple de profils de vitesse dans la zone de restructuration.

Toutefois, comme le montre la fig. 10, les profils de vitesse obtenus pour une même valeur (H = 2,2) du paramètre de forme H possèdent quel que soit α une structure très voisine analogue à celle d'une couche limite destabilisée proche du décollement.

2.3.2 - Epaisseurs caractéristiques et paramètres de forme.

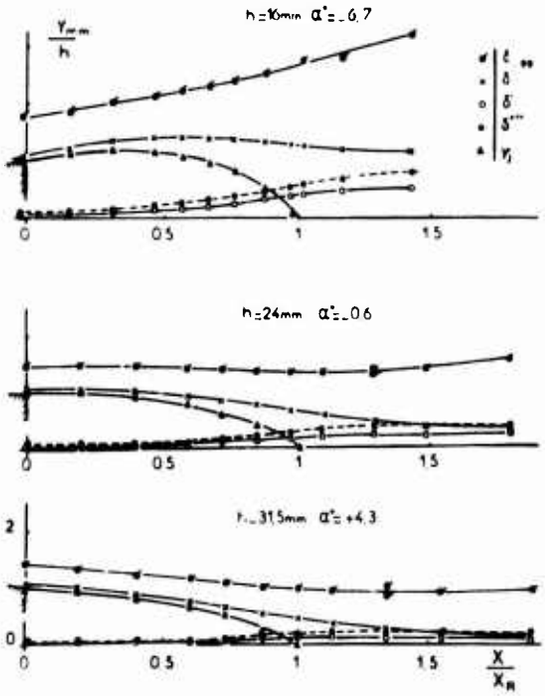

Fig. 11 - Evolution des épaisseurs caractéristiques en aval du décollement.

Un exemple d'évolution avec l'abscisse des différentes épaisseurs caractéristiques $\delta, \delta^*, \delta'', \delta''', y_j$ dans la zone décollée et en aval est donnée fig. 11 pour les 3 configurations typiques précédemment examinées (α = -0,7, -0,6, 4,3).

On notera l'épaississement important que subit la couche dissipative dans le cas où l'écoulement extérieur est ralenti (α=-6,7°).

L'existence d'une famille de profils de vitesse dans le domaine proche du recollement en amont et en aval de celui-ci, indépendante de la configuration géométrique étudiée qui avait été suggérée par l'analyse locale (fig. 9 et 10) est ici confirmée au niveau des grandeurs caractéristiques globales. Une relation fonctionnelle unique entre les divers paramètres de formes définis par le rapport de deux épaisseurs caractéristiques quelconques en est notamment la preuve. Une telle relation est parfaitement vérifiée en ce qui concerne l'évolution $\bar{H}$ (H) par exemple (fig. 12); elle cesse dès que l'on pénètre dans le domaine ischare du décollement pour les raisons indiquées en 2.3.1.

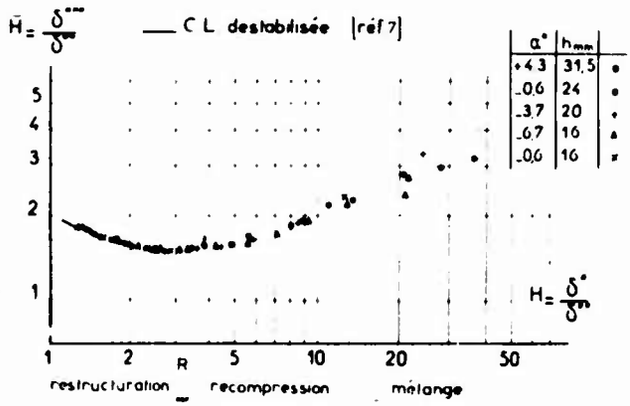

Fig. 12 - Corrélation expérimentale $\bar{H}$(H).

Un regroupement moins satisfaisant est obtenu fig. 13 dans la représentation $\tilde{H}$ (H), la dispersion des résultats et les écarts par rapport aux mesures de Head en particulier pouvant être en grande partie imputés à l'imprécision intervenant nécessairement dans la définition de l'épaisseur δ .

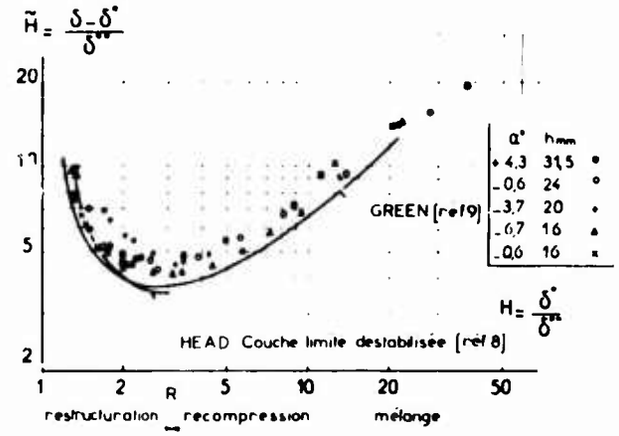

Fig. 13 - Corrélation expérimentale $\tilde{H}$ (H).

2.3.3 - Fonctions caractéristiques de l'écoulement dissipatif.

Parallèlement à l'examen détaillé des relations existant entre les divers paramètres de forme, une étude expérimentale des fonctions caracté-

ristiques intervenant dans le calcul des couches dissipatives par des méthodes intégrales a été effectuée.

L'évolution avec H de la fonction d'entraînement [8 - 10] définie par la relation :

$$F = \frac{1}{u_e} \frac{d}{dx} \left[u_e (\delta - \delta^*) \right]$$

et déduite de nos mesures est donnée fig. 14.

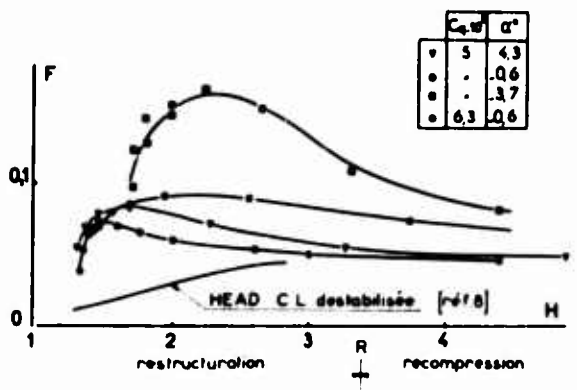

Fig. 14 - Fonction d'entraînement.

Ces résultats mettent en évidence l'impossibilité de retenir l'hypothèse d'une relation universelle reliant F et H dans les domaines de recompression et de restructuration; des effets marqués liés à l'importance de la couche limite initiale (paramètre C_q) et à la configuration géométrique (α) entraînant une dispersion importante dans le plan F, H.

En ce qui concerne la fonction de dissipation $\Phi = \frac{1}{\rho_e u_e^3} \int_0^\delta \tau \frac{\partial u}{\partial y} dy$, calculée par la relation (5c) § 3.2, une telle hypothèse ($\Phi = \Phi(H)$) semble mieux assise, bien qu'imparfaitement vérifiée, les écarts par rapport à une courbe moyenne demeurant modérés (fig. 15).

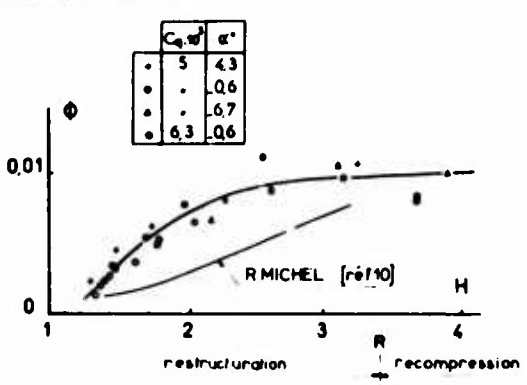

Fig. 15 - Fonction de dissipation.

2.3.4 - Remarques diverses.

a) Evolution de la turbulence :

Dans le cadre de l'analyse détaillée des couches dissipatives, le taux de fluctuation de la vitesse longitudinale $\sqrt{\overline{u^2}}/u_0 = u_{eff}/u_0$ a été mesuré pour la configuration $\alpha \simeq -0,6$ et deux valeurs de l'épaisseur relative δ_1/h de la couche limite initiale ($\delta_1/h = 0,6$ et $1,7$) une exploration assez complète n'ayant été effectuée que pour $\delta_1/h = 1,7$.

L'évolution transversale de u_{eff}/u_0 présente un maximum au sein de la couche dissipative étroitement lié à celui qui apparaît pour le profil de cisaillement turbulent [12].

La fig. 16 montre l'évolution de $\left| \frac{u_{eff}}{u_e} \right|_{max}$ en fonction de l'abscisse réduite X/δ obtenue au cours de ces expériences, évolution qui a été comparée à celle obtenue par Tani dans le cas de valeurs δ_1/h plus faibles.

Dans tous ces exemples on constate que $\left| \frac{u_{eff}}{u_e} \right|_{max}$ présente une évolution croissante jusqu'au point de recollement et décroît ensuite progressivement dans la zone de restructuration, l'extremum ainsi obtenu dépendant fortement de δ_1/h.

La partie croissante de la courbe est quasi universelle pour une couche limite initiale donnée et représente la transition entre l'état de turbulence propre à cette couche limite et celui qui correspond à un processus de mélange asymptotique, celui-ci est obtenu lorsque l'épaisseur de la couche limite initiale est faible devant l'étendue de la zone décollée (Tani, $\frac{\delta_1}{h} \sim 0,27$).

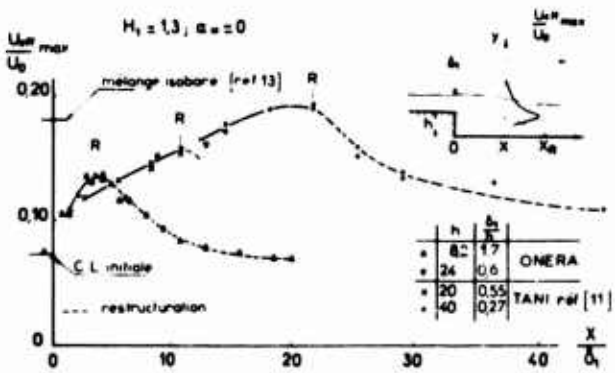

Fig. 16 - Evolution de la fluctuation maximale de vitesse en aval du décollement.

Ces expériences confirment qu'un état d'équilibre est atteint pour les profils de vitesse dans une couche de mélange bien avant que cet équilibre ne soit établi pour la turbulence interne.

b) Effet d'une couche limite épaisse ($C_q > 0,7.10^{-2}$) :

Tant que la couche limite initiale est mince, la couche dissipative abordant la zone de recollement possède un profil de vitesse sensiblement figé dans sa forme, même si la structure de la turbulence ne présente pas la même situation. Dans ces conditions on a pu mettre en évidence des propriétés assez générales concernant l'évolution des vitesses moyennes et la recompression jusqu'au point de recollement.

Par contre lorsque δ_1 devient significatif devant l'étendue de la zone décollée, ces propriétés ne sont plus conservées, le fluide conservant au-delà de X_i la mémoire du profil de vitesse à l'origine du décollement.

Cela se traduit comme le montrent les fig. 17 par une différence importante sur la forme des profils de vitesses, en particulier au point de recollement (fig. 17a et 17b), qui entraîne la modification de la relation fonctionnelle $\overline{H}(H)$ (fig. 17c).

Par contre l'évolution du saut des pression au recollement reste monotone (fig. 4) et la loi d'évolution des pressions est peu influencée du moins tant que C_q n'excède pas 10^{-2}.

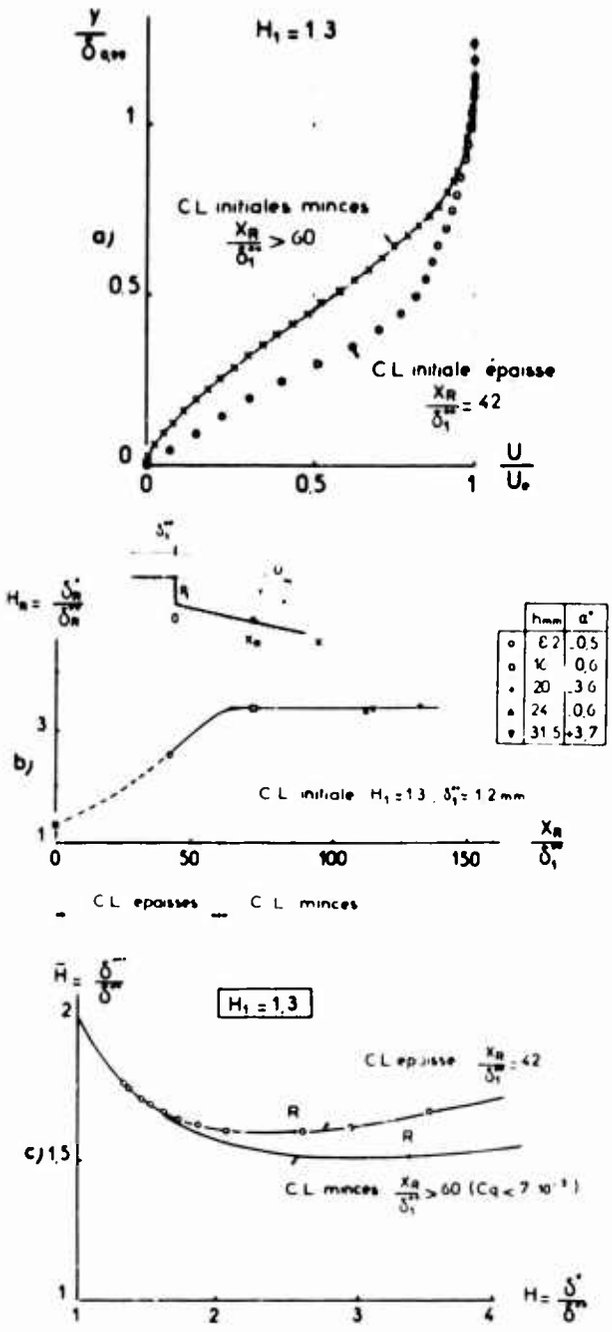

Fig. 17 - Influence de la couche limite initiale.
a) Profil de vitesse au recollement
b) Paramètre de forme H au recollement
c) Corrélation $\bar{H}(H)$.

Signalons enfin que dans le cas d'une couche limite initiale destabilisée ($H > 1,4$) les propriétés relatives aux couches limites minces établies pour $H < 1,4$ sont conservées.

c) Influence des gradients de pression normaux :

Un examen de ces effets est présenté en annexe.

3 - CALCUL DE L'ECOULEMENT.

3.1 - La connaissance de la solution de fluide parfait glissant sur la paroi suffit généralement pour estimer en première approximation l'épaisseur de déplacement δ^* de la couche limite à l'aide des équations de Prandtl. Un second calcul de fluide parfait sur cette frontière de déplacement détermine alors la pression, toute adjonction d'itérations sur δ^* n'apportant en principe que des retouches négligeables. Cette procédure qui est relative à une couche limite asymptotique régulière [14] se révèle inadéquate dès qu'apparaît une forte interaction entre couche dissipative et écoulement extérieur, comme on le constate dans des régions de décollement, de recollement, ou de couches limites rapidement déstabilisées.

Bien souvent néanmoins, l'observation des phénomènes indique que les effets dissipatifs demeurent confinés dans une couche voisine de la paroi tandis que la plus grande partie de l'écoulement conserve un comportement essentiellement non visqueux. Une solution pratique peut dans ces conditions être légitimement demandée à une analyse de type couche limite, moyennant la définition d'une structure asymptotique appropriée. Quelques éléments dégagés de l'étude expérimentale permettent de penser que, si la couche limite initiale est mince, la structure ordinaire "fluide parfait irrotationnel - couche limite de Prandtl" peut constituer une première approche raisonnable pour le calcul du recollement en aval d'une marche.

Les grandeurs étant adimensionnalisées par une vitesse et une longueur convenables, $u(x,y)$ et $v(x,y)$ désignant les composantes de la vitesse de l'écoulement potentiel $\bar{u}(x,\bar{y})$ et $\bar{v}(x,\bar{y})$ celles de la couche limite, on admet la validité dans la majeure partie du domaine d'interaction des développements habituels par rapport à l'épaisseur normalisée δ de la couche limite :

$$u(x,y) = u_0(x,y) + \delta \cdot u_1(x,y) + \dots$$
$$v(x,y) = v_0(x,y) + \delta \cdot v_1(x,y) + \dots$$
$$\bar{u}(x,\bar{y}) = \bar{u}_0(x,\bar{y}) + \delta \cdot \bar{u}_1(x,\bar{y}) + \dots$$
$$\bar{v}(x,\bar{y}) = \quad + \delta \cdot \bar{v}_0(x,\bar{y}) + \dots$$

Un effet visqueux plus intense qu'une perturbation d'ordre δ peut être obtenue en envisageant des solutions d'auto-induction où l'écoulement de base est indéterminé à l'ordre 0.

L'indétermination est levée par un appel à l'ordre suivant qui conduit à une définition implicite de δ^*, $[u = u_0]$, $[v = v_0 + \delta v_1]$.

Pour une paroi $y = 0$:

$$(1) \quad \lim_{\bar{y}\to\infty} \{\bar{u}(x,\bar{y})\} = u(x,0)$$

$$(2) \quad \frac{d\delta^*}{dx} + \frac{\delta^*}{u(x,0)} \cdot \frac{du(x,0)}{dx} = \frac{v(x,0)}{u(x,0)}$$

La résolution de ce problème, introduite par Crocco et Lees [19] a été abondamment utilisée en supersonique [20] [21] [22] et plus récemment en transsonique par Klineberg et Steger [23]. Nous utiliserons toutefois (2) sous la forme équivalente :

$$(3) \quad \frac{d\delta^*}{dx} = \frac{v(x,\delta^*)}{u(x,\delta^*)} \qquad u(x,\delta^*) = u(x,0)$$

de préférence à la forme utilisée par les précédents auteurs :

$$(4) \quad \frac{d\delta^*}{dx} - \frac{\delta - \delta^*}{u(x,\delta)} \frac{du(x,\delta)}{dx} = \frac{v(x,\delta)}{u(x,\delta)}$$
$$u(x,\delta) = u(x,0)$$

pour des raisons dictées par l'expérience (Annexe). Dans le cas présent, la recherche de la solution sera grandement facilitée par la connaissance d'une loi empirique constituant une approximation suffisante de $u(x,0)$ dans la zone décollée, et conduisant à la procédure que nous allons maintenant examiner.

3.2 - Calcul de la couche dissipative.

Le caractère nécessairement itératif de la résolution numérique du problème implicite défini par (1) et (2), et le souci de construire un moyen de calcul assez rapide ont amené à sélectionner les méthodes les plus simples possibles.

Hors du bulbe de décollement, les couches dissipatives seront décrites par une méthode intégrale.

Dans la région décollée, l'existence pour la pression pariétale d'une loi de corrélation empirique à un paramètre $\left(\frac{p-p_1}{p_R-p_1} = f\left(\frac{x}{x_R}, \theta_R\right)\right)$ constitue un moyen sûr de construire $u(x,0)$, et de définir avec précision l'épaisseur de déplacement après calcul du champ potentiel. L'usage de cette loi de corrélation, établie dans des variables normalisées, nécessite la connaissance de la longueur x_R du bulbe ainsi que du niveau de recompression $\frac{p_R-p_1}{q_1}$ entre le culot et le point de recollement. Une seconde loi expérimentale sera introduite pour relier ce niveau à l'état de la couche limite initiale (fig. 4) tandis que x_R sera déterminé par le calcul lui-même.

La méthode intégrale est construite en faisant l'hypothèse que les grandeurs caractéristiques de la couche limite (épaisseurs, paramètres de forme, etc....) ne dépendent que des deux inconnues principales, vitesse $V(x)$ et épaisseur de déplacement $\delta^*(x)$, et d'un seul paramètre auxiliaire qui est le paramètre de forme usuel $H(x)$. Les données expérimentales ont montré que cette hypothèse convient à deux conditions :

a)- la couche limite avant décollement doit être mince. Les profils de vitesse moyenne dans la région de calcul forment alors une famille de profils à un paramètre sensiblement confondue avec celle des couches limites lentement destabilisées et on dispose des relations permettant de définir tout paramètre de forme en fonction de l'un d'eux.

b)- il faut retenir pour équation auxiliaire celle de l'énergie cinétique du mouvement moyen pour les raisons indiquées § 2.3.3.

Ajoutons que la loi de Ludwig-Tiellman est adoptée pour le frottement pariétal, son influence sur l'écoulement dans la région de recollement étant d'ailleurs minime.

Soit $\theta(x)$ la direction de l'écoulement potentiel au niveau de la frontière de déplacement. Le problème consiste à déterminer les quatres inconnues $\delta^*(x)$, $V(x)$, $\theta(x)$, $H(x)$

On dispose des trois équations différentielles globales de continuité, de quantité de mouvement et d'énergie cinétique :

$$(5)\begin{cases} \dfrac{d\delta^*}{dx} = \operatorname{tg}\theta \quad (a) \\ \dfrac{1}{\delta^*}\dfrac{d\delta^*}{dx} + (H+2)\dfrac{dLogV}{dx} - \dfrac{1}{H}\dfrac{dH}{dx} = \dfrac{H}{\delta^*}\dfrac{Cf}{2} \\ \bar{H}(H-1)\dfrac{dLogV}{dx} - \dfrac{d\bar{H}}{dH}\dfrac{dH}{dx} = \dfrac{H}{\delta^*}\left(\bar{H}\dfrac{Cf}{2} - 2\Phi\right) \quad (c) \end{cases}$$

avec les définitions : $\delta^* = H\,\delta^{**}$

$\delta^{**} = \bar{H}\,\delta^{***}$ épaisseur d'énergie cinétique

$\Phi = \dfrac{1}{\rho V^3}\int_0^\delta \tau\,du$ fonction de dissipation

On dispose en outre des relations empiriques auxilaires :

$$\begin{cases} \Phi = \Phi(H) \\ \bar{H} = \bar{H}(H) \\ Cf = \dfrac{0.246}{\mathcal{R}_{\delta^*}^{0.268}}\, 10^{-0.678H} \end{cases}$$

Le système est fermé par une relation fonctionnelle $\mathcal{R}\{V(x), \theta(x)\}$ exprimant que V et θ sont effectivement le module et la direction de la vitesse dans l'écoulement potentiel le long de la ligne de courant $\delta^*(x)$.

Le caractère elliptique de $\mathcal{R}(V,\theta)$ impose une solution itérative consistant en une succession de calculs potentiels et de calculs de couche limite, l'inconnue principale de $\mathcal{R}$ pouvant être soit $V(x)$ soit $\theta(x)$.

Dans le premier cas, $V(x)$ étant supposé connu par $\mathcal{R}$, les inconnues principales de (5) sont alors δ^*, H, θ. L'examen de ce système, une fois les termes en $\frac{dLogV}{dx}$ placés au second membre montre qu'une singularité apparaît lorsque $\frac{d\bar{H}}{dH} = 0$. Cette circonstance se produit au voisinage immédiat du point de recollement, $H \simeq 3$, et nous remarquerons que l'équation (5c) se réduit alors à :

$$(5d)\quad \left[\delta^* \frac{dLogV}{dx}\right]_R = \left[\frac{-2\Phi H}{\bar{H}(H-1)}\right]_R \text{ puisque } Cf \simeq 0$$

relation simple entre δ^*_R et $\left[\frac{dLogV}{dx}\right]_R$ dès que les valeurs de Φ, H et $\bar{H}$ sont connues. Klineberg et Steger [23] [24] ont montré que cette difficulté n'est pas intrinsèque au problème couplé, mais est artificiellement introduite par l'adoption d'un calcul de couche limite à vitesse $V(x)$ imposée. Ce mode de calcul, qualifié de direct ne doit donc être considéré comme le procédé adéquat que lorsque l'interaction visqueuse est faible.

Par contre, dans les régions où l'interaction visqueuse est forte, on choisira pour inconnues principales de (5) δ^*, H, V, l'évolution $\theta(x)$ étant cette fois demandée à $\mathcal{R}$. On est alors ramené au système suivant :

$$(6)\begin{cases} \dfrac{d\delta^*}{dx} = \operatorname{tg}\theta \quad (a) \\ \delta^*\dfrac{dH}{dx} - \delta^* H(H+2)\dfrac{dLogV}{dx} = H\left(\operatorname{tg}\theta - H\dfrac{Cf}{2}\right) \quad (b) \\ \delta^*\dfrac{d\bar{H}}{dH}\dfrac{dH}{dx} - \delta^*\bar{H}(H-1)\dfrac{dLogV}{dx} = H\left(2\Phi - \bar{H}\dfrac{Cf}{2}\right) \quad (c) \end{cases}$$

qui n'est singulier que si $\delta^* = 0$, situation exclue pour les régions considérées. Cette procédure, qualifiée d'inverse, présente de plus l'avantage d'autoriser la substitution d'une loi empirique de vitesse $V(x)$ au système intégral (6), toutes les fois que c'est nécessaire ou commode. Cette facilité sera exploitée dans la région du bulbe de décollement qui ne peut être traitée dans sa totalité par les équations (6) (fig. 18).

On notera enfin que le système inverse (6) calcule $\operatorname{Log} V(x)$ à partir de $\theta(x)$ par une intégration tandis que le système direct (5) déterminait $\theta(x)$ d'après $\operatorname{Log} V(x)$ au

moyen d'une dérivation. Le calcul de l'écoulement potentiel attribuant un rôle symétrique aux fonctions Log V et θ, le mode inverse introduit un effet de lissage intéressant sur le plan numérique dont la contre-partie est un effet de dérive risquant de compromettre son utilisation sur des régions étendues, spécialement si l'interaction visqueuse est faible.

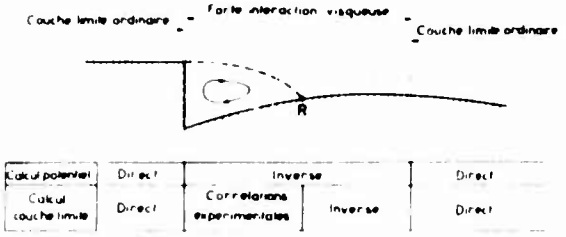

Fig. 18 - Domaines de calcul du recollement.

3.3 - Calcul de l'écoulement potentiel.

L'écoulement non visqueux, plan, incompressible et irrotationnel admet une vitesse complexe dont le logarithme $U = \text{Log}|V| - i\,\theta$ est une fonction analytique de $(x + iy)$ sur un domaine borné inférieurement par la frontière de déplacement, et limité éventuellement par une paroi supérieure quelconque.

Substituant à la variable physique $(x + iy)$ le potentiel complexe $(\varphi + i\,\psi)$, on se ramène à un domaine simple : $0 < \psi < \text{cste}$. Une transformation conforme applique enfin cette bande sur un demi-plan où la fonction analytique U est étudiée.

L'adoption d'un processus de couplage en mode tantôt direct, tantôt inverse (fig. 18) conduit pour U à un problème à données mixtes sur la frontière, tantôt θ tantôt V, de type Volterra. Sa résolution dans le demi-plan, pour laquelle on renvoit à [25] se ramène à celle d'un problème de Dirichlet pour l'équation de Laplace et par suite à des quadratures.

3.4 - Mise en oeuvre de la solution complète.

L'utilisation dans la région du bulbe d'une loi de pression empirique normalisée par une échelle longitudinale x_R inconnue à priori conduit à satisfaire la condition de couplage en deux étapes.

Dans une première étape, x_R est arbitrairement fixé. La solution couplée est alors obtenue au terme d'un algorithme numérique adapté au découpage représenté sur la fig. 18. Désignant par V_i et θ_i les valeurs discrétisées des fonctions inconnues $V(x)$ et $\theta(x)$, on itère sur le vecteur composite ξ :

$$\xi = \begin{cases} \xi_i = \theta_i & \text{dans les régions de calcul direct} \\ \xi_i = V_i & \text{" " " inverse} \end{cases}$$

Le problème est écrit sous la forme implicite :

$$\xi_i = \mathcal{F}_i(\xi_j)$$

où $\mathcal{F}$ désigne l'opérateur qui consiste à appliquer successivement un calcul potentiel et un calcul de la couche dissipative. Le schéma itératif habituel :

$$\xi^{n+1} = \mathcal{F}(\xi^n)$$

se révèle insuffisant. La convergence est obtenue en introduisant une sous relaxation assez importante :

$$\xi^{n+1} = \xi^n + \omega\left[\mathcal{F}(\xi^n) - \xi^n\right]$$

La difficulté d'analyse de l'opérateur $\mathcal{F}$ amène à choisir pour ω une constante scalaire réelle $0 < \omega < 1$ susceptible de satisfaire aux conditions de convergence :

$$|1 - \omega(1 - \lambda_k)| < 1$$

où les λ_K sont les valeurs propres de la matrice jacobienne $\left(\frac{\partial \mathcal{F}_i}{\partial \xi_j}\right)$

la valeur de ω déterminée par tâtonnements est de l'ordre de 0,15.
L'étape finale consistera à déterminer l'échelle x_R qui convient.

Au total, l'organisation du calcul complet est schématisée sur la fig. 19. L'initialisation du vecteur ξ est nécessaire pour amorcer l'algorithme précédent. En ce qui concerne V(x), le choix de la longueur x_R et du paramètre θ_R assure sa définition à l'intérieur du bulbe. A l'extérieur, l'évolution $V(x)$ est approchée par une loi d'aire s'il s'agit d'un canal, par une vitesse constante si l'écoulement est illimité. La loi $\theta(x)$ est estimée à partir de la direction de la paroi elle-même.

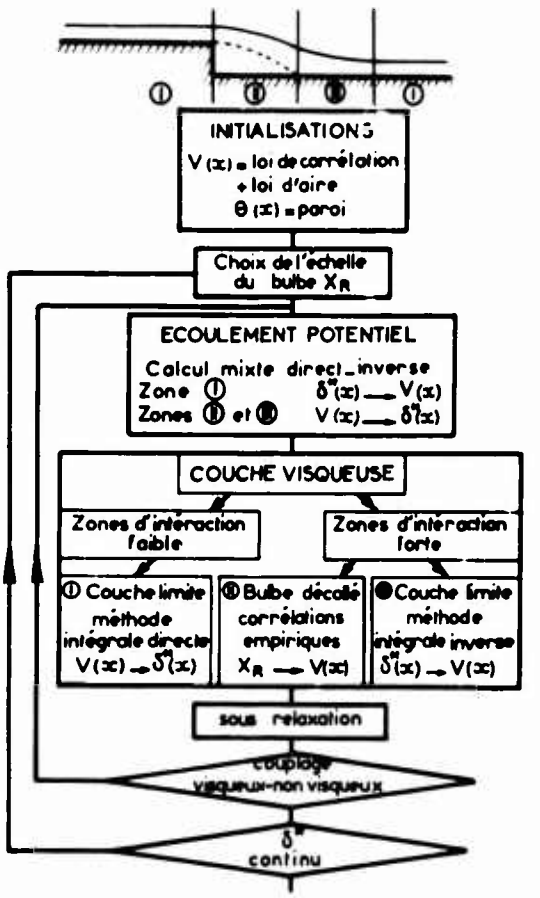

Fig. 19 - Organigramme schématique du calcul du recollement.

Au cours de la boucle d'itération interne qui correspond à l'étape intermédiaire où la longueur x_R est arbitraire, le calcul visqueux est interrompu dans le domaine II, ce qui impose pour reprendre l'application de la méthode intégrale en aval de R la définition de conditions initiales en ce point. La connaissance de H_R et de $\left[\frac{d\,\text{Log}\,V}{dx}\right]_R$ fixe δ^*_R en vertu du système différentiel (5). Choisissant $H_R = 3$, on obtient explicitement δ^*_R de la relation (5d) qui s'écrit alors :

$$\delta^*_R \cdot \left[\frac{d\,\text{Log}\,V}{dx}\right]_R = \left[\frac{-2\,\phi_H}{H(H-1)}\right]_{H=3} \approx 0{,}018$$

Au terme de cette boucle d'itérations, on dispose donc, pour une valeur de x_R arbitrai-

rement fixée, de deux lois $\theta(x)$, $v(x)$ satisfaisant des conditions de couplage strictes, mais ne correspondant pas nécessairement au décrochement de paroi imposé. En effet, il est possible de définir la frontière de déplacement dans le plan physique par intégration de $\theta(x)$, et de mettre en place une paroi fictive de calcul par la connaissance de δ^*_R .

L'échelle X_R sera donc finalement ajustée afin de superposer cette paroi fictive et la paroi véritable.

3.5 - Résultats.

La durée d'un calcul complet reste modérée. L'ordre de grandeur est 7 minutes sur CII/IRIS 80 pour une discrétisation assez raffinée comprenant 100 points de calcul dont 20 dans le bulbe.

La comparaison calcul-expérience est satisfaisante pour des couches limites initiales modérément épaisses $\left[\frac{\delta}{h} < 1\right]$. La fig. 20a présente deux résultats de recollement dans un canal dont les parois sont presque parallèles.

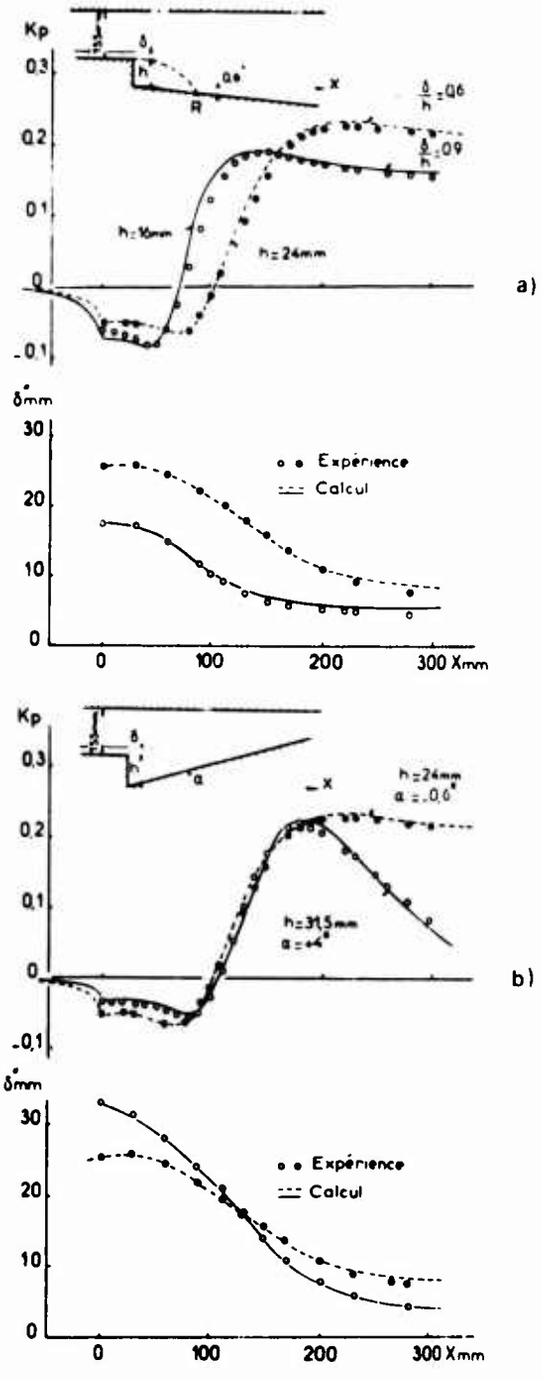

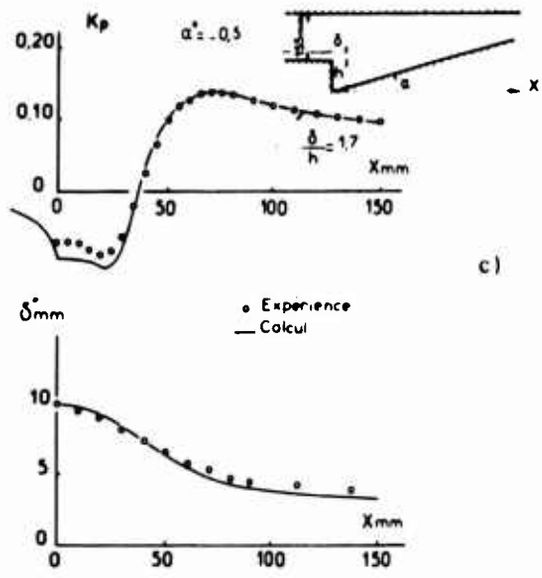

Fig. 20 - Comparaisons calcul-expérience.
a) Prédiction de l'effet de couche limite initiale
b) Prédiction de l'influence de l'écoulement potentiel
c) Cas d'une couche limite initiale épaisse.

La couche limite initiale δ est sensiblement la même et la hauteur de la marche a varié de 50%. La prévision de l'effet de la couche limite initiale, caractérisée par le paramètre δ/h est correcte tant en ce qui concerne la longueur du bulbe que le niveau de pression.

La fig. 20b illustre l'influence d'une modification sensible du champ potentiel provoqué par un changement de la géométrie du canal. Les deux configurations sont choisies pour que les effets visqueux soient similaires, c'est-à-dire que les longueurs de bulbe ainsi que les niveaux de recompression entre le culot et le point de recollement soient très peu différents. On observe une prédiction correcte de l'évolution de la pression de culot. Enfin on notera que dans tous les cas une définition satisfaisante de l'épaisseur de déplacement et du paramètre de forme de la couche limite est obtenue.

La fig. 20c montre le résultat d'une application abusive de la méthode à une configuration de couche limite initiale épaisse $\frac{\delta}{h} \simeq 1{,}7$. Dans ce cas en effet, l'universalité des fonctions empiriques utilisées est mise en défaut, en particulier pour les lois $\bar{H}(H)$ et $\Phi(H)$, et la prédiction de la pression de culot devient grossière.

4 - CONCLUSION.

Une étude expérimentale détaillée du recollement turbulent incompressible a été conduite sur un modèle bidimensionnel simple, comportant essentiellement une marche descendante de hauteur variable suivie d'une paroi de recollement rectiligne d'inclinaison réglable.

En cas de couche limite initiale mince, c'est-à-dire donnant naissance à une couche de mélange atteignant effectivement son état asymptotique avant le recollement, des lois empiriques ayant un caractère de généralité intéressant ont été dégagées pour la couche dissipative en présence d'un écoulement extérieur globalement accéléré ou ralenti :

- profils de vitesse moyenne constituant une famille à un paramètre confondue avec celle des couches d'équilibre (loi $\bar{H}(H)$).

- définition de l'évolution $\Phi(H)$ de la fonction de dissipation globale caractéristique du phénomène de restructuration et distincte de celle gouvernant les couches d'équilibre.

- répartitions de pression pariétale dans le bulbe décollé obéissant à une loi à un paramètre.

- loi de corrélation reliant le niveau de recompression entre le culot et le point de recollement avec l'état de la couche limite initiale.

La partie théorique envisage le recollement comme une interaction auto-induite entre une couche limite de Prandtl et un écoulement extérieur de fluide parfait tant que la couche limite initiale est mince. Le cas où la couche limite initiale est épaisse, nécessitant la prise en considération d'une région rotationnelle n'est pas envisagée ici.

La résolution du problème est dans son principe analogue à la méthode proposée par Klineberg et Steger [23] pour le calcul des profils transsoniques. Excepté dans les régions où l'interaction est faible, on adopte un mode de calcul inverse, la pression devenant une inconnue du calcul de couche limite. On évite ainsi l'introduction artificielle des singularités qui apparaissent au décollement et au recollement dans la résolution des équations de Prandtl à pression imposée. Cette procédure inverse permet en outre d'introduire la loi empirique d'évolution des pressions dans la région décollée.

La comparaison calcul-expérience est satisfaisante tant en ce qui concerne la prédiction des distributions de pression à la paroi, et notamment de la pression de culot, que des épaisseurs caractéristiques des couches dissipatives, pourvu que la couche limite au décollement soit modérément épaisse $\left[\frac{\delta}{h} \leq 1\right]$.

ANNEXE

INFLUENCE DES GRADIENTS DE PRESSION NORMAUX.

L'existence de gradients de pression normaux dans le domaine de décollement recollement est illustrée fig. 21 par une comparaison entre l'évolution longitudinale de la pression à la paroi et à l'ordonnée δ de la couche dissipative, pour trois configurations typiques. Ces gradients, sensiblement de même signe et de même intensité que dans l'écoulement potentiel extérieur, suivent l'évolution de la courbure des lignes de courant voisine de δ .

Abandonnant les approximations de la couche limite, mais ne retenant que les termes prépondérants, l'équation de quantité de mouvement longitudinale pour la couche dissipative peut s'écrire sous l'une des formes intégrales a/ b/ c/ de la figure 22, selon les termes négligés. La vitesse U_e est celle déduite de la pression à la frontière δ . L'intégration de ces équations différentielles pour des répartitions $U_e(x)$, $H(x)$, $\int_0^\delta [p(x)-p_e(x)]\,dy$, déduites de l'expérience conduit aux résultats présentés figure 22 où la condition initiale est fixée au point de recollement R . On constate que les valeurs expérimentales sont correctement prévues par les équations retenant les termes de gradient de pression normal (b/ et c/), et que le frottement pariétal peut être négligé (b/). Ces conclusions ne sont pas altérées si l'on transfère la condition initiale à l'abscisse X_i par exemple.

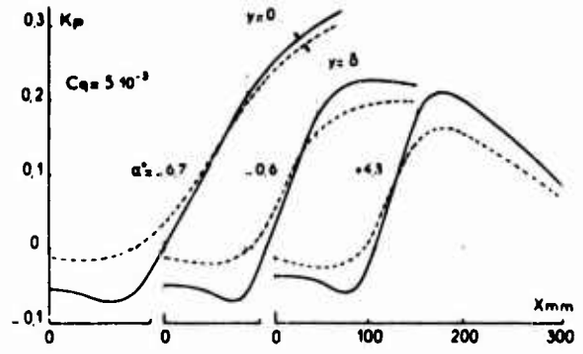

Fig. 21 - Gradients de pression normaux en aval du décollement.

a) $\frac{d\delta^{**}}{dx} + \delta^{**}(H+2)\frac{dU_e}{U_e dx} = 0$

b) $\frac{d\delta^{**}}{dx} + \delta^{**}(H+2)\frac{dU_e}{U_e dx} = \frac{1}{\rho U_e^2}\frac{d}{dx}\int_0^\delta (P-P_e)dy$

c) $\frac{d\delta^{**}}{dx} + \delta^{**}(H+2)\frac{dU_e}{U_e dx} = \frac{1}{\rho U_e^2}\frac{d}{dx}\int_0^\delta (P-P_e)dy + \frac{Cf}{2}$

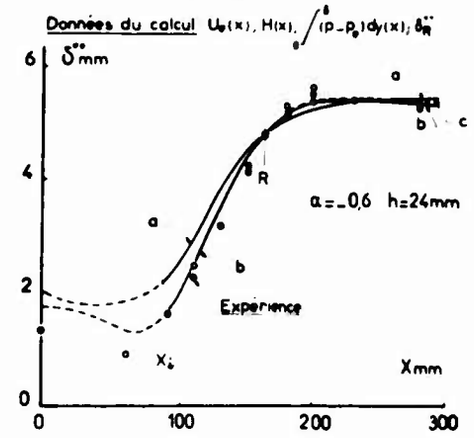

Fig. 22 - Effet du gradient de pression normal sur le calcul de δ^{**} (référence de vitesse Ue)

$\frac{d\delta^{**}}{dx} + \delta^{**}(H+2)\frac{dUp}{Up dx} = \frac{Cf}{2} \quad (\frac{dp}{dy}=0)$

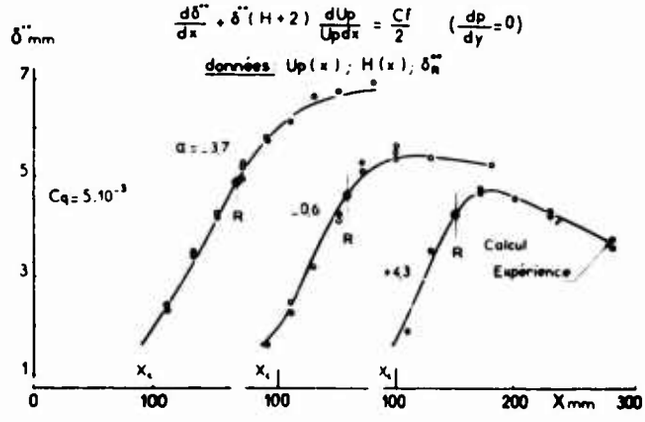

Fig. 23 - Effet du gradient de pression normal sur le calcul de δ^{**} (référence de vitesse Up).

En revanche, la prise en compte du terme de gradient de pression normal ne s'impose plus, semble-t-il, pour calculer ces couches dissipatives si, conservant la formulation habituelle de la couche limite, on définit la vitesse extérieure $U_p(x)$ à partir de la pression pariétale. Cette propriété a été vérifiée sur l'équation de Karman pour trois configurations d'écoulement ralenti ($\alpha < 0$), uniforme ($\alpha \sim 0$), ou accéléré ($\alpha > 0$) (figure 23).

Par ailleurs, le calcul du fluide parfait montre que si la ligne de courant frontière admet la même répartition de pression $p(x)$

qu'à la paroi, elle coïncide sensiblement avec la frontière de déplacement expérimentale $\delta^*(x)$. Cette seconde propriété, ajoutée à la précédente, valide un calcul couplé des deux régions fluides selon le concept habituel de l'effet de déplacement.

REFERENCES.

[1] R. Fouillot - Contribution au calcul du recollement turbulent subsonique - mémoire du CNAM Paris (Nov. 1970).

[2] M. Sirieix, J. Délery et J. Mirande - Recherches expérimentales fondamentales sur les écoulements séparés et applications. VIIIème Symposium polonais de dynamique des fluides. Tarda (Sept. 1967).

[3] A. Rosko et J.C. Lau - proceeding of the 1965 heat transfer and fluid mechanics institute (Standford University Press).

[4] P. Carriere et M. Sirieix - Facteurs d'influence au recollement d'un écoulement supersonique - 10ème congrès de mécanique appliquée Stresa (1960).

[5] M. Sirieix et J.L. Solignac - Contribution à l'étude expérimentale de la couche de mélange turbulent isobare d'un écoulement supersonique AGARD conférence Proceedings Rhode Ste Genèse (Mai 1966).

[6] F.N. Kirk - An approximate theory of base pressure in two-dimensional flow at supersonic speeds - RAE TN 2377 (Déc. 1959).

[7] E.C. Mueller, H.H. Korst, W.L. Chow - On the separation reattachment and redevelopment of incompressible turbulent shear flow. Journal of Basic engineering (Juin 1964)

[8] R. Head - Entrainement in the turbulent boundary layer - Aeronautical research concil R.M. 3152 (1958).

[9] J.E. Green - Two-dimensional turbulent reattachment as, a boundary-layer problem - RAE TR 66059 (Février 1966).

[10] R. Michel, C. Quémard et R. Durant - Application d'un schéma de longueur de mélange à l'étude des couches limites turbulentes d'équilibre. ONERA - N.T. 154 (1969).

[11] I. Tani, M. Iuchi, H. Komoda - Experimental investigation of flow separation - University of Tokyo - Report N° 364 (Avril 1961).

[12] P. Bradshaw et F.Y.F. Wong - The reattachement and relaxation of a turbulent shear layer - Journal of fluid mechanics - volume 52 part 1 (14 Mars 1972).

[13] I. Wygnanski et H.E. Fiedler - The two-dimensional mixing region Boeing scientific research laboratories D1-82-0951 (Février 1970).

[14] J. Piquet - Couplage singulier entre écoulement potentiel et couche limite turbulente - Publication ONERA N° 153 (1973).

[15] Nguyen Van Noi - Etude théorique et expérimentale du recollement subsonique incompressible d'un écoulement plan turbulent à sa frontière. Thèse présentée à la Fac. des Sciences de Paris (Janv. 1971).

[16] Stewartson K. et Williams P.G. - Self-induced separation Proc. Roy. Soc. A. 312, pp 181 - 206 (1969).

[17] Délery J. et Masure B. - Action d'une variation brusque de pression sur une couche limite turbulente et application aux prises d'air hypersoniques. La Recherche Aérospatiale N° 129 (Mars - Avril 1969).

[18] Délery J. et Le Balleur J.C. - Recherches sur l'interaction choc-couche limite turbulente. Note technique ONERA non publiée (Avril 1973).

[19] Crocco L. et Lees L. - A mixing theory for the interaction between dissipative flows and nearly isentropic streams- J.A.S. Vol. 19, N° 10 (Octobre 1952).

[20] Lees L. et Reeves B.L. - Supersonic Separated and reattaching laminar flows- I general theory and application to adiabatic boundary layer shock-vave interaction. AIAA Journal, Vol. 2, N° 10 (1964).

[21] Klineberg J.M. - Theory of laminar viscous-inviscid interactions in supersonic flow - California Inst. of Technology - Ph. D. Thesis (Mai 1968).

[22] Reyhner T.A. et Flügge-Lotz - The interaction of a Shock Wave with a laminar boundary layer Standford Univers., Div. Of Engineering Mechanics (Nov. 1966).

[23] Klineberg J.M. et Steger J.L. - Calculation of separated flows at subsonic and transonic speeds - Proceedings of the International Conference on Numerical Methods in Fluid Mechanics, Spring-Verlag, Vol. II, 1973, pp. 161-168.

[24] Klineberg J.M. et Steger J.L. - On laminar boundary layer separation - AIAA Paper N° 74-94 (Janvier - Février 1974).

[25] Jacob C. - Introduction mathématique à la Mécanique des Fluides - Gauthier-Villars, Paris (1959) pp 111-116.

THREE DIMENSIONAL DISTURBANCES IN REATTACHING SEPARATED FLOWS

G. R. Inger
Department of Aerospace and Ocean Engineering
Virginia Polytechnic Institute and State University
Blacksburg, Virginia 24061, USA

SUMMARY

Two possible causes of the pronounced periodic spanwise disturbances that have been observed in nominally two-dimensional or axi-symmetric reattaching laminar and turbulent separated flows are studied theoretically. Approximate analytical compressible small disturbance flow models for both a local vortex instability mechanism and the effect of a row of incoming streamwise vortices are set up, solved and compared with available experimental data on surface disturbance pattern, pressure and heat transfer. The results on all counts confirm the predictions of the vortex instability model. It is also shown that Reynolds analogy does not apply to the disturbance skin friction and heat transfer.

LIST OF SYMBOLS

a	Local speed of sound	γ	Specific heat ratio
B	Stagnation velocity gradient, $(du/dx)_s$	δ	Boundary layer thickness
f	Similarity solution stream function	ϵ	Small perturbation parameter
g	Total enthalpy ratio H/H_s	η	Similarity coordinate
h,H	Static and total enthalpy	λ	Spanwise wavelength of disturbance pattern
M	Mach number	μ	Coefficient of viscosity (laminar)
p,p'	Static pressure and pressure perturbation	μ_t	Eddy viscosity coefficient (turbulent)
q	Heat transfer rate	ν	Kinematic viscosity (μ/ρ)
T	Absolute static temperature	ρ	Density
u,v,w	Streamwise, normal and sidewash velocity components	τ	Shear stress
		Subscripts	
x,y,z	Streamwise coords. measured from reattachment line, distance normal to surface and spanwise distance.	e	Edge of boundary layer
		1	Perturbation values
v^*	v_1/g_o	o	Basic two-dimensional flow
α	Inverse wavelength parameter $(2\pi/\lambda)$	s,R	Stagnation line conditions
$\bar{\alpha}$	$\alpha\sqrt{\nu_{o_s}/B}$	w	Wall surface

1. INTRODUCTION

The study of separated flows and their reattachment continues to be of basic importance in a wide variety of fluid mechanics and heat transfer problems, especially in the presence of three dimensional effects. A particularly important type of three-dimensionality is that associated with the presence of vortices in the flow. In recent years, an appreciable body of evidence has accumulated showing that significant vortex-like lateral-periodic variations in shear, pressure and heat transfer occur in nominally two-dimensional reattaching separated laminar and turbulent flows under both low and high speed flow conditions [Ref. 1-9]. For example, Fig. 1 illustrates a typical such reattachment pattern downstream of a rearward-facing step in supersonic flow as observed by Ginoux[4] using a sublimating surface film technique, while Fig. 2 shows the corresponding periodic lateral total pressure variations measured in this flow.

The following major properties of these three dimensional disturbances have been observed over a wide range of Mach and Reynolds numbers in both two-dimensional and axi-symmetric reattaching flows regardless of the particular upstream cause of separation (backward facing steps, compression ramp, etc.). (a) The disturbances are laterally-periodic with a wavelength comparable to the Taylor-Görtler value of 2 to 4 boundary layer thicknesses. (b) They have a definite vortex-like structure consisting of a layer of alternating vortex pairs located roughly at the edge of the boundary layer with a maximum sidewash around the center of the layer and rapid damping near the wall surface. (c) Pronounced lateral peaks (10-25% of mean) in the pitot pressure, skin friction and heat transfer occur which are strongly correlated with each other and with the spanwise location of the vortices and which increase markedly with Mach number. (d) Provided that there is some kind of upstream streamwise vorticity disturbance, however

weak and irregular, the three-dimensional disturbances amplify and assume a characteristic well-organized form only following the occurance of reattachment.

These observations suggest two possible physical mechanisms as the cause of such disturbances. (1) The birth of vortices during reattachment due to a local disturbance mode unique to this type of flow (e.g. the Taylor-Görtler instability associated with the concave streamlines*). In this case the faint random incoming disturbances merely act as an initial "trigger" and have no significant effect on the final steady state behavior, thus giving rise to an eigenvalue problem. (2) Possible amplification during reattachment of streamwise vorticity already present in the incoming separated flow. Here, the incoming vorticity (which can be due to a variety of upstream histories such as convex streamlines in the separation region[10] or streamwise vorticity-formation from small surface shape distortions as described by Tobak[11]) is the primary forcing function of the problem.

The present paper describes the results of a theoretical investigation of three dimensional disturbances in reattaching flows and a comparison with experimental observations. Our approach is to formulate an approximate analytical flow model of reattachment and to consider within it the behavior of each of the two aforementioned vortex-like small disturbance mechanisms that might cause the observed three-dimensional effects. Solutions are obtained for each, including the effects of compressibility and heat transfer and the derivation of useful engineering expressions for the three-dimensional pressure, heat transfer and skin friction disturbances at reattachment. Typical numerical results are given and then compared with available experimental data, thereby identifying one of the theoretical models as the likely explanation of the disturbances. Finally, we conclude with a brief discussion of some recommended improvements and extensions of the present work.

2. FORMULATION OF THEORETICAL APPROACH

2.1 Assumptions

The detailed analysis of even a two-dimensional reattaching high speed flow is in itself a difficult problem (Fig. 3). Consequently, as a first step toward developing a general theory of three-dimensional effects in such flows an approximate analysis is formulated by introducing some simplifying assumptions, as follows. (1) The flow is composed of a basic two-dimensional incoming flow u_o, v_o, ρ_o, p_o, H_o plus small linearized three-dimensional steady state perturbations u', w', p', ρ', H'. Note, however, that the "parallel shear flow" model of the basic flow common to many small disturbance theories is not used since the streamwise change $(\partial u_o/\partial x)$ is very important in the present problem.[12] (2) We confine our attention to a neighborhood of the reattachment line (Region A, Fig. 3) which is small compared to both the incoming flow width and the overall scale of the reattachment region; consequently, in the leading approximation we may idealize the incoming basic flow outside the boundary layer as an infinite uniform inviscid flow undergoing a stagnation-like reattachment normal to the surface as shown in Fig. 4. We thus neglect the adverse pressure gradient effect of the overall compressive shock-boundary layer interaction on the local three-dimensional disturbance field, and the vorticity and finite width effects of the incoming shear flow. Based on contemporary studies of such high speed reattaching flows[13], these approximations are judged acceptable within a region $x \leq 10\delta$ (which is more than ample size for the present purposes) provided the flow is not hypersonic. (3) Under the presumed high Reynolds number flow conditions of interest the viscous and heat conduction effects, wherever important, are treated on the basis of boundary layer-type approximations. This is accurate unless very small disturbance wavelengths or fine scale features of the flow are of interest. (4) The laminar density-viscosity product is constant and equal to its basic flow value $(\rho\mu = \rho_o\mu_o = \rho_{wo}\mu_{wo})$ with a unit Prandtl number. (5) In the case of turbulent flow, the correlations between the disturbance field and the turbulent fluctuations are assumed negligible, thereby permitting the turbulent case to be treated as a quasi-laminar mean flow with an appropriate eddy-viscosity $\mu_{o,t}$. Moreover, by virtue of simplification (2) we can further neglect the contribution of any incoming flow turbulence to $\mu_{o,t}$ since Bearman[14] has shown that the larger turbulent scales that might so contribute attenuate strongly during stagnation, while Traci and Wilcox[15] have also indicated that the influence of such turbulence on the incoming flow can be neglected.

2.2 General Disturbance Flow Equations

Confining our attention to the immediate vicinity of the reattachment (stagnation) point and introducing the compressibility-transformed similarity variables $\eta = Y\sqrt{B/\rho_w\mu_w}$, $dY = \rho_o dy$, the basic non-adiabatic two-dimensional flow is thus self-similar and described by the relations $u_o = Bxf_o'(\eta)$, $\rho_o v_o = -\sqrt{B\rho_w\mu_w}f_o(\eta)$, $H_o = H_{os}g_o(\eta)$ with $p_o = p_{os} - (\rho_{os}B^2x^2/2)$ where $B = (du_{o,e}/dx)_s$ is the stagnation velocity gradient. The velocity and enthalpy distribution function are given by the solution to the well-known momentum and energy equations

$$f_o f_o'' + f_o'' = (f_o')^2 - g_o \tag{1}$$

$$f_o g_o' + g_o'' = 0 \tag{2}$$

subject to the boundary conditions $f_o'(\infty) = g_o(\infty) = 1$ and $f_o(0) = f_o'(0) = 1, g_{ow} = h_w/H_{os} \simeq T_w/T_{os}$ in the absence of mass transfer through the surface of given wall temperature T_w.

Using the aforementioned simplifying assumptions in the compressible Navier-Stokes equations, arbitrary steady state small three-dimensional disturbances $u'(x,y,z) = u-u_o$, $v'(x,y,z) = v-v_o$, $w = w'(x,y,z)$, $p'(x,y,z) = p-p_o$, $H'(x,y,z) = H-H_o$, $\rho'(x,y,z) = \rho-\rho_o$ are found to be governed by the set of linear equations

*The local maximum concave radii of curvature in the observed reattaching flows are ten to a hundred times larger than the minimum critical value defined by the Taylor-Görtler theory.

$$\rho_o^{-1}\frac{\partial}{\partial x}(\rho_o u' + \rho' u_o) + \frac{\partial}{\partial Y}(\rho_o v' + \rho' v_o) + \frac{\partial w'}{\partial z} = 0 \tag{3}$$

$$\frac{\partial}{\partial x}\left(u'u_o\right) + \rho_o v_o \frac{\partial u'}{\partial Y} + \left(\rho_o^{-1}\frac{\partial p'}{\partial x} - \frac{\rho'}{\rho_o^2}\frac{\partial p_o}{\partial x}\right) + \rho_o v' \frac{\partial u_o}{\partial Y} =$$

$$= \rho_{ow}\mu_{ow}\frac{\partial}{\partial Y}\left[\left(1 + 2\frac{\mu_{o,t}}{\mu_o}\right)\frac{\partial u'}{\partial Y'}\right] \tag{4}$$

$$u_o\frac{\partial w'}{\partial x} + \rho_o v_o \frac{\partial w'}{\partial Y} + \rho_o^{-1}\frac{\partial p'}{\partial z} = \rho_{ow}\mu_{ow}\frac{\partial}{\partial Y}\left[\left(1 + \frac{\mu_{o,t}}{\mu_o}\right)\frac{\partial w'}{\partial Y}\right] \tag{5}$$

$$u_o\frac{\partial H'}{\partial x} + \rho_o v_o \frac{\partial H'}{\partial Y} + \rho_o v' \frac{\partial H_o}{\partial Y} =$$

$$= \rho_{ow}\mu_{ow}\frac{\partial}{\partial Y}\left[\left(1 + \frac{\mu_{o,t}}{\mu_o}\right)\frac{\partial H'}{\partial Y} + \frac{\mu_{o,t}}{\mu_o}\left(\frac{\partial H_o/\partial Y}{\partial u_o/\partial Y}\right)\frac{\partial u'}{\partial Y}\right] \tag{6}$$

$$\frac{p'}{p_o} = \frac{\rho'}{\rho_o} + \frac{H' - u_o u'}{H_o - \frac{1}{2}u_o^2} = \frac{\rho'}{\rho_o} + \frac{T'}{T_o} \tag{7}$$

which represent disturbance field continuity, streamwise and spanwise and spanwise momentum conservation, energy and ideal gas equation of state, respectively. These equations generalize an earlier theory of three-dimensional disturbances[16] to the case of non-parallel shear flow.* The pressure disturbance is governed by the following equation derived from combining the normal momentum equation with the others:

$$\left[1 - \left(\frac{v_o}{a_o}\right)^2\right]\frac{\partial^2 p'}{\partial y2} + \frac{\partial^2 p'}{\partial x2} + \left[1 - M_o^2(x,y)\right]\frac{\partial^2 p'}{\partial x2} - M_o\left(\frac{v_o}{a_o}\right)\frac{\partial^2 p'}{\partial x \partial y} -$$

$$- 2\left\{\frac{\partial M_o/\partial y}{M_o} + \left[\frac{1-(\gamma+1)M_o^2}{\gamma}\right]\frac{v_o}{u_o}\left(\frac{\partial p_o/\partial x}{p_o}\right)\right\}\frac{\partial p'}{\partial y} -$$

$$- 2\left[\frac{\partial M_o/\partial x}{M_o} + \left(\frac{\gamma+1}{\gamma}\right)\left(1 - M_o^2\right)\left(\frac{\partial p_o/\partial x}{p_o}\right)\right]\frac{\partial p'}{\partial x} + \left(\frac{\gamma+1}{\gamma}\right)\left(1 - M_o^2\right)\left(\frac{\partial p_o/\partial x}{p_o}\right)^2 p' =$$

$$= 2\frac{\partial p_o}{\partial x}\left[\left(1-M_o^2\right)\frac{\partial w'/\partial z}{u_o} + \frac{\partial}{\partial x}\left(\frac{u'}{u_o} - \frac{T'}{2T_o}\right) + \frac{\partial(M_o^2)/\partial x}{1-M_o^2}\left(\frac{u'}{u_o} - \frac{T'}{2T_o}\right)\right] \tag{8}$$

where $M_o = u_o/a_o$ and $a_o^2 = \gamma RT_o = \gamma p_o/\rho_o$. Eq. (8) is a generalization to nonparallel flows of the well-known pressure perturbation equation for parallel-type shear flows.[16] It indicates that sizeable normal pressure gradients may occur in the present problem (as indeed will be seen below). The right hand side further shows that the pressure disturbance field is strongly coupled to the lateral velocity perturbations by the axial pressure gradient effect in the basic reattaching flow. Finally, note that the term v_o^2/a_o^2 (the Mach number squared of the flow normal to the surface) is always very small compared to unity and can hereafter be neglected.

2.3 Vortex-Instability Mechanism

As previously discussed we here imagine that a purely local instability has lead to a steady state, laterally-periodic disturbance field. In view of the stagnation-like character of the basic reattaching flow, we are thus lead to postulate the following functional forms for this field in the neighborhood of the reattachment line (neglecting terms of order x^2 compared to unity):

$$\begin{aligned}
u'(x,y,z) &= Bxu_1(\eta)\cos\alpha z \\
v'(x,y,z) &= -\sqrt{B\nu_{os}}\,v_1(\eta)\cos\alpha z \\
w'(x,y,z) &= \alpha\nu_{os}w_1(\eta)\sin\alpha z \\
p'(x,y,z) &= \rho_{os}B\nu_{os}P_1(\eta)\cos\alpha z \\
H'(x,y,z) &= H_{os}g_1(\eta)\cos\alpha z
\end{aligned} \tag{9}$$

where $\alpha = 2\pi/\lambda$ and λ is the characteristic wavelength of the laterally-periodic disturbance field. Then under the aforementioned assumptions and taking into account the basic flow relations the perturbation distribution functions u_1, v_1, etc. for a non-adiabatic compressible flow are found to be governed by

*Since $\mu_{o,t} \sim x\partial u_o/\partial y \sim x^2$ near reattachment, this term (which represents the downstream growth of boundary layer turbulence following reattachment) may be hereafter neglected in the present approximation.

the following ordinary differential equations:

$$(P_1'/g_o)' - \bar{\alpha}^2 g_o P_1 - 2\frac{(f_o'/\sqrt{g_o})'\sqrt{g_o}}{g_o f_o'} P_1' = -2\frac{\bar{\alpha}^2 g_o}{f_o'} w_1 \tag{10}$$

$$u_1 - (v_1/g_o)' + \bar{\alpha}^2 w_1 = -f_o(g_1/g_o)' \tag{11}$$

$$f_o u_1' - 2f_o' u_1 + (v_1/g_o)f_o'' + u_1'' = -g_1/g_o \tag{12}$$

$$f_o w_1' + w_1'' + g_o p_1 = 0 \tag{13}$$

$$f_o g_1' + g_1'' + g_o'\left[(v_1/g_o) - (g_1 f_o/g_o)\right] = 0 \tag{14}$$

where $\rho_1/\rho_{o_s} = -g_1/g_o^2$, $\bar{\alpha}^2 = \alpha^2\nu_{o_s}/B$ and a prime here denotes differentiation with respect to η. To this order of approximation, only the x-component of disturbance vorticity $\zeta' = (\partial w'/\partial y) - (\partial v'/\partial z) = \bar{\alpha}B[g_o^{-1}(dW_1/d\eta) - V_1]\sin\alpha z$ is significant; hence the disturbance field is connected with vortices parallel to the wall that develop in the turning reattachment flow. Eqs. (11)-(13) resemble those previously derived for the vortex-disturbance problem in incompressible stagnation point flow[12]; the present formulation, however, extends the theory to high speed laminar or turbulent flow by including the compressibility and heat transfer effects plus an explicit equation for the corresponding pressure changes. Note that the pressure and sidewash velocity perturbations are intimately coupled, but are independent of the other disturbances.

The appropriate wall boundary conditions on these equations require zero slip, no mass transfer and a fixed surface temperature and hence that $u_1 = v_1 = w_1 = g_1 = dP_1/d\eta = 0$ as $y \to 0$. On the other hand, when the disturbances are presumed to originate during the act of reattachment process itself they must all vanish far from the body, giving a set of outer boundary conditions which are also homogeneous: $u_1(\infty) = v_1(\infty) = w_1(\infty) = g_1(\infty) = P_1(\infty) = 0$. Thus we get an eigenvalue problem where non-trivial disturbance solutions exist only for certain values of α, as discussed below. Once these solutions are found, their gradients can be used to evaluate the streamwise and lateral wall shear stresses, respectively, as follows:

$$\tau_{w,x} = \mu_{o_w}\left(\frac{\partial u_o}{\partial y} + \frac{\partial u'}{\partial y}\right)_w = \rho_{o_s}\sqrt{\nu_{o_s}\beta^3}\, x\left[F_o''(0) + u'(0)\cos\alpha z\right] \tag{15A}$$

$$\tau_{w,z} = \mu_{o_w}\left(\frac{\partial w'}{\partial y}\right)_w = \rho_{o_s} B\, o_s \bar{\alpha} w_1'(0)\sin\alpha z \tag{15B}$$

while the corresponding first order approximation to the surface heat transfer at reattachment is

$$\dot{q}_w = \rho_{os}\sqrt{\nu_{o_s} B}\, H_{s_o}\left[g_o'(0) + g_1'(0)\cos\alpha z\right] \tag{16}$$

2.4 Forced Disturbance Model

The alteration of incoming vorticity in a stagnation-like reattachment flow has been studied previously for the case where the vortex filaments are parallel to the x axis, i.e., parallel to the basic flow streamlines near the boundary[17] and also when the filaments are perpendicular to the plane of the basic flow[18]. However, no consideration has apparently yet been given to the presence of streamwise vorticity in the incoming flow, although in fact this case is often encountered in practice[19] and may be an alternative source of three-dimensional reattachment disturbances.

As a representative model of such incoming streamwise disturbances, we consider the case of a row of discrete counter-rotating vortex pairs lying in the y-z plane, their (small) amplitude ε and spacing being regarded as known. Far from the reattachment surface, these vortices induce a two-dimensional adiabatic velocity disturbance field given by the Biot-Savart law† as

$$u'(x, y \to \infty, z) = \varepsilon\, G(x,z)\cosh\alpha z \sin\alpha z \tag{17}$$

$$v'(x, y \to \infty, z) = 0$$

$$w'(x, y \to \infty, z) = -\varepsilon\, G(x,z)\sinh\alpha x \cos\alpha z \tag{19}$$

---

†Although this point is often ignored in studies of vortices outside boundary layers[19], it is important that the assumed mathematical disturbance form satisfy Biot-Savart if it truly pertains to actual vortices (rather than simply being "vortex-like").

where $G(x,z) = (\cosh^2 \alpha x - \cos^2 \alpha z)^{-1}$. The functional character of these relations and some preliminary study then lead us to postulate the following expressions for the resulting disturbance field near the surface:

$$u'(x,y,z) = \varepsilon\, U_1(\eta)\, G(x,y) \cosh \alpha x \sin \alpha x \tag{20}$$

$$v'(x,y,z) = \varepsilon\, \alpha \sqrt{\nu_{os}/B}\, V_1(\eta) \sinh \alpha x\, (\cosh^2 \alpha x + \cos^2 \alpha z) G^2(x,z) \sin \alpha z \tag{21}$$

$$w'(x,y,z) = -\varepsilon\, W_1(\eta)\, G(x,y) \sinh \alpha x \cos \alpha z \tag{22}$$

$$p'(x,y,z) = \varepsilon\, \rho_{o_s} Bx P_1(\eta) \csc \alpha z \tag{23}$$

$$H'(x,y,z) = \varepsilon\, H_{s_o} x H_1(\eta) \sinh \alpha x\, (\cosh^2 \alpha x + \cos^2 \alpha z)\, G^2(x,z) \sin \alpha z \tag{24}$$

Substituting these relationships into the small disturbance equations and using the previously-discussed basic flow relations and simplifying assumptions yields the following perturbation distribution function equations:

$$dP_1/d\eta = 0 \tag{25}$$

$$U_1 - W_1 - (V_1/g_o)' = 0 \tag{26}$$

$$f_o U_1' - f_o' U_1 + U_1'' = g_o P_1 \tag{27}$$

$$f_o W_1' - f_o' W_1 + W_1'' = g_o P_1 \tag{28}$$

$$f_o H_1' - f_o' H_1 + H_1'' = (g_o'/g_o)\alpha\, V_1/B \tag{29}$$

Evidently the induced velocity field of these vortices causes no normal pressure gradient, at least to first order.

As in the previous disturbance model, the wall boundary conditions are homogeneous: $U_1(0) = V_1(0) = W_1(0) = H_1(0) = 0$. However, when streamwise vortices are present in the incoming flow, the outer boundary conditions far from the surface are non-homogeneous; taking into account Eqs. (17)-(19), they are $U_1(\infty) = W_1(\infty) = 1$, $V_1(\infty) = H_1(\infty) = 0$ and $P_1(\infty) = -1$. Solutions of Eqs. (25)-(29) are thus possible for all values of α.

3. ANALYTICAL RESULTS

3.1 Vortex Instability Model

To assist their numerical solution a detailed analytical study of Eqs. (10)-(14) was made to determine the inviscid asymptotic solution behavior outside the viscous boundary layer ($\eta \geq 4$-5) where $f_o' = g_o = 1$. This analysis, which is described in Reference 22, indicates that the disturbance vorticity and normal velocity decay algebraically like $f_o^{-1} \sim (\eta-k)^{-1}$ leading to an $(\eta-k)^{-2}$ decay of both the pressure and sidewash, whereas the corresponding streamwise velocity u_1 and energy disturbance g_1 are exponentially small. Using these results in conjunction with a standard Runge-Kutta integration routine, numerical solutions of the two point eigenvalue problem were obtained by a straightforward "guess-and-shoot" method. From the investigations of Kestin and Wood[20] and of Weiss[21], we expect that our underlying assumption of effectively-infinite width for the incoming reattaching flow will result in solutions throughout a finite band of $\bar{\alpha}$ between zero and a value on the order of unity rather than for a single $\bar{\alpha}$ eigenvalue. This was indeed found to be the case: a continuum of eigensolutions was found to exist only for $0 \leq \alpha \leq \alpha_{max}$, where $\bar{\alpha}_{max}$ is unity for adiabatic walls and increases slightly with increasing wall cooling ($T_w/T_{s_o} < 1$) as shown in Fig. 5.

A representative set of disturbance field profiles across the reattachment region is shown in Fig. 6 for a typical value of $\bar{\alpha} = 2/3$ on a cooled wall. Additional results for other $\bar{\alpha}$, g_w combinations can be found in Appendix B of Ref. 22. It is seen that the spanwise disturbance velocity vanishes and changes sign around $\eta = 3.4$ (which is slightly outside the basic reattachment flow boundary layer), indicating the presence of the vortex core at this level. The effects of viscosity and heat conduction on the disturbance field become important about half-way into the basic boundary layer thickness ($y \leq 1/2\beta_o$) and serve to damp out the perturbations. A significant lateral pressure drop occurs owing to the suction associated with the vortices, most of this developing in the "inviscid disturbance" region.

From such results, the detailed disturbance flow structure can be constructed and it is seen to involve pairs of counter-rotating vortices which develop along the basic two-dimensional flow streamlines as they turn and become parallel to the surface during reattachment (see Fig. 7). The cores of these vortices ultimately stand parallel to the surface outside the basic flow boundary layer as mentioned above. The corresponding spanwise disturbance flow streamline pattern very near the surface is also sketched in Fig. 7 and is seen to inline similar to the alternating node-saddle point pattern suggested in Ref. 23.

Practical engineering relations for the prediction of important physical quantities such as pressure, shear stress and heat transfer at the wall are directly forthcoming from the equations of the present analysis and the tabulated values of $P_1(0)$, $w_1'(0)$, etc. From Eq. 9, for example, the spanwise pressure variation along the reattachment line is

$$p_w'(z) = \rho_{o_s} P_1(0) \cos\left(\bar{\alpha} z \sqrt{B/\nu_{o_s}}\right) \tag{30}$$

where values of $P_1(0)$ are tabulated in Table 1. This pressure fluctuation has a wavelength on the order of the basic boundary layer thickness δ_o since $\delta_o \sim \sqrt{\nu/B}$. At $z = 0$ the negative $P_1(0)$ given by this solution indicates that the suction associated with the local vortex pair decreases the total stagnation pressure slightly. The relative heat transfer disturbance for a fixed wall temperature can be expressed from Eq. (16) by

$$\frac{\Delta q_w(z)}{q_{w_o}} = \frac{g_1'(0)}{g_o'(0)} \cos\left(\tilde{\alpha} z \sqrt{B/\nu_{o_s}}\right) \tag{31}$$

and can be quite significant in practice since $g_1'(0)/g_o'(0) \approx .2$-$.4$ for highly cooled walls (see Table 1). Since $g_1'(0)$, $p_1(0)$ and $w_1'(0)$ are all negative, the heat transfer and wall pressure perturbations are in phase with each other but 90° out of phase with the lateral shear stress disturbance (Eq. 15) which maximizes at the spanwise positions of the vortices as illustrated in Fig. 8. Reynolds analogy is clearly <u>not</u> applicable between these three dimensional heat transfer and skin friction disturbances.

Several additional features of the wall cooling effect on the vortex disturbance field are worth nothing. First, since $\alpha \sim \lambda^{-1}$ Fig. 5 shows that cooling slightly decreases the spanwise wavelength of the pattern. Second, it can be seen from Table 1 that cooling also slightly increases and decreases the wall pressure and spanwise shear stress perturbations, respectively, while strongly enhancing both the heat transfer and streamwise shear disturbances. Third, an examination of the various disturbance profile results (as summarized in Table 2) shows that the maximum sidewash height in the boundary layer (η for w'_{max}) moves inward toward the wall as a result of cooling, although with little corresponding change in the sidewash magnitude itself.

3.2 <u>Forced Disturbance Model</u>

Owing to its simpler mathematical character, several important features of this solution can be discerned by direct examination of Eqs. (25)-(29). First, because of the constant pressure (Eq. 25), Eqs. (27) and (28) plus the boundary conditions immediately show that $U_1(\eta) = W_1(\eta)$. Consequently, it is found from Eq. (26) that $V_1(\eta)$ is zero everywhere. Physically, this means that throughout the flow at reattachment the incoming vortices are simply carried straight inward toward the surface, suffering only a change in amplitude due to the combined effects of the basic flow compressibility and viscosity. The fluid mechanics of the problem thus reduces to the solution of the relatively simple uncoupled two-point boundary value problem associated with either Eq. (27) or (28). Without carrying this out in detail, however, one can estimate the qualitative character of the disturbance flow pattern near the surface which is associated with this model; the result is illustrated schematically in Fig. 9. It is obviously quite different from that associated with the vortex instability model, having a "cats-eye" appearance.

Another important feature of this disturbance mode that is readily discerned is its thermodynamic behavior. Since $V_1(\eta)$ vanishes and both the inner and outer boundary values of H_1 are zero, energy Eq. (29) yields the solution

$$H_1(\eta) = 0 \tag{32}$$

Hence in the linearized disturbance approximation the compressibility and heat transfer effects of the basic flow on the forced vortex perturbation field are zero in the absence of any normal velocity disturbances; consequently these incoming vortices cause no spanwise heat transfer perturbations along the reattachment line.

3.3 <u>Comparison with Experiment</u>

Figure 10 shows a picture of the disturbance flow pattern observed in the reattachment region following a rearward-facing step using a surface oil coating method.[5] It is seen that this experimental pattern clearly exhibits a distinct lateral periodicity of an alternating "node - saddle point" character, very similar to what is predicted by the eigenvalue vortex disturbance theory (compare Figs. 7 and 10) but completely different to the theoretical pattern associated with the non-vanishing incoming streamwise vorticity model (Fig. 9). Of the two, the former mode would thus appear to be the likely cause of the observed disturbances.

This conclusion is further strengthened by an examination of the heat transfer perturbations. Figure 11 compares the present theory with measurements made by Ginoux[4] in the reattachment region following a two-dimensional rearward-facing step on a pre-cooled model with $T_w/T_o = .30$. In marked contrast with the negligible heat transfer associated with the "forced disturbance" vortex solution, the predictions of the vortex instability theory (Eq. 31) are in excellent agreement with the experimental data. These laterally-periodic heat transfer variations are seen to be very pronounced indeed, having an amplitude of almost 40% about the mean in this example.

Another aspect of the theory that can be checked against experiment is the spanwise wavelength of the disturbance vortex pattern. The present theory and previous studies[12,15,20] suggest that the most unstable (highly amplified) disturbance corresponds to an eigenvalue around $\tilde{\alpha} = 1$. Then working back through the compressibility transformation to calculate the boundary thickness, we obtain the following theoretical estimate for λ/δ_o that depends only on the wall temperature ratio: $\lambda/\delta_o \approx 2\pi/(1.8 + .8g_{o_w})$. This result agrees with experiment on two counts. First, the prediction that λ/δ_o is essentially Mach and Reynolds number-independent is confirmed by experiments over a wide range of flow conditions. Second, the theoretical values of λ/δ_o range from 2.4 on an adiabatic wall to 3.5 on a very cold wall ($g_{o_w} \to 0$) and these are in excellent agreement with the spread of values $2 \leq \lambda/\delta_o \leq 4$ quoted as being observed in <u>all</u> the reported experimental studies.[1-9]

Another feature of interest is the velocity disturbance field. Confining attention to the immediate vicinity of the reattachment line where $u' \sim x$ and $u_o \sim x$ both vanish, the flow field consists of normal and spanwise perturbations v', w' on the incoming basic flow normal to the surface v_o. From the foregoing vortex instability theory relations for these quantities, we thus obtain the following expressions for relative magnitudes of the velocity perturbations:

$$\frac{w'}{v_o} = \frac{g_{o_w}}{g_o(n)} \frac{w_1(n)}{f_o(n)} \quad , \quad \frac{v'}{v_o} = \frac{g_{o_w}}{g_o(n)} \frac{v_1(n)}{f_o(n)} \tag{33}$$

The implications of Eqs. (33) also show a two-fold agreement with experiment, as follows. (a) Examination of the disturbance profile solutions for $\bar{a} = 1$ shows that the average location of the maximum v_1 and w_1 is $n_{max} = 1.9$. According to hot wire studies in adiabatic flows[24], the maximum velocity perturbations occur around $y/\delta = .5$ which corresponds here to an $n = 1.6$ and which roughly agrees with the aforementioned n_{max}. (b) Corresponding to n_{max} our numerical solutions and Eq. (33) yield the adiabatic wall estimates $|w'/v_o|^2 = .12$, $|v'/v_o|^2 = .64$ and these agree roughly with the value range .2-.4 for the spanwise variations in mean square hot wire signals measured by Ginoux[24] at $y/\delta = .5$.

Finally, it is possible to approximately check the pressure disturbance solution of the vortex instability model. Based on the analysis of reattachment described in the Appendix it is shown that the mean reattachment pressure is approximately proportional to the kinetic energy of the incoming stagnation like-flow v_o at the edge of the boundary layer: $P_R = K\rho_{s_o} v_o^2(\delta)/2$, where K is a constant of proportionality. Using this and the boundary layer expression for v_o, the relative static pressure perturbation near the wall at reattachment is found from Eq. (30) to be

$$\frac{p'(z)}{p_R} = \frac{2g_{o_w}^2 \; P_1(0)}{K f_o^{\,2}(n_e)} \cos(2\pi z/\lambda) \tag{34}$$

In the case of $M = 2.25$ flow past an adiabatic rear-facing step, application of data given in Ref. 24 yields the estimate $K = 9.3$ (see Appendix). Using the previously-discussed disturbance solution properties, the resulting prediction for the spanwise pressure variation is shown in Fig. 12 along with experimental data obtained from a static pressure probe survey near the reattachment line of this flow.[24] The theory is in fairly good agreement, overestimating slightly the disturbance amplitude. It is noteworthy here that the relative pressure disturbances are nearly an order of magnitude smaller than the corresponding spanwise heat transfer perturbations (compare with Fig. 11).

4. CONCLUDING DISCUSSION

The encouraging results of the present study warrant further improvement and extension of the theoretical approach in several respects. (1) The vortex instability analysis should be modified to incorporate an incoming flow of finite width, thereby leading to a single unique eigensolution. (2) Although a single row of incoming vortices in the forced disturbance model is felt to be the most likely configuration encountered in practice, a double row configuration might also be worth studying from the scientific standpoint.[26] (3) To extend it to hypersonic flow, the present two-dimensional reattachment flow model should be improved by including the effects of incoming flow vorticity and the adverse pressure gradient induced by viscous-inviscid interaction. The right side of Eq. 8 suggests that the latter may have a significant influence on the size of the three-dimensional disturbances. In this connection, there is a definite need for additional experimental data at hypersonic speeds ($M_\infty = 4 - 10$) to establish the effect of high Mach number on the magnitude and wavelength of spanwise heat transfer and pressure disturbances at reattachment. (4) Finally, since it is the heat conduction within the surface which ultimately determines its temperature response to spanwise heat transfer perturbations such as shown in Fig. 10, a theoretical study of the three-dimensional surface material response aspect (temperature and even possible ablation) analogous to the work on cross-hatching[16,27] would be useful.

REFERENCES

1. Ginoux, J., "Experimental Evidence of Three-Dimensional Perturbations in the Reattachment of a Two-Dimensional Laminar Boundary Layer at M = 2.05," Von Karman Institute TN-1, Brussels, Belgium, 1958.

2. Hopkins, E. J., S. J. Keating and A. Bandettini., "Photographic Evidence of Streamwise Arrays of Vortices in Boundary Layer Flow," NASA TN D-328, September 1960.

3. Miller, D. S., et. al, "Mach 8 to 22 Studies of Flow Separations due to Deflected Control Surface," AIAA Journal, 2. 1964.

4. Ginoux, J., "Streamwise Vortices in Laminar Flow," AGARDograph 97, 1965, Part II.

5. Roshko, A. and G. J. Thomke, "Observations of Turbulent Reattachment Behind an Axi-symmetric Downstream Facing Step in Supersonic Flow," AIAA Journal, 4, June 1966, pp. 975-980.

6. Sfeir, A., "Supersonic Flow Separation on a Backward Facing Step," University of California (Berkeley), Aero. Sci. Div. Report AS-66-18, 1966.

7. Persen, L. N., "Investigation of Streamwise Vortex Systems Generated in Certain Classes of Curved Flow," Air Force Aerospace Res. Labs. Rep. ARL68-0134, July 1968.

8. Gartling, K. K., "Tests of Vortex Generators to Prevent Separation of Supersonic Flow," University of Texas Applied Res. Lab. Rep. TR-70-44, 1970.

9. Rockwell, D.O. and J. A. Owczarek, "An Experimental Investigation of Three-Dimensionality of Wall Jet Flows," ASME Paper 72-Flcs-7, March 1972.

10. Tani, I., "Production of Longitudinal Vortices in the Boundary Layer Along a Concave Wall," Journal of Geophys. Res., 1962, 67(8), 3075-3080.

11. Tobak, M., "Hypothesis for the Origin of Cross-Hatching," AIAA Journal, 8, 1970, pp. 330-334.

12. Hämmerlin, G., "Zur Instabilitates Theroie der ebenen Staupunktströmung," 50 Jahre Grenzschichtforschung, Vieweg, braunchweig, 1955, p. 315.

13. Chow, W. L., "Recompression of a Two-Dimensional Supersonic Turbulent Free Shear Layer," in Devel. in Mechanics, Vol 6: Proc. 12th Midwestern Mech. Conf., p. 319-333.

14. Bearman, P. W., "Some Measurements of the Distortion of Turbulence Approaching a Two-Dimensional Bludd Body," Journal of Fluid Mech. 53, Pt. 3, 1972, p. 451-466.

15. Traci, R. M. and D. C. Wilcox, "Analytical Study of Freestream Turbulence Effects on Stagnation Point Flow and Heat Transfer," AIAA Paper 74-515, June 1954.

16. Inger. G. R., "Three Dimensional Heat Transfer and Ablation Disturbances in High Speed Flows," AIAA Journal, 10, 1972, pp. 1641-1646.

17. Sutera, S. P., "Vorticity Amplification in Stagnation Point Flow and Its Effect on Heat Transfer," Journal of Fluid Mech., 21, 1965, pt. 3, pp. 513-534.

18. Stuart, J. T., "Viscous Flow Near a Stagnation Point When the External Flow Has Uniform Vorticity," Journal Aero/Space Sciences, 26, 1959, pp. 124-127.

19. Fannelop, T. K., "Effects of Streamwise Vortices on Laminar Boundary Layer Flow," ASME Trans. Journal Appl. Mech., 35, June 1968, pp. 424-426.

20. Kestin, J. and R. T. Wood, "On the Stability of Two-Dimensional Stagnation Flow," Journal of Fluid Mech., 44, 1970, pt. 33, pp. 461-479.

21. Weiss, R. F., "Stability of the Stagnation Region to Three-Dimensional Disturbances," Thesis, New York University, April 1963.

22. Inger, G. R., "Three Dimensional Disturbances in Two Dimensional Reattaching Flow," VPI & SU Report Aero-011, AFOSR TR-74-0610, August 1974.

23. Ginoux, J., "Streamwise Vortices in Reattaching High Speed Flows: A Suggested Approach," AIAA Journal, 9, April 1971, pp. 759-760.

24. Ginoux, J., "On Some Properties of Reattaching Laminar and Transitional High Speed Flows," Von Karman Institute Report TN-53, Brussels, Belgium, September 1969.

25. Chang, P. F., "Separation of Flow," Pergamon Press, N. Y., 1970, pp. 570-605.

26. Gersten, K. and J. Steinheuer, "Untersuchungen im Institut fur Aerodynamik auf dem Gebiet der Grenzschictstromungen, DFL-Mitteilungen, Heft 7, 1967 (Schlicting Anniversary Vol.), 311-325.

27. Inger, G. R., "Compressible Boundary-Layer Flow Past a Swept Wavy Wall with Heat Transfer and Ablation," Astronautica Acta, 16, pp. 325-338.

ACKNOWLEDGEMENT

This work was supported by AFOSR under Grant 72-2173.

Table 1

Vortex Eigensolution Values at Wall

$\bar{\alpha}$	$P_1(0)$	$W_1'(0)$	$k_1'(0)$	$u_1'(0)$
		$Bo_w = .15$ $[g_o'(0) = .441]$		
.20	-2.313	-2.129	-0.034	-0.583
.50	-2.051	-1.465	-0.119	-2.342
2/3	-1.728	-1.176	-0.140	-3.155
1.00	-1.344	-0.876	-0.189	-5.011
1.19	-1.153	-0.743	-0.211	-5.926
		$Bo_w = .50$ $[g_o'(0) = .271]$		
.20	-2.165	-2.235	-0.027	-0.115
.50	-1.990	-1.866	-0.066	-0.495
2/3	-1.632	-1.513	-0.064	-0.668
1.00	-1.208	-1.113	-0.062	-1.043
1.09	-1.094	-1.006	-0.062	-1.115
		$Bo_w = 1.00$ $[g_o'(0) = 0]$		
.20	-2.114	-2.711	0.0	-0.019
.50	-1.959	-2.298	0.0	-0.038
2/3	-1.528	-1.863	0.0	-0.037
1.00	-1.070	-1.304	0.0	-0.036

Fig. 1

Typical Streaked Disturbance Pattern

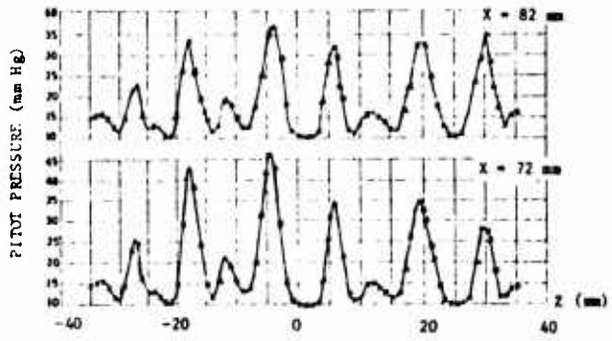

Fig. 2

Laterally-Periodic Total Pressure Variations at Reattachment (Measurements of Ginoux, M = 2.25)

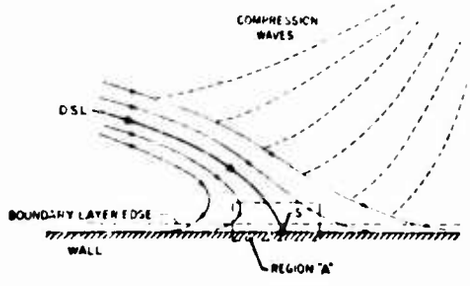

Fig. 3 Reattachment Flow Configuration

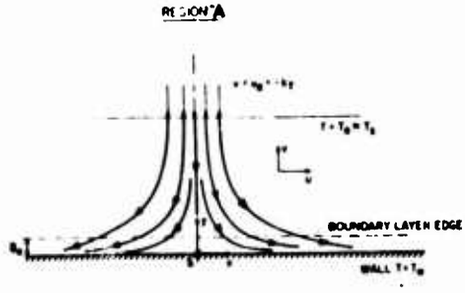

Fig. 4 Idealized Reattachment Flow Model

Fig. 5

Maximum Non-Dimensional Vortex Instability Wavelength vs. Wall Temperature Ratio

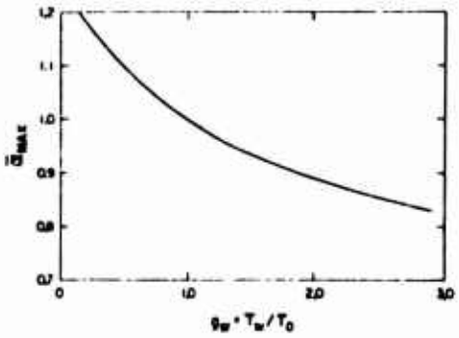

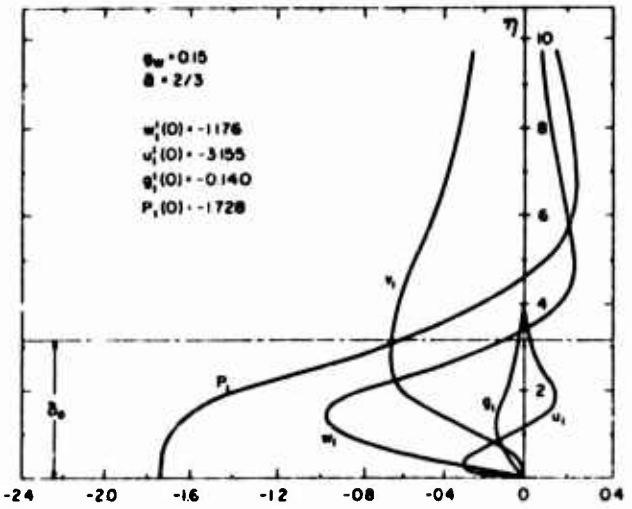

Fig. 6 Eigenvalue Disturbance Profiles Across Boundary Layer

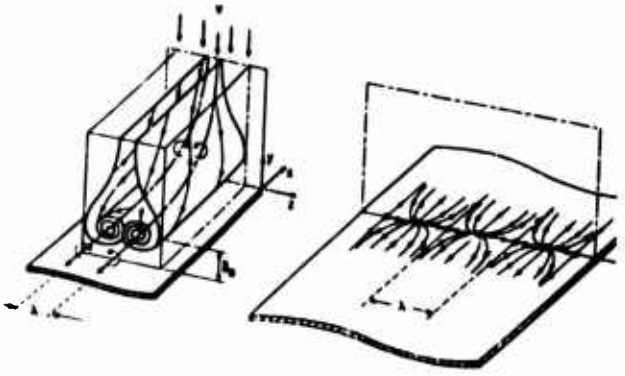

Fig. 7

Vortex-Instability Disturbance Flow (Schematic)

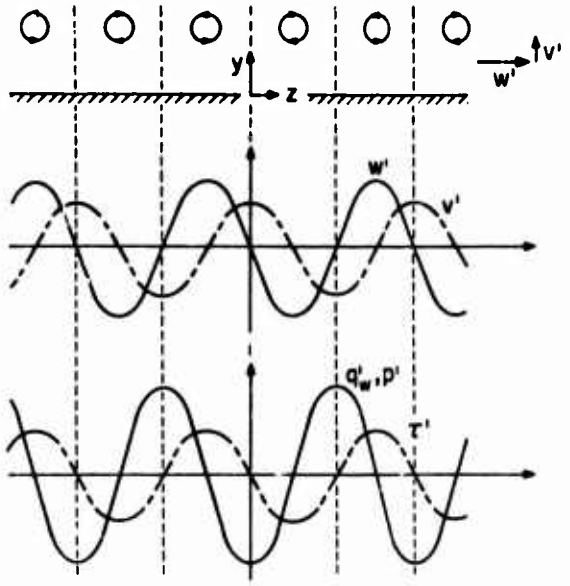

Fig. 8

Spanwise Phasing of Disturbance Field

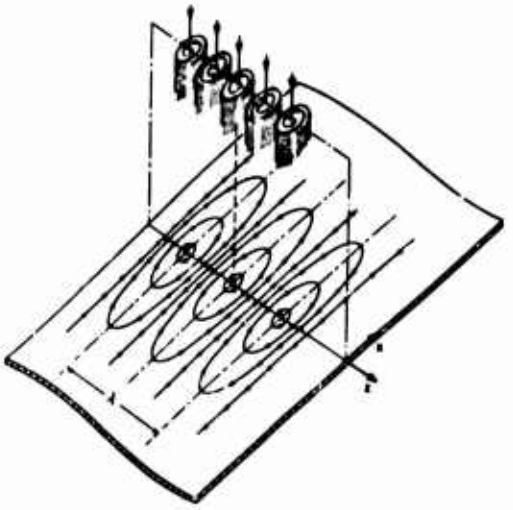

Fig. 9

Incoming Streamwise Vortex Disturbance Flow

Fig. 10

Experimental Oil Flow Visualization of Reattachment Flow Pattern (Roshko and Thomke)

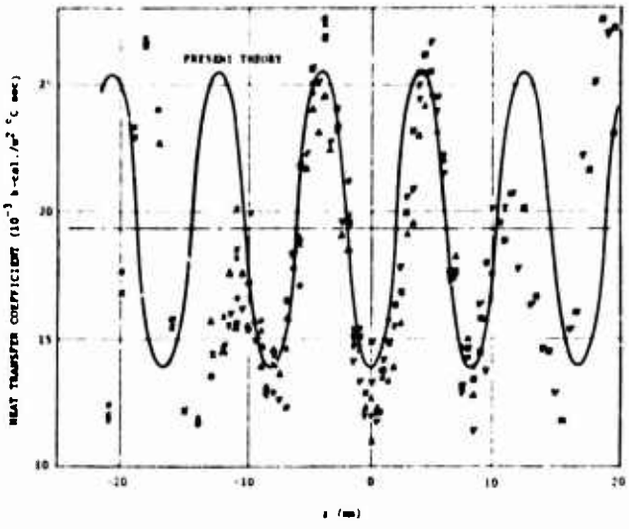

Fig. 11

Comparison of Theoretical Heat Transfer Disturbances with Experiments of Ginoux ($M = 2.25$, $T_w/T_o = .30$)

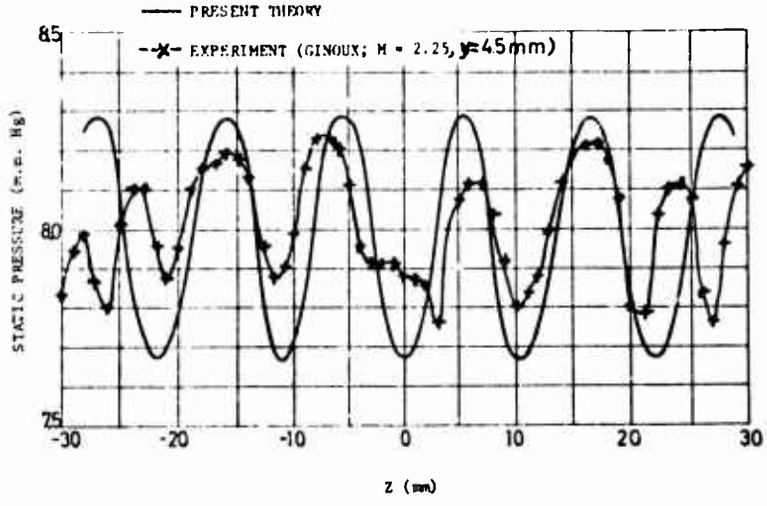

Fig. 12

Comparison of Theory and Experiment for Spanwise Static Pressure

APPENDIX

APPROXIMATE ANALYSIS OF REATTACHMENT PRESSURE FOR BASIC FLOW

We consider a separated two-dimensional shear flow reattaching to a flat surface as schematically illustrated in the accompanying sketch. The incoming flow along the dividing streamline before the compressive turning associated with reattachment is denoted by the subscript "d", while the corresponding local inviscid conditions outside the shear layer are indicated by subscript "i". This inviscid flow is in turn imagined to have been produced by isentropic expansion of some known reference flow M_∞, p_∞.

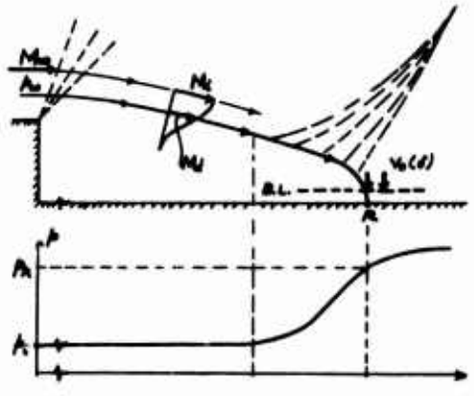

Along the dividing streamline we follow Chapman and approximate the pressure rise by an isentropic compression from $p_d = p_i$ to some pressure p_r and low speed velocity $v_o(\delta)$ (normal to the surface) just outside the boundary layer. Thus if p_{total} is the (constant) total pressure along this streamline, we have

$$p_r \simeq p_{total} - \rho_{so} \frac{v_o^2(\delta)}{2} \qquad \text{(C-1)}$$

Then introducing the reasonable assumption that the actual pressure increase $p_r - p_i$ during reattachment is some fraction β of the maximum possible pressure rise $p_{total} - p_i$,

Eq. (C-1) yields the following equation governing p_R:

$$p_r = p_i + \left(\frac{1-\beta}{\beta}\right)\frac{\rho_{so}}{2} v_o^2(\delta) \tag{C-2}$$

The parameter β can be estimated as follows. From the aforementioned assumption that $p_r - p_i = \beta(p_{total} - p_i)$ and the isentropic relationship between p_{total} and p_i, we thus get

$$\beta \approx \frac{(p_r - p_i)}{p_i}\left\{\left[1 + \left(\frac{\gamma-1}{2}\right)M_d^2\right]^{\frac{\gamma}{\gamma-1}} - 1\right\}^{-1} \tag{C-3}$$

Now following Chang[25] (p. 576, 597) we introduce the reattachment pressure ratio parameter $N \equiv (p_r - p_i)/(p_\infty - p_i)$ and the Mach number ratio $\phi \equiv M_d/M_i$, and so obtain from (C-3) that

$$\beta \approx N\left(\frac{p_\infty}{p_i} - 1\right)\left\{\left[1 + \left(\frac{\gamma-1}{2}\right)\phi^2 M_i^2\right]^{\frac{\gamma}{\gamma-1}} - 1\right\}^{-1} \tag{C-4}$$

where M_i is related to M_∞ by the isentropic relation

$$M_i^2 = \frac{2}{\gamma-1}\left\{\left(\frac{p_\infty}{p_i}\right)^{\frac{\gamma}{\gamma-1}}\left[1 + \left(\frac{\gamma-1}{2}\right)M_\infty^2\right] - 1\right\} \tag{C-5}$$

with p_i/p_∞ being a known function of M_∞ (interpreted as base pressure) as given in Ref. 24 (page 577). Generally speaking, it is found that the first term on the RHS of (C-2) is very small (1/20 to 1/30) compared to the second, and so can be neglected giving

$$p_r = K\frac{\rho_{so}}{2} v_o^2(\delta) \tag{C-5}$$

where $K \equiv (1-\beta)/\beta$

Example: for an $M_\infty = 2.25$ flow, we have from p. 577, Ref. 25 that $p_{base}/p_\infty = p_i/p = .30$ while p.576, Ref. 25 yields $\phi = .67$. Substituting into Eq. (C-4) we find a value of $\beta = .097$ so $K \simeq 9.32$; thus from C-2,

$$p_r = .3\, p_\infty + 9.32\frac{\rho_{so}}{2} v_o^2(\delta)$$

and indeed the second term is predominant, justifying approximation C-5.

Table 2

Heat Transfer Effect on Maximum Sidewash

($\bar{\alpha} = 2/3$)

g_w	r @ max w_1	$w_{1,max}$
.15	1.40	-0.94
.50	1.25	-1.02
1.00	1.15	-1.06
2.00	0.90	-1.00

AN EXPERIMENTAL INVESTIGATION OF THE COMPRESSIBLE TURBULENT BOUNDARY-LAYER SEPARATION INDUCED BY A CONTINUOUS FLOW COMPRESSION

Robert L. P. Voisinet
Naval Surface Weapons Center
White Oak Laboratory
Silver Spring, Maryland 20910

SUMMARY

Flow-field measurements of a compressible turbulent boundary-layer separation are presented. The boundary layer chosen for investigation was formed on the nozzle wall of the Naval Surface Weapons Center (NSWC) Boundary Layer Channel. A continuous compression of the nozzle flow was imposed on the thick nozzle-wall boundary layer to produce a streamwise pressure rise of sufficient strength to cause separation. This manner of separating the boundary layer produced a separated flow field which was free of incident shock waves, wall discontinuities, and wall curvature.

Tests were conducted at an adiabatic-wall condition, for a nominal initial Mach number of 4.9, and Reynolds numbers based on initial boundary-layer thickness from 1.4×10^5 to 1.4×10^6. Comprehensive flow-field measurements included wall static-pressure distributions, boundary-layer surveys of static pressure, Pitot pressure and stagnation temperature, wall shear-stress distributions and wall heat-transfer measurements throughout the entire region of interaction.

The effects of Reynolds number on the separation phenomena are presented. For Reynolds numbers below $8. \times 10^5$ the separation length was found to increase with increasing Reynolds number, whereas for Reynolds numbers above $8. \times 10^5$ the reverse trend was observed. This reversal in the separation length versus Reynolds number trend was consistent with the reversal observed for incipient separation versus Reynolds number correlations.

NOTATION

C_f	-	skin-friction coefficient
d	-	diameter of skin-friction balance sensing element
h	-	heat-transfer coefficient $q/(T_w-T_{aw})$
M	-	Mach number
P	-	pressure
r_f	-	recovery factor
Re/ft	-	unit Reynolds number per foot = $\rho_e u_e/\mu_e$
Re_δ	-	Reynolds number based on δ
t	-	thickness of skin-friction balance sensing element
T	-	temperature
u	-	velocity
u_τ	-	shear velocity = $\sqrt{\tau_w/\rho_w}$
u*	-	Van Driest transformed velocity (Eqn. 1)
x	-	distance along test plate from nozzle throat
y	-	distance normal to test plate
δ	-	boundary-layer thickness
δ^*	-	displacement thickness
θ	-	momentum thickness
μ	-	dynamic viscosity
ν	-	kinematic viscosity
ρ	-	density
τ	-	shear stress

Subscripts

aw	-	adiabatic-wall conditions
e	-	boundary-layer edge conditions
I	-	conditions at start of interaction
inc	-	incipient separation conditions
o	-	tunnel supply conditions
oil	-	determined from oil flow
PK	-	peak pressure-rise conditions
PP	-	determined by Preston probe
R	-	reattachment conditions
S	-	separation conditions
t	-	stagnation conditions
w	-	wall conditions

Superscripts

'	-	"ideal" properties calculated from P, P_t, T_t

1. INTRODUCTION

Compressible turbulent boundary-layer separation is a phenomenon of such complexity that its analysis has been primarily empirical in nature. The need for experimental data has been great and continues to grow with each new theory and numerical technique which is introduced. However, the requirement is not only for more data but for more comprehensive data. With this objective in mind, an experimental investigation was conducted for the purpose of obtaining more comprehensive measurements of a separated flow field with particular attention given to the evaluation of the boundary-layer flow structure and its interaction with the external flow field. A thick nozzle-wall boundary layer was chosen for investigation in order that detailed measurements could be obtained for a large-scale interaction.

Tests were conducted at an adiabatic-wall condition for a nominal Mach number of 4.9. The Reynolds number, the only parameter systematically varied in the tests, ranged from 1.4×10^5 to 1.4×10^6. Data in this Reynolds number range are of particular interest because they lie between the comprehensive low Reynolds number data of Kuehn[1] and high Reynolds number data of Thomke and Roshko.[2]

The boundary-layer separation was accomplished by imposing a continuous compression of the nozzle flow onto the boundary layer so as to produce a continuous streamwise pressure rise of sufficient magnitude to cause separation. This technique of separating the boundary layer differs from shock-induced separations in that the incident compression is isentropic and occurs over a finite distance. Curved ramp models produce similar isentropic compressions; however, longitudinal curvature effects are present in these configurations. The present test provided for a separated flow field which was free of incident shock waves, wall discontinuities and wall curvature. Presumably, the analytical modeling of such a flow would be simplified because of the elimination of these factors.

2. EXPERIMENTAL SETUP AND TEST CONDITIONS

The experiment was performed in the NSWC Boundary Layer Channel[3] shown in Figure 1. The two-dimensional supersonic half nozzle, the main component of the facility, has for one wall a flat test plate, eight feet long and twelve inches wide, along which the boundary-layer measurements were made. The test plate boundary layer developed naturally along the smooth flat nozzle wall to a thickness of between two and three inches. This boundary-layer flow has been investigated extensively in the past and is well documented for a range of Reynolds number, heat-transfer, and pressure-gradient conditions.[4,5,6] The opposite nozzle wall, a flexible contoured plate, was adjusted to produce a strong adverse-pressure-gradient flow along the flat test plate downstream of the initial flow expansion. The influence of the flexible nozzle wall contour on the opposite wall pressure distribution is illustrated in Figure 2. The nozzle contour provided for an initial expansion of the flow to Mach 4.9 as in conventional supersonic nozzles, followed by a region of zero pressure gradient. The nozzle flow then underwent a continuous flow compression of sufficient strength to cause separation of the flat test plate boundary layer. This was followed by a flow expansion to meet nozzle exit conditions. The nozzle contour was designed using a method-of-characteristics computer program together with a correction for the boundary-layer displacement thickness. Provision was made for a smooth transition between the various pressure-gradient regimes with no shock-wave interference. The nozzle configuration was not changed during the test. Therefore, the strength of the compression imposed on the boundary layer remained the same for all test conditions. Figure 3 illustrates how the boundary layer responded to this incident compression.

Tests were conducted at tunnel supply pressures between 10 and 150 psia. The tunnel supply temperature was 595°R and the wall temperature was ambient (535°R) except for the region of the nozzle throat where the nozzle wall was heated to the local adiabatic-wall temperature. These conditions provided a range of Reynolds number per foot from 5.6×10^5 to 8.5×10^6 at a wall-to-adiabatic-wall temperature ratio very near 1.0. Boundary-layer profiles ahead of the interaction, wall-pressure distributions, and separation lengths were measured for the range of Reynolds numbers investigated. However, the comprehensive boundary-layer and flow-field measurements and the wall shear-stress and heat-transfer measurements through the interaction were only obtained at an intermediate Reynolds number of $Re_{\delta I} = 7.7 \times 10^5$.

3. TRAVERSING TEST PLATE MODEL

With the realization that flow measurements were to be made at many incremental streamwise locations throughout the separation region, a special traversing plate model was designed and fabricated. The model, pictured in Figure 4, consisted of a flat test plate replacement for the existing nozzle wall of the facility. The model was fitted with aerodynamic fences which were necessary for the elimination of the cross flow emanating from the thick sidewall boundary layers (see discussion later). One distinctive feature of the model was the eight-inch wide central strip of the test plate which could be traversed 8.5 inches in the streamwise direction. The leading edge of this strip slid under a 0.030-inch-thick stainless steel sheet. Appropriate sealing was provided on all surfaces to eliminate leakage from the tunnel plenum chamber to the flow surface. With this model, the need for duplication of instrumentation was minimized and the streamwise measuring resolution was greatly increased. For example, continuous wall static-pressure distributions were obtained by monitoring only four static-pressure orifices along the test plate during a traverse. Access ports along the traversing test plate provided for the installation of a variety of instrumentation.

4. INSTRUMENTATION

Continuous distributions of wall shear stress and heat transfer were obtained by direct measurement using skin-friction balances and a heat-transfer gage installed in the traversing test plate instrumentation ports. Figure 5 pictures the balances used in this investigation. The large NSWC designed balance[7] and the small balance of DRL design[8] provided redundancy in measuring instrument. In addition, the effect of sensing element size was tested by masking off portions of the sensing area and substituting smaller sensing elements.

Heat-transfer measurements were made using a thermopile gage mounted on the surface of an instrumentation port insert. The thermopile consisted of two thermocouples connected in series and located on opposite sides of a thin thermal barrier. The heat flux measured was proportional to the temperature across the thermal barrier. Since the test conditions were near adiabatic, a heater button was mounted to the back of the gage to produce selected heat flux conditions. This allowed for the measurement of the heat-transfer coefficient in addition to the measurement of the adiabatic-wall temperature and recovery factor.

A Preston probe was traversed through the interaction region to establish the location of the separation and reattachment points. A 0.040-inch-diameter probe was mounted in both a forward and rearward facing mode. The points of flow reversal were determined when the pressure differential between the probe and wall static pressure became zero. An oil flow technique was also used to determine these points. A small amount of oil was allowed to flow from a static pressure orifice in the test plate. The separation and reattachment points were determined by traversing the test plate and orifice beneath the interaction and observing when the direction of oil flow changed from the streamwise to rearward direction.

In addition to the measurements of wall properties, surveys of the boundary layer and external flow field were made by using a boundary-layer traverse and probes which were inserted through the test plate instrumentation ports. Generally, boundary-layer surveys were obtained at one-inch increments in the streamwise direction in the region of interaction. Surveys of Pitot pressure, static pressure, and total temperature were obtained using a variety of instrumentation as shown in Figure 6. Typically, Pitot-pressure probes were of the flattened-tip configuration with a 0.003 x 0.100-inch rectangular opening. The static-pressure probe consisted of a 0.750-inch-diameter flat-surfaced disc with a sharp, 10-degree bevel on its edge and a static orifice at its center. The total temperature through the boundary layer was measured using the fine-wire probe design of Yanta[9] with a 0.002-inch diameter x 0.127-inch-long sensing wire exposed to the flow. Probe supports were of varying design with extensions provided for the probes when sting support interference was suspected.

All boundary-layer traverses were made from the free stream toward the plate with a maximum movement of 4.5 inches. Data were recorded with the probes at rest and only when the probe pressures and/or temperatures were observed to have reached equilibrium conditions. The data acquisition system simultaneously recorded eight channels of data on digital voltmeters and converted the information directly to a computer card output.

5. DATA REDUCTION

The data-reduction schemes used in this test were very nearly identical to those reported earlier by the author;[4,5,6] therefore, only a brief description will be given here. The introduction of the static-pressure variation normal to the test plate into profile and integral parameter definitions was of utmost necessity for this flow field. The procedure used was to define "ideal" flow properties which are calculated from the local static pressure, total pressure and stagnation temperature using isentropic relations. These properties represent the "inviscid" flow field which would exist if the boundary layer was not present. The boundary-layer thickness was defined as the distance from the wall where $M/M' = 0.995$, i.e. the point where the viscous and inviscid distributions differed by half a percentage. The primed (') quantities refer to the "ideal" flow parameters.

6. TWO-DIMENSIONALITY

Measurements of boundary-layer flows in a two-dimensional facility of this type are usually questioned as to the two-dimensionality of the flow. This question is always intensified when any mention of separation is made.[10] Two investigations into identifying the two-dimensionality of the present flow were conducted. The first was by observation of surface oil flow patterns. Figure 7 shows oil flow patterns on the test plate in the region of interaction for test configurations with and without aerodynamic "fences." As can be seen, fences were found to be a necessity in eliminating the cross flows which were emanating from the thick sidewall boundary layers and feeding the separation process. With the introduction of the fences the flow field became more nearly two-dimensional. The incoming flow did not exhibit cross-flow tendencies and the separation and reattachment lines were well defined and straight across a good portion of the test plate. (It should be noted that these photographs were obtained in preliminary shakedown tests. The detached flow at the leading edge of the fences was eliminated in the final tests by an improved fence design.) It should be further noted that the boundary layer would not separate when the fences were installed until the strength of the pressure rise imposed on the boundary layer was increased.

The second evaluation of two-dimensionality was made by comparing the wall static-pressure distributions on and two inches off centerline of the test plate as shown in Figure 8. Differences between the on and off centerline distributions were slight for both configurations, indicating how insensitive the lateral distribution of wall pressure is to cross-flows and three-dimensional effects. However, the streamwise position of the interaction and the overall degree of separation did differ significantly between the configurations with and without fences indicating the strong influence of cross-flows on separation lengths and incipient separation criteria. These findings are consistent with the studies of Reda and Murphy[10,11] on shock-induced separations.

7. FLOW-FIELD DEFINITION

The complex flow field encountered in this test is illustrated in Figure 9 through schlieren photographs and an isobar mapping of the interaction region. The isobar mapping was compiled from many static-pressure surveys through the flow field. Strong static-pressure gradients were observed through the interaction except for the region of the subsonic separation bubble where the static pressure normal to the wall appeared to be constant. The schlieren photographs showed the separation shock emanating from deep within the boundary layer.

Boundary-layer velocity profiles ahead of the interaction are shown in Figure 10 for the range of Reynolds numbers tested. The profiles are presented in law-of-the-wall coordinates using the Van Driest[12] transformed velocity, u^*, in the form

$$u^* = \frac{u_e}{A}\left\{\sin^{-1}\left(\frac{2A^2\left(\frac{u}{u_e}\right) - B}{\sqrt{B^2 + 4A^2}}\right) + \sin^{-1}\left(\frac{b}{\sqrt{B^2 + 4A^2}}\right)\right\} \qquad (1)$$

where: $$A = \sqrt{\frac{T_e}{T_w} r_f \, 0.2 \, M_e^2} \quad \text{and} \quad B = \frac{T_{aw}}{T_w} - 1$$

The shear velocity, u_τ, was determined from a best fit of the transformed profile data in the logarithmic region of the boundary layer to the relation

$$\frac{u^*}{u_\tau} = 2.5 \ln\left(\frac{y \, u_\tau}{\nu_w}\right) + 5.1 \qquad (2)$$

All the profiles exhibited the usual turbulent boundary-layer characteristics of a laminar sublayer, a logarithmic region, and a wake region. A summary of the boundary-layer parameters is given in Table 1 for the range of Reynolds numbers tested. For Reynolds numbers per foot below 4.5×10^5, the flow was below the turbulent flow limit of the facility.

8. WALL-PRESSURE DISTRIBUTIONS

The wall-pressure distributions through the interaction region are shown in Figure 11. Shown for comparison is a best approximation of the "inviscid" pressure field which was imposed on the boundary layer. This "inviscid" distribution was computed using a method-of-characteristics solution from measured streamwise static-pressure distributions outside the boundary layer and ahead of the interaction. An overall "inviscid" pressure rise of between 8 and 10 was imposed on the boundary layer from the incident compression. The "inviscid" pressure drop which followed the compression was caused by the subsequent expansion of the nozzle flow. For this reason, the actual pressure rise through the interaction only reached about half the peak "inviscid" value.

Of particular interest in Figure 11 is the effect of the Reynolds number on the wall-pressure distribution. For Reynolds numbers per foot above 3.4×10^6, the upstream propagation decreased with increasing Reynolds number, whereas for Reynolds numbers per foot below 3.4×10^6, the opposite trend was observed. This trend reversal becomes more vivid in Figures 12 and 13, where the location of the separation and reattachment points and the non-dimensional separation distance are plotted respectively versus Reynolds number. This reverse phenomenon can best be explained with the use of Figure 14 which shows incipient separation pressure-rise data for different Mach numbers and Reynolds numbers. Shown on the figure are the data of Kuehn,[1] Thomke and Roshko[2] and Sterrett and Emery[13] together with the correlation of Elfstrom.[14] Consider the test conditions of this study in terms of the reversal trend in the incipient separation pressure rise-Reynolds number correlation. As the Reynolds number is increased for a constant $P/P_I = 9$ and $M_I = 4.9$, the state of the boundary layer transforms from being unseparated to being incipiently separated and strongly separated; then it reverts back to being incipiently separated and unseparated. Over the limited Reynolds number range of the present study the flow acted as predicted with the degree of separation increasing and then decreasing with increasing Reynolds number. Although it has been argued that the geometry of the experiment and the choice of a criterion for detection of incipient separation could account for the reversal trend seen in Figure 14, the present tests tend to discount these arguments because of the single test configuration and measurement technique. The reversal trend appears genuine.

The free-interaction concept as proposed by Chapman, Kuehn and Larson[15] states that certain characteristics of the separated flow should not depend on the object shape or mode of inducing separation. This concept requires the fulfillment of two criteria. The ratio of the separation-point pressure to the initial pressure must remain invarient and the shape of the distribution of pressure up to the separation point must be the same. Figures 15 and 16 show that the first criterion was fulfilled for the Reynolds numbers tested with $P_S/P_I = 2.18$. Similarly a type of free interaction appeared in the reattachment region with $P_R/P_{PK} = 0.67$. These pressure values were based on the separation and reattachment points determined from Preston probe measurements. Oil flow measurements of the separation and reattachment point locations were also obtained (see Figure 12), but they were not considered correct based on the low P_S/P_I value (1.2 to 1.5) which was indicated. This discrepancy in the oil flow results was also noted by Driftmyer[16] for a similar test configuration.

The second free-interaction criterion, the invariance in the shape of the pressure distribution up to the separation point, was not fulfilled according to the guidelines of Ref. 15. Although the pressure distributions were similar in shape, a scaling factor appeared necessary in the length parameter. Zukoski[17] proposed that the length coordinate be non-dimensionalized to the boundary-layer thickness providing for a ratio $(X_S-X_I)/\delta_I$ which is constant and equal to a value of 2.5. Values of $(X_S-X_I)/\delta_I$ for this investigation varied from 1.15 to 1.73 for decreasing $Re_{\delta I}$ over the Reynolds number range tested. Because the parameters X_S and X_I are difficult to measure and subject to varying interpretation, the maximum pressure gradient in the free interaction appeared to be an easier and more consistent parameter to evaluate. It would seem logical that the larger the pressure gradient the smaller the free-interaction length, X_S-X_I. Figure 17 shows pressure-gradient data compiled from a number of experiments plotted versus Reynolds number for several Mach numbers. Although there was a sizeable scatter in the data, the maximum pressure gradient in the interaction region showed a consistent trend of increasing with increasing Reynolds number for a given Mach number. This pressure gradient appeared to be independent of the overall pressure rise after the free interaction,[2,16] the heat-transfer condition,[14] and the mode of separation. The concept of a free-interaction region appears valid; however, proper scaling of the length parameter must be found to correlate the variation with Mach number and Reynolds number.

9. WALL HEAT-TRANSFER AND SHEAR-STRESS

The recovery-factor and heat-transfer coefficient distributions through the separation region are presented in Figure 18. The value of the local recovery factor was observed to increase sharply at separation, remain somewhat constant through the separation region, and relax back to its original value after reattachment. The value of the heat-transfer coefficient also showed a sharp increase at separation; however, the value thereafter decreased to a lower value at the center of the separation region before increasing again through the reattachment.

Wall shear-stress measurements are presented in Figure 19. The data were obtained by direct measurement using skin-friction balances. Large corrections to the data were needed to compensate for pressure-gradient effects on the shear balances; consequently, results can only be considered in qualitative terms. The pressure-gradient effects resulted primarily from the integral pressure force acting on the edge of the measuring element. This pressure force was proportional to the local pressure gradient and thickness of the measuring element; therefore, the greatest errors occurred in the separation and reattachment regions where the pressure gradients were strongest. Since the wall shear stress was small in these same regions, it is questionable whether skin-friction balances can be considered as valid and accurate tools to the evaluation of separation criteria.

10. CONCLUSIONS

An experimental investigation of a compressible turbulent boundary-layer separation was conducted with emphasis placed on the collection of a comprehensive set of flow-field measurements. A continuous compression of a nozzle flow provided a separated flow field which was free of incident shock waves, wall discontinuities and wall curvature. The compression-induced-separation data could be correlated with data obtained for other test configurations and models. A traversing plate model was shown to be of great advantage in minimizing instrumentation duplication and increasing streamwise measuring resolution. Aerodynamic fences were found to be a necessity for the elimination of cross-flows emanating from large sidewall boundary layers.

The important conclusions reached in this study are:

1. The separation length, $(X_R-X_S)/\delta_I$, was found to increase with increasing Reynolds number for $Re_{\delta I} < 8. \times 10^5$, whereas the opposite trend was found for $Re_{\delta I} > 8. \times 10^5$. This reversal in the separation length versus Reynolds number trend is consistent with the reversals observed for incipient separation versus Reynolds number correlations.

2. The pressure rise to separation was found to be invarient with Reynolds number for a given Mach number. The free-interaction length, $(X_S-X_I)/\delta_I$, and the maximum pressure gradient in the free-interaction region, $[d(P/P_I)]/[d(X/\delta_I)]$, were found to be a function of Reynolds number and Mach number. No reversals were observed in the interaction length versus Reynolds number trend; $(X_S-X_I)/\delta_I$ decreased for increasing $Re_{\delta I}$.

ACKNOWLEDGEMENTS

The author is grateful for the support and encouragement of the members of the Boundary Layer Group, Dr. Roland E. Lee, Chief, and Drs. William J. Yanta and David F. Gates. The assistance of Messrs. F. W. Brown and F. C. Kemerer is also gratefully acknowledged for their efficient operation of the facility and preparation of instrumentation.

This research was performed under the sponsorship of the Naval Air Systems Command, Washington, D. C., U. S. A., Task No. A 32 320/292/69/R009-02-030.

REFERENCES

1. Kuehn, D. M., "Experimental Investigation of the Pressure Rise Required for the Incipient Separation of Turbulent Boundary Layers in Two-Dimensional Supersonic Flow," NASA Memo 1-21-59A, Feb 1959

2. Thomke, G. J. and Roshko, A., "Incipient Separation of a Turbulent Boundary Layer at High Reynolds Number in Two-Dimensional Supersonic Flow Over a Compression Corner," NASA CR-73308, 1969

3. Lee, R. E., Yanta, W. J., Leonas, A. C. and Carner, J., "The NOL Boundary Layer Channel," NOLTR 66-185, Nov 1966

4. Voisinet, R. L. P. and Lee, R. E., "Measurements of a Mach 4.9 Zero-Pressure-Gradient Turbulent Boundary Layer with Heat Transfer - Part 1, Data Compilation," NOLTR 72-232, Sep 1972

5. Voisinet, R. L. P. and Lee, R. E., "Measurements of a Supersonic Favorable-Pressure-Gradient Turbulent Boundary Layer with Heat Transfer - Part 1, Data Compilation," NOLTR 73-223, Dec 1973

6. Voisinet, R. L. P., Lee, R. E. and Yanta, W. J., "An Experimental Study of the Compressible Turbulent Boundary Layer with an Adverse Pressure Gradient," Paper No. 9, Turbulent Shear Flows, AGARD CP-93-71, Sep 1971

7. Bruno, J. R., Yanta, W. J. and Risher, D. B., "Balance for Measuring Skin Friction in the Presence of Heat Transfer," NOLTR 69-56, Jun 1969

8. Fenter, F. W., "The Turbulent Boundary Layer on Uniformly Rough Surfaces at Supersonic Speeds," DRL Report 437, CM 941, Jan 1960

9. Yanta, W. J., "A Fine-Wire Stagnation Temperature Probe," NOLTR 70-81, Jun 1970

10. Reda, D. C. and Murphy, J. D., "Shock Wave-Turbulent Boundary Layer Interactions in Rectangular Channels," AIAA Paper 72-715, Jun 1972

11. Reda, D. C. and Murphy, J. D., "Shock Wave-Turbulent Boundary Layer Interactions in Rectangular Channels - Part II, The Influence of Sidewall Boundary Layers on Incipient Separation and Scale of the Interaction," AIAA Paper 73-234, Jan 1973

12. Van Driest, E. R., "Turbulent Boundary Layer in Compressible Fluids," JAS, Vol. 18, No. 3, Mar 1951

13. Sterrett, J. R. and Emery, J. C., "Experimental Separation Studies for Two-Dimensional Wedges and Curved Surfaces at Mach Numbers of 4.8 to 6.2," NASA TN D-1014, 1962

14. Elfstrom, G. M., "Turbulent Separation in Hypersonic Flow," I.C. Aero Report 71-16, Sep 1961

15. Chapman, D. R., Kuehn, D. M. and Larson, H. K., "Investigation of Separated Flows in Supersonic and Subsonic Streams with Emphasis on the Effect of Transition," NACA Report 1356, 1958

16. Driftmyer, R. T., "A Forward Facing Step Study - The Step Height Less Than The Boundary-Layer Thickness," NOLTR 73-98, May 1973

17. Zukoski, E. E., "Turbulent Boundary-Layer Separation in Front of a Forward-Facing Step," AIAA Journal, Vol. 5, No. 10, Oct 1967

P_o psia	Re/ft $x10^{-6}$	δ inches	$\delta^{*'}_w$ inches	θ_w' inches	Re_δ $x10^{-5}$	C_f $x10^3$
150.	8.5	2.0	0.68	0.058	14.16	0.636
105.	6.0	2.1	0.73	0.062	10.5	0.665
75.	4.2	2.2	0.79	0.066	7.7	0.703
60.	3.4	2.26	0.83	0.070	6.4	0.733
45.	2.5	2.36	0.88	0.074	4.92	0.786
30.	1.7	2.5	0.94	0.078	3.54	0.835
25.	1.4	2.57	0.98	0.081	3.00	0.804
20.	1.12	2.65	1.02	0.086	2.47	(0.860)
15.	0.85	2.75	1.09	0.090	1.95	0.895
12.	0.67	(2.85)	(1.15)	(0.094)	(1.59)	(0.980)
10.	0.56	2.95	1.19	0.098	1.38	1.07

( ) Interpolated Values

TABLE 1

BOUNDARY LAYER PROPERTIES AHEAD OF THE INTERACTION, X = 67 INCHES

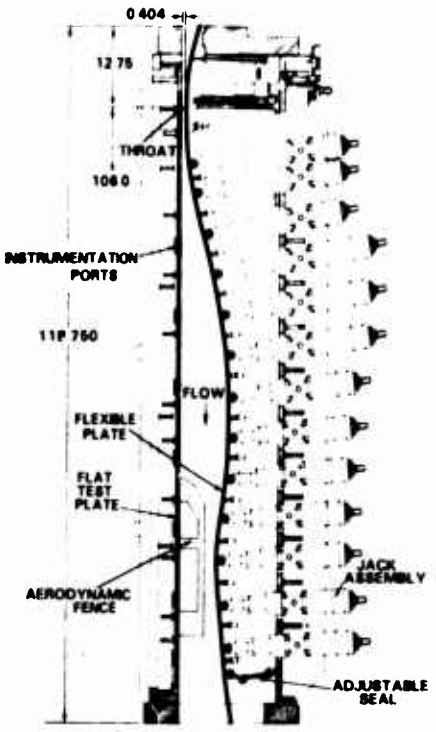

FIG. 1 - NSWC BOUNDARY LAYER CHANNEL

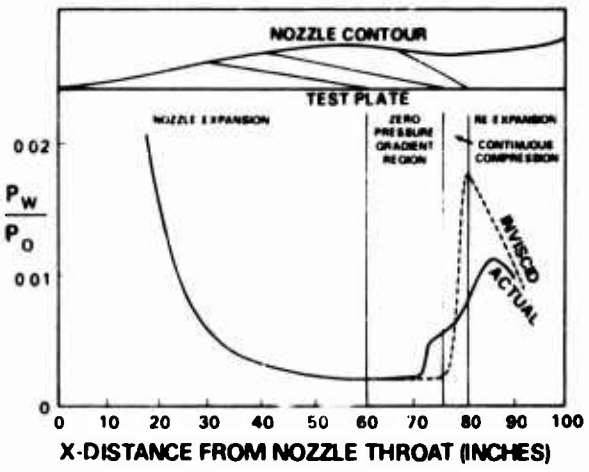

FIG. 2 - NOZZLE CONTOUR INFLUENCE ON TEST PLATE PRESSURE DISTRIBUTION

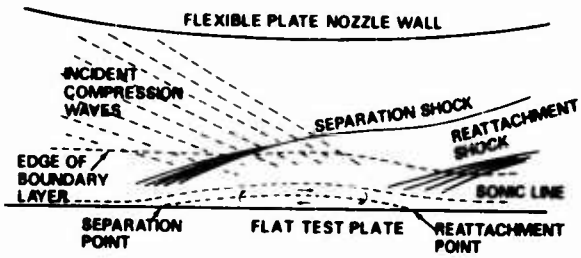

FIG. 3 - FLOW SEPARATION INDUCED BY A CONTINUOUS NOZZLE FLOW COMPRESSION

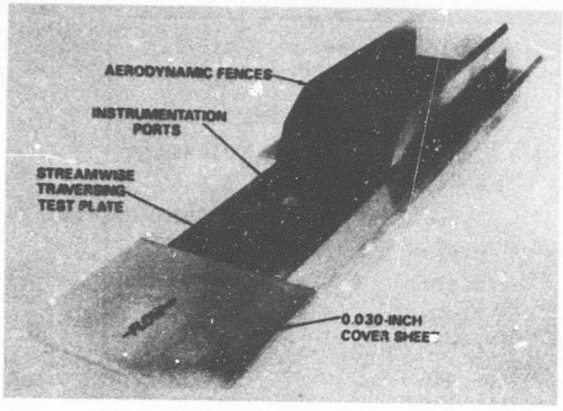

FIG. 4 - TRAVERSING TEST PLATE MODEL

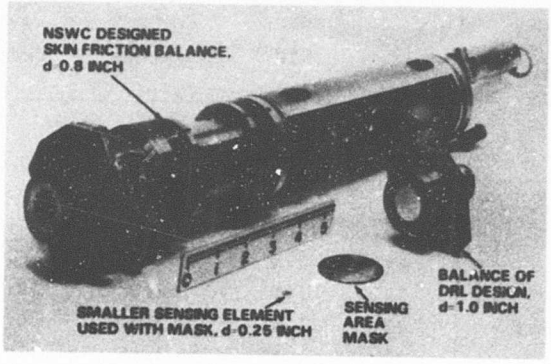

FIG. 5 - SKIN-FRICTION BALANCES

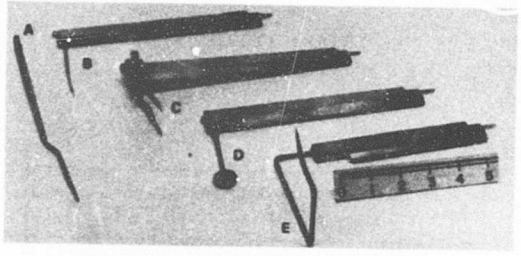

A FLATTENED TIP PITOT PROBE WITH EXTENSION
B FLATTENED TIP PITOT PROBE
C DOUBLE PROBE HOLDER WITH PITOT AND FINE WIRE STAGNATION TEMPERATURE PROBE
D 0 75 INCH DIAMETER DISC STATIC PRESSURE PROBE
E REVERSE FLOW PITOT PROBE

FIG. 6 - BOUNDARY-LAYER PROBES

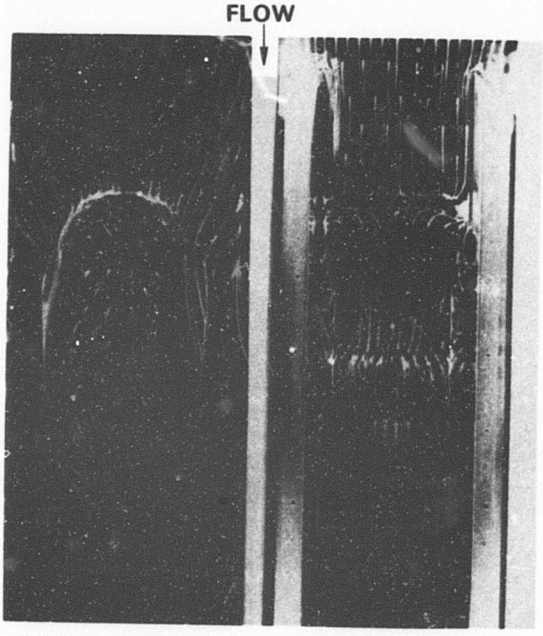

OIL FLOW PATTERN WITHOUT AERODYNAMIC FENCES

OIL FLOW PATTERN WITH AERODYNAMIC FENCES

FIG. 7 - SURFACE OIL FLOW PATTERNS

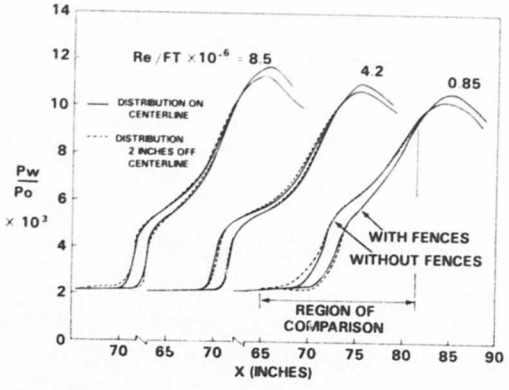

FIG. 8 - STREAMWISE WALL-PRESSURE DISTRIBUTIONS ON AND OFF CENTERLINE WITH AND WITHOUT FENCES

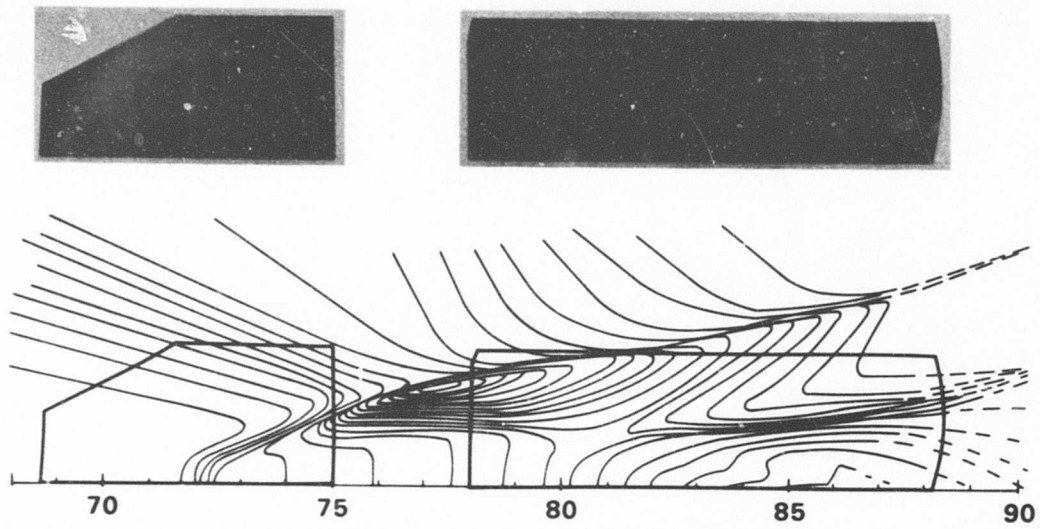

FIG. 9 - SCHLIEREN PHOTOGRAPHS AND STATIC-PRESSURE ISOBAR MAPPING, $Re_{\delta I} = 7.7 \times 10^5$

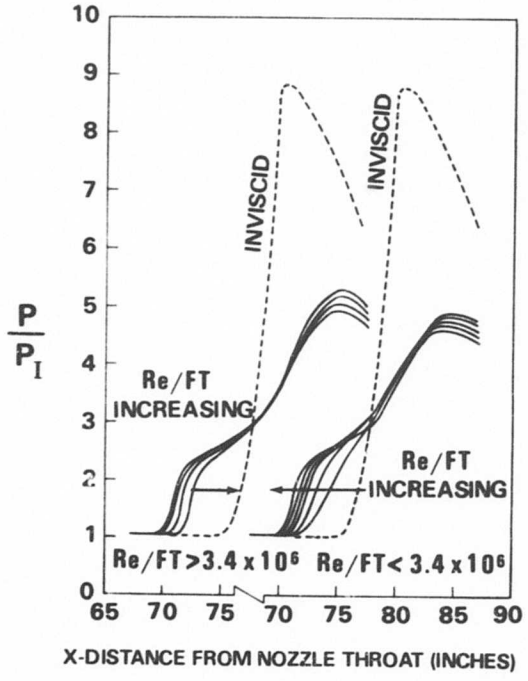

FIG. 11 - REYNOLDS NUMBER EFFECT ON THE WALL-PRESSURE DISTRIBUTION

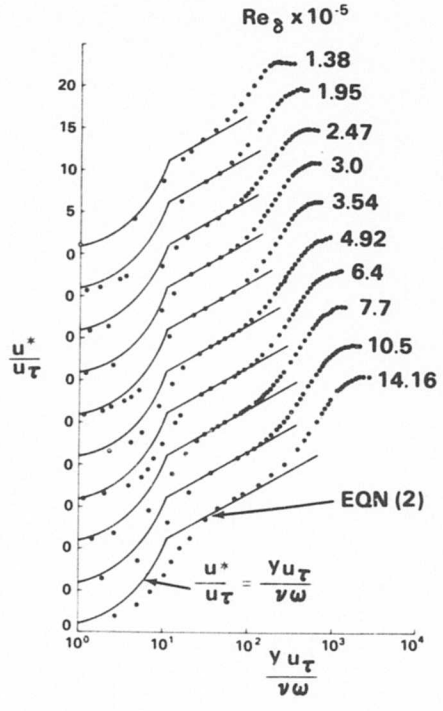

FIG. 10 - REYNOLDS NUMBER EFFECT ON THE LAW-OF-THE-WALL VELOCITY CORRELATION AHEAD OF THE INTERACTION, X = 67 INCHES

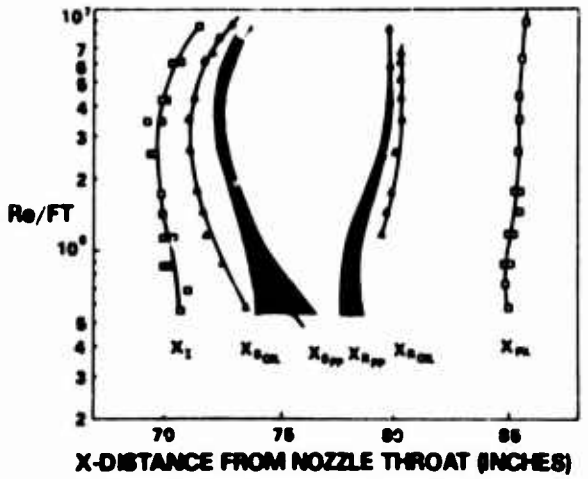

FIG. 12 - VARIATION OF SEPARATION AND REATTACHMENT LOCATIONS WITH REYNOLDS NUMBER

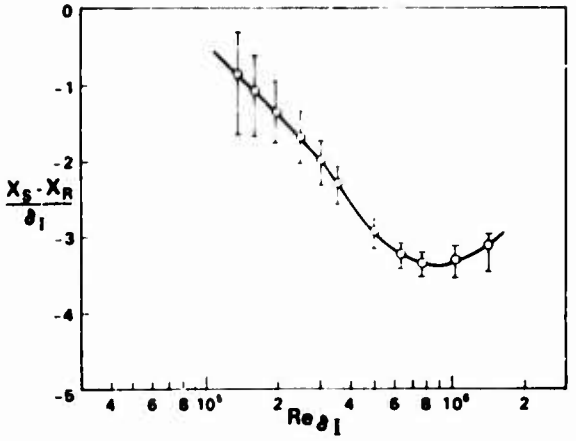

FIG. 13 - SEPARATION LENGTH VARIATION WITH REYNOLDS NUMBER

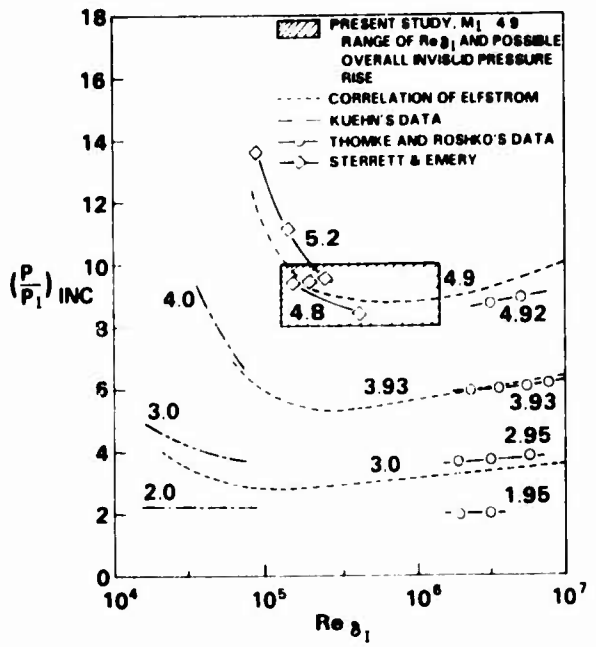

FIG. 14 - REYNOLDS NUMBER EFFECT ON THE PRESSURE RISE TO INCIPIENT SEPARATION

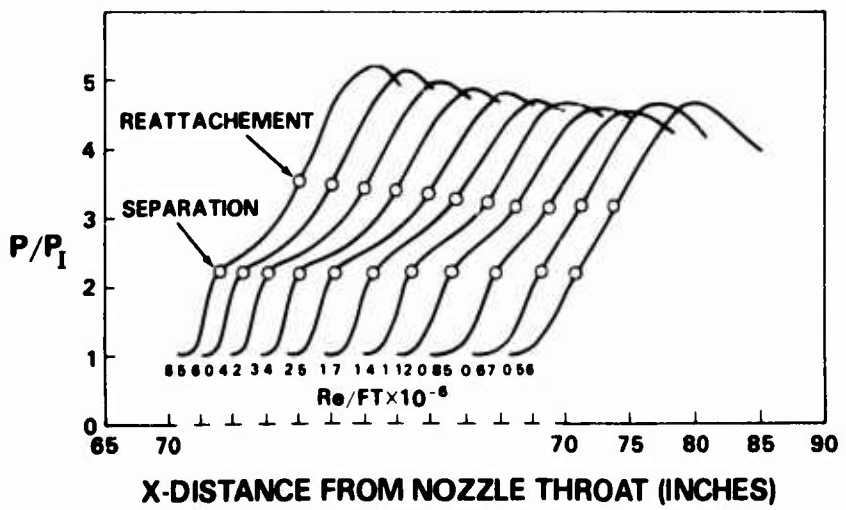

FIG. 15 - REYNOLDS NUMBER EFFECT ON THE WALL-PRESSURE DISTRIBUTION

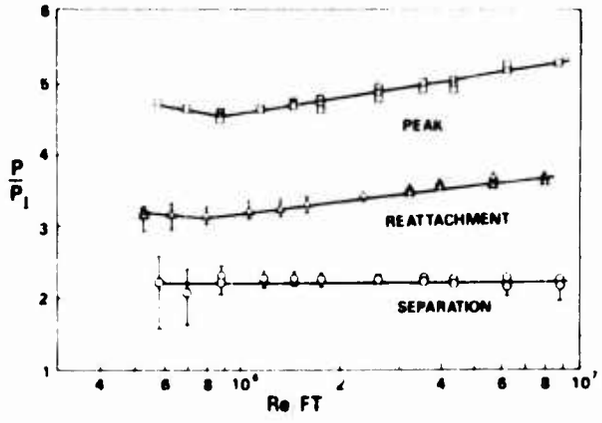

FIG. 16 - PRESSURE RISE VARIATION WITH REYNOLDS NUMBER

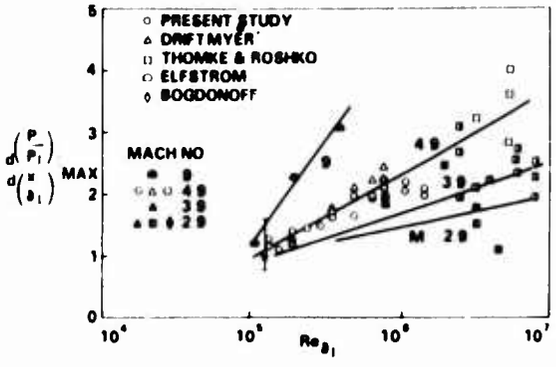

FIG. 17 - VARIATION OF THE MAXIMUM PRESSURE GRADIENT IN THE FREE-INTERACTION REGION WITH REYNOLDS NUMBER

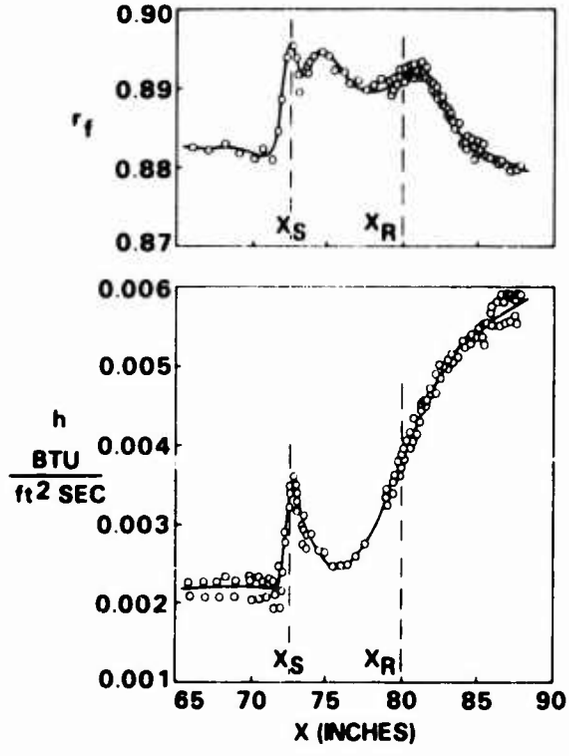

FIG. 18 - RECOVERY FACTOR AND HEAT-TRANSFER COEFFICIENT DISTRIBUTIONS
$Re_{\delta I} = 7.7 \times 10^5$

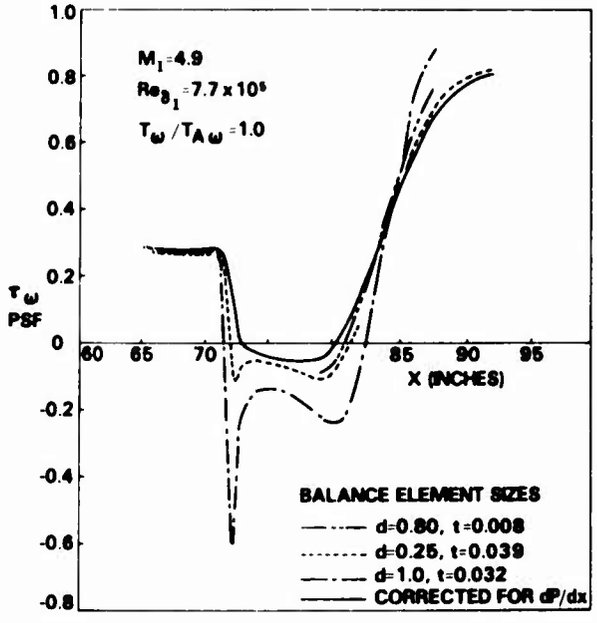

FIG. 19 - WALL SHEAR-STRESS DISTRIBUTIONS
$Re_{\delta I} = 7.7 \times 10^5$

Laminar and Turbulent Boundary-Layer Separation at Supersonic and Hypersonic Speeds

John L. Stollery
Aerodynamics Division,
College of Aeronautics,
Cranfield Institute of Technology,
Cranfield, Bedford MK43 OAL, England

SUMMARY

The paper discusses a number of theoretical and experimental investigations of shock-boundary layer interaction. Both laminar and turbulent layers are considered, growing over two-dimensional and axi-symmetric bodies.

For laminar flow a simplified version of the well-known Lees-Reeves momentum integral method has been developed by Georgeff and used to predict incipient separation. A number of comparisons between experiment and theory for attached, incipient and well separated flows are included.

For turbulent flow the 'three layer' model proposed by Elfstrom is shown to give good quantitative estimates of incipient separation and to explain the Reynolds number trend found experimentally. Since the turbulent boundary layer is more resistant to shock interference a very simple attached flow theory is derived, which gives good predictions of both pressure and heat transfer at hypersonic speeds.

LIST OF SYMBOLS

C	constant in temperature-viscosity law.	δ	boundary layer thickness.
C_f	skin friction coefficient.	δ^*	displacement thickness.
$f_{1,2,3}$	function of.	θ	streamline slope.
h	enthalpy.	μ	viscosity.
k	constant.	ρ	density.
L	value of x at corner.	$\bar{\chi}$	viscous interaction parameter.
M	Mach number.	SUFFICES	
p	pressure.	e	edge of boundary layer.
P	p/p_∞.	i	incipient.
$\dot{q}$	heat transfer rate.	L	corner.
$Re_{(\ )}$	Reynolds number, $\rho_\infty u_\infty (\ )/\mu_\infty$	r	recovery.
St	Stanton number.	s	strong.
T	temperature.	w	weak or wall.
u	velocity	o	total
x,y	distance along and normal to free stream.	∞	freestream
α	incidence.	$-$	average value.

1. INTRODUCTION

At supersonic and hypersonic speeds separation is usually caused by shock-boundary layer interference. Indeed the problem is one of strong viscous interaction. This paper brings together the results of a number of theoretical and experimental studies using two-dimensional wedge compression corner and axisymmetric cylinder-flare models to investigate incipient separation and the subsequent separated flow.

2. THEORY

The basic problem is to solve the viscous flow around a given shape in an interdependent, and hence initially unknown, pressure distribution. If the boundary layer approximation is acceptable then the problem reduces to the simultaneous solution of three equations:

$$\delta^* = f_1(P) \tag{1}$$

$$P = f_2(Y_e) \tag{2}$$

$$Y_e = f_3(\delta^*) \tag{3}$$

The first equation expresses the boundary layer displacement thickness growth $\delta^*(x)$, in terms of the pressure gradient, $P(x)$, which in turn depends on the effective shape of the body $Y_e(x)$. The viscous flow equations dictating the growth of δ^* and the inviscid equations governing the pressure distribution, are coupled by equation (3) which relates the effective shape to the geometric shape. A number of different approximations, covering a wide range of accuracy and complexity, are possible for each of the three equations so that the total number of methods of solving the complete problem are legion.

3. LAMINAR FLOW

One of the most widely used methods for laminar flow is Klineberg's[1] or Holden's[2] extension of the Lees-Reeves[3] momentum integral technique in which the momentum, moment of momentum and energy equations are solved using the Cohen-Reshotko catalogue of similarity solutions to provide profile data. For a time the utility of the method was obscured by fruitless discussion of details which were subsequently shown to have no physical significance (see, e.g., Stollery and Hankey[4]). More recently Georgeff[5] has made a detailed study of the method. He found that it was important in cold wall flows to uncouple the velocity and enthalpy parameters by solving the energy integral equation in addition to the momentum and moment of momentum equations. However, Georgeff also showed that the moment of momentum equation could be replaced by the much simpler momentum equation at the wall, thereby 'hooking' the pressure gradient to local values of the dependent variables, with no loss of accuracy. Neither was the choice of profile quantities too sensitive and he was able to generalise the Cohen-Reshotko profiles to cover any wall temperature ratio.

The result is that with integral boundary layer equations representing relation (1), shock-expansion theory for equation (2) and the correct coupling equation

$$\frac{d\delta^*}{dx} - (\delta - \delta^*)\frac{d\,\ell n(\rho_e u_e)}{dx} = \tan(\theta_e - \alpha_w) \tag{4}$$

a method exists for predicting laminar attached, incipient and fully separated flows. Agreement with experiment at supersonic speeds is extremely good. At hypersonic speeds some predictions of Georgeff are compared with the experimental data of Bloy[6] in Fig. 1.

3.1 Laminar Incipient Separation

Both the mathematical formulation of the problem and dimensional reasoning suggest that the important parameters are $M_\infty^2\alpha^2$, $\bar{\chi}$ and T_w/T_o. The simple analysis of Cheng[7] shows that when incidence and displacement effects are present it is the ratio $M_\infty^2\alpha^2/\bar{\chi}$ which is important. For laminar flow $\bar{\chi} \equiv M_\infty^3\sqrt{C}/\sqrt{Re_x}$ so that we might expect the incipient separation angle to be given by

$$M_\infty \alpha_i = k\,\bar{\chi}_L^{\frac{1}{2}} \quad \text{or} \quad \alpha_i = k\left\{\frac{M_\infty^2}{Re_x}\right\}^{\frac{1}{4}} \tag{5}$$

The results of experiments using compression corner and incident shock flows are compared with Georgeff's predictions of incipient separation in Fig. 2. Both experiment and prediction do support an approximate relation of the type

$$M_\infty \alpha_i = k\,\bar{\chi}_L^{\frac{1}{2}}.$$

Other experiments and calculations indicate that cooling the wall has a small but beneficial effect in increasing the incipient separation angle.

4. TURBULENT FLOW

In principle the momentum-integral approach can also be applied to turbulent flow but progress is hampered by lack of knowledge of turbulent boundary layer profiles for a wide range of pressure gradients. Todisco and Reeves[8] developed the method for adiabatic turbulent flow but were forced to use empirical profile data for attached and incipient conditions together with laminar similarity solutions for the reversed flow since little else was available at that time. Subsequently Reeves[9] proposed a two-layer model in which an analytical solution for the inner part, based on a compressible law of the wall, is matched with a moment integral method in the outer layer. The paucity of detailed profile data encouraged semi-empirical methods and correlations of experimental measurements at the wall. A recent collection of incipient separation data is shown in Fig. 3. One interesting feature is immediately obvious, the trend reversal of α_i with Re_{δ_L} at high values of Reynolds number. Until recently the evidence for this trend reversal was primarily from Roshko and Thomke's[10] measurements on a wedge placed on the floor of a supersonic tunnel. Law[11] has now confirmed this trend with tests on a flat-plate-plus-wedge model mounted centrally in the ARL high Reynolds number supersonic tunnel.

Following a suggestion by Green, Elfstrom[12] has given an explanation of this trend reversal and has obtained quantitative estimates of the incipient separation angle. It is obvious from schlieren pictures (Fig. 4) that the oblique shock wave penetrates well into the turbulent boundary layer and it is reasonable to divide the layer into an outer primarily inviscid but rotational zone and a thin inner viscous layer, the dividing line being drawn through the 'corner' of the velocity profile as in Fig. 5. Roshko and Thomke used a similar model to explain their measured pressure distributions. So far as separation is concerned we assume that the inner region is the important one and that a relevant Mach number (M_w) can be obtained by extrapolating the inviscid outer profile to the wall as shown in Fig. 5. The further assumption that separation occurs when a normal shock is formed in the corner region (i.e., the inviscid shock detachment condition appropriate to M_w) gives the wedge angle α_i. If the profile shape remained constant then a single value of α_i, independent of Reynolds number, would be obtained. However, the various parts of a fully developed turbulent profile grow at different rates so that the Mach number M_w increases slightly with Reynolds number. Thus the expected trend from this argument is one of slowly increasing α_i with Re_{δ_L}, precisely the one found by Roshko and Thomke and now by Law. The reason for the decreasing α_i with Re_{δ_L} at low values of Re_{δ_L} is due to the slow development of the wake component of the turbulent velocity profile. This wake component development is particularly slow at high Mach numbers and very high values of Re_{δ_L} are needed before a fully developed profile is obtained. Elfstrom has used the Coles[13] incompressible profile with the wake function recommended by Alber and Coats[14] then transformed to the real non-adiabatic compressible flow profile using the method of Van Driest[15] and the Crocco linear temperature-velocity relation. With these profiles and the assumptions described earlier, the predictions of α_i shown in Fig. 6 have been made. The agreement with experiment is very good considering the simplicity of the model. The predicted Mach number profile can also be used to calculate the pressure distribution by splitting the profile into a number of layers as shown in Fig. 7a. Each layer is assumed to turn throught the wedge angle via an oblique shock of the appropriate strength. The predictions and mesurements are compared in Fig. 7b. Of course these simple techniques are only valuable up to incipient separation but fortunately this occurs at quite high angles, particularly at high Mach numbers.

The heat transfer rate measurements complementary to Elfstrom's pressure distributions have been made by Coleman[16]. They show a striking resemblance even in the well separated regions. This increase in heat transfer in turbulent separated flow regions is now well established and is one of the most significant differences between laminar and turbulent flow, Fig. 8.

A simple relation between pressure and heat transfer rate has been obtained by Stollery and Bates[17] following similar arguments to those used for laminar viscous interaction by Hayes and Probstein[18].

Starting from the assumption that the Stanton number St can be expressed in terms of a Reynolds number based on average boundary layer properties then,

$$St \equiv \frac{\dot{q}}{\bar{\rho} u_\infty (h_r - h_w)} \sim \left\{ \frac{\delta u_\infty x}{\bar{\nu}} \right\}^{1/5} . \tag{6}$$

If $\bar{T}/T_\infty \sim M_\infty^2$ and $\bar{\mu}/\mu_\infty = C_\infty \bar{T}/T_\infty$ then the final expression is

$$M_\infty^3 St_\infty \sim \{M_\infty^9 C_\infty / Re_x\}^{1/5} P^{4/5} \tag{7}$$

where P is the pressure ratio $p(x)/p_\infty$ and $\{M_\infty^9 C_\infty / Re_x\}^{1/5} \equiv \bar{\chi}_w$, the weak viscous interaction parameter for the turbulent flow. A more rigorous analysis in the same paper suggests that

$$M_\infty^3 St_\infty = \frac{0.204}{(1 + 2.5 T_w/T_o)^{3/5}} \bar{\chi}_w P^{4/5} \tag{8}$$

The connection between St_∞ and the pressure distribution is obvious. Figure 9 compares equation (8) with some of Coleman's two-dimensional compression corner data. The agreement is reasonable except in the well separated case ($\alpha = 38^\circ$) when there is no reason to think that the analysis would be valid

4.1 Turbulent Incipient Separation

It is easy to show that the strong viscous interaction parameter for turbulent flow is

$$\bar{\chi}_s \equiv \left\{\frac{M_\infty^9 C}{Re_x}\right\}^{2/7} .$$

Similar reasoning to that used for laminar flow would suggest that

$$M_\infty^2 \alpha_i^2 \sim (M_\infty^9 C/Re_L)^{2/7} \qquad (9)$$

or

$$\alpha_i \sim (M_\infty^2 C/Re_L)^{1/7} \qquad (10)$$

instead of

$$\alpha_i \sim (M_\infty^2 C/Re_L)^{1/4} \qquad (11)$$

as for laminar flow.

Reference to the compilation of experimental data (Fig. 3) shows that the true picture is far more complex but the data do show α_i increasing with M_∞.

4.2 Turbulent Axi-symmetric Flow

Completely two-dimensional experimental data are impossible to achieve because of end-effects and non-uniformities in the model and test stream. They are often unfairly criticized on this score and in fact many quasi two-dimensional data are perfectly reliable guides to the ideal situation. Nevertheless one way of avoiding end effects is to test the equivalent axi-symmetric model. Coleman and Stollery[19] have tested a hollow cylinder-flare model under identical conditions to those used for the wedge compression corner measurements. They found that the pressure distributions in the neighbourhood of the corner were very similar (Fig. 10) and that the incipient separation angles differed by only 1° (in about 30°) being slightly higher for the axi-symmetric tests. Kuehn[20] found a similar but more marked trend as shown in Fig. 11.

Coleman[21] made further tests using cone-cylinder-flare and hemisphere-cylinder-flare models. Despite the very different nose sections and hence a marked change in flow conditions approaching the flare, the incipient separation angle remained much the same (approx. 30° at $M_\infty = 9$). Assuming the flow is quasi two-dimensional which is reasonable until well past the cylinder flare junction then equation (8) is relevant. The measured pressure and heat transfer rate distributions for all three axi-symmetric bodies are compared with the prediction of equation (8) in Fig. 12.

5. CONCLUSIONS

For laminar two-dimensional flow the momentum integral method has been effectively developed and tested against experiment so that it can now be used to predict attached, incipient and well separated flows. The method has, so far, been less successful for turbulent flow because the velocity profile development is far more complex and insufficient information either experimental or theoretical, is available to guide development. In the meantime some simple but sensible ideas such as those given by Elfstrom enable the incipient separation condition to be predicted over a very wide range of Mach number and Reynolds number. The pressure distribution for unseparated flow can also be calculated and a simple connection can be established between heat transfer and pressure. There are sufficient measurements to support these relationships for both two-dimensional and axi-symmetric flow at hypersonic Mach numbers though there are conflicting data at supersonic speeds.

6. REFERENCES

1. KLINEBERG, J.M. AIAA J., 7, 2211-2221, (1969).

2. HOLDEN, M.S. AIAA J. 9, 84-93, (1971)

3. LEES, L and REEVES, B.L. AIAA J., 2, 1907-1920 (1964).

4. STOLLERY, J.L. and HANKEY, W.L. AIAA J. 8, 1349-1351, (1970).

5. GEORGEFF, M.P. Ph.D. Thesis, University of London (1972). See also AIAA J., 12, 1393-1400 (1974).

6. BLOY, A.W. and GEORGEFF, M.P. J. Fluid Mech., 63, 431-447, (1974)

7. CHENG, H.K., HALL, J.G., GOLIAN, T.C. and HERTZBERG, A. J. Aero. Sci., 28, 353-382, (1961)

8. TODISCO, A. and REEVES, B.L. ARL Symposium on Viscous Interaction Phenomena in Supersonic and Hypersonic Flow, University of Dayton Press, (1969).

9. REEVES, B.L. AGARD Conference Proceedings No. 93 (1971).

10. ROSHKO, A. and THOMKE, G.J. ARL Symp. on Viscous Interaction Phenomena in Supersonic and Hypersonic Flow, University of Dayton Press, (1969).

11. LAW, C.H. AIAA J., 12, 794-797, (1974).

12. ELFSTROM, G.M. J. Fluid Mech., 53, 113-127, (1972).

13. COLES, D.E. Rand Corp. Rep. 4-403-PR, (1962).

14. ALBER, E.I. and COATS, D.E. AIAA Paper No. 69-689, (1969).

15. VAN DRIEST, E R. J. Aero. Sci., 18, 145-160.

16. COLEMAN, G.T. Ph.D. Thesis, University of London (1973).

17. STOLLERY, J.L. and BATES, L. J. Fluid Mech., 63, 145-156 (1974).

18. HAYES, W.D. and PROBSTEIN, R.F. Hypersonic Flow Theory, Academic Press, (1959).

19. COLEMAN, G.T. and STOLLERY, J.L. AIAA J. 12, 119-120 (1974).

20. KUEHN, D.M. NASA Memo 1-21-59A, (1959).

21. COLEMAN, G.T. Imperial College, Aero. Rep. 73-06, (1973).

22. APPELS, C. and BACKX, E. VKI Rep. (unpublished), (1971).

23. BALL, K.O.W. and KORKEGI, R.H. AIAA J. 5, 1224-1230, (1968).

24 COLEMAN, G.T. and STOLLERY, J.L. J. Fluid Mech., 56, 741-742, (1972).

25 DROUGGE, G. FFA Rep. Sweden, No. 47, (1953).

26 GRAY, K.D. and RHUDY, R.W. AEDC-Tr-70-235, (1971).

27 HARVEY, W.D. NASA Tech. Note, D-4671, (1968).

28 HOLDEN, M.S. AIAA Paper No. 72-74, (1972).

29 KESSLER, W.C. REILLY, J.F. and MOCKAPETRIS, L.V. McDonnell Douglas Corp. Rep. MOC59800, (1970).

30 KUEHN, D.M. NASA TR R-117, (1961).

31 MILLER, D.S., HYMAN, R. and CHILDS, M.E. AIAA J., 2, 312-321, (1964).

32 NEEDHAM, D.A. Ph.D. Thesis, University of London, (1965).

33 RICHARDS, B.E. and ENKENHUS, K.R. AIAA J. 8, 1020-1025, (1970).

34 SPAID, F.W. and FRISHETT, J.C. AIAA J. 10, 915-922, (1972).

35 STERRETT, J.R. and EMERY, J.C. NASA Tech Note, D-1014, (1962).

36 THOMKE, G.J. and ROSHKO, A. McDonnell Douglas Corp. Rep. DAC 59819, (1969).

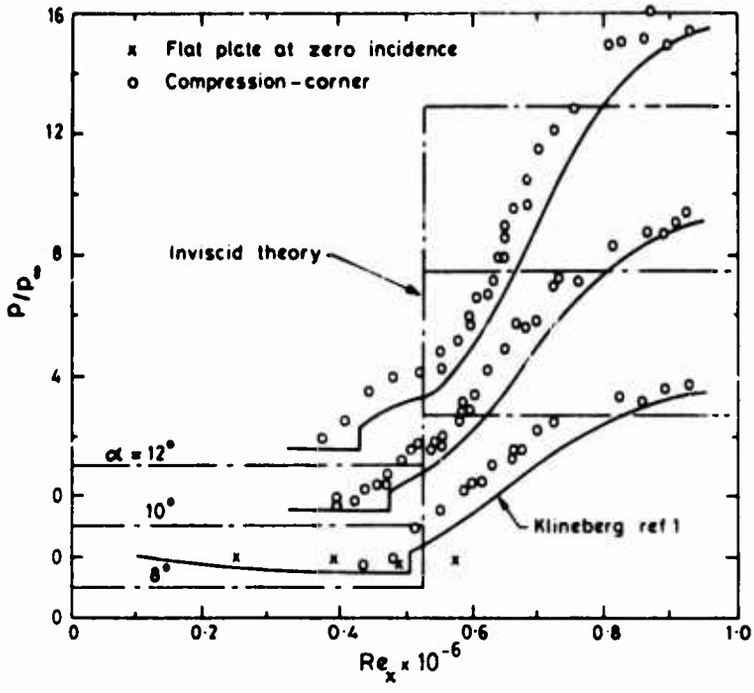

Figure 1a. Pressure distribution on the compression-corner model;

$M_\infty = 12.2$,

$Re_\infty = 0.87 \times 10^5 in.^{-1}$,

$T_w/T_o = 0.22$.

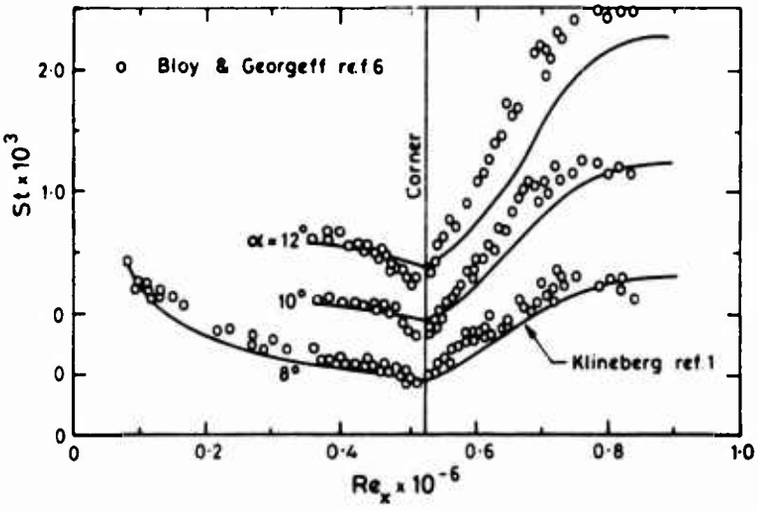

Figure 1b. Heat-transfer rate distribution on the compression-corner model;

$M_\infty = 12.2$,

$Re_\infty = 0.87 \times 10^5 in.^{-1}$,

$T_w/T_o = 0.22$.

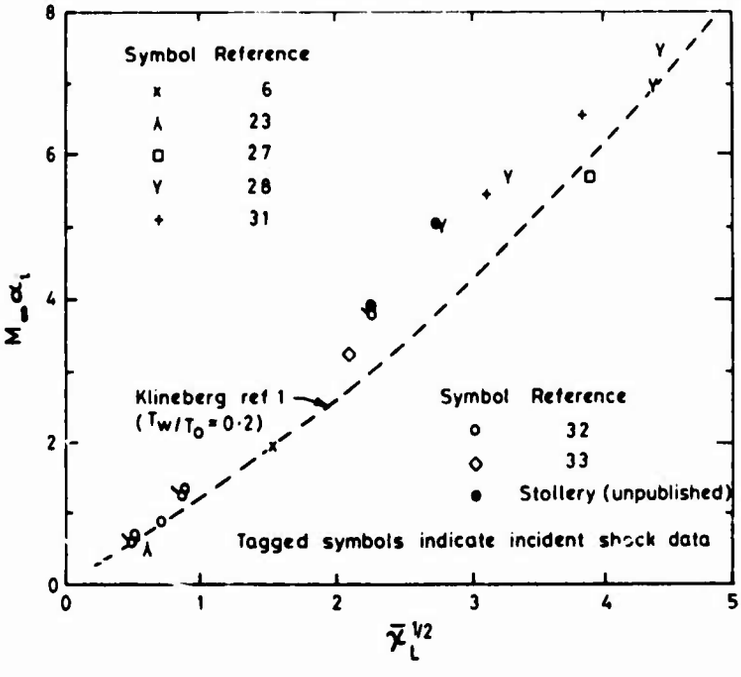

Figure 2. Correlation of hypersonic, cold wall, incipient separation data.

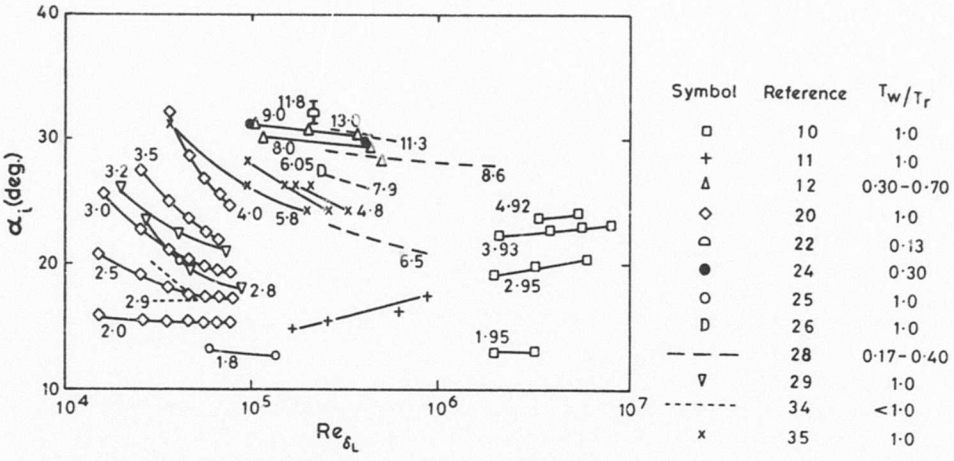

Figure 3. Incipient separation at a wedge compression corner.

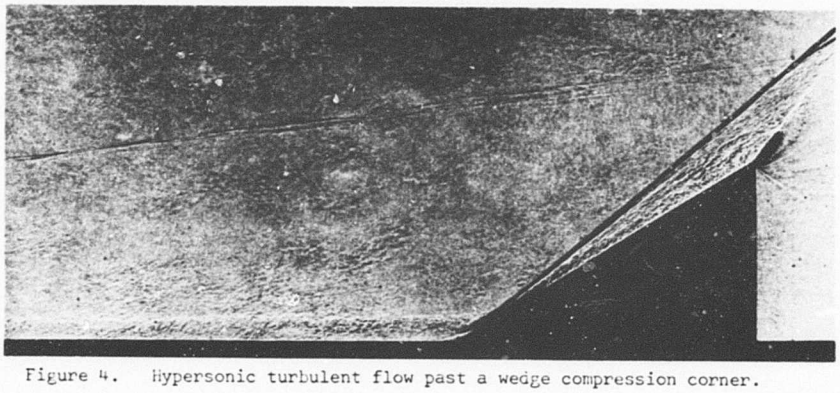

Figure 4. Hypersonic turbulent flow past a wedge compression corner.

$M_\infty = 9.22$, $Re_L = 24 \times 10^6$, $\alpha = 30^\circ$, $\frac{T_w}{T_o} = 0.28$

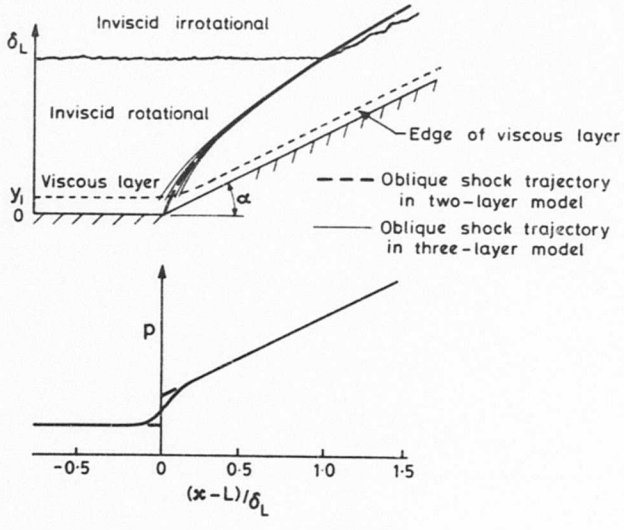

Figure 5a. Three-layer model of an attached flow field at a wedge-compression corner.

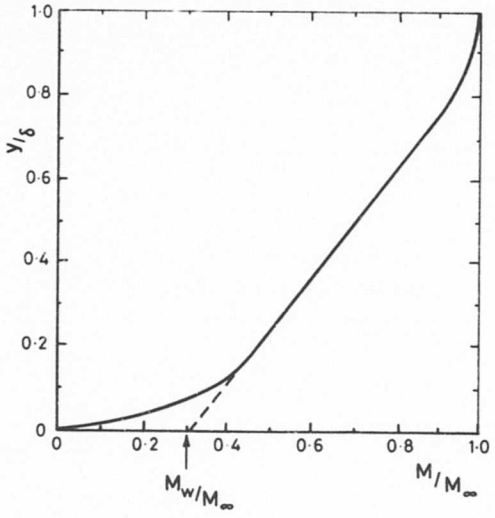

Figure 5b. Definition of M_w from Predicted Profile.

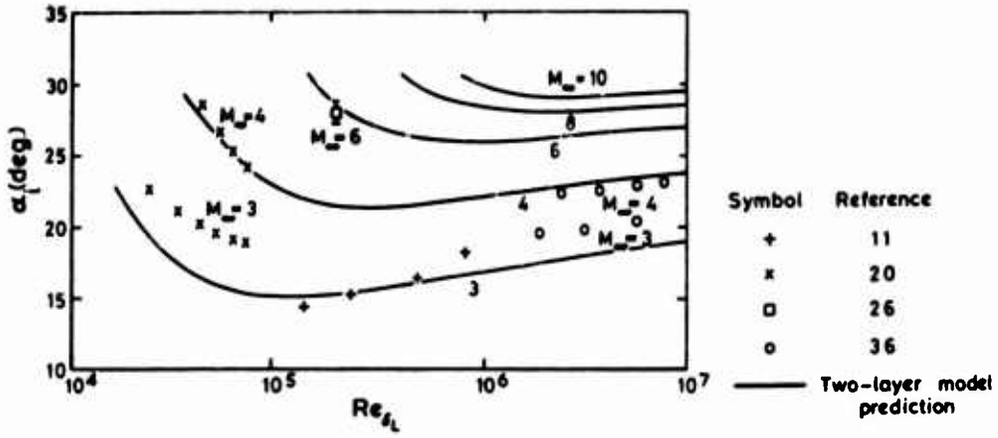

Figure 6a. Estimation of incipient separation for adiabatic wall conditions.

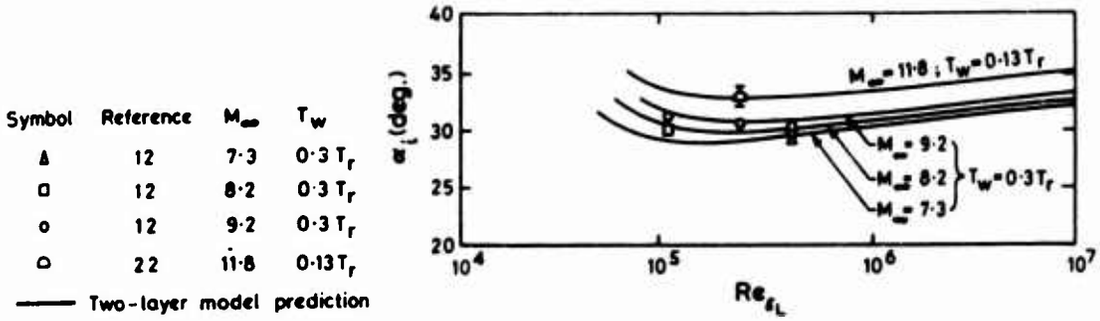

Figure 6b. Estimations of incipient separation of non-adiabatic wall conditions.

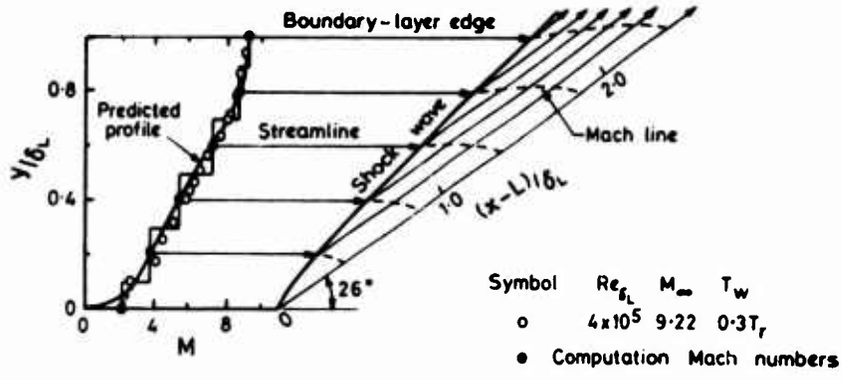

Figure 7a. Example of the construction of an attached flow field at a wedge-compression corner.

Figure 7b. Prediction of attached flow static pressure distribution at a wedge-compression corner.

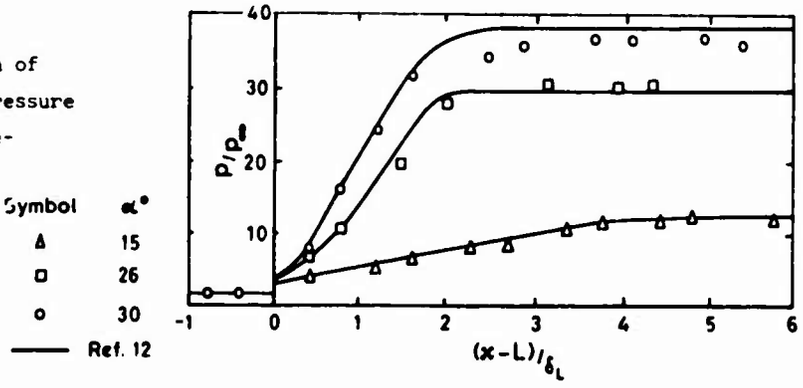

$M_\infty = 9.22$, $Re_{\delta_L} = 4 \times 10^5$, $T_w = 0.3 T_r$;

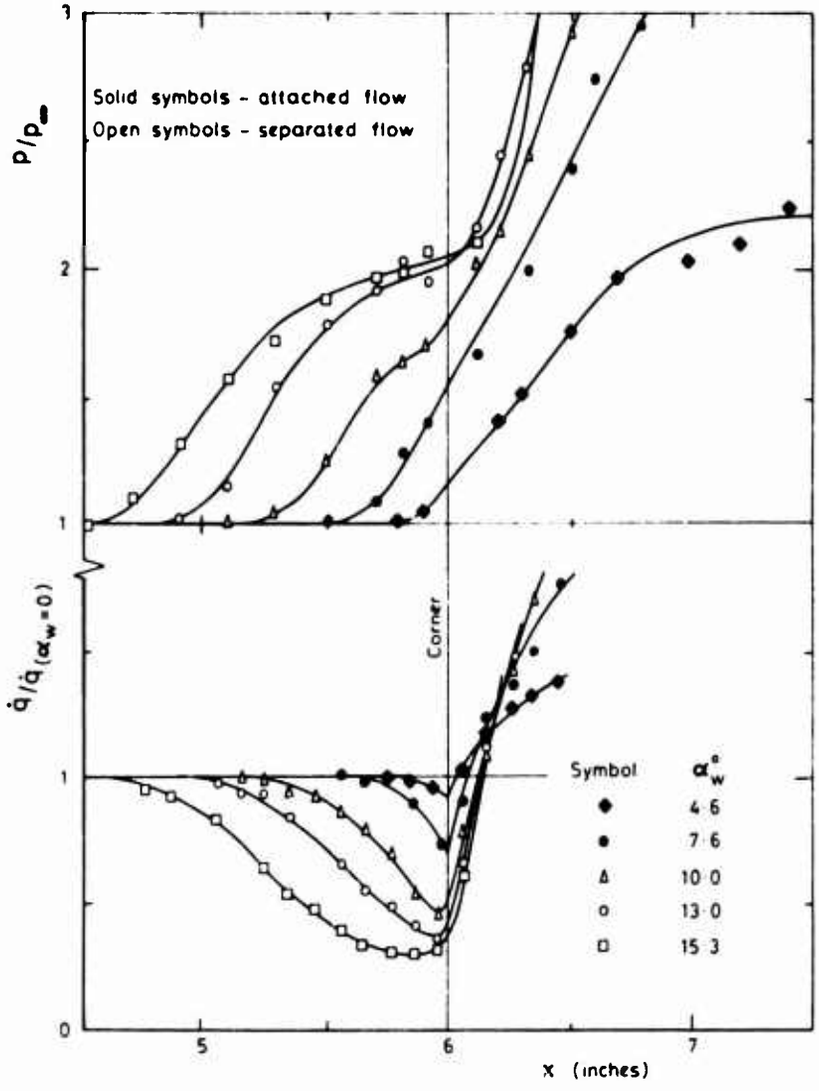

LAMINAR FLOW

Ref. 32

$M_\infty = 9.7$

$Re_L = 0.95 \times 10^6$

$T_w/T_o = 0.22$

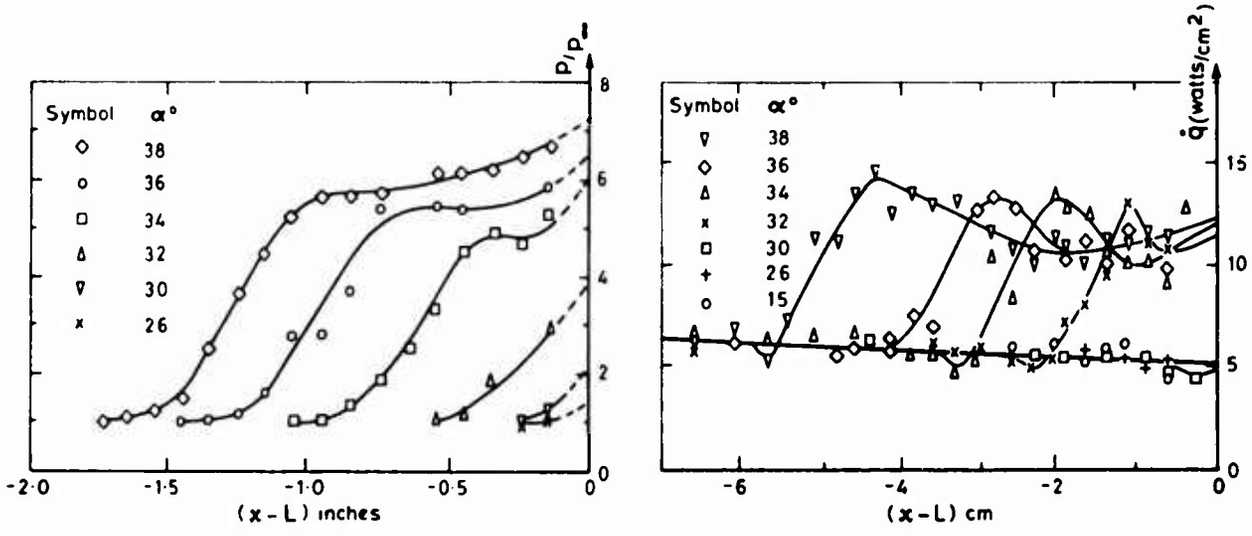

TURBULENT FLOW Ref. 16

$M_\infty = 9.22$ $Re_L = 28 \times 10^6$ $T_w/T_o = 0.28$

Figure 8. Flow past a wedge-compression corner. A comparison between the laminar and turbulent values of pressure and heat transfer.

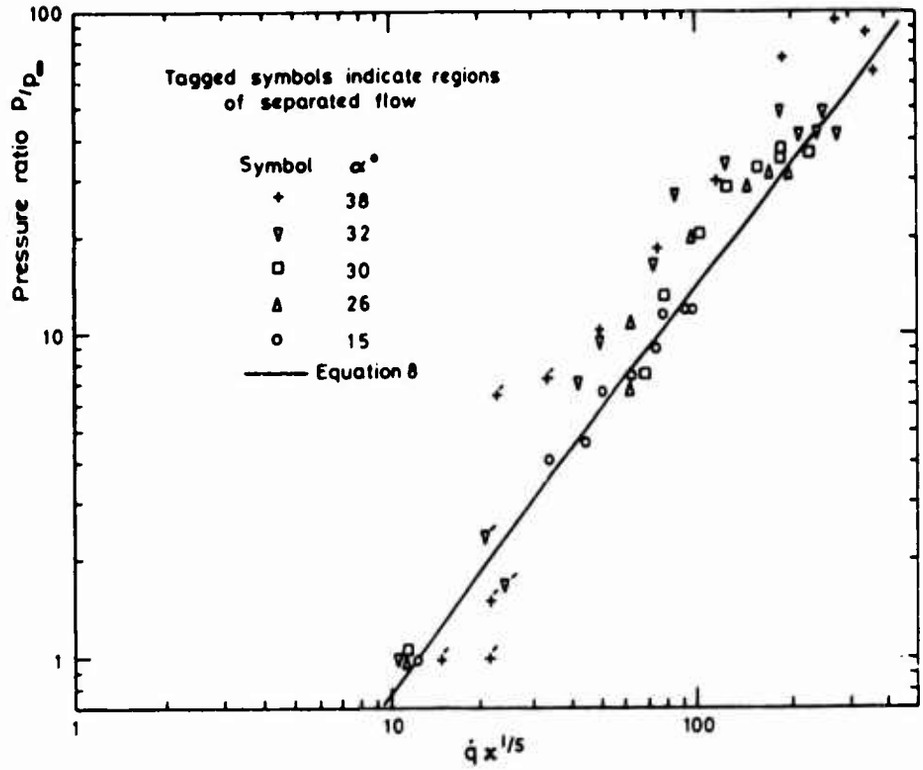

Figure 9. The pressure and heat transfer measurements of Coleman on a two-dimensional wedge-compression-corner compared with a simple prediction method.
M_∞ = 9.22, Re_L = 26 x 10^6, T_w/T_o = 0.28.

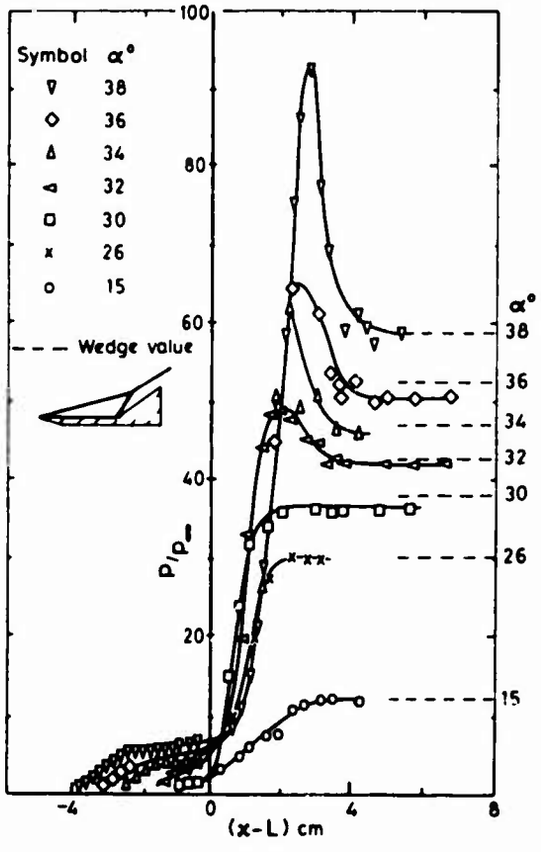

Pressure distributions on a wedge-compression corner.
M_∞ = 9.22, T_w/T_r = 0.28, $Re\delta_L$ = 3.4 x 10^5. Refs. 19&12

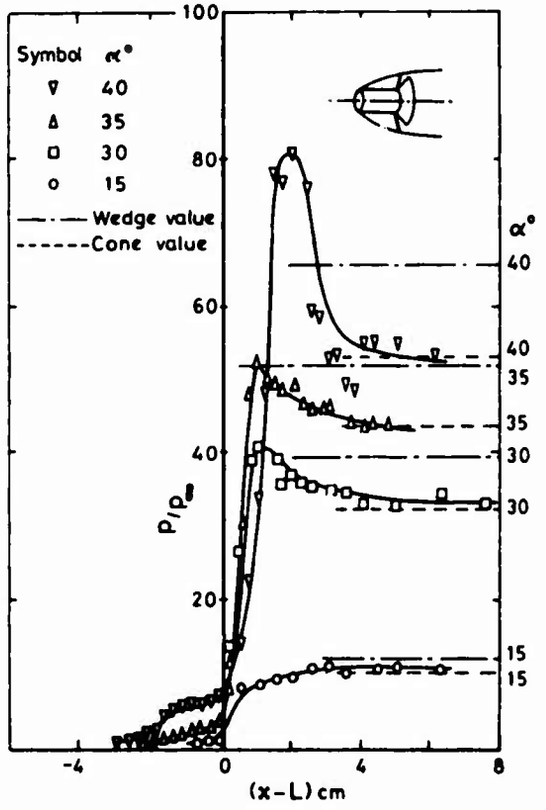

Pressure distributions on a hollow cylinder-flare
M_∞ = 9.22,
T_w/T_r = 0.28, $Re\delta_L$ = 2.14 x 10^5. Refs. 19&21

Figure 10. A comparison between two-dimensional and axially symmetric flow.

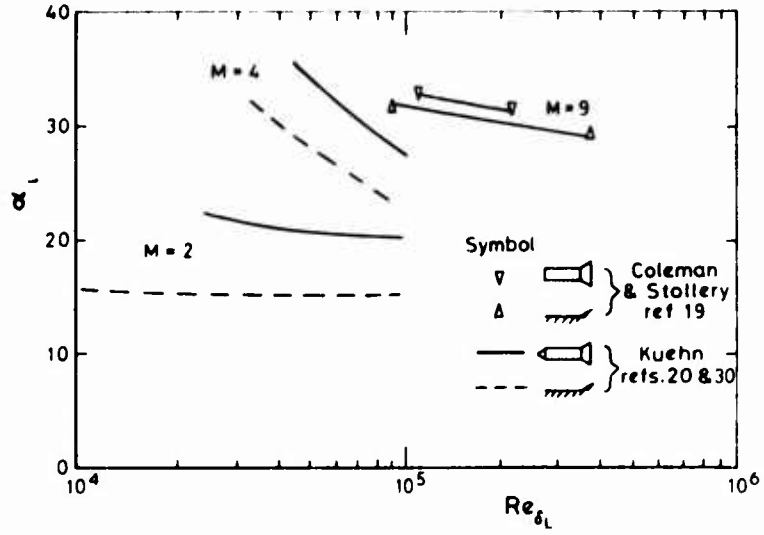

Figure 11. Comparison with wedge compression corner results. Incipient Separation on a Cylinder-Flare.

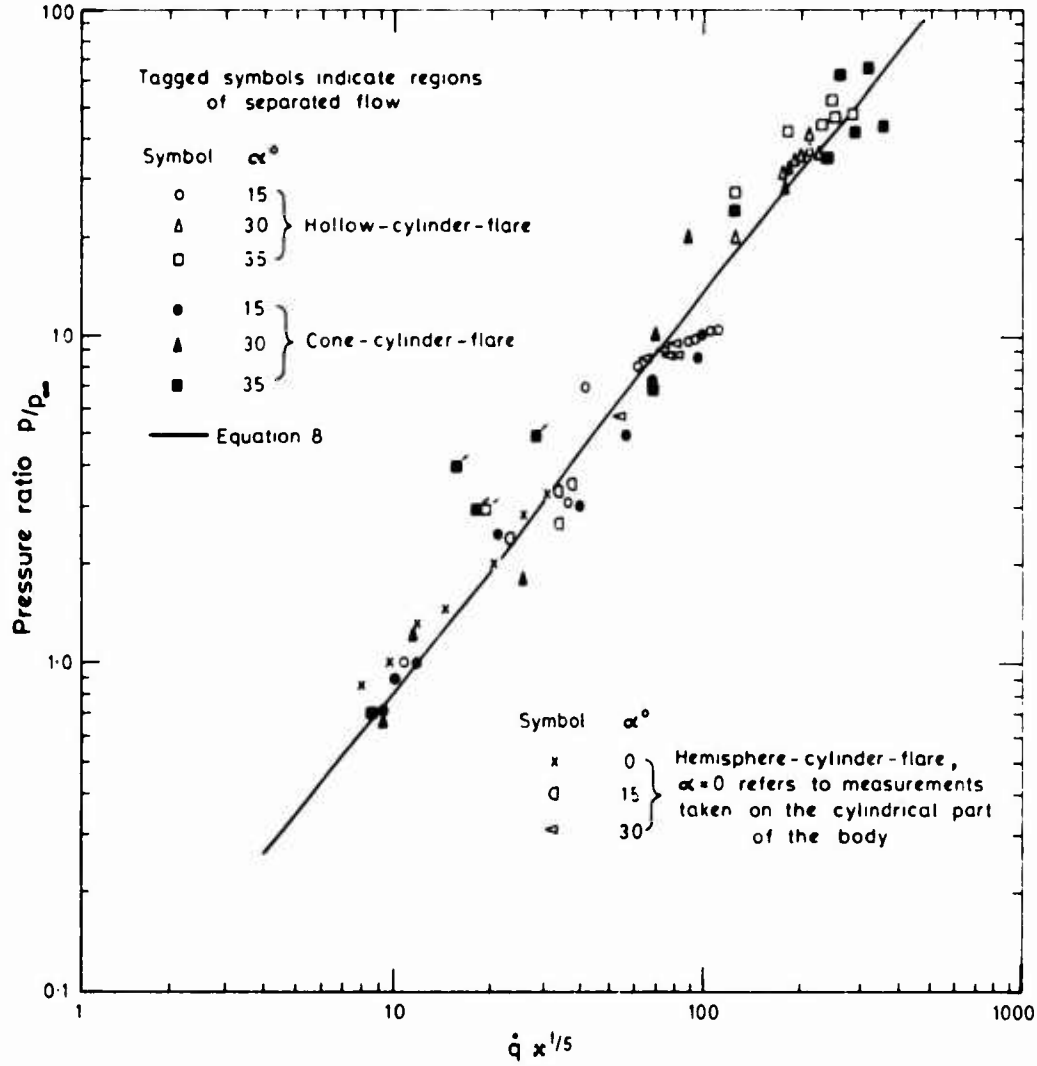

Figure 12. The pressure and heat transfer measurements of Coleman on a series of axi-symmetric flared bodies compared with a simple prediction method.

$M_\infty = 9.22$, $Re_L = 26 \times 10^6$, $T_w/T_o = 0.28$.

INCIPIENT SEPARATION OF A COMPRESSIBLE TURBULENT BOUNDARY LAYER

by

C. Appels, Research Assistant
B.E. Richards, Associate Professor
von Karman Institute for Fluid Dynamics
72 Chaussée de Waterloo
1640 Rhode-Saint-Genèse
Belgium

SUMMARY

The paper describes an experimental study of the separation of a turbulent boundary layer developed on nozzle walls induced by a compression corner at Mach numbers of 3.5 and 5.4 over a range of Reynolds numbers based on boundary layer thickness of 10^5-10^6. Careful application of liquid line and schlieren flow visualisation techniques were used to detect separated lengths down to one tenth of the boundary layer thickness. In this way separation was detected at lower flap angles than has been previously found at these conditions. The related finding of low incipient separation angle, α_i, implies that flow reversal may occur initially only in the laminar sublayer, and this is confirmed by the successful prediction of α_i by applying simple laminar correlations to this layer. This measured value of α_i is found to be little dependent on Mach number and it is concluded that the large dependence of α_i with this parameter found earlier by researchers is explained by each experiment detecting a different degree of onset of separation. The measured variation of α_i with Reynolds number appears to follow the trend of development of the wake component in the undisturbed boundary layer.

DECOLLEMENT IMINENT D'UNE COUCHE LIMITE TURBULENTE COMPRESSIBLE

RESUME

Cette communication décrit une étude expérimentale du décollement d'une couche limite turbulente se développant aux parois d'une tuyère, à des nombres de Mach de 3.5 et de 5.4 et des nombres de Reynolds basés sur l'épaisseur de couche limite variant entre 10^5 et 10^6. Une utilisation très soignée des techniques de visualisations de l'écoulement par strioscopie et par film liquide a conduit à la détection des longueurs de décollement aussi petites qu'un dixième de l'épaisseur de la couche limite. C'est ainsi qu'il a été possible de détecter le décollement à des angles de rampe plus faibles que précédemment dans de telles conditions. Le fait que le décollement se produise à de faibles angles α_i implique que la recirculation de l'écoulement se produit dans la sous-couche laminaire uniquement. Ce point de vue est confirmé par le fait qu'il est possible de calculer l'angle α_i d'une manière satisfaisante en appliquant une corrélation laminaire simple à cette sous-couche. On a trouvé que la valeur mesurée de α_i dépendait très peu du nombre de Mach. La très grande dépendance du nombre de Mach pour α_i, observée antérieurement par les chercheurs est expliquée par le fait que dans chaque expérience précédente, on détectait le décollement à des états différents. La variation de α_i mesurée en fonction du nombre de Reynolds apparait suivre la tendance de développement de la composante de l'onde dans une couche limite non perturbée.

NOMENCLATURE

C_f	skin friction coefficient
C_p	pressure coefficient
k	von Karman constant
L_s	distance between the separation point and the hinge line
M	Mach number
n	power-law velocity profile exponent
P	pressure
R	radius of curvature of axi-symmetric models
$Re_{( )}$	Reynolds number based on quantity ( )
Re_-	unit Reynolds number
T	temperature
T_r	recovery temperature
U	velocity component parallel to surface

U_τ friction velocity $\sqrt{\frac{\tau_w}{\rho}}$

y distance normal to the surface

α compression corner angle

β $\sqrt{M^2 - 1}$

δ boundary layer thickness

ν kinematic viscosity

ρ mass density

τ local shear stress

Subscripts

0 free stream conditions

e conditions at the edge of the boundary layer

i incipient separation conditions

L conditions at the edge of the sublayer

t total conditions

w conditions at the wall

INTRODUCTION

The separation of compressible turbulent boundary layers has been studied in some detail during the last 15 years. Since the onset of separation entirely changes the flow field, an important parameter of interest is one defining incipient separation. The first extensive investigation in this field was that of Kuehn (Ref.1, 1959) who used the appearance of a kink in the wall pressure distribution to detect incipient separation. Since then, several detection methods have been developed and the amount of experimental data has strongly increased; however, with it, the disagreement between results has become larger. The following influences on compression corner angle at incipient separation, α_i, are considered in this paper : the effect of Mach and Reynolds number, the state of the turbulent boundary layer (flat plate or nozzle wall boundary layer, fully developed or near-transitional boundary layer) and the method used to detect incipient separation. A brief survey of the literature is presented in a later discussion.

The primary aim of the present investigation was to make very careful measurements of α_i using techniques that could detect very small separation regions. This enabled a statement by Kuehn (Ref.1) to be examined, that when incipient separation conditions according to his detection method were reached, some evidence for the existence of small separation bubbles was found. He mentioned that these small separated regions were "primarily of academic interest", since they did not perceptibly affect the wall pressure distribution. Although this seems to be correct for the thin boundary layers prevalent in ground facilities, it is possible that on full scale models (e.g. re-entry vehicles) with very thick boundary layers these relatively small separated regions can become so large, that their effects can no longer be ignored. Furthermore, the understanding of the existence of these regions is of importance for any theoretical approach to the problem. Such a study has led to an explanation for the lack of agreement between several experimental investigations on incipient separation and a better understanding of the phenomenon.

EXPERIMENTAL PROCEDURE

The wind tunnels used in the experiments were blowdown facilities, both having two-dimensional contoured nozzles. The S4 supersonic tunnel with a Mach number of 3.5 has an 80mm x 100mm test section. The stagnation temperature is normally 6°C and the stagnation pressure can be varied between 2 and 17 kg/cm^2 giving unit Reynolds numbers from 10^7 to 10^8/m. The thickness of the boundary layer on the nozzle wall at the exit is between 6 and 7mm resulting in values for Re_δ of 9.10^4 to 7.10^5. The H1 pebble bed heated hypersonic 140mm x 145mm tunnel (Ref.2) with a Mach number of 5.4 can be operated at stagnation pressures varying from 13 to 33 kg/cm^2. All the tests reported herein were carried out at a temperature of approximately 200°C giving a range of unit Reynolds numbers from 10^7 to 3.10^7/m. The boundary layer thickness at the wall was somewhat less than 20mm and hence Re_δ could be varied between 2.10^5 and 6.10^5. A list of the free stream conditions used in this study is given in Table 1.

Pitot pressure traverses were made only through the undisturbed tunnel wall boundary layer at the position of the corner for all relevant test conditions in both tunnels. The wall static and pitot pressures were measured using very sensitive Ultradyne (Type 4184-10-1D) and Validyne (Type DP 15TL) transducers respectively, and the pitot pressure profile was directly recorded on an X-Y plotter through the use of a linear transducer. Different pitot probes were used in the two tunnels : a circular probe with an external diameter of 0.75mm for the M = 5.4 tunnel and a flat probe with

a height of 0.6mm for M = 3.5 tunnel. Both probes were calibrated against large circular versions in the free stream.

The model configurations used consisted of wedges of different angles (α) mounted at the same position on the tunnel wall; i.e., at the nozzle exit in the Mach 5.4 tunnel, and downstream of the nozzle exit in the Mach 3.5 tunnel. The test set-up in both tunnels is shown in Fig.1. The leading edge thickness of the wedge was small in order to attempt to eliminate steps at the hinge lines which could cause small separation bubbles. To avoid an interaction between the flow over the wedge and the boundary layers on the tunnel side walls, the span of the wedge was smaller than the width of the test section. The ratio of the span of the wedge to the undisturbed boundary layer thickness was 14 for the supersonic tests. However, this ratio was only 6.5 for the hypersonic tests so that it was impossible in this case to study large separated regions which could be classed as two-dimensional because of three-dimensional effects due to outflow.

Oil flow visualisation was one method used to detect the separation line. A liquid, consisting of oil, dye and oleic acid, was smeared on the wall or the wedge before the test. During the test, pictures of the resulting oil pattern were recorded. For large separated regions the oil film is expected to have a negligible interference on the separation behaviour and therefore oil was put on the hinge line and upstream of the separated region. A typical oil pattern seen during a test is shown in Fig.2. It is possible to see the complete separation line coincident with the accumulation of oil. This is the so-called "liquid line" method of detecting the separation line.

The main arguments that have been stated against the use of liquid line methods in the past are : the unsteady character of the separated region, the interaction between the liquid and the separation bubble due to their comparable thicknesses and finally the "buoyancy" effect (Ref.3). High speed schlieren pictures (5000 frames per second) of a small separated region taken during the present study (reported more fully in Ref.4) illustrated that the effect of the first factor is negligible. During the test, the separation length appeared to remain constant and the shape of the separation shock hardly changed. The two latter factors can be expected to be of importance only in small separated regions. To avoid interaction between the liquid and the separation bubble, observations of the separated length were made before the oil accumulated, so that the effect of the strong adverse pressure gradient on the oil (i.e. buoyancy) was negligible. In that case the driving force of the oil is the wall shear stress and not drag forces or pressure gradients. A few tests with much longer running times and strong accumulation of oil were carried out and they showed that after a while, at spanwise positions where the oil accumulation was greatest, entrainment of the oil into the separated region occurred and the separation bubble was filled up with oil. This demonstrates the existence of a close contact between the separation region and the oil accumulation line and so, even in this case, the accumulation is the result of a reversed flow and not of the balance between wind and buoyancy forces.

For small separated regions, however, one has to be very careful not to disturb the separation bubble by the introduction of the oil itself. Therefore only a very small quantity of oil was put ahead of the expected position of the separated region but not on the hinge line itself, so that during the test individual streamwise streaks of oil were formed, which stopped (at different times and spanwise positions) when encountering a region of reversed flow. Fig.3 helps to illustrate that with these precautions the interaction between the separation bubble and the oil flow will be negligible. The separation line was then visualised by only a few discrete points in any one test, however, exactly the same position was detected in repeat tests at different spanwise locations. In order to prove that the stagnation of the oil close to the hinge line for small wedge angles is due to a reversal in skin friction (and hence to a separation line), and not due to insufficient skin friction, several tests were carried out in which oil was put on the wedge close to the hinge line. The result is that the oil flows forward and stagnates at exactly the same position as found if the oil is placed upstream of the separated region. The effect of wedge leading edge thickness on the oil stagnation was proved to be negligible since no stagnation at all was detected in tests on compression corners at low deflection angles in which attached flow was expected.

Another method used to detect the separation line was through the use of a single pass schlieren system with a horizontal knife edge. The position of the separated line was determined by extrapolating the separation shock to the wall. The error on this extrapolation is relatively small as the shock is formed well within the boundary layer, very close to the wall (see Fig.4).

RESULTS AND DISCUSSION

Undisturbed boundary layer

Figs 5 and 6 show for both tunnels the Mach number profiles at two typical Reynolds numbers. The velocity profiles were obtained using the quadratic law

$$\left(\frac{U}{U_e}\right)^2 = \frac{T_t - T_w}{T_{t_e} - T_w}$$

which is often used in connection with tunnel wall boundary layers as an alternative to the linear Crocco law. The results from these calculations are also given in Figs 5 and 6. Examination of the fullness of these profiles reveals that the power law exponent n in the relation $U/U_e = (y/\delta)^{1/n}$ is increasing with increasing Reynolds number. A Van Driest transformation (Ref.5) was applied to these compressible profiles in order to compare them with generalised incompressible profiles. This particular method was chosen since, according to Ref.6 it gives the best correlation for the law-of-the-wall region. As the skin friction coefficient, required for these transformations, could not be measured, it was calculated using Spalding and Chi (Ref.7). The transformed profiles were compared in Fig.7 with Coles law-of-the-wall (Ref.8) and with the following logarithmic law :

$$\frac{U}{U_\tau} = \frac{1}{k} \ln \frac{yU_\tau}{\nu} + C$$

The deviation from these two laws in the outer part of the boundary layer shows that in all the profiles a strong developed wake component exists, which is in agreement with other tunnel wall data. The low values of U/U_τ, close to the wall in the Mach 3.5 profiles are due to probe-wall interference; this effect is of no importance in the M = 5.4 profiles because in that case the probe size is relatively much smaller, as is shown in Figs 5 and 6.

The variation of separation length with wedge angle

The wedge angle for incipient separation, the behaviour of which is discussed in the next section, was found by extrapolating the separation length for different wedge angles to zero. The development of the oil flow technique to detect very small bubbles described earlier allowed a reduction in the error involved in the extrapolation. The most well-defined separated length available from the visualisation techniques selected was the distance from the separation line to the corner. This length is called L_s in this study.

For typical values of Reynolds number, the values of L_s at Mach numbers of 3.5 and 5.4 using these techniques are plotted against wedge angle α in Figs 8 and 9. It is noted that the greater uncertainty in locating the separation line from the schlieren photographs is illustrated by the error bars placed on the appropriate data point. These results show clearly the existence of small separation bubbles at very low wedge angles and the considerable change in the rate of growth when the length of the separated region increases. The shape of the $L_s \sim \alpha$ curve can be explained physically as follows. As the wedge angle is increased from zero and the adverse pressure gradient generated becomes of the same value as the wall shear stress, initially only the inner (low velocity) part of the boundary layer near the corner will be decelerated and then reversed. The very small separated region generated this way is then only expected to be controlled by the conditions in the lower portion of the boundary layer. By further increasing the wedge angle, a larger proportion of the boundary becomes so influenced and the separated region grows. As this region is controlled by a larger proportion of the boundary layer, the rate of growth will change until the wedge angle (and hence the pressure gradient) is large enough to influence the whole boundary layer. Further increase in α will cause the separation bubble to grow, but the rate of growth will remain unchanged.

Definition of incipient separation

When using flow visualisation methods the angle of incipient separation is found by extrapolating the separation length, as a function of α to zero. However because of the change in the rate of growth of L_s, extrapolation of this curve L_s vs. α is highly dependent on the available number of data points and on the range of α for which these points were found. To illustrate this, two different extrapolation curves are shown in the Figs 8 and 9, one in which all the experimental results are used and a second in which the results below a certain value of α were neglected. This value was chosen such that the remaining curve has approximately the same form as those obtained by other investigators, whose measuring techniques had not adequate resolution to detect the smaller separated regions. The difference between the two extrapolations is shown in Figs 8 and 9 where the arrow indicates what value of separation length still exists when, according to the second extrapolation, incipient separation is apparently reached. Figs 10 and 11, in which curves faired through all the data taken in this test series have been plotted, show that for the same Mach number, the trend in separation length behaviour is the same for all Reynolds number cases. The angles of incipient separation determined from the two extrapolations of these curves are plotted against Reynolds number based on boundary layer thickness and compared with all the experimental data obtained by other investigators that was available for two-dimensional configurations as summarized in Table 2 (Refs 1,9-20). For completeness results from axisymmetric configurations are given in Table 2 (Refs 21-23) and plotted in Fig.13 compared with their two dimensional counterparts at similar conditions.

The most striking feature seen in these two figures is a lack of agreement in the magnitude of α_i even at similar conditions. This lack of agreement has been ascribed to differences in boundary layer properties (e.g. boundary layers on nozzle walls, boundary layers on flat plates, boundary layers at different stages of development, etc.) and to

the use of different methods of detecting incipient separation. The importance of each of these factors is still under discussion. Concerning the detection method Fig.12 shows that some investigators (Refs 17 and 19) found extremely low angles, using liquid line or similar techniques (most commonly used is the oil flow method). The careful examination of this technique described earlier provides strong evidence to its accuracy despite criticisms given in Refs 14 and 17. Another proof of the reliability of the oil flow method in particular, lies in comparison with other methods. Spaid and Frishett (Ref.19) found good agreement between their oil flow data, the results of a powder deposition technique and the extrapolation of the shock to the wall. In the axi-symmetric case Rose et al (Ref.23) used an alcohol injection technique and found values of α_i which are comparable with the two-dimensional liquid line data of Spaid and Frishett (Ref.19) and the present study. Finally, for the present study, Figs 8 and 9 show the very good agreement between oil flow data and results obtained by extrapolating the shock to the wall.

The large differences between most of the methods of detecting incipient separation can now be explained in terms of the existence of these very small separation bubbles, which in the beginning grow very slowly with increase in wedge angle. The accuracy of each method depends on the smallest size of separated region that can be detected. One of the most commonly employed methods has been the detection of the kink in the pressure distribution (Kuehn Ref.1). In the original report, Kuehn indicated that possibly some of his so-called attached flows could have had very small separation regions. More recently, several investigators (Refs 14, 19 and 23) showed that indeed the separated region has to reach a certain minimum size before an inflection in the pressure distribution occurs, even when very dense pressure instrumentation is used. It is also obvious that the spacing of the pressure taps changes the accuracy of detecting this inflection point. Because these small separated regions hardly effect the pressure distribution, the method of Roshko and Thomke (Ref.18), which assumes that α_i coincides with an inflection in the variation of pressure near the corner with α, cannot be accurate either. In other methods, Refs 18 and 23, probes or dams are introduced into the flow (surface pitots, orifice dams, etc.). The sizes of these objects relative to the size of the very small separation regions are not negligible, so that these methods are likely to be inaccurate as well. For hypersonic flows, the appearance of a pressure overshoot at re-attachment is used to detect incipient separation (Refs 9 and 13) but as this method is based on the existence of a double shock compression again it cannot be expected to detect small separation bubbles. The extrapolation of the length of relatively large separated regions, measured on schlieren pictures, to $L_s = 0$ (Refs 11 and 13) can result in large errors in α_i. This is illustrated in Figs 8 and 9, where the extent of separation present at the incipient separation angles obtained using such an extrapolation, is shown actually to be between 0.15 and 0.40 times the boundary layer thickness. Finally, there is the more positive method of measuring the reversal in skin friction, using floating element balances (Ref.14), which is theoretically the ideal approach to the problem. However, the development of these rather complicated measuring devices is in some cases still in an early stage, and apart from the fact that these gauges are often rather large compared to small separated regions, the reliability of these balances when used in complex flow fields like separation and re-attachment regions, is still in question.

As a conclusion, one can say that the incipient separation angles indicated in Fig.12 in most cases, do not represent incipient separation conditions, but the conditions at which a certain extent of separation occurs. This "certain extent" is a function of the detection method used. This explains why agreement between the data can be found when the same or similar methods are used. As an example, the results obtained by detecting a kink in the pressure distribution are in rather good agreement except for some disagreements caused probably by a lack of densely spaced instrumentation.

The effect of Reynolds number on incipient separation

Figs 12 and 13 show that the angle of incipient separation changes with Reynolds number. At first glance no obvious trend is apparent. Until recently, experiments indicated that α_i decreased with increasing Reynolds number except at very high Reynolds numbers where Roshko and Thomke found an opposite trend. Recent experiments (Refs 17 and 19) showed that for similar free stream conditions completely different trends are found. These differences can again be explained using arguments concerning the disturbance occurring at different stages of development of the turbulent boundary layers and the method of detecting incipient separation.

Spaid and Frishett proved in their experiments (Ref. 19, see the four curves in Fig.12 obtained using different techniques) that the latter factor can indeed influence the effect of Reynolds number on α_i. This could be due to the fact that these values of α_i represent a certain degree of onset of separation and if the growth of the separated region is a function of Reynolds number, the methods which detect small regions will suggest different Reynolds number trends than methods which detect only large regions. This argument of course, does not explain the different trends observed when using the same technique and therefore it is believed that the most important factor is the stage of development of the turbulent boundary layer. Elfstrom (Ref.13) indicated that the reversal in the α_i trend with Re_δ closely follows the development of the wake component in the velocity profile and hence the power law exponent n in the relation $U/U_e=(y/\delta)^{1/n}$. A stronger developed wake (higher n, fuller velocity profile) results in a more energetic boundary layer which is more resistant to separation. Studies in turbulent boundary layers on flat plates (Ref.24) proved that close to transition n decreases with increasing

Reynolds number (so-called overshoot in n) and at high Reynolds number, when the boundary layer is fully developed, n increases with Re. Up to now no experiments on turbulent separation (with the probable exception of one very recent study by Holden, Ref.15) have been carried out in this high Reynolds number region. Ref. 24 also shows that this overshoot in n does not exist in boundary layers on nozzle walls, because of the favourable pressure gradient, and therefore, in this case n (and hence α_i) increases even at low Reynolds numbers. This trend was also shown in the undisturbed boundary layer profiles described earlier. Combining the information in Table 2 and Figs 12 and 13, there appear to be no exceptions to Elfstrom's statement. Indeed comparison of the present data on tunnel walls with that of Ref.14 on flat plates but at similar freestream condition shows the expected opposite trend of α_i with Re_δ. It should be noted that the flat plate data of Law (Ref.17) appears contrary to this argument, but since the model is placed well into the nozzle, the boundary layer growth is expected to be the same as on nozzle walls.

The effect of the value of wall-to-recovery temperature ratio is neglected in this study, because previous investigations indicated that it is small and most of the experimental data considered are at approximately adiabatic conditions.

Empirical prediction of incipient separation

Several of the correlation methods for incipient separation conditions have been outlined in Ref.9 and some of these (e.g. that of Roshko and Thomke, Ref.18, shown in Fig.14) gave rather good agreement for most of the experimental results. However, this figure also shows that the very low incipient separation conditions detected in the present study, cannot be correlated in the same way. In order to account for these very small separated regions, new methods have to be developed. As discussed earlier, these small separation bubbles are probably a result of the flow reversal occurring initially only in the laminar sublayer, hence parameters based on this sublayer should be considered. In order to prove that this is the correct approach to the problem, a very simple method for predicting these low values of α_i was developed. The laminar sublayer was considered to have the separation characteristics of a laminar boundary layer, assuming that the conditions at the edge of the sublayer are the free stream conditions for this equivalent laminar boundary layer; hence, the influence of the outer part of the boundary layer is neglected. This assumption can be made as a first approximation since as the wedge angle is increased from a low angle, the separation will be restricted to a very small region (at the hinge line) deep in the turbulent boundary layer. A prediction method for laminar separated flows was then used to calculate incipient separation in that boundary layer.

The edge of the laminar sublayer was defined as being the position at which, in the transformed velocity profile :

$$\frac{yU_\tau}{\nu} = 15 \quad (\text{or} : \frac{U}{U_\tau} = 11.5).$$

The appropriate skin friction coefficient to be applied to this method was calculated from the actual skin friction coefficient assuming constant static pressure through the laminar sublayer, hence :

$$\frac{C_{f0}}{C_{fL}} = \frac{M_L^2}{M_0^2} .$$

For predicting laminar separation the correlation of Hakkinen et al. (Ref.25) was used :

$$\frac{P_s - P_\infty}{P_\infty} = 1.0 \sqrt{\frac{M_\infty^4 \cdot C_{f_\infty}}{\beta_\infty}}$$

where the index ∞ denotes free stream conditions which are, for this application, the conditions (L) at the edge of the laminar sublayer.

The method was applied to the undisturbed boundary layer profile data of the present study and of the investigation of Spaid and Frishett. The latter was the only work found that contained enough information to apply the method. The results are compared with the experimental data in Fig.12 and the degree of agreement is shown to be highly dependent on the Reynolds number. This could be connected with the thickness of the sublayer δ_L relative to the overall boundary layer thickness δ. As indicated in Ref.26, the sublayer is much thinner at higher Reynolds numbers and a factor of 10 difference was found for δ_L/δ between low Reynolds number experiments of Spaid and Frishett (Ref.19) and the high Reynolds number data of the present study. The poor prediction at high Reynolds numbers of the experimental values of α_i using the liquid line technique, are hence ascribed in part to the very crude prediction method, in which the interaction between the laminar sublayer and the rest of the turbulent boundary layer is neglected. Another reason may come from lack of resolution in measuring separation lengths, even

using careful application of oil flow techniques, at small wedge angles at high Reynolds numbers. This would result in difficulty in obtaining accurate measurements of α_i from extrapolation of the data. The good agreement achieved at low Reynolds numbers, when significantly the resolution of the technique for measuring separation length is of the order of the, now larger, sublayer thickness, gives good confidence in this empirical prediction method.

It is further encouraging to note that in the present study the Mach number trend of α_i is the same for the experiments and the prediction method, however, this trend is so small that one can only conclude that the Mach number dependence of α_i, when taking into account the very small separated regions, is almost negligible.

CONCLUSIONS

The present study shows that, with care, methods using oil flow visualisation are reliable for aiding the detection of incipient separation. The two visualisation methods (oil flow and schlieren) gave very similar values of the separation line of turbulent separated regions for each condition examined. For all test conditions the results of the tests indicate that very small separated regions exist at low deflection angles and that when the wedge angle is increased, initially a change in the rate of growth of the separation bubble occurs until the full boundary layer is influenced and large separated regions are formed. The disagreement between the present results and those obtained using other detection techniques (e.g. a kink in the pressure distribution) at similar conditions appears to arise from each method detecting a different degree of onset of separation. The general change in angle of incipient separation with Reynolds number follows closely the trend of the development of the wake component in the undisturbed boundary layer (as suggested by Elfstrom). The results of an approximate correlation method, consisting of a laminar incipient separation criterion applied to the laminar sublayer in the turbulent boundary layer, are in good agreement with liquid line data at relatively low Reynolds number. Both the experiments and the correlation method seem to indicate, when taking into account α_i as determined in the case of small separated regions that the Mach number dependence of the incipient separation angle is very weak. This would mean that the strong trends found using other detection methods, appear to represent the Mach number dependence of the growth of the small separated regions.

REFERENCES

1. Kuehn D.M. : "Experimental investigation of the pressure rise required for the incipient separation of turbulent boundary layers in two-dimensional supersonic flow", NASA Memo 1-21-59A, February 1959.
2. Korkegi R.H. : "The intermittent hypersonic wind tunnel H-1", TCEA(VKI) TM 15, March 1963.
3. Chapman D.R., Kuehn D.M., Larson H.K. : "Investigation of separated flows in supersonic and subsonic streams with emphasis on the effect of transition", NACA, Tech.Report 1356, 1958.
4. Appels C. : "Incipient separation of a compressible turbulent boundary layer", VKI TN 99, April 1974.
5. Van Driest E.R. : "Turbulent boundary layer in compressible fluids", IAS Journal, Vol.18, N°3, pp.145-160, 216, March 1951.
6. Keener E.R., Hopkins E.J. : "Turbulent boundary layer velocity profiles on a non-adiabatic flat plate at Mach number 6.5", NASA TN D-6907, August 1972.
7. Spalding D.B., Chi S.W. : "The drag of a compressible turbulent boundary layer on a smooth flat plate with and without heat transfer", J.F.M., Vol.18, part I, pp.117-144, January 1964.
8. Coles D. : "Measurements in the boundary layer on a smooth flat plate in supersonic flow, Part I : the problem of a turbulent boundar layer", Report 20-69, Jet Propulsion Lab., California Institute of Technology, June 1953.
9. Appels C. : "Turbulent boundary layer separation at Mach 12", VKI TN 90, September 1973.
10. Batham J.P. : "An experimental study of turbulent separating and re-attaching flows at a high Mach number", J.F.M., Vol.52, Part 3, pp.425-437, April 1972.
11. Coleman G.T., Stollery J.L. : "Heat transfer in hypersonic turbulent separated flow", I.C. Aero Report 72-05, March 1972.
12. Drougge G. : "An experimental investigation of the influence of strong adverse pressure gradients on turbulent boundary layers at supersonic speeds", FFA Report 47, 1953.
13. Elfstrom J.M. : "Turbulent separation in hypersonic flow", I.C. Aero Report 71-16, September 1971.
14. Holden M.S. : "Shock wave - turbulent boundary layer interaction in hypersonic flow", AIAA Paper 72-74, January 1972.
15. Holden M.S. : "Experimental studies of shock wave boundary layer interaction", VKI Lecture Series LS 62, January 1974.
16. Kessler W.C., Reilly J.F., Mockapetris L.J. : "Supersonic turbulent boundary layer interaction with an expansion ramp and compression corner", McDonnell Douglas Report, MDC EO 264, 1970.
17. Law H.C. : "Supersonic turbulent boundary layer separation measurements at Reynolds numbers of 10^7 to 10^8. AIAA Paper, N° 73-665, July 1973.

18. Roshko A., Thomke G.J. : "Supersonic turbulent boundary layer interaction with a compression corner at very high Reynolds number". Proceedings of the 1969 Symposium on "Viscous interactions phenomena in supersonic and hypersonic flow", A.R.L. pp.109-139, 1969.
19. Spaid F.W., Frishett J.L. : "Incipient separation of a supersonic turbulent boundary layer including effects of heat transfer", AIAA Journal, Vol.10, N°7, pp. 915-923, July 1972.
20. Sterrett J.R., Emery J.C. : "Experimental separation studies for two-dimensional wedges and curved surfaces at Mach numbers of 4.8 to 6.2", NASA TN D-1014, 1962.
21. Coleman G.T., Stollery J.L. : "Incipient separation of axially symmetric hypersonic turbulent boundary layers", AIAA Journal, Vol.12, N°1, pp.119-120, January 1974.
22. Kuehn D.M. : "Turbulent boundary layer separation induced by flares on cylinders at zero angle of attack", NASA TR R117, 1961.
23. Rose W.C., Page R.J., Childs M.E. : "Incipient separation pressure rise for a Mach 3.8 turbulent boundary layer", AIAA Journal, Vol.11, N°5, pp.761-764, May 1973.
24. Johnson C.B., Bushnell D.M. : "Power law velocity profile exponent variations with Reynolds number, wall cooling, and Mach number in a turbulent boundary layer, NASA TN D-5753, April 1970.
25. Hakkinen R.J., Greber I., Trilling L., Abarbanel S.S. : "The interaction of an oblique shock wave with a laminar boundary layer", NASA MEMO 2-18-59W, March 1959.
26. Kemp J.H., Owen F.K. : "Experimental study of nozzle wall boundary layers at Mach numbers 20 to 47", NASA TN D-6965, October 1972.

ACKNOWLEDGEMENTS

The authors thank the following persons : Mr. R. Conniasselle, Technical Engineer, Mr. J. Borrès, Electronics Engineer, Mr. J.C. Lobet, Photographic Technician and their helpers who assisted in the experiments and Mrs. L. Rigaux who carried out the typing. One of the authors (C. Appels) was financially supported by the I.W.O.N.L. (Instituut ter Aanmoediging van het Wetenschappelijk Onderzoek in Nijverheid en Lanbouw).

TABLE 1 : SUMMARY OF TEST CONDITIONS

P_t kg	T_t °K	M	T_w/T_R	Re_∞ /m	δ mm	Cf_0
2	278	3.46	1.0	$1.28\ 10^7$	7.3	$1.64\ 10^{-3}$
5	278	3.46	1.0	3.20	6.5	1.40
8	278	3.46	1.0	5.13	6.3	1.30
11	278	3.46	1.0	7.05	6.2	1.22
14	278	3.46	1.0	8.97	6.0	1.18
17	278	3.46	1.0	10.89	5.9	1.14
13	470	5.45	.72	1.46	19.8	1.04
20	470	5.45	.72	2.16	18.3	.96
33	470	5.45	.72	3.66	18.2	.88

TABLE 2 : REVIEW OF INCIPIENT SEPARATION DETECTION METHODS

INVESTIGATOR	METHOD OF DETECTION OF INCIPIENT SEPARATION	TEST CONFIGURATION
1. Appels Ref.9	- Disappearance of the overshoot in the wall pressure distribution	Flat plate - wedge δ = 6.5mm
2. Batham Ref.10	- Distance between separation and re-attachment shocks measured on schlieren pictures - Appearance of a kink in the wall pressure distribution	Flat plate - wedge δ = 4.8 - 6.5mm

Table 2 (Cont'd)

3. Coleman Ref.11	- Distance between separation and re-attachment shocks measured on schlieren pictures. Linear extrapolation of L_s to zero.	Flat plate - wedge δ = 7.6 - 8.2mm
4. Drougge Ref.12	- Appearance of a kink in the wall pressure distribution - Change in angle of shock-wave, due to the formation of a double shock system	Flat plate - wedge at low Reynolds numbers Tunnel wall - wedge at high Reynolds numbers
5. Elfstrom Ref.13	- Disappearance of the overshoot in the wall pressure distribution - Distance between separation and re-attachment shocks measured on schlieren pictures. Linear extrapolation of L_s to zero. - Inflection in the variation of pressure near the corner with α.	Flat plate - wedge δ = 8mm
6. Holden Refs 14-15	- Separation length measured on schlieren pictures - Detection of flow reversal using skin friction balances	Flat plate - wedge
7. Kessler et al. Ref.16	No information available	
8. Kuehn Ref.1	- Appearance of a kink in the wall pressure distribution	Flat plate - wedge Use of boundary layer trip δ = 2 - 4mm
9. Law Ref.17	- Appearance of a kink in the wall pressure distribution - Inflection in the variation of pressure in front of the corner with α - First appearance of the deflection of the boundary layer measured on schlieren pictures - Oil flow method	Flat plate - wedge Leading edge of flat plate far upstream of nozzle exit, hence large favourable pressure gradient. δ = 4mm
10. Roshko & Thomke Ref.18	- Inflection in the variation of pressure near the corner with α - Detection of separation and re-attachment using orifice dams	Tunnel wall - wedge δ = 75 - 140mm
11. Spaid & Frishett Ref.19	- Oil flow method - Powder deposition technique - Extrapolation on schlieren pictures of the separation shock to the wall - Change in shock wave angle, due to the formation of a double shock system - Inflection in the variation of pressure in front of the corner with α.	Tunnel wall - wedge δ = 8mm
12. Sterrett & Emery Ref.20	- Appearance of a kink in the wall pressure distribution	Flat plate - wedge with and without roughness trips δ = 4 - 8mm
13. Present study (also Ref.4)	- Oil flow method - Extrapolation, on schlieren pictures, of the separation shock, to the wall	Tunnel wall - wedge δ = 6 & 20mm
14. Coleman Ref.21	Similar techniques as Elfstrom's and Coleman's two-dimensional tests, see N°3 and 5	Hollow cylinder-flare δ = 4mm R/δ = 8
15. Kuehn Ref.22	- Appearance of a kink in the wall pressure distribution	Cone-cylinder-flare δ = 4.5mm R/δ = 3.65

Table 2 (Cont'd)

16. Rose et al. Ref.23	- Injection of oil in the separated region (liquid line method) - Detection of separation and re-attachment using orifice dams - Appearance of a kink in the wall pressure distribution - Appearance of a kink in the surface pitot pressure distribution	Axi-symmetric tunnel wall Shock induced separation δ = 5mm R/δ = 5

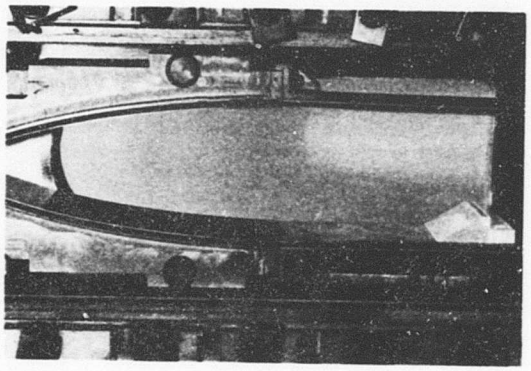

Fig. 1a : Compression corner on the wall of the M=3.5 tunnel

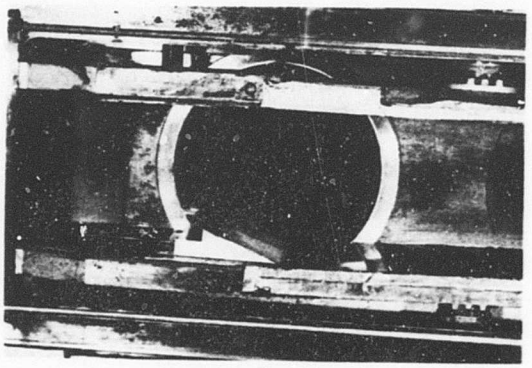

Fig. 1b : Compression corner on the wall of the M=5.4 tunnel

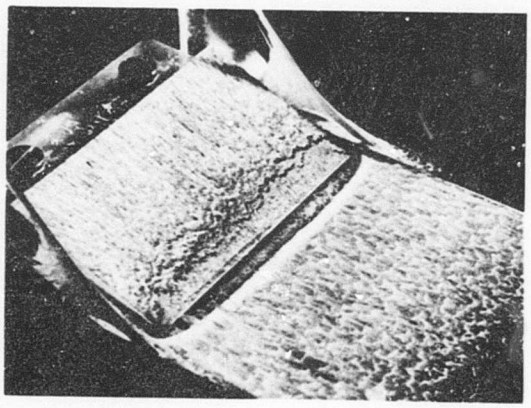

Fig. 2 : Oil flow pattern for large separated regions

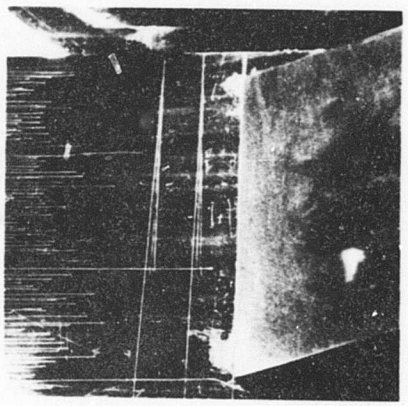

Fig. 3 : Oil flow pattern for small separated regions

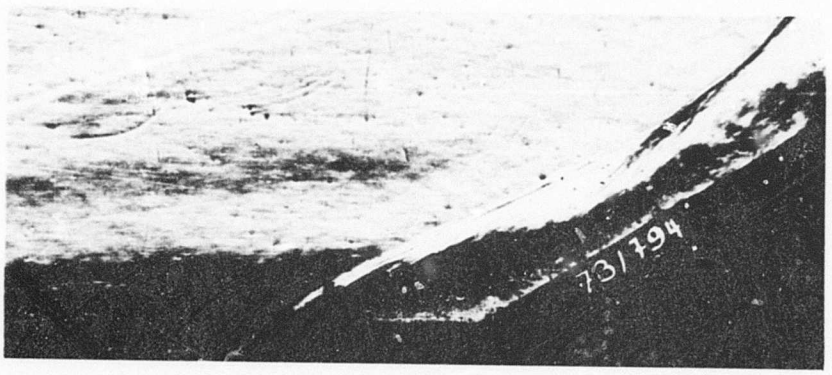

Fig. 4 : Schlieren picture of a separated flow

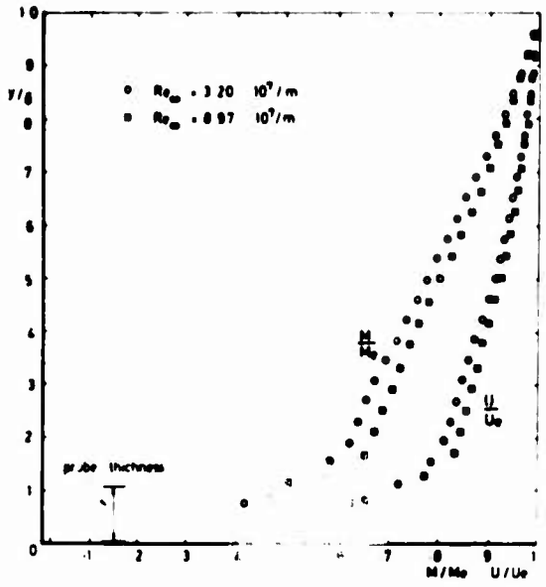

Fig. 5 : Mach number and velocity profiles for the turbulent boundary layer on the M=3.5 tunnel wall

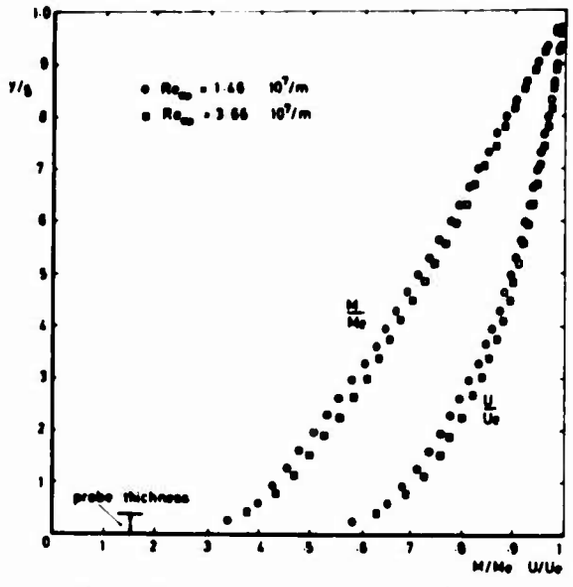

Fig. 6 : Mach number and velocity profiles for the turbulent boundary layer on the M=5.4 tunnel wall

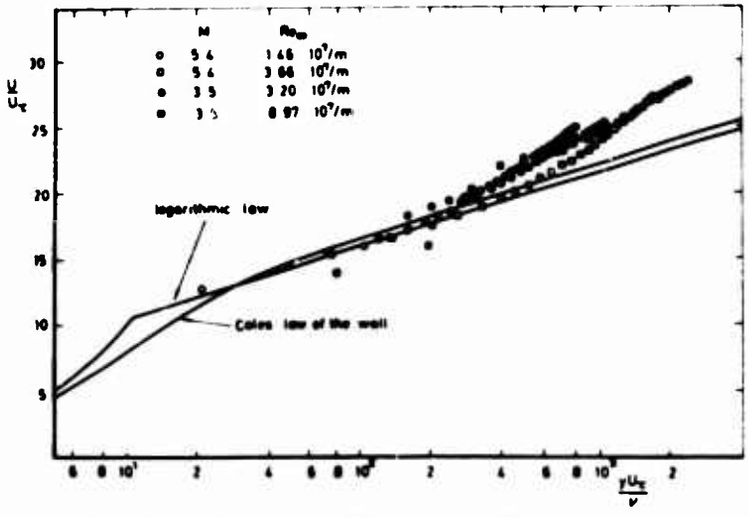

Fig. 7 : Compressibility transformation of Van Driest applied to the boundary layer velocity profiles

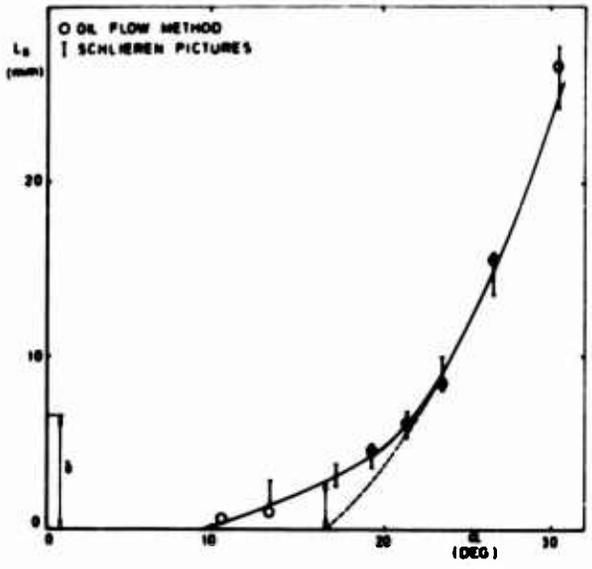

Fig. 8 : Separation length as function of the wedge angle, M=3.5, $Re_\delta = 2.07 \times 10^5$

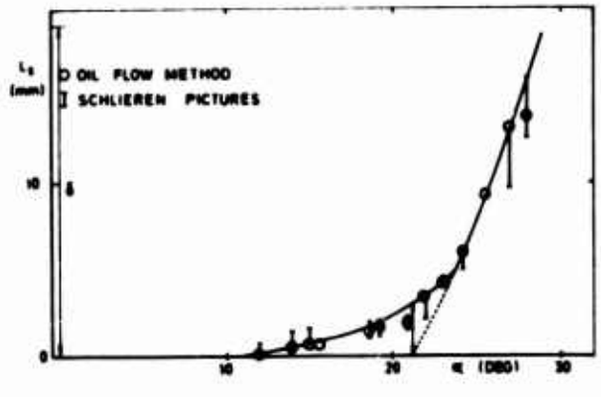

Fig. 9 : Separation length as function of the wedge angle, M=5.4, $Re_\delta = 6.67 \times 10^5$

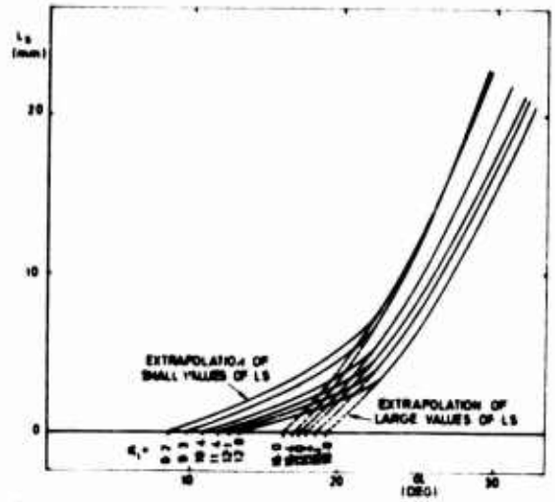

Fig. 10 : Detection of incipient separation by extrapolating the separation length M=3.5

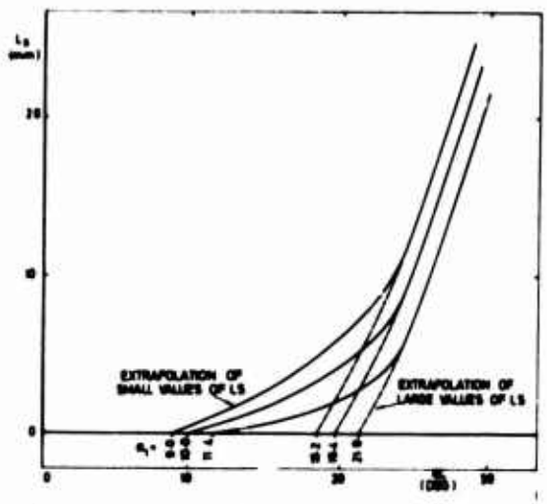

Fig. 11 : Detection of incipient separation by extrapolating the separation length M=5.4

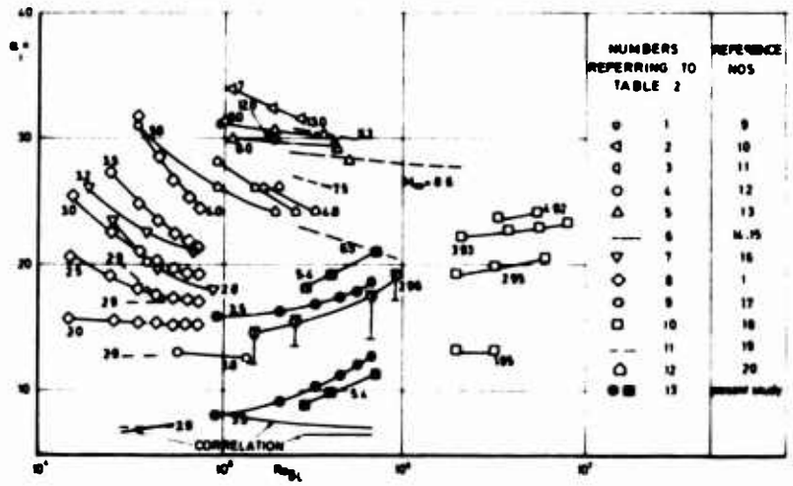

Fig. 12 : Incipient separation angles for two-dimensional configurations

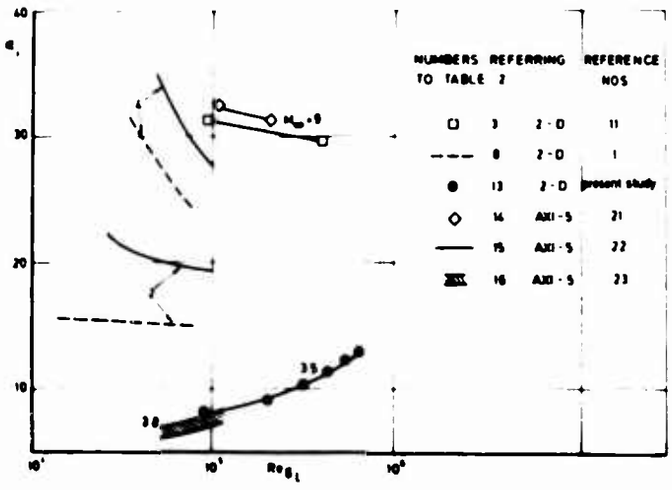

Fig. 13 : Comparison of incipient separation angles between two-dimensional and axisymmetric configurations

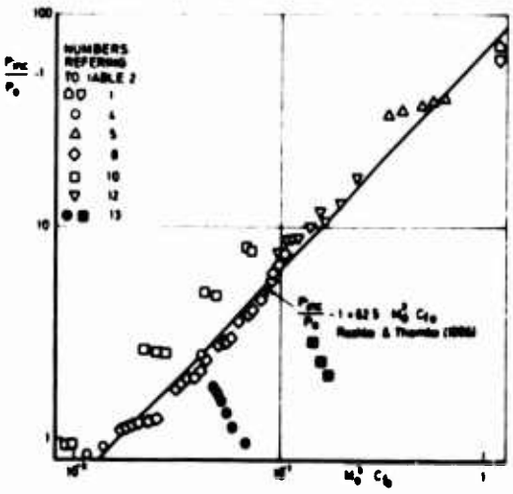

Fig. 14 : Correlation method for the pressure rise to incipient separation

ON THE CALCULATION OF SUPERSONIC SEPARATING AND REATTACHING FLOWS

By John D. Murphy, Leroy L. Presley, and William C. Rose
Ames Research Center, NASA
Moffett Field, California, 94035

SUMMARY

A method is developed for solving the laminar and turbulent compressible boundary-layer equations for separating and reattaching flows. Results of this method are compared with experimental data for two laminar and three turbulent boundary-layer, shock-wave interactions. Several Navier-Stokes solutions are obtained for each of the laminar boundary-layer, shock-wave interactions considered. Comparison of these solutions indicates a first-order sensitivity in C_f to the computational mesh selected in *both* the viscous and inviscid portions of the flow.

Three turbulent boundary-layer, shock-wave interactions were considered: one unseparated interaction at $M = 3$ and two separated interactions at $M = 1.47$ and 3. Boundary-layer theory appeared to be adequate to describe the first two of these interacting flows; however, for the separated interaction at $M = 3$, boundary-layer theory failed.

Comparison of the present boundary-layer solutions with the Navier-Stokes solutions and with data for a given Mach number indicates that as long as the separation bubble is small, the boundary-layer approximation yields solutions whose accuracy is comparable to the Navier-Stokes solutions.

NOMENCLATURE

C	Chapman-Rubesin constant
C_f	skin-friction coefficient, $C_f = \tau_w/(1/2)\rho_0 u_0^2$
DC	difference coefficient multiplying quantities at x
DM	difference coefficient multiplying quantities at $x - \Delta x$
DP	difference coefficient multiplying quantities at $x + \Delta x$
E	Eckert number, $u_e^2/2H_e$
F	defined in Eq. (12)
f	dimensionless stream function
H	total enthalpy $h + (u^2/2)$
h	static enthalpy
ℓ	mixing length
M_0	initial Mach number
M	number of nodes in x direction
N	number of nodes in y direction
n	iteration number
Pr	Prandtl number
Pr_T	turbulent Prandtl number
p	pressure
R	gas constant
r	body radius
S	entropy
T	temperature
U	defined in Eq. (12)
u	velocity component in x direction
v	velocity component in y direction
x	streamwise variable
y	cross stream variable
α	weighting factor in type dependent differencing
β	boundary-layer pressure gradient parameter $= (2\xi/u_e)(du_e/d\xi)$
γ	ratio of specific heats
δ	boundary-layer thickness or stream angle
δ^*	displacement thickness
ϵ	residual error
ζ	y_u/y_ℓ
η	transformed y variable
μ	viscosity or Mach angle $[\mu = \sin^{-1}(1/M)]$
ξ	transformed x variable
ρ	density
σ	defined in Eq. (18)
τ	shear stress
τ_T	turbulent shear stress
$(\,)'$	differentiation with respect to η

Subscripts

e	evaluated at boundary-layer edge
f	evaluated at final conditions downstream of interaction
i	evaluated at ith x-point
j	evaluated at jth y-point
ℓ	lower boundary
o	evaluated on initial line
t	evaluated at stagnation conditions
u	upper boundary
w	evaluated at wall conditions

INTRODUCTION

It is generally agreed that the problem of separating and reattaching flows is one of the more challenging and technologically relevant problems in computational fluid mechanics. In recent years, the computational attack has taken place on two fronts - the engineering approach by way of boundary-layer theory and the pure numerical approach by way of the Navier-Stokes equations. Reasonably complete summations of the status of these two approaches up to about 1970 are contained in References 1 through 3. During the past two or three years, substantial additional progress has been made in the boundary-layer theory approach by Klineberg and Steger (Ref. 4) and Carter (Ref. 5), and in the Navier-Stokes equation approach (Refs. 6 through 11). The basic position taken by each of these schools of thought can be summarized as follows: the Navier-Stokes equations are undoubtedly the correct equations for describing the flow fields in question and, since we can solve them it is unnecessary to settle for approximations. The boundary-layer contingent would concur with the above but they would add that the cost of Navier-Stokes solutions both now and in the near future is far too high to permit their use as design tools.

The present study examines these positions in some detail. In particular, we are concerned with establishing, at least qualitatively, the limits of applicability of the boundary-layer approximation for both laminar and turbulent separating and reattaching flows. Secondly, we are concerned with the development of an economical and reasonably accurate engineering calculation scheme for such flows.

ANALYSIS

Viscous-flow calculations

The procedure used to solve the viscous-flow portion of the calculation is a generalized Galerkin method (Refs. 12 and 13) applied to the boundary-layer equations. The equations considered are

$$\frac{\partial \rho u r^k}{\partial x} + \frac{\partial \rho v r^k}{\partial y} = 0 \tag{1}$$

$$\rho u \frac{\partial u}{\partial x} + \rho v \frac{\partial u}{\partial y} = - \frac{dP}{dx} + \frac{\partial}{\partial y}\left(\mu \frac{\partial u}{\partial y} + \rho \tau_T\right) \tag{2}$$

$$\rho u \frac{\partial H}{\partial x} + \rho v \frac{\partial H}{\partial y} = \frac{\partial}{\partial y}\left[\frac{\mu}{Pr} \frac{\partial H}{\partial y} + \frac{\mu}{2}\left(1 - \frac{1}{Pr}\right)\frac{\partial u^2}{\partial y}\right] + \frac{\partial}{\partial y}\left\{\rho \tau \left[\frac{1}{Pr_T} \frac{\partial H/\partial y}{\partial u/\partial y} + u\left(1 - \frac{1}{Pr_T}\right)\right]\right\} \tag{3}$$

$$P = \rho R T \tag{4}$$

$$\rho \tau_T = \rho \ell^2 \left|\frac{\partial u}{\partial y}\right| \frac{\partial u}{\partial y} \tag{5}$$

Only adiabatic flows with $Pr = Pr_T = 1$ are treated here; hence, Eq. (3) is replaced by $h + (u^2/2) = \text{const}$. To suppress the streamwise growth of the boundary layer and to facilitate initialization, Eqs. (1) and (2) are combined under the Levy-Lees-Dorodnitsyn transformation $(x,y) \rightarrow (\xi,\eta)$ where

$$\xi = \int_0^x \rho_e u_e \mu_e r^{2k}\, dx, \qquad \eta = \frac{\rho_e u_e r^k}{\sqrt{2\xi}} \int_0^y \frac{\rho}{\rho_e}\, dy$$

$$f = \frac{1}{\sqrt{2\xi}} \int_0^y \rho u\, dy, \qquad f' = \frac{u}{u_e}$$

which results in

$$(Cf'')' + ff'' + \beta\left(\frac{\rho_e}{\rho} - f'^2\right) + K_1 \rho \tau - 2\xi\left(f' \frac{\partial f'}{\partial \xi} - f'' \frac{\partial f}{\partial \xi}\right) = 0 \tag{6}$$

where $K_1 = \sqrt{2\xi}/u_e r^k$ and the primes indicate differentiation with respect to η. The following analysis closely parallels that of Kendall and Bartlett (Ref. 13). The present method extends that of Reference 13 to treat separated flow and is restricted to calorically and thermally perfect gases.

η-dependent differencing. To apply the generalized Galerkin method, the approximations for the stream function, velocity, and shear between adjacent nodes are chosen as

$$f_{j+1} = f_j + f'_j \Delta\eta + f''_j \frac{\Delta\eta^2}{2} + f'''_j \frac{\Delta\eta^3}{3} + f'''_{j+1} \frac{\Delta\eta^3}{24} \tag{7}$$

$$f'_{j+1} = f'_j + f''_j \Delta\eta + f'''_j \frac{\Delta\eta^2}{3} + f'''_{j+1} \frac{\Delta\eta^2}{6} \tag{8}$$

$$f''_{j+1} = f''_j + f'''_j \frac{\Delta\eta^2}{2} + f'''_{j+1} \frac{\Delta\eta^2}{2} \tag{9}$$

These relations are obtained by a Taylor series expansion to terms including f^{IV} and substitution of $f^{IV}_j = (f'''_{j+1} - f'''_j)/\Delta\eta$. Equations (7) through (9) are substituted in Eq. (6) and the results integrated with respect to a unit square-wave weighting function from η_j to η_{j+1} to yield:

$$Cf''\Big|_{\eta_j}^{\eta_{j+1}} + ff'\Big|_{\eta_j}^{\eta_{j+1}} - \left(1 + \frac{2\beta}{2 - E}\right)\sum_{k=1}^{4} f_j^k XPK + \frac{\beta}{2 - E}\,\eta\Big|_{\eta_j}^{\eta_{j+1}} + K_1 \tilde{\tau}\Big|_{\eta_j}^{\eta_{j+1}} - 2\xi\int_{\eta_j}^{\eta_{j+1}} f' \frac{\partial f'}{\partial \xi}\, d\eta + 2\xi\int_{\eta_j}^{\eta_{j+1}} f'' \frac{\partial f}{\partial \xi}\, d\eta = 0 \tag{10}$$

where

$$\sum_{k=1}^{4} f_j^k XPK = f'_j XP1 + f''_j XP2 + f'''_j XP3 + f'''_{j+1} XP4 = \int f'^2\, d\eta$$

and

$$XP1 = \Delta\eta\left(f'_j + f''_j \frac{\Delta\eta}{2} + f'''_j \frac{\Delta\eta^2}{8} + f'''_{j+1} \frac{\Delta\eta^2}{24}\right)$$

$$XP2 = \frac{\Delta\eta^2}{2}\left(f'_j + f''_j\frac{2\Delta\eta}{3} + f'''_j\frac{11\Delta\eta^2}{60} + f'''_{j+1}\frac{\Delta\eta^2}{15}\right)$$

$$XP3 = \frac{\Delta\eta^3}{8}\left(f'_j + f''_j\frac{11\Delta\eta}{15} + f'''_j\frac{66\Delta\eta^2}{315} + f'''_{j+1}\frac{5\Delta\eta^2}{63}\right)$$

$$XP4 = \frac{\Delta\eta^3}{24}\left(f'_j + f''_j\frac{4\Delta\eta}{5} + f'''_j\frac{5\Delta\eta^2}{21} + f'''_{j+1}\frac{2\Delta\eta^2}{21}\right)$$

The two terms remaining to be integrated are discussed under x-Dependent Differencing. This procedure yields a consistent differencing method that is fourth-order accurate in η and Eqs. (7) through (9) ensure that the stream function, velocity, and shear are defined everywhere (not only at nodal points) and are continuous everywhere. Equations (7) through (10) provide a sequence of 4(N-1) equations in 4N unknowns, where N is the number of nodes normal to the wall. Note that 3(N-1) of these equations are linear algebraic equations while (N-1) equations are nonlinear ordinary differential equations. The remaining four equations are imposed as boundary conditions:

$$f = f' = 0 \quad \text{at} \quad \eta = 0$$

$$f' = 1, \quad f'' = 0 \quad \text{at} \quad \eta = \infty$$

We note in passing that while the differential equation is only third order, the high-order differencing method requires an additional boundary condition. The complete system is solved by use of a Newton-Raphson iteration scheme by differentiating with respect to f_j, f_{j+1}, . . . , f'''_j, f'''_{j+1}; for separated flows f''_1 is specified and we differentiate with respect to β. This yields

$$J(f)\Delta f^k_j = -\epsilon^k_j$$

where $J(f)$ is the $(4N \times 4N)$ Jacobian, ϵ is the residual error, and Δf^k_j is the incremental change in the solution parameters per iteration.

To speed up the iteration process, the equations are ordered so that the 3(N-1) linear algebraic equations plus the boundary condition $f'(0) = 0$ occupy the first 3N-2 matrix rows. The matrix has the partitioned form (see Ref. 14):

$$\begin{bmatrix} L_1 & L_2 \\ NL_1 & NL_2 \end{bmatrix}\begin{bmatrix} \Delta f_L \\ \Delta f_{NL} \end{bmatrix} = -\begin{bmatrix} \epsilon_L \\ \epsilon_{NL} \end{bmatrix}$$

The submatrix L_1 is a function of the nodal configuration only and can be inverted just once and used in all subsequent calculations. Formal manipulation and back substitution yield

$$\Delta f_{NL} = \left[NL_2 - NL_1L_1^{-1}L_2\right]^{-1}\left[-\epsilon_{NL} + NL_1L_1^{-1}\epsilon_L\right]$$

$$\Delta f_L = -L_1^{-1}\left[\epsilon_L + L_2\Delta f_{NL}\right]$$

The matrix $[NL_2 - NL_1L_2]$ must be inverted every iteration, but it is only of order (N+2).

x-dependent differencing. The streamwise differencing is carried out in a manner similar to that of Reference 4. The term

$$-2\xi\int_{\eta_j}^{\eta_{j+1}} f'\frac{\partial f'}{\partial\xi}\,d\eta$$

is decomposed and integrated by parts as

$$-\int_{\eta_j}^{\eta_{j+1}} f'\left[DPf'_{i+1} + DCf'_i + DMf'_{i-1}\right]d\eta = -\left[DP\sum f^k_{i+1,j}XPK + DC\sum f^k_{i,j}XPK + DM\sum f^k_{i-1,j}XPK\right]$$

where, for attached flow,

$$DP = 0\,, \quad DC = 2/\ell n\ \xi_i/\xi_{i-1}\,, \quad DM = -DC$$

and for separated flow

$$DP = (1 - \alpha)/\ell n\ \xi_{i+1}/\xi_i\ ; \quad \alpha = 1 \quad \text{for} \quad f' > 0.01$$

$$DM = -(1 + \alpha)/\ell n\ \xi_i/\xi_{i-1}\ ; \quad \alpha = 100f'\,, \quad -0.01 \le f' \le 0.01$$

$$DC = -(DP + DM) \quad ; \quad \alpha = -1\,, \quad f' < -0.01$$

This procedure incorporates backward differencing when the flow is in the mainstream direction, forward differencing when the flow is reversed, and a central difference on the zero velocity streamline. The remaining term is decomposed as above, integrated by parts, and expanded in Taylor series to yield:

$$2\xi\int_{\eta_j}^{\eta_{j+1}} f''\frac{\partial f}{\partial \xi}\,d\eta = DCf_if_i'\Big|_{\eta_j}^{\eta_{j+1}} + DPf_{i+1}f_i'\Big|_{\eta_j}^{\eta_{j+1}} + DMf_{i-1}f_i'\Big|_{\eta_j}^{\eta_{j+1}} + DC\sum f_{i,j}^k XPK_i + DP\sum f_{ij}^k XPK_{i+1} + DM\sum f_{ij}^k XPK_{i-1}$$

where, for attached flow, excluding the points of separation and reattachment yields

$$DC = 2/\ln \xi_i/\xi_{i-1}\ , \qquad DP = 0\ , \qquad DM = -DC$$

and for separated flow,

$$DC = 0\ , \qquad DP = 2/\ln \xi_{i+1}/\xi_{i-1}\ , \qquad DM = -DP$$

As shown, a straightforward marching routine is used in the attached flow while, for separated flow, the entire separation region must be relaxed simultaneously.

The present method requires no under relaxation and a typical well-separated flow with 20 η points and 10 ξ points can be relaxed to a maximum residual $O(10^{-4})$ in about 22 iterations compared to 800 for the method of Reference 4 and 100 to 200 iterations for the method of Reference 5. Although the present method may require more operations per iteration, it is at least competitive with other methods cited. Typical computing time required for the solution of the above is 150 sec on the IBM 360 or 10 sec on the CDC 7600.

Inviscid-flow equations and coupling schemes

In this section, the technique used to solve for the inviscid flow field and to obtain the effects due to the boundary layer on that flow is described. A technique for obtaining fully coupled interactive solutions of the inviscid and viscous flows is being developed, but is not sufficiently advanced to discuss here in detail. Rather, at this point, boundary-layer solutions for a pressure and skin-friction distribution, appropriate to the data of Reference 13, have been obtained and various schemes for matching this solution with the inviscid flow have then been investigated. The inviscid flow is for supersonic flow between a shock-wave generator and some matching line given by the boundary-layer solution.

Inviscid-flow equations. The basic equation used in the inviscid flow-field analysis is similar to that of Reference 15. The key features, however, are described here for completeness. In a Cartesian coordinate system, the steady, inviscid, two-dimensional fluid dynamic equations (continuity, x and y momentum) are written in conservative form as

$$\tilde{U}_x + \tilde{F}_y = 0 \tag{11}$$

The three components of the vectors $\tilde{U}$ and $\tilde{F}$, which represent the conservative variables, are defined as

$$\tilde{U} = \begin{bmatrix} \rho u \\ kp + \rho u^2 \\ \rho uv \end{bmatrix}\ , \qquad \tilde{F} = \begin{bmatrix} \rho v \\ \rho uv \\ kp + \rho v^2 \end{bmatrix} \tag{12}$$

where $k = (\gamma - 1)/2\gamma$. The units of these equations were normalized by dividing both pressure and density by their respective stagnation conditions, while the velocities were divided by the maximum adiabatic velocity. With this normalization and the further restriction that the flow be adiabatic, the energy equation can be written:

$$\frac{p}{\rho} + u^2 + v^2 = 1 \tag{13}$$

To calculate two-dimensional flow between two nonparallel walls, in this case the shock-wave generator and the lower coupling boundary, it is most convenient to normalize the coordinate system so that the upper and lower boundaries become parallel. The transformed coordinates are

$$\left.\begin{aligned} x &= x \\ \xi &= \frac{y - y_\ell}{y_u - y_\ell} = \frac{y - y_\ell}{\zeta} \end{aligned}\right\} \tag{14}$$

where $y_u = y_u(x)$ and $y_\ell = y_\ell(x)$. Applying this transformation to Eq. (11) results in

$$U_x + F_\xi = 0 \tag{15}$$

where $U = \zeta U$ and $F = F + U[y_\ell'(\xi - 1) - y_u']$. (In this section, the primes denote differentiation with respect to x.)

The above differential equation is integrated using MacCormack's second-order-accurate differencing scheme (see Ref. 15). For flow-field points, that is, points on neither the upper nor lower boundary, the predictor and corrector equations are

$$\bar{U}_j^{n+1} = U_j^n - \left(\frac{\Delta x}{\Delta \xi}\right)\left(F_{j+1}^n - F_j^n\right) \qquad \text{(predictor)} \tag{16}$$

Subscript j identifies particular points on a data line as follows: 1, lower body point; 2, 3, . . ., $N_{\xi-1}$, flow-field points; and N_ξ, upper body point. The data lines are identified by the superscripts n and $n+1$. The bars indicate a predicted value.

$$U_j^{n+1} = \frac{1}{2}\left[U_j^n + \bar{U}_j^{n+1} - \left(\frac{\Delta x}{\Delta \xi}\right)\left(\bar{F}_j^{n+1} - \bar{F}_{j-1}^{n+1}\right)\right] \qquad \text{(corrector)} \tag{17}$$

The above equations are applied to the three vector components of U.

The step size in the x direction is found by determining the maximum slope of the characteristic surface, inclined at the local Mach angle μ relative to the local stream angle δ, for each point as follows:

$$\sigma_j^n(\pm) = |\tan(\pm\mu + \delta)_j^n| \tag{18}$$

where the $\pm$ denote positive and negative directions of the Mach angle from each point. The entire data line n is surveyed to determine $|\sigma_j^n(\pm)|_{max}$. Depending on the sign associated with the maximum slope, Δx is found from

$$\Delta x(+) = K\left[\frac{\xi_{j+1}^{n+1}\zeta^{n+1} - \xi_j^n\zeta^n - y_\ell^n + y_\ell^{n+1}}{\sigma_j^n(+)_{max}}\right] \tag{19}$$

or

$$\Delta x(-) = K\left[\frac{\xi_j^n\zeta^n - \xi_{j-1}^{n+1}\zeta^{n+1} - y_\ell^{n+1} + y_\ell^n}{\sigma_j^n(-)_{max}}\right] \tag{20}$$

where K is a constant that controls the step size. If $K = 1$, the CFL condition is satisfied identically.

Application of the finite-difference Eqs. (16) and (17) yields predicted and corrected values of the three components of the conservative-variable vector U on the new data line. These must be decoded after the predictor step and corrector step in turn. This decoding into physical variables is accomplished by solving the following:

$$\left.\begin{aligned} v &= \left.\frac{U_1}{U_2}\right|_j^{n+1} \\ u &= \left.\frac{U_2 + \sqrt{U_2^2 - 4U_1^2k(1-k)(1-v^2)}}{2U_1(1-k)}\right|_j^{n+1} \\ \rho &= \left.\frac{U_1}{\zeta u_1}\right|_j^{n+1}; \qquad p = \rho(1 - u^2 - v^2) \end{aligned}\right\} \tag{21}$$

Constructing a technique that will give a physically realistic solution of the conditions on a solid boundary is difficult in a predictor-corrector sequence since strict application requires an imaginary point inside the body. Abbett (Ref. 16) developed a technique that satisfies the surface tangency condition and relies on information provided by the finite-difference equations. For the upper and lower surfaces, respectively, the predictor equations are written as

$$\overline{U_{N_\xi}^{n+1}} = U_{N_\xi}^n - \left(\frac{\Delta x}{\Delta\xi}\right)\left(F_{N_\xi}^n - F_{N_\xi-1}^n\right) \tag{22}$$

and

$$\overline{U_1^{n+1}} = U_1^n - \frac{\Delta x}{\Delta\xi}\left(F_2^n - F_1^n\right) \tag{23}$$

Modified corrector equations that maintain second-order accuracy at the upper and lower surfaces, respectively, are given by

$$U_{N_\xi}^{n+1} = \frac{1}{2}\left[U_{N_\xi}^n + \overline{U_{N_\xi}^{n+1}} - \frac{\Delta x}{\Delta\xi}\left(\overline{F_{N_\xi}^{n+1}} - \overline{F_{N_\xi-1}^{n+1}}\right) - \frac{\Delta x}{\Delta\xi}\left(F_{N_\xi}^n - 2F_{N_\xi-1}^n + F_{N_\xi-2}^n\right)\right] \tag{24}$$

and

$$U_1^{n+1} = \frac{1}{2}\left[U_1^n + \overline{U_1^{n+1}} - \frac{\Delta x}{\Delta\xi}\left(\overline{F_2^{n+1}} - \overline{F_1^{n+1}}\right) - \frac{\Delta x}{\Delta\xi}\left(F_3^n - 2F_2^n - F_1^n\right)\right] \tag{25}$$

After the corrector equations are decoded at the boundaries, the flow variables will not necessarily satisfy the boundary conditions at the wall. The technique for satisfying the lower boundary conditions depends on a scheme for matching the boundary-layer solution.

The coordinates of the upper boundary are determined from

$$y_u = y_{u_o} + x\tan\delta_u \tag{26}$$

where δ_u is the deflection angle of the upper wall. When matching to the output of the boundary-layer solution, the lower boundary is specified by a table of coordinates. These coordinates are used to fit a parabola of the form

$$y = ax^2 + bx + c \tag{27}$$

between each set of three consecutive input boundary points. The three points used to determine the coefficients in the above equation were chosen so that two of these points should have $x > x^{n+1}$. The slope of the boundary is found from the derivative of Eq. (27).

Matching scheme. Two techniques for matching the inviscid and viscous solutions were investigated: (1) requiring tangency along a chosen matching contour, and (2) forcing the inviscid solution to agree with the u and v velocity components from the viscous solutions along a matching line. In the first matching scheme, two matching contours were considered. The first was the contour defined by the displacement thickness δ^* and the second contour was a streamline along which the flow remained supersonic throughout and was taken from the viscous flow solution. The slope of the matching line was used to specify the relationship between u and v in the inviscid solution as follows:

$$\delta = \tan^{-1} \frac{v}{u}$$

The second matching scheme forced the inviscid solution to match values of u and v given by the viscous solution along the boundary-layer edge. This technique does not impose the tangency condition along the matching boundary, but rather allows for mass exchange from the inviscid to viscous portions of the flow, a physically realistic situation.

Although some difficulty was encountered in the vicinity of the shock impingement point, the above methods yield comparable results for those flows for which the boundary-layer approximation is appropriate.

The above cited difficulties and the restriction to flows for which the boundary-layer equations are appropriate are discussed in a subsequent section.

Navier-Stokes solutions

Solutions to the Navier-Stokes equations presented here were obtained from several sources. Solutions of MacCormack (Ref. 3), MacCormack and Baldwin (Ref. 11), Messina (private communication), and Skoglund and Gay (Ref. 6) were obtained from the sources cited, while additional solutions were obtained in the present study using the computer codes of MacCormack and Baldwin (Ref. 11) and Carter (Ref. 10).

Space does not permit a detailed description of the differences and similarities of the several codes considered. There are, however, some striking differences and similarities in the several solutions presented which warrant discussion in some detail. Figure 1 shows the envelope of four Navier-Stokes solutions obtained from Reference 3 and References 10 through 12, together with the data of Hakkinen, et al. (Ref. 17), for an unseparated, laminar-boundary-layer, shock-wave interaction at M = 2.

Two points immediately come to mind: first, the large discrepancy in skin friction and the relatively small discrepancy in surface pressure. At first glance, this implies a low sensitivity of the pressure distribution to the skin-friction distribution and a lack of uniqueness in the Navier-Stokes solutions. However, a sequence of solutions obtained here using MacCormack and Baldwin's (Ref. 11) code, with successive mesh refinement in the outer inviscid flow, shows differences in C_f of the same order as those shown in Fig. 1. This arises from the fact that for the coarsest mesh considered, the externally generated shock wave takes on a thickness that, when projected onto the boundary layer, is of the same order as the length of interaction. The viscous flow is then responding to a continuous compression rather than an imposed shock wave. As the nodal structure was refined, the skin-friction distribution approached a single curve.

Figure 2 shows a similar envelope of Navier-Stokes solutions obtained from References 6, 8, 10, and 11, together with experimental data for a well-separated, laminar-boundary-layer, shock-wave interaction (Ref. 17). The results here are similar to those discussed above and the same conclusions can be drawn.

The point of the foregoing presentation is not to show how poorly Navier-Stokes solutions perform but rather to induce the user to Navier-Stokes codes to examine his results critically and, in particular, to examine the computational mesh dimensions in the light of the smallest relevant physical scale in the problem under consideration.

In subsequent sections, the boundary-layer calculation scheme developed is compared to the Navier-Stokes solutions of MacCormack (Ref. 3).

RESULTS

The results of the inverse boundary-layer method are compared with Navier-Stokes solutions and with experimental data. The flows considered all occur on a flat plate and the pressure rise is caused by an externally generated shock wave. The specific flow parameters and experiments considered are listed below.

Reference	M_o	Re	p_f/p_o	Remarks
17*	2	1.84×10^5	1.2	Laminar
17*	2	1.96×10^5	1.4	Laminar
18	1.47	4×10^6/ft	2.25	Turbulent
19	2.93	5.7×10^7/m	2.5	Turbulent
19*	2.93	5.7×10^7/m	5.0	Turbulent

*Navier-Stokes solutions available

Finally, we will describe the progress made, to date, in coupling the inverse boundary-layer method to the inviscid calculation scheme to provide a complete flow-field prediction method.

Laminar-boundary-layer, shock-wave interaction

Two laminar-boundary-layer, shock-wave interactions are considered: an unseparated interaction at M = 2.0 having an overall pressure rise p_f/p_o of 1.2 and a well-separated interaction at M = 2.0 having an overall pressure rise p_f/p_o of 1.4. These two interactions correspond to the experiments of Hakkinen, et al., as reported in Reference 17 where they are shown as Figures 6a and 6b, respectively. For convenience, these two interactions are subsequently referred to here as Hakkinen (6a) and Hakkinen (6b).

Note that in this and all subsequent comparisons with Navier-Stokes solutions, the skin-friction distribution obtained from the Navier-Stokes solution was input to the inverse boundary-layer method. This procedure ensures that a comparison of other parameters, that is, velocity and pressure distributions, provides a true measure of the validity of the boundary-layer assumption, without the peripheral considerations of downstream boundary conditions or matching conditions between viscous and inviscid flow. However, some differences can arise even in this case because of the order of the difference approximation used. The present inverse method is third-order accurate in wall shear as opposed to first-order accuracy imposed by assuming a linear variation of velocity with distance away from the wall in the Navier-Stokes solutions. An examination of the differences attributable to this assumption indicates that C_f can vary ·10 percent for the same velocity profile, depending on the order of curve fit used to deduce the derivative at the wall.

Figure 3 compares the pressure distribution obtained from present methods with a refined mesh Navier-Stokes calculation using Hung and MacCormack's code (Ref. 9) for Hakkinen (6a). The two solutions are nearly indistinguishable everywhere and they are in reasonable agreement with the data. In Fig. 4, the velocity distributions at the x location corresponding to the minimum value of C_f (Fig. 3) are compared. The differences between the present method and MacCormack's solution are not large and are principally attributable to differences in transport properties; that is, Pr = 1 and $\mu/\mu_0 = T/T_0$ in the present method and Pr = 0.72 and . from the Sutherland law in MacCormack's code.

Figure 5 shows the streamwise pressure distribution for Hakkinen (6a) for $y = 0, \delta/2, \delta$, as computed by MacCormack (Ref. 3). These curves are essentially indistinguishable and hence, within the boundary layer, $\partial p/\partial y \approx 0$. This, in turn, implies a trivial solution to the y momentum equation which, from the usual boundary order-of-magnitude arguments, indicates that the boundary-layer equations are adequate for this flow.

Figure 6 compares the pressure distribution obtained from the present method with that of MacCormack's solution for Hakkinen (6b). For this case, a slight difference in surface pressure distribution is obtained near $x/L = 0.15$. Figure 7 compares the velocity profiles obtained from the present method and from MacCormack's method for Hakkinen (6b). Differences between the profiles are explicable in terms of differences in transport properties discussed previously. Figure 8 shows the streamwise pressure distributions for Hakkinen (6b), as computed by MacCormack (Ref. 3). This figure shows the normal pressure gradient developing in about the same region noted in Fig. 6 ($x/L = 0.15$ corresponds to $x/\delta x = 20$). This normal pressure gradient appears to be an inertial effect associated with strong streamline curvature in the outer portion of the boundary layer where $M(y) \cdot M_e$. For this case, the boundary-layer method predicts a relatively large value of v_e/u_e (not shown), which indicates the beginning of a breakdown of the boundary-layer approximation.

It should be pointed out that the boundary-layer equations will also fail based on viscous flow parameters for large separation bubbles. Oswatitsch (Ref. 20) has shown that the Navier-Stokes equation requires that

$$\left.\frac{\partial p}{\partial y}\right|_w = -\frac{\partial^2 w}{\partial x^2} = \frac{1}{3}\tan \alpha \frac{\partial p}{\partial x}$$

where α is the angle at which the dividing streamline leaves the wall. It is clear from this analysis that the boundary-layer equations are never valid in an exact mathematical sense for separating flows; however, as long as the separation bubble is not too large, α will remain small and $\partial p/\partial y \ll \partial p/\partial x$ so that the boundary-layer equations will provide an adequate approximation. It appears that for supersonic laminar flows that the inertially induced breakdown will occur before the viscous breakdown of the boundary-layer approximation.

Turbulent boundary-layer, shock-wave interaction

The question of the utility of boundary-layer thoery in turbulent boundary-layer, shock-wave interactions is somewhat less clear than for the laminar case. This is true for three reasons. First, few Navier-Stokes solutions with simple turbulence models are available for comparison. Second, the current turbulence models are demonstrably inadequate for flows with rapidly changing boundary conditions and, third, only a few experiments are available in supersonic turbulent flow which are sufficiently detailed to permit a useful comparison. Because of these facts, only a cursory comparison of results of the present method with both Navier-Stokes solutions and experimental data can be made.

Figure 9 compares the present method with the data of Seddon (Ref. 18), for a normal shock-wave, turbulent-boundary-layer interaction with an initial Mach number of 1.47. For this case, the experimentally determined value of $C_f(x)$ was input to the inverse boundary-layer method in the attached-flow regime. For the reversed-flow region, where no data were available, three estimates of C_f were made (defined by the solid, dashed, and dot-dashed lines in the upper half of Fig. 9). The corresponding pressure distributions are shown in the lower half of Fig. 9. Two conclusions can be drawn from this figure: first, the boundary-layer equations are capable of reproducing the observed behavior and, second, the pressure distribution is sufficiently sensitive to variations in C_f to permit a coupled solution to distinguish between similar distributions of skin-friction coefficient.

Figure 10 shows a comparison of a direct calculation using the present method with the data of Reference 19. The experimental skin-friction distribution shown was deduced from the measured mean velocity profiles using the method of Reference 21. These data were taken at a free-stream Mach number of 2.93 and a unit Reynolds number of 5.7×10^7 m^{-1}. The pressure rise was effected by a shock generator set at 7° incidence to the oncoming flow. As noted above, the predicted results were obtained for this case by calculation in the direct mode, that is, P(x) was specified and C_f computed. The two predicted skin-friction distributions shown in the upper portion of Fig. 10 result from two turbulence models used for this calculation. The equilibrium model is that described above while the exponential lag model is that suggested by Rose and Johnson (Ref. 22) and similar to the one used with some success in the Navier-Stokes calculations of References 23 and 24. One may conclude then that, given the appropriate turbulence model, the boundary-layer equations are adequate to describe flows of this type.

The last case considered was also taken from References 19 and 21. The initial flow properties were the same as those discussed in Fig. 10 but the shock generator angle was set at 13° to the oncoming flow. As shown in the upper portion of Fig. 11, the flow has an extensive region of separation: $(X_{reatt} - X_{sep}) \approx 46$. For this case, the inverse boundary-layer method failed. The predicted pressure distribution shown in Fig. 11 indicated nearly twice the pressure rise observed experimentally. Direct solutions employing the experimentally observed pressure distribution failed to predict any separation. This might be attributed to three-dimensional effects in the experiment except that the Navier-Stokes solutions of Baldwin and Rose (see Ref. 24), using a similar turbulence model, did a plausible job of predicting the flow. An examination of this solution shows extensive regions of significant normal pressure gradient together with no significant contributions from the elliptic terms or the shear terms in the y momentum equation except in the immediate vicinity of the shock wave.

This implies that the primary cause of failure of the boundary-layer approximation is the inviscidly driven normal pressure gradient. In turn this implies that if one were to use a system of equations consisting of continuity, boundary-layer x momentum, and inviscid y momentum equations, the utility of spatially parabolic equations could be substantially extended (see section entitled Truncated Navier-Stokes Equations).

Coupled solutions

Some of the results obtained from the inviscid-viscous coupling techniques are shown in Fig. 12. The surface pressure distributions (one with tangency specified and one with u and v specified) resulting from the two matching schemes for the Hakkinen (6b) case are compared with that given by the Navier-Stokes program of Reference 3. Both techniques demonstrate overall qualitative agreement with the solution of the Navier-Stokes equations, except in the region of the shock impingement point. This disagreement arises from the tendency of the inviscid technique used to smear the shock waves over several grid points and to overshoot the pressure rise through a shock wave reflection. It is anticipated that at least part of this difficulty may be removed by incorporating a discrete shock calculation into the inviscid calculation scheme.

Truncated Navier-Stokes equations

To circumvent the difficulties encountered in coupling viscous and inviscid flows, an alternative procedure was considered. Rather than solve coupled viscous and inviscid equations in an iterative mode, we proposed to solve the following system of equations:

$$\frac{\partial \rho}{\partial t} + \frac{\partial \rho u}{\partial x} + \frac{\partial \rho v}{\partial y} = 0$$

$$\frac{\partial \rho u}{\partial t} + \rho u \frac{\partial u}{\partial x} + \rho v \frac{\partial u}{\partial y} + \frac{\partial p}{\partial x} = \frac{\partial \tau_{xy}}{\partial y}$$

$$\frac{\partial \rho v}{\partial t} + \rho u \frac{\partial v}{\partial x} + \rho v \frac{\partial v}{\partial y} + \frac{\partial p}{\partial y} = 0$$

together with an equation of state and a consistent energy conservation relation. This was accomplished by simply removing the appropriate terms from the computer code of MacCormack and Baldwin (Ref. 11). These equations converged everywhere within 1 percent of full Navier-Stokes solution for the Hakkinen cases (6a) and (6b) using the same mesh configuration (results not shown). The above method is slightly more efficient than the solution of the full Navier-Stokes equations because fewer operations need to be performed in the computer code.

One may deduce from the above that this truncated system can be solved, and that with this system no coupling problems exist. Further, since the equations are parabolic in the streamwise variable, the steady-state equations should be solvable, for attached flow, by a streamwise marching procedure and in the separated region by a relaxation procedure. This latter procedure would allow a first-order improvement in computational efficiency. Unfortunately, these conclusions were reached very late in the present study, and time did not permit significant exploitation of the properties of these equations.

CONCLUDING REMARKS

We have demonstrated the validity of the boundary-layer equations applied to certain shock-wave, boundary-layer interactions. As has been suggested (e.g., Ref. 2), solutions to the boundary-layer equations begin to depart significantly from those of the Navier-Stokes equations under the same conditions for which nontrivial normal pressure gradients are first observed in the Navier-Stokes solutions. Based on the physical argument that high-velocity flow, turning through a large angle, requires the action of a large force over a short distance, one may deduce that the normal pressure gradient arises primarily from the inviscid characteristics of the flow field. From this, one may conclude that when some parameter involving both Mach number and turning angle, for example, $M_e|v_e/u_e|$, exceeds a critical value, boundary-layer theory will fail.

Despite the fact that boundary-layer theory can be shown to fail at high supersonic Mach numbers when extensive separations occur, it would appear that, for many technological problems, boundary-layer theory is quite satisfactory. This should be particularly true in the design of transonic airfoils and for engine inlets to be used on transonic and low supersonic flight vehicles.

Although the present coupled solutions do not as yet provide a practical predictive capability, it is the belief of the authors that the difficulties encountered are in no way fundamental and that with some additional development can provide a useful design tool applicable to many real technological problems.

The truncated Navier-Stokes equations considered above, appear to offer substantial potential advantage for the treatment of interacting flow fields at higher Mach numbers than the boundary-layer equations can cope with.

REFERENCES

1. Brown, S. N.; and Stewartson, K.: Laminar Separation. Edited by W. R. Sears and M. Van Dyke, Annual Review of Fluid Mechanics, Vol. 1, Annual Reviews, Inc., Palo Alto, Calif., 1969, pp. 45-72.

2. Murphy, J. D.: A Critical Evaluation of Analytic Methods for Predicting Laminar Boundary-Layer, Shock-Wave Interaction. NASA TN D-7044, 1971.

3. MacCormack, R. W.: Numerical Solution of the Interaction of a Shock Wave With a Laminar Boundary Layer. Proceedings of the 2nd International Conference on Numerical Methods in Fluid Dynamics, Lecture Notes in Physics, Vol. 8, Springer-Verlag, 1971.

4. Klineberg, J. M.; and Steger, J. L.: The Numerical Calculation of Laminar Boundary-Layer Separation. NASA TN D-7732, 1974.

5. Carter, J. E.: Solutions for Laminar Boundary Layers With Separation and Reattachment. AIAA Paper 74-583, 1974.

6. Skoglund, V. J.; and Gay, B. D.: Improved Numerical Techniques and Solution of a Separated Interaction of an Oblique Shock Wave and a Laminar Boundary Layer. Bur. of Engin. Res. Rept. ME 41(69)S-068, Univ. of New Mexico, June 1969.

7. Staiano, E. F.: A General Numerical Procedure for Solutions of Viscous Compressible Flows With Shock Waves. Ph.D. dissertation, Univ. of New Mexico, May 1967.

8. MacCormack, R. W.: An Introduction to the Numerical Solution of the Navier-Stokes Equations. AIAA Paper 75-1, 1975.

9. Hung, C. M.; and MacCormack, R. W.: Supersonic and Hypersonic Laminar Flows Over a Two-Dimensional Compression Corner. AIAA Paper 75-2, 1975.

10. Carter, J. E.: Numerical Solutions of the Navier-Stokes Equations for the Supersonic Laminar Flow Over a Two-Dimensional Compression Corner. NASA TR R-385, 1972.

11. MacCormack, R. W.; and Baldwin, B. S.: A Numerical Method for Solving the Navier-Stokes Equations With Application to Shock Boundary-Layer Interactions. AIAA Paper 75-1, 1975.

12. Murphy, J. D.: Application of the Generalized Galerkin Method to the Computation of Fluid Flow. Presented at the AIAA Computational Fluid Dynamics Conference, Palm Springs, Calif., July 19-20, 1973.

13. Kendall, R. M.; and Bartlett, E. P.: Non-Similar Solutions of the Multicomponent Laminar Boundary Layer by an Integral Matrix Method. AIAA Preprint 67-218, 1967.

14. Lanczos, C.: Applied Analysis. Prentice-Hall, Englewood Cliffs, N. J., 1964.

15. Presley, L. L.; and Kutler, P.: Comparison of a Discrete-Shock Finite-Difference Technique and the Method of Characteristics for Calculating Internal Supersonic Flows. Presented at the AIAA Computational Fluid Dynamics Conference, Palm Springs, Calif., July 19-20, 1973.

16. Abbett, M. J.: Boundary Condition Calculation Procedures for Inviscid Supersonic Flow Fields. Presented at the AIAA Computational Fluid Dynamics Conference, Palm Springs, Calif., July 19-20, 1973.

17. Hakkinen, R. J.; Greiber, I.; Trilling, L.; and Abarbanel, S. S.: The Interaction of a Oblique Shock Wave With a Laminar Boundary Layer. NASA Memo 2-18-5914, 1959.

18. Seddon, J.: The Flow Produced by Interaction of a Turbulent Boundary Layer With a Normal Shock Wave of Strength Sufficient to Cause Separation. ARC R & M 3502, 1967.

19. Reda, D. C.; and Murphy, J. D.: Shock Wave Turbulent Boundary-Layer Interaction in Rectangular Channels: Part II. The Influence of Side Wall Boundary Layers on Incipient Separation and Scale of the Interaction. AIAA Paper 73-234, 1973.

20. Oswatitsch, K.: Die Ablösungsbedingung von Grenzschichten. Boundary-Layer Research, Edited by H. Görtler, Springer-Verlag, 1958, pp. 357-367.

21. Rubesin, M. W.; Murphy, J. D.; and Rose, W. C.: Wall Shear in Strongly Retarded and Separated Turbulent Boundary Layers. AIAA J., Vol. 12, No. 10, Oct. 1974, pp. 1442-1444.

22. Rose, W. C.; and Johnson, D. A.: A Study of Shock Wave Turbulent Boundary-Layer Interaction Using Laser Velocimeter and Hot Wire Anemometer Techniques. AIAA Paper 74-95, 1974.

23. Shang, J. S.; and Hankey, W. L., Jr.: Numerical Solutions of the Navier-Stokes Equations for Supersonic Turbulent Flow Over a Compression Corner. AIAA Paper 75-4, 1975.

24. Baldwin, B. S.; and Rose, W. C.: Calculation of Shock-Separated Turbulent Boundary Layers. Presented at NASA Conference on Aerodynamic Analyses Requiring Advanced Computers, March 4-6, 1975.

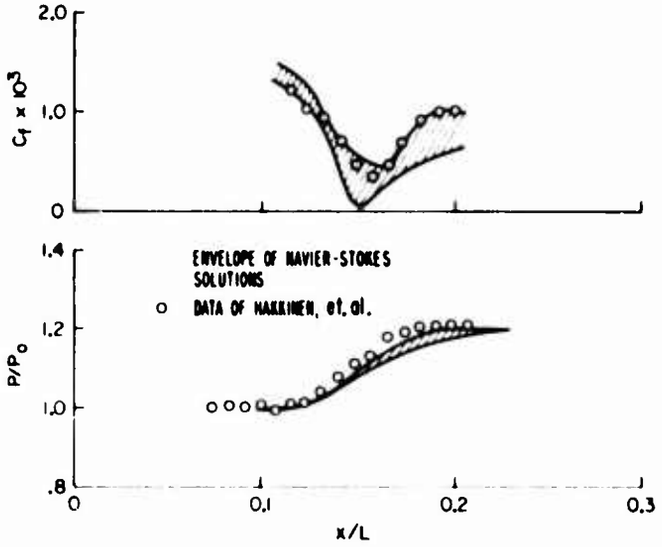

Fig. 1 Comparison of envelope of four Navier-Stokes solutions with the data of Hakkinen, et al.; $M = 2$, $Re_{shock} = 2.84 \times 10^5$, $p_f/p_0 = 1.20$.

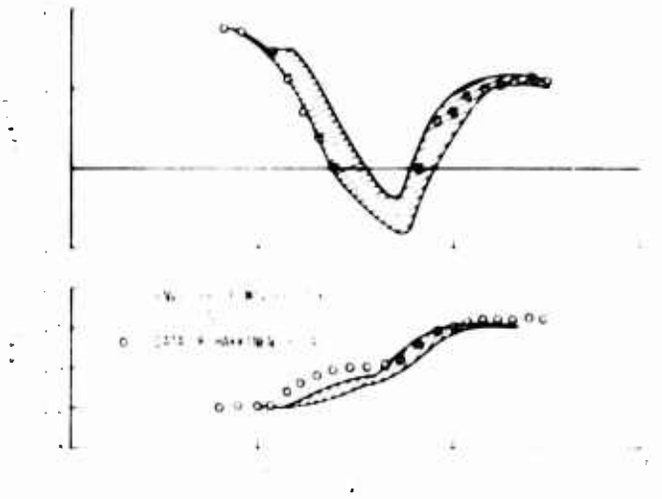

Fig. 2 Comparison of envelope of four Navier-Stokes solutions with the data of Hakkinen, et al.; $M = 2$, $Re_{shock} = 2.96 \times 10^5$, $p_f/p_0 = 1.40$.

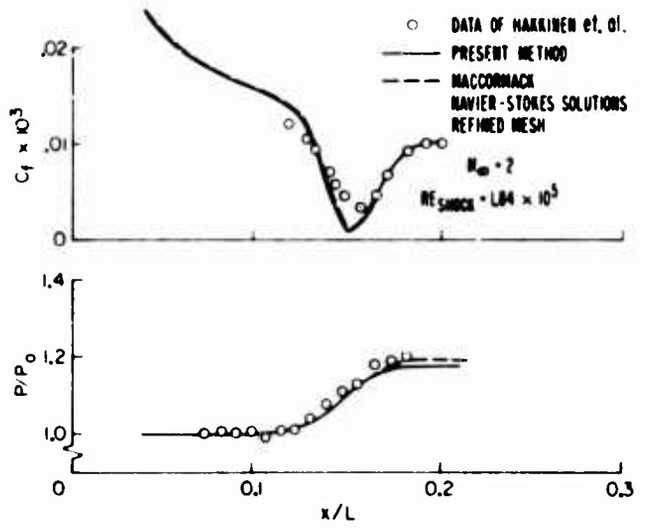

Fig. 3 Comparison of results of the present method with refined mesh calculations using MacCormack code.

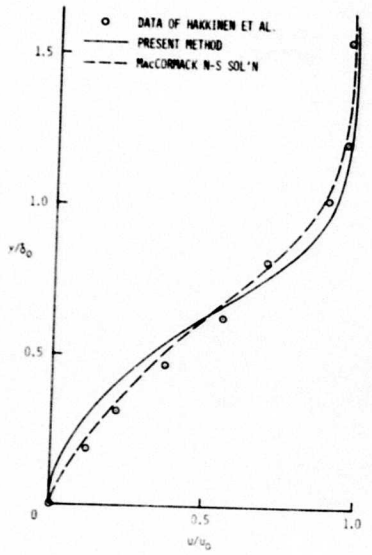

Fig. 4 Comparison of predicted velocity profiles at minimum C_f.

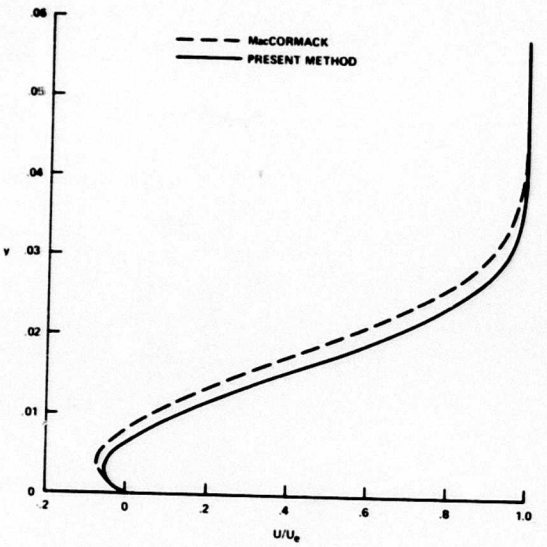

Fig. 7 Comparison of predicted velocity profiles at minimum C_f.

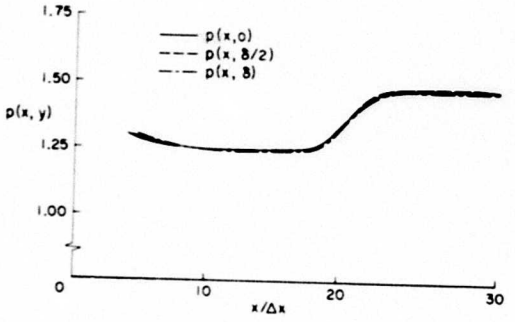

Fig. 5 Predicted pressure distributions for an unseparated laminar boundary-layer, shock-wave interaction; calculations of MacCormack.

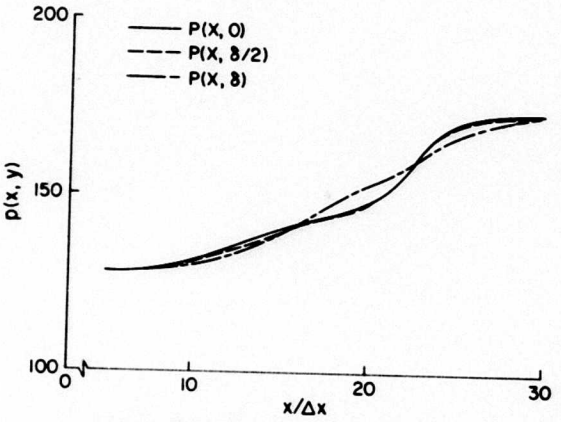

Fig. 8 Predicted pressure distributions for a separated laminar boundary-layer, shock-wave interaction; calculations of MacCormack.

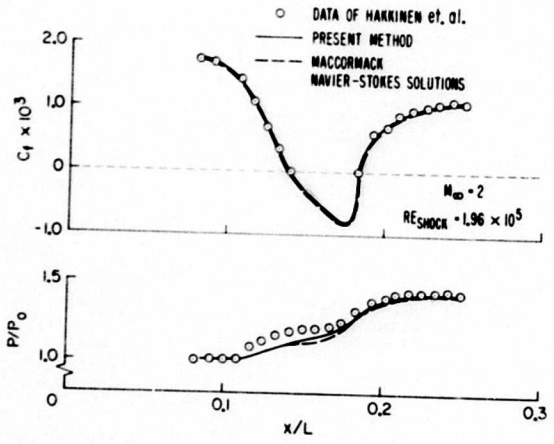

Fig. 6 Comparison of results of present method with calculations of MacCormack.

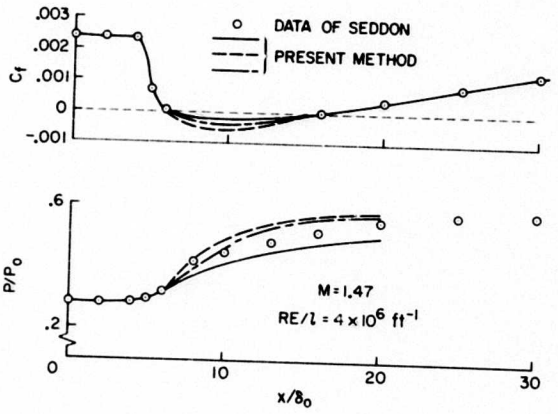

Fig. 9 Comparison of the results of the present method with the data of Seddon (Ref. 18).

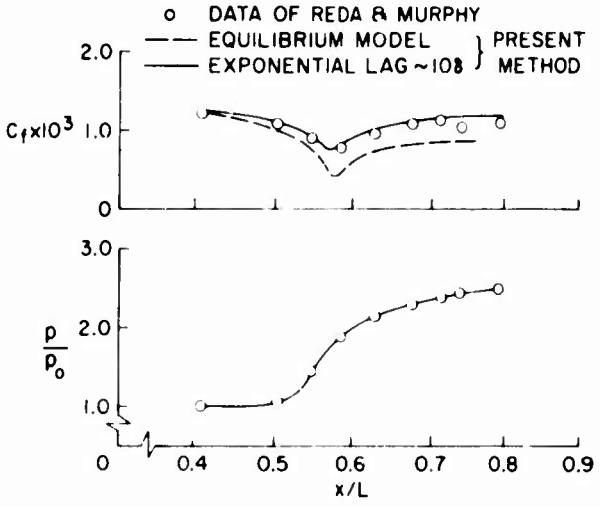

Fig. 10 Comparison of the present method with the data of Reference 19; turbulent unseparated flow.

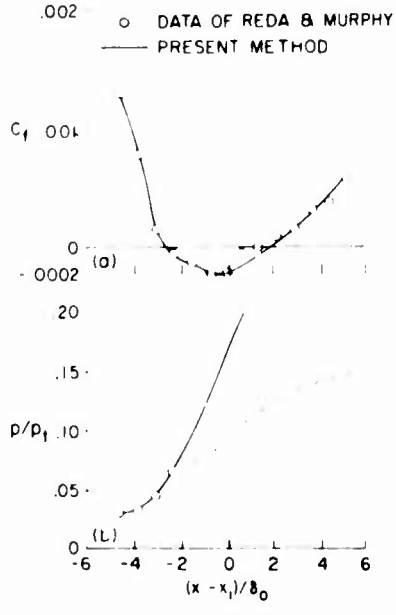

Fig. 11 Comparison of the present method with the data of Reference 20; turbulent separated flow.

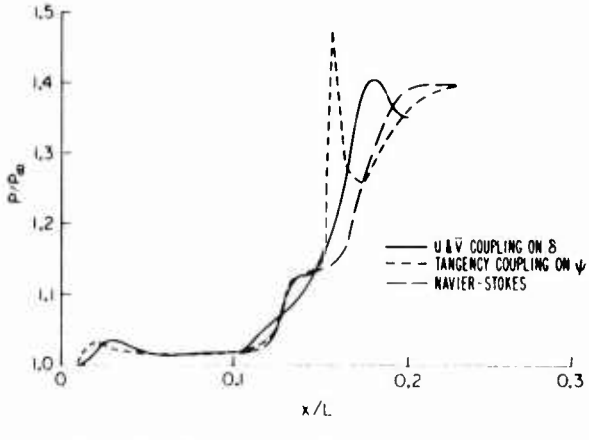

Fig. 12 Comparison of coupling schemes.

SUPERSONIC TURBULENT SEPARATED FLOWS UTILIZING THE NAVIER STOKES EQUATIONS

by

J. S. Shang, Aerospace Engineer

and

W. L. Hankey Jr., Senior Scientist
Aerospace Research Laboratories
Wright-Patterson Air Force Base, OH 45433
USA

SUMMARY

A modified eddy viscosity model is incorporated into the compressible Navier-Stokes equations and numerical solutions obtained for separated flows. The modification attempts to reproduce the response of a turbulent boundary layer to a severe pressure gradient by introducing a simple rate equation to account for the relaxation phenomenon. The system of equations is solved by MacCormack's time-splitting explicit numerical scheme for a series of compression corner configurations. Computations are performed for ramp angle varying from 15 to 25 degrees at a Mach number of 2.96 and Reynolds number of 10^7. An incident oblique shock impingement case is also computed at these same conditions and included for comparison with a ramp induced separation case. Calculations utilizing the modified eddy viscosity for the interacting turbulent flow compare very well with experimental measurements for the compression ramps, particularly, in the prediction of the upstream pressure propagation and location of the separation and reattachment points. Good agreement is also attained between the measured and the calculated density profiles in the viscous-inviscid interaction region.

LIST OF SYMBOLS

C_f	skin-friction coefficient $\frac{2\tau_\omega}{\rho_e U_e^2}$
D	Van Driest Damping factor, equation 14.
e	Specific energy
e_i	specific internal energy, $c_v T$
F,G	Vector fluxes in mean flow equations
h	maximum vertical dimension of the computational domain
L	length of the leading plate, 1ft
P	static pressure
P_r	molecular Prandtl number
P_{r_t}	turbulent Prandtl number
$q = u\cos\alpha + v\sin\alpha$	
S	distance along the surface
t	time
T	temperature
u,v	velocity components in the Cartesian coordinates
U_{max}	maximum velocity in the shock layer
U	vector of conserved properties in mean flow equations
x,y	Cartesian coordinates
α	transformation variable defined by equation 1.
δ	boundary-layer thickness
ε	eddy viscosity coefficient
θ_1	the deflection angle of impinging shock wave generator
θ_ω	wedge angle
μ	molecular viscosity coefficient
λ	relaxation length scale
ξ,η	skewed coordinates defined by equation 1.
ρ	density
τ_ω	shear stress along this contour

SUBSCRIPT

i	denotes initial condition
j	index of computational mesh points
∞	denotes the free stream condition

1. INTRODUCTION

Flow separation around compression ramps and shock impingement on boundary layers has long been identified to be an inviscid-viscous interaction problem. Interacting boundary layer solutions over two-dimensional corners have been employed for laminar flows[1,2,3]. More recently, an asymptotic solution on the identical subject also has been accomplished[4]. For all these solving schemes, either an iterative or a matching procedure must be implemented to accomodate simultaneously the high shear stress region and the associated inviscid stream. On the other hand, numerical solutions of the time dependent Navier-Stokes equations have also been reported[5,6,7,8]. This direct approach automatically accomplishes the inviscid-viscous interaction. Crocco[9] indicates that the time dependency of the governing equations allows the solution to progress naturally from an initial guess to an asymptotic steady state. MacCormack developed a two-step difference method for solving the time-dependent Navier-Stokes equations and successfully investigated the interaction of a shock wave with a laminar boundary layer[5]. Recently, Baldwin and MacCormack[6] generalized the numerical scheme by including a turbulence model to analyze the turbulent interaction flow field in the hypersonic regime. The flow field structure of the shock impingement problem bears a close analogy to the flow over a compression corner. Carter[7] used the Brailovskaya finite difference scheme to study successfully, the laminar flow separation over a compression corner. The first documented solution of turbulent flows on the compression ramp is probably due to Wilcox[8]. He adopted an explicit time-marching first order finite difference scheme (AFTON 2pt code) with Saffman's turbulent model[10] to investigate two-dimensional separated turbulent flows. Comparisons of his numerical solutions and experimental data for the compression corner reveals substantial disparity. Wilcox offers two possible explanations for the discrepancy; first, the uncertainty of the two-dimensionality of the experimental data; and secondly, the eddy viscosity concept may be inappropriate, primarily due to the mean-flow streamline curvature. Nevertheless, one perceives that only a further refinement of the turbulence model is necessary to improve the accuracy of numerical solutions.

The present authors recently implemented a simple but effective relaxation eddy viscosity model to evaluate the turbulent flow over a series of compression ramps[11]. This relaxation model of eddy viscosity in essence is a particular solution of the rate equation similar to that suggested by Bradshaw[12] for his correction factor. The local effective eddy viscosity coefficient is a combination of the local equilibrium value and the unperturbed upstream value with an exponential decay. The numerical results when compared with the experimental data indicate a significant improvement over the local equilibrium eddy model[13]. Particularly, the relaxation model predicts correctly, the extent of upstream pressure propagation for all the ramp configurations considered. Furthermore, the predictions of the detailed flow field also agrees very well with the direct experimental measurements.

The present analysis utilizes the two-dimensional time-dependent Navier-Stokes equations as developed by MacCormack with an explicit finite differencing scheme[6] (alternating direction explicit). The concept of splitting reduces the set of two-dimensional equations into two sets of one-dimensional equations while retaining second order accuracy. Cebeci-Smith's[13] eddy viscosity model provides the closure of the system of equations. The dependent variables thus degenerate into time-average properties of this fluid motion. It is well-known that this composite algebraic eddy viscosity model is derived from the concept of an "equilibrium" turbulent boundary layer. The simple diffusive eddy viscosity model in its' original form is incapable of explicitly, conveying any information about the "history" of this flow field. The present investigation intends to improve on this characteristic in order to produce a relatively simple engineering tool. A simple but effective means is to modify the eddy viscosity model to allow for a lag in the response of the turbulence to a sudden application of a severe adverse pressure gradient. In essence, the present analysis attempts to model a relaxation phenomenon within the above mentioned frame work.

Two obvious objectives of the present effort can be summarized. The primary aspiration is to develop an engineering method capable of predicting turbulent flow separation near a compression ramp and the flow separation due to the shock wave-turbulent boundary layer interaction. The shock impingement problem is included to clarify the uncertainty regarding the departure from two-dimensionality of experimental efforts observed by Green[14]. Substantiation of this approach and its' range of validity is acquired through comparison with experimental data. Further understanding of this complicated turbulent flow phenomenon is also planned, and hopefully the additional understanding may aid in the future development of turbulence modeling.

Governing Equations

The governing equations of the present analysis are the unsteady compressible Navier-Stokes equations in terms of mass-averaged variables. The adoption of the eddy viscosity coefficient and the turbulent Prandtl number reduces the conservation equations to the nearly identical form for laminar flows[6]. In order to avoid extensive interpolation of boundary conditions on the compression ramp, a skewed coordinate system is used. The relationship between the skewed and the Cartesian coordinate system is given by Carter[7] as:

$$\xi = x \sec \alpha \tag{1-a}$$

$$\eta = y - x \tan \alpha \tag{1-b}$$

where $$\alpha = \begin{cases} 0 & x \le x_c \\ \theta_\omega & x \ge x_c \end{cases}$$

The corresponding spatial derivatives of the coordinate system can be easily obtained as follows[7]:

$$\frac{\partial}{\partial x} = \sec \alpha \frac{\partial}{\partial \xi} - \tan \alpha \frac{\partial}{\partial \eta} \tag{2-a}$$

$$\frac{\partial}{\partial y} = \frac{\partial}{\partial \eta} \tag{2-b}$$

One observes that the above equations are valid for both the straight segments of this compression ramp

configuration. Carter[7] reveals that the derivative with respect to ξ requires special treatment in order to maintain second-order accuracy in the corner region. Applying this spatial coordinate transformation, the two-dimensional mean flow governing equations acquire the following form:

$$\frac{\partial U}{\partial t} + \sec\alpha \frac{\partial F}{\partial \xi} + \frac{\partial}{\partial \eta}(G - \tan\alpha F) = 0 \tag{3}$$

The vector components are:

$$U = \begin{Bmatrix} \rho \\ \rho u \\ \rho v \\ \rho e \end{Bmatrix} \tag{4}$$

$$F = \begin{Bmatrix} \rho u \\ \rho u^2 - \sigma_x \\ \rho uv - \tau_{xy} \\ (\rho e - \sigma_x) u - \tau_{xy} v - \dot{q}_x \end{Bmatrix} \tag{5}$$

$$G = \begin{Bmatrix} \rho v \\ \rho uv - \tau_{yx} \\ \rho u^2 - \sigma_y \\ (\rho e - \sigma_y) v - \tau_{xy} u - \dot{q}_y \end{Bmatrix} \tag{6}$$

Where the apparent stress components are given by:

$$\sigma_x = -p - 2/3(\mu + \epsilon)\left(\sec\alpha \frac{\partial u}{\partial \xi} - \tan\alpha \frac{\partial u}{\partial \eta} + \frac{\partial v}{\partial \eta}\right) + 2(\mu + \epsilon)\left(\sec\alpha \frac{\partial u}{\partial \xi} - \tan\alpha \frac{\partial u}{\partial \eta}\right) \tag{7}$$

$$\sigma_y = -p - 2/3(\mu + \epsilon)\left(\sec\alpha \frac{\partial u}{\partial \xi} - \tan\alpha \frac{\partial u}{\partial \eta} + \frac{\partial v}{\partial \eta}\right) + 2(\mu + \epsilon)\frac{\partial v}{\partial \eta} \tag{8}$$

$$\tau_{xy} = \tau_{yx} = (\mu + \epsilon)\left(\frac{\partial u}{\partial \eta} + \sec\alpha \frac{\partial v}{\partial \xi} - \tan\alpha \frac{\partial v}{\partial \eta}\right) \tag{9}$$

$$\dot{q}_x = \gamma(\mu/P_r + \epsilon/P_{r_t})\left(\sec\alpha \frac{\partial e_i}{\partial \xi} - \tan\alpha \frac{\partial e_i}{\partial \eta}\right)$$

$$\dot{q}_y = \gamma(\mu/P_r + \epsilon/P_{r_t})\frac{\partial e_i}{\partial \eta}$$

The mean specific total energy is defined by the mass-averaged specific internal energy e; as:

$$e = e_i + (u^2 + v^2)/2 \tag{10}$$

Owing to the particular eddy viscosity model we selected, an additional approximation was required. Namely, the specific turbulent energy in equation 10 was omitted (ref. 6).

Auxiliary relationships included in the system of equations are the equation of state, perfect gas assumption, and Sutherland's viscosity equation. Upon the specification of the eddy viscosity model, molecular Prandtl number (0.72) and turbulent Prandtl number (0.90) the system of equations is completed.

1. The Initial and Boundary Conditions for the Compression Ramp

The associated initial and boundary conditions are prescribed as follows: the initial conditions and upstream boundary conditions are prescribed for all the dependent variables.

A detailed description of the upstream boundary condition will be deferred to a latter section of the discussion. At the downstream boundary, gradients of all properties are assumed to vanish[5,6].

$$\frac{\partial U}{\partial \xi} = 0 \quad \xi > \xi_{corner} \text{ (Predictor)} \tag{11-a}$$

The outer boundary conditions for the present analysis consists of two regions, upstream and downstream of the coalescing waves. The former is satisfied by permitting the flow to approach its' unperturbed freestream value.

$$U(t, \xi, h) = U_\infty \tag{11-b}$$

The region downstream of the coalescing shock system is fulfilled by the Rankine-Hugoniot relations.

$$U(t, \xi, h) = U(M_\infty, \theta_\omega) \tag{11-c}$$

The boundary condition on the solid contour is given as:

$$u(t, \xi, 0) = 0, \quad v(t, \xi, 0) = 0 \tag{11-d}$$

$$T(t, \xi, 0) = T_\omega \text{ (constant)} \tag{11-e}$$

and a derived condition for pressure, i.e., $\frac{\partial p}{\partial \eta} \approx 0$, or

$$p(t, \xi, \Delta\eta) = p(t, \xi, -\Delta\eta) \tag{11-f}$$

2. The Initial and Boundary Conditions for Shock Impingement

First of all, the simple geometry for the shock impingement problem reduces the numerical procedure significantly. The coordinate transformation is no longer needed. In the computational process, the parameter α is set equal to zero. The upstream and downstream boundary condition is identical to that of the compression ramp. The outer boundary condition of the incident oblique shock is merely the freestream value,

$$U(t, \xi, h) = U_\infty \tag{12-a}$$

while the region downstream of the incident oblique shock wave is prescribed by the Rankine-Hugoniot relations

$$U(t, \xi, h) = U(M_\infty, \theta) \tag{12-b}$$

The boundary conditions on the solid contour is given as

$$U(t, \xi, 0) = 0 \ , \ V(t, \xi, 0) = 0 \tag{12-c}$$

$$T(t, \xi, 0) = T_\omega \text{ (constant)} \tag{12-d}$$

and the derived pressure relationship is

$$\frac{\partial \sigma_x}{\partial \eta} = - \frac{\partial \tau_{xy}}{\partial \xi}$$

or

$$\frac{\partial P}{\partial \eta} = \frac{\partial}{\partial \xi} \left(\mu_\omega \frac{\partial u}{\partial \eta} \right) + 4/3 \frac{\partial}{\partial \eta} \left(\mu_\omega \frac{\partial v}{\partial \eta} \right) \tag{12-e}$$

The Diffusive Eddy Viscosity Model

From the view point of engineering calculations, the compression ramp encounters severe difficulty mainly arising from the lack of knowledge concerning the fundamental representation of turbulence. In the corner region, the flow not only experiences a strong adverse pressure gradient, but also must negotiate a sharp corner. Bradshaw[12] in his work on the effects of streamline curvature on turbulent flows thoroughly discussed and summarized the various effects which could substantially alter the structure of turbulence. He also suggested several correction schemes to be used in the calculation methods. Uncertainty remains regarding the applicability of these corrections to the present problem.

Wilcox's[8] numerical solutions of separated turbulent flows resolves some of the unknowns. In short, he successfully demonstrates that the interacting turbulent flow inclusive of the separation phenomenon can be predicted by numerical analysis. His rate equation for turbulence in principle should be more suitable for interacting flows than the simple eddy viscosity model. The latter possesses no means of explicitly carrying any information about the history of the flow field. For the sole purpose of comparison, a 25 degree compression ramp solution by the Cebeci-Smith's eddy viscosity model is presented in Figure 1, together with the Wilcox's solution and the experimental data of Law[15]. It becomes obvious that neither turbulence model can produce an acceptable engineering solution, at least for the pressure distribution on the contour. The comparison is particularly poor in the initial phase of the intense interaction region. It should also be pointed out that this is the worst comparison of the 6 cases that Wilcox presented. The pronounced discrepancy in the leading portion of the pressure distribution seems to suggest a dramatic response of turbulence to the sudden adverse pressure gradient. Perhaps it reveals as Bradshaw asserted[12] that at supersonic Mach numbers, the effects of compression dominate over the effects of surface curvature.

Recently, several research efforts indicate that the Reynolds shear stress nearly remains frozen at its initial value and is convected along streamlines in highly accelerated (or decelerated) flows[16,17]. The measurements[17] also indicate the Reynolds stress approaches a new equilibrium state exponentially. A reasonable explanation of this phenomenon has been given by Bradshaw[12]. He also suggests an empirical ordinary differential equation for a correction factor. Without more data on the relaxation phenomenon, one realizes it would be unrealistic to allow a complex correction. In the present analysis, the "history" effects are given by this following simple equation.

$$\lambda \frac{d\varepsilon}{dx} = \varepsilon_{equil} - \varepsilon \tag{13}$$

The length scale λ is a measure of the memory of the stress-containing eddies. Bradshaw estimates the "time scale" by the ratio of the turbulent energy to the rate of production of turbulent energy. He concludes that for a turbulent boundary layer $\lambda \approx 10\delta$ and $\lambda \approx 2\delta$ for a free mixing layer.

If the ε equilibrium in equation 13 retains a constant value, a particular solution of the rate equation is readily given as

$$\varepsilon - \varepsilon_{equil} = (\varepsilon_{upstream} - \varepsilon_{equil}) \, e^{\frac{-\Delta x}{\lambda}} \tag{14}$$

Equation 14 is identical to the expression proposed by Rose and Johnson[18] for the mixing length. This simple relaxation eddy viscous model was adopted by the present authors to investigate turbulent flow over a series of compression ramps. The numerical results exhibit an encouraging improvement over the local equilibrium viscosity model, and in some aspects, even yields better agreement with data than the numerical results with a rate equation for turbulence[8]. In our early effort,[11] this relaxation eddy viscosity model is technically assumed to have an identical characteristic relaxation time scale for the entire turbulent shear layer. This specific conjecture was incorporated mainly for convenience in the

computational procedure. In reality, perhaps the significant relaxation phenomenon would be identifiable only in the outer portion of the turbulent shear layer where the large scale eddies dominate, e.g., Bradshaw[12] suggests that the inner region be considered near equilibrium. In this sense, only the relaxation of the outer portions of the turbulent shear layer will be treated. The composite eddy viscosity we have adopted, is perfectly suitable for this procedure. In the present analysis, the rate equation (13) is applied only to the outer region of the turbulent shear layer and matched to the local equilibrium inner eddy viscosity. The present procedure offers a more realisitc representation of the relaxation phenomenon of turbulence due to a sudden pressure disturbance and also explicitly considers the rate of change of the local equilibrium eddy viscosity.

The two-layer mixing length model of Cebeci and Smith is adopted in the following fashion; In the inner region, the original form of the Cebeci-Smith model is retained with the Van Driest's modification for the sublayer

$$\varepsilon_i = \rho k_1^2 y^2 \left|\frac{\partial q}{\partial n}\right| D^2 \tag{15}$$

Where k_1 is the von Karman's constant (0.4) and D is the Van Driest's damping factor

$$D = 1 - \exp\left(-y\sqrt{\tau_\omega/\rho_\omega}/26\nu_\omega\right) \tag{16}$$

In the law of the wake for the outer region, the modified Clauser's defect law is employed.

$$\varepsilon_o = 0.0168\ \rho u_{max} \delta^*_i \tag{17}$$

In the outer region, the basic scaling δ^*_i is the kinematic displacement thickness

$$\delta^*_i = \int_0^\infty (1-u/u_{max})\, dy \tag{18}$$

The outer region eddy viscosity coefficient is calculated by equation 17 and satisfied the rate equation, 13. Then the result is matched into the inner equilibrium value by a comparative process. A modification on Cebeci-Smith's eddy viscosity model is also required on the normalizing velocity (u_{max}) in equation 17 to prevent a possible numerical anomaly in the transient phase of the computations. More importantly, one must appreciate that the outer edge of an intensely interacting boundary layer cannot be clearly defined. For this same reason, the intermittency correction in the law of the wake is also omitted. Technically, the Cebeci-Smith's eddy viscosity model is generalized from a boundary layer application to the Navier-Stokes flow regime.

Numerical Procedure

The present analysis adopts MacCormack's alternating-direction-explicit numerical scheme[5]. In the present version [19], it contains two special procedures specially designed to eliminate several types of nonlinear instabilities. One is the averaging process, the other is the rather novel fourth-order product damping term in the predictor and corrector. The later is essential for the analysis of flow fields with severe pressure gradients.

For the compression ramp configuration, the contour geometry is piecewise continuous. At present, no special treatment has been provided at the interface between the plate and the wedge. According to Carter[7], an interpolation process is required to maintain a second-order accurate solution. An improvement in numerical resolution is made possible by overlapping the computational domains. However, the over-lapping capability also serves the purpose of providing an identical upstream boundary condition for all the subsequent inviscid-viscous interacting cases. The leading segment of the calculation domain is defined by a rectangle with the dimensions of 12 x 0.72 inches. The height of the computational plane is roughly six times the boundary-layer thickness. A flat plate solution is allowed to develop on the leading plate with the unperturbed freestream as the initial condition. Solutions in this region compare very well with calculations by an implicit turbulent boundary-layer program developed previously[20]. The difference between the two solutions is within a few percent of both the skin-friction coefficient and velocity profile. All the necessary information is then stored at a given streamwise location to be used as the upstream boundary condition for the following corner region. On the compression ramp the computational region is defined by a trapezoid with the lower surface parallel to the wedge surface.

In the calculation, a 64 x 22 computational mesh is employed. Grid spacing in the ξ direction is uniformly distributed for each computational domain. However, a different increment in ξ has been used for the flat plate region ($\Delta\xi$= 0.01695 ft.) and downstream of the overlapping location ($\Delta\xi$= .00565 ft.). The grid system consists of an exponentially varying inner region (16 points) and an equal-spaced outer region[19]. The finest step size in η is assigned to the viscous sublayer with a dimension of 10^{-4} ft.

The calculation is performed on a CDC 6600 digital computer. The rate of data processing is 0.028 seconds per grid point for each time step. The evolution of the dependent variables is monitored until consecutive calculations indicate no significant change (<.1%), then the result is considered to be the asymptotic solution. A typical calculation requires about 300 time cycles (1 1/2 hours) to achieve convergence.

Discussion of Results

Numerical results are presented in three groups. The first portion examines the feasibility of employing the eddy viscosity model with an empirical relaxation correction for predicting interacting turbulent flows with separation. The second portion of the presentation is devoted to the verification of this concept through a comparison with experimental data. Finally, corresponding compression ramps and shock impingement cases are compared in an attempt to delineate some of the important features of "free interacting" flows. Before we proceed further in this discussion, clarification of the terminology is needed. In this present analysis, the "equilibrium" flow solution is defined as the calculation by

means of the Cebeci-Smith's eddy viscosity model. "Frozen" flow then is designated as the result obtained by holding the eddy viscosity profile constant at the undisturbed upstream value. We have selected the location to be 0.929 ft from the leading edge of the flat plate for all cases computed. In principle, a sophisticated criterion can be utilized by freezing the eddy viscosity along a streamline as a function of the gradient. However, to demonstrate the cause and effect of relaxing the eddy viscosity, a more complicated model is not warranted at the present time. The relaxation solution is described to be the calculation with the eddy viscosity model given by equation 18 or equation 14. We emphasize that this eddy viscosity model is a simplified version originated by Bradshaw[12] and Rose et al[18]. They both propose a length scale adjustment on the eddy viscosity coefficient of about ten boundary-layer thicknesses. The present correction only attempts to represent the flow "history" effect due to a strong compression, with no additional correction for the effects of streamline curvature, etc. incorporated.

In Figure 2, the static pressure measurements of Law[15] along with three different numerical results are presented for the 25° compression ramp. The free stream Mach number is 2.96 and the Reynolds number based upon the leading plate length is 10^7. The equilibrium calculation fails completely in predicting the pressure variation in the corner region, in that it underpredicts the extent of the upstream propagation and produces a very short pressure plateau. In addition, the pressure approaches the inviscid asymptote at a more rapid rate than the experimental data indicates. The frozen solution on the other hand produces too large a separation region. The correct solution apparently is somewhere between these two extremes. A relaxation model employing equation 14 produces a solution with marked improvement over the two aforementioned calculations. Significant discrepancy between the data and the present calculation only appears in the pressure plateau, near the corner.

The calculated skin-friction coefficient distributions are present in Figure 3. The striking feature of this presentation is the drastic difference in the shear stress distributions for the three calculations. The difference is perhaps anticipated in view of the three substantially different surface pressure variations. Interestingly enough, the unusual "dual-minimum" skin friction distribution is also encountered for laminar flows with extensive separation regions[1,2,3,4]. Unfortunately, no experimental skin-friction data are available for this case, however, oil flow measurements indicated the separation and reattachment points of the flow.

Excellent agreement in the location of separation and reattachment is observed in that the discrepancy between the data and the relaxation calculation is within a fraction of the boundary-layer thickness. However, the equilibrium and the frozen calculations significantly under and over predict these locations respectively. In short, the present relaxation scheme seems able to adequately predict the important engineering features of the ramp problem. Therefore it appears logical to seek further verification of the present assertions in the prediciton of the detailed flow field properties.

In Figure 4, we present a comparison between the measured and calculated density profiles at two streamwise locations. The experimental data are direct measurements from an interferogram by means of evaluating the fringe shifts[21]. The affinity between data and the relaxation calculation upstream and in the separated flow region is obvious.

Up to this point, we have only presented the numerical results associated with the algebraic relaxation eddy viscosity model, equation 14. It has been mentioned previously that the algebraic expression is a special solution of the empirical rate equation (equation 13). The relaxation eddy viscosity rate equation model possesses two aesthetically pleasing features over the algebraic model: First, the general solution includes the rate of change of the local equilibrium value and secondly, applies only to the outer portions of the turbulent boundary layer. The latter implies the inner region of the turbulent boundary layer remains in the state of local equilibrium, as has been experimentally observed[12]. In the present numerical procedure, the rate equation model requires an additional data storage to process the accumulation rate of change for the local equilibrium eddy viscosity coefficient. However, the rate of data processing is comparable to the simple algebraic model. A specific comparison of the two relaxation eddy viscosity models is summarized in the next two figures.

The streamwise pressure distribution, over a 25° compression ramp are presented in Figure 5 for the two relaxation models computed under identical conditions. Minor differences are apparent only near the forward portion of the interaction. In Figure 6, the skin friction coefficient distributions are presented. Again, the discrepancy between the two relaxation models is comparable to the experimental data scatter.

In view of the fact that the present analysis claims to be no more than an engineering prediciton scheme and the small numerical difference between the relaxation eddy viscosity models does not indicate an obvious preference to be recommended, therefore, the remainder of the presentation will be restricted to the results provided by only the algebraic relaxation eddy viscosity model.

Encouraged by these preliminary results, a series of calculations were performed in an attempt to establish the range of validity of the relaxation eddy viscosity model. The investigated ramp angles span a range from 15 to 25 degrees at an interval of 2 degrees apart. The computed surface pressure distributions together with the corresponding experimental data[15] are given in Figure 7. In general, the difference between the data and numerical results is small. Excellent prediction of the pressure propagation upstream of the corner has been achieved. Significant discrepancies between the data and calculations appear only in the corner region for the high ramp angle (Figure 2).

The skin-friction coefficient distributions for the compression ramp at six different ramp angles are presented in Figure 8. Experimental data[15,21] of this separation location (using several techniques) for different ramp angles are also provided in this graph. For the 15 degree ramp, the calculations indicate a very small region of separation with a dimension less than 2/3 of the boundary-layer thickness. The corresponding experimental observation reveals even a smaller region of the separated flow. In general, the calculations predict accurately the point of separation. For all the investigated cases, the predictions are well within the data scatter band of the different experimental techniques. In this graph, one observes a systematic evolution of the skin-friction coefficient from a single-minimum distribution into

a dual-minima behavior as the separation domain increases substantially. This trend has also been observed for separated laminar flows[1,2,3,4].

In Figure 9, the complete interacting flow field including the separation region is presented. Upstream of the corner a clearly defined outer edge of the turbulent boundary layer can be discerned. The normal velocity component in the boundary layer first reveals significant adjustment in magnitude, then exhibits a rapid pressure rise in the wall region as the corner is approached. Adjacent to the separation point, the coalesence of compression waves is evident. The penetration of the separation induced shock wave reaches the shear stress dominated inner region. Extensive separation exists around the corner; the boundary layer growth increases rapidly but still reveals a clearly identifiable outer edge. Further downstream of the corner, a second coalescing shock wave at reattachment also becomes detectable. The second shock eventually intersects the leading separation shock producing an obvious change in the slope of the wave front. Downstream of this intersection point, no distinctive outer edge of the boundary layer can be clearly defined. Instead a rotational field produces a streamwise velocity gradient. The numerical result essentially duplicates the experimental observations (Figure 10). The experimental data are obtained chiefly from the optical and oil-flow studies of the 25° degree ramp configurations by Havener, and Radley[21] and Law[15].

The comparison of the density profiles at several streamwise locations between the data and calculation is presented in Figure 11. The data are directly evaluated from the fringe shifts[21, 22] observed in Figure 10, therefore, this outer limit of the data either represents the encountering of a shock wave or a uniform flow region. All the data and calculated density profiles are presented in the coordinate perpendicular to the surface. Interpolation of the computed results downstream of the corner is required to present the information in this format. In general, the numerical results predict the measured density profiles within few percent.

In Figure 12, we present several streamwise velocity profiles in the body orientated coordinates. One observes a sequence of turbulent boundary layer through this interaction region which separates, reattaches and finally exits as a confined shear layer. Havener, et al, also deduced several velocity profiles from their optical measurements[21,22]. They obtained the velocity data through the Crocco relationship and by linearly interpolating the pressure across the boundary layer. The comparison between the data and the calculation reveals good conformity throughout. Conclusions on the agreement with the experiment should be based on the density distribution (Figure 11) where a direct comparison may be performed.

The two-dimensional flow over a compression ramp and the oblique shock impingement on a turbulent boundary layer have been identified as "free interaction" problems. The present understanding of the detailed flow structures is not complete. However, Green[14] has correctly pointed out that the wave system produced by an incident oblique shock may be considered to be a variant of the compression ramp configuration He concludes that a compression corner with a stream deflection of $2\theta_I$ and an incident shock of a stream deflection of θ_I will produce virtually the same overall pressure rise. The experimental data however indicate a large discrepancy between the scales of the flow separation region[14]. The source of the discrepancy between tests has been attributed to the departure from two dimensionality of the two-dimensional experimental arrangements. The present analysis perhaps would contribute some understanding to the uncertainty in this area. At least, the present analysis will provide a two-dimensional numerical solution of the shock impingement problem.

In Figure 13, the surface pressure distributions of a 25° compression ramp and the incident oblique shock generating by a deflection angle of 12.5 degree are presented together. Both computations are carried out with the identical unperturbed upstream conditions. The abscissa, S/L=1.0, denotes the corner location of the compression ramp configuration. For the shock impingement problem, this location is designated as the intersection of the extended incident shock and the flat plate. Referred to the common origin, the surface pressure distribution of the shock impingement case shifted upstream at the compression ramp value by roughly the boundary layer thickness (.17 inch). More importantly, the overall pressure rise between the two investigated cases differs by only one percent. The corresponding skin friction coefficient distributions are presented in Figure 14 and also show an upstream shift.

Concluding Remarks

For some time now it has been possible to obtain excellent agreement between experimental data and numerical calculations for turbulent flows with zero pressure gradient. However these turbulence models (eigher the eddy viscosity model[13,20] or the more sophisticated model equations[10]) have failed to predict turbulent flows with strong adverse pressure gradients. In the present analysis, a simple relaxation of the turbulence has been incorporated into an eddy viscosity model. The relaxation eddy viscosity model is combined with the Navier-Stokes equations to form a closed system of equations. The results demonstrate that the turbulence model adequately predicts tne inviscid-viscous interacting turbulent flow, including the separation phenomenon.

Two versions of the relaxation model have been examined under identical conditions and only small differences observed. The comparisons with experimental data at Mach 3 of Law[15], Havener and Radley[20,21] for compression ramps (and shock impingement) indicate that the present method accurately predicts the upstream pressure propagation and location of the separation and the reattachment points. Good agreement is also obtained between the measured and calculated density profiles throughout the viscous-inviscid flow field.

REFERENCE

1. Dwoyer, D. L., "Supersonic and Hypersonic Two-Dimensional Laminar Flow Over a Compression Corner" Proceedings AIAA Computational Fluid Dynamics Conference, July, 1973, p. 69

2. Werle, M. J., and Vatsa, V. N., "Numerical Solution of Interacting Supersonic Boundary Layer Flows Including Separation Effects" ARL 73-0162. Aerospace Research Laboratories, Wright-Patterson AFB, Ohio Dec. 1973.

3. Holden, M. S., "Theoretical and Experimental Studies of Laminar Flow Separation on Flat Plate-Wedge Compression Surfaces in the Hypersonic Strong Interaction Regime" ARL 67-0112. Aerospace Research Laboratories, Wright-Patterson AFB, Ohio May 1967.

4. Jensen, R., Burggraf, O. R., and Rizzetta, D. P., "Asymptotic Solution for Supersonic Viscous Flow Past a Compression Corner" Proceedings of th International Conference on Numerical Methods in Fluid Dynamics, Boulder, Col. June 1974

5. MacCormack, R. W., "Numerical Solutions of the Interaction of a Shock Wave with a Laminar Boundary Layer" Lecture notes in Physics, Vol. 8, Springer-Verlag, New York, 1971, p. 151

6. Baldwin, B. S., and MacCormack, R. W., "Numerical Solution of the Interaction of a Strong Shock Wave with a Hypersonic Turbulent Boundary Layer" AIAA paper 74-558, AIAA 7th Fluid and Plasma Dynamics Conference Palo Alto, Cal. June 17-19, 1974

7. Carter, J. E., "Numerical Solution of the Supersonic Laminar Flow Over a Two-Dimensional Compression Corner" Lecture notes in physics, Vol. 19, Springer-Verlag, New York, 1973, p. 69

8. Wilcox, D. C., "Numerical Study of Separated Turbulent Flows" AIAA paper 74-584, AIAA 7th Fluid and Plasma Dynamics Conference Palo Alto, Cal. June 17-19, 1974

9. Crocco, L., "A Suggestion for the Numerical Solution of the Navier-Stokes Equations" AIAA J., Vol. 3, No. 10, Oct. 1965, p. 1824

10. Saffman, P. G., and Wilcox, D. C., "Turbulence Model Predictions for Turbulent Boundary Layer" AIAA J., Vol. 12, No. 4, April 1973, p. 541

11. Shang, J. S., and Hankey, W. L. Jr., "Numerical Solution of the Navier-Stokes Equations for Supersonic Turbulent Flow over a Compression Ramp" AIAA paper 75-3, AIAA 13th Aerospace Science Meeting, Pasadena Cal. January 20-22 1975

12. Bradshaw, P., "Effects of Streamline Curvature on Turbulent Flow" AGARDograph, No. 169, (AGARD-AG-169) August 1973

13. Cebeci, T., Smith, A. M. O., and Mosinskis, G., "Calculations of Compressible Adiabatic Turbulent Boundary Layers" AIAA J., Vol. 8, No. 11, 1970, p. 1974

14. Green, J. E., "Interactions Between Shock Waves and Turbulent Boundary Layer" in progress in Aerospace Sciences, Vol. 11, pp. 235-340, Pergamon Press, 1970

15. Law, C. H., "Supersonic Turbulent Boundary-layer Separation" AIAA J., Vol. 12, No. 6, June 1974, p. 794

16. Deissler, R. G., "Evolution of a Moderately Short Turbulent Boundary Layer in a Severe Pressure Gradient" J., Fluid Mechanics, Vol. 64, Part 4, 1974, p. 763

17. Narasimha, R., and Prabhu, A., "Equilibrium and Relaxation in Turbulent Wakes" J., Fluid Mechanics, Vol. 54, Part 1, 1972. p. 1

18. Rose, W. E., and Johnson, D. A., "A Study of Shock-Wave Turbulent Boundary Layer Interaction Using Laser Velocimeter and Hot-wire Anemometer Techniques" AIAA paper 74-95, AIAA 12th Aerospace Sciences Meeting, Washington, D. C., Jan 30-Feb 1, 1974

19. MacCormack, R. W., "Numerical Methods for Hyperbolic Systems" Lecture notes for short course on Advances in Computational Fluid Dynamics. The University of Tennessee Space Institute, Tullahoma, Tennesse, Dec., 10-14, 1973

20. Shang, J. S., Hankey Jr., W. L., and Dwoyer, D. L., "Numerical Analysis of Eddy Viscosity Models in Supersonic Boundary Layer" AIAA J., Vol. 11, No. 12, Dec. 1973, p. 1677

21. Havener, A. G., and Radley, R. J., "Turbulent Boundary-Layer Flow Separation Measurements Using Holographic Interferometry." AIAA J., Vol. 12, No. 8, August, 1974, p. 1071

22. Havener, A. G., and Radley, R. J., "Supersonic Wind Tunnel Investigations Using Pusled Laser Holography" ARL 73-0148, Aerospace Research Laboratories, Wright-Patterson AFB, Ohio, Oct 1973

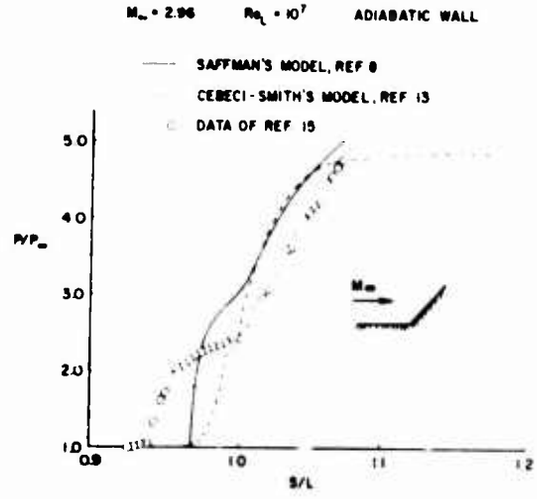

Figure 1. Comparison of Different Turbulent Models with Experiment

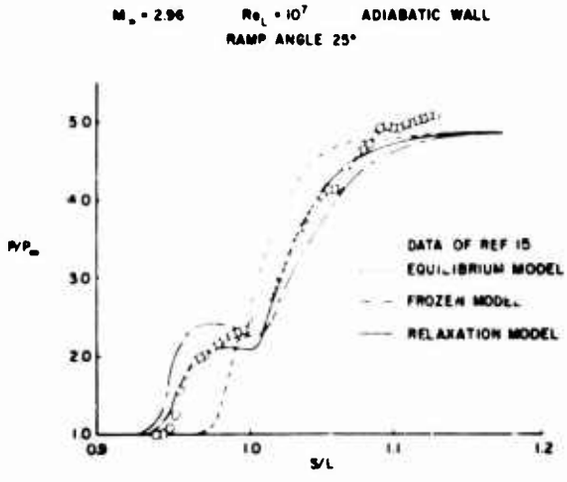

Figure 2. Pressure Distribution for Equilibrium, Frozen and Relaxation Eddy Viscosity Models

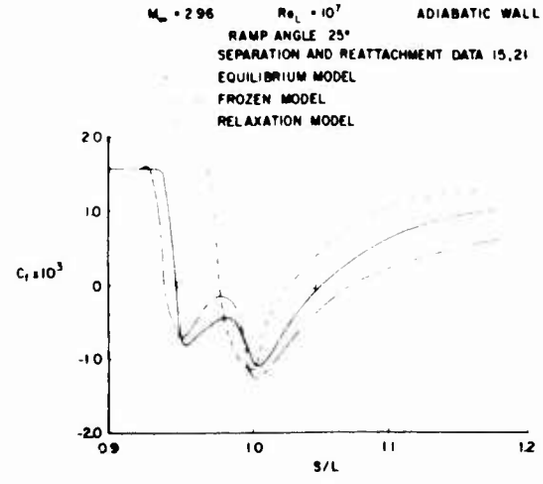

Figure 3. Skin-friction Coefficient Distributions for Equilibrium, Frozen and Relaxation Eddy Viscosity Models

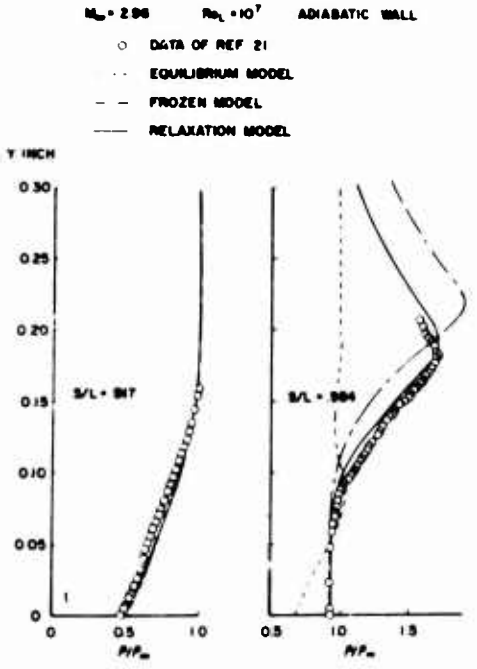

Figure 4. Density Profiles for Equilibrium, Frozen and Relaxation Eddy Viscosity Models

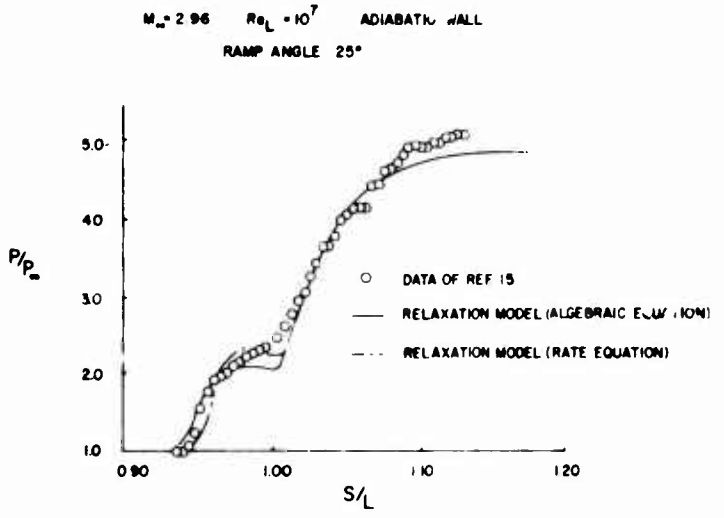

Figure 5. Comparison of Pressure Distribution for Two Relaxation Models

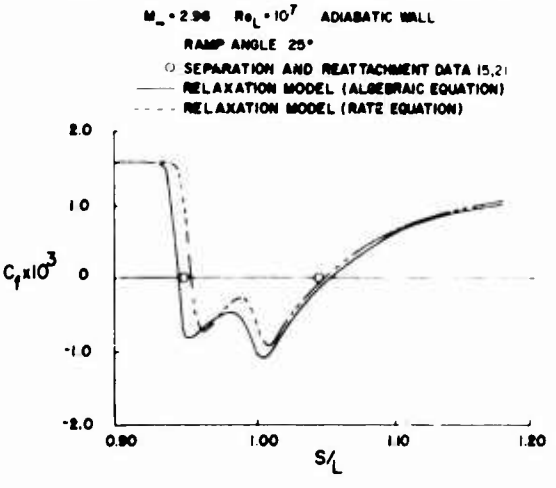

Figure 6. Comparison of Skin-friction Distributions for Two Relaxation Models

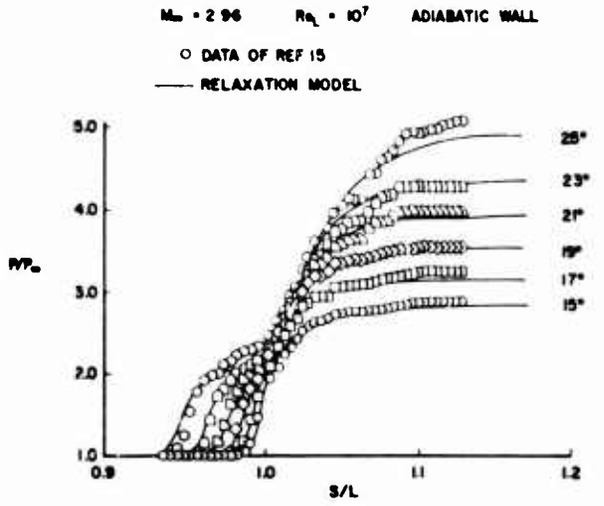

Figure 7. Pressure Distributions for Various Compression Ramp Angles

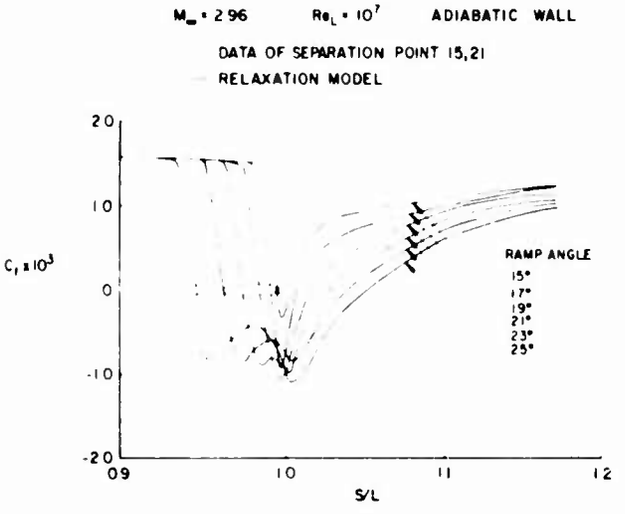

Figure 8. Skin-friction Coefficient Distributions for Various Compression Ramp Angles

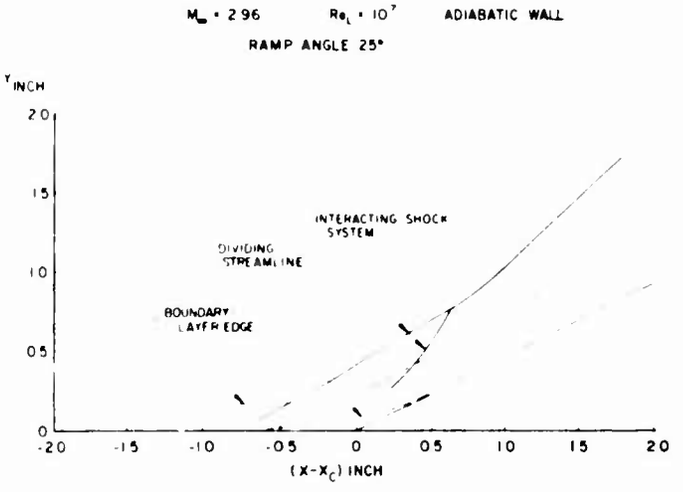

Figure 9. Computed Flow Field Structure for a 25° Compression Ramp

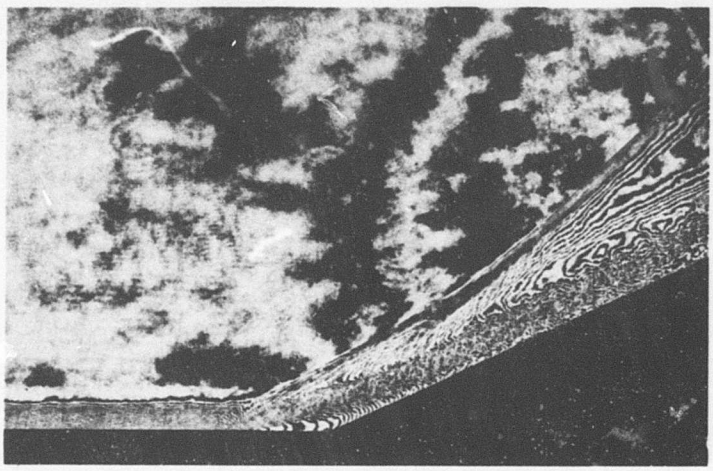

Figure 10. Interferogram for the Flow Over a 25° Compression Ramp

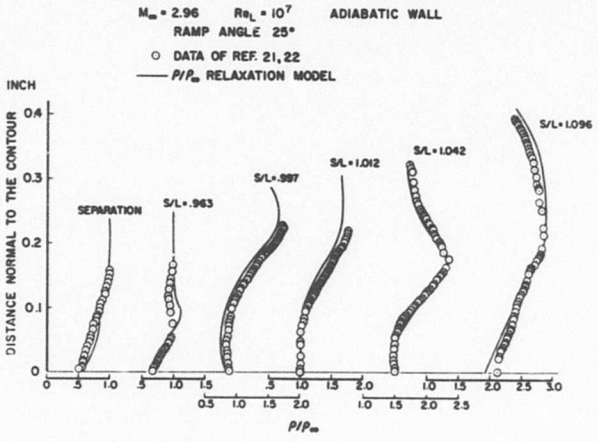

Figure 11. Density Profiles for a 25° Compression Ramp

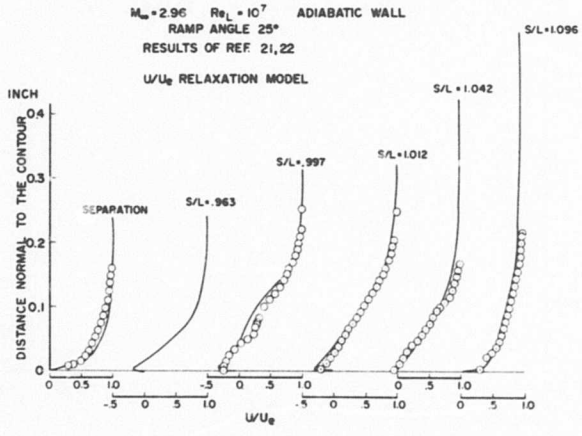

Figure 12. Velocity Profiles for a 25° Compression Ramp

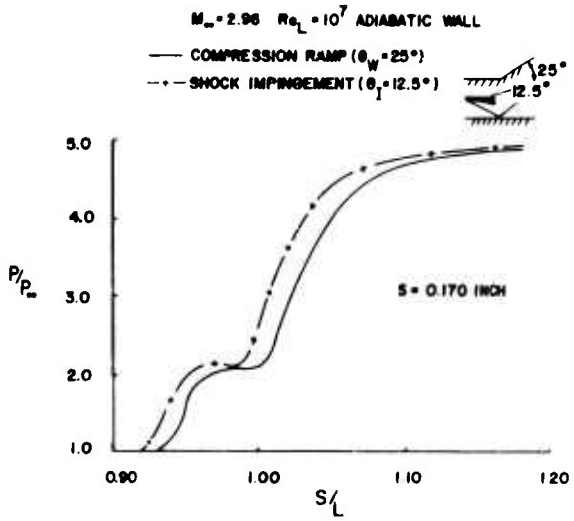

Figure 13. Comparison of the Pressure Distributions for a Compression Ramp and Shock Impingement

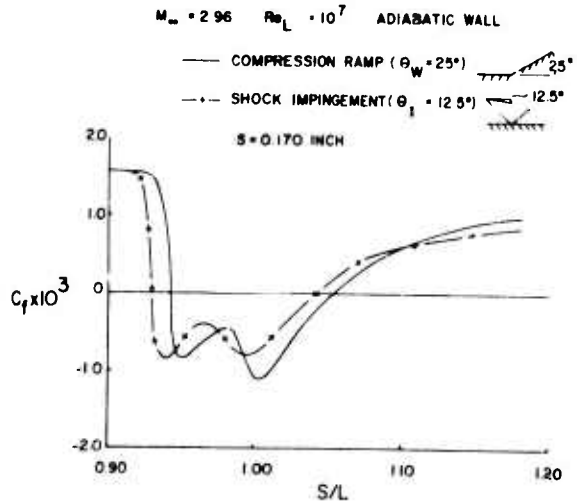

Figure 14. Comparison of the Skin-friction Coefficients for a Compression Ramp and Shock Impingement

AN EXPERIMENTAL AND NUMERICAL INVESTIGATION OF SHOCK-WAVE INDUCED TURBULENT BOUNDARY-LAYER SEPARATION AT HYPERSONIC SPEEDS

J. G. Marvin,* C. C. Horstman,**
M. W. Rubesin,† T. J. Coakley,†† M. I. Kussoy††
Ames Research Center, NASA
Moffett Field, California 94035, USA

SUMMARY

This paper describes a thoroughly documented experiment that was specifically designed to test and guide computations of the interaction of an impinging shock wave with a turbulent boundary layer. Detailed mean flow-field and surface data are presented for two shock strengths which resulted in attached and separated flows, respectively. Numerical computations, employing the complete time-averaged Navier Stokes equations along with algebraic eddy viscosity and turbulent Prandtl number models to describe shear stress and heat flux, are used to illustrate the dependence of the computations on the particulars of the turbulence models. Models appropriate for zero-pressure-gradient flows predicted the overall features of the flow fields, but were deficient in predicting many of the details of the interaction regions. Improvements to the turbulence model parameters were sought through a combination of detailed data analysis and computer simulations which tested the sensitivity of the solutions to model parameter changes. Computer simulations using these improvements are presented and discussed.

NOTATION

A, A_w^+ van Driest damping parameter, Eqs. (5) and (6)

c_p specific heat at constant pressure

c_v specific heat at constant volume

C_F local skin friction coefficient, $\tau_w/(1/2)\rho_\infty u_\infty^2$

C_H local Stanton number, $q_w/\rho_\infty u_\infty c_p(T_t - T_w)$

e total specific energy per unit volume, $\rho[c_v T + (v^2 + u^2)/2]$

F,G,H mass-averaged fluxes, Eqs. (1) and (2)

I intermittency factor, Eq. (9)

k thermal conductivity

ℓ mixing length, Eqs. (4) and (20)

p time-averaged pressure

Pr molecular Prandtl number, $\mu c_p/k$

Pr_t turbulent Prandtl number

q_x axial heat flux, $-c_p(\mu/Pr + \rho\varepsilon/Pr_t)\partial T/\partial x$

q_r, q_y radial heat flux, $-c_p(\mu/Pr + \rho\varepsilon/Pr_t)\partial T/\partial r$

r radial coordinate, distance from model centerline

t time

T temperature

u mass-averaged velocity component in axial direction

U mass-averaged conservation variables, Eqs. (1) and (2)

v mass-averaged velocity component in radial direction

x axial coordinate, distance from leading edge of shock-wave generator

y distance normal to model surface

α shock-wave generator leading-edge angle

δ boundary-layer thickness

δ_0 boundary-layer thickness at the upstream location of the first measured profile station

δ_i^* kinematic displacement thickness, Eq. (8)

δ_c^* compressible displacement thickness, Eq. (11)

ε eddy viscosity, Eqs. (4) and (20)

κ von Karman constant, Eq. (5)

μ viscosity

ρ time-averaged density

σ_r radial normal stress, $p - 2\mu_T \frac{\partial v}{\partial r} + \frac{2}{3}\mu_T \left(\frac{v}{r} + \frac{\partial v}{\partial r} + \frac{\partial u}{\partial x}\right)$

σ_x axial normal stress, $p - 2\mu_T \frac{\partial u}{\partial x} + \frac{2}{3}\mu_T \left(\frac{v}{r} + \frac{\partial v}{\partial r} + \frac{\partial u}{\partial x}\right)$

σ_θ azimuthal normal stress, $p - 2\mu_T \frac{v}{r} + \frac{2}{3}\mu_T \left(\frac{v}{r} + \frac{\partial v}{\partial r} + \frac{\partial u}{\partial x}\right)$

τ, τ_{xr} total shear stress, Eq. (3)

Subscripts

f final axial grid location

i initial axial grid location

max maximum

o location of incident shock impingement on cylinder surface in the absence of a boundary-layer

---

*Chief, Experimental Fluid Dynamics Branch
**Ass't Chief, Experimental Fluid Dynamics Branch
†Sr. Staff Scientist
††Research Scientist

r	radial direction	x	axial direction
t	stagnation conditions	w	wall
T	total	∞	local free stream ahead of interaction

1. INTRODUCTION

The availability of larger, faster computers, the need to reduce wind-tunnel testing, which is time consuming and costly, and to provide alternate simulation capability for test conditions beyond the reach of practical wind-tunnel design have resulted in increased emphasis on computational fluid mechanics. Computations that were not feasible several years ago are now being performed routinely. For example: inviscid three-dimensional computations for speeds ranging from transonic to hypersonic are possible (refs. 1 and 2); even flows where dominant viscous interactions occur, such as the interaction of a shock with a boundary layer, are being computed (refs. 3 and 4). These interacting flows present the greatest challenge, however, because most of the practical applications occur at high Reynolds numbers where the flow is turbulent and little is known about turbulence modeling.

Until recently, most of the techniques for predicting the flow behavior in the vicinity of shock boundary-layer interactions were based on experimental correlations or approximate solutions to the boundary-layer equations. But advances in numerical methods and increased computer speed and capacity have resulted in successful attempts to obtain steady-state solutions of the complete time-dependent Navier Stokes equations. Computations of laminar interactions have been used to illustrate the utility and accuracy of these techniques (refs. 3 and 4). Very recent examples for turbulent flows (refs. 5-7) illustrate that such computations using the time-dependent, time-averaged‡ Navier Stokes equations are also feasible and that they describe the qualitative features of the flow interactions. In these examples, closure of the conservation equations was accomplished by describing the turbulent shear stress and heat flux by eddy-viscosity models and turbulent Prandtl numbers. However, a lack of sufficient detailed experimental data precluded verification of these models and efforts to modify them so that the quantitative flow features could be more aptly described.

The present study was undertaken to provide a formidable first step toward understanding the mechanisms that must be modeled before successful numerical calculations of these complicated flows can be made. It combines experimental and numerical methods to guide and verify turbulence modeling for two shock boundary-layer interaction flows, one with and one without separation. An axisymmetric experimental arrangement was chosen to assure purely two-dimensional flow (ref. 8). Shocks of two different strengths were impinged on an established turbulent boundary layer to set up both unseparated and separated flows in the interaction zone. Detailed measurements, consisting of surface-pressure, skin-friction, heat-transfer, and boundary-layer profiles of velocity, static pressure, and temperature were obtained at finely spaced intervals along the surface. Analysis of these data was undertaken to define the detailed behavior of the turbulence parameters used to describe the shear stresses throughout the interaction regions. Computations were made using the time-dependent, time-averaged Navier Stokes equations employing the exact experimental boundary conditions and algebraic eddy-viscosity descriptions for the turbulent shear stress. The authors reported preliminary progress on the separated case in ref. 9.

2. APPARATUS AND PROCEDURES

2.1 Facility

The experiment was conducted in the NASA Ames Research Center 3.5-Foot Hypersonic Wind Tunnel. This facility operates in a blowdown mode and utilizes contoured axisymmetric nozzles to achieve a uniform Mach number, and an open-jet type test core approximately 0.7 m in diameter and 4 m in length. The present tests were all performed at a nominal free-stream Mach number of 7.2 and with nominal values of total temperature and pressure of 695° K and 34 atmospheres, respectively. The corresponding nominal value of free-stream unit Reynolds number was 10.9×10^6 m^{-1} and the useful test time was about 3 min.

2.2 Model

A cone-ogive cylinder, 330 cm in length and 20.3 cm in diameter was used as the test surface (see fig. 1). An annular shockwave generator, 51 cm in diameter, mounted concentric with the cylinder axis was used to generate shock waves of two different strengths by beveling the sharp leading edge at either 7.5° or 15°. The generator could be translated in a direction parallel to the cylinder axis so that the entire interaction region could be passed over selected survey stations.

Interchangeable instrumentation ports, 12 cm in diameter and specifically contoured to match the cylindrical surface, were located at 25 cm intervals along the cylinder in a single line, and every 50 cm in another line 180° around the body. One port was instrumented with a floating element skin-friction balance. Another was used to accommodate either pitot and static pressure probes or total temperature probes. The probes were positioned by a mechanism contained inside the cylinder and automatically actuated from outside the tunnel test section. The remaining ports were instrumented with thermocouples spot-welded to the inner surface every 1.25 cm and with static pressure taps. Static pressure taps were also located every 5 cm along the entire cylinder between ports.

2.3 Test procedure

Data were collected from a series of tests with the tunnel operating at the nominal conditions described above. In separate tests without the generator it was determined that a fully developed turbulent

‡Time averaging in these equations is over periods long compared to turbulence time scales, but short compared to the time variations of the flow field as a whole.

boundary layer with negligible axial pressure gradient was established over the cylinder surface between 100 and 300 cm from the model tip (ref. 10). With the generator in place, the nominal measured boundary-layer parameters ahead of the interaction for the 7.5° and 15° generator angles, respectively, were: edge Mach number, 6.7 and 6.9; boundary-layer thickness, 3.2 cm and 2.7 cm; and Reynolds number based on boundary-layer thickness, 0.23×10^6 and 0.2×10^6. The model wall temperature was essentially constant at a value of 300° K.

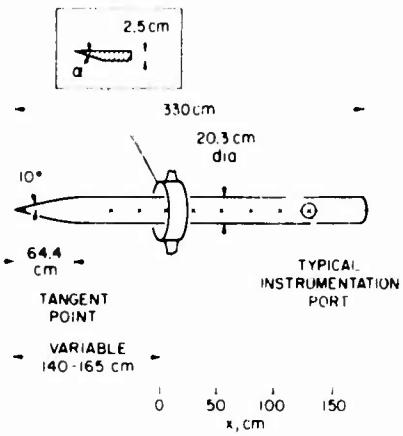

Fig. 1 Test model.

Surface pressure, skin friction, and heat transfer were obtained at small intervals by moving the shock-wave generator in an axial direction during the tests. The boundary-layer thickness increased about 10% over the distance of 25 cm which corresponded to the difference between the farthest upstream and downstream positions of the generator. The difference in boundary-layer thickness had little influence on the results, provided they were compared at equivalent distances from the leading edge of the generator.

Skin friction was measured with a contoured floating-element balance whose sensible element was 0.95 cm in diameter. Calibrations of the gage before and after each test run were repeatable to within 5%. The skin-friction data were corrected for buoyancy effects resulting from the axial pressure gradient. Corrections were less than 10% of the measured values, except in the regions of minimum skin friction for the 7.5° generator tests and near separation and reattachment for the 15° generator tests, where they were as high as 50% of the measured upstream zero pressure gradient values. The heat-transfer rate was measured using the thin-wall transient technique. Longitudinal conduction errors were computed and found to be less than 5% of the measured rates and so no corrections were applied to these data.

Velocity, density, and pressure profiles were obtained from pitot and static pressure and total temperature surveys. Each survey was taken during a single test run, and its axial location was established prior to the run by prepositioning the shock generator. In the interaction region, surveys were obtained every 2 cm for the 7.5° generator tests and every 2.5 cm for the 15° generator tests. Downstream of the interaction the corresponding distances between survey stations were increased to 4 cm and 5 cm, respectively, for the two generator angles. In the reversed flow region established with the 15° generator, pitot measurements were obtained in upstream and downstream directions to help establish the extent of separation. When traversing the boundary layer, the probes were stopped at each location for a few seconds to avoid time lags in the measurements, and static pressures at the model surface were monitored continuously to verify interference-free data.

To verify that the model was aligned with the free-stream flow direction, surface-pressure measurements at selected axial positions were obtained at 90° intervals around the model, and skin-friction measurements at selected axial positions 180° apart. Comparisons of these data around the model showed variations that were within the experimental accuracy of the measurements. For the 15° generator tests, separation and reattachment lines around the model were also measured using a surface oil film technique. The results verified an axisymmetric separation zone.

A more complete description of the test procedure and data accuracy along with tabulations of all the test data are given in ref. 11.

3. GOVERNING EQUATIONS AND NUMERICAL PROCEDURES

The equations and numerical procedures were first presented by the authors in ref. 9. For completeness, some of that information is presented again in this section.

3.1 Equations and boundary conditions

The mass-averaged Navier Stokes equations for compressible flow, expressed in cylindrical coordinates with axial symmetry assumed, were used to predict the flow throughout the interaction region. The equations and the concept of mass averaging are discussed in ref. 12. The turbulent Reynolds stress and heat-flux terms in these equations are related to the mean flow gradients of velocity and temperature by eddy-transport coefficients that are added to the molecular-transport coefficients. Additional restrictions on the equation system include the perfect gas assumption, constant specific heats, the Sutherland viscosity law, and zero bulk viscosity. The resulting equations are

$$\frac{\partial U}{\partial t} + \frac{\partial F}{\partial x} + \frac{\partial G}{\partial r} = H \tag{1}$$

$$U = r\begin{pmatrix}\rho\\ \rho u\\ \rho v\\ e\end{pmatrix} \qquad F = r\begin{pmatrix}\rho u\\ \rho u^2 + \sigma_x\\ \rho uv \qquad \tau_{xr}\\ (e + \sigma_{\ldots} + \tau_{xr}v + q_x\end{pmatrix}$$

$$H = r\begin{pmatrix} 0 \\ \sigma \\ \sigma_\theta \\ 0 \end{pmatrix} \qquad G = r\begin{pmatrix} \rho v \\ \rho uv + \tau_{xr} \\ \rho v^2 + \sigma_r \\ (e + \sigma_r)v + \tau_{xr}u + q_r \end{pmatrix} \tag{2}$$

Figure 2 shows the computational domain. The conditions on the upstream boundary were prescribed by a combination of an inviscid, method of characteristics program (ref. 13), and a boundary-layer program (ref. 14) modified for turbulent flows by Marvin and Sheaffer. At the upstream boundary position, the experimental and computed incident shock waves were aligned and the boundary-layer program was run for an x distance that ensured a match of experimentally and numerically determined displacement thicknesses. Along the cylinder surface, $r = r_w$ or $y = 0$, the boundary conditions used were the viscous, no-slip conditions, $u = v = \partial p/\partial r = 0$, $T = T_w$, while along the outer boundary they were the inviscid, free-slip conditions, $v = \partial p/\partial r = \partial u/\partial r = \partial T/\partial r = 0$. At the downstream boundary the simple extrapolation relation, i.e., $\partial(u)/\partial x = 0$, was used. The initial conditions within the computation domain used to start the solutions were obtained by setting the values of all variables equal to their inflow boundary values at the same vertical station, i.e., $f(x, r, o) = f(x_i, r, o)$, $x_i \le x \le x_f$. To restart solutions or make modifications to turbulence parameters, initial values of the variables were set equal to their computed values obtained during the last time-step of the previous solution.

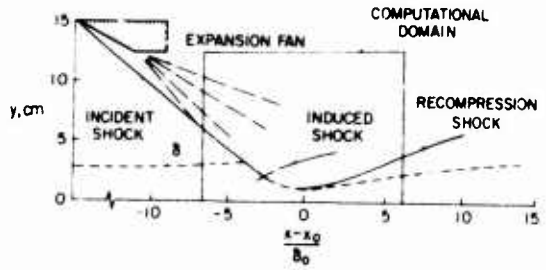

Fig. 2 Flow-field sketch and computational domain.

3.2 Numerical procedures

The finite difference scheme used to solve eq. (1) is the same as that developed originally by MacCormack (ref. 3) and applied more recently to two-dimensional turbulent shock boundary-layer interactions by Baldwin and MacCormack (ref. 15). The numerical techniques employed in the present study, along with all the pertinent difference equations, and some special procedures, are reported in ref. 9. The computational domain was subdivided into four subgrids with each subgrid divided into a number of uniform grid cells with spacing Δy. Finer spacing was employed near the wall. A total of 78 cells in the y direction was used; uniformly spaced grid with 48 cells in the x direction was used with spacing $\Delta x = 0.80$ or 0.635 cm for the 7.5 and 15° cases, respectively. Some of the solutions presented later cover axial distances greater than those obtained with the 48 cells in the x direction. Those solutions were achieved by redefining the upstream boundary to coincide with a position about 3 cm ahead of the downstream boundary from converged solutions and then continuing the solutions on downstream for another 48 x cell points.

The solutions were advanced in time following the procedure described in ref. 9. Steady-state convergence was assumed when solutions from at least 20 successive time steps showed little or no change. Computation times to achieve these fully converged solutions on a CDC 7600 were 3-4 hrs for the 15° generator cases and about 1 hr for the 7.5° cases.

4. RESULTS AND DISCUSSION

4.1 Experimentally determined flow-field features

Figure 2 depicts the major features of the shock-wave, boundary-layer interaction zone. The sketch is based on boundary-layer survey measurements and shadowgraphs taken during the experiments using both the 7.5° and 15° shock-wave generators. The incident shock wave, weakened and curved somewhat by the expansion fan emanating from the corner formed by the leading edge and the body of the shock-wave generator, impinges on the incoming boundary layer. The subsequent increases in surface pressure cause the boundary layer to thicken, or even separate in the case of the strongest incident shock wave, and induce a shock wave. Thereafter rapid flow turning and boundary-layer thinning occur and a recompression shock is formed.

Figure 3 shows the surface measurements obtained for the two shock-wave generator angles. Surface-pressure, skin-friction, and heat-transfer coefficients are shown as functions of a normalized interaction distance centered about x_o, the location of the intersection of the inviscid incident shock wave with the body surface in the absence of a boundary layer. With the 7.5° generator, the pressure rises continually through the interaction, the skin friction decreases initially in the presence of the adverse pressure gradient, and rises thereafter in the recompression region where the boundary layer thins. The heat transfer follows a behavior similar to that of the pressure. No separation was observed in this case, either from the skin-friction measurements or from oil-flow patterns that were established and photographed during some special tests. In contrast, with the 15° generator the initial increase in pressure levels off in a plateau, and negative values of skin friction were measured, both characteristics typically associated with separation. Rapid increases in pressure and skin friction occur downstream of reattachment. The heat transfer rises continually through the interaction until the surface pressure decreases. For both generator angles, the decay in pressure, skin friction, and heat transfer downstream of the interaction is a direct result of the expansion fan emanating from the corner of the generator.

Figures 4 and 5 present constant static pressure and velocity contours and illustrate further the details of the two interaction cases under investigation. The contours were constructed from the profiles of velocity and static pressure across the boundary layer obtained from pitot and static pressure and total temperature measurements taken at small Δx and Δy intervals. Complete tabulations of these profile

data can be found in ref. 11. Locations of the incident, induced, and recompression shocks are easily recognized in the pressure contours. Note that for the 15° generator the pressures are higher than the wall-peak pressure in the compression region downstream of the intersection of the incident and induced shocks. The velocity contours illustrate more dramatically the differences between the two flow cases. For the larger generator angle the flow velocity near the wall in the vicinity of the interaction is highly retarded and achieves negative values associated with the reversed flow in the separated zone.

A precise determination of separation and reattachment points for the separated case was made difficult because of the unsteady nature of the separated flow and the relatively large diameter of the skin friction element. A detailed discussion of this unsteady phenomenon is given in ref. 9. A best estimate of the extent of the time-averaged separation region was obtained from data obtained with forward and backward facing pitot tubes. These data, obtained at fixed values of y with x varied by moving the shock generator, indicated a separated region extending from $(x - x_0)/\delta_0 = -3.15$ to -1.68. This region is somewhat larger than the skin-friction measurements indicated. Locations of the separation and reattachment points from the pitot measurements are shown on the abscissa of the skin-friction plot.

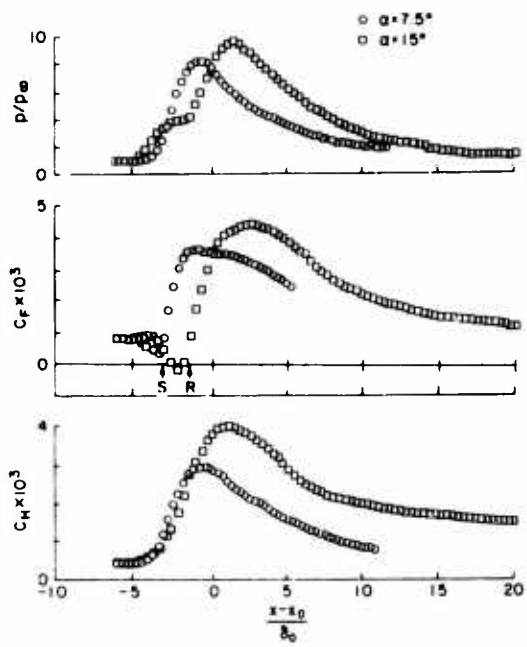

Fig. 3 Measurements along the model surface.

Fig. 4 Static pressure contours obtained from flow-field measurements.

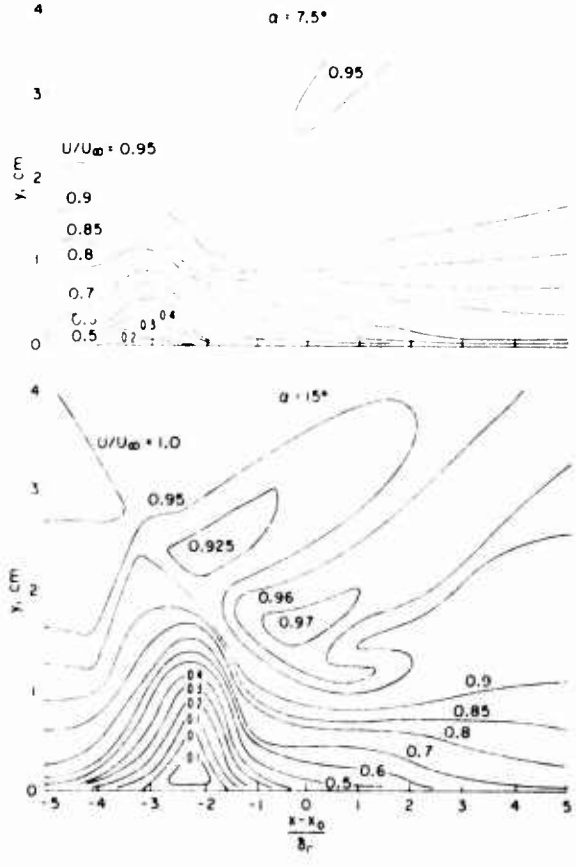

Fig. 5 Velocity contours obtained from flow-field measurements.

4.2 Numerically simulated flow-field features

As previously mentioned, the turbulent Reynolds stress and heat-flux terms in eq. (2) were assumed to be related to the mean flow gradients of velocity and temperature by algebraic eddy-transport coefficients that were simply added to the molecular transport coefficients. Mainly, this choice was dictated by considerations of economy in the computer program. Although such a model may be restrictive in its application to other new flow situations, it suits our current objectives of (1) defining the eddy viscosity field that results when a shock impinges on a turbulent boundary layer, and (2) determining whether improvements

in the eddy viscosity description used in the numerical simulations can be made by a close examination of the experimental data.

4.2.1 Results using a baseline turbulence model. The first numerical simulations were obtained with a modified, two-layer, Cebeci-Smith (ref. 16) eddy viscosity model. Modifications suggested by Cebeci to account for pressure gradient effects were not used. The shear was expressed as:

$$\tau = -\tau_{xr} = (\mu + \rho\epsilon)\left(\frac{\partial u}{\partial r} + \frac{\partial v}{\partial x}\right) \tag{3}$$

In the inner layer the following mixing length description for the eddy viscosity was used:

$$\epsilon = \epsilon_{inner} = \ell^2\left(\left|\frac{\partial u}{\partial r} + \frac{\partial v}{\partial x}\right|\right) \tag{4}$$

where

$$\ell = \kappa y\left[1 - \exp\left(\frac{-y}{A}\right)\right] \tag{5}$$

$$A = A_w^+ \frac{\mu_w}{\sqrt{|\tau_w|\rho_w}} \tag{6}$$

with the von Karman constant $\kappa = 0.4$ and the van Driest constant $A_w^+ = 26$. In the outer layer, the eddy viscosity was given, following Clauser, by:

$$\epsilon = \epsilon_{outer} = 0.0168 \frac{u_{max}\delta_1^*}{I} \tag{7}$$

where

$$\delta_1^* = \int_0^{y_{max}} \left(1 - \frac{u}{u_{max}}\right)\frac{r_w + y}{r_w}\, dy \tag{8}$$

$$I = 1 + 5.5\left(\frac{y}{\delta}\right)^6 \tag{9}$$

$$\delta = 1.735\, \delta_c^* \tag{10}$$

$$\delta_c^* = \int_0^{y_{max}} \left(1 - \frac{\rho u}{(\rho u)_{max}}\right)\frac{r_w + y}{r_w}\, dy \tag{11}$$

The above definitions of the displacement thicknesses differ somewhat from the conventional ones. The present choice was dictated by the fact that, in the first stages of developing the Navier Stokes code for the shock interaction problem, overshoots in the velocity profiles during early time-steps made it difficult to select the edge of the viscous layer. Therefore, the value of y_{max} was simply taken as the boundary-layer thickness ahead of the interaction, and u_{max} and $(\rho u)_{max}$ were taken as the local maximum values between the wall and y_{max}. The boundary between the two layers was determined by the value of y where $\epsilon_{inner} = \epsilon_{outer}$.

The heat flux was expressed in terms of the eddy viscosity by:

$$q = q_r = -\left(\frac{\mu}{P_r} + \frac{\rho\epsilon}{P_{r_t}}\right) c_p \frac{\partial T}{\partial r} \tag{12}$$

where $P_{r_t} = 0.9$.

Results of the computations using this baseline turbulence model are compared with the experimental data in figs. 6, 7, and 8. Overall, the computations predict the qualitative features of the two flows remarkably well considering the simplicity of the turbulence model, but a closer examination of the comparisons points out the major limitations of the computations.

The overall surface pressure rise for the flow with the 7.5° shock-wave generator (fig. 6a), is predicted reasonably well, except for the location of the initial rise in pressure. The corresponding predicted rises in both skin friction and heat transfer lag the data in the interaction region, reflecting the inability of the simple turbulence model to predict any upstream influence, but the final predicted levels downstream agree reasonably well with the data. The skin friction prediction shows separation at the surface but the measurements do not. The pressure contour comparisons (fig. 7a), show that the computation predicts only the incident and reflected shocks whereas the experimental data show the presence of an induced shock. The comparison of the streamline contours (fig. 8a), shows the prediction of a zero velocity line just off the surface accompanied by a small region of reversed flow which is not present in the experimental data.

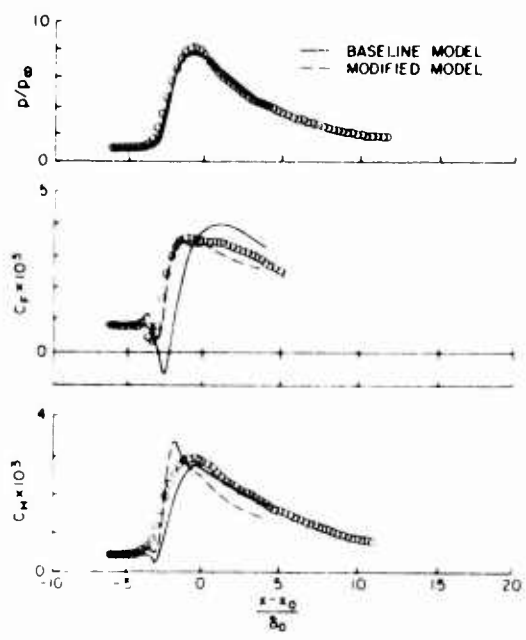

(a) $\alpha = 7.5°$.

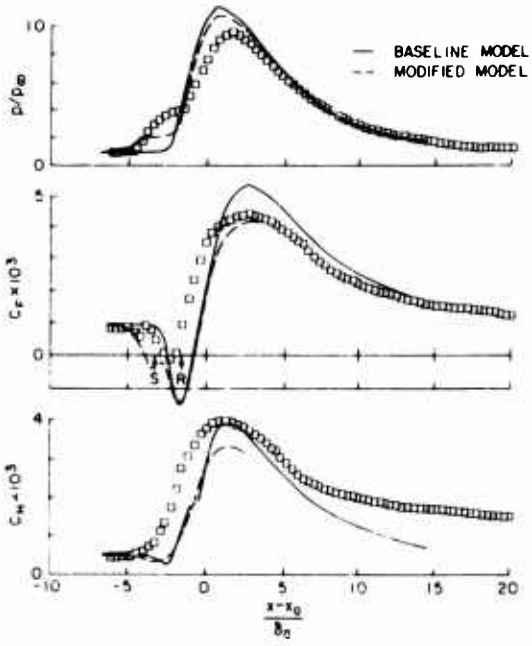

(b) $\alpha = 15°$.

Fig. 6 Comparisons of computations and measurements along the model surface.

Similar conclusions can be made from comparisons of the numerical computations and the data for the flow with the 15° shock-wave generator (figs. 6b, 7b, and 8b). With the baseline turbulence model, no upstream influence is predicted and in this separated flow case no plateau pressure is predicted. The induced shock wave caused by the large separation in the experiment is not predicted because the computation predicts such a small separation height. For this separated flow case, the baseline turbulence model results in good prediction of the overall pressure and skin friction rises and their subsequent decay; but the heat transfer is substantially underpredicted (see fig. 6b).

4.2.2 Baseline model modifications. Attempts were made to guide changes in the turbulence model by combining data analysis and trial and error solutions in the actual Navier Stokes code. Ideally, these changes could have been guided entirely from data if absolutely reliable shear-stress measurements had been available. But, since attempts to directly measure the shear stress through these interactions have so far produced unsatisfactory results, the boundary-layer profile data were used. A significant degree of uncertainty is introduced in this procedure, however, because the inertial forces dominate the momentum balance, especially in the outer portions of the flow. Conversely, relying solely on trial and error solutions to the code itself to guide modeling changes would be time consuming and perhaps unsuccessful if attention was not confined to physically meaningful changes.

The shear-stress and heat-flux distributions through the boundary layer were evaluated by the use of experimental profile data to solve the following equations based on the boundary-layer approximation:

$$\tau = \frac{1}{(r_w + y)}\left[r_w\tau_w + \frac{\partial}{\partial x}\int_0^y (r_w + y)(p + \rho u^2)dy - u\frac{\partial}{\partial x}\int_0^y (r_w + y)\rho u\, dy\right] \tag{13}$$

and

$$q - u\tau = \frac{1}{(r_w + y)}\left[r_w q_w + c_p T_t \frac{\partial}{\partial x}\int_0^y (r_w + y)\rho u\, dy - \frac{\partial}{\partial x}\int_0^y (r_w + y)\rho u c_p T_t\, dy\right] \tag{14}$$

By performing integration with respect to y before differentiation with respect to x and by employing the conservative form of the variables, e.g. $(p + \rho u^2)$, it was expected that errors in the momentum and energy balances could be minimized. Despite these precautions, not all the shear profiles approached zero at large distances from the wall where they should have. In some of these cases it was possible to adjust the inertial balance across the boundary layer so that zero shear was achieved at the edge of the thermal boundary layer. These adjustments were usually small for the 7.5° shock wave generator profiles, but somewhat larger for the 15° generator profiles.

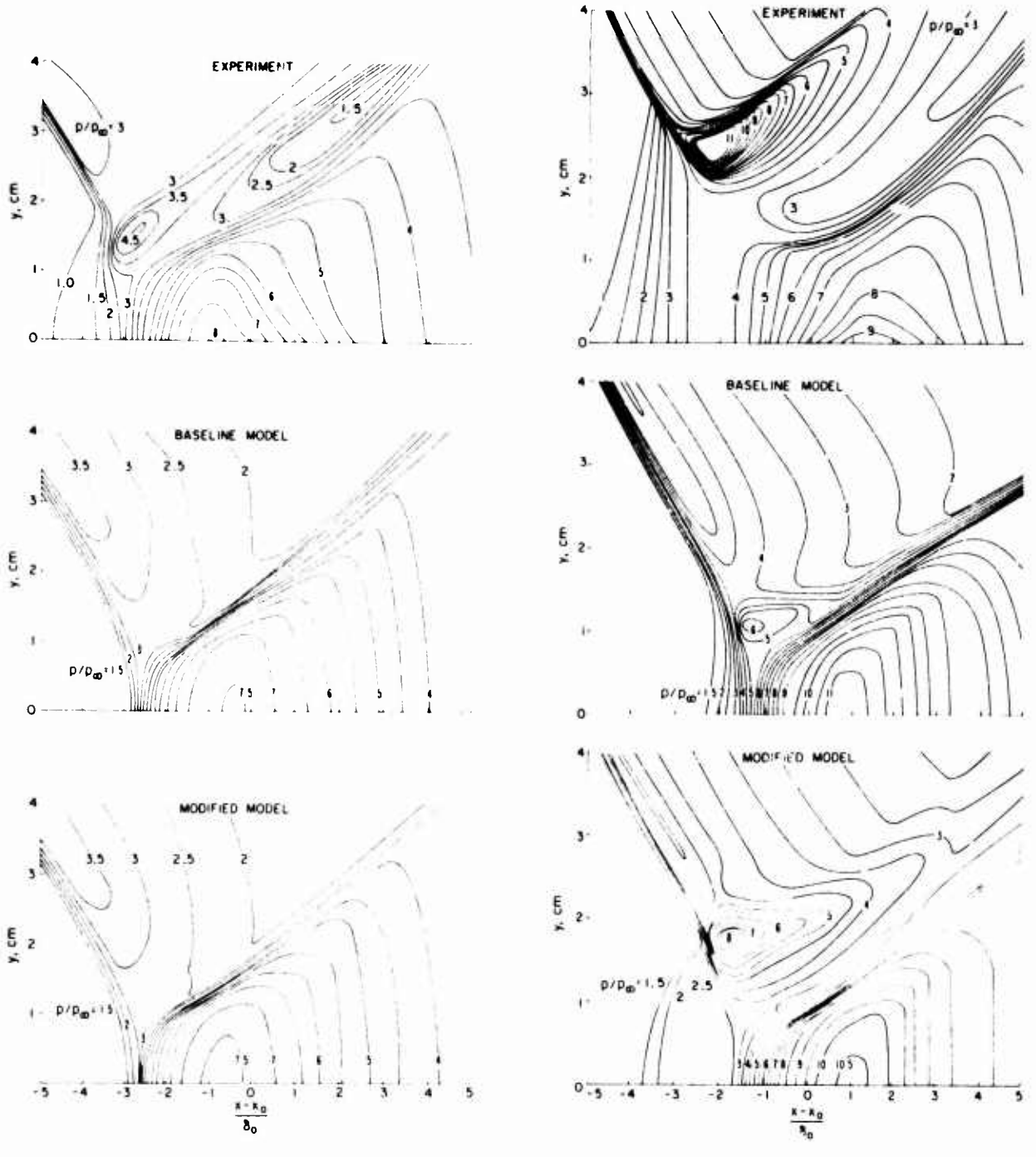

(a) α = 7.5°. (b) α = 15°.

Fig. 7 Comparisons of static pressure contours from computations and experiment.

Figure 9 shows the shear profiles resulting from these momentum and energy balances for axial locations ahead, within, and downstream of the two interaction regions. For the flow with the 7.5° generator the maximum shear stress within the boundary layer builds up rapidly within the interaction region as the adverse pressure gradient increases; after peak pressure is reached this maximum shear relaxes toward its initial level but at a very slow rate. At the farthest downstream location where the pressure gradient is favorable the shear near the wall decreases and subsequently increases, indicating that the shear in the outer extremes of the boundary layer is adjusting to the local flow gradients more slowly than the shear near the wall. Similar conclusions can be reached for the separated case using the 15° generator. In this case, data were available for a larger downstream interaction distance, and the shear appears to have adjusted to the local flow gradients. Also, for this separated case, the maximum shear in the boundary layer continues to increase downstream of reattachment and slightly beyond the location of peak pressure.

A maximum mixing length was determined at each of the profile survey stations by dividing the experimentally deduced shear distributions by the measured velocity gradients, plotting the results, and choosing the maximum value of mixing length. For those cases where the mixing length continuously increased with distance from the wall, the value of maximum mixing length was chosen at the point where the first significant departure from a linear mixing length distribution occurred. These maximum values are shown

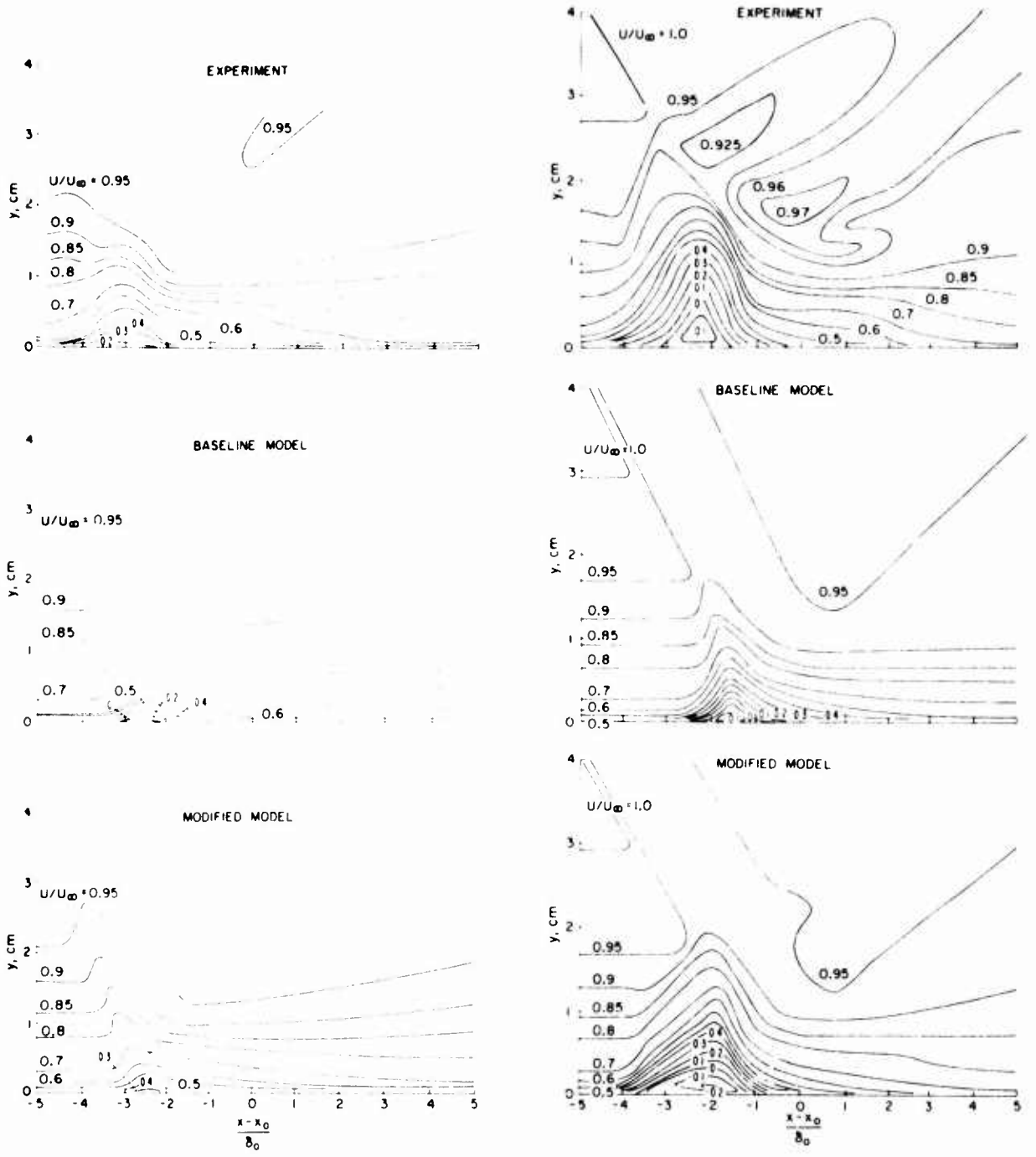

(a) α = 7.5°. (b) α = 15°.

Fig. 8 Comparisons of velocity contours from computations and experiment.

in fig. 10 as a function of the interaction length parameter. The extremes on the bars represent the uncertainty introduced by using shear profiles evaluated either directly from the momentum balances or from momentum balances modified by adjusting the inertial terms to insure zero shear at the edge of the thermal boundary layer. The uncertainty was largest in the region downstream of reattachment for the 15° generator case. In both cases the maximum mixing lengths tend to decrease in regions of adverse pressure gradient where the boundary layer thickens, and to increase in regions of favorable pressure gradient.

Near the surface where the importance of the inertia and convection terms in the momentum and energy balances diminished, attempts were made to evaluate κ and A_w^+. The shear profiles at each survey station were analyzed by integrating the following system of equations to obtain values of velocity and temperature as a function of y out to distances where the estimated errors in the inertial balance became significant compared to the magnitude of the local shear (usually this consisted of about 9 measured points away from the wall):

$$\tau = \left(\mu + \rho \ell^2 \left|\frac{\partial u}{\partial y}\right|\right) \frac{\partial u}{\partial y} \tag{15}$$

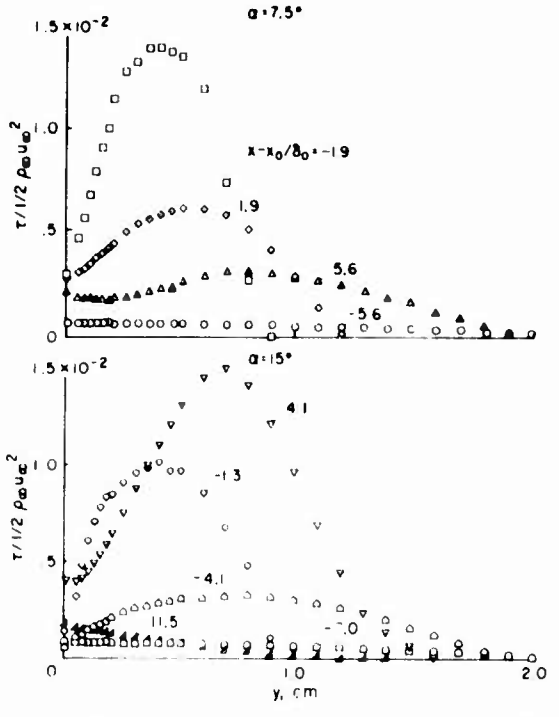

Fig. 9 Shear profiles for various axial locations along the model.

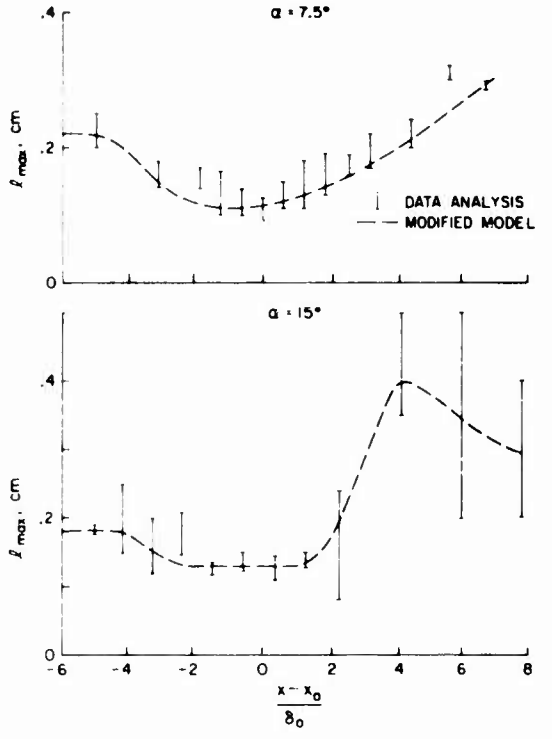

Fig. 10 Axial variation of maximum mixing lengths.

$$\ell = \kappa y\left[1 - \exp\left(\frac{-y}{A}\right)\right] \tag{16}$$

$$A = \frac{\mu_w}{\sqrt{|\tau_w|\rho_w}} A_w^+ \tag{17}$$

$$q = -\left(\frac{\mu}{P_r} + \frac{\rho \ell^2}{P_{r_t}}\left|\frac{\partial u}{\partial y}\right|\right)\frac{\partial T}{\partial y} \tag{18}$$

Best fits to the velocity and temperature profile data near the wall were achieved by repeated integration of these equations until the sum of the root mean square of the differences between the predicted and measured velocities and temperatures were minimized. The procedure was automated for solution on a CDC 7600 and initiated by inputting shear and temperature profiles from the momentum and energy balances along with the measured values of wall shear. An optimization routine‡‡ was initiated and values of κ and A_w^+ and q_w were sought to satisfy the minimization criteria. The root mean square of the residuals never exceeded 5% and in most cases was less. Exceptions to this residual band occurred for the 15° generator case in the separated region. However, it was still possible to achieve this band at these profile stations, provided the input wall shear was also considered part of the optimization routine along with the other parameters. This was not surprising, however, since accurate skin-friction measurements were difficult to make in this separated region. An example of the best fits to the velocity and temperature data near the upstream edge of the separated region are shown as the solid lines in fig. 11. Two important aspects of this example are noteworthy. First, as this station, the wall shear needed to achieve a best fit was -5.28 N/m^2 whereas the direct measurement was 12.1 N/m^2. Considering that the station is near the separation point where experimental accuracy is poor and that the separation point is unsteady, this disparity is not unreasonable. Second, at this station, values of κ and A_w^+ are significantly lower than their corresponding undisturbed values, 0.4 and 26.

Figure 12 presents the values of κ and A_w^+ required to achieve these best fit velocity and temperature profiles for both of the interaction cases being studied. The error bands on the symbols again represent the uncertainty introduced by using shear profiles evaluated either directly from the momentum balances or from momentum balances modified by adjusting the inertial terms to insure zero shear at the edge of the thermal boundary layer. The results for the 7.5° generator show that A_w^+ decreases in the vicinity of the interaction while κ increases. These results are interpreted as indicating a higher eddy-viscosity throughout the region than that predicted by the baseline turbulence model. This could explain why the numerical simulations using the baseline turbulence model predicted separation. For the 15° generator case where separation was present, similar trends in κ and A_w^+ are apparent. However, the uncertainties within the separated region precluded any precise determination of the parameters. Apparently, both κ and A_w^+ decrease ahead of and in the upstream portions of the separated region. At the downstream edge of the separated region near reattachment κ has increased considerably and A_w^+ is also increasing. The physical interpretation of these results suggests that ahead of separation the

‡‡The optimization routine, described in ref. 16, was developed by Garret Vanderplaats of NASA Ames Research Center. His assistance in helping to implement it for this application is appreciated.

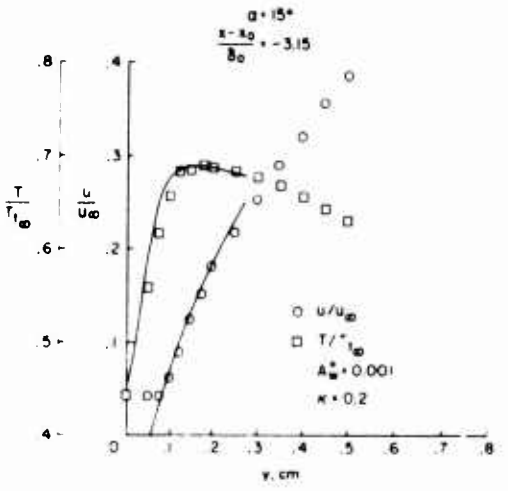

Fig. 11 Comparison of experimental and best fit velocity and temperature profiles employing a modified inner eddy-viscosity model.

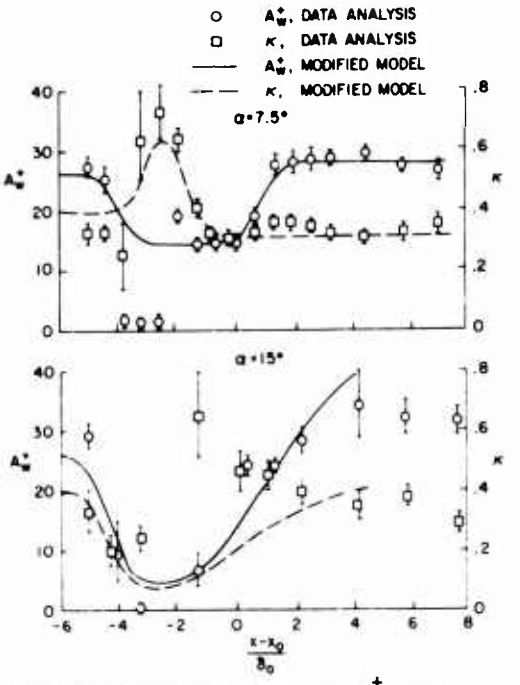

Fig. 12 Axial variation of A_w^+ and κ.

sublayer or inner region has a somewhat higher eddy-viscosity than the baseline model would predict, but in the logarithmic region the viscosity is somewhat lower than the baseline model would predict. In the separated region, an interpretation is more difficult to arrive at, but apparently, at least near the reattachment point, the eddy viscosity is higher across the sublayer and logarithmic regions than would be predicted by the baseline model.

The turbulence model mixing length formulation suggested by the foregoing data analysis was introduced into the Navier Stokes computer code in the following way.

$$\tau = -\tau_{xr} = (\mu + \rho\varepsilon)\left(\frac{\partial u}{\partial r} + \frac{\partial v}{\partial x}\right) \tag{19}$$

$$\varepsilon = \ell^2\left[\left(\frac{\partial u}{\partial r}\right)^2 + \left(\frac{\partial v}{\partial x}\right)^2\right]^{1/2} \tag{20}$$

In the inner region

$$\ell = \kappa(x)\left[1 - \exp\left(\frac{-y}{A}\right)\right] \tag{21}$$

$$A = A_w^+(x)\,\frac{\mu_w}{\sqrt{|\tau_w|\rho_w}} \tag{22}$$

In the outer region

$$\ell = \ell_{max}(x) \tag{23}$$

Employing ℓ_{max} in this model formulation eliminated the need for arbitrarily defining compressible and incompressible displacement thickness as was the case with the baseline model. The boundary between the two regions is determined by the value of y where $\ell = \ell_{max}$. The heat flux equation remained the same as for the baseline model (see eq. 12).

Computer simulations were next obtained using the experimental data analysis as a guide for evaluating the parameters $\ell_{max}(x)$, $\kappa(x)$, and $A_w^+(x)$. First, values directly from the data analysis were used. Examination of the resulting computer simulations made it apparent that adjustments to the parameters would be needed before the simulations would predict the experimentally determined features of the flow fields in the interaction region. Therefore, a trial and error procedure was initiated to arrive at more appropriate distributions of the turbulence parameters. The procedure is still underway at this time. Before discussing the results of this procedure to date, some interesting observations can be pointed out. The simulations were all more sensitive to modifications of the inner region model parameters than the outer maximum mixing length parameter. In the inner region itself, $A_w^+(x)$ modifications tended to affect the solutions more than those for $\kappa(x)$, especially in the separated case. However, best results have been achieved with modification to both $A_w^+(x)$ and $\kappa(x)$.

4.2.3 Results using a modified turbulence model. The turbulence parameter variations used in the latest computer simulations employing the complete Navier Stokes equations are shown as the solid and dashed lines in figs. 10 and 12. The maximum mixing length variation (fig. 10), employed in all simulations corresponded to the mean variation exhibited by the data analysis. In the inner layer region (fig. 12), values of A_w^+ and κ had to be altered to obtain better predictions of the experimental surface and

flow-field data. For the 7.5° generator case these variations in A_w^+ and κ follow the trends exhibited by the data analysis. The largest disparity between the values used in the simulations and those deduced from data analysis is in A_w^+ at the beginning of the interaction region. As noted before, decreasing A_w^+ and increasing κ both result in a larger eddy viscosity in the inner layer region. For the 15° generator case the variations in the inner layer turbulence parameters follow the same trends as the data analysis except near reattachment. Part of the reason for this disparity is that the data analysis in this region was completed only recently and there was insufficient time to obtain converged simulations before preparing this manuscript.

The results of the computer simulations using the turbulence parameter variations described above are presented in figs. 6, 7, and 8. For the 7.5° generator case there is obvious improvement over the baseline predictions of skin friction and heat transfer in the interaction region (see fig. 6a). Separation is not predicted and the upstream influence of the interaction coincides with that observed from the data. Downstream of the peak pressure location the heat-transfer prediction is not as good as the baseline model predictions, but this could be explained by an incorrect choice of a constant turbulent Prandtl number. At this stage of model development this disparity in heating prediction is not considered crucial because the solutions of the momentum and energy equations are loosely coupled. The turbulence model changes had little effect on the surface pressure prediction. The pressure and velocity contours (figs. 7 and 8) are not changed significantly from those for the baseline model, except that no reversed flow region is predicted with the modified model. The reflected shock observed in the data is still not predicted. The main reason for this is that the numerical simulations fail to show a significant thickening of the boundary layer at the start of the interaction region.

Results using the turbulence model modifications for the 15° generator case are also shown in figs. 6, 7, and 8. The predicted separation bubble size increased considerably with a corresponding prediction of upstream influence and a plateau in the surface pressure. The pressure contours show the presence of an induced shock wave similar to that observed in the experiment. Obviously, substantial deficiencies still exist in the prediction using the modified model. The separated bubble size is still smaller in height than the experiment indicates; the plateau pressure is only about half the measured value; and all three surface quantities show substantial differences with the measurements in the interaction region. It is felt, however, that a significant improvement in the surface predictions can be made by including the latest data analysis values of A^+ and κ near reattachment. This should shorten the extent of predicted separation and shift the rise in skin-friction and heat-transfer upstream.

5. CONCLUDING REMARKS

A detailed experimental investigation of the mean flow throughout two shock-wave boundary-layer interaction regions, one with separation and one without, has been presented. Although the interactions were very complex, the mean data were of sufficient detail and quality to assess the validity of numerical simulations and to guide turbulence model changes.

Numerical solutions, employing the full time-averaged Navier Stokes equations along with algebraic eddy viscosity models appropriate for zero-pressure-gradient flows, predicted the overall features of the flow fields, but they were seriously deficient in predicting the details of the interaction regions. Through a combination of data analysis and trial and error computer simulations, which tested the sensitivity of the solutions to turbulence model parameter changes, the agreement between numerical predictions and experiment was improved.

Although the improvements fell short of identifying an optimum model, several important trends regarding the two-layer, algebraic eddy-viscosity model can be noted. The inner layer model parameters had substantially more influence on the numerical simulations than the outer layer parameter. Where the boundary layer was unseparated, the eddy-viscosity in the inner layer region had to be increased substantially over that predicted by a zero-pressure-gradient, two-layer model, otherwise separation was predicted. Therefore the simple zero-pressure gradient model cannot be used to predict locations of separation. Where separation did occur, the results were less clear, but the eddy viscosity in the sublayer region had to be increased while in the logarithmic region it had to be reduced somewhat, otherwise the separation bubble size was substantially underpredicted.

REFERENCES

1. Balhaus, W. F.; and Bailey, F. R.: Numerical Calculation of Transonic Flow About Swept Wings. AIAA Paper 72-677, June 1972.

2. Rakich, J. V.; and Kutler, P.: Comparison of Characteristics and Shock Capturing Methods with Application to the Space Shuttle Vehicle. AIAA Paper 72-191, Jan. 1972.

3. MacCormack, R. W.: Numerical Solution of the Interaction of a Shock Wave with a Laminar Boundary Layer. Lecture Notes in Physics, Vol. 8, Springer Verlag, New York, 1971, p. 151.

4. Hung, M.; and MacCormack, R. W.: Supersonic and Hypersonic Laminar Flows Over a Two-Dimensional Compression Corner. AIAA Paper 75-2, Jan. 1975.

5. Baldwin, B. S.; and MacCormack, R. W.: Numerical Solution of Interaction of a Strong Shock Wave with a Hypersonic Turbulent Boundary Layer. AIAA Paper 74-558, June 1974.

6. Wilcox, D. C.: Numerical Study of Separated Turbulent Flows. AIAA Paper 74-584, June 1974.

7. Deiwert, G. S.: Numerical Simulation of High Reynolds Number Transonic Flows. AIAA Paper 74-603, June 1974.

8. Redda, D. C.; and Murphy, J. D.: Shock Wave Turbulent Boundary Layer Interactions in Rectangular Channels, Part II: The Influence of Sidewall Boundary Layers on Incipient Separation and Scale of the Interaction. AIAA Journal, Vol. 11, No. 10, Oct. 1973, pp. 1367-1368.

9. Horstman, C. C.; Kussoy, M. I.; Coakley, T. J.; Rubesin, M. W.; and Marvin, J. G.: Shock Wave Induced Turbulent Boundary-Layer Separation at Hypersonic Speeds. AIAA Paper 75-4, Jan. 1975.

10. Horstman, C. C.; and Owen, F. K.: Turbulent Properties of a Compressible Boundary Layer. AIAA Journal, Vol. 10, No. 11, Nov. 1972, pp. 1418-1424.

11. Kussoy, M. I.; and Horstman, C. C.: An Experimental Documentation of a Hypersonic Shock-Wave Turbulent Boundary-Layer Interaction Flow — With and Without Separation. NASA TM X-62,412, 1975.

12. Rubesin, M. W.; and Rose, W. C.: The Turbulent Mean-Flow Reynolds-Stress, and Heat Flux Equations in Mass-Averaged Dependent Variables. NASA TM X-62,248, March 1973.

13. Sorensen, V. L.: Computer Program for Calculating Flow Fields in Supersonic Inlets. NASA TN D-2897, July 1965.

14. Marvin, J. G.; and Sheaffer, Y. S.: A Method for Solving the Nonsimilar Boundary-Layer Equations Including Foreign Gas injection. NASA TN D-5516, Nov. 1969.

15. Baldwin, B. S.; and MacCormack, R. W.: Interaction of Strong Shock Wave with Turbulent Boundary Layer. Proceedings of the 4th International Conference on Numerical Methods in Fluid Dynamics, Boulder, Colorado, June 1974.

16. Vanderplaats, Garret N.: CONMIN - A FORTRAN Program for Constrained Function Minimization User's Manual. NASA TM X-62,282, August 1973.

PREDICTION OF TURBULENT SEPARATED FLOW AT SUBSONIC AND TRANSONIC SPEEDS INCLUDING UNSTEADY EFFECTS

by Gary D. Kuhn, Research Engineer
and Jack N. Nielsen, President
Nielsen Engineering & Research, Inc.
510 Clyde Avenue, Mountain View, CA 94043

SUMMARY

An integral boundary-layer method is extended to calculation of separated turbulent boundary layers in steady flow and to unsteady turbulent boundary layers. Separated boundary layers are calculated by treating the pressure as a dependent variable and prescribing the wall shear variation. The boundary-layer method and a suitable potential flow method are used in an iterative procedure to produce a method for predicting the characteristics of separated flows. The interaction between the boundary layer and the inviscid flow is accounted for by augmenting the physical surface by the boundary-layer displacement thickness. Good comparisons are shown between the theory and data for a separated turbulent boundary layer on the wall of a transonic wind tunnel. Modifications are derived by which the displacement thickness can be prescribed and an improved iteration developed. Analytical solutions developed from a small perturbation analysis indicate the method is valid for unsteady flow over a certain range of frequencies. Good comparisons were obtained between the linearized theory and results produced by a finite-difference solution of the complete nonlinear unsteady boundary-layer equations. Examination of the nature of the integral equations in the vicinity of a point of zero wall shear stress indicates that the shear stress gradient decreases approaching the point of zero shear in agreement with the results of other researchers.

SYMBOLS

A_{ij}	coefficients in Eqs. (26), (27), and (31)
A^t_{ij}, A^x_{ij}	coefficients in Eqs. (38) and (39)
A_δ	amplitude of time-dependent part of δ, Eq. (55)
A_τ	amplitude of time-dependent part of U_τ, Eq. (52)
B^x_i, B^x_i	coefficients in Eqs. (38) and (39)
D	quantity defined by Eq. (49)
f	weighting function, Eq. (21); also unsteady part of U_τ, Eqs. (41) and (45)
g	unsteady part of δ, Eqs. (42) and (46)
k	constant denoting whether flow is two-dimensional or axisymmetric, Eqs. (1), (2), and (3)
L	reference length
P	quantity defined by Eq. (47)
p	pressure
Q	quantity defined by Eq. (48)
R_1	terms in Eqs. (38) and (39)
r	radius
S	enthalpy parameter $T_t/T_{te} - 1$
T_t	total temperature
t	transverse curvature factor, Eq. (14)
U,V	velocity components in incompressible plane
U_o	arbitrary wall velocity
U_1	wake parameter, Eq. (22)
U_τ	friction velocity, Eq. (23)
u,v	velocity components in physical coordinate system
X,Y	transformed coordinates in incompressible plane
x,y	physical coordinates, x is measured along the surface, y is normal to the surface with y = 0 at the surface
$\tilde{x},\tilde{y}$	coordinates in transformed axisymmetric system
Y^+	$\lvert U_\tau \rvert Y/\nu$
α	angle between the body axis and a longitudinal tangent to the body at x
α_δ	phase angle of δ, Eq. (56)
α_τ	phase angle of U_τ, Eq. (53)
β	eddy viscosity parameter, $1 + \epsilon/\mu$
δ	boundary-layer thickness
δ^+	$\lvert U_\tau \rvert \delta/\nu$
δ^*	displacement thickness, $\int_0^\delta (1 - U/U_e)\, dY$
δ_1	axisymmetric displacement thickness, Eq. (28)
δ_2	axisymmetric momentum thickness, Eq. (29)
ϵ	eddy viscosity $-\rho(\overline{u'v'})/(\partial u/\partial y)$; also amplitude of unsteady flow, Eqs. (40) and (50)
μ	molecular viscosity
ν	kinematic viscosity
ρ	density
θ	$\tan^{-1}(V_e/U_e)$
τ	shear stress
ω	frequency

SUBSCRIPTS AND SUPERSCRIPTS

e	edge of boundary layer	w	refers to variable evaluated at surface
o	refers to reference station or initial value	$( )_x$	refers to a derivative with respect to x (also y and t)
s	refers to steady-state solution	$( )'$	denotes turbulent fluctuations

INTRODUCTION

During the last several years an integral method for predicting the two-dimensional or axisymmetric flow field through turbulent separation and reattachment at transonic or subsonic speeds has been under development. During that time a number of significant advances have been achieved. The development of a method for calculating a boundary layer smoothly through a separation point led to the first successful calculation of the complete velocity field for a separating and reattaching turbulent boundary layer at transonic speeds, excluding base flows. In addition, application of the integral method to unsteady turbulent separation has indicated that the method can produce results for small time-dependent disturbances in good agreement with the results of other researchers.

In this paper, the application of the integral boundary-layer method to steady, turbulent, viscous-inviscid flow interactions taking account of the elliptical nature of the problem and to time-dependent boundary layers under prescribed free-stream conditions is described. For steady viscous-inviscid flow interactions, the technique combines the integral boundary-layer method developed by the authors (ref. 1) and a finite-difference potential flow method described in reference 2. The boundary-layer characteristics and the inviscid flow field are calculated by an iteration procedure in which the boundary layer and inviscid flow are calculated alternately by separate calculative programs. In attached flow regions, the pressure calculated from the inviscid flow is prescribed for the boundary-layer calculation, and the displacement thickness of the boundary layer is used to augment the surface coordinate to provide a boundary condition for the inviscid flow. In the separated region, the pressure cannot be prescribed in the boundary-layer calculations. Instead, the wall shear stress or the displacement thickness is prescribed and the corresponding pressure distribution is calculated from the boundary-layer method. The iterative process is continued until the pressure distributions produced by the viscous solution and the inviscid solution agree.

For time-dependent boundary layers, the same integral boundary-layer method is used with the addition of time-dependent terms which are omitted for steady flows. Analytical solutions are derived from a small perturbation analysis described in reference 3 to study the frequency range of validity of the equations. The nature of the equations in the vicinity of a point of zero wall shear stress is also examined.

GOVERNING EQUATIONS FOR STEADY FLOWS

The governing equations for the steady flow of a compressible turbulent boundary layer for both two-dimensional and axisymmetric configurations in terms of curvilinear cylindrical coordinates tangential and normal to the body surface are

$$(r^k \rho u)_x + (r^k \rho v)_y = 0 \tag{1}$$

$$\rho u u_x + \rho v u_y = -p_x + \frac{1}{r^k} (r^k \mu \beta u_y)_y \tag{2}$$

$$\rho u S_x + \rho v S_y = \frac{1}{r^k} (r^k \mu \beta S_y)_y \tag{3}$$

wherein $k = 0$ for two-dimensional flows and $k = 1$ for axisymmetric flows, both laminar and turbulent Prandtl numbers are assumed to be unity, and the term ρv is a time-averaged quantity defined by

$$\rho v = \overline{\rho v} + \overline{\rho' v'} \tag{4}$$

The quantity S is the enthalpy parameter, defined as

$$S = \frac{T_t}{T_{t_e}} - 1 \tag{5}$$

Transformation of Axisymmetric Boundary-Layer Equations to Almost Two-Dimensional Form

The Probstein-Elliott transformation (ref. 4) is

$$d\tilde{x} = \left[\frac{r_w(x)}{L} \right]^2 dx \tag{6}$$

$$d\tilde{y} = \frac{r(x,y)}{L}\,dy \tag{7}$$

where $r_w(x)$ is the radius of the body, measured perpendicular to the axis of the body and $r(x,y)$ is given by

$$r(x,y) = r_w(x) + y\cos\alpha \tag{8}$$

where α is the angle between the body axis and a longitudinal tangent to the body at x, with $y = 0$ at the body surface. The transformed continuity equation has the form

$$(\rho\tilde{u})_{\tilde{x}} + (\rho\tilde{v})_{\tilde{y}} = 0 \tag{9}$$

where

$$\tilde{u} = u \tag{10}$$

and

$$\tilde{v} = \frac{rL}{r_w^2}\,v - \frac{L^2}{r_w^2}\,\frac{\partial\tilde{y}}{\partial x}\,u \tag{11}$$

Applying the transformation to the momentum and energy Eqs. (2) and (3) yields the transformed equations

$$\rho\tilde{u}u_{\tilde{x}} + \rho\tilde{v}u_{\tilde{y}} = -p_{\tilde{x}} + \left[(1 + kt\tilde{y})\mu\rho u_{\tilde{y}}\right]_{\tilde{y}} \tag{12}$$

$$\rho\tilde{u}S_{\tilde{x}} + \rho\tilde{v}S_{\tilde{y}} = \left[(1 + kt\tilde{y})\mu\rho S_{\tilde{y}}\right]_{\tilde{y}} \tag{13}$$

where t is the transverse curvature factor

$$t = \frac{2L\cos\alpha}{r_w^2} \tag{14}$$

and

$$\tilde{y} = \frac{r_w}{L}\,y + \frac{\cos\alpha}{2L}\,y^2 \tag{15}$$

For flows in which the transverse curvature terms are negligible, letting $k = 0$ in Eqs. (12) and (13) produces the equations of a two-dimensional boundary layer.

Transformation of the Compressible Boundary-Layer Equations

The Stewartson transformation (ref. 5) along with the assumption that the viscosity varies linearly with the temperature and laminar and turbulent Prandtl numbers are unity, reduces the equations of a compressible boundary layer to those of an incompressible boundary layer

$$U_X + U_Y = 0 \tag{16}$$

$$UU_X + VU_Y = (S + 1)U_e(U_e)_X + \nu_{e_o}\left[(1 + kt\tilde{y})\beta U_Y\right]_Y \tag{17}$$

$$US_X + VS_Y = \nu_{e_o}\left[(1 + kt\tilde{y})\beta S_Y\right]_Y \tag{18}$$

The coordinate $\tilde{y}$ is not transformed in the transverse curvature terms because numerical integration of the equations across the boundary layer is anticipated and only corresponding values are needed in those terms.

In the remainder of this report, the solution of the energy Eq. (18) will be approximated by the Crocco relation

$$S = S_w\left(1 - \frac{U}{U_e}\right) \tag{19}$$

Thus, the velocity profiles found to be valid for incompressible two-dimensional turbulent boundary layers can be used by simply transforming the input quantities to the incompressible plane, performing the calculation for an equivalent incompressible boundary layer, and then transforming the results back to the compressible plane, and for an axisymmetric flow, back to the axisymmetric coordinates.

INTEGRAL BOUNDARY-LAYER METHOD FOR INCOMPRESSIBLE FLOW

Integral Equations

Because it was anticipated that, for predicting turbulent separated boundary-layer characteristics, an iterative scheme would be developed requiring multiple calculations and because questions of existence and convergence of solutions arise, it was desired to use the simplest possible theories for the boundary-layer flow and the inviscid flow which still retain the essential physical features of the flow. The method chosen to calculate the boundary layer is an integral method similar to that presented by Nash

and Hicks (ref. 6). Different velocity profiles and eddy viscosity models are used in this work. The method used herein was described in detail in reference 7.

Families of integral equations are derived by eliminating V between the momentum and continuity equations and then taking weighted integrals of the resulting equation across the boundary layer.

$$\int_0^{\delta}\left[UU_X - U_Y\int_0^Y U_X d\eta - (S+1)U_e(U_e)_X - \nu(\beta U_Y)_Y\right]f(Y)\,dY = 0 \tag{20}$$

In the present case the functions

$$f = Y^n;\ n = 0,1 \tag{21}$$

produce the momentum and moment of momentum integral equations, respectively.

Velocity Profiles

The Y dependence of the integral equations is eliminated by substituting an appropriate parametric formulation for the velocity profiles. The function used for the present theory is a modification of Coles' family (ref. 8) with a laminar sublayer added and the wake function approximated by a cosine.

$$U = U_\tau\left[2.5\ \ln(1+Y^+) + 5.1 - (3.39\ Y^+ + 5.1)e^{-0.37Y^+}\right] + \frac{1}{2}U_\beta\left[1 - \cos\left(\pi\frac{Y}{\delta}\right)\right] \tag{22}$$

The parameter U_τ is the usual friction velocity, modified to accommodate separated flows.

$$U_\tau = (\tau_w/|\tau_w|)\,(|\tau_w|/\rho)^{1/2} \tag{23}$$

The other parameters in Eq. (22) are δ, the boundary-layer thickness and U_β a wake velocity. The exponential terms and the additional unit in the logarithmic term provide a smooth transition from the turbulent flow to the wall through a laminar sublayer.

Eddy Viscosity

The eddy viscosity model used in this work is an extension of the two-layer model used by Kuhn (ref. 9) including an intermittency function for the outer layer and a modification of the outer layer for adverse pressure gradients and separated flows. In the inner layer of attached flows, the eddy viscosity parameter, β, is represented by an exponential expression based on the law of the wall. In the outer layer Clauser's expression, modified for adverse pressure gradients, is used along with an intermittency function giving

$$\epsilon = \left[0.013 + 0.0038\ \exp(-\delta^* p_X/15\tau_w)\right]U_e\delta^*/\left[1 + 5.5(Y/\delta)^6\right] \tag{24}$$

For favorable pressure gradients, the exponential term in Eq. (24) is taken to be unity.

For separated flows, the eddy viscosity across the entire layer is represented by a relation based on the velocity profile above the $U = 0$ line.

$$\beta = 0.013\left[1 + 5.5(Y/\delta)^6\right]^{-1}\frac{U_e}{\nu}\int_{Y_{u=0}}^{\delta}\left(1 - \frac{U}{U_e}\right)dY \tag{25}$$

Equations Solved

Substitution of Eq. (22) into the two equations produced by Eqs. (20) and (21) produces two ordinary differential equations for the variation of the variables U_τ, U_β, δ and U_e with x. A third equation produced by evaluating Eq. (22) at $Y = \delta$ allows the elimination of U_β from the equations, leaving a set of two equations

$$A_{11}(U_\tau)_X + A_{12}\delta_X + A_{13}(U_e)_X = -U_\tau|U_\tau|/U_e\delta \tag{26}$$

$$A_{21}(U_\tau)_X + A_{22}\delta_X + A_{23}(U_e)_X = -\frac{\nu}{U_e\delta^2}\int_0^{\delta}\beta U_Y dY \tag{27}$$

Anticipating the development of a viscous-inviscid interaction, we consider the velocity, U_e to be a dependent variable. The coefficients A_{ij} are functions of the variables U_τ, δ and U_e. The usual procedure for solving Eqs. (26) and (27) for attached boundary layers is to prescribe the pressure distribution, or the free-stream velocity distribution, U_e. However, if separation occurs, the pressure distribution cannot be prescribed arbitrarily in the separated region. If an adverse pressure gradient is prescribed for an attached boundary layer, the value of U_τ can approach zero. When U_τ vanishes,

the coefficients A_{11} and A_{12} in Eqs. (26) and (27) also vanish, producing a singularity. The singularity can be removed by rearranging the equation so that U_τ can be prescribed and U_e (or p) calculated as a dependent variable. The precise manner in which U_τ must be prescribed is determined using an iterative procedure in which the boundary layer and the inviscid flow are calculated alternately until the pressure distribution calculated for the boundary layer, hereafter called the "viscous pressure," agrees with that calculated for the inviscid flow. The iterative procedure becomes predictive by the introduction of a model for the interaction between the viscous and inviscid flows. That model will be described subsequently.

VERIFICATION OF THE BOUNDARY-LAYER THEORY

Before the boundary-layer theory was used to develop a viscous-inviscid interaction model, it was desirable to verify that the theory provides an adequate description of a real boundary layer. This verification was accomplished by applying the boundary-layer theory to two sets of experimental boundary-layer measurements. Either the experimental velocity distribution, U_e, or the friction distribution represented by U_τ were prescribed; and the other appropriate boundary-layer quantities such as the displacement and and momentum thickness distributions and velocity profiles were calculated and compared with the experimental data. If the calculated boundary-layer quantities agree well with the experimental values, the boundary-layer theory is considered to be verified.

The two cases used for comparison between the theory and experimental data are the data of Fernholtz and Gibson (ref. 10) for an incompressible, axisymmetric flow on a cylinder and those of Alber, et al., (ref. 11) for a bump on the wall of a transonic wind tunnel.

Comparison with Axisymmetric Incompressible Flow

The configuration of reference 10 is shown schematically in figure 1. The boundary layer is formed on a plexiglass cylinder in the annulus between that cylinder and a porous outer cylinder. An adverse pressure gradient is produced by an adjustable end plate, with localized control of the pressure gradient accomplished by adjusting the distribution of the porosity of the outer cylinder. For the case considered here, a separated flow region was indicated by negative wall shear as observed from sublayer fences. The separated region was observed to be axisymmetric by the agreement of measurements at different circumferential locations. As shown in figure 1, the theoretical boundary-layer thickness exceeds the height of the annulus near the end of the test region. Since the theory does not account for the upper boundary, it cannot calculate the boundary-layer quantities accurately where the boundary layer nearly fills the annulus.

In figure 2 are shown the velocity at the edge of the boundary layer and the measured and calculated skin-friction coefficient, C_f. In the calculations for these data, a smooth curve was fitted to the experimental U_e distribution and the fitted data were provided as input into the computer program. Ahead of the separation point, U_e was prescribed and U_τ was calculated. Slightly before U_τ reached zero, the procedure was reversed and an extrapolation of U_τ was prescribed while U_e was calculated. A short distance downstream of the separation point, the procedure was again reversed, the calculated U_e distribution was then faired smoothly into the given curve and the U_τ distribution was calculated in the same manner as ahead of separation. A series of trial-and-error calculations was necessary to find the best extrapolation of U_τ. The results, shown in figure 2, agree very well with the experimental separation point location and with the measured values of C_f. Experimental values of C_f in the region of reversed flow were not given in reference 10 since the sublayer fences were not calibrated for reversed flow.

After separation the calculations show that there is a region of reversed flow followed by a return to a flow with essentially zero wall shear. This is also in good agreement with the measured wall shear.

The results for the axisymmetric displacement and momentum thicknesses

$$\delta_1 = \int_0^\delta \left(1 - \frac{U}{U_e}\right)\left(1 + \frac{Y}{r}\right)dy \tag{23}$$

and

$$\delta_2 = \int_0^\delta \frac{U}{U_e}\left(1 - \frac{U}{U_e}\right)\left(1 + \frac{Y}{r}\right)dy \tag{29}$$

are shown in figure 3. The comparison is good for δ_2 but poor for δ_1. The deviation of the theoretical results from the experimental values of δ_1 is explained in part by the fact mentioned previously that the experimental boundary-layer growth is affected by the proximity of the outer cylinder which is not accounted for in the theory. That effect is smaller on the momentum thickness, δ_2, since that quantity is more dependent on the velocities near the wall than on those at the outer edge of the boundary layer.

Comparison with Two-Dimensional Transonic Flow

The configuration used in reference 11 is shown in figure 4. A bump of circular-arc shape was placed on the floor of a transonic wind tunnel with the ends of the bump smoothly faired into the floor by cosine-shaped fairings. The ceiling in the wind tunnel was contoured to approximate a streamline of the flow. Boundary-layer characteristics corresponding to the experimental surface pressure distribution were calculated and compared with measured boundary-layer characteristics. The case chosen for comparison corresponded to $M_\infty = 0.7325$ with the separation indicated downstream of a shock wave due to an adverse pressure gradient. Ahead of the shock wave occurring slightly downstream of the peak of the bump, the measured pressure distribution was prescribed for the calculations. Since the shock-wave, boundary-layer interaction was not a part of this investigation, the boundary-layer calculations were stopped at the beginning of the shock pressure rise and restarted slightly downstream using the measured boundary-layer quantities at the downstream point. From this point downstream, the friction velocity U_τ was specified. The distribution of U_τ along the surface was altered through several trials until the resulting viscous pressure distribution matched the experimental pressure distribution.

The calculated boundary-layer quantities are presented in figures 5 to 8. Figure 5 shows the pressure distributions as prescribed upstream of the shock wave and as calculated downstream of the shock wave. In figure 6 is shown the skin-friction coefficient corresponding to the prescribed U_τ distribution compared with the values given by reference 11. It should be noted that C_f from reference 11 is quasi-experimental having been obtained from fitted velocity profiles not from direct measurement. The agreement is very good except at a point near the end of the test section, after reattachment. As shown in figure 7, the specified U_τ distribution allows a smooth variation of the displacement thickness through both separation and reattachment. The calculated δ^* values are in very good agreement with the values as presented by reference 11. Also shown in figure 7 for illustration are the $U = 0$ line, the dividing streamline and several other streamlines as well as the boundary-layer thickness, δ.

Velocity profiles at several points of the flow are compared in figure 8. The initial values of U_τ and δ^* were chosen so the velocity profile at station zero was matched. The comparison between the calculated and measured profiles at stations 10 and 14.5 is good.

The generally good results of the comparisons between the present theory and the data of references 10 and 11 is verification that the present boundary-layer theory is an adequate approximation for real boundary layers in both incompressible and compressible flows.

PREDICTIVE METHOD FOR TURBULENT SEPARATION

Viscous-Inviscid Interaction Model

A significant question bearing on the interaction model is whether the displacement thickness of the boundary layer will account for the effect of the interaction between the inner and outer flows through its effect on the pressure distribution. In figure 9 is shown the experimental pressure distribution on the model of reference 11 compared with two pressure distributions predicted from the theory of reference 2. The pressure distribution shown by the solid line corresponds to the bare bump. The dashed line corresponds to the pressure for a surface defined by the bare bump augmented by the experimental displacement thickness. The displacement thickness causes a substantial forward movement of the normal shock along with a decrease in the peak pressure behind the shock. The inviscid theory including the effect of the displacement thickness gives results in much better agreement with experiment than the theory neglecting it. On the whole, the δ^* model accounts adequately for the observed difference between experiment and theory to the accuracy of the discontinuous normal shock produced by the theory of reference 2. Since it has been demonstrated previously that the boundary-layer theory can provide a good approximation to the measured displacement thickness for a case such as that of figure 9, the boundary-layer theory can now be coupled with the inviscid flow theory to produce a predictive method. It should be noted that the method of Tai (ref. 12) developed subsequent to this work, includes the shock-wave, boundary-layer interaction and produces a continuous pressure distribution for the entire model.

Iterative Procedure

Because the viscous and inviscid flow fields of subsonic and transonic flows are coupled in an elliptical fashion, the interaction between them is conveniently handled by iteration. In this section an iteration will be described in which the boundary-layer method described previously and an inviscid flow theory requiring the surface slope as a boundary condition can be used alternately to calculate the two flow fields.

The iteration procedure used in the prediction of turbulent flows begins with the calculation of the inviscid flow on the surface under consideration with no boundary layer. The next step is to calculate the boundary layer on the surface. The displacement thickness is then added to the surface and a new inviscid flow solution is calculated based on the augmented surface. This procedure is continued until convergence is achieved. If the flow contains no significant adverse pressure gradient regions, the boundary layer will always be attached; and convergence in terms of decreasing differences between successive iterations usually requires only four or five iterations. Such a flow is usually described as a weak interaction.

The presence of a region of significant adverse pressure gradients may lead to separation of the boundary layer, implying a strong interaction. In such a case, the pressure distribution due to the bare surface calculated in the first step of the iteration will usually cause the calculated boundary layer to separate. That is, with the pressure prescribed, a singularity will be encountered in the flow where $U_\tau = 0$. Subsequent boundary-layer calculations are made in two parts. The pressure distribution is prescribed in the weak interaction regions and U_τ is prescribed in the strong interaction region. Convergence is achieved in the weak interaction regions as described previously. In the strong interaction region convergence is achieved when the pressure distributions calculated by the inviscid theory and the boundary-layer theory agree within a desired tolerance.

CALCULATIVE EXAMPLE FOR TRANSONIC FLOW ON A BUMP

A predictive calculation of the boundary layer on the bump of reference 11 was performed for the transonic flow described previously. In calculating the theoretical flow, the only experimental information used was the velocity profile at the beginning of the test section and an approximate variation of δ^* through the shock wave. The theory of reference 2 was used for the inviscid flow field. That theory is based on transonic small-disturbance theory using a line relaxation method to solve the finite-difference equations.

The experimental data of reference 11 indicate that the velocity profiles are distorted by the shock so that Eq. (22) is not a good representation of the profiles in the vicinity of the shock. The profiles return to the form of Eq. (22) immediately after the shock with values of U_τ and δ smaller than existed ahead of the shock. Since precise theory of the local shock-wave, boundary-layer interaction in the immediate neighborhood of the shock was not a part of the research effort, it was decided to use the experimental results to provide approximate values of δ and U_τ to start the calculation downstream of the shock. A smooth fairing for δ^* across the shock was used to provide a smooth boundary condition for the inviscid flow calculation.

For the predictive calculation, the location of the beginning of the strong interaction solution was chosen as a point immediately after the shock wave. During early iterations, where the shock-wave location changed for each iteration, the location of the beginning of the strong interaction solution thus also changed.

In figure 10 are shown the results for a "converged" solution. The viscous and inviscid solutions agree within one percent. For comparison, the experimental δ^* and pressure distribution are also shown in figure 10. The predicted pressure is seen to be slightly higher than the experimental data in the same manner as observed in figure 9. This is attributed to discrepancies between the wind-tunnel ceiling contour and that of an actual free streamline as required by the theory. The predicted δ^* is in excellent agreement with the data upstream of the shock wave while it is slightly lower than the δ^* data downstream of the shock probably due to slight uncertainty in specifying the initial boundary-layer conditions for starting the calculations downstream of the shock. As mentioned previously, a more recent analysis by Tai (ref. 12) includes the local shock-wave, boundary-layer interaction. That is an important development since such a capability is necessary to improve this aspect of the calculation and to handle the case of separation right at the shock wave.

IMPROVEMENT OF ITERATION PROCEDURE

This study provides several insights into the viscous-inviscid interaction problem which suggest methods of improving the prediction method. The physical insight into the iterative method would be improved if the problem were formulated so that δ^* would be specified instead of U_τ. Examination of the relation between the viscous and inviscid solutions indicates that a convergent iteration scheme could be developed with such a formulation. For intermediate iterations, when the inviscid solution corresponds to a δ^* distribution which is above the converged δ^* distribution, the resulting viscous pressure distribution is above the inviscid pressure distribution. Conversely, subsequent calculations where the δ^* distribution was below the converged δ^* distribution were characterized by the viscous pressure curve being below the inviscid curve. Thus, it should be possible to develop a more rapidly convergent viscous-inviscid interaction procedure based on δ^*.

Recent work by other researchers (refs. 12 and 13) indicates that the integral continuity equation

$$\int_0^\delta U_x dy = -U_e \tan\theta \tag{30}$$

where

$$\tan\theta = \frac{V_e}{U_e}$$

provides an additional relation by which the singularity present when U_τ is treated as a dependent variable in Eqs. (26) and (27) can be removed by prescribing the variation of $\tan\theta$. Encouraging results have been demonstrated by Tai (ref. 12) using that approach coupled with an integral method for calculating the inviscid flow. However, it should be noted that the singularity at $U_\tau = 0$ is not removed by the simple addition

of Eq. (30) to the set if the resulting equation is expressed in the same form as Eqs. (26) and (27). The resulting equation in that case is

$$A_{31}(U_\tau)_x + A_{32}\delta_x + A_{33}(U_e)_x = -U_e \tan\theta \tag{31}$$

where A_{3i} are functions of U_τ, δ and U_e, and A_{31} vanishes when $U_\tau = 0$. Thus, the set of Eqs. (26), (27), and (31) are singular, and the expedient of prescribing $\tan\theta$ will not remove the singularity. Tai (ref. 12) has developed a procedure in which the singularity is avoided by calculating the solution up to the point where U_τ vanishes and then finding a value of U_τ to restart the calculation downstream of the separation point by iteration. Apparently, the effect of prescribing the $\tan\theta$ is to keep the slopes of δ and U_e finite, even though $(U_\tau)_x$ can become infinite.

Another method of avoiding the singularity at $U_\tau = 0$ is now suggested. If the displacement thickness, δ^*, is expressed in terms of U_τ, δ and U_e and the result is differentiated with respect to x, a fourth equation is developed.

$$A_{31}(U_\tau)_x + A_{32}\delta_x + A_{33}(U_e)_x + U_e\delta^*_x = 0 \tag{32}$$

where the A_{3i} are the same as in Eq. (31). It can be shown that A_{11}/A_{31} and A_{21}/A_{31} are both finite when $U_\tau = 0$. This allows the four Eqs. (26), (27), (31), and (32) to be reduced to three ordinary differential equations in the three dependent variables, δ^*, δ and U_e. The resulting equations are:

$$\frac{A_{11}}{A_{31}}U_e\delta^*_x + \left(\frac{A_{11}}{A_{31}}A_{32} - A_{12}\right)\delta_x + \left(\frac{A_{11}}{A_{31}}A_{33} - A_{13}\right)(U_e)_x = \frac{U_\tau|U_\tau|}{U_e\delta} \tag{33}$$

$$\frac{A_{21}}{A_{31}}U_e\delta^*_x + \left(\frac{A_{21}}{A_{31}}A_{32} - A_{22}\right)\delta_x + \left(\frac{A_{21}}{A_{31}}A_{33} - A_{23}\right)(U_e)_x = \frac{\nu}{U_e\delta^2}\int_0^\delta \beta U_Y dY \tag{34}$$

$$U_e\delta^*_x + (\delta^* - \delta)(U_e)_x = U_e\tan\theta \tag{35}$$

Although the nature of these three equations has not been investigated completely, calculation of the determinant of coefficients for a wide range of values of U_τ indicates that they are not singular at $U_\tau = 0$ nor at other values of U_τ. Thus, the singularity can be avoided since U_τ can be obtained directly by solving the nonlinear relation

$$\delta^* = f(U_\tau, \delta, U_e) \tag{36}$$

Prescribing the distribution of δ^* in Eqs. (33) and (34) and obtaining U_τ from Eq. (36) is equivalent to prescribing U_τ as described previously. Thus, the problem is now formulated so that viscous-inviscid interactions can be calculated in a more direct manner than when U_τ was prescribed. It should be possible to use this formulation in a calculative method such as that of Tai. It should also be possible to develop an automated iterative calculation by using the inviscid flow method of reference 2 to calculate $\tan\theta$ along a line corresponding to $Y = \delta$ in the inviscid flow with δ^* being used as described previously to augment the surface shape.

INTEGRAL METHOD FOR TIME-DEPENDENT, TURBULENT, INCOMPRESSIBLE BOUNDARY LAYERS

For the study of time-dependent boundary layers, the governing equations were taken to be Eqs. (16) and (17) with the addition of the time derivative of the velocity to Eq. (17) and the assumption that S_w is zero so that Eq. (18) is not necessary. Thus, the momentum equation is

$$U_t + UU_x + VU_y = (U_e)_t + U_e(U_e)_x + \frac{\tau_y}{\rho} \tag{37}$$

Since the emphasis in this study was on the nature of the integral equations, it was not necessary to choose a specific turbulence model. Various approaches have been taken by other researchers including use of an unsteady eddy viscosity model (refs. 14 and 15) and direct calculation of the turbulent shear stress by introduction of an additional equation for the turbulence kinetic energy (refs. 16, 17, and 18). In the present analysis, the shear stress is simply included in the equations under study as a function with certain assumed properties.

The velocity profiles are assumed to be represented by Eq. (22) as for the steady flows discussed previously. It is recognized that such profiles are based on equilibrium concepts and therefore will be unable to calculate flows which deviate significantly from equilibrium. Nevertheless, their use can allow some insight to be gained into the nature of the integral equations for unsteady flows and some of the limitations on their applicability to such flows.

The integral equations are derived in the same manner as discussed previously, producing two partial differential equations in U_τ, δ, and U_e of the form

$$A^t_{11}(U_\tau)_t + A^t_{12}\delta_t + A^x_{11}(U_\tau)_x + A^x_{12}\delta_x = B^t_1(U_e)_t + B^x_1(U_e)_x + R_1 \tag{38}$$

$$A_{21}^{t}(U_\tau)_t + A_{22}^{t}\delta_t + A_{21}^{x}(U_\tau)_x + A_{22}^{x}\delta_x = B_2^{t}(U_e)_t + B_2^{x}(U_e)_x + R_2 \tag{39}$$

where the coefficients A_{ij} and B_i and the terms R_i are functions of U_τ, δ, and U_e defined in reference 3.

ANALYTICAL STUDIES OF UNSTEADY BOUNDARY LAYERS

Response to Time-Dependent, Free-Stream Conditions

The response of the integral boundary-layer equations to an oscillatory disturbance of the free-stream velocity is examined. It is assumed that the free stream consists of a steady flow plus a small amplitude disturbance

$$U_e = U_{e_s}(x) + \epsilon \sin \omega t \tag{40}$$

It is further assumed that the solutions for U_τ and δ can be expressed in the same way as a steady part plus an unsteady part. Thus,

$$U_\tau = U_{\tau_s}(x) + f(x,t) \tag{41}$$

$$\delta = \delta_s(x) + g(x,t) \tag{42}$$

where $U_{\tau_s}(x)$ and $\delta_s(x)$ are the steady-state solutions of U_τ and δ in response to the imposed distribution $U_{e_s}(x)$, and the functions f and g are unknown functions to be calculated.

The steady solution is assumed to be far from separation so that f is assumed to be small compared to U_{τ_s}. Similarly, because of the small perturbation assumption, g is small compared to δ_s. With these assumptions, it is possible to approximate the coefficients of Eqs. (38) and (39) by their steady-state values. When these quantities are substituted into Eqs. (38) and (39) and the equations for the steady-state solution are subtracted from the results, Eqs. (38) and (39) become, to first order

$$A_{11}^{t}f_t + A_{11}^{x}f_x + A_{12}^{t}g_t + A_{12}^{y}g_x = -2\left|u_{\tau_s}\right| f + B_1^{t}\omega\epsilon \cos \omega t \tag{43}$$

$$A_{21}^{t}f_t + A_{21}^{x}f_x + A_{22}^{t}g_t + A_{22}^{x}g_x = B_2^{t}\,\omega\epsilon \cos \omega t - \frac{1}{\rho}\int_0^{\delta} \tau' dy \tag{44}$$

McDonald and Shamroth (ref. 19) noted that an equilibrium model of the turbulence would be a valid approximation and the time rate of change of turbulent intensity would be negligible for typical frequencies. It is assumed that frequencies of interest here satisfy the condition

$$\omega << \frac{U_e}{\delta}$$

For such cases, according to McDonald and Shamroth, the unsteady shear stress integral in Eq. (44) can be neglected.

In reference 3 it was shown by order-of-magnitude analysis that the x derivatives in Eqs. (43) and (44) can also be neglected. The solutions of the resulting equations are then found to be

$$f = \left(f_o - \frac{QP\omega}{\omega^2 + P^2}\right)e^{-Pt} + \frac{QP\omega}{\omega^2 + P^2}\cos \omega t + \frac{Q\omega^2}{\omega^2 + P^2}\sin \omega t \tag{45}$$

$$g = \left(\frac{B_2^{t}}{A_{22}^{t}}\epsilon - \frac{A_{21}^{t}}{A_{22}^{t}}\frac{Q\omega^2}{\omega^2 + P^2}\right)\sin \omega t - \frac{A_{21}^{t}}{A_{22}^{t}}\frac{QP\omega}{\omega^2 + P^2}\cos \omega t$$

$$- \frac{A_{21}^{t}}{A_{22}^{t}}\left(f_o - \frac{QP\omega}{\omega^2 + P^2}\right)e^{-Pt} + g_o + \frac{A_{21}^{t}}{A_{22}^{t}}f_o \tag{46}$$

where

$$P = \frac{2\left|U_{\tau_s}\right|}{D} \tag{47}$$

$$Q = \frac{(B_1^{t} - A_{12}^{t}B_2^{t}/A_{22}^{t})}{D} \tag{48}$$

$$D = \frac{A_{11}^{t} - A_{12}^{t}A_{21}^{t}}{A_{22}^{t}} \tag{49}$$

The sign of the quantity P determines whether the transient part of these solutions is decaying or growing. From Eq. (47) the sign of P clearly depends on the sign of the quantity D, Eq. (49).

In reference 3 the value of D is calculated using the results of Singleton and Nash (ref. 17) for a flat plate with oscillating free-stream velocity of the form

$$\frac{U_e}{U_{e_o}} = 1 + \epsilon \sin \omega t \tag{50}$$

where U_{e_o} is constant. For a disturbance amplitude (ϵ) of 0.125, the resulting value of D is 0.156. Thus, for this case the quantity P is positive. Eqs. (45) and (46) thus show that the boundary-layer thickness and friction velocity undergo an initial transient period when the free-stream oscillations are imposed impulsively on the flow, but after a sufficient time the solutions take on the forms

$$U_\tau = U_{\tau_s} + A_\tau \sin(\omega t + \alpha_\tau) \tag{51}$$

$$A_\tau = QW/(\omega^2 + P^2)^{1/2} \tag{52}$$

$$\alpha_\tau = \tan^{-1}(P/\omega) \tag{53}$$

and

$$\delta = \delta_s + A_\delta \sin(\omega t + \alpha_\delta) \tag{54}$$

where

$$A_\delta = \left\{ \left(\frac{A^t_{21}}{A^t_{22}} P \right)^2 + \left[\frac{B^t_2 \epsilon (\omega^2 + P^2)}{A^t_{22} Q \omega} - \frac{A^t_{21}}{A^t_{22}} \omega \right]^2 \right\}^{1/2} \frac{Q\omega}{\omega^2 + P^2} \tag{55}$$

and

$$\alpha_\delta = \tan^{-1} \frac{A^t_{21} P}{A^t_{21} \omega - \frac{\omega^2 + P^2}{Q\omega} B^t_2 \epsilon} \tag{56}$$

Since P is positive, the phase angle, α_τ, of U_τ (Eq. (51)) is leading. It varies between $\pi/2$ for zero ω and 0 for $\omega \to \infty$. According to the results of Singleton and Nash (ref. 17), the phase angle of τ_w is nearly constant over a wide range of frequencies and does not increase significantly as $\omega \to 0$. This contradiction is probably due to the assumptions used to derive the present theory and may be useful in defining the range of applicability of this theory. The phase angle of δ may be either leading or lagging depending on the frequency.

The variation of τ_w and δ^* over a period of oscillation of the free-stream disturbance were calculated for several frequencies in order to compare with the results of Singleton and Nash. The results are shown in figures 11 and 12. The steady-state boundary-layer conditions used were those at the trailing edge of the flat plate as described previously.

In figure 11(a), the wall shear stress, τ_w, calculated by the present theory is compared with the results of Singleton and Nash for $\omega = 1.57$. The variation of the free-stream velocity, U_e, is also shown for reference. The two theories exhibit fair agreement. The agreement for the displacement thickness shown in figure 11(b) is poor.

For a higher frequency, the agreement between the present theory and that of Singleton and Nash is much better. In figure 12 is shown comparisons between the two theories for $\omega = 15.7$. The agreement for τ_w shown in figure 12(a) is excellent while the agreement for δ^* shown in figure 12(b) is good in terms of the magnitude of the quantity, but poor in terms of the phase angle.

Clearer comparison of the phase angles of the two theories is presented in figure 13 where the phase angles for τ_w and δ^* for the two theories are plotted as a function of ω. The present theory predicts that the phase angles of both δ^* and τ_w are always leading and that they both increase for small ω and approach zero for large ω. The theory of Singleton and Nash, on the other hand predicts that the phase angle of τ_w is nearly constant over the frequency range considered, while their results for the phase angle of δ^* indicate a trend similar to that of the present theory, but with a negative asymptote for large ω.

It will be recalled that the present theory was considered to be valid in a frequency range $U_e/L \ll \omega \ll U_e/\delta$. For the case presented in figures 12 and 13, this becomes approximately $1 \ll \omega \ll 44$. Thus, the calculations which agree best with the nonlinear theory, figure 12, correspond to a frequency well within the range of validity of the theory.

The results presented here are encouraging even though the amplitude of the disturbance was rather large and the steady-state components of U_τ and δ are not much larger than the disturbances f and g for all times as assumed. The comparisons suggest that the velocity profile formulation should be accurate for a certain range of frequencies. Comparison with experimental data is necessary to verify this conclusion, however.

The discrepancies noted between the present theory and that of reference 17 are probably due to two factors. First, the velocity profiles used in the present method are restricted to having the shape prescribed by Eq. (22) while no such restrictions are imposed by the finite-difference method of reference 17. Second, no explicit shear stress model was used in the present method while in reference 17, the turbulent shear stresses were calculated by generalizing the shear stress transport equations used in steady flows to include the unsteady convective terms. It should also be noted that both of the methods consitutute numerical experiments and can be validated only by comparisons with experimental data. The recent work of reference 15 indicates similar agreement with the present method and that of reference 17 using an eddy viscosity model generalized for unsteady flow.

Solutions in the Vicinity of Vanishing Wall Shear

Of major concern in calculations of boundary-layer characteristics in unsteady as well as steady flows is the question of the nature of the equations in the vicinity of a point of vanishing wall shear stress. When the free-stream velocity, U_e, is prescribed, the steady equations are known to exhibit a singular behavior in which the slope of the wall shear stress $(\tau_w)_x$ increases without bound as the point of zero τ_w is approached. The free-stream velocity cannot be prescribed arbitrarily in such a region. On the other hand, Nash (ref. 18) has recently shown that in unsteady flows, the gradient $(\tau_w)_x$ may decrease as the point of zero τ_w is approached, thus suggesting removal of the singularity. This in turn suggests that the distribution of U_e with x can be prescribed arbitrarily in an unsteady flow even including the point where τ_w is zero. The exact reason for this is not completely understood at this time.

The work described previously indicated that the singularity in the steady boundary-layer equations could be removed if the free-stream velocity is not arbitrarily prescribed but is treated as a dependent variable. The success of that method for steady turbulent flows is encouraging for the application of integral methods to unsteady flows. Even though the validity of Coles' formulation of the velocity profiles at a separation point has been questioned (ref. 11), the formulation has been found to be quite adequate for representing the velocity profiles at other locations both upstream and downstream of the separation point. In unsteady flows, according to the work of Sears and Telionis (ref. 20), a point of zero wall shear stress can occur without separation of the flow from the boundary. Such results were also obtained by Kuhn and Nielsen (ref. 21) studying the unsteady flow of two-dimensional estuaries where reversal of the shear at the bottom of a channel occurred out of phase with the reversal of the surface (corresponding to the boundary-layer edge) flow, with no indication of a singularity at the point of zero wall shear.

With these considerations the equations will now be examined for vanishing U_τ. It will be assumed that U_τ is so small that not only is $U_\tau \ll 1$, but also $\delta^+ \ll 1$. The coefficients of Eqs. (38) and (39) must then be evaluated by writing the velocity profiles for small δ^+. The details of this evaluation are presented in reference 3. When the velocity profiles are expanded for small δ^+, the Eqs. (38) and (39) can be expressed after some algebraic manipulation in terms of powers of U_τ. Collecting terms of the same order yields the following results:

Zeroth-order terms

$$\frac{1}{2}(U_e - U_o)\delta_t - \left[\frac{1}{8}U_e^2 + \frac{1}{4}U_o\left(U_e - \frac{3}{2}U_o\right)\right]\delta_x = \frac{1}{2}\delta(U_e)_t + \left(\frac{3}{4}U_e - \frac{1}{4}U_o\right)\delta(U_e)_x \tag{57}$$

$$\frac{1}{2}\left(\frac{4}{\pi^2} - 1\right)(U_e - U_o)\delta\delta_t + \left[\left(\frac{1}{\pi^2} - \frac{3}{16}\right)(U_e - U_o)^2 - \frac{1}{2}(U_e - U_o)U_o\left(1 - \frac{4}{\pi^2}\right)\right]\delta\delta_x =$$

$$\frac{1}{4}\left(1 - \frac{4}{\pi^2}\right)\delta^2(U_e)_t + \left[\frac{1}{2}\left(1 - \frac{4}{\pi^2}\right)U_e + \frac{1}{2}\left(1 + \frac{8}{\pi^2}\right)U_o\right]\delta^2(U_e)_x - \int_o^\delta \tau\, dy \tag{58}$$

where U_o is an arbitrary wall velocity.

First-order terms

$$|U_\tau|(U_\tau)_x = 0 \tag{59}$$

$$\left(\frac{1}{6} - \frac{2}{\pi^2}\right)\delta^3\frac{|U_\tau|}{\nu}(U_\tau)_t + \left[U_e\left(\frac{1}{\pi^2} - \frac{1}{6}\right) - U_o\left(\frac{7}{\pi^2} - \frac{1}{3}\right)\right]\delta^3\frac{|U_\tau|}{\nu}(U_\tau)_x = 0 \tag{60}$$

Eqs. (57) and (58) show that at $U_\tau = 0$ there is a unique relationship between the boundary-layer thickness gradient and the free-stream velocity gradient for steady flow with zero wall velocity. The equations reduce to

$$\frac{1}{8}U_e^2\delta_x + \frac{3}{4}U_e\delta(U_e)_x = 0 \tag{61}$$

$$\left(\frac{1}{\pi^2} - \frac{3}{16}\right)U_e^2\delta_x - \frac{1}{2}\left(1 - \frac{4}{\pi^2}\right)U_e\delta^2(U_e)_x = -\int_o^\delta \tau\, dy \tag{62}$$

These equations show that the free-stream velocity gradient cannot be prescribed arbitrarily at $U_\tau = 0$. The gradients of U_e and δ must satisfy both of these equations.

Eq. (50) says that the singularity occurring in U_τ is integrable for steady or unsteady flows. Assuming that

$$U_\tau \sim x^n$$

then

$$U_\tau (U_\tau)_x = n x^{2n-1}$$

and

$$\lim_{x \to 0} U_\tau (U_\tau)_x = 0 \quad \text{if} \quad n > \frac{1}{2}$$

In references 1 and 7, physical considerations were used to determine how U_τ would be varied across the separation point. In order to obtain a smooth variation of the displacement thickness it is necessary to avoid the development of very large slopes. This is accomplished by letting U_τ vary linearly with x across the separation point ($n = 1$). With Eq. (59), Eq. (60) suggests that similar circumstances exist for the unsteady case, since

$$|U_\tau| (U_\tau)_t = 0 \tag{63}$$

The meaning of this condition appears to be that at a fixed location, the time variation of the solution also has an integrable singularity. Evidence that such a condition may exist is found in references 17 and 18 where the displacement thickness is shown to increase significantly when the wall shear stress approaches zero. This suggests that the singularity found in steady flows when $U_e(x)$ is prescribed may be present in unsteady flows when $U_e(t)$ is prescribed.

A variation of U_τ with constant $(U_\tau)_x$ at $U_\tau = 0$ has the following results for the wall shear stress. From Eq. (23)

$$\frac{\tau_w}{\rho} = U_\tau |U_\tau| \tag{64}$$

so that

$$\frac{(\tau_w)_x}{\rho} = 2|U_\tau| (U_\tau)_x \tag{65}$$

and

$$\frac{(\tau_w)_{xx}}{\rho} = 2|U_\tau| (U_\tau)_{xx} + 2 \frac{U_\tau}{|U_\tau|} \left[(U_\tau)_x\right]^2 \tag{66}$$

Thus, the gradient $(\tau_w)_x$ is negative on both sides of the point of zero shear while the second derivative changes sign. This makes the point of zero shear stress a point of inflection. Of course, the limitation that this analysis only applies for U_τ so small that $\delta^+ \ll 1$ makes it applicable to a very small neighborhood of the zero shear stress point. Nevertheless, these results are consistent with the results observed by other researchers using finite-difference calculation methods for unsteady boundary-layer flows. Nash (ref. 18) and Sears (ref. 20) and others have found that in unsteady flows the solution is not singular at the point of zero shear and the shear stress tends to approach zero with decreasing slope.

CONCLUDING REMARKS

An *a priori* turbulent boundary-layer separation prediction has been achieved by coupling an integral boundary-layer method and a finite-difference inviscid flow method through an iterative interaction model. The interaction model was developed through examination of the relationship between experimental boundary-layer quantities and calculated inviscid flow quantities. Those studies indicated that the change of the inviscid flow created by the boundary layer could be well approximated by the addition of the boundary-layer displacement thickness to the physical surface. Calculations in a transonic flow produced results in good agreement with experiment. Insights gained from this study suggest a method in which the separation singularity can be removed and a completely automated calculation method developed by combining a modified version of the present boundary-layer method with an appropriate inviscid flow method.

The integral boundary-layer method was also examined briefly for its applicability to unsteady turbulent flows. A small perturbation analysis produced good comparison with results of the nonlinear finite-difference method of reference 17 for frequencies within the range of validity of the linearized theory even for fairly large amplitude perturbations. The results indicate that the integral boundary-layer method using an analytical formulation based on equilibrium velocity profiles can be extended to unsteady flows. It may be possible to extend the range of frequencies over which the method is valid by including a time-dependent turbulent shear stress model and by solving the complete nonlinear boundary-layer equations.

Another aspect of the problem of calculating unsteady boundary layers that was examined is the nature of the solution in the vicinity of vanishing wall shear. It was demonstrated in reference 1 that the singularity occurring at a point where $U_\tau = 0$ in steady flow is integrable and can be removed. In unsteady flow, the same kind of

situation was found to exist for the time-dependent solution. The conditions found to apply at a point of zero wall shear stress was found to be consistent with a decreasing shear stress gradient approaching the point in agreement with the results of other researchers.

REFERENCES

1. Kuhn, G. D. and Nielsen, J. N.: Prediction of Turbulent Separated Boundary Layers. AIAA Paper No. 73-663 presented at the 6th Fluid and Plasma Dynamics Conference, Palm Springs, CA, July 16-18, 1973.

2. Murman, E. M. and Cole, J. D.: Calculation of Plane Steady Transonic Flows. AIAA Jour., vol. 9, no. 1, Jan. 1971, pp. 114-121.

3. Kuhn, G. D. and Nielsen, J. N.: Studies of an Integral Method for Calculating Time-Dependent Turbulent Layers. Project SQUID Tech. Rept. NEAR-2-PU, Oct. 1973.

4. Probstein, R. F. and Elliott, D.: Transverse Curvature Effect in Compressible Axially-Symmetric Laminar Boundary-Layer Flow. J. Aero. Sci., vol. 23, 1956, p. 208.

5. Stewartson, K.: Correlated Incompressible and Compressible Boundary Layers. Proc. of the Royal Soc. A., vol. 200, 1949, pp. 85-100.

6. Nash, J. F. and Hicks, J. G.: An Integral Method Including the Effect of Upstream History on the Turbulent Shear Stress. Proceedings - Computation of Turbulent Boundary Layers - 1968 AFOSR-IFP-Stanford Conference, vol. 1, editors S. J. Kline, et al.

7. Kuhn, G. D. and Nielsen, J. N.: An Analytical Method for Calculating Turbulent Separated Flows Due to Adverse Pressure Gradients. Project SQUID, Tech. Rept. NEAR-1-PU, Oct. 1971.

8. Coles, D.: The Law of the Wake in the Turbulent Boundary Layer. J. Fluid Mech., vol. 1, 1956, p. 191.

9. Kuhn, G. D.: Calculation of Compressible Nonadiabatic Boundary Layers in Laminar, Transitional and Turbulent Flow by the Method of Integral Relations. NASA CR-1797, Nov. 1971.

10. Fernholz, H. and Gibson, P.: Experiments on Turbulent Boundary Layers Along a Circular Cylinder with and Without Separation. Tech. Rept. No. 91, M.I.T. Gas Turbine Laboratory, July 1967.

11. Alber, I. E., Bacon, J. W., Masson, B. S., and Collins, D. J.: An Experimental Investigation of Turbulent Transonic Viscous-Inviscid Interactions. AIAA Jour., vol. 11, no. 5, May 1973, pp. 620-627.

12. Tai, T. C.: Transonic Turbulent Viscous-Inviscid Interaction Over Airfoils. AIAA Paper No. 75-78 presented at the 13th Aerospace Sciences Meeting, Pasadena, CA, Jan. 20-22, 1975.

13. Gerhart, P. M.: On Prediction of Separated Boundary-Layers with Pressure Distribution Specified. AIAA Jour., vol. 12, no. 9, Sept. 1974, pp. 1278-1279.

14. Abbott, D. E. and Cebeci, T.: The General Analysis of Unsteady Boundary Layers - Laminar and Turbulent. Fluid Dynamics of Unsteady, Three-Dimensional and Separated Flows. Project SQUID Workshop, GA Inst. Tech., June 10-11, 1971, pp. 202-227.

15. Telionis, D. P. and Tsahalis, D. T.: Unsteady Turbulent Boundary Layers and Separation. AIAA Paper No. 75-27 presented at the 13th Aerospace Sciences Meeting, Pasadena, CA. Jan. 20-22, 1975.

16. Bradshaw, P.: Calculation of Boundary Layer Development Using the Turbulent Energy Equation. Part 6: Unsteady Flow. Nat'l Phys. Lab. Rept. No. NPL-Aero-1288, Feb. 1969.

17. Singleton, R. E. and Nash, J. F.: A Method for Calculating Unsteady Turbulent Boundary Layers in Two- and Three-Dimensional Flows. Proceedings AIAA Computational Fluid Dynamics Conference, Palm Springs, CA, July 19-20, 1973, pp. 84-91.

18. Nash, J. F., Carr, L. W., and Singleton, R. E.: Unsteady Turbulent Boundary Layers in Two-Dimensional, Incompressible Flow. AIAA Paper No. 73-650 presented at the 6th Fluid and Plasma Dynamics Conference, Palm Springs, CA, July 16-18, 1973.

19. McDonald, H. and Shamroth, S. J.: An Analysis and Application of the Time-Dependent Turbulent Boundary-Layer Equations. AIAA Jour., vol. 9, no. 8, Aug. 1971, pp. 1553-1560.

20. Sears, W. R. and Telionis, D. P.: Unsteady Boundary Layer Separation. Fluid Dynamics of Unsteady, Three-Dimensional and Separated Flows. Project SQUID Workshop, GA Inst. Tech., June 10-11, 1971, pp. 285-309.

21. Kuhn, G. D. and Nielsen, J. N.: Application of Boundary-Layer Theory to Dispersion in Well-Mixed Estuaries. NEAR TR 63, Nielsen Engineering & Research, Inc., Sept. 1974.

ACKNOWLEDGEMENT

The ability to achieve fundamental advances in the state of the art of boundary-layer calculative methods is greatly enhanced by an atmosphere in which free inquiry is encouraged. For this the authors gratefully acknowledge the support and encouragement of the United States Office of Naval Research Project SQUID under Contract 4965-29.

The assistance of Dr. E. M. Murman in making available his computer programs for transonic inviscid flow is also gratefully acknowledged.

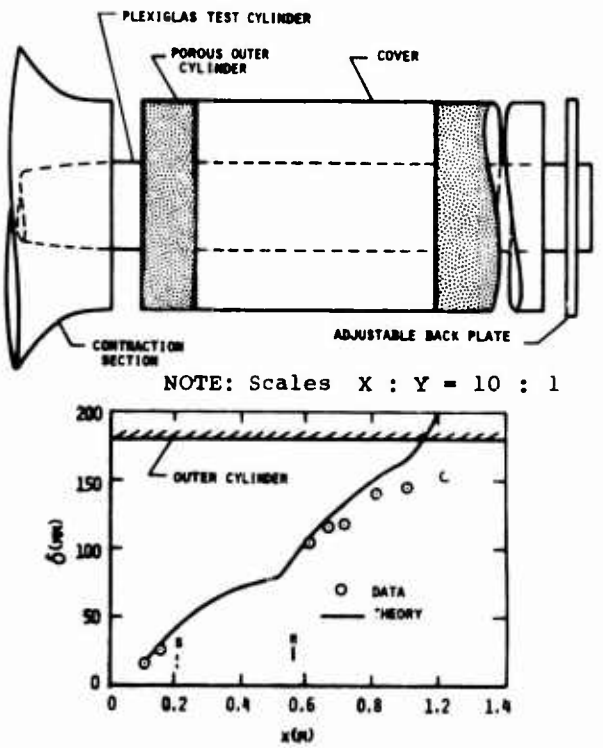

Figure 1.- Fernholz and Gibson configuration and boundary-layer growth (ref. 10).

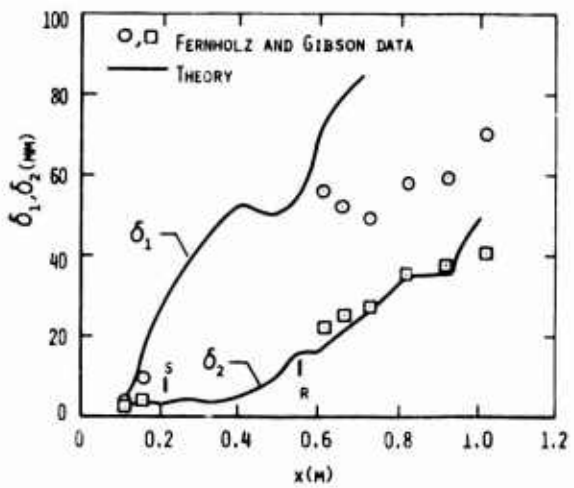

Figure 3.- Comparison with data on a circular cylinder.

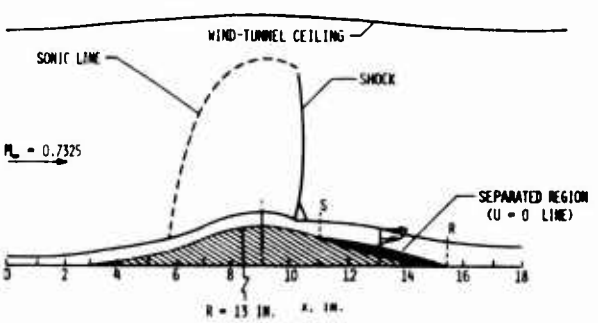

Figure 4.- Transonic flow field over a bump (ref. 11).

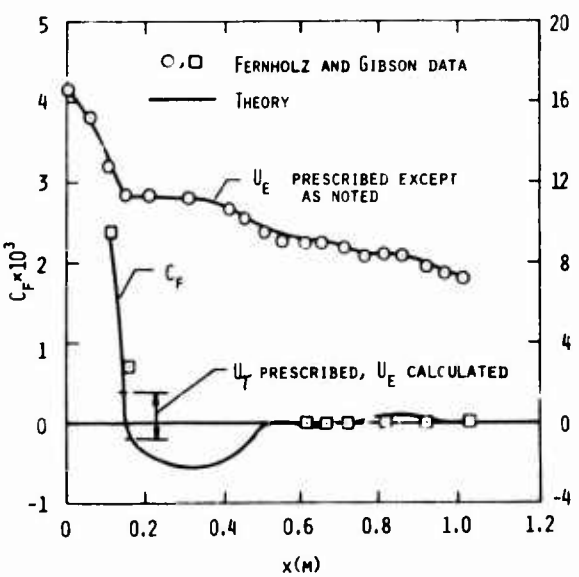

Figure 2.- Comparison with data on a circular cylinder.

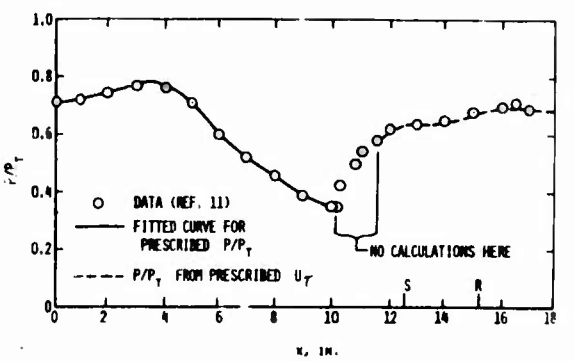

Figure 5.- Experimental and theoretical pressure distributions for verification of boundary-layer theory.

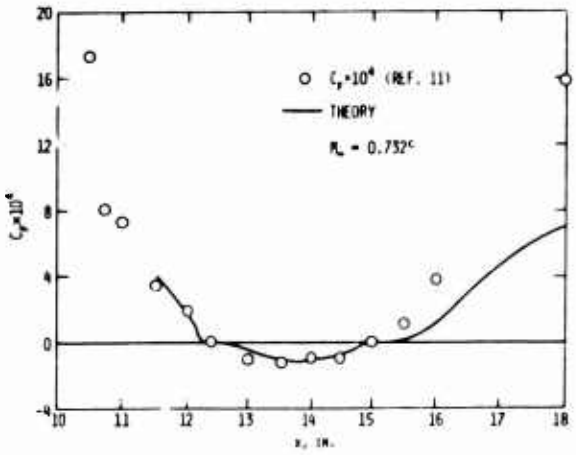

Figure 6.- Skin-friction coefficient on a bump in transonic flow.

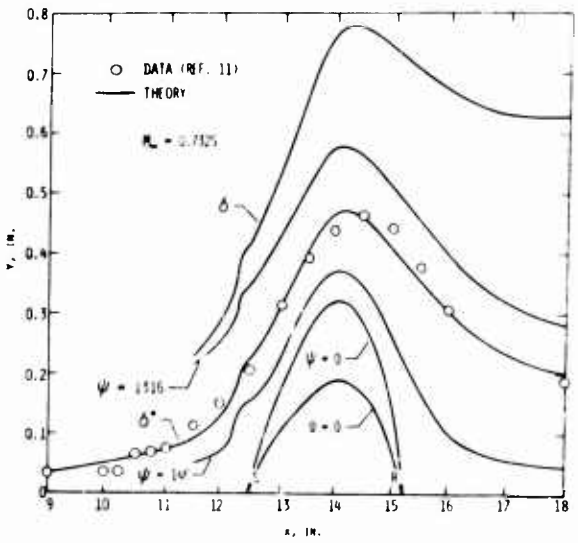

Figure 7.- Displacement thickness and other characteristic lines of boundary layer on a bump in transonic flow.

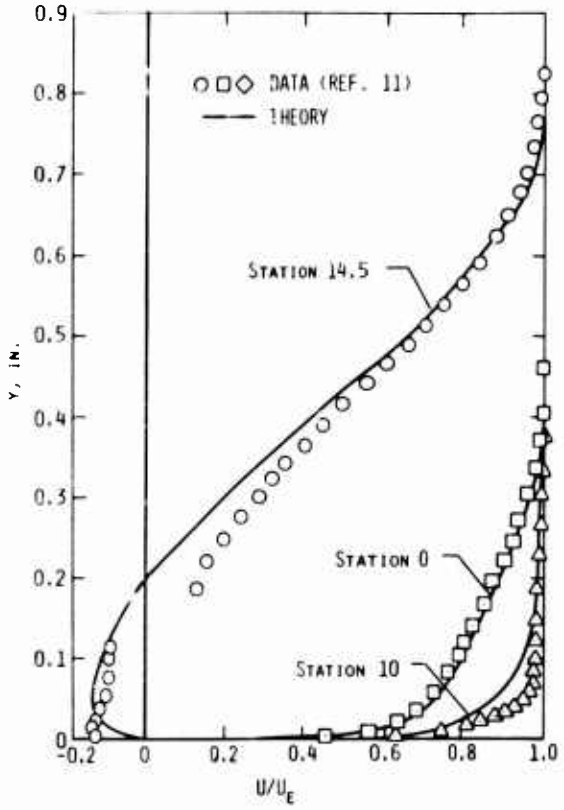

Figure 8.- Velocity profiles of boundary layer on a bump in transonic flow.

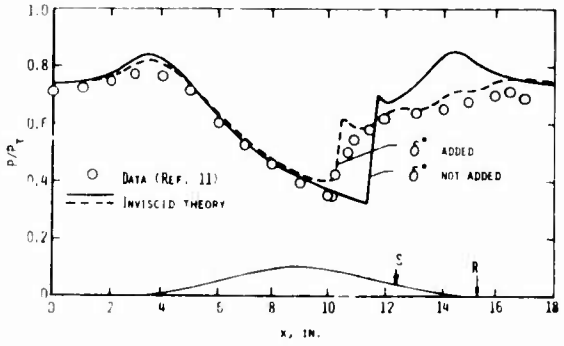

Figure 9.- Comparison of inviscid pressure distributions with data, M_∞ = 0.7325.

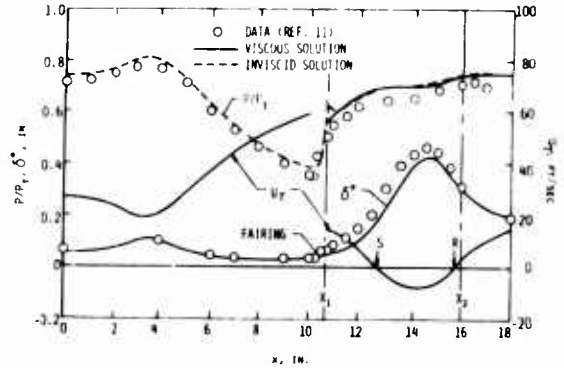

Figure 10.- Converged solution compared with data.

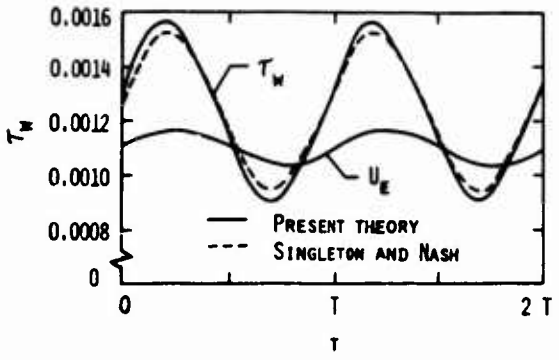

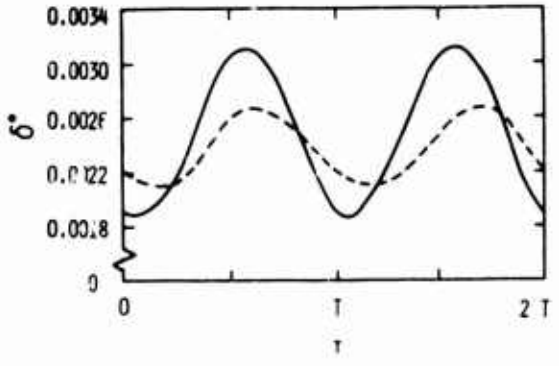

(b) Displacement thickness.

Figure 11.- Comparison of linearized theory and nonlinear theory for oscillating flow on a flat plate, $\epsilon = 0.125$, $\omega = 1.57$.

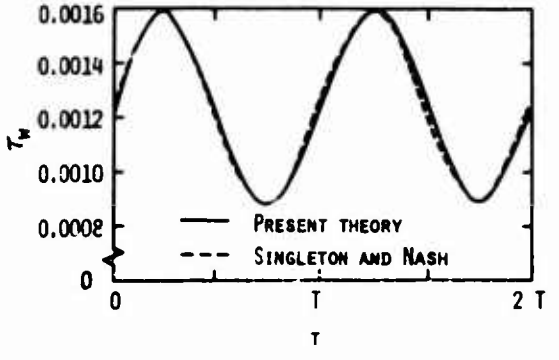

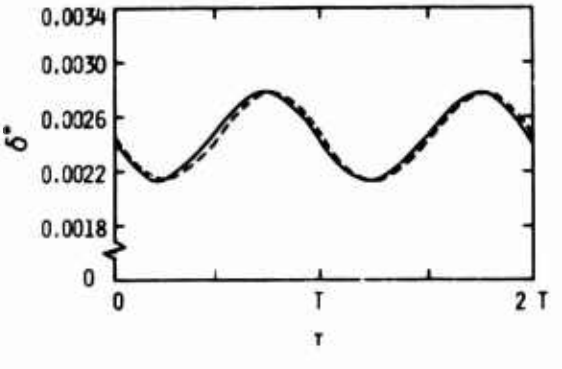

(b) Displacement thickness.

Figure 12.- Comparison of linearized theory and nonlinear theory for oscillating flow on a flat plate, $\epsilon = 0.125$, $\omega = 15.7$.

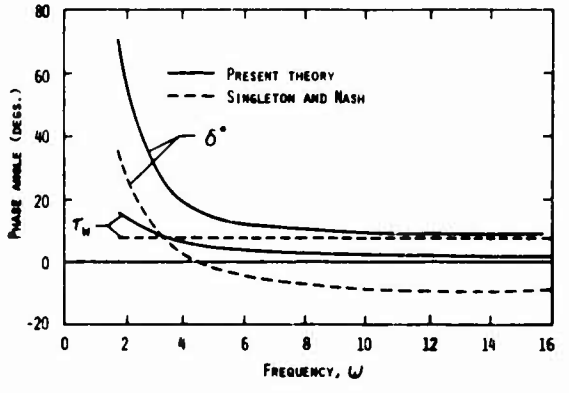

Figure 13.- Phase angles of δ^* and τ_w for oscillating flow on a flat plate, $\epsilon = 0.125$.

INTERACTION VISQUEUSE AVEC DÉCOLLEMENT EN ÉCOULEMENT TRANSSONIQUE

par J. DÉLERY, J.J. CHATTOT et J.C. LE BALLEUR

Office National d'Etudes et de Recherches Aérospatiales (ONERA)
92320 CHATILLON (France)

RESUME

Les écoulements transsoniques autour des profils portants sont le siège d'interactions visqueuses fortes qui entraînent un épaississement important de la couche limite avec, fréquemment, l'apparition d'une zone décollée. Dans ces conditions, le calcul de l'écoulement doit faire appel aux théories d'interaction rapide dont l'application en transsonique et dans le cas d'une couche limite turbulente est examinée en liaison avec l'analyse expérimentale. Cette dernière a été conduite dans une soufflerie continue dont la veine bidimensionnelle a 120 cm^2 de section. Le dispositif d'essai consiste en un demi-profil placé sur la paroi inférieure de la soufflerie. Les mesures ont consisté en une analyse détaillée de l'écoulement en utilisant l'interférométrie, moyen d'investigation puissant qui évite toute perturbation de l'écoulement. Parallèlement à cette expérimentation on cherche à développer une méthode de calcul inspirée de l'approche de Klineberg. Le principe de la théorie consiste à diviser l'écoulement en deux domaines : une zone d'interaction faible, là où le gradient de pression est soit négatif, soit modérément positif, et une zone d'interaction rapide dans les régions où un décollement est susceptible de se produire.

VICOUS INTERACTION WITH SEPARATION IN A TRANSONIC FLOW

SUMMARY

Strong viscous interactions which are present in transonic flows past airfoils give rise to an important thickening of the boundary layer with, the frequent formation of a separated region. Under such conditions, the calculation of the flow must call upon rapid interaction theories whose application for the case of a turbulent boundary layer is examinated in conjunction with experimental analysis. The experiments have been conducted in a continuous wind tunnel equiped with a two-dimensional nozzle having a 120 cm^2 section. The experimental installation is made of a half profile mounted on the lower wall of the transonic channel. A detailled analysis of the flow field has been made by using interferometry, a measuring technique which avoids any disturbance of the flow. At the same time one's tries to develop a method of calculation similar to Klineberg's approach. The principle of this theory is to divide the flow into two domains : a "weak" interaction region where the pressure gradient is negative or positive but moderate, and a "rapid" interaction region if separation is likely to occur.

NOTATIONS.

Symboles

- ℓ : largeur de veine.
- B : constante de la loi de Gladstone-Dale (ici $B = 0{,}227510^{-3}$ m^3/kg).
- Cf : coefficient de frottement pariétal.
- Cf_i : " " " incompressible.
- D : point de décollement.
- e : épaisseur du profil.
- H_i : paramètre de forme incompressible.
- K_p : coefficient de pression.
- L : corde du profil.
- M : nombre de Mach.
- n : numéro d'une frange sur le cliché à l'arrêt.
- N : numéro d'une frange sur le cliché en marche.
- p : pression.
- P : nombre de pression de Busemann.
- q : pression dynamique $(q = \frac{1}{2}\rho V^2)$
- r : facteur de récupération pariétal ($r = 0{,}9$ en turbulent).
- $\mathcal{R}_\delta$: nombre de Reynolds calculé avec δ .
- T : température absolue.
- u, v : composantes du vecteur vitesse selon Ox et Oy respectivement.
- u^* : vitesse critique.
- u_τ : vitesse de frottement : $\left(u_\tau = \sqrt{\frac{\tau_p}{\rho_p}}\right)$
- x, y : coordonnées cartésiennes.
- α : paramètre de forme $\left(\alpha = \frac{\delta_{H_i}}{\delta}\right)$
- β : angle de divergence ou de convergence de la veine.

γ : rapport des chaleurs spécifiques à pression et à volume constant.

δ : épaisseur physique de la couche limite.

δ_1 : " de déplacement.

δ_2 : " de quantité de mouvement.

δ_3 : " d'énergie cinétique.

δ_{1i} : " de déplacement incompressible.

δ_{2i} : " de quantité de mouvement incompressible.

η : ordonnée réduite $(\eta = \frac{z}{\delta})$

θ : déflexion induite par la couche limite.

λ : longueur d'onde de la radiation lumineuse utilisée (ici $\lambda = 0{,}5461\ \mu m$).

ν : viscosité cinématique et indice de réfraction.

ρ : masse spécifique.

τ : frottement.

φ_p : angle de la paroi.

ϕ : intégrale de dissipation.

Indices.

i : désigne les conditions génératrices.

e : " " à la frontière de la couche limite.

0 : désigne les conditions à l'origine d'une interaction.

∞ : désigne les conditions de référence.

INTERACTION VISQUEUSE AVEC DECOLLEMENT EN ECOULEMENT TRANSSONIQUE.

1 - INTRODUCTION.

Au cours des dernières années, plusieurs méthodes ont été proposées pour calculer l'écoulement de fluide parfait autour d'un profil en transsonique. Les méthodes en principe les plus exactes sont basées sur la résolution numérique des équations d'Euler instationnaires [1-2-3]. Elles présentent toutefois l'inconvénient de nécessiter des temps de calcul très longs, ce qui limite fortement leurs possibilités d'application pratique. Les autres techniques numériques utilisent l'équation du potentiel, soit complète [4], soit sous la forme linéarisée correspondant à l'hypothèse des petites perturbations transsoniques [5-6]. Les résultats fournis par ces différentes méthodes présentent déjà des sources de désaccord, en ce sens que les schémas numériques adoptés permettent une résolution plus ou moins exacte des équations. La confrontation avec l'expérience est encore moins bonne. La cause première du désaccord réside dans l'hypothèse consistant à négliger complètement la viscosité. On sait qu'en règle générale la détermination précise de l'écoulement autour d'un obstacle doit tenir compte de l'effet de déplacement produit par la couche limite. Aux vitesses subsoniques ou supersoniques, la correction sur les pressions pariétales qui en résulte est le plus souvent faible, hormis les cas où un décollement existe. En transsonique, par contre, la solution dépend beaucoup plus fortement de la forme effective de l'obstacle, cette influence se faisant surtout sentir, en supercritique, sur la position de l'onde de choc.

L'importance des effets visqueux en transsonique est illustrée par la figure 1 où trois méthodes de calcul sont comparées à l'expérience. L'exemple choisi est celui d'un demi-profil circulaire, d'épaisseur relative 12%, monté sur une des parois d'un canal bidimensionnel. On note un très grand écart entre la théorie et l'expérience sur la partie aval du profil où la recompression entraîne un épaississement rapide de la couche limite.

L'interaction entre la zone dissipative et l'écoulement extérieur, considéré comme non visqueux, joue un rôle essentiel dans les cas où un décollement se forme. La figure 2 montre quels sont alors, d'après Pearcey [7], les différents schémas d'écoulement qui peuvent s'établir sur la partie aval du profil. En a, un bulbe de décollement prend naissance au pied de l'onde de choc; en b un deuxième décollement apparaît

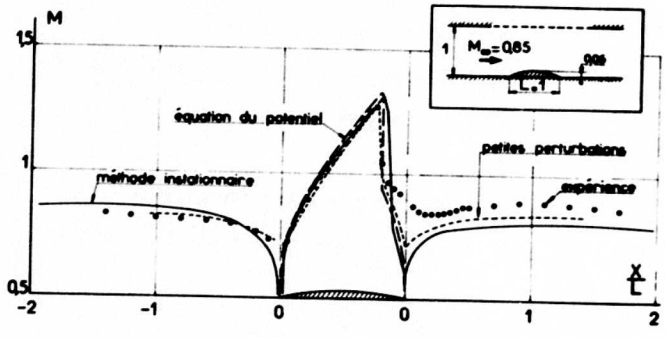

Fig. 1 CALCULS DE L'ÉCOULEMENT AUTOUR D'UN PROFIL TRANSSONIQUE

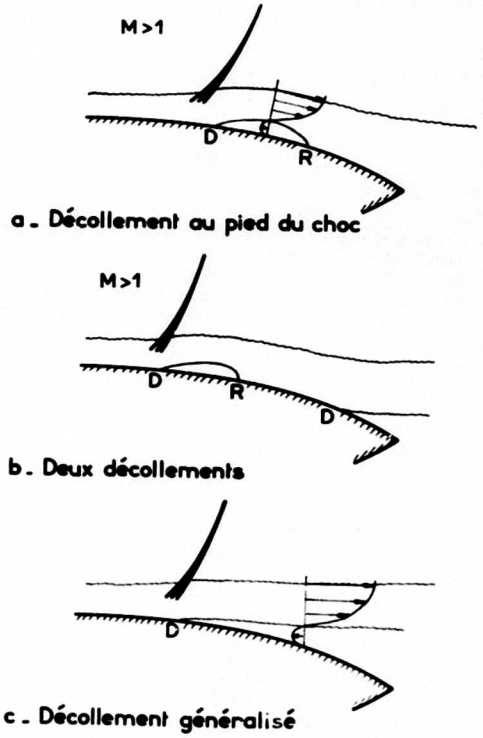

Fig. 2 - INTERACTIONS VISQUEUSES EN TRANSSONIQUE (d'après PEARCEY)

au cours de la recompression plus progressive qui suit l'onde de choc. Enfin, en c, les deux régions décollées se sont rejointes pour former un bulbe étendu.

Dans ces conditions, la détermination de la répartition de pression sur le profil nécessite le calcul conjoint de l'écoulement extérieur non visqueux et de la couche dissipative. Pour les interactions sans décollement, les méthodes de couplage classiques peuvent être appliquées. En revanche, si un décollement est susceptible de se produire, les équations de la couche limite sous la forme où elles sont habituellement intégrées deviennent singulières. Cette circonstance oblige à modifier la procédure par l'adoption de modes de calcul inverses [8-9] qui seront discutés plus loin.

Dans tous les cas, l'amélioration des méthodes de calcul des écoulements transsoniques passe par une connaissance approfondie des effets visqueux. En particulier, il est essentiel de pouvoir prédire le comportement de la couche limite à la traversée de l'onde de choc et d'être en mesure de décrire la structure des zones décollées.

Sur le plan fondamental, les phénomènes en question ont fait l'objet de quelques études expérimentales, certaines déjà anciennes [10], d'autres plus récentes [11-12]. Les renseignements tirés des sondages détaillés des couches dissipatives sont très instructifs, bien que de portée encore limitée. Afin d'étendre ces résultats, une étude de base a été entreprise à l'ONERA. Son originalité réside dans l'emploi de l'interférométrie comme moyen d'investigation.

La première partie de cette communication présentera une analyse expérimentale de l'écoulement autour d'un demi-profil avec forte interaction visqueuse. La deuxième partie sera consacrée à un examen des méthodes de calcul développées pour traiter ce genre de problème.

2 - ETUDE EXPERIMENTALE.

2.1 - Montage d'essai et techniques de mesure.

Les expériences ont été effectuées dans une veine transsonique bidimensionnelle dont la largeur est de 120 mm et la hauteur, à l'entrée du canal, de 100 mm. La soufflerie fonctionne en continu, les conditions génératrices étant voisines de l'ambiante, soit :

- pression $p_i \simeq 1$ bar,
- température $T_i \simeq 290$ K.

Le schéma de l'installation est donné figure 3. Le demi-profil étudié est fixé sur la paroi inférieure de la veine. Cette disposition a été adoptée afin que, dans la zone de mesure, la couche limite soit pleinement turbulente et assez épaisse pour se prêter à une analyse détaillée de sa structure (immédiatement en amont du bord d'attaque du profil l'épaisseur physique δ est voisine de 5 mm).

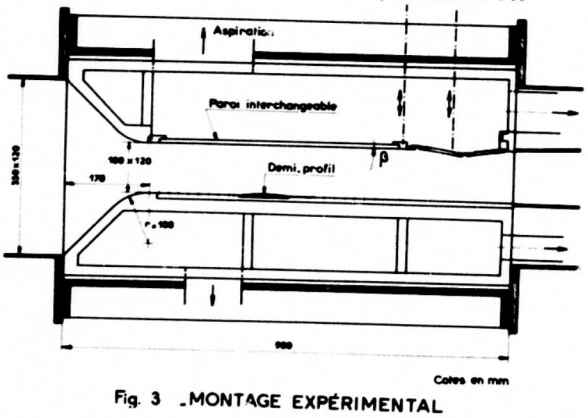

Fig. 3 .MONTAGE EXPÉRIMENTAL

La paroi supérieure du canal est constituée d'une plaque plane très rigide qui peut être pleine ou perforée. Le champ aérodynamique autour d'un profil de forme donnée peut être régulé en agissant sur les trois paramètres suivants :

- angle β de convergence ou de divergence de la paroi supérieure,
- hauteur du deuxième col,
- intensité et répartition de l'aspiration au travers de la plaque perméable.

Soulignons que les essais, dont les résultats vont être présentés, ont tous été effectués avec une paroi supérieure pleine. Les dimensions géométriques des profils essayés sont données figure 4. Le premier profil est symétrique, de forme circulaire; sa corde est égale à 100 mm et son épaisseur à 7 mm. Le deuxième profil a un contour asymétrique. La moitié amont est une courbe de degré 6 qui assure la continuité de la pente et de la courbure au raccordement avec le plancher amont rectiligne. La partie aval est de forme circulaire. Chaque profil est équipé de prises de pression statique disposées longitudinalement dans le plan de symétrie.

L'analyse des phénomènes d'interaction visqueuse en transsonique fait le plus largement appel à l'interférométrie quantitative, technique de mesure qui présente le double avantage de fournir un très grand nombre de renseignements sur la structure du champ aérodynamique et d'éviter l'introduction de sondes au sein de l'écoulement [13-14].

Rappelons le principe de la mesure de la masse

a - Profil symétrique

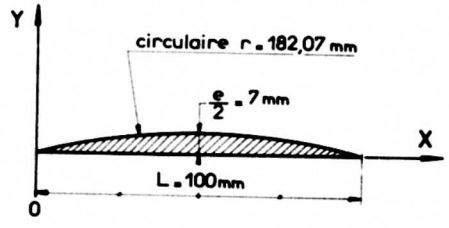

b - Profil asymétrique

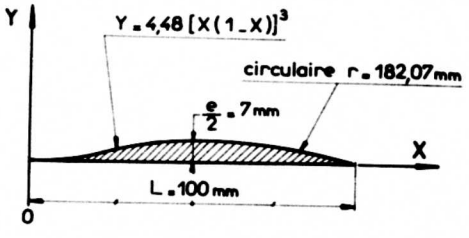

Fig. 4 .DÉFINITION DES PROFILS

spécifique au sein d'un écoulement par interférométrie. L'appareil utilisé est du type Mach Zehnder. Il peut être réglé, soit en "teinte plate", soit en "franges serrées". Dans le premier mode de fonctionnement, les variations d'éclairement sur l'interférogramme pris en marche correspondent directement aux variations de la masse spécifique ρ . La méthode permettant alors de calculer ρ est résumée figure 5.

Le réglage en teinte plate donne une représentation de la structure du champ aérodynamique puisque, dans ce cas, les franges sont des courbes iso-ρ , donc également des iso-Mach dans les régions où l'écoulement est isentropique. Cependant, comme en pratique, seuls les

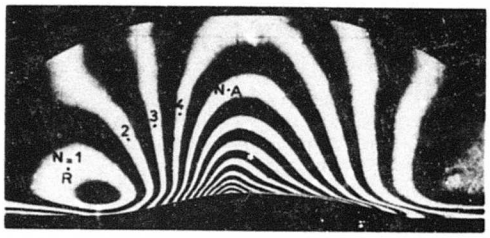

$$\nu = 1 + B\rho \qquad \text{(Loi de GLADSTONE-DALE)}$$

$$\frac{\rho_A}{\rho_{i_0}} = \frac{\lambda}{b\,B\,\rho_{i_0}} (N_A - N_R) + \frac{\rho_R}{\rho_{i_0}}$$

$\lambda = 0{,}5461\ \mu m$ (longueur d'onde)

$b = 0{,}12\ m$ (largeur de veine)

$B = 0{,}2275\ 10^{-3}\ m^3/kg$ (pour 0,5461 μm)

Fig. 5 PRINCIPE DU DÉPOUILLEMENT
RÉGLAGE EN TEINTE PLATE

milieux des franges peuvent être repérés avec précision, ce mode de réglage ne permet pas de déceler des variations de ρ correspondant à moins d'une demi-frange, ce qui restreint le nombre des points de mesure dans les régions où la masse spécifique varie peu. Aussi, afin d'améliorer la précision, en multipliant les pointés, on adopte plutôt le réglage en franges serrées qui consiste à introduire une différence de marche variable d'un point à l'autre du champ par rotation d'une lame séparatrice ou d'un miroir autour d'une droite de son plan. Le phénomène aérodynamique superpose alors en chaque point la différence de marche qui lui est propre à celle qui provient du réglage initial.

Le calcul de la masse spécifique à partir d'un interférogramme en franges serrées s'effectue de la façon suivante (voir figure 6). Il est d'abord procédé au numérotage des franges sur le cliché pris à l'arrêt. Celles-ci sont ensuite numérotées sur le cliché pris en marche. Désignons par R un point du champ où la masse spécifique ρ_R est connue, par N_R et n_R les numéros de frange en R en marche et à l'arrêt respectivement. Soit un point A où les numéros sont N_A et n_A.

La masse spécifique en A est donnée par :

$$\frac{\rho_A}{\rho_{i_0}} = \frac{\lambda}{b\,B\,\rho_{i_0}} \left[(N_A - n_A) - (N_R - n_R) \right] + \frac{\rho_R}{\rho_{i_0}}$$

Le repérage très précis du milieu des franges (blanches et noires) est obtenu par analyse des clichés sur un microdensitomètre Joyce-Loebl. Pour chaque configuration étudiée, les interférogrammes pris à l'arrêt, puis en marche, sont explorés selon un certain nombre de directions perpendiculaires à la corde $X'X$ du profil.

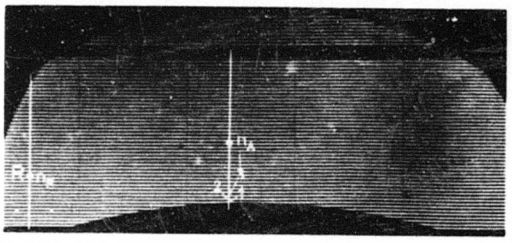

a - cliché à l'arrêt

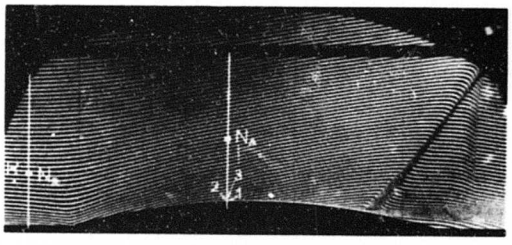

b - cliché en marche

$$\frac{\rho}{\rho_{i_0}} = \frac{\lambda}{b\,B\,\rho_{i_0}} \left[N_A - n_A - (N_R - n_R) \right] + \frac{\rho_R}{\rho_{i_0}}$$

Fig. 6 PRINCIPE DU DÉPOUILLEMENT
RÉGLAGE EN FRANGES SERRÉES

Dans les régions où l'écoulement est isentropique, la connaissance de la masse spécifique suffit pour déterminer les autres grandeurs aérodynamiques, telles le nombre de Mach, la pression ou encore le module de la vitesse. En revanche, dans les zones dissipatives le calcul de la vitesse nécessite soit une mesure supplémentaire, soit l'adoption d'une hypothèse permettant de relier μ et ρ . Pour les dépouillements présentés ici, nous avons utilisé la loi de Crocco modifiée.

Désignant par :

T_p la température de paroi,

T_f " " frottement,

T_e " " à la frontière ,

cette relation s'écrit :

$$\frac{T}{T_e} = \frac{T_p}{T_e} + \frac{T_f - T_p}{T_e} \frac{u}{u_e} - \left(\frac{T_f}{T_e} - 1 \right) \left(\frac{u}{u_e} \right)^2$$

En régime permanent $T_p = T_f$, la température de frottement étant donnée par :

$$\frac{T_f}{T_e} = 1 + r\,\frac{\gamma - 1}{2} M_e^2 \qquad (r = 0{,}9 \text{ en turbulent})$$

Si la couche limite est transversalement isobare:

$$\frac{T}{T_e} = \frac{\rho_e}{\rho}$$

Cette hypothèse n'est pas toujours vérifiée dans le cas présent où les couches limites ont une épaisseur non négligeable devant la corde du profil et où les accélérations longitudinales sont importantes, spécialement lors de la détente sur la partie amont du profil. Dans ces conditions :

$$\frac{T}{T_e} = \frac{\rho_e}{\rho}\,\frac{\pi}{\pi_e}$$

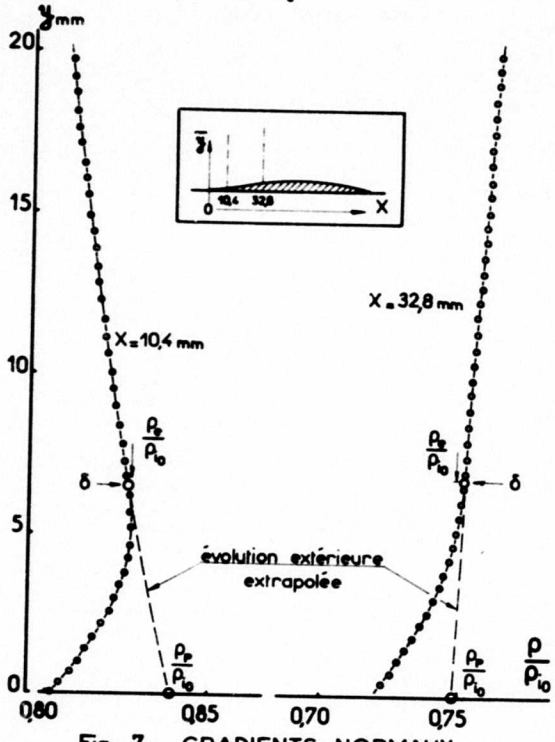

Fig. 7 GRADIENTS NORMAUX DANS LA COUCHE LIMITE_PROFIL ASYMÉTRIQUE

La mesure de la pression statique s'avérant malaisée et peu sûre dans un écoulement rapidement variable, il a été jugé préférable de déterminer $\pi(y)$ en extrapolant l'évolution extérieure de ρ jusqu'à la paroi (voir figure 7) π et ρ étant reliées par la relation de détente isentropique :

$$\frac{\pi}{\pi_e} = \left(\frac{\rho}{\rho_e}\right)^{\gamma}$$

Une telle façon de procéder est justifiée par le fait que la pression déduite de la valeur "paroi" ρ_p est en bon accord avec les mesures pariétales.

2.2 - Résultats obtenus.

Les répartitions de nombre de Mach, déduites des mesures de pression effectuées sur les parois supérieures et inférieures du canal, sont données figures 8a et 8b pour le profil symétrique et 9a et 9b pour le profil asymétrique. Lorsque la veine présente une divergence importante (β voisin de 1°), l'écoulement demeure entièrement subsonique. La diminution progressive de β entraîne une détente de plus en plus grande de l'écoulement. Il se forme en premier lieu une poche supersonique terminée par un choc, d'abord très faible (configuration 2). Le nombre de Mach maximal augmentant, le choc devient plus intense alors que la distribution de pression sur le profil, en amont, est pratiquement figée. En aval de l'onde de choc, l'évolution $M(x)$ est largement commandée par le comportement de la couche limite. A partir des configurations 4 , l'allure des courbes reflète un processus de décollement - recollement caractérisé par l'existence d'un quasi-plateau suivi d'une recompression très progressive. Dans les deux cas, l'étendue de la zone décollée est maximale pour la configuration 4. Le décollement s'étend alors du pied du choc jusqu'au voisinage aval du bord de fuite. La longueur du bulbe décollé diminue ensuite progressivement au fur et à mesure que l'onde de choc recule. Pour la configuration 7, dans le cas du profil symétrique, elle est quasi nulle. Il est à noter que, lorsqu'il y a décollement, le rapport M_1/M_0 des nombres de Mach après et avant décollement est compris entre 0,75 et 0,77, valeur en bon accord avec le critère simplifié souvent utilisé en turbulent. Au cours de décollements de ce type, l'écoulement non visqueux, contigu à la zone dissipative, demeure supersonique après séparation, comme on

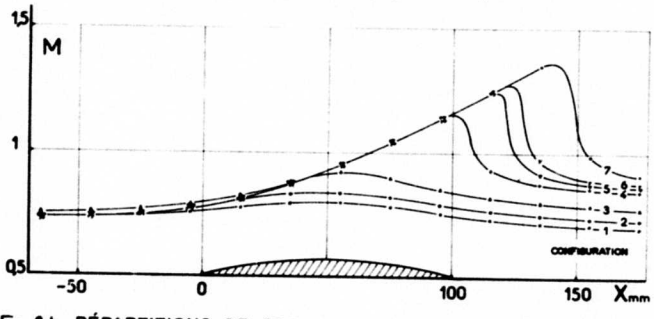

Fig. 8 b RÉPARTITIONS DE PRESSION SUR LA PAROI SUPÉRIEURE PROFIL SYMÉTRIQUE

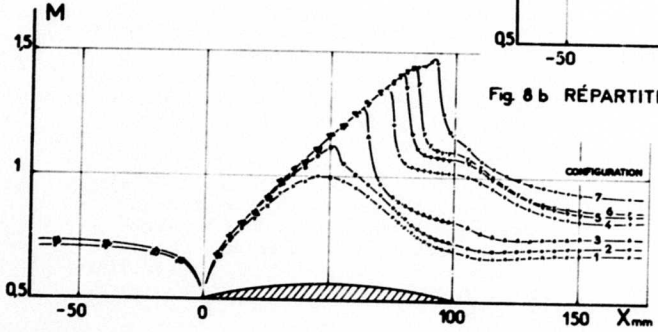

Fig. 8 a RÉPARTITIONS DE PRESSION SUR LA PAROI INFÉRIEURE PROFIL SYMÉTRIQUE

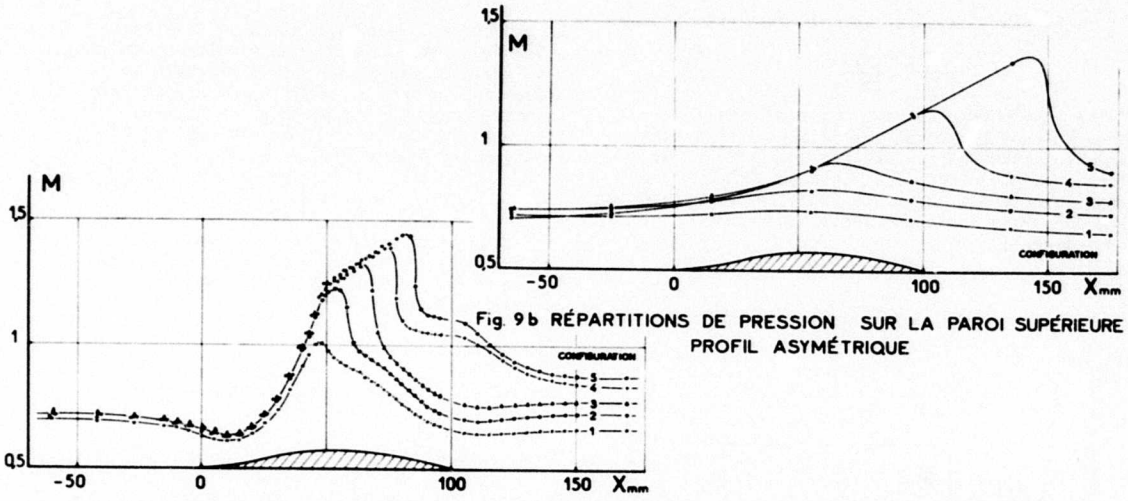

Fig. 9b RÉPARTITIONS DE PRESSION SUR LA PAROI SUPÉRIEURE PROFIL ASYMÉTRIQUE

Fig. 9a RÉPARTITIONS DE PRESSION SUR LA PAROI INFÉRIEURE PROFIL ASYMÉTRIQUE

peut le constater figures 8a et 9a. En conséquence, le processus semble pouvoir être décrit par le modèle d'interaction libre initialement proposé par Chapman [15] puis généralisé au cas des écoulements non uniformes par Carrière et al [16]. La figure 10 montre les valeurs de la fonction de corrélation $\mathcal{F}$ évaluées pour les différentes configurations décollées. Rappelons que $\mathcal{F}$ est définie par la relation :

$$\mathcal{F} = \sqrt{\frac{P - P_0}{q_0} \quad \frac{P - \bar{P}}{C_{f_0}}}$$

où q est la pression dynamique $(q = \frac{1}{2}\rho V^2)$

P " le nombre de pression

$\bar{P}$ " " " à la même abscisse, s'il n'y avait pas décollement

C_f est le coefficient de frottement.

L'indice 0 désigne les conditions à l'origine de l'interaction.

(Le coefficient de frottement C_{f_0} a été estimé à partir de différents calculs de couche limite; la valeur moyenne $C_{f_0} = 0{,}004$ à été retenue).

On constate, figure 10, un très bon regroupement de $\mathcal{F}$ autour de la courbe de corrélation universelle, ce qui met en évidence le caractère essentiellement supersonique du décollement qui intervient au cours d'un processus interaction choc-couche limite en transsonique.

Les figures 11 à 14 montrent des interférogrammes de l'écoulement relatifs aux configurations 2, 3, 5 et 7 pour le profil symétrique. Ils correspondent à des cas jugés comme les plus typiques. Les figures comportent également la répartition de pression associée à chaque visualisation. On remarquera la cassure des franges qui marque la frontière δ de la couche limite sur la partie amont du profil.

A peine perceptible pour la configuration 2 (figure 11), le choc devient très apparent sur le deuxième interférogramme (figure 12). Dans le troisième cas (configuration 5, figure 13), il se produit un phénomène de choc en lambda : un premier choc oblique prend naissance près du bord de fuite du profil; la zone faiblement supersonique qui lui succède est limitée par un choc droit très peu intense. Enfin, le dernier interférogramme montre un choc oblique situé pratiquement au bord de fuite. On constate que, dans ce cas, l'épaississement de la couche dissipative est nettement moins important que dans les exemples 3 et 5 précédents.

Nous allons maintenant examiner les résultats de l'exploitation des répartitions de masse spécifique au travers de la couche limite pour le profil symétrique de forme circulaire.

Dans le premier cas analysé (configuration 3), un choc quasi-normal se forme à environ 70% de la corde, l'écoulement dans le canal n'étant pas bloqué. Les figures 15a et 15b montrent, à titre d'exemple, quelques unes des répartitions de vitesse mesurées dans la couche limite, d'abord en amont de l'onde de choc (figure 15a), puis en aval de celle-ci (figure 15b). En amont du choc, les profils de vitesse sont fortement déformés sous l'effet du gradient de pression négatif intense. Cette altération se traduit par un remplissage des distributions au voisinage de la paroi, sans que l'épaisseur δ de la couche dissipative diminue sensiblement. Ainsi, u/u_e est voisin de 0,9 à une hauteur relative y/δ égale à 0,05. Ce phénomène a déjà été observé par Alber et al. [12] dans des expériences effectuées sur un montage analogue au nôtre. En aval du choc, les profils sont sensiblement modifiés par la recompression rapide. Les régions à basse vitesse voient leur importance relative augmenter considérablement. On notera surtout, après une variation rapide près de la paroi, une tendance très progressive de u/u_e vers 1, ce qui donne lieu à une quasi-cassure dans la forme des distributions de vitesse. Les strioscopies à court temps d'exposition de la figure 16 montrent quelle est l'origine de ce phénomène : on y observe la formation d'une zone tourbillonnaire en aval de l'onde de choc. L'apparition de ces tourbillons est probablement due à une oscillation de l'onde de choc à fréquence élevée. Il en résulte un épaississement très important de la couche dissipative et, dans les sondages, il est difficile de faire la part entre la couche limite proprement dite et la région tourbillonnaire adjacente.

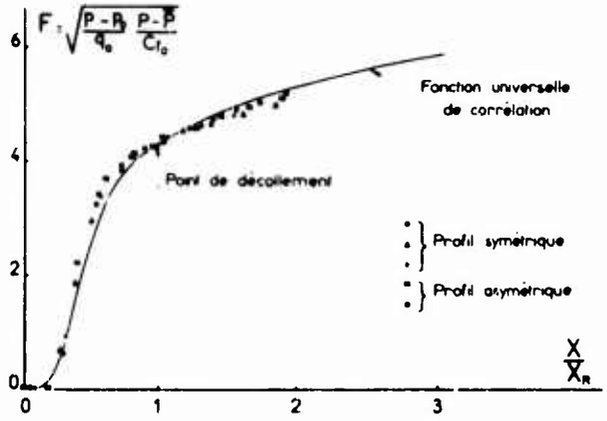

Fig. 10 INTERACTION AVEC DÉCOLLEMENT
CORRÉLATION DES PRESSIONS

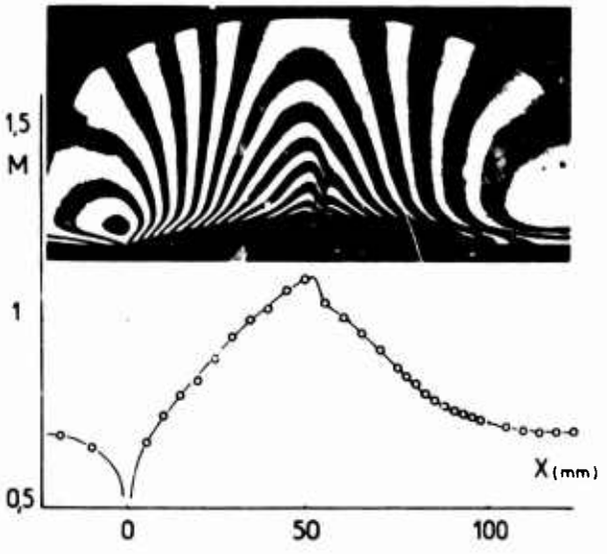

Fig. 11 INTERFÉROGRAMME DE L'ÉCOULEMENT
PROFIL SYMÉTRIQUE - CONFIGURATION 2

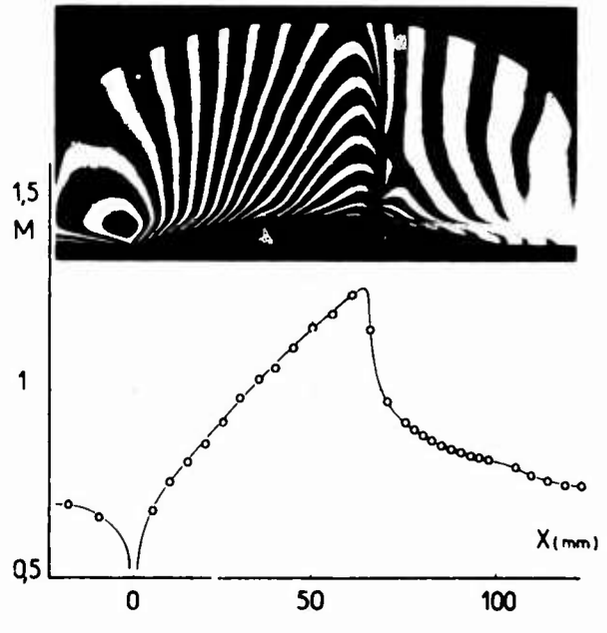

Fig. 12 INTERFÉROGRAMME DE L'ÉCOULEMENT
PROFIL SYMÉTRIQUE - CONFIGURATION 3

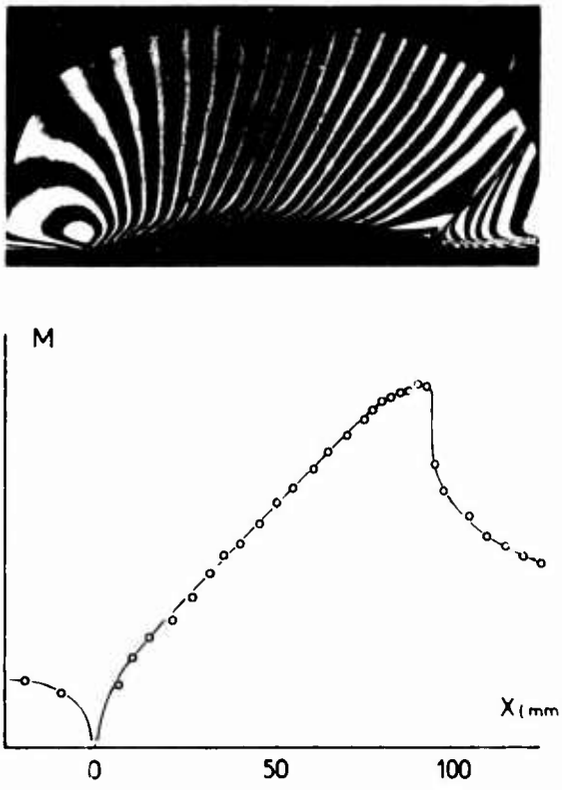

Fig. 14 INTERFÉROGRAMME DE L'ÉCOULEMENT
PROFIL SYMÉTRIQUE - CONFIGURATION 7

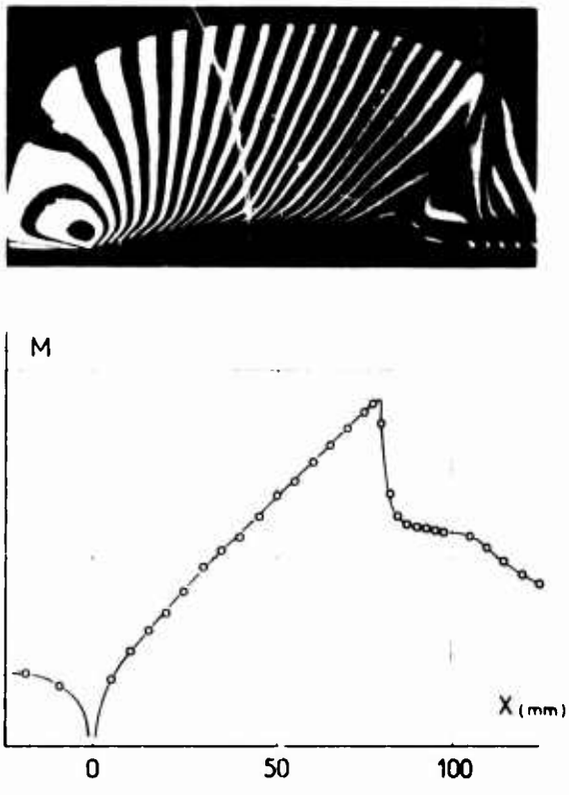

Fig. 13 INTERFÉROGRAMME DE L'ÉCOULEMENT
PROFIL SYMÉTRIQUE - CONFIGURATION 5

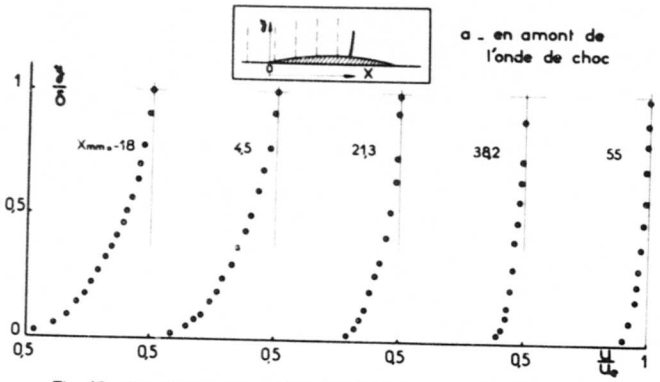

Fig. 15a PROFILS DE VITESSE DANS LA COUCHE LIMITE
PROFIL SYMÉTRIQUE - CONFIGURATION 3

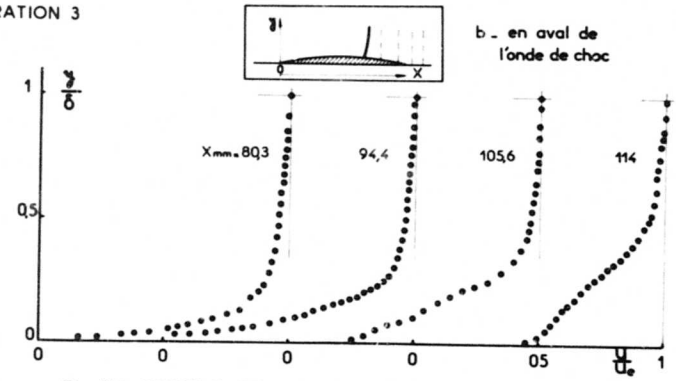

Fig. 15 b PROFILS DE VITESSE DANS LA COUCHE LIMITE
PROFIL SYMÉTRIQUE - CONFIGURATION 3

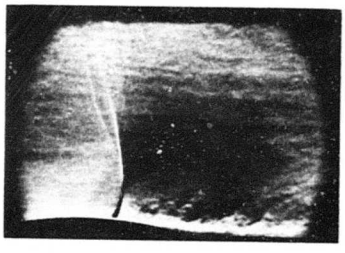

a - couteaux horizontaux

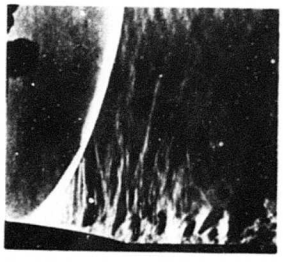

b - couteaux verticaux

Fig. 16 VISUALISATIONS DE L'ECOULEMENT
PAR STRIOSCOPIE ECLAIR ($t \simeq 1\,\mu s$)

La figure 17 montre les évolutions des épaisseurs caractéristiques δ_1 et δ_2 ainsi que du paramètre de forme incompressible H_i (H_i est défini à partir des épaisseurs "incompressibles" :

$$\delta_{1i} = \int_0^\delta \left(1 - \frac{u}{u_e}\right) dy \quad , \quad \delta_{2i} = \int_0^\delta \frac{u}{u_e}\left(1 - \frac{u}{u_e}\right) dy \quad \text{par } H_i = \frac{\delta_{1i}}{\delta_{2i}}$$

La très forte détente en amont de l'onde de choc entraîne une décroissance importante de δ_1 et δ_2, ainsi que de H_i qui tend vers des valeurs proches de l'unité ($H_i \simeq 1{,}07$).

En aval du choc, l'existence des tourbillons dont il a été question plus haut conduit à une augmentation considérable de δ_1 et δ_2, sans que H_i croisse dans des proportions aussi grandes. La valeur de H_i en aval du choc, proche de 1,5, indique que la couche limite ne décolle pas. En revanche, au bord de fuite du profil, on observe une croissance rapide de δ_1, δ_2 et H_i causée par la discontinuité de pente qui provoque, vraisemblablement, un décollement localisé.

La figure 18 présente les résultats relatifs à la configuration 5 où l'interaction se fait par choc oblique avec décollement de la couche limite. On note une augmentation plus modérée de δ_1 et δ_2 à la traversée de l'onde de choc puis une forte croissance de ces quantités corrélative au décollement. Le paramètre de forme H_i atteint une valeur proche de 2 derrière le choc, il tend ensuite à décroître en aval du profil. Il est à noter que si l'on évalue, grossièrement, la discontinuité de pente au niveau du choc en dérivant $\delta_1(x)$, on trouve une déflexion proche de 7° qui est rapprocher de la valeur 8° déterminée par les relations de choc oblique à partir des nombres de Mach Mo et M1 de part et d'autre du choc. Compte tenu de l'imprécision dans l'estimation de $d\delta_1/dx$, on peut considérer que l'accord est satisfaisant.

Dans le cas de la configuration 7 (voir figure 19), l'interaction a lieu sans décollement perceptible de la couche limite. En outre, quand l'écoulement extérieur demeure entièrement supersonique au cours du processus, on n'observe pas les instabilités affectant la configuration 3. Pour ces deux raisons, la croissance de δ_1, δ_2 et H_i est sensiblement moins forte que dans les exemples précédents.

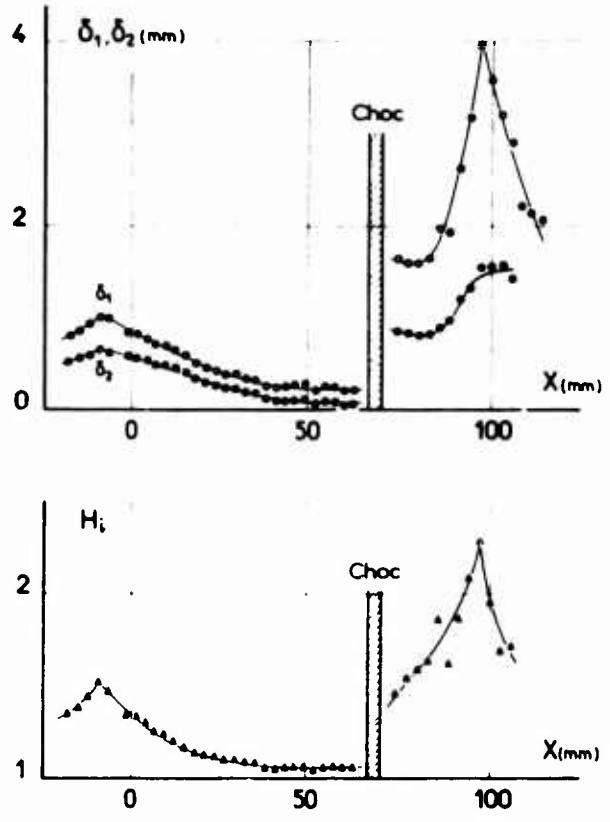

Fig. 17 GRANDEURS CARACTÉRISTIQUES DE LA COUCHE LIMITE
PROFIL SYMÉTRIQUE - CONFIGURATION 3

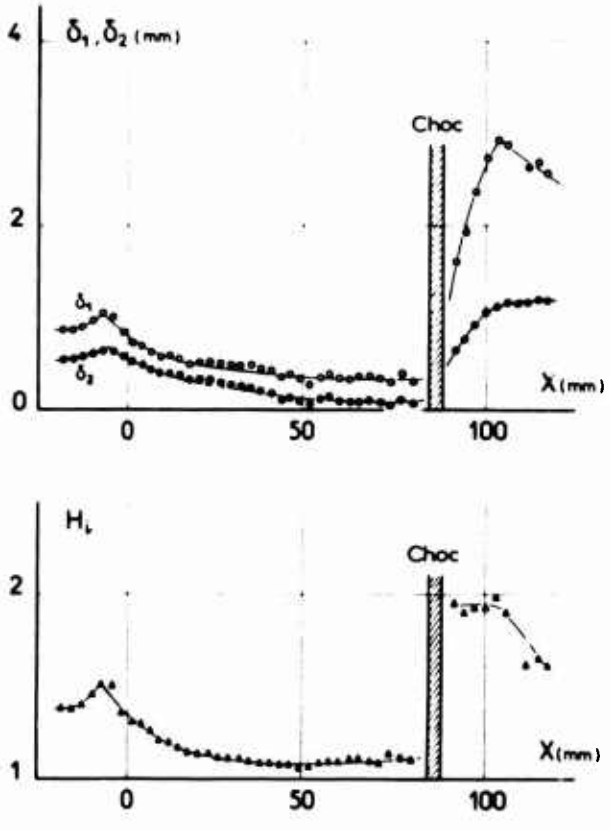

Fig. 18 GRANDEURS CARACTÉRISTIQUES DE LA COUCHE LIMITE
PROFIL SYMÉTRIQUE - CONFIGURATION 5

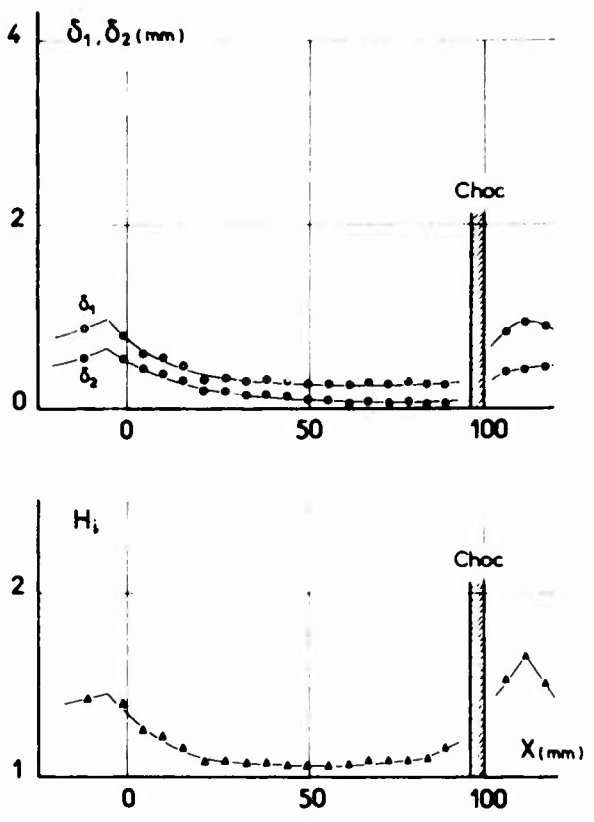

Fig. 19 GRANDEURS CARACTÉRISTIQUES DE LA COUCHE LIMITE
PROFIL SYMÉTRIQUE - CONFIGURATION 7

3 - DISCUSSION DES PROBLEMES DE CALCUL.

3.1 - Principe général d'une méthode permettant la prise en compte des effets visqueux.

Les expériences présentes ont été effectuées de manière à servir de guide pour le développement d'une méthode de calcul des écoulements transsoniques avec forte interaction visqueuse, inspirée du modèle proposé par Klineberg [6]. En gros, cette technique consiste à coupler le calcul du champ extérieur considéré comme non visqueux et celui de la zone dissipative dont l'évolution est décrite par les équations de la couche limite. Dans les méthodes usuelles qui tiennent compte de l'effet de déplacement, le calcul de fluide parfait fournit la répartition $M_e(x)$ à imposer sur la frontière de la couche limite pour déduire $\delta_1(x)$ dont la connaissance permet de corriger la condition de pente à afficher sur le profil, soit :

$$\varphi_p + \theta$$

θ étant la déflexion causée par les effets visqueux.

Une telle façon de procéder devient inapplicable lorsqu'un décollement se produit car, alors, le calcul de couche limite diverge à l'approche du point de séparation. Pour éviter cette singularité, l'écoulement autour du profil est divisé en deux zones : sur la partie amont, l'interaction visqueuse est considérée comme faible et on procède de la manière habituelle, la distribution $M_e(x)$ étant donnée par le calcul de fluide parfait. Dans la région aval ou l'interaction est susceptible de conduire à un décollement, c'est $\varphi_p + \theta$ qui est demandé au champ non visqueux. Utilisant une méthode inverse, la résolution des équations de la couche limite donne alors $M_e(x)$. Un

nouveau calcul de l'écoulement extérieur est effectué en imposant comme conditions aux limites $\varphi_p + \theta$ dans la zone d'interaction faible, puis $M_e(x)$ dans la région d'interaction forte. Il en résulte deux nouvelles répartitions, $M_e(x)$ en amont et $\theta(x)$ en aval qui permettent d'entamer un nouveau cycle. Le processus est répété jusqu'à convergence sur $\theta(x)$, par exemple.

Afin d'appliquer ce modèle théorique au problème d'un profil placé dans un canal transsonique, deux méthodes ont été développées pour calculer le champ non visqueux d'une part, la couche limite d'autre part.

3.2 - Calcul de l'écoulement de fluide parfait.

On utilise la méthode de relaxation pour les composantes de la vitesse en théorie transsonique des petites perturbations. Le choix de ces variables est en effet commode pour le traitement des problèmes aux limites.

Soient x et y les variables indépendantes du plan de l'écoulement. L'axe Ox est choisi parallèle et orienté dans la direction de l'écoulement non perturbé, u et v sont respectivement les composantes longitudinale et transversale de la vitesse de perturbation, la vitesse de référence U_∞ ainsi que le nombre de Mach M_∞ étant choisis pour l'écoulement non perturbé.

Le système d'équations aux dérivées partielles du premier ordre auquel doivent satisfaire u et v s'écrit alors de la façon classique :

$$\frac{\partial \sigma}{\partial x} + \frac{\partial v}{\partial y} = 0$$

$$-\frac{\partial v}{\partial x} + \frac{\partial u}{\partial y} = 0$$

avec :

$$\sigma = \sigma(u) = \left(1 - M_\infty^2 - \frac{\gamma+1}{2} M_\infty^2 u\right) u$$

les équations couplées sont non linéaires par l'intermédiaire du terme σ et du type mixte : lorsque $u < u^*$ le système est du type elliptique et hyperbolique si $u > u^*$

La ligne parabolique (ligne sonique) correspond à $u = u^*$ où

$$u^* = \frac{1 - M_\infty^2}{(\gamma+1) M_\infty^2}$$

Nous considérons ici des écoulements transsoniques autour de demi-profils montés sur la paroi inférieure d'un canal parallèle ou faiblement divergent à grande distance.

Sur les parois du canal deux types de conditions aux limites sont possibles :

- la pente locale du profil ou de la paroi est donnée. La condition de glissement linéarisée pour la paroi inférieure s'écrit :

$$v_0 = f'(x) \quad (f(x) \text{ est l'équation de la paroi})$$

On dira que dans ce cas le calcul est effectué en mode direct.

- la pression locale est donnée. On connait alors u ; en effet, la théorie montre que le coefficient de pression est relié à u par $K_p = -2u$. La condition s'écrira par exemple :

$$u_0 = -\frac{K_p(x)}{2}$$

On dira que le calcul est effectué en mode inverse. Sur la paroi supérieure, nous supposerons que l'écoulement est toujours subsonique et que les gradients de vitesse sont modérés. Nous y appliquerons une condition de glissement.

Dans le cas d'un canal parallèle à grande distance et de sections d'entrée et de sortie égales, on appliquera à l'amont et à l'aval des conditions de retour à l'écoulement uniforme non perturbé, soit :

$$u, v \to 0 \quad \text{si} \quad x \to \pm\infty$$

Dans les autres cas, on choisit de raccorder la solution avec une solution asymptotique possible des équations correspondant à un canal divergent:

$$\begin{cases} \sigma = \sigma(x) = \alpha + \beta x \\ v = v(y) = -\beta y + \gamma \end{cases}$$

où α, β, γ sont des constantes.

La méthode de relaxation généralisée de Steger et Lomax [4] permet de résoudre des systèmes d'équations aux dérivées partielles du premier ordre. Cette méthode consiste à évaluer les dérivées $\frac{\partial}{\partial y}$ au moyen d'un schéma implicite décentré à trois points, alternativement vers le haut et vers le bas. Les inconnues colonnes sont alors solution d'un système dont la matrice est tridiagonale, à diagonale dominante et dont l'inversion par une méthode directe est rapide et stable. Bailey et Steger [18] ont étendu cette méthode aux écoulements transsoniques tridimensionnels en mode direct. Steger et Klineberg [19] ont effectué des calculs inverses bidimensionnels qui leur ont permis d'aborder le problème du couplage fluide-parfait - fluide visqueux en subsonique et transsonique. C'est cette approche que nous avons choisi. Les schémas utilisés ici ont été rendus entièrement conservatifs par l'introduction d'un "point choc" pour l'évaluation des dérivées $\frac{\partial}{\partial x}$, comme l'indique Murman [20] et par une modification du schéma de discrétisation des dérivées $\frac{\partial}{\partial y}$.

La figure 20 montre l'application de cette méthode sur un cas modèle. La répartition de vitesse $u_0(x)$ sur un profil bi-convexe dans un canal parallèle est obtenue en mode direct. A partir de ce résultat, on effectue un calcul en mode mixte : mode inverse pour $0{,}5 \leq x \leq 1{,}1$, mode direct pour le reste du profil. L'intégration de la singularité au bord de fuite fait apparaître un léger décalage en v.

3.3 - Calcul de la couche dissipative.

Dans le but d'analyser les phénomènes d'interaction visqueuse en transsonique une nouvelle méthode intégrale pour le calcul de la couche limite a été développée. La première relation utilisée est l'équation de Von Karman qui s'écrit :

$$(1)\quad \frac{d\delta_2}{dx} + \delta_2 \left[(H+2)\frac{1}{u_e}\frac{du_e}{dx} + \frac{1}{\rho_e}\frac{d\rho_e}{dx}\right] = \frac{C_f}{2}$$

La deuxième relation est l'équation intégrale

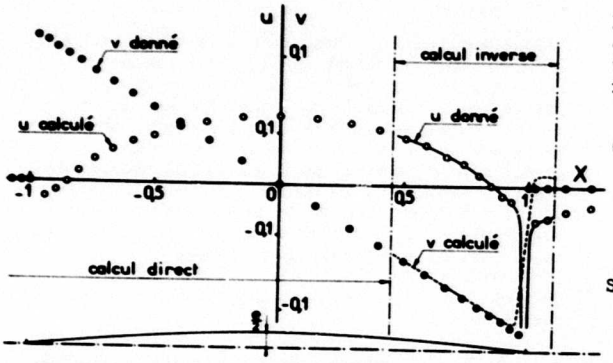

Fig. 20 . CALCUL DE L'ÉCOULEMENT DE FLUIDE PARFAIT
MÉTHODE DE RELAXATION GÉNÉRALISÉE
$\mathcal{R}_\delta = 006$ $M_\infty = 0.7$

de l'énergie cinétique :

$$(2)\quad \frac{d\delta_3}{dx} + \delta_3 \frac{d}{dx}\left(\log \rho_e u_e^3\right) - (\delta - \delta_1)\frac{d}{dx}\left(\log u_e^2\right) - \frac{2}{\rho_e u_e^2}(\delta - \delta_{1i})\frac{dp}{dx} = \phi$$

où δ_3 est l'épaisseur d'énergie cinétique :

$$\delta_3 = \int_0^\delta \frac{\rho u}{\rho_e u_e}\left(1 - \frac{u^2}{u_e^2}\right) dy$$

et ϕ l'intégrale de dissipation

$$\phi = \frac{2}{\rho_e u_e^3}\int_0^\delta \tau \frac{\partial u}{\partial y}\, dy$$

Les profils de vitesse turbulents adoptés sont inspirés de la famille proposée par Coles [20]. En incompressible, ils sont représentés par :

$$(3)\quad \frac{u}{u_e} = 1 + C_1 \log \eta - C_2 f(\eta) \quad \text{avec } \eta = \frac{y}{\delta}$$

$$C_1 = \frac{u_\tau}{0{,}41\, u_e} \qquad C_2 = 2{,}24\,(\alpha - C_1)$$

$f(\eta)$ est un polynôme de degré 10 en $\sqrt{\eta}$ qui est une forme améliorée de la composante sillage de la loi de Coles [22]. Rappelons que u_τ est la vitesse de frottement définie par :

$$u_\tau = \sqrt{\frac{\tau_p}{\rho_p}}$$

d'où

$$\frac{u_\tau}{u_e} = \sqrt{\frac{1}{2} C_{fi}}$$

Le "paramètre de forme" α est ici identifié au rapport :

$$\alpha = \frac{\delta_{1i}}{\delta}$$

où δ_{1i} est l'épaisseur de déplacement "incompressible" :

$$\delta_{1i} = \int_0^\delta \left(1 - \frac{u}{u_e}\right) dy$$

Raisonnant toujours en incompressible, le coefficient de frottement C_{fi} est calculé en fonction de α et $\mathcal{R}_\delta$ à partir de la relation donnée par Coles :

$$(4)\quad \frac{u}{u_e} = \frac{u_\tau}{u_e}\left(\frac{1}{0{,}41}\log \frac{y\, u_\tau}{\nu_p} + 5\right) + 2{,}24\left(\frac{\delta_{1i}}{\delta} - \frac{u_\tau}{0{,}41\, u_e}\right)(1 - f)$$

Se plaçant en $y = \delta$ (4) donne

$$1 = \frac{u_\tau}{u_e}\left[\frac{1}{0{,}41}\log\left(\mathcal{R}_\delta \frac{u_\tau}{u_e}\right) + 5\right] + 2{,}24\left(\frac{\delta_{1i}}{\delta} - \frac{u_\tau}{0{,}41\, u_e}\right)$$

d'où

$$(5)\quad \frac{\delta_{1i}}{\delta} = \frac{1}{2{,}24}\left\{-\frac{u_\tau}{u_e}\left[\frac{1}{0{,}41}\left(\log \mathcal{R}_\delta \frac{u_\tau}{u_e}\right) + 5 - \frac{2{,}24}{0{,}41}\right] + 1\right\}$$

Pour $\alpha = \frac{\delta_{1i}}{\delta}$ et $\mathcal{R}_\delta$ donnés, (5) constitue une équation implicite permettant de calculer u_τ/u_e, dont on déduit immédiatement C_{fi}.

Dans le cas compressible, si le nombre de Mach M_e est modéré ($M_e < 2$), l'expérience montre que l'on peut encore représenter les profils de vitesse par la relation (3), C_1 et C_2 étant calculés à partir de C_{fi} . Quant au coefficient de frottement compressible, on le calcule par la formule :

$$\frac{C_f}{C_{fi}} = \frac{1}{1 + \frac{\gamma - 1}{2} M_e^2}$$

qui, en l'absence de flux de chaleur, est en très bon accord avec d'autres évaluations.

L'intégrale de dissipation ϕ , supposée indépendante du nombre de Mach M_e et du nombre de Reynolds, est calculée à partir des résultats théoriques d'Alber [23]. L'indépendance de ϕ à l'égard de M_e est évidemment une approximation qui n'est vérifiée que pour les nombres de Mach M_e modérés ($M_e < 2$). En outre l'évolution $\phi(\alpha)$ adoptée n'est valable que si $\mathcal{R}_\delta$ est de l'ordre de 10^5 ce qui correspond sensiblement aux conditions des présents essais.

Si la couche limite décolle, les profils (3) sont remplacés par des profils de sillage d'équation :

$$(6)\quad \frac{u}{u_e} = 1 - 2{,}24\,\frac{\delta_{1i}}{\delta} f$$

qui peuvent comporter une zone de retour près de la paroi. Les distributions définies par (6) ont une vitesse non nulle à la paroi, néanmoins l'expérience montre, qu'en turbulent, ces profils sont très proches de la réalité. De plus, il est supposé que dans ces régions le frottement pariétal est nul.

Pour traiter les problèmes d'interaction visqueuse forte, on adjoint aux équations (1-2) une relation de couplage qui est obtenue en intégrant selon y , entre 0 et δ , l'équation locale de continuité D'où la relation :

$$(7)\quad \frac{d\delta_1}{dx} - (\delta - \delta_1)\frac{d}{dx}\left(\log \rho_e u_e\right) = \frac{1}{2}\theta$$

où θ est l'angle par rapport à la paroi du vecteur vitesse à la frontière δ de la couche limite. Une forme simplifiée de (7) souvent utilisée s'écrit :

$$(8) \qquad \frac{d\delta_1}{dx} = \gamma\,\theta$$

Afin de contrôler la validité de cette méthode, un calcul a été effectué à partir des résultats expérimentaux relatifs à la configuration 3 L'écoulement sur le profil est divisé en deux zones : en amont de l'onde de choc, l'interaction visqueuse étant considérée comme faible, la distribution $M_e(x)$ est celle fournie par l'expérience. La résolution du système (1-2) permet de déterminer toutes les grandeurs caractéristiques de la couche limite. Le calcul en mode inverse est démarré un peu en amont du choc. On impose alors, comme donnée, la déflexion $\theta(x)$ déduite des mesures de couche limite. La pente totale $\varphi_p + \theta(x)$ est tracée figure 21a. Elle se caractérise par une quasi-discontinuité au niveau du choc. Résolvant alors le système (1-2-8), où les inconnues sont une épaisseur, le paramètre de forme et le nombre de Mach, on en déduit la répartition $M_e(x)$ dans la zone d'interaction forte. Le résultat porté figure 21b est en bon accord avec l'évolution $M_e(x)$ mesurée, compte tenu de l'imprécision assez grande dans l'estimation de la déflexion θ à partir des expériences. Le calcul de couche limite prévoit l'existence d'une région décollée (DR) au voisinage du bord de fuite du profil.

Un tel résultat est très encourageant pour la mise au point d'une méthode de couplage puisqu'il montre que le comportement de la couche limite peut être convenablement prévu à la traversée de l'onde de choc, à condition d'adopter une procédure de calcul inverse.

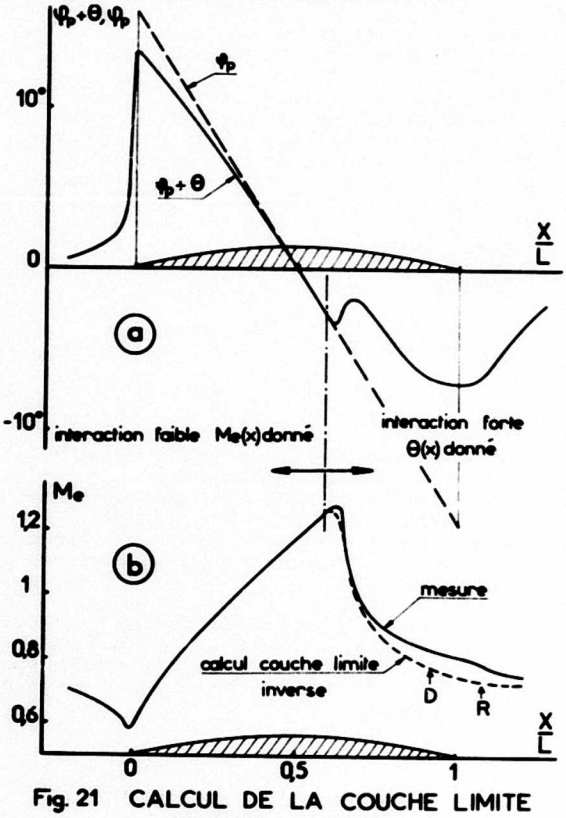

Fig. 21 CALCUL DE LA COUCHE LIMITE EN MODE INVERSE

4 - CONCLUSION.

L'écoulement autour d'un profil, en transsonique, est largement influencé par le développement de la couche limite, spécialement dans le cas où la présence d'une onde de choc engendre une interaction visqueuse notable. Afin d'approfondir la connaissance de ces phénomènes, une étude expérimentale de base est effectuée en écoulement plan. Le montage consiste en un demi-profil monté à la paroi inférieure de la veine d'essai. Dans le but d'éviter toute perturbation par l'introduction de sondes, il est largement fait appel à l'interférométrie quantitative. Les résultats obtenus jusqu'à présent ont mis en évidence les points suivants :

- la forte accélération qui précède l'onde de choc provoque une importante déformation des profils de vitesse (le paramètre de forme incompressible H_i devient voisin de l'unité),

- l'interaction avec le choc entraîne un épaississement notable de la couche limite et une déformation sensible des distributions de vitesse. Ces deux effets se traduisent par une quasi discontinuité des épaisseurs de déplacement et de quantité de mouvement. Il semble que, dans certains cas, l'épaississement de la région dissipative soit amplifié par des phénomènes instationnaires,

- l'apparition d'un bulbe d'écoulement décollé est fonction de l'intensité du choc et de la forme du profil. Lorsque le processus est entièrement supersonique il obéit aux règles de similitude de la corrélation de Chapman.

Parallèlement à cette expérimentation, et s'appuyant sur elle, on s'efforce de développer une méthode de calcul inspirée de l'approche de Klineberg. Le principe de cette théorie consiste à diviser l'écoulement en deux zones : dans les régions où le gradient de pression est soit négatif, soit modérément positif, on adopte le procédé de couplage classique entre le champ non visqueux et la couche limite. Dans les régions de compression notable, où un décollement est susceptible de se produire, une procédure inverse est utilisée ; la déflexion du vecteur vitesse à la frontière δ est donnée par l'écoulement non visqueux et imposée dans le calcul de couche limite qui fournit alors $M_e(x)$. Afin de mettre en oeuvre cette théorie, deux méthodes ont été développées, l'une pour la couche dissipative, l'autre pour l'écoulement non visqueux. La première est une technique intégrale qui utilise une famille de profils de vitesse proche de la loi de Coles. La seconde résoud les équations de l'écoulement transsonique dans l'hypothèse des petites perturbations. Elle permet d'afficher comme condition aux limites sur l'obstacle et en aval, soit l'angle, soit le module de la vitesse. Le couplage entre les deux zones converge et donne de bons résultats dans les cas subcritiques, en revanche sa mise au point n'est pas encore achevée lorsqu'il y a apparition d'une onde de choc.

REFERENCES.

[1] MAGNUS R. et YOSHIHARA H. "Inviscid transonic flow over airfoils" AIAA Journal, Vol. 8, N° 12 (1970).

[2] GROSSMAN B. et MORETTI A. "Time dependant computation of transonic flows" AIAA Paper 70-1322 (1970).

[3] LAVAL P. "Méthode de calcul de l'écoulement supercritique sur un profil placé dans une tuyère" N.T. ONERA N° 189 (1972).

[4] GARABEDIAN P.R. et KORN D.G. "Analysis of transonic airfoils" Com. Pure and Appl. Math., Vol 24, pp 841-851 (1971).

[5] MURMAN E.M. et COLES J.D. "Calculation of plane steady transonic flows" AIAA Journal, Vol. 9, N° 1 (1971).

[6] MURMAN E.M. "Computation of wall effects in ventilated transonic wind tunnels" AIAA Paper 72.1007 (1972).

[7] PEARCEY H.H. "Some effects of shock induced Separation of turbulent boundary layers in transonic flow post airfoils". NPL. FM 2261 (1955).

[8] KLINEBERG J.M. et STEGER J.L. "Calculations of separated flows at subsonic and transonic speeds". Proceedings of the 3 rd International Conference on Numerical Methods in Fluid Dynamics, Springer Verlag, Lecture Notes in Physics (1972).

[9] KUHN G.D. et NIELSEN J.N. "Prediction of turbulent Separated boundary layers" AIAA Paper N° 73.663 (1973).

[10] MICHEL R. "Couches limites en écoulement supersonique ralenti. Interaction couche limite - onde de choc" N.T. du Ministère de l'Air N° 73 (1958).

[11] ALBER I.E., BACON J.W., MASSON B.S. et COLLINS J.D. "An experimental investigation of turbulent transonic viscous - inviscid interactions" AIAA Journal. Vol. 11 N° 5 (1973).

[12] STANEWSKY E. et LITTLE B.H. "Separation and reattachment in transonic airfoil flow" Journal of Aircraft. Vol. 8., N° 12 (1971).

[13] GUIENNE P. et BOUNIOL F. "Détermination du champ des vitesses en aval d'un choc détaché à partir d'un interférogramme" - La Recherche Aéronautique N° 53 (1956).

[14] SOLIGNAC J.L. "Exemples d'application des méthodes de mesures optiques à des recherches fondamentales d'aérodynamique" AGARD - Rapport 398 (1960).

[15] CHAPMAN D.R., KUHN D.M. et LARSON H.K. "Investigation of separated flows in supersonic and subsonic streams with emphasis on the effect of transition" NACA Report 1356 (1958).

[16] CARRIERE P., SIRIEIX M. et SOLIGNAC J.L. "Propriétés de similitude des phénomènes de décollement laminaire ou turbulent en écoulement supersonique non uniforme" XIIème Congrès International de Mécanique appliquée - Stanford (1968) et TP ONERA 659 F (1968).

[17] STEGER J.L. et LOMAX H. "Generalized Relaxation methods applied to problem in transonic flows" Proceedings of the second International Conference on Numerical Methods in Fluid Dynamics Vol. 8 of Lecture Notes in Physics, Springer-Verlag (1971).

[18] BAILEY F.R. et STEGER J.L. "Relaxation techniques for three dimensional transonic flow about wings" AIAA Journal, Vol. 11, N° 3 (1973).

[19] STEGER J.L. et KLINEBERG J.M. "A finite difference method for transonic airfoil design" AIAA Paper 72-679 (1972).

[20] MURMAN E.M. "Analysis of embedded shock waves calculated by relaxation methods" AIAA Journal, Vol. 12, N° 5 (1974).

[21] COLES D.E. "The law of the wake in turbulent boundary layer" Journal of Fluid Mech., Vol. 1, part 2, pp 191-226 (1956).

[22] NGUYEN VAN NOI "Etude théorique et expérimentale du recollement subsonique incompressible d'un écoulement plan turbulent à sa frontière". Faculté des Sciences de l'Université de Paris, Thèse d'Ingénieur-Docteur (1971).

[23] ALBER I.E "Similar solutions for a family of separated turbulent boundary layers". AIAA Paper N° 11-203 (1971).

UNSTEADY SHOCK WAVE-BOUNDARY LAYER INTERACTION ON PROFILES IN TRANSONIC FLOW

Klaus Finke
Aerodynamisches Institut der RWTH Aachen, 51 Aachen, Templergraben 55
Germany

SUMMARY

Many unsteady flows are characterized by the interaction of shock waves with separated boundary layers. In particular shock oscillations occur on thick airfoils at high angles of attack and transonic free stream Mach numbers. Measurements were carried out in an intermittent indraft tunnel to study shock oscillations on various two dimensional wings. Several optical methods (Schlieren-, shadow-, interferogram, streak interferogram) were used together with single-spark, multi-sparks and high-speed films for flow visualisation and measurements. The frequency of oscillation was determined with a Laser-Schlieren technique. Unsteady pressure measurements were obtained with transistor probes, and measurements of velocity-and temperature fluctuations with hot films. Alternating separation and attachment at the leading edge is the observed severest type of the unsteady flow conditions. For this case multi-spark interferograms show periodical oscillations of the circulation of the wing, accompanied by the same oscillation of the circulation in the opposite sense in the wake. Large periodical disturbances exist throughout the entire flow field with defined phase shifts. The primary source of the observed instability is the shock induced separation of the boundary layer on the profile.

1. INTRODUCTION

Many unsteady flow phenomena are initiated by the interaction of shock waves with separated boundary layers. For example the flow over airfoils with a trailing edge flap (Refs. 1, 2, 3 and 4), in supersonic intakes (Refs. 5, 6, 7, 8 and 9), over the aft portion of rockets in transonic flows (Refs. 10 and 11), over a wing with extended flap at high angles of attack at hypersonic flows (Refs. 12 and 13). The associated shock oscillations are particularly intense on thick airfoils at large angles of attack at high subsonic free-stream Mach numbers. The physical mechanism of the shock oscillations is not yet fully understood, although a number of investigations dealing with this subject has been carried out during the past thirty years.

Ferri (Ref. 14) first observed unsteady flow effects on profiles in the transonic regime. According to Liepmann (Ref. 15), the reason for the shock oscillations, generally visible in transonic wind tunnel flows, is to be sought in the velocity fluctuations of the tunnel, especially when the tunnel does not operate with a choking devise downstream from the model. First systematic investigations of shock oscillations were carried out experimentally at the NPL (Refs. 16 and 17). Upstream running waves which disturbed the local supersonic flow were observed outside of the supersonic region. Tamaki (Ref. 18) attributed to these waves the high-frequency shock oscillations on thin airfoils at small angles of attack. Shock-wave oscillations on thick airfoils at large angles of attack were reported in Refs. 19 and 20. Also Naumann (Refs. 21 and 22) investigated the unsteady interaction mechanism between a shock wave and the boundary layer on profiles experimentally with various techniques. He was able to find out that shock oscillations with large amplitudes were caused by a separated boundary layer. In addition to these investigations at the Aerodynamische Institut the interaction between unsteady shock waves and a vortex street were studied in transonic flows past circular cylinders (Refs. 23, 24). The influence of the Reynolds number, air humidity and different tunnel walls (closed walls, semiopen tunnel, slotted walls) on transonic attachment at the leading edge was investigated in Ref. 25, where an attempt was made to explain unsteady alternating flow separation and attachment at the leading edge as an unbalanced mechanism.

Shock induced separation of turbulent boundary layers, alternating with the flow attachment at the leading edge, was considered experimentally by Dyment and Gryson (Ref. 26). Meyer and Hiller (Refs. 27 and 55) observed shock oscillations in an especially perforated transonic wind tunnel without a model. The shock oscillations could be damped out by boundary layer suction on the tunnel walls.

Wind tunnel noise and turbulence also may cause unsteady effects in transonic flows (Refs. 28, 29 and 30). Schmidt (Ref. 31) on the other hand explained the shock oscillations he observed on biconvex circular-arc airfoils with tunnel choking effects. Only few theoretical investigations deal with unsteady interaction between shock wave and boundary layer. Dore (Ref. 32) and Schneider (Ref. 33) made the first attempt to investigate the upstream influence of an unsteady shock wave in an attached supersonic boundary layer. Trilling (Ref. 34), Dvorak (Refs. 35 and 36) and Karashima (Ref. 37) using simplifying assumptions for the upstream influence, treated the unsteady interaction between shock wave and locally separated boundary layer as a stability problem.

In this paper experimental investigations of unsteady shock wave boundary layer interaction on various airfoils in transonic flows will be described. The results presented herein are part of a research programme carried out at the Aerodynamische Institut on unsteady flow phenomena about airfoil sections in transonic flows. Several experimental techniques are being used and although a definite and final description cannot be given, several physically possible mechanisms will be discussed in detail. This research programme was initiated by Prof. Naumann whom the author is indebted for suggesting this topic to him. He also provided many stimulating discussions.

2. EXPERIMENTAL SET UP AND DISCUSSION OF RESULTS

The measurements were carried out in an intermittent indraft tunnel with a closed test section of 400 x 75 mm^2, operating with a choked diffusor downstream from the model. Condensation effects were avoided by drying the air before entering the tunnel with a large silicagel filter. The Reynolds number per meter at a Mach number 0.75 was 1.3×10^7. Since the flow at this Re-number is predominantly laminar, transition to turbulent flow was enforced artificially by boundary-layer trips. A symmetric NACA 63_1-012, a quasi-elliptical NLR-profile and a biconvex circular-arc section, with different chord lengths, were investigated at Mach numbers ranging from 0.65 to 0.75 and angles of attack from 0^o to 10^o. The shock oscillations were studied with several optical methods, schlieren-, shadow-, interferogram, streak interferogram, in form of single-spark, multi-sparks and high-speed films. The frequency of the oscillation was determined with a Laser-schlieren technique. Unsteady pressure measurements were carried out with transistor probes, and measurements of velocity- and temperature-fluctuations with the hot-film technique.

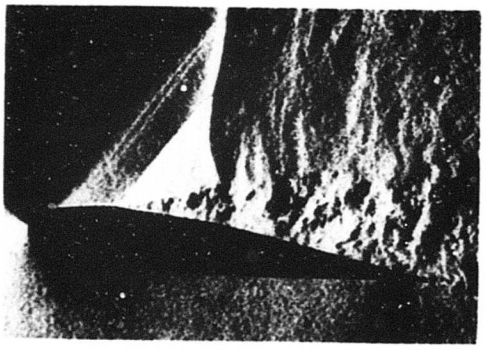

a) laminar ($\alpha = 8^o$)

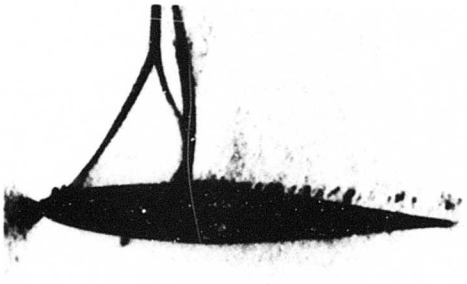

b) turbulent ($\alpha = 3^o$)

Fig. 1 Laminar and turbulent interaction NACA 63_1-012, c = 100 mm, $M_\infty = 0.71$, $Re = 1.25 \cdot 10^7 m^{-1}$

The single-spark schlieren pictures of Fig. 1 show the difference between the steady interaction of a normal shock wave with a laminar boundary layer and a tripped turbulent boundary layer. It can be seen that the length of the turbulent interaction region is much smaller. The reason for this behaviour is to be sought in the ability of the turbulent boundary layer to withstand the larger adverse pressure gradients caused by the shock wave in comparison to the laminar boundary layer. The positions of the shock wave on the profile are different for the two cases at the same angle of attack, strongly effected by the scaling (Refs. 38 and 39). The weak oblique shock wave which can be seen at $x/c = 0.03$ in Fig. 1b is caused by the boundary layer trip mentioned earlier. The results for laminar interaction were obtained in the following way: First the unsteady flow was recorded by Fastax-movies. The evaluation of the flow pictures recorded on the film yielded the results depicted in the following five Figs. 2, 3, 4, 5, 6 for the NACA 63_1-012 section. Figs. 2 and 3 show the mean shock-wave position and the angle of attack versus Mach number, for which leading edge separation, alternating flow separation and attachment, and shock induced separation occur. The maximum of the mean position of the shock indicates the beginning of shock-induced separation. The theoretical buffet boundary in Fig. 3 after GADD (Ref. 40) falls together with the beginning of shock-induced separation. Alternating flow separation and attachment at the leading edge is the severest case of the unsteady flow behaviour (Fig. 3). In Figs. 4 and 5 the amplitudes and the reduced frequencies of the shock oscillations are plotted versus angle of attack with the free stream Mach number as parameter. The frequencies exhibit a minimum for a certain angle of attack. At the minimum the oscillations are periodic. Fig. 6 shows lines of constant shock-wave ampitudes as a measure for the interaction between the unsteady shock and the boundary layer.

The local velocity fluctuations downstream of the unsteady shock were detected with hot films. Fig. 7 shows an unfiltered and a filtered oscillogram. The location of the gauge has been choosed in such a way that the mean position of the shock wave reaches the edge of the separated boundary layer. The hot film was periodically exposed to the boundary-layer flow and the outer inviscid flow; the former causes the large noise in the unfiltered oscillogram. The shock oscillation was also investigated by a Laser-schlieren technique: A Laser beam was focused on the mean shock wave position. Since the actual shock wave is not an exact discontinuity, the diffraction of the Laser beam caused by the shock oscillation could be

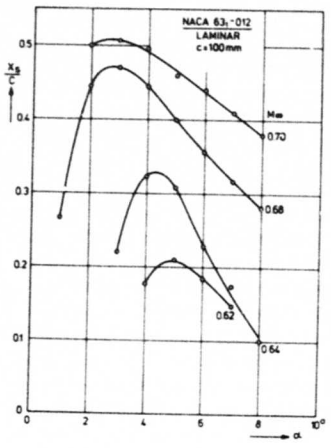

Fig. 2 Mean shock-wave position

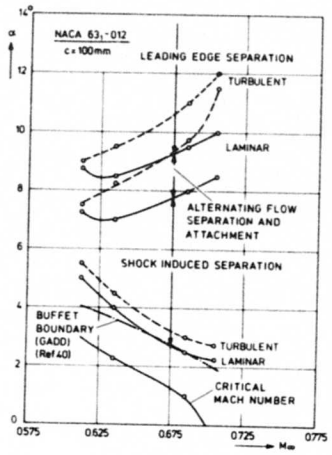

Fig. 3 Transonic flow regions

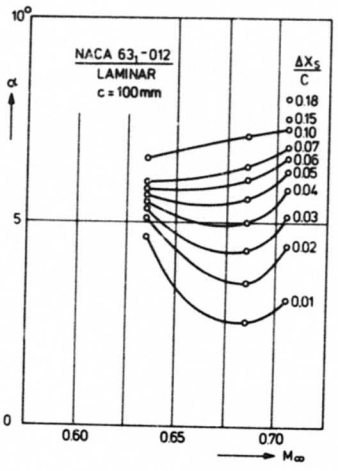

Fig. 6 Lines of constant shock-wave amplitude

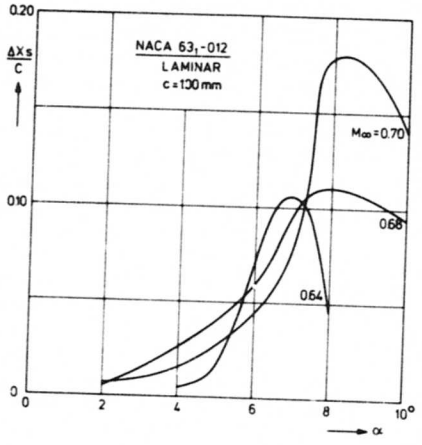

Fig. 4 Shock-wave amplitude

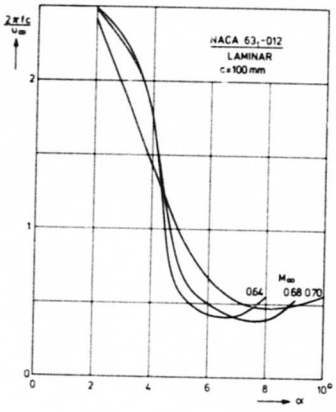

Fig. 5 Reduced frequency

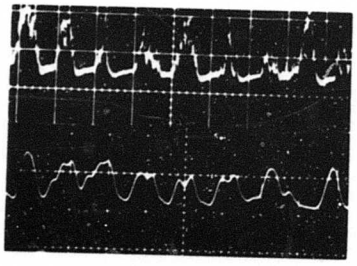

Fig. 7 Hot-film oscillograms
NACA 63_1-012, c = 100 mm
M_∞ = 0.66, α = 7°,
Re = 1.2×10^7 m^{-1}, 1 cm = 5 ms

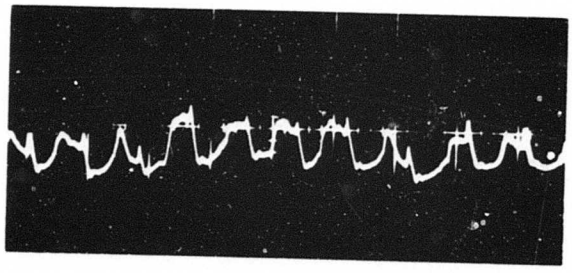

Fig.8 Laser-schlieren measurement
NLR 0.1025-0.6750-1.300, c= 80 mm
M_∞ = 0.71 , α = 5°,
Re = 1.25×10^7 m^{-1}, 1 cm = 5 ms

detected with a photo multiplier (Fig. 8). Eventually this method can be used to determine the frequencies of the oscillation with a frequency analyser.

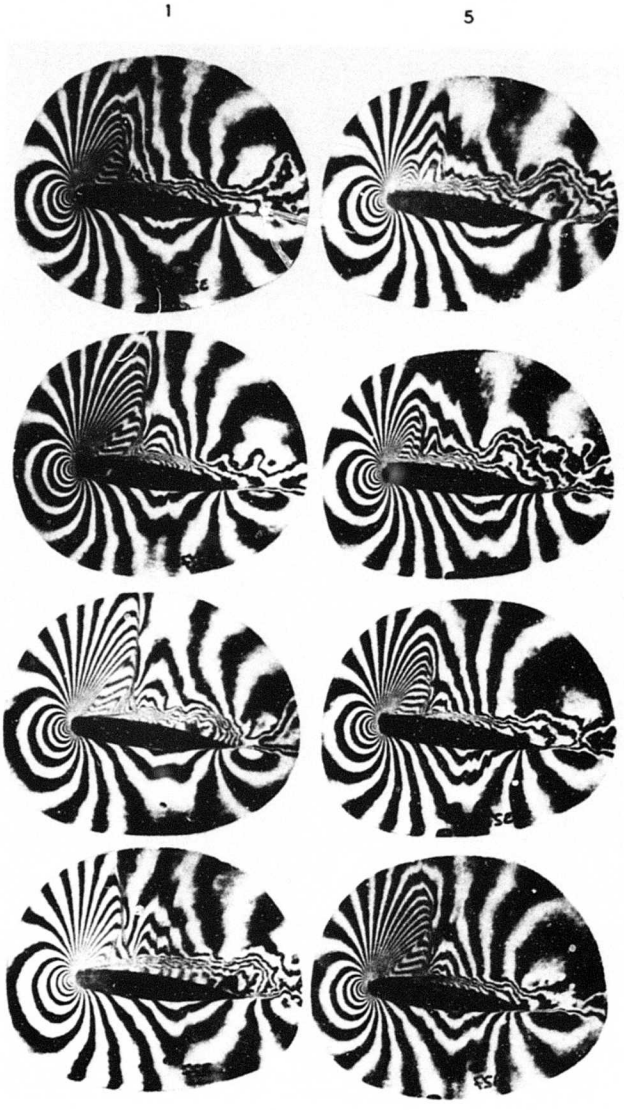

Fig. 9 NLR 0.1025-0.6750-1.300
c = 80 mm , M_∞ = 0.71 , α = 5°
Re = 1.25×10^7 m^{-1} , Δt = 700 µs

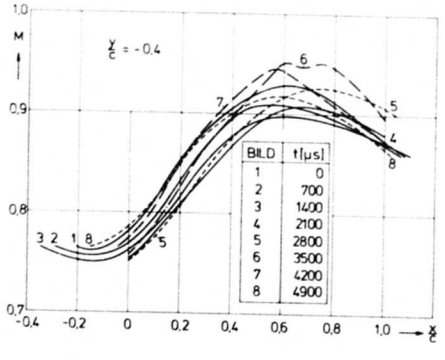

Fig. 10 Local Mach numbers
NLR 0.1025-0.6750-1.300 , c = 80 mm
M_∞ = 0.71 , α = 5° , y/c = -0.4

With the 8-sparks camera (Ref. 41) of the Aerodynamische Institut which makes use of the Cranz-Schardin prinziple, the time dependent development of the shock oscillations could be studied in detail. The Mach-Zehnder interferograms in Fig. 9 show about one full period of oscillation. The pictures with lines of constant density are depicted in intervals of 700 micro seconds. This alternating separation is characterized by a periodical change of the flow separation at the leading edge and at the upstream foot of the lambda shock. The separation point follows the shock movement; the separation region extends from the instantaneous position of the shock wave to the trailing edge. In picture 3 the shock was positioned at 40 percent chord, in picture 5 the shock degenerates to a Mach wave and leading-edge separation alone determines the flow. From the multi-spark interferograms the time dependent local Mach numbers were determined with the assumption of isentropic flow in the entire flow field. Figs. 10, 11 and 12 show typical results for the lower side (y/c = - 0.4), the geometrical stagnation line (y/c = 0) and the upper side of the profile (y/c =+0.4) , with the time as parameter. The position of a point in the flow field is given by the co-ordinates x and y , measured from the leading edge of the profile, in and normal to the direction of the chord. On the lower side the flow is predominantly subsonic (Fig. 10).

In Fig. 12 downstream of the shock wave expansion regions are visible, already observed by Ackeret (Ref. 49) at pressure measurements, and analysed theoretically by Zierep (Ref. 50) for inviscid flows. Near the trailing edge on the lower side the maximum Mach number is reached when the shock wave on the upper side is in its furthest position. Large Mach number fluctuations can be noticed in the entire flow field. Figs. 13 and 14 show the periodical character of the flow for y/c = -0.4 and y/c = +0.4. In particular phase shifts of the waves can be recognised. The extrem positions of the shock wave at the upper side are also indicated for the orientation. Apparently pressure waves propagate clockwise around the profile, outside the separated boundary layer. Within the separated boundary layer and near the leading edge the motion of the waves cannot clearly recognised. The pressure measurements on the wing surface carried out in the separated region by Sorenson (Ref. 54) , confirm the clockwise propagation of large disturbances.

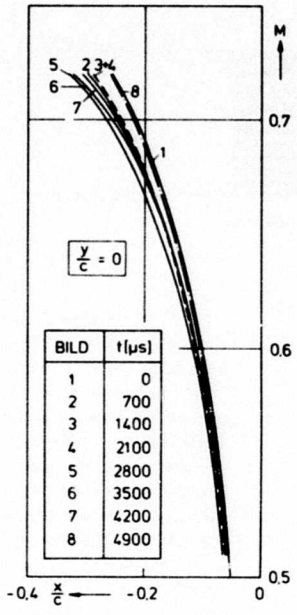

Fig. 11 Local Mach numbers
NLR 0.1025-0.6750-1.300
c = 80 mm , M_∞ = 0.71
α = 5° , y/c = 0

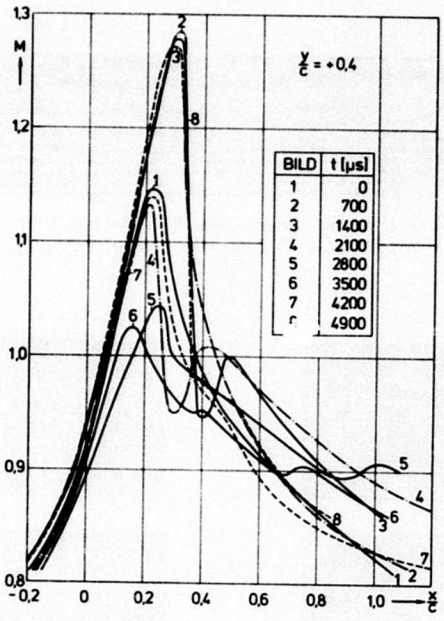

Fig. 12 Local Mach numbers
NLR 0.1025-0.6750-1.300
c = 80 mm , M_∞ = 0.71
α = 5° , y/c = +0.4

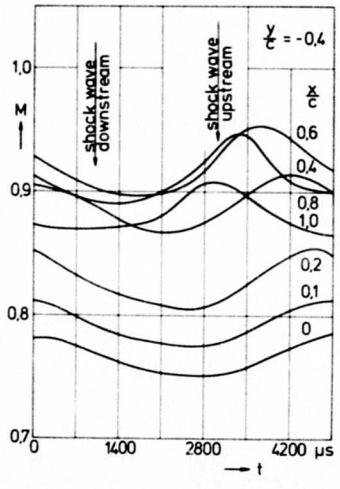

Fig. 13 Local Mach numbers
NLR 0.1025-0.6750-1.300
c = 80 mm , M_∞ = 0.71
α = 5° , y/c = - 0.4

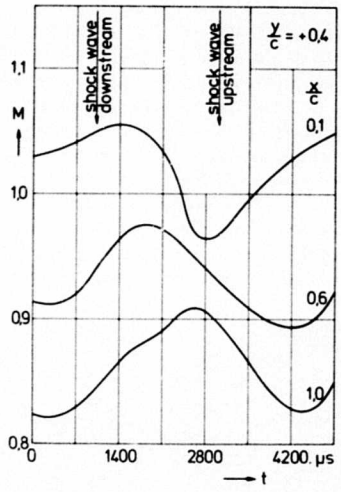

Fig. 14 Local Mach numbers
NLR 0.1025-0.6750-1.300
c = 80 mm , M_∞ = 0.71
α = 5° , y/c = + 0.4

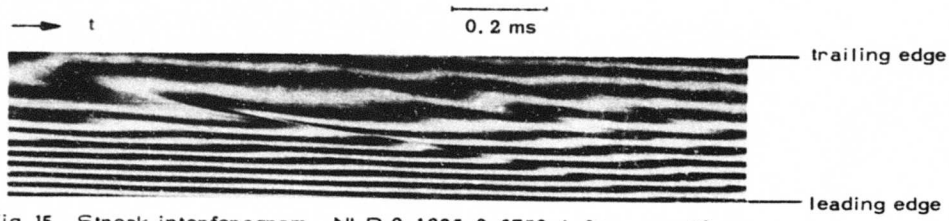

Fig. 15 Streak interferogram , NLR 0.1025-0.6750-1.3oo , c = 80 mm
$M_\infty = 0.71$, $\alpha = 5^o$, $Re = 1.25 \times 10^7\ m^{-1}$, y/c = -0.30

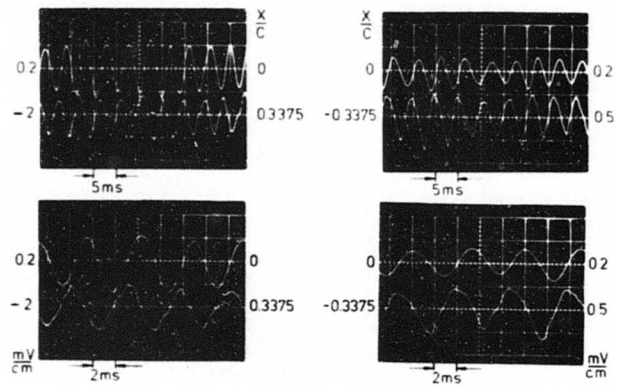

Fig. 16 Pressure measurements
NLR 0.1025-0.6750-1.300 , c = 80 mm
$M_\infty = 0.71$, $\alpha = 5^o$, $Re = 1.25 \times 10^7\ m^{-1}$
x/c = 0.3375 upper side
x/c = -0.3375 lower side

Fig. 15 shows a detail of a typical streak interferogram , taken with the slit at y/c = -0.3 . The pressure wave propagating upstream can clearly be recognized. The periodical character of the flow can be seen in the entire streak interferogram. Measurements of the unsteady pressure on the airfoil surface (Fig. 16) also show the very regular behaviour of fluctuations on the upper side, the lower side and the geometrical stagnation point, with clearly recognisable phase shifts. These measurements also confirm the upstream motion of the waves on the lower side.

Fig. 17 demonstrates the unsteady transonic flow over a 20 percent thick biconvex circular-arc airfoil at zero angle of attack. The alternating upstream motion of the lambda shocks on the upper and on the lower side of the profile is of particular interest. Near the leading edge the shock waves degenerate in sound waves without further boundary layer separation. The sound waves leave the airfoil and propagate upstream. The flow is fully periodical and the interferograms indicate the periodical change of the expansion regions on the upper and lower side. Fastax films also show the periodical character of the flow near the stagnation point, and the results indicate that there are some analogies to the transonic flow past circular cylinders as shown in Fig. 18 (see also Ref. 23). The observation is confirmed by the appearance of a vortex street downstream of the wing (Fig. 19). The entire wake exhibits crosswise oscillations with the frequency of the shock wave motion. The wake flow of the NLR-airfoil section also shows periodical character (Fig. 20). Busemann (Ref. 53) predicted that vortex-street formation would occur in transonic airfoil flow away from the design point.

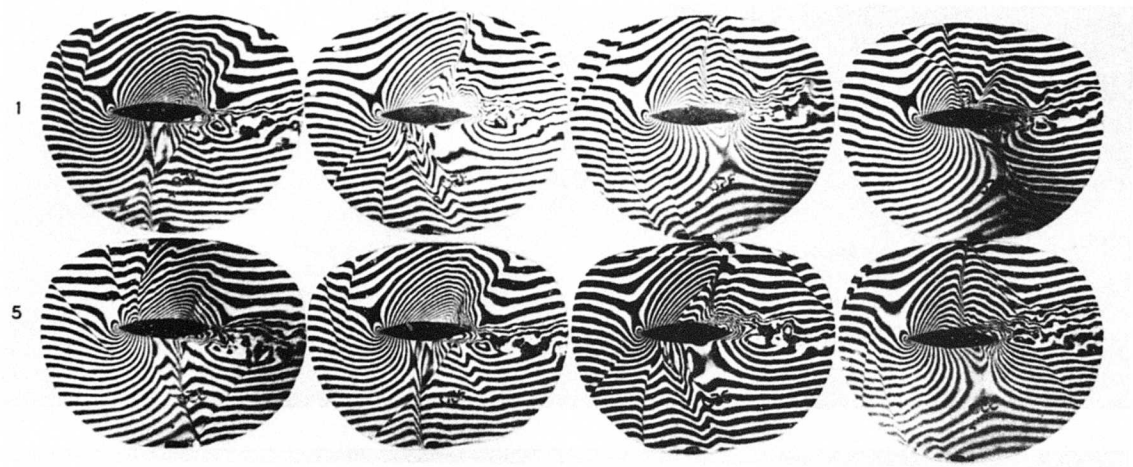

Fig. 17 Biconvex circular-arc , c = 50 mm , $M_\infty = 0.71$, $\alpha = 0^o$, $Re = 1.25 \times 10^7\ m^{-1}$, $\Delta t = 250\ \mu s$

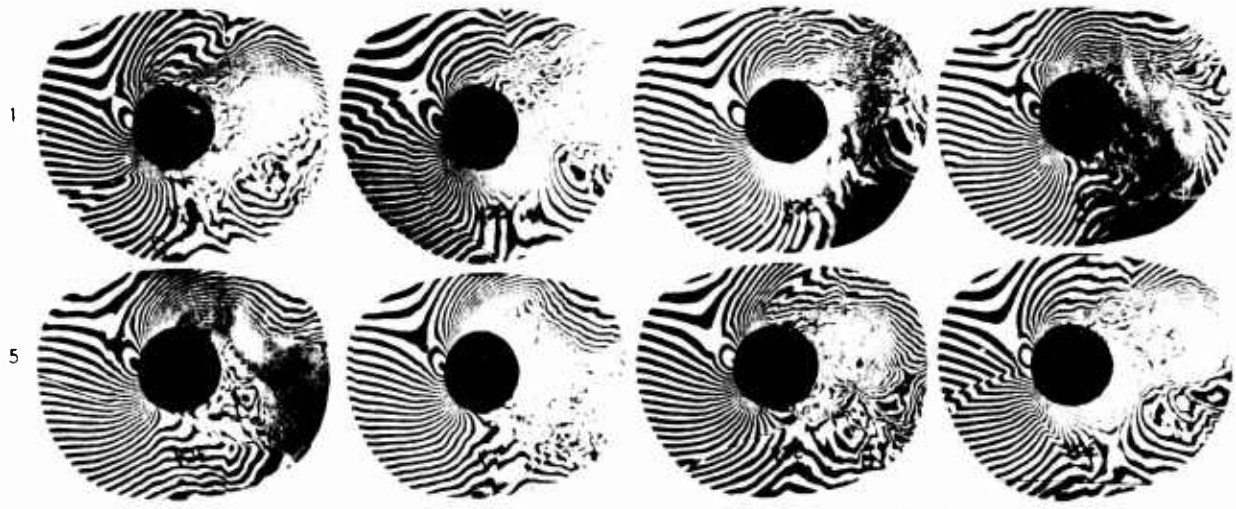

Fig. 18 Circular cylinder , d = 40 mm , M_∞ = 0.55 , Re = 1.03x10^7 m^{-1} , Δt = 150 µs

Fig. 19 Vortex street
Biconvex circular-arc
c = 50 mm, M_∞ = 0.71, α = 0°

Fig. 20 Vortex street
NLR 0.1025-0.6750-1.300
c = 80 mm, M_∞ = 0.71, α = 5°

Fig. 21 Choking condition
Circular arc, α = 0°
c = 150 mm, M_∞ = 0.7

In order to detect the influence of possible blockade or choking effects in the tunnel on the shock oscillations, the chord lenght of the NLR-profile (c = 40, 80, 160 mm) and of the biconvex circular-arc airfoil (c = 25, 50, 100, 150 mm) was varied for constant freestream conditions. For the circular-arc with 150 mm chord the shock waves were essentially steady (Fig. 21). The choking Mach number, calculated from the one-dimensional theory without separation (Ref. 42), is M_∞ = 0.695. The shock wave was not completely steady for the largest NLR-section (c = 160 mm) at five degrees angle of attack and M_∞ = 0.71, because choking between the lower side of the profile and the lower tunnel wall could not be reached. In all other cases regular shock oscillations occured with the same reduced frequency referenced to the chord lenght, for a definite airfoil. It can therefore be concluded that the frequency of the shock oscillation depend on the chord lenght, and is not caused by the tunnel effects. For the biconvex circular-arc airfoil at zero angle of attack the theoretically determinedchoking Mach numbers for c = 25, 50, 100 mm are M_∞ = 0.877, 0.827, 0.755, so that it is safe to assume that the flow in the test section at M_∞ = 0.71 was not choked (see also Ref. 43). This conclusion is confirmed by the interferograms. Only at the largest profiles (c = 160, respectively c = 150 mm) did the sonic lines reach the tunnel walls.

3. UNSTEADY FLOW MECHANISMS

The following four possible unsteady flow mechanisms can be identified in flows with shock oscillations.

1. If a small pressure disturbance appears during the interaction, it propagates upstream in the subsonic part of the boundary layer (Ref. 36). This disturbance will result in flow changes in the boundary layer, and in an upstream shift of the separation point. For laminar shock-boundary layer interaction (λ-shock pattern), the upstream propagated disturbances will cause changes in the outer supersonic flow and thereby a change in the strength of the first shock-wave and a downstream propagated pressure disturbance. It is the latter which gives rise to the unsteady oscillation of the interacting inviscid and viscous flow. Dvorak (Ref. 36) made an attempt to solve the unsteady interaction problem as a stability problem of the small disturbance propagation. The comparison (Fig. 22) between experiment and this theory shows that for small angles of attack the trend of the reduced frequency is in principle predicted for high-frequency oscillations. The diagram, however, also shows that another mechanism becomes predominant at higher angles of attack.

II. After Tamaki (Ref. 18) the shock-wave oscillations may be considered as the repetition of the following process: The upstream traveling disturbances tend to accumulate at a certain point (Busemann, Refs. 45 and 46) , but their pressure rise can be transfered upstream through the subsonic region outside (confirmed by Fig. 23 , see also Ref. 48), where upstream motion of the disturbances is possible. Then the flow returns to the initial state and repeats the same process.
With the models I and II the high-frequency oscillations with small amplitudes at small angles of attack (Fig. 5) can in principle be explained.

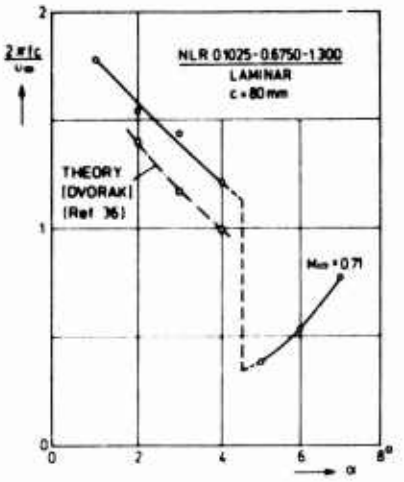

Fig. 22 Reduced frequency, Re = 1.25×10^7

Fig. 23 Shadow-pictures, NLR 0.1025-0.6750-1.300 , c = 80 mm , $M_\infty = 0.71$, $\alpha = 5^\circ$
Re = 1.25×10^7 m^{-1} , $\Delta t = 60$ µs

III. The following mechanisms are believed to describe the small-frequency-shock-wave oscillations with large amplitudes at large angles of attack. For these cases the separation of the boundary layer extends from the instantaneous position of the shock wave to the trailing edge. Disturbances now also travel upstream in the subsonic region at the lower side of the profile and pressure readings on the lower side clearly confirm periodical pressure fluctuations with definite phase shifts (Fig. 16). The pressure waves on the lower side made visible with the multi-spark technique (Fig. 24), are visible around the whole airfoil. The "divergence" of the trailing edge pressure, as defined by Pearcey (Ref. 38), may give the first triggering impuls for the upstream movement of the disturbances on the lower side. Arround the airfoil periodical oscillations of the circulation exist, connected with unsteady flow near the trailing edge so that the Kutta condition can be satisfied. The oscillation of the circulation cause oscillations of the circulation in the wake but with the opposite sign.

IV. Inspection of Fastax-high-speed films indicate that the separated boundary layer carried out crosswise oscillations, which are synchronous with the shock wave movement, in analogy to the transonic aileron buzz (Ref. 44). The mechanism can be explained as follows: If the boundary layer at the rear portion of the wing separates, unsteady pressure disturbances are produced in the outer subsonic flow which propagate downstream and upstream. The upstream propagating disturbances meet the shock and force it to move upstream. The shock wave travels in regions of smaller Mach numbers; the angle between the edge of the separated boundary layer and the free stream direction is reduced; negative pressure disturbances in the outer flow downstream of the shock wave are produced and the shock wave is forced to move downstream again. The crosswise oscillation of the wake is particularly intense at the biconvex circular-arc airfoil.

Fig. 24 Shadow-pictures , NLR 0.1025-0.6750-1.300 , c = 80 mm , $M_\infty = 0.71$, $\alpha = 5^o$
$Re = 1.25 \times 10^7\ m^{-1}$, $\Delta t = 100\ \mu s$

4. COMMENTS ON EXISTING THEORIES

Because of the strong coupling between the boundary layer and the inviscid flow theoretical analysis is difficult, in particular in the case of separated boundary layers. In the present problem unsteady effects are essential. In the interest of the problem investigated here, unsteady methods as for example the one proposed by Yoshihara (Ref. 47) would be most useful for the prediction of unsteady inviscid and viscous transonic flows. Application of the Navier-Stokes equations may be a successful way to describe the flow about the airfoil as were for example done successfully for low Reynolds number flows in Refs. 51 and 52 . There are similarities to the starting process of an airfoil, which may result from the same mechanism as the periodical behaviour of the wake flow downstream from the profile.

5. CLOSING REMARKS

Measurements of the unsteady shock wave-boundary layer interaction on various airfoils were carried out at transonic Mach numbers. The shock oscillations induced by boundary layer separation characterise the flow; the separation extends from the instantaneous position of the shock wave to the trailing edge. Small-frequency shock oscillations with large amplitudes at large angles of attack show large periodic oscillations of the circulation on the profile, compensated apparently by the circulation of the vortices in the wake but in the opposite sence.

An analogy seems exist to the transonic flow over circular cylinders with a vortex street in the wake. The influence of possible choking effects in the wind tunnel were eliminated. It was shown that the frequency of the shock oscillation varies inversely proportional to the chord length and is not caused by tunnel effects. The influence of the wind tunnel walls is presently being studied by means of a finite-difference solution for the exact potential equation.

6. REFERENCES

1. Lambourne, N.C., "Some instabilities arising from the interactions between shock waves and boundary layers", AGARD Rep. No. 182, 1958
2. Coupry, G., Piazzoli, G., "Étude du flottement en régime transsonique", La Recherche Aéronautique No. 63, Mars-avril 1958
3. Lambourne, N.C., "Control-surface buzz", ARC R.+M. No. 3364, 1964
4. Nakamura, Y., "Some contributions on a control-surface buzz at high subsonic speeds", J. Aircraft, Vol. 5, No. 2, March-April 1968, 118-125
5. Ferri, A., Nucci, L.M., "The origin of aerodynamic instability of supersonic inlets at subcritical conditions", NACA RM L 50K30, 1951
6. Hermann, R., "Supersonic inlet diffusers and introduction to internal aerodynamics", Minneapolis, Minneapolis-Honeywell, 1956
7. Oswatitsch, K., Teipel, I., "Die Pulsationen von Stoßdiffusoren", ZAMP, Vol. IXb, 1958, 462-478
8. Neale, M.C., Armstrong, F.W., "Some recent research on supersonic intakes at NGTE", AGARD-CP-71-71, 1971
9. Nagashima, T., Obokata, T., Asanuma, T., "Experiment of supersonic air intake buzz", ISAS Report No. 481 (Tokyo), 1972
10. Chevalier, H.L., Robertson, J.E., "Pressure fluctuations resulting from an alternating flow separation and attachment at transonic speeds", AEDC-TDR-63-204, 1963
11. Ericsson, L.E., Reding, J.P., Guenther, R.A., "Effects of shock-induced separation", Lockheed Missiles + Space Comp., Techn. Summary Report L-87-69-1, 1969
12. Ericsson, L.E., Reding, J.P., "Dynamic stability problems associated with flare stabilizers and flap controls", J. Spacecraft, Vol. 7, No. 2, Febr. 1970, 132-137
13. Goldman, R.L., Obremski, H.J., "Experimental investigation of hypersonic buzz on a delta configuration", AIAA Journ., Vol. 11, No. 10, Oct. 1973, 1361-1362
14. Ferri, A., "Experimental results with airfoils tested in the high-speed tunnel of Guidonia", Atti di Guidonia, No. 17, 1939
15. Liepmann, H.W., "Shock-wave oscillations in wind tunnels", J. Aeron. Sci., May 1947, 295-302
16. Hilton, W.F., Fowler, R.G., "Photographs of shock wave movement", NPL, Reports and Memoranda No. 2692, Dec. 1947
17. Holder, D.W., North, R.J., "A high-speed camera for the photography of shock-wave oscillations in a wind tunnel", NLP, Reports and Memoranda No. 2901, Aug. 1949
18. Tamaki, F., "Experimental studies on the stability of the transonic flow past airfoils", Journ. of the Phys. Soc. of Japan, Vol. 12, No. 5, May 1957, 544-549
19. Daley, B.N., Humphreys, M.D., "Effects of compressibility on the flow past thick airfoil sections", NACA TN No. 1657, 1948
20. Humphreys, M.D., "Pressure pulsations on rigid airfoils at transonic speeds", NACA RM L51I12, 1951
21. Naumann, A., "Strömungsbilder an Profilen bei hohen Geschwindigkeiten", Jahrb. WGL, 1953, 129-131
22. Naumann, A., "Stoßschwingungen an Profilen", Abh. aus dem Aerodyn. Inst. der TH Aachen, Heft 18, 1965, 9-13
23. Pfeiffer, H., "Strömungsuntersuchungen an Kreiszylindern bei hohen Geschwindigkeiten", Forschungsbericht des Landes NRW, Nr. 1062, 1962
24. Kramer, C., "Strömungsuntersuchungen an Zylindergittern", Diss. TH Aachen, 1966
25. Lindsey, W.F., Landrum, E.J., "Compilation of information on the transonic attachment of flows at the leading edges of airfoils", NACA TN 4204, 1958
26. Dyment, A., Gryson, P., "Example of aerodynamic instability under supercritical conditions about profiles", Coll. d'Aérodyn. Appl., 10th, Univ. de Lille, France, Nov. 7-9, 1973, paper 26
27. Meyer, G., Hiller, W., "An experimental investigation of unsteady transonic flow by high-speed interferometric photography", AGARD CP No. 35, 1968, paper 9
28. Mabey, D.G., "The influence of flow unsteadiness on windtunnel measurements at transonic speeds", LaWs-Paper No. 38
29. Timme, A., "Effects of turbulence and noise on wind-tunnel measurements at transonic speeds", AGARD Rep. No. 602, paper 5, 1973
30. Cox, R.N., Freestone, M.M., "Sound fields generated by transonic flows over surfaces having circular perforations", AGARD-CP-83-71 (1971), paper 24
31. Schmidt, B., "Schallnahe Profilumströmung mit Kondensation", ACTA MECHANICA, Vol. II/2, 1966, 194-208
32. Dore, B.D., "The upstream influence ahead of a weak, uniformly moving shock or expansive wave", Quart, Journ. Mech. and Appl. Math., Vol. XX, Pt. 3, 1967, 333-345
33. Schneider, W., "Upstream propagation of unsteady disturbances in supersonic boundary layers", Journ. Fluid Mech., Vol. 63, Part 3, 1974, 465-485
34. Trilling, L., "Oscillating shock boundary-layer interaction", Journ. Aeron. Sci., May 1958, 301-304
35. Dvorak, R., "Unsteady phenomena in transonic flow past aerofoils" (in Czech), Czech. Acad. of Sci., Inst. Mech. Eng., Rep. No. 151/62, Prague 1962
36. Dvorak, R., "On the unsteady boundary layer-shock wave interaction in the lower transonic region", Fiuid Dynamics Transactions, Vol. 2, 1965, Ed. W. Fiszdon

37. Karashima, K., "Instability of shock wave on thin airfoil in high subsonic flow", Aeronautical Research Inst., Univ. of Tokyo, Rep.No. 363, March 1961, 39-118
38. Pearcey, H.H., Osborne, J., Haines, A.B., "The interaction between local effects at the shock and rear separation - a source of significant scale effects in wind-tunnel tests on aerofoils and wings", AGARD CP No. 35, paper 11, 1968
39. Hartzuiker, J.P., "Scale effects at transonic speeds, basic considerations", VKI Lecture Series 42, Jan. 1972
40. Thomas F., "Die Ermittlung der Schüttelgrenzen von Tragflügeln im transonischen Geschwindigkeitsbereich", Jahrb. WGLR, 1966, 126-144, Bild 5
41. Hermanns, E., Kramer, C., Meszerits, M., Schultz, S., "Entwicklung einer Mehrfunken-Kamera fur Stromungsuntersuchungen", Abh. aus dem Aerodyn. Inst., TH Aachen, Heft 20, 1970, 15-19
42. Zierep, J., "Theoretische Gasdynamik", Bd. 2, "Schallnahe u. Hyperschallströmungen", Braun, Karlsruhe, 1972, S. 6
43. Jungbluth, H., "Experimentelle Untersuchungen der schallnahen, ebenen Umströmung einer welligen Wand im blockierten Kanal", Diss. Univ. Karlsruhe, 1969
44. Eckhaus, W., "On the theory of transonic aileron buzz", MIT Fluid Dynamics Research Laboratory Report No. 60-6, 1960
45. Busemann, A., "Das Abreißen der Grenzschicht bei Annäherung an die Schallgeschwindigkeit", Tagung "Abgasstrahlantrieb", Dresden 1939, Bericht 118, 41-44, Lilienthal-Gesellschaft für Luftfahrtforschung
46. Busemann, A., "The drag problem at high subsonic speeds", Journ. Aeron. Sci., June 1949, 337-344
47. Yoshihaha, H., "Some recent developments in planar inviscid transonic airfoil theory", AGARDograph 156, 1972
48. Spee, B.M., "Investigations on the transonic flow around aerofoils", NLR TR 69122 U, 1971
49. Ackeret, J., Feldmann, F., Rott, N., "Untersuchungen an Verdichtungsstößen und Grenzschichten in schnell bewegten Gasen", Mitt. aus dem Inst. für Aerodynamik der ETH Zürich, Nr. 10, 1946
50. Zierep, J., "Der senkrechte Verdichtungsstoß am gekrümmten Profil", DVL-Bericht Nr. 51, 1958
51. Mehta, U.B., "Starting vortex, separation bubbles and stall - a numerical study of laminar unsteady flow around an airfoil", Illinois Inst. of Technology, Ph.D., 1972, Engineering, mechanical
52. Lugt, H.J., Haussling, H.J., "Laminar flow past an abruptly accelerated elliptic cylinder at 45° incidence", Journ. Fluid Mech., Vol. 65, part 4, 711-734, 1974
53. Busemann, A., "Widerstand bei Geschwindigkeiten nahe der Schallgeschwindigkeit", Verhandlungen des III. Internationalen Kongresses für technische Mechanik, Stockholm, 1930, Bd. I, S. 282-286
54. Sorenson, R.M., Wyss, J.A. Kyle, J.C., "Preliminary investigation of the pressure fluctuations in the wakes of two-dimensional wings at low angles of attack", NACA RM A51G10, Fig. 22, 1951
55. Meier, G.E.A., "Ein instationäres Verhalten transonischer Strömungen", Mitt. Max-Planck-Inst. f. Stromungsforsch. u.d. AVA, Göttingen, 1974

SHOCK INDUCED FLOW OSCILLATIONS

by

G.E.A. Meier
Max-Planck-Institut für Strömungsforschung
D 34,Göttingen, Böttingerstr. 4-8, Germany

SUMMARY

The physical system consisting of a shock wave and the downstream separated flow causes oscillatory instabilities in three cases described here: transonic flow in a curved channel; flow over a symmetric profile at angle of attack; and flow in a Laval nozzle. The shock-boundary layer interaction creates or displaces a separation bubble, thereby changing the flow field downstream of the shock root. This process usually strengthens the shock wave by increasing the back pressure. The shock wave then becomes unsteady, moving the separation point with it in an upstream direction, so that a self-preserving instability occurs, thus reducing the flow velocity in the whole transonic field. By means of the later reattachment of the boundary layer, the entire flow is accelerated and tends to return to the initial condition, i.e., the process is cyclic. The length of the oscillation periods can be estimated. Using a one-dimensional model for the Laval nozzle flow, it can actually be calculated. Consideration of the gasdynamics of the process leads to limits in terms of pressure or Mach number for the existence of oscillations, these limits being in good agreement with experimental results.

INTRODUCTION

Several years ago we observed nonsteady behavior of transonic flows in a curved tunnel when shocks with a certain minimum strength of pressure jump occurred at the end of a supersonic region embedded in a subsonic flow [1]. The great similarity to phenomena connected with buffeting [2] on wings suggested a parallel investigation of both types of flow with regard to the detection of an oscillation mechanism.

In an attempt to find a simple model for the complex phenomena observed in the two-dimensional nonsteady flows, we found we could predict, based on considerations of the mechanisms, that supersonic Laval-nozzle flows must also show this behavior for a certain pressure ratio and certain geometrical forms. Experiments with a nozzle of this type have confirmed the prediction, and moreover provided an explanation for the nonsteady behavior of flows occasionally observed in supersonic tunnels and valves. The reduction of the problem to nonsteady behavior of nozzle makes it possible to treat the mechanism of oscillation theoretically in a one-dimensional model by a modified current tube theory.

The most important result of the investigation is that the oscillation is generated by a local instability which is based on an interaction of the boundary layer and shock wave. In the acceleration phase, a shock wave forms at the end of the supersonic flow. The pressure jump in the shock wave is capable of detaching the boundary layer or displacing the point of detachment. The effect is a local increase of pressure behind the shock wave, which causes the latter to move upstream. In this process the shock wave moves the separation point away with it, so that a self-preserving instability occurs, which may result in canceling the whole supersonic flow. The shock wave leaves the region in which the oscillation is generated in many cases as an acoustic bang wave through the subsonic flow. In the acceleration phase the boundary layer reattaches to the wall.

The process described here should not be confused with another type of shock boundary layer interaction, which was described by L. Trilling [3]. This instability is restricted to the case of λ - type shock waves separating laminar boundary layers. The influenced area where the distortions propagate is very small and the oscillation frequencies are therefore much higher than in the case treated in this paper.

INSTRUMENTATION

The different channels are connected with a vacuum chamber and fed with dried atmospheric air. The flow volume is controlled by a variable supersonic nozzle.

The central flow field is observed with a Mach-Zehnder-Interferometer. With air at atmospheric pressure inside the duct, the interferometer is adjusted to infinite width the interference fringes. Thus the fringes will be lines of constant density in the photographs of the flow field. As long as no entropy changes occur, all other variables of state and magnitude of flow velocity will be constant on interference fringes.

The unsteady flow phenomena are recorded by high speed photography. A single photograph has an exposure time $t \cong 10^{-6}$ s. The interframe time Δt is given in the corresponding subscripts.

Pressure measurements were made by mercury columns for the stationary component of static pressure. The unstationary component was measured by piezoelectric transducers with resonance frequencies

f_r = 80 kHz. Signals are recorded on film from an eight trace oscilloscope and for further evaluation on magnetic tape.

OSCILLATIONS IN A CURVED CHANNEL

Two examples of interferograms of an oscillation cycle in a curved channel are shown in Fig. 1 and Fig. 2 (in these tests suction was applied at the convex boundary; for more details see [1] and [3]).

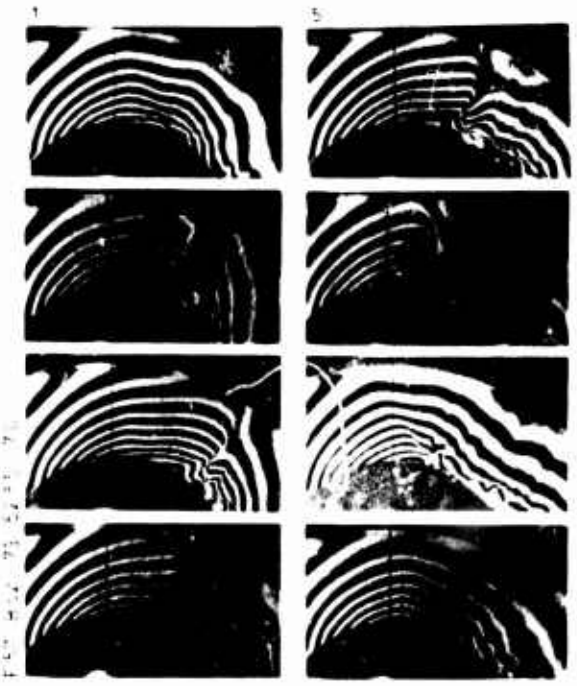

Fig. 1 Interferograms of an oscillation cycle of transonic flow with intermediate separation in a channel of h = 40 mm depth and d = 45 mm distance between top and bottom walls at the smallest cross section. Highest Mach number at the smallest cross section at the lower wall M_{max} = 1.5. Suction velocity at the convex contour v_s = 3 m/s. Interframe time Δt = 0.3 ms. Flow direction from left to right.

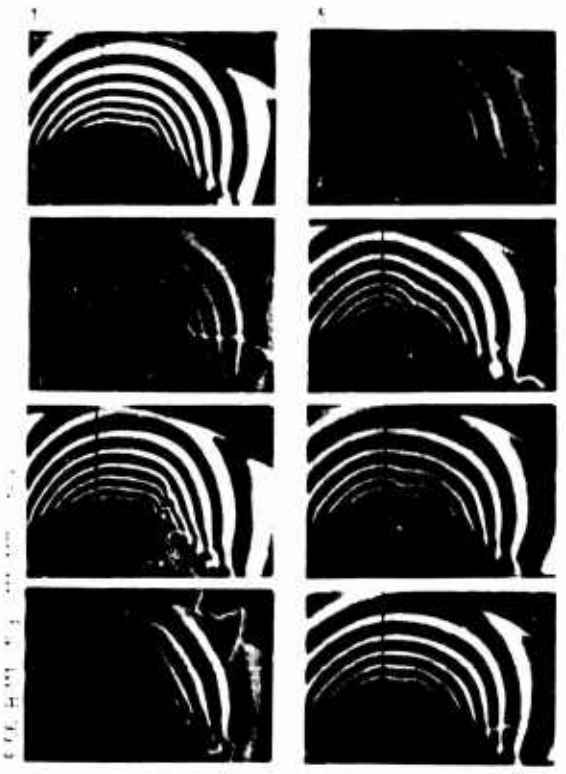

Fig. 2 Interferograms of an oscillation cycle of transonic flow with intermediate separation in a channel of 40 mm x 45 mm smallest cross section. Mach number at the zenith of the boundary M_{max} = 1.4. Suction velocity at the convex contour v_s = 3 m/s. Interframe time Δt = 0.6 ms. Flow direction from left to right.

Fig. 1 represents the most common case, that of a shock wave being established during frames 1-3 at the end of a growing supersonic flow regime, creating a separation bubble in frame 3. The main flow around the newly-created separation bubble is similar to that around a convex contour (see frames 4 and 5), with highest density and pressure values just behind the shock wave. This pressure can be additionally amplified by acoustic waves resonating in the duct [4]. The density or pressure behind the shock wave therefore becomes too high for a stationary shock and it moves upstream (frames 4-7). The boundary layer separation point for the beginning of the separation bubble is moved with the shock root. Thus the high density or pressure field just behind the shock persists during the main part of the motion. Therefore we call this a phase of self-preserving instability. The duration of the deceleration phase is essentially determined by the acceleration of the secondary flow inside the separation bubble and the propagation velocity of the shock wave against the main flow. When the shock wave becomes too weak to maintain separation (see frame 7) the boundary layer is reattached very quickly with the velocity of downstream convected turbulence elements. The following acceleration phase is extended over the whole flow field as an expansion wave starting from the area of reattachment (see frames 7-1)

Fig. 2 shows that a very similar oscillation cycle can occur without complete separation of the boundary layer. The turbulent layer after the shock wave is considerably thickened after the shock has reached a certain strength in the acceleration phase (see frames 4 and 5). The thickened boundary layer also creates a pressure wave running upstream and driving the shock wave at the end of the supersonic flow regime to a more upstream position (see frames 5-7). As can be seen from other measurements [4] the magnitude of the pressure wave is amplified by acoustic resonance in parts of the duct. The amplitude of the oscillation depends on this and thus cannot be easily predicted.

The evaluation of interference pictures shown in Fig. 2 leads to the density curves shown in Fig. 3 and Fig. 4. It can easily be seen from Fig. 3, traces 18 and 22, how the shock wave suddenly increases the

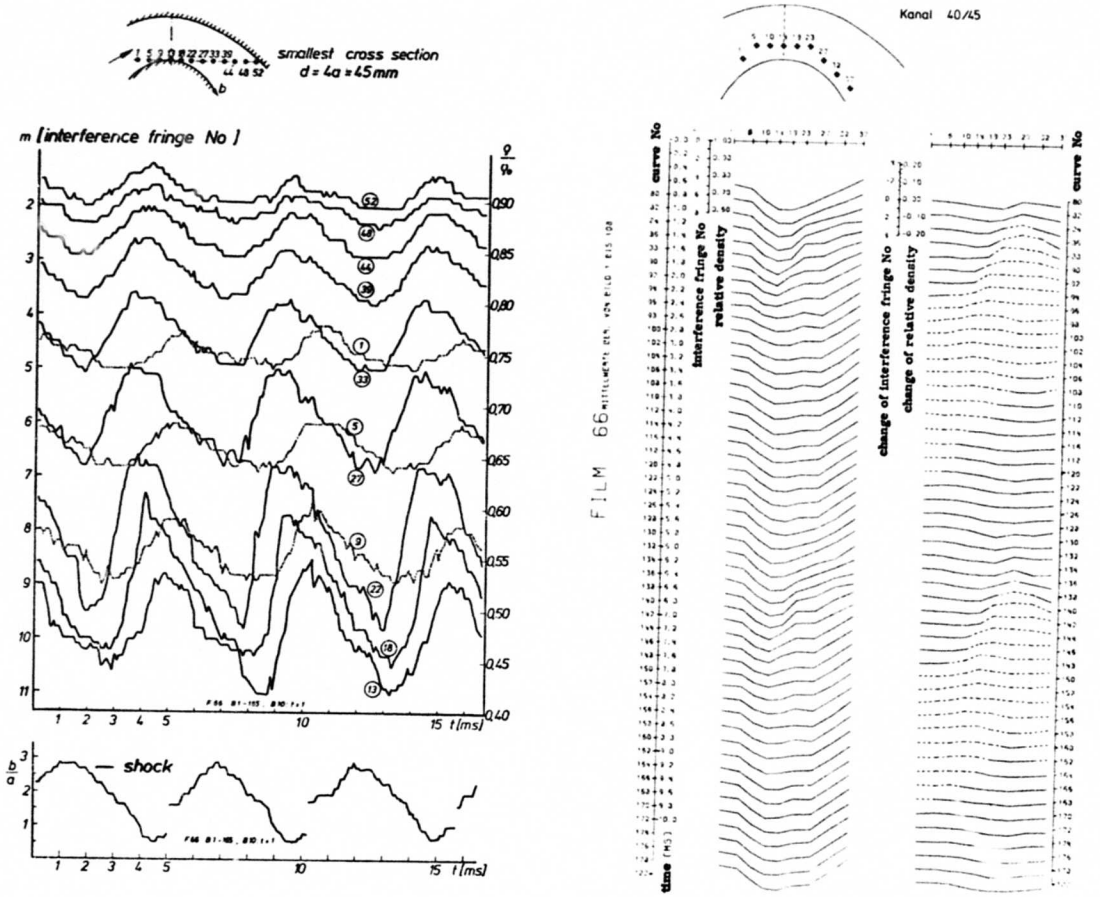

Fig. 3 Time dependence of density and shock position. Plot of density at certain points marked in the sketch of the channel and on the individual curves. Plot of shock position in dimensionless distance downstream of smallest cross section measured on the convex boundary.

Fig. 4 Time sequences of density and density changes in the connection line of the shown scanning points. High density in the changes is marked by dashed lines.

density by $\Delta\varrho/\varrho_0 \cong 0.15$ passing the corresponding points in the flow field. But also the density changes in the subsonic flow, for instance trace 1 or 52, show changes of $\Delta\varrho/\varrho_0 \cong 0.05$. Corresponding pressure changes have the same order of magnitude and therefore have great capability for immediate destruction or for producing material fatigue.

Estimation of the shock velocity from the lower part of Fig. 3 leads to values $|v_s| \cong 10$ m/s. Small values like this occur only in cases of small pressure waves and fluctuations. More usual values, corresponding to oscillations like those shown in Fig. 1, are shock velocities $|v_s| \cong 30$ m/s.

Looking at the maxima of the density curves a phase shift becomes obvious. This indicates that density or pressure increase starts in the area just behind the shock wave when the flow velocity in the supersonic flow tends to reach its maximum. The reasons for this pressure drop are the increasing strength of the shock wave and the change in the boundary contour by the growing separation bubble. Fig. 4 shows in the left-hand part of the diagram time sequences of the density distribution in the flow along the shown scanning points. Development of the shock wave at the end of the supersonic flow can clearly be seen here. The right-hand curves of density differences show how the densities above average are propagated from the area just behind the shock wave into the whole flow field. From this diagram it can also be seen that acceleration, i.e., decrease of density values, starts in approximately the same area. The reason for this seems to be the fact that the boundary layer first reattaches in this area. The velocity of expansion waves taken from these diagrams seems to be higher than shock wave velocities in the upstream direction. Typical values are $|v_e| \cong 50$ m/s.

OSCILLATIONS ON A PROFILE

Transonic flows around profiles can show similar unsteady behavior if the flow tends toward separation. Fig. 5 presents one cycle of oscillation for a symmetric profile with $\alpha = 8^\circ$ angle of attack. In the case

of this profile, oscillations occur only in an area of angles of $6^{o} \leq \alpha \leq 10^{o}$. These limiting angles correspond to permanent attachment and permanent detachment of boundary layer, respectively. In the case of more rounded profiles the oscillation regime will be greater.

A typical difficulty for measurements like this is the proper match of wall impedance of the transonic tunnel simulating the real free field conditions. If for instance the flow in the tunnel is more like a jet, separation will not occur at small angles of attack: oscillations will then be prohibited. If on the other hand walls are too hard, separation occurs in nearly any case with pressure increase, and oscillations thus occur in a too-extensive regime of parameters. To overcome this difficulty without changing the tunnel it may be helpful to make models as small as possible by requirements of Reynolds number.

In the case of Fig. 5 the model thickness was approximately 4 % of the duct width of w = 350 mm. It can be seen that on this profile the flow switches from complete attachment of a flow with high Mach numbers in the supersonic part of the field (frame 1; M = 1.3) to completely separated flow with only a very small supersonic flow regime at the shoulder of the profile, where separation starts (frame 6).

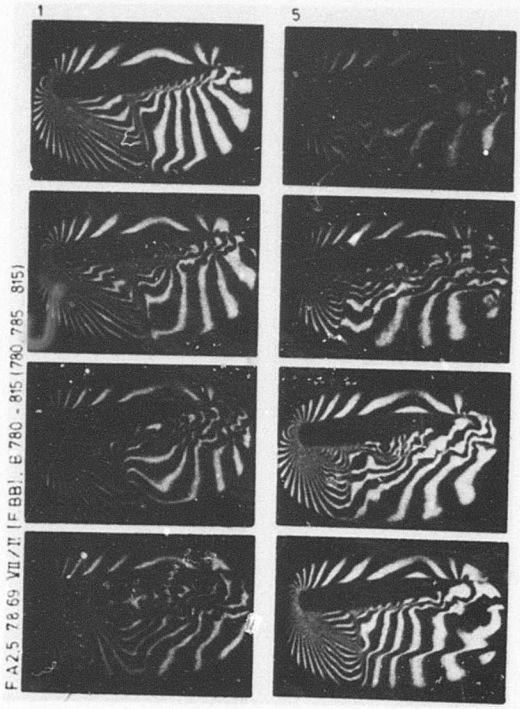

Fig. 5 Interferograms of an oscillation cycle of transonic flow around a symmetric profile (NLR 0.1 - 0.675 - 1.6) of l = 126.5 mm chord length with $\alpha = 8^{o}$ angle of attack. Highest Mach number at the profile $M_{max} \cong 1.3$. Interframe time Δt = 1 ms. Flow direction from left to right.

The separation bubble grows in two directions (see frames 2-5) from the position of the strong shock wave in frame 1. On the one hand it is established downstream with the velocity of turbulent elements, i.e., nearly flow velocity ($|v_t| \cong 100$ m/s). On the other hand it is penetrating below the supersonic flow regime with the velocity of the inclined part of the shock wave ($|v_s| \cong 20$ m/s). This value is then comparable with the upstream flow velocity in the secondary flow regime of the separation bubble which certainly balances static pressure perpendicular to the mixing layer all the time. Therefore it is obvious that this secondary flow is accelerated strongly in the first moment when the separation bubble is formed by the pressure gradient of the shock wave (see frames 2 and 3).

The evaluation of density from a longer portion of the film shown in Fig. 6 demonstrates a more statistical behavior of this type of oscillation. Time scale and amplitudes show this behavior. The reason for this is the missing synchronizing effect of a cavity resonance like that in the case of the curved channel. As can be seen from the shock and separation point movement plotted in the lower part of the diagram, the separation bubble has a very irregular expansion with time. It is also interesting to notice that the velocities of shock and boundary layer separation point, taken from the slopes of these curves, have mostly the same value. This leads to the conclusion that the irregularities come from stabilizing effects in certain states of the oscillation cycle.

The density trace corresponding to point 48 on the high pressure side of the profile shows antiphase oscillation compared with the other traces. This indicates low velocities here when the low pressure side has high average values of velocity and vice versa. So one simply can conclude that large circulation fluctuations are connected with the oscillations of the flow field.

Time sequences of density and density changes in Fig. 7 show behavior very similar to the case at the curved channel. Two differences should be noted and can be seen from the dashed density difference curves: first, the acceleration in this case starts from the shoulder of the wing, which is in agreement with the observation that reattachment of the boundary layer starts here; second, the density in the trailing edge regime is lower although the whole flow field shows higher densities in the deceleration phase. The reason for this can be the more constant mass flow in the duct here compared to the previous and the following case.

OSCILLATIONS IN A LAVAL NOZZLE

As stated before, consideration of the mechanism of oscillations led to experiments with Laval nozzle flow. Fig. 8 shows interferograms of the observed oscillation at a pressure ratio of $p_1/p_o = 0.76$. The pressures p_1 and p_o are the rest pressures in the receiver and supply reservoirs, respectively.

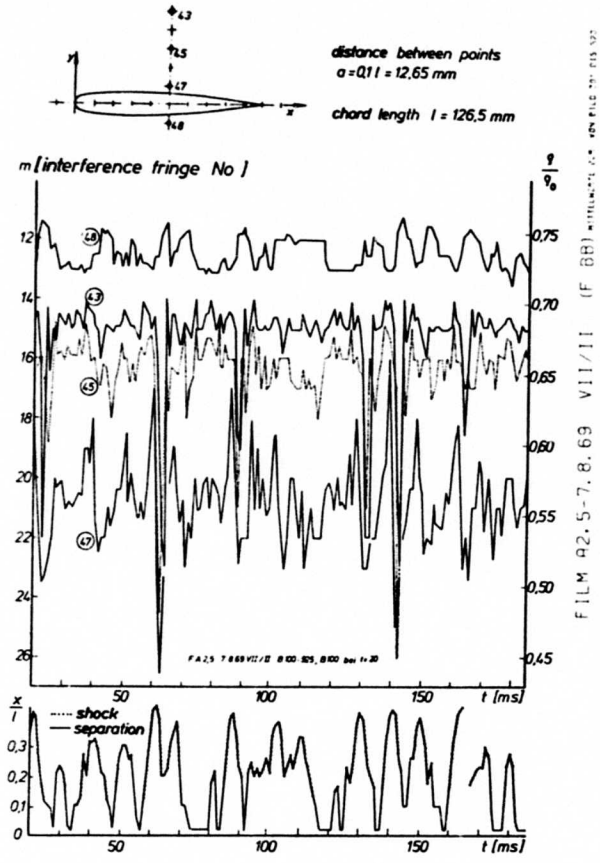

Fig. 6 Time dependence of density and shock position for unsteady profile flow. Plot of density at certain points of the flow field marked in the sketch of the profile. Plot of shock position and separation point in dimensionless distance downstream of profile nose. Angle of attack $\alpha = 8^{\circ}$.

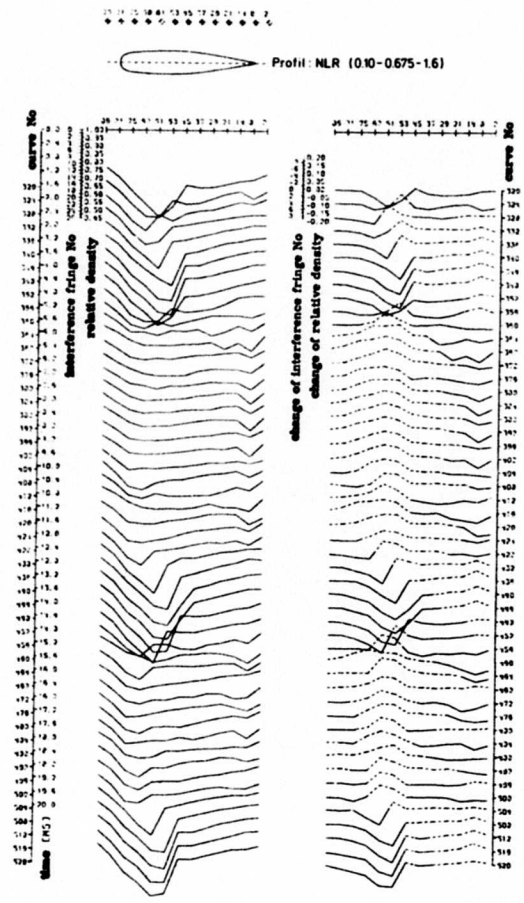

Fig. 7 Time sequences of density and density changes for the line of scanning points shown. High density in the changes is marked by dashed lines.

Frame 1 in Fig. 8 shows a shock wave just at the position of the smallest cross section, which is marked by a vertical line in these pictures. This shock later penetrats the subsonic intake flow, leaving the intake of the duct as a bang wave. Frame 2 shows complete subsonic flow in the nozzle.

Separation is permanent in this type of nozzle flow corresponding to the applied pressure ratio p_1/p_0. In the case of subsonic flow, separation is maintained by very small pressure or density gradients (see frame 2). The boundary layer is separated only at one boundary of the duct. This is due to another type of instability, which in the case of two separation bubbles causes the higher one to grow by centrifugal pressure differences in a curved flow. So at the beginning of any experiment it is decided on which boundary separation will take place.

By means of the applied pressure ratio the flow is accelerated in the frames 3-5. In this acceleration phase the boundary layer is further stabilized and the shock wave is not concentrated in a certain position (see frame 5). If the shock is formed (see frame 7), the separation point switches to the position of the shock root. Thus the shock gets additional back pressure and the separation bubble starts growing (see frames 7-9). The shock wave then penetrats the whole supersonic flow, transforming it to subsonic flow (see frames 8-10 and 1). So the cycle is completed.

The density fluctuations, shown in Fig. 9, look very similar to the fluctuation in the curved channel Fig. 3. The very great changes in trace 2 of $\Delta\varrho/\varrho_0 \cong 0.35$ are due to the fact that the flow Mach number changes from $M \cong 1.2$ in the supersonic flow phase to $M \cong 0.7$ in the subsonic flow phase. This indicates the more one-dimensional behavior of this duct flow with no further possibilities of radiation or equalisation of time-dependant distortions other than in the axial dimension. In other words: although the behavior of the flow is a reaction to a separation at only one of four boundaries the reaction influences a single cross section nearly uniformly. This is the main assumption for the gasdynamic considerations on the mechanism.

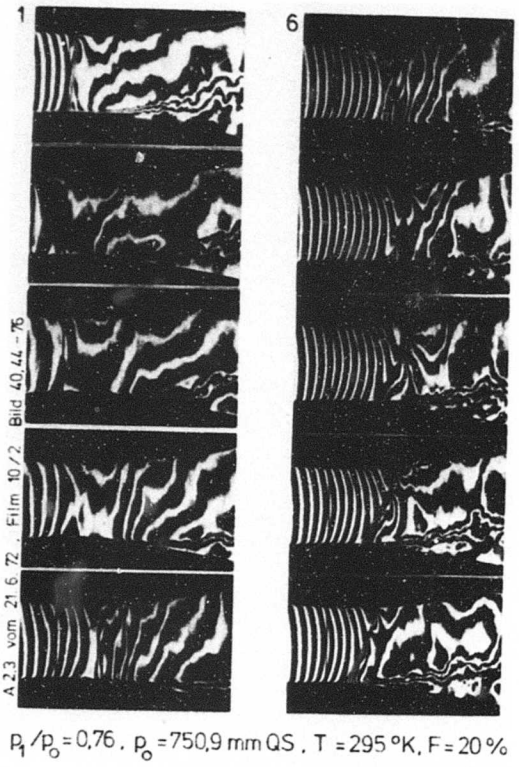

Fig. 8 Interferograms of an oscillation cycle for transonic flow with permanent separation in a Laval nozzle of d = 50 mm wall distance at the smallest cross section. Depth of channel h = 100 mm. Pressure ratio $p_1/p_o = 0.76$. Interframe time $\Delta t = 0.5$ ms. Flow direction left to right.

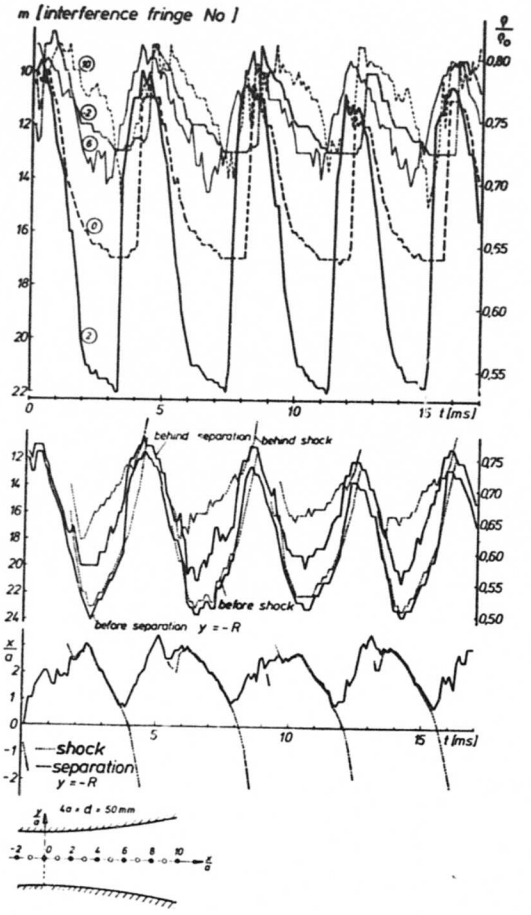

Fig. 9 Time dependence of the density at certain points and of the density before and after shock or separation point respectively. Position of shock wave and separation point in dimensionless distance from zenith.

A plot of the densities just before and behind the shock wave and separation point is shown in the central part of Fig. 9. Differences between these values become great at the end of the acceleration phase. The differences become smaller during the deceleration phase. It is interesting to note that the density itself behind the shock wave is still growing during deceleration. This is due to an amplification of the driving pressure wave, which is not included in the later considerations on the mechanism but can be included in a calculation of a one-dimensional model flow.

The lowest part of Fig. 9 is a plot of position of shock and boundary layer separation point versus time. It is obvious that the downstream velocity of the separation point in the acceleration time is fairly high. Typical values of velocity $|v_p| \cong 30$ m/s are observed. This values correspond to velocities in the lower boundary layer. The outer shape of the separation bubble is changed with much higher velocity. This corresponds to convection velocity of turbulence elements and typical values of $|v_p| = 100$ m/s are observed from interferograms.

The motion of the shock wave, also plotted in the lowest part of Fig. 9, is coupled to the motion of the separation point in the deceleration phase up to a certain position downstream of the smallest cross section. Here they split with remarkable quickness. This sudden splitting is associated with the tendency of the separation point to move to a more downstream position where the duct geometry and boundary layer characteristics are more favorable to separation, i.e., the coupling between the shock wave and the separation point becomes too weak to carry the separation further upstream. After the splitting the shock wave increases its velocity from typical values of $|v_s| \cong 25$ m/s up to $|v_s| \cong 50$ m/s, penetrating the first part of the subsonic inlet flow.

The time sequences of density and density changes of the nozzle flow are plotted in Fig. 10. The motion of the shock wave and the supersonic flow regime as a whole can clearly be recognized from the left-hand density sequence. In the right-hand sequence one can see that the density increase starts just behind the shock wave and is propagated up- and downstream (note that densities greater than the time average are

indicated by dashed lines). The acceleration starts in the same area of the duct and is propagated in the upstream direction with somewhat higher velocity than in the downstream direction; deceleration shows the opposite behavior. All of these phase velocities are in the interval 40 m/s $\leq |v_p| \leq$ 100 m/s.

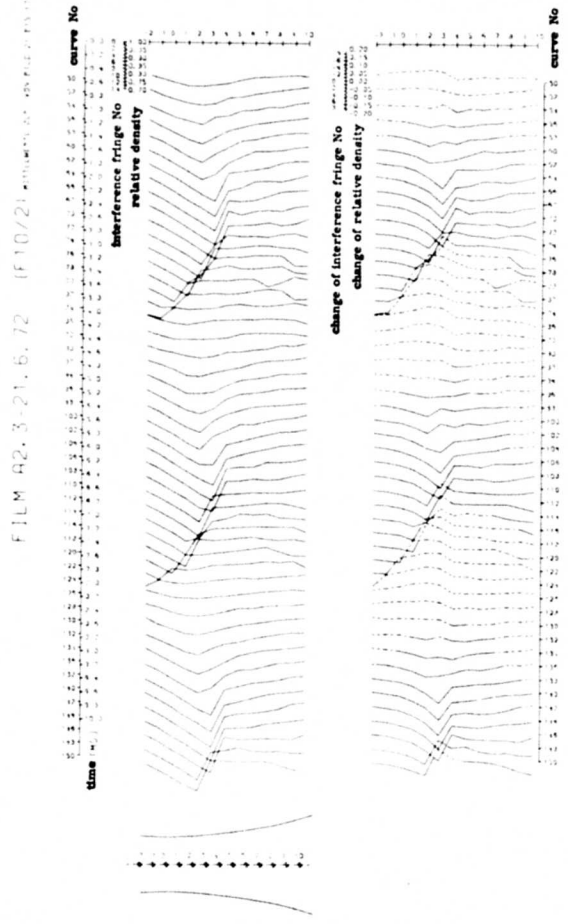

Fig. 10 Time sequences of density and density changes at the center line of Laval nozzle. High density in the changes is marked by dashed lines.

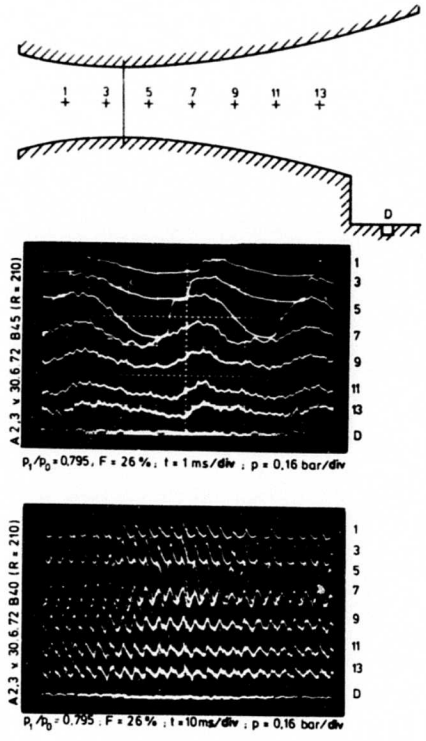

Fig. 11 Pressure oscillations in the Laval nozzle flow in time. The drawing shows the position of the pressure transducers.

Fig. 1i demonstrates, if compared with Fig. 9, the close relation of density and pressure fluctuations. At certain points on the side walls pressure transducers were mounted flush to the wall. The signal trace 7 in the upper diagram shows initially increasing pressure. This is in agreement with the observation from density traces. The penetration of the shock wave can be studied from traces 5, 3 and 1. The traces 7, 9, 11, and 13 show that the pressure increase starts later, downstream of the "center of oscillation" between point 7 and 5. These traces have also decreasing amplitudes like the upstream traces 3 and 1. Trace D indicates that inside of the receiver reservoir only small pressure fluctuations occur.

The lower part of Fig. 11 shows the pressure fluctuations over a longer period of time. The overall behavior is quite regular although some changes in amplitude and cycle length occur. These changes are typical for relaxation oscillations like those discussed here. Small changes of parameters, for instance by interaction with turbulence or sound waves, can influence the single oscillation cycle in a nonpredictable manner.

CONSIDERATIONS OF MECHANISM AND TREATMENT

One can get some further ideas about the oscillation mechanism from a one-dimensional model of the Laval nozzle flow. Fig. 12 shows a sketch of the duct in the upper part and the corresponding pressure values for steady flow in the lower part. The dashed lines give the pressure distribution for nozzle flow without separation. We can get additional information by introducing some knowledge of the boundary layer separation and pressure conditions to this diagram. Curve A shows a pressure distribution in the duct corresponding to frame 2 in Fig. 9 with subsonic flow and separation at the marked point. If we now treat the oscillation mechanism in a quasistatic model, we see that one can reach distributions like B and C without much change in the inlet and outlet pressure. It is important that shock waves B and C lead only to a certain

back pressure given by

$$\frac{p_2}{p_o} = \frac{2\gamma M_1^2 - (\gamma - 1)}{(\gamma + 1)} \left[\frac{2}{(\gamma - 1) M_1^2 + 2} \right]^{\frac{\gamma}{\gamma - 1}} .$$

This pressure is plotted as a dotted line for different front Mach numbers M_1. They are simple functions of the dimensionless length l/d or cross section F/F^* in the diagram:

$$\frac{F}{F^*} = \left(\frac{\gamma + 1}{2}\right)^{-\frac{\gamma + 1}{2(\gamma - 1)}} M_1 \left(1 + \frac{\gamma - 1}{2} M_1^2\right)^{\frac{\gamma + 1}{2(\gamma - 1)}} .$$

The value of $\gamma = 1.4$ for air leads to a maximum of the back pressure curve at $M_m = 1.48$.

We see from the diagram that there is a mismatch between the back pressure of the shock waves and the pressure distribution of the separation bubble, which can be overcome by a very steep increase of pressure along the corresponding dashed curve. This steep increase after the pressure jump of the shock wave will not be tolerated by a normal boundary layer in a divergent duct. Thus the separation point jumps to the shock root. This has two consequences with respect to pressure distribution. The pressure gradient on the separated flow is increased; so this back flow is accelerated and the bubble is growing. The pressure jump in the shock wave becomes too high for a stationary shock and it moves upstram, taking separation point and therefore its instability with it. This situation is indicated in Fig. 12 by extension of the shock wave to the point just above the dotted line.

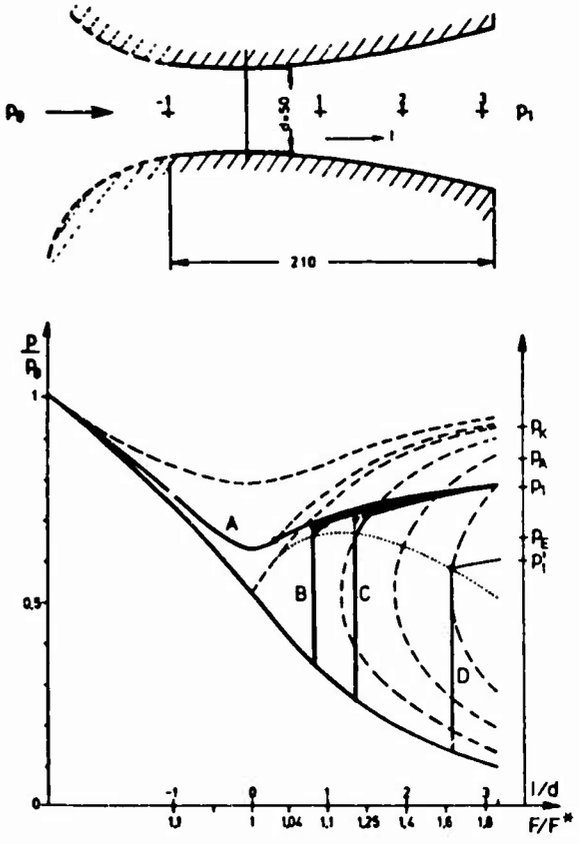

Fig. 12 Gasdynamic pressure distributions in the Laval nozzle flow plotted versus dimensionless length or cross section.

From these considerations we also obtain some information about the instability regime of transonic flows for oscillations described here. If we take for instance a receiver pressure p_1' leading to a pressure distribution like curve D, no instability will occur. Being below the maximum p_e of the back pressure curve an additional pressure increase, to reach the common pressure distribution of separated flow, is not needed. Therefore the shock position is stable in this case. In other words: if the shock wave is moved upstream, pressure increase in the separated flow tends to zero and the backflow decreases.

Another limit for oscillations is obviously the critical pressure p_k. The nozzle flow can reach supersonic velocity, which is essential for the mechanism, only with discharge pressure below p_k. In fact this limit is shifted down to a certain value $p_a < p_k$ by pressure loss in the separation, which depends on the apparatus.

The oscillation regime in terms of discharge pressure therefore is $p_m/p_o = 0.67 < p_1/p_o < p_a/p_o < p_k/p_o$ or in terms of Mach number in front of the shock wave $1 < M_1 < 1.48$. Both the limits are in excellent agreement with experimental results for the Laval nozzle flow. Last penetration of shock waves in the subsonic intake flow was found for $p_1/p_o = 0.66$. The disappearance of oscillations was found for $p_1/p_o = 0.86$, which in this case is the value for p_a/p_o. The value for $p_k/p_o = 0.925$ for thic nozzle is essentially greater: the difference is due to the pressure loss by separation.

In principle these considerations are not restricted to the case of Laval nozzle flow. They are also applicable to the two-dimensional flow fields in the curved duct or around profiles. If λ-shocks occur the considerations are also similar.

The amplitudes of oscillations can be calculated exactly only in the quasi one-dimensional case of the Laval nozzle flow. In the case of two-dimensional flow fields, with the possibility of free propagation of pressure waves in two dimensions, the calculation appears to be more difficult.

We have treated the one-dimensional case with the nonlinear gasdynamic equations, with simple conditions for the coupling of pressure and boundary layer separation. In a first approximation it is assumed that the receiver pressure p_1 is coupled to shock position by means of the coupling of shock wave and separation point in the deceleration phase. The result, an exact solution of the equations, shows good agreement with experiment. We will report on this and more sophisticated solutions in another paper.

The frequency of the oscillations can also be calculated for the one-dimensional case from these solutions. A more practical method, which is also valid for the other cases, was also tried with fairly good results.

The oscillation period was estimated by adding all phase durations of interest:

$t = \sum_{a=1}^{n} g_a \cdot l_a / v_a$ [s], which leads to frequencies $f = 1/t$ [Hz]. The length l_a is a typical length of the structure, for instance the length of the supersonic flow regime, separation bubble, profile, or inlet of the duct. The velocity v_a is the corresponding phase velocity of the phenomenon, for instance the shock velocity, backflow velocity, flow velocity, or velocity of sound. The factor g_a includes constants of proportionality for the values of l_a and v_a respectively and a weighting factor for time overlapping of the phases. The application of this method needs a substantial knowledge of the oscillation process: if this is available the influence of different parameters on the oscillation frequency can be estimated.

In addition to the flow configurations treated in this paper there are other often more complicated configurations where oscillations of the same mechanism occur. Some of the cases already treated, for instance supersonic diffusor intake flow [5], or flow through the sudden enlargement of a duct [6], seem to be closely related. We hope that we can get further results on shock separation interaction in the future.

REFERENCES

[1] Meier, G. and Hiller, W.: An Experimental Investigation of Unsteady Transonic Flow by High-Speed Interferometric Photography. 1968 AGARD CP No. 35, pp. 9-1 ... 9-9.

[2] Pearcy, H.H. and Holder, D.W.: Simple Methods for the Prediction of Wing Buffeting Resulting from Bubble Type Separation. 1962 NPL Aero Rep. 1024.

[3] Trilling L.: Oscillating Shock Boundary-Layer Interaction. 1958 Journ. Aero Sci. Vol. 25, No. 5.

[4] Meier, G.E.A.: Ein instationäres Verhalten transsonischer Strömungen. 1974 Mitt. MPI/AVA Nr. 59.

[5] Dailey, C.L.: Supersonic Diffuser Instability. 1955 J. Aer. Sci. Vol. 22, No. 11.

[6] Jungowski, W.M.: Investigation of Flow Pattern Boundary Conditions and Oscillations Mechnism in a Compressible Flow through Sudden Enlargement of a Duct. 1968 Prace Naukowe, Mechanika Nr. 3 Wydawnictwa Politechniki Warszawskiej.

EXPERIMENT ON TRANSONIC SHOCK-WAVE BOUNDARY LAYER INTERACTION

by

J.W. Kooi
NATIONAL AEROSPACE LABORATORY NLR
Anthony Fokkerweg 2
Amsterdam-1017
The Netherlands

SUMMARY

An experiment is described in which a normal shock interacts with a two-dimensional turbulent boundary layer in an unif rm flow with a Mach number of 1.4. The Reynolds number based on shock position was 20 x 10^6 and based on the momentum thickness at the start of the interaction 2.2 x 10^4. The wall pressure distribution in the interaction region was measured and detailed pitot and static pressure surveys were made. The flow field was analysed and no supersonic tongue was found downstream of the shock. The velocity profiles were integrated to obtain the integral properties whereas the skin friction was derived from Clauser plots. From the distribution of skin friction and the behaviour of the integral properties it has been concluded that the boundary layer separated at the f ot of the shock and reattached 4.5 undisturbed boundary layer thickness downstream of the separation point. The velocity profiles at the start of the interaction and downstream of the reattachment point correlate well with the logarithmic velocity distribution in the wall region. The velocity profile at separation is similar to Stratford's separation profile. The boundary layer at 30 undisturbed boundary layer thickness downstream of the start of the interaction has a skin-friction coefficient, which is still 30 percent less than the equivalent flat plate value.

LIST OF SYMBOLS

C_f	local skin-friction coefficient
C_p	static pressure coefficient, $2(p-p_\infty)/\rho_\infty U_\infty^2$
F	compressibility factor on skin friction, Eq. (5)
H	shape factor, δ^*/θ
k	von Karman's constant, k = 0.41
M	Mach number
n	exponent of power-law profile, $U/U_e = (y/\delta)^{1/n}$
p	static pressure
p_o	tunnel settling chamber total pressure
p_t	pitot pressure
Re_s	Reynolds number based on shock position
Re_x	Reynolds number based on x
T_t	total temperature in deg. Kelvin
U	mean velocity in x-direction
U_τ	friction velocity, $U_\tau = \sqrt{\tau_w/\rho_e}$
x	distance from the leading edge, see figure 1
$\bar{x}$	non-dimensional distance from start of interaction, $\bar{x} = (x-x_u)/\delta_u$
y	distance normal to the plate, see figure 1
$\bar{y}$	non-dimensional distance normal to the plate, $\bar{y} = y/\delta_u$
β	empirical constant in Stratford's separation criterion, Eq. (2)
δ	boundary layer thickness
δ_u	boundary layer thickness at $\bar{x} = 0$, δ_u = 6.6 mm
δ^*	displacement thickness, Eq. (8)
θ	momentum thickness, Eq. (9)
ν	kinematic viscosity
ρ	density
τ_w	wall shear stress
ω	Prandtl-Meyer function

Subscripts

e	conditions at outer edge of viscous layer
i	ideal properties calculated from p, $(p_t)_e$, $(T_t)_e$
u	undisturbed conditions at start of interaction
w	wall conditions
∞	free-stream conditions

Supercript

i	equivalent incompressible values

1 INTRODUCTION

For a number of years it was thought that the transonic flow with shocks over a wing of a model was adequately simulated, compared with full-scale conditions, as long as the boundary layer was turbulent at the beginning of the interaction region. However, with the introduction of the modern highly-loaded, transonic airfoils, transition upstream of the shock turned out to be not sufficient. The cause of this must be found in the boundary layer development at and downstream of the shock. In order to extrapolate the wind tunnel results to the flight Reynolds number the boundary-layer characteristics downstream of the interaction must be quantitatively similar. This can be achieved by the use of wind tunnels with Reynolds numbers, much higher than those of present-day wind tunnels. Another future possibility to extrapolate to high Reynolds numbers may be the use of calculation methods. For the development of these calculation methods it is necessary to have a good insight in shock-wave boundary-layer interaction. This insight will also be of use to establish a minimum Reynolds number for new high Reynolds number wind tunnels.

In the past experimental investigations of the interaction of a boundary layer and a normal shock have been performed by Ackeret (Ref. 1), Seddon (Ref. 2), Gadd (Ref. 3) and Vidal (Ref. 4). Ackeret investigated the transonic flow with a shock over a curved plate. He found that at low Reynolds numbers the boundary layer was laminar and there was an extensive separation at the foot of the shock. The shock bifurcated and a so-called "lambda" foot was formed. When the Reynolds number was increased so that the transition from laminar to turbulent boundary layer took place in front of the shock the lambda foot disappeared and the turbulent layer remained attached. The highest Mach number in front of the shock for the turbulent interaction in Ackeret's experiment was 1.3. In Seddon's experiment a flat plate was used, while the Mach number of the uniform flow in front of the shock was 1.47. The boundary layer was again turbulent. The pressure rise associated with the normal shock was strong enough to separate the boundary layer. The shock wave was bifurcated. Surprisingly enough Seddon found behind the shock wave a region of supersonic flow which compressed isentropically to subsonic speed. Separation at a much lower Mach number (1.2) was observed by Gadd. In his investigation a normal shock was created in a tube. The shock interacted with the turbulent boundary layer on the tube wall. Gadd was unable to observe the shock so that no conclusion could be drawn whether the shock was bifurcated or not. Recently Vidal published the results of his investigation. A pressure distribution of a supercritical airfoil was similated on a flat plate with the use of the transonic nozzle of a Ludwig tube. The normal shock in this experiment interacted with a turbulent boundary layer. The Mach number in front of the shock was 1.4. Results were obtained at two different Reynolds numbers ($Re_s = 9 \times 10^6$ and $Re_s = 36 \times 10^6$). At both Reynolds numbers the boundary layer was separated. The length of the separation bubble was the smallest at the highest Reynolds number.

In the above four investigations wall pressure distributions and boundary layer velocity profiles were measured. Although some of these investigations are quite detailed, they do not provide enough data to study the influence of all parameters which are believed to play an important role in shock-wave boundary-layer interaction. These parameters are: Mach number in front of the shock, Reynolds number and imposed pressure gradient downstream of the shock. When a research program was initiated at NLR with the final aim to develop a calculation method for the interaction region in a two-dimensional flow, it was considered necessary to start with an experimental investigation to provide additional information of the influence of the above mentioned parameters and to improve the physical insight in the interaction.

The model used in the present experimental investigation was quite similar to that of Seddon (Ref. 2). The exclusion of wall curvature which is believed to have an important influence on the interaction, leads to a model of this type. The Mach number in front of the shock in the present experiment was 1.40. This Mach number was chosen equal to that of the experiment of Vidal (Ref. 4). This was done to enable the influence of the Reynolds number at a constant Mach number to be studied. The Reynolds number based on shock position in the present experiment was 20×10^6, compared to 9×10^6 and 36×10^6 in Vidal's experiment. The influence of the Mach number on the interaction will be discussed with the use of the results of Ackeret (Ref. 1), Seddon (Ref. 2) and Gadd (Ref. 3).

2 EXPERIMENT

2.1 Wind tunnel and test conditions

The tests were performed in the supersonic wind tunnel CSST of NLR. At low supersonic speeds this tunnel was operated as an intermittent blow-down facility. The tunnel is equipped with a variable nozzle and has a test section of 27×27 cm^2. A transonic insert with slotted upper and lower walls was placed between the test section and the diffuser. More details of the wind tunnel are given in reference 5.

The Mach number in front of the shock was 1.40 with maximum variations of $\pm$ 0.002 between different runs. The settling chamber total pressure was 2.9 kg cm^{-2}. The mean tunnel total temperature was 278° K and varied a few degrees Kelvin during the course of the experiment due to changes in the ambient conditions. The maximum running time for these conditions was 10 minutes. The unit Reynolds number was 45×10^6 per meter.

2.2 Model

The model consisted of two flat plates mounted in the transonic insert as shown schematically in figure 1. The lower plate was a 72 cm long steel plate spanning the tunnel and supported by two side plates which were fixed to the lower wall of the transonic insert. Air leakage between the tunnel side wall and the side plate was prevented by O-ring seals. To generate and locate a normal shock a second flat plate, the shock generator, was mounted 8 cm above the other one. The leading edge of the shock generator was 45 cm downstream of the leading edge of the lower plate. The shock generator was fixed to the upper wall of the transonic insert by means of two side plates. A wedge was mounted at the trailing edge of the lower plate. This wedge could be moved in upstream and downstream direction by means of an electric driving unit. In this way the height at the exit of the channel formed by the two plates could be reduced until the flow became choked and a normal shock was formed at the entrance of the channel.

During preliminary tests it was found that in the test section disturbances were present created by the transition of the solid upper wall to the slotted wall. As these disturbances were unacceptably large, the slotted upper wall had been partly covered with a solid plate such that the slotted wall started at the leading edge of the shock generator.

To measure the wall pressure in the interaction region the lower plate was equipped with 69 pressure holes arranged around the centerline with a minimum spacing of 2.5 mm. The diameter of the pressure holes were 0.3 mm. A number of pressure holes had the same streamwise location but different distances to the centerline to verify the absence of three-dimensional effects. On the centerline there were 13 ports with a diameter of 8 mm and a streamwise spacing of 15 mm. These ports were used to pass the stem of the probes

for the boundary layer measurements. The traversing mechanism to which the probes were attached consisted of a micrometer, a gearbox and a stepping motor. Probes of different lengths could easily be plugged into the traversing mechanism. Up to a distance of y = 10 mm the probe pressure was recorded at intervals of 0.1 mm after a delay time of approximately 0.5 s. At larger y's the steps were 1 mm. Probe wall contact was sensed electrically.

The position of boundary layer transition on the lower flat plate was fixed using a roughness band which consisted of carborumdum grains. The roughness band was located 40 mm downstream of the leading edge of the lower plate.

2.3 Probes

To be able to make boundary layer surveys at streamwise intervals of 5 mm, 3 flattened pitot probes with the same head geometry but with different lengths have been used. The probes had a tip opening of 0.16x0.49 mm and a wall thickness of approximately 0.07 mm. The distance from stem centerline to probe tip was 20.0 mm, 25.0 mm and 30.0 mm respectively.

To measure the static pressure, the pitot probes were replaced by static pressure probes. For these probes a design had been selected that was previously used in transonic wake experiments (Ref. 6). The static pressure probes, which had a 1.5 mm outside diameter and were equipped with 4 static holes disposed around the circumference at equal intervals. Two static pressure probes have been used with distances from the stem centerline to the static pressure holes of 25.5 mm and 34.6 mm. These probes had a hemispherical nose. A third probe with a conical nose was used when the tip of the probe protruded into the supersonic flow in front of the shock. The distance from the stem centerline to the static pressure holes for this third probe was 25.5 mm. The static pressure measurements of the short probes were slightly influenced by the stem. All measurements with the short probes have been corrected for this error.

2.4 Test procedure and data reduction

In the first test run the position of the wedge was varied until a stable shock position was obtained. The shock position was monitored using the tunnel schlieren system. The shock position was so stable that no change in wedge position was needed for all subsequent tests.

After a supersonic flow was established in the test section, the probe was lowered until contact was made with the wall. Then the probe was moved one step of 0.1 mm away from the wall and the pressure was recorded. In a number of cases the pitot pressure recording was used to check the accuracy of this procedure of probe positioning. This has been done in the following way. As long as the probe was in contact with the wall the pressure was constant but as soon as the probe started to move into the boundary layer the recorded pressure increased. The agreement between both methods was excellent. Probe displacement and data acquisition were controlled automatically by the data acquisition system. Wall static pressure distributions and pitot pressure profiles in the boundary layer were measured simultaneously. The corresponding static pressure profile was measured in a separate test run because the traversing gear could accomodate only one probe at the time. The settling chamber total pressure was measured simultaneously to account for small changes in settling chamber total pressure.

The Mach number distribution in the boundary layer was calculated from the measured pitot and local static pressure. The distance to the wall of the first data point depended on the dimensions of the probe and in general static pressures were not measured at the same y position as total pressures. In these cases the static pressure was interpolated linearly. Besides, an interpolation in streamwise direction was necessary because at a number of stations no static survey was made. These measurements were not required because static pressures varied only gradually and a simple linear interpolation technique was adequate. The velocity profiles were calculated using the assumption that the total temperature across the local boundary layer was constant. In reference 7 it was concluded that integral properties calculated with this assumption give the best agreement with those calculated from measured temperature distributions.

The two dimensionality of the flow was investigated using oil dots applied to the flat plate. From the oil traces it was estimated that the flow is two-dimensional over at least half of the model span. The Mach number variation in spanwise direction was in agreement with the results of the flow visualization. This variation was less than $\pm$ .006 over half the model span.

3 ANALYSIS OF THE RESULTS

3.1 Description of the flow field

A schlieren picture of the bifurcated shock system is shown in figure 2. In figure 3 a schematic drawing of the flow field is given. The flow direction in both figures is from left to right. Just downstream of the start of the interaction (station 16, Fig. 3) a dip in the boundary layer thickness is found. This was observed in schlieren pictures and measured in boundary layer velocity profiles. The flow inside and outside the boundary layer, starting at station 18 is compressed. It is likely that this compression in the supersonic part of the flow takes place in the form of Prandtl-Meyer compression waves. Outside the boundary layer the compression waves coalesce and the forward oblique shock is formed. The oblique shock joins a rear shock to form the upper shock at about 4 δ_u above the plate. This point will be called "bifurcation point". The shock above the bifurcation point is slightly curved; the curvature decreases with increasing distance to the plate. The upper shock is of the strong type i.e. the flow downstream of the shock is subsonic. The rear shock of the bifurcated system is also of the strong type. This is necessary because the pressure of the flow passing through the upper shock just above the bifurcation point must be equal to the pressure of the flow passing through both the oblique and the subsequent rear shock just below the bifurcation point. This can only be achieved by a rear shock of the strong type. The combined pitot pressure losses through the oblique shock and the rear shock are significantly less than the pitot pressure losses through the single upper shock. The regions of different pitot pressure losses are separated by a vortex sheet.

Behind the forward oblique shock the boundary layer grows rapidly and passes over a separation bubble, which has been found to be relatively thin. The boundary layer reattaches some 4.5 δ_u downstream of the separation point.

3.2 Wall pressure distribution

The ratio of measured wall pressure to settling chamber total pressure has been plotted in figure 4. The dimensionless streamwise co-ordinate $\bar{x}$ is defined as the distance downstream of the start of the interaction divided by the thickness of the boundary layer at the start of the interaction. In figure 3 the loca-

tion of the start of the interaction with regard to the shock position is sketched. It is clear from figure 4 that the steepest slope is observed at the start of the interaction. The separation point which is determined with help of the skin-friction distribution, is located at the end of this nearly linear pressure increase ($\bar{x} = 2.4$). The ratio of the wall pressure at the separation point to the wall pressure at $\bar{x} = 0$ is equal to 1.45. This correlates well with the values measured at the same Mach number by Vidal (Ref. 4), and by Little (Ref. 8) in his transonic diffuser experiment. The pressure rise up to the shock is the result of a rapid increase of the boundary layer displacement thickness due to pressure signals of the shock propagating upstream in the subsonic region of the boundary layer. At the edge of the boundary layer, the streamlines turn away from the wall and the supersonic flow in front of the shock is compressed. This compression is - at least at the edge of the boundary layer - isentropic. This is called the "free interaction". In many calculation methods for the supersonic interaction this "free interaction" principle is used to calculate the pressure rise up to the shock impingement point. Free interaction can mathematically be expressed in the following formula:

$$\frac{d\delta^*}{dx} = \tan\left(\omega(M_u) - \omega(M_e)\right) \qquad (1)$$

In Eq. (1) ω (M) is the Prandtl-Meyer function and the subscript u refers to the undisturbed initial conditions. Using the measured δ^* distribution, the pressure distribution has been calculated from Eq. (1) and the results have been plotted in figure 4. The agreement with the measured pressure distribution is very good. At $\bar{x} = 3.8$ the calculated pressure decreases rapidly, but it is precisely at this position that the rear limb of the bifurcated shock wave impinges on the boundary layer. The maximum Prandtl-Meyer angle turning obtained in the present experiment is 7.9°, which is the same as in Seddon's experiment. Figure 4 also presents the pressure distributions measured by Vidal (Ref. 4) at the Reynolds numbers based on shock position, Re_s, of 9×10^6 and 36×10^6. From this graph it can be seen that increasing the Re_s results in an increase of the slope of the pressure distribution at the start of the interaction. It is note worthly that in neither experiment the normal shock recovery is obtained at the wall far downstream of the interaction region. A possible reason for this is the increase of the boundary layer downstream of the interaction resulting for the inviscid flow in a converging channel. Another factor is that the shock is not a simple normal shock but curved and bifurcated which implies a lower downstream pressure.

For incompressible flow, Stratford (Ref. 9) has derived a formula to calculate the separation point on the basis of the measured pressure distribution only. Vidal (Ref. 4) has shown that this formula for incompressible flow can also be used to predict the separation point in transonic shock-wave boundary-layer interaction. Stratford assumed that the initial boundary-layer profile can be approximated by a power-law profile and his separation criterion in its general form is:

$$C_p^{\frac{n-2}{4}} \sqrt{x \frac{dC_p}{dx}} = \left(\frac{n-2}{n+1}\right)^{\frac{n-2}{4}} \left(\frac{3}{n+1}\right)^{\frac{1}{4}} \frac{2.161\ \beta (Re_x)^{1/10}}{\sqrt{(n+1)(n+2)}} \qquad (2)$$

where 1/n is the exponent of the power-law profile and β is a constant equal to 0.66. The undisturbed profile is best fitted with n equal to 8.3. Separation can be expected when the left hand side (LHS) exceeds the value of the right hand side (RHS). The value of the RHS for the present experiment is almost constant and equal to 0.32. The LHS of Eq. (2) is plotted in figure 5 together with the measured pressure coefficient C_p. The point of zero skin friction lies 0.8 δ_u downstream of the theoretical separation point.

3.3 Static pressure distribution

In figure 6 the static pressure profiles at the stations 18 ($\bar{x} = 0.8$), 27 ($\bar{x} = 3.0$), 29 ($\bar{x} = 3.8$) and 52 ($\bar{x} = 12.9$) has been plotted as a function of the non-dimensional normal distance $\bar{y}$. Downstream of the start of the interaction the wall pressure increases, while the static pressure of the inviscid flow in front of the bifurcated shock is constant and equal to the undisturbed value. This means that the static pressure varies through the boundary layer (station 18). Just downstream of the rear shock (station 29) the wall pressure is much lower than the pressure obtained behind the bifurcated shock and again there is a pressure gradient but not of opposite sign. This pressure gradient is not confined to the boundary layer. Also indicated in figure 6 is the wall pressure measured in the absence of the static pressure probes. The difference between the two is less than 0.3 °/o of the measured static pressure. Another check on the accuracy of the measurements is the reading of the static probe in the undisturbed flow. The agreement between the static pressure of the uniform, undisturbed flow measured along the flat plate and the reading of the static pressure probe outside the boundary layer (station 18) is excellent. At station 18 and $\bar{y} = 6.5$ a weak disturbance in the oncoming flow is present originating from the leading edge of the lower plate.

In figure 7 the static pressure distribution at constant $\bar{y}$ is given as a function of $\bar{x}$. The results are plotted for values of $\bar{y}$ of 0.0, 2.3, 3.8, 5.3 and 6.8. An examination of figure 7 shows that the pressure jump for a normal shock is not reached. As discussed in section 3.1 schlieren pictures indicate that the upper shock is curved; the curvature decreases with increasing $\bar{y}$. At $\bar{y} = 5.3$ the measured pressure corresponds to a pressure rise through an oblique shock with a shock angle of 76° and at $\bar{y} = 6.8$ this angle is equal to 80°. The angles measured from the schlieren pictures are in good agreement with these values.

3.4 Total pressure distribution in the inviscid flow

Pitot profiles have been plotted in figure 8. Upstream of the shock an increase in recorded pressure means a decrease in Mach number in front of the pitot probe. The upstream profile is taken at station 25 ($\bar{x} = 2.3$). From this profile it can be concluded that close to the boundary layer a region exists with a local Mach number smaller than the undisturbed value. The observed region with the lower Mach number corresponds with the flow downstream of the forward oblique shock of the bifurcated shock system. The angle between the flow direction and the front leg of the bifurcated system measured from schlieren pictures is about 53°. The local Mach number downstream of a shock of this strength is 1.2 and the flow deflection angle is about 5°. A deflection angle of 5° corresponds well with the calculated Prandtl-Meyer angle change up to

this station. The local Mach number calculated with help of Raleigh's pitot formula is 1.2 and is in agreement with the Mach number calculated from the oblique shock relations.

A remarkeble feature of the pitot pressure distribution downstream of the shock is the very low pitot pressure losses behind the rear shock of the bifurcated shock system. This is the result, as indicated in section 3.1, of a compression through the oblique shock and the subsequent rear shock. At $\bar{y}$ greater than 5.0 the pitot pressure losses are close to the theory for normal shocks. A small difference exists between the measured values upstream and downstream of the shock. This difference is partly due to the fact that the - nominally normal - upper shock was slightly curved and partly due to the use of two different pitot probes. The vortex sheet originating at the bifurcation point has an almost constant thickness of about 0.5 δ_H and is present in all measured profiles. The pitot pressure profiles measured by Gadd (Ref. 3) and Ackeret (Ref. 1) have been included in figure 8 to illustrate a possible relation between separation and bifurcation. The Mach number in the experiment of Gadd was 1.25 and the effective Reynolds number 12×10^6. This effective Reynolds number is calculated from the free-stream conditions and a length equal to the length of a flat plate giving the same boundary layer thickness at the start of the interaction. The boundary layer at the region of shock interaction was separated.

The curve resembles the one of the present experiment. In contrast to these two curves is the one measured by Ackeret (Ref. 1). In his turbulent interaction the Mach number was 1.28; the Reynolds number based on shock position was 0.65×10^6. The shock did not bifurcate and the boundary layer remained attached. Gadd (Ref. 3) has pointed out that wall curvature, as in Ackerets experiment, will increase the Mach number at which separation occurs first. The pitot pressure distribution of Ackeret does not show a region of very low pitot pressure losses. This is undoubtly related to the absence of shock bifurcation. It remains an open question whether separation and shock bifurcation are directly related to each other.

3.5 Boundary layer profiles

From a combination of pitot and static pressure the Mach number may be calculated. The resulting Mach number distribution at station 29 ($\bar{x} = 3.8$) is shown in figure 9. This station is just downstream of the bifurcated shock system. Contrary to Seddon (Ref. 2) no supersonic tongue is found behind the shock. It is likely that this is due to the lower free-stream Mach number of the present experiment, 1.40, compared with 1.47 in the experiment of Seddon. As is shown in figure 9, a region of high velocities, close to the local speed of sound, is found at the edge of the boundary layer. It seems likely that a supersonic tongue may be found in this region already at a slightly higher free-stream Mach number.

The wall pressure at station 16 ($\bar{x} = 0$) has not been influenced by the shock and the characteristics of this velocity profile have therefore been compared with the empirical relations for the flate plate boundary layer. This profile is given in figure 10. The skin-friction coefficient of the measured velocity profile is calculated with help of a Clauser plot. The law of the wall of Winter and Gaudet (Ref. 10) is used:

$$\frac{U}{U_\tau^i} = 6.05 \log \frac{yU^i}{\nu_e} + 4.05 \qquad (3)$$

with

$$U_\tau^i = (C_f{}^i/2)^{1/2} U_e \qquad (4)$$

To find the equivalent incompressible skin friction coefficient a compressibility factor is defined by

$$C_f{}^i = F.C_f$$

with

$$F = (1 + 0.2 M_e^2)^{1/2} \qquad (5)$$

For this station the skin friction deduced from the Clauser plot and corrected for compressibility is 0.00190. Winter and Gaudet give a relation of the skin-friction coefficient for a flat plate boundary layer as a function of the Reynolds number based on the streamwise position. For station 16 a skin-friction coefficient of 0.00192 is obtained.

Method	C_f	Θ(mm)	δ(mm)
Winter and Gaudet flat plate correlation	0.00192	.49	
from measured velocity profiles	0.0019	.49	6.6
boundary layer thickness according to Eq.(6)			6.4

Table 1: Characteristics of boundary layer profile at station 16 ($\bar{x} = 0$)

The close agreement between the values of Winter and Gaudet and the results of the present experiment indicates that the boundary layer is indeed a normal flat plate boundary layer.

The boundary layer thickness $\delta_{.999}$ has been calculated with the formula given by Winter and Gaudet:

$$\delta_{.999} = \frac{1}{3.3} (C_f{}^i/2)^{-1/2} \frac{H}{(1 + M_e^{2/3})} \Theta (1 + .056 M_e^2) \qquad (6)$$

The RHS of Eq. (6) was evaluated using the experimental values $C_f{}^i$, H and Θ. The experimental boundary layer thickness was determined from pitot pressure profiles. It turned out that due to the small stepsize in the surveys it was possible to determine accurately the point in the pitot pressure profile beyond which the pitot pressure became constant. This point is taken as the edge of the boundary layer. The agreement between the experimental δ and $\delta_{.999}$ from Eq. (6) is very good.

The velocity profiles, measured in the interaction region and made dimensionless with the local velocity at the boundary layer edge, have been plotted in figure 11. The velocity distribution outside the boundary layer is given in figure 12. Semi-logarithmic plots of the boundary layer velocity profiles (Fig. 13) indicate the existance of a logarithmic region upstream of the shock. When the boundary layer is retarded due to the pressure rise in the interaction region the extend of this region decreases. Instead of this logarithmic region the profiles at the stations 25 ($\bar{x} = 2.3$), 27 ($\bar{x} = 3.0$) (not shown) and 29 ($\bar{x} = 2.8$) (see Fig. 11) develop close to the wall a form similar to Stratford's separation profile:

$$U = \left(\frac{4}{\rho k^2}\frac{\partial p}{\partial x}\right)^{1/2} y^{1/2} \qquad (7)$$

where k is von Karman's constant. The factor at the RHS of Eq. (7) is evaluated from the measured wall pressure. The best agreement between Eq. (7) and the measured velocity profile is obtained for stations 25 and 27 (see Fig. 14). A well-defined area of reversed flow which is characteristic for local flow separation can not be distinguished. It is, however, believed that the boundary layer is separated from station 29 ($\bar{x}$ = 3.8) to 42 ($\bar{x}$ = 7.6). Very close to the wall the pitot pressure is still 1 °/o higher than the wall pressure. A similar result has been found by Vidal (Ref. 4). He argued that this is caused by the fact that the pitot probe does not only measure the mean velocity but also the time-average of the fluctuating components. With vanishing mean velocities the contribution of the fluctuating velocity components becomes more important and can result in a too high pitot pressure reading. A second effect leading to a reduction of the velocity at a given distance to the wall is obviously the probe-wall interference. A reliable method for separated flows to correct for the fluctuating velocity components and probe-wall interference does not exist and no attempt has been made to account for this. A third factor which can explain the absence of a well-defined region of reversed flow in the experimental data may well be the dimensions of the pitot probe in comparison with the height of a bubble. The height of the bubble can be estimated from the measured velocities which are considered reliable. The thus found bubble height is about 3 times the thickness of the probe. Note that in Seddon's experiment where a well-defined reversed flow region existed the bubble height was 10 times the probe height.

Downstream of station 42 ($\bar{x}$ = 7.6) the boundary layer profile exhibits again a logarithmic part. The height of this region increases with streamwise distance. At station 64 ($\bar{x}$ = 26.5) the velocity distribution is still not in agreement with a fully developed flat plate boundary layer. This agrees with the result found by Seddon. In his experiment the velocity profile resembles again a normal flat plate profile downstream of $\bar{x}$ = 50.

3.6 Integral properties

The skin-friction coefficient was calculated with the aid of Clauser plots. The logarithmic law of the wall with the compressibility transformation of Winter and Gaudet (Ref. 10) was chosen (see Eq. (3) and Eq. (5)). From station 21 ($\bar{x}$ = 1.5) to station 25 ($\bar{x}$ = 2.3) the determination of the skin-friction was not possible because of the absence of a region with a logarithmic velocity distribution. In these cases a formal value for C_f was determined on the basis of the data point closest the wall. The skin-friction distribution found in this way is shown in figure 15. To find the location of the separation point the skin-friction distribution was extrapolated to zero. The separation point was found to lie between station 25 ($\bar{x}$ = 2.3) and station 27 ($\bar{x}$ = 3.0). As discussed in section 3.5 the velocity profiles measured at these stations agreed very well with Stratford's separation profile. Closely related to this is the fact that Stratford's separation criterion predicted also separation at this location.

During flow visualization tests it was observed that oil dots between station 29 ($\bar{x}$ = 3.8) and station 42 ($\bar{x}$ = 7.6) did not move after the shock system was formed. Upstream of station 29 oil was accumulated along a straight line normal to the model centerline and a regular streamwise oil trace pattern was formed downstream of station 42.

The end of the separated region was also found by extrapolating the skin-friction distribution to zero This resulted in a reattachement point close to station 40 ($\bar{x}$ = 6.8). The length of the separated region is approximately 4.5 δ_u. Downstream of the separated region the skin friction increases gradually but even at station 63 the value is still some 30 °/o lower than the normal flat plate value at the corresponding free-stream Mach number and Reynolds number.

In the case of a static pressure variation through the boundary layer the conventional definitions of the integral properties have to be modified. Myring (Ref. 11) has proposed modified definitions having the advantage that von Karman's momentum integral equation is not altered. According to reference 12 the modified definitions can be conveniently expressed in the conventional definitions and an additional correction term. This correction term is calculated from the so-called "ideal" flow properties. The ideal flow properties are computed from the measured local static pressure inside the boundary layer, the pitot pressure at the edge of the boundary layer and the total temperature at the edge of the boundary layer. The modified definitions are:

displacement thickness:

$$\delta^* = \int_0^\delta \left(1 - \frac{\rho U}{\rho_{iw} U_{iw}}\right) dy - \int_0^\delta \left(1 - \frac{\rho_i U_i}{\rho_{iw} U_{iw}}\right) dy \qquad (8)$$

momentum thickness:

$$\Theta = \int_0^\delta \frac{\rho U}{\rho_{iw} U_{iw}} \left(1 - \frac{U}{U_{iw}}\right) dy - \int_0^\delta \frac{\rho_i U_i}{\rho_{iw} U_{iw}} \left(1 - \frac{U_i}{U_{iw}}\right) dy \qquad (9)$$

The subscript "i" indicates the ideal flow properties.

The boundary layer integral properties δ^*, Θ and H are plotted in figure 16. The momentum thickness Θ and the displacement thickness δ^* were made dimensionless with the thickness of the undisturbed boundary layer at station 16 ($\bar{x}$ = 0). The displacement thickness increases mainly at the start of the interaction. The maximum value is reached close to the reattachment point. Downstream of this point the displacement thickness decreases gradually until at the most downstream station the decrease levels off. In general this behaviour agrees with Seddon's results. In Seddon's experiment the maximum δ^* in the separated region was 5.8 times the undisturbed value whereas in the present experiment this maximum is 4.6 times the undisturbed value. It is interesting to note that the contribution of the correction term in the definition of δ^* is at maximum 5 °/o of the total value. This maximum contribution is found at station 18 ($\bar{x}$ = 0.8). Further downstream the magnitude of the correction term falls off rapidly. The correction term for the momentum thickness is much higher: e.g. at station 18 ($\bar{x}$ = 0.8) the contribution of the correction term is 18 °/o and in the separated region it is still 10 °/o. The momentum thickness increases continuously with increasing $\bar{x}$.

The shape factor H is plotted in figure 16. It is generally assumed that the boundary layer is separated when the shape factor exceeds a certain value; in reference 2 and reference 13 this value is about 2.6. In figure 16 the value of 2.6 is exceeded between station 25 and station 27. This is in agreement with the results of other separation criteria as discussed before. At the reattachement point the value of H is some-

what lower than in Seddon's experiment. After reattachement H decreases.

4 CONCLUSIONS

The interaction of a normal shock and a turbulent boundary layer at a Mach number of 1.4 has been investigated experimentally. The analysis of the data has led to the following conclusions.

1. The wall pressure distribution in the interaction region at a Reynolds number of 20×10^6 correlates well with the pressure distribution measured by Vidal (Ref. 4) at the same Mach number but at Reynolds numbers based on shock position of 9×10^6 and 36×10^6.
2. The measured initial pressure rise agrees well with the one calculated from the measured displacement thickness using the Prandtl-Meyer function.
3. From schlieren pictures it is observed that the shock is bifurcated. The pitot pressure losses through the bifurcated shock are less than 0.5 °/o. Downstream of the bifurcated shock system no supersonic flow is found, in contrast with what has been reported by Seddon at a Mach number of 1.47.
4. Upstream as well as downstream of the normal shock the static pressure varies appreciably through the boundary layer.
5. From Stratford's separation criterion, the skin-friction distribution obtained from Clauser plots and the value of the shape factor H it is concluded that the boundary layer separates at the foot of the shock. The length of the separated region is about 4.5 δ_u. The height of the separation bubble is too small to be accurately estimated from the measured velocity profiles.
6. In the region of the sharp initial pressure rise the logarithmic velocity distribution close to the wall disappears. The velocity profiles close to the separation point are well described by Stratford's separation profile.
7. At 30 δ_u downstream of the shock the boundary layer has not yet obtained normal flat plate characteristics.

5 REFERENCES

1. Ackeret, J., Feldmann, F., Rott, N. — Untersuchungen an Verdichtungsstössen und Grenzschichten in schnell bewegten Gasen. Bericht Nr. 10 a.d. Inst. f. Aerodynamik ETH Zürich, 1946.
2. Seddon, J. — The flow produced by interaction of a turbulent boundary layer with a normal shock wave of strength sufficient to cause separation. ARC R and M 3502, 1960.
3. Gadd, G.E. — Interactions between normal shock waves and turbulent boundary layers. ARC 22, 559 - F.M. 3051, 1961.
4. Vidal, R.J., Wittliff, C.E., Catlin, P.A., Sheen, B.H. — Reynolds number effects on the shock wave turbulent boundary layer interaction at transonic speeds. AIAA paper No. 73-661, 1973.
5. Erdmann, S.F.A.H.P., Vicq, R.F. de — Short review on wind tunnel facilities of the NLR. NLR GG.47, 1964.
6. Zwaaneveld, J., Egmond, J.A. van — Grenslaag en zogmetingen aan quasi-elliptisch profiel 0.1-0.675-1.6. NLR TR 69108, 1969.
7. Nothwang, G.J. — An evaluation of four experimental methods for measuring mean properties of a supersonic turbulent boundary layer. NACA Rep. 1320, 1957.
8. Little, B.N. — Effects of initial turbulent boundary layer on shock-induced separation in transonic flow. Von Karman Institute for Fluid Dynamics Tech. Note 39, 1967.
9. Stratford, B.S. — The prediction of separation of the turbulent boundary layer. JFM Vol. 5, Pt. 1, Jan. 1959, pp 1-16.
10. Winter, K.G., Gaudet, L. — Turbulent boundary-layer studies at Mach numbers between 0.2 and 2.8. RAE TR 70251, 1970.
11. Myring, D.F. — The effects of normal pressure gradients on the boundary layer momentum integral equation. RAE TR 68214, 1968.
12. Zwaaneveld, J. — Comparison of various methods for calculating profile drag from pressure measurements in the near wake at subcritical speeds. AGARD Conference on Aerodynamic Drag, AGARD-CP-124, 1973.
13. Alber, I.E., Bacon, J.W., Masson, B.S., Collins, D.J. — An experimental investigation of turbulent transonic viscous-inviscid interactions. AIAA Paper 71-565, 1971.

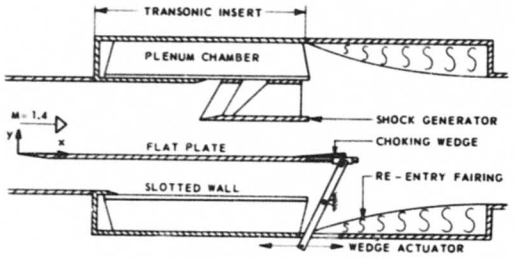

Figure 1: Model in test section

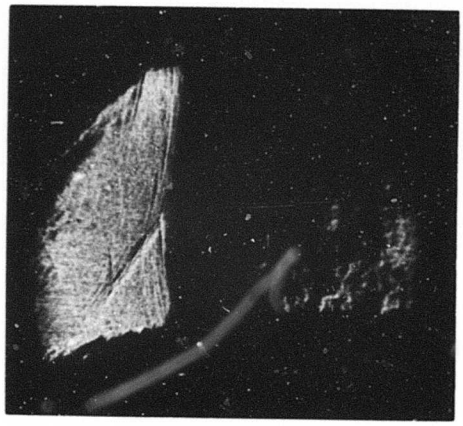

Figure 2: The bifurcated shock system

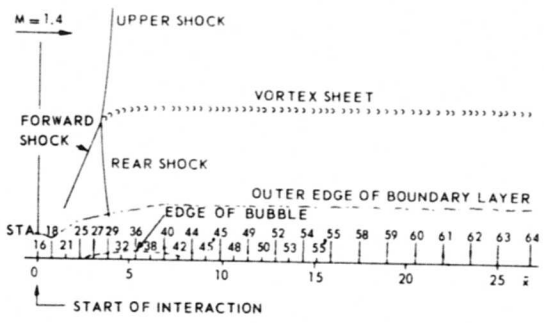

Figure 3: Position of survey stations

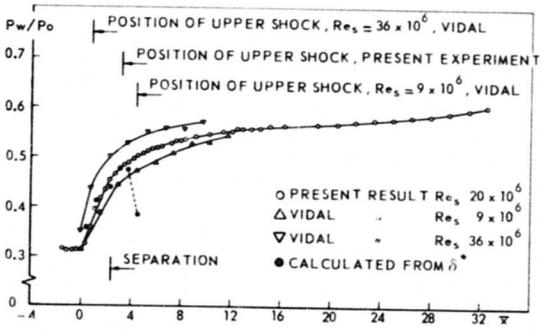

Figure 4: Wall pressure distribution

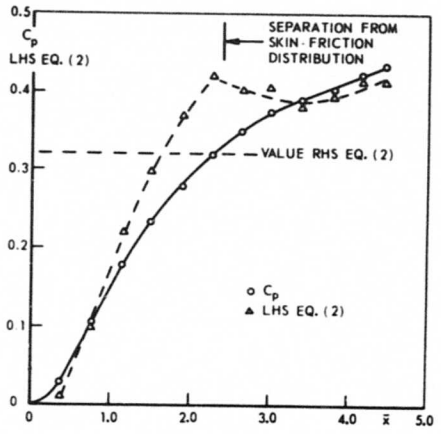

Figure 5: Calculation of separation point with Stratford's criterion

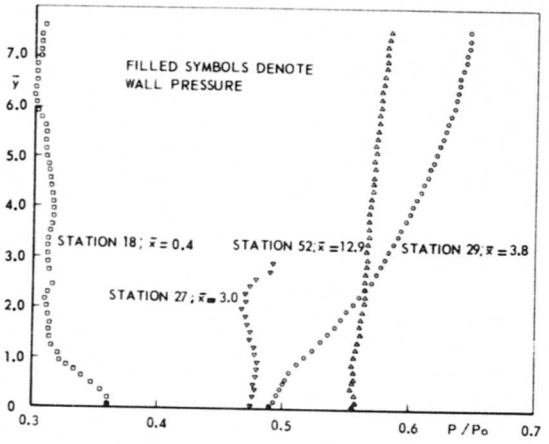

Figure 6: Static pressure profiles normal to the wall

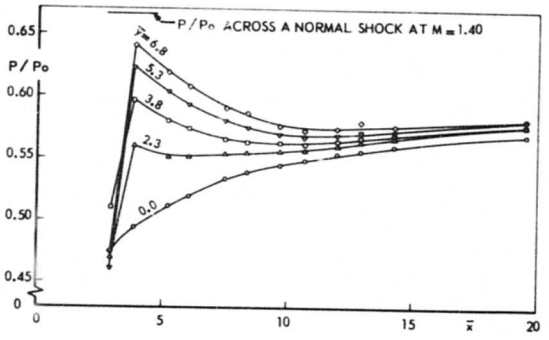

Figure 7: Static pressure distribution downstream of shock at varies distances to the wall

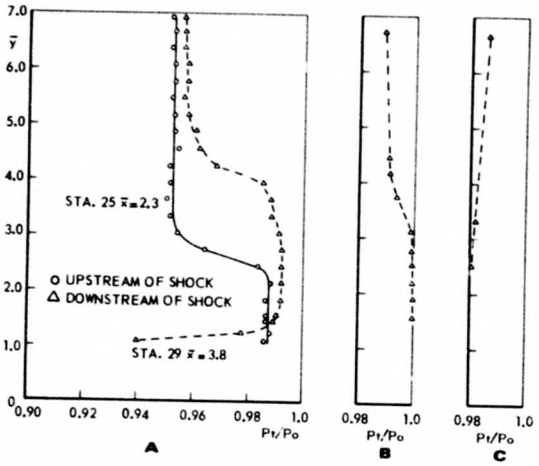

Figure 8: Pitot pressure profiles of the present experiment (a); Gadd's result for a Mach number of 1.25 (b) and Ackeret's result for a Mach number of 1.28

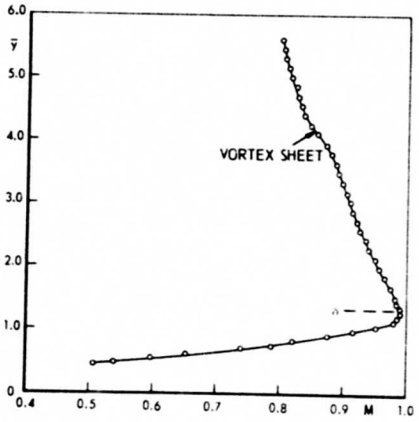

Figure 9: Mach number profile downstream of shock (station 29, $\bar{x} = 3.8$)

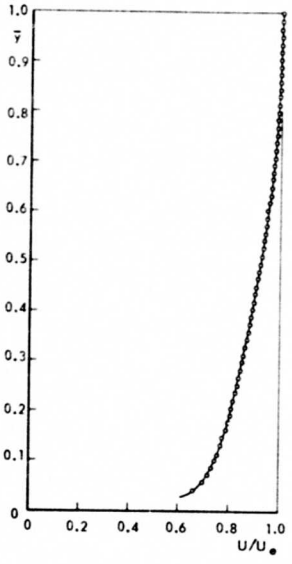

Figure 10: Non-dimensional velocity profile of the undisturbed boundary layer (station 16, $\bar{x} = 0$)

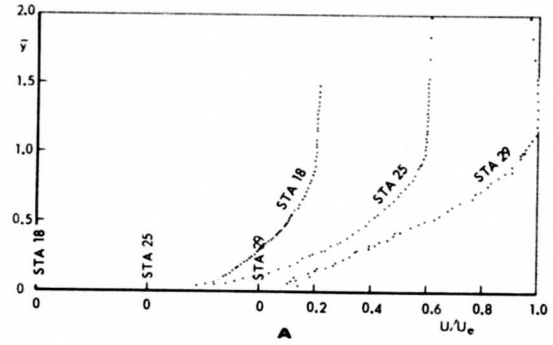

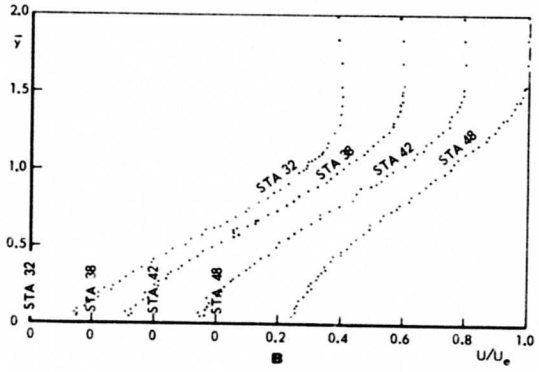

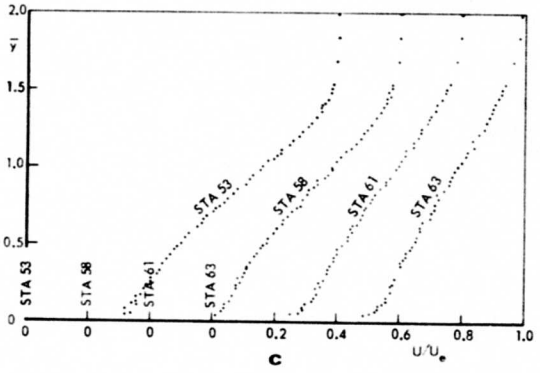

Figure 11: Non-dimensional boundary layer velocity profiles in the interaction region

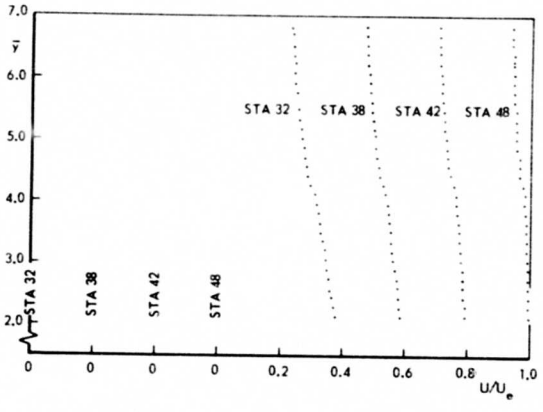

Figure 12: Non-dimensional velocity profile downstream of shock outside the boundary layer

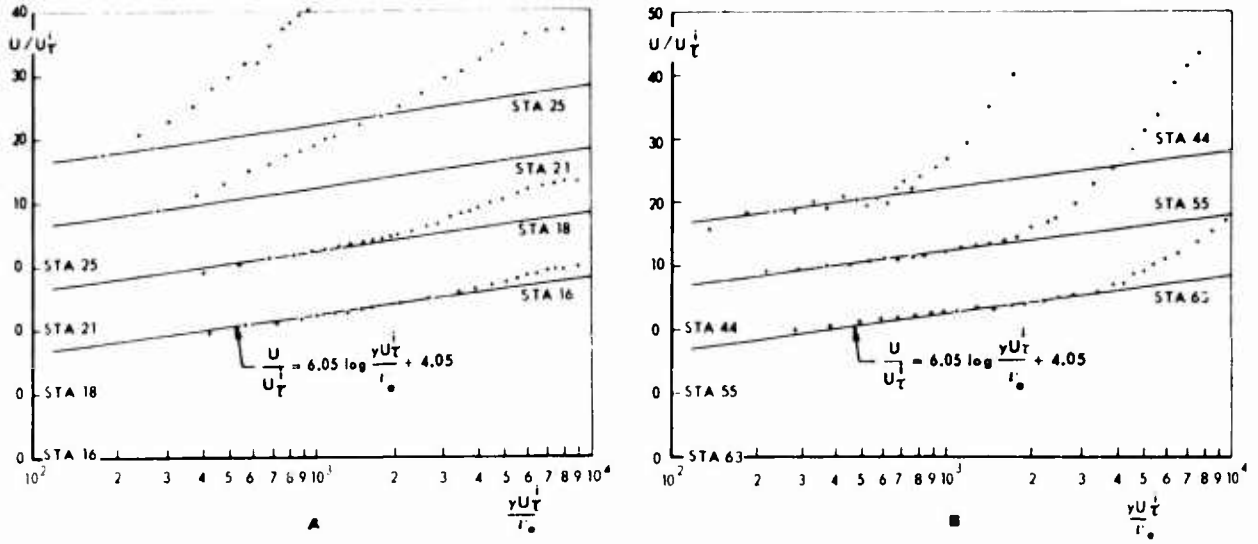

Figure 13 Logarithmic velocity profiles

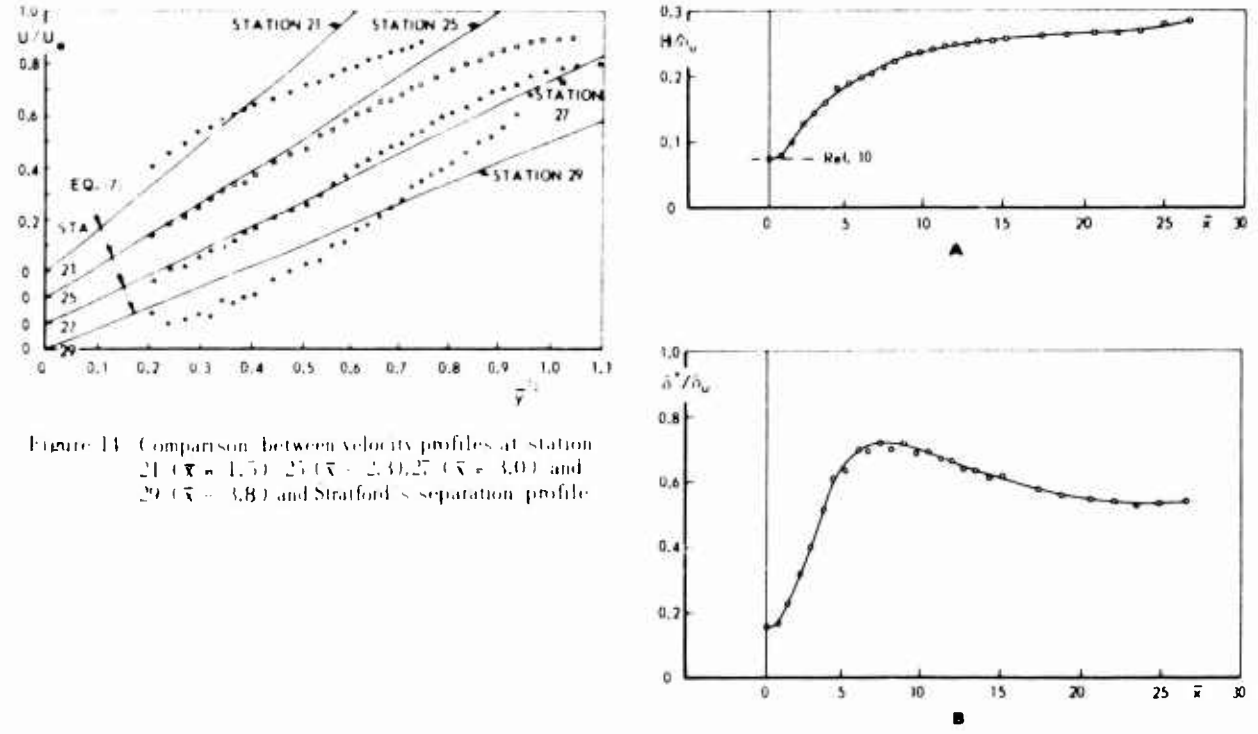

Figure 14 Comparison between velocity profiles at station 21 ($\bar{x} = 1.53$), 25 ($\bar{x} = 2.33$), 27 ($\bar{x} = 3.03$) and 29 ($\bar{x} = 3.83$) and Stratford's separation profile

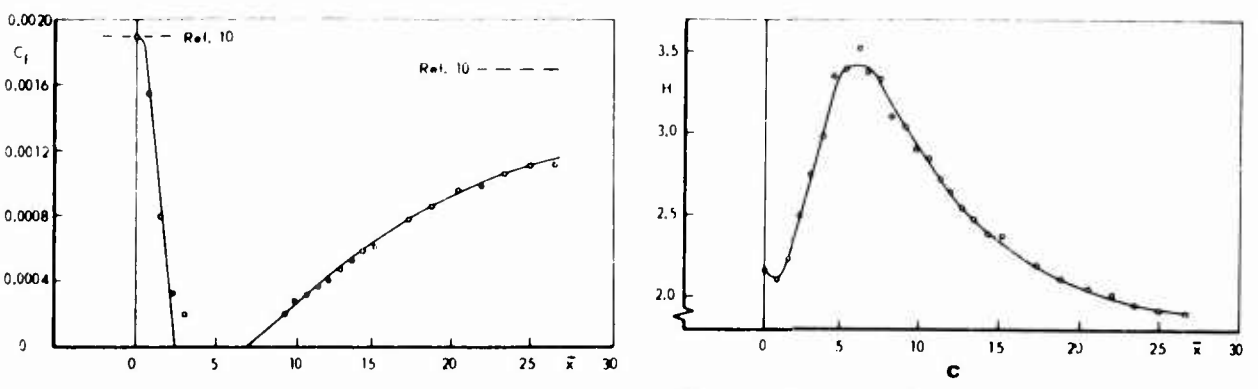

Figure 15 Skin-friction distribution in interaction region

Figure 16 Momentum, displacement and shape factor distribution in interaction region

A REVIEW OF SEPARATION IN STEADY, THREE-DIMENSIONAL FLOW

by
J. H. B. Smith
Royal Aircraft Establishment
Farnborough, Hants, UK

SUMMARY

Recent work which aims to explain the nature of three-dimensional separation, to predict its occurrence and to represent the behaviour of separated flow is reviewed. Despite the diversity of problems and methods, an attempt is made to present a unified view which leads from a consideration of the structure of the problem and the role of modelling, through the partial solutions which have been found, to some illustrations of the application of three-dimensional flow separation in aircraft design.

Much of the work reported is only partially three-dimensional, in the sense that boundary layers are calculated for flows over cones or infinite sheared wings and that slender-body theory is used to calculate the separated flow. These treatments reveal the limitations of some two-dimensional concepts like re-attachment and present an exciting range of problems and possibilities. Such glimpses as we have of the fully three-dimensional situation suggest a still richer field, but also warn us against relying on properties which are limited to quasi-two-dimensional situations.

Behind the presentation is the view that separation is an essential feature of the aerodynamics of lift and propulsion, that it is nearly always three-dimensional, and that there are benefits to be found in encouraging its three-dimensionality.

1 INTRODUCTION

The simplest way to categorize flow separations is in terms of their causes, and in the aeronautical field these are mainly

(1) obstacles protruding from a wall,
(2) blowing normal to a wall,
(3) shock waves,
(4) adverse external flows over smooth walls,
(5) salient edges.

Important examples of the first of these are the separation of the fuselage boundary layer caused by the wing and the separations provoked by excrescences on the otherwise smooth surface of the aircraft. The effects of large protuberances were discussed in some detail in a review by Peake, Rainbird and Atraghi[1] and the effects of small excrescences were discussed in a recent AGARD paper by Gaudet and Winter[2]. In principle the larger scale separations of this type can be regarded as special cases of types 4 and 5 and I shall not discuss them specifically.

Blowing normal to a wall presents itself in two extreme forms: the penetration of a transverse jet into the main stream for purposes of lifting, control or mixing; and the smoothly distributed injection of fluid, which is a favourite problem in two-dimensional boundary layer theory and describes some cooling schemes. The major difficulties in modelling the overall behaviour of a jet emerging normal to a wall (see, e.g. Ref.3) have discouraged attempts to examine its effect on the wall boundary layer. The presence of turbulent shear stress normal to the wall and of entrainment into the jet must clearly affect the structure of those regions both upstream and downstream of the jet, in which separation would be found if the jet were a solid obstacle. The surface oil-flow patterns of McMahon and his colleagues[4,5] offer a challenge which does not seem to have been taken up. Nor has much been done about the effects of distributed blowing on three-dimensional separation.

The interactions between shock waves and boundary layers have been extensively studied, including the central problems of whether the shock separates the boundary layer and, if it does, what form the separation takes. Green[6] reviewed work in this field in 1970. Work on situations involving three-dimensional interactions has continued fairly intensively since then, particularly in the specialist areas of wing design for high subsonic flight and of the off-design performance of supersonic intakes. As would be expected, the presence or potential presence of shock waves does nothing to simplify the problems. As would also be expected the types of separation which arise[7] are not different in kind from those familiar elsewhere and extensions of two-dimensional correlations for incipient separation are possible[6]. I shall not attempt to up-date Green's extensive survey.

Most of the specific examples to which I shall refer later are either of separation induced on a smooth body by a smoothly varying external flow or else of separation produced at a salient edge of a body. Typical examples of the former are the flow over bodies of revolution at incidence, the flow over the upper surfaces of swept wings, the outboard flow over the upper surface of a delta wing beneath the primary vortex, and the flow past upswept rear fuselages. With the exception of the flow over the rear of fuselages, which was reviewed recently by Peake, Rainbird and Atraghi[1], these examples will be discussed later. Both laminar and turbulent separations are of practical interest. Separations at salient edges occur at trailing edges where boundary layers are thick and turbulent and pressure gradients are usually adverse, at sharp leading edges where boundary layers are thin and sometimes laminar and pressure gradients are favourable, and at the lips of cavities. In flows over smooth surfaces the emphasis is on predicting where separation will occur. In flows over salient edges the emphasis is on modelling the separated flow. Although more work is needed on both of these aspects, the next important task is to bring them together, so that a model of the separated flow is incorporated in the method which predicts where separation will occur.

We also need to consider the relevance of our studies to the design of aircraft. It is perhaps worth pointing out that the flight of heavier-than-air craft only became possible through the exploitation of

separation from the sharp trailing edges of wings and propeller blades. For a long time the application of flow separation in design stopped there and advances in the efficiency of flight came about as the aerodynamicist applied his art to the elimination of separation forward of the trailing edge. Intentional separations were confined to spoilers, dive-brakes and vortex generators, the role of the last being to prevent larger-scale separation.

The task of avoiding separation became harder as the demands made on lifting surfaces became more extreme, in terms of the ranges of speed and angle of incidence over which they had to work. Military aircraft are now designed to manoeuvre with extensive regions of separated flow[9] and civil aircraft like Concorde take off and land with large-scale flow separations[10]. Slender missiles and flare-stabilised re-entry vehicles encounter flow separations which lead to guidance and heating problems. Unfortunately our ability to model the phenomena of separated flow and to incorporate its features in rational design procedures has not kept pace with its occurrence in practice.

This review begins with an attempt to define the problems involved and the relations between them, and a discussion of the role of flow modelling. Some of the differences between separated flow in two and in three dimensions are described. The main part of the review deals successively with the nature, the prediction and the modelling of flow separation in three dimensions. In conclusion, some applications of separated flow in the aerodynamic design of aircraft are briefly discussed.

2 PROBLEM DEFINITION

We can now attempt to define areas of interest. First there is the large area in which separation is unwanted and, we believe, avoidable. Either we know it is positively harmful, perhaps increasing drag or reducing lift, or it is a nuisance, introducing such complexities as forebody vortices into a simpler design concept. This is the area of classical aircraft design, in which separation takes place at sharp trailing edges only. We need to know what the causes of separation are, how to avoid them and how to minimize the effects of unavoidable separation. The sort of mathematical models that help us are models of inviscid flows over specified boundaries, models of wakes shed from sharp trailing edges and models of boundary-layer flows. The boundary-layer calculation method must be capable of predicting separation, at least in the sense that it only breaks down when separation is imminent and that it does not proceed past separation lines without indicating their presence. This area is fairly well understood, in the sense that the remaining problems can be isolated, not that they are necessarily close to solution. Advances are being made and will continue to be made by working separately on the computation of the inviscid flow and of the boundary layer, and then putting the methods together for design applications.

As soon as this area of essentially attached flow is left behind, models of the separated flow are needed. However, it is useful to distinguish an area of some importance in which it is sufficient to have a model of the separated flow, without the need to predict where separation occurs. If the separation takes place from a salient edge, its occurrence is independent of the boundary layer structure, at least for high Reynolds number. A shear layer forms at the salient edge and, again for high Reynolds number, this can be modelled by a vortex sheet. The role of viscosity is to produce the separation: its location is determined geometrically. Inviscid models can then be constructed.

A typical flow of this kind is found on wings with highly-swept, sharp leading edges, when the shear layers shed from the leading edges roll up into vortices with a spiral structure. Simple flows of this kind are fairly well understood, but the presence of free boundaries makes computation difficult, and there are still some conceptual difficulties, in particular in relation to the formation of multiple centres of rotation.

The next stage in complexity is reached when we have a model of the separated flow but the origin of the separation is not fixed by the shape of the body. A simple example is the slender circular cone at incidence. Separation gives rise to shear layers, which we can model by vortex sheets rolling up into spiral vortices. It is fairly certain that, if the separation lines are specified, the resulting inviscid problem with the embedded vortex sheets will have a sensible solution. The position of the separation line should emerge from a boundary-layer calculation carried out for an external flow in which the separated flow is represented. An iteration process should then lead eventually to a consistent representation in which boundary-layer separation is predicted along a line from which a vortex sheet originates.

The final category of problems is the one in which we have no adequate model of the separated flow. Precisely which problems we place in this category is a matter for individual judgement, but we should all agree that there are some separations for which no adequate model exists. Two lines of approach are then needed: detailed and careful experimental studies and sound thinking about the physical mechanisms involved. Experiments in separated flow are difficult, because the flow field must be investigated in depth, in spite of its sensitivity to interference from measuring probes. Optical methods, so useful in two-dimensional flow, become much more complex in three-dimensional flows[11]. The unsteadiness of many separated flows at frequencies lower than those characteristic of turbulence is a basic difficulty affecting both experimental technique and the construction of helpful mental concepts.

The classification of problems which I have been attempting is summarized in Fig.1. The representation is entirely topological and the sizes of the regions are not meant to indicate their importance or the extent of our knowledge.

3 LEVELS OF MODELLING

It is necessary at this point to defend an extended discussion of models. It is possible to maintain that the only model we need to consider is the set of Navier-Stokes equations governing the motion of a viscous, compressible, heat-conducting fluid. Progress with special sub-models for particular forms of separated flow is slow and essentially limited; many separated flows of practical concern are extremely complex; progress in computer hardware and in numerical methods for solving differential equations is very rapid.

For instance, calculations of laminar, three-dimensional separated flow by the numerical solution of the Navier-Stokes equations have already been reported by Li[12]. He considers a body consisting of a hemispherical nose followed by a circular cylinder and terminated by a conical flare with a flat base. For the region between this body and the bow shock wave he marches in the time direction until an essentially stationary condition is reached. Typically, for an angle of incidence of 20°, a Mach number of 3 and a Reynolds number of 10^4, he describes the flow by 9000 interior points. 20 points lie on each line between the body and shock, concentrated near the body, and there are 18 azimuthal stations between the leeward and windward meridians. About 2000 time steps are needed and the process takes 100 hours on an IBM 360-75. The published results all relate to the body surface, but they show, as indications of separation, the vanishing of the azimuthal component of skin friction on the cylinder just aft of the spherical nose, and the vanishing of the longitudinal component of skin friction on the cylinder just ahead of the flare.

Other large-scale computations of this kind have made use of some simplification of the Navier-Stokes equations for steady flow. Lin and Rubin[13] at Brooklyn and Lubard and Helliwell[14] in California have studied the laminar flow past a cone at incidence at high Mach number. In this flow, separation is found downstream of a region near the apex in which the shock wave and boundary layer merge in a single viscous region, and it is this downstream flow, in which a boundary layer is distinguishable, that they consider. A spherical polar system of coordinates is then natural. If r is the radial distance measured from the apex of the cone, then the essential simplification is to neglect viscous diffusion in the r direction. This leads to a system of equations which is parabolic in r, so that a marching technique can be used. Diffusion in the circumferential direction is retained, in addition to the representation of diffusion normal to the surface, as in the usual boundary-layer model. Initial conditions at the upstream end of the computed region are required. These can be taken from a solution for the merged layer on a sharp cone or a solution for the flow over a blunt nose.

Lin and Rubin[13] assume in addition that, at high Reynolds numbers, viscous effects are confined to a thin layer and that the flow external to this layer is conical. The external pressure field is taken from measurements. Within the viscous layer they find vortex structures when the incidence is moderately large. The flow attaches in the plane of symmetry on the windward side and then leaves the surface along separation lines on the leeward side. There is a second attachment in the plane of symmetry on the leeward side. At smaller angles of incidence the flow leaves the surface in the plane of symmetry on the leeward side. This can be regarded as a separation, but it is a trivial one, since no vorticity is being shed from the 'separation line', owing to the symmetry of the flow. Agreement with experimentally observed separation is good, with various calculated and measured values of the azimuthal angle of separation lying within a band of about 10° width. The position of separation is apparently unaffected by heat transfer, but increasing Mach number delays separation and reduces the extent of the vortex structures.

The same authors have recently extended their method to treat a spinning cone[15]. An angular velocity of 10^4 revolutions per minute has remarkably little effect on the symmetry of the lee-side vortices, displacing them by no more than a degree or two in a typical case ($M = 8$, $Re = 10^5$, $\iota = 12^{\circ}$, $\sigma = 10^{\circ}$). In this case the flow is unsteady and the identification of the separation line presents difficulties.

Lubard and Helliwell[14] solve a similar set of equations, but treat the whole flow field between the cone and the bow shock as a single viscous region, so no interaction with an external flow arises. In their reported work they use an artificial starting procedure, but this is not an essential feature. They find they need to take steps in the marching direction which are larger than a certain minimum size, in order to obtain stability. The results found agree well with experiment, separation being predicted about 6° of azimuth ahead of its observed position in a typical case ($M = 14$, $Re = 8.3 \times 10^5$, $\iota = 8^{\circ}$, $\sigma = 5.6^{\circ}$).

In spite of the demonstrated achievements of these integrated approaches to the prediction of separated flow, two arguments persuade me that the continued consideration of local or sub-models is worthwhile. The first argument is technical, the second philosophical. The technical argument is just that the representation of turbulence, at least upstream of separation, is vitally important in many practical problems. Representing turbulence directly through the time-dependent Navier-Stokes equations makes such enormous demands on the capacity and power of computers that it is difficult to imagine its effective implementation. Some closure hypothesis then becomes necessary and we are led away from the conceptual simplicity of the Navier-Stokes equations and back to sub-models.

The philosophical argument naturally concerns ends rather than means. If our aim is to reproduce our bit of the real world in a computer, then the solution of the Navier-Stokes equations is a possible approach, at least for laminar flows. We may hope to obtain more precise information, more quickly and more cheaply than by making measurements in real fluids, and this is well worth doing. However, as scientists we wish to understand things, and as engineers we wish to alter things. In both of these processes the acquisition of data needs to be accompanied by the growth of conceptual frameworks which can account for the data we already have and show us where more is needed. It is such conceptual frameworks which enable us to formulate intelligent ways of modifying and controlling our bit of the universe. They are built of models, some far-reaching and all-embracing, but some quite special. I do not see the need for special models disappearing in our field. In particular, I expect the distinction between the external inviscid flow and the boundary layer, on which the science of aerodynamics has been built, to continue, supplemented locally by special models of separation phenomena.

4 'RE-ATTACHMENT' AND 'SEPARATED REGIONS'

The kind of local model needs to be rather different in three-dimensional flow from those familiar in steady two-dimensional flow. If a boundary layer in a plane flow separates from the body, either it re-attaches to the body downstream or it gives rise to a wake flow. In either case we can label a region of the flow as 'separated' and discuss its properties. This is not generally so with three-dimensional separations. Those fluid particles which leave the surface of the body along a separation line only return to the body in exceptional circumstances.

Since it is almost impossible to draw fully three-dimensional flow fields, I have chosen in Fig.2 to represent the conical flow past a thin, slender, sharp-edged delta wing at incidence. The picture is

familiar, but it is worth remembering what the lines on it represent[12]. If you can imagine all the streamlines of the flow being projected from the apex of the wing on to this plane, then these lines are just those projections. Alternatively, if you consider all those stream surfaces which pass through conical rays, then these lines are the intersections of those stream surfaces with the plane. What the picture does is to present how the fluid particles progress from one conical ray to another, ignoring how they travel along each ray. Consequently, the free stream appears as an inward flow. The particles leaving the leading edge are special, since they carry vorticity. They do not return to the wing, but end up in the leading-edge vortex, as do all the particles between the streamlines ending at A_1 and A_2. There is a temptation to describe the conical ray through A_1 as a re-attachment line, by analogy with two-dimensional flow. In fact the fluid approaching the body near this line comes from the free stream, just as it does in the case of the attachment line through A_2. In particular, new, initially laminar, boundary layers develop on the two sides of A_1, although the free shear layer becomes turbulent soon after it is shed from the leading edge. The boundary layer flowing outboard from A_1 is distinct from the free shear layer above it and, in fact, separates again to form a secondary vortex. This secondary separation may be laminar or turbulent. Note that we cannot point to a closed region of separated flow: the upstream flow penetrates everywhere.

This is, of course, an extreme case chosen to bring out the unexpected features of three-dimensional separation. It is easy to imagine how, at a smaller angle of sweep-back and a smaller angle of incidence, the scale of the separation becomes much smaller, in particular in relation to the thicknesses of the free shear layer and the wing boundary layer. The free shear layer on its return towards the leading edge then merges with the boundary layer on the wing and the flow reaching the wing inboard of the vortex is contaminated by the turbulence in the free shear layer, as indicated in Fig.3. When this happens we have a region of turbulent rotating flow near the leading edge, with a turbulent boundary layer downstream of it. In the figure, the mean streamlines are again to be regarded as conical streamlines, although I am not suggesting that conical conditions will be found in subsonic flow at these smaller angles of sweep-back. If the flow were conical, the turbulent region would be growing in size, roughly in proportion to the distance downstream from the apex. What is more frequently realized in experiments is an approximation to the flow past an infinite sheared wing, in which the flow, although three-dimensional, is independent of spanwise position. This corresponds to a conical flow in which the vertex has receded to infinity. The region of turbulent flow would then become of constant size and could well be described as a bubble.

At Queen Mary College in London, Prof. Young and his students have made a number of explorations of bubble flows, starting with unswept bubbles. Their first study of a swept bubble, by Horton[16], was reported briefly to the last AGARD meeting on separated flows in 1966. His bubble was generated on a flat plate by a lifting cylinder placed above it, the whole configuration being swept through 26.5°. Recently Delpak[17] has completed a study of the effects of increasing the sweep to 45°. With the same external pressure field imposed, he finds a 'separated region' whose size depends on Reynolds number. At high wind-speeds, a separated region resembling a short bubble is found, with constant length across the span. At a lower speed, the flow at the upstream end remains much the same, but the size of the bubble increases across the span and the larger separation outboard is associated with a reduced suction peak. At a lower speed still, the larger separation is found across the span and uniform conditions are not obtainable. Strong outboard flows are found in the separated region, analogous to the high axial velocities in the cores of leading-edge vortices. Much of what takes place can be interpreted in terms of modifications of two-dimensional flow patterns, but a considerable residue seems to need a model which is three-dimensional from the start.

5 ATTACHMENT

Having used a picture of conical flow to illustrate the difference between two- and three-dimensional separation, I ought to draw attention to an over-simplification which can arise from reliance on conical and sheared-wing flow patterns. This concerns not separation, but attachment. Flow attachment takes place at upstream stagnation points, but when a flow has a plane of symmetry there is usually an attachment line in it. This line has a number of properties:

(1) it is a streamline of the external flow,
(2) it is a limiting streamline (skin-friction line),
(3) there is no pressure gradient normal to it,
(4) both sets of surface streamlines diverge from it,
(5) the boundary layers which develop on either side of it are independent, and
(6) it is a geodesic on the surface.

There is not time to discuss the various interdependencies between these properties. I want to point out that lines with the same properties arise away from planes of symmetry in conical flows and in sheared-wing flows. However, in more general three-dimensional flows it does not seem that all the properties occur together, except in planes of symmetry.

If we consider, for instance, a swept wing at incidence, then there will be a limiting streamline which runs roughly parallel to the leading edge and divides those limiting streamlines which pass above the wing from those which pass below it. We might call this limiting streamline an attachment line of the surface flow. Similarly, in the flow external to the boundary layer, there will be a streamline, also roughly parallel to the leading edge, which divides the external flow passing above the wing from that passing below it, and we might call this streamline an attachment line of the external flow. However, there is no reason why either of these attachment lines should be geodesics on the surface, nor why the pressure gradient normal to either of them should vanish. If the boundary-layer model is entirely consistent there should be a stream surface of the real flow which passes through both of them, but this will not be normal to the surface of the body. The two attachment lines will be displaced laterally. There will be an attachment region in the boundary layer along the leading edge of the wing which will affect the flow over both the upper and lower surfaces, and this attachment region will contain the attachment lines of the surface flow and of the external flow.

6 NATURE OF SEPARATION

When we come to separation lines we find a rather curious situation. Most people are quite confident that separation lines can be recognized in patterns of limiting streamlines, whether these are obtained experimentally by oil-flow techniques or numerically from flow calculations. On the other hand, the actual definition of a separation line gives rise to a lot of discussion, much of it stemming from ideas put forward by Maskell[18,19]. Two approaches can be distinguished: a local approach, which is needed in order to recognize separation as it happens; and a global approach, which is needed to establish the consistency of postulated flow patterns.

The local approach seeks to identify the separation line in terms of the behaviour of the limiting streamlines near it. Maskell[18] described it as an envelope and cusp locus of the limiting streamlines. The mathematical expression of this definition gives it a precision which invites controversy[20]. To pursue the controversy it is necessary to be clear about whether it is solutions of the laminar boundary-layer equations or of the Navier-Stokes equations that are relevant and which definition of envelope is to be adopted (see, e.g. Ref.21). It seems to me that 'envelope' is a good descriptive word for what is observed and has not been improved upon. In the context of the laminar boundary-layer equations, the behaviour of the shear stress near the separation line is relevant to the controversy as well as being of intrinsic interest. Is there a singular behaviour or not? The work first of Brown[22] and then of Buckmaster[23] shows that a singular behaviour is possible, just as Goldstein found in two-dimensional flow. It is still possible to argue about whether it occurs.

The global approach starts with a recognition[18] that two different sets of limiting streamlines come together at a separation line. Stewartson[24] made this more precise by distinguishing points on the surface which are accessible from the upstream attachment point from those which are not, giving a definition which includes the two-dimensional behaviour. In the case of a slender body at moderate incidence, however, separation lines form which are fed on both sides by fluid from the upstream stagnation point. One scheme of limiting streamlines in such a flow is shown in Fig.4, taken from Legendre[25]. BD is a separation line, fed on both sides by fluid from the upstream stagnation point A. Eichelbrenner[26] gives essentially the same definition of a separation line as Stewartson. In addition he distinguishes between separation proper and a 'clash' of boundary layers. It seems he would regard the situation shown in Fig.4 as a clash. We certainly need to consider such flows. Lighthill[27] defines a separation line as a line which issues from both sides of a saddle point of separation and, after embracing the body, disappears into a nodal point of separation. In Legendre's scheme, B is such a saddle point of separation and one streamline through it, BD, fits Lighthill's definition. However, in the other direction it ends in the spiral point C. Whether BC is itself a separation line or whether separation only occurs from the point C is discussed briefly by Legendre in a later paper[28]. The streamline patterns in the vicinity of these various types of singular points have been drawn by Oswatitsch[29].

Maskell[18] also showed separation originating on a slender body from a separation line which starts at an ordinary point of the surface. This removes the complication of the saddle point and spiral point from Fig.4. Wang[30] has revived this idea recently in the course of a lively discussion of possible separation patterns. In physical terms, with separation envisaged as arising from the close approach of the limiting streamlines, the scheme is attractive. It is particularly easy to imagine a trivial separation of this kind developing in a plane of symmetry, with streamlines converging on both sides, and with no definite point at which the separation could be said to start. It is less easy to imagine when the cross-flow is non-zero and the separation results in the shedding of vorticity. The details of how the separation line starts are in any case unimportant compared with the realisation that the separation line need not cross the plane of symmetry, so that the separation is entirely fed from the upstream stagnation point of attachment.

Even when the separation line does cross the plane of symmetry, as in Fig.5, so that a downstream point of attachment has to be introduced, it does not follow that the separation forms a closed bubble. It is possible for a vortex-sheet separation in the form of a horse-shoe or a hairpin to form, fed on both sides with air from the free stream. A closed separation line does not necessarily give rise to a closed separation surface, and it is the form of the separation surface which is the more significant.

7 PREDICTION OF SEPARATION

It might have been hoped that the calculation of the three-dimensional boundary layer, apart from difficulties with starting in an attachment region and with recognizing separation as it occurs, would prove to be a straightforward numerical problem. Unfortunately, even with laminar flows numerical difficulties arise near separation, and conceptual uncertainties in the modelling of turbulence become more important near separation. This is not the place to attempt a review of boundary-layer calculation methods and I shall only pick out a few examples relevant to the prediction of separation.

Several years ago, Cooke[31] calculated the laminar boundary layer on a circular cone at incidence, using a conical external flow. Separation can then only occur along a conical ray. His solution starts from the windward generator and marches round the cone. He found that, as separation was approached, it was necessary to reduce the step size in the marching process so much that effective progress became impossible. However, he was able to use the analytical form derived by Brown[22] for the solution near separation to extrapolate convincingly for the position of the separation line. Separation is predicted to occur earlier than it was observed by Rainbird, Crabbe and Jurewicz[32], typically by 15 to 20° in azimuthal angle when the incidence and semi-angle of the cone are both 7.5°. Calculations reported by Jaffe and Smith[33] agree with those of Cooke, although they were not carried so close to separation. Cooke suggested that the discrepancy in his prediction of separation might have arisen either from the use of slender-body theory for the external flow field or from the absence of any representation of separation in the external flow. The latter seems more likely, since calculations by Tsen and Arnaudon[34] for cones at incidence in supersonic flow used exact external flow solutions and still found discrepancies in separation position of about the same size. They treat the compressible laminar boundary layer by an integral method and introduce the cross-flow through an iterative procedure. Their results show an appreciable effect of

heat transfer on the magnitude of the cross-flow, but very little effect on the location of separation, in agreement with Cooke's finding[35] and with the work of Lin and Rubin[13].

Cooke's method is equally applicable to the flow over infinite sheared wings and has been programmed for this case by Beasley[36] for incompressible flow and by Hirschel[37] for compressible flow. Cooke also extended his method to treat laminar boundary layers in 'quasi-conical' external flows, defined by the property that the direction of the external velocity is constant along each ray, although its magnitude varies along the rays. This extension[38] enabled him to obtain good agreement with measurements by Hummel[39] of the boundary layer on the upper surface of a delta wing, including the secondary separation of the flow swept outboard under the primary vortex.

For fully three-dimensional laminar boundary layers, the pioneering work of Raetz[40], Der[41] and Hall[42] is now bearing fruit. Three numerical procedures have recently been reported, by Blottner and Ellis[43], by Wang[44] and by Geissler[45]. The calculations of Blottner and Ellis have not been carried far enough to encounter separation. Wang has presented detailed results[44] for the incompressible flow over a prolate ellipsoid of axis ratio 1:4 at 30° incidence, and, subsequently[46], at 45° incidence. His calculation extends as far as the line on the body along which the circumferential component of skin friction vanishes. Away from the extremities of the ellipsoid, this line is almost a meridian, so its position is probably a good indication of the position of the separation line. Unfortunately he shows no comparison with observations, such as those of Peake, Rainbird and Atraghi[1].

Geissler[45] uses a coordinate system based on the external streamlines, in contrast to Wang's use[44] of a system related to the geometry of the body. He calculates incompressible flow over three prolate ellipsoids and a combination of an elliptic forebody with a cylindrical afterbody. He finds the limiting streamlines running together to form separation lines like those of Wang, but the absence of a common test case precludes quantitative comparisons. The displacement thickness grows rapidly near the upstream origin of the separation line. As the separation line is approached, the numerical method becomes unstable, a feature which Geissler claims is characteristic of separation when the calculation is effected in streamline coordinates. It is of some interest that he finds the separation line on his cylindrical afterbody in about the same circumferential position as Schönauer[47] found the separation point in the two-dimensional flow past a cylinder.

When the boundary layer is turbulent it is again easiest, both conceptually and computationally, to start with problems in which there are essentially only two independent variables. For the turbulent boundary layer on a cone, this requires a further assumption about the growth of the boundary layer along a generator. Mewlem and Smith[48] describe an integral method based on such an assumption, but their calculations of flow on a cone do not extend to separation.

The slightly artificial case of the infinite sheared wing does not require such an assumption and provides a problem in two independent variables which exhibits features of fully three-dimensional flow. For test cases we have the pioneering experiments of Cumpsty and Head[49] and the more recent measurements by van den Berg and Elsenaar[50]. Calculations have been published by Bradshaw[51], Wesseling and Lindhout[52], P.D. Smith[53], Fannelöp and Humphreys[54], Krause[55] and Cebeci[56]. We hope to hear more from NLR at this meeting. These methods generally show good agreement with experiment well upstream of separation. Closer to separation, calculation seems to diverge from experiment, though it seems there are usually variations in the methods which can be exploited to improve the agreeement. Bradshaw calculated the measured flow of Cumpsty and Head and found a very pronounced effect from a term he introduced to account for the effect of the longitudinal curvature of the wall. When this term was introduced, separation moved upstream from $x = 0.77$ to 0.60, passing through its measured position at $x = 0.66$. He also showed significant differences between the predictions of his own differential method and Head's integral method, separation being particularly sensitive.

P.D. Smith[53] applied his integral method, based on Head's entrainment concept, to the measurements of van den Berg and Elsenaar[50], in which surface curvature effects were avoided. He calculates separation to occur between stations 7 and 8 using Johnston profiles for the cross-flow and between stations 9 and 10 using Mager profiles. Separation actually occurred between stations 8 and 9. The need to choose a profile family is avoided by the use of a differential method, but some closure assumption is still needed.

Fannelöp and Humphreys[54] use an eddy viscosity formulation, recommending a reduced eddy viscosity for the cross-flow. With the measured pressure distribution of van den Berg and Elsenaar, they fail to predict separation. However, they noticed that the measured external-flow direction was not consistent with the measured pressure distribution, assuming the flow was really part of an infinite-sheared-wing flow. Using a modified pressure distribution derived from the measured external-flow direction, they calculate separation slightly upstream of its observed position.*

Krause[55] has recently applied his method[57] for calculating fully three-dimensional boundary layers to the same experimental situation. His object was to test three different eddy viscosity formulations, all isotropic, in the sense that the same relations are used for both components of the Reynolds stress. Changes in the eddy viscosity formulation lead to significant variations in the predicted skin friction but variations of about the same size arise from changing the difference scheme used in the calculations from a second-order formula to a fourth-order formula. Neither change has much effect on the cross-flow. Agreement with experiment deteriorates as the measured separation line is approached, and, as in the original calculation of Fannelöp and Humphreys[54], separation is not predicted. Krause attributes this failure to the inadequacy of the closure assumptions, in particular to their isotropic nature. In this connection it is appropriate to refer to an analysis by East[58] of his own data and that of other workers. He concludes that the shear stress in a three-dimensional turbulent boundary layer is not parallel to the velocity gradient, but does not propose a better representation.

Since so many problems arise in sheared-wing boundary layers, it may seem absurd to proceed to examine fully three-dimensional turbulent flows. However, there is a successful prediction of separation to report. P.D. Smith[53] has applied his integral method to the turbulent boundary layer on the upper surface of a delta wing, as measured by East[58]. Although the cross-flow angles are exaggerated by the

* According to a later paper[122], this was the result of an error, and separation is not predicted with the modified pressure distribution

calculation and the amount of the exaggeration depends on the profile family used, the position of the secondary separation is predicted to within 2.5% of the local semi-span of the wing. The success of the calculation is related to the fact that the flow, and consequently the regions of influence, are broadly aligned with the generators of the almost conical external field; whereas for the infinite sheared wing the flow crosses the generators, which are the lines of constant percentage chord.

From this cursory examination of a complex field, I conclude that, for laminar flow in three dimensions, existing boundary-layer methods are probably adequate to carry out the task of predicting separation. This places the emphasis on the formulation of adequate models of the separated flow and of schemes for including these in calculations which embody the interaction between the boundary layer and the external, separated flow. For turbulent flow much more is needed. If integral methods are to become reliable, better ways to represent the cross-flow must be sought. Current methods of representing turbulent processes in differential methods seem to become inadequate as three-dimensional separation is approached; so that, although differential methods offer the better long-term prospect, at present they provide no advantage over integral methods.

8 MODELS OF SEPARATED FLOW

The only three-dimensional separated flows to have been modelled extensively are those which arise from highly-swept separation lines, giving rise to rolled-up shear layers. Before dealing with these it is convenient to mention two extensions to three dimensions of techniques for treating separation in two-dimensional flow.

The first concerns the basic problem of how the laminar boundary layer approaching the trailing edge changes into the wake behind it. In two dimensions, Stewartson and others have shown that the flow has a triple-deck structure, with outer regions which are asymptotically thicker than the boundary layer. Recently Guiraud[59] has provided an extension of this work to three-dimensional flow, treating the flow near the trailing edge of a swept plate with a small edge angle at zero incidence.

The second of these extensions concerns the separation ahead of a ramp in supersonic flow. Werle, Vatsa and Bertke[60] consider an infinite, swept ramp, with a uniform flow along the ramp and a supersonic flow normal to it. Their solution depends on a double iteration. In the inner loop the external flow and the boundary-layer parameters are matched locally at each point. The outer loop determines the pressure at separation, by requiring that the pressure downstream of reattachment returns to its inviscid value. It is not clear from their account how this fits in with the upstream flow. They find that the extent of the separated region increases as the angle of sweep increases, in spite of the reduction in the Mach number of the flow normal to the ramp.

Coming now to separation from highly-swept separation lines, I want to start with the simple case in which the position of the separation line is fixed, through the presence of a salient edge. It is reasonable, for large enough Reynolds number, to model the shear layer springing from the edge by a vortex sheet. Since the rolled-up sheet is infinite in extent, a simplified representation of the inner part of it is needed. Several asymptotic solutions for the inner part exist (see, e.g. Küchemann and Weber[61] and references therein) but they have not so far been included in calculations of the whole flow field. Instead, slender-body theory approximations are introduced and the inner part of the rolled-up sheet is replaced by a line vortex. The resulting model is illustrated (Fig.6) for the flat-plate delta wing at incidence. It is sufficient to consider a cross-section of the flow, perpendicular to the centre-line of the wing. In this plane, a slit represents the wing, there are finite lengths of vortex sheet, and isolated vortices are joined to the free ends of the sheets by cuts. The vortex and the cut together represent the inner part of the spiral sheet. The component of the free stream provides a flow at infinity. A solution of Laplace's equation in this plane is to be found in which the wing slit is a streamline, the velocity at the leading edges is finite, the pressure is continuous across the vortex sheet and the vortex sheet forms part of a three-dimensional stream surface. A pressure difference inevitably arises across the cut and this is balanced by a force acting on the isolated vortex, to provide a model which is force-free overall. The longer the outer part of the sheet, the less circulation remains in the isolated vortex and the smaller are the local forces which arise. This is the basic representation whose properties were investigated by Mangler and myself[62,63] several years ago.

This work has since been extended to combinations of delta wings and elliptic cones by Levinski and Wei[64], to delta wings with conical camber in the form of circular-arc cross-sections by Barsby[65], to delta wings with thickness in the form of rhombic cones by myself[66], to yawed delta wings by Fullin[67] and by Jones[68,69] (see Fig.7). The same model of the flow can also be applied when the configuration is not conical, provided it is still slender. I described some special similar solutions[70] for wings with lengthwise camber and curved leading edges in Moscow in 1972; subsequently Clark[71] has treated the general slender wing with straight, thin cross-sections. The wing undergoing small plunging or pitching oscillations about a fixed incidence has been treated by Cooper[72]. The flow past a slender wing and cylindrical fuselage rolling continuously at zero incidence has been calculated by Jones[68] (see Fig.8). It has also proved possible to incorporate a representation of a thin jet blown from the leading edge of the wing within the same framework[73].

This is an impressive collection of applications of a model and goes some way towards the provision of an aerofoil theory for slender wings with leading-edge separation. However, it must be remembered first of all that the theory is nonlinear, so that the various effects cannot be superposed; and secondly that the use of slender-body theory means that important effects have been omitted, rather as they are in two-dimensional aerofoil theory. This leaves a great deal of work to be done. Some studies in which the limitations of slender-body theory are avoided will be mentioned later.

In all the examples which have been listed, separation takes place at a salient edge at which a Kutta-Joukowski condition is imposed. It emerges that, for the basic example of the flat-plate delta wing at incidence, solutions of this kind can only be obtained for angles of incidence which are not too small. Barsby[74] has shown that, for very small values of the incidence parameter ($\alpha/\gamma < 0.04$ α = angle of incidence, γ = semi-angle of wing apex) a solution can be found in which separation takes place from the

flat surface of the wing, a short distance inboard of the leading edge. At the leading edge itself, where the Kutta condition is applied, the flow attaches smoothly instead of separating. It appears that, in the calculation, the effect of enforcing the Kutta condition is to fix the position of the separation line on the upper surface of the wing. Since there is no reason to expect attached flow at the leading edge, it is likely that the physically appropriate solution involves separation both at the leading edge and elsewhere on the wing, with the position of the inboard separation line being fixed by the boundary layer flow. Since the angles of incidence at which the anomalous behaviour arises are so small, the behaviour of the solution is only a scientific curiosity. The practically significant feature is that Barsby encountered no special difficulty in calculating the properties of a vortex sheet springing tangentially from a smooth surface.

When the vortex sheet leaves a salient edge, we know something of its local behaviour. For trailing-edge separation in incompressible flow, Mangler and I[75] wrote down the conditions under which the vortex sheet is tangential to the upper or lower surface of the wing and Legendre[28] generalised our results to unsteady flow. Recently Clapworthy and Mangler[76] have given a much more detailed account for the case of leading-edge separation, assuming conical flow and using slender-body theory.

The outstanding difficulty in modelling flows with separation at a sharp leading edge by vortex sheets lies in knowing where to introduce additional spiral centres. For instance, on a double-delta wing at small angles of incidence, there are separate spiral sheets from the two parts of the leading edge, since the vortex formed at the apex does not follow the change in the sweep of the leading edge, but tears off and streams back over the wing, while a new core originates near the kink in the leading edge. At a larger angle of incidence a single vortex will form along the whole leading edge. It is not clear how calculation could predict the angle of incidence at which the change occurs. If the kink in the leading edge is smoothed out, there is a further difficulty in knowing where along the leading edge the second spiral forms. Clark[71] encounters a similar difficulty in calculating the flow over a wing with lengthwise camber at an attitude for which the local incidence passes through zero somewhere along the length of the wing. His existing calculation method breaks down just as a second vortex, with the opposite sense of rotation, seems to be developing on the lower surface of the wing. A similar difficulty arises in modelling the rolling-up of the wake behind a wing with deflected part-span flaps.

In spite of the number of problems tackled successfully by various authors, there is no doubt that representing vortex sheets in numerical calculations does still present initial difficulties and many people have preferred to use assemblages of line vortices. For instance, Sacks, Lundberg and Hanson[77] introduce up to 96 vortices springing from the leading edge of a slender wing of general planform, calculating their paths by a downstream integration of a set of ordinary differential equations. This sort of calculation leads to stability problems, which they overcome[78] by imposing a particular spiral form on the line joining the vortices. In this context the recent work of Moore[79] and of Fink and Soh[80] is worthy of attention. Moore treats the two-dimensional time-dependent problem of the rolling-up of an initially plane vortex sheet, with an elliptic distribution of circulation, representing it by an array of line vortices. He succeeds in calculating the flow accurately and consistently up to large times and removes much of the mystery that has grown up around the problem. Fink and Soh exploit the essentially simple idea of spacing the vortices evenly along the sheet at the start of the calculation and then, after every step forward in time, redistributing the circulation among the vortices so that they are once again equally spaced along the sheet. This increases the accuracy of the calculation and at the same time reduces the growth of extraneous disturbances.

The use of isolated vortices to model the shed vorticity also makes it possible to calculate the fully three-dimensional incompressible flow past wings with distorted vortex sheets shed from their salient edges. The rolling-up of trailing vortices has been treated by Belotserkovskii[81], Clements and Maull[82], Butter and Hancock[83], Labrujere[84], Maskew[85], Rehbach[86], and Rom, Portnoy and Zorea[87], among others. The proximity of the wing makes the leading-edge problem more awkward; but Rehbach[88] has produced an ingenious method in which he starts from his previous solution[89] for a side-edge separation on a rectangular wing and progresses through a succession of trapezoidal wings in which the length of the unswept part of the leading edge is gradually reduced to zero and the wing becomes a delta. The starting solution for each wing is the converged solution for the previous one. He obtains results for lift and pitching moment which are quite close to measured values, using 10 line vortices shed from each leading edge. The representation of the vortex sheet by these 10 vortices in the plane of the trailing edge looks very reasonable, but there must be some doubt about the adequacy of the representation further forward with fewer vortices. A similar model of the flow has been used by Mook and his collaborators[90,91], but their calculated configurations of vortices show an apparent reluctance to roll up.

There are of course intrinsic difficulties in using vortex lines which are either kinked or curved, because of the infinite self-induced velocities to which they give rise. The correct treatment follows from a consideration of what it is that the line vortex is representing. If it is part of a sheet, then the local self-induced velocity is zero, to first order. If, on the other hand, it represents the core of a vortex, its self-induced velocity depends on the structure of the core which it represents (see, e.g. Widnall and Bliss[92]) and is, in general, non-zero, but still finite.

Many other methods have been used to predict the forces and moments on wings with leading-edge separation, but few of them can be regarded as modelling the separation in a fluid mechanical sense. In particular, for supersonic flow, when leading-edge separation still occurs if the Mach number normal to the edge is less than about 0.7, no model which is entirely satisfactory seems to exist. If all the shed vorticity is collapsed on to the plane of the wing a simple model, proposed by Küchemann[93] in the context of slender-body theory, is obtained. This has been extended by Squire[94] and by Carafoli[95] to supersonic conical flow. If all the shed vorticity is collapsed into a single line vortex another simple model is obtained, which was treated by Brown and Michael[96] within slender-body theory. An attempt to extend this to supersonic conical flow has been made by Nenni and Tung[97].

We turn now to the modelling of separation from highly swept separation lines which lie on smooth surfaces. Most prediction methods for flows of this kind use the cross-flow analogy (see, e.g. Marshall and Deffenbaugh[98]), which cannot be regarded as providing a model of a three-dimensional flow. The work of Barsby[74] referred to earlier, in which a vortex sheet was calculated springing from a separation line

inboard of the leading edge of a delta wing, shows that no difficulty need arise in treating a vortex sheet leaving a smooth surface. His example is quite untypical in that the position of the separation line was determined by imposing a Kutta condition at the leading edge. In general, the position of the separation line on a smooth surface must be supplied before the inviscid model of the separated flow can be calculated. It seems likely that, if the position of the separation line is specified, the usual boundary conditions on the vortex sheet will be sufficient to determine it completely. The specification of the separation line can be taken from experimental observations or from the result of a boundary-layer calculation.

The same situation arises if the separated flow is modelled by an array of line vortices, rather than a vortex sheet. Angelucci[99] has formulated such a model for the flow over a body of revolution at incidence, and presented the results of sample calculations which show encouraging agreement with experiment when an observed separation line is introduced. He represents the free shear layers by arrays of vortices, continually adding to them as the calculation advances downstream, rather as Sacks[77] does for the flow over a slender wing. A subsequent paper[100] extending the model to bodies of general cross-section is marred by an error in the formulation of the attached flow. A recent attempt by Wardlaw[101] to model asymmetric separation on a body of revolution depends on a number of assumptions whose basis is not very clear.

When the shear layer is represented by an array of vortices there is some doubt about the boundary condition to be applied at the separation line. Angelucci imposes a stagnation condition on the cross-flow. If a vortex sheet is used to model the free shear layer it is possible to represent the flow near the separation line more completely. We can see first that the sheet must be tangential to the wall along the separation line, if the fluid on both sides of the sheet originates from upstream, as is usually the case with a highly-swept separation line. Since the pressure is continuous across the sheet and the Bernoulli constant is the same on both sides of it, the magnitude of the velocity is also continuous. If the sheet left the wall at a non-zero angle, the direction of the velocity would also be the same on both sides and so no vorticity would be shed from the separation line. Hence a non-trivial separation is tangential.

With the sheet tangential to the wall, we can distinguish between an upstream side, on which the inviscid velocity is only constrained to be parallel to the wall, and a downstream side, on which the inviscid velocity must be parallel to the separation line. This constraint on the velocity on the downstream side provides an appropriate boundary condition on the inviscid flow, which replaced the Kutta condition appropriate to a salient edge. On the upstream side the inviscid external velocity is unconstrained by the separation, but the limiting streamline of the viscous flow must be parallel to the separation line, in accordance with our general picture of three-dimensional separation. On the downstream side, the viscous flow is harder to visualize, since the free shear layer merges with the boundary layer on the wall. Fortunately it is the more straightforward behaviour of the boundary layer on the upstream side that has to be regarded as the 'cause' of separation.

As a specific example, we might consider a circular cone at incidence in a supersonic stream, with a laminar boundary layer, so that the separation line is straight. The external flow can then be regarded as conical, but it is of course affected by the separation. To calculate a model of the separated flow, the separation line must be known, and to find the separation line the boundary layer on the upstream, or windward, side must be calculated. This requires a knowledge of the external flow. In such a situation an iterative approach suggests itself, although there is no guarantee of convergence. In a related two-dimensional problem, Lighthill[102] considered the flow along a horizontal flat plate at the end of which a second, vertical plate was fixed. A free streamline, representing a separation bubble, can be drawn from an arbitrary point of the horizontal plate to pass through the top edge of the vertical plate. The intention was to determine this point as the point at which the boundary layer on the horizontal plate separated under the external field in which the appropriate free streamline appeared. However, the adverse pressure gradient on the plate becomes infinite at the origin of the free streamline. Existing methods for predicting laminar separation related it to a finite value of the pressure gradient and so would always predict separation upstream of the position represented in the model. Lighthill circumvented the difficulty by using a separation criterion which depends on the magnitude of the pressure rise. So far as I know the problem has not been treated using a finite difference method for the boundary-layer calculation.

It is not clear how relevant such a two-dimensional situation is to our concern with three-dimensional separation. However, some recent analysis of my own suggests that in two important respects the situations are similar. It appears that the curvature of a vortex sheet leaving a smooth wall along a highly-swept separation line is infinite at the separation line; and that the pressure gradient upstream of a highly-swept separation line on a smooth wall is adverse, and infinite at the line itself.

Assuming, in spite of this, that the iteration process can be made to converge for the simple case of the cone, what happens more generally? So long as the external separated flow can be calculated by a downstream marching process, it is possible to envisage the downstream development of the boundary layer being calculated in parallel. The position of separation at each streamwise station would have to be found iteratively before proceeding to the next station downstream. A more elaborate treatment would be needed if it were necessary to allow for upstream influence.

The most obvious circumstances in which upstream influence must be taken into account arise in subsonic flow, with separation lines which are not highly swept. However, we are then faced with the more fundamental problem of having no adequate model of the separated flow. Regions of the flow field arise into which the upstream flow either fails to penetrate, or only penetrates after suffering turbulent exchanges, or only penetrates intermittently. A displacement effect of separation arises. Unsteadiness of the flow becomes more evident and more important to the designer, and it may be more profitable to consider the unsteady aspects of the flow from the start, rather than regarding them as something to be superimposed on a steady flow modelled independently.

9 SEPARATED FLOW IN DESIGN

As suggested in the introduction, most design is concerned with avoiding separation, as evidenced by the title of the useful account by Cooke and Brebner[19]. Some design is aimed at controlling separation and a little is concerned with using it to advantage. In the commonest design application, the vortex generator,

a small-scale, well-controlled, highly three-dimensional separation is used to prevent a large-scale uncontrolled separation, frequently almost two-dimensional in character.

To illustrate the themes of avoiding, controlling and using separation, it is convenient to consider slender-wing aircraft. The first requirement is to control the primary separation from the leading edge. This means making the leading edge effectively sharp, so that the separation line is fixed along the leading edge, and choosing the planform and the camber and twist distribution so that circulation is shed smoothly and continuously along the length of the leading edge. The ideal is to have a single vortex on each side of wing which follows the leading edge throughout the range of flight conditions encountered. To achieve this, rapid changes in the local angle of sweep back should be avoided, and the camber and twist should be chosen so that there is an angle of incidence at which the flow attaches along the whole of the leading edge.

Many distributions of camber and twist satisfy this requirement, which is simply for the leading edge to be drooped until it points into the local flow direction. Some droop of this kind is advantageous from the viewpoint of aerodynamic efficiency[10,103]. The question then arises, whether, with flow attachment along the leading edge, subsequent separation ahead of the trailing edge can be avoided. Maskell and Weber[104] showed that this could be done, at least at supersonic speeds. By considering the possible configurations of the surface streamlines in the external flow and relating the configurations of limiting streamlines to these, they were able to show that separation cannot occur if the longitudinal pressure gradient is favourable in the streamwise direction and the lateral pressure gradient is favourable in the inboard direction. They went on to provide examples of wings on which the calculated pressure distribution was doubly favourable in this sense over the whole wing. Such a design is, of course, conservative, since appreciable unfavourable pressure gradients can be withstood by turbulent boundary layers, and, indeed, such pressure gradients cannot be avoided in subsonic flow.

Given the possibility of achieving a wholly attached flow by sufficient leading-edge droop, the question[105,106] which arises is how much droop should the designer choose. In practice the requirements of various off-design conditions affect this, but we can isolate a specific problem. If we have a given planform and thickness distribution, and we consider a particular type of camber and twist capable of producing attached flow, how much of the camber and twist should be applied in order to produce the lowest drag at a particular operating lift coefficient? Enough to produce attached flow, more than enough, none at all, a negative amount? Empirical evidence suggests that sufficient droop should be incorporated to produce attached flow at about half the operating lift coefficient. The results of some calculations by Barsby[65] are shown in Fig.9. The configuration is a thin, conically-cambered delta wing, whose cross-section is a circular arc. The curves show the lift-dependent drag factor for various fixed lift coefficients. At the smaller lift coefficients the drag has a clear minimum when the camber is rather less than that needed to produce attached flow, that is when there is a small leading-edge vortex above the drooped part of the wing.

Turning from the use of separated flow to reduce drag to the use of separated flow to obtain high lift, we come to the Viggen, whose design has been described by Röed[103]. This close-coupled canard configuration is arranged so as to maximize the interference between the separated flows over its lifting surfaces at high angles of incidence. For the canard to be effective it is necessary to postpone to very high angles of incidence the breakdown of the vortices which form from its leading edges. This is achieved by exploiting the favourable effect of the low pressure above the main wing. At the same time, the main wing vortices deflect the fore-plane vortices downwards and outwards, clear of the fin. So far, a solution like this can only be found by wind tunnel experimentation, but theoretical calculations[107] have provided a partial explanation for the success of the concept.

The lift of a slender wing at given incidence can be increased by blowing in a thin jet from the leading edge of the wing. This both strengthens the leading-edge vortices and moves them outboard. The flow fields produced have recently been investigated by Spillman and Goodridge[108]. Barsby's calculations[73] for blowing in the plane of a flat delta wing in conical flow show that the greatest lift increment comes from blowing normal to the leading edge. The rate of increase of lift with blowing momentum falls off somewhat at the higher rates of blow. Comparison with experiment shows that the extra lift produced by blowing is reduced by the failure of the slenderness approximation in the same proportion as the basic lift at the same incidence. Further calculations by Barsby of the effect of downward blowing from a cambered wing should soon become available.

Blowing is a powerful tool for preventing and controlling separation. Blowing from the leading edge of a delta wing removes the secondary separation from the upper surface of the wing[109]. Blowing along the axis of a leading-edge vortex postpones the occurrence of vortex breakdown[110]. Werlé and Gallon[111] have recently shown that the bubble separation occurring at the leading edge of a thin unswept wing can be coverted into a steady separation of vortex type by blowing in the spanwise direction. This directs the low-energy air which tends to accumulate in the bubble outboard towards the tip of the wing. From there it can escape downstream in a steady fashion, rather than escaping intermittently from the rear of the bubble. Roy[112] has provided a simple theoretical model of the process. Lateral blowing not only improves the quality of the flow but also increases the lift[113].

Another way to introduce a desirable three-dimensionality into a leading-edge bubble on a two-dimensional aerofoil is to serrate the leading edge. Schwind and Allen[114] found high frequency pressure fluctuations in a leading-edge bubble, which they interpreted in terms of self-induced oscillation, affecting the size and position of the bubble. A small serrated comb protruding from the leading edge near the stagnation line reduced the unsteadiness by up to 40%. Beneficial effects, particularly reductions in base drag, can be produced by introducing swept separation lines into base flows. The work of Tanner (e.g. Ref.115) on rectangular wings with blunt bases has shown that the pressure drag can be reduced to about a third of its original value by breaking up the two-dimensionality of the base flow with variously-shaped indentations.

A more obviously important, but little understood, example of the use of separated flow in design is the strake of low aspect ratio fitted ahead of a wing of moderate sweep and aspect ratio. Such strakes are already in evidence on the YF16 and 17. They seem to offer a number of advantages, of which the most significant is probably the extension of the manoeuvre envelope, particularly at high subsonic speeds[116,117].

In these conditions, the flow separating at the leading edge of the strake forms a vortex which tears off at the junction with the main wing and streams back along the side of the fuselage. The flow over the main wing is attached, with a rear shock wave. Küchemann[118] has suggested that the vortex avoids the necessity for the formation of the usual forward branch of the shock pattern by providing a 'soft' boundary for the flow turning inboard over the leading edge, instead of the 'stiff' boundary provided by the side of the fuselage.

Finally, we may indulge in a little speculation about the role of three-dimensional separation in the design of aircraft for low noise levels. Most obviously, the action of many of the silencers fitted to engine nozzles may be regarded as the introduction of properly three-dimensional elements into an axisymmetric flow pattern. Once noise has been produced, it is desirable to direct it away from the ground, particularly on take-off. Here the refractive effects of vortices can be significant (see, e.g. Broadbent[119]) and benefits can come by suitably disposing noise sources in relation to the separation lines from which vortices form. Another significant problem is the production of vibrations in the aircraft structure and of noise within the aircraft from unsteadiness in the external flow. Legendre[120] has recently discussed how the flow in the wing-body junction contributes to this and has drawn attention to the role of vortex generators in bringing under control the fluctuating patterns of separation which arise there. As progress is made with engine silencing and noise shielding, a significant part of the noise perceived on the ground, particularly on the approach to the airfield, derives from the aerodynamic noise of the airframe itself. At a high angle of incidence, with high-lift devices deployed, substantial areas of separated flow are likely, on the flaps and the aft fuselage, and these are likely to be important sources of noise. Two promising general lines of approach to this problem are to fix the origins of separation at sharp edges, so reducing the scope for unsteadiness, and to render the separations as three-dimensional as possible, since a three-dimensional separation is more likely to be steady than a two-dimensional one.

REFERENCES

1. D.J. Peake, W.J. Rainbird and E.C. Atraghi: Three-dimensional flow separations on aircraft and missiles. AIAA Journ. 10, 5, 1972, pp.567-580.
2. L. Gaudet and K.G. Winter: Measurements of drag of some characteristic aircraft excrescences immersed in turbulent boundary layers. *In* AGARD CP 124, 1973.
3. – : Analysis of a jet in a subsonic cross-wind. NASA SP-218, 1969.
4. H.M. McMahon and D.K. Mahurt: Experimental investigation of pressures induced on a flat plate by a jet issuing into a subsonic cross-wind. *In* NASA SP-218, 1969.
5. W. Mikdowski and H. McMahon: An experimental investigation of a jet issuing from a wing in crossflow. Journ. of Aircraft 10, 9, 1973, pp.546-553.
6. J.E. Green: Interactions between shock waves and turbulent boundary layers. Progress in Aerospace Sciences, 11, Pergamon, Oxford, 1970, pp.235-340.
7. T.J. Goldberg: Three-dimensional separation for interaction of shock waves with turbulent boundary layers. AIAA Journ. 11, 11, 1973, pp.1573-5.
8. R.H. Korkegi: A simple correlation for incipient turbulent boundary-layer separation due to a skewed shock wave. AIAA Journ. 11, 11, 1973, pp.1578-9.
9. W.R. Burris and J.T. Lawrence: Aerodynamic design and flight test of US Navy aircraft at high angles of attack. *In* Fluid Dynamics of Aircraft Stalling, AGARD CP 102, 1972.
10. M.B. Morgan: A new shape in the sky. 60th Wright Brothers' Lecture, 1971, Aeron. Journ. 76, 733, 1972, pp.1-18.
11. D. Pierce and D.A. Treadgold: Some examples of the use of a conical shadowgraph technique. RAE Tech. Note Aero 2955; ARC CP 763, 1964.
12. C.P. Li: A numerical study of laminar flow separation on blunt flared cones at angle of attack. AIAA Paper 74-585, 1974.
13. T.C. Lin and S.G. Rubin: Viscous flow over a cone at incidence. Part 2: Boundary layer. J. Fluid Mech., 59, 3, 1973, pp.593-620.
14. S.C. Lubard and W.S. Helliwell: Calculation of the flow on a cone at high angle of attack. AIAA Journ. 12, 1974, pp.965-974.
15. T.C. Lin and S.G. Rubin: Viscous flow over spinning cones at angle of attack. AIAA Journ. 12, 7, 1974, pp.975-985.
16. A.D. Young and H.P. Horton: Some results of investigations of separation bubbles. *In* Separated Flows, AGARD CP 4, 1966, pp.779-811.
17. H.T. Delpak: An investigation of three-dimensional laminar separation bubbles on a 45° swept plate. Ph.D. Thesis, University of London, Queen Mary College, 1973.
18. E.C. Maskell: Flow separation in three dimensions. RAE Rep. Aero 2565, ARC 18063, 1955.
19. J.C. Cooke and G.G. Brebner: The nature of separation and its prevention by geometric design in a wholly subsonic flow. *In* Boundary Layer and Flow Control (Ed. Lachmann), Pergamon, Oxford, 1961, pp.144-181.
20. S.N. Brown and K. Stewartson: Laminar separation. *In* Annual Review of Fluid Mechanics, 1, Ann. Rev. Inc., Palo Alto, 1969, pp.45-72.
21. H.T.H. Piaggio: Elementary treatise on differential equations and their applications. 2nd ed., G. Bell, London, 1928, p.192.
22. S.N. Brown: Singularities associated with separating boundary layers. Phil. Trans. R. Soc. Lond. A 257, 1084, 1965, pp.409-444.
23. J. Buckmaster: Perturbation technique for the study of three-dimensional separation. Phys. of Fluids, 15, 12, 1972, pp.2106-13.

24. K. Stewartson: Theory of laminar boundary layers in compressible fluids. OUP, Oxford, 1964.

25. R. Legendre: Lignes de courant d'un écoulement continu. Rech. Aérosp. No.105, 1965, pp.3-9.

26. E.A. Eichelbrenner: Three-dimensional boundary layers. *In* Annual Review of Fluid Mechanics, 5, Ann. Rev. Inc., Palo Alto, 1973, pp.339-360.

27. M.J. Lighthill: *In* Laminar boundary layers (Ed. Rosenhead), OUP, Oxford, 1963, p.78.

28. R. Legendre: La condition de Joukowsky en écoulement tridimensionnel. 13th Int. Cong. Theor. Appl. Mech., Moscow, 1972; Rech. Aérosp. 5, 1972, pp.241-8; RAE Lib. Transl. 1709, 1973.

29. K. Oswatitsch: Die Ablösungsbedingung von Grenzschichten. IUTAM Symp. on Boundary Layer Research, Freiburg, Springer, Berlin, 1957, pp.357-367.

30. K.C. Wang: Separation patterns of boundary layer over an inclined body of revolution. AIAA Journ. 10, 8, 1972, pp.1044-50.

31. J.C. Cooke: The laminar boundary layer on an inclined cone. RAE Tech. Rep. 65178; ARC R & M 3530; AGARDograph 97, Part II, 1965, pp.909-931.

32. W.J. Rainbird, R.S. Crabbe and L.S. Jurewicz: A water-tunnel investigation of the flow separation about circular cones at incidence. NRC Aero Rep. LR-385, 1963.

33. N.A. Jaffe and A.M.O. Smith: Calculation of laminar boundary layers by means of a differential-difference method. Progress in Aerospace Sciences, 12, Pergamon, Oxford, 1972, pp.49-212.

34. L.F. Tsen and J.F. Arnaudon: Calcul par itération d'une couche limite tridimensionelle et comparison experimentale. Int. Journ. Heat and Mass Transfer, 15, 7, 1972, pp.1373-94.

35. J.C. Cooke: Supersonic laminar boundary layers on cones. RAE Tech. Rep. 66347, ARC CP 1063, 1966.

36. J.A. Beasley: Calculation of the laminar boundary layer and prediction of transition on a sheared wing. RAE Tech. Rep. 73156, 1974.

37. E.H. Hirschel: The influence of the free-stream Reynolds number on transition in the boundary layer on an infinite swept wing. *In* Fluid Motion Problems in Wind-Tunnel Design, AGARD Rep. 602, 1973.

38. J.C. Cooke: Laminar boundary layer calculations compared with measurements by Hummel. RAE Tech. Rep. 67227, ARC CP 1096, 1967.

39. D. Hummel: Experimentelle Untersuchung der Strömung auf der Saugseite eines schlanken Deltaflügels. Zeit. fur Flugwissenschaften, 13, 1965, pp.247-252.

40. G.S. Raetz: A method of calculating three-dimensional laminar boundary layers of steady compressible flows. Northrop Aircraft Inc. Rep. No. NAI-58-73, 1957.

41. J. Der and G.S. Raetz: Solution of general three-dimensional boundary-layer problems by an exact numerical method. Inst. Aeron. Sci. Paper 62-70, 1962.

42. M.G. Hall: A numerical method for calculating steady three-dimensional laminar boundary layers. RAE Tech. Rep. 67145, ARC 29525, 1967.

43. F.G. Blottner and Molly A. Ellis: Finite-difference solution of the incompressible three-dimensional boundary layer equations for a blunt body. Computers and Fluids, 1, 1973, pp.133-158.

44. K.C. Wang: Boundary layer over a blunt body at high incidence with an open type of separation. Proc. R. Soc. Lond. A, 340, 1974, pp.33-55.

45. W. Geissler: Berechnung der dreidimensionalen laminaren Grenzschicht an schrägangeströmten Rotationskorper mit Ablösung. Ingen.-Arch. 43, 1974, pp.413-425.

46. K.C. Wang: Laminar boundary layer over a body of revolution at extremely high incidence. Phys. of Fluids, 17, 7, 1974, pp.1381-5.

47. W. Schönauer: Ein Differenzenverfahren zur Lösung der Grenzschichtgleichung für stationäre, laminare inkompressible Strömung. Ingen.-Arch. 33, 1964, pp.173-189.

48. A.R. Mowlem and R.A. Smith: Analysis of compressible turbulent flow over a yawed cone. AIAA Journ. 12, 9, 1974, pp.1171-2.

49. N.A. Cumpsty and M.R. Head: The calculation of three-dimensional turbulent boundary layers. Part IV: Comparison of measurements with calculations on the rear of a swept wing. Aeron. Quart. 21, 1970, pp.121-132.

50. B. van den Berg and A. Elsenaar: Measurements in a three-dimensional incompressible turbulent boundary layer in an adverse pressure gradient under infinite swept wing conditions. NLR TR 72092U, 1972.

51. P. Bradshaw: Calculation of three-dimensional turbulent boundary layers. J. Fluid Mech. 46, 3, 1971, pp.417-445.

52. P. Wesseling and J.P.F. Lindhout: A calculation method for three-dimensional incompressible turbulent boundary layers. *In* Turbulent Shear Flows, AGARD CP 93, 1971, pp.8.1-8.13.

53. P.D. Smith: An integral prediction method for three-dimensional, compressible, turbulent boundary layers. RAE Tech. Rep. 72228, ARC R & M 3739, 1973.

54. T.K. Fannelφp and D.A. Humphreys: A simple finite-difference method for solving the three-dimensional turbulent boundary-layer equations. AIAA Paper 74-13, 1974.

55. E. Krause: Analysis of viscous flow over swept wings. 9th ICAS Congress, Haifa, 1974, ICAS Paper 74-20.

56. T. Cebeci: Calculation of three-dimensional boundary layers: I-Swept infinite cylinders and small cross flow. AIAA Journ. 12, 6, 1974, pp.779-786.

57. E. Krause, E.H. Hirschel and W. Kordulla: Fourth-order "Mehrstellen" - integration for three-dimensional turbulent boundary layers. AIAA Conf. on Computational Fluid Dynamics, Palm Springs, 1973.

56. L.F. East: Measurements of the three-dimensional turbulent boundary-layer induced on the surface of a slender delta wing by the leading-edge vortex. RAE Tech. Rep. 73141, ARC 35269, 1974.

59. J.-P. Guiraud: Ecoulement au voisinage d'un bord de fuite. Comptes Rendus, Paris, 276A, 1973, pp.399-401.

60. M.J. Werle, V.N. Vatsa and S.D. Bertke: Sweep effects on supersonic separated flows. AIAA J rn. 11, 12, 1973, pp.1763-5.

61. D. Küchemann and J. Weber: Vortex motions. ZAMM 45, 7/8, 1965, pp.457-474.

62. K.W. Mangler and J.H.B. Smith: A theory of the flow past a slender delta wing with leading-edge separation. Proc. R. Soc. Lond. A, 251, 1959, pp.200-217.

63. J.H.B. Smith: Improved calculations of leading-edge separation from slender delta wings. Proc. R. Soc. Lond. A 306, 1968, pp.67-90.

64. E.S. Levinsky and M.H.Y. Wei: Nonlinear lift and pressure distribution on slender conical bodies with strakes at low speeds. NASA CR 1202, 1968.

65. J.E. Barsby: Flow past conically-cambered slender delta wings with leading-edge separation. RAE Tech. Rep. 72179, ARC R & M 3748, 1972.

66. J.H.B. Smith: Calculation of the flow over thick, conical slender wings with leading-edge separation. RAE Tech. Rep. 71057, ARC R & M 3694, 1971.

67. D.I. Pullin: Calculations of the steady conical flow past a yawed slender delta wing with leading-edge separation. Imperial Coll., London, Aero Rep. 72-17, 1972.

68. I.P. Jones: Leading-edge vortex flows. Thesis, University of East Anglia, Norwich, 1974.

69. I.P. Jones. Flow separation from yawed delta wings. *To appear in* Computers and Fluids, 1975

70. J.H.B. Smith: Similar solutions for slender wings with leading-edge separation. 13th Int. Cong. Th r. Appl. Mech., Moscow, 1972.

71. R.W. Clark: Non-conical flow past slender wings with leading-edge vortex sheets. Euromech Colloq. 41, 1973, *to appear as* RAE Tech. Rep.

72. R.K. Cooper: Unpublished work in the Dept. of Engineering Mathematics, Queen's University, Belfast.

73. J.E. Barsby: Calculations of the effect of blowing from the leading edges of a slender delta wing. RAE Tech. Rep. 71077, ARC R & M 3692, 1971.

74. J.E. Barsby: Separated flow past a slender delta wing at low incidence. Aeron. Quart. 24, 2, 1973, pp.120-128.

75. K.W. Mangler and J.H.B. Smith: Behaviour of the vortex sheet at the trailing edge of a lifting wing. Aeron. Journ. 74, 719, 1970, pp.906-8.

76. G.J. Clapworthy and K.W. Mangler: The behaviour of a conical vortex sheet on a slender wing near the leading edge. RAE Tech. Rep. 74150, 1974.

77. A.H. Sacks, R.E. Lundberg and C.W. Hanson: A theoretical investigation of the aerodynamics of slender wing-body combinations exhibiting leading-edge separation. NASA CR-719, 1967.

78. A.H. Sacks and E.G. Tickner: An exploratory study of the vortex sheets shed from the leading edges of slender wings. NASA CR 73048, 1966.

79. D.W. Moore: A numerical study of the roll-up of a finite vortex sheet. J. Fluid Mech. 63, 2, 1974, pp.225-235.

80. P.T. Fink and W.K. Soh: Calculation of vortex sheets in unsteady flow and applications in ship hydrodynamics. Univ. of New South Wales, School of Mech. Engg., Nav/Arch 74/1, 1974.

81. S.M. Belotserkovskii: Calculation of the flow about wings of arbitrary planform at a wide range of angles of attack. Mech. Zhid. Gaza 4, 1968, pp.32-44, RAE Lib. Transl. 1433, 1970.

82. R.R. Clements and D.J. Maull: The rolling up of a trailing vortex sheet. Aeron. Journ. 77, 745, 1973, pp.46-51.

83. D.J. Butter and G.J. Hancock: A numerical method for calculating the trailing vortex system behind a swept wing at low speed. Aeron. Journ. 75, 728, 1971, pp.564-8.

84. T.E. Labrujere: A numerical method for the determination of the vortex sheet location behind a wing in incompressible flow. NLR-TR-72091, 1972.

85. B. Maskew: On the influence of camber and non-planar vortex wake on wing characteristics in ground effect. ARC CP 1264, 1971.

86. C. Rehbach: Etude numérique de l'influence de la forme de l'extremité d'une aile sur l'enroulement de la nappe tourbillonaire. Rech. Aérosp. 1971-6, 1971, pp.367-9.

87. J. Rom, H. Portnoy and C. Zorea: Investigations into the formation of wing-tip vortices. Israel Technion TAE Rep. 199, 1974.

88. C. Rehbach: Etude numérique de nappes tourbillonaires issues d'une ligne de décollement prés du bord d'attaque. Rech. Aérosp. 1973-6, 1973, pp.325-330.

89. C. Rehbach: Calcul d'écoulements autour d'ailes sans épaisseur avec nappes tourbillonaires évolutives. Rech. Aérosp. 1973-2, 1973, pp.53-61, NASA TT-F-15183.

90. D.T. Mook and S.A. Maddox: Extension of a vortex-lattice method to include the effects of leading-edge separation. Journ. of Aircraft 11, 2, 1974, pp.127-8.

91. O.A. Kandil, D.T. Mook and A.H. Nayfeh: Nonlinear prediction of the aerodynamic loads on lifting surfaces. 7th AIAA Fluid and Plasma Dynamics Conf., June 1974, AIAA Paper 74-503.

92. S.E. Widnall and D.B. Bliss: Self-induced motion and stability of concentrated vortex filaments. Arch. of Mech. 26, 3, 1974, pp.459-478.

93. D. KUchemann: A non-linear lifting-surface theory for wings of small aspect ratio with edge separations. RAE Rep. Aero 2540, ARC 17769, 1955.

94. L.C. Squire: The estimation of the non-linear lift of delta wings at supersonic speeds. Journ. R. Aeron. Soc. 67, 1963, pp.476-480.

95. E. Carafoli: Wing theory in supersonic flow. Pergamon, Oxford, 1969.

96. C.E. Brown and W.H. Michael: On slender delta wings with leading-edge separation. Journ. Aeron. Sci. 21, 1954, pp.690-4 and 706.

97. J.P. Nenni and C. Tung: A second-order slender-wing theory for wings with leading-edge separation in supersonic flow. NASA CR 1860, 1971.

98. F.J. Marshall and F.D. Deffenbaugh: Separated flow over bodies of revolution using an unsteady discrete-vorticity crosswake. NASA CR 2414, 1974.

99. S.B. Angelucci: A multivortex method for axisymmetric bodies at angle of attack. Journ. of Aircraft 8, 12, 1971, pp.959-966.

100. S.B. Angelucci: Multivortex model for bodies of arbitrary cross-sectional shapes. AIAA Paper 73-104, 1973.

101. A.B. Wardlaw: Prediction of yawing force at high angle of attack. AIAA Journ. 12, 8, 1974, pp.1142-4.

102. M.J. Lighthill: On boundary layers and upstream influence. I: A comparison between subsonic and supersonic flows. Proc. R. Soc. Lond. A217, 1953, pp.344-357.

103. A. Roëd: Development of the SAAB-SCANIA Viggen. Can. Aeron and Space Journ. 18, 6, 1972, pp.167-175.

104. E.C. Maskell and J. Weber: On the aerodynamic design of slender wings. Journ. R. Aeron. Soc. 63, 1959, pp.709-721.

105. A. Spence and J.H.B. Smith: Some aspects of the low-speed and supersonic aerodynamics of lifting slender wings. Proc. 3rd ICAS Congr., Stockholm, 1962, Spartan Books, Washington, 1964, pp.553-567.

106. P.J. Davies: The design of a series of warped slender wings for subsonic speeds. ARC CP 1263, 1971.

107. D. Finkleman: Nonlinear vortex interactions on wing-canard configurations. Journ. of Aircraft 9, 6, 1972, pp.399-406.

108. J. Spillman and M. Goodridge: Flow characteristics about a delta wing at 15° incidence with and without edge blowing. Coll. of Aeronautics, Cranfield, Rep. Aero 9, 1972.

109. A.J. Alexander: Experiments on a delta wing using leading-edge blowing to remove the secondary separation. Coll. of Aeronautics, Cranfield, Rep. 161, 1963.

110. R.G. Bradley and W.O. Wray: A conceptual study of leading-edge vortex enhancement by blowing. Journ. of Aircraft 11, 1, 1974, pp.33-38.

111. H. Werlé and M. Gallon: Contrôle d'écoulements par jet transversal. l'Aeronautique et l'Astronautique No.34, 1972, pp.21-33.

112. M. Roy: Staticnnarité et stabilisation de tourbillons rectilignes en écoulement plan. Comptes Rendus, Paris, 274A, 1972, pp.1659-62.

113. C.J. Dixon: Lift augmentation by lateral blowing over a lifting surface. AIAA Paper 69-193, 1969.

114. R.C. Schwind and H.J. Allen: Effects of leading-edge serrations on reducing flow unsteadiness about airfoils. AIAA Paper 73-89, 1973.

115. M. Tanner: Basisdruckmessungen zur Optimierung gebrochener Hinterkanten. DLR-FB 73-60, 1973.

116. E.J. Ray, L.W. McKinney and J.G. Carmichael: Maneuver and buffet characteristics of fighter aircraft. *In* Fluid Dynamics of Aircraft Stalling, AGARD-CP-102, 1972.

117. W. Staudacher: Verbesserung der Manoeverleistungen im hohen Unterschall. DGLR Symp. Göttingen, Paper 72-126, 1972, NASA TT-F-15406, 1974.

118. D. KUchemann: On the possibility of designing wings that combine vortex flows with classical aerofoil flows. RAE unpublished, 1971.

119. E.G. Broadbent: Acoustic ray theory applied to vortex refraction in two dimensions with reference to geometry and symmetry. RAE Tech. Rep. 74148, 1974.

120. R. Legendre: Congés à l'emplanture d'une aile sur un fuselage. Rech. Aérosp. 1973-1, 1973, pp.1-4.

121. J.H.B. Smith: Remarks on the structure of conical flow. Progress in Aerospace Sciences 12, Pergamon, Oxford, 1972, pp.241-272.

122. T.K.Fanneløp and D.A.Humphreys: The solution of the laminar and turbulent three-dimensional boundary layer equations with a simple finite difference technique.FFA Report 126, Stockholm 1975.

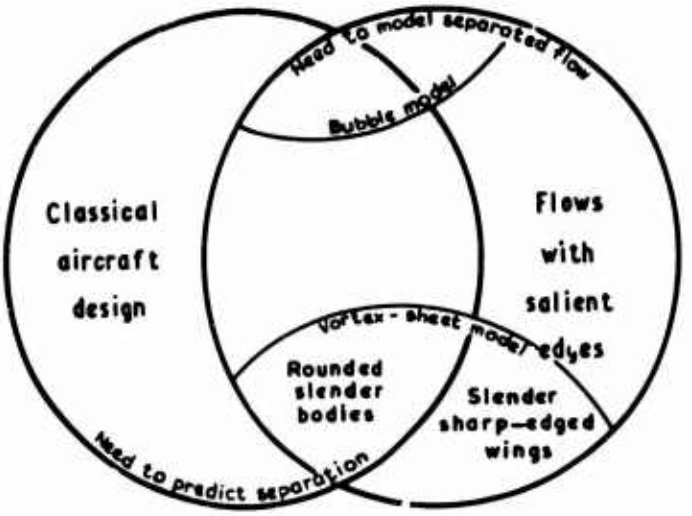

Fig.1 Classification of problems in three-dimensional flow separation

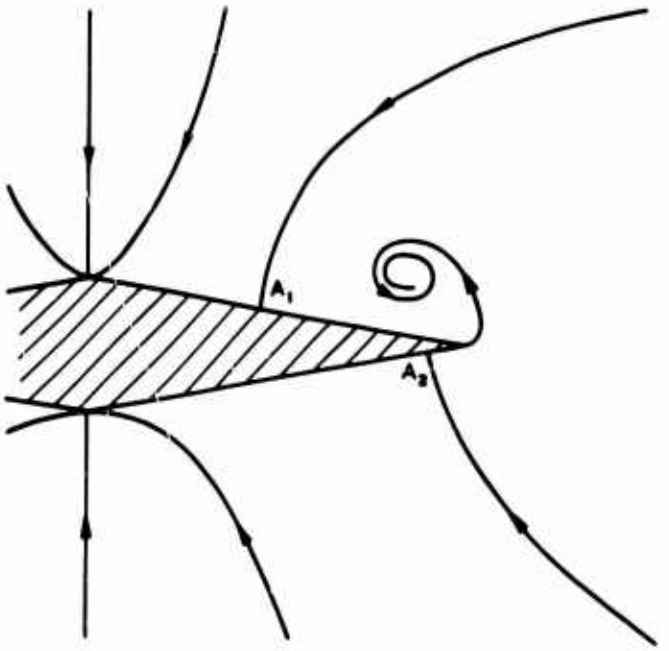

Fig.2 Conical streamlines - slender delta wing

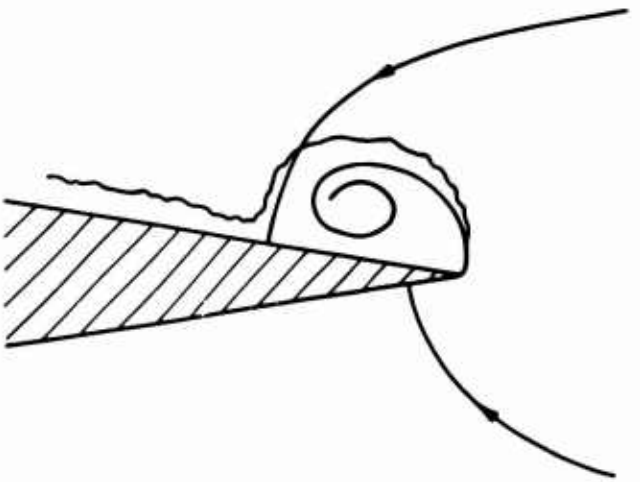

Fig.3 Attachment line contaminated by turbulence of free shear layer

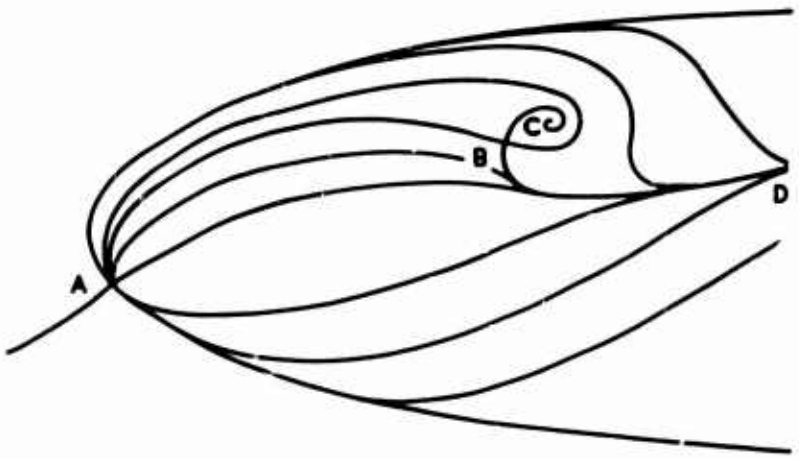

Fig. 4 Limiting streamlines on a forebody, after Legendre[25]

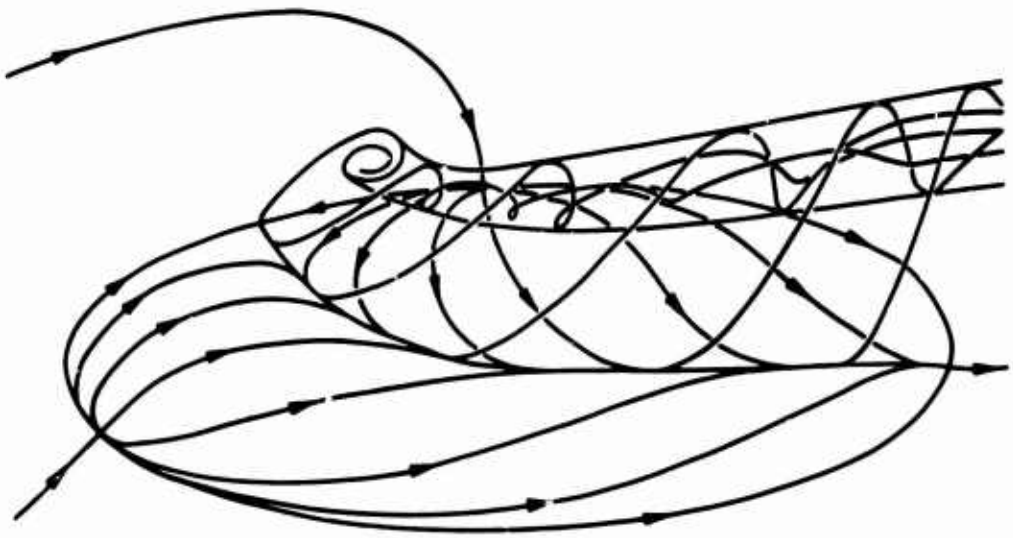

Fig.5 Side view of an open separation surface springing from a closed separation line

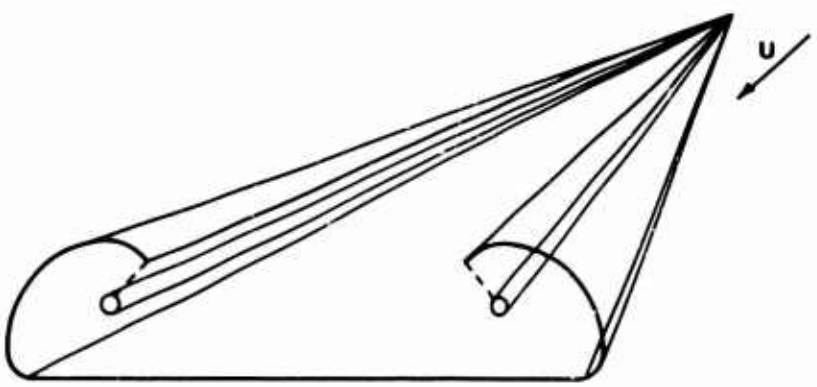

Fig.6 Model of flow separated from leading edges of delta wing

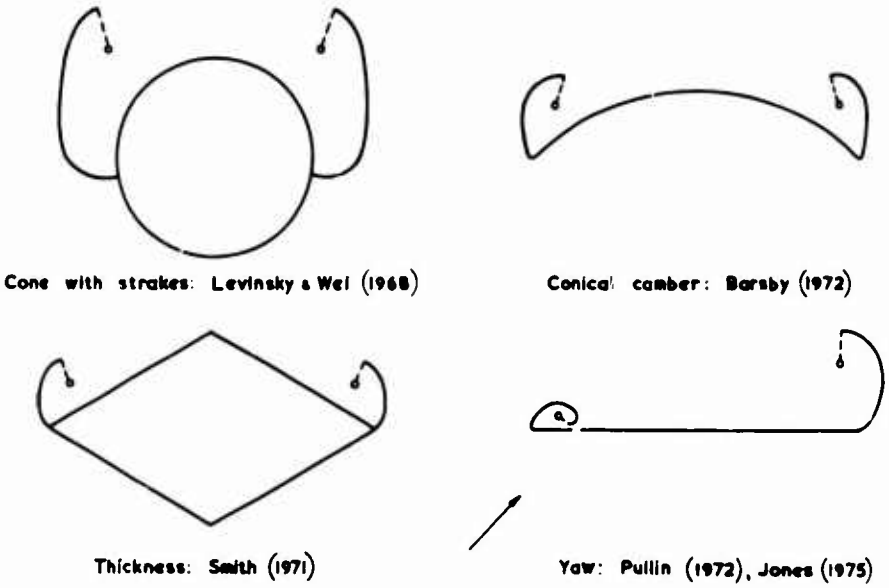

Fig 7 Some conical flow fields involving leading-edge separation

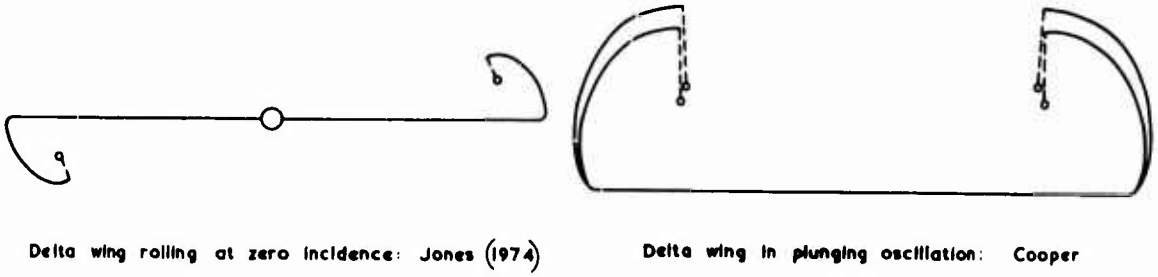

Fig. 8 Some non-conical flow fields involving leading-edge separation

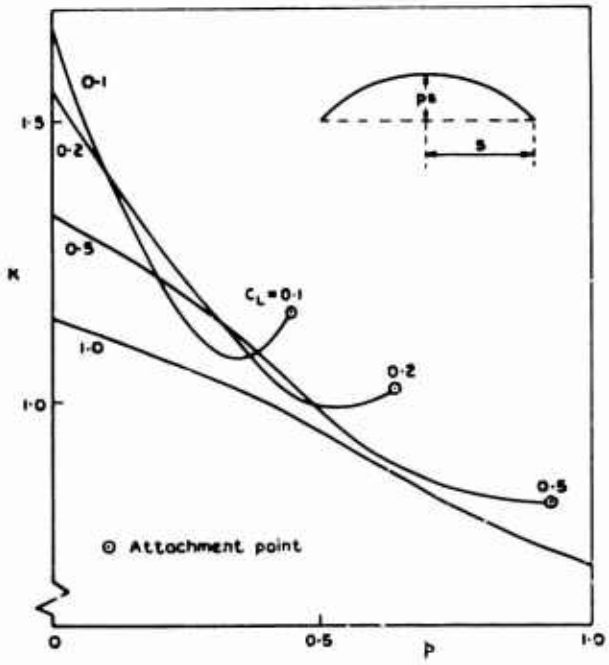

Fig.9 Lift-dependent drag factor of conically-cambered delta wings, for lift coefficients corresponding to Λ=72·5°, after Barsby[65]

LAMINAR SEPARATION ON A BLUNTED CONE AT HIGH ANGLES OF ATTACK*

by
Dr. Stephen C. Lubard
R&D Associates
Post Office Box 3580
Santa Monica, California 90403

SUMMARY

This report demonstrates a new technique for calculating the entire flowfield on spherically blunted cones at high angles of attack and high laminar Reynolds numbers. An approximate system of parabolic equations obtained from the steady Navier-Stokes equations by assuming the viscous, streamwise derivative terms are small compared to the viscous normal and circumferential derivatives is the basis of the calculations. These equations are valid for both the inviscid and viscous regions, including the circumferential separation zone that develops on the leeward side at high angles of attack. Two different methods are used to obtain the initial conditions for these equations at the sphere cone tangency plane. For small nose Reynolds numbers, an axisymmetric merged layer solution around a sphere is rotated to provide a three-dimensional initial plane of data. For large nose Reynolds numbers, the nose region is solved using an inviscid, three-dimensional time-dependent solution combined with a boundary layer solution for the viscous flow. The computed flowfield including the leeward separation region is described and compared with data for two cases. The first case is a "sharp" (0.003 inch nose radius) 7° half-angle cone at 10° angle of attack with a Mach number of 16.1 and a Reynolds number of 10^6 (based on vehicle length). The second case is a blunt 15° half-angle cone with a 1.0-inch nose radius at 15° angle of attack with a Mach number of 10.6 and Reynolds number of 2.1×10^6. In both cases, good agreement with the available data is obtained.

LIST OF SYMBOLS

CA_F	Forebody axial force coefficient
CMO	Pitching moment coefficient about the cone apex. The axial length is the reference length
CN	Normal force coefficient
Cp	Specific heat at constant pressure divided by the freestream value
CPP	Pressure coefficient using pitot pressure
CPS	Pressure coefficient using static pressure
H, h	Static enthalpy divided by the freestream value
k	Conductivity divided by freestream value
L	Reference length
M_∞	Freestream Mach number
P, p	Static pressure divided by twice the freestream dynamic pressure
Pr	Freestream Prandtl number
r	Metric for the ϕ coordinate; $x \sin\theta + y \cos\theta$
RN	Nose radius
RB	Base radius
Re_L, RE, Re	Freestream Reynolds number based on the reference length
U, u	Velocity component along the cone rays divided by the freestream velocity
V, v	Velocity normal to the cone divided by the freestream velocity
V_∞	Freestream velocity
W, w	Circumferential velocity divided by the freestream velocity
X, x	Distance along the cone rays divided by the reference length
XN/RN	Axial distance from nose divided by nose radius
y	Coordinate normal to the surface divided by L
α	Angle of attack
θ_c, θ	Cone half angle
ϕ	Circumferential angle from the windward ray
γ	Ratio of specific heats
η	Transformed normal coordinate
λ	Bulk viscosity divided by freestream viscosity$(-2/3)\mu$
μ	Viscosity divided by freestream viscosity
ξ	Bow shock standoff distance divided by L
ρ	Density divided by freestream density
Subscripts	
∞	Value in the freestream

1. INTRODUCTION

Increased emphasis has recently been placed on developing a technique that will predict flowfields on conical-type geometries at high angles of attack. This emphasis is due, in part, to the current interest in the NASA Space Shuttle. In this paper, only the circular cross-section cone will be considered, although the method which is developed can be extended to other geometries. In addition, the analytical approach will emphasize the blunted nose case at the higher laminar Reynolds numbers (10^6).

Experimental data [1] indicate that at angles of attack of approximately 3/4 the cone half-angle, the flow on the leeward side separates in a circumferential mode and forms two counter-rotating longitudinal vortices. This separation zone occurs for both the sharp and blunted cone cases. Based on the oil flow data (Figure 1 taken from Reference 1), this separation zone first appears downstream of the sharp tip or blunted nose region.

Most of the previous theoretical solutions to this problem are invalid on the leeward side for angles of attack at which flow separation occurs. These theories assume a weak interaction between the viscous region and the inviscid flow. A solution to the inviscid flow is first obtained [2-4] and then a system of boundary-layer equations is used to solve for the viscous flow region [5-7]. This approach develops a singularity on the leeward side at approximately the point where flow separation occurs [6-7].

One possible method for computing the separated flow region on a cone at angle of attack is to use the time-dependent technique for solving the steady Navier-Stokes equations. However, computing time and storage requirements will be extremely large if one wishes to solve for the flow over the entire cone.

*This work is supported under NASA Contract NAS2-8113.

An alternate approach, and the one presented in this paper, is to use a single system of three-dimensional parabolic equations [8]. These equations are obtained from the steady Navier-Stokes equations and are valid from the body to the bow shock. They include the circumferential shear stress terms and thus are capable of predicting the flow within the separation zone on the leeward side. In addition, since the equations contain the full inviscid equations as a subset, they are capable of predicting the pressure distribution on the body and also the viscous-inviscid effects.

Figure 1. Oil Flow Photograph of the Leeward Separation on a 30% Blunt 5.6° Cone at 10° Angle-of-Attack in a Mach 14 Airstream

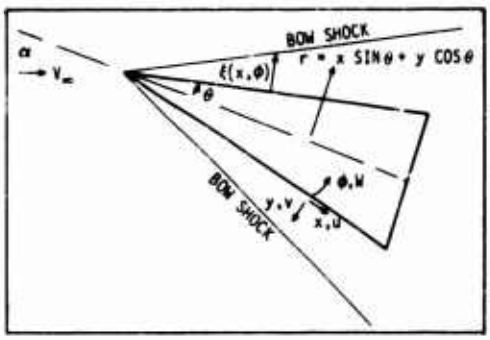

Figure 2. Coordinate System Used on the Cone

In Reference 8, these equations are used to compute the flowfield on sharp cones at high angles of attack. Lin and Rubin [9] have also analyzed the sharp cone case by using a system of modified boundary layer equations, which include the circumferential viscous shear stress terms. The initial data plane which is necessary for their approach is provided by a merged layer solution for the sharp tip region [10]. Their formulation requires the static pressure distribution on the cone to be known and, in fact, the pressure is assumed conical in the solutions obtained by Lin and Rubin. This approach is difficult to extend to the blunted cone case.

To obtain a solution for the blunted cone using the single layer system of equations, one must first compute a fully-viscous three-dimensional initial plane of data. Two different methods are used to obtain the data based on the nose Reynolds number. For small nose Reynolds numbers (sharp), an axisymmetric merged layer solution around a sphere [11] is rotated to provide a three-dimensional initial plane of data. For large nose Reynolds numbers, initial conditions at the sphere cone tangency plane are obtained by an inviscid solution added to a viscous-boundary layer. The inviscid solution is calculated by using a three-dimensional time-dependent approach [12]. Both of these approaches are based on the experimental observation [1] that the nose region in unseparated and therefore not a strong interaction region.

The computed flowfield including the leeward separation region is described and compared with data for two cases. The first case is a "sharp" (0.003-inch nose radius) 7° half-angle cone at 10° angle of attack. The freestream Mach number is 16 and the freestream Reynolds number is 10^6 based on cone length. The second case is a 15° half-angle cone with a 1-inch nose radius at 15° angle of attack. The freestream Mach number is 10.6 and the freestream Reynolds number is 2.1×10^6. Good agreement with the available data in both cases is obtained.

2. ANALYSIS

As indicated in the Introduction, the method for predicting flowfields on blunted cones at high angles of attack is based on an approximate system of equations obtained from the steady Navier-Stokes equations. This system assumes the viscous, streamwise derivative terms are small in comparison with the viscous normal and circumferential derivatives. In a body-oriented coordinate system (Figure 2), these equations become

$$\frac{\partial(\rho u r)}{\partial x} + \frac{\partial(\rho v r)}{\partial y} + \frac{\partial(\rho w)}{\partial \phi} = 0 \tag{1}$$

$$\frac{\partial(\rho u^2 r)}{\partial x} + \frac{\partial(\rho u v r)}{\partial y} + \frac{\partial(\rho w u)}{\partial \phi} - \rho w^2 \sin\theta + r\frac{\partial p}{\partial x} = \frac{r}{Re}\left\{\frac{\partial}{\partial y}\left(\mu\frac{\partial u}{\partial y}\right) + \frac{1}{r^2}\frac{\partial}{\partial \phi}\left(\mu\frac{\partial u}{\partial \phi}\right)\right\} \tag{2}$$

$$\frac{\partial(\rho u v r)}{\partial x} + \frac{\partial(\rho v^2 r)}{\partial y} + \frac{\partial(\rho w v)}{\partial \phi} - \rho w^2 \cos\theta + \frac{r\partial p}{\partial y} = \frac{r}{Re}\left\{\frac{\partial}{\partial y}([\lambda+2\mu])\frac{\partial v}{\partial y} + \frac{1}{r^2}\frac{\partial}{\partial \phi}\left(\mu\frac{\partial v}{\partial \phi}\right) + \frac{1}{r}\frac{\partial}{\partial y}\left(\lambda\frac{\partial w}{\partial \phi}\right) + \frac{1}{r}\frac{\partial}{\partial \phi}\left(\mu\frac{\partial w}{\partial y}\right)\right\} \tag{3}$$

$$\frac{\partial(\rho u w r)}{\partial x} + \frac{\partial(\rho v w r)}{\partial y} + \frac{\partial(\rho w^2)}{\partial \phi} + \rho u w \sin\theta + \rho v w \cos\theta + \frac{\partial p}{\partial \phi} = \frac{r}{Re}\left\{\frac{\partial}{\partial y}\left(\mu\frac{\partial w}{\partial y}\right) + \frac{1}{r^2}\frac{\partial}{\partial \phi}\left([\lambda+2\mu]\frac{\partial w}{\partial \phi}\right) + \frac{1}{r}\frac{\partial}{\partial y}\left(\mu\frac{\partial v}{\partial \phi}\right) + \frac{1}{r}\frac{\partial}{\partial \phi}\left(\lambda\frac{\partial v}{\partial y}\right)\right\} \tag{4}$$

$$\frac{\partial(\rho u h r)}{\partial x} + \frac{\partial(\rho v h r)}{\partial y} + \frac{\partial(\rho w h)}{\partial \phi} - r(\gamma-1)M_\infty^2 \times \left(u\frac{\partial p}{\partial x} + v\frac{\partial p}{\partial y} + \frac{w}{r}\frac{\partial p}{\partial \phi}\right) = \frac{r}{Re\,Pr}\left\{\frac{\partial}{\partial y}\left(\frac{k}{Cp}\frac{\partial h}{\partial y}\right) + \frac{1}{r^2}\frac{\partial}{\partial \phi}\left(\frac{k}{Cp}\frac{\partial h}{\partial \phi}\right)\right\} + \frac{(\gamma-1)M_\infty^2 r}{Re}\left\{\mu\left(\frac{\partial u}{\partial y}\right)^2 + \frac{\mu}{r^2}\left(\frac{\partial u}{\partial \phi}\right)^2 + (\lambda+2\mu)\left(\frac{\partial v}{\partial y}\right)^2 + \frac{\mu}{r^2}\left(\frac{\partial v}{\partial \phi}\right)^2 + \mu\left(\frac{\partial w}{\partial y}\right)^2 + \frac{(\lambda+2\mu)}{r^2} \times \left(\frac{\partial w}{\partial \phi}\right)^2 + 2\frac{\lambda}{r}\frac{\partial v}{\partial y}\frac{\partial w}{\partial \phi} + 2\frac{\mu}{r}\frac{\partial v}{\partial \phi}\frac{\partial w}{\partial y}\right\} \tag{5}$$

All the quantities appearing in Eqs. (1-5) have been non-dimensionalized with the appropriate free-stream quantities. Details on the derivation and solution of these equations are included in Reference 14. The complete inviscid equations appear on the left-hand side of these equations. In addition to the differential equations, other equations are necessary to complete the system, namely an equation-of-state that relates the density to the pressure and enthalpy, and equations that relate the viscosities and specific heat to the enthalpy.

These equations have previously [8] predicted the flowfield for sharp cones at high angles of attack, including the circumferential separation vortices which develop on the leeward side. Based on experiment [1,15] and analysis [10], these vortices are known to form downstream of the nose region in both the sharp and blunted cone cases. This distance will be a function of nose bluntness, Mach number, cone angle, etc.

The approximate parabolic system of equations requires a starting solution at (or downstream of) the nose-cone tangency plane which is appropriate to the blunt nose region. This initial data plane must be given from the body to the bow shock and from the windward to the leeward side.

For small Reynolds numbers based on nose radius ($\lesssim 10^3$), the following approximate procedure is used. A merged layer, zero angle of attack solution for a sphere is computed using the time-dependent technique for solving the Navier-Stokes equations developed in Reference 11. This solution is computed to an angle around the sphere of $(90°-\theta+\epsilon)$. The flowfield from this calculation for angles from $(90°-\theta-\epsilon)$ to $(90°-\theta+\epsilon)$ around the sphere is then rotated and converted at the sphere cone tangency point into the cone coordinate system using the equations given in Appendix A of Reference 16. This approach provides an exact solution at the tangency point on the windward side but only an approximation to the flow for other circumferential stations. The results of Reference 8 indicate that effects of errors at the tangency plane will die out within a few nose radii.

For large Reynolds numbers based on nose radius ($\gtrsim 10^4$), the flowfield on the nose can be specified by using an inviscid solution combined with a viscous boundary layer. In the present study, the inviscid flow is determined by a three-dimensional, time-dependent, blunt-body technique developed by Morretti [12] and a Method of Characteristics (MOC) code developed by Rakich [17]. This inviscid solution is used to compute the inviscid streamlines and surface quantities along these streamlines using the method outlined in Reference 18. Non-similar axisymmetric boundary layer solutions are then calculated [13] along these inviscid streamlines from the stagnation point to the nose-cone tangency plane. The inviscid solution is then added to the viscous solution, and the resultant profiles are transformed into the cone surface normal coordinate system (Figure 2).

This procedure for obtaining the initial conditions is approximate in two ways. The first approximation is in splitting the flow into a viscous and an inviscid region and neglecting any interaction between them. This is felt to be a good approximation at the higher Reynolds numbers which are the major concern here. The second approximation is in using an axisymmetric boundary layer code and calculating the viscous flow along the inviscid streamlines. This approximation is adequate (see Section 3) for the spherical nose case; however, it may be poor for other nose geometries. A three-dimensional boundary layer solution [19,20] could eliminate this difficulty.

3. NUMERICAL RESULTS

In this section, calculated results for two cases are presented. The first is for a "sharp" (RN = 0.003 inch) 7° half-angle cone at 10°, 5° and 1° angle of attack and a Mach number of 16.1. The free-stream conditions and other necessary inputs used in the calculations for this example are given in Table 1. The conditions and geometry for this case have been chosen to correspond closely to the experiments performed in Tunnel F at AEDC [21].

Table 1. Parameters Used in the Calculations for Tunnel F Case

CONE ANGLE	7°
NOSE RADIUS	0.003 INCHES
MACH NUMBER	16.1
LENGTH	1.19 FEET
REYNOLDS NUMBER	0.83×10^6/FT
WALL/FREESTREAM TEMPERATURE	540°R/82°R
PRANDTL NUMBER, CONSTANT	0.72
TEST GAS	NITROGEN
RATIO OF SPECIFIC HEATS	1.4
ANGLE OF ATTACK, α	10°, 5°, 1°
VISCOSITY CALCULATED USING SUTHERLAND LAW	
PERFECT GAS EQUATION OF STATE	

Initial conditions for this case were obtained by using an axisymmetric merged layer solution* for a sphere and transforming it as described in Section 2. This provides a three-dimensional plane of data at the sphere cone tangency plane. The approximate parabolic Navier-Stokes equations (Eqs. 1-5) are then used to continue the solution downstream. The computed results at $\alpha = 10°$ for surface pressure distribution as a function of distance downstream is shown in Figure 3 for various circumferential stations. The initial sharp increase in pressure is due to the parabolic equations adjusting the approximate initial conditions. The computations indicate that a circumferential separation zone first appears on the leeward side at 300 nose radii downstream.

* These computations were performed by Dr. George Widhopf of the Aerospace Corporation.

For this case, only integrated coefficient experimental force data are available for comparison with the computations. Figure 4 gives the comparison between the computed and measured coefficients. The differences are all within the reported [21] experimental uncertainty. A breakdown of the various contributors to the total integrated force coefficients is given in Table 2.

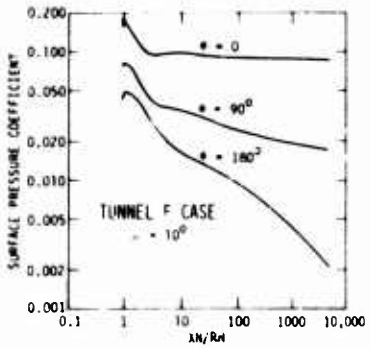

Figure 3. Streamwise Pressure Variations for Tunnel F Case = 10°

In addition to the results available for the conditions indicated in Table 1, the method of computation automatically outputs the force and moment coefficients at smaller (length) Reynolds numbers. However, since the cone has a slight bluntness (0.003 inches), there is a corresponding increase in bluntness ratio at the smaller Reynolds numbers. Figure 5 gives the center of pressure as a function of Reynolds number with the bluntness ratio indicated. This figure clearly indicates the significant increase in center of force/axial length as the Reynolds number decreases (and bluntness increases).

Table 2. Breakdown of Integrated Force Coefficients for Tunnel F Case

ANGLE OF ATTACK	10°	5°	1°
RESOLUTION	(100,19)	(50,19)	(50,10)
CMO	-0.2318	-0.1132	-0.02318
CN	0.3406	0.1657	0.03384
CA_F	0.0989	0.0772	0.06695
-CMO/CN	0.6805	0.6828	0.6849
CMO (pressure)	-0.2262	-0.1096	-0.02234
CN (pressure)	0.3338	0.1614	0.03288
-CMO (pressure/ CN (pressure)	0.6779	0.6790	0.6793
CMO (circumferential shear)	-0.0055	-0.0036	-0.00084
CN (circumferential shear)	0.0092	0.0059	0.00138
CN (axial shear)	-0.0024	-0.0016	-0.00041
CA_F (pressure)	0.0606	0.0424	0.03544
CA_F (axial shear)	0.0383	0.0348	0.03151

Figure 6 gives the distribution of flow vectors in a plane perpendicular to the cone at its base for $\alpha = 10°$. The separation zone on the leeward side is clearly indicated. This leeward separation first appears in the calculations at approximately a tenth of the way down the cone (approximately 300 nose radii). Additional flowfield results for this case are given in Figures 7-12 and include profiles of the flow variables normal to the body for $\alpha = 10°$ at various circumferential stations on the leeward side at a streamwise station 0.3 normalized to the reference length. Figure 12 gives the shock standoff distance for this same station.

The results of computations for the second case are presented in the following paragraphs. This case is a 15° half-angle cone with a 1-inch nose radius at Mach number of 10.6. The freestream conditions, and other inputs used in the calculations for this case are listed in Table 3. The angle of attack is equal to the cone half angle so that a leeward separation zone forms as the solution proceeds downstream. This case was chosen to correspond with experiments performed by Cleary [15,22,23] so that comparisons with data could be obtained. These data included both surface heat transfer and surface pressure measurements on the cone and also pitot and static pressure profile surveys at two streamwise stations. Comparisons with calculated surface pressures provided by Rakich [24] and obtained using a three-dimensional MOC code are also presented.

Table 3. Parameters Used in the Calculations for Cleary's Case

CONE HALF ANGLE	15°
NOSE RADIUS	1 INCH
ANGLE OF ATTACK	15°
MACH NUMBER	10.6
REYNOLDS NUMBER	$1.2*10^6$ PER FOOT
WALL TEMPERATURE	530° R
TOTAL TEMPERATURE	2000° R
PRANDTL NO.; CONSTANT	0.72
RATIO OF SPECIFIC HEAT; CONSTANT	1.4
PERFECT GAS EQUATION OF STATE	
SUTHERLAND VISCOSITY LAW	
REFERENCE LENGTH, SLANT LENGTH	1.932 FEET

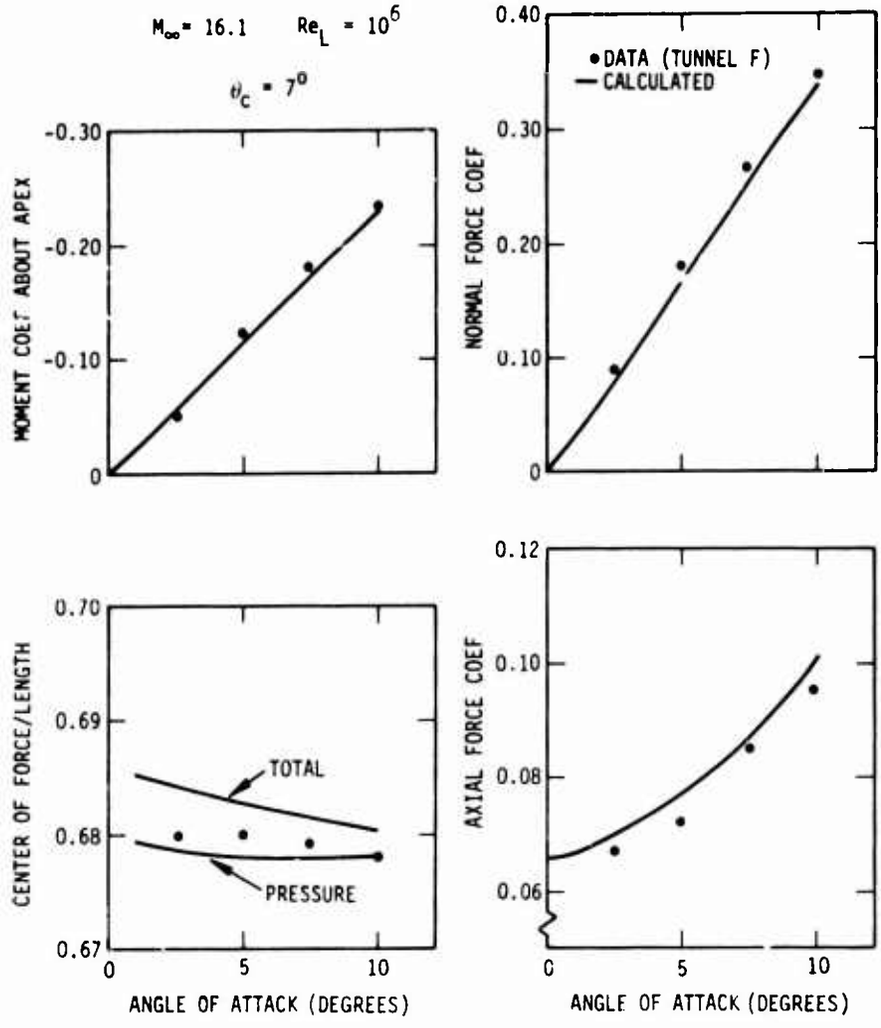

Figure 4. Calculated Aerodynamics for a Sharp 7° Half-Angle Cone

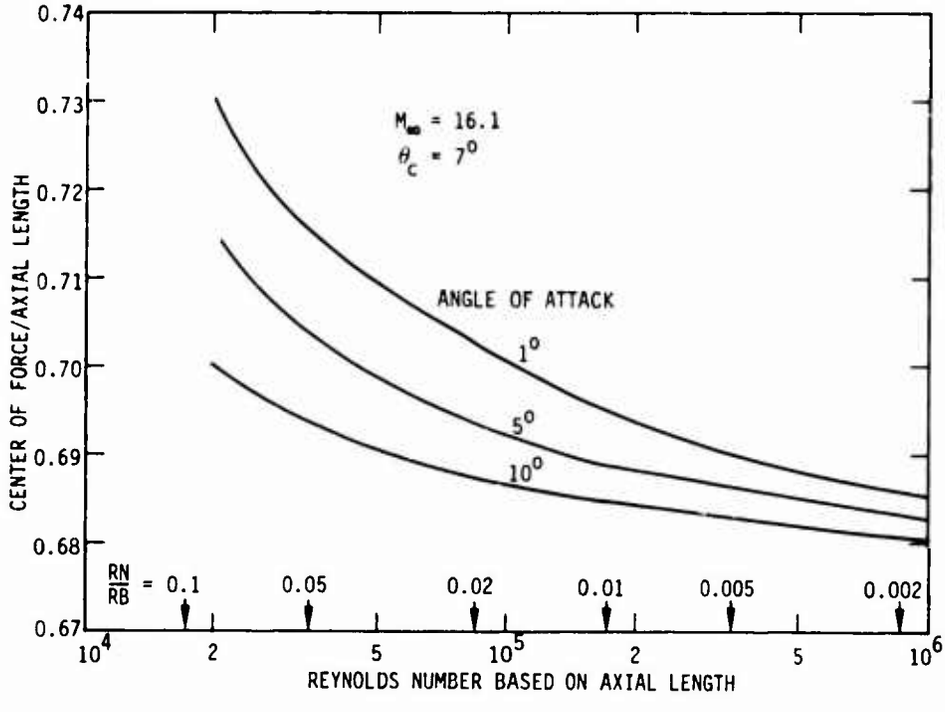

Figure 5. Center of Force vs Reynolds Number

For this case, the Reynolds number based on nose radius is large ($\approx 10^5$); therefore, initial conditions at the tangency plane are obtained by adding the inviscid computations to the viscous boundary layer predictions* as described in Section 2. Further details on these combined initial profiles are given in Reference 25. These combined profiles are used as initial conditions for Eqs. (1-5). These profiles do not satisfy the differential equations exactly, and therefore the first few streamwise steps are made very small to allow for flowfield adjustments. An indication of these adjustments is an oscillation of the surface pressure near the tangency plane (Figure 13). These oscillations disappear after the first few steps, and the remainder of the integration is straightforward.

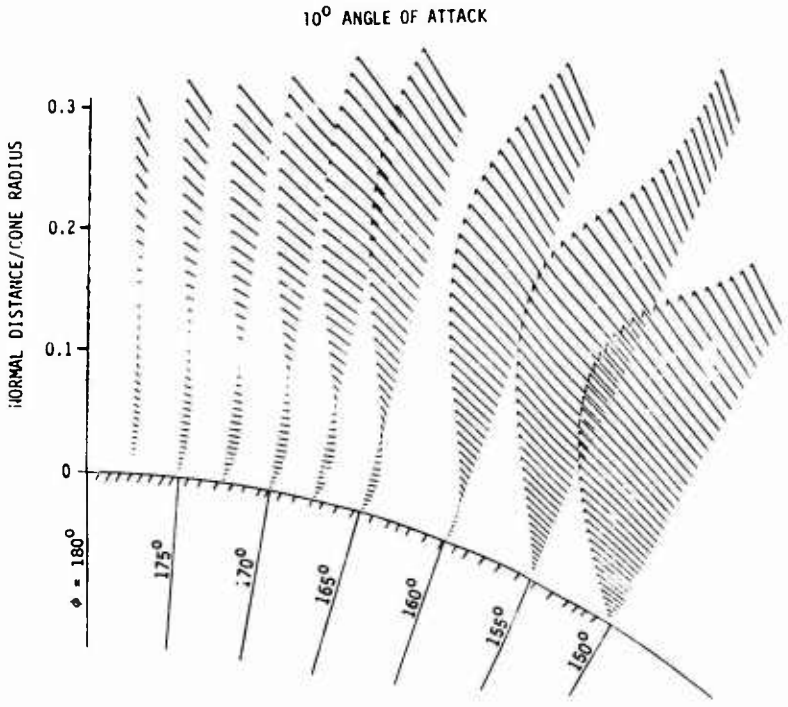

Figure 6. Cross Plane Vector Distribution

Figure 13 shows a comparison between the calculated and measured surface pressure distributions on the cone. The calculated results were obtained using the wall temperature indicated in Table 3. The experimental pressure data were obtained using an uncooled model which had a considerably higher surface temperature than that used in the calculations. Even with this difference, the agreement for all circumferential stations is within the experimental accuracy except for the surface pressure near the sphere-cone tangency point. These pressure differences are probably due to the approximations used in obtaining the initial profiles. Figure 13 also shows the MOC results for the same case [24]. The agreement on the windward side is very good; however, as expected, the inviscid calculations show disagreement with the data and the present results on the leeward side.

Figure 14 shows a comparison between the measured and calculated heat transfer distributions along the cone. The agreement for all the circumferential stations is within the experimental accuracy except for the heat transfer near the base on the leeward side. This disagreement in heat transfer is very likely due to transition occurring in the experiment. The experimental error quoted by Cleary for the heat transfer data is $\pm 20\%$ for the lowest heating rates.

Comparisons between the measured and calculated pressure surveys are shown in Figures 15 and 16 for the two stations where data were obtained. In these figures, CPS and CPP represent the pressure coefficient using the static and pitot pressures respectively. The calculated pitot pressure is obtained using the total velocity. The general agreement between the calculations and data is again excellent for all the circumferential stations. The calculations indicate a shock location which is slightly greater than the measurements at the station closer to the nose (XN/RN = 3.4). This disagreement is felt to be due to the initial viscous-inviscid profiles used at the tangency point. The inviscid solution was simply added to the viscous solution; thus, the calculated initial shock standoff distance is larger than its actual value. This effect almost disappeared by the second station (XN/RN = 14.8). The differences between the calculated CPP and data at $\phi = 60°$ and 90° for XN/RN = 14.8 probably result from flow angle effects in the measurements.

The calculations indicate that the circumferential separation zone for this case first appears on the leeward side at an XN/RN of approximately 8. This separated flow is clearly indicated in Figure 17, which gives the cross plane vector distribution on the leeward side at XN/RN = 14.8. The vortex which forms at a circumferential station of approximately 155° can be discerned. The leeward heating and pressure distributions are compared with the data for various streamwise stations in Figures 18 and 19. The increased pressure and heating at $\phi = 180°$ at the larger XN/RN due to the viscous-inviscid interaction should be noted. Profiles of streamwise and circumferential velocity, enthalpy and entropy, and shock standoff distance at XN/RN = 14.8 are given in Figures 20 to 24. Additional profile results are included in Reference 25.

*These computations were performed by John Rakich of the NASA Ames Research Center.

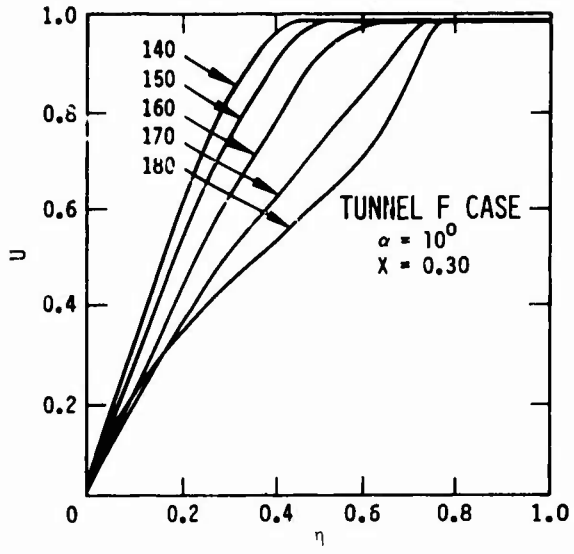

Figure 7. Streamwise Velocity Profiles on the Leeward Side

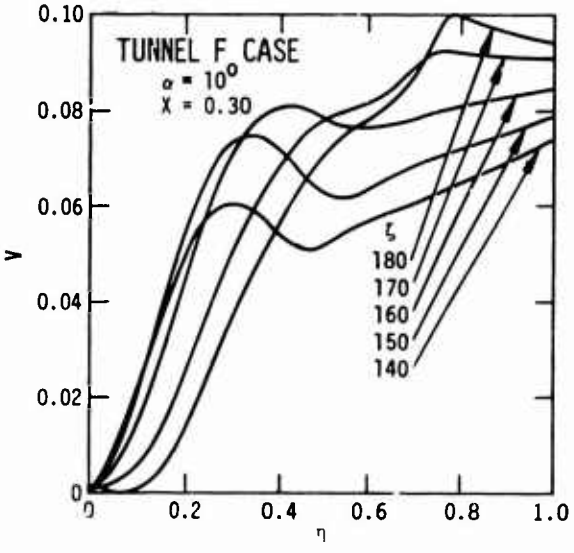

Figure 8. Normal Velocity Profiles on the Leeward Side

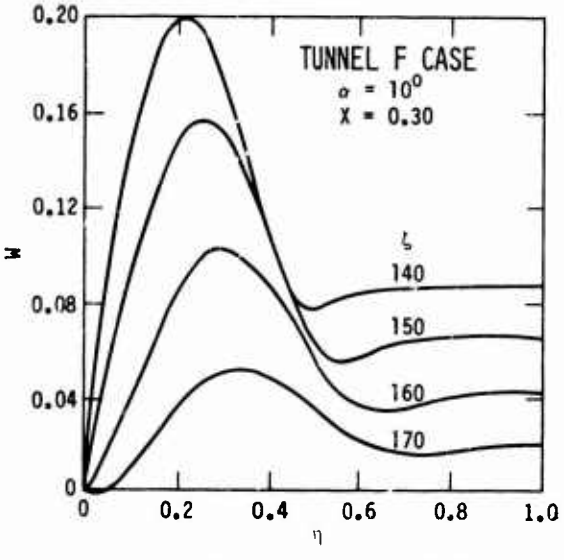

Figure 9. Circumferential Velocity Profiles on the Leeward Side

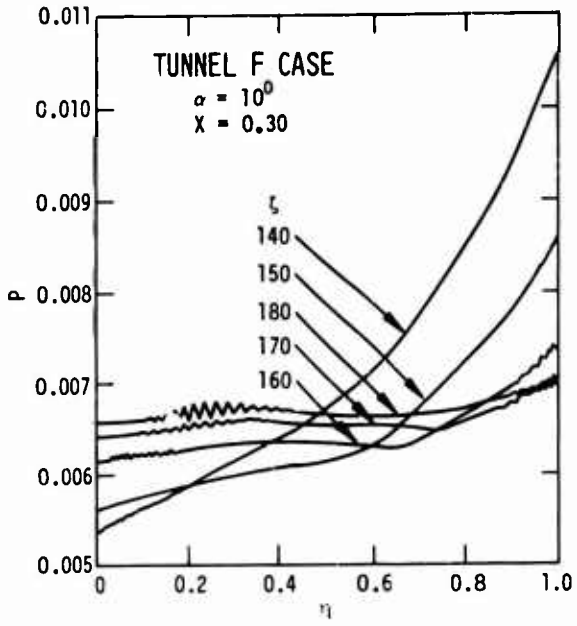

Figure 10. Pressure Profiles on the Leeward Side

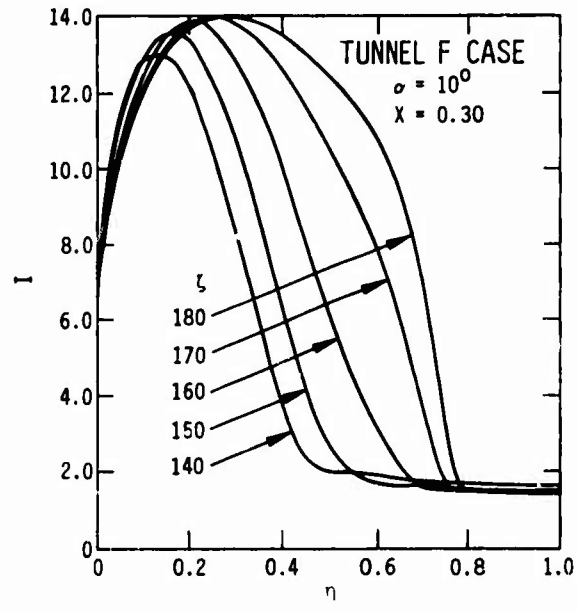

Figure 11. Enthalpy Profiles on the Leeward Side

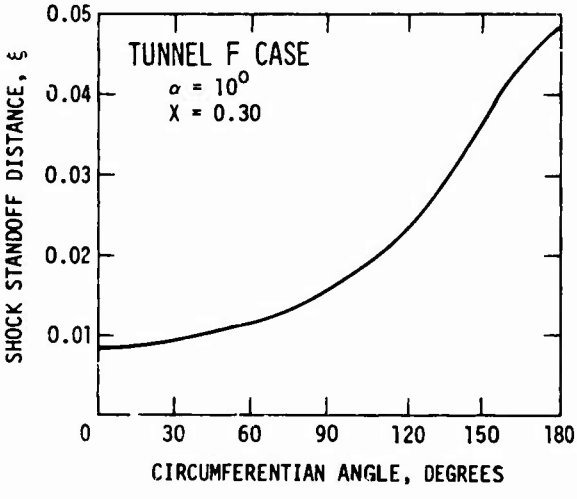

Figure 12. Shock Standoff Distance

The implicit numerical method used to integrate the equations in both these cases has been described in detail in Reference 26. Computations for both cases were run on a CDC 7600 computer. Because of the very small nose radius (0.003 inch) in the Tunnel F case, the initial step size in the marching direction must also be very small. Consequently, for the $\alpha = 10°$ case, 130 steps in the axial direction were required to reach a distance of 1/10 the length of the cone. This phase of the run required approximately 1/2 hour of computing on a CDC 7600. The remaining part of the run (from 1/10 to 1 cone length) took an additional 60 steps and also required about 1/2 hour of CDC 7600 computer time. Approximately 100 unequally spaced points normal to the cone and 19 equally spaced circumferential stations were used in this case.

The computations for Cleary's case required 20 minutes to run 80 steps in the streamwise direction to XN/RN = 17. Fifty unequally spaced points normal to the cone and 19 equally spaced circumferential stations were used to obtain the solution.

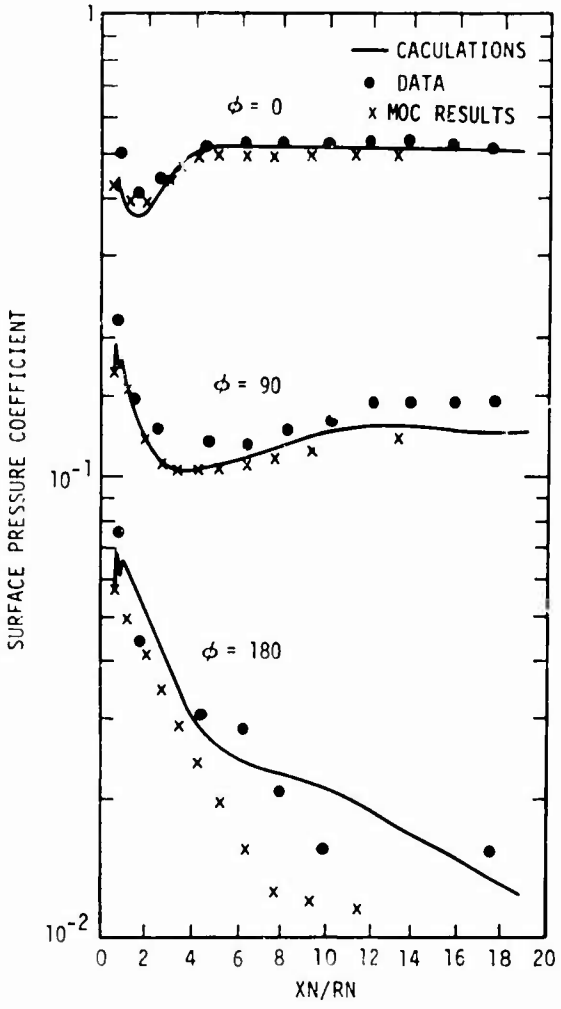

Figure 13. Comparison Between Calculated and Measured Surface Pressure Distributions

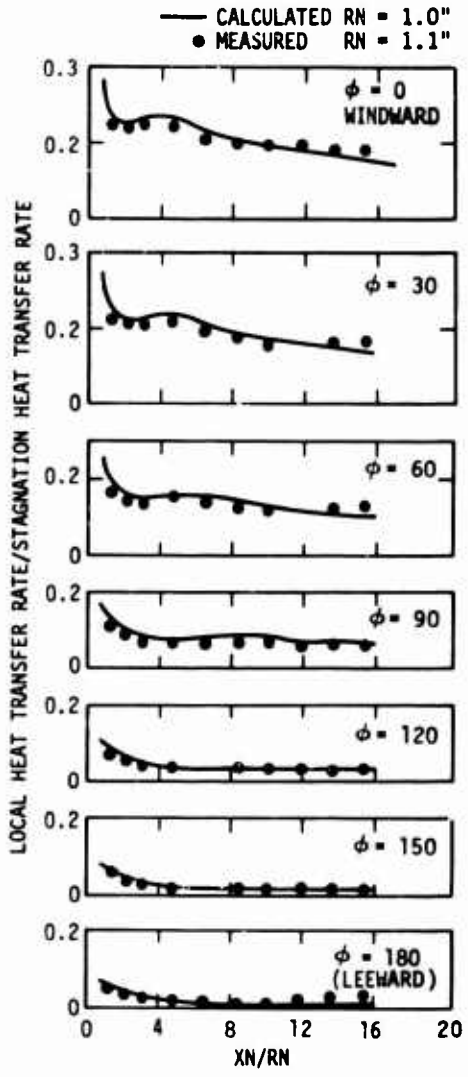

Figure 14. Comparison Between Calculated and Measured Heat Transfer Distributions

4. DISCUSSIONS AND CONCLUSIONS

In conclusion, a new method for calculating the entire flowfield on a blunted cone at high angles of attack and high Reynolds numbers is described in this paper. The method has demonstrated the ability to predict the development and growth of the circumferential separation zone on the leeward side. Both cases with small nose Reynolds number and large nose Reynolds number have been considered. The effects of viscous-inviscid interaction and entropy gradients due to both the curved bow shock and angle of attack are automatically included. Calculated results are compared with surface pressure, heat transfer, pressure profile and integrated force coefficient data, and show very good agreement.

At present, only the case of spherically blunted circular cone has been solved. However, for large nose Reynolds numbers, the concept of using a time-dependent inviscid solution combined with a boundary layer solution to solve the unseparated nose region and provide initial conditions for the "parabolic" steady Navier-Stokes equations is applicable to other nose tip geometries. For low nose Reynolds numbers, three-dimensional merged layer time-dependent solutions of the Navier-Stokes equations are in the process of being computed [27] for more complicated geometries, and the output will be used directly. In addition, work is now in progress to solve the flowfield on more arbitrary geometries at angle of attack using the same approximate parabolic system of equations.

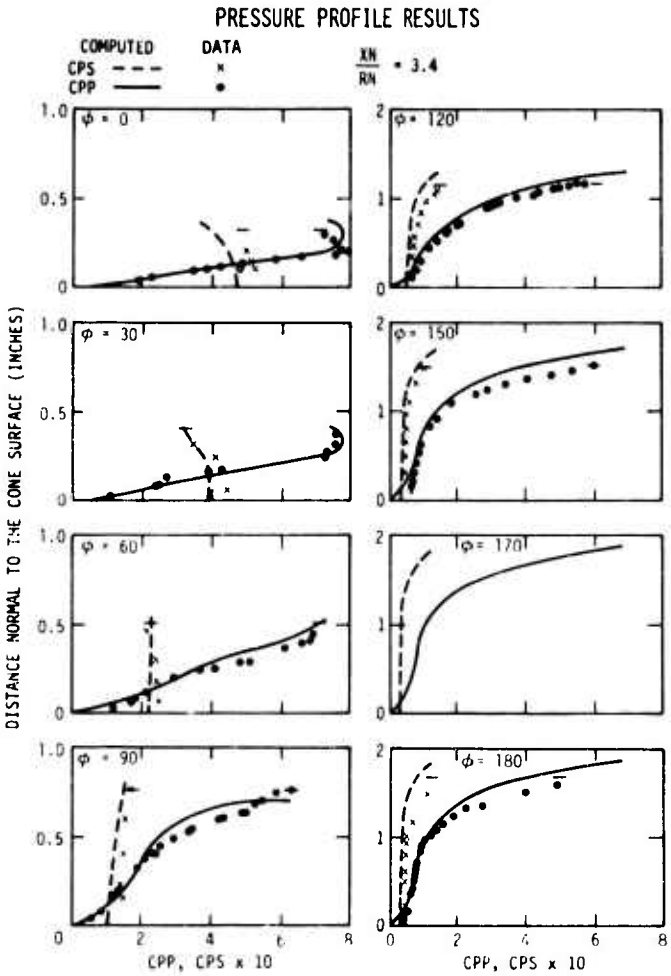

Figure 15. Comparison Between Calculated and Measured Pressure Profiles: XN/RN = 3.4

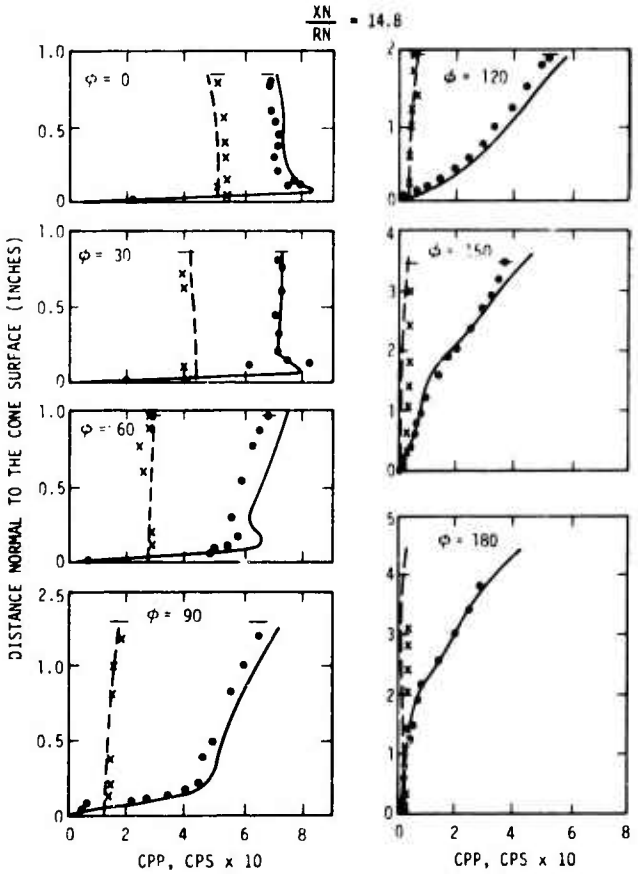

Figure 16. Comparison Between Calculated and Measured Pressure Profiles: XN/RN = 14.8

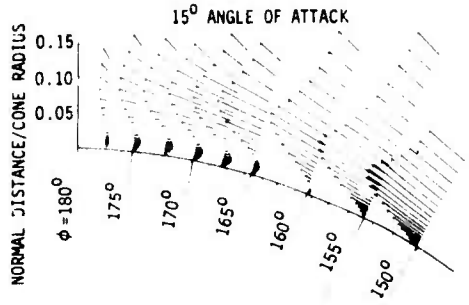

Figure 17. Cross Plane Vector Distribution XN/RN = 14.8

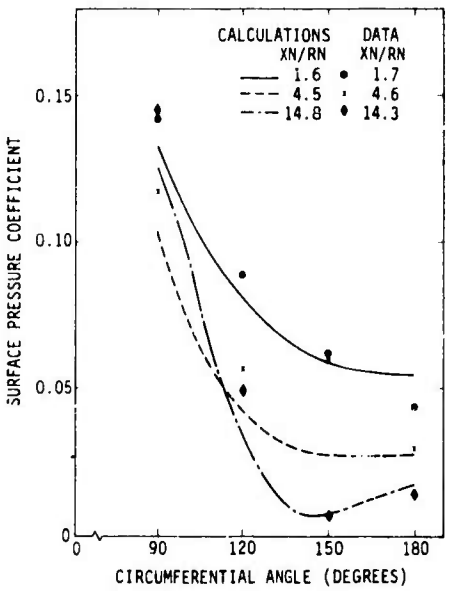

Figure 18. Leeward Surface Pressure Distribution

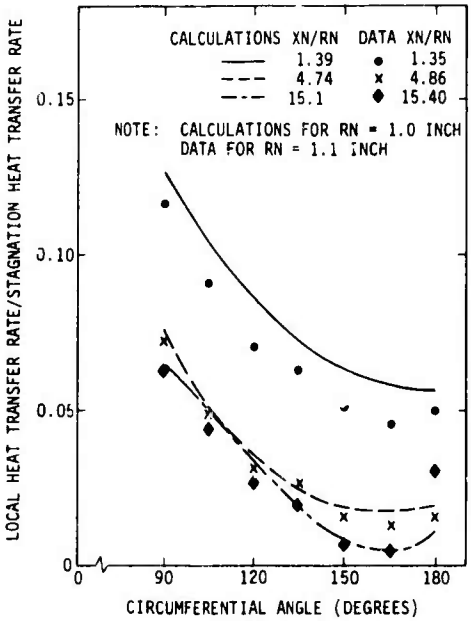

Figure 19. Leeward Heating Distribution

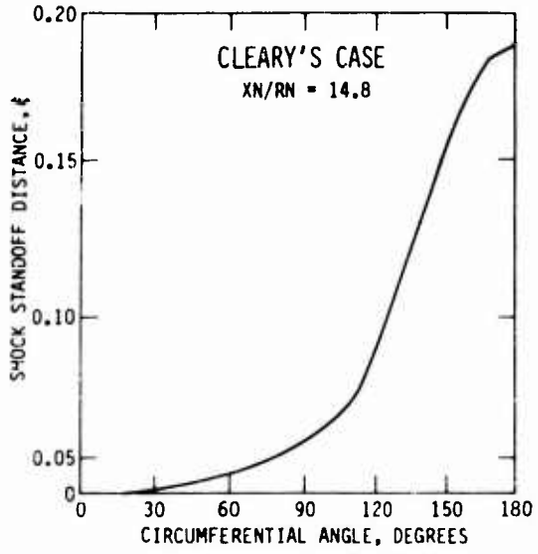

Figure 20. Shock Standoff Distance versus Circumferential Angle for Cleary's Case

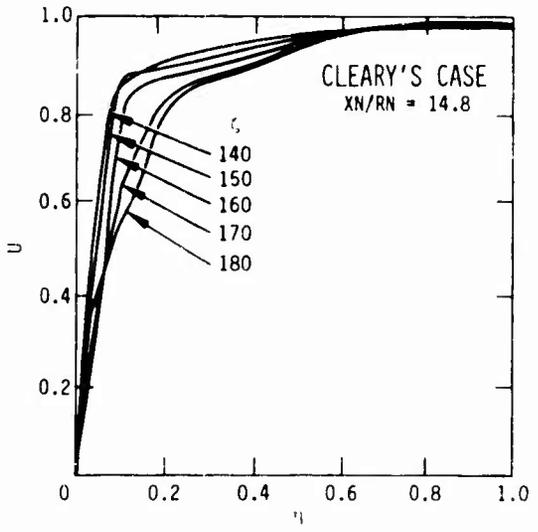

Figure 21. Streamwise Velocity Profiles on the Leeward Side for Cleary's Case

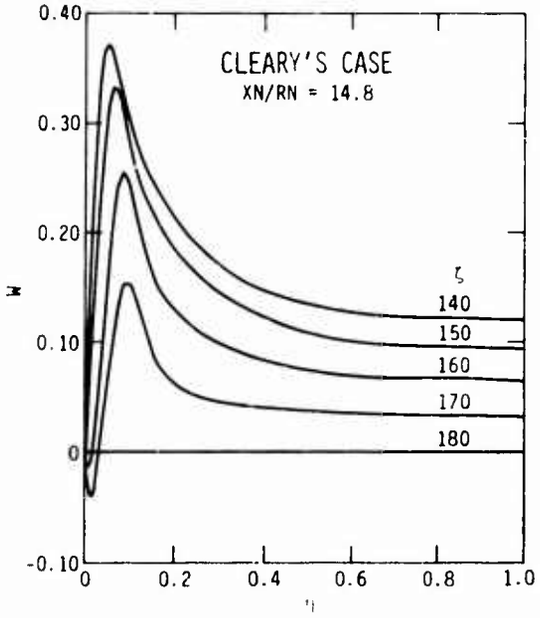

Figure 22. Circumferential Velocity Profiles on the Leeward Side for Cleary's Case

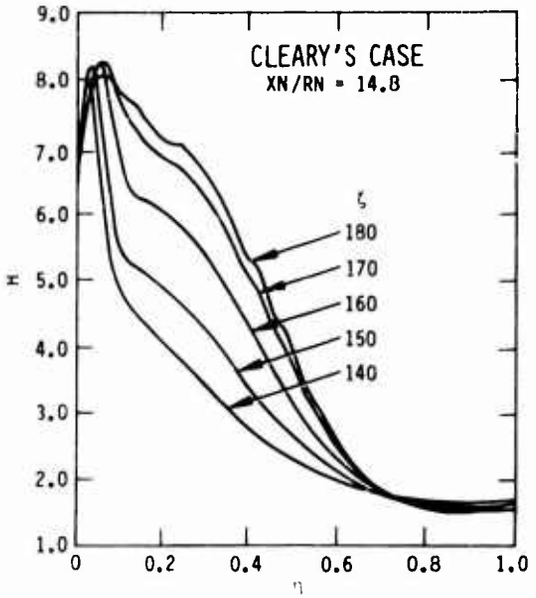

Figure 23. Static Enthalpy Profiles on the Leeward Side for Cleary's Case

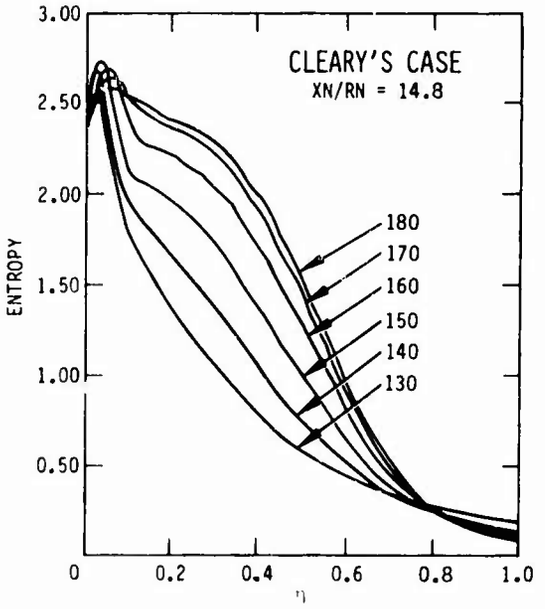

Figure 24. Entropy Profiles on the Leeward Side for Cleary's Case

REFERENCES

1. K. F. Stetson, "Boundary-Layer Separation on Slender Cones at Angle of Attack," AIAA Journal, Vol. 10, No. 5, May 1972, pp. 642-648.
2. A. H. Stone, "On the Supersonic Flow Past a Slightly Yawing Cone, Part II," Journal of Mathematics and Physics, Vol. 30, No. 4, January 1952, pp. 304-312.
3. J. C. Cook, "Supersonic Laminar Boundary Layers on Cones," November 1966, Royal Aircraft Establishment, Farnborough, England, TR 66347.
4. G. Moretti, "Inviscid Flow Field Past a Pointed Cone at an Angle of Attack," December 1965, General Applied Science Labs., Inc., Westbury, N.Y., TR 577.
5. F. K. Moore, "Laminar Boundary Layer on Cone in Supersonic Flow at Large Angle of Attack," 1953, NACA, TR 1132.
6. R. R. Boericke, "Laminar Boundary Layer on a Cone at Incidence in Supersonic Flow," AIAA Journal, Vol. 9, No. 3, March 1971, pp. 462-468.
7. H. A. Dwyer, "Boundary Layer on a Hypersonic Sharp Cone at Small Angle of Attack," AIAA Journal, Vol. 9, No. 2, February 1971, pp. 277-284.
8. S. C. Lubard and W. S. Helliwell, "Calculation of the Flow on a Cone at High Angle Attack," AIAA Journal, Vol. 12, No. 7, July 1974, pp. 965-974.
9. T. C. Lin and S. G. Rubin, "Viscous Flow over a Cone at Incidence, Part 2: Boundary Layer," Journal of Fluid Mechanics, Vol. 1, July 1973, pp. 593-620.
10. T. C. Lin and S. G. Rubin, "Viscous Flow Over a Cone at Incidence, Part 1: Merged Layer," Journal of Computers and Fluids, Vol. 1, January 1973.
11. K. J. Victoria and G. F. Widhopf, "Numerical Solution of the Unsteady Navier-Stokes Equations in Curvelinear Coordinates: The Hypersonic Blunt Body Merged Layer Problem," presented at the Third International Conference on Numerical Methods in Fluid Mechanics, University of Paris-Orsay, published in Lecture Notes in Physics, No. 19, Vol. III, Springer-Verlag.
12. G. Morretti and G. Blich, "Three-Dimensional Flow Around Blunt Bodies," AIAA Journal, Vol. 5, No. 9, 1967.
13. E. P. Barttlet and R. M. Kendall, Non-Similar solution of the Multicomponent Laminar Boundary Layer by an Integral Matrix Method, Aerothem Corporation, March 1967, Technical Report 66-7, NASA CR-1062.
14. S. C. Lubard and W. S. Helliwell, "Calculation of the Flow on a Cone at High Angle of Attack," February 1973, RDA-TR-150.
15. J. W. Cleary, An Experimental and Theoretical Investigation of the Pressure Distribution and Flow Fields on Blunted Cones at Hypersonic Mach Numbers, August 1965, Ames Research Center, NASA TN D-2969.
16. S. C. Lubard, "Calculation of the Hypersonic Flow on a Sharp 7° Cone at Angle of Attack," July 1974, RDA-TR-5004-002.
17. J. V. Rakich, A Method of Characteristics for Steady Three-Dimensional Supersonic Flow with Application to Inclined Bodies of Revolution, (to be published), Ames Research Center.
18. J. V. Rakich and G. G. Mateer, "Calculation of Metric Coefficients for Streamline Coordinates," AIAA Journal, Vol. 10, No. 11, November 1972, pp. 1538-1540.
19. J. Der, Jr., "A Study of General Three-Dimensional Boundary Layer Problems by an Exact Numerical Method," AIAA Journal, Vol. 9, No. 7, July 1971.
20. F. G. Blottner and M. A. Ellis, "Finite Difference Solution of the Incompressible Three-Dimensional Boundary Layer Equations for a Blunt Body," presented at the Symposium on Applications of Computers to Fluid Dynamic Analysis and Design, Polytechnic Institute of Brooklyn, Graduate Center, Farmingdale, N.Y., January 1973.
21. S. R. Pate, Summary of Sharp Cones Static Force Measurements in AEDC VKF Tunnels A, B, C, F, Arnold Engineering Development Center, Tullahoma, Tennessee, May 1974.
22. J. W. Cleary, Effects of Angle of Attack and Bluntness on the Shock Layer Properties of a 15° Cone at Mach Number 10.6, Ames Research Center, November 1968, NASA TN D-4909.
23. J. W. Cleary, Effects of Angle of Attack and Bluntness on Laminar Heating Rate Distribution on a 15° Cone at Mach Number of 10.6, Ames Research Center, October 1969, NASA TN D-5450.
24. J. V. Rakich, Personal Communication, June 1974.
25. S. C. Lubard, "Calculation of the Flow on a Blunted Cone at High Angle of Attack," September 1974, RDA-TR-6100-002.
26. W. S. Helliwell and S. C. Lubard, "An Implicit Method for Three-Dimensional Viscous Flow with Application to Cones at Angle of Attack," presented at the Symposium on Computers and Fluids, Polytechnic Institute of Brooklyn, Brooklyn, N.Y., January 1973.
27. C. P. Li, "A Numerical Study of Laminar Flow Separation on Blunt Flared Cones at Angle of Attack," AIAA 7th Fluid and Plasma Dynamics Conference, June, 1974.

ACKNOWLEDGMENTS

The support of Mr. John Swan and Dr. Donald Fletcher in performing the calculations for the study is gratefully acknowledged.

CALCULATION OF THE THREE-DIMENSIONAL LAMINAR BOUNDARY LAYER AROUND BODIES OF REVOLUTION AT INCIDENCE AND WITH SEPARATION

by

Wolfgang Geißler
Deutsche Forschungs- und Versuchsanstalt für Luft- und Raumfahrt e. V.
- Aerodynamische Versuchsanstalt Göttingen -
Institut für Aeroelastik
3400 Göttingen, Bunsenstraße 10, Germany

SUMMARY

A numerical method is presented to calculate the three-dimensional laminar incompressible boundary layer over bodies of revolution at incidence. The inviscid flow velocities used for the boundary condition at the outer edge of the boundary layer are determined numerically by a singularity method. The boundary layer calculation is carried out in a streamline coordinate system. The coordinates are fixed to the streamlines and equipotential lines of the inviscid flow.

The boundary layer equations are integrated by an implicit finite difference method.

As a result of the numerical calculation process the velocity profiles in directions of streamlines and equipotential lines are known for each mesh point of the coordinate system. It is shown that this method can be used to determine the separation lines on the body surface. The results of the boundary layer calculation and the determination of flow separation are in very good agreement with numerical and analytical results of other investigators.

LIST OF SYMBOLS

ξ, η, ζ	System of rectangular coordinates, oriented with regard to the potential flow, (Fig. 1)
ξ	in direction of streamlines
η	in direction of equipotential lines
ζ	coordinate normal to body surface
x, r, φ	cylindrical coordinates (Fig. 1)
L	total length of body
ds	length element in streamline direction
dy	length element in equipotential line direction
u, v, w	velocity components in the boundary layer (in ξ, η, ζ-directions respectively)
U	velocity of potential flow
U_m	meridional component of U
U_φ	circumferential component of U
U_∞	velocity of undisturbed flow
Φ	velocity potential
α	angle of incidence of the body
ρ	density
ν	kinematic viscosity
μ	dynamic viscosity
p	static pressure

q_∞ dynamic pressure of undisturbed flow, $q_\infty = \frac{1}{2} \rho U_\infty^2$

Re Reynoldsnumber, $Re = U_\infty \cdot L/\nu$

τ_0 wall shearing stress

c_f local skin friction coefficient $c_f = \frac{2\tau_0}{\rho U_\infty^2}$

$c_{f\xi}$ component of c_f in streamline direction (Fig. 7)

$c_{f\eta}$ component of c_f in potential line direction (Fig. 7)

1. INTRODUCTION

The exact prediction of the position of boundary layer separation for bodies at angle of attack is a problem of great practical importance in aircraft design. Methods to calculate boundary layers which are based on one of the common simplifications such as similarity, small crossflow, small perturbation are not very suitable to determine the position of boundary layer separation. Some methods even fail near the separation point or line.

We have developed a method at DFVLR - AVA in Göttingen where no simplifications or limitations are introduced: The complete three-dimensional laminar boundary layer equations are solved numerically by an implicit finite difference technique. The boundary layer calculation is carried out in a streamline coordinate system. The advantage of such coordinates with the physical significant separation into primary and secondary flow within the boundary layer has already been pointed out by L. Prandtl [1] in 1945. Later on E. A. Eichelbrenner and A. Oudart [2] have been the first who used streamline coordinates for the boundary layer calculation on ellipsoids of revolution at incidence. This method is a quasi two-dimensional integral method.

Recently, F. G. Blottner and M. A. Ellis [3] and K. C. Wang [4] have presented methods which are based on finite difference concepts. A discussion of separation patterns over inclined bodies of revolution was given by K. C. Wang [5]. Both authors use coordinate systems which are fixed to the body geometry. This concept is very simple with respect to the determination of the coordinate lines themselves. But complications in the flow calculation process occur both near the front stagnation point, which is in general no special point of that geometrical coordinate system, and in regions, where the direction of the potential flow is reversed and finally near separation.

The application of the two methods mentioned above is limited to simple bodies of revolution like prolate spheroids or elliptic paraboloids. These are the very few cases where the inviscid flow data can be determined by an analytical formula.

In the present method the coordinates are represented by the streamlines and potential lines of the outer inviscid flow. Using streamline coordinates the extension of the numerical boundary layer calculation over the entire body surface beginning near the front stagnation point and generally ending at the separation line or point is a straightforward process. No transformation from one into another coordinate system is necessary. Using the finite difference scheme which has been investigated by M. G. Hall [6] it is possible to include the lines of symmetry of the flow into the calculation process. This is a great simplification as compared with Blottner's and Wang's methods who both have to specify initial data along the lines of symmetry by a separate numerical calculation process. In the present method the outer inviscid flow data, serving as a boundary condition are calculated by a singularity method which has been developed by the author [7]. This method is applicable to bodies of revolution with arbitrary cross-sections even for inlets and cowls.

2. GOVERNING EQUATIONS

Fig. 1 gives the notation of the streamline coordinate system: the rectilinear coordinate system ξ, η, ζ is oriented in the direction of streamlines, equipotential lines and normal to the surface respectively. The corresponding velocity components in these directions are u, v, w, whereas U is the velocity of the outer inviscid flow, U_∞ is the undisturbed mainflow and α the angle of attack.

If all length are made dimensionless with the total body length L, all velocities with U_∞ and pressures with ρU_∞^2 where ρ is the density and if the quantities ζ and w are multiplied in addition by $Re^{1/2}$ the boundary layer equations for steady three-dimensional laminar incompressible flow are:

Equation of continuity

$$\frac{\partial u}{h_1 \cdot \partial \xi} + \frac{\partial v}{h_2 \cdot \partial \eta} + \frac{\partial w}{\partial \zeta} - K_1 u - K_2 v = 0 \quad . \tag{1}$$

Equation of momentum in ξ-direction

$$u \cdot \frac{\partial u}{h_1 \cdot \partial \xi} + v \cdot \frac{\partial u}{h_2 \cdot \partial \eta} + w \cdot \frac{\partial u}{\partial \zeta} - K_2 \cdot u \cdot v + K_1 \cdot v^2 = - \frac{\partial p}{h_1 \cdot \partial \xi} + \frac{\partial^2 u}{\partial \zeta^2} \quad . \tag{2}$$

Equation of momentum in η-direction

$$u \cdot \frac{\partial v}{h_1 \cdot \partial \xi} + v \cdot \frac{\partial v}{h_2 \cdot \partial \eta} + w \cdot \frac{\partial v}{\partial \zeta} - K_1 \cdot u \cdot v + K_2 \cdot u^2 = - \frac{\partial p}{h_2 \cdot \partial \eta} + \frac{\partial^2 v}{\partial \zeta^2} \quad . \tag{3}$$

The boundary conditions are:

$$\begin{aligned} u = v = w = 0 \qquad & \text{at} \quad \zeta = 0 \quad , \\ u = U, \; v = w = 0 \quad & \text{at} \quad \zeta \to \infty \quad . \end{aligned} \tag{3a}$$

The local curvature parameters K_1, K_2 are defined as follows:

$$K_1 = - \frac{1}{h_1 \cdot h_2} \frac{\partial h_2}{\partial \xi} \quad , \qquad K_2 = - \frac{1}{h_1 \cdot h_2} \frac{\partial h_1}{\partial \eta} \quad . \tag{4}$$

The terms of equations (2) and (3) containing K_1 and K_2 are centrifugal and coriolis forces caused by the curvature of the coordinate system.

In Eqs. (1) to (4) h_1 and h_2 are the metric coefficients such that $h_1 \cdot d\xi = ds$ is the actual differential length along streamlines and $h_2 \cdot d\eta = dy$ is the actual differential length along equipotential lines.

3. CALCULATION PROCESS

The differential equations (1) to (3) represent a mixed initial value and boundary value problem. Before the actual numerical boundary layer calculation can start, initial boundary layer profiles near the front stagnation point as well as potential flow data at the outer edge of the boundary layer have to be specified.

So the calculation process must be carried out in the following four steps:

1. Numerical calculation of the inviscid flow data by a singularity method.
2. Numerical calculation of a net formed by streamlines and equipotential lines.
3. Determination of initial boundary layer profiles along potential lines in the vicinity of the front stagnation point. Here the method developed by L. Howarth [8] is used.
4. Numerical boundary layer calculation by a finite difference method.

Steps 1 and 3 are described elsewhere (see [7], [8]). The following two chapters are concerned with steps 2 and 4.

4. STREAMLINE COORDINATES

The surface streamline equation can be expressed in the form:

$$\frac{U_\varphi}{U_m} = \frac{r \cdot d\varphi}{ds_m} \tag{5}$$

where U_m is the inviscid velocity component in meridional direction and U_φ the component in circumferential direction (see Fig. 1). Furthermore, r is the radius of the body at station x, φ is the circumference angle and ds_m is the arc length along meridians. Eq. (5) is integrated numerically by the Runge-Kutta method. Equipotential lines are determined by the condition $\Phi = \text{const}$ ($\Phi \mathrel{\hat{=}}$ velocity potential) on different streamlines. Φ is defined by

$$\Phi = \int_{\xi_0}^{\xi} U \cdot h_1 \cdot d\xi \tag{6}$$

with integration along streamlines.

With Eqs. (5) and (6) a complete set of streamlines and equipotential lines can be calculated. But with respect to the finite difference method the mesh sizes of the coordinate system may not be arbitrary. Two conditions have to be fulfilled:

1. The mesh sizes must be small in order to limit the truncation error of the difference method.

2. The ratio of mesh sizes ($\Delta s/\Delta y$) where Δs is the arclength in streamline and Δy the arclength in equipotential line direction respectively, must be unity or slightly smaller than one with respect to the numerical stability condition of the finite difference method (see next chapter).

Fig. 2 shows a coordinate net with such controlled mesh sizes for an ellipsoid of revolution (axis ratio $a/b = 6$) at $\alpha = 10^{\circ}$ angle of attack.

5. FINITE DIFFERENCE METHOD

For the numerical solution of the boundary layer equations (1) to (3) all differential quotients must be replaced by appropriate finite difference quotients. In the present method central differences of the type investigated by M.G. Hall [6] are used. Hall described a method which is implicit in the direction normal to the body surface but explicit in the two directions in the surface.

The three boundary layer equations are solved by an iteration process. For each step of this iteration the boundary layer equations are solved by a system of linear equations with tridiagonal coefficient matrices. During each iteration step the coefficients are supposed to be constant.

A three-dimensional finite difference method even if implicit is not unconditionally numerical stable. A stability condition (Courant-Friedrich-Levy condition) must be satisfied, which takes the form

$$\left| \frac{v}{u} \frac{\Delta s}{\Delta y} \right| \leq 1 \quad . \tag{7}$$

This condition is based on the concept of the zone of dependence. One can read from Eq. (7) that the ratio of mesh sizes ($\Delta s/\Delta y$) plays an important part: if $\Delta s/\Delta y$ is already equal to or even smaller than one, the ratio v/u (secondary velocity component over primary component) within the boundary layer has to be greater than one before condition (7) is violated. Experiences with this finite difference technique have shown, that large secondary velocity components compared with the primary component occur in the vicinity of flow separation. Using streamline coordinates the condition (7) can serve as a criterion to determine boundary layer separation. This is investigated more in detail in the following chapter.

6. RESULTS

The discussion of results starts with an ellipsoid of revolution (axis ratio $a/b = 6$) at $\alpha = 10^{\circ}$ angle of attack as a first example.

Fig. 3 to 5 show the development of the boundary layer profiles in primary and secondary flow direction respectively. Fig. 3 gives the profiles in some netpoints along a potential line in the vicinity of the front stagnation point. The primary profiles are of Blasius type. The secondary components are small and in positive direction (directed from the windward to the leeside symmetry line). Fig. 4 shows tne flow conditions further downstream. There is a netpoint close to the upper symmetry line where negative secondary velocities within the boundary layer occur for the first time. These negative components grow very rapidly as one marches in streamwise direction. In Fig. 5 a position is reached where the negative secondary components exceed the positive components on the windward side of the body. The corresponding primary profile has a point of inflection: It is well known from two-dimensional theory that this type of boundary layer profiles occurs near flow separation

In Fig. 6 the boundary layer displacement thickness δ_1 is plotted versus the circumference angle φ of different equipotential lines. Going downstream an increasing δ_1-maximum is formed ending in a small peak along the equipotential line of Fig. 5.

One step Δs downstream of the last equipotential line of Fig. 6 just behind the δ_1-peak the numerical stability condition, Eq. (7), is violated for the first time.

In order to clear the flow situation around this first point of numerical instability, Fig. 7 shows the vectors of the wall shearing stress in a simplified quadratic net. Point i gives the location of the first instability point. The wallstreamlines or limiting streamlines as calculated by numerical integration of the vector field of the wall shearing stresses are indicated in Fig. 7. It is possible to continue the boundary layer calculation downstream of point i. One starts the calculation at the windward symmetry line and marches along equipotential lines until numerical instability occurs. Fig. 7 shows very clearly that the wallstreamlines coalesce in the vicinity of the instability points forming an envelope. The boundary layer thickness is growing very rapidly near this envelope. This flow phenomenon can be interpreted as one type of three-dimensional boundary layer separation which has already been described by E.C. Maskell [9]. Fig. 8 shows two examples of Maskell's qualitative investigation of separation in three dimensions. The first type of separation, Fig. 8a, is the bubble type where a flowfield is completely separated from the surrounding mainflow and the second type of three-dimensional separation, Fig. 8b, is the free vortex layer which can occur for example on the surface of a swept wing. This latter type of boundary layer separation can also occur on the entire surface of a blunt body at incidence. The free vortex layer is

characterized by coalescing wallstreamlines combined with a steep increase of the boundary layer thickness. The thickened boundary layer has the tendency to roll up and create a pair of body vortices which have been measured by numerous investigators (see for instance [10]). It must be emphasized that the coincidence of the location of numerical instability with the separation line must be referred to the application of a streamline coordinate system in connection with controlled meshsize ratios ($\Delta s/\Delta y$) over the whole body surface.

Fig. 9 shows the complete separation lines in topview and sideview respectively. The separation lines run into a point on the windward symmetry line where a quasi two-dimensional type of separation occurs.

Simular results have been obtained with other geometrical configurations and angles of incidence.

Fig. 10 shows the streamline net and the separation line for the ellipsoid of revolution with axis ratio $a/b = 4$ at $\alpha = 15^{\circ}$ angle of attack and Fig. 11 gives the same results for the thick ellipsoid of axis ratio $a/b = 2$ at $\alpha = 20^{\circ}$ angle of attack.

Fig. 12 shows the coordinate net and the corresponding separation lines for a half ellipsoid (axis ratio $a/b = 6$) with cylindrical afterbody at 10° angle of attack. The afterbody is assumed to be very long. The separation lines run into parallels of the body axis within the cylindrical part. The circumferential locations of these parallels come out to be nearly identical in different investigated incidence cases ($\alpha = 5^{\circ}, 10^{\circ}, 15^{\circ}$) as is demanded by the theory for infinite cylinders in crossflow. This last result confirms the usefulness and effectiveness of the numerical stability condition as a separation criterion.

7. CONCLUSIONS

A method has been described to calculate the three-dimensional laminar boundary layer over bodies of revolution at incidence by means of an implicit finite difference technique. The inviscid flow data serving as a boundary condition at the outer edge of the boundary layer as well as initial velocity profiles near the front stagnation point are calculated separately by numerical methods. The boundary layer calculation is carried out in a streamline coordinate system. The mesh sizes formed by the streamlines and equipotential lines are controlled in such a way that all mesh size ratios are favourable with respect to the numerical stability condition of the finite difference technique. Results have shown that in this case the numerical instability condition serves as a useful criterion to determine three-dimensional separation.

8. REFERENCES

[1] Prandtl, L.
Über Reibungsschichten bei dreidimensionalen Strömungen
Betz-Festschrift 1945, pp. 134-141 or Gesammelte Abhandlungen 2
Springer-Verlag, Berlin/Göttingen/Heidelberg (1961) pp. 679-686

[2] Eichelbrenner, E. A., Oudart, A.
Methode de calcul de la couche limite tridimensionelle. Application a un corps fusele sur le vent
ONERA, Publ. No. 76 (1955)

[3] Blottner, F. G., Ellis, M. A.
Finite difference solution of the incompressible three-dimensional boundary layer equations for a blunt body
Computers and Fluids, Pergamon Press, Vol. 1 (1973) pp. 133-158

[4] Wang, K. C.
Three-dimensional boundary layer near the plane of symmetry of a spheroid at incidence
J. Fluid Mech., Vol. 43, Part 1 (1970) pp. 187-209

[5] Wang, K. C.
Separation patterns of boundary layer over an inclined body of revolution
AIAA Journ., Vol. 10, No. 8 (1972) pp. 1044-1050

[6] Hall, M. G.
A numerical method for calculating steady three-dimensional laminar boundary layers
RAE TR 67145 (1967)

[7] Geißler, W.
Berechnung der Potentialströmung rotationssymmetrischer Rümpfe, Ringprofile und Triebwerkseinläufe
Z. Flugwiss. 20 (1972) pp. 457-462

[8] Howarth, L.
The boundary layer in three-dimensional flow.
Part 2: The flow near a stagnation point
Phil. Mag., Vol. 42 (1951) pp. 1433-1440

[9] Maskell, E. C.
Flow separation in three dimensions
RAE Rep. Aero 2565 (1955)

[10] Grosche, F.-R.
Wind Tunnel Investigation of the Vortex-System Near an Inclined Body of Revolution with and without Wings
AGARD CP 71 (1971) pp. 2-1 to 2-13

[11] Geißler, W.
Berechnung der dreidimensionalen laminaren Grenzschicht an schräg angeströmten Rotationskörpern mit Ablösung
Ing.-Archiv, Vol. 43, No. 6 (1973/74) pp. 413-425

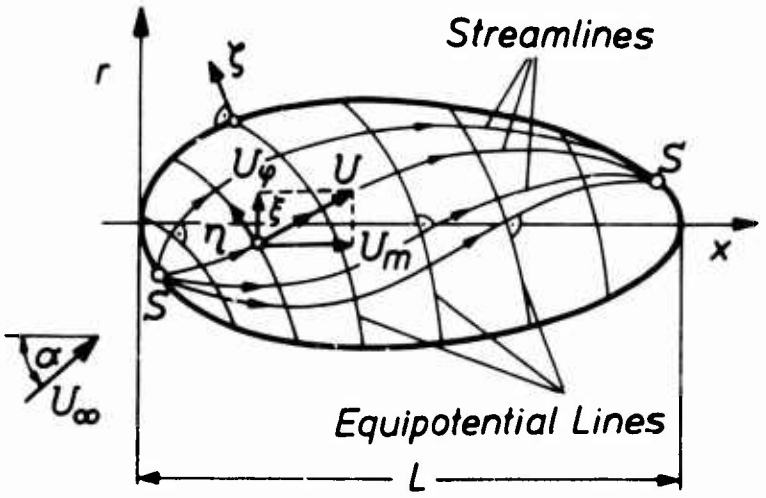

Fig. 1: Streamline coordinates

S ≙ stagnation point of potential flow

ξ ≙ coordinate in streamline direction

η ≙ coordinate in potential line direction

ζ ≙ coordinate normal to body surface

U ≙ velocity of potential flow

$U \triangleq \sqrt{U_m^2 + U_\varphi^2}$

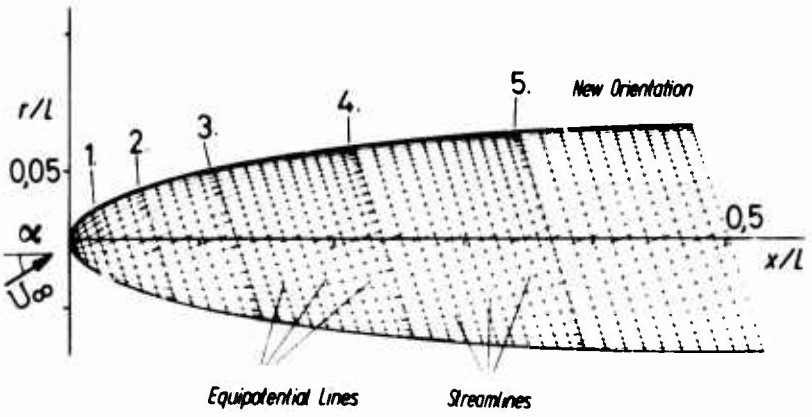

$a/b = 6 \; ; \quad \alpha = 10^\circ$

Fig. 2: Streamline net for ellipsoid of revolution ($a/b = 6$, $\alpha = 10^\circ$)

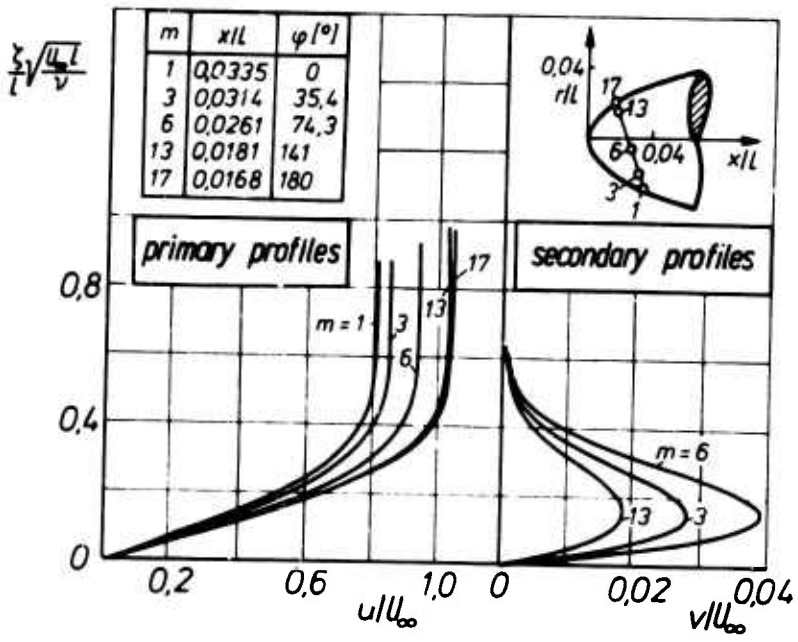

Fig. 3: Boundary layer profiles for ellipsoid of revolution
(a/b = 6 , $\alpha = 10^{o}$) $x_1 = 0,034$ (at $\varphi_1 = 0^{o}$)

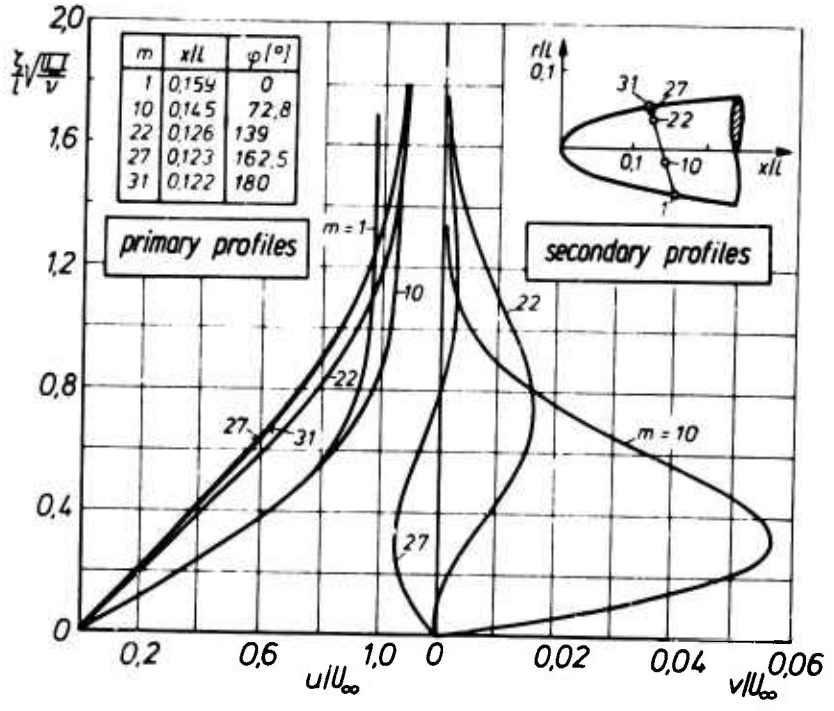

Fig. 4: Boundary layer profiles for ellipsoid of revolution
(a/b = 6 , $\alpha = 10^{o}$) $x_1 = 0,159$ (at $\varphi_1 = 0^{o}$)

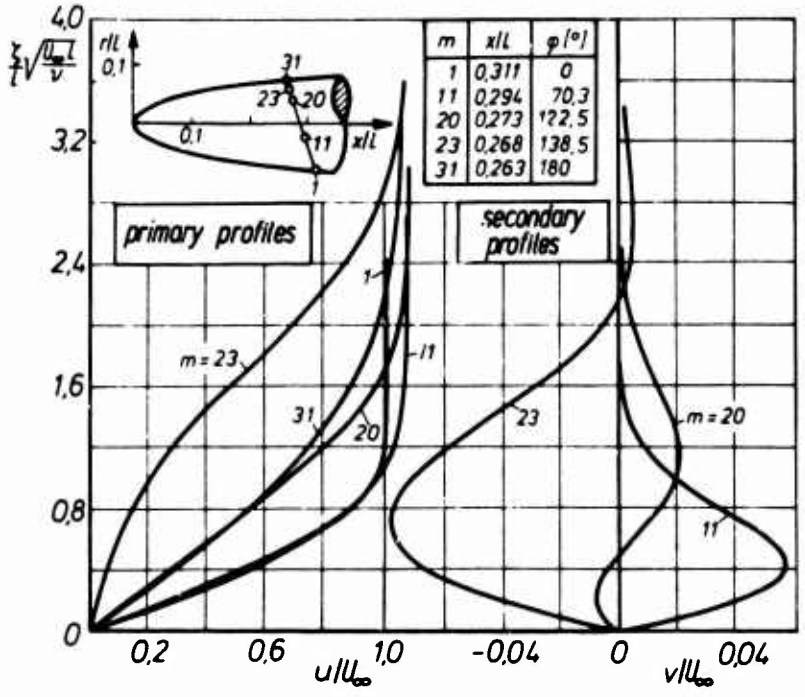

m	x/l	φ [°]
1	0,311	0
11	0,294	70,3
20	0,273	122,5
23	0,268	138,5
31	0,263	180

Fig. 5: Boundary layer profiles for ellipsoid of revolution (a/b = 6, $\alpha = 10^{\circ}$) $x_1 = 0,311$ (at $\varphi_1 = 0^{\circ}$)

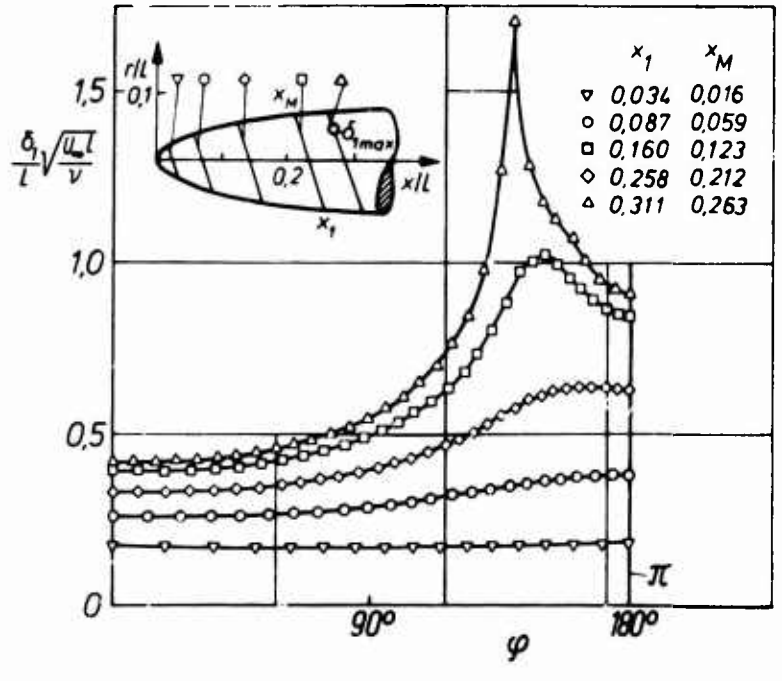

x_1	x_M
0,034	0,016
0,087	0,059
0,160	0,123
0,258	0,212
0,311	0,263

Fig. 6: Displacement thickness δ_1 (a/b = 6, $\alpha = 10^{\circ}$)

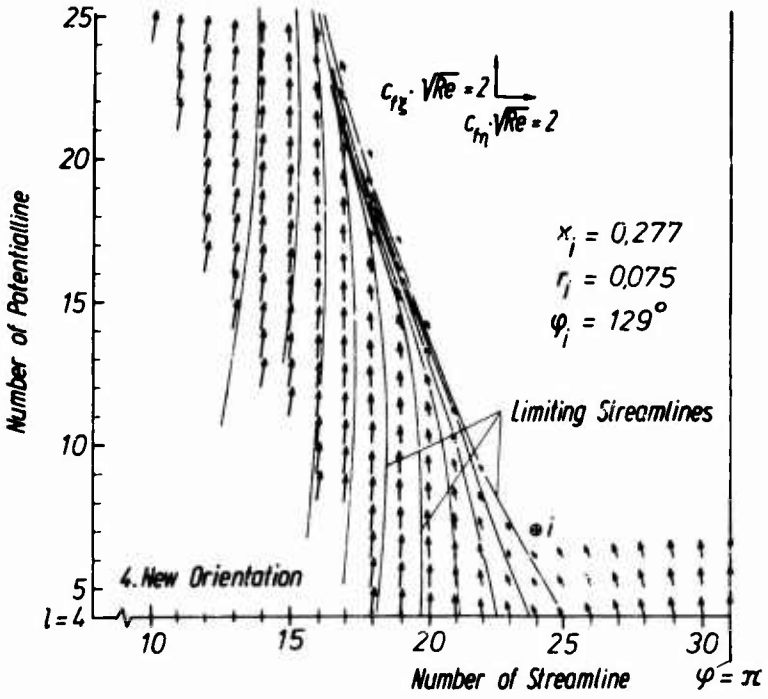

Fig. 7: Vectors of the local skin friction coefficient c_f and limiting streamlines (a/b = 6, $\alpha = 10^{\circ}$)

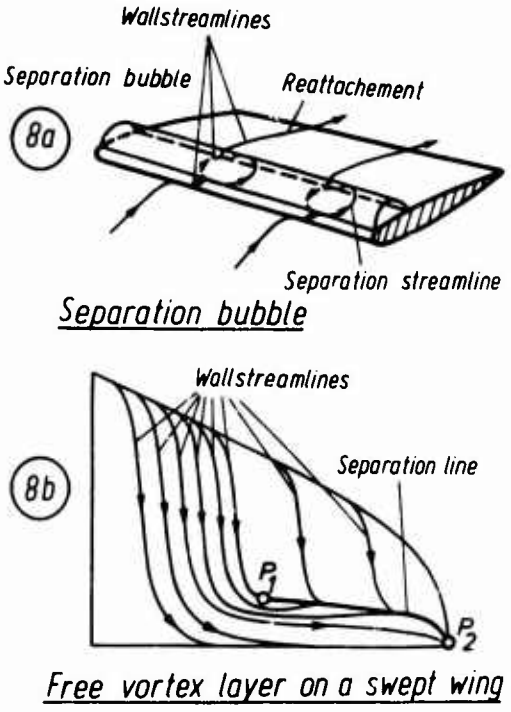

Fig. 8: Separation in three dimensions after Maskell [9]

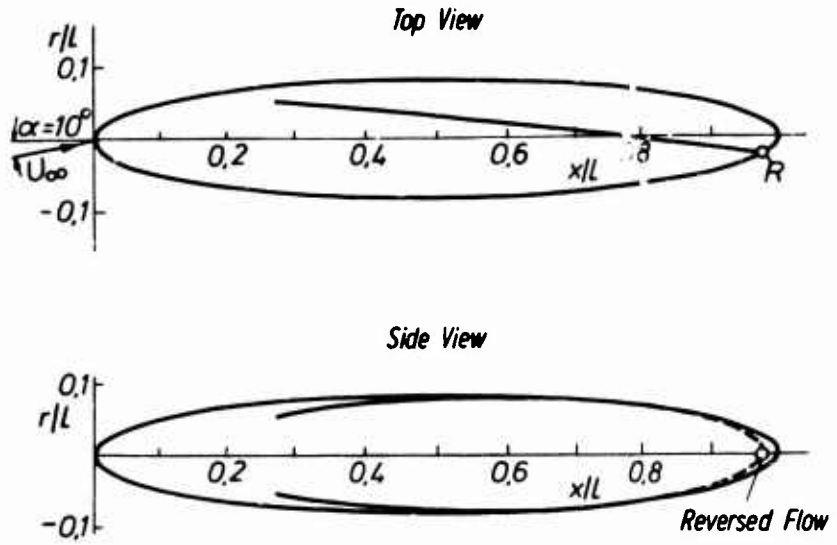

Fig. 9: Separation lines (a/b = 6, $\alpha = 10^{o}$)

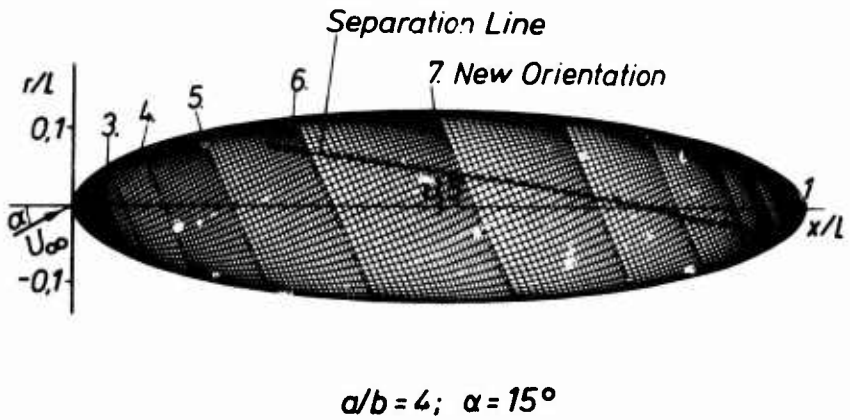

a/b = 4; $\alpha = 15°$

Fig. 10: Streamline net with separation line (a/b = 4, $\alpha = 15^{o}$)

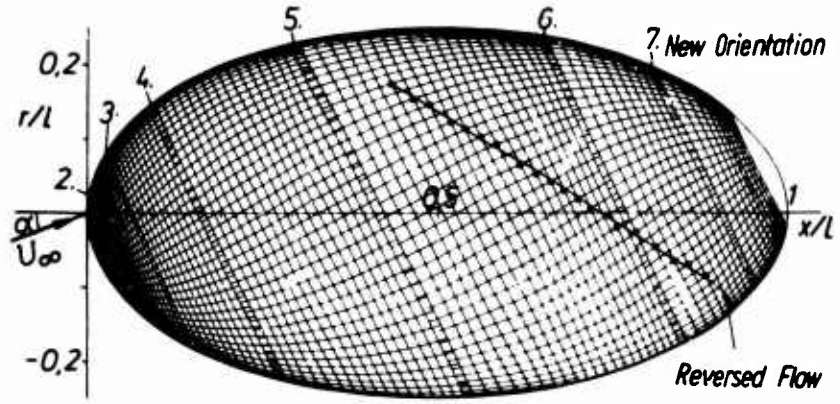

$a/b = 2\ ;\ \alpha = 20°$

Fig. 11: Streamline net with separation line ($a/b = 2$, $\alpha = 20^{\circ}$)

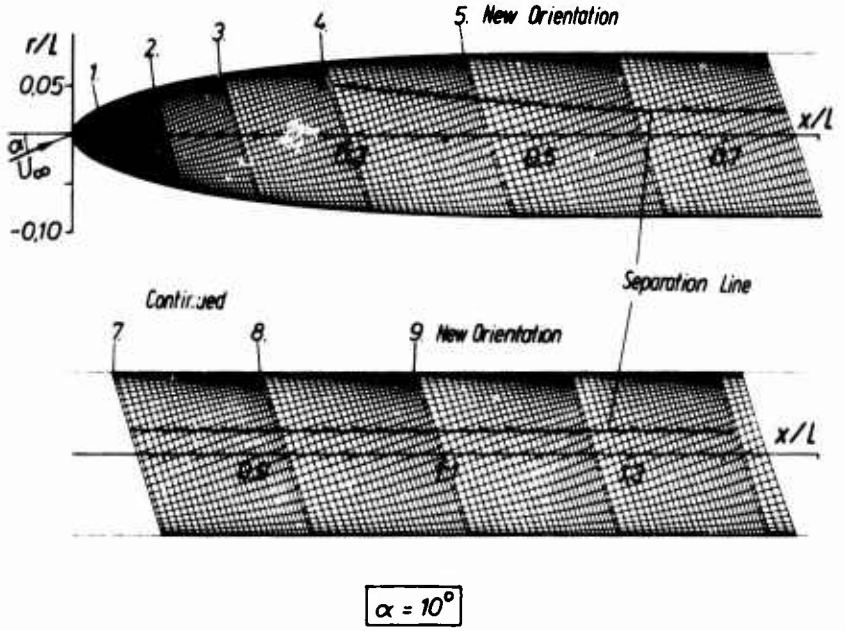

$\alpha = 10°$

Fig. 12: Halfellipsoid with cylindrical afterbody ($a/b = 6$, $\alpha = 10^{\circ}$)

THREE-DIMENSIONAL SEPARATION OF AN INCOMPRESSIBLE TURBULENT BOUNDARY LAYER ON AN INFINITE SWEPT WING

by

A. Elsenaar, B. van den Berg and J.P.F. Lindhout
NATIONAL AEROSPACE LABORATORY NLR
Anthony Fokkerweg 2
Amsterdam-1017
The Netherlands

SUMMARY

An experiment is described in which a three-dimensional boundary layer flow under infinite swept wing conditions is simulated. A description is given of the development of the boundary layer in a region of an adverse pressure gradient leading to increased cross flows and finally terminating in a three-dimensional separation.

Measurements are reported of the mean velocity profiles, the wall shear stress and the components of the Reynolds stress tensor. These measurements reveal a decreasing mixing length with increased cross flow and a substantial difference between the direction of the shear stress and the velocity gradient.

After the separation line a region with an almost spanwise flow is observed.

Calculations are presented of the boundary layer development with a finite difference method using semi-empirical shear stress relations based on the turbulent energy equation. This method fails to predict separation. When empirical modifications, based on the experimental results are introduced, the agreement improves. Close to separation, however, the calculations are very sensitive to the pressure distribution and this might be related to a Goldstein-type singularity at separation.

RÉSUMÉ

Ce rapport décrit un essai, dans lequel on a simulé une couche limite tri-dimensionnelle sur une aile en flèche d'envergure infinie. La couche limite se développe dans une région d'un gradient de pression positif qui conduit à une augmentation de la vitesse transversale, suivi par un décollement tri-dimensionnal.

Les résultats des mesures des profils de vitesse moyenne sont présentés, ainsi que le frottement à la paroi et les composantes des tensions de Reynolds. Ces mesures montrent que la longueur de mélange diminue avec une augmentation de vitesse transversale et qu'il y a une difference remarquable entre la direction du frottement et le gradient de la vitesse moyenne.

Après le point du décollement on a observé une région avec un écoulement à peu près dans la direction de l'envergure.

On a présenté les résultats d'un calcul par différences finies du développement de la couche limite. Cette méthode de calcul utilise des relations de frottement semi-empiriques basées sur l'équation de l'énergie turbulente. Il paraît que cette méthode ne réussit pas à prédire le point de décollement. Si on introduit des modifications empiriques les résultats des calculs sont plus en accord avec les résultats expérimentaux. Cependant près du point de décollement les calculs sont très sensitifs pour la répartition de pression et probablement ce phénomène est lié avec une singularité au point de décollement d'un type de Goldstein.

LIST OF SYMBOLS

a_1	$= \frac{\tau/\rho}{q^2/2}$, ratio of turbulent shear stress and turbulence intensity
c_f	$= \tau_w / \frac{1}{2}\rho U_e^2$, skin-friction coefficient
c_p	static pressure coefficient, relative to station 1
E	DC-component of hot-wire voltage
e	AC-component of hot-wire voltage
G	diffusion function
K	= dE/dU, velocity sensitivity of hot-wire
K	= 0.41, von Karman constant
ℓ	mixing length
L	dissipation length
N_e	$= \frac{\overline{vw}/\overline{uv}}{\partial W/\partial y / \partial U/\partial y}$ ratio of eddy viscosity components
p	static pressure
q^2	$= \overline{u^2} + \overline{v^2} + \overline{w^2}$, total turbulence intensity
Q	mass flow inside the boundary layer per unit span
r	$= -\tan \gamma$, directional sensitivity of hot-wire
s	$= v. \sin \phi + w. \cos \phi$, effective component of transverse velocity fluctuation
S	distance from leading edge in measuring plane
U	velocity magnitude in local streamline co-ordinate system

U_e	velocity magnitude at boundary layer edge
U_x, U_y, U_z	velocity components in wing co-ordinate system
U_s, U_c	streamwise and crosswise velocity components in external streamline co-ordinate system
u_τ	$= \sqrt{\tau_w/\rho}$ friction velocity
$\left\|\frac{dU}{dy}\right\|$	$= \sqrt{(\frac{\partial U}{\partial y})^2 + (\frac{\partial W}{\partial y})^2}$, magnitude of velocity gradient vector
u, v, w	fluctuating velocity components in local streamline co-ordinate system
$\overline{u^2}, \overline{v^2}, \overline{w^2}$	turbulence intensities
$\overline{uv}, \overline{uw}, \overline{vw}$	turbulent shear stresses
V	vertical velocity component
V_δ	vertical velocity component at boundary layer edge
V_{ent}	entrainment velocity
$\frac{\partial W}{\partial y}$	y-derivative of transverse velocity in local streamline co-ordinate system
x, y, z	co-ordinates in wing co-ordinate system
y	distance to the wall
α	flow angle at boundary layer edge, relative to tunnel axis
β	flow angle in the boundary layer, relative to velocity at boundary layer edge
β_w	wall shear stress angle
γ	hot-wire angle
δ	boundary layer thickness
δ_2	$= -\int_0^\delta \frac{U_c}{U_e} dy$, crosswise displacement thickness
δ_x	$= \int_0^\delta (1-\frac{U_x}{U_{x_{edge}}}) dy$, chordwise displacement thickness
ν	kinematic viscosity
ρ	density
$\|\tau\|$	$\rho\sqrt{(\overline{uv})^2 + (\overline{vw})^2}$, magnitude of shear stress vector
τ_w	wall shear stress
τ_x, τ_z	shear stress components in chordwise and spanwise direction
τ_{max}	maximum shear stress inside the boundary layer
θ_{11}	$= \int_0^\delta (1-\frac{U_s}{U_e}) \frac{U_s}{U_e} dy$, streamwise momentum thickness
φ_τ	$= \beta + \text{atan}(\overline{vw}/\overline{uv})$, direction of shear stress relative to velocity at boundary layer edge
φ_{grad}	$= \beta + \text{atan}(\frac{\partial W}{\partial y}/\frac{\partial U}{\partial y})$, direction of velocity gradient vector relative to velocity at boundary layer edge
ω	roll angle of hot-wire probe

co-ordinate systems

- wing co-ordinate system: the boundary layer equations are written in this co-ordinate system; the x-axis is taken in chordwise direction (perpendicular to the leading edge), the z-axis in spanwise direction (parallel to the leading edge) and the y-axis perpendicular to the wall; the velocity components along the three axes are U_x, U_y and U_z.
- local streamline co-ordinate system (Fig. 4): the velocity components are related to the local flow direction inside the boundary layer; U is taken in the direction of the local velocity, but parallel to the wall and makes an angle β with the velocity at the boundary layer edge; the mean transverse velocity component W is zero by definition, but the derivative $\partial W/\partial y$ is generally not equal to zero; the vertical velocity is perpendicular to the wall and positive away from the wall; U, V and W with their fluctuating components u, v and w form a right-handed co-ordinate system; the results of the turbulence measurements are presented in this co-ordinate system.
- external streamline co-ordinate system: the components of the mean velocity in a plane parallel to the wall are taken in the direction of the velocity at the boundary layer edge (streamwise component, U_s) and perpendicular to the velocity at the boundary layer edge (crosswise component, U_c); these velocity components are used for the evaluation of the integral parameters θ_{11} and δ_2.

1. INTRODUCTION

The prediction of the development of a turbulent boundary layer on a swept wing is an essential step before the calculation of the real flow over such a wing, including the interactions between the viscous and potential flow field, can be made. The boundary layer on a swept wing is three-dimensional and at present only a few calculation methods can deal with this kind of flow (Ref. 1 to 9).

The ultimate test of such a calculation method is the prediction of separation of the turbulent boundary layer. The definition of separation in three-dimensional flows is more complicated than in two dimensions and involves a knowledge of the pattern of the skin-friction lines. In the case of an infinite swept wing, however, the separation line can be defined as the skin-friction line with a direction parallel to the leading edge (Ref. 10).

Boundary layer calculation methods still rely on empirical information. Momentum integral methods use empirical velocity profile families and if they are extended to three-dimensional flows, assumptions must be made with regard to the cross flow families (e.g. Ref. 3). The attraction of a generalisation of a field method such as the turbulent energy method of reference 11 is that this can be done without much prior knowledge on three-dimensional flows although measurements are needed to prove the validity of the generalisation.

Parallel to the development of the three-dimensional calculation method by Wesseling and Lindhout (Ref. 2) based on the turbulent energy approach,a research program has been conducted at NLR to investigate experimentally the three-dimensional boundary layer under infinite swept wing conditions. Measurements of the mean flow properties and the wall shear stress are reported in reference 12. These results have been compared with the calculation method of Wesseling and Lindhout (Ref. 13) and other methods (Refs. 3, 4, 8 and 14). It turns out that the separation position is not well predicted by most of these methods and that cross flow angles are generally underestimated.

For the verification of the turbulence model as used in some of the calculation methods measurements of the Reynolds stress tensor are very much wanted. They might give some answer to the question how the direction of the shear stress must be determined and to what extent the three-dimensionality of the flow affects the two-dimensional empirical relations. Only a few measurements of this type are reported in the literature (Refs. 15, 16 and 17).

Therefore measurements of the Reynolds stress tensor were carried out on the same model as used for the mean velocity measurements. These measurements are reported in reference 18. The present paper gives an assessment of the results of these measurements especially with respect to the development of a calculation method and the prediction of separation.

2. EXPERIMENT

2.1. Description of model

The experimental model was designed with three considerations in mind. First there is a considerable advantage in simulating the flow over an infinite swept wing. From a physical point of view the boundary layer on an infinite swept wing is not different from a general three-dimensional boundary layer. But since ideally the flow properties are constant in spanwise direction, it is sufficient to measure the boundary layer development in one section only. Also this flow is mathematically much easier to handle and this will facilitate the comparison with theory. Secondly a pressure variation is required such that the boundary layer is almost two-dimensional at the beginning, followed by a region of an adverse pressure gradient causing increased cross-flow with a three-dimensional separation close to the trailing edge. In this way the initial boundary layer profile is well defined and the full development of a three-dimensional boundary layer, including separation, is covered. The third condition is that the boundary layer must develop on a flat plate to eliminate unknown effects of surface curvature on the turbulent structure.

On the basis of these conditions a model was designed (Fig. 1) made up of a smooth plate and an airfoil-like body mounted near the plate. Plate and body spanned the 3x2 meter cross section of the wind tunnel and were fixed to the tunnel side walls under a sweep angle of 35 degrees. In this way a diverging channel was obtained between plate and body. Appropriate flow blockage at the end of the channel and curved guiding vanes at the two sides of the diverging channel were used to obtain the desired pressure distribution and to eliminate side wall effects. The free stream velocity was about 35 m/sec giving a Reynolds number per meter of 2.4×10^6.

A large number of static pressure holes were located in the testplate for accurate measurements of the pressure distribution. Boundary layer probes could be brought into the flow in one section (the measurement plane) at ten measuring stations (stations 1 till 10), although additional measurements could be made at both sides in spanwise direction of the first measuring station (Fig. 1). The boundary layer probes could be positioned inside the boundary layer by means of a traversing mechanism mounted on the back side of the flat plate to avoid interference.

For a more detailed description of the experimental set-up and the mean velocity measurements can be referred to reference 12. Details of the measurements of the Reynolds stress tensor are given in reference 18.

2.2. External flow field

The static pressure coefficient (relative to the static pressure and dynamic head at the first measurement station) in the measurement plane and at the plate surface is shown in figure 2. In the same figure the pressure coefficient, derived from the measured flow velocity at the edge of the boundary layer by means of a pitot-static pressure tube, is indicated. Good agreement is obtained, but after station 8 small differences are noticeable. They are due to a slight static pressure variation (of the order of 1 or 2 $^0/_0$) across the boundary layer.

Calculations of the flow angle at the boundary layer edge using the measured static pressure variation and assuming quasi two-dimensional flow showed good agreement with the flow angles measured by means of a cylindrical yaw tube. Only after station 7 differences of at most 1 degree could be detected, indicating the accuracy of the experimental approximation of a quasi two-dimensional flow.

2.3. Mean velocity profiles

Mean velocity profiles were obtained with a small rotatable hot-wire probe (Fig. 3). Since the probe dimensions are very small, interference with the boundary layer flow can almost be neglected. Measurements are taken as close to the wall as 0.2 mm. The direction of the flow is found by rotation of the probe at constant distance from the wall and the subsequent determination of the symmetry line. When the wire is perpendicular to the local flow direction the velocity can be deduced from the hot-wire calibration.

Magnitude and direction of the velocity vector are shown in the figures 5 and 6. Chordwise velocity profiles are shown in figure 7. Close to station 9 the y-derivative of the chordwise velocity component vanishes and consequently three-dimensional separation can be expected to occur in this region.

Velocity profiles measured left and right in spanwise direction of the first measuring station did not reveal any significant spanwise variation of the initial boundary layer profiles.

2.4. Wall shear stress measurements

Wall shear stress measurements are made with wall pitots of the Stanton type with slit heights of 0.1 and 0.2 mm. These devices were calibrated in a fully developed pipe flow. The direction of the wall shear was determined by rotation of the wall pitot.

If the magnitude of the velocity is plotted versus the logaritm of the wall distance y (the so-called "Clauser plots"; reference 19) a straight line over an apreciable distance is encountered in the wall region of the flow (Fig. 8), with a slope depending on the local wall shear stress. The wall shear stress derived from this technique is compared with the value deduced from the calibrated wall pitots and good agreement is obtained (Fig. 9). The skin friction coefficient exhibits a distinct minimum close to station 9, that is at or very close to the three-dimensional separation line.

The direction of the wall shear stress is also shown in figure 9. The values obtained by rotation of the wall pitot agree well with an extrapolation of the measured direction of the mean velocity towards the wall (Fig. 6). Due to the rapid rotation of the velocity vector in the viscous sublayer, the direction of the wall shear stress might be underestimated by 1 or 2 degrees. A photograph of the oil flow pattern of the skin-friction lines is shown in figure 10.

2.5. Measurements of Reynolds stress tensor

In turbulent boundary layer flows the shear stresses are mainly determined by the action of turbulence except very close to the wall where the turbulent motion is suppressed and viscous stresses are dominant. The Reynolds stress tensor has the form:

$$\begin{vmatrix} \overline{u^2} & \overline{uv} & \overline{uw} \\ \overline{uv} & \overline{v^2} & \overline{vw} \\ \overline{uw} & \overline{vw} & \overline{w^2} \end{vmatrix}$$

The tensor is symmetric. The diagonal terms represent the turbulence intensities and the off-diagonal terms the turbulent shear stresses. In the boundary layer approximation only the shear stress components $\overline{uv}$ and $\overline{vw}$ are retained and they can then be viewed as the two components of the shear stress vector. Only a few measurements of the Reynolds stress tensor are reported in the literature (Refs. 15, 16 and 17). Therefore some more attention will be paid to the details of this technique as applied in the present experiment.

The turbulence measurements were carried out with an X-wire probe (Fig. 11). Since the probe-tip was located 25 mm in front of the rotation axis, the probe-tip will describe a helix when the probe is transversed inside the three-dimensional boundary layer and aligned with the local flow direction. The displacement of the tip in chordwise direction, however, is sufficiently small to be neglected. A special feature of the probe is that it can also be rotated along an axis co-inciding with the local flow direction. This rotation is indicated by the roll angle ϕ (see Fig. 12).

When the plane of the X-wire is perpendicular to the wall (ϕ = 90 or 270 degrees) the fluctuating velocity components u and v will be measured. For different settings of the roll angle, different components of the fluctuating velocity can be measured. In general one can say:

$$e = K.\,(u + r.s)$$

with e, the fluctuating voltage of the hot-wire,
u, the fluctuating velocity in the direction of the mean flow U,
s, the transverse fluctuating velocity in the plane of the X-wire and perpendicular to the mean velocity U,
K, the velocity sensitivity of the hot-wire defined by K = dE/dU and given by the hot-wire calibration of the mean voltage E as a function of the mean velocity U,
r, the directional sensitivity, depending on the wire angle γ and approximated by $r = -\tan\gamma$. In fact r was determined from a yaw calibration.

The transverse velocity component s can be expressed as (Fig. 12):

$$s = v.\sin\phi + w.\cos\phi$$

The fluctuating voltages of the two wires of an X-wire e_1 and e_2 can be combined electronically to give the mean square values $\overline{(e_1+e_2)^2}$, $\overline{(e_1-e_2)^2}$ and $\overline{e_1^2 - e_2^2}$. Substitution of the relation between e, u and s yields 3 equations that can be solved for the correlations $\overline{u^2}$, $\overline{s^2}$ and $\overline{us}$, if the values of K_1, K_2, r_1 and r_2 are known from calibration.

$\overline{u^2}$ is always measured, irrespective of the roll angle ϕ. The other turbulence intensities are determined from:

$\phi = 0^\circ$ or 180° $\quad \overline{w^2} = \overline{s^2}$

$\phi = 90^\circ$ or 270° $\quad \overline{v^2} = \overline{s^2}$

In principle $\overline{uv}$ and $\overline{uw}$ can also be determined from these positions but instead two separate measurements have been made:

I: $\phi = 45^\circ$ $\quad \overline{us}_I = (\overline{uv} + \overline{uw})/\sqrt{2}$

II: $\phi = 315^\circ$ $\quad \overline{us}_{II} = (-\overline{uv} + \overline{uw})/\sqrt{2}$

and one can find that:

$$\overline{uv} = (\overline{us}_I - \overline{us}_{II})/\sqrt{2}$$

$\overline{uv}$ can also be derived from the combination of probe settings $\phi = 135^\circ$ and 225°. In the same way $\overline{uw}$ can be derived by combination of the measurements with $\phi = 45^\circ$ and 135° or $\phi = 225^\circ$ and 315°. Finally the value of $\overline{vw}$ is found from the so-called quarter-square technique:

I: $\phi = 45^\circ$ or 225° $\quad \overline{s_I^2} = \overline{(v + w)^2}/2$

II: $\phi = 135^\circ$ or 315° $\quad \overline{s_{II}^2} = \overline{(v - w)^2}/2$

and is follows that:

$$\overline{vw} = (\overline{s_I^2} - \overline{s_{II}^2})/2.$$

At each station 8 boundary layer traverses were made with the roll angle ϕ varying from 0^o till 360^o in steps of 45^o. In this way each component is measured twice and the average value of the two is given as the final result.

It is well known that large errors can occur in this type of measurements. The procedure outlined above reduces at least part of the error caused by differences between the angles (γ_1 and γ_2) of the two wires. A more detailed discussion of this can be found in reference 18. The measurements are corrected for temperature drift, but no other corrections (as for finite wire length, non-linearity, frequency limitations) are applied. Care has been taken of the effects caused by upwash inside the boundary layer. In some cases the vertical velocity inside the boundary layer can be as large as 10 ^{o}/o of the mean velocity. The upwash was measured by the X-wire itself and the wire angles were corrected accordingly. The final results are given in the local streamline co-ordinate system (Fig. 4).

The accuracy of the measurements is estimated at 10 ^{o}/o. One must realize that an error of this order of magnitude might be present in the data.

The six components of the Reynolds stress tensor have been measured at station 1 and station 4 till 10. However, due to the configuration of the X-wire probe the measurements are taken 25 mm in front of the positions where the mean velocity and wall shear stress were measured. The closest reading was taken at 2.5 mm away from the wall.

The turbulent shear stresses and turbulence intensities have been made dimensionless with the friction velocity u_τ defined by $u_\tau^2 = \tau_w/\rho$ and measured independently with the wall pitot as discussed previously. As a result of this $-\overline{uv}/u_\tau^2$ must approach a value of 1 at the wall and $\overline{vw}/u_\tau^2$ a value of 0. It can be seen from figure 13 and 14 that this is the case. Some examples of the turbulence intensity are shown in the figures 15, 16 and 17.

3. ANALYSIS OF THE FLOW FIELD

3.1. Separated region

If three-dimensional separation on an infinite swept wing is defined by a vanishing component of the wall shear stress in a direction perpendicular to the leading edge (Ref. 10) separation occurs close to station 9 as one can infer from the figures 9 and 10.

The skin-friction lines after the separation line are almost parallel to the trailing edge. The flow at the surface after the separation line is not initiated at the leading edge, but at the upstream guiding vane (Fig. 1). At the separation line the skin-friction lines that started from the leading edge coalesce and the shear stress reaches a very distinct minimum (Fig. 9). The wall shear stress does not fall to zero, as is the case in two-dimensional separation: only the chordwise component vanishes. The rapid increase after the separation line indicates an acceleration of the flow in the wall region also noticeable in the mean velocity profiles (Fig. 5). Throughout the flow development at and after separation the well-known logarithmic velocity distribution is maintained (Fig. 8).

Very remarkable changes can be observed in some of the components of the Reynolds stress tensor after the separation line. In front of this line the value of $-\overline{uv}$ increases when moving away from the wall while a maximum value is reached about half way the boundary layer thickness. Further outwards the shear stress decreases again till a value of zero is reached near the boundary layer edge. This is the usual pattern in a boundary layer with an adverse pressure gradient (Ref. 20). After the separation line, at station 10, a very pronounced dip in $-\overline{uv}$ is encountered in the wall region, followed by an increase till a maximum value at about two third of the boundary layer thickness and a subsequent fall-off at the boundary layer edge (Fig. 13). The distribution of $-\overline{uv}$ close to the wall is very similar to the shear stress distribution inside a zero pressure gradient boundary layer, although the co-incidence with the shear stress distribution at station 1 is fortuitous. A similar dip can be found in the distribution of the longitudinal turbulence intensity $\overline{u^2}$ at station 10 (Fig. 17). Probably the increased wall shear is linked to the intensified turbulence production close to the wall. These results suggest two distinct layers after the separation line: a thin "fresh" boundary layer, mainly in spanwise direction with an increased turbulence production and a shear stress distribution resembling a two-dimensional zero pressure gradient boundary layer, and on top of this a second layer with a shear stress distribution similar to the upstream shear stress profiles. These two layers merge very gradually into each other.

Another remarkable effect is the increase in $\overline{w^2}$ intensity when moving downstream till it almost equals the $\overline{u^2}$ intensity (Figs. 16 and 17).

3.2. Magnitude of shear stress

For a calculation method the flow development ahead of the separation line is of great practical importance. The question is if the turbulence model as presently used in calculation methods needs to be modified to predict adequately three-dimensional separation. Since the three-dimensional boundary layer program that is used at NLR is based on Bradshaw's turbulent energy method (Ref. 11) we will restrict ourselves to those parameters that are of relevance in the present context.

The basic problem of any turbulent field method is to describe the turbulent shear stress, both in magnitude and direction. The magnitude of the turbulent shear stress can be inferred from a mixing length approach. The relevant relation is:

$$|\tau| = \rho \ell^2 \cdot \left|\frac{dU}{dy}\right|^2$$

where $|\tau|$ is the shear stress magnitude and $\left|\frac{dU}{dy}\right|$ the magnitude of the velocity gradient vector defined by:

$$\left|\frac{dU}{dy}\right|^2 = \left(\frac{\partial U}{\partial y}\right)^2 + \left(\frac{\partial W}{\partial y}\right)^2$$

The mixing length ℓ, made dimensionless with the local boundary layer thickness δ has been calculated from the measured shear stress and mean velocity profiles. The result is shown in figure 18 for the stations 1, 5, 7, 9 and 10. In the wall region of the flow all data reduce to the usual relation $\ell = 0.41.y$. This is in agreement with a logarithmic velocity distribution when τ is approximately constant in the wall region. In the outer region of the boundary layer, however, a remarkable decrease in the mixing length is found between station 1 (where $\ell/\delta \approx 0.08$, which is a normal value for a two-dimensional zero pressure gradient boundary layer; Ref. 11), and station 7 (with $\ell/\delta \approx 0.05$). At and after separation this value remains almost constant or increases slightly. The measurements indicate that the value of the mixing length in the outer region of the flow might be influenced significantly by three-dimensional effects.

3.3. Direction of shear stress

In the literature is some discussion on the direction of the shear stress in three-dimensional turbulent boundary layers. The most simple assumption in calculation methods and in accordance with laminar three-dimensional boundary layers is to take the shear stress in the direction of the velocity gradient (Ref. 9). A refinement is introduced in the turbulent kinetic energy method of Bradshaw (Ref. 1) and Wesseling and Lindhout (Ref. 2) where small departures from the direction of the velocity gradient are possible by the effects of convection and diffusion as will be discussed in section 4.1. Measurements of Johnston (Ref. 15) and Bradshaw (Ref. 16) do indicate differences between the two directions. More recent calculations by Vermeulen (Ref. 21) and East (Ref. 22) suggest that the shear stress is in between the direction of the velocity gradient and the mean flow velocity. They calculated the shear stress direction from the momentum balance using measured velocity profiles.

The present experiment seems to confirm these findings as can be seen from the figures 19, 20 and 21. Also it is noticeable from these figures that the difference between the two directions decreases when moving downstream. This is even more pronounced in the wall region. At station 10 the two directions almost coincide.

Both Vermeulen and East use a factor N_e to express the direction of the shear stress. N_e represents the ratio of the eddy viscosity component normal to the local flow direction and the component in the local flow direction. This can be written as:

$$N_e = \frac{\overline{vw}/\overline{uv}}{\frac{\partial W}{\partial y}/\frac{\partial U}{\partial y}} = \frac{\tan(\varphi_\tau - \beta)}{\tan(\varphi_{grad} - \beta)}$$

Vermeulen and East found an almost constant value across the boundary layer of 0.5 and 0.4 respectively. In this experiment N_e varies from 0.5 at station 4 till 0.7 near separation. After separation larger values up to 1.0 are found (Fig. 22). One may conclude that there is a strong experimental evidence that in general appreciable differences between the velocity gradient and shear stress direction exist. The present experiment does not support a constant value of N_e.

3.4. Entrainment

The proces of entrainment of non-turbulent fluid inside the boundary layer is explicitely represented in some boundary layer calculation methods. The entrainment velocity V_{ent} is defined by:

$$V_{ent} = \frac{1}{\rho}\frac{dQ}{dx}$$

where Q is equal to the mass flow per unit span inside the boundary layer. In the turbulent kinetic energy method the entrainment is controled by the value of the diffusion term (see Section 4.1) at the boundary layer edge. In two-dimensional boundary layers Bradshaw (Ref. 11) proposes the relation:

$$\frac{V_{ent}}{U_e} = 10\left(\frac{\tau_{max}}{\rho U_e^2}\right)$$

with U_e the velocity at the boundary layer edge and τ_{max} the maximum value of the shear stress inside the boundary layer. In this experiment the entrainment velocity has been calculated from:

$$V_{ent} = \frac{d}{dx}\left[U_{x_{edge}}(\delta - \delta_x)\right]$$

where the velocity $U_{x_{edge}}$ and the chordwise displacement thickness δ_x are evaluated in a direction perpendicular to the leading edge. The calculation shows that the entrainment velocity in this example of a three-dimensional boundary layer is almost constant and not significantly different for the stations 1 to 7 from the empirical relation in two-dimensional boundary layer flows (Fig. 23). Only at and after separation (station 8, 9 and 10) $\tau_{max}/\rho U_e^2$ increases at an almost constant value of V_{ent}/U_e.

3.5. Turbulent kinetic energy

In two-dimensional turbulent boundary layer flows an almost constant ratio is often found between the shear stress and the turbulent kinetic energy, expressed as:

$$a_1 = \frac{|\tau|/\rho}{(\overline{u^2}+\overline{v^2}+\overline{w^2})} = \frac{|\tau|/\rho}{q^2}$$

In this experiment a decrease of a_1 can be noticed in downstream direction (Fig. 24). At station 1 a value of $a_1 = 0.15$ is found in accordance with other data (Ref. 11) but close to separation a value of 0.12 is observed.

4. COMPARISON WITH CALCULATIONS

4.1. Description of the calculation method

At NLR a calculation method has been developed based on a generalisation of Bradshaw's turbulent kinetic energy method (Ref.11). The method is discussed in great detail in the references 2 and 23. The set of equations is:

continuity: $$\frac{\partial U_x}{\partial x} + \frac{\partial U_y}{\partial y} + \frac{\partial U_z}{\partial z} = 0$$

x-momentum: $$\rho\frac{DU_x}{Dt} = -\frac{\partial p}{\partial x} + \frac{\partial \tau_x}{\partial y}$$

z-momentum: $$\rho\frac{DU_z}{Dt} = -\frac{\partial p}{\partial z} + \frac{\partial \tau_z}{\partial y}$$

the empirical shear stress equations are:

$$\frac{1}{2a_1}\frac{D\tau_x}{Dt} = |\tau|\cdot\frac{\partial U_x}{\partial y} - \left(\frac{|\tau_{max}|}{\rho}\right)^{1/2}\frac{\partial}{\partial y}(G\tau_x) - \left(\frac{|\tau|}{\rho}\right)^{1/2}\frac{\tau_x}{L}$$

$$\frac{1}{2a_1}\frac{D\tau_z}{Dt} = |\tau|\cdot\frac{\partial U_z}{\partial y} - \left(\frac{|\tau_{max}|}{\rho}\right)^{1/2}\frac{\partial}{\partial y}(G\tau_z) - \left(\frac{|\tau|}{\rho}\right)^{1/2}\frac{\tau_z}{L}$$

(1) (2) (3) (4)

In the last two equations a_1 is a constant (taken as 0.15) and G and L are prescribed functions of y/δ (Ref. 11). The dominant terms are the production term (2) and the dissipation term (4). When the other terms representing convection (1) and diffusion (3) are neglected the mixing length relation is recovered:

$$|\tau| = \rho.L^2.\left|\frac{dU}{dy}\right|^2$$

with

$$\frac{\tau_x}{\tau_z} = \frac{\partial U_x/\partial y}{\partial U_z/\partial y}$$

This last expression shows that in this special case the shear stress acts in the direction of the velocity gradient. However, when the diffusion and convection terms are no longer neglected, small deviations from the direction of the velocity gradient will be found.

The 5 partial differential equations are hyperbolic as a consequence of the formulation of the diffusion terms. The external pressure distribution is supposed to be known. The equations are solved numerically by means of a simple, linear, explicit finite difference scheme based on a generalisation of the two-dimensional Courant-Isaacson-Rees scheme.

The empirical shear stress equations are not valid close to the wall since the viscous shear stresses are neglected. Also the velocity gradients are very steep there and therefore it is very attractive to use an analytical expression in that region. The first mesh-point, at some distance away from the wall, can then be coupled with the boundary condition at the wall. In two dimensions the familiar "law of the wall" is often used. Recently van den Berg (Ref. 24) derived a three-dimensional "law of the wall" by taking into account in an approximate way the effect of pressure gradient as well as inertial effects.

In the case of a quasi two-dimensional flow the z-derivatives (in spanwise direction) can be ignored and the calculations are greatly simplified. Assuming such a flow the calculations, presented next, have been made using the measured pressure distribution and the mean velocity profile at station 1 as input data.

4.2. Comparison with original calculation method

A very sensitive parameter for comparison with theory is the angle of the wall shear stress β_w as shown in figure 25. The agreement is good up to station 5, but becomes increasingly worse further downstream. After station 7 the shear stress angle decreases again and separation is not predicted at all. The same applies for the comparison of the calculated integral parameters like Θ_{11} and δ_2 (Fig. 26). Again good agreement is obtained only up to station 5. After this station the cross flow angles are underestimated and this influences to a large extent the downstream development of the boundary layer. A more detailed discussion of this can be found in reference 13.

4.3. Modifications to original calculation method

From this result it is clear that the shear stress equations as formulated in section 4.1 are not accurate enough to describe three-dimensional boundary layers with large cross-flows. They fail to predict separation adequately. The turbulence measurements are of great help to modify the empirical shear stress equations. The difference between the direction of the velocity gradient and the shear stress and the downstream reduction of the mixing length both act to increase the cross flow angles inside the boundary layer. Three tentative modifications are proposed. Since they are based on one experiment only they can not be more than an empirical modification for this special case. More comparisons with different experiments are needed to prove their validity in a general way.

First the direction of the shear stress has been taken more in accordance with the experimental results. This is done by the introduction of a factor C, representing the difference between the velocity gradient angle φ_{grad} and the shear stress angle φ_τ in the absence of the effects of diffusion and convection:

$$C = \tan(\varphi_\tau - \varphi_{grad})$$

Combination of the two shear stress equations of section 4.1 yields the scalar equation for the turbulent energy as used in the two-dimensional method:

$$\frac{1}{2a_1}\frac{D|\tau|}{Dt} = |\tau|\cdot\left|\frac{dU}{dy}\right| - \left(\frac{|\tau_{max}|}{\rho}\right)^{1/2}\frac{\partial}{\partial y}(G|\tau|) - \left(\frac{|\tau|}{\rho}\right)^{1/2}\cdot\frac{|\tau|}{L}$$

One would like to retain this property in the modified shear stress equations. It then follows that the dissipation term in the equation for τ_x must be written as:

$$\left(\frac{|\tau|}{\rho}\right)^{1/2}\cdot\frac{1}{L}(\tau_x + C\tau_z)$$

and in the equation for τ_z as:

$$\left(\frac{|\tau|}{\rho}\right)^{1/2}\cdot\frac{1}{L}(\tau_z - C\tau_x)$$

It must be noted here that there is no physical model underlying the proposed modifications of the dissipation terms. They only act to give the shear stress equations the required properties. The value of C still has to be determined and as a first trial C is related to the eddy viscosity ratio N_e as defined by East and Vermeulen. C can then be expressed as:

$$C = \frac{(N_e-1)\tan(\varphi_{grad}-\beta)}{1+N_e\tan^2(\varphi_{grad}-\beta)}$$

In this relation $\varphi_\tau - \beta$ represents the difference in direction between the shear stress φ_τ and the mean velocity β. N_e is taken constant across the boundary layer and equal to 0.5 as an average value for the data of Vermeulen, East and the present experiment.

The seond modification is related to the reduction of mixing length as observed in the experiment. The turbulent energy equation represents a balance between production and dissipation of turbulent energy. This balance is linked to the turbulence structure. Bradshaw (Ref. 25) noticed that small extra rates of strain may have a large effect on the turbulence structure. Townsend (Ref. 26) more specifically stressed the importance of the lateral strain $\partial V/\partial y$ and more recently Morel and Torda (Ref. 27) use a similar parameter for empirical changes in L and a_1 for jet and wake flows. In the empirical shear stress equations the nature of this balance can be affected if the dissipation length L is related to the extra rate of strain $\partial V/\partial y$. In two-dimensional boundary layers (if not to close to separation) and in moderately three-dimensional boundary layers $\partial V/\partial y$ is very small. However, when the cross flow increases, the vertical velocity inside the boundary layer will increase as well by the effect of streamline convergence. Therefore a modification of the dissipation length is proposed related to the non-dimensional lateral strain, approximated by:

$$\frac{\partial V/\partial y}{\partial U/\partial y} \approx \frac{V_\delta/\delta}{U_e/\delta} = \frac{V_\delta}{U_e}$$

V_δ and U_e are the vertical and horizontal velocity at the boundary layer edge respectively. The dissipation length L in the shear stress equation will now be described by:

$$\text{if } y \leq \frac{L_{max}}{K} \qquad L = K.y$$

$$\text{and if } y > \frac{L_{max}}{K} \qquad L = L_{max} = 0.084.\delta.(1-5.3V_\delta/U_e)$$

The constant 0.084 is in accordance with a two-dimensional constant pressure boundary layer and the additional constant 5.3 is determined from a correlation with the measured shear stress distribution. The measured mixing length could not be used in this respect since mixing length and dissipation length are different outside the wall region due to the effects of convection and diffusion.

The validity of this correction can only be assessed if a great number of two- and three-dimensional boundary layers are re-calculated and compared with experiments. In the context of this paper the correction can be viewed as an empirical modification to obtain good agreement with the measured shear stress distributions.

When it is assumed that the lateral strain $\partial V/\partial y$ has an effect on the turbulence structure, the variation of a_1 as observed in the experiment, can be represented accordingly. Therefore a_1 is written as:

$$a_1 = 0.15\ (1-3.5\frac{V_\delta}{U_e})$$

This modification is not of great importance. The effect on the calculations is very small.

Renewed calculations were performed with the modifications as outlined above. The result is shown in figure 25 for the variation of the wall shear stress angle and in figure 26 for the momentum and displacement thickness. Good agreement is now obtained till station 7 but, surprisingly, separation is not yet predicted.

4.4. Influence of pressure distribution

In an attempt to investigate the cause of the difference between the experimental results and the modified calculations the pressure gradient at the most rearward stations was slightly increased. In fact, the static pressure, measured at the boundary layer edge instead of the value at the plate surface (Fig. 2) was used as an input for the calculations. This amounts to an increase in pressure coefficient of 0.005 at station 8 and 0.01 at station 9. The result of this calculation is also shown in figure 25. Separation is now predicted between station 7 and 8! The exercise shows that a small variation in the pressure distribution causes a large shift in the predicted separation position.

This particular phenomenon close to separation as shown in figure 25 suggests a singular behaviour at separation. Moreover in the calculation with separation the vertical velocity V as calculated in the finite difference scheme, rises very rapidly near the separation point. Very similar phenomena are known to occur in two-dimensional laminar boundary layer flows near separation (see the classical article of Goldstein; (Ref. 28). Golstein proved that when separation is approached $\tau_w \longrightarrow 0$ while $V \longrightarrow \infty$. More recently Tsahalis and Telionis (Ref. 29) showed a similar singularity to exist in two-dimensional turbulent flows. The singularity only exists if the pressure distribution is specified as an independent boundary condition. The singularity can be removed if the wall shear stress or the displacement thickness is prescribed and the boundary layer equations are then solved for the pressure distribution (Ref. 30 and 31).

In the case of a laminar three-dimensional separation on an infinite swept wing the boundary layer equations in chordwise direction can be solved independently of the spanwise flow (the "independence principle"). Therefore the same singularity will occur at the three-dimensional laminar separationline on an infinite swept wing. When the flow is turbulent this independence principle does not hold anymore since the shear stresses are coupled by the additional equations for the shear stresses. It is possible that the singularity is not affected by this.

To investigate this point further, calculations have been made with an interaction model for the pressure and the boundary layer development. Since the experimental configuration is basically a duct flow the interaction between the boundary layer flow and the potential core can easily be taken into account. The pressure gradient in the duct is a function of the variation of channel height and the displacement thickness of the boundary layer. Conversely the displacement thickness is an, apparently strong, function of the pressure gradient. In the finite difference calculations the potential flow equation can be coupled with the boundary layer equations such that at each step in the numerical scheme the pressure gradient is determined by the channel height and the displacement thickness. At each step a few iterations are needed to ensure convergence. This process failed to converge close to the separation point, but as indicated in figure 27 the solution follows closely the experimental curve. The so calculated pressure gradient is shown in figure 28 and compared with the experimental pressure gradient at the wall and at the boundary layer edge. The differences are very small indeed, illustrating the sensitivity of the calculations for the pressure distribution.

It is of interest to know where the separation would have been predicted with the original boundary layer equations as formulated in section 4.1. The result of this calculation is also shown in figure 27.

Deviations from the experimental results can be observed downstream of station 5. Separation is predicted close to station 10 instead of station 9.

The example shows that an accurate prediction of the separation position in this case is only possible when the problem is re-formulated in terms of a dependence of the potential flow on the boundary layer development. This may be generally true, although the interaction in this special case of a duct flow might be much more dramatic as in the case of a real swept wing where the local pressure gradient is affected by the potential flow around the complete wing. The calculations indicate, however, that a singularity exists at the separation point that can only be avoided if the pressure distribution is not prescribed.

5. CONCLUSIONS

Measurements of the mean flow and the Reynolds stress components in a three-dimensional turbulent boundary layer under infinite swept wing conditions indicate a two-layer structure after the separation line. There is a region close to the wall with a flow mainly in spanwise direction and with an increased turbulence intensity. On top of this a second layer can be observed with a structure similar to the upstream boundary layer.

In the three-dimensional boundary layer development a marked decrease in mixing length and an appreciable difference between the directions of shear stress and velocity gradient has been observed. The entrainment did not seem to be influenced by the three-dimensionality of the flow.

Theoretical calculations of the boundary layer development, based on the turbulent energy equation, did not predict separation. Improvement was obtained with modifications derived from the measured turbulent shear stresses but the calculations showed to be very sensitive for the pressure distribution close to separation. There are strong indications that this sensitivity is related to a Goldstein-type singularity at separation as a consequence of the prescribed pressure distribution. When the boundary layer calculation was directly coupled to the potential flow equation the agreement was encouraging, but the calculations failed to converge close to the separation line.

6. REFERENCES

1. Bradshaw, P. — Calculation of three-dimensional turbulent boundary layers. J. Fluid Mech. Vol. 46, part 3 (1971), p.417.

2. Wesseling, P.; Lindhout, J.P.F. — A calculation method for three-dimensional incompressible turbulent boundary layers. AGARD Conf. Proc. No. 93 (1971).

3. Smith, P.D. — An integral prediction method for three-dimensional compressible turbulent boundary layers. A.R.C. TR 72228 (1973).

4. Fanneløp, T.K.; Humphreys, D.A. — A simple finite-difference method for solving the three-dimensional turbulent boundary layer equations. Proc. of the 12th Aerospace Sciences Meeting, AIAA, Washington (1974).

5. Michel, R.; Cousteix, J.; Quémard, C. — Methode practique de prévision des couches limites turbulentes bi- et tridimensionelles. La Recherche Aérospatiale No. 1 (1972).

6. Pierce, F.J.; Klinsiek, W.F. — An implicit numerical solution of the turbulent three-dimensional incompressible boundary layer equations. Virginia Polytechnic Inst. VPI-E-71-14 (1971).

7. Shanebrook, J.R.; Sumner, W.J. — A small cross flow theory for three-dimensional compressible turbulent boundary layers on adiabatic walls. AIAA Journal 11, p. 950 (1973).

8. Krause, E. — Numerical treatment of boundary layer problems. AGARD Lecture Series No. 64 (1973).

9. Nash, J.F. — The calculation of three-dimensional turbulent boundary layers in incompressible flow. J. Fluid Mech. Vol. 37 (1969) p.625.

10. Maskell, E.C. — Flow separation in three dimensions. A.R.C. Rept.Mem. 18063 (1955)

11. Bradshaw, P.; Ferriss, D.H.; Atwell, N.P. — Calculation of boundary layer development using the turbulent energy equation. J. Fluid Mech. Vol. 28, part 3 (1967) p.593.

12. Berg, B. van den; Elsenaar, A. — Measurements in a three-dimensional incompressible turbulent boundary layer in an adverse pressure gradient under infinite swept wing conditions. NLR TR 72092 U (1972).

13. Berg, B. van den; Elsenaar, A.; Lindhout, J.P.F.; Wesseling, P. — Measurements in an incompressible three-dimensional turbulent boundary layer under infinite swept wing conditions and a comparison with theory. NLR MP 74005 U (1974).

14. Bradshaw, P. — Private communication

15. Johnston, J.P. — Measurements in a three-dimensional turbulent boundary layer induced by a forward-facing step. J. Fluid Mech. 42 (1970) p.823.

16. Bradshaw, P.; Terrill, M.C. — The response of a turbulent boundary layer on an "infinite" swept wing to the sudden removal of pressure gradient. NPL Aero.Rep. 1305 (1969).

17. Pierce, F.J. Duerson, S.H. — Measurements of the Reynolds Stress Tensor in a three-dimensional turbulent boundary layer. Virginia Polytechnic Inst. VPI-E-74-4 (1974).

18. Elsenaar, A. Boelsma, S.H. — Measurements of the Reynolds stress tensor in a three-dimensional turbulent boundary layer under infinite swept wing conditions. NLR TR 74095 U (1975).

19. Clauser, F.H. — Turbulent boundary layers in adverse pressure gradients. J. Aero.Sci. 21 (1954) p.91.

20. Bradshaw, P. — The turbulence structure of equilibrium boundary layers. J. Fluid Mech. Vol. 29, part 4 (1967) p.625.

21. Vermeulen, A.J. — Measurements of three-dimensional turbulent boundary layers. Ph. D. Thesis, Dept. of Eng. Cambridge (1971).

22. East, L.F. — Measurements of the three-dimensional incompressible turbulent boundary layer induced on the surface of a slender delta wing by the leading edge vortex. RAE, TR 73141 (1974).

23. Lindhout, J.P.F. — An ALCOL program for incompressible three-dimensional turbulent boundary layers. NLR report (to be published).

24. Berg, B. van den — The law of the wall in two- and three-dimensional turbulent boundary layers. NLR TR 72111 U, (1972).

25. Bradshaw, P. — The strategy of calculation methods for complex turbulent flows. Imperial College, London, I.C. Aero. Report 73-05 (1973).

26. Townsend, A.A. — The structure of turbulent shear flow. University Press, Cambridge (1956), p.238.

27. Morel, T. Torda, T.P. — Calculation of free turbulent mixing by the interaction approach. AIAA Journal, Vol. 21, No. 4 (1974) p.533.

28. Golstein, S. — On laminar boundary layer flow near a position of separation. Quart. J. Mech. Appl. Math. 1, (1948), p.43

29. Trahalis, D.Th. Telionis, D.P. — On the behaviour of turbulent boundary layers near the point of zero wall shear. Virginia Polytechnic Institute, VPI-E-74-20 (1974).

30. Catherall, D. Mangler, K.W. — The integration of the two-dimensional laminar boundary layer equation past the point of vanishing skin friction. J. Fluid. Mech. Vol. 26 part 1 (1966) p.163.

31. Cebeci, T. Mosinskis, G.J. Smith, A.M.O. — Calculation of separation points in incompressible turbulent flows. Journal of Aircraft, Vol. 9, No. 9 (1972) p.618.

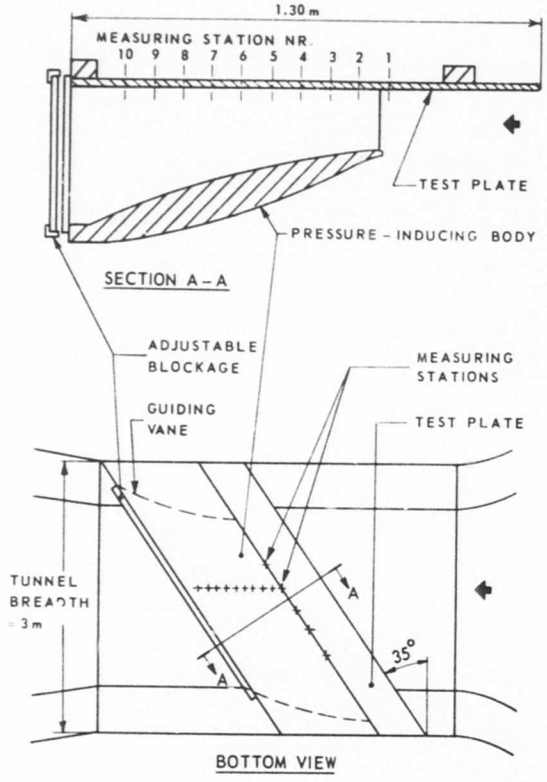

Figure 1: Sketch of the model

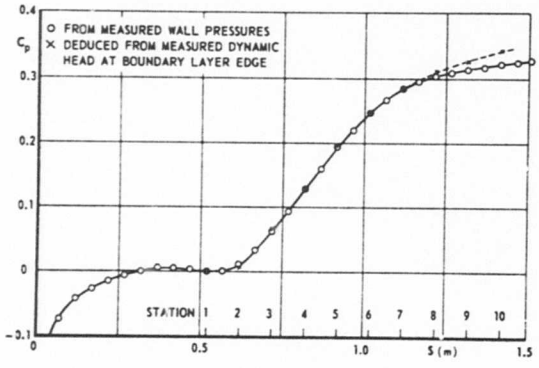

Figure 2: The pressure distribution at the measurement plane

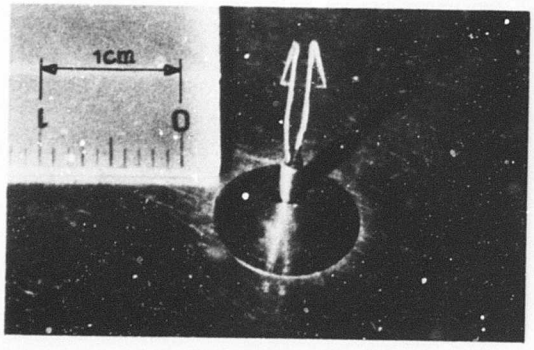

Figure 3: Rotatable hot-wire probe

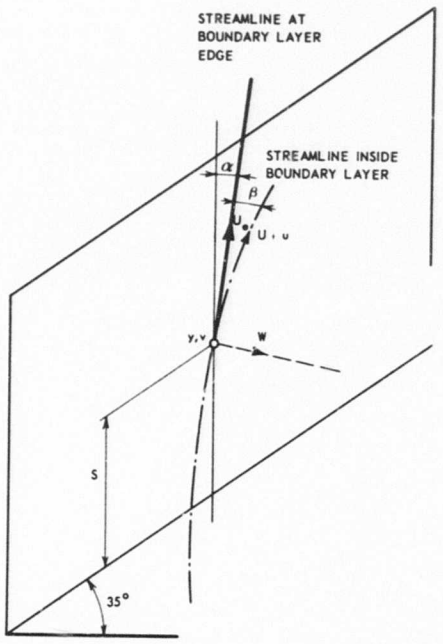

Figure 4: Boundary layer co-ordinate system

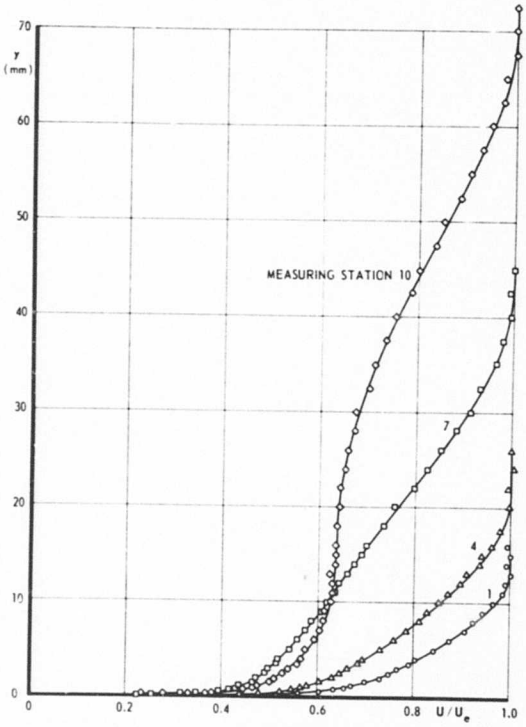

Figure 5: Measured magnitude of velocity

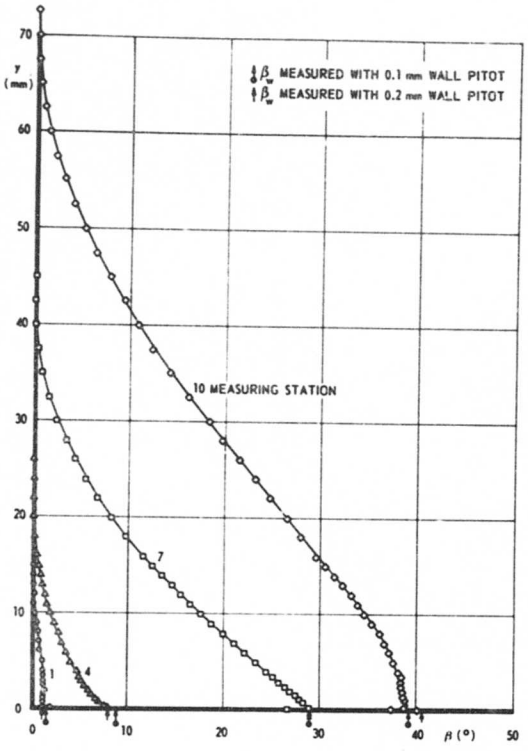

Figure 6: Measured flow angles

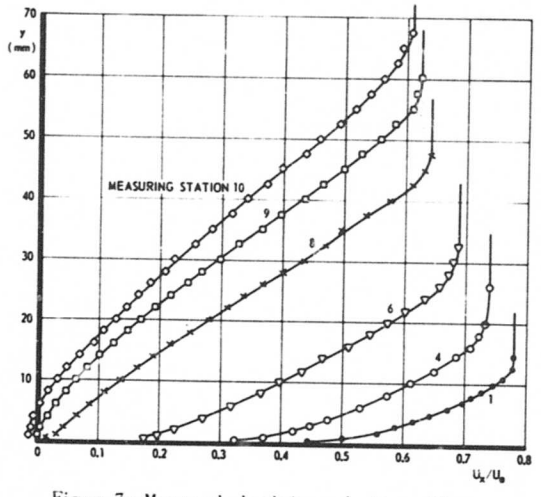

Figure 7: Measured chordwise velocity profiles

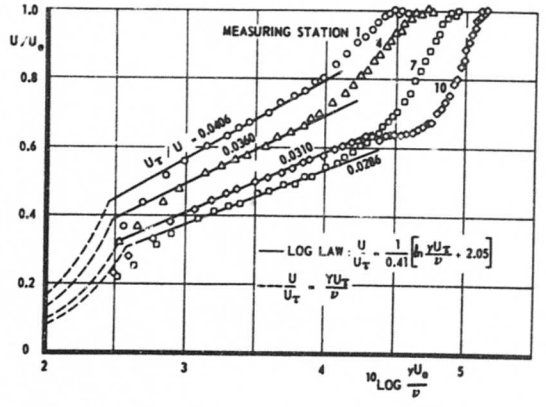

Figure 8: Clauser plot of the velocity magnitude

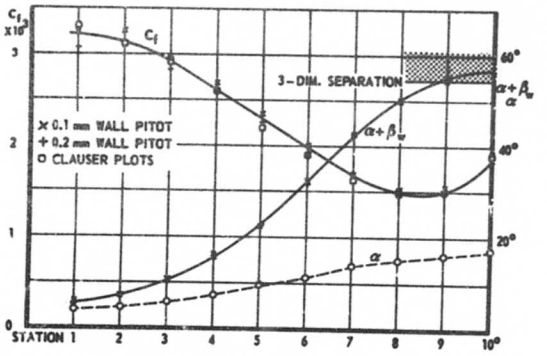

Figure 9: Measured flow angle at boundary layer edge and magnitude and direction of skin-friction

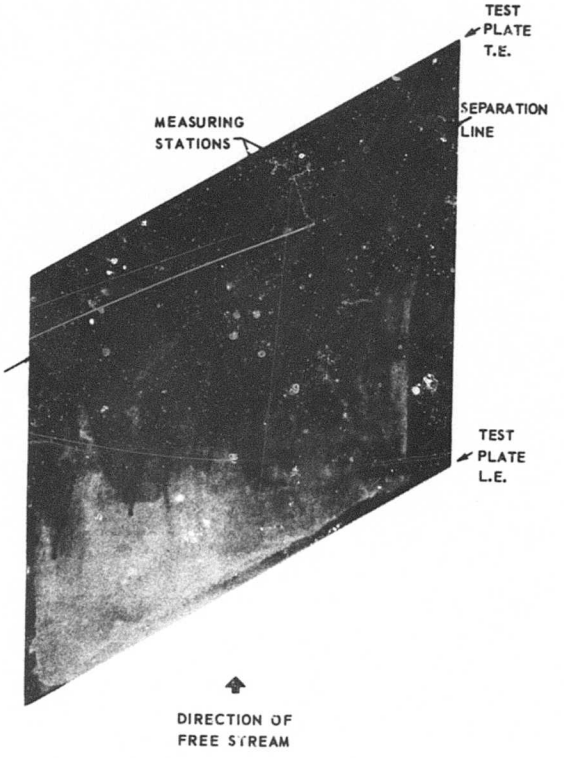

Figure 10: Photograph of the oil flow pattern on the test plate

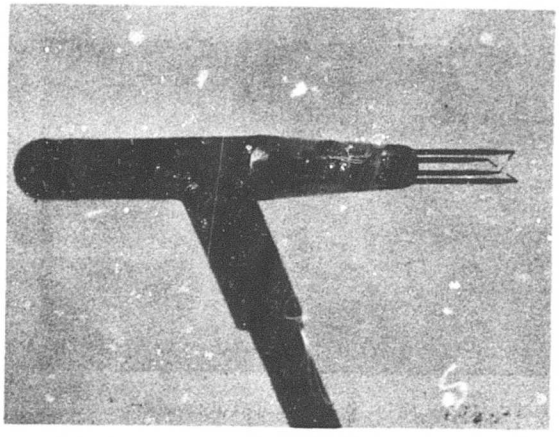

Figure 11: X-wire probe for turbulence measurements

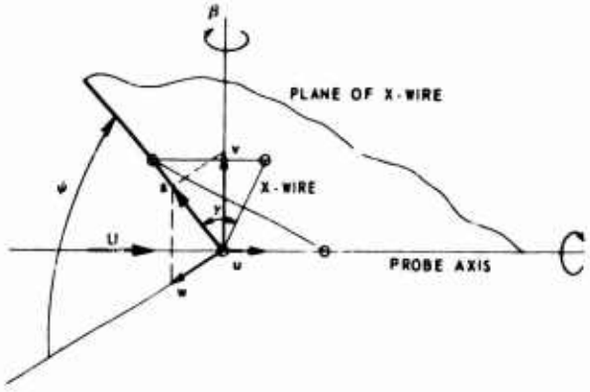

Figure 12: Definition of x-wire position

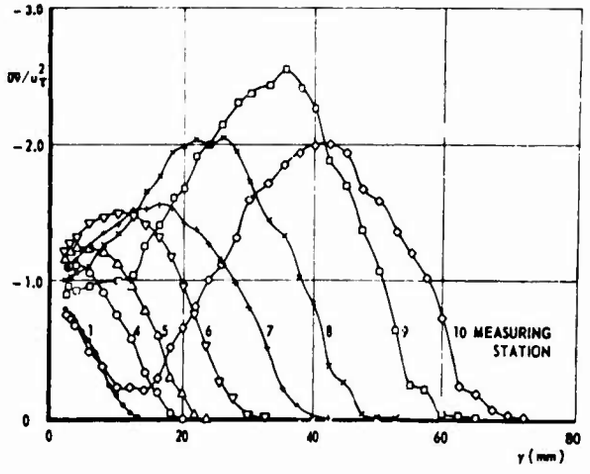

Figure 13: $\overline{uv}$-profiles at the measuring stations

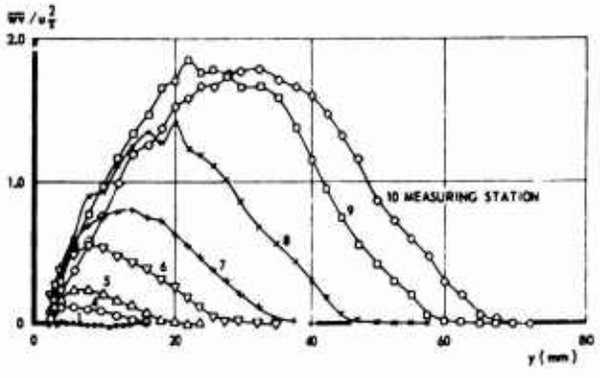

Figure 14: $\overline{uv}$ profiles at the measuring stations

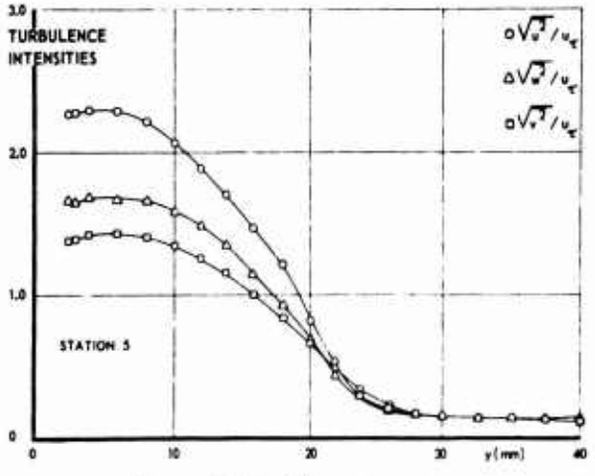

Figure 15: Turbulence intensities

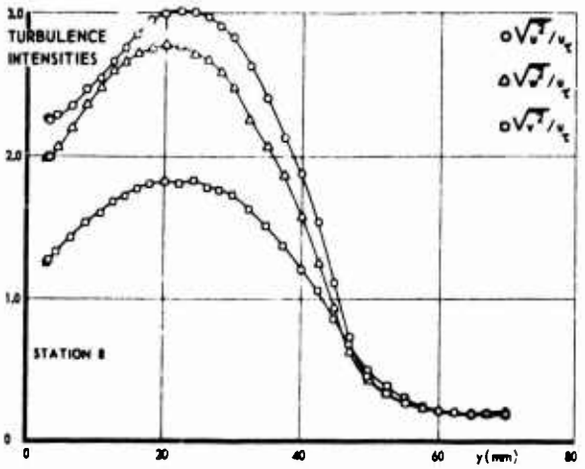

Figure 16: Turbulence intensities

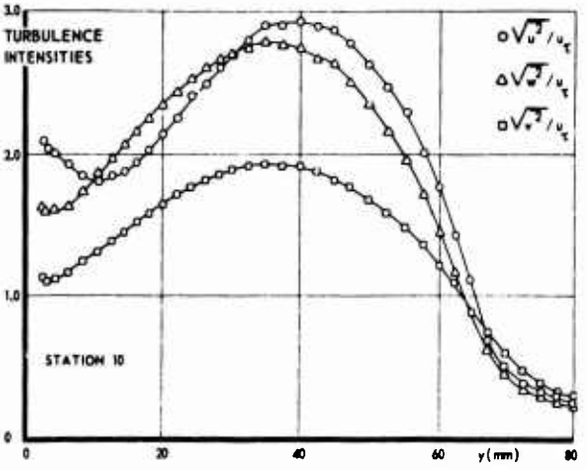

Figure 17: Turbulence intensities

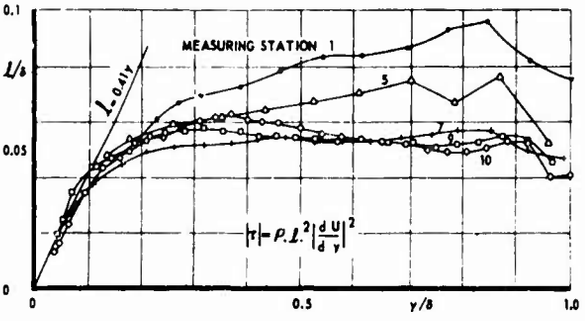

Figure 18: Measured mixing length distribution

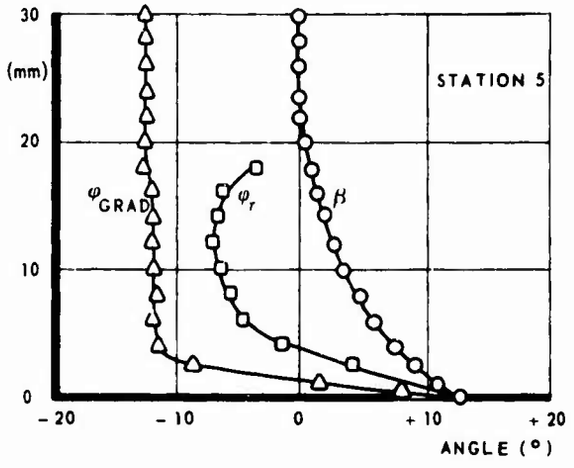

Figure 19: Direction of velocity, velocity gradient and shear stress

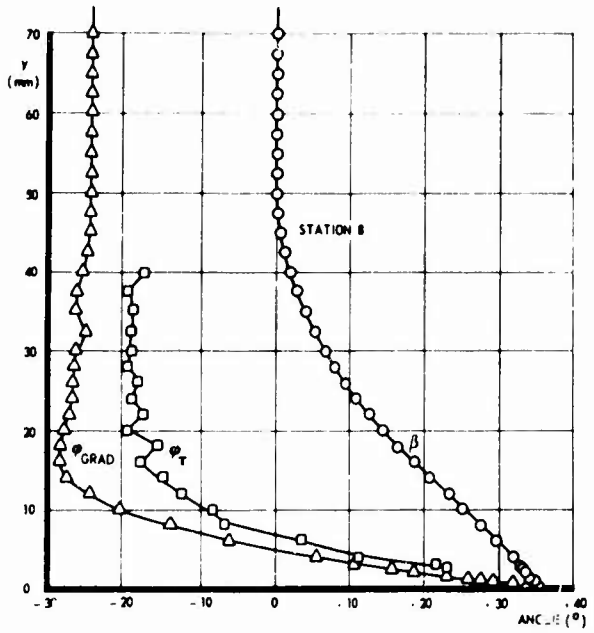

Figure 20: Direction of velocity, velocity gradient and shear stress

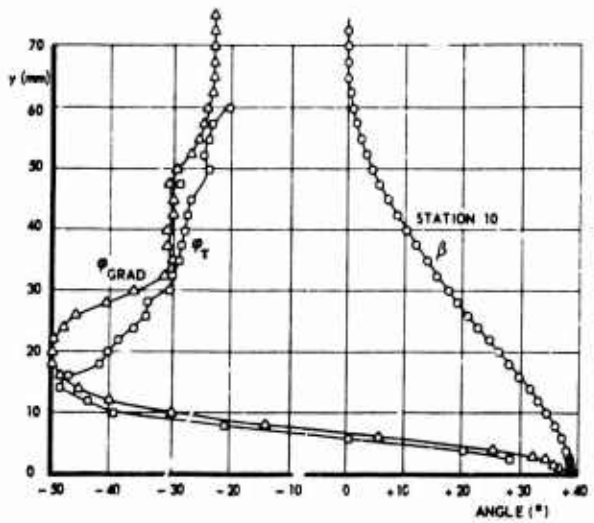

Figure 21: Direction of velocity, velocity gradient and shear stress

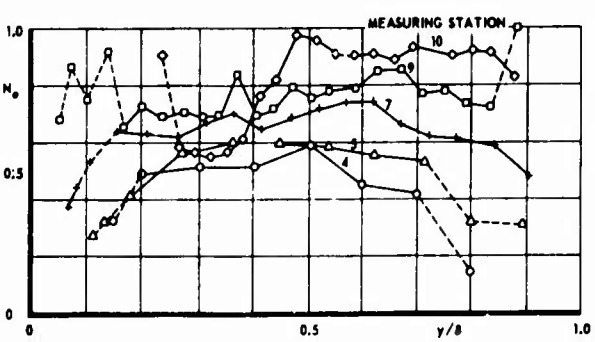

Figure 22: Ratio of components of eddy viscosity

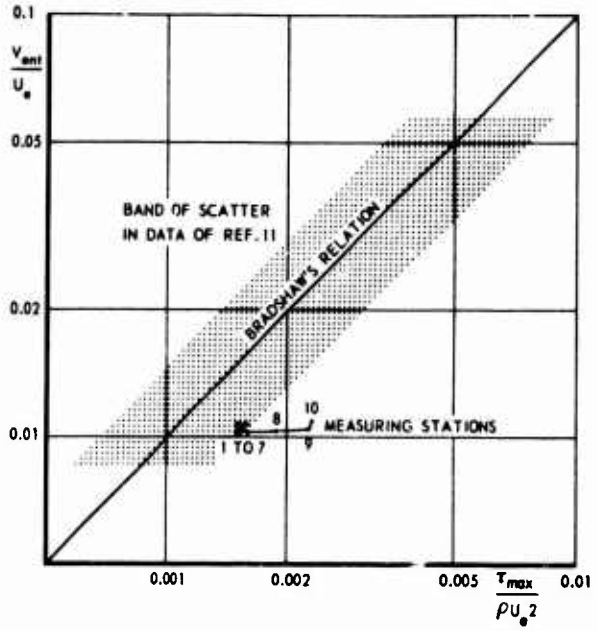

Figure 23: Entrainment relation

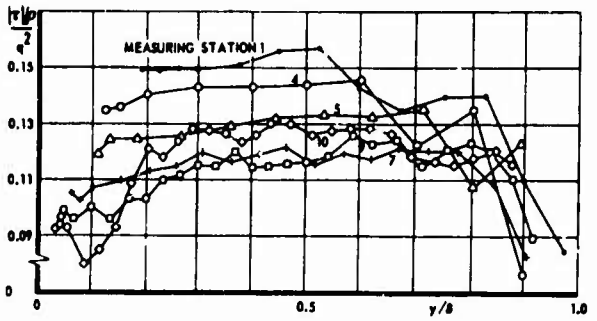

Figure 24: Ratio of shear stress and turbulent energy

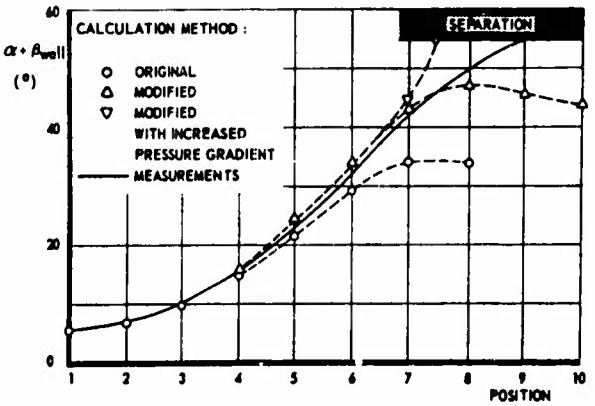

Figure 25: Comparison of measured wall shear stress angles with calculations

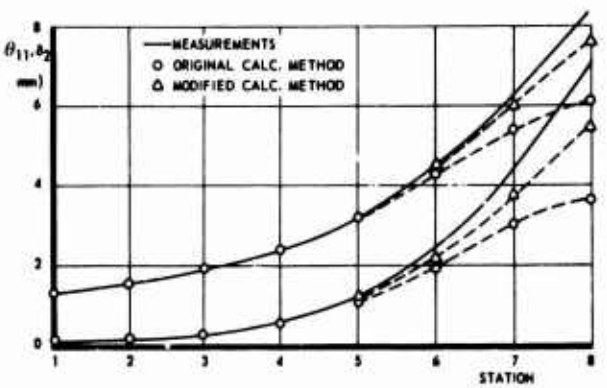

Figure 26: Comparison of measured integral parameters with calculations

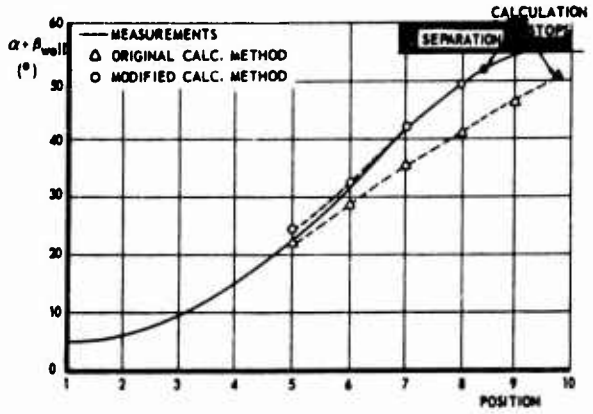

Figure 27: Calculation with interaction model

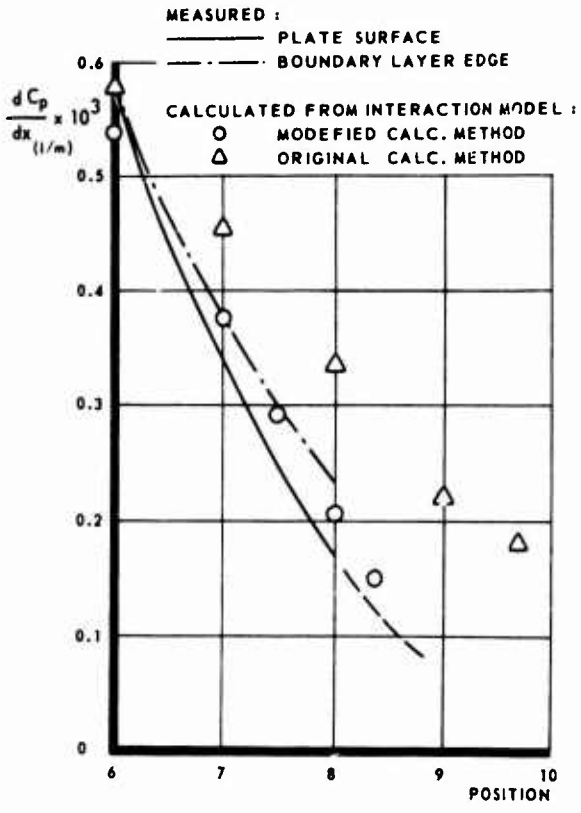

Figure 28: Measured and calculated pressure gradients

DISCUSSION ON PAPER 34

by

Roger L.Simpson
Institute of Technology
Southern Methodist University
Dallas, Texas, 75275

The purpose of this discussion is to point out the importance of additional turbulence energy production terms in this separating three-dimensional turbulent boundary layer and to point out the several similarities of the modified calculation method presented here to the normal stress modified model presented in paper 14. The production terms of the turbulence energy equation for three dimensions are

$$-\overline{uv}\frac{\partial U}{\partial y} - \overline{wv}\frac{\partial W}{\partial y} - \overline{uw}\frac{\partial W}{\partial x} - \overline{uv}\frac{\partial V}{\partial x} - (\overline{u^2} - \overline{v^2})\frac{\partial U}{\partial x} + \overline{v^2}\frac{\partial W}{\partial z}$$

where the first four are shear production and the last two are normal stress production (Bradshaw, 1973, paper 14). The first two are normally the only two retained; however, the remaining terms play a more important role as separation is approached. The accompanying figure shows the ratio of the last four terms to the first two terms for stations 7, 8, and 9, i.e., F-1 where F is the ratio of total production to shear production from the traditional first two terms. These estimates were calculated in the local streamline co-ordinate system using the tabulated experimental results from Reference 18. The fifth term is the main additional production term with the fourth term being very small and the third and sixth terms nearly cancelling each other.

From these results, it is clear that the additional production terms account for about 10 percent of the turbulence energy produced. Then $a_1 F$ should represent the ratio of the total turbulence production to the turbulence energy produced and Equation (16) of paper 14 should be used for the dissipation length. If one uses these modified parameters, one will obtain approximately the same numerical values for a_1 and the dissipation length as Elsenaar, et al. report in this paper. In other words, near separation, with the relations

$$a_1 = \frac{0.15}{F} \quad \text{and} \quad \frac{L}{\delta} = \frac{0.084}{F^{3/2}}$$

and $F \approx 1.15$, a_1 is about 0.13 and L/δ is about 0.068 while with a V_δ/U_e of about 0.05 (Elsenaar, private discussion) a_1 is about 0.124 and L/δ is about 0.062 from the equations in the Elsenaar, et al. paper. Thus, as in the two-dimensional case described in paper 14, the additional turbulence energy production terms can account for the modification of the structure parameters a_1 and L. Since the parameter F arises naturally from turbulence energy considerations, it would seem to be a preferable explanation of why a_1 and L decrease near separation.

In both the results of paper 14 and the three-dimensional results presented here, improved predictions near separation are achieved by accounting for reduced a_1 and L values.

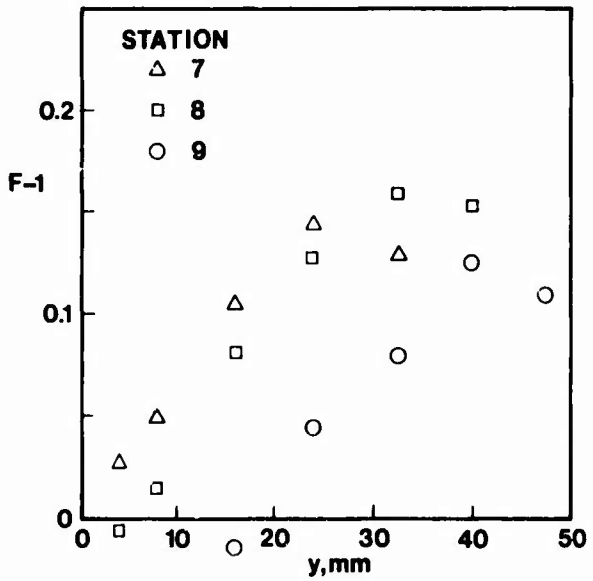

THREE DIMENSIONAL BOUNDARY LAYER SEPARATION IN SUPERSONIC FLOW

by
William D. Bachalo, Post Doctoral Fellow*
and
Maurice Holt, Professor
University of California
Berkeley, California 94720 U.S.A.

SUMMARY

An account is given of a detailed experimental investigation of three dimensional boundary layer separation in supersonic flow. The experiments were performed in the 15.2 cm x 15.2 cm Supersonic Wind Tunnel of the Fluid Mechanics Laboratory at the University of California at Berkeley. Prior to the current work, supersonic separation in two dimensional flow was investigated in the same wind tunnel by Sfeir using a plane compression corner as a model. In investigating three dimensional effects on supersonic separation, models were chosen which exhibited departures from two dimensional flow in the simplest way. The plane compression corner (formed by two intersecting plane plates) was replaced by a plate attached to a swept back wedge formed by two obliquely intersecting planes. Maintaining a constant tunnel Mach number of 2.5, surface pressure measurements were made on these models at static orifices spaced along the centerline and along three parallel lines. The flow parameters in the boundary layer and separated regions adjacent to the model surface were measured by traversing hot wire and pitot probes. The traverses were taken across the boundary layer and reversed flow regions in a direction normal to the body surface; they were made in several vertical planes, including the plane of symmetry.

SOMMAIRE

Les études expérimentales concernant le décollement d'une couche limite tridimensionnelle dans un écoulement supersonique sont présentées. Les mesures ont été effectuées dans la soufflerie supersonique (15,2 cm X 15,2 cm) du Laboratoire de Mécanique des Fluides de l'Université de Californie à Berkeley. Les études expérimentales d'écoulement de couche limite bidimensionnelle avaient préalablement été effectuées dans la même soufflerie par Sfeir, qui avait utilisé un coin de compression plan comme maquette. Pour examiner les effets tridimensionnels sur le décollement supersonique, on a choisi des maquettes qui ont exposé les différences entre les écoulements bi-et tridimensionnels de façon la plus simple. Le coin de compression plan (formé de deux plaques planes sécantes) fût remplacé par une plaque attachée a un dièdre en flèche formé de deux plans se croisant obliquement. En gardant le nombre de Mach de l'écoulement à une valeur constante de 2,5, les mesures des pressions sur la surface de ces maquettes ont été effectuées par des orifices de prise de pression statique qui sont situées aussi bien le long de l'axe cental que le long de trois lignes parallèles à l'axe central sur la surface des maquettes. Les mesures des paramètres d'écoulement, aussi bien dans la couche limite que dans les zones de séparation adjacentes à la surface de la maquette, ont été effectuées en déplaçant un tube de pitot et un fil chaud à travers ces zones. La direction de leur déplacement étant normale à la surface de la maquette dans plusieurs plans verticaux, y compris le plan de symétrie.

1. INTRODUCTION

Separation of laminar boundary layers in supersonic flow has been investigated extensively in two dimensions, both experimentally and theoretically. By contrast, corresponding flows in three dimensions have received comparatively little attention. In the present paper experimental measurements of the characteristics of three dimensional laminar boundary layers near simple bodies are investigated in detail, with particular attention given to separated regions.

In two dimensional flow separation of a laminar boundary layer on a smooth body is associated with the vanishing of skin friction coefficient and a change in sign in the velocity gradient at the wall. In three dimensions, on the other hand, the velocity component within the boundary layer parallel to the wall has variable direction. Separation occurs when only one component of this tangential velocity changes sign and this condition will not in general coincide with that of zero wall shearing stress.

We shall consider flow of a uniform supersonic stream parallel to a flat plate with a swept back wedge attached. In this case the separated region can be defined in the sense used by Eichelbrenner,[1] namely, as a region inaccessible to fluid particles originating far upstream of the wedge. In the present problem the particles within this region are confined to a recirculating zone and are unable to penetrate regions either far upstream or far downstream.

The present experiments were carried out in the Berkeley Supersonic Wind Tunnel. They were preceded by an investigation in the same tunnel by Sfeir,[2] dealing with supersonic separation in two dimensions, using a plane concave corner to induce the compression. Sfeir demonstrated that this type of separation is dominated by a free interaction process, namely that once the pressure outside the boundary layer begins to increase the subsequent boundary layer growth and pressure distribution are independent of the angle in the compression corner. On the other hand, the position of the beginning of interaction is influenced by downstream geometry (in particular by the location of the compression corner). The condition fixing this position is that of smooth reattachment, more precisely, that the pressure approaches uniform conditions downstream of reattachment. Sfeir also verified another result of free interaction theory, namely, that the pressure normal to the separated layer is constant and, at any station, corresponds to the pressure in inviscid supersonic flow past an effective body thickened by the displacement thickness.

---

*Now NRC Associate, NASA Ames Research Laboratory, Moffett Field, California 94035.

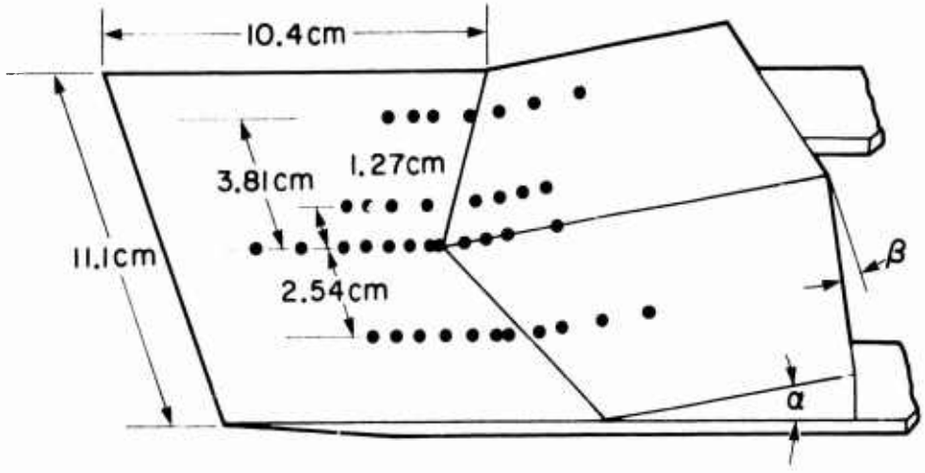

Fig. 1. Typical model configuration and pressure tap distribution

In seeking to extend the investigation of these properties to three dimensions, it was desirable to depart from two dimensional conditions in the simplest way and also to study experimental configurations which could be investigated theoretically without introducing unnecessary geometrical complications. After considering a number of three dimensional forms the basic model chosen for the present experiment was the swept back wedge formed by making two oblique, symmetric cuts in a plane compression corner. This is shown in Fig. 1. With this model, the undisturbed stream approaches a compression corner in each vertical plane, but since the height of the wedge varies on either side of the central plane of symmetry the effective compression angle varies also. Separation is two dimensional only in the plane of symmetry and is increasingly dominated by cross flow effects as we move to stations away from this plane. The separation region is increased in extent and the transverse flow becomes stronger at successive spanwise stations away from the plane of symmetry.

The characteristics of the flow past models of this type, when introduced into the tunnel working section maintained at a uniform free stream Mach number of 2.5, were measured in as much detail as possible. Use was made of static pressure measurements at orifices distributed over the model and of hot wire measurements obtained from a traversing probe which could scan the disturbed flow region in three orthogonal directions.

It is intended to compare flow characteristics derived from these observations with calculated characteristics for the same configurations and flow conditions. The calculations are based on an integral technique developed by Modarress[3] which has already been applied successfully to a series of three dimensional boundary layer flows.

There has not been much previous experimental work on three dimensional separation, probably because the probing techniques needed have only been developed very recently. The closest investigation to that described here is by Avduyevskii and Gretsov,[4] who investigated supersonic flow past half cone-plate combinations, with varying semi cone angles and angles of inclination to the free stream. Location of the lines of turbulent boundary layer separation and reattachment and the effects on the inviscid flow were inferred from flow visualization techniques and pressure measurements. Avduyevskii and Gretsov claim that separation in the case of flow around semi cones with apex angle $< 35°$ may be considered two dimensional in planes normal to the line of separation. This appears to have been concluded from the fact that a pressure curve exists along this normal that is quantitatively similar to that of separation of the turbulent boundary layer in the plane case. The angle of the separated flow zone in a plane normal to the separation (arctan $d\delta/dn$) was found to be practically coincident with its value for plane two dimensional separation.

Attention is directed in our experiment to the relationship between the extent of the displacement on the inviscid flow and the degree of the cross flow. The cross flow also affects the extent of separated region as noted by Dwyer[5] and Mager.[6] It can be argued that the diversion of streamwise momentum to transverse momentum in the boundary layer would delay reattachment. Furthermore, if the reattachment lines slope downstream with respect to the inviscid flow direction then the separated fluid turning upstream initially has a positive streamwise velocity component. For this reason the viscous shear stress would not be as significant in dragging the fluid downstream as it is in two dimensional separation wherein the flow is reversed directly in the separation region.

This, and other significant differences between two and three dimensional behavior are given careful consideration in this investigation.

2. EXPERIMENTAL APPARATUS

2.1 Wind Tunnel

An overall view of the experimental equipment used is shown in Fig. 2. The three dimensional boundary layer flows examined in this experiment were produced in the 15.2 cm x 15.2 cm closed circuit continuous flow supersonic wind tunnel of the Fluid Mechanics Laboratory at the University of California,

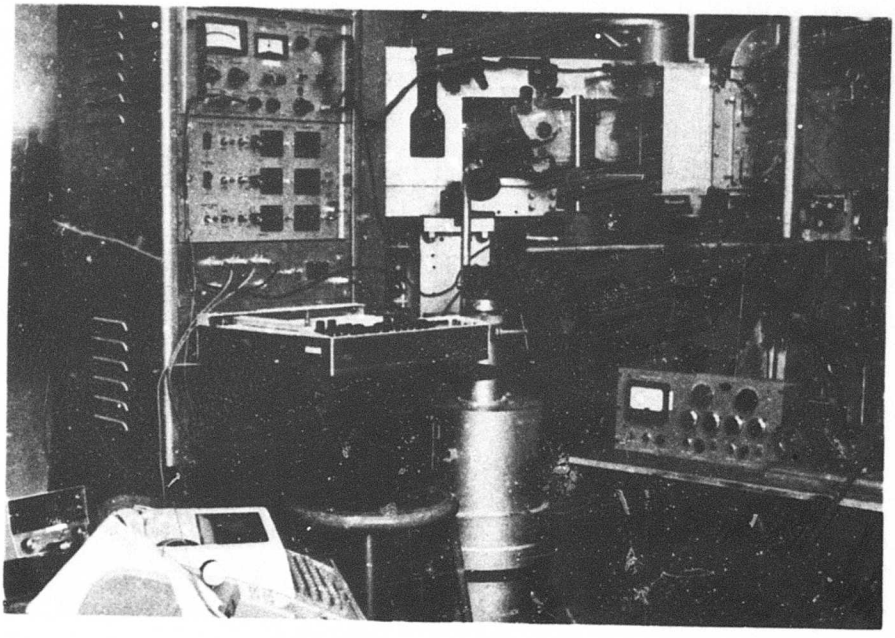

Fig. 2. Experimental apparatus

Berkeley. The tunnel can be run at stagnation temperatures in the range $10°C < T_t < 66°C$ and stagnation pressures in the range $10 < p_t < 175$ kPa. The corresponding attainable range of Reynolds number per meter is 4.9×10^5 to 17.2×10^6. The total pressure in the tunnel can be maintained to within ±0.2 kPa, while the total temperature can be held to within ±1.0°C of the set values.

2.2 Model Description

Model configurations were selected which exhibited departure from two dimensional flow in the simplest fashion. The plane compression corner (used in Sfeir's earlier experiments[2]), formed by two intersecting plane plates, was replaced by a plate attached to a swept back wedge formed by two obliquely intersecting planes (Fig. 1). In each vertical plane the undisturbed stream approaches a compression corner. However, due to the swept back configuration, the greater the distance from the plane of symmetry, the further downstream inviscid flow encounters the wedge. As a result a transverse pressure variation is created. Three such models were used; one with streamwise slope $\alpha = 10°$, and cross slope, $\beta = 7.5°$, the others with $\alpha = 10°$, $\beta = 5°$, and $\alpha = 20°$, $\beta = 5°$; they are referred to as the 10°/7.5°, 10°/5°, and 20°/5° models. The models were drilled for static pressure orifices (0.51 mm diameter) with a distribution similar to that shown in Fig. 1.

Side plates of thickness 0.51 mm were attached to the model to isolate the plate boundary layer from the disturbed high pressure flow under the plate and from the tunnel boundary layer on the side wall. The side plates were cut at an angle of 10° to the model surface to minimize their disturbances. The model leading edge was machined to a sharp edge and was free from irregularities.

2.3 Probe Design

The probe used for the hot wire traverse measurements is shown in Fig. 3. Jeweller's cutting broaches, which have a uniform taper (dimensions 0.20 to 4.6 mm) with tips tapered down to 0.051 mm to match the diameter of the unetched Wollaston process wire, were used. Silver plated 10% rhodium platinum wire 10.2 μm in diameter was used for the anemometer. The wire was soft soldered to the broaches and the central portion was etched with dilute nitric acid (needle spacing 4mm, etched 1.5 mm). A thin film of epoxy (≈ 10 μm) was applied to the connection points and the unetched wire to prevent electrical shorting when the model was brought into contact with the model.

This method appeared to be most suitable for minimum flow disturbance and aided in the visual positioning of the wire parallel to the model surface. Measurements could now be made very close to this surface. The probes used to resolve both magnitude and direction of the flow were set at 65.0° and 115° to the free stream direction (wire normal to the free stream flow being 90°). The probe was supported in the tunnel on a sting probe support.

2.4 Probe Positioning

A traversing mechanism was designed to simplify accurate positioning of the probe in the three coordinate directions. The traverse had Slo-Syn bifilar stepping motors driving micrometer quality stainless steel lead screws which had insignificant thread backlash. The device could be placed in a given position with an accuracy of within ±30 μm. Location of the probe was controlled by presetting a reference zero position and setting subsequent positions on digit switches of the digital logic position control system.

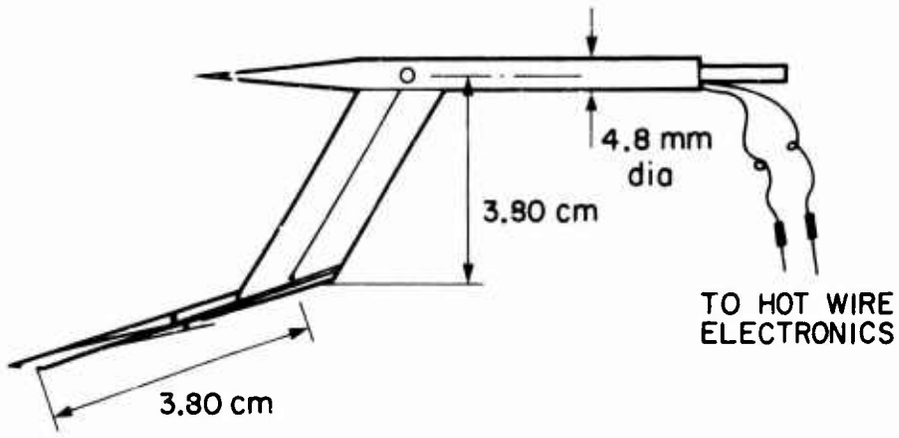

Fig. 3. Hot wire probe support

The transistor-transistor logic (TTL) electronics circuit was designed to allow movement to precise preset positions at an exact rate. Speeds in the individual directions could be set to produce motion in a desired resultant linear direction.

2.5 Data Acquisition

An electronics circuit was designed to control the acquisition and recording of data. A model 33 Teletype with send/receive capability and paper tape punch was the main data recording device. The Teletype was also linked to the Berkeley CDC 6400 computer and could be switched from a data monitoring mode to a remote terminal mode for data reduction and testing results.

A 7004B X-Y plotter was used to display the analog voltage outputs. The function of the recorder was to observe the qualitative aspects of the boundary layer profile. The recorder was an invaluable instrument for the determination of data density requirements, the direction of the flow (whether forward or reversed), and the location of the lines of separation and reattachment. Starting and stopping of the recorder was effected automatically, synchronizing with the traverse control logic circuit.

3. EXPERIMENTAL TECHNIQUES

3.1 Flow Establishment

In order to explore the details of the three dimensional separated region it is essential to establish fully developed two dimensional boundary layer flow of the Blasius type upstream of the interaction region. Observations must therefore begin at a distance sufficiently far from the leading edge to permit the damping out of longitudinal disturbances in the boundary layer generated by leading edge effects.

The tunnel boundary layer can separate in the working section as a result of flow blockage below the model. To minimize disturbances from this cause the tunnel nozzle was diverted under the model. As a consequence, supersonic flow was maintained in this region and undesirable separation effects were eliminated.

3.2 Two Dimensional Flow

Side plates were used to isolate the plate boundary layer from the disturbed flow beneath and at the sides of the plate. To cancel out the compression waves generated by the leading edges of the side plates and displacement effect of the corresponding boundary layer the plates were mounted with a divergent angle of 0.1 mm in 2 cm. The joints between the side plates and model were made airtight to prevent blowing from the higher pressure region beneath the model.

3.3 Laminar Flow

To make sure that the boundary layer was laminar throughout the region of interest, boundary layer profiles were plotted. The influence on the profile of relative curvatures at the free stream end and of the gradients near the wall was noted. Chapman's[7] designations of purely laminar, transitional, and turbulent separation were adhered to. For purely laminar conditions the separation must be truly unaffected by transition. That is, transition must not occur in the separated region nor in the near vicinity of the reattachment lines. Purely laminar separation was achieved with a total temperature of 18.3°C and a total pressure of 20.7 kPa, which resulted in a Reynolds number of 1.8×10^6/m.

3.4 Turbulent Flow

At Reynolds numbers above 5.0×10^6/m the boundary layer became turbulent upstream of the separation with the 20°/5° wedge. The existence of turbulence was confirmed by observing the radical downstream shift of the separation line and the increase in velocity gradients near the wall.

3.5 Hot Wire Anemometry

A constant temperature hot wire anemometer was used to determine velocity magnitude and direction, temperature and Mach number of the flow field. The hot wire anemometer was suitable for this purpose because of the relatively small size of the probe and its directional sensitivity characteristics. Because the hot wire responds to mass flow rate, with the low density required to maintain laminar flow, the hot wire data reduction scheme became quantitatively inaccurate in the inner region of the boundary layer. However, the qualitative shape characteristics of the boundary layer profiles indicating regions of reversed flow and cross flow were believed to be accurate.

The hot wire anemometer measures the local mass flux of a flowing fluid by determining the rate of heat transfer from a heated wire (10.2 μm diameter). Heat transfer is determined by measuring the electrical resistance of the wire and voltage drop across it.

The theoretical analysis of heat transfer from circular cylinders need not be considered here. Extensive empirical data dealing with the heat transfer rates from infinitely long circular cylinders in terms of Nusselt number have been published. We have

$$Nu_m = \frac{q_m d}{(Tw_m - Te_m)K_o}$$

where Nu_m is the measured Nusselt number, q_m is the heat dissipated from the wire per unit area, d is the diameter of the wire, K_o is the thermal conductivity of the surroundings at stagnation conditions, Te_m is the equilibrium (adiabatic recovery) temperature of the wire and Tw_m is the heated wire temperature. The data have been related as a function of the non-dimensional flow parameters; Mach number and Reynolds number. The data were reduced by Dewey[8] to a set of universal correlation curves. The curves were used to determine the Mach and Reynolds numbers (based on wire diameter) from the measured heat transfer relations corrected for the effects of finite wire length.

For a finite length of wire there is heat loss to the wire supports in addition to the convective and radiated heat loss. The conduction end losses resulted in a symmetric but nonuniform temperature distribution along the wire. The end losses also affect the adiabatic recovery temperature of the wire, which in turn affects the heat transfer rate of the finite wire as compared to the infinite wire length case. Therefore corrections to the adiabatic recovery temperature of the wire were made. The end loss effects of the finite length of wire were quantitatively important (end conduction heat loss could be as large as 50 percent of the total heat loss for wires with aspect ratios of 100). Because of this fact a careful theoretical analysis of the end loss was carried out.

The details of the hot wire anemometer reduction procedure are given in a report by Klopfer.[9] This was written in collaboration with the present authors for use in the current experiment.

Local flow direction was determined using the fact that heat loss is primarily dependent on the flow normal to the axis of the wire. Two measurements with different wire orientations in the plane of the model surface were taken at each point. The Mach number components at the two different wire orientations were used as follows.

The resultant local flow direction relative to the free stream direction of the wind tunnel was determined by

$$\theta = \tan^{-1}\left|\frac{M_1 \sin\theta_2 - M_2 \sin\theta_1}{M_1 \cos\theta_2 - M_2 \cos\theta_1}\right| .$$

The resultant Mach number is (Fig. 4)

$$M = M_1/\cos\left(\frac{\pi}{2} - \theta_1 + \theta\right)$$

$$= M_2/\cos\left(\frac{\pi}{2} - \theta_2 + \theta\right) .$$

Two profiles were measured separately at each position on the model with one-wire angle probes, one at each angle. Such a procedure was possible with the accurate probe positioning system. The two-wire crossed probe technique was not used because of its inherent flow disturbance and the necessity of having the wires at the same level above the model.

In the near proximity of the model the hot wire loses heat to the model as well as to the fluid. With the model at the adiabatic recovery temperature (≈ 55°F) and the wire at approximately 250°F a substantial heat loss via molecular conduction may occur in the presence of the model.

Tests were made of this phenomenon with no flow thus isolating the wall heat loss from the loss due to forced convection. When heat loss versus distance from the wall was plotted a logarithmic profile was found. The no-flow distance from the wall where the effect became negligible was of the order of 0.25 mm.

To reduce the effect of heat loss to the model a wire temperature as low as possible was used. For regions of two-dimensional flow observations of the analog plots of the boundary layer profile showed the effect to be confined to 0.13 mm of the model. Therefore, no corrections were made for this effect. A discussion of possible correction schemes may be found in Wills.[10]

3.6 Visual Data

The flow pattern adjacent to the surface was made visible by applying discrete dots of a mixture of titanium dioxide, oleic acid, and oil to the model surface. A grid was then established to determine where boundary layer traverses would be made.

3.7 Pressure Measurements

Each model has four rows of static pressure taps distributed over the model; rows falling along the centerline, and at 1.27 cm, 2.54 cm and at 3.81 cm from the centerline. The pressure lines were connected via manifolds to a Dibutylphthalate micromanometer. Repeated measurements showed good agreement. The averaged pressures were plotted to form a pressure plane for the model.

3.8 Hot Wire Traverses

A low power microscope was initially used to position the hot wire axis parallel to the model surface. The microscope was also used to establish how close to the wall the probe could reach (50 μm from the wall was possible). On the wedge the traverses were taken normal to the model. Data points were recorded at a spacing of 8.45 μm.

A complete set of profiles was recorded and then repeated. The data sets were then combined; each set at one hot wire angle was combined with all sets at the other hot wire angle. In this manner the primary source of error, the inaccuracy of the position in the boundary layer at which the measurement was recorded, was reduced.

Concerning accuracy, repeated measurements established that the experimental errors in velocity and pressure were less than 2% and 1%, respectively. The velocity direction was believed to be accurate to within 5% accuracy except at very low speed regions.

4. RESULTS AND DISCUSSION

The principal measurements made during the investigation were static pressure distributions on the model and velocity profiles across the boundary layer at a sufficient number of stations to cover the whole interaction region, extending from upstream of separation to downstream of reattachment. In addition, maps of skin friction lines (equivalent to the wall streamlines referred to by Eichelbrenner) were obtained from surface oil traces.

Most of the results given here correspond to laminar separation and reattachment in the 10° (incidence) 7.5° (cross slope) wedge, dominated by strong cross flow. A few results for the weak laminar cross flow case are included ($\alpha = 10°$, $\beta = 5°$) and velocity profiles are shown for the turbulent case $\alpha = 20°$, $\beta = 5°$.

4.1 Pressure Distributions

Static pressure distributions for the 10°/7.5° wedge are shown in Figs. 4 and 5. Figure 4 shows the variation in the main stream direction (X increasing) at constant spanwise stations (Y = constant). Figure 5 shows distributions in planes normal to the main stream, giving the pressure variations in the spanwise direction at stations X = constant. In the streamwise direction the pressure rises continuously in all vertical planes and the plateau observed in two dimensions is not attained in any plane, although the distributions away from the plane of symmetry show a region of very gradual increase in the neighborhood of the wedge corner. In the heart of the separated zone the spanwise pressure falls rapidly near the plane of symmetry and this effect is responsible for the strong cross flow on the 10°/7.5° wedge. Beyond reattachment the spanwise pressure increases at first with distance Y and then falls rapidly after reaching a maximum. This behavior is connected with the geometry of the displacement thickness surface in the reattachment region. Figure 6 gives the spanwise pressure distributions in the 10°/5° case and it is evident that the spanwise gradients are much smaller than in the 10°/7.5° case, leading to a more gentle cross flow. The streamwise distributions in this case show little change from plane to plane; also the two dimensional plateau behavior is completely absent.

4.2 Surface Geometry in the Separated Regions

Figure 7 shows, for the 10°/7.5° wedge, sections of two important surfaces in the separated region, firstly that traced out by the effective boundary between the viscous and inviscid regions, and secondly, the outer boundary of the reversed flow region (where the axial velocity component changes sign). Traces of a third surface are also shown, representing the boundary of a secondary transverse flow very near the wedge leading edge; the experimental evidence for the existence of this is quite strong. Two special features of the inviscid boundary should be noted. Firstly, the height of the region reaches a pronounced maximum above the wedge leading edge, near the center of the separated zone. Secondly, while this maximum height increases significantly in the spanwise direction, the height of the region in a spanwise plane downstream of reattachment is almost constant. This is in conformity with the changes in spanwise pressure distributions shown in Fig. 5. The corresponding boundary traces in the 10°/5° case are shown in Fig. 8. Here the changes in behavior with span are much less pronounced, as would be expected.

4.3 Velocity Profiles

The development of measured velocity profiles for the 10°/7.5° wedge is shown in two views in Figs. 9 and 10. Figure 9 shows profiles of the u velocity component in four planes parallel to the plane of symmetry. All the profiles are laminar in character with inflection points characteristic of retarded flow regions. Reversal of sign of the u component is confined mainly to the neighborhood of the plane of symmetry, in sharp contrast to the situation in two dimensional flow. Figure 10 shows the profiles of the transverse v component in three spanwise planes and emphasizes the importance of cross

flow in the separated region. Figure 11 combines the information in Figs. 9 and 10 and shows the velocity profiles in three dimensional form over the whole separated region near the wedge.

4.4 Separation and Reattachment

To resolve the flow behavior in the separation region a flow visualization technique was used. Since the skin friction is minimal in the laminar cases, particularly where the boundary layer is inflected near the wall in regions of pre-separation and in regions where separation has occurred, a very low viscosity mixture was required. A mixture of light machine oil, titanium dioxide and oleic acid was used. The oleic acid serves to break up the particles of titanium dioxide. The mixture was applied in discrete dots to the surface of the model with an excess near the leading edge. Although start-up transients carried some of the mixture away, a sufficient quantity of the trace material remained to be rearranged into the mapping of the directions of the skin friction lines of the steady state flow, after a sufficient amount of time had elapsed.

Separation was found to stand upstream of the forward tip of the wedge-plate intersection line approximately 1.5 cm on the plane of symmetry in the case of the 10°/7.5° wedge but extended forward with respect to the wedge-plate intersection line with distance from the plane of symmetry. This resulted from the shock strength increasing with distance from the plane of symmetry. Displacement of the inviscid flow was relatively small on the plane of symmetry, as was the slope to separation (Fig. 7). The separation line was swept back with distance from the centerline (Fig. 12), forming a blunt hyperbolic curve with asymptotes that appeared to be parallel to the wedge-plate intersection (this could not be confirmed because of the aspect ratio limitations). The separation line in the case of the 10°/5° wedge formed a more flattened curve about the plane of symmetry.

Accumulation of the trace material occurred on the separation line at the model plane of symmetry. This point is a singular point of flow where

$$\left.\frac{\partial u}{\partial z}\right|_{z=0} = \left.\frac{\partial v}{\partial z}\right|_{z=0} = 0 \quad .$$

A very slow lateral flow existed along the separation line at stations away from the centerline. The pressure plot (Fig. 4) indicates a relatively small lateral pressure gradient forward of the wedge-plate intersection line that is driving this flow.

Skin friction lines originating at nodes of attachment upstream of the separation began turning at distances as great as 1 cm upstream of the separation line and approached it asymptotically. Skin friction lines approaching the separation line from downstream originated at the reattachment line beginning from a direction tangent to the reattachment line; a direction with a positive u component. These traces formed large arcs turning into a direction approximately upstream and then back to merge asymptotically with the separation line. The separation line is thus the line of demarcation dividing the surface into a region accessible to skin friction lines attaching at nodal points upstream and those attaching at nodal points downstream and eventually turning upstream.

In the neighborhood of the wedge-plate intersection line, a small embedded flow region was discovered wherein the flow direction was found to follow the wedge-plate intersection line. The reversed flow approaching this region appeared to depart from the wall and move over the region, reattaching again upstream.

Hot wire measurements indicated that the boundary layer was inflected near the model surface well upstream of separation. This large extent of upstream influence is an inherent result of the self-sustaining interaction between the boundary layer and the supersonic stream outside. Stewartson and Williams[11] used a theory developed by Lighthill[12,13] to demonstrate that the propagation upstream could occur anywhere in the boundary layer provided the main stream was supersonic and had a pressure rise downstream of the free interaction zone.

Within the separation bubble, hot wire measurements confirmed the existence of a very slow moving two dimensional separation vortex on the plane of symmetry. However, the vortex developed a spiral component with distance from the plane of symmetry. The rate of increase of the transverse velocity in the neighborhood of the separation line near the plane of symmetry was very small. Although the u component of velocity reversed direction, the velocity vector within the separated region at stations displaced from the plane of symmetry did not become zero. Instead, the velocity vector showed a continuous rotation into the free-stream direction as the boundary layer was traversed. The extent and growth behavior of the region of the reversed component of velocity can be seen in Fig. 7. As the wedge was approached, the cross flow component became progressively greater in magnitude and extent, while the reversed u component was diminished. It can be seen in Fig. 11 that as reattachment is attained the cross flow velocity profile progressively approaches and attaches to the model and then decreases uniformly in normal extent. In general, the magnitude of the reversed velocity component within the separation bubble is very small.

Reattachment was subject to severe three dimensional effects. In response to the strong transverse pressure gradient on the wedges (Figs. 4 and 7), relatively large cross flow components existed (Fig. 11). Evidence of any increase in the displacement of the inviscid flow as a result of the lateral migration of low momentum fluid could not be confirmed here because the effect of cross flow could not be isolated from the effect of the increase of the shock strength with lateral distance. In fact, the weak cross flow model (10°/5°) wedge demonstrated a greater reattachment boundary layer displacement increase with distance from the plane of symmetry. Although the displacement of the inviscid flow over the separated region was similar in extent for the 10°/5° wedge and the 10°/7.5° models, the reattached boundary layer was much thinner in the case of the 10°/7.5° model. Results for the 10°/5° case are discussed more fully in Bachalo.[14]

The reattachment line in the case of the 10°/7.5° model moved downstream with distance from the model symmetry line (Fig. 12) and appeared to become asymptotic to a line parallel to the wedge-plate intersection line. (Once again, this cannot be confirmed here because of the limitations on the model aspect ratio.) Rapid growth of the boundary layer displacement and the extent of the separation zone occurred with distance from the model centerline. This may be seen in Figs. 7 and 8. This is, as aforementioned, a result of the increasing shock strength with distance from the plane of symmetry. However, the transverse pressure gradient would approach a constant value at large distances from the model plane of symmetry. Therefore it may be postulated that the separation and reattachment lines would, in fact, become parallel to the wedge-plate intersection lines.

Since the transverse pressure gradient on the wedge is zero on the plane of symmetry and large in the neighborhood, an accelerated cross flow velocity with respect to lateral displacement, $\partial v/\partial y$, may be expected there. This is evident in Fig. 11 wherein a relatively large cross flow velocity exists at a station slightly displaced (2.5 mm) from the plane of symmetry.

4.5 Turbulent Case

Figure 13 shows a sample of three dimensional turbulent mean velocity profiles. Only the $\bar{u}$ component has been shown at streamwise stations in the neighborhood of separation. In this case (20°/5° wedge) the separation is essentially confined to the foot of the shock at the wedge-plate intersection line. The separation has been delayed as compared to the laminar case as a result of the increased diffusion of momentum. Retardation of the flow in the inner region of the boundary layer occurred far upstream of the compression corner but diminished with distance downstream due to increasing turbulence intensity. The separation and reattachment lines were approximately parallel to the wedge-plate intersection at 0.5 cm upstream and 0.4 cm downstream of the intersection, respectively.

A strong cross flow existed within the separated region. The skin friction lines formed a well-defined saddle point of separation about the forward stagnation point and a nodal point of reattachment about the plane of symmetry.

The separation in this case resulted in a minimal disturbance to the inviscid flow field.

REFERENCES

1. Eichelbrenner, E. A., "Three Dimensional Boundary Layers," Annual Reviews of Fluid Mechanics 5, 1973, 339-360.
2. Sfeir, A. A., "Interaction d'une couche limite laminaire avec une onde de choc dans un coin de compression," Rév. Roum. Sci. Techn. Méc. Appl. 15, 1970, 1375-1391.
3. Modarress, D., "Application of the Method of Integral Relations to Three Dimensional Boundary Layer Flows with Separation," Ph.D. Thesis, University of California, Berkeley, June 1974.
4. Avduyevskii, V. S. and Gretsov, V. K., "Investigation of a Three-Dimensional Separated Flow Around Semicones Placed on a Plane Plate," NASA Technical Translation F-13, 1971, p. 578.
5. Dwyer, H. A., "Solution of a Three-Dimensional Boundary-Layer Flow with Separation," AIAA J. 6, 1968, 7.
6. Mager, A., "Three-Dimensional Laminar Boundary Layer with Small Cross Flow," J. Aeronaut. Sci. 21, 1954, 834-45 [480].
7. Chapman, D. R., Kuehn, D. M., and Larson, H. R., "Investigation of Separated Flows in Supersonic and Subsonic Streams with Emphasis on the Effect of Transition," NACA Report 1356, 1958.
8. Dewey, C. F., Jr., "A Correlation of Convective Heat Transfer and Recovery Temperature Data for Cylinders in Compressible Flow," Int. J. Heat and Mass Transfer 8, 1965, 245-252.
9. Klopfer, G., "Constant Temperature Hot Wire Anemometry Data Reduction Procedure," University of California, Berkeley, College of Engineering Report No. FM-74-1, 1974.
10. Wills, J. A. B., "The Correction of Hot Wire Readings for Proximity to a Solid Boundary," J. Fluid Mech. 12, 1962, 388.
11. Stewartson, K., and Williams, P. G., "Self-Induced Separation," Proc. Roy. Soc. A31?, 1969, 181-206.
12. Lighthill, M. J., "Reflection at a Laminar Boundary Layer of a Weak Steady Disturbance to a Supersonic Stream, Neglecting Viscosity and Heat Conduction," Qtr. J. Mech. Applied Math. 3, Part III, 1950, 303-325.
13. Lighthill, M. J., "On Boundary Layers and Upstream Influence," Proc. Roy. Soc. A,(I) 217, 1953, 344; A,(II) 217, 1953, 478.
14. Bachalo, W. D., "Experiments on Supersonic Boundary Layer Separation in Three Dimensions," ASME Applied Mechanics Western Conference, 1975.

This work was supported by NASA Ames Research Center under the Grant for the Graduate Research Program in Aeronautics and Air Transportation at the University of California, Berkeley.

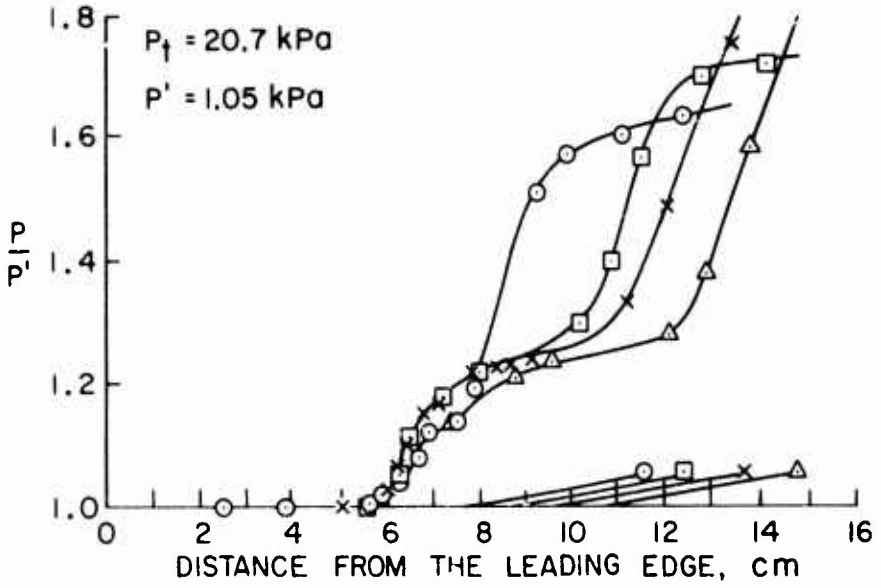

Fig. 4. Static pressure profiles, laminar separation, $\alpha = 10°$, $\beta = 7.5°$

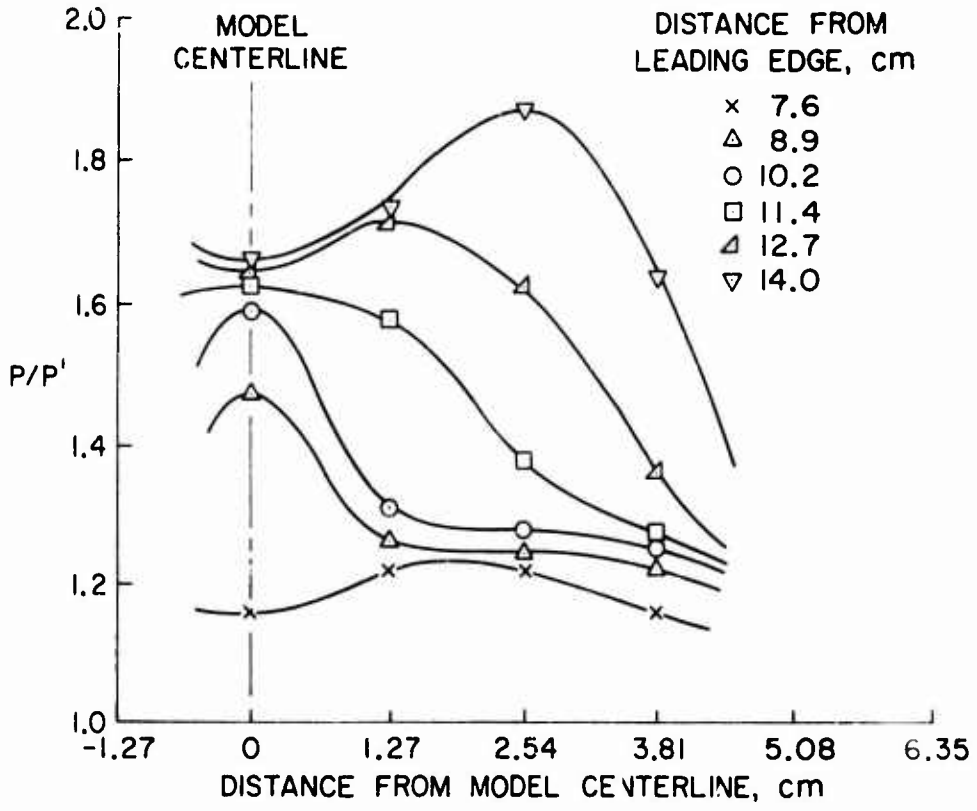

Fig. 5. Transverse static pressure profiles, laminar separation, $\alpha = 10°$, $\beta = 7.5°$

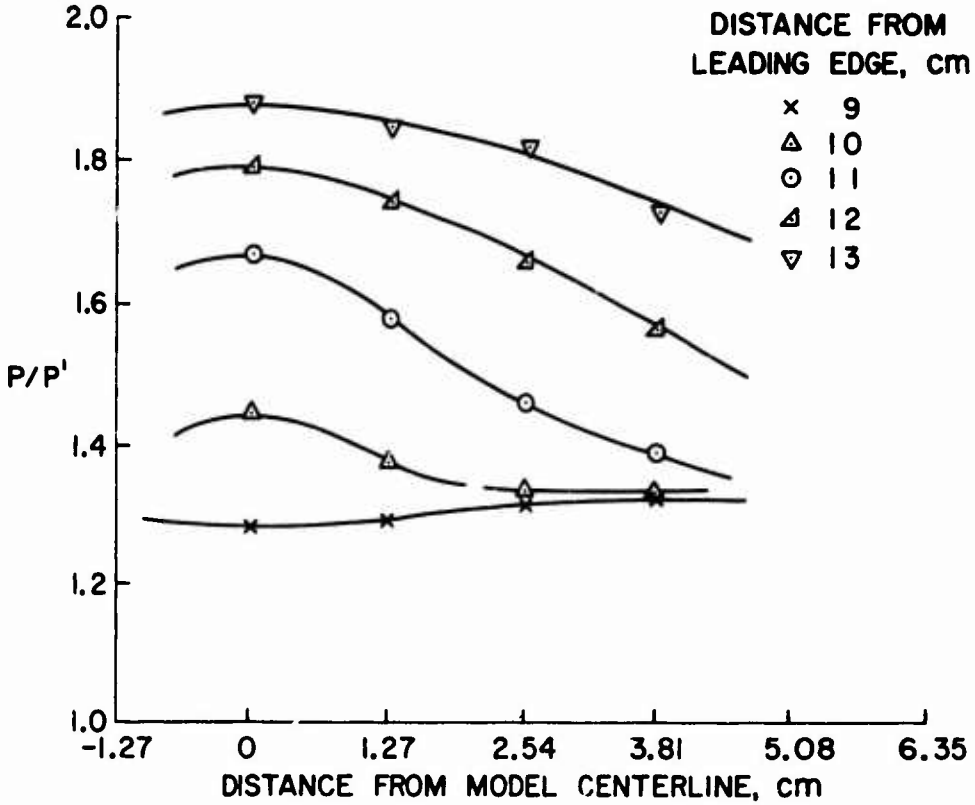

Fig. 6. Transverse static pressure profiles, laminar separation, $\alpha = 10°$, $\beta = 5°$

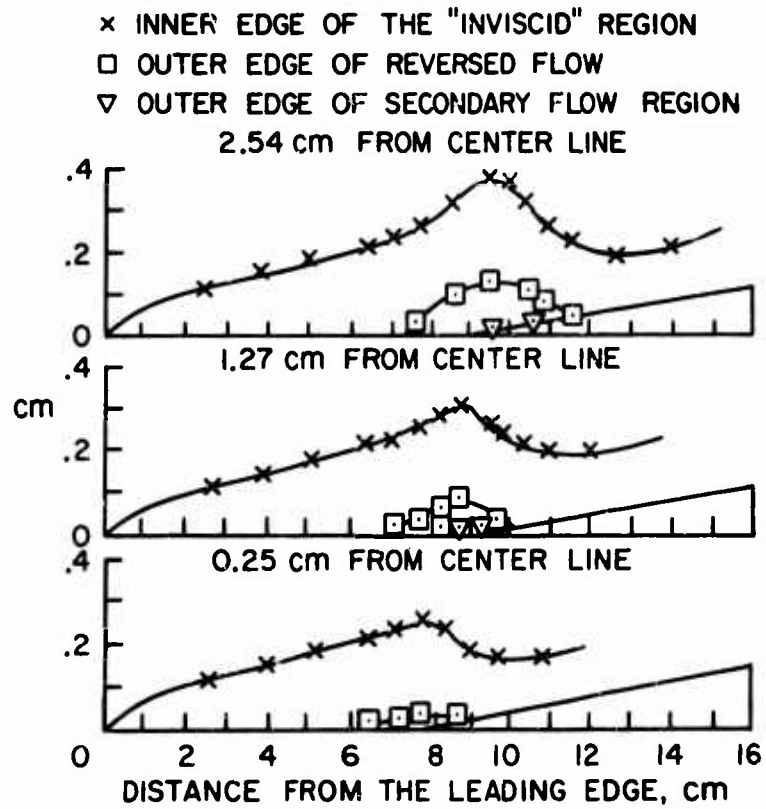

Fig. 7. Profile views of separated flow, 10°/7.5° wedge

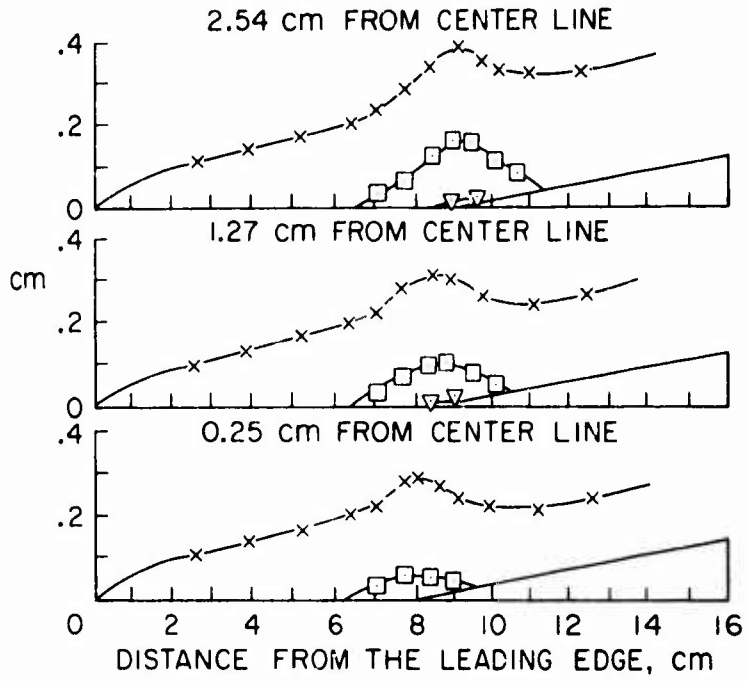

Fig. 8. Profile view of separated flow, 10°/5° wedge

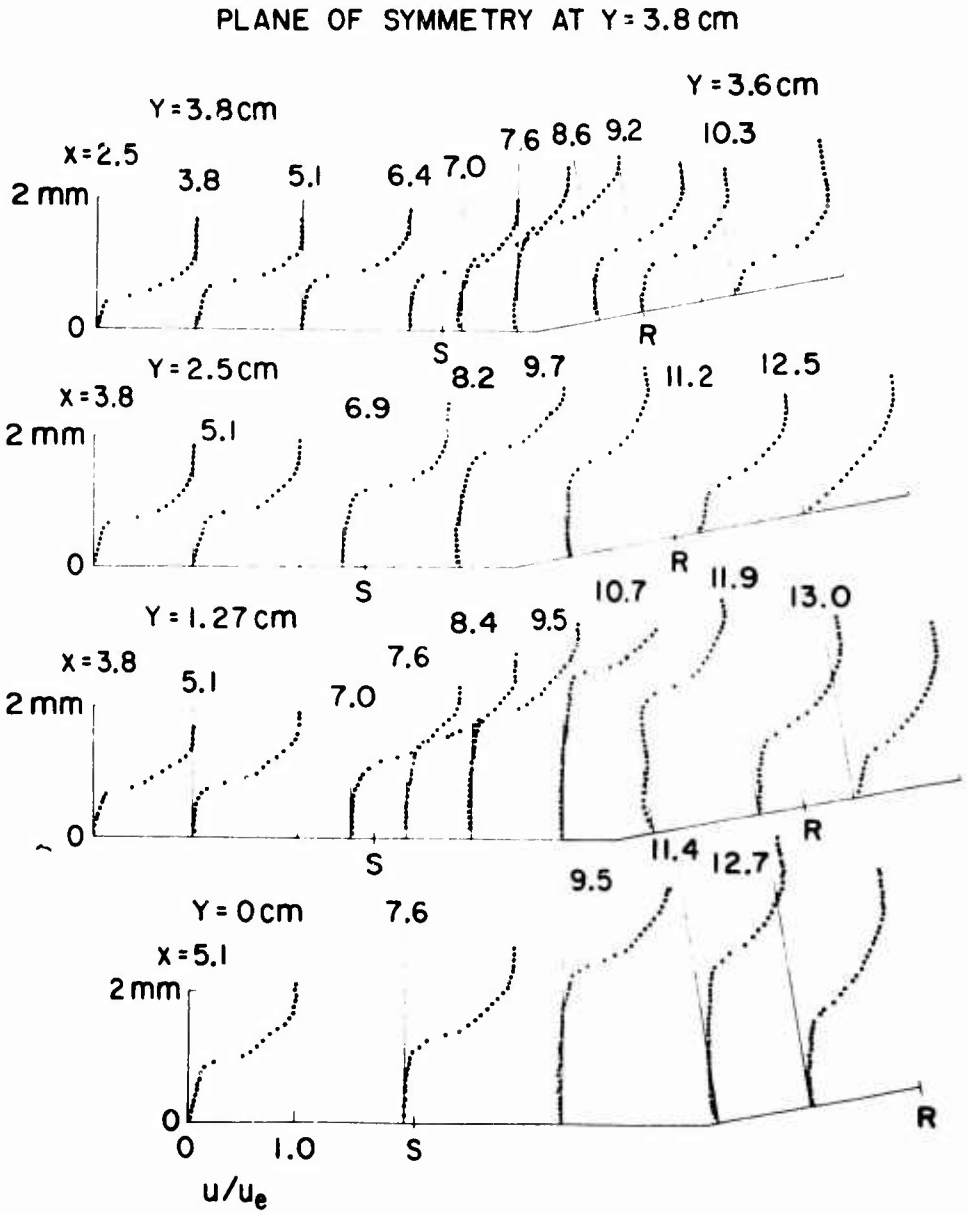

Fig. 9. Laminar separation, 10°/7.5° wedge, u (axial) velocity profiles

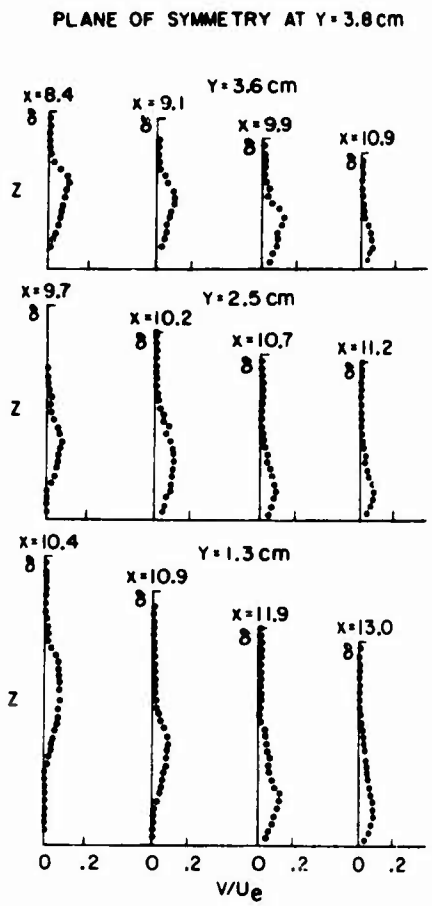

Fig. 10. Laminar separation, 10°/7.5° wedge, v (transverse) velocity profiles

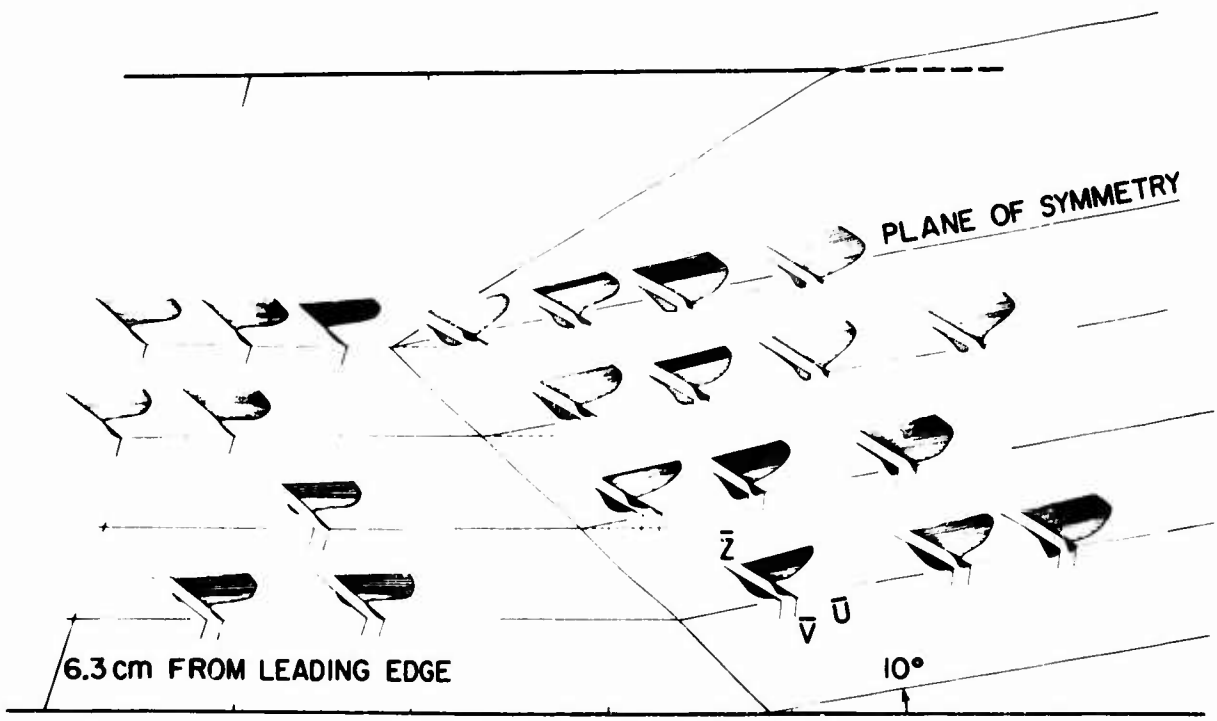

Fig. 11. 10°/7.5° Wedge, laminar separation velocity field

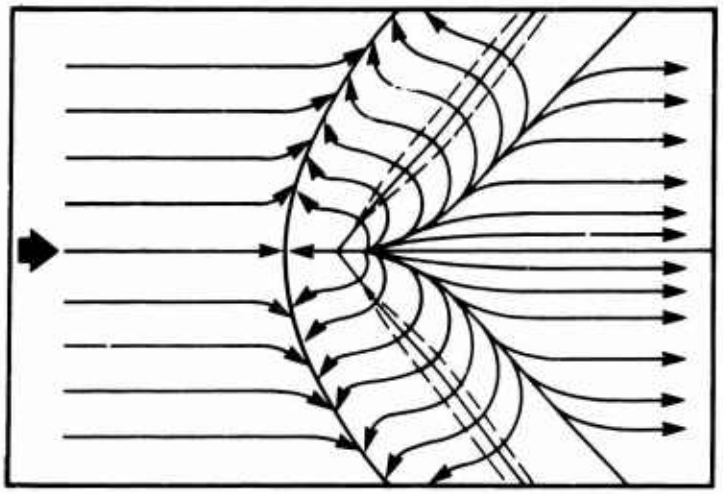

Fig. 12. Sketch of the skin friction lines for laminar separation on 10°/7.5° wedge

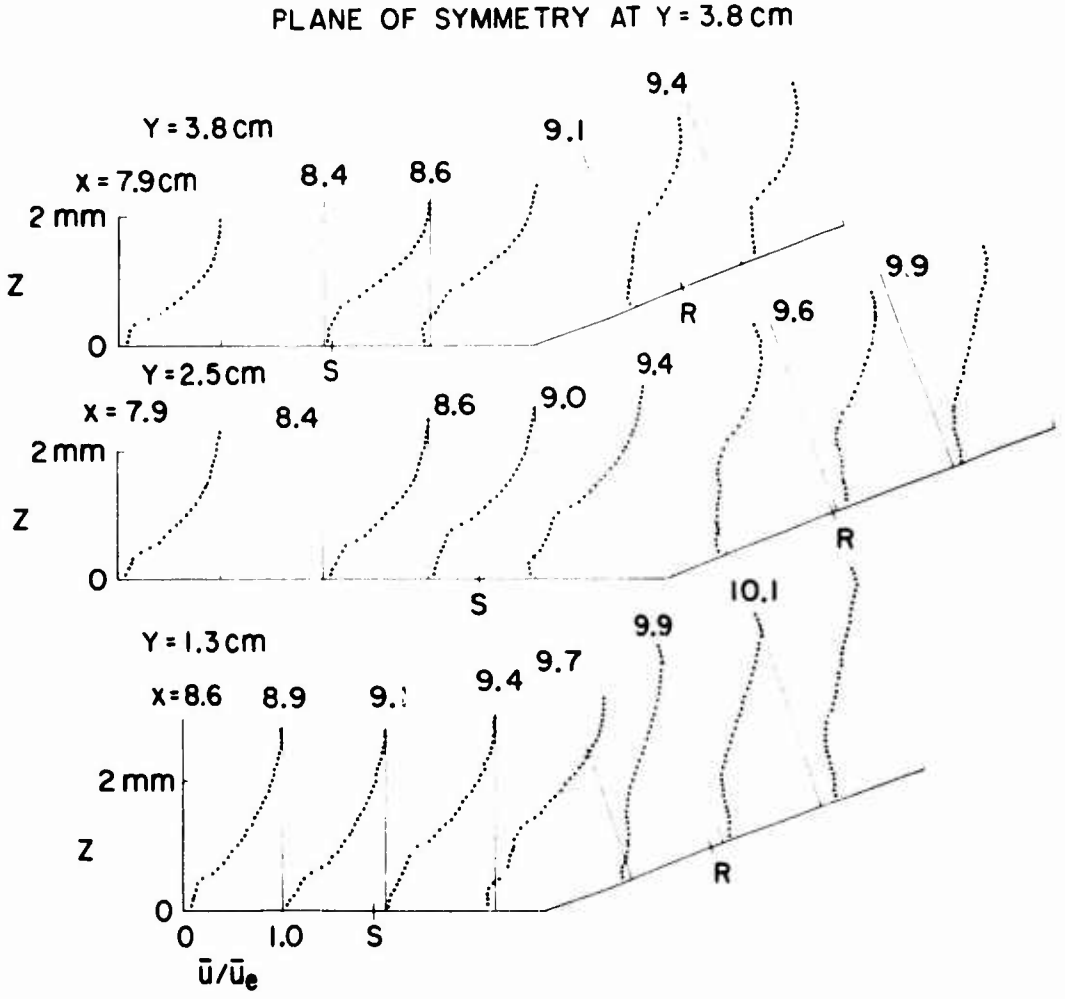

Fig. 13. $\bar{u}$ velocity profiles, turbulent separation, 20°/5° wedge

PRESSURE RISE TO SEPARATION IN CYLINDRICALLY SYMMETRIC SHOCK WAVE - TURBULENT BOUNDARY LAYER INTERACTION

BY
Dr D F MYRING
Department of Mechanical Engineering
University of Salford
Salford M5 4WT

SUMMARY

Integral equations governing the three-dimensional flow in a cylindrically symmetric shock wave - turbulent boundary layer interaction are written in the form of momentum equations for directions normal to and aligned with the line of the shock, plus an entrainment equation. By neglecting the contributions of surface friction and mass entrainment, direct dependence on spatial derivatives is removed and solutions are obtained using the Mager cross flow profiles and power-law profiles for the streamwise flow. Results are produced for angles of sweep greater than 45° which show good agreement with experimental measurements of pressure rise to separation. For smaller angles of sweep the theory suggests that the skin friction becomes vanishingly small at separation, which in turn suggests the need for a modified separation criterion.

SYMBOLS

c_{f1}	component of surface friction coefficient in x direction
c_{f2}	component of surface friction coefficient in y direction
c_{ps}	pressure coefficient at separation
E	pressure gradient coefficient (equations 23 and 1.14)
F	entrainment coefficient
F_{11}, F_{21}, F_1	ratios Θ_{11}/Θ_{11}, Θ_{21}/Θ_{11}, Δ_1/Θ_{11} respectively
$f_{12}, f_{21}, f_{22}, f_2$	functions of H_i (equations 1.15 to 1.18)
H	shape parameter $\int_0^\delta (1 - \frac{\rho u}{\rho_e u_e}) dz / \Theta_{11}$
H_i	shape parameter $\int_0^\delta \frac{\rho}{\rho_e}(1 - \frac{u}{u_e}) dz / \Theta_{11}$
H_1	shape parameter $\int_0^\delta \frac{\rho u}{\rho_e u_e} dz / \Theta_{11}$
I_{pt}	total pressure loss integral (equation 39)
J_1	ratio
M	Mach number just external to boundary layer
M_n	component of M in the x direction
P	static pressure
P_t	total pressure
t	$\tan\beta$ for Mager profiles
U	boundary layer velocity component in direction of external stream
u	boundary layer velocity component in direction of x axis
v	boundary layer velocity component in direction of y axis
x, y, z	rectangular cartesian axes, z normal to body surface, x normal to shock front
α	angle of external streamline relative to x axis
β	angle between skin friction line and external streamline
Δ_1	$\int_0^\delta \frac{(\rho_e u_e - \rho u)}{\rho_e u_e} dz$
δ	value of z at edge of boundary layer
Θ_{11}	$\int_0^\delta \frac{\rho u}{\rho_e u_e^2}(u_e - u) dz$
Θ_{21}	$\int_0^\delta \frac{\rho u}{\rho_e u_e^2}(v_e - v) dz$
Θ	$\Theta_{11} \rho_e u_e \sec\alpha$
$\bar{\Theta}$	Θ/Θ_0
Θ_{11}	streamwise momentum thickness $\int_0^\delta \frac{\rho u}{\rho_e u_e}(u_e - u) dz$
ϕ	$\tan\alpha \cdot \tan\beta$
λ	angle between x and y axes

SUBSCRIPTS

2D	two-dimensional flow
3D	three-dimensional flow
e	edge of boundary layer
o	beginning of pressure rise to separation
s	separation

INTRODUCTION

Shock wave - boundary layer interaction is a phenomenon which can have an important bearing on several aspects of aeronautical design. The role played by this interaction in influencing the performance of items such as wings and engine intakes in supersonic flows has long been recognised and has formed the basis of a great deal of study.

Broad features of the interaction of a shock wave with a boundary layer are well understood to the extent that in certain cases working theoretical models of the flows have been constructed which can adequately predict measured characteristics. Of particular interest is the prediction of the pressure rise to separation in cases where the shock wave in strong enough to produce a region of reverse flow in the boundary layer. Under these conditions it is well known that substantial departures from the flow patterns predicted by inviscid flow theory take place. The pressure rise to separation is one of the salient features identified by various investigators and is important since the pressure at separation is only just lower than the almost constant pressure in the 'plateau' region of the reverse flow, which can have such a profound effect on features such as wing pitching moment and control surface effectiveness.

However, the major part of the investigation has dealt with nominally two-dimensional flows, whereas in practice many flows possess a strong element of three-dimensionality; flow over a swept wing is a prime example. As a result, present knowledge and understanding of three-dimensional interactions cannot be said to equal that of two-dimensional flows. Whilst the general physical mechanisms are undoubtedly similar important details such as the definition and effects of separation differ considerably. To match the level of understanding of two-dimensional flows much more experimental and theoretical work is needed.

In general three-dimensional flows a boundary layer separation line is defined[1] as a skin-friction line joining a separation saddle-point to a separation node. In certain cases where the flow exhibits some form of symmetry it is possible to identify the orientation of the separation line simply from consideration of the symmetry. For instance, if a cylindrically symmetric flow is postulated then the separation node and saddle-point lie at plus and minus infinity referred to an axis aligned with isobars, and the separation line will in fact coincide with one member of the family of isobars which will be straight, parallel lines. Under these conditions separation is therefore deemed to occur when skin friction lines have been turned through an angle sufficient to bring them parallel with an isobar.

In determining separation position experimentally it is usual to rely on some form of surface flow visualisation such as pigmented oil-flow techniques[2]. Unfortunately of the few published results of three-dimensional interaction experiments only in certain cases is skin-friction line visualisation included. Stanbrook[3] examined the interaction produced by a swept normal shock and the side-wall boundary layer of a wind-tunnel in the Mach number range $M = 1.5 - 2.0$; from oil-flow results and surface pressure measurements he was able to determine the pressure rise to separation. McCabe's[4] work was quite similar in technique though in this case tests at a higher Mach number of $M \simeq 3$ were carried out. The experiments of Stalker[5] on the other hand did not include detailed measurements of separation position but rather concentrated on the determination of pressure rise to reattachment and upstream influence.

Of the three investigations mentioned above only that of McCabe included a theoretical attempt to look in detail at the flow inside the boundary layer. By considering the effects of the vorticity convected by the boundary layer through the interaction region McCabe was able to derive an approximate relationship between external flow deflection and skin-friction line deflection and hence effectively determined the separation pressure rise. Some rather bold assumptions were necessary in order to complete the derivation but in many respects the comparisons with experimental results appeared to indicate a definite match.

In the following sections existing knowledge of three-dimensional boundary layer flows is applied to the prediction of pressure rise to separation in the simplest case of three-dimensional shock interaction with a turbulent boundary layer; that is a flow with cylindrical symmetry in which conditions along the plane of the shock wave are invariant. Comparison with the few available experimental measurements mentioned above shows an encouraging confirmation of the predictions.

The basis for the theory is an integral method[6] for the prediction of three-dimensional turbulent boundary layer growth. In the general form the method was derived in terms of non-orthogonal curvilinear co-ordinates and was designed for use with either the Mager[7] or Johnson[8] cross flow models. The entrainment method combined with power-law velocity profiles for the external streamwise flow were adapted for use in the general coordinate system (x,y,z). In essence the integral parameters in the x and y directions (z was taken normal to the surface) were related to those in the external streamwise direction in terms of the assumed velocity profile families. The basic method was applied to compressible flows by Smith[9] who made the usual modifications to account for density changes across the boundary layer. Because of their generality the governing integral equations as derived in ref 6 provide a most convenient basis for the analysis which follows.

In some previous treatments of shock-boundary layer interactions,[10,5] especially for nominally two-dimensional turbulent flows, the governing equations have been simplified on the assumption that surface shear stress and mass entrainment terms can be regarded

as being negligible in the interaction region. In view of the rather large change in boundary layer flow occurring over a small streamwise distance this appears to be quite a plausible assumption and is one which will be made here. In consequence it becomes possible to relate changes in momentum defects and shape parameters to changes in free-stream pressure directly without reference to distances x and y. In particular it is possible to relate changes in the direction of skin-friction lines to changes in pressure and by so doing determine the pressure rise to separation.

As a consequence of neglecting the surface friction terms, a definite advantage arises in the use of Mager cross flow profiles as opposed to those of Johnston, which involve the surface friction coefficient as a parameter. Whilst the merits of the two families of profiles are arguable the simplicity of the Mager family in the present application makes the choice a clear one. The results of the analysis which are here restricted to adiabatic flows indicate that for shock sweeps greater than 45° the pressure rise to separation is directly proportional to the product of dynamic head based on velocity component normal to the shock and a function of boundary layer shape parameter H of the undisturbed flow. For sweeps of less than 45° values of shape parameter H at separation become unrealistically large. Compared with results obtained for two-dimensional flows it is possible to deduce that for angles of sweep α_o greater than 45° the pressure rise to separation is smaller than that for a two-dimensional interaction in an identical undisturbed flow by a factor of $2\cos^2\alpha_o$.

THEORY

(1) BOUNDARY LAYER FLOW

It is assumed that the shock interaction region is cylindrically symmetric with the y-axis in the plane of the shock and parallel to the surface which is taken to be adiabatic. Conditions along the y axis will then be invariant. The x-axis is assumed to be orthogonal to the y-axis and also parallel to the surface. This arrangement is depicted in fig 1. Because of the assumed symmetry all derivatives with respect to y in the integral equations will be zero and since the axes are orthogonal the mixed metric will be zero. If x and y are now taken to be distances measured along the x and y axes the momentum integral equation for the x direction may be taken from ref 6 in the form

$$\frac{d}{dx}\left(\rho_e U_e^2 \Theta_{11}\right) + \Delta_1 \rho_e U_e \frac{du_e}{dx} = c_{f1} \tag{1}$$

Here Θ_{11} is the momentum thickness for the x direction, ρ_e and U_e are the density and resultant velocity just external to the boundary layer and u_e is the component of external velocity in the x direction. The term cf1 is the coefficient of surface friction in the x direction and Δ_1 is directly related to the displacement thickness. If momentum thickness in the external streamwise direction is Θ_{11} it may be shown[6] that

$$\Theta_{11} = F_{11}\ \Theta_{11}, \tag{2}$$

where for orthogonal axes F_{11} is a function of the external flow angle relative to the x - axis, α, the cross flow angle β (directly for Mager profiles, indirectly for Johnston profiles) and the streamwise shape parameter H_i. The parameter H_i is defined as

$$H_i = \frac{\int_0^\delta \rho/\rho_e \left(1 - \frac{U}{U_e}\right) dz}{\int_0^\delta \frac{\rho U}{\rho_e U_e}\left(1 - \frac{U}{U_e}\right) dz} \tag{3}$$

where U is the component of velocity in the direction of the external stream and δ is boundary layer thickness.

The momentum integral equation for the y-direction may be obtained in the form

$$\frac{d}{dx}\left(\Theta_{21} \rho_e U_e^2\right) = c_{f2} \tag{4}$$

where cf2 is the coefficient of surface friction and Θ_{21} is the momentum thickness for the y-direction. As before Θ_{21} may be related to Θ_{11} directly, in this case by the equation

$$\Theta_{21} = F_{21} \cdot \Theta_{11} \tag{5}$$

where F_{21} is a function of α, β and H_i.

To complete the set of governing equations for the boundary layer flow the entrainment equation may be obtained in the form

$$\frac{d}{dx}\left(\rho_e U_e \Theta_{11} J_1\right) = \rho_e U_e F \tag{6}$$

where J_1 is another function of α, β and H_i and F is the entrainment coefficient. The three functions F_{11}, F_{21} and J_1 are derived in ref 6 and are included here in appendix A1.

In deriving (1) it has been assumed that the external flow is isentropic in order that the second term on the left-hand side, which is essentially a pressure gradient term, may be written in terms of the gradient of velocity in the x-direction.

It is now assumed that since pressure rise to separation occurs rapidly, then over the region of this pressure rise skin friction makes a negligible contribution to the momentum balance and entrainment contributions to boundary layer mass flow rate are also

negligibly small. Hence the three governing equations,((1), (4) and (6)), may be approximated by

$$d\left(\rho_e U_e^2 \Theta_{11}\right) + \Delta_1 \rho_e U_e \, dU_e = 0 , \tag{7}$$

$$\frac{\Theta_{11}}{F_{11}} \cdot F_{21} \rho_e U_e^2 = \text{const.}, \tag{8}$$

and

$$\rho_e U_e \Theta_{11} \frac{J_1}{F_{11}} = \text{const.}, \tag{9}$$

where the streamwise momentum thickness in (6) has been written in terms of Θ_{11} using the relationship given by (2), and Θ_{21} in (4) has been replaced by $\Theta_{11} \cdot \frac{F_{21}}{F_{11}}$ using (2) and (5).

Separation in the case of cylindrically symmetric flows is identified by the condition that at separation the skin friction lines are parallel to, in this case, the y-axis. It follows quite readily that if ϕ is defined as

$$\phi = \tan\alpha \cdot \tan\beta \tag{10}$$

then at separation, denoted by subscript s,

$$\phi_s = 1 \tag{11}$$

Further, if it is assumed that at the start of the pressure rise there is no cross flow in the boundary layer (collateral flow) then

$$\phi_o = 0 \tag{12}$$

where subscript o refers to conditions at the beginning of the pressure rise.

In appendix A1 it is shown that for Mager profiles

$$\frac{J_1}{F_{11}} = \frac{\sec\alpha \left(H_1 + f_2 \phi\right)}{1 - (f_{21} + f_{12})\phi + f_{22}\phi^2} \tag{13}$$

where f_{12}, f_{21} and f_{22} are all functions of H_i only and are derived in ref 6. The shape parameter H_1 is defined as

$$H_1 = \frac{\int_0^\delta \frac{\rho U}{\rho_e U_e} dz}{\int_0^\delta \frac{\rho U}{\rho_e U_e}\left(1 - \frac{U}{U_e}\right) dz} \tag{14}$$

There is some evidence, both experimental and theoretical, to suggest that values of H_1 and H_i are related in a substantially unique way and here the power law relationship

$$H_1 = \frac{2 H_i}{(H_i - 1)} \tag{15}$$

will be assumed.

If the parameter Θ, defined as

$$\Theta = \Theta_{11} \rho_e U_e \sec\alpha \tag{16}$$

is introduced then by applying (9) between the start of the pressure rise and separation it follows that

$$\bar{\Theta}_s = \frac{H_{1o}(1 - f_{21s} - f_{12s} + f_{22s})}{H_{1s} + f_{2s}} \tag{17}$$

where

$$\bar{\Theta}_s = \Theta_s / \Theta_o \tag{18}$$

It is therefore clear that for a given value of H_{1o}, $\bar{\Theta}_s$ is uniquely related to the value of H_{is}. The relationship between $\bar{\Theta}_s$ and H_{is} is shown in fig 2 for a value of H_{io} of 1.286 (1/7th power law).

Similarly by taking the expression for F_{21}/F_{11} as derived in Appendix A1 and applying (8) between the start of the pressure rise and separation it may be shown that

$$\bar{\Theta}_s = \frac{1 - f_{21s} - f_{12s} + f_{22s}}{1 - f_{12s} + (f_{21s} - f_{22s}) \cot^2\alpha_s} \tag{19}$$

By eliminating $\bar{\Theta}_s$ between equations (17) and (19) it readily follows that

$$\tan^2\alpha_s = \frac{H_{1o}(f_{21s} - f_{22s})}{H_{1s} + f_{2s} + H_{1o}(f_{12s} - 1)} , \tag{20}$$

from which it may be seen that for a given value of H_{io} (and hence H_{1o}), the

external flow angle α_s is a function of H_{is} only. The relationship between α_s and H_{is} is shown in fig 3 for $H_{io} = 1.286$. The upper limiting value for α_s of 90° corresponds to the limit in which shock sweep tends to 90° and β_s tends to zero. At this limit it will be seen that a lower limiting value for H_{is} of 1.48 arises (for $H_{io} = 1.286$). For values of H_{is} in the region of 2.1 - 2.2, where typically separation in two-dimensional flows may be expected, α_s lies in the range 60° - 58°. At these high values of H_{is} the various assumed relationships between shape parameters and also the cross flow profiles become of dubious validity. Consequently a value of 2.1 for H_{is} will be taken as an upper working limit. Hence the theory as laid down may be expected to apply to interactions in which α_s lies in the range 60° - 90°.

Reference to fig 2 then enables limits of 4.40 to approximately 4.32 to be put on the value of $\bar{\Theta}_s$. Thus if a mean value of $\bar{\Theta}_s$ of 4.36 is taken then over the range of application of the theory $\bar{\Theta}_s$ varies by less than ±1%. In what follows therefore a constant value for $\bar{\Theta}_s$ of 4.36 will be taken.

In terms of the compound variable Θ equation (7) may be written

$$d(\Theta u_e) + \left(\frac{\Delta_1 \cos\alpha}{\Theta_{11}}\right)\Theta\, du_e = 0 \tag{21}$$

where the relationship

$$u_e = U_e \cos\alpha \tag{22}$$

has been invoked. Writing

$$E = \frac{\Delta_1 \cos\alpha}{\Theta_{11}}, \tag{23}$$

the assumption that E remains substantially constant over the pressure rise to separation enables equation (21) to be approximated by

$$d\left(\ln\left\{\Theta\, u_e^{1+E}\right\}\right) = 0 \tag{24}$$

or

$$\Theta u_e^{1+E} = const. \tag{25}$$

Justification for taking E to be approximately constant may be derived from appendix A1 where it is shown that the value of E is set by the three parameters H_i, ϕ and M whose influences tend to cancel each other. The value of E tends to be increased by an increase in H_i as separation is approached but tends to decrease as Mach number falls; increasing values of ϕ tend to increase E near the start of the pressure rise but have an opposite effect near separation. The combined effect depends in detail on the values of M_o and H_{is} but in broad terms E tends to change by only a small amount.

At the start of the pressure rise it is shown in appendix A1 that

$$1 + E = H_o + 1 = 2.286(1 + 0.2M_o^2), \tag{26}$$

so that by applying (25) between stations o and s it is clear that

$$\frac{u_{es}}{u_{eo}} = 4.36^{\frac{1}{2.286(1+0.2M_o^2)}} \tag{27}$$

Here the value of $\bar{\Theta}_s$ determined previously has been substituted.

(2) EXTERNAL FLOW

In cases of swept shock interaction the appropriate model for the external flow is not readily apparent. If, as may be the case, the generated shock is embedded in the boundary layer, then the external flow will be non-isentropic. If the increase in entropy through the shock is large then equation (1) is not valid since it would in these circumstances lack a term involving the x-wise gradient of total pressure. However, for shocks of moderate strength the increase in entropy is also moderate and the absence of total pressure gradient terms in (1) may be justified within the limits of the approximations already made.

If a separation pressure rise coefficient is defined as

$$C_{ps} = \frac{p_s - p_o}{\tfrac{1}{2}(\rho_e U_{eo}^2)} \tag{28}$$

then because the component of external velocity in the direction of the y axis remains constant, equation (28) may be expressed as

$$C_{ps} = \left\{\left[1 + \frac{\gamma-1}{2} M_{No}^2\left(1 - \frac{u_{es}^2}{u_{eo}^2}\right)\right]^{\frac{\gamma}{\gamma-1}} - 1\right\}\frac{2\cos^2\alpha_o}{\gamma M_{No}^2} \tag{29}$$

in isentropic flow, where

$$M_{No} = M_o \cos\alpha_o \tag{30}$$

Using the binomial theorem (29) may be expanded to give

$$C_{ps} = \cos^2\alpha_0 \left\{ 1 - \frac{u_{es}^2}{u_{e0}^2} + \frac{\gamma-1}{4\gamma} M_{n0}^2 \left(1 - \frac{u_{es}^2}{u_{e0}^2}\right)^2 + \cdots\cdots \right\} \qquad (31)$$

Under conditions in which the change of total pressure in the external stream may be assumed to be small it may be expected that a good approximation to (31) can be obtained by neglecting all but the first two terms giving

$$C_{ps} \doteq \cos^2\alpha_0 \left\{ 1 - \frac{u_{es}^2}{u_{e0}^2} \right\} \qquad (32)$$

To the same order of approximation this may be written

$$C_{ps} = 2\cos^2\alpha_0 \left\{ 1 - \frac{u_{es}}{u_{e0}} \right\}, \qquad (33)$$

which takes the form of the familiar small perturbation approximation. It is interesting to note that (33) is exactly the expression which would be obtained on the assumption that the increase in pressure $P_s - P_0$ is effected by a single normal shock wave aligned with the y-axis. Thus even for flows in which substantial changes in total pressure occur and for which clearly the approximation of (32) is not valid, equation (33) may be expected to remain within adequate limits of accuracy.

Hence from the combination of (33) and (25) it follows that

$$\frac{C_{ps}}{2\cos^2\alpha_0} = 1 - 4.36^{\frac{2.26(1+0.2M_0^2)}{}} \qquad (34)$$

For given boundary conditions of α_0 and M_0 therefore (34) provides a prediction of the pressure rise coefficient C_{ps}.

The condition that the component of external velocity in the y direction remains constant leads quite readily to the relationship

$$\tan\alpha_s = \tan\alpha_0 \left(\frac{u_{e0}}{u_{es}}\right) \qquad (35)$$

Thus using (25) the value of α_s may be calculated and hence H_{is} may be obtained from fig 3.

COMPARISON WITH EXPERIMENTAL RESULTS

There are few experimental investigations of three-dimensional flows which have been reported in detail sufficient to permit values of C_{ps} to be determined. Here the results of McCabe[4] and Stanbrook[3] will be compared with the predictions.

Both investigators generated a swept normal shock using a wedge spanning a wind tunnel working section. From the recorded value of wedge face incidence just sufficient to turn skin friction lines to run parallel with the plane of the shock, it is possible to deduce the value of C_{ps} and the shock incidence α_0. Hence the group $C_{ps}/2\cos^2\alpha_0$ may be plotted against the working section Mach number M_0 and the trends compared with those predicted by (34). Fig 4 shows this comparison; even though with the few available points firm conclusions are difficult to draw, it can be said that broadly the level of agreement is quite good, there being some indication that the predicted trends with changes in free-stream Mach number are valid. Results at the two lower Mach numbers from Stanbrook's work are in fact border-line cases for the present theory since values of α_s are below the limit of 58°-60°. Overall therefore the agreement shown by fig 4 is very encouraging.

A comparison with results obtained for nominally two-dimensional flows (Refs 11,12,13,14, 15) is presented in fig 5 where it will be seen that the theoretical trend of C_{ps2D} with Mach number derived in ref 16 closely resembles the trend of $C_{ps3D}/2\cos^2\alpha_0$ derived here. Since the predicted values of C_{ps2D} agree well with the measured values shown, it may be argued that the relationship

$$\left[C_{ps3D}\right]_{M_0} = 2\cos^2\alpha_0 \left[C_{ps2D}\right]_{M_0} \qquad (36)$$

is valid provided always that α_s is greater than the lower limit of between 58° and 60° for the three-dimensional flows. Subscript M_0 here indicates that the upstream Mach number is identical in the flows being compared.

At a lower limit of 60° for α_s the variation in shock sweep α_0 with free-stream Mach number M_0 is shown in fig 6 where it will be seen that in the supersonic range α_0 is always greater than 45°. It is therefore possible to conclude from (36) that C_{ps} for a swept shock interaction is always less than the value appropriate to a two-dimensional flow at the same Mach number.

DISCUSSION

In setting up the theoretical model it was assumed that cylindrical symmetry existed. In the experiments from which results were taken as a comparison there was some evidence that the interaction region was spreading with distance along the shock-wave, and thus strict cylindrical symmetry could not be assumed. However for the small rate of spread which was evident, terms in the equations representing gradients in the y-direction can be said to be negligible, making the assumption of cylindrical symmetry an acceptable approximation. The possibility of total pressure losses in the flow just external to the boundary layer has already been noted. However, if substantial losses in total pressure P_t occur, equation (21) should have an extra term and should appear in the form

$$d\left(\ln\{\Theta u_e\}\right) + E\,d(\ln u_e) - \frac{E}{\gamma M_N^2}\,d\left(\ln p_t\right) = 0 \qquad (37)$$

On integration this gives

$$\ln\left\{\Theta u_e^{1+E}\right\} = E\int \frac{d(\ln p_t)}{\gamma M_N^2} + \text{const.}, \qquad (38)$$

where the total pressure integral will be negative. Hence writing

$$E\int_0^s \frac{d(\ln p_t)}{\gamma M_N^2} = I_{pt} \qquad (39)$$

we have

$$\frac{u_{es}}{u_{eo}} = \bar{\Theta}_s^{\frac{-1}{1+E}} \exp\left\{\frac{I_{pt}}{1+E}\right\} \qquad (40)$$

Since changes in total pressure will not affect the value of $\bar{\Theta}_s$ it may be inferred that u_{es}/u_{eo} will be overestimated by equation (25) if the flow just external to the boundary layer is not isentropic. Hence, because equation (33) remains a good approximation even when large changes of total pressure occur it is to be expected that under these circumstances C_{ps} will be underestimated; an improved prediction should be possible by evaluating I_{pt} given by (39). From an estimate of I_{pt} derived from normal shock-wave relationships it may be shown that provided M_{No} is below 1.70 then errors in C_{ps} caused by the assumption of isentropic flow for the momentum equation should be less than 5%.

It has been assumed that there is zero cross flow at the start of the pressure rise to separation. With an initial cross flow in the sense of that produced by the interaction it follows from the analysis that the pressure rise to separation would be smaller than that predicted here and vice-versa. However, in the latter case a profile family which embraced the cross-over profile would be needed rendering both the Mager and Johnston families inappropriate.

By eliminating the direct dependence of the governing equations on spatial derivatives certain singular behaviour of the equations has been avoided. For two-dimensional adiabatic flows singular behaviour upstream of separation can be inferred[16] to result theoretically from the neglection of changes in static pressure across the boundary layer. Similar problems arise in three-dimensional flows but it may be inferred just as in two-dimensional flows,[17] that provided the integral parameters are defined as integrals along isobars in the (x,z) plane then the form of the governing equations is unchanged and pressure changes along a surface normal (z axis) are automatically accommodated. Thus on condition that the velocity profile families assumed here are representative of those arising along isobars, the analysis can be said, by a change of interpretation, to account for changes in static pressure across the boundary layer.

It has been shown that the analysis cannot be expected to apply to interactions in which shock-wave sweep is less than the lower limits shown in fig 6 as a function of undisturbed free-stream Mach number M_o. Below these limits the predicted value of H_{is} exceeds the range of values in which surface friction falls to zero in two-dimensional flows. A common assumption in three-dimensional turbulent flows is that the streamwise component of surface friction can be derived from two-dimensional data; by inference therefore values of H_{is} above approximately 2.1 imply that surface friction is virtually zero in three-dimensional flows also. Thus in the range of sweeps 0° to 45° the flow at separation apparently exhibits features of both two-dimensional separation, in which the surface friction is always zero, and three-dimensional separation in which except at saddle-points or nodes surface friction is generally non-zero.

Prediction methods for this lower range of sweep therefore require modifications to either the velocity profiles or the effective definition of separation.

The result given by (34) can be shown to support the inference made by Stalker[5] to the effect that the influence of sweep on peak pressure ratio may be expressed simply in terms of free-stream Mach number component normal to the line of sweep. Here the pressure ratio at separation is considered. From (28)

$$\frac{p_s}{p_o} = 1 + \frac{C_{ps}}{2}\gamma M_o^2$$

so that on substitution for C_{ps} from (34)

$$\frac{p_s}{p_o} = 1 + M_{No}^2 \cdot f(M_o) \qquad (41)$$

Thus if sweep is changed in a flow at a given Mach number M_o, then the pressure ratio at separation depends only on M_{No}. However, two flows with the same value of M_{No} but different values of M_o will clearly produce different pressure ratios at separation. Furthermore, although certain similarities with two-dimensional results have been noted equation (41) will not of course embrace these results since the region of sweep 0 - 45° is excluded.

CONCLUSIONS

The problem of predicting the pressure rise to separation in a cylindrically symmetric shock wave - turbulent boundary layer interaction has been analysed using a momentum integral method. By neglecting surface friction and mass entrainment a simple expression

for the pressure coefficient at separation has been derived, valid in the range of sweeps from approximately 45° upwards. At smaller angles of sweep conditions at separation exhibit features which suggest vanishingly small values of surface friction as in two-dimensional flows. Prediction of separation in the range of sweeps from 45° downwards therefore demands a modified separation criterion which may be beyond the scope of the velocity profile families utilised here.

Comparison with experimental results shows an encouraging agreement, although more measurements are needed to support firmer comment. Within the limits of the theory it has been shown that in flows at the same undisturbed free-stream Mach number, increasing sweep leads to smaller pressure rises to separation, maximum values being obtained for two-dimensional flows.

REFERENCES

NO	AUTHOR	TITLE ETC
1	M J Lighthill	Laminar Boundary Layers Oxford Press 1963
2	A Stanbrook	The surface oil flow technique used in high speed wind tunnels RAE TN 2712 1960
3	A Stanbrook	An experimental study of the glancing interaction between a shock-wave and a turbulent boundary layer ARC CP 555 1960
4	A McCabe	The three-dimensional interaction of a shock wave with a turbulent boundary layer Aero Quart Vol.XV11 1966
5	R J Stalker	Sweepback effects in turbulent boundary layer-shock wave interaction J Aero Sci Vol 27 1960
6	D F Myring	An integral prediction method for three-dimensional turbulent boundary layers in incompressible flow RAE TR 70147 1970
7	A Mager	Generalisation of boundary layer momentum integral equations to three-dimensional flows including those of rotating systems NACA Rpt 1067 1952
8	J P Johnston	Three-dimensional turbulent boundary layer MIT Gas Turbine Lab Rpt 39 1957
9	P D Smith	An integral prediction method for three-dimensional compressible turbulent boundary layers R & M 3739 1972
10	L Crocco R F Probstein	The peak pressure rise across an oblique shock emerging from a turbulent boundary layer over a plane surface Princeton Aero Lab Rpt 254 1954
11	J R Sterrett J C Emery	Extension of boundary layer separation criteria to a Mach number of 6.5 by utilising flat plates with forward facing steps NASA TN-618 1960
12	S M Bogdonoff	A study of shock wave boundary layer interaction Princeton University Aero Eng Dept Rpt No 222

13	J Seddon	The flow produced by interaction of a turbulent boundary layer with a normal shock wave of strength sufficient to cause separation R & M 3502 1960
14	G E Gadd D W Holder J D Regan	An experimental investigation of the interaction between shock waves and boundary layers Proc Rory Soc A226 1954
15	D F Chapman D M Kuehn H K Larson	Investigation of separated flows in supersonic and subsonic streams with emphasis on the effects of transition NACA TN 3869 1957
16	D F Myring	The interaction of a turbulent boundary layer and a shock at hypersonic Mach numbers AGARD con proc No 30 1968
17	D F Myring	The effects of normal pressure gradients on the boundary layer momentum integral equation RAE TR 68214 1968

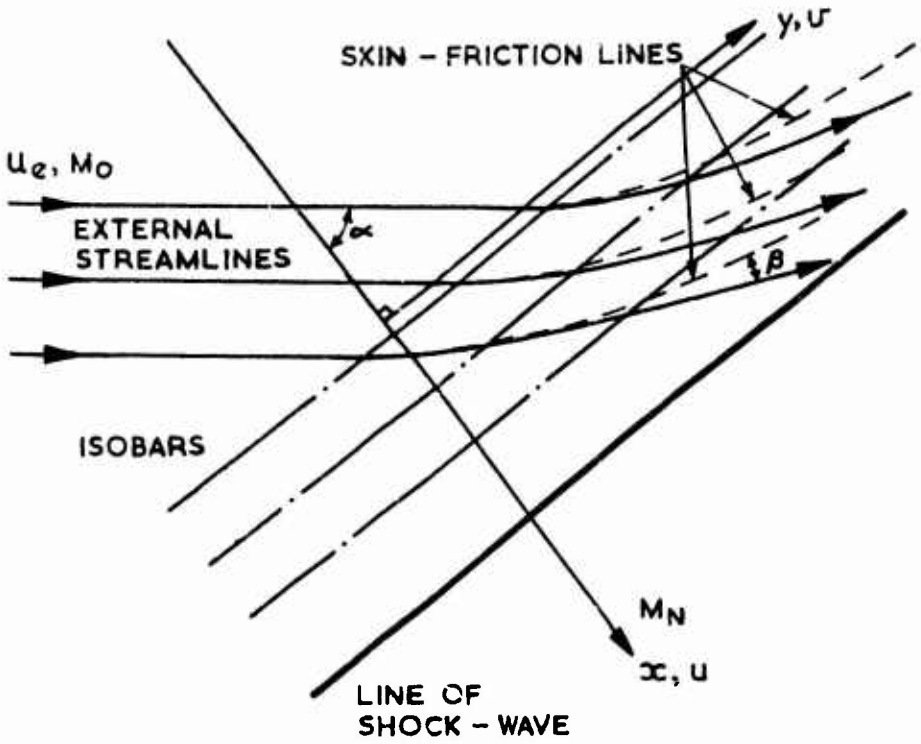

Fig.1 Plan-view of surface

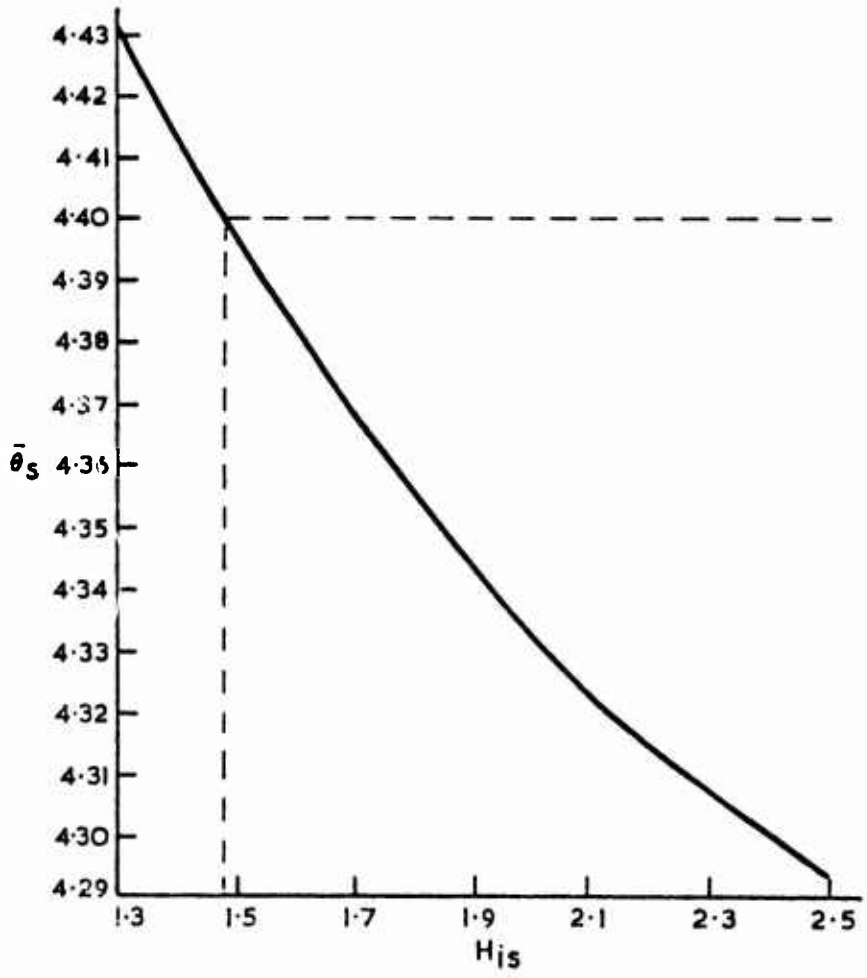

Fig.2 Momentum function versus shape parameter at separation

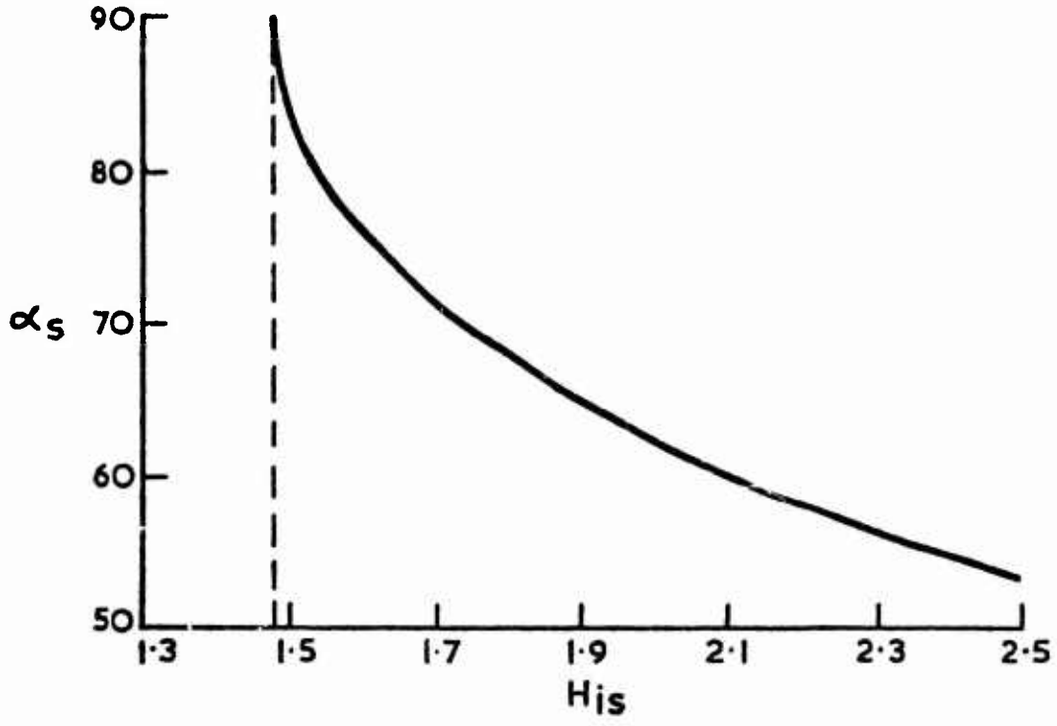

Fig.3 External flow angle versus shape parameter at separation

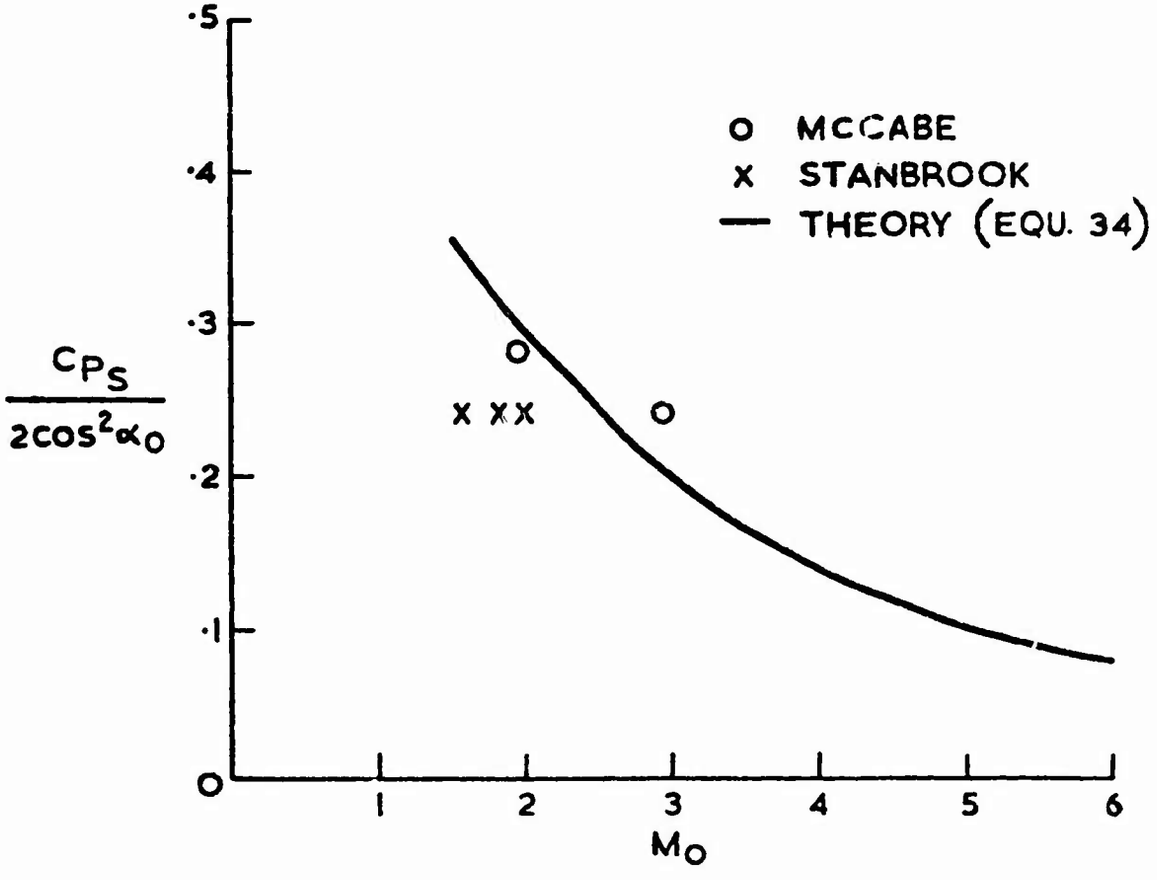

Fig.4 Pressure coefficient at separation versus free-stream Mach number in three-dimensional flows

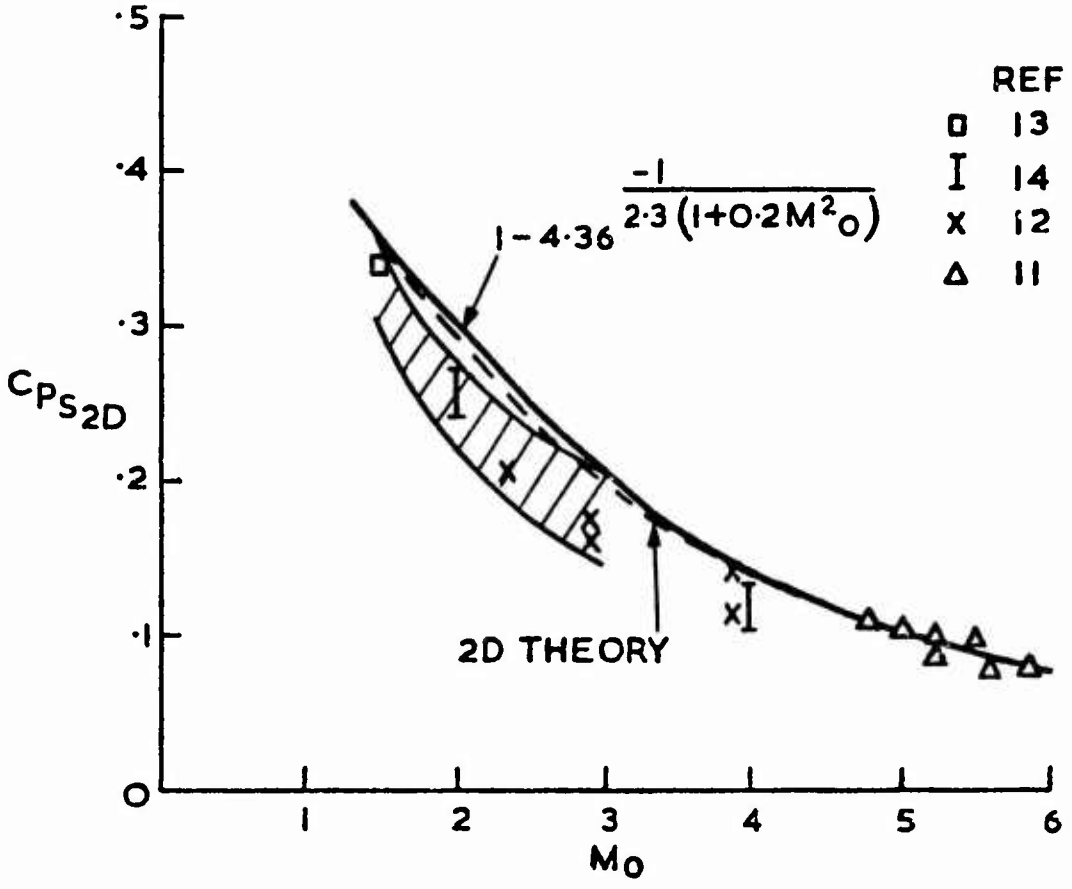

Fig.5 Pressure coefficient at separation versus free-stream Mach number in two-dimensional flows

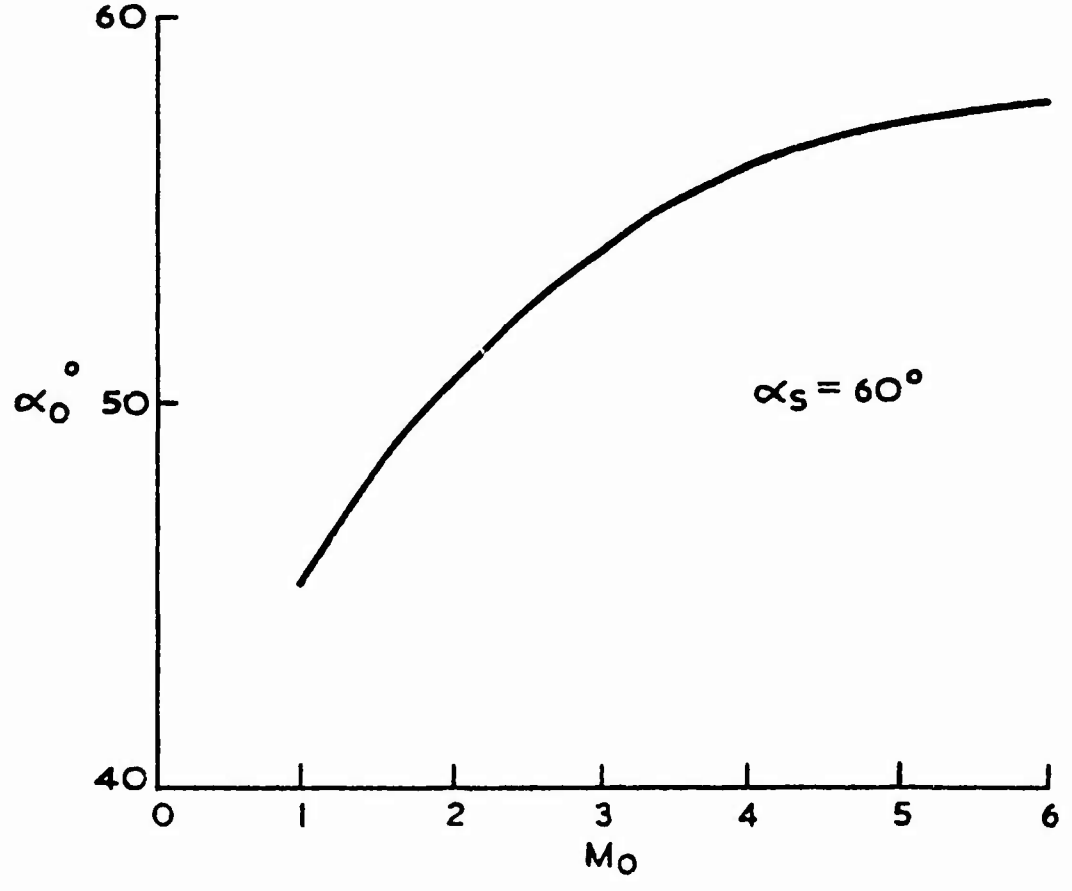

Fig.6 Shock sweep versus free-stream Mach number

APPENDIX A1
INTEGRAL PARAMETER COEFFICIENTS

From appendix D of ref 1 the coefficients F_{11}, F_{21} and J_1 may be extracted as

$$F_{11} = \left\{\sin^2(\lambda-\alpha) - (f_{12}+f_{21})\sin(\lambda-\alpha)\cos(\lambda-\alpha)\,t + f_{22}\cos^2(\lambda-\alpha)\,t^2\right\}/\sin^2\lambda \quad 1.1$$

$$F_{21} = \left\{\sin\alpha\sin(\lambda-\alpha) + \left[f_{21}\cos\alpha\sin(\lambda-\alpha) - f_{12}\sin\alpha\cos(\lambda-\alpha)\right]t - f_{22}\cos\alpha\cos(\lambda-\alpha)\,t^2\right\}/\sin^2\lambda \quad 1.2$$

$$J_1 = \left\{H_1\sin(\lambda-\alpha) + f_2\cos(\lambda-\alpha)\,t\right\}/\sin\lambda \quad 1.3$$

where λ is the angle between the x and y axes and for Mager profiles $t = \tan\beta$.

By putting $\lambda = \pi/2$, $\phi = \tan\alpha\tan\beta$ these equations become

$$F_{11} = \cos^2\alpha\left\{1 - (f_{12}+f_{21})\,\phi + f_{22}\,\phi^2\right\} \quad 1.4$$

$$F_{21} = \frac{\cos^3\alpha}{\sin\alpha}\left\{\tan^2\alpha + f_{21}\,\phi - f_{12}\tan^2\alpha\,\phi - f_{22}\,\phi^2\right\} \quad 1.5$$

$$J_1 = \cos\alpha\left\{H_1 + f_2\,\phi\right\} \quad 1.6$$

Thus

$$\frac{J_1}{F_{11}} = \frac{\sec\alpha\,(H_1 + f_2\,\phi)}{(1 - (f_{12}+f_{21})\,\phi + f_{22}\,\phi^2)} \quad 1.7$$

and

$$\frac{F_{21}}{F_{11}} = \frac{\cos\alpha\left\{\tan^2\alpha\,(1-f_{12}\,\phi) + f_{21}\,\phi - f_{22}\,\phi^2\right\}}{\sin\alpha\left\{1-(f_{12}+f_{21})\,\phi + f_{22}\,\phi^2\right\}} \quad 1.8$$

The term E is defined as

$$E = \frac{\Delta_1\cos\alpha}{\Theta_{11}} \quad 1.9$$

and this may be written

$$E = \frac{\Delta_1}{\Theta_{11}}\cdot\frac{\Theta_{11}}{\Theta_{11}}\cos\alpha = \frac{F_1}{F_{11}}\cos\alpha \quad 1.10$$

where F_1 may be taken from ref 6 as

$$F_1 = H\cos\alpha - f_2\sin\alpha\,t$$
$$= \cos\alpha\left\{H - f_2\,\phi\right\} \quad 1.11$$

Hence

$$E = \frac{H - f_2\,\phi}{1-(f_{12}+f_{21})\,\phi + f_{22}\,\phi^2} \quad 1.12$$

Now by assuming that total temperature remains constant across the boundary layer it may be shown that

$$H = (H_i + 1)\,(1 + 0.2M^2) - 1 \quad 1.13$$

where H_i is defined by (3) and M is the Mach number just external to the boundary layer.

Therefore on substitution for H from 1.13, 1.12 becomes

$$E = \frac{(H_i+1)(1+0.2\,M^2) - 1 - f_2\,\phi}{1-(f_{12}+f_{21})\,\phi + f_{22}\,\phi^2}. \quad 1.14$$

Expressions for f_{12}, f_{21}, f_{22} and f_2 may be shown to be identical to those derived in ref 6 except that H_i replaces H for compressible flows. Thus

$$f_{12} = \frac{2(7H_i+15)}{(H_i+2)(H_i+3)(H_i+5)} \quad 1.15$$

$$f_{21} = \frac{-2}{(H_i-1)(H_i+2)} \quad 1.16$$

$$f_{22} = \frac{12}{(H_i+3)(H_i+4)} \quad 1.17$$

and

$$f_2 = \frac{-16\,H_i}{(H_i-1)(H_i+3)(H_i+5)} \quad 1.18$$

The effect of variations in H_i, M and ϕ on E can therefore be found numerically.

For zero cross-flow $\phi = 0$ and 1.14 becomes

$$E = (H_i + 1)\,(1 + 0.2M^2) - 1 \quad 1.19$$

Therefore at the beginning of the pressure rise to separation, a value of $H_{io} = 1.286$ gives

$$1 + E = H_o + 1 = 2.286\ (1 + 0.2M_o^2) \qquad 1.20$$

THE STRUCTURE OF THREE-DIMENSIONAL SEPARATED FLOWS IN OBSTACLE, BOUNDARY-LAYER INTERACTIONS

RAYMOND SEDNEY
CLARENCE W. KITCHENS, JR.

Ballistic Research Laboratories
Aberdeen Proving Ground, MD 21005

SUMMARY

The subject is studied using some flow visualization techniques; the turbulent boundary layer on the wall of a continuous supersonic wind tunnel is used. Sizeable separated flow regions can be studied since the wall width is 38cm and the boundary layer is typically 2.5cm thick. The large scale of the experiment is required to resolve the fine details of the flow structure. The flow visualization techniques are discussed. The variation of primary separation distance is presented as a function of M, R, and obstacle dimensions. Some scaling laws that have been proposed are not supported by our results. The structure of the separated flow upstream of the obstacle changes with relatively small changes in R; the number of vortices varies from 6 to 4 to 2 as R changes. Data are presented for large and small protuberances, but the latter are emphasized.

INTRODUCTION

Although the history of the study of boundary-layer or shear flows over obstacles is a long one, the recorded history extending back to Leonardo da Vinci, several aspects of such flows remain elusive. The main qualitative feature, the horseshoe vortex system, is well documented. The twin tornado-like vortices that rise up from the near wake and become the trailing vortex system have been studied for small obstacles. The third universal feature of the flow is the downstream persistence of these two vortex systems. A survey of the effects of small protuberances on boundary-layer flows[1] shows that the above three features are common to a wide range of conditions: laminar and turbulent boundary layers for all speeds up to hypersonic. However, more detailed examination of the flow structure is lacking except for laminar, low speed flow. One purpose of the present paper is to describe the flow structure for turbulent, supersonic boundary-layer flows over protuberances. Most of our experiments concern small obstacles; i.e., $k < \delta$, where k is the obstacle height and δ is the 99% boundary-layer thickness. However, data for large and intermediate obstacles are shown and their relationships with small obstacle data are discussed.

Since the flow structure, mainly the number and positions of vortices, is complex, the paucity of information on it is not surprising. The flow structure is needed not only to achieve an intuitive understanding of the flow but also to understand the pressure, heat transfer and shear distributions near and on the protuberance. These distributions and this understanding are needed for the well known applications in aerodynamics, ballistics and hydraulics; there are also applications in meterology and geology. Recently, some features of the flow structure were used to interpret erosion patterns on Mars[2]. Data on pressure and/or heat transfer are available in many references, mostly for large protuberances. Most of these are discussed in either Ref. 1, the survey by Korkegi[3], or the report of Kaufman et al[4]. The very high values of pressure, pressure gradient, and heat transfer measured on and in the vicinity of large protuberances in supersonic flow are a most remarkable aspect of this separated flow. Such high values are not found in the relatively few experiments on small protuberances. The unusual, and practically important, feature of this case is the fact that the disturbance caused by the small protuberance can persist for hundreds of protuberance heights downstream[1].

Understanding the flow structure and correlating the vast amount of data available is made difficult by the number of parameters that must be considered. The dimensions (three lengths), shape and orientation (sweep) of the obstacle are important. The undisturbed velocity profiles (laminar or turbulent, 2-D or 3-D) and δ must be considered as well as Mach number, M, and the Reynolds numbers that can be formed with the various lengths. The undisturbed velocity, u_k, at the height k off the surface has been found important in low speed flows. Heat and mass transfer and turbulent shear should be considered. (We are unaware of any experiments which systematically vary these.) This plethora of parameters is relieved somewhat for large protuberances; if $k \gtrsim 2\delta$ then the height no longer influences the flow interactions. But the number of parameters is still large and unwieldy. Therefore, any success at correlating important flow features with the various non-dimensional combinations of parameters is important.

Such a correlation was given by Westkaemper[5] using a large collection of data on primary separation distance, S. This is defined as the distance from the leading edge of the obstacle to the most upstream location of separation. However, different definitions of separation were used in the data he collected. All the protuberances were cylinders of diameter D, with $k > \delta$; the boundary layer was supersonic and turbulent. His conclusions were: $S/D = 2.65$ for $k/D > 1.13$ and $S/D = 2.42\ (k/D)^{0.7}$ for $k/D < 1.13$; he proposes this correlation for $2 \leq M \leq 20$ and for all Reynolds numbers provided the boundary layer is turbulent. A critique of this is given later. Unfortunately, as more data become available, the deviation of the data from this correlation increases. However, this work indicates that S/D is essentially independent of k, D, and Reynolds number; the variation with M is significant but not strong. Thus for large cylindrical protuberances the possibilities for correlation are favorable but this is not so for small protuberances, even if restricted to cylinders. Our data show that for constant Mach and Reynolds numbers, S does not even scale with D. The number of models tested is not sufficient for us to arrive at definitive correlations.

The main point of this work is to determine as much as possible of the flow structure. For this purpose flow visualization was used. The optical-surface indicator technique[6,7] was employed to visualize the flow patterns on the surface over which the boundary layer flows. More conventional techniques were

used on the surface of the protuberance. The optical-surface indicator technique is particularly suited to this application and yields a vast amount of detail. For visualization off the surface, the vapor screen method was used since it is the only tracer method that will work in supersonic, turbulent flows. Although it provided some useful data, it cannot approach the smoke method, so useful in low speed, laminar flow, in the amount of detail observed. It could not, for example, resolve the multiple vortex pattern upstream of the obstacles revealed by the optical-surface indicator visualization.

For a given protuberance and M we find 2, 4, or 6 vortices between the protuberance and primary separation, depending on Reynolds number. On physical grounds there is no reason why several vortices cannot exist there, but in the experiments on turbulent boundary layer - obstacle interactions, at either high or low speeds, two are almost always observed. The only exception known to us is the work of Winkelman[8]; he used a surface-indicator method in a high speed, turbulent boundary layer. The interpretation of our surface flow patterns was aided by the results of Norman[9], who used the smoke technique in a low speed, laminar boundary layer and obtained remarkably detailed information on the streamlines and vortices in the separated region. The structure in the separated flow upstream of the obstacle is fairly clear now but there are some features that must be clarified. The sensitivity of the number of vortices to changes in unit Reynolds number, R/ℓ, is an interesting fact for which we have no explanation at present.

Although we concentrate here on the upstream separated flow, many other features are revealed in our visualizations. Further work is required to gain sufficient insight into, e.g., the fascinating near wake flow. Obtaining this insight and making progress on the items discussed at the end of the previous paragraph would be much easier if a model of this complex flow existed. On the other hand, the model can only be formulated after sufficient flow visualization is accomplished. This paper represents one stage in this iteration process.

FLOW VISUALIZATION TECHNIQUES

In our experiments we visualize the flow in the following ways: (1) the optical-surface indicator method giving plan-view shadowgraphs that show surface flow patterns and shock fronts; (2) the conventional surface indicator method providing the flow pattern on the protuberance; (3) conventional, side-view shadowgraph and schlieren methods showing the trace of the shock surfaces and an indication of the edge of the boundary layer; (4) the vapor screen method giving shock surfaces, a boundary-layer edge and, to some extent, vortices. Because of the constraints of the wind tunnel facility and for reasons of time and economy, we could not fully exploit all of these techniques. Most of our data was obtained with (1), considerably less with (3) and (4), and the least with (2). A more effective tracer method than the vapor screen technique is needed.

The tests were conducted in one of the continuous, supersonic wind tunnels at B.R.L. The interactions were studied by placing the protuberances in the wall boundary layer, having a typical thickness of 2.5 cm. The essence of the optical-surface indicator method requires mounting the obstacle on a tunnel window which is in the sidewall. Obtaining the side-view shadowgraph and schlieren pictures requires placing the obstacle on the floor (or ceiling) of the tunnel. To determine the properties of and compare these boundary layers, pitot pressure surveys were made with no protuberance in the flow. The data were taken at the point where the center of the protuberance would be. Figure 1 shows one set of the results; a separate report will contain all of them. The 99% velocity thickness, δ, is given as a function of unit Reynolds number, R/ℓ, and Mach number, M, for the sidewall and floor boundary layers. The only significant difference between these occurs at M = 3.50 for the lowest value of R/ℓ. We suspect the same trend exists at M = 4.50 but the results at small R/ℓ are not available for the sidewall boundary layer. Similar comparative results and trends are shown for displacement and momentum thickness. Thus for most test conditions a valid quantitative comparison can be made between results for the protuberance in the two locations.

The optical-surface indicator method will be described briefly; for more details see Refs. 6 and 7. The obstacle is mounted on a test section window which is in a vertical plane. Figure 2 shows a schematic view of the experimental set-up and a sketch of some features of the flow over a small protuberance. A small amount of lightweight, transparent oil is placed on the window before and/or after the flow is started. After the surface flow pattern is established, typically in 1 minute, a shadowgraph or schlieren picture is taken; we refer to these as plan-view pictures. They show the surface (window) flow pattern and parts of the shock surfaces. An example is shown in Figure 3. The relation between the streaks and flow near the surface is discussed in Ref. 10.

The window used for these tests is one that has several pits and scratches from long use but is otherwise a "schlieren quality" window. The window defects will be evident on the shadowgraphs to be shown. The model is bolted to the window. Schlieren pictures are taken by flashing a BH-6 tube. The schlieren light source and one parabolic mirror are used for continuous viewing on a frosty mylar screen. Shadowgraphs are taken with a spark light source of 1 μs duration.

Several methods of introducing oil onto the window are used. In the first method a light machine oil is sprayed on the window in a fine mist, usually upstream of the region where the primary separation of the boundary layer occurs. A second technique is to place regularly spaced dots on the window, usually near the model. A third method of introducing oil made use of a static pressure tap located 40 cm upstream of the model. Two or more drops of light machine oil are aspirated into the tunnel wall boundary layer. Some of the oil flowed along the wall and window and some atomized into the flow off the wall. The mist formed in this manner was carried in the flow to the region immediately upstream of the protuberance. Some impinged on the window, thus drawing the surface streamlines, and some was deposited on the protuberance. This was the only way that an attachment line, labeled A below, could be consistently visualized.

The clearest definition of the surface flow pattern is obtained when the oil drops are drawn out into streaks of height 0.1 mm or less. The intensity of the image of the streak is then about 50% of the undisturbed intensity; it appears gray. If the cross-section of the streak is such that its image is almost opaque, the spacing must be considerably greater to obtain a clear pattern, which decreases the resolution.

The observed variation in intensity can be predicted approximately by geometrical optics calculations[7].

In Figure 3 most of the streaks are gray. Several prominent features are labeled. The attachment line A is difficult to see in a reproduction unless the region is enlarged, see Refs. 1 and 7 for examples of that. If oil is placed near and upstream of the model before flow is started, it is mostly wiped away by the time a shadowgraph is taken. If oil is introduced through the pressure tap, a clear image of A is obtained for a few minutes. This is the region of highest shear and, from the results of other investigators, e.g., Ref. 8, highest heat transfer. Further discussion of this is given in a later section. As in all shadowgraphs, a shock wave surface will produce a shadow only if there are light rays at nearly grazing incidence to the surface. Since the cylinder in Figure 3 is a large protuberance, the shock pattern is not like the side view sketched in Figure 2. It consists of a bow shock which intersects a separation shock, well below the top of the cylinder, resulting in a Mach stem plus other complex structure. A visualization of this will be shown in Figure 5. For the conditions of Figure 3, the bow shock is steady and hence has a distinct shadow; the Mach stem is unsteady which explains its irregular shadow. This unsteadiness is shown in our side-view shadowgraphs and has been found by other investigators. The dominant frequency of the oscillation, from other kinds of shock intersection studies, is probably on the order of 1000 Hz. The shear at the wall, which forms the surface flow pattern, has a dominant frequency which is presumed to be much less At any rate a surface indicator method can only give an indication of an average flow pattern.

The usual surface indicator method of coating the model with a pigmented oil was used to observe the flow pattern on the protuberance. A variation of this, which incorporates the idea of taking a shadowgraph of transparent oil streaks, was also used. The model was wrapped with a transparent plastic sheet and oil was introduced through the upstream pressure tap with flow in the tunnel, as explained above. At the end of the run the wrapping was removed and a shadowgraph of it was taken. Obviously this method is only convenient if the surface of the protuberance is developable. Surface flow patterns on the front half of a large and a small cylindrical protuberance are shown in Figure 4. Somewhat different patterns are obtained for a large cylindrical protuberance depending on k/δ, D/δ, M, and R/ℓ, see, e.g., Refs. 8 and 11. The pattern shown in Figure 4A is like that of Ref. 11 except for the upper portion. In that reference k/δ was large enough so that the circumferential, 2-D flow, was approached. We are unaware of other work that shows the surface flow patterns on a small protuberance. A distinguishing feature of the pattern shown in Figure 4B is the attachment point on the central generator at the top of the cylinder. There is an intimate relation between the separation line near the bottom of each cylinder and the attachment line A mentioned above; this will be discussed later.

There is no need to discuss the side-view shadowgraph and schlieren visualizations except to say that a sampling of the unsteady behavior of the Mach stem and some weak waves from the separated shear layer was obtained by taking a sequence of shadowgraphs using the 1 μs light source.

The vapor screen method is the only tracer method available for the flow under consideration, leaving aside the use of tufts. It is described fully by McGregor in Ref. 10. Our version of the method is different from the standard practice only in the way the light sheet is generated. This is done in a simple fashion[12] using a low power CW laser (e.g., 15 mW), a cylindrical lens (a glass rod is adequate), and a small slit to cut off some undesirable side bands of light. Some further details of this are given in Ref. 7. The small diameter beam is diverged by the lens into a sheet of thickness equal to the beam diameter. The sheet is rotated by rotating the lens and is easily translated because the apparatus weighs little.

In the vapor screen method one observes the light scattered by the liquid or solid particles which are usually water. Shock waves and vortices are easily detected. An example is shown in Figure 5. The illumination is determined by the density of scattering centers and this is changed by mechanical and thermodynamic effects. Near the window heat transfer effects also enter. These heat transfer effects, together with the fact that some of the vortices we wish to see are small and closely spaced, have prevented us from resolving some of the more interesting flow patterns. Finally, care must be taken if quantitative results are desired since the condensation process alters the flow properties.

MODELS AND TEST CONDITIONS

The tests were conducted in one of the continuous, supersonic wind tunnels at B.R.L. The test section is 33 x 38 cm in cross-section and the protuberances were mounted on the 38 cm wall. Data were taken at M = 1.5, 2.5, 3.5, 4.0, and 4.5, but mostly at M = 2.5 and 3.5. The unit Reynolds number was varied over the allowable limits which are shown by the values in Figure 1. The stagnation temperature is nominally 90°F. The experiments were performed using obstacles of simple geometrical shape: circular cylinder, hemisphere, parallelepiped, truncated cone, and bar. The last was used in a study of side plate design so that the flow over a projectile rotating band could be simulated; that work will be reported separately. For the first four obstacles we also added a small perturbation to the basic shape but space limitations preclude discussion of the results. For the same reason we give no details for the flow patterns about the hemisphere, parallelepiped, and truncated cone. Table I gives the dimensions of the models, the notation used in referring to them (e.g., 2C), and the symbols used when plotting results for several models on the same figure.

PRIMARY SEPARATION

One of the quantities of main interest in obstacle-boundary layer interaction is the extent of the separated flow. This boundary is called the primary separation line. This would be required to estimate the loads on the surface. If the obstacle is a large cylinder or fin, so that there is a plane of symmetry in the flow, the distance from the leading edge of the obstacle to primary separation, S, can be used, together with some empirical correlations, to estimate the position of the triple shock intersection and the maximum pressure on the leading edge. This was done by Westkaemper[5]; the estimate of pressure was 20% high in one case. We shall only present data for S in this section. The primary separation line is easily determined from our plan-view shadowgraphs but it is only practical to discuss the behavior of S. Because

we simultaneously visualize the bow shock, correlation of it with the primary separation line is straightforward. This will not be presented here; we only remark that the measured bow shock detachment distances for models 1D and 2D agree with those in the literature for 2-D flow over cylinders to within 5%.

A question arises as to how separation is defined from experimental measurements. In the kinds of flows considered here it has been defined using pressure or heat transfer distributions, side-view schlieren or shadowgraph photographs, and surface indicator techniques. The fact that these give different results has been discussed in the literature (especially for 2-D flows); we will not elaborate on this. Note that Price and Stallings[13] make a distinction between the disturbed flow region, as determined by pressure measurements for example, and the separated flow region, as determined by surface indicators. General use of such a convention would obviate confusion. Unsteady effects, which certainly exist in the flow, will affect the experimental definition of separation in different ways for the various measurement techniques. Suffice it to say that the surface indicator technique, with its extremely slow response time, gives an indication of an average surface flow pattern that is clear and repeatable. Unsteadiness in flows of the type considered here is discussed in Ref. 4 with respect to static pressure measurements; the conclusion is reached that the pressure distributions are not repeatable.

The accuracy of the measured values of S is, in most cases, ± 1%. At the lowest stagnation pressures (i.e., R/ℓ) at each Mach number this becomes ± 3%. These error bounds include effects from both repeatability of the pattern and reading accuracy. Additionally, there is a slight amount of geometrical magnification in the images on the shadowgraph because we use the diverging light from the spark source. This systematic error is easily accounted for. Most often this correction is negligible, but in some cases it amounts to 5% in the ratio S/D.

The primary separation distance, for cylinders say, is a function of the following variables: D, k, δ, free stream velocity, U_k (for small protuberances), kinematic viscosity, sound velocity, density, and a measure of the turbulent shear. We have no measure of the turbulent shear and we find that U_k is not significant as an independent variable, so these are left out of the dimensional analysis. This yields

$$S/D = f(k/D,\ D/\delta,\ R_D,\ M);$$

where R_D is Reynolds number based on D and free stream velocity. Of course this can be written in other, equivalent forms, so that, e.g., k/δ and R_k appear as two of the four non-dimensional parameters. It is often convenient to use the three ratios of lengths even though they are not independent. Likewise, three Reynolds numbers could be defined. We do not have enough points in parameter space to tell which of these is most meaningful. The variation of S/D with any of these Reynolds numbers is weak compared to the other three non-dimensional parameters.

Curves of S/D vs. k/δ are given in Figure 6 to show the approach to an "infinite length" cylinder. For each of the curves three of the four possible dimensionless parameters are constant, viz., D/δ, R_D, and M. From the data in the literature, and as expected, S/D approaches a constant as k/δ increases. If a large protuberance is defined on that basis, then clearly models 1D and 2D, with $k/\delta = 4.5$, are large. Other definitions are possible, e.g., requiring 2-D flow on some portion of the cylinder. On that basis these models are not large, see the cylinder surface flow sketched in Figure 4; a much larger k/δ would be needed. We shall adopt the definition based on S/D. These results in Figure 6 show that the rate of approach to the asymptote depends on D/δ.

The same conclusions are reached if the data for M = 3.5 are plotted in the same way. Instead this data is presented in Figure 7 with the roles of k/δ and D/δ interchanged. Again, models 1D and 2D with $k/\delta = 3.69$ are large protuberances; the variation of S/D with D/δ is only slightly larger than the estimated error in S/D. Thus these two data points are consistent with the results of many other investigators, viz., that S/D is independent of D for a large cylindrical protuberance. Contrast this with the conclusion for the small protuberance, e.g., S/D changes by more than a factor of 2 for $k/\delta = 0.37$. The simple and satisfying scaling law valid for large protuberances is not valid for small ones.

Another conclusion reached in some other studies of separation caused by large, cylindrical obstacles is that S/D is weakly dependent on M. This dependence, for the large cylinders, 1D and 2D, is shown in Figure 8. The variation in S/D is more than 50%; whether or not this is a weak dependence is a matter of interpretation since the term is not a precise one. The data points are connected with straight lines as a reading aid. For the small protuberances a variation of S/D with M is established only for model 2B; but the trend of increasing S/D with M is clear for all models. Note that, even though R/ℓ is constant, δ varies because M changes. Thus the change of S/D with M and k/D, shown in Figure 8, is effected by other parameters.

The following two figures are presented to give a partial evaluation of the correlation for large protuberances proposed by Westkaemper[5] and to see to what extent our small protuberance data agrees with it. In Figures 9 and 10 data for S/D vs. k/D are shown together with the correlation of Ref. 5, already discussed in the Introduction. Since R/ℓ and M are fixed in each case, δ is constant. Points for constant k/δ or D/δ can be connected with the help of Table 1. At M = 2.5 our two points for large k/δ are well below the correlation, as are the two from Ref. 4 and the five points from Ref. 14; the latter are for an "infinite effective height" but unspecified k/D. The data from these two references are for the same M but for a larger R/ℓ; they were determined using surface indicator methods. The small k/δ points bear little relationship to the correlation as might be expected; Westkaemper[5] cautions against using the correlation for cylinders "that do not extend to the outer edge of the boundary layer." From our previous discussion (Figure 6) the condition would be more restrictive than that. Thus at M = 2.5 the correlation is not very successful. The situation is a little better at M = 3.5. Our points are closer to the correlation but the two points from Ref. 4 are not. The latter are for M = 3.0 and 4.0. Our data, for M = 1.5, 4.0, 4.5, are consistent with the trend shown in Figures 9 and 10. The data points for the large protuberances agree with the correlation for M = 4.0 and lie above it for M = 4.5. The data, from various sources, used in establishing the correlation extend over the range $2 \leq M \leq 20$, but separation was determined in several ways

in the different sources. In several of these, separation was determined by noting the first change, in a pressure or heat transfer gauge reading, from the undisturbed, upstream reading. That method will give a separation distance larger than the surface indicator method. The latter was used by Westkaemper[5] to obtain his own data points that went into the correlation. The surface flow pattern was visualized in his experiments by injecting a liquid through an orifice upstream of primary separation. From a photograph of the pattern it is seen that a horseshoe vortex from the injection orifice interacts with primary separation; this has been noted by others, see, e.g., Ref. 7. This interaction will introduce an error in S of unknown amount. If the interference of the orifice vortex and wake flows with primary separation acts to increase S, then some unclear points about the correlation could be understood.

Regardless of the agreement of the data with this particular correlation, it is evident that the spread in the data for small protuberances is reduced most by plotting S/D vs. k/D. One tentative possibility for correlation, including small and large cylinders, would be to consider S/D as a function of k/D for fixed M, but variable Reynolds number; e.g., by fairing a curve through the points of Figure 9. A wider range of the other parameters, D/δ, etc., is needed to arrive at a more firm conclusion. The result that S/D is almost independent of D but depends on M for large cylindrical protuberances is reasonable if the inviscid pressure field is considered. There is then only a bow shock and its detachment distance, Δ, scales with D. The pressure change across this nearly 2-D shock is independent of D but depends on M. Thus the pressure gradient imposed on the boundary layer has the same dependence. For the small cylindrical protuberances, the inviscid flow bow shock position depends on k/D and M and the pressure change across it depends on M. Therefore, it is reasonable that, for this case, k/D and M have a significant effect on S/D. That is what our data show.

Variations of S/D with a Reynolds number will not be shown. To obtain a significant change in, say, R_D by changing D and also keeping the other dimensionless parameters approximately constant, would require many more models than we have used. Because of limitations of the wind tunnel and small changes in δ with R/ℓ, even a factor of two change in R_D would be difficult to achieve. Therefore, changes in R/ℓ must be utilized. Examples of S/D vs. R/ℓ are included in the figures discussed in the next section. For all of our models the conclusions are that: (1) for fixed D and k, S/D changes by 30% at most for the maximum allowable variation in R/ℓ, with most of that change taking place at the lower end of the range of R/ℓ; (2) S/D sometimes decreases while for other models it increases as R/ℓ increases; for several models S/D is a non-monotonic function of R/ℓ. This variety in the behavior of S/D is related to the changes in the flow structure as R/ℓ is varied.

FLOW STRUCTURE

Detecting the magnitude and kinds of changes of S/D with R/ℓ just mentioned by means of pressure or heat transfer measurements on the surface would be extremely difficult and impossible using side-view shadowgraphs. With conventional surface indicator techniques it is more likely, but this has not been done. The optical-surface indicator technique can detect this behavior without much difficulty when used with a little care; it visualizes many other features of the flow, many of which are discussed here.

Upstream For convenience we shall divide the flow into the regions upstream and downstream of the center of the cylinder. It is best to start the description of the upstream flow in the plane of symmetry and its neighborhood. Separation and attachment lines have a special appearance in that plane. The 3-D vortices implied by these lines have helix-like streamlines and the pitch of the helix goes to zero as the symmetry plane is approached. Because of symmetry, there is no flow across this plane but there is flow out of or into it so that streamlines can appear to end in a side view of this plane, being tangent to it. We shall use the same symbol, e.g., S for primary separation, to represent a point in the plane of symmetry, its distance from the leading edge of the cylinder, and its continuation as separation or attachment lines. These lines show that there must be vortices off the surface and it is convenient to describe the flow structure in terms of the number of these vortices. There would be additional vortices further off the surface which leave no trace; the complete flow off the surface is discussed later.

An example of two vortices is shown in Figure 3; there is one separation point, S, and one attachment point, A, in the plane of symmetry. The two-vortex pattern is most often found in turbulent boundary layer-obstacle interactions. The streamwise extent of the large vortex is about 25 times that of the small one.

For a given small or large cylinder, at fixed M, the number of vortices changes with R/ℓ. Our results show as many as 6 of them. The separation and attachment lines for 6 are shown in Figure 11a; the change to 4 and then to 2 is sketched in Figures 11b and 11c. Note that S and A are always present, but the structure between them changes. A plan view shadowgraph obtained by the optical-surface indicator technique is shown in Figure 12, as an example of 6 vortices. The sequence in Figure 11a, b and c illustrates the number of vortices decreasing as R/ℓ changes. These sketches are not to scale, but the sequence is that shown in Figure 13 as R/ℓ increases. We shall refer later to a 4-inner vortex configuration. This denotes the situation of 11b wherein A2 and S2 are not present. If A1 and S1 have disappeared, but A2 and S2 remain, this is called a 4-outer vortex configuration.

The distances from the cylinder leading edge to these points, normalized with D, are shown in Figures 13, 14, and 15. The abscissa is the stagnation pressure P_o, which, for fixed M, is proportional to R/ℓ; a value of which is noted to facilitate conversion to R/ℓ. In particular the variation of S/D with R/ℓ, discussed in the last section, is given. The scatter in S/D for the low values of P_o, mentioned before, is also illustrated. The most difficult position to determine is A2. The main problem is to introduce the oil in such a way that there is some in the neighborhood of A2 after flow is established. If oil is aspirated into the tunnel, after flow is established, some will reach S2 but a clear pattern at A2 is not obtained. In Figures 13 - 15 straight lines connect the points or their average, for ease in following the trends. In addition, dashed lines are used to extend the trend. The paths followed by the various points will be described for Figure 13. At the lowest P_o there are 3 attachments and 3 separations, therefore 6

vortices. Point A stays fixed; it is associated with S and is always present. The distance S decreases suddenly between 35 and 50 cm Hg and thereafter changes little. This decrease appears to be related to the disappearance of A2 and S2 which takes place for P_o between 35 and 40 cm Hg. Point A1 does not change much but S1 approaches it and then they disappear. This is the sequence of events depicted in Figure 11. The sequence is different in Figure 14, which shows the same type of data for the same small protuberance but for M = 3.50. For $P_o \leq 150$ the 4-inner vortex structure exists, but disappears for $P_o > 150$. The 4-outer vortex structure appears for some $P_o \leq 150$. For $P_o = 150$ we have 6 vortices. As P_o increases the number of vortices goes from 4 to 6 to 4 to 2. That such phenomena also take place for large protuberances is shown by Figure 15 which is for M = 3.50. The paths of the points are very much like those in Figure 14. There is no data in the small range of P_o between the 4-inner and 4-outer structures, so we cannot definitely say that 6 vortices exist. For the three cases illustrated and the others where we have enough data to draw conclusions, the relatively rapid decrease in S/D for a small increase in P_o is associated with the disappearance of A2 and S2.

The details of the process by which an attachment and a separation line merge and then disappear, in or near the symmetry plane, have been observed. From these visualizations the sketches shown in Figure 16 were drawn, for a 4-inner vortex structure. Parts a and b illustrate the motion of A1 and S1 towards each other. When they meet, part c, an unusual pattern is obtained; it is like one-half of the pattern that would be obtained at a nodal point of attachment juxtaposed with the separation line; Ref. 7 for an example. Upstream of S, the pattern is like that shown in Figure 4b. Finally, S1 bifurcates so that near the plane of symmetry the separation line has disappeared and there is flow through the center of S1. The two branches of S1 are still separation lines; they are similar to the open type separation lines that have been found in the flow over inclined bodies of revolution, see for example Ref. 15.

We have not yet detected any regularity in these changes in flow structure. They occur for rather small variations in Reynolds number. This suggests there may be a delicate balance in the flow which is upset by changing R/ℓ so that one structure easily changes to another. Note that the results of Figures 13 - 15 are repeatable from test to test and can be obtained either by starting tunnel flow at a certain P_o or varying it continuously during a test. Therefore, it would not seem proper to call these changes an unstable behavior. Similar flow structure changes have been observed in low speed, laminar flow over small protuberances; e.g., in Ref. 9. Norman states that "We have seen one, three, five, and even seven steady vortices forming in front of upright cylinders and fences of varying widths as k/δ and/or U_∞ increased." He observed the changes in the number of vortices to occur in "discrete jumps." The odd number of vortices observed by Norman is consistent with our even number. He did not observe the small vortex at the base of the protuberance, or the attachment point A; the size of this vortex makes such observation difficult.

We shall now discuss the flow off the surface but still in the neighborhood of the plane of symmetry. This involves some conjecture since we mostly have surface data; the vapor screen technique could not resolve the multiple vortex structure just discussed. Elementary fluid dynamic reasoning allows possible vortex structures to be determined. An attempt at this was made in Ref. 6, with insufficient surface data to support the conjecture. We use the work of Norman[9] to aid our conjecturing and give it a more firm basis. His careful use of the smoke technique gave him some beautiful views of streamline patterns. Some of these are shown and discussed by Morkovin[16]. From the visualization in the neighborhood of the plane of symmetry, two possible models of the vortex structure were determined, called the "jet-maze" and "stairstep" models; the former was preferred. We have adapted and modified his rendition of the jet-maze model, with 6 vortices, in Figure 17a. The modifications are: (1) we have no attachment point on the protuberance, since the surface flow on small cylinders showed none, see Figure 4b; (2) we have separation near the base at point P for the same reason; (3) we have an attachment point, A, already discussed. The sketches are not to scale and the streamwise dimensions are magnified compared to cross-stream dimensions for clarity. For the same reason the shock surfaces are omitted. Figures 17b, c, and d show the 4-outer, 4-inner, and 2 vortex structures assuming the jet-maze model applies to all of them. The distances from the junction of the plane and cylinder to points A and S are approximately equal. But A and S cannot be connected by a streamline to have a closed vortex, by conservation of mass. The flow near A comes from high energy flow near the edge of the boundary layer, which is probably why the high shear exists there, as discussed before. In Winkelman's experiments[8], A is in the center of the highest heat transfer region on the surface. Norman[9] did see a smoke line following the tortuous path leading to A2 in 17a, which is not present in the stairstep model. In our experiments, when oil is introduced through the pressure tap, some is deposited near S1, A1, S2, and, to a lesser extent, near A2. Since we have no quantitative measure of the distribution of droplets through the boundary layer, this information does not allow a deduction in favor of either the jet-maze or stairstep model. To appreciate Figure 17 it is well to refer back to Figures 11 - 15. The delicate balance of the vortex structure, mentioned above, may be associated with the existence of the free stream stagnation points shown in Figure 17.

If we now briefly consider the flow away from the symmetry plane, the primary separation line, S, remains distinct over the field of view. But for some of the smaller models, for which more of the flow field is visible, this line becomes very hard to distinguish. The attachment at A continues as a fairly distinct attachment line to at least behind the model, see Figure 3. The other attachment lines, when they exist, become less distinct more quickly. This is also true for S2, but usually not for S1, which may mean that S2 lifts off the surface but S1 remains near it. A vapor screen photograph, with the light sheet perpendicular to the cylinder axis, clearly shows one horseshoe-shaped dark region indicating that the horseshoe vortex remains intact to at least 3 diameters downstream. Some painstaking work gave Norman a visualization of his flow around the side of the obstacle and some sketches of the vortex structure. These could help us interpret our surface patterns but this will not be done here.

Downstream This part of the flow contains a number of fascinating features, some of which will be briefly discussed. More detail will be given in a separate paper. Outside the wake there is still at least one vortex, meaning one leg of the horseshoe vortex. A secondary separation line exists even if there is

none immediately upstream of the model. The horseshoe vortex, in fact, persists for hundreds of protuberance heights downstream[1]. The near wake patterns of all of our small protuberances listed in Table 1 are the same, topologically. From this statement it can be seen that model 1C should not be called small as it was in our definition; actually, it is perilously close to being large, see Figure 6. A sketch of one of these patterns is shown in Figure 18. An attachment line is shown as a dashed line; this is almost certainly the impingement of the flow that separates from the top and/or the sides of the protuberance. Flow from this attachment line, in addition to other parts of the flow field as shown, feed into the two large dots in a swirling manner. In the shadowgraphs we see two oil accumulation dots, as in Figure 3; this shows a large protuberance flow pattern but the phenomenon is the same. The small protuberance near wake surface pattern illustrates Morkovin's base flow-through module[16] for high speed turbulent flow. Some further discussion of this can be found in Ref. 1. Suffice it to say that these dots appear for all of our small-obstacle near wake flows. They are the surface traces of the two tornado-like vortices discovered by Gregory and Walker[17]; they rise up from the surface, bend over into the free stream direction, and continue as the trailing vortex pair. For different orientations of the light sheet, the vapor screen shows only a dark region in the new wake; apparently it cannot resolve this complex structure, at least not near a wall. When the sheet of light was placed normal to the surface (and free stream) at distances between 1.5 and 4.0 diameters downstream of the cylinder leading edge, contrasting light and dark regions were observed. Specifically, a dark region of oval shape was seen; the width to height ratio was typically 3.0. The long axis was parallel to the surface and the bottom was roughly (0.1) k off the surface. The position of the two ends, along the major axis of the oval, correlates with attachment lines in the oil flow surface pattern. If the trailing vortices remained stable we would expect to see two distinct, dark regions indicating their cross-sections. We suppose there are two such regions which are not resolved; this requires more investigation. The surface pattern, as seen in Figure 18, is consistent with the conjectured interpretation. If the direction of rotation observed in the vortices normal to the surface (the dots) is continued downstream, as in the trailing vortices, then the centerline of the wake would be a separation line and there should be two, symmetrically located attachment lines. This is what we observe, as in Figure 18, for all small protuberances. Since our shadowgraphs for all small protuberances show the two dots and separation along the wake center line, we are fairly certain that the above conjecture is correct, at least in an average sense, for the first few diameters downstream. As the vapor screen is translated downstream the dark region changes shape and gradually rises off the surface. The changes in the near wake as R/ℓ is varied are minor. The effect of M is more noticeable; the change from M = 1.5 to 2.5 being greater than that from M = 2.5 to 4.5. These are not qualitative changes, as mentioned at the beginning of this subsection.

In contrast, for large protuberances there are qualitatively different near wake patterns as R/ℓ and M vary; compare the shadowgraph in Figure 3 with the sketch of the near wake presented in Figure 19. For instance the dot-swirl feature is shown in the former but not in the latter. Sometimes we see oil accumulation dots attached to the cylinder, fed in the manner shown in Figure 19. The dots are generally on the model for low values of R/ℓ and move downstream monotonically as R/ℓ increases, at a fixed M. (Figures 3 and 19 are for different values of M.) That no attachment line is observed, such as the one normal to the centerline in Figure 18, is understandable. One feature is common to all of our large protuberance cases, now including model 1C. That is, the centerline of the far wake is always an attachment line. Contrast this with the small protuberance finding. The far wake, as visualized by the vapor screen, is considerably more complex for large protuberances, compared to the small protuberance case. More analysis of our vapor screen results remains to be done. An example of one view of the wake, in a plane three diameters downstream of the leading edge of a large cylinder, is shown in Fig. 20. Some of the intricate detail, at a distance k off the surface, is lost in the reproduction. Near the surface, instead of the dark region being oval-like, as for the small protuberance, it is shaped more like a triangle with curved sides and rounded vertices, with the bottom "side" parallel to the surface. To explain the flow pattern of Figure 19 there must be two vortices in the bottom part of the triangle, with circulation such as to produce the attachment line. Understanding such a 3-D wake requires more visualization of the flow structure.

REFERENCES

1. Sedney, R., "A Survey of the Effects of Small Protuberances on Boundary Layer Flows," AIAA Journal, Vol. 11, No. 6, June 1973, pp. 782-792.

2. Greeley, R., Iversen, J. D., Pollack, J. B., Udovich, N., and W[illiams] B., "Wind Tunnel Studies of Martian Aeolian Processes," Proc. Roy. Soc. Lond. A., Vol. 341, No. [illegible], 10 Dec. 1974, pp. 331-360. See also "Wind Tunnel Simulations of Light and Dark Streaks on Mars," Science, Vol. 183, Mar. 1974, pp. 847-849.

3. Korkegi, R. H., "Survey of Viscous Interaction Associated with High Mach Number Flight," AIAA Journal, Vol. 9, No. 5, May 1971, pp. 771-784.

4. Kaufman, L. G. II, Korkegi, R. H., and Morton, L. C., "Shock Impingement Caused by Boundary-Layer Separation Ahead of Blunt Fins," AIAA Journal, Vol. 11, No. 10, October 1973, pp. 1363-1364. See also ARL 72-0118, Aerospace Research Laboratories, August 1972.

5. Westkaemper, J. C., "Turbulent Boundary-Layer Separation Ahead of Cylinders," AIAA Journal, Vol. 6, No. 7, July 1968, pp. 1352-1355.

6. Sedney, R., "Visualization of Boundary Layer Flow Patterns Around Protuberances Using an Optical-Surface Indicator Technique," The Physics of Fluids, Vol. 15, No. 12, December 1972, pp. 2439-2441.

7. Sedney, R., Kitchens, C. W. Jr., and Bush, C. C., "The Marriage of Optical, Tracer, and Surface Indicator Techniques in Flow Visualization - A Survey," Record of the 1973 International Congress on Instrumentation in Aerospace Simulation Facilities, IEEE Publication No. 73CHC 784-9AES, pp. 155-171.

8. Winkelmann, A. E., "Flow Visualization Studies of a Fin Protuberance Partially Immersed in a Turbulent Boundary Layer at Mach 5," NOLTR 70-93, Naval Ordnance Laboratory, May 1970.

9. Norman, R. S., "On Obstacle Generated Secondary Flows in Laminar Boundary Layers and Transition to Turbulence," Ph.D. Thesis, Illinois Institute of Technology, Dec. 1972.

10. Maltby, R. L., "Flow Visualization in Wind Tunnels Using Indicators," AGARD-ograph 70, AGARD-NATO Fluid Dynamics Panel, 1962.

11. Voitenko, D. M., Zubkov, A. I., and Panov, Y. A., "Existence of Supersonic Zones in Three-Dimensional Separation Flows," Izv. AN SSSR. Mekhanika Zhidkosti i Gaza, Vol. 2, No. 1, 1967, pp. 20-24.

12. Private communication from R. K. Matthews, Arnold Engineering and Development Center, to C. J. Nietubicz, Ballistic Research Laboratories, 1972 and 1973.

13. Price, E. A., and Stallings, R. L., "Investigation of Turbulent Separated Flows in the Vicinity of Fin-Type Protuberances at Supersonic Mach Numbers," NASA TN D-3804, Feb. 1967.

14. Voitenko, D. M., Zubkov, A. I., and Panov, Y. A., "Supersonic Gas Flow Past a Cylindrical Obstacle on a Plate," Mekhanika Zhidkosti i Gaza, Vol. 1, No. 1, 1966, pp. 121-125.

15. Maskell, E. C., "Flow Separation in Three Dimensions," Rept. No. Aero 2565, Royal Aircraft Establishment, Farnborough, Nov. 1955.

16. Morkovin, M. V., "An Approach to Flow Engineering via Functional Flow Modules," Beiträge zur Strömungsmechanik, insbesondere zur Grenzschichttheorie, Porz-Wahn, DLR F Vol. 2, pp. 270-301, 1972.

17. Gregory, N., and Walker, W. S., "The Effect on Transition of Isolated Surface Excrescences in the Boundary Layer," R & M 2779, Pt. I, 1955, Aeronautical Research Council, England.

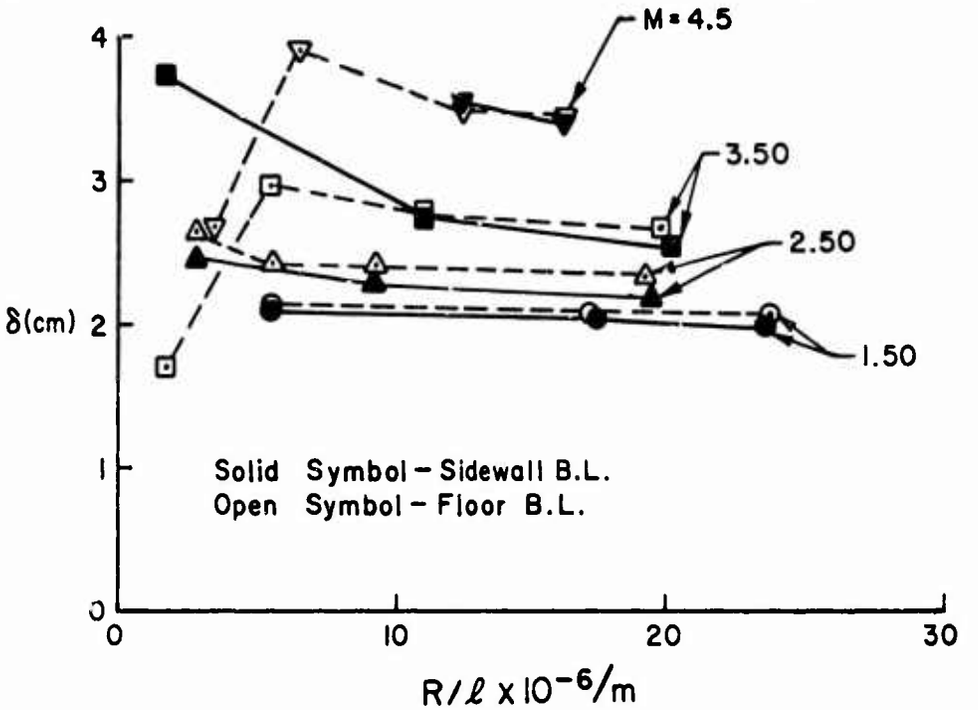

Fig. 1. Boundary-Layer Thickness (δ) vs. Unit Reynolds Number from Pitot Surveys.

Table 1. Model Dimensions (cm), Designation (e.g., 2C) and Plotting Symbols.

CYLINDERS

		A	B	C	D
1	k	1.02	2.03	4.06	10.16
	D	1.91 ♦	1.91 ●	1.91 ■	1.91 ▲
2	k	1.02	2.03	4.06	10.16
	D	3.81 ◊	3.81 ◊	3.81 ◻	3.81 △
3	k	1.02	2.03	4.06	
	D	7.62 ◊	7.62 ○	7.62 ◻	
4	k	1.91 HEMISPHERE			
	D	3.81			
5	k	2.03 TRUNCATED CONE			
	D	3.81 (Base) 1.91 (Top)			
6	k	2.03 PARALLELEPIPED			
		2.54 (Width) 2.03 (Depth)			

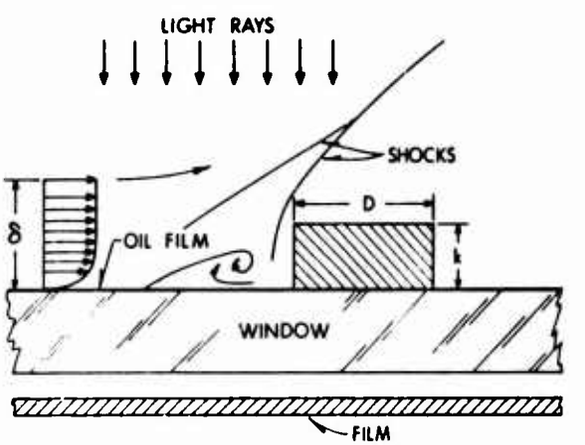

Fig. 2. Schematic of Optical-Surface Indicator Technique Showing Small Protuberance Immersed in Supersonic Turbulent Boundary Layer.

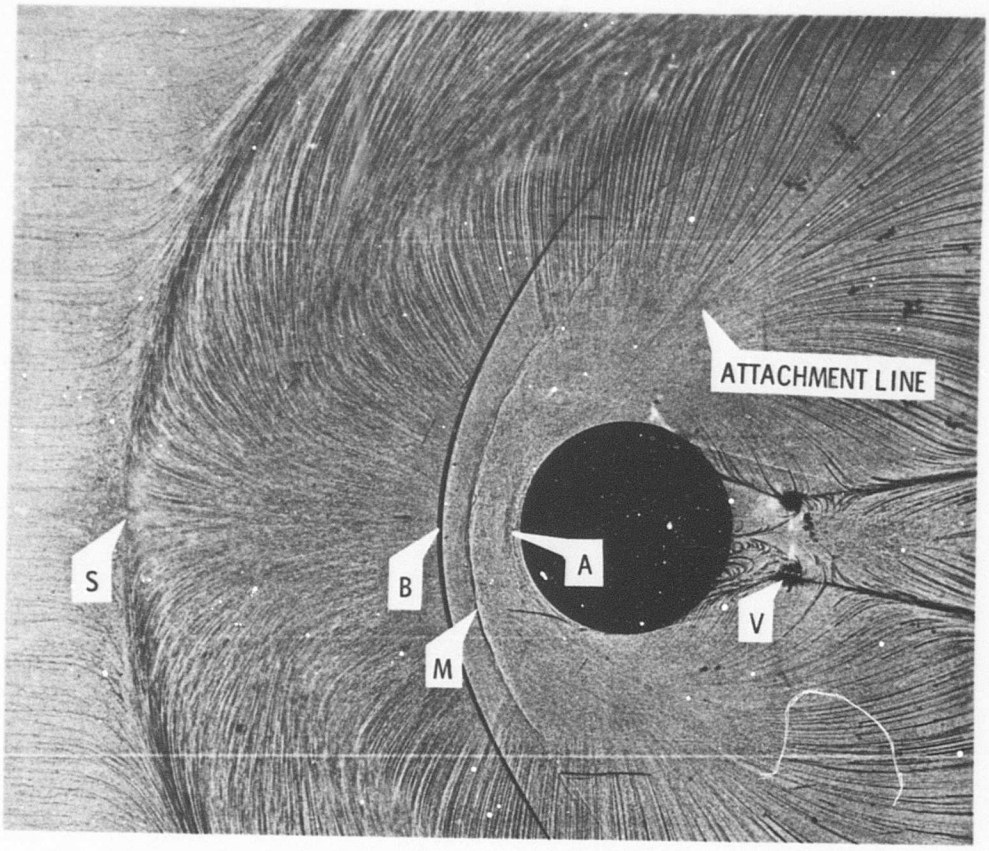

Fig. 3. Plan-View Shadowgraph for Large Protuberance, Model 2D, M = 2.50, $R/\ell = 19.3 \times 10^6$/m. S - Primary Separation, B - Bow Shock, M - Mach Stem, A - Attachment Line, V - Vortex Core. Attachment Line Indicated Originates at Point A.

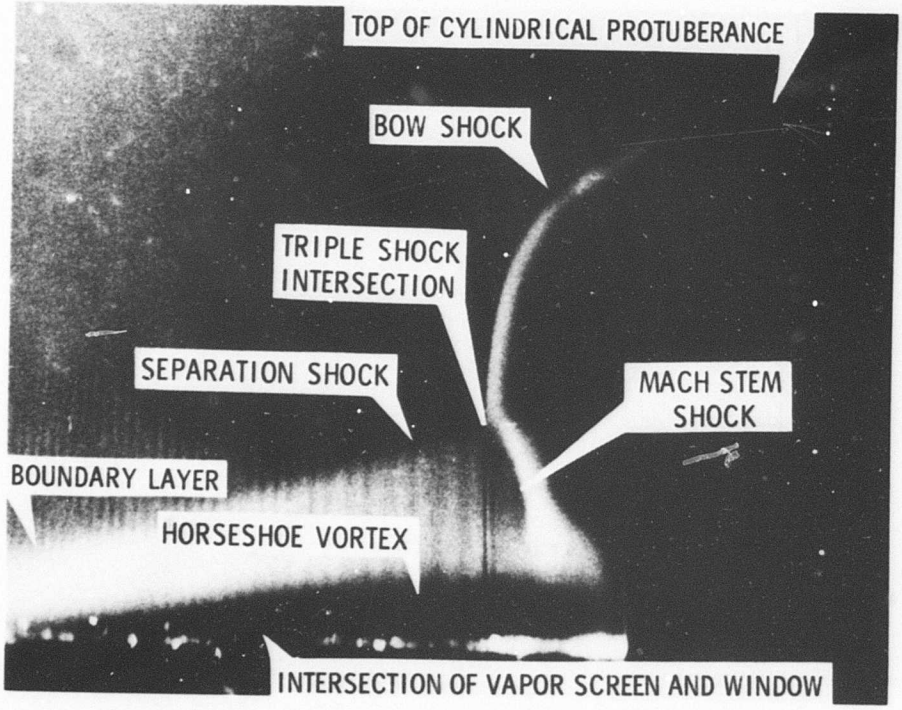

Fig. 5. Vapor Screen Photograph for Large Protuberance, Model 2D, with Light Sheet in Symmetry Plane and Camera at 30° to Sheet, M = 2.50, $R/\ell = 9.3 \times 10^6$/m.

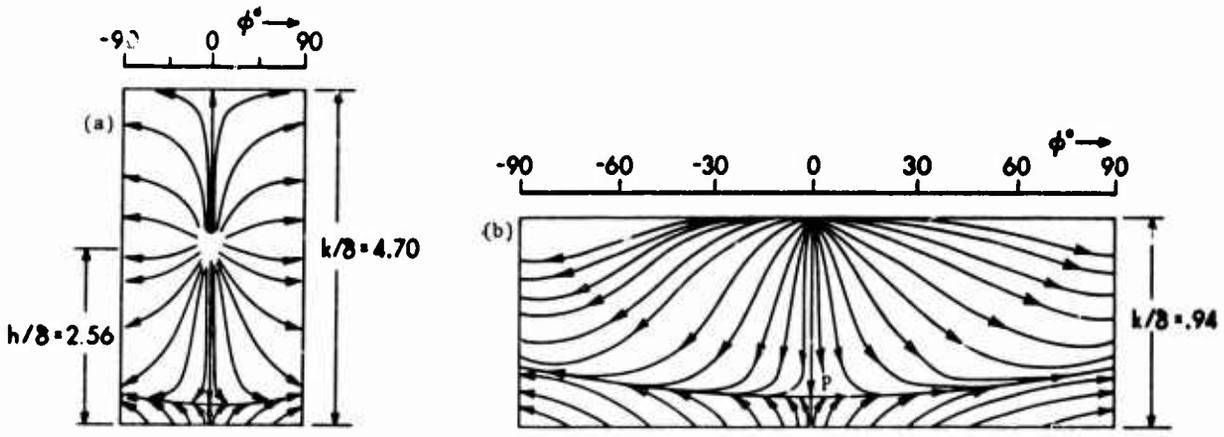

Fig. 4. Sketch of Protuberance Surface Patterns, M = 2.50, R/ℓ = 9.3×10^6/m, δ = 2.25 cm. (4a) Large Protuberance, Model 2D; (4b) Small Protuberance, Model 2B; Protuberance Leading Edge at ϕ = o.

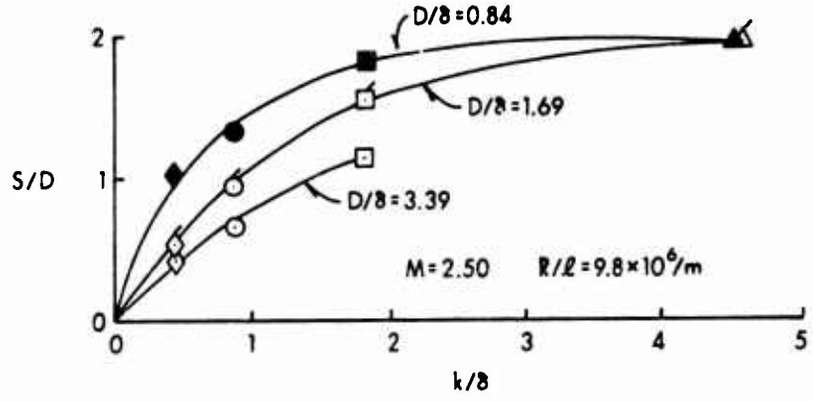

Fig. 6. Primary Separation Distance (S/D) vs. Protuberance Height $(k/\delta)_\ell$, M = 2.50, R/ℓ = 9.8×10^6/m, δ = 2.25 cm.

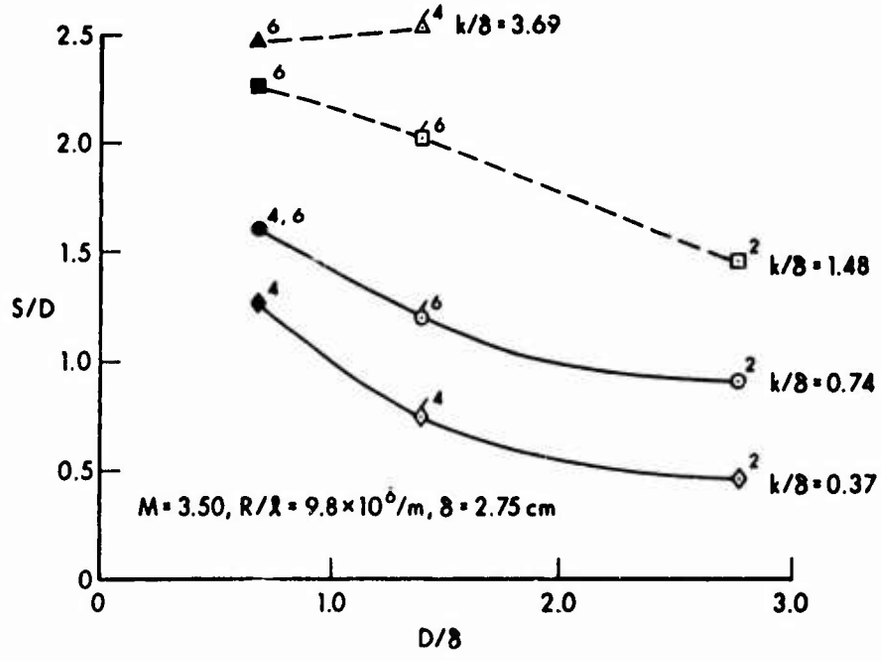

Fig. 7. Primary Separation Distance (S/D) vs. Protuberance Diameter (D/δ), M = 3.50, R/ℓ = 9.8×10^6/m, δ = 2.75 cm.

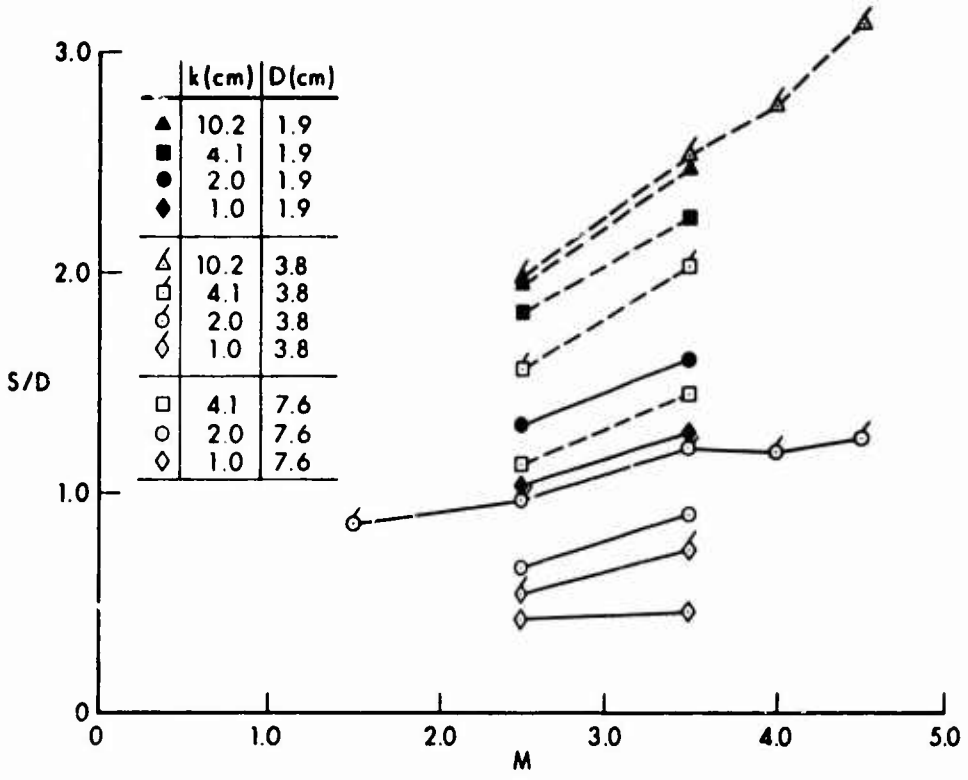

Fig. 8. Primary Separation Distance (S/D) vs. Mach Number (M), $R/\ell = 9.8 \times 10^6$/m.

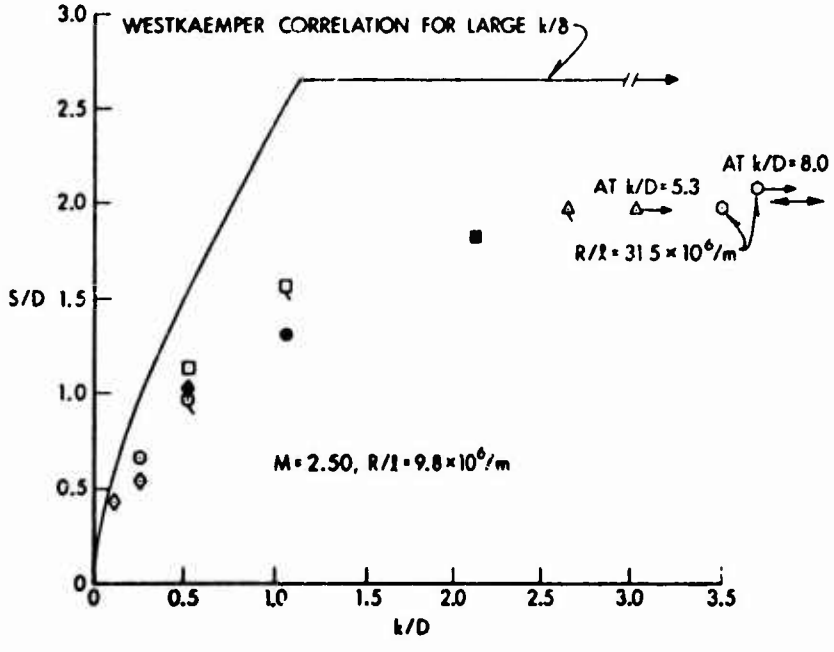

Fig. 9. Primary Separation Distance (S/D) vs. Protuberance Height (k/D), M = 2.50, $R/\ell = 9.8 \times 10^6$/m, $\delta = 2.25$cm. ◯ - Ref. 4; ⟷ 5 Points from Ref. 14.

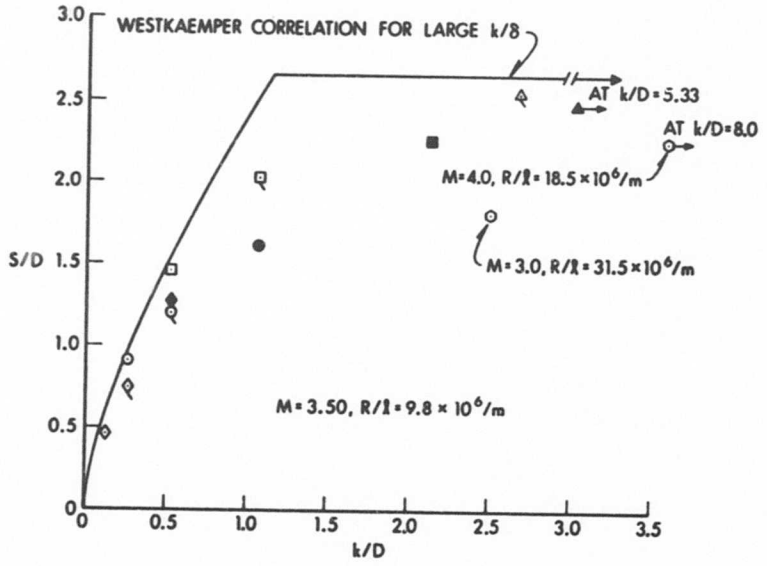

Fig. 10. Primary Separation Distance (S/D) vs. Protuberance Height (k/D), M = 3.50, $R/\ell = 9.8 \times 10^6$/m, δ = 2.75cm. ⬡ - Ref. 4.

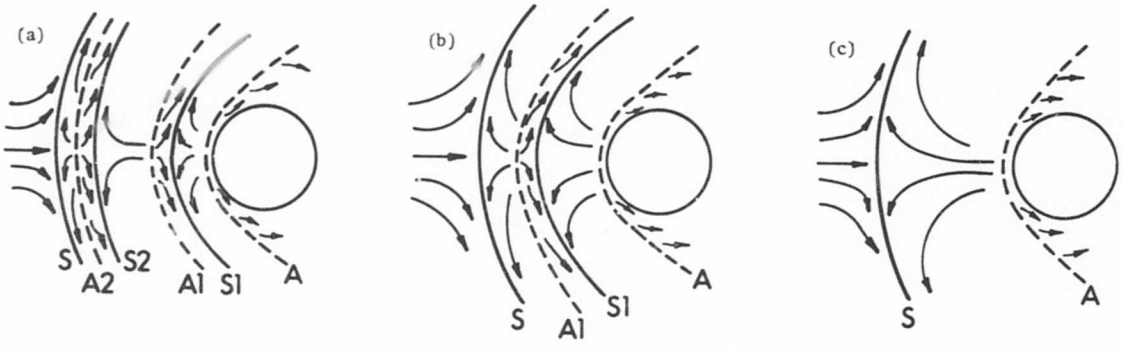

Fig. 11. Plan-View Sketches of Separation and Attachment Upstream of Cylindrical Protuberance; (a) Six Vortices; (b) Four Vortices; (c) Two Vortices.

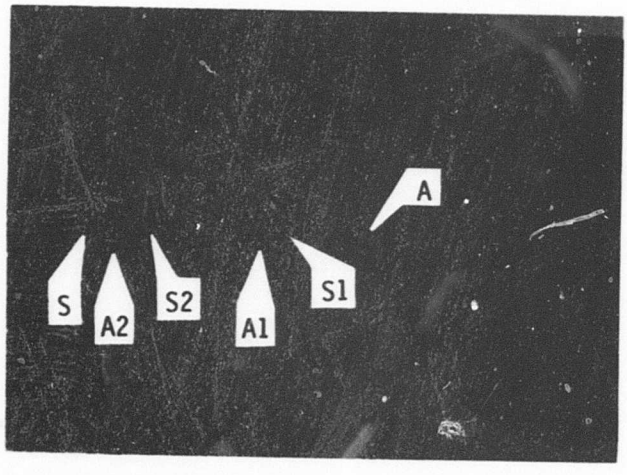

Fig. 12. Plan-View Shadowgraph Illustrating Six-Vortex Configuration for Model 3B, M = 2.50, $R/\ell = 3.0 \times 10^6$/m. S - Primary Separation; S1, S2 - Secondary Separations; A1, A2 - Attachment Lines.

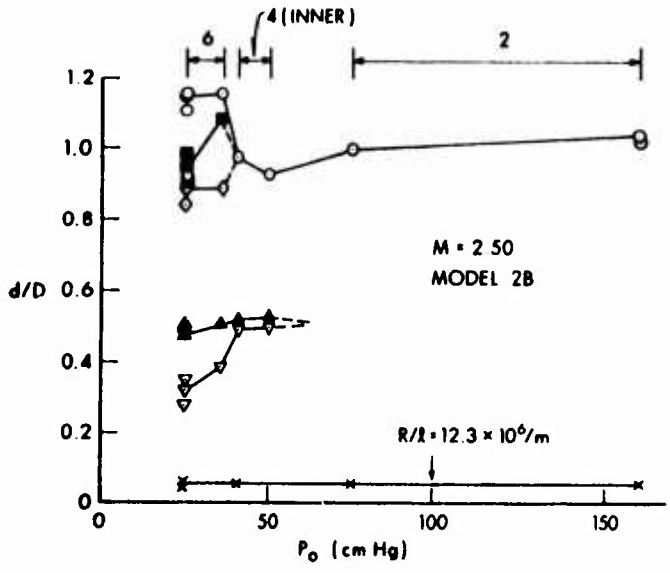

Fig. 13. Position of Separation and Attachment Points vs. Stagnation Pressure (P_o), Model 2B, M = 2.50, $3.0 \times 10^6/m \leq R/\ell \leq 19.3 \times 10^6/m$. Symbols Defined in Fig. 14.

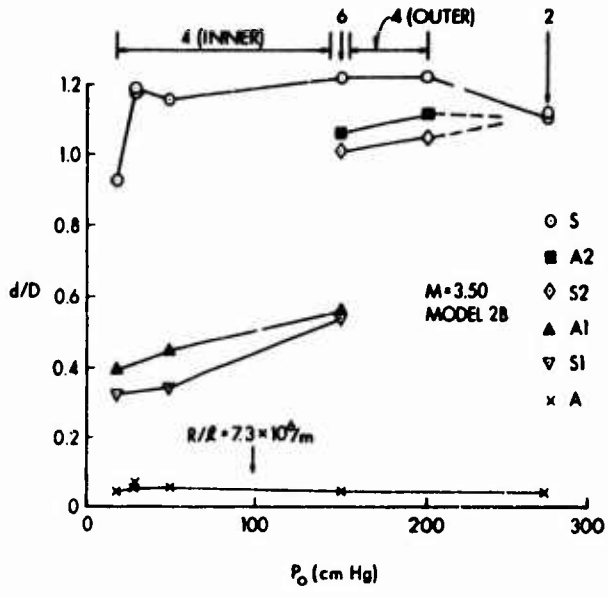

Fig. 14. Position of Separation and Attachment Points vs. Stagnation Pressure (P_o), Model 2B, M = 3.50, $1.8 \times 10^6/m \leq R/\ell \leq 19.9 \times 10^6/m$.

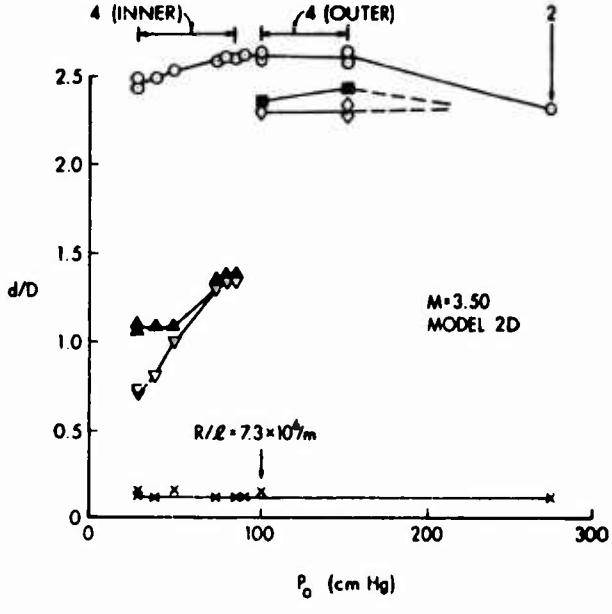

Fig. 15. Position of Separation and Attachment Points vs. Stagnation Pressure (P_o), Model 2D, M = 3.50, $1.8 \times 10^6/m \leq R/\ell \leq 19.9 \times 10^6/m$. Symbols Defined in Fig. 14.

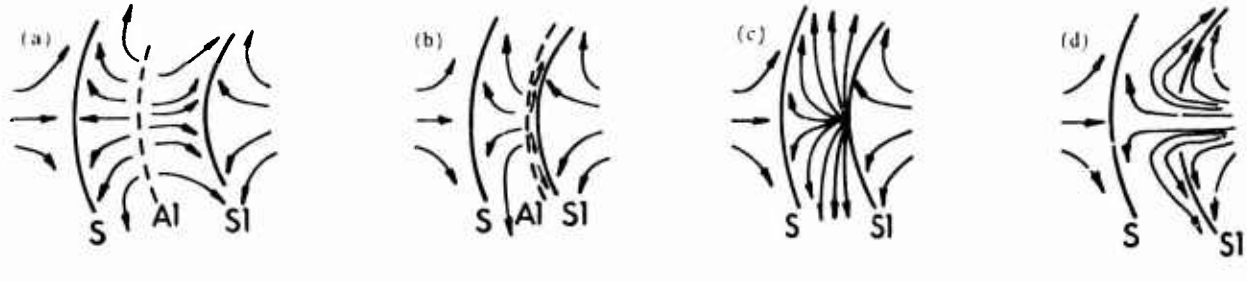

Fig. 16. Plan-View Sketches Showing Merging of Separation and Attachment Lines. (a) Secondary Separation S1 Distinct from Attachment A1; (b) S1 Moves Closer to A1; (c) S1 Merges with A1, Forming One-Half of a Nodal Point of Attachment; (d) Open-Type of Secondary Separation S1, with Flow-Through Center.

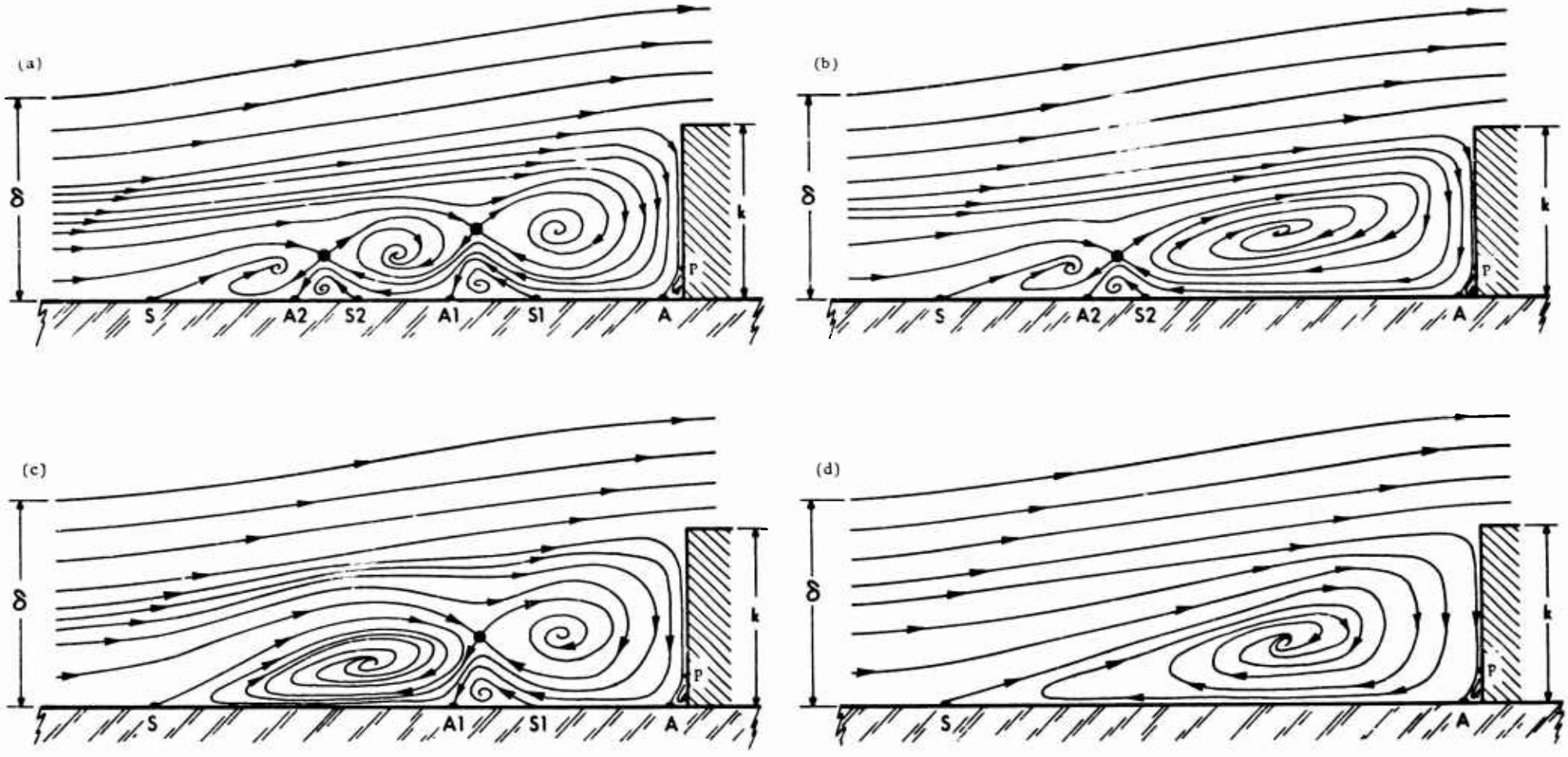

Fig. 17. Side-View in Plane of Symmetry of Small Protuberance Separated Flow Showing Various Vortex Configurations; Adapted from Jet-Maze Model of Ref. 9. (a) Six Vortices; (b) Four-Outer Vortices; (c) Four-Inner Vortices; (d) Two Vortices. For Clarity, Shock Waves Are Omitted and Horizontal Scale Is Stretched.

Fig. 18. Plan-View Sketch of Near Wake for Small Protuberance, Model 2B, M = 3.50, $R/\ell = 19.9 \times 10^6/m$. Separation Line Downstream in Symmetry Plane.

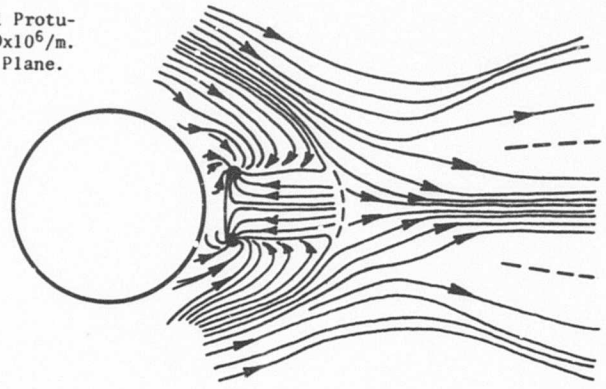

Fig. 19. Plan-View Sketch of Near Wake for Large Protuberance, Model 2D, M = 3.50, $R/\ell = 19.9 \times 10^6/m$. Attachment Line Downstream in Symmetry Plane.

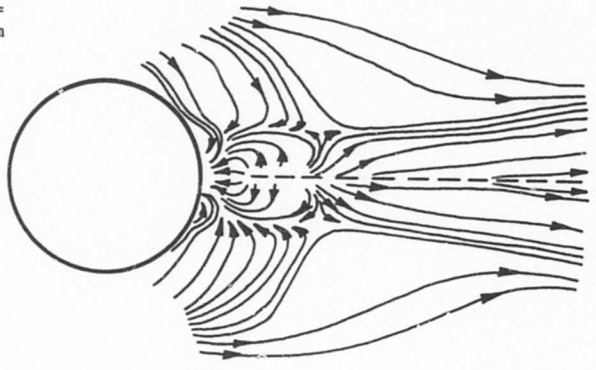

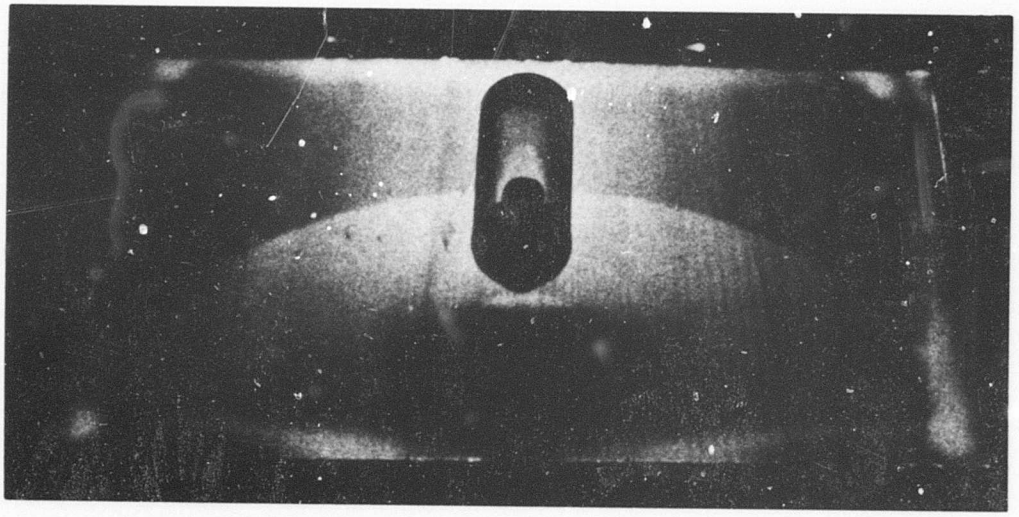

Fig. 20. Vapor Screen View of the Wake Looking Downstream, from Below; Light Sheet at 3 Diameters Downstream. Model 2D, M = 2.50, $R/\ell = 9.3 \times 10^6/m$.

CINEMATOGRAPHIC STUDY OF SEPARATED FLOW REGIONS

R.H. Page and C.E.G. Przirembel
Professor and Associate Professor
Dept. of Mechanical, Industrial, and Aerospace Engineering
Rutgers University
New Brunswick, New Jersey
08903
U.S.A.

SUMMARY

A cinematographic study utilizing high speed motion picture photography was carried out for a series of supersonic separated flow configurations. A two-dimensional variable Mach number wind tunnel was used to produce flow fields about several sting-supported models, including a sphere, a blunt body with a leading spike and a missile. The flow in the wake of a blunt-based, axisymmetric model was studied in a unique, support-interference free, wind tunnel. Color Schlieren and shadowgraph techniques were the primary diagnostic tools used in these studies. For some film sequences, these flow visualization techniques were enhanced by the addition of small particles.

The chief results of these studies are presented in a 16mm color motion picture film. Excellent qualitative descriptions of various supersonic, separated flow fields have been obtained by viewing these high speed motion pictures on a reduced time scale or on a frame-by-frame basis. These films assist researchers in obtaining the physical understanding of separated flow fields essential for making theoretical analyses of these complex regions.

1.0 INTRODUCTION

The intellectual curiosity of humans has resulted in observations of air and water flows which have been recorded over the ages. Air is invisible and water transparent. Hence, the earliest observations were of the paths of debris transported by the motion of these fluids. Thus our atmosphere and rivers served as prime opportunities for observations of flow patterns using natural flow visualization techniques. From such observations conclusions were drawn about flow path lines and streamlines. From this early start (such as described by Leonardo da Vinci[1]) flow visualization has progressed from an art to a science. Outstanding progress in flow visualization has been made during the past decade.[2-6]

Many flow visualization techniques have been used in the study of separated flows. These include surface treatments which optically alter the interaction between a wall (surface) in a fluid as well as those that optically alter a surface between a liquid and a gas.[7-9] The flow visualization of separated flows has also included internal treatments which include methods that optically alter the flow itself such as by the introduction of smoke, dyes, neutral density heads, etc.[10]

Although earlier investigators were convinced that they could "see" the flow of optically transparent fluids (such as air and water) through the introduction of foreign particles, many experimenters soon recognized that the foreign particles may not be behaving in precisely the same manner as the fluid itself. Early investigators also recognized that a probe inserted in the flow for measurement purposes had an influence on the motion of the fluid. The discovery and development of methods by which an optical system could be used to visualize transparent flows through direct observation of the optical properties of the flowing fluid (without the necessity for instrumentation probes and the introduction of foreign particles) was a major step forward in flow visualization.[11,12] Such methods provide a technique for photographically recording all the information observed by the optical system.[13,14] The results reported in this paper relied primarily on the application of such optical techniques.

2.0 FLOW VISUALIZATION TECHNIQUES

A number of flow visualization techniques have been utilized effectively for separated flow studies at Rutgers University. The optical techniques of Schlieren, shadowgraph, and interferometry have played a major role as experimental diagnostic tools. Many past investigations with optical methods have involved the use of image photography to obtain a photograph of instantaneous flow phenomena. A good example is the steady flow wave pattern about a model in a supersonic wind tunnel. In such a case, single photographs were sufficient for obtaining the desired information. However, the need for optical methods which can record time varying phenomena has developed. The combustion of fuel droplets, the motion of waves in reactive gases, the flow patterns about an accelerating body, and the oscillations of various flow patterns are all examples of time-dependent phenomena which are best studied with image recording on film.[15,16,17]

Transient flow phenomena involving separated flow regions have been studied at Rutgers utilizing high-speed motion picture cameras. Preliminary research[18] indicated that direct motion picture photography of optical images was possible and practical at high framing rates. The cinematographic studies used the optical techniques of conventional Schlieren, color Schlieren, and shadowgraph.

2.1 Conventional Schlieren

A conventional Schlieren system of the standard Toepler type is shown in Figure 1. The light from a source is focused by a mirror into a parallel beam which passes through the glass wall of the test section of the wind tunnel. If there are no density gradients normal to the light axis in the wind tunnel test section (for example, when the tunnel is turned off) the light emerges from the test section in an undisturbed, parallel beam. It is then forcused into an image of the source at the focal plane of the second

parabolic mirror. Generally, the knife edge is inserted at this focal plane in such a way that it intercepts about one-half of the source image. The image of the object in the test section is brought to focus at the film plane of the camera by an auxiliary lens.

Figure 2 illustrates the refraction pattern for conventional Schlieren system. The undisturbed light rays converge to form an image of the source at the knife edge. If the knife edge is adjusted for maximum sensitivity, approximately one-half of the light from the source is cut off and a uniform grey image is produced at the film plane. Density gradients in the test section could cause refraction of light rays as shown by the dotted lines in the lower two sketches of Figure 2. The refracted rays in the center sketch missed the knife edge entirely thus causing a bright white illumination of the upper portion of the film. In the bottom sketch the opposite case of refracted rays being intercepted by the knife edge and thus causing the absence of light on the upper half of the film is shown. The light reinforcement or cancellation on the grey image background produces the familiar black and white Schlieren images. It is obvious, from Figure 2, that density gradients which refract light rays parallel to the knife edge will result in no change in illumination at the film plane. A Schlieren system is only sensitive to density gradients having a component normal to the knife edge.

2.2 Color Schlieren

The Rutgers color Schlieren system[19,20] is simply a black and white system with a knife edge replaced by a tri-color filter. Figure 3 shows how the tri-color filter is used to produce color images. The undisturbed light rays of the top sketch all pass through the narrow blue slit and result in a uniform blue illumination of film. When a density gradient is present which causes refraction of some of the light rays a different color appears on the film image. The center sketch of Figure 3 shows light rays refracted so that they pass through the yellow filter. The bottom sketch shows light rays refracted in the opposite direction so that the refracted rays now pass through the red filter, thus causing a red image on the top half of the film. This color Schlieren system, like the black and white system, is only sensitive to density gradients having a component normal to the axis of the blue filter.

2.3 Shadowgraph

The direct-shadow method of flow visualization (shadowgraph) utilizes an optical system identical to that shown in Figure 1, except that there is no knife edge or color filter present. Therefore, the illumination of the image is no longer sensitive to density gradients having a component normal to a particular axis. In fact, it can be shown, that the change of illumination at the film plane becomes proportional to the rate of change of the density gradient in the test section. Because of its simplicity, the shadowgraph technique is ideal for visualizing phenomena involving large changes in the second derivative of the density (such as shock waves).

2.4 Particle Addition

The motion picture films of non-steady separated flow regions utilizing color Schlieren and shadowgraph images provide a great deal of information about the flow fields. The location of shock waves and expansion fans which vary with time may be readily determined. However, in addition to determining the overall flow fields of separated regions in this manner, the flow within the separated region was visualized by the introduction of particles. Particles were selected which would follow the recirculation flow paths. Because of the large range of velocities in a separated region bounded by supersonic flow, it was impossible to select a particle size and density such that the particles would at all times follow all mean streamlines in the separated region. A number of different particle materials and sizes were tested. Talc particles proved to be convenient to handle, non-toxic, and of the proper size distributions, shape and density in order to follow the mean streamlines in a recirculating region. Because of their irregular shape, talc particles have a higher drag coefficient than spherical particles. The talc particles utilized had an average effective diameter of 0.05mm with a distribution of larger and smaller size particles. Of course, the resolution of the optical system was not sufficient to identify individual particles of such a small diameter. Nevertheless, groups of particles which followed mean streamlines could be easily identified. The optical superpositioning of the paths of these particle groups on the cinematographic images greatly enhanced the visualization of the separated flow regions.

2.5 Image Recording

A 16mm Hycam camera (Red Lake Model) was used to obtain high speed motion pictures of the optical images generated by the above flow visualization techniques. The camera, which utilized a rotating prism for optical compensation, had a capacity of 30.48 m [100 feet] of film. The frame rate was adjustable from 150 to 8000 frames per second.

An auxiliary lens was used to focus the optical image in the plane of the film. The exposure was controlled by regulating the size of the light source. Since the light source size had to be adjusted for each frame rate, an empirical correlation of light intensity versus frame rate was developed.

In most instances, standard movie color film (GAF-Anscochrome) with an ASA rating of 200 was used. A timing light, which placed small blips of light on the edge of the film, was used to determine the precise frame rate. The timing light was usually operated at 1000 cycles per second.

3.0 EXPERIMENTAL FACILITIES

3.1 Emil Buehler Wind Tunnel

Two different supersonic wind tunnels at Rutgers were utilized in these cinematographic studies. Table I summarizes the essential features of these facilities. The first series of separated flow regions were associated with models in the Emil Buehler Wind Tunnel (EBWT). This facility is a blowdown, supersonic wind tunnel, with an approximate maximum run time of two minutes. A schematic of the tunnel is shown in Figure 4.

The asymmetric, fixed geometry, variable Mach number nozzle was designed by the method of characteristics. The nominal test section cross-section is 10.16 cm x 11.43 cm (4.0 inches x 4.5 inches). The test section Mach number can be varied continuously between 1.3 to 4.0. The flow angle deviation is less than ± 0.5%.

The 17.2 x 10^4 N/m^2 (250 psig) air supply system consists of two non-lubricated compressors in series, aftercoolers, moisture separator, air dryer and storage tanks. The latter were located outside of the laboratory area, and, therefore, the stagnation temperature is essentially equal to the atmospheric temperature. The air dryer provided air with a dew point of -73.3°C (-100°F) at 8.6 x 10^4 N/m^2 (125 psig), which is equivalent to 0.25 parts per million of moisture on a weight basis. The effective elimination of moisture and oil resulted in a very adequate supply of compressed air for optical studies of supersonic flow phenomena.

The stagnation pressure for the EBWT is controlled by a single-seat globe valve in conjunction with an electro-pneumatic control system. This system maintains a constant pressure within ±3% of the stagnation pressure set point.

The test section is enclosed by two optical quality windows which are located parallel to each other and perpendicular to the light path of the Schlieren system. The test models were mounted with stings on the tunnel support system, which was attached to the roof of the constant area section following the test section. The angle of attack of each model was adjustable by controls outside of the tunnel.

3.2 Rutgers Axisymmetric Near-Wake Tunnel

The second facility utilized in this study was the Rutgers Axisymmetric Near-Wake Tunnel (RANT). It is a blowdown supersonic wind tunnel with an average run time of 20 seconds. It uses dry, oil-free, compressed air from the same air supply system described above as the working fluid. RANT is shown schematically in Figure 5. A detailed description of RANT has been reported by Przirembel.[21]

The annular nozzle was designed by the method of characteristics and produces a uniform flow field at a nominal Mach number of 4. The centerbody and test models are integral parts of the nozzle configuration and have constant outside diameters of 7.62 cm (3.00 inches). This design eliminates model support interference effects on the near wake. The centerbody is hollow, thus allowing pressure and temperature leads to pass from the test models to measuring instruments located outside of the tunnel.

The stagnation pressure for the tunnel is controlled by a single-seat globe valve. The control system for the valve is primarily pneumatic; however, electrical timers and solenoid valves are used for automatic start-up and shut down. The stagnation pressure was maintained within ±3.4 x 10^3 N/m^2 (0.5 psia) during each test run. The timer for the high speed motion picture camera was also wired into the tunnel control system.

The test section is equipped with rectangular windows to allow for visualization studies of the wake flow. The transition between the flat windows and the circular walls was designed to keep the main tunnel flow attached to the windows and to avoid detrimental shock formation caused by the nozzle test section junction.

The experiments were conducted at a stagnation pressure of 1.05 x 10^6 N/m^2 (152.5 psia), a free stream Mach number of 3.88 and a corresponding Reynolds number of 4.9 x 10^6 per m (1.6 x 10^7 per foot). The model boundary layer approaching the base was turbulent. The boundary layer was characterized by the following parameters:

Thickness (δ) = 8.74 mm (0.344 inches)
Displacement thickness (δ^*) = 3.56 mm (0.140 inches)
Momentum thickness (θ) = 0.434 mm (0.017 inches)

Detailed pressure measurements on the model and in the near-wake have been reported by Sieling, Przirembel and Page.[22] Of particular importance to this flow visualization study is the location of the rear stagnation point. By comparing the centerline pitot and static pressures, the average position of this point was 0.84 model diameters from the base.

4.0 DISCUSSION OF RESULTS

The essence of this study is a 16 mm high speed motion picture film[23], which depicts various subsonic and supersonic separated flow fields. A summary of the various film sequences is shown in Table II. Some comments about the content of each sequence and some conclusions which can be drawn from the film by a frame-by-frame analysis are given below.

4.1 Cone-Flow Transients

During the subsonic portion of the flow, the wake, as made visible by density gradients in the free shear layer, is open and reasonably steady. As a result of the asymmetric tunnel nozzle, the upper portion of the wind tunnel test section reaches supersonic conditions first. The starting normal shock system generates some very interesting shockwave-boundary layer interactions on the nozzle wall. The model wake closes after the starting shock has passed through the test section. The wake remains reasonably steady after that.

4.2 Cone-Aeroelastic Transients

The starting process for the wind tunnel at M = 3.3 is significantly different from that at M = 1.9. There is no longer a distinct normal shock. Due to the elastic properties of the sting and the asymmetric starting shock, severe oscillations of the model occur during the start-up. Of particular interest are the dynamic changes of the wake region as the model changes its angle of attack.

4.3 Axisymmetric Cavity-Steady Flow

The supersonic free stream approaching the model is steady with time. This can be easily verified by observing the conical shock formed around the leading cone. The free shear layer formed behind this model does not close, but jumps across the gap to reattach on the second model. Since the reattachment surface is not a smooth wall aligned with the free stream, the reattachment region is very unsteady. The recompression shock system moves about erratically.

4.4 Front Spike-Steady Flow

In this case, the free stream is as steady, as for the flow field of Section 4.3. However, the free shear layer associated with the forward separated flow region does not have a suitable place to reattach. Hence, this separated region is very unsteady. The flow disturbances propagate downstream, and influence the model base region. Both the free shear layer and the recompression shocks display significant oscillations.

4.5 Sphere-Transient Flow

As observed in the cone flow, the subsonic wake appears to be open, and wake closure only occurs after the supersonic flow has been established. The entire flow field in the vicinity of the model is steady.

4.6 Blunt Base-Transient/Steady

Since the support system and model are an intrinsic part of the nozzle, there is no forebody flow field to observe nor to influence the wake flow region. During the subsonic portion of the flow-time history, the wake is extremely turbulent. An open wake is observed as the tunnel starting shock system moves along the model. As this tunnel shock reaches the corner of the blunt base, the free shear layer is parallel to the model. As the starting shock passes through the wake, the near wake closes and a distinct recompression shock system is established. No visual evidence of a lip shock was observed. This qualitative observation was verified quantitatively by pitot tube pressure measurements reported by Przirembel.[21] After the main flow has been established, some unsteadiness of the near and far wake was observed.

4.7 Blunt Base-Transient/Steady-Particle Injection

In order to obtain some indication of time-averaged streamlines and to enhance the visual quality of the flow field, talc particles were injected into the base region. During the subsonic free stream flow conditions, there was some indication of three-dimensional vortices in the wake. However, their behavior was not periodic by any means. Prior to the passing of the tunnel starting shock system, the particles seemed, at times, to move in the upstream direction. As the starting shock reached the base, the free shear layer, which formed an envelope for the injected particles, was again parallel to the model and aligned with the free stream. As the free shear layer entrained fluid from the base region, an intermittent recirculation pattern could be observed. After the near wake closure, a mean recirculation flow pattern was established. Although the resolution of the optical system was not adequate to study the path of single particles, it was possible to trace an aggregate of talc particles. The resulting path lines are shown in Figure 6. It was observed that all particles are contained within an hour glass-shaped region outlined by the dashed lines.

5.0 CONCLUDING REMARKS

Excellent qualitative descriptions of separated flow fields have been obtained by viewing motion picture films of Schlieren images. Color Schlieren images, in which the density gradient's algebraic sign is discriminated by means of color changes, are easily obtained and clarify the visual interpretation of the Schlieren field. The cinematographic photography of the motion of talc particle clusters in the recirculation region was also productive of good results.

Viewing of these films on a reduced time scale, or frame-by-frame, enables researchers to obtain a good physical understanding of both transient and steady flows. These techniques are useful in establishing accurate descriptions of the flow field. At Rutgers, the information from the cinematographic studies has been extremely helpful in the development of theoretical models of separated flow fields.

The film referred to in this paper and entitled, "Cinematographic Study of Separated Flow Regions" is available on a loan basis from the authors.

REFERENCES

1. da Vinci, Leonardo, "Del Moto e Misura dell'Acqua", edited by E. Carusi and A. Favaro, Bologna, Italy, 1924.

2. Ragsdale, W.C., "Flow Visualization Workshop Report", Naval Ordnance Laboratory, Silver Spring, Md., NOLTR 72-94, May 1972.

3. Thompson, D.H., "The Use of Dyes for Water Tunnel Flow Visualization", Aeronautical Research Laboratories, Australian Defence Scientific Service, Melbourne, Australia, Aerodynamics Note 339, Feb. 1973.

4. Mueller, T.J. and Hall, C.R., Jr., "Supersonic Wake Flow Visualization", AIAA J., V.7, N. 11, p.2151-2155, Nov. 1969.

5. Merzkirch, W., Flow Visualization, Academic Press, N.Y. and London, 1974.

6. Clutter, D.W., Smith, A.M.O., and Brazier, J.G., "Techniques of Flow Visualization Using Water as the Working Medium", Douglas Aircraft Company Report #ES29075, April 1959.

7. "Symposium on Flow Visualization", Summary of Presentations, ASME, New York, N.Y., Nov. 1960.

8. Merzkirch, W.F., "Making Flows Visible", International Science and Technology, N. 58, p. 46-56, Oct. 1966.

9. Clayton, B.R. and Massey, B.S., "Flow Visualization in Water: A Review of Techniques", J. of Scientific Instrumentation, V. 44, p. 2-11, 1967.

10. Prandtl, L. and Tietjens, O.G., Applied Hydro- and Aeromechanics, Dover Publication, N.Y., N.Y., 1957.

11. Toepler, A., "Beobachtungen Nach Einer Neuen Optischen Methode", Ostwalds Klassiker der Exacten Wissenschaften, N. 157, Leipzig, 1906.

12. Schardin, H., "Toepler's Schlieren Method - Basic Principles for its Use and Quantitative Evaluation", David Taylor Model Basin, U.S.N., Translation 156, July 1947.

13. Holder, D.W. and North, R.J., "Optical Methods for Examining the Flow in High Speed Wind Tunnels - Part I: Schlieren Methods", AGARDograph 23, Nov. 1956.

14. Wood, G.P., "Optical Methods for Examining the Flow in High Speed Wind Tunnels - Part II: Interferometer Methods", AGARDograph 23, Nov. 1956.

15. North, R.J. and Stuart, C.M., "Flow Visualization and High-Speed Photography in Hypersonic Aerodynamics", Proceedings of Sixth International Congress on High-Speed Photography, 1963.

16. Havener, A.G. and Radley, R.J., Jr., "Turbulent Boundary Layer Flow Separation Measurements Using Holographic Interferometry", AIAA J., Vol. 12, No. 8, p. 1071-1075, 1974.

17. Baltakis, F.P., "Wind-Tunnel Study of Oscillating Flow-Induced Surface Pressures on a Tension-Cone Geometry Model", Naval Ord. Lab., Silver Spring, Md., NOLTR 74-134, Jan. 1974.

18. Page, R.H., Kessler, T.J., and Kuebler, A.A., "Color Schlieren Studies of Transient Flows with High Speed Motion Picture Photography", Proceedings 4th Space Congress, Cocoa Beach, Florida, April 1967.

19. Kessler, T.J. and Hill, W.G., Jr., "A Color Schlieren System", College of Engineering, Rutgers U., TR 105-ME-F, Sept. 1965.

20. Kessler, T.J. and Hill, W.G., Jr., "Schlieren Analysis Goes to Color", Astronautics and Aeronautics, V.4, N.1, front cover and p. 38-40, Jan. 1966.

21. Przirembel, C.E.G., "Construction and Operation of RANT", Dept. of Mechanical and Aerospace Engineering, Rutgers U., New Brunswick, N.J., Technical Report N. 110-ME-F, November 1966.

22. Sieling, W.R., Przirembel, C.E.G., and Page, R.H., "The Turbulent Near-wake of Infinite Axisymmetric Bodies at Mach Four", Proceedings of the 12th Midwestern Mechanics Conference, Developments in Mechanics, V. 6, U. of Notre Dame, August 1971.

23. Page, R.H. and Przirembel, C.E.G.", Cinematographic Study of Separated Flow Regions", 10 min - 16mm silent color film, Department of Mechanical, Industrial, and Aerospace Engineering, Rutgers University, 1974.

TABLE I

Rutgers Supersonic Wind Tunnels Used for Cinematographic Studies

	EBWT	RANT
Name	Emil Buehler Wind Tunnel	Rutgers Axisymmetric Near-Wake Tunnel
Test section geometry	Two-Dimensional	Axisymmetric
Test section size	10.16 cm x 11.43cm (4 inch x 4.5 inch)	20.32 cm diam. (8 inch diameter)
Mach No. range	1.2 to 4.0	3.0 and 3.88
Stagnation Temperature	Atmospheric	Atmospheric
Stagnation Pressure	Automatic control up to 10 atm.	Automatic control up to 14 atm.
Compressed Air Moisture Content	1 part per million	1 part per million
Mode of Operation	Intermittent with constant stagnation pressure control	Intermittent with constant stagnation pressure control
Control System	Electro-pneumatic	Electro-pneumatic

	EBWT	RANT
Test Time Duration	Programmable by event timer (30 seconds common)	Programmable by event timer (20 seconds common)
Model Support	Conventional sting mount with variable angle of attack	Special design with complete support by upstream sting, which is an integral part of the nozzle
View Ports	Optical Glass 43.18 cm x 12.06 cm (17 inch x 4.75 inch)	Optical Glass 22.86 cm x 10.16 cm (9 inch x 4 inch)

TABLE II

Summary of Film Scenes

Film Sequence	Exp. Facility	Model Schematic	Flow Visualization Techniques	Flow Field	Frame Rate
1. Cone-Flow	EBWT M = 1.90		Color Schlieren	Transient	2500
2. Cone-Flow	EBWT M = 3.30		Color Schlieren	Transient (Aeroelastic)	2500
3. Axisymmetric Cavity	EBWT M = 3.25		Color Schlieren	Steady	7000
4. Front Spike	EBWT M = 3.10	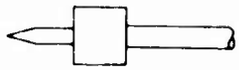	Color Schlieren	Steady	7000
5. Sphere	EBWT M = 3.10	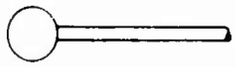	Color Schlieren	Transient	3000
6. Blunt Base	RANT M = 3.88		Color Schlieren	Transient	5500
7. Blunt Base	RANT M = 3.88		Color Schlieren	Steady	5500
8. Blunt Base	RANT M = 3.88		Color Schlieren Talc Particles	Transient	5500
9. Blunt Base	RANT M = 3.88		Shadowgraph Talc Particles	Transient	5500
10. Blunt Base	RANT M = 3.88	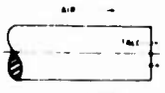	Shadowgraph Talc Particles	Steady	5500
11. Blunt Base	RANT M = 3.88		Shadowgraph Talc Particles	Transient	5500

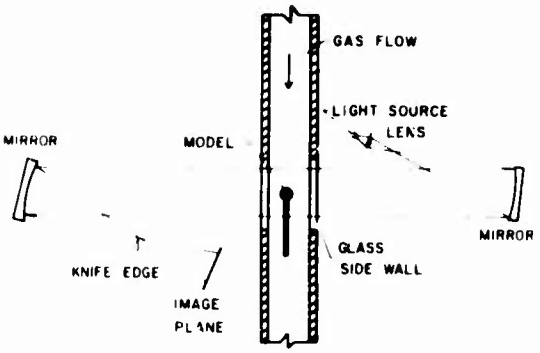

Fig. 1. Standard Toepler Schlieren System

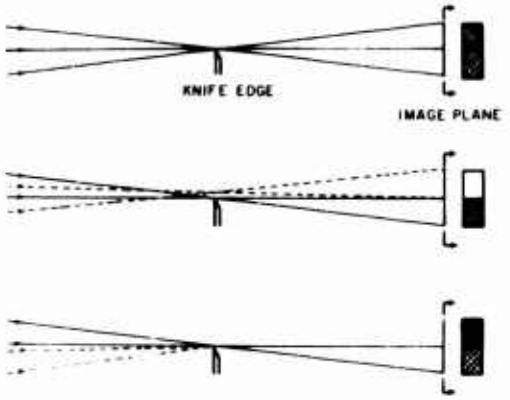

Fig. 2. Conventional Refraction Pattern

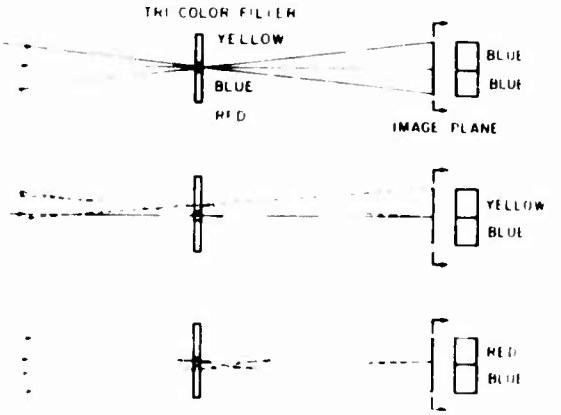

Fig. 3. Tri-Color Filter Refraction Pattern

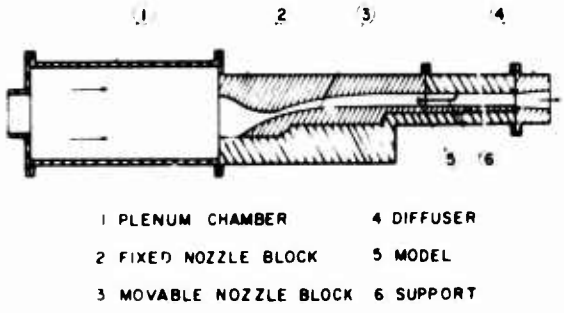

Fig. 4. EBWT Schematic

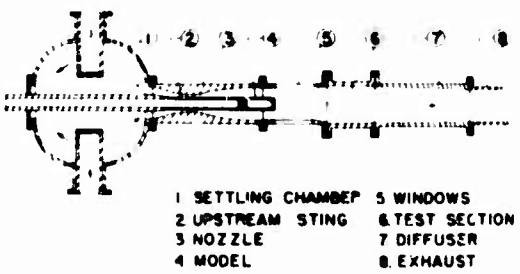

Fig. 5. RAMT Schematic

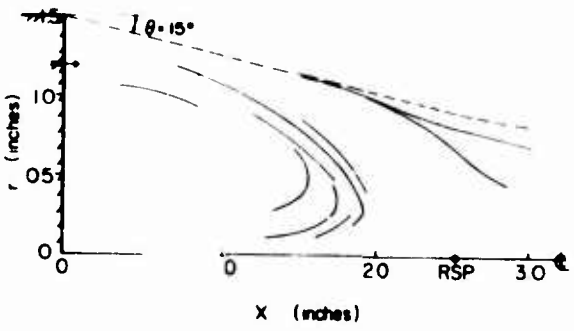

Fig. 6. Path Lines

ÉCOULEMENTS DÉCOLLÉS

ÉTUDE PHÉNOMÉNOLOGIQUE A PARTIR DE VISUALISATIONS HYDRODYNAMIQUES*

par Henri WERLÉ

Office National d'Etudes et de Recherches Aérospatiales (ONERA)
92320 CHATILLON (France)

RÉSUME

Grâce aux visualisations d'écoulements effectuées au tunnel hydrodynamique de l'ONERA depuis de nombreuses années, il a été possible d'entreprendre l'étude physique des phénomènes de décollement autour d'une grande variété d'obstacles.

De ces résultats obtenus à faible vitesse se dégage un certain nombre de schémas fondamentaux qui correspondent aux principaux types de décollements observés en écoulement bi- ou tridimensionnel : leur analyse détaillée en précise les singularités et en souligne les aspects transitionnels, tourbillonnaires et instationnaires.

A partir de ces éléments, il est tenté une synthèse, qui a pour but de caractériser les décollements tridimensionnels par rapport aux décollements qui se produisent en courant plan ou en écoulement de révolution.

(*) Quelques exemples ont été groupés dans le film ONERA 817 [F1] présenté en cours de séance.

SEPARATED FLOWS

A phenomenologic study based on hydrodynamic visualizations

SUMMARY

Thanks to flow visualizations obtained at the ONERA water tunnel since many years, it has been possible to undertake the physical study of separations around a broad variety of obstacles.

From these results, obtained at low speed, emerge a number of fundamental schemes which correspond to the main types of separations observed in two- or three-dimensional flow ; their detailed analysis emphasizes their singularities as well as their transitional, vortex-like and unsteady aspects.

From these elements we attempted a synthesis aiming at the characterization of three-dimensional separations as compared to those occurring in plane or axisymmetrical flow.

Note : A few examples are assembled in the ONERA film n° 817, presented at the Symposium.

INTRODUCTION

Dans le cadre restreint du présent mémoire, la description des écoulements décollés a dû être limitée à un certain nombre de cas fondamentaux observés autour de modèles schématiques et visualisés au tunnel hydrodynamique de Châtillon [1]. Mieux structurés et surtout moins complexes que les décollements qui se produisent autour de maquettes plus élaborées, telles qu'elles sont mises en jeu en aérodynamique appliquée [2, F2], les principaux phénomènes de base peuvent ainsi faire l'objet d'une analyse sûre et précise.

Ce document, largement inspiré par les études antérieures faites dans ce domaine par E.C. Maskell [3], E.A. Eichelbrenner [4], R. Legendre [5], M. Roy [6] et bien d'autres [7 - 9], se bornera simplement à mettre à jour les observations faites sur les points, angles, lignes, surfaces et caractères remarquables mis en évidence par les visualisations à basse vitesse, et à en dégager un répertoire des principales singularités rencontrées, plus particulièrement dans le cas des décollements tridimensionnels.

TECHNIQUE EXPERIMENTALE

La technique pratiquée au tunnel depuis sa mise en service en 1952 est trop connue pour être rappelée ici : le lecteur intéressé trouvera, avec de nombreux exemples à l'appui, dans [1] toutes les caractéristiques et applications de ce tunnel vertical, et dans [10 - 12, F3 & F4] tous les détails relatifs aux méthodes qui y sont pratiquées. Précisons simplement que les visualisations qui illustrent ce document ont pour la plupart été obtenues à l'aide de traceurs liquides colorés de même densité que l'eau, procédé convenant particulièrement pour les écoulements pariétaux (par ex. fig.3 et 7). Dans un certain nombre de cas, ces images ont été complétées ou recoupées par celles de trajectoires de traceurs gazeux en suspension dans l'eau :

- bulles d'air obtenues au moment du remplissage du réservoir et mettant en évidence la totalité du champ dans des plans de coupe longitudinaux (par ex. fig.2b, d, f et g) ou transversaux (par ex. fig.5i, j et o) ;
- bulles d'hydrogène dégagées par électrolyse et limitées à la seule surface de courant qui s'appuie sur la cathode, par ex. à la nappe issue d'un bord d'attaque en flèche (fig. 5k, m et n).

RAPPELS RELATIFS AUX ECOULEMENTS NON DECOLLES

Aussi bien pour familiariser le lecteur avec l'examen des images ainsi obtenues que pour compléter cette analyse en opposant les éléments remarquables des écoulements non décollés et décollés, cette revue phénoménologique évoque d'abord quelques résultats simples qui, quoique évidents, ne sont pas toujours présents à l'esprit. Les différentes vues de la fig. 1 mettent clairement en évidence les différences fondamentales existant entre les points et lignes d'arrêt amont en courant plan et en écoulement de révolution, et les points d'arrêt et lignes de partage en écoulement tridimensionnel. Pour les premiers, les lignes de courant pariétales se détachent perpendiculairement de part et d'autre de la ligne d'arrêt (fig. 1a et c) et dans le cas limite d'un modèle de révolution axial et sans incidence (fig. 1e et f), le point d'arrêt avant (et arrière lorsqu'il existe) est un ombilic selon la terminologie adoptée par H. Poincaré [5] (voir aussi fig.5j, k et m). A ce point de divergence isotrope des lignes de courant pariétales s'oppose le point d'arrêt amont non isotrope (noeud) qui apparait en écoulement tridimensionnel par suite de l'inclinaison ou de la forme de la maquette (fig.1g, h et i). De ce noeud est issue la (ou les) ligne(s) de partage qui se forme(nt) sur l'intrados ou sur les bords des modèles (fig.1i, j, k, l et 7g). Suivant les cas, elle sépare les courants d'intrados et d'extrados ($\alpha = 0°$) ou les différents courants d'intrados ($\alpha > 0°$) qui se déversent au bord d'attaque et au bord de fuite. Une ligne de partage n'est pas une ligne d'arrêt, mais une ligne de courant pariétale remarquable, de part et d'autre de laquelle se détachent tangentiellement les autres lignes de courant pariétales. La trace de cette ligne dans un plan de coupe perpendiculaire peut être assimilée au point d'arrêt du pseudo-écoulement transversal.

Notons enfin que dans le cas d'un écoulement irrotationnel, la surface de courant contenant ces lignes de partage ou d'arrêt est perpendiculaire à la surface du modèle, comme le montre l'expérience (par ex. fig.1b et d).

DECOLLEMENTS EN COURANT PLAN ET EN ECOULEMENT DE REVOLUTION

Rapidement et sans entrer dans les détails (*), la présente étude se doit de passer en revue les principaux types de décollements observés en courant plan et en écoulement de révolution, ce dernier étant bien souvent le seul "cas bidimensionnel" correctement réalisé au cours des essais, c'est-à-dire exempt de tout effet parasite dû aux parois entre lesquelles sont montés les modèles "courant plan".

C'est ce qui peut être décelé sur certaines vues de la fig. 2 qui illustre les cas bidimensionnels classiques suivants :

- décollement généralisé sur un cylindre (fig.2a), exemple de structure avec point de décollement libre ;
- décollement devant un ressaut de paroi (fig. 2b et c), structure formée avec point de décollement libre, mais avec point de recollement fixé sur la paroi normale près de l'arête supérieure ;
- décollement derrière un décrochement de paroi (fig.2d, e et f) structure fermée avec point de décollement fixé au bord du décrochement, le point de recollement (laminaire ou turbulent suivant les conditions des essais) restant libre ;
- enfin, décollement localisé dans une cavité de paroi (fig.2g) avec points de décollement et de recollement fixés tous les deux.

Les vues groupées sur la fig.3 complètent cette revue dans le cas de modèles "courant plan" sans discontinuité de pente (fig.3a à h) et l'étendent à celui de maquettes axiales à écoulement de révolution (fig.3i à m). Dans tous les exemples ci-dessus, les lignes de courant pariétales situées de part et d'autre des lignes de

(*) Seuls sont présentés dans ce mémoire des écoulements avec décollement laminaire dont la structure est clairement mise en évidence par les traceurs utilisés pour la visualisation. En régime entièrement turbulent, les observations sont non seulement plus difficiles en raison des fluctuations de vitesse, mais aussi fortement gênées par la diffusion du colorant et les trajectoires désordonnées des bulles d'air servant de traceurs.

décollement (ou de recollement) s'y rattachent (ou s'en détachent) à peu près normalement.

Ces visualisations qui précisent en outre l'organisation et les caractères des zones décollées ont permis de dégager le schéma physique des principaux types de décollement observés en courant plan :

- décollement généralisé sur paroi incurvée (fig.4a) que caractérisent une émission périodique de tourbillons emportés par le courant et une turbulence aval ;
- décollement localisé devant un ressaut de paroi, zone de recirculation qui est le siège de tourbillons stationnaires, (fig.4b).

Dans les conditions des essais réalisées au tunnel, la surface de séparation, frontière de ces zones décollées, se détache toujours sous un angle faible ou nul.

Le cas d'un décollement fixé par une singularité géométrique du modèle telle que le bord d'un décrochement de paroi est schématisé sur les vues 4d (zone de recirculation entièrement laminaire derrière un décrochement de faible hauteur) et 4e (eau morte laminaire côté amont et zone turbulente côté aval derrière un grand décrochement). La structure de ces zones décollées finies présente une grande analogie avec celle des bulbes décollés qui se forment au bord d'attaque d'un profil portant [13, F5]. Dans toutes les expériences avec recollement de l'écoulement non imposé par la présence d'une paroi normale faisant obstacle, le rattachement de la surface de séparation sur la paroi aval s'effectue sous un angle relativement faible ou nul.

Enfin, il semble utile de revenir sur le cas d'un montage "courant plan" si souvent utilisé en soufflerie pour insister sur les effets tridimensionnels dus aux parois latérales et qui tendent à se développer particulièrement lorsque l'écoulement décolle sur le modèle :

- dans le meilleur des cas, cela se traduit par une légère incurvation vers l'aval, de la ligne de décollement de part et d'autre du plan de symétrie (par ex. fig.2a) ;
- dans d'autres cas, auxquels il convient de faire très attention si l'on ne veut pas aboutir à des conclusions erronées, l'importance des décollements parasites sur les côtés est telle qu'elle provoque la formation d'un col et entraîne un recul non réaliste du point de décollement dans la zone médiane (formation d'un point de partage reculé) [1].

Seule la ligne de décollement qui ceinture un corps fuselé de révolution sans incidence (fig.3i, j et k) est exempte de point de partage : le tube décollé ainsi formé prolonge le modèle dont il constitue le sillage ; mais il peut aussi en venant se rattacher autour d'un parallèle, enfermer un bulbe annulaire entièrement laminaire ou mixte et à recollement turbulent.

CARACTERISATION DES DECOLLEMENTS TRIDIMENSIONNELS PAR RAPPORT AUX DECOLLEMENTS PRECEDENTS

Les fig.4c et 4f schématisent pour les deux types d'exemples analysés ci-dessus, les modifications fondamentales qui se produisent dans l'écoulement sous l'effet d'une composante transversale. Ainsi se forme-t-il devant un ressaut de paroi d'envergure limitée (fig.4c) des tourbillons-puits alimentés par une mince couche de courant et s'échappant de part et d'autre de l'obstacle. Devant un cylindre fixé à la paroi (fig.5a et b), ces tourbillons sont incurvés en "fer à cheval" comme la ligne de décollement qui les précède et qui se développe de part et d'autre d'un point de partage avancé (voir fig.6d) du type "col" [5].

Derrière un décrochement de paroi, l'effet d'une composante transversale importante n'est pas moindre (fig.4f), qu'elle s'établisse naturellement en raison de la géométrie du modèle, par exemple dans le cas d'un décrochement en chevron (fig.5h, i et j) ou artificiellement, telle que la provoque un jet transversal [14, F6]. Ces courants transversaux, dont l'importance a été soulignée à plusieurs reprises [6, 15], ont pour effet de provoquer l'enroulement de la nappe, qui se détache au bord du décrochement, autour d'un tourbillon-puits (fig.4f). Ce tourbillon est alimenté par une couche de fluide dont la frontière vient se rattacher sur la paroi aval sous un angle voisin de 90°.

Sur l'extrados d'une aile delta mince avec incidence, on retrouve une organisation identique des tourbillons issus de l'apex et qui résultent de l'enroulement en "cornet" des nappes qui se détachent des bords d'attaque (fig.5k à o) [6, F7] : le schéma correspondant est classique (configuration tourbillons séparés), il reste valable même en supersonique [16].

Quand aucune singularité géométrique du modèle (pointe, arête, bord, etc.) ne fixe la ligne de décollement sur la surface du modèle, les décollements tridimensionnels présentent une structure plus complexe et des différences notables suivant la forme, l'élancement ou l'attitude du modèle.

Ainsi peut-on distinguer sur l'extrados d'une ogive [17, 9, F8] ou d'une aile delta épaisse [6, F1] :

- un décollement unique issu d'un point de partage axial avancé (col) et siège d'un tourbillon en "fer à cheval" dont les deux branches s'incurvent vers l'aval (fig. 5c, 6a et 7h) ;
- 2 plages décollées séparées par un couloir axial sain non décollé (fig.5d, 6b et 7i, j, k), chaque ligne de décollement issue d'un point de partage avancé comportant en outre un foyer (fig.6d), point de convergence spirale d'où s'élève un tourbillon-trombe [5, 18] ;
- une plage unique, mais résultant de la jonction, à incidence élevée, d'un décollement localisé à l'avant (bulbe) et d'un décollement généralisé arrière, par exemple sur une ogive à nez relativement plat (fig.5e) ou sur une aile annulaire [17, 19].

Enfin, le cas des décollements arrière tels qu'ils se produisent à incidence faible ou nulle, notamment sur des modèles finis et sans arêtes comme par exemple des ellipsoïdes (fig.5f et g) a été examiné dans des publications précédentes [4], qui, les premières, ont révélé l'aspect caractéristique de la ligne de décollement tridimensionnelle, asymptote (pratiquement assimilée à une enveloppe) des lignes de courant pariétales (fig.6d), ainsi que l'existence de cols (points de partage) et de noeuds (points de convergence non spirale) : voir par exemple fig. 5f et g.

Le lecteur attentif saura distinguer sur les fig.5 et 7 les différentes singularités passées en revue ci-dessus et que l'on retrouve aussi bien à la surface de parois avec obstacles et de voilures que sur des corps fuselés.

De l'ensemble des observations faites au cours de ces essais ressortent les résultats fondamentaux suivants applicables aux écoulements permanents en moyenne :

- de même qu'en écoulement bidimensionnel (bulbe de bord d'attaque, bulbe annulaire), les décollements tridimensionnels peuvent, dans quelques cas relativement rares, être fermés (bulbe d'envergure limitée, par exemple au nez d'une ogive insuffisamment profilée ou au bord d'attaque d'une aile annulaire) ;

- alors qu'en courant plan et qu'en écoulement de révolution les zones décollées mises en évidence sont toujours fermées vers l'amont, les structures tridimensionnelles peuvent s'ouvrir en des points et lignes singulières (point de partage, ligne de décollement, point de convergence spirale qui donne naissance à un tourbillon trombe) pour capter une couche de fluide et alimenter les tourbillons concentrés autour desquels s'enroulent les nappes émises le long des lignes de décollement.

Dans ce cas, ces structures tridimensionnelles sont nécessairement ouvertes vers l'aval pour évacuer le débit ainsi introduit, débit que l'on retrouve dans le sillage et plus particulièrement dans les noyaux des tourbillons.

Par contre, les structures ouvertes vers l'aval sans évacuation de débit capté (parce que fermées vers l'amont) finissent toujours par se refermer au sein du fluide en des points ou lignes singulières dont la position dépend surtout du gradient de pression antagoniste.

SINGULARITES AU SEIN DU FLUIDE

Cette étude des écoulements décollés ne serait pas complète si elle ne comportait pas une évocation, ne serait-ce que sommaire, des phénomènes de confluence ou d'éclatement se produisant au sein du fluide.

Sous l'effet d'un gradient favorable, tel qu'il peut être réalisé par l'artifice d'une prise d'air aval à débit d'entrée élevé (fig.8a et b), le décollement qui se produit au culot d'un obstacle bidimensionnel, plan ou axisymétrique, peut être réduit à une zone de recirculation fermée, dont l'extrémité, point de confluence des courants extérieurs, est pointue (voir aussi fig.3h). Par contre, dans le cas d'un décollement tridimensionnel, comme il se produit derrière un cylindre en dérapage (fig.8d, e et f), la confluence des courants extérieurs, telle que la révèle une coupe transversale (fig.8f), s'effectue normalement au plan de symétrie et en un point qui prend l'apparence d'un point de partage. Cette confluence est due au courant transversal qui s'établit naturellement lorsque le dérapage du cylindre est suffisant. La même organisation de l'écoulement peut être observée au-dessus d'une aile delta aux incidences élevées : en effet, la configuration "tourbillons rejoints" [16, F9] est caractérisée par la rencontre au sein du fluide des couches qui alimentent les tourbillons d'extrados de chaque côté de l'aile ; vue en coupe, elle s'effectue en un point de partage du pseudo-écoulement transversal.

C'est au contraire devant un gradient défavorable, tel qu'il résulte d'un effet d'obstacle, que se produit l'éclatement d'un sillage de couche limite au sein du fluide (fig.8g).

En écoulement tridimensionnel, le même procédé a permis de provoquer l'éclatement artificiel d'un tourbillon de voilure (fig.8i, j et k) [21, F11], phénomène qui se produit naturellement sur une aile delta aux incidence élevées [21, F9]. Comme pour les décollements, il existe différents types d'éclatement, aussi bien des poches fermées et quasi-stationnaires (par ex. fig.8h) que des éclatements à structure ouverte et très instationnaire (par exemple fig.8k).

STRUCTURES DECOLLEES INSTATIONNAIRES

Cette revue phénoménologique des décollements dans le cadre restreint de ce mémoire restera forcément incomplète par suite du nombre élevé et de la complexité des cas existants. En instationnaire, elle se limitera à quelques remarques au sujet des décollements et sillages à caractère périodique ou momentanément instationnaire.

En courant plan, l'exemple de ce type le plus connu est celui des tourbillons alternés de Bénard - Karman (fig.3g) qui caractérise la plupart du temps le sillage d'un obstacle fixe.

En écoulement de révolution, le sillage instationnaire correspondant est marqué par une émission périodique de tourbillons toriques (fig.3l). Souvent ce phénomène ne débute qu'en aval d'une zone d'eau morte laminaire dont l'importance croît avec les dimensions du culot (fig.6c) ; mais ce qui caractérise la formation de ces tourbillons, c'est l'ouverture périodique de la structure décollée vers l'amont, alternativement de chaque côté du modèle plan, ou sur toute la périphérie en écoulement axisymétrique.

Ainsi contrairement aux observations faites en régime permanent, les structures décollées bidimensionnelles peuvent s'ouvrir vers l'amont en instationnaire.

Il en est ainsi a fortiori dans le cas de maquettes en mouvement.

En courant plan, l'exemple classique est celui d'un profil animé d'oscillations harmoniques en tangage autour d'une incidence voisine de l'angle de décrochement [22, F11] ; le décollement instationnaire que l'on enregistre au cours de chaque cycle comporte les phases suivantes :

- apparition et développement au bord d'attaque d'un bulbe, siège d'un tourbillon-puits ;
- déplacement du bulbe vers l'aval et échappement dans le sillage.

Cette structure à volume variable s'ouvre donc alternativement vers l'amont (formation) et vers l'aval (échappement) : elle "respire" selon la terminologie utilisée par R. Legendre.

Le cas symétrique ou axisymétrique du tourbillon-puits qui se forme au cours d'un mouvement de démarrage, par exemple derrière une plaque disposée normalement à la direction de la vitesse Vo (fig.3m) [20, F10], est encore un exemple de structure bidimensionnelle momentanément ouverte vers l'amont, comme seul en instationnaire cela peut se produire. Il reste à évoquer le cas des structures instationnaires tridimensionnelles.

Les exemples de sillages tridimensionnels à caractère instationnaire accentué et issus de modèles fixes sont nombreux et il suffit de citer celui du sillage d'une structure soumise au vent (immeuble-tour, cheminée, etc) [20, F10] et de remarquer que bien souvent des effets tridimensionnels apparaissent même en bidimensionnel (en dehors des parois ou supports de montage), par suite de déchirures de la nappe qui s'enroule autour des tourbillons, sur la périphérie ou le long de l'envergure, par exemple sur un cylindre [23].

Quant aux exemples relatifs à des modèles en mouvement, on peut mentionner ceux d'une aile en flèche animée d'un mouvement d'oscillations harmoniques en tangage ou de translations alternées normales à la vitesse Vo (mouvement de pilonnement) [20, F10]. Les structures décollées mises en évidence pour une incidence moyenne non nulle sont, comme en stationnaire, caractérisées par la formation de tourbillons concen-

trés, et de ce fait ouvertes vers l'amont et l'aval (débit des noyaux), mais ce débit capté et évacué est modulé périodiquement par le mouvement, et en particulier s'annule chaque fois que l'incidence effective du modèle passe par 0°.

Enfin, l'exemple de structure tridimensionnelle observée lors d'un mouvement de démarrage, qui clôture cette longue série de résultats, est le décollement qui se forme sur un ellipsoïde de révolution allongé avec incidence [1] : quand la vitesse Vo croît à partir de 0, cette structure ouverte vers l'avant capte un débit qui provoque la remontée vers l'amont, de la ligne de décollement non fixée par une arête (comme sur une plaque normale à Vo) jusqu'à sa position de régime permanent (fig.7f).

CONCLUSION

L'étude à partir de visualisations, des points, lignes et surfaces remarquables au sein du fluide et sur les obstacles fournit aux théoriciens et aux expérimentateurs des informations utiles et non dénuées d'intérêt, qui sont loin d'être évidentes. Puissent-elles, en dépit de leur caractère qualitatif, leur permettre de mieux interpréter leurs propres résultats et inspirer ou guider les recherches effectuées en vue d'une meilleure connaissance des écoulements décollés.

REFERENCES

[1] Werlé H. - Le tunnel hydrodynamique au service de la Recherche Aérospatiale - Publication n° 156 (à paraître en 1975).

[2] Werlé H. - Applications aérospatiales, industrielles et maritimes de la visualisation hydrodynamique des écoulements - ATMA (Session 1975).

[3] Maskell E.C. - Flow separation in three dimensions - RAE Rep. Aero. 2565 (Novembre 1965).

[4] Eichelbrenner E.A. & Oudart A. - Le décollement laminaire à trois dimensions - Rech. Aéron. n° 47 (1955).

Eichelbrenner E.A. & Oudart A. - Méthode de calcul de la couche limite tridimensionnelle - ONERA Publication n° 76 (1955).

Eichelbrenner E.A. - Décollement laminaire en trois dimensions sur un obstacle fini - ONERA Publication n° 89 (1957).

Eichelbrenner E.A., Laval P. & Werlé H. - Décollement sur une aile delta placée sans incidence dans un écoulement laminaire - Rech. Aéron. n° 70 (1959).

[5] Legendre R. - Séparation de l'écoulement laminaire tridimensionnel - Rech. Aéron. n° 54 (1956).

Legendre R. - Lignes de courant d'un écoulement continu - Rech. Aérosp. n° 105(1965).

[6] Roy M. - De la formation des zones tourbillonnaires dans les écoulements à faible viscosité - (3ème Conf. L. Prandtl) - Z. Flugw., Heft 8 (1959) et publié par l'ONERA.

[7] Rainbird W.J., Crabbe R.S., Peake D.J. & Meyer R.F. Some examples of separation in three-dimensional flows - NRCC Ottawa (April 1966) - Reprint DME/NAE Quarterly Bulletin n° 1966 (1).

[8] Werlé H. - Partage et rencontre d'écoulements fluides - Rech. Aéron. n° 79 (1960).

[9] Wang K.C. - Separation patterns of boundary layer over an inclined body of révolution - AIAA Journal vol. 10 n° 8 (August 1972).

[10] Werlé H. - Méthodes d'étude, par analogie hydraulique, des écoulements subsoniques, supersoniques et hypersoniques. AGARD Rapport 399 (1960).

[11] Werlé H. - Hydrodynamic flow visualization - Annual Review of Fluid Mechanics vol. 5 (1973) p. 361 - 382.

[12] Werlé H. - Méthodes de visualisation hydrodynamique des écoulements "Techniques de mesure dans les écoulements" Eyrolles, Paris (1974).

[13] Werlé H. - Sur l'écoulement au bord d'attaque d'un profil portant - Rech. Aerosp. n° 1973-4.

[14] Werlé H. & Gallon M. - Contrôle d'écoulements par jet transversal-l'Aéron. et l'Astron. n° 34 (1972-2).

[15] Roy M. - Stationnarité et stabilisation de tourbillons rectilignes en écoulement plan - C.R.Acad. Paris, t.274 (1972), série A p. 1659-1662.

[16] Monnerie B. & Werlé H. - Etude de l'écoulement supersonique et hypersonique autour d'une aile élancée en incidence. AGARD CP n° 30 p.23-1 à 23-19.

[17] Werlé H. - Le décollement sur les corps de révolutions à basse vitesse - Rech. Aéron. n° 90 (1962).

[18] Legendre R. - La condition de Joukowski en écoulement tridimensionnel - Rech. Aerosp. n° 1972-5.

[19] Hansen A.G. - Symposium on fully separated flows - ASME, Philadelphie, Mai 1964 p. 1 à 9 (article de E.A. Eichelbrenner).

[20] Werlé H. - Visualisation hydrodynamique des écoulements instationnaires - ONERA Note Technique n° 180 (1971).

[21] Werlé H. - Sur l'éclatement des tourbillons - ONERA Note Technique n° 175 (1971).

[22] Werlé H. & Gallon M. - Ecoulement plan autour d'un modèle animé d'un mouvement périodique - ONERA Note Technique n° 239 (1975).

[23] Gerrard J.H. - La structure tridimensionnelle du sillage d'un cylindre circulaire - J. of Fluid Mech. 5/66, 25 part. 1.

CINEMATHEQUE

[F1] Film ONERA n° 817 - (1975)
Ecoulements décollés.

[F2] Film ONERA n° 812 - (1975)
Applications aérospatiales, industrielles et maritimes de la visualisation hydrodynamique des écoulements.

[F3] Film ONERA n° 355 - (1960)
Etude de courants fluides par analogie hydraulique.

[F4] Film ONERA n° 757 - (1973)
Méthodes de visualisation hydrodynamique des écoulements.

[F5] Film ONERA n° 745 - (1974)
Sur l'écoulement au bord d'attaque d'un profil portant.

[F6] Film ONERA n° 649 - (1972)
Contrôle de l'écoulement par jet transversal.

[F7] Film ONERA n° 802 - (1975)
Nappes en cornet issues d'ailes minces élancées.

[F8] Film ONERA n° 432 - (1963)
Visualisations d'écoulements hydrauliques.

[F9] Film ONERA n° 755 - (1973)
Tourbillons concentrés.

[F10] Film ONERA n° 666 - (1971)
Ecoulements instationnaires.

[F11] Film ONERA n° 575 - (1968)
Ecoulements à grandes fluctuations de vitesse.

Nota : tous ces films (16 mm, sonores, durée de 10 à 30 mn) peuvent être prêtés ou achetés : voir catalogue édité par l'ONERA (s'adresser au Service des Relations Publiques).

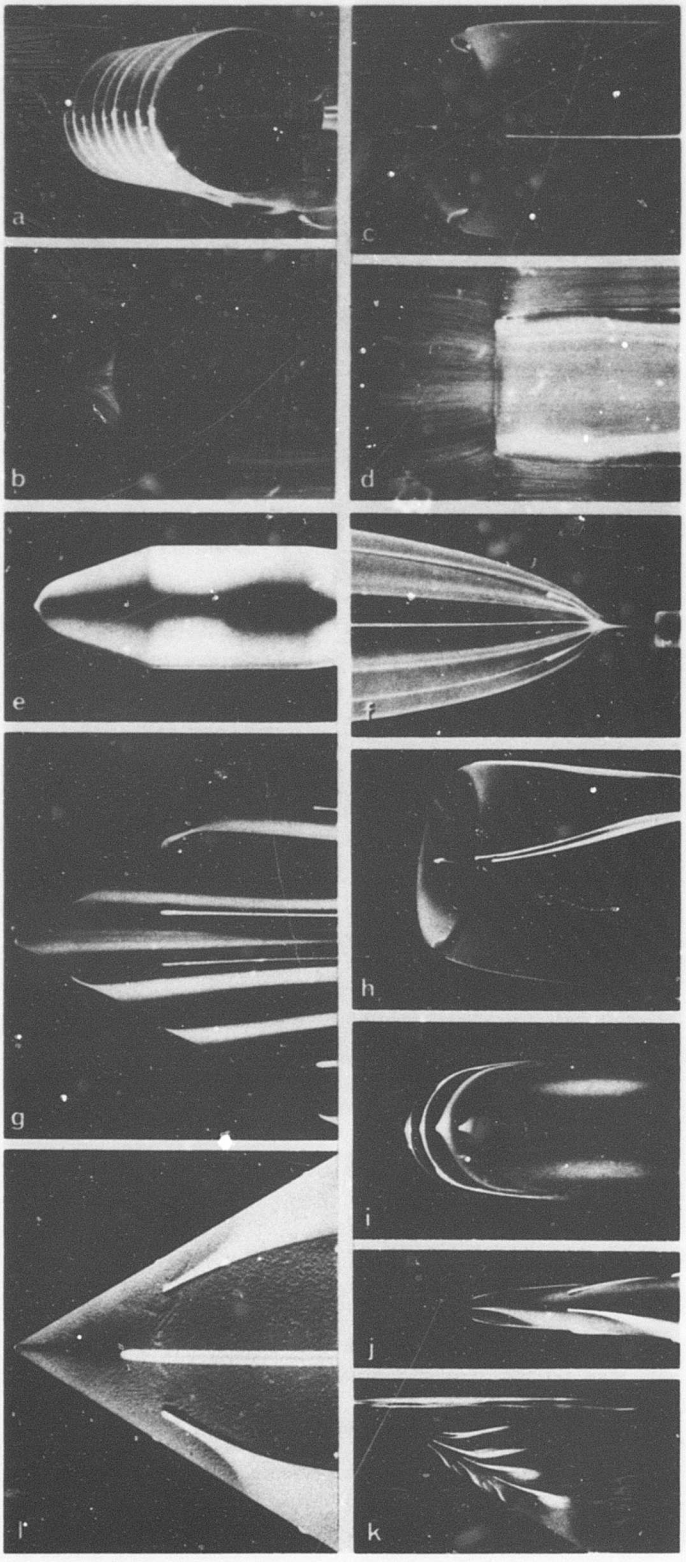

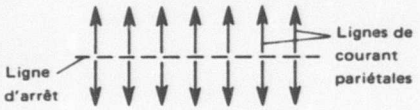

Ligne d'arrêt à l'avant d'un cylindre monté entre parois (a) et d'une prise d'air circulaire (c) sans incidence.

Visualisations complémentaires (b et d) de l'écoulement dans le plan de symétrie des modèles (méthode des bulles d'air).

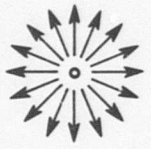

Ombilic, point de divergence (convergence) isotrope des lignes de courant pariétales

Point d'arrêt (ombilic) à l'avant (e) et à l'arrière (f avec aspiration du sillage) d'un corps fuselé de révolution sans incidence.

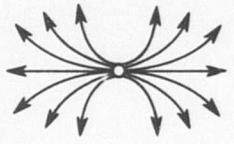

Nœud, point de divergence non isotrope des lignes de courant pariétales

Points d'arrêt (nœuds) à la pointe d'une aile delta (g) sans incidence, sur les lèvres inférieure et supérieure d'une prise d'air (h) avec incidence et sur le bord d'attaque arrondi d'un disque (i) sans incidence.

Lignes de partage se formant sur l'intrados aux incidences élevées :

Ligne unique sur un cône élancé (j) et sur une aile cylindrique en dérapage (k), ligne double sur une aile delta (l).

FIG. 1 – SINGULARITÉS CARACTÉRISANT L'ÉCOULEMENT NON DÉCOLLÉ SUR UN MODÈLE.
(Visualisation par émissions colorées pariétales).

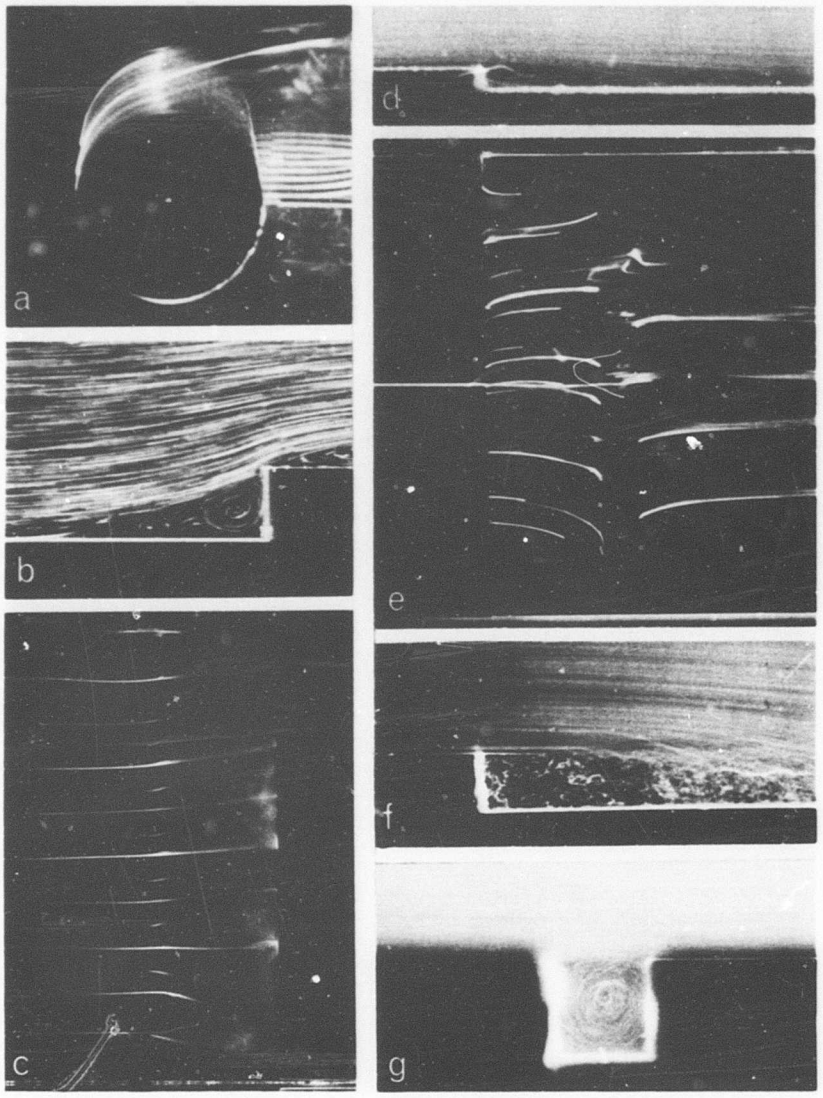

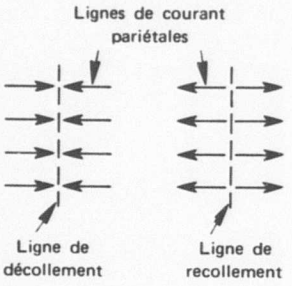

a cylindre avec décollement généralisé.

b et **c** paroi plane avec décollement localisé devant un ressaut.

d et **e** paroi plane avec décollement localisé derrière un petit décrochement.

f paroi plane avec décollement derrière un grand décrochement (transition).

g paroi plane avec cavité (zone de recirculation).

Visualisation par bulles d'air (plan de symétrie) et par émissions colorées pariétales.

FIG. 2 – LIGNES ET SURFACES CARACTÉRISANT LES DÉCOLLEMENTS EN COURANT PLAN.

FIG. 3 – PRINCIPAUX TYPES DE DÉCOLLEMENTS ET SILLAGES OBSERVÉS EN COURANT PLAN ET EN ÉCOULEMENT DE RÉVOLUTION [1]

a à **d** décollement généralisé le long d'une paroi incurvée (a : zone laminaire côté amont; **b** à **d** : zone turbulente côté aval - vues extraites d'un film d'essai).

e décollement localisé du type bulbe avec recollement laminaire } sur un profil.

f décollement localisé du type bulbe avec recollement turbulent }

g tourbillons de Bénard Karman dans le sillage d'une plaque mince sans incidence.

h sillage derrière les cylindres d'une maquette de faisceau tubulaire.

i sillage à l'extrémité d'un corps fuselé sans incidence.

j décollement localisé à recollement laminaire autour d'une tête d'engin sans incidence.

k décollement localisé à recollement turbulent autour d'une ogive à nez presque plat sans incidence.

l sillage au culot droit d'un corps de révolution sans incidence en régime permanent.

m tourbillon torique observé derrière un disque normal au vent au cours d'un mouvement de démarrage.

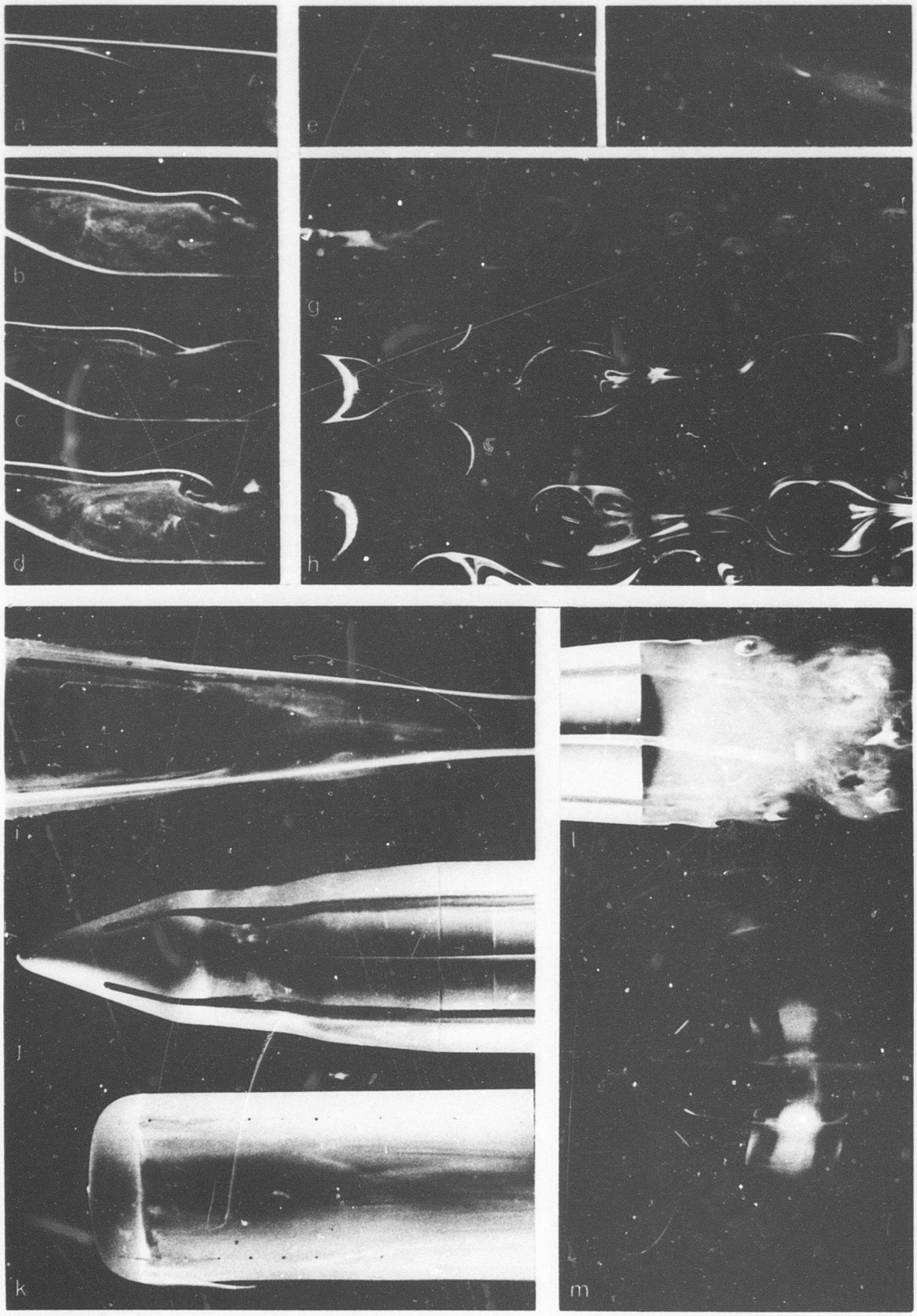

FIG. 4 – SCHÉMAS D'ÉCOULEMENTS LE LONG D'UNE PAROI

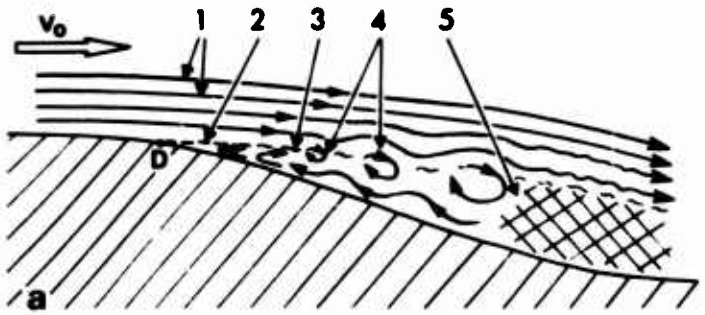

a paroi incurvée

1. lignes de courant (écoulement laminaire);
2. frontière de la zone décollée, stable côté amont, fluctuante côté aval;
3. transition; D point de décollement;
4. tourbillons emportés par le courant;
5. zone décollée turbulente.

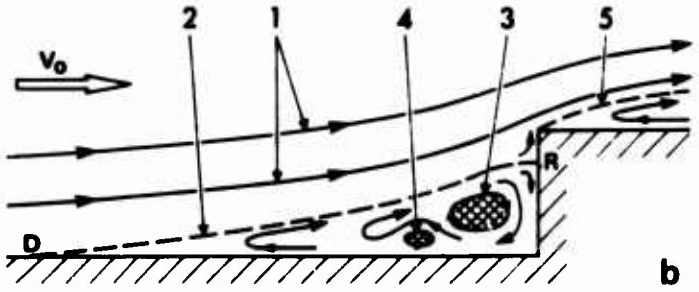

b paroi plane avec ressaut (marche > 0)

1. lignes de courant;
2. frontière de la zone décollée devant le ressaut;
3. tourbillon principal;
4. tourbillon secondaire;
5. frontière de la zone décollée sur le ressaut.

D point de décollement.

R point de recollement.

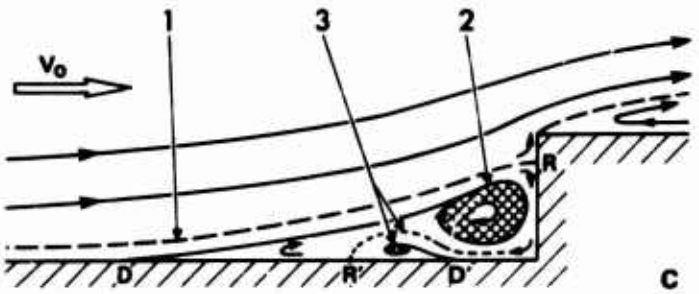

c paroi plane avec ressaut d'envergure limitée (écoulement tridimensionnel)

1. surface de séparation aboutissant le long de la ligne de recollement R;
2. tourbillon-puits principal (échappement transversal) autour duquel s'enroule la surface de séparation issue le long de la ligne de décollement D;
3. tourbillon-puits et surface de séparation secondaires.

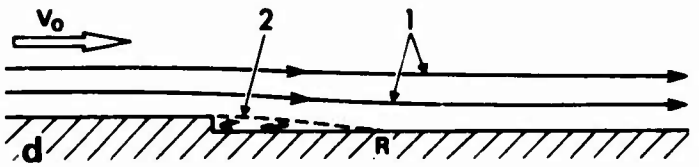

d paroi plane avec petit décrochement

1. lignes de courant;
2. frontière de la zone décollée fermée.

R zone de recollement laminaire.

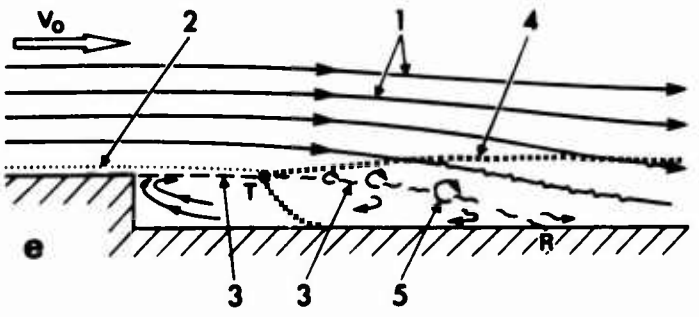

e paroi plane avec grand décrochement

1. lignes de courant;
2. couche limite;
3. frontière de la zone décollée, stable côté amont, fluctuante côté aval;
4. frontière de la zone turbulente;
5. tourbillons emportés par le courant.

T transition.

R point de recollement turbulent.

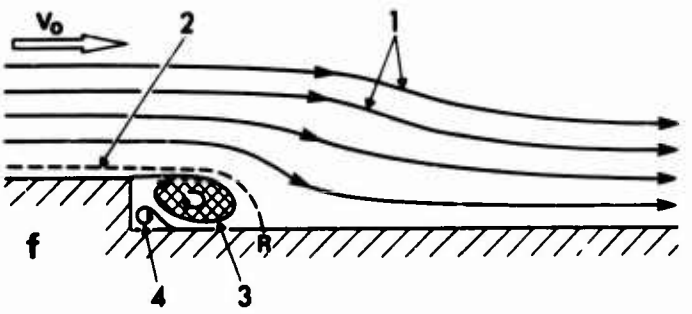

f paroi plane avec grand décrochement (écoulement tridimensionnel)

1. lignes de courant;
2. surface de séparation aboutissant le long de la ligne de recollement R;
3. tourbillon-puits principal (échappement transversal) autour duquel s'enroule la surface de séparation qui se détache au bord du décrochement;
4. tourbillon-puits et surface de séparation secondaires.

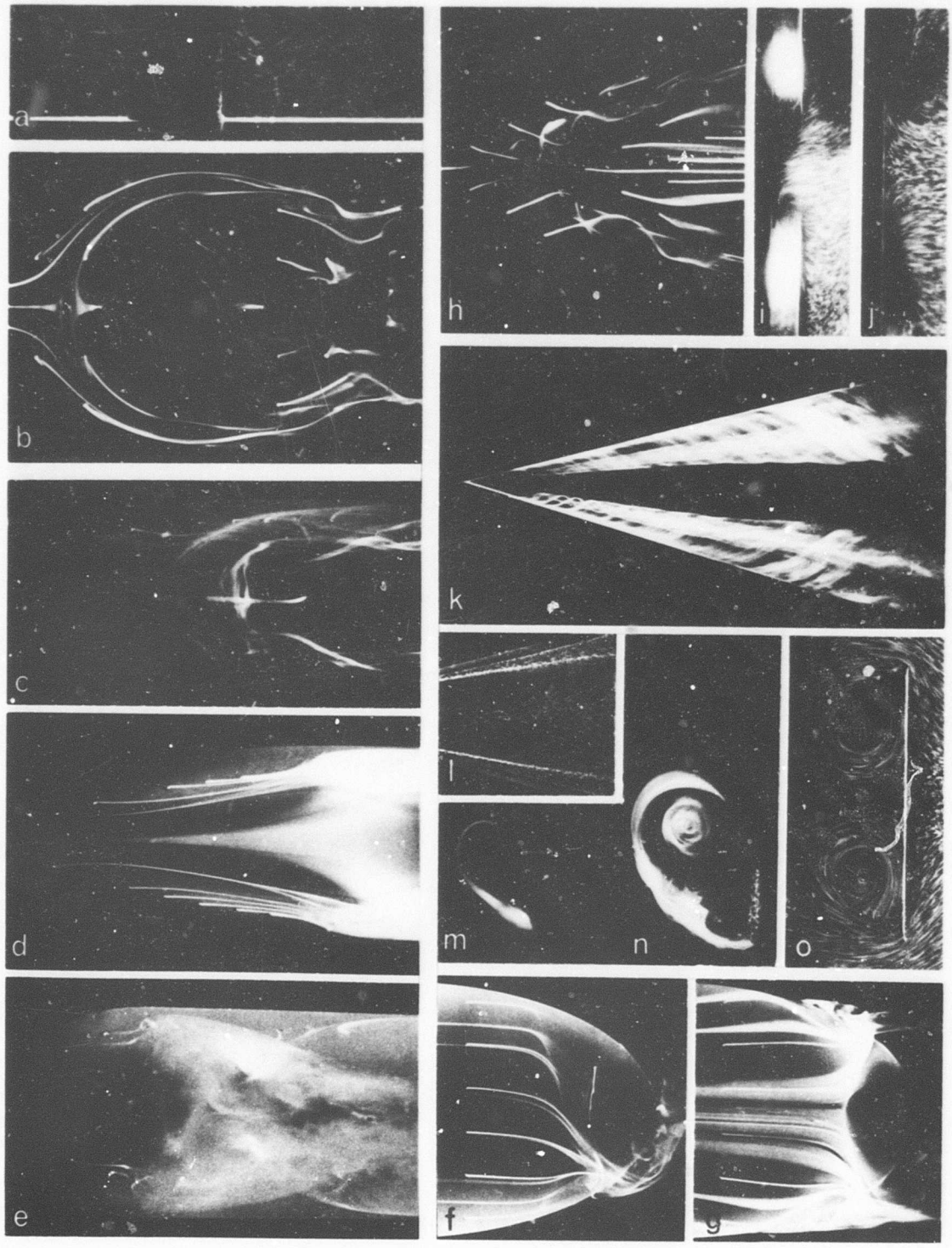

FIG. 5 – SINGULARITÉS CARACTÉRISANT LES DÉCOLLEMENTS TRIDIMENSIONNELS.

a et **b** décollement devant un cylindre fixé à la paroi.
c, d et **e** décollement sur l'extrados d'une ogive plus ou moins profilée avec incidence.
f et **g** décollement arrière sur un ellipsoïde aplati (a = 6 b = 2 c).
h, i et **j** nappes en «cornet» issues des bords d'un décrochement de paroi en «chevron»
k à **o** nappes en «cornet» issues des bords d'attaque d'une aile delta mince avec incidence.

Visualisation par émissions colorées (**b** à **h**), par bulles d'air (**a, i, j, l** et **o**) et par bulles d'hydrogène (**k, m** et **n**).

FIG. 6 – SCHÉMAS DE L'ÉCOULEMENT SUR L'EXTRADOS D'UNE AILE DELTA.

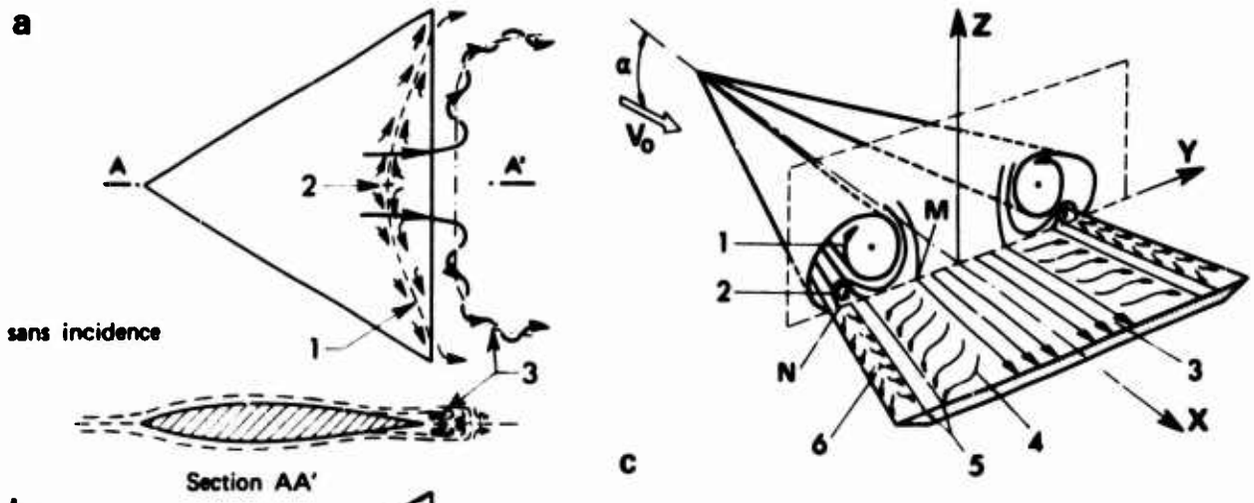

AILE DELTA MINCE AVEC INCIDENCE

1. nappe en «cornet» formant le tourbillon principal d'extrados;
2. nappe en «cornet» formant le tourbillon secondaire;
3. zone médiane non tourbillonnaire;
4. zone balayée par le tourbillon principal;
5. lignes d'accumulation de bulles d'air situées entre 4 et 6;
6. zone balayée par le tourbillon secondaire.

M frontière entre les zones 3 et 4.

N frontière entre la zone 6 et la zone située près du bord d'attaque et soumise à l'effet de la nappe 1.

AILE DELTA MOYENNEMENT ÉPAISSE

1. ligne de décollement;
2. point de partage de l'écoulement pariétal;
3. tourbillon de bord de fuite;
4. point de convergence spirale;
5. tourbillon d'extrados issu de 4.

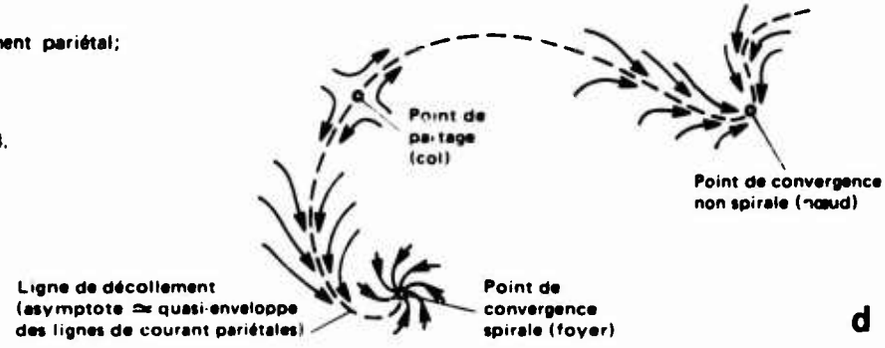

PRINCIPALES SINGULARITÉS OBSERVÉES

FIG. 7 – EXEMPLES D'ÉCOULEMENTS PARIÉTAUX OBSERVÉS A LA SURFACE DES MODELES [1]

a paroi plane sans obstacle

b paroi plane avec dièdre à culot droit ($\delta_{pointe} = 10°$) } obstacles

c paroi plane avec plaque à avant arrondi et retreint arrière ($\alpha = 0°$) } «courant plan»

d } aile trapézoïdale (NACA 0012) { $\alpha \simeq 2°$ / $\alpha \simeq 5°$ (vues de l'extrados)

e }

f ellipsoïde de révolution allongé : a/b = 6, $\alpha = 10°$ (vue de profil)

g aile delta (e/ℓ = 7 %, $\varphi_{BA} = 60°$) : vue partielle de l'avant côté intrados ($\alpha = 18°$)

h, i, j, k } aile delta (e/ℓ = 10 %, $\varphi_{BA} = 60°$) : vues partielles de l'arrière côté extrados { $\alpha = 0°$ / $\alpha = 6°$ / $\alpha = 8°$ / $\alpha = 10°$

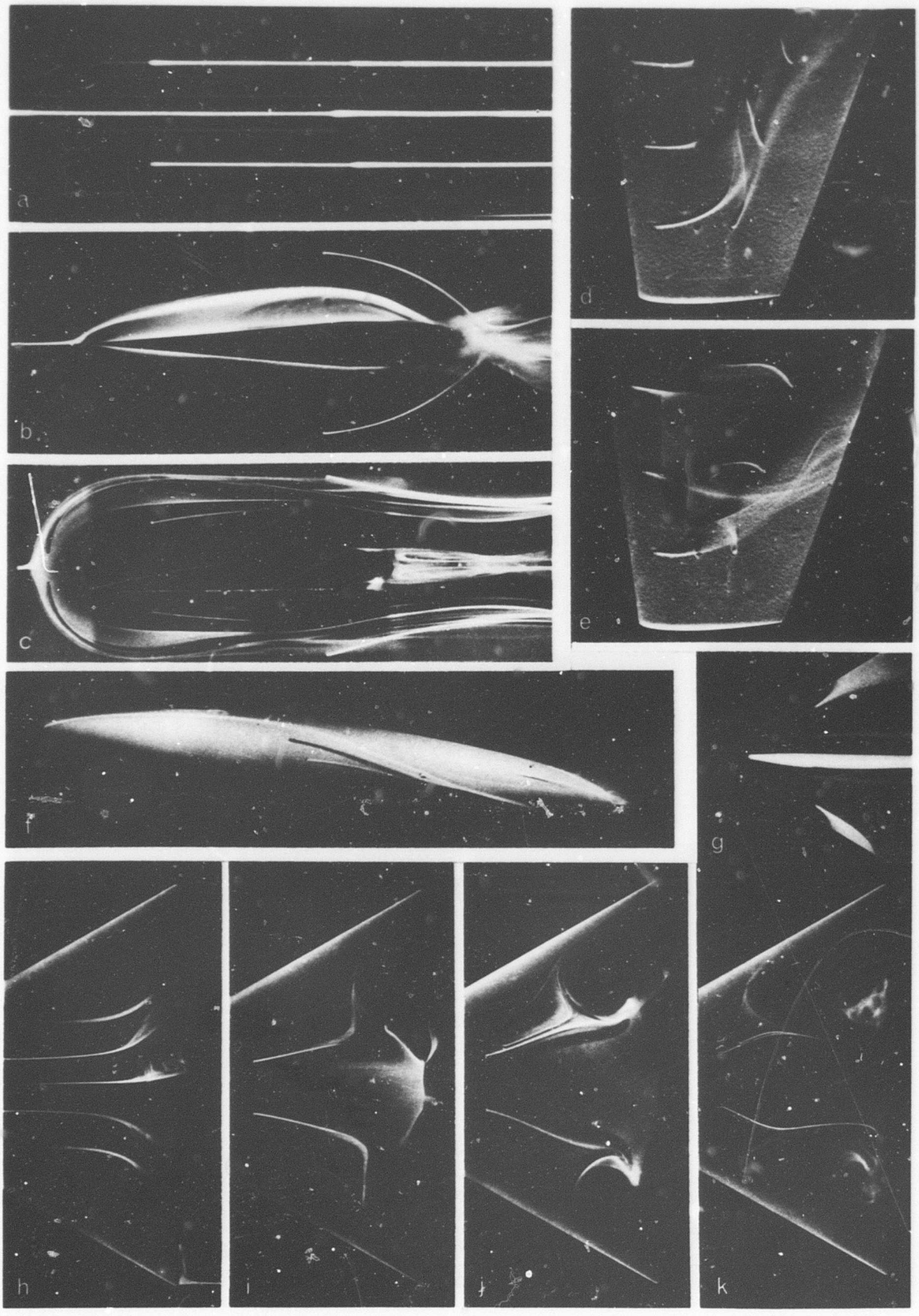

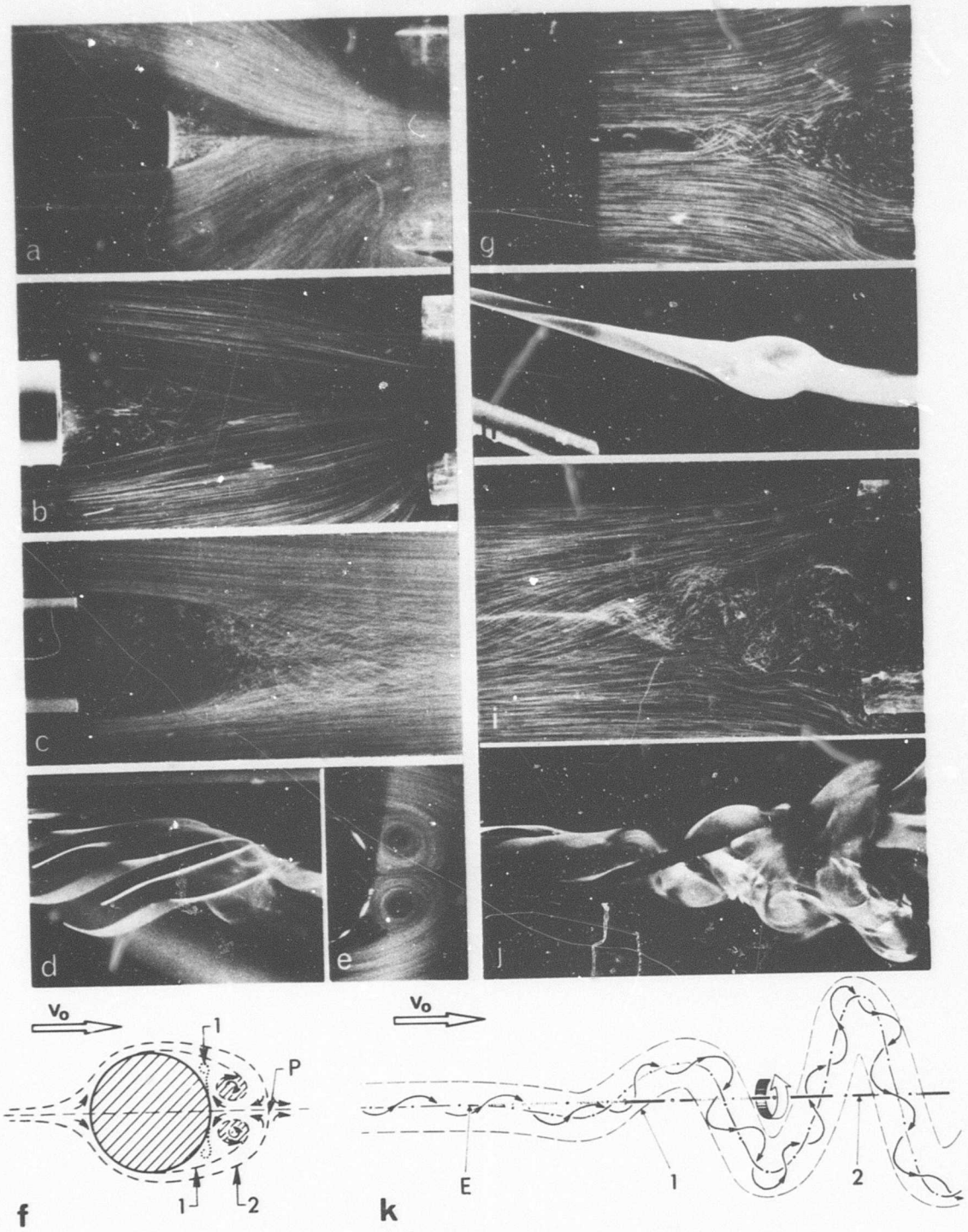

FIG. 8 – DÉCOLLEMENTS AU SEIN DU FLUIDE.

– Sillage fini en courant plan (a) et en courant de révolution (b), fermé sous l'effet d'aspiration.
– Comparaison avec un sillage naturel (c) comportant une eau morte finie amont et une zone turbulente aval.
– Sillage fermé derrière un cylindre en dérapage (d, e, f)
  1. nappes s'enroulant autour des tourbillons principaux et secondaires
  2. frontière de la couche alimentant les tourbillons
  P point de partage.
– Eclatement d'un sillage en courant plan (g) sous l'effet d'un obstacle.
– Eclatement localisé (h) d'un tourbillon de voilure (poche décollée finie).
– Eclatement généralisé (i, j, k) d'un tourbillon de voilure sous l'effet d'un obstacle
  E point d'éclatement
  1. partie d'un noyau déformé par l'éclatement
  2. axe du tourbillon.

THE THREE-DIMENSIONAL SEPARATION OF A TURBULENT BOUNDARY LAYER BY A SKEWED SHOCK WAVE; AND ITS CONTROL BY THE USE OF TANGENTIAL AIR INJECTION

by

David J. Peake
National Aeronautical Establishment, Ottawa, Canada

and

William J. Rainbird
Carleton University, Ottawa, Canada

SUMMARY

The three-dimensional interaction of a skewed shock wave with a turbulent boundary layer, that is generated by a variable-angle wedge standing normal to a flat test wall, has been systematically investigated at nominal mainstream Mach numbers of 2 and 4, up to and beyond shock strengths sufficient to cause incipient three-dimensional separation. The Reynolds number based on the undisturbed test boundary-layer thickness of 0.2-inch, growing along the nozzle sidewall of the NAE 5 × 5-inch blowdown wind tunnel, was $\sim 2 \times 10^5$. The experimental measurements, made under essentially zero heat transfer conditions, included extensive mapping of the test surface static pressures, selected pitot pressure and stagnation temperature profiles obtained with a servo-controlled 3-tube yawmeter; Preston tube impact pressures, and oil dot surface flow visualization. Some limited Schlieren investigations were made to verify shock angles.

In the Mach number 2 flowfield, with wedge deflection angles of 8 and 11.5°, blowing air at Mach 3 (also at ambient stagnation temperature) was introduced upstream of the interaction and tangential to the wall, through a rearward-facing step. The objective was to control and remove the three-dimensional separation. The jet excess momentum for this control situation was slightly more than the momentum deficit of the undisturbed boundary layer. In addition to the control of the magnitude of the blowing momentum, the direction of the wall jet could also be changed by rotating the line of the jet efflux. The optimum direction of blowing was found to be along a line somewhere between the deflected surface of the wedge and the line of the oblique shock wave (or the 3D separation).

NOTATION

β	Angle between local resultant velocity vector in the viscous flow and external stream resultant velocity vector at the outer edge of the boundary layer
β_{CL}	Angle between resultant velocity vector in the viscous flow and tunnel centre-line
C_F	Local skin friction coefficient
d_s	Diameter of static pressure orifice
δ	Boundary-layer thickness
δ_{995}	Boundary-layer thickness where local resultant velocity is 0.995 of velocity at boundary-layer edge
δ_1^*	Streamwise displacement thickness = $\int_o^{h_E} \left(1 - \frac{\rho u}{\rho_E u_E}\right) dh$
δ_2^*	Crossflow displacement thickness = $-\int_o^{h_E} \frac{\rho v}{\rho_E u_E} dh$
δ_o	Reference undisturbed boundary-layer thickness in empty wind tunnel
δ_W	Deflection angle of wedge shock generator measured with respect to tunnel centre-line
h	Height above test surface
H	Shape factor of streamwise boundary-layer profile, = δ_1^*/θ_{11}
$\dot{m}_j$	Mass flux of blc jet
M	Local mean Mach number
M_J	Local Mach number at exit of supersonic jet blowing nozzle for blc
M(P/PO)	Mach number calculated from ratio of static to stagnation pressure
M(P/PIT)	Mach number calculated from Rayleigh pitot relation
p	Static pressure
p_B	Pressure measured in static hole immediately upstream of obstacle block
p_1	Static pressure at reference measuring station 1
p_2	Calculated static pressure, downstream of swept shock, according to 'Oblique Shock Tables'
P_o, PO	Stagnation pressure of undisturbed mainstream flow

P_{oj}	Stagnation pressure of blc jet blowing air
P_p	Pitot pressure
R_{δ_o}	Reynolds number based on boundary-layer thickness, δ_o, and local mainstream conditions
$R_{\theta_{11}}$	Reynolds number based on streamwise momentum thickness of boundary layer and local mainstream conditions
ρ	Mean density within boundary layer
ρ_E	Mean density at outer edge of boundary layer
T_{AW}, TAW	Adiabatic wall temperature
T'	Intermediate temperature
T_o	Stagnation temperature measured in settling chamber of wind tunnel
T_{PC}	Corrected total temperature at cobra probe thermocouple
T_{PCE}	Corrected total temperature at outer edge of boundary layer
T_W	Wall temperature
θ_j	Rotation of blc jet blowing nozzle unit with respect to perpendicular to tunnel centre-line in (x,y)-plane
θ_{11}	$\int_o^{h_E} \frac{\rho u}{\rho_E u_E}\left(1 - \frac{u}{u_E}\right) dh$, momentum thickness of streamwise flow
u	Component of mean velocity within boundary layer parallel to direction of external streamline at outer edge of boundary layer - called streamwise flow
u_B	Resultant mean velocity within boundary layer, (in 2D flow, $u_B \equiv u$)
u_E	Mean velocity at outer edge of boundary layer
u_j	Mean velocity of blc jet blowing air at jet nozzle exit
v	Component of mean velocity within boundary layer normal to direction of external streamline at outer edge of boundary layer - called crossflow
x, X	Axial distance from centre of rotation of turntable jet blowing nozzle on tunnel centre-line
XT	Location of traverse station of cobra probe or circular pitot tube orifices along x-axis
XWLE	Axial location of leading-edge of movable wedge shock generator
XSWINV	Axial location of calculated shock wave from deflected wedge, assuming inviscid flow on either side of shock
y	Lateral distance in plane of tunnel floor from centre of rotation of turntable jet blowing nozzle. Positive is in direction away from deflection test surface of wedge shock generator

ABBREVIATIONS

blc	boundary-layer control
2D	two-dimensional
3D	three-dimensional

SUBSCRIPTS

E	outer edge of boundary layer
j	jet
w	wall

1.0 INTRODUCTION

The three-dimensional interaction between a turbulent boundary layer developing along a surface and a perpendicular, glancing oblique shock wave (sometimes called a 'skewed' shock wave) - see Figure 1 - is a phenomenon of considerable importance in the design of swept wings, wing/body and tail/body junctions, and quasi 2D intakes. Despite several previous investigations[1,2,3,4], Green noted[5] that there was little quantitative understanding of interactions between swept shock waves and turbulent boundary layers, although Stalker[1] and Stanbrook[2] introduced some qualitative features in their early work, while later investigations by McCabe[3] and Lowrie[4] provided some insight into the crossflows developing in the interaction. Much of the existing analysis has been developed for so-called 'infinite' swept flows, and so is of a quasi two-dimensional nature; while most experiments have been conducted using the nozzle boundary layers in relatively small supersonic wind tunnels At a given mainstream Mach number, the flow deflection angle for so-called 'incipient separation' has usually been determined as when the limiting streamlines became parallel to the projection of the shock wave (in the external stream) on to the wall, and Korkegi[6] has made a simple correlation of incipient separation data from References 3 and 4.

In an attempt to remedy some of the deficiencies of the earlier investigations, a systematic series of experiments was planned and executed, utilizing the NAE 5 × 5-inch blowdown (pilot) wind tunnel. In these experiments, the mean flow features including wall static pressure, surface impact pressure and limiting streamline direction, and pitot and stagnation temperature profiles, were gathered through swept interactions at mainstream Mach numbers of 2 and 4, up to and beyond flow deflection angles through the shock wave that produced three-dimensional separation. The Reynolds number based upon the mainstream conditions and the undisturbed boundary-layer thickness, δ_o, of 0.2-inch, was $\sim 2 \times 10^5$.

Subsequently, for the Mach 2 flow, a small convergent/divergent tangential wall jet nozzle was installed in the test wall (Figure 2) upstream of the interaction region, to investigate whether a strong three-dimensional shock-induced separation could be controlled or destroyed by a Mach number 3 supersonic wall jet. (The planning of the 3D experiment followed the criteria established by Peake[7] for supersonic blowing boundary-layer control in a two-dimensional shock/boundary-layer interaction). The direction of the jet efflux could be orientated at various angles with respect to the line of separation, as we see on the diagrammatic sketch of Figure 1.

This experiment was planned as one of several at NAE, to ascertain the fluid mechanics of three-dimensional separations in low and high-speed flows. A full compilation of the 3D shock/boundary-layer interaction results is presented in Reference 8, while a review of other NAE work is published in Reference 9.

2.0 EXPERIMENT

Figure 2 illustrates the outlet of the 5 × 5-inch Mach number 2 supersonic nozzle that comprises one of the test sections of the pilot wind tunnel. It is composed of flat top and bottom plates (the usual nozzle sidewalls) that are separated by the two contoured nozzle blocks. Nozzle block pairs providing nominal mainstream Mach numbers of 2 and 4 were used in the tests. One of each pair of nozzle blocks has two slots to accept the support struts of the vertical, plane/triangular-sectioned wedge shock generator. The generator can translate parallel to the tunnel axis and can be pitched about its leading-edge.

The test boundary layer with free transition, developed along the bottom plate of the wind tunnel. The nominal two-dimensional boundary layer in the empty tunnel (about 0.2-inch thick) was traversed with a 0.0164-inch dia. pitot tube which was also used as a Preston tube at the wall. The three-dimensional boundary layer was investigated with a 'cobra' probe comprising a flattened three-tube measuring head (Figure 3) where the two outer tubes are each chamfered back at 45-degrees to form a yawmeter, while the centre tube (0.028-inch wide × 0.012-inch high) is a rectangular pitot. As the probe is traversed out through the viscous flow, from an initial position at the wall to a maximum extension of about 0.8-inch, a yaw servo-system turns the probe head to align it with the oncoming flow direction. Local flow angles in a plane parallel with the test floor, and pitot pressures, can hence be measured at the wall and through a skewed boundary layer. Probe height above the surface accurate to better than ±0.001-inch and yaw angle to ±0.2°, are measured by geared multi-turn potentiometers. The pitot pressure was recorded by a close-coupled 50 psia pressure transducer. The probe extension rate can be pre-selected: a traverse height of 0.5-inch was usually sampled in about 15→30 seconds.

Figure 4 shows the assembly of the cobra probe and its appearance above a test wall.

To measure the variation of stagnation temperature through the viscous flow, an unshielded iron-constantan thermocouple, of bead diameter 0.002-inch, was mounted above the pitot orifice - see Figure 3 - so permitting pneumatic and temperature measurements to be taken simultaneously. The temperature probe design was similar to the stagnation line probe introduced by Bradfield et al[10] and Harris[11], the installation of which was particularly suitable for adapting to the cobra probe. Upon calibration of the thermocouple in the tunnel mainstream flow, at various Mach numbers downstream of the shock wave from the variable-angle wedge, the recovery factors were found to be 0.960 ± 0.003, being slightly less than the factors found in Reference 10.

The local near adiabatic wall temperature was measured using flush-mounted thin plate elements to which thermocouples were attached on the side away from the flow.

A rectangular cut-out was machined in the test floor, to accept alternative and removable inserts that are fitted with instrumentation and equipment for the interaction phase (wall static pressure orifices, yawmeter traverse and wall temperature stations) and for the control phase: the blowing nozzle, as seen on Figure 2. The throat dimension of the blowing nozzle could be changed in order to provide a variable Mach number of the injection air, of between 1.5 and 4.5. (Only jet Mach numbers of 3 were used, however). The jet slot height of 0.1-inch was half of the undisturbed boundary-layer thickness, while jet stagnation pressures could be varied up to 20 atmospheres at ambient stagnation temperature.

The maximum values of stagnation pressure used in the mainstream flow at Mach numbers 2 and 4 (limited by the strength of the wedge strut supports) were 2.4 and 12 atmospheres respectively.

3.0 RESULTS

3.1 Empty Tunnel Flow

Some initial tests in the empty wind tunnel were conducted to determine the two-dimensionality of the undisturbed test boundary layer on the tunnel floor at nominal Mach numbers of 2 and 4. The uniformity of the flow was assessed by reviewing wall static pressures, surface oil flow visualization, mean velocity profiles at several lateral positions and at two axial stations in the working section, and local surface skin friction. For brevity, we shall only comment upon the Mach 2 flow.

Figure 5 shows surface pressure and oil dot flow visualization results at Mach 2, with a stagnation pressure in the mainstream flow of 34 psia (corresponding with a Reynolds number based on the undisturbed boundary-layer thickness, δ_o = 0.2-inch, equal to 150,000). This value of blowing pressure was used for all of the Mach 2 traverse measurements through the swept interaction to be discussed later. The surface pressures were made non-dimensional by reference to the static pressure at a station labelled 1 in the upstream part of the working-section. The surface pressures and oil flow visualization in Figure 5 indicate reasonable uniformity across the width of the test section. The lines of 0.015-inch diameter static pressure orifices, labelled Y, Z, ℄, A, B, D and E on the test floor, and the two axial stations numbered 4 and 18 where circular pitot traverses were taken, may be identified on Figure 5. We should note that the origin of the X-abscissa is arbitrarily set at the position of the turntable centre-line of the blowing experiment (see Figure 2) - this is for convenience in referencing the later data with blowing. Such origin is situated 8.625-inches upstream of the exit of the tunnel working section, and 11.14-inches downstream of the throat of the Mach 2 nozzle.

Figure 6 displays mean velocity profiles at Mach 2 as deduced from the traverse measurements with the circular pitot tube at the axial stations numbered 4 and 18. The velocity profiles were computed assuming, through the boundary layer, constant static pressure equal to the local wall condition in the absence of the pitot tube; and constant stagnation temperature equal to the tunnel settling chamber temperature. The boundary-layer thickness, $\delta_{99.5}$, is that where the local mean velocity reaches 99.5 percent of the local boundary-layer 'edge' or mainstream velocity, and the displacement correction for the circular tube corresponds with that of Reference 12.

We see on Figure 6, that the uniformity is acceptable at both stations 4 and 18. The locations C and X are 1.25-inches or $6\delta_o$ on either side of the tunnel centre-line. At station 18, the nominal two-dimensional profiles are described better by a 1/7th than a 1/9th power law, although towards the edge of the boundary layer, the profiles indicate more fullness than either power law would predict. A contributing factor might be the presumed high mainstream turbulence level resulting from intense pressure fluctuations generated at the tunnel control valve and measured in the tunnel working section[13] ($\Delta p_{rms}/P_o \sim 0.7$ percent at Mach 2), producing, in conjunction with the rapid acceleration of the boundary layer from tunnel throat to Mach 2 conditions and associated non-equilibrium situation, an increase in width of the zone of intermittency[14]. Other profiles obtained with the cobra probe compared satisfactorily with the circular tube results[8].

Boundary-layer integral parameters and local surface skin friction results for the empty tunnel Mach 2 flow, as deduced from the circular pitot and cobra probes, are plotted on Figure 7. We see only a very small increase in boundary-layer thickness, displacement thickness and momentum thickness, along more than 3-inches of the test region (equivalent to about 150 momentum thicknesses). The results from the circular pitot seem to provide thicknesses slightly less than from the cobra probe: neither changes in the rectangular flattened tube displacement correction used for the cobra probe[15] (which is debatable), nor inserting T_o = constant across the boundary layer, instead of using the cobra measured total temperature distribution, made substantial effect upon this comparison.

Pitot pressures at the wall expressed in terms of the corresponding local skin friction coefficients according to the correlation of Bradshaw and Unsworth[16], are also shown on Figure 7. The surface pitot measurements from the cobra probe provide us with a local skin friction coefficient consistently less than that given by the circular tube by $\Delta C_F \cong 0.00035$. Although the measurements of skin friction by Quarmby and Das[17] with rectangular pitot tubes in incompressible flow demonstrated insignificant differences from the circular tube calibration of Patel[18] (where the height of the probe was used in correspondence with the outer diameter of the circular tube) we interpret the cobra probe geometry with its chamfered flattened side tubes, to require a calibration in a high Reynolds number pipe flow. It is worthy of note that a chamfered three-tube surface yaw probe, but with three circular tubes affixed together, was used in conjunction with Patel's calibration[18] in Reference 19, when the surface direction of the flow was initially unknown. We further note on Figure 7, that the circular tube result from Bradshaw's and Unsworth's correlation[16] is less by $\Delta C_F \cong 0.0004$ than the adiabatic wall, Spalding/Chi[20] result at the corresponding momentum thickness Reynolds number. The discrepancy is in all likelihood bound up with the recovery of the test boundary layer from its large degree of three-dimensionality in the expanding nozzle flow to one with a very small residual convergence (toward the centre-line) in the working section.

3.2 Surface Pressure Distributions and Flow Visualization at Mach 2 In the Presence of the Wedge

The static pressure distributions along the test surface and a selection of photographs of oil dot streak patterns obtained with the vertical-standing wedge in the test section, are shown on Figure 8. On each pressure distribution, we observe the theoretical shock pressure rise in inviscid flow corresponding with the mainstream Mach number, while the origin of the abscissa is the calculated shock wave position where it intersects the given line of pressure holes. The abscissa scale is normalized with respect to the nominal undisturbed boundary-layer thickness, δ_o, of 0.2-inch. Each pressure distribution is in the direction of the undisturbed stream parallel to the tunnel centre-line at different y-values or lateral distances from the wedge apex, and for clarity, only those measurements from lines Z through B have usually been plotted. The flow is from left-to-right, and the triangular cross-section of the wedge has been outlined in ink. The wedge

at 8° to the centre-line). Constant reference to Figure 11 will assist the reader with the ensuing discussion.

The measurements from the cobra probe (prior to their manipulation into velocity profiles) are shown on Figures 12 and 13 as simultaneously gathered pitot pressures, total temperatures and yaw angles (with respect to the tunnel centre-line direction) plotted against vertical distance from the test surface, h-inches. The relative dispositions of the changes in the profile shapes are clear on Figure 12.

The profiles exhibited on Figure 13 are those taken along the tunnel centre-line only, where, as on the static pressure plots, the calculated shock wave location is the origin for the abscissa. The flow is from left-to-right.

The scale for the pitot pressure profiles as related to the settling chamber stagnation pressure is given at the top of Figure 13, and the local wall static pressures are written beneath the abscissa. The upstream profiles display the characteristics of the nominal two-dimensional flow existing there. At $2\delta_o$ upstream of the calculated shock position, we observe a substantial outward movement of the sonic line, coupled with a rapid decrease in pitot pressure signal as the local mainstream is approached. This pitot pressure deficit would be consistent with passage through a densely packed fan of compression waves that commences ahead of the location of the calculated shock front. This outer gradient of pitot pressure disappears suddenly at the calculated shock position, indicating a sudden increase in local Mach number as h → 0.5-inch. With further distance downstream, the sonic line slopes back towards the wall. We note that especially through the interaction, near the calculated shock position, the pitot pressure adjusts very slowly towards the level in the local mainstream flow.

The centre graphical display of Figure 13 shows the measured total temperature profiles, referenced to the stagnation temperature in the tunnel settling chamber: 1 percent of T_o is roughly 5°R. The total temperature rises rapidly in the laminar sublayer immediately adjacent to the wall, before assuming some constancy in the wall law region. Thereafter, it continues to increase and to overshoot the mainstream flow level by typically one half of one percent of T_o. The presence of the overshoot in the temperature distributions (which moves further from the wall with progression through the interaction) means that the total enthalpy defect in the layer

$$\int_o^\delta \frac{\rho u_B}{\rho_E u_E} \left(1 - \frac{T_{PC}}{T_{PCE}}\right) dh$$

should be small, tending to zero for a boundary layer on a thermally insulated surface.

If the total temperature distributions are expressed in terms of the quotient

$$F = \frac{T_{PC} - T_W}{T_{PCE} - T_W}$$

they can be compared against the Crocco relationship[21] put into a 3D formulation,

$$F = \frac{u_B}{u_E}$$

where u_B is the resultant velocity in the viscous flow. We noted that when plotting the ratio of temperature differences as ordinate versus u_B/u_E as abscissa, the results were situated well above the line of 100 percent correlation on the graph. The parabolic relation of Walz[22],

$$F = \left(\frac{u_B}{u_E}\right)^2$$

provided even worse comparison. Neither of these frequently assumed 2D type temperature distributions appear to exist, therefore, in the swept interaction presently under discussion.

The yaw angle distributions corresponding with the pitot and total temperature plots just discussed, are shown on the lowest of the three sets of profiles on Figure 13. The skew at the wall, in a direction that turns away from the deflected wedge surface, begins to increase from its nominal 2D value, at least $3\delta_o$ upstream of the calculated shock wave location. As we move downstream (but still upstream of the shock) the extent of the yawed flow region normal to the wall, and the maximum yaw angle grow progressively; while at the prescribed boundary-layer edge, the yaw angle has not returned to the nominal mainstream flow direction parallel to the tunnel centre-line. The yaw angle continues to reduce up to $2\delta_o$ away from the surface (see profile no. 8, for instance). Immediately upstream of the shock, at profile no. 11, we note the opposite behavior - see Figure 12 - above the boundary-layer edge, the yaw angle increases slowly, this trend carrying over into the recovering flow downstream of the calculated shock location.

We recollect that our diagnosis of the oil flow visualization records on Figure 8 contended that no 3D separation existed at $\delta_W = 8°$. The raw profile information that we have just examined would seem to support this view, for we shall see in Section 3.6, that the stagnation temperature profiles appear to be sensitive indicators of three-dimensional separated flow regions. In contrast, the Mach 2, $\delta_W = 8°$ temperature profiles on Figure 13 display no sudden variation in characteristics.

at 8° to the centre-line). Constant reference to Figure 11 will assist the reader with the ensuing discussion.

The measurements from the cobra probe (prior to their manipulation into velocity profiles) are shown on Figures 12 and 13 as simultaneously gathered pitot pressures, total temperatures and yaw angles (with respect to the tunnel centre-line direction) plotted against vertical distance from the test surface, h-inches. The relative dispositions of the changes in the profile shapes are clear on Figure 12.

The profiles exhibited on Figure 13 are those taken along the tunnel centre-line only, where, as on the static pressure plots, the calculated shock wave location is the origin for the abscissa. The flow is from left-to-right.

The scale for the pitot pressure profiles as related to the settling chamber stagnation pressure is given at the top of Figure 13, and the local wall static pressures are written beneath the abscissa. The upstream profiles display the characteristics of the nominal two-dimensional flow existing there. At $2\delta_o$ upstream of the calculated shock position, we observe a substantial outward movement of the sonic line, coupled with a rapid decrease in pitot pressure signal as the local mainstream is approached. This pitot pressure deficit would be consistent with passage through a densely packed fan of compression waves that commences ahead of the location of the calculated shock front. This outer gradient of pitot pressure disappears suddenly at the calculated shock position, indicating a sudden increase in local Mach number as $h \to 0.5$-inch. With further distance downstream, the sonic line slopes back towards the wall. We note that especially through the interaction, near the calculated shock position, the pitot pressure adjusts very slowly towards the level in the local mainstream flow.

The centre graphical display of Figure 13 shows the measured total temperature profiles, referenced to the stagnation temperature in the tunnel settling chamber: 1 percent of T_o is roughly 5°R. The total temperature rises rapidly in the laminar sublayer immediately adjacent to the wall, before assuming some constancy in the wall law region. Thereafter, it continues to increase and to overshoot the mainstream flow level by typically one half of one percent of T_o. The presence of the overshoot in the temperature distributions (which moves further from the wall with progression through the interaction) means that the total enthalpy defect in the layer

$$\int_o^\delta \frac{\rho u_B}{\rho_E u_E}\left(1 - \frac{T_{PC}}{T_{PCE}}\right) dh$$

should be small, tending to zero for a boundary layer on a thermally insulated surface.

If the total temperature distributions are expressed in terms of the quotient

$$F = \frac{T_{PC} - T_W}{T_{PCE} - T_W}$$

they can be compared against the Crocco relationship[21] put into a 3D formulation,

$$F = \frac{u_B}{u_E}$$

where u_B is the resultant velocity in the viscous flow. We noted that when plotting the ratio of temperature differences as ordinate versus u_B/u_E as abscissa, the results were situated well above the line of 100 percent correlation on the graph. The parabolic relation of Walz[22],

$$F = \left(\frac{u_B}{u_E}\right)^2$$

provided even worse comparison. Neither of these frequently assumed 2D type temperature distributions appear to exist, therefore, in the swept interaction presently under discussion.

The yaw angle distributions corresponding with the pitot and total temperature plots just discussed, are shown on the lowest of the three sets of profiles on Figure 13. The skew at the wall, in a direction that turns away from the deflected wedge surface, begins to increase from its nominal 2D value, at least $3\delta_o$ upstream of the calculated shock wave location. As we move downstream (but still upstream of the shock) the extent of the yawed flow region normal to the wall, and the maximum yaw angle grow progressively; while at the prescribed boundary-layer edge, the yaw angle has not returned to the nominal mainstream flow direction parallel to the tunnel centre-line. The yaw angle continues to reduce up to $2\delta_o$ away from the surface (see profile no. 8, for instance). Immediately upstream of the shock, at profile no. 11, we note the opposite behavior - see Figure 12 - above the boundary-layer edge, the yaw angle increases slowly, this trend carrying over into the recovering flow downstream of the calculated shock location.

We recollect that our diagnosis of the oil flow visualization records on Figure 8 contended that no 3D separation existed at $\delta_W = 8°$. The raw profile information that we have just examined would seem to support this view, for we shall see in Section 3.6, that the stagnation temperature profiles appear to be sensitive indicators of three-dimensional separated flow regions. In contrast, the Mach 2, $\delta_W = 8°$ temperature profiles on Figure 13 display no sudden variation in characteristics.

3.4 Crossflow and Streamwise Flow

Let us now examine selected profiles on Figure 14 obtained with the cobra probe at the three lines of traverse stations (see Figure 11). Where profiles at nominally the same distances upstream or downstream of the calculated shock position along each of the lateral traverse lines (y/δ_o = constant) have been gathered, they will be overplotted, and a mean line drawn through them.

Taking the measured values of total temperature and pitot pressure, coupled with the assumption of constant static pressure across the viscous flow equal to the local wall value, the distribution of resultant mean velocity can be calculated. We might interject that since at any given Mach number in the flow, the resultant velocity, u_B, depends only upon the half power of the local absolute stagnation temperature, whether we use a constant stagnation temperature through the boundary layer equal to T_o, or whether we use that measured locally in the flow, causes insignificant change in the calculated result for u_B. Of greater significance, is the assumption of constant static pressure across the boundary layer. We can see from Figures 8, 9 and 10 for example, that upstream of the calculated shock wave location, the wall pressure is potentially greater than in the mainstream, whereas downstream, it is potentially less, if the distribution of pressure rise in the mainstream follows the pattern of the inviscid flow calculation. In Reference 23, at a nominal Mach number of 3, we saw that a linear reduction in static pressure of 16 percent from the wall to the mainstream, made about a 2 percent difference in both normalized density and velocity ratios when compared with using a constant static pressure across the flow. These differences tended to be self-compensating. Hence, the overall effect was for only a 2 percent reduction in displacement thickness. On the other hand, there was a massive increase in local momentum thickness of about 80 percent (due to the lower values of velocity ratio) thereby reducing the local shape factor. If indeed, the static pressures are monotonically increasing or decreasing substantially across the 3D viscous flow, we would not expect to view major variations in the resultant normalized velocity profiles, but momentum thickness parameters might be in doubt.

Knowing the local flow direction and mean velocity at the boundary layer edge, u_B can be resolved into streamwise flow and crossflow components, u and v, where $u = u_E$ and $v = 0$ at $h = \delta$. Representative boundary-layer u and v profiles of the Mach 2, $\delta_W = 8°$ flow, are shown on Figure 14. The traverse height perpendicular to the wall and the velocities have been normalized by local values of δ_{995} and u_E respectively.

The wall static pressure ratio increases in the downstream direction when proceeding 'downstairs', to the left for the crossflow, and to the right for the corresponding streamwise flow. The symbol code at the top left-hand corner distinguishes the traverse locations and Figure 11 should be sought to identify the traverse positions relative to the calculated shock wave location.

The difficulties of finding adequate representation for the crossflow profiles is illustrated on the left-hand side of Figure 14, where the experimental measurements at the calculated shock location are compared against the parabolic form suggested by Mager[24], which is

$$\frac{v}{u_E} = \frac{u}{u_E}\left(1 - \frac{h}{\delta}\right)^2 \tan \beta$$

The angle, β, on the test surface, is between the local limiting streamline direction and the projection on to the surface of the inviscid streamline at the boundary-layer edge. This profile representation clearly forces agreement immediately adjacent to the surface*, but is more full throughout the boundary layer than its experimental counterpart. The maximum value of crossflow velocity ratio and flow angle, tends almost to a constant value downstream of the calculated shock position. The thesis of Lowrie[4] dealt almost exclusively with representing chosen velocity profiles in a swept interaction region by Johnston's[25,26,27] triangular model for crossflow. Such a representation does not work for the present flow[8].

It remains to be seen whether the family of hodograph crossflow models suggested by Shanebrook and Hatch[28] and discussed in terms of the compressible, 3D turbulent boundary layer in Reference 29, would yield any satisfactory degree of comparison in a non-equilibrium boundary layer, such as in the swept interaction. Comparisons between selected members of the hodograph family of Shanebrook and Hatch[28] and the nozzle wall crossflow profile data of Hall and Dickens[24] were good. But to find analytical profiles, the method of least squares must be used to fit the experimental hodographs with the crossflow models from the theoretical subfamilies[29]. Such a technique is not too helpful when attempting to calculate a flowfield before experimental results are taken. For reasons such as these, the use of a three-dimensional boundary-layer calculation method such as that due to Nash that is based upon the turbulent kinetic energy equation[30] would appear a more worthwhile pursuit, in which no assumptions about crossflow profile shapes have to be made. In fact, the Nash programme[31] in which the experimental $\delta_W = 8°$ pressure distribution and the upstream 2D boundary-layer properties were boundary conditions, was used to calculate the flowfield and the calculated profiles were in good qualitative agreement

*There is a discrepancy, however, between the flow near the surface from the cobra probe traverse and that on the parabolic distribution. This is due to the fact that the local wall shear stress direction from the oil flow visualization has been inserted for β, rather than the cobra probe determined yaw angle closest to the wall.

with the cobra probe measurements[8].

In contradistinction with the crossflow profiles, the streamwise flow on Figure 14 demonstrates an almost self-preserving character once into and through the region of strong interaction, but with a profile much less full than that given by the 2D, 1/7th power law.

3.5 Integral Parameters, Local Skin Friction and Wall Conditions at Mach 2 with $\delta_W = 8°$

Figures 15, 16 and 17 illustrate the growth of the boundary layer through the $\delta_W = 8°$, Mach 2 swept interaction region. All of the profile data are plotted, taken along both the tunnel centre and off/centre-line stations (at $y/\delta_o = 0.14$ and 0.75). The three lines of results are identified with different symbols. The shaded symbols are at those two traverse stations along the projected inviscid streamline, downstream of the calculated shock wave position. We note that the qualitative interpretation of the results is the same, whether we stay on one line of traverse measurements, or whether we follow the inviscid streamline path.

In the axial direction, there is a lag in the growth of the streamwise and crossflow thickness parameters, until about $1\delta_o$ downstream from the commencement of the pressure rise, where the local static pressure gradient is at its maximum. (We note on Figure 17, however, that the deflection, β, of the limiting streamlines responds immediately to the application of the pressure rise). During the following $2\delta_o$ of downstream distance, the component displacement and momentum thickness parameters show rapid growth until the calculated shock position is reached, after which the pressure gradient begins to reduce significantly. Nevertheless, in the streamwise flow sense at least, changes in density are more-or-less compensated by the local changes in velocity: for the streamwise shape factor, $H (= \delta_1^*/\theta_{11})$, on Figure 15, shows only a small overall reduction through the interaction region. This is what we would expect from the appearance of the streamwise flow profiles on Figure 14.

In addition, on Figure 16 we detect a thickening of the viscous flow with increase of lateral distance from the wedge apex, so that in the range of measurement, the flow appears more quasi-conical than quasi-cylindrical, as we discussed in Reference 32.

On Figure 16, we show the thickness parameters along the tunnel centre-line, calculated by the compressible 3D turbulent boundary-layer method of Nash[30,31], for this Mach 2, $\delta_W = 8°$ flow case. The calculated results offer a near invariancy of boundary-layer thickness, and only a small increase in the growth of the true displacement surface[33,34] with distance downstream through the swept interaction, in contrast with the rapid growth of the measured individual streamwise and crossflow components. The plot of displacement thickness on Figure 16, illustrates, perhaps, that the viewing of the components in the streamwise and crossflow directions does not necessarily provide the correct physical impression of the true displacement effect. In a qualitative sense, the true displacement thickness differs from the streamwise flow value because the boundary layer causes some flow at right angles to the direction of the external streamlines[34].

The measured distribution of surface pressure shown on Figure 15 is not unlike that found in an unseparated, two-dimensional flow[35], while the slightly elevated temperature of the test wall indicates less change in temperature gradient along the wall than the corresponding adiabatic wall temperature distribution.

The distribution of the local skin friction coefficient C_F (Figure 17) obtained using the streamwise momentum deficit thickness in the intermediate temperature formulation of Sommer and Short[36], also possesses the same qualitative form as in 2D flow: a rapid fall in C_F as the shock induced pressure ratio increases to its maximum pressure gradient condition, followed by a more gentle reduction where the pressure gradient is virtually constant, to a near exponential return to equilibrium further downstream. The Nash calculation method utilizing a law of the wall formula to give C_F provides satisfactory agreement with this particular correlation of the velocity profile data according to the Sommer/Short C_F method[36].

On Figure 17, we have plotted, as reference datums, the empty tunnel C_F values for the circular pitot tube and the cobra probe calculated according to the correlation of Bradshaw and Unsworth[16], and the offset between them that we discussed in Section 3.1. Data points from the cobra profiles in the undisturbed boundary layer upstream of the interaction (Sommer/Short) are in good agreement with the empty tunnel results of the circular Preston tube measurements at the wall (Bradshaw/Unsworth).

In the region of the static pressure rise (Figure 15) $-4 \leq (XT\text{-}XSWINV)/\delta_o \leq -2$, where the initial pressure gradient is largest and virtually constant, the local streamwise flow C_F values indicate a smaller reduction with downstream distance than the corresponding resultant C_F measured by the cobra probe at the wall. (For the latter results, the correlation of Bradshaw and Unsworth[16] using local adiabatic wall temperature and Mach number computed from the local wall pressure to upstream stagnation pressure ratio, compare relatively well with the correlation of Hopkins and Keener[37] using the intermediate temperature hypothesis and local Mach number from static to pitot pressure ratio). The limiting streamline deflection increases progressively in the region, so that the crossflow shear stress at the wall must be increasing at a rate faster than the shear stress in the streamwise flow direction is decreasing. On this basis, we would

expect that the magnitude of the resultant surface shear stress should fall less rapidly than the streamwise component alone, when the opposite appears to occur. Tentatively, these differences might perhaps be reconciled from our earlier discussion where we indicated that if there were a substantial static pressure gradient normal to the wall, in which the pressure reduces towards the mainstream, an enhanced streamwise momentum deficit thickness would result, leading to an overall reduction in the streamwise C_F component.

The lower graph on Figure 17 displays the rapid initial growth in the divergence of the local limiting streamline direction with respect to the undisturbed flow, followed by a virtually constant value of β_{CL} and a subsequent region of slow decay. We note that the limiting streamline direction through the interaction region as measured from the oil flow visualization, always leads the nearest value of yaw angle to the wall that is obtained from the cobra probe; but that in the relaxing region downstream of the calculated shock position, the measurements recover to one of good comparison. Since good agreement was previously obtained between cobra probe and oil flow directions at the wall in 3D boundary-layer experiments on right-circular cones[38], where a substantial region of collinear flow existed adjacent to the wall, we infer from the present discrepancy in β_{CL} through the interaction region, that yaw conditions near the wall, between the wall and the first data point measurable with the cobra probe, are still changing rapidly, and that regions of collinear flow are very small.

In the 3D boundary-layer calculation of Nash, the method is formulated to deal with swept flows with side stream surfaces parallel to the oncoming flow. Hence, the forced omission of the deflected wedge surface as a boundary constraint in the calculation, causes the computed skew angle at the wall downstream of the shock to be less than that measured, by an amount roughly equal to the deflection angle of the wedge.

3.6 In a Three-Dimensional Separated Flow at Mach 4

What features different and distinct from the Mach 2, $\delta_W = 8°$ flow would we expect in the presence of a 3D separation? To answer the question, we look at a flow example at Mach 4. Incipient separation at Mach 4 would appear to occur at a flow deflection angle, δ_W, close to 6° – see reference 8 – so that increasing the wedge angle by a further 10°, produces a strong three-dimensional separation region that is shown on Figure 18. The upper photographs demonstrate limiting streamline motion beneath the calculated and experimental shock wave positions, toward a separation envelope situated at about $5\delta_o$ upstream of the shock wave, along the tunnel centre-line. (The nominal undisturbed boundary layer thickness is about the same at Mach 4 as at Mach 2, for the tunnel run conditions used). The leading expansion wave from the wedge trailing-edge is now relatively much closer to the calculated shock location, and attenuates the pressure rise sharply at $6\delta_o$ aft of the calculated shock intersection point with the tunnel centre-line. The view of the wedge surface at the bottom of Figure 18 shows a divergent limiting streamline pattern on the wedge face close to the corner (this may also be observed more clearly towards the top of the wedge). The attachment surface continues across to the wedge trailing-edge, and on to the tunnel floor as we see by the divergent limiting streamline pattern just ahead of the projection of the trailing-edge expansion.

The sidewall limiting streamline pattern demonstrates a cellular structure not unlike that found on 2D aerofoils in transonic flow[39], and in no way may this be considered as a quasi-2D separation!

Figures 20 and 21 illustrate the cobra probe pitot, total temperature and yaw profiles along the tunnel centre-line through this Mach 4, $\delta_W = 16°$ separated flow. A map of the seven stations relative to the calculated shock wave location is given on Figure 19. These centre-line stations were chosen to provide profile measurements from upstream of the three-dimensional separation line to a position downstream of the calculated shock wave location.

The pitot pressure profiles on the top graph of Figure 21 are sufficiently close in spacing through the interaction to allow a construction of the forward oblique leg of the shock bifurcation at the foot of the wedge shock. The position of the oblique shock leg is given by the noticeable and sudden deficit in pitot pressure observable on the plotted distributions, and as we might expect, the 3D separation line is situated near to the intersection of this oblique shock wave and the test surface. Downstream of the 3D separation line, the presence of shear layers with heat transfer is indicated by rapid changes and troughs in the pitot distributions that are matched closely in position by troughs on the temperature plots.

From these distributions, we may postulate that the deficit troughs correspond with the core flow of a flattened vortex structure of the rolled-up shear layer from the 3D separation line, much like the flow model proposed by Cooper and Hankey in Reference 40. The axis of the vortex would appear just ahead of the line of the calculated shock wave (the origin of which is the wedge apex) where the 'overshoot' towards 0° on the yaw profile is at its maximum. Along a traverse, in the region of the flattened vortex core structure, we would expect the yaw angle to increase initially from the surface due to the outboard movement of the underside of the vortex. But this is not measured.

From these measurements, therefore, the significant changes in the total temperature distributions are a good indicator of a three-dimensional separated flowfield.

3.7 Tangential Air Injection into a Swept Shock/Turbulent Boundary-Layer Interaction in a Mach 2 Mainstream Flow

In our statement of objectives, we indicated that the goal of the present investigation was the control by tangential air injection of a three-dimensional separated flow region caused by a swept shock wave. As a follow-on to the successful two-dimensional boundary-layer control experiment reported in Reference 7, we planned to use a Mach 3 wall jet (with variable flow direction) beneath a Mach 2 mainstream, to provide a jet velocity greater than that of the mainstream, coupled with an excess of jet momentum flux somewhat more than the momentum deficit of the undisturbed test boundary layer upstream of the jet slot.

Why should we wish to control or destroy a shock-induced 3D separation, when we know that in some instances, a 3D separation and its associated vortices can be of benefit: the delta wing at landing and take off, for instance?* Nevertheless on swept wings, especially in transonic flow, the viscous vortex from a 3D separation can sometimes burst over the wing, leading to unpleasant difficulties in airplane control; while in the quasi-2D supersonic intake, once 3D separations are present on the sidewalls, they appear to promote high fluctuation and destortion levels at the compressor face further downstream. But perhaps the most significant aspect of 3D separated flows in the hypersonic régime, is the high heat transfer to the surface in the region of flow reattachment, which poses severe problems of skin cooling[41]. The particular losses caused by the pitot pressure deficit in the rolled-up viscous vortex, and the associated skin friction increases in reattachment zones, have not been quantified to the authors' knowledge.

In Section 2.0, we described the jet blowing apparatus consisting of a 2D convergent/divergent supersonic nozzle installed in the wind tunnel floor as part of a turntable, the jet exit of which was situated upstream of the leading-edge of the wedge shock generator at a distance along the tunnel of up to 14 δ_o. The so-called 'mixing length' along which distance the jet and original boundary layer flows merge together, may conveniently be defined as the distance between the jet exit and the calculated shock wave position along the line of the jet. Hence, for any given rotation of the jet efflux, and shock wave angle from the wedge, the local mixing length will vary substantially along the length of the shock front.

Figure 22 is a schematic diagram of the wall jet mixing with the boundary layer prior to applying the adverse pressure gradient from the shock pressure rise. In a physical evaluation of the flow, it is possible to subdivide the flow of the jet/boundary-layer combination (Reference 7) into (a) the new wall boundary layer under the jet and a consideration of jet peak characteristics; and (b), the wake or mixing region between the jet and the original boundary layer. To prevent flow reversal in an adverse pressure gradient, in either of (a) or (b) above, it was necessary to choose a length downstream for mixing so that (i) the wake trough total pressure was greater than the local static pressure from the applied pressure gradient – otherwise reversal of the wake flow resulted; and (ii), the fall-off in jet peak total pressure was not severe. The indication in Reference 7 was that at best, the wake trough total pressure approached a constant value of about 0.6 of the mainstream total pressure for undisturbed Mach numbers similar to those used in the present experiments. The initial rate of mixing between the jet and the original boundary layer within the range tested was much the same for all injection stagnation pressures and jet excess momentum rates.

Tests showed that with a jet excess momentum† slightly more than the momentum deficiency of the undisturbed boundary layer ($M_J \simeq 2.4$) and a mixing region extent of 6 to 10 δ_o (or approximately 100 undisturbed momentum deficit thicknesses), control of shock-induced separation could be maintained at least up to static pressure ratios of 3 in a Mach 1.8 mainstream. An empirically derived equation was presented that correlated the minimum velocity in the wake with distance downstream of the injection point. The wake velocity defect was shown to be roughly proportional to the inverse square root of the distance downstream of the injection point. With reasonable satisfaction of the momentum integral equation, the equation was considered[7] to be a useful first step in predicting the compressible flow characteristics of a jet mixing with either a boundary layer or wake.

Before commenting upon the degree of control exercised by blowing into a swept interaction region, we first of all look at the downstream penetration qualities of the Mach 3 wall jet in the empty tunnel flow. Figure 23 illustrates the surface pressure distributions and oil flow visualization from one such configuration, where the jet flow (displayed by the superposed small black arrows) exits at $\theta_J = -12°$ relative to the normal to the nominal mainstream flow direction (large clear arrow). The negative sign ascribed to the jet exit setting indicates anti-clockwise rotation of the turntable (i.e. away from the wedge surface direction) from the zero line with the jet exit plane perpendicular to the mainstream flow, when we view the floor from above and the mainstream flow is from left-to-right. The turntable periphery is visible from the dark material inserts used in

---

*We have seen[8] that the 3D separation develops slowly and progressively with increase of shock strength and would not be expected to suddenly produce a catastrophic situation on an airplane configuration – unlike the stalling of high aspect ratio wings, where nominal 2D separations are present.

†The excess momentum flux at the jet exit, is defined as $[\dot{m}_J(u_J - u_E)]_{exit}$, in order to correspond with the momentum deficiency of a boundary layer. The definitions are virtually the same except for sign for $\rho_E u_E^2 \theta_{11} = \int \rho u(u_E - u)dy = \int (u_E - u)d\dot{m}$.

its construction, while the rearward facing steps situated between the extremities of the jet nozzle and the tunnel endwalls introduce regions of disturbed flow bordering the jet.

The surface oil streaks on Figure 23 indicate negligible change in direction of the jet flow about its redirected centre-line along the test floor. The jet stagnation pressure of 167 psia yields a calculated static pressure in the Mach 3 jet flow about equal to the Mach 2 mainstream static pressure. The abrupt change in slope of 4° between the jet nozzle wall and the tunnel floor in the plane of the jet exit generates a shock wave and consequent increase in local static pressure, which is almost immediately cancelled by the reflection of the shock wave within the jet, as an expansion from the free jet boundary – see Figure 23. At 10 jet slot heights ($5\delta_o$) downstream of the jet exit, the wall static pressure has returned to the nominal mainstream value within the limits of ±10 percent of the reference undisturbed static pressure, p_1.

What of the uniformity of the jet flow across the width of the jet nozzle exit? Because of the large number of static pressure orifices in the wind tunnel floor, and the obstruction of the supply pipe to the blowing nozzle (see Figure 2) it was not possible to install either the cobra probe or the circular pitot probe traversing gear. Instead, as well as relying on local static pressure distributions we chose to use the obstacle block indirect skin friction measuring devices that Nituch[42] had investigated (following the suggestion of Rainbird) in a low speed tunnel flow. The optimum dimensions and geometry that Nituch found for the obstacle block are shown on Figure 24, where the height, width and length of the block are typically 3, 4.5 and 9 times the diameter of the static hole against which the block is to be abutted. A semi-circular cut-out, positioned at the centre of the forward facing side of the block, along with a drill bit in the static hole, facilitates the accurate and positive location of the block with respect to the inside of the static hole. As with the geometrically similar Preston tube devices, the disturbance to the local flow produced by a congruent family of obstacle blocks, provided they are immersed within the law of the wall region of a turbulent boundary layer, will be governed only by wall variables and a characteristic size of the obstacle (the height). The blocks can be calibrated in a pipe flow and Vinh[43] has demonstrated that under high Reynolds number conditions, the calibration for the geometry of block described is similar to that of Patel's calibration[18] for the Preston tube.

Figure 24 shows the static and obstacle block pressures across the wind tunnel at 17.5 slot heights or almost $9\delta_o$ downstream of the jet exit, with the Mach 3 wall jet on and off. (For a qualitative determination of the variation of local wall shear stress, we can clearly observe the disturbance pressure due to the obstacle block and compare it against the undisturbed static pressure, p_1, at the reference station 1).

We see on Figure 24 that the static pressure distribution across the tunnel is unaltered by the addition of the jet flow at this station downstream of the jet slot. In contrast, the block pressure ratios display a non-uniform distribution reminiscent of a preferential cellular type flow; that the tunnel flow itself was not responsible for the unevenness is shown by the jet-off block pressure ratios measured with the same blocks, which indicate relatively good spanwise uniformity of surface shear stress. Hence the jet flow provided a high mean level of local wall shear stress, modulated by a periodicity across the span of the jet. As the local skin friction coefficient is very roughly proportional to $(p_B/p_1 - 1)$, all other parameters being equal, we can see that the jet flow has introduced a wall shear stress about 5 times that existing in the empty wind tunnel, with a typical amplitude of modulation of about 0.7 times the level of the wall shear stress in the undisturbed flow.

Sections 3.2 and 3.3 have included a discussion of the flow in the swept interaction region at Mach 2, generated by an 8° wedge deflection. We recollect that in spite of substantial skewing of the boundary layer, 3D separation had not yet begun. This flow régime, therefore, provides an initial datum against which to check the effects of adding the Mach 3 jet.

Figure 25 is comprised of a series of illustrations (oil-dot flow visualizations and pressure distributions) depicting the jet efflux issuing beneath and at various angles to the direction of the undisturbed boundary-layer flow, of between -20° and +30°, where the mixing distance between the jet exit and the shock front varies from about 2 to 20 δ_o, depending on θ_j.

We might think that blowing at say $\theta_j = 30°$ would offer the most benefit for controlling the 3D separated flows, for in so doing, the direction of the jet surface shear must be turned through more than 60° for it to follow the line of a typical 3D separation at Mach 2, generated by a wedge standing normal to the floor. In other words, the penetration ability of the jet should be sufficient to erase the separation. With the geometrical constraints of the experimental configuration, however, the wedge obstruction acts as a bluff protuberance to produce a near normal shock to the oncoming jet flow, and a consequent massive 3D separation that we view on the lowest photograph of Figure 25.

If we now rotate the jet efflux such that it is parallel with the undisturbed boundary layer at the jet slot, we still perceive a 3D separation. We now have a flow with substantial separation with the jet on as compared with the swept interaction at $\delta_W = 8°$ with no jet, where no separation existed! Incipient separation of the new boundary layer growing beneath the wall jet peak will occur at δ_W corresponding with the local jet peak Mach number, provided the latter is greater than the Mach number of the mainstream. We remember from Sections 3.2 and 3.6 that δ_W for incipient separation decreases as the local oncoming Mach number to the wedge increases. Clearly, with $M_j \cong 3$, the wedge angle

for incipient separation is less than 8°. Under these circumstances, the enhanced surface shear stress provided by the jet is insufficient to remove the 3D separation at the given 'initial' mixing distance of about $4\delta_o$ between the jet exit and the wedge leading-edge.

If we follow the progression of photographs from the centre of Figure 25 to the top of the page, we observe that by aligning the jet efflux somewhere between the wedge deflection angle of 8° and the shock wave deflection angle of 37° (at Mach 2), the 3D separation line is caused to disappear.

On the left-hand side of Figure 25, some representative wall static pressure distributions along the centre-line and line A for $\theta_j = +30°$ and $-20°$ are plotted. We see that one aspect of the controlling mechanism, for instance, with θ_j at $-20°$ is the reduction in overall shock pressure rise generated by the jet flow expanding locally around the wedge leading-edge, to a value less than the calculated shock pressure rise. In addition, the jet is now blowing in a direction along which, from the wedge apex, there exists a favourable pressure gradient (in the absence of the jet) due to the relaxation along the shock direction, of maximum pressure rise with distance from the wedge leading-edge.

For these reasons, coupled with the substantial wall shear stress introduced by the jet flow, the 3D separation would also appear to be erased at $\theta_j = -25°$ and $\delta_w = 11.5°$, as we see on Figure 26.

We have measured no mean flow profiles in the 3D jet/boundary-layer combination, and consequently we can only rely on our 2D results[7] as a qualitative guide. In the limited number of experiments with blowing that we have managed in the present constrained geometrical conditions, it is not clear, for example, whether the advised direction of blowing herein would carry over to controlling a 3D shock-induced separation on say a swept wing or body flow with internal shock waves[38].

More work clearly needs to be done on a flow model producing a 3D separation without the constraint of a solid vertical wall in proximity to the jet.

4.0 CONCLUSIONS

Based on measurements of the near-zero heat transfer turbulent boundary layer on a flat wall in a swept interaction region at Mach 2 and 4, generated by a wedge standing normal to the test wall, and at a Reynolds number of $\sim 2 \times 10^5$ based on the undisturbed boundary-layer thickness, δ_o, of 0.2 inch, we conclude that:

1. The development of the viscous flow in the swept interaction region leading eventually to 3D separation with increasing deflection angle of the wedge, is a gradual, progressive, relatively steady, and essentially quasi-conical process near the wedge, in which the flow leaves the 3D separation line as a shear layer that rolls up into a flattened vortex within the depth of the original undisturbed boundary layer. There appears to be no sudden eruption of viscous vortical fluid from the test surface. In fact, the precise wedge angle at which incipient separation occurs is particularly elusive, unless the observation of parallelism of the limiting streamlines with the calculated (or visualized) shock wave is adopted as the incipient separation criterion.

2. The optimum direction of a Mach 3 supersonic wall jet to control the shock-induced separation (caused by the aforementioned wedge in a flow at Mach 2) is along a line between the wedge deflection angle and its shock wave angle (or the 3D separation line).

REFERENCES

1 Stalker, R.J., "Sweepback Effects in Turbulent Boundary-Layer/Shock Wave Interaction", Jour. Aero. Sci., vol. 27, No. 5, May 1960, pp. 348-356.

2 Stanbrook, A., "An Experimental Study of the Glancing Interaction Between a Shock Wave and a Turbulent Boundary Layer", ARC CP 555, 1961.

3 McCabe, A., "The Three-Dimensional Interaction of a Shock Wave with a Turbulent Boundary Layer", Ph.D. Thesis, Univ. of Manchester, October 1963; Aero. Quart., vol. XVII, August 1966, pp. 231-252.

4 Lowrie, B.W., "Cross-Flows Produced by the Interaction of a Swept Shock Wave with a Turbulent Boundary Layer", Ph.D. Thesis, Univ. of Cambridge, December 1965.

5 Green, J.E., "Interactions Between Shock Waves and Turbulent Boundary Layers", RAE TR 69098, May 1969; Progress in Aerospace Sciences, vol. 11, Pergamon Press at Oxford, 1970, pp. 235-340.

6 Korkegi, R.H., "A Simple Correlation for Incipient Turbulent Boundary-Layer Separation due to a Skewed Shock Wave", AIAA J, vol. 11, No. 11, November 1973, pp. 1578-1579.

7 Peake, D.J., "The Use of Air Injection to Prevent Separation of the Turbulent Boundary Layer in Supersonic Flow", NGTE R256, Nov. 1973; ARC CP 890, 1966; M. Sc. Thesis, University of Bristol, 1962.

8 Peake, D.J., "The Three-Dimensional Interaction of a Swept Shock Wave with a Turbulent Boundary Layer and the Effects of Air Injection on Separation", Ph.D. Thesis, Carleton University, Ottawa, Canada, March 1975.

9 Peake, D.J., Rainbird, W.J., Atraghji, E., "Three-Dimensional Flow Separations on Aircraft and Missiles", AIAA J, vol. 10, No. 5, May 1972, pp. 567-580.

10 Bradfield, W.S., Hanson, A.R., Sheppard, J.J., "Design, Calibration and Application of a Miniature Total Temperature Probe", Jour. Heat Transfer (ASME), Aug. 1964, pp. 462-464.

11 Harris, H., "An Investigation of Turbulent Boundary-Layer Characteristics with Particular Reference to the Effects of Heat Transfer and Pressure Gradient", Ph.D. Thesis, London University, 1970.

12 MacMillan, F.A., "Experiment on Pitot Tubes in Shear Flow", ARC R and M 3128, 1957.

13 Westley, R., "Aerodynamic Sound and Pressure Fluctuations in a Supersonic Blowdown Wind Tunnel", National Research Council of Canada Aero. Report LR-274, January 1960.

14 Fiedler, H., Head, M.R., "Intermittency Measurements in the Turbulent Boundary Layer", J. Fluid Mech., vol. 25, part 4, pp. 719-735, 1966.

15 Ozaropoglu, V., "Measurements in Incompressible Turbulent Flow", Ph.D. Thesis, Laval University, June 1973.

16 Bradshaw, P., Unsworth, K., "A Note on Preston Tube Calibrations in Compressible Flow", Imperial College Aero Report 73-07, Sept. 1973.

17 Quarmby, A., Das, H.K., "Measurement of Skin Friction Using a Rectangular-Mouthed Preston Tube", Aero. Jour., vol. 73, No. 699, March 1969, pp. 228-230.

18 Patel, V.C., "Calibration of the Preston Tube and Limitations on its Use in Pressure Gradients", J. Fluid Mech., vol. 23, 1965, p. 185.

19 Rajaratnam, N., Muralidhar, D., "Yaw Probe Used as Preston Tube", Aero. Jour., vol. 72, No. 696, December 1968, pp. 1059-1060.

20 Spalding, D.B., Chi, S.W., "The Drag of a Compressible Turbulent Boundary Layer on a Smooth Flat Plate with and without Heat Transfer", Jour. Fluid Mech., vol. 18, part 1, 1964, pp. 117-143.

21 Crocco, L., "Transformation of the Compressible Turbulent Boundary Layer with Heat Exchange", AIAA J, vol. 1, No. 12, December 1963, pp. 2723-2731.

22 Walz, A., "Compressible Turbulent Boundary Layers", Mechanics of Turbulence, Gordon and Breach Science Publishers, New York, 1964.

23 Peake, D.J., Romeskie, J., Brakmann, G., "Comparisons Between Some High Reynolds Number Turbulent Boundary-Layer Experiments at Mach 4, and Various Recent Calculation Procedures", AGARD CP - 93, September 1971.

24 Hall, M.G., Dickens, H.B., "Measurements in a Three-Dimensional Turbulent Boundary Layer in Supersonic Flow", ARC R and M 3537, 1968.

25 Johnston, J.P., "On the Three-Dimensional Turbulent Boundary Layer Generated by Secondary Flow", J. Basic Eng., Series D, Trans. ASME, vol. 82, 1960, p. 223.

26 Johnston, J.P., "Three-Dimensional Turbulent Boundary Layers", MIT Gas Turbine Lab., Rept. 39, May 1957.

27 Wheeler, A.J., Johnston, J.P., "Three-Dimensional Turbulent Boundary Layers - an Assessment of Prediction Methods", Stanford Univ. Rept. MD-30, July 1971.

28 Shanebrook, J.R., Hatch, D.E., "A Family of Hodograph Models for the Crossflow Velocity Component of Three-Dimensional Turbulent Boundary Layers", ASME Paper 71-FE-1, 1971.

29 Shanebrook, J.R., Summer, W.J., "Crossflow Profiles for Compressible Turbulent Boundary Layers", J. Aircraft, vol. 8, No. 3, 1971, pp. 188-189.

30 Nash, J.F., Scruggs, R.M., "Three-Dimensional Boundary-Layer Computations for a Finite Swept Wing", NASA CR-112158, 1973.

31 Nash, J.F., Private Communications, 1974.

32 Peake, D.J., Jones, D.J., Rainbird, W.J., "The Half-Cone Pressure Field and its Significance to Side-Mounted Intakes", AGARD CP - 71, 1971.

33 Moore, F.K., "Displacement Effect of a Three-Dimensional Boundary Layer", NACA Rept. 1124, March 1952.

34 Lighthill, M.J., "On Displacement Thickness", J. Fluid Mech., vol. 4, 1958, pp. 383-392.

35 Kuehn, D.M., "Experimental Investigation of the Pressure Rise Required for the Incipient Separation of Turbulent Boundary Layers in Two-Dimensional Supersonic Flow", NASA Memo 1-21-59A, Feb. 1959.

36 Sommer, S.C., Short, B.J., "Free-Flight Measurements of Turbulent Boundary-Layer Skin Friction in the Presence of Severe Aerodynamic Heating at Mach Numbers from 2.8 to 7.0", NACA TN 3391, 1955. (Also, J. Aero Sci., vol. 23, No. 6, June 1956).

37 Hopkins, E.J., Keener, E.R., "Study of Surface Pitots for Measuring Turbulent Skin Friction at Supersonic Mach Numbers - Adiabatic Wall", NASA TN D-3478, 1966.

38 Rainbird, W.J., "Turbulent Boundary-Layer Growth and Separation on a Yawed Cone", AIAA J, vol. 16, No. 12, December 1968, pp. 2410-2416.

[39] Peake, D., Yoshihara, H. et al., "Transonic Lift Augmentation of Two-Dimensional Supercritical Aerofoils by means of Aft Camber, Slot Blowing and Jet Flaps, in High Reynolds Number Flow", ICAS Paper 74-11, August 1974.

[40] Cooper, J.R., Hankey, W.L., "Flowfield Measurements in an Asymmetric Axial Corner at M = 12.5", AIAA J, vol. 12, No. 10, October 1974, pp. 1353-1357.

[41] Rainbird, W.J., Crabbe, R.S., Peake, D.J., Meyer, R.F., "Some Examples of Separation in Three-Dimensional Flow", CASI Jour., vol. 12, No. 6, December 1966, pp. 409-423.

[42] Nituch, M.J., "The Use of Congruent Obstacle Blocks for the Indirect Measurement of Turbulent Skin Friction on Smooth Surfaces", M. Eng. Thesis, Carleton University, Ottawa, August 1972.

[43] Vinh, N., Private Communication, 1974.

ACKNOWLEDGEMENTS

The authors would like to thank Pamela Godding and Doug Thomason for assistance with the illustrations; and to Frank Kisko, for maintaining the operational performance of the 5 × 5-inch wind tunnel.

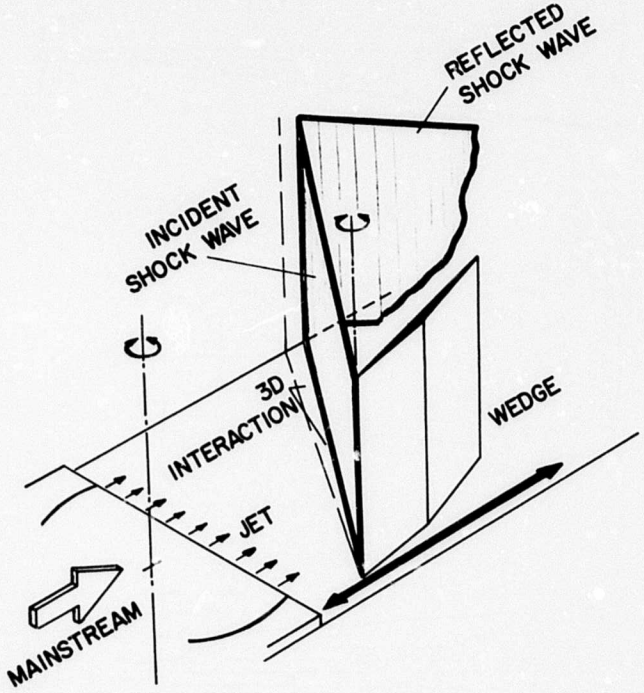

Fig.1 Flow configuration

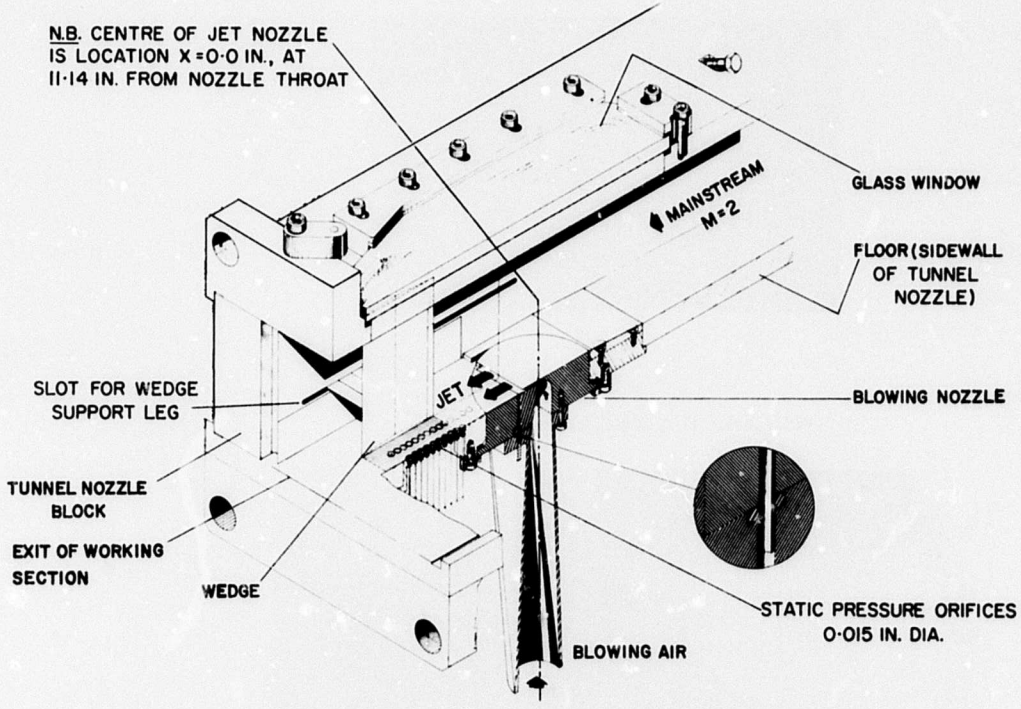

Fig.2 Typical assembly of working section of 5 x 5 in wind tunnel for BLC

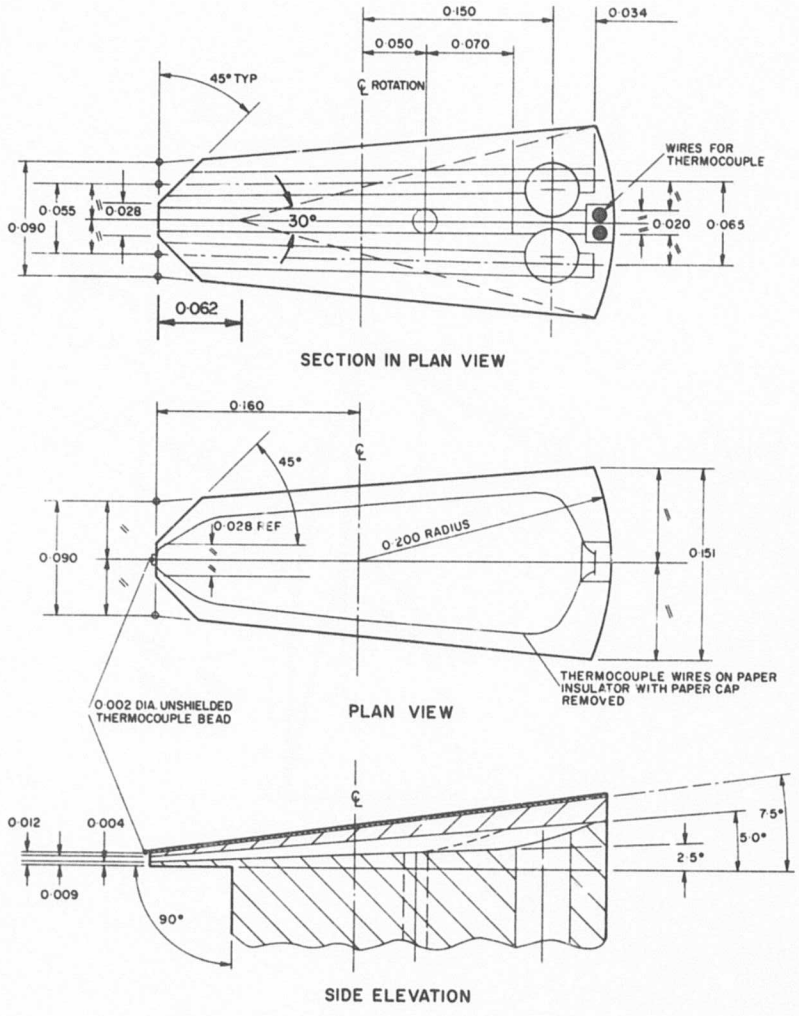

Fig.3 Head of cobra probe, design dimensions

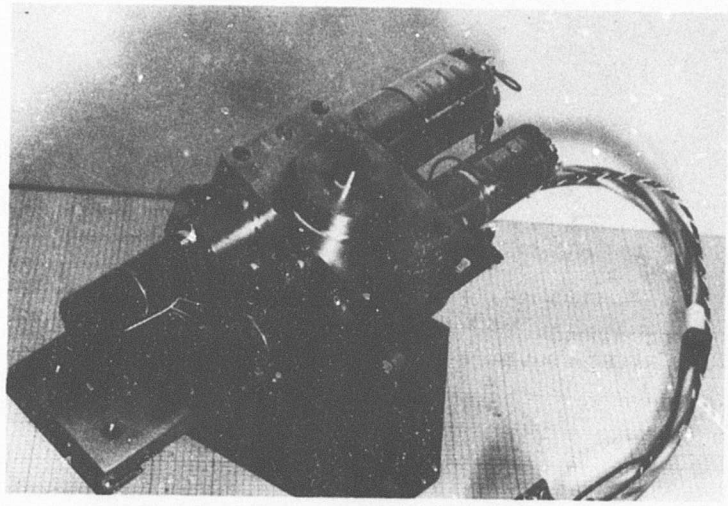

YAW AND TRAVERSING MECHANISM

SIDE VIEW OF HEAD AND STEM SUPPORT

Fig.4 Assembly of cobra yaw probe

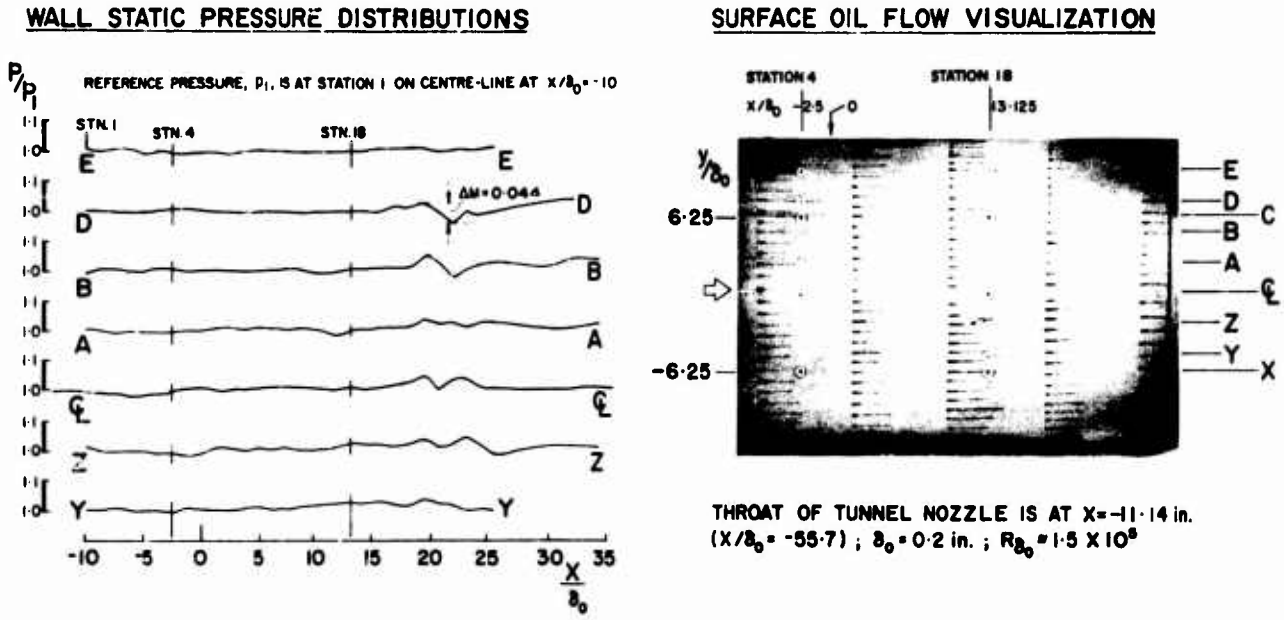

Fig.5 Pressure distributions and flow visualization. Empty tunnel flow at Mach 2

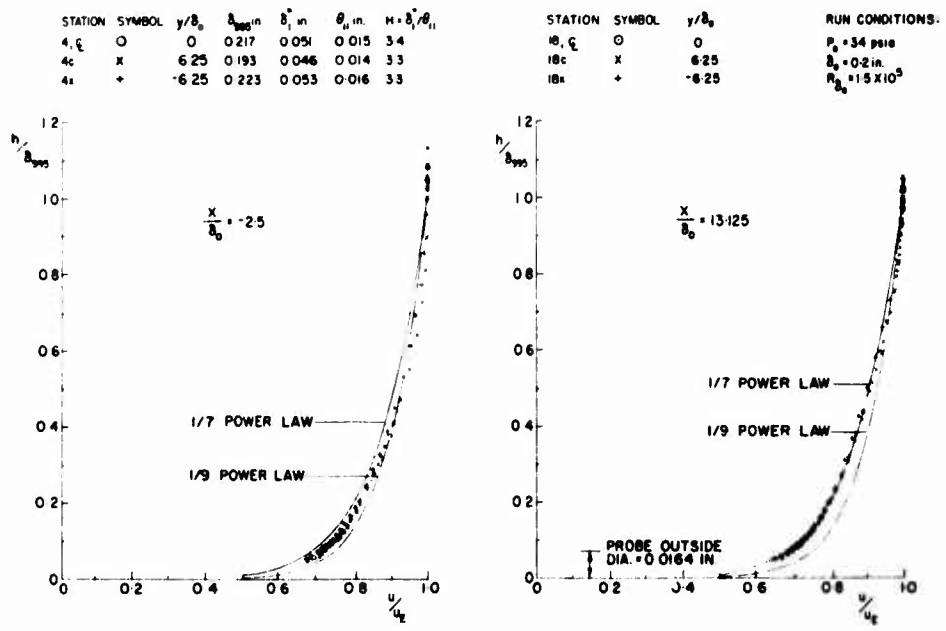

Fig.6 Spanwise symmetry: velocity profiles in empty tunnel at Mach 2 measured with circular pitot tube

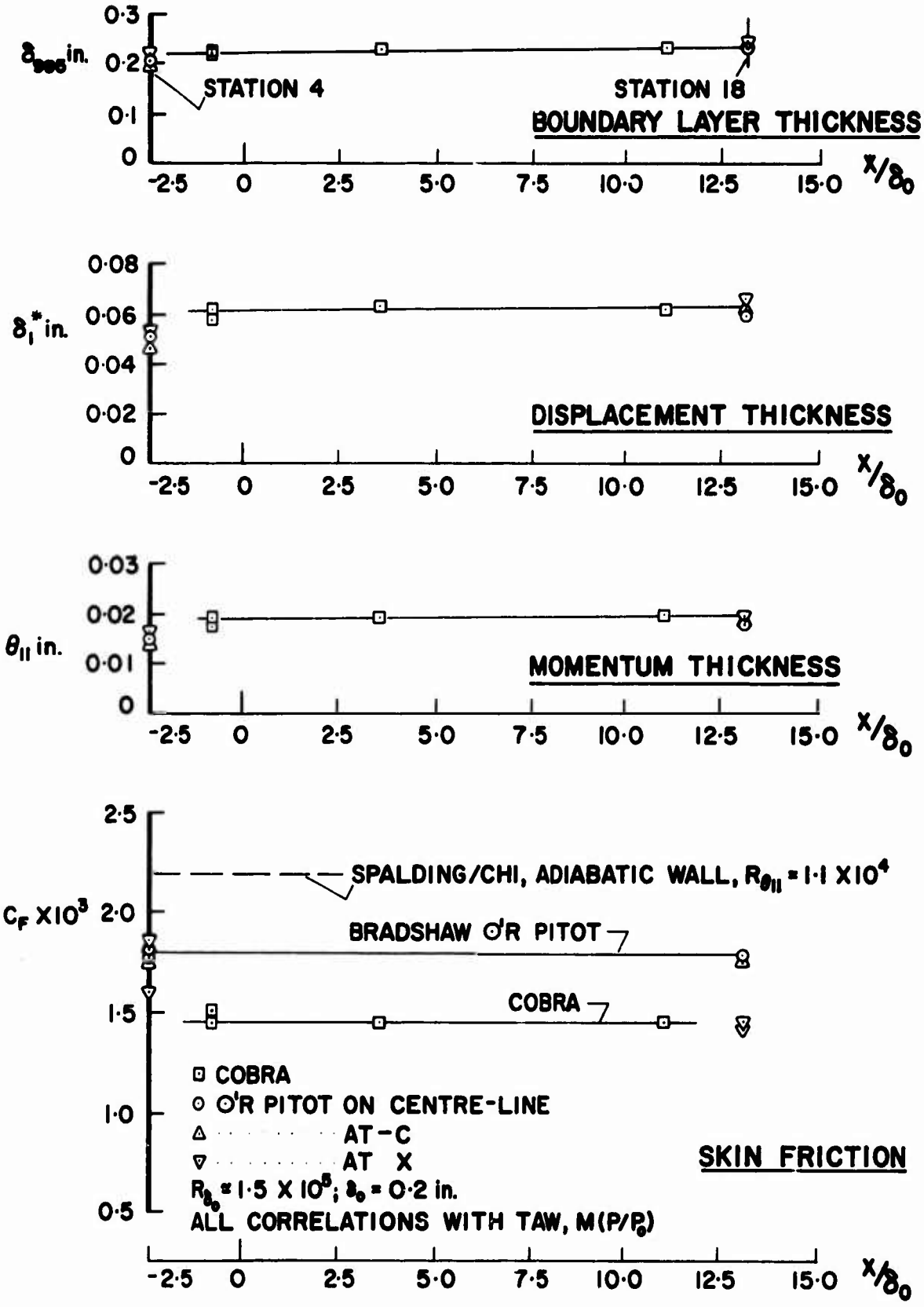

Fig.7 Integral parameters and local skin friction for flow in empty tunnel at Mach 2

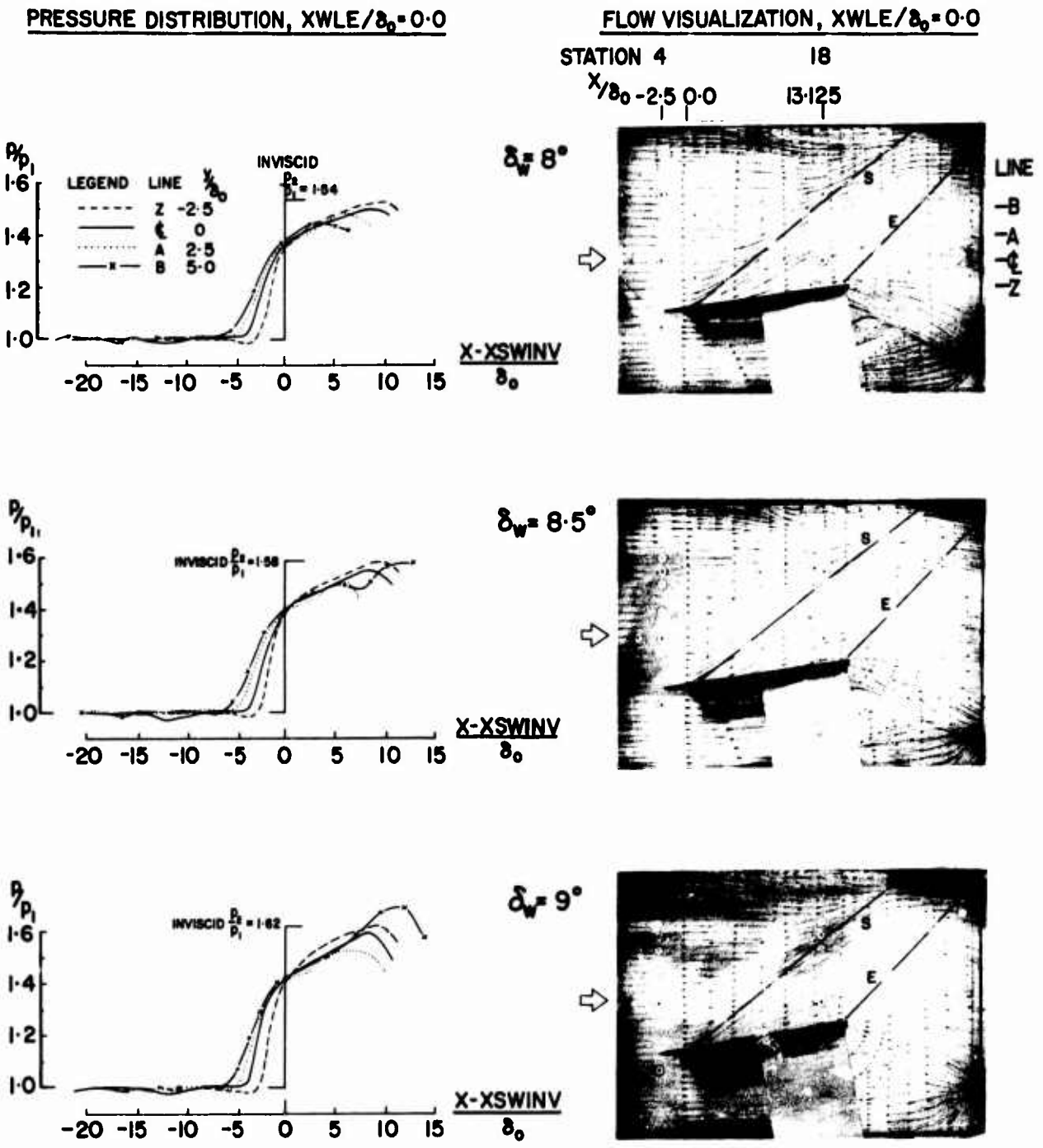

Fig.8 Flow at Mach 2 with $\delta_w = 8°$, 8.5° and 9°

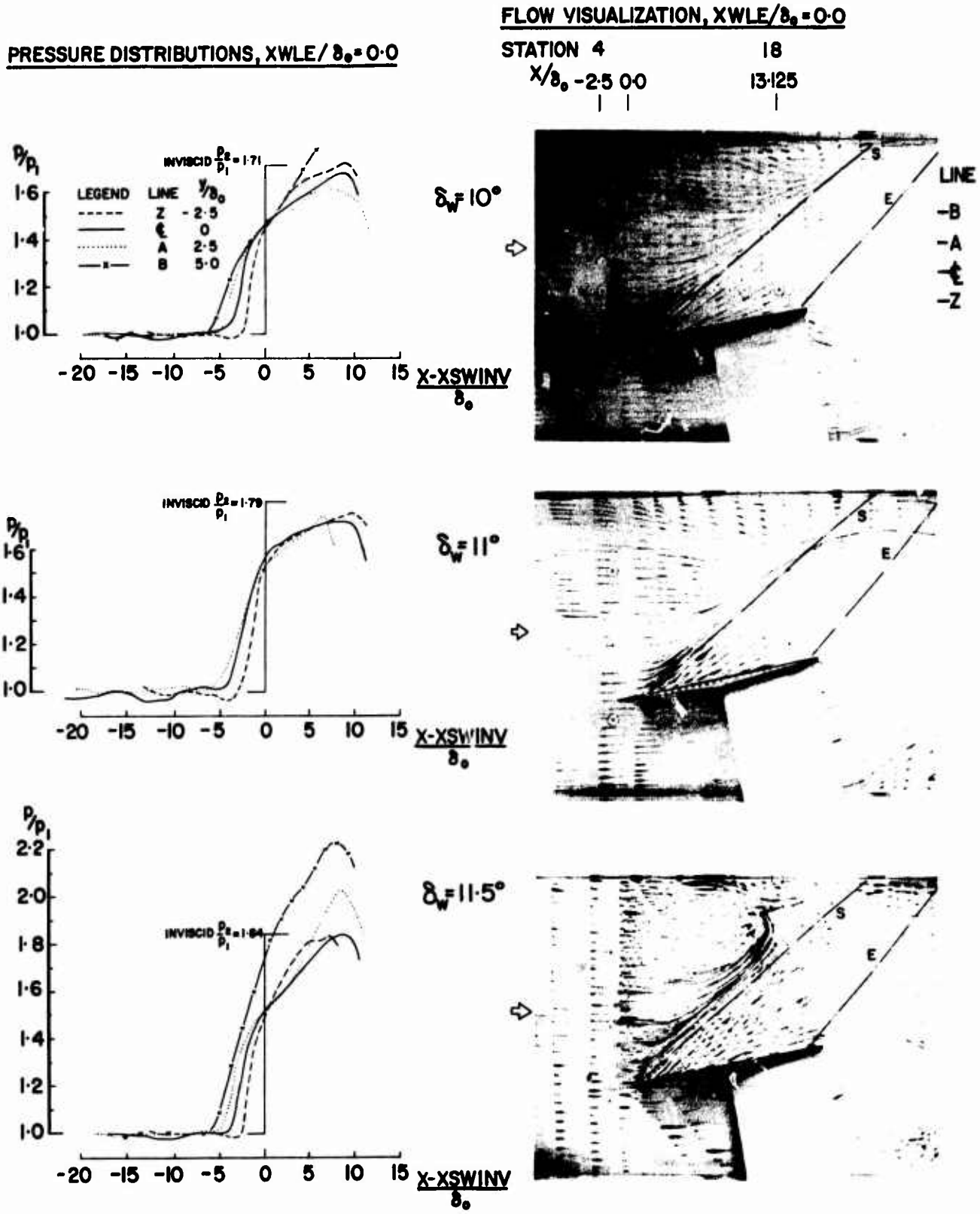

Fig.9 Flow at Mach 2 with δ_w = 10°, 11° and 11.5°

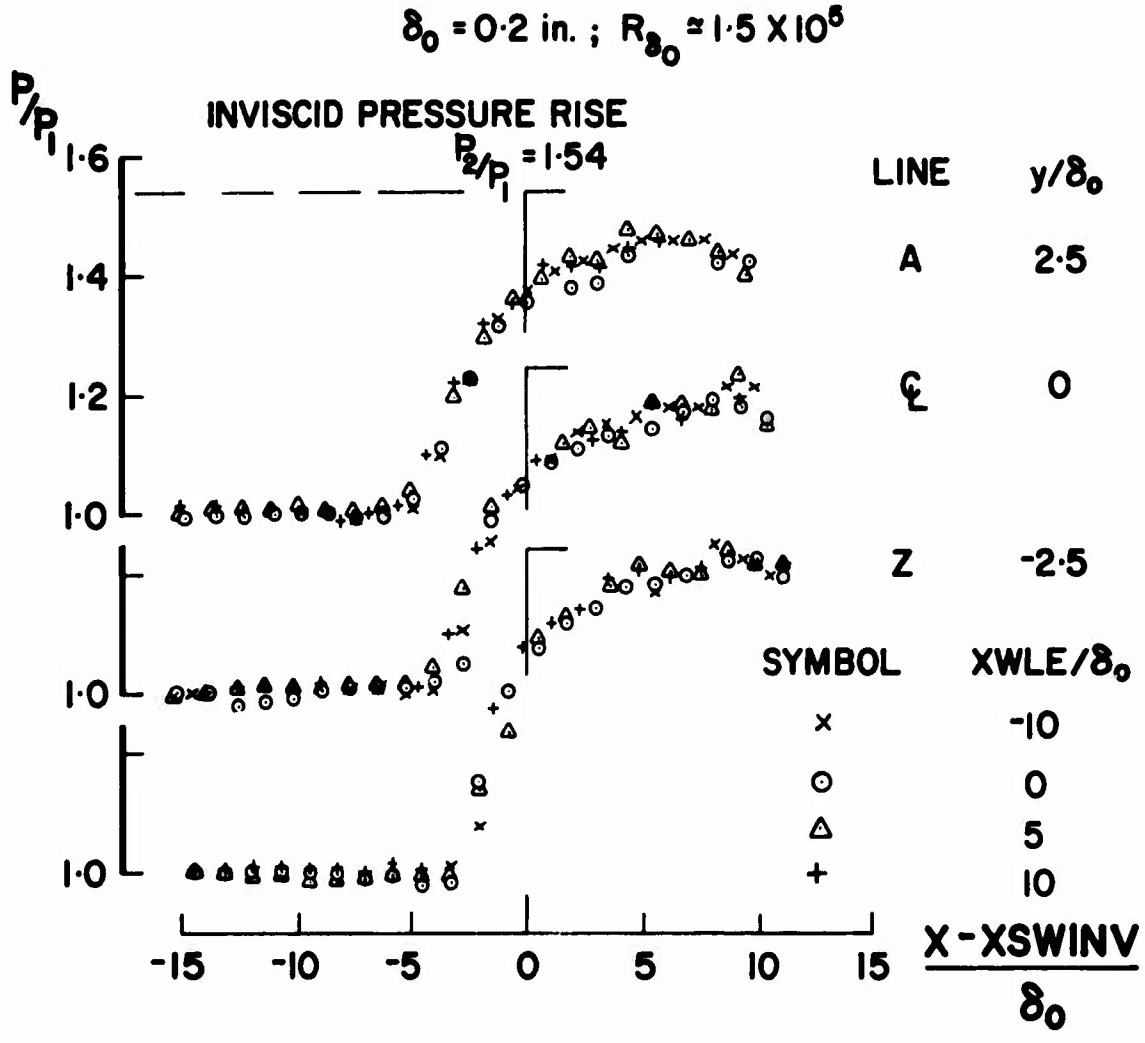

Fig.10 Surface pressures along lines A, ℄, and Z at Mach 2; $\delta_w = 8°$, for various longitudinal wedge positions

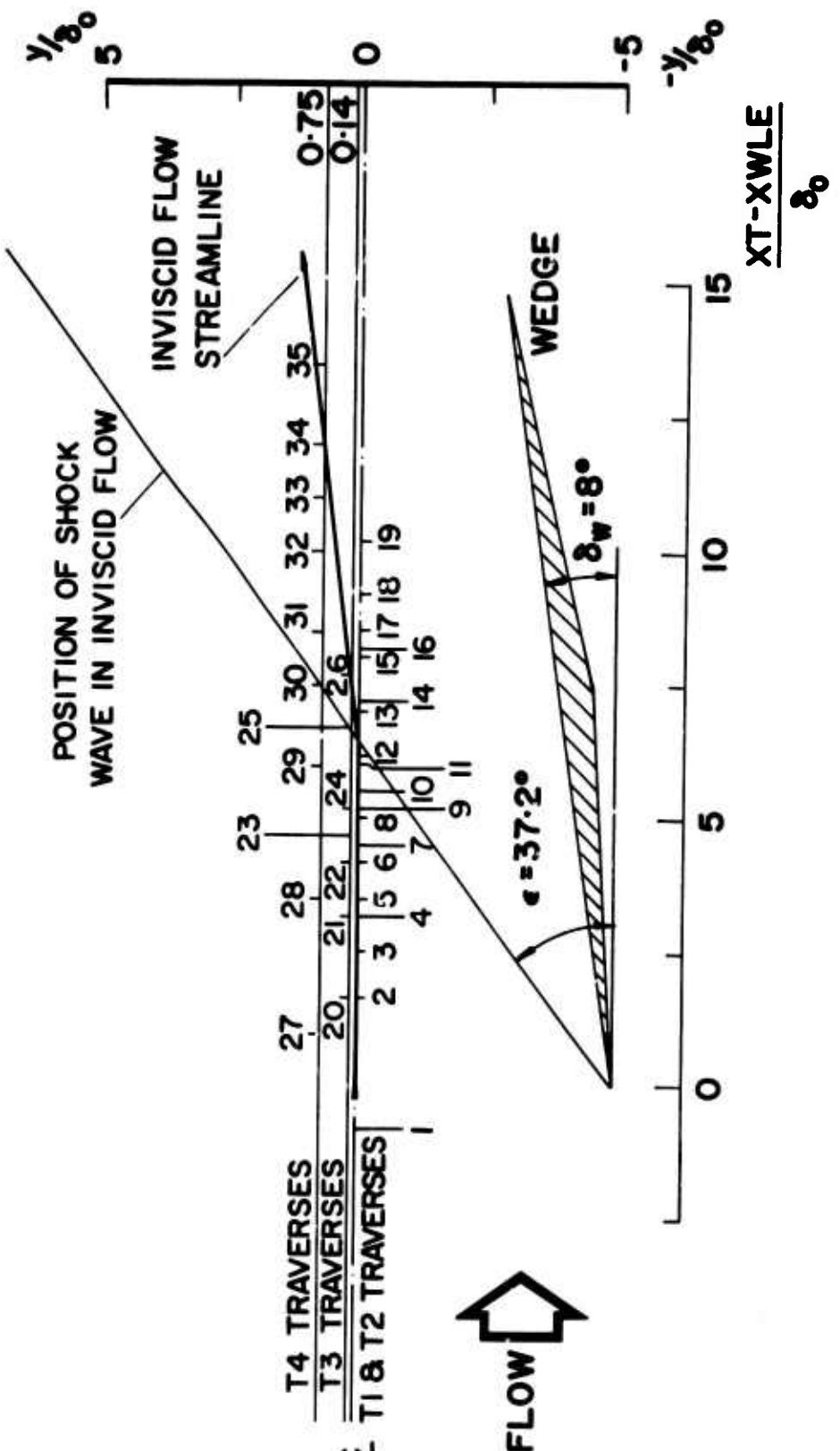

Fig.11 Map of cobra probe traverse locations at Mach 2, $\delta_w = 8°$

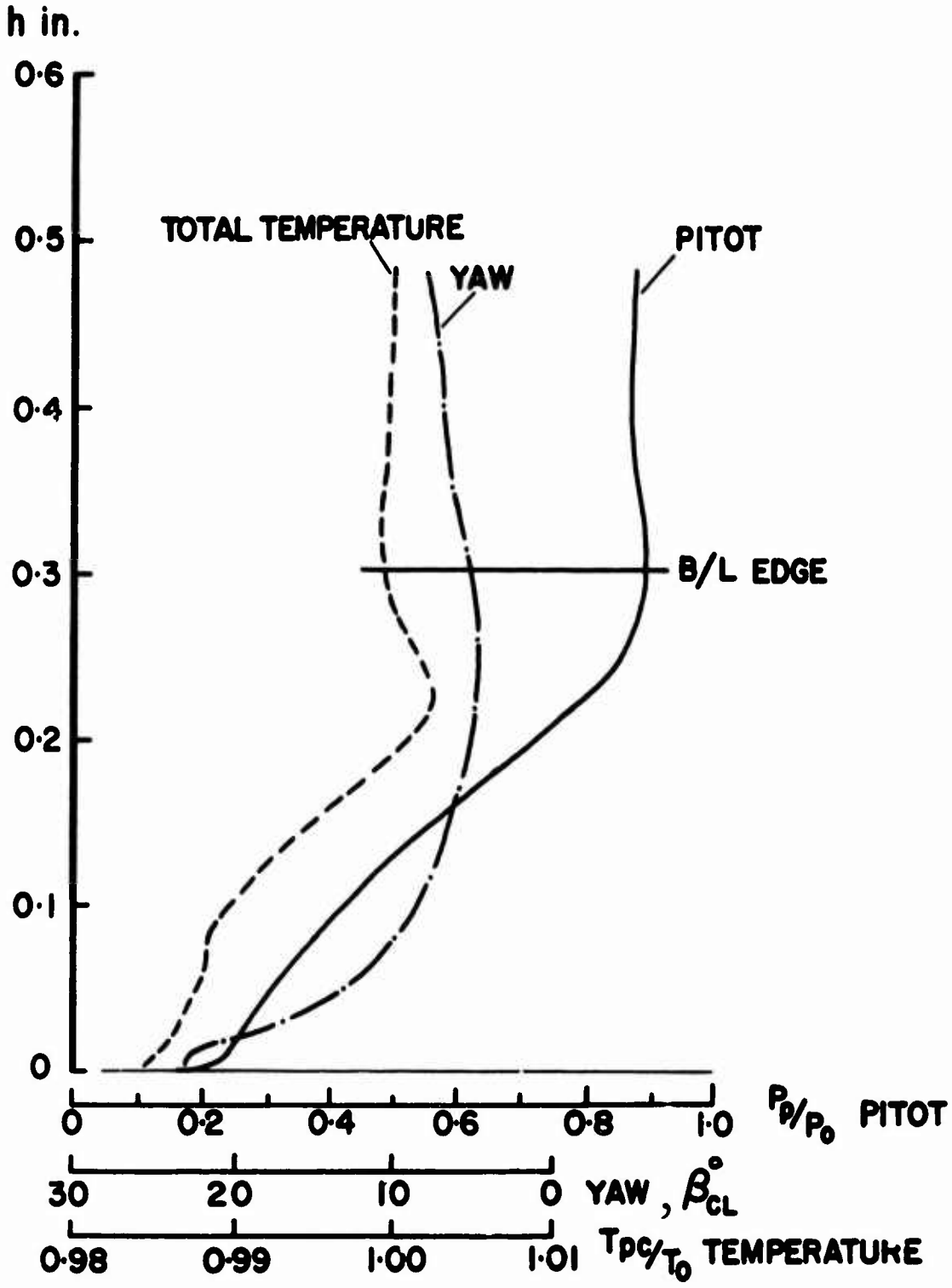

Fig.12 Pitot, total temperature and yaw angle distributions for station II near inviscid shock wave location; for $\delta_w = 8^\circ$ at Mach 2

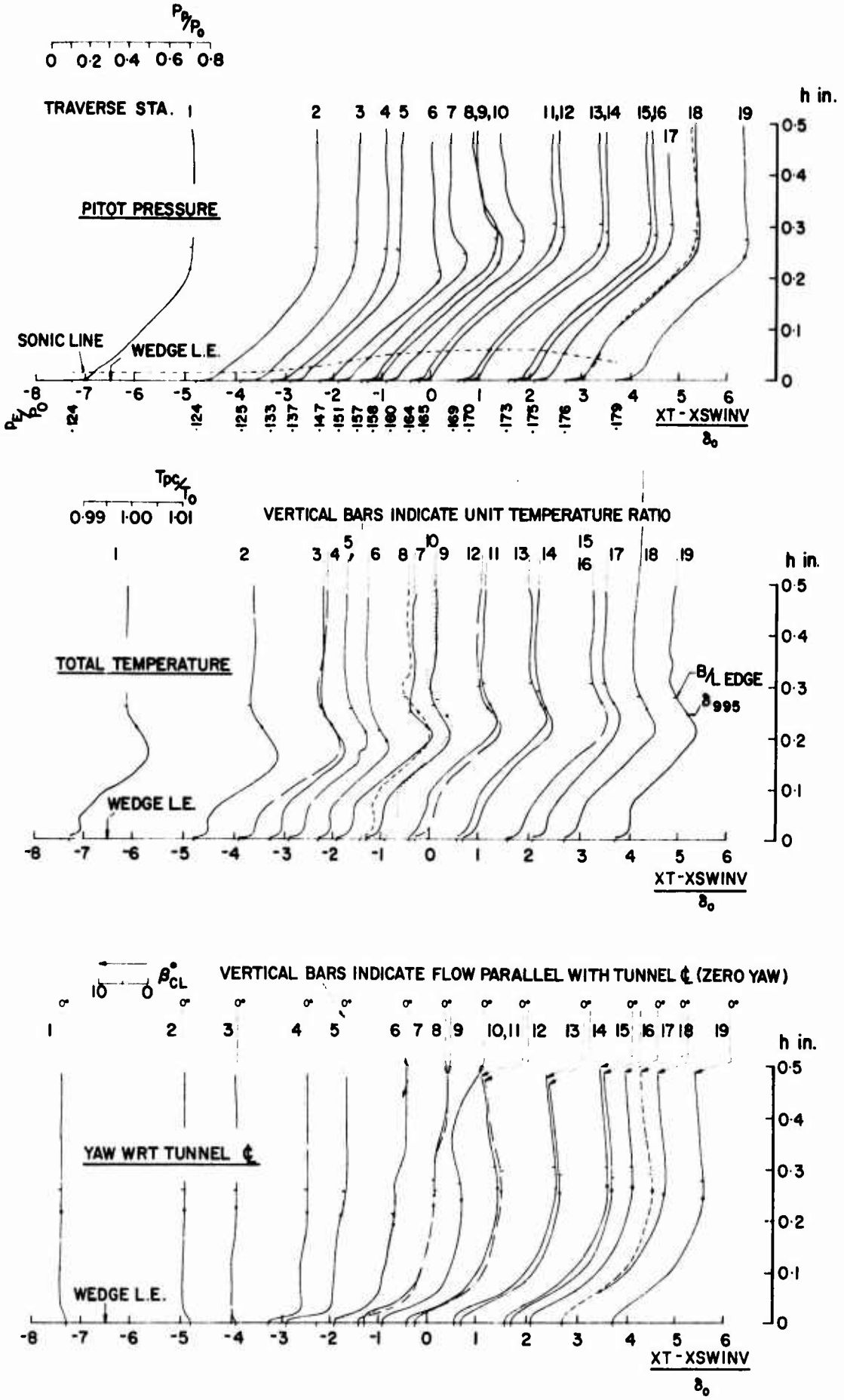

Fig.13 Cobra probe measurements along tunnel ℄ at Mach 2 and $\delta_w = 8°$

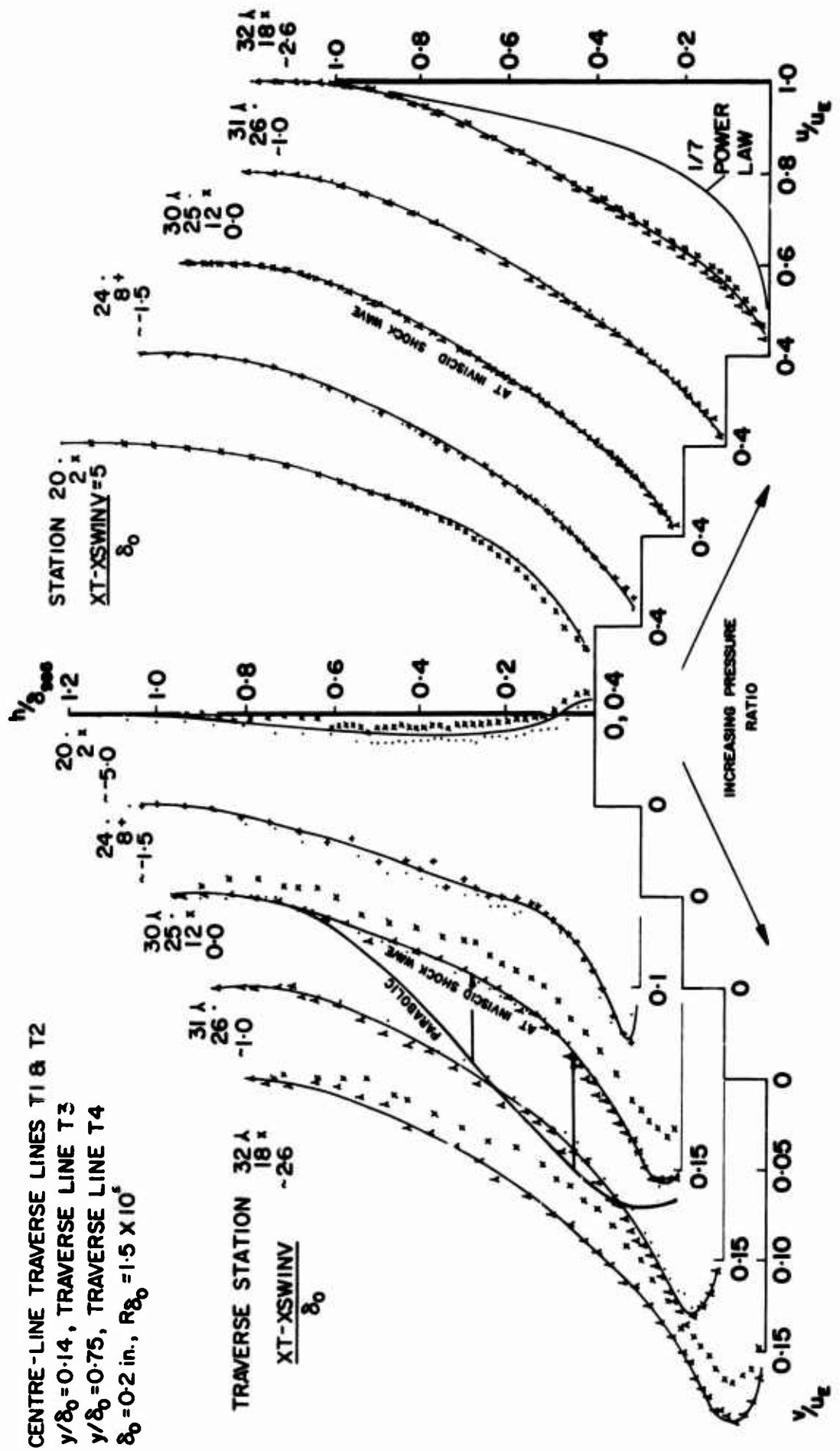

Fig.14 Crossflow and streamwise flow velocity profiles for $\delta_w = 8°$ at Mach 2

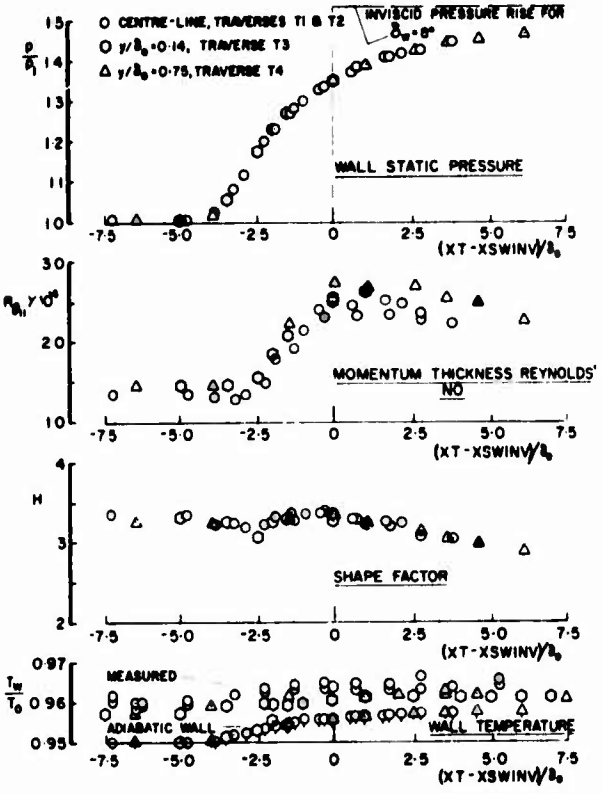

Fig.15 Streamwise integral parameters and wall conditions for $\delta_w = 8°$ at Mach 2

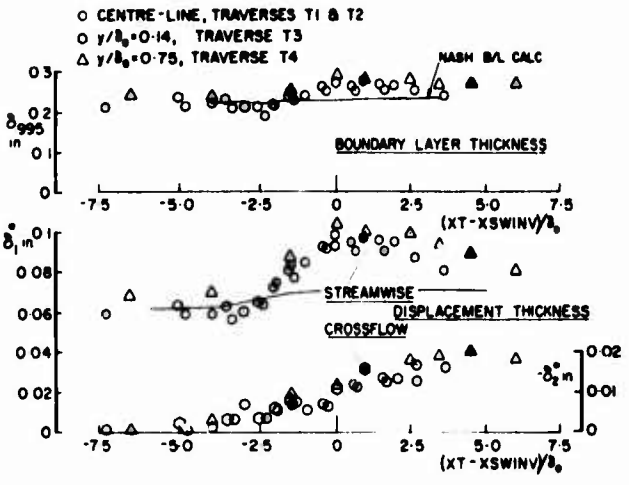

Fig.16 Boundary layer thickness for $\delta_w = 8°$ at Mach 2

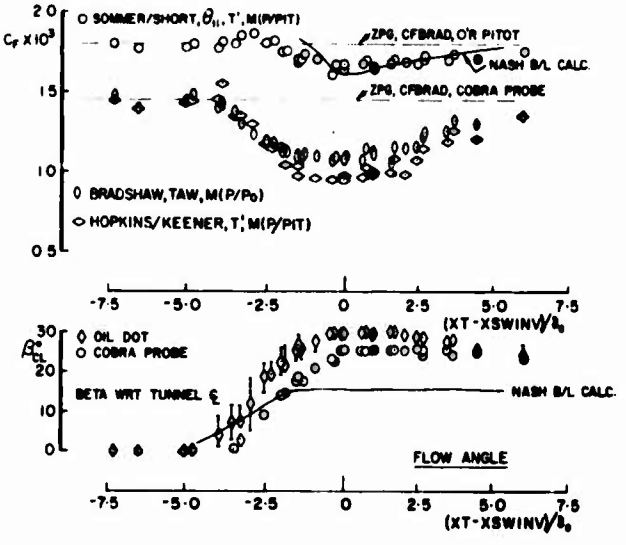

Fig.17 Local skin friction and flow deflections for for $\delta_w = 8°$ at Mach 2

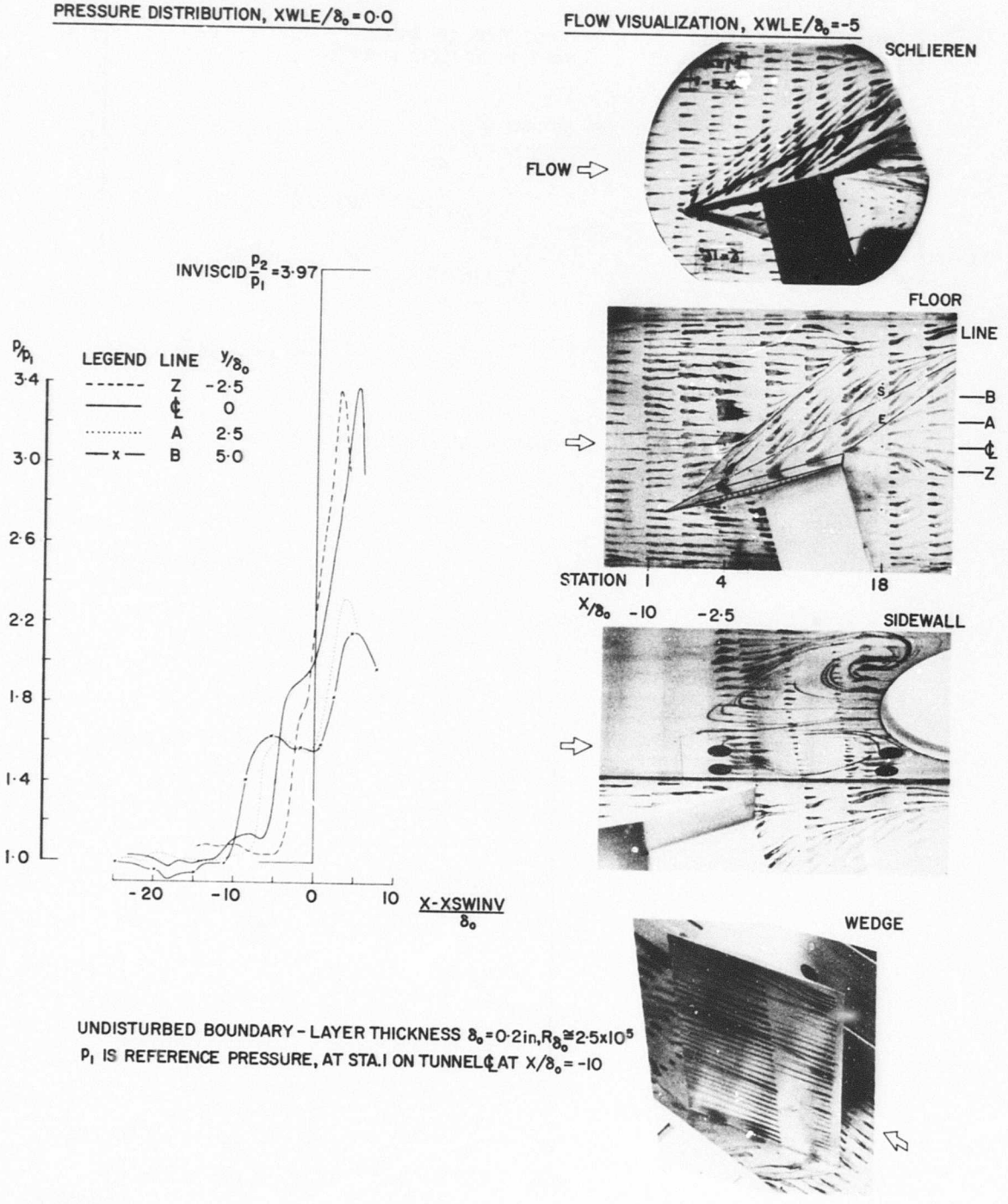

Fig.18 3-D separation with $\delta_w = 16°$ at Mach 4

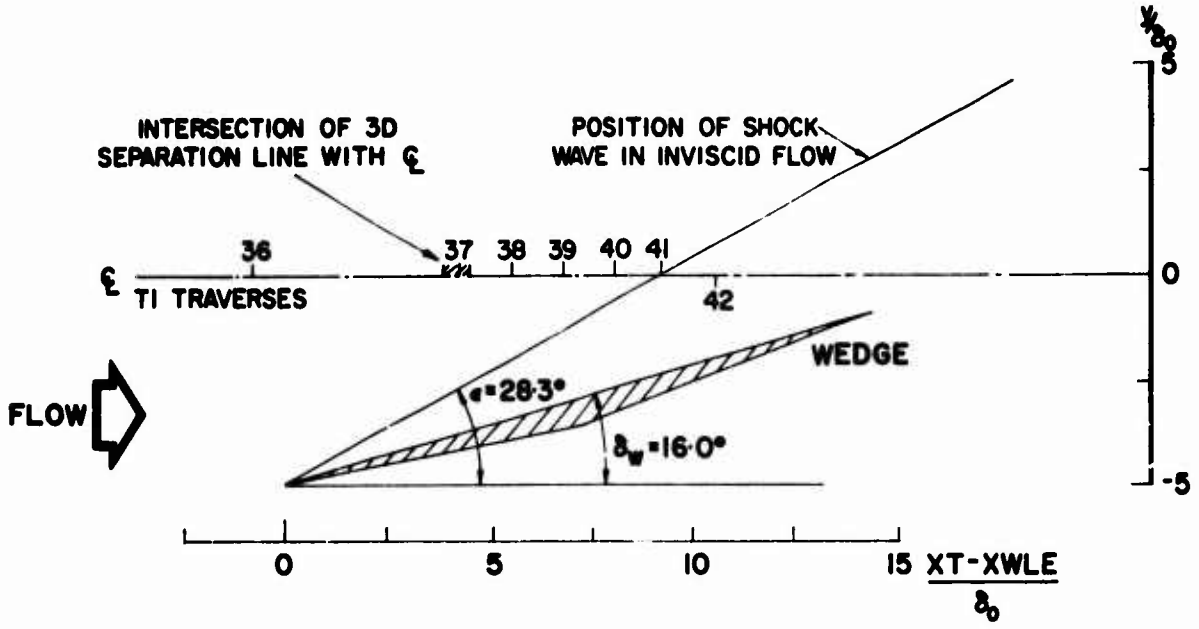

Fig.19 Map of cobra probe traverse locations at Mach 4, $\delta_w = 16°$

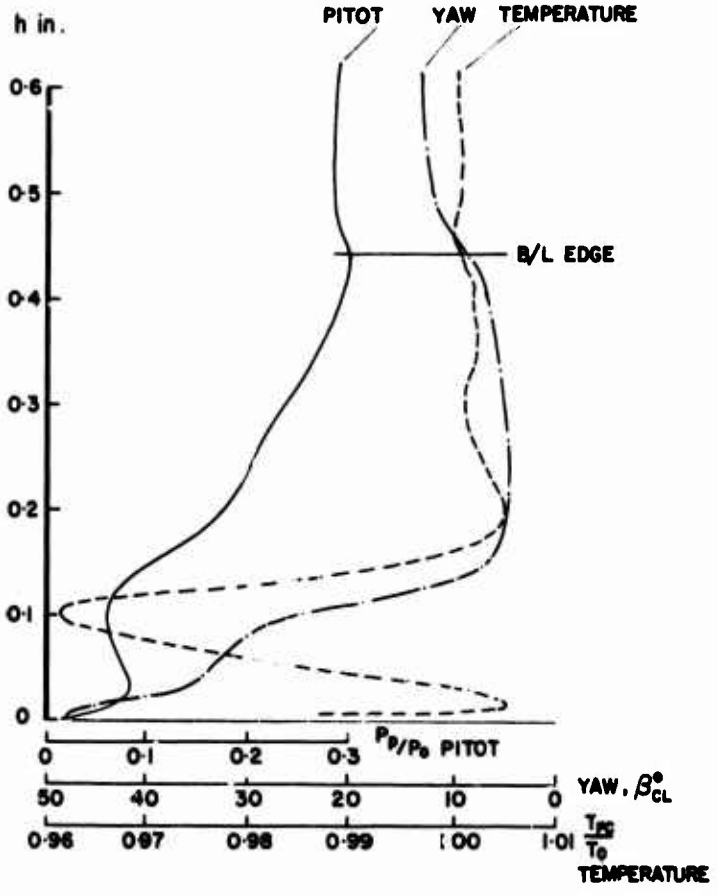

Fig.20 Pitot, total temperature and yaw angle distributions for station 41 near inviscid shock wave location; for $\delta_w = 16°$ at Mach 4

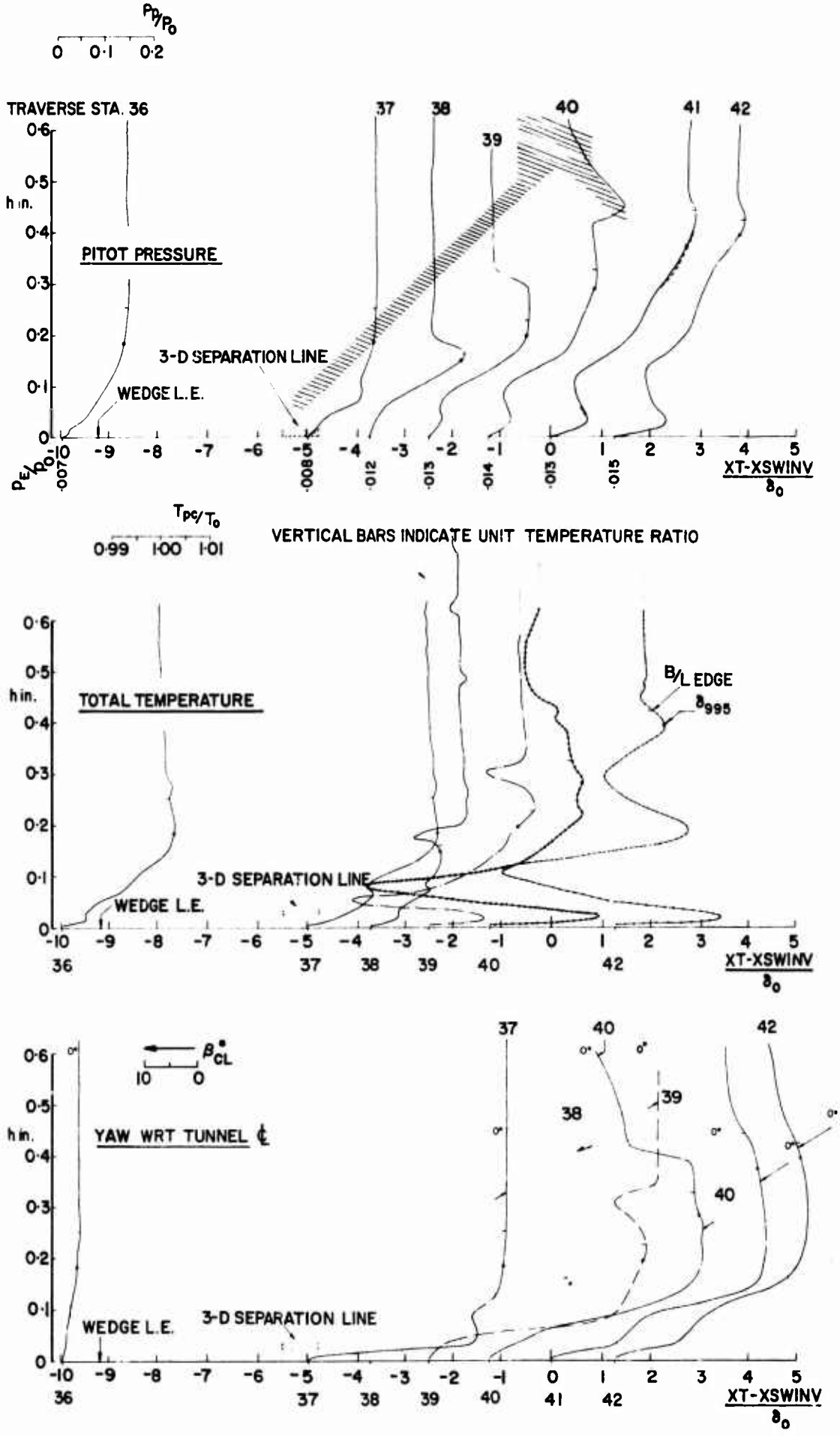

Fig.21 Cobra probe measurements along tunnel ℄ at Mach 4 and $\delta_w = 16°$

h IS DISTANCE PERPENDICULAR
TO WALL

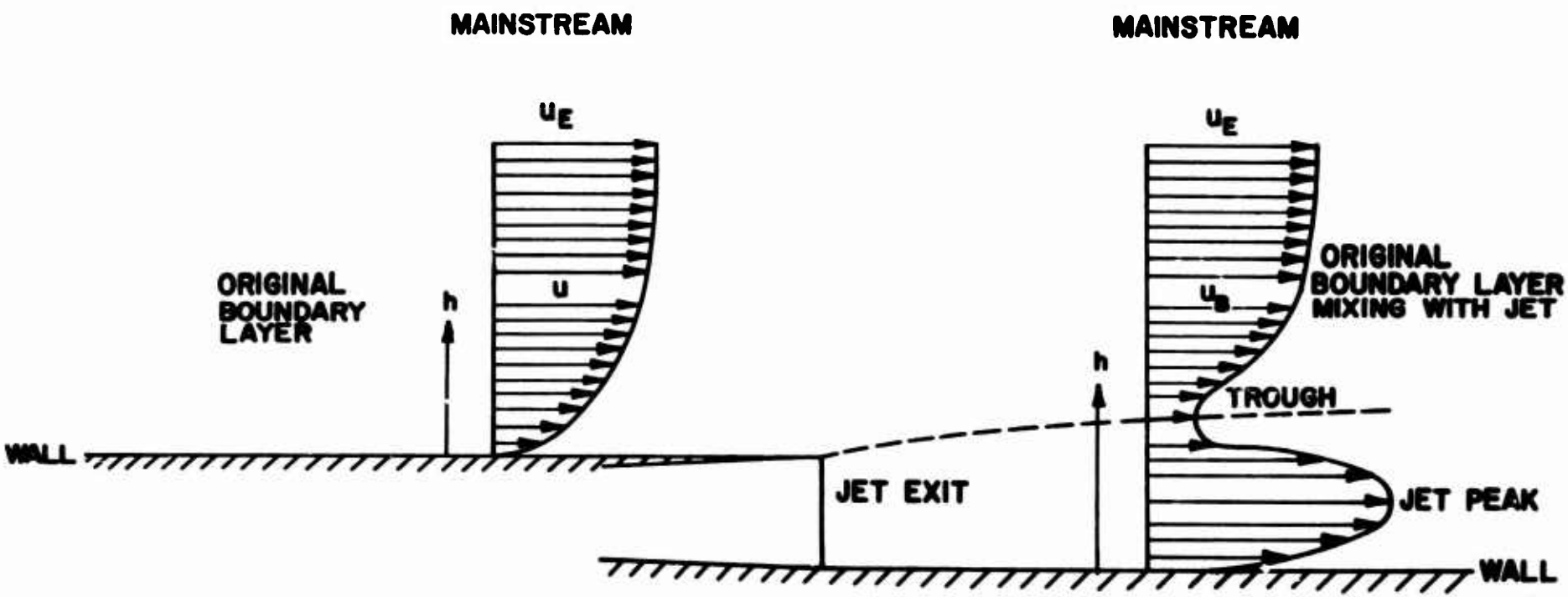

Fig.22 Definition of jet peak and wake trough

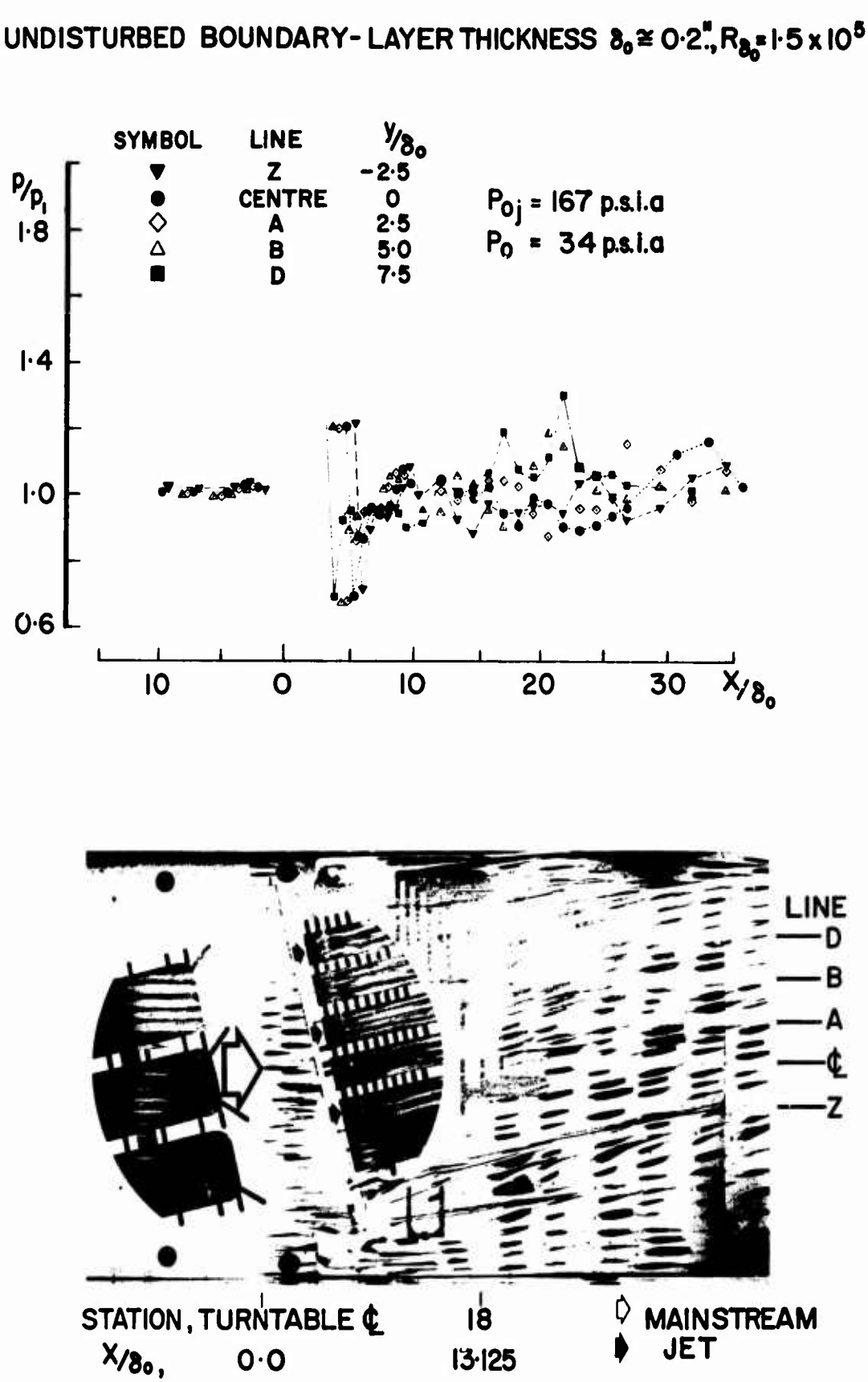

Fig.23 Downstream penetration of jet in empty tunnel: with $\theta_j = -12°$, $M_j = 3$, at Mach 2

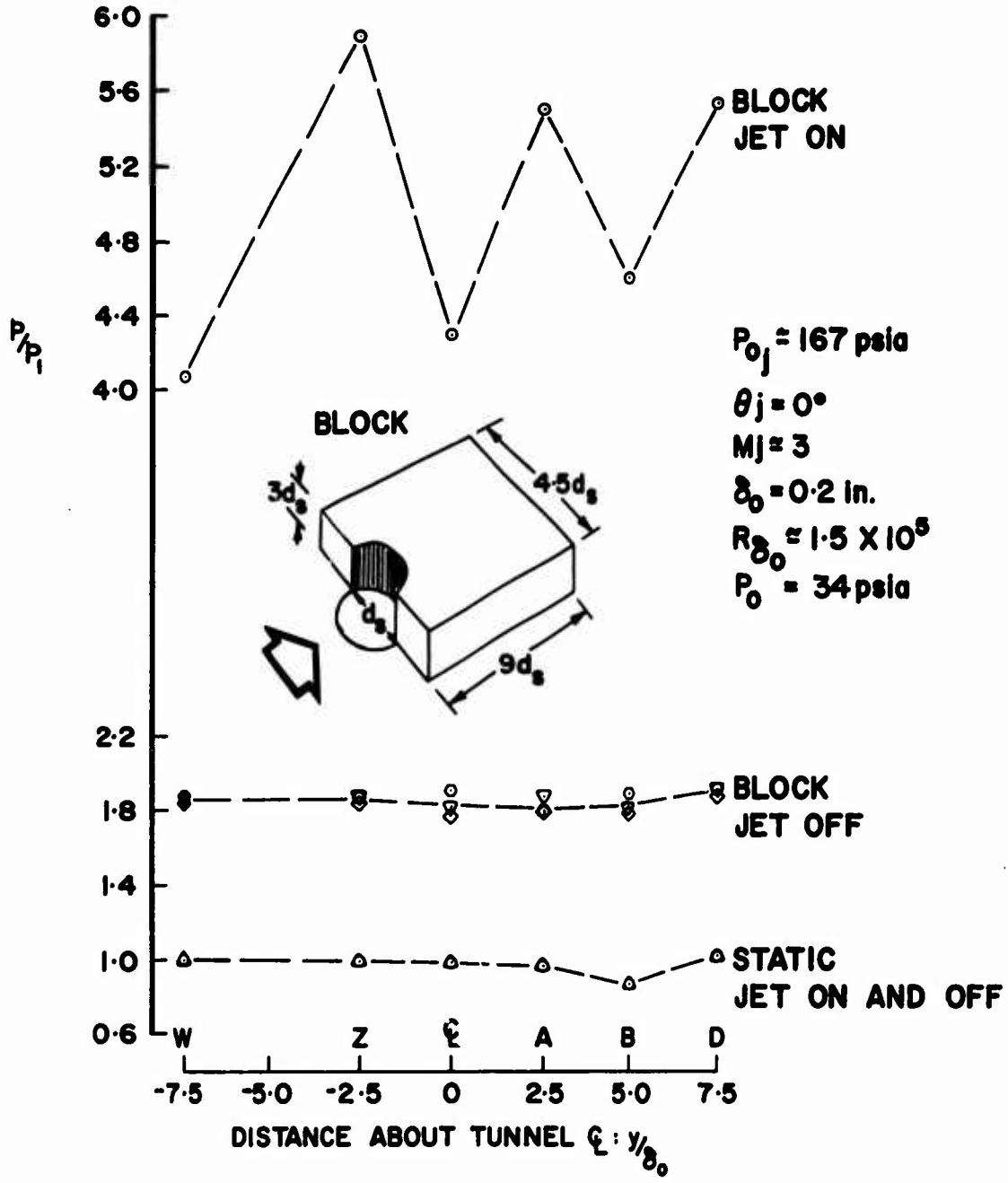

Fig.24 Static and obstacle block pressures downstream of jet slot at $X/\delta_0 = 11.88$

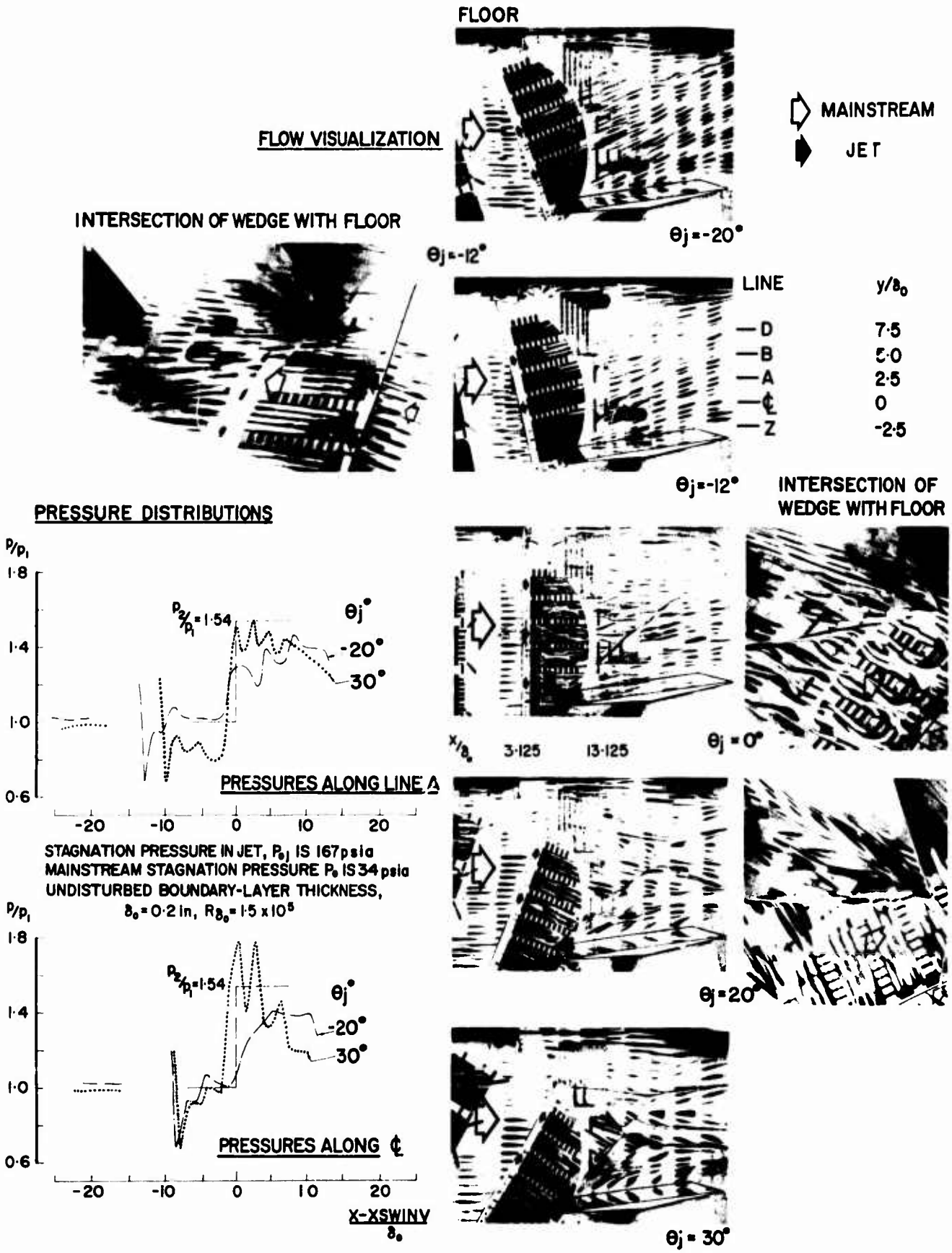

Fig.25 Air injection: effect of θ_j at $M_j \cong 3$ for $\delta_w = 8°$ at Mach 2 with $XWLE/\delta_0 = 7.5$

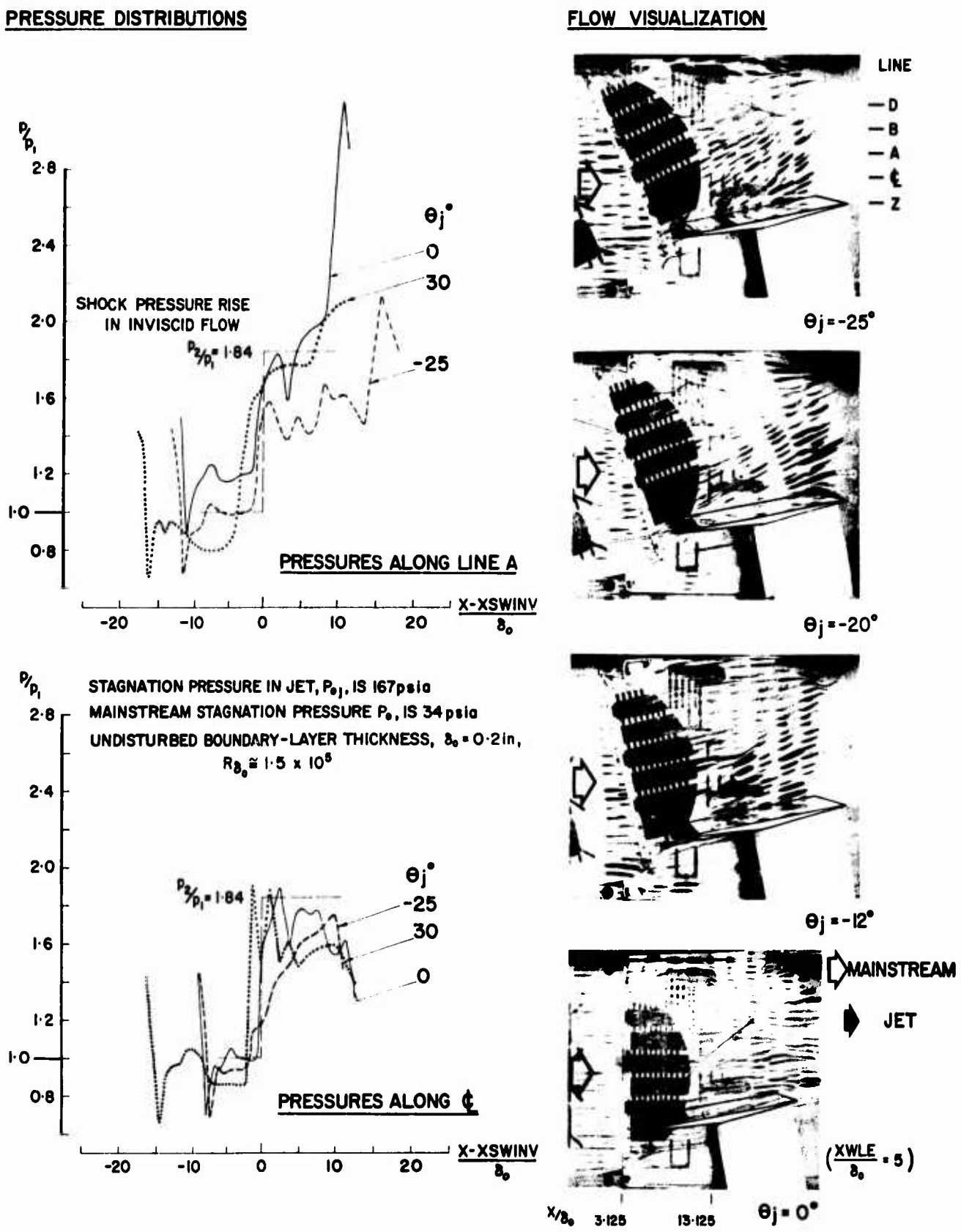

Fig.26 Air injection: effect of θ_j at $M_j \cong 3$ for $\delta_w = 11.5°$ at Mach 2 with $XWLE/\delta_0 = 7.5$

AN EXPLORATORY STUDY OF A THREE-DIMENSIONAL SHOCK WAVE BOUNDARY LAYER INTERACTION AT MACH 3

by

B. Oskam, I. E. Vas and S. M. Bogdonoff
Princeton University
Princeton, New Jersey 08540, U.S.A.

SUMMARY

An exploratory experimental investigation has been carried out on the three dimensional flow fields caused by the interaction of oblique shock waves and a planar turbulent boundary layer. The study was performed at a free stream Mach number of 2.95, a Reynolds number per inch of 1.6×10^6 and near adiabatic wall conditions. The interaction was studied on two experimental configurations having different initial boundary layer thicknesses (δ = 0.13 and 0.55 inches). Both surface measurements as well as complete flow field surveys were performed.

The main contributions of the present investigation are two experimentally derived flow field models for shock generator angles of 4^o and 10^o. Based upon both static pressure and surface flow patterns, as well as heat transfer data, the interaction region can be characterized as quasi-two-dimensional along the shock direction in the region studied.

A critical examination of the occurance of "ordinary" flow separation and its character, as applied to the present problem, was carried out. It was concluded that McCabe's criterion, as used by the previous investigators, is not a sufficient condition to determine the onset of flow separation.

LIST OF SYMBOLS

a	local speed of sound
C_p	specific heat at constant pressure
$C_f = \frac{\tau_w}{\frac{1}{2}\rho_1 u_1^2}$	local skin friction coefficient
$C_h = \frac{q_c}{\rho_1 u_1 C_p (T_w - T_{aw})}$	local heat transfer coefficient
$M = \frac{\sqrt{u^2+v^2}}{a}$	Mach number
p	static pressure
q_c	convective heat transfer
$Re_\delta = \frac{\rho_1 u_1 \delta}{\mu_1}$	Reynolds number based on δ
t	time
T	temperature
T_{aw}	adiabatic wall temperature
u,v,w	velocity components in X, Y and Z directions
u_{inc}	u-velocity transformed by van Driest transformation of Ref. 8
$u_\tau = \sqrt{\frac{\tau_w}{\rho_w}}$	skin friction velocity
X	coordinate parallel to tunnel axis measured from leading edge of shock generator
X_s	coordinate parallel to X-axis measured from calculated shock position
Y	coordinate normal to X-axis in plane of the test surface measured from leading edge of shock generator
Z	coordinate normal to X- and Y-axis measured from test surface
$\alpha = \arctan(\frac{v}{u})$	yaw angle
α_o	angle between oil line and X-axis
$\alpha_{o_{max}}$	maximum of α_o for fixed shock generator angle
α_G	effective shock generator angle measured with respect to X-axis
$\beta = \arctan(\frac{w}{u})$	pitch angle
δ_1	boundary layer thickness at ($X_s = -\Delta X$) for fixed Y
δ_{ave}	average δ_1 (as defined in Section 4.3)
δ^*	displacement thickness
ΔX	upstream extent of interaction
θ	momentum defect thickness
μ	viscosity
ρ	density
τ_w	surface shearing stress
ν	kinematic viscosity

Subscripts

1	as in free stream ahead of interaction
2	uniform conditions behind shock wave as calculated from oblique shock theory

Subscripts (Cont'd)		Superscripted variables	
w	wall conditions	$\bar{p}$	corresponds to $\frac{p}{p_1}$
vD	van Driest	$\bar{u}$, $\bar{v}$, $\bar{w}$	corresponds to $\frac{u}{u_1}$, $\frac{v}{u_1}$, $\frac{w}{u_1}$
		$\overline{X_s}$, $\bar{Z}$	corresponds to $\frac{X_s}{\delta_1}$, $\frac{Z}{\delta_1}$

1. INTRODUCTION

Since the early studies of supersonic flow, there has been continued research on the problems of the interaction of shock waves and turbulent boundary layers. These studies have been concerned with geometries where the pressure gradients were imposed in the streamwise direction, resulting in planar, two-dimensional flows. In most cases of practical importance, there are probably significant three-dimensional effects. In nominally two-dimensional flows this three-dimensionality is associated with end or corner restraints and involves gradients in flow properties in all three directions. However, there is a large class of three-dimensional flows which contain one particular direction along which flow properties vary only slowly. In this class of shock wave/boundary layer interactions, one might expect a quasi-two-dimensional character and therefore a simplification over the full three-dimensional problem.

The study presented herein deals with such a quasi-two-dimensional interaction between an oblique shock wave and the turbulent boundary layer on a surface parallel to the stream but perpendicular to the plane of the shock. Interactions of this kind are found, for example, on the sidewalls of rectangular supersonic air intakes or oblique shock diffusers. The geometry produces both streamwise as well as transverse pressure gradients resulting in significant cross flows in the boundary layer. These complex three-dimensional flows have been the subject of only a few studies, primarily because of the experimental difficulty involved in the full resolution of the flow phenomena. McCabe[1] and Lowrie[2] have studied the problem both experimentally and theoretically. McCabe presented an approximate inviscid theory, based on vorticity arguments, which relates the limiting surface streamline angle to the shock conditions. This theory incorporates some fairly sweeping assumptions, which result in an oversimplification of the physical situation and therefore severely limits the understanding that can be gained from it. A more complicated and also more realistic treatment has been given by Lowrie. His analysis is primarily based on the argument that the pressure gradient term in the momentum equation is much larger than the shear stress term and, consequently, the problem is treated as inviscid rotational fluid flow. The development of cross flows within the boundary layer can be predicted in this way, but only in an initial region of the interaction where the pressure gradient is indeed the dominant effect. It should be noted that Lowrie assumed constant static pressure in the direction normal to the wall in both his theory and his experiments. He reported that boundary layer profiles that showed a static pressure variation of more than 5% were discarded.

Token[3] and Neumann[4] have concentrated on surface heat transfer as it is most important for direct practical applications. Although McCabe, Lowrie and Token provide a large amount of information about the three-dimensional interaction of an oblique shock wave with a turbulent boundary layer each of these studies leaves a significant part of the phenomenon unresolved.

The present study involves the same general problem as examined by the previous investigators but with a somewhat different objective; to examine, in a well-defined experimental set-up, the complete flow field of the interaction and to directly connect this flow field with the surface phenomena. The goal is to provide a better understanding of the phenomena by considering many different aspects of the complete interaction and to form a framework for future experimental and theoretical studies.

Variable strength shock waves, at a Mach number of 2.95, interacting with a high Reynolds number turbulent boundary layer were the general framework of the experimental program. The shock interaction studied was at some distance from the shock generator to try to determine the characteristics of the interaction in a region not directly influenced by the streamwise corner formed by the shock generator and the test surface. Major concentration was on the study of the interaction using one relatively thick turbulent boundary layer (Model 1), but the scope of the study was extended to a much thinner turbulent boundary layer (Model 2) to examine scaling effects.

Special attention was paid to the phenomenon of flow separation in three dimensions. It should be noted that a unique characteristic of three-dimensional flow is that it can separate from the surface without the mean surface shear stress becoming zero. This type of flow separation, known as ordinary separation, has to be distinguished from singular separation whose principal characteristic is that the mean wall shear stress is zero at the separation point (e.g., the separation in planar, two-dimensional flows is singular). Previous investigators of the present problem have indicated the occurance of ordinary separation along a line defined on the basis of surface oil flow patterns. The present investigation examines this ordinary separation on the basis of <u>both</u> surface phenomena as well as flow field measurements.

2. EXPERIMENTAL PROGRAM

2.1 Geometrical Arrangements

A schematic of the experimental configuration, showing the region of detailed measurement, is presented in Fig. 1. The oblique shock was generated by a variable angle shock generator which spanned the tunnel between top and bottom wall. As noted, the region of study extends upstream of the interaction to establish the incoming boundary layer characteristics. The test region does not extend to the shock generator, and is limited in extent by the expansion from the trailing edge of the shock generator and the reflection of the shock from the wall opposite to the shock generator. In any such experimental set-up, extraneous interference effects from the boundaries of the region of study can be expected and great effort

was made to evaluate these effects. The length of the shock generator was made long enough so that the expansion from the trailing edge did not interfere with the region of study and a detailed examination was made of the region of influence of the reflection of the shock wave from the opposite wall.

One of the key parameters of the study is the effect of shock strength which was varied by changing the deflection angle of the shock generator. Two configurations of this general format (Fig. 2) were studied in detail; their main difference was the thickness of the boundary layer coming into the interaction region. Most of the studies were carried out on Model 1, because the relatively thick turbulent boundary layer allowed high resolution measurements to be made throughout the interaction region. The configuration of Model 2 incorporates a much smaller incoming boundary layer thickness and thus covers a larger region of the interaction in terms of boundary layer thickness than Model 1. A more detailed description of the experimental geometries is given in Ref. 5.

2.2 Wind Tunnel

The experimental study was carried out in the Princeton University blowdown wind tunnel. The test section has a cross area of 8 inches by 8 inches. The test conditions for the present tests were a Mach number of 2.95, a stagnation pressure of 100 psia, an average stagnation temperature of 472°R and a tunnel wall temperature of 10 to 20% above the adiabatic wall temperature. These test conditions resulted in a Reynolds number per inch of 1.6×10^6 and a maximum test time of 6 minutes. Details of the basic facility are given in Ref. 6.

Previous measurements had indicated that the boundary layer flow over the bottom and top walls were equivalent and planar, two-dimensional. The bottom wall boundary layer was used as the test layer for the Model 1 study. Windows positioned in the top and bottom walls were used either as observation or instrumentation ports. In general, pressure distribution studies were carried out with instrumentation mounted in the bottom window. The top window was used as an observation port for photography of oil flow patterns.

2.3 Surface Measurements

Oil flow studies: A technique developed for the present test conditions used a fluorescent oil applied upstream of the region of study before the tunnel was started. Approximately 10 seconds after the tunnel was operating, photographs were taken of the oil pattern. The particular mixture used consisted of clear motor oil and green fluorescent dye thinned with kerosene. The oil patterns were illuminated by a high intensity ultra violet light source. This particular combination of ultra violet excitation and green fluorescence made it possible to filter out the ultra violet reflections coming from the metal test surface. Good results were obtained under all test conditions.

Surface static pressure: Measurements were made on Model 1 using an instrumented plate which fitted into the bottom window port. A large number of static pressure taps was necessary to map the full flow field involving the interaction and to account for the change in shock location when the shock generator angle was varied. During a test, a fixed shock generator position was held while a scanivalve measured the static pressure distribution. The basic static pressure window port could not be used for Model 2, so the test surface itself was instrumented with an arrangement of static pressure orifices.

Heat transfer: Several techniques were investigated to measure the heat transfer rate over the test area. The method finally chosen was a quasi-transient method using a slug calorimeter since it matched best to the tunnel operating procedures, gave reasonable spatial resolution and is rather simple to manufacture. Figure 3 shows a photograph of the heat transfer plug and the insert which provides the hot air. A line drawing of the slug calorimeter arrangement is given in Fig. 4.

To determine the heat transfer rate from the wall to the gas at uniform wall temperature conditions it is necessary that the test piece (slug) be heated to a temperature higher than the surrounding wall temperature. This heating was provided by impinging a tiny jet of hot air to the inside of each slug calorimeter. After the hot air heating is stopped, the slug would attempt to reach the wall recovery temperature as time progresses. At an intermediate time, t_o, while the slug temperature is dropping it equals to the wall temperature. From an exponential curve fitted to the measured slug temperature-time data points, the temperature-time gradient was evaluated at t_o. The convective heat transfer follows from this temperature-time derivative and the calorimeter properties. Heat conduction from the slug to the surrounding wall was minimized by separating the slugs from the aluminum plug by nylon insulation. It was determined that no correction due to insulation losses were necessary.

Skin friction: The Preston tube was used to get some indication of the skin friction. As the present problem involves both pressure gradients and cross flows, there will be uncertainties in the results, particularly for the case of large cross flows. The Preston probe was first aligned with the surface oil flow direction, then rotated 10^o in both directions. Although the Preston tube reading was relatively insensitive to such rotation, the largest measured value was used to evaluate the skin friction. The calibration scheme proposed by Bradshaw[7] was used to evaluate the skin friction. He extended the subsonic calibration equation to compressible flow in an alternate way. Instead of using calibration factors to transform to the subsonic calibration coordinates, he added a compressibility correction function to the subsonic calibration equation. This new function has variables which are based upon wall conditions only.

2.4 Flow Field Measurements

To carry out detailed flow field measurements in the interaction region, a probe drive system with two degrees of freedom was used. It moved the probes normal to the wall and yawed them. The probes themselves were supported by a streamlined section which extended from the top wall down towards the bottom wall boundary layer where the measurements were taken.

Pitot-yaw surveys: To determine the flow angles in the X-Y plane throughout the flow field, a cobra probe has been employed. The cobra probe was traversed and yawed in such a way that the two side pressures remained equal so that the flow yaw angle and pitot pressure could be determined at the same time.

Static pressure surveys: Since it was clear that significant variations in the static pressure would take place within the interaction region, it was necessary to determine the local static pressure in order to evaluate the local flow velocities and density. To obtain a measure of the local values, a small cone-cylinder probe was designed to be used in conjunction with the probe drive mechanism noted previously. The static pressure orifices were located 11 diameters downstream of the tip. The probe rotated in the X-Y plane about the orifice location and was kept aligned with the known flow direction. A calibration of the angle sensitivity of the probe in uniform flow was performed and it was found that over $\pm$ 4°, the static pressure varied less than 2% from the correct value.

Total temperature surveys: To complete the measurements from which the local velocities can be obtained, measurements were made of the total temperature throughout the interaction region. Although the wall temperature was approximately 15% above its adiabatic value, the measurement of small variations of total temperature provide for increased accuracy of the deduced flow field data. The probe used was a fine wire probe which had a thermocouple junction in the middle of the wire. This thermocouple consisted of the junction between alumel and chromel wires which had a thickness of 0.002 inches diameter.

A more detailed description of the experimental techniques used is given in Ref. 5.

3. INCOMING BOUNDARY LAYER CHARACTERISTICS

The boundary layers that interacted with the shock wave were surveyed extensively and were shown to be two dimensional across the width of the wind tunnel. It should be noted, however, that the upstream boundary of the interaction region, as determined from the start of the wall static pressure increase, is a swept line which is approximately parallel to the shock wave. This results in a variation in thickness of the boundary layer coming into the interaction region since the boundary layer is growing in the streamwise direction. The boundary layer that interacted with the shock wave in the Model 1 configuration originated from the tunnel nozzle and increased in thickness from 0.52 to 0.58 inches along a typical interaction region for a 10 degree shock generator angle. The boundary layer for Model 2 was generated on a flat test plate which spanned the tunnel and was located 2 inches above the tunnel bottom wall. The corresponding increase in thickness of this thinner Model 2 boundary layer was much larger because of its shorter running length and amounted to a variation of 0.11 to 0.16 inches. These increases of the incoming boundary layer thickness along the shock wave have to be taken into account when the scale of the interaction length is evaluated in terms of a local boundary layer thickness.

Boundary layer parameters derived from the measurements are tabulated for two typical initial profiles for Model 1 and 2, respectively:

	δ(inches)	δ^*(inches)	θ(inches)	C_f	Re_{inch}
Model 1	0.540	0.162	0.052	0.00119	1.6×10^6
Model 2	0.132	0.040	0.008	0.00150	1.6×10^6

The corresponding velocity profiles were transformed to the incompressible law of the wall variables by using the van Driest transformation as given in Ref. 8. These profiles are then compared with the incompressible wall-wake law as given by

$$\frac{u_{inc}}{u_\tau} = \frac{1}{k} \ln \left(\frac{y u_\tau}{\nu_w}\right) + C + \frac{\Pi}{k} W \left(\frac{y}{\delta}\right) \qquad (1)$$

where $W(\frac{y}{\delta}) = 1 - \cos(\pi \frac{y}{\delta})$, $C = 5.0$, $k = 0.41$, $\Pi = 0.52$.

The comparison (see Fig. 5) shows that the test boundary layers can be described as fully developed, "equilibrium", turbulent boundary layers.

The overall size of the region of study for both Model 1 and 2 in terms of boundary layer thickness is represented in Fig. 6 and compared with those of previous studies by McCabe, Lowrie and Token. Model 1 provides results in an area which is also covered by McCabe and Lowrie, but outside the region studied by Token. Model 2 covers a larger range not heretofore explored.

The general coordinate system used in obtaining and presenting the data is also shown in Fig. 6. The shock location, calculated from the oblique shock theory, is used as the origin for the X_s coordinate.

4. ANALYSIS OF RESULTS AND DISCUSSION

4.1 Three-Dimensional Separation

The notion of flow separation on planar surfaces in both two-dimensional as well as three-dimensional flow is that a boundary layer, flowing tangentially alongside a solid surface, breaks away from this surface due to an adverse pressure gradient. In planar, two-dimensional flows the customary definition of separation requires that the mean wall shear stress vanishes at the separation point. This definition is quite satisfactory for such cases as it implies the start of flow reversal. In three-dimensional flow, however, the situation is more complicated, illustrated by the fact that three-dimensional separation has a two-fold mechanism (see Lighthill, Ref. 9). This mechanism is explained by using the concept of limiting surface streamlines (or skin friction lines). If one considers a streamline at a small distance from the surface, then it follows from the continuity equation that this streamline has to depart from the surface not only in case of vanishing wall shear-stress, but also in a case where the topography of the limiting

surface streamlines is such that they converge. They can coalesce and form a line of ordinary separation. Although the notion of flow separation as applied to two- or three-dimensional flow is the same, the main mechanism through which flow separation takes place can be different; for example, three-dimensional flow can separate from the wall along a separation line without the mean surface shear stress becoming zero. This type of flow separation is known as ordinary separation (see Maskell, Ref. 10) and has to be distinguished from singular separation whose main characteristic is that the mean wall shear stress vanishes at the separation point.

In applying these ideas of flow separation to the present problem, previous investigators have proposed several ways in which the onset of flow separation, over any region of significant size, can be determined from surface flow patterns. The main characteristic of a line of ordinary separation is the tangential convergence of the surface streamlines into one single line. Maskell proposed that the order of magnitude of the rate of this convergence be the same on each side of the separation line. Rogers and Hall[11] have relaxed this criterian for separation, by suggesting that for the condition of incipient separation the limiting surface streamlines converge toward the separation line only in the upstream region, immediately downstream they are parallel to it and further downstream they turn progressively away from it.

Although these criteria of ordinary flow separation are based upon limiting surface streamlines, and thus have to be verified by actual flow field measurements, they are believed to be physically correct. Care, however, must be taken in applying these criteria especially in turbulent boundary layers where the equivalence between limiting surface streamlines (skin friction lines) and oil flow lines is not an obvious matter. In the following sections, there are several discussions specifically aimed at trying to clarify questions about this ordinary flow separation. Finally, objections will be raised against McCabe's criterion for separation as used in other investigations (Refs. 1-4) of the present problem.

4.2 Surface Flow Patterns

Some results obtained during the oil flow studies are presented in Figs. 7 through 10 with $\alpha_G = 4$ and 10 degrees for both Model 1 and 2. The oil lines for $\alpha_G = 4^o$ downstream of the calculated shock location are deflected to a maximum angle of about 10^o, which is about twice the shock generator angle but remains well below the shock wave angle. For $\alpha_G = 10^o$ the oil lines turn to angles which are substantially larger than the shock wave angle and coalescence of the oil streaks occurs as a consequence. Special attention should be paid to the difference in scale of an average boundary layer thickness between Model 1 and 2. Because of this large region of Model 2 (see Fig. 6) there emerges an area downstream of the shock wave for $\alpha_G = 10^o$ where the oil streak lines are parallel to the shock generator again. This region (II) is indicated on Fig. 10.

The interpretation is that the interaction is completed and the boundary layer has again reached a planar, two-dimensional character in this area indicated. The implication of this observation is that, for example, in the case of $\alpha_G = 10^o$, Y = 2.25 inches, it takes about 30 boundary layer thicknesses downstream of the shock wave before all cross flows have disappeared from the boundary layer. This length of the downstream extent of the interaction has never been observed in previous investigations and is a direct result of the large region covered by Model 2. The fact that the end of the interaction does not appear on the surface flow patterns for α_G smaller than 6^o is an indication that the downstream extent of the interaction in the X-direction is larger for smaller shock generator angles.

These surface flow patterns can be reduced to quantitative data by measuring the angles of local oil lines with respect to the X-direction along a line of Y = constant. Results obtained from that process for shock generator angles ranging from 2 up to 12 degrees are presented in Fig. 11 for Model 2. The theoretical shock wave angles are shown to the left hand side of these figures. From Fig. 11 it can be seen that the rate of decrease of the local oil line angles with distance X_s for small generator angles, $\alpha_G \leq 6^o$, is much smaller than for the larger α_G's . This results in a larger downstream extent for weaker shocks. The explanation of this seemingly contradictory result lies in the topography of the flow field that is associated with the surface flow patterns.

For $\alpha_G = 6^o$ and smaller, the total yaw angles occurring in the flow field remain smaller than the shock wave angle. These flow fields are similar to a classical three dimensional boundary layer flow that negotiates a transverse pressure gradient. This transverse pressure gradient causes the slower moving fluid in the bottom portion of the boundary layer to deflect to larger angles than the faster moving fluid in the outer portion of the boundary layer. This process in which cross flows are produced by the transverse pressure gradient is an instantaneous process or in other words the cross flows are created at the physical location where the transverse pressure gradients are present. These pressure gradients disappear in going downstream of the shock location. The cross flows, however, do not vanish instantaneously, but rather decay slowly. The driving force in this decay process is the magnitude of the cross flow itself. So as the cross flow gets smaller, the rate of decay decreases, and the downstream limit of no cross flow is only reached asymptotically, resulting in very large downstream extent for $\alpha_G \leq 6^o$.

For larger generator angles ($\alpha_G \geq 8^o$) other processes play a role in the decay of cross flows. Since the yaw angles are no longer smaller than the shock angle, it can no longer be considered as regular flow field, but rather a flow with large secondary flows imbedded in it. The fluid in which the large cross flows are produced is transported along the shock direction and thus out of the plane of observation, the X-Z plane. This reorganization process of the flow, as described in a later section on the flow model, causes fluid in which much smaller cross flows are present to pitch down toward the wall resulting in a strong decay of oil line angles with distance X_s for $\alpha_G \geq 8^o$.

McCabe[1] has proposed a simple approximate secondary flow theory. This theory assumes that the limiting streamline angle does not vary with distance downstream of the shock wave. This is an oversimplification of the actual situation as can be seen from Fig. 11. However, if the predicted limiting streamline angle is assumed to be a representation of the maximum of the distribution of oil line angles for a given shock generator deflection, $\alpha_{o_{max}}$, then the theory is a good approximation of the present experimental data, as shown in Fig. 12. The theoretical shock wave angle is also indicated in the figure.

McCabe has also suggested a criterion for ordinary separation which defines the flow as separated if the oil lines are deflected to an angle larger than the shock wave angle. This criterion indicates that the flow is separated for $\alpha_G > 7.5^o$ from the present data (see Fig. 12). The justification of this criterion, however, is very much in question since it would not coincide with the first appearance of an ordinary separation line as shown by McCabe himself. This criterion also implies that the minimum shock generator angle needed for flow separation decreases indefinitely as the shock wave angle decreases with increasing Mach number (see Korkegi, Ref. 12). This last observation indicates that even the practical value of McCabe's criterion is not at all clear.

4.3 Static Pressure Distributions

A typical static pressure distribution is shown in Fig. 13. The distance X_s is normalized by the boundary layer thickness, δ_1 , at the beginning of the pressure rise. The upstream extent of the interaction region measured from the shock position is about 12 δ_1 and largely independent of the shock strength at this station of Y = 2.25 inches of Model 2. The downstream extent is more difficult to define in terms of the static pressure distribution because this limit is reached asymptotically. The observation that the scale of this downstream extent is of the order of 20 to 30 times the incoming boundary layer thickness at Y = 2.25 inches is of quite some significance. This scale was also extracted from the surface flow patterns.

Static pressure distributions obtained along several instrumentation lines of Y = constant were also cross plotted as isobar patterns. A typical isobar pattern is shown in Fig. 14 for $\alpha_G = 10^o$, Model 1. As can be noted, the lines of constant static pressure are approximately parallel to the shock wave and only to a small amount diverging along the shock direction. This indicates that the pressure distribution is quasi-two-dimensional in the sense that this flow quantity is constant in the shock direction to a good approximation.

Some comparison can be made with the data obtained by other investigators. The test conditions are listed in the following table:

	Mach Number	δ_{ave} (inches)	Re_{inch}	$Re_{\delta_{ave}}$
Lowrie (Ref.2)	3.44	0.412	1.02×10^6	4.20×10^5
McCabe (Ref.1)	2.94	0.230	2.06×10^5	0.47×10^5
Token (Ref.3)	3.71	6.0	2.91×10^5	17.5×10^5
Model 1	2.95	0.55	1.6×10^6	8.8×10^5
Model 2	2.95	0.133	1.6×10^6	2.1×10^5

The test Mach number of all these studies is around 3 and the wall temperatures are all near adiabatic. The boundary layer thickness, however, varies by a factor of 40. If the intersection of a line drawn tangent to the maximum slope of a static pressure distribution and the line $\bar{P} = 1$, is taken as the beginning of interaction, then the upstream extent, ΔX , can be defined as the distance between the calculated shock location and this beginning. The upstream extent of the interaction, nondimensionalized by the local incoming boundary layer thickness, is shown in Fig. 15. The Y coordinate in this plot is nondimensionalized by the boundary layer thickness, δ_1 , averaged over the distance between the shock generator leading edge and the station Y = constant considered. This average of δ_1 is indicated by δ_{ave} .

The general agreement of the data in Fig. 15, despite the difference in Mach number and deflection angles, has an important implication. If one recalls that δ_1 varies by a factor of 40, one can reach the conclusion that the boundary layer thickness can provide a basis for scaling parameters in this type of problem.

4.4 Heat Transfer Distribution

The heat transfer results are presented as a nondimensional ratio of the local heat transfer coefficient divided by the flat plate value predicted by the van Driest method[13] for the test conditions upstream of the interaction. It should be noted that the local heat transfer coefficient is defined as the local heat transfer rate nondimensionalized by free stream conditions ahead of the interaction. The wall temperature conditions are uniform throughout the interaction region.

The results indicate, as shown in Fig. 16, that heat transfer rate decreases somewhat as the shock is approached in the streamwise direction, and increases almost linearly with the downstream distance from the shock position. No conclusion about the peak heat transfer could be reached as the maximum occurred at the boundary of the region of study of Model 1. The heat transfer results are also cross plotted as a heat transfer pattern in the X-Y plane and an example is given in Fig. 17 for $\alpha_G = 10^o$, Model 1. The results show a general uniformity of the heat transfer field and demonstrate again the quasi-two-dimensional nature of the interaction region.

4.5 Preston Tube Measurements

The skin friction was deduced from Preston tube measurements taken along Y = 4.0 inches on Model 1 for $\alpha_G = 2^o$ to 10^o. These results of these measurements are shown in Fig. 18 where the skin friction has been nondimensionalized by the upstream flat plate value. The most significant observation is that the skin friction distribution is almost equivalent to the heat transfer distribution. This implies that the Reynolds analogy is valid as a first approximation. If ordinary separation occurs it is not required that the skin friction vanish, therefore, no conclusion about separation can be reached by these results.

4.6 Analysis of Complete Flow Field Data

A complete picture of the mean flow field in the X-Z plane can be constructed from the measured quantities, pitot pressure, yaw angle, static pressure, and total temperature. If the static pressure and the pitot pressure at a point in the field are known, the Mach number can be calculated directly from the isentropic relations for subsonic conditions, and from the Rayleigh Pitot formula in an iterative cycle for supersonic cases. The total energy equation was then applied to give the static temperature and thus the density and u,v velocity components. In addition, the velocity component in the Z-direction, w , can be deduced from the density and u,v velocity distributions by integrating the continuity equation and using the boundary condition $w = 0$ at $z = 0$. Hence:

$$w = -\frac{1}{\rho} \int_0^z \left\{ \frac{\partial}{\partial x} (\rho u) + \frac{\partial}{\partial y} (\rho v) \right\} dz' \qquad (2)$$

The derivatives in the integrand were obtained by locally fitting a second order polynomial through three data points followed by a differentiation of the polynomial. Data was taken in one X-Z plane only. To overcome this difficulty of evaluating the $\frac{\partial}{\partial y}$ derivative, the data in the X-Z plane at $Y = 4.0$ inches was projected along the shock direction to higher and lower values of Y . This procedure assumes that the interaction region is perfectly two-dimensional along the shock direction, but it was found that the resultant w was not sensitive to small changes of the projection direction, e.g., a slight divergence of the projection directions through the interaction. The accuracy of the w component obtained by differentiation and integration of the original data is less than that of u and v . After the w-component is computed, the pitch angle β (defined as $\beta = \arctan(\frac{w}{u})$) can be found. It should be noted that the measurement technique of obtaining u and v is only valid if w remains small compared to $\sqrt{u^2 + v^2}$. This requirement was checked a posteriori and found to be satisfied.

The static pressure distribution in the X-Z plane at $Y = 4.0$ inches for $\alpha_G = 10^o$, shown in Fig. 19, indicates that within the interaction there is no major region (in terms of δ) where the static pressure is uniform. The flow ahead of the shock is characterized by compression waves extending to well outside the incoming boundary layer. The static pressure field downstream of the shock has a more complicated distribution. The Mach number distribution in this X-Z plane is mostly supersonic, Fig. 20. A shallow subsonic region was measured close to the wall near the shock location.

Large yaw angles are measured in the interaction region (see Fig. 21). The largest yaw angles of 55^o occurred a small distance from the wall and $\overline{X_s} \approx 3$. Despite this small region where the yaw angles are larger than the shock wave angle, there is an extensive region downstream of the shock wave where the yaw angles are substantially less than the shock generator angle ($\alpha_G = 10^o$).

The pitch angle β through the interaction (shown in Fig. 22) provides some additional information. The compression waves ahead of the shock do not only cause increasing yaw angles but also increasing pitch angles. Going through the shock wave these pitch angles don't seem to decrease initially, however, at $\overline{X_s} \approx 3$ rapid changes take place and the pitch angle becomes negative.

In view of the question about ordinary separation, it should be noted from this figure that the pitch angle tends to zero as the wall is approached. This observation is of particular importance at the position ($\overline{X_s} \approx -3$) where the oil lines tend to coalesce. This is the region where one would expect locally large pitch angles. The surveys were taken at stations one boundary layer thickness, δ, apart. Keeping this streamwise resolution in mind it can be concluded that a local coalescence of oil flow lines is not necessarily related to locally large streamline inclination with respect to the wall surface. There is, however, a tendency of the flow to depart from the wall (β positive) but it is uniformly spread out over many boundary layer thicknesses.

4.7 Flow Models and Separation

To depict the flow field in the X-Z plane at $Y = 4.0$ inches, the following flow model is constructed for $\alpha_G = 10^o$, see Fig. 23. The region A is the undisturbed uniform flow ahead of the interaction with a planar turbulent boundary layer at the wall. The typical character of region B is that it has very slowly increasing yaw angles which remain lower than the shock generator angle ($\alpha_G = 10^o$) even in subregions B_2 and B_3 and only reach the 10^o level far downstream. In region C (the area extending downward from region B and approaching the wall) large yaw angles prevail ($10^o \leq \alpha \leq 55^o$). Yaw angles larger than the shock wave angle ($\alpha_{sh} = 28^o$) occur in subregion C_2. The far flow field downstream of the shock and outside region B contains waves originating from the interaction, region D. The decrease in pitch angles β observed by going from subregion B_2 to B_3 generates expansion waves in the external flow (subregion D_1). Compression waves are present in subregion D_2 where the flow has to turn parallel to the wall again.

The corresponding flow model for $\alpha_G = 4^o$ is also presented, see Fig. 24. The measurements on which this model is based are given in Ref. 5. Unlike the $\alpha_G = 10^o$ case, the yaw angles in this case remain well below the shock wave angle. This means that no reorganization process occurs as in the case of $\alpha_G = 10^o$ where the net transport of fluid along the shock direction incurred negative values of β . Although it was determined that the maximum pitch angles were quite small (1.5^o), they are significantly larger than those associated with boundary layers developing under zero pressure gradient conditions.

It is obvious that for $\alpha_G = 4^o$, although the streamlines are slightly departing from the wall ($\beta \leq 1.5^o$), that there is no question about separation. For the $\alpha_G = 10^o$ case, however, the question of whether the boundary layer should be called separated is not an obvious matter. If one examines the oil flow patterns for $\alpha_G = 10^o$ (Figs. 8 and 10) more carefully, the observation can be made that although the oil lines are converging and tend to coalesce upstream of the calculated shock position, they do not converge into one single line. The region in which coalescence occurs is growing in size in the direction

along the shock. This observation is consistent with the idea that the size of the interaction region is increasing with distance along the shock. It is exactly this gradual increase in size that permits the oil lines to converge without incurring locally large pitch angles β corresponding to separation of the flow from the wall. This directly leads to the conclusion that the flow is also unseparated for $\alpha_G = 10^o$.

The results clearly indicate that the qualitative difference between attached flows and flows with ordinary separation for the present problem cannot be taken for granted. The definition of ordinary separation becomes then a matter of some conjecture but does not seem to be as crucial as its counterpart in planar two-dimensional flow concerning singular separation.

5. CONCLUSIONS

A detailed study was carried out of the three-dimensional flow fields caused by the interaction of oblique shock waves and a planar turbulent boundary layer. The main results are the following:

1. Two flow field models have been constructed based on experimental data for shock generator angles of 4^o and 10^o. The measurements give a complete description of the flow fields.

2. Based on the 10^o flow field data, it is concluded that McCabe's criterion for incipient separation is not sufficient to define flow separation.

3. The interaction region is quasi-two-dimensional in an area at sufficient distance from the shock generator. This means that although all three velocity components play an important role, the fluid variables vary only slowly along the shock direction.

4. The heat transfer rate decreases as the shock is approached in the streamwise direction and increases almost linearly with downstream distance from the shock location.

5. Reynolds analogy is valid as a first approximation to the problem.

6. Boundary layer thicknesses will provide a basis for scaling parameters of the upstream extent as a function of the transverse distance Y.

7. The downstream extent of the interaction in X-direction is at least four times as large as the upstream one.

REFERENCES

1. McCabe, A.: "The Three-Dimensional Interaction of a Shock Wave with a Turbulent Boundary Layer", Aeronautical Quarterly, August 1966, pp. 231-252.

2. Lowrie, B. W.: "Cross Flows Produced by the Interaction of a Swept Shock Wave with a Turbulent Boundary Layer", 1965, Ph.D. Thesis, Univ. of Cambridge.

3. Token, K. H.: "Heat Transfer Due to Shock Wave Turbulent Boundary Layer Interaction on High Speed Weapon Systems", 1974, AFFDL-TR-74-77.

4. Neumann, R. D.: "Recent Notes on Interference Heating", 1972, AFFDL-TR-72-12.

5. Oskam, B., Bogdonoff, S. M. and Vas, I. E., "Study of Three-Dimensional Flow Fields Generated by the Interaction of a Skewed Shock Wave with a Turbulent Boundary Layer", 1975, AFFDL-TR-75-21, to be published.

6. Vas, I. E. and Bogdonoff, S. M.: "A Preliminary Report on the Princeton University High Reynolds Number 8" x 8" Supersonic Tunnel", 1971, Internal Memorandum No. 39, Gas Dynamics Laboratory, Princeton University.

7. Bradshaw, P. and Unsworth, K.: Comment on "Evaluation of Preston Tube Calibration Equations in Supersonic Flow", AIAA Journal, Vol. 12, No. 9, September 1974, p. 1293.

8. Hopkins, E. J., et.al.: "Hypersonic Turbulent Skin-Friction and Boundary Layer Profiles on Nonadiabatic Flat Plates", AIAA Journal, Vol. 10, No. 1, January 1972, p. 40.

9. Lighthill, M. J.: "Laminar Boundary Layers", Ch. II, Oxford University Press, Edited by L. Rosenhead, 1963.

10. Maskel, E. C.: "Flow Separation in Three-Dimensions", 1955, RAE-Rp-Aero-2565.

11. Rogers, E. W. E. and Hall, I. M.: "An Introduction to the Flow About Plane Sweptback Wings at Transonic Speeds", J. Roy. Aero. Soc., Vol. 64, 1960, p. 449.

12. Korkegi, R. H.: "A Simple Correlation for Incipient Turbulent Boundary-Layer Separation Due to a Skewed Shock Wave", AIAA Journal, Vol. 11, No. 11, November 1973, p. 1578.

13. Hopkins, E. J. and Inouye, M.: "An Evaluation of Theories for Predicting Turbulent Skin Friction and Heat Transfer on Flat Plates at Supersonic and Hypersonic Mach Numbers", AIAA Journal, Vol. 9, No. 6, June 1971.

ACKNOWLEDGEMENT

This research was supported by the Air Force Flight Dynamics Laboratory, Wright-Patterson Air Force Base, Contract Number F33615-73-C-3133.

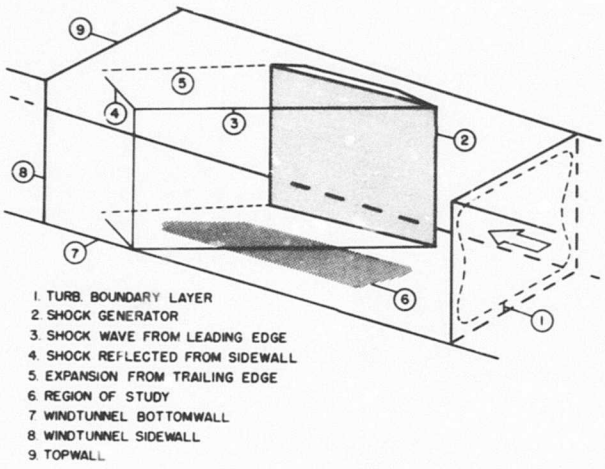

Fig. 1: Schematic of Experimental Configuration

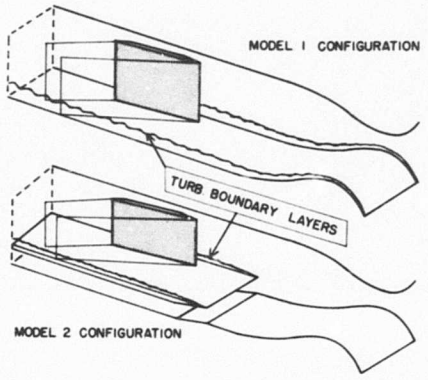

Fig. 2: Model 1 and 2 Configurations

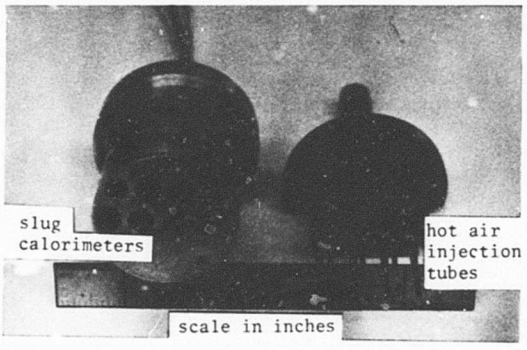

Fig. 3: Heat Transfer Plug

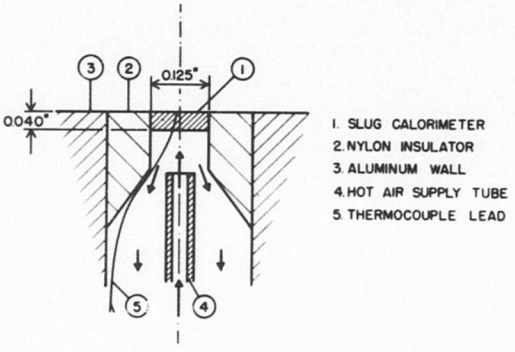

Fig. 4: Slug Calorimeter Arrangement

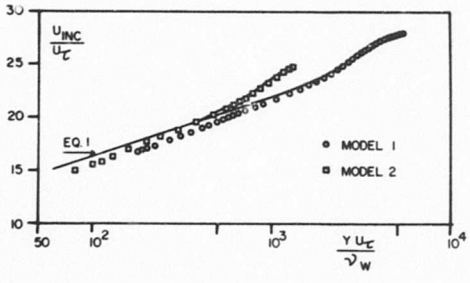

Fig. 5: Transformed Velocity Profiles

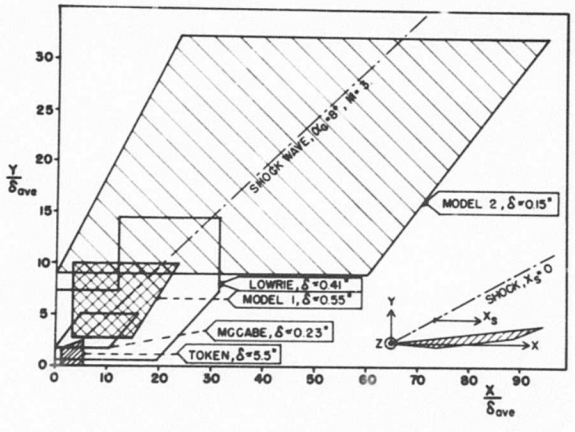

Fig. 6: Regions of Study and Coordinate System

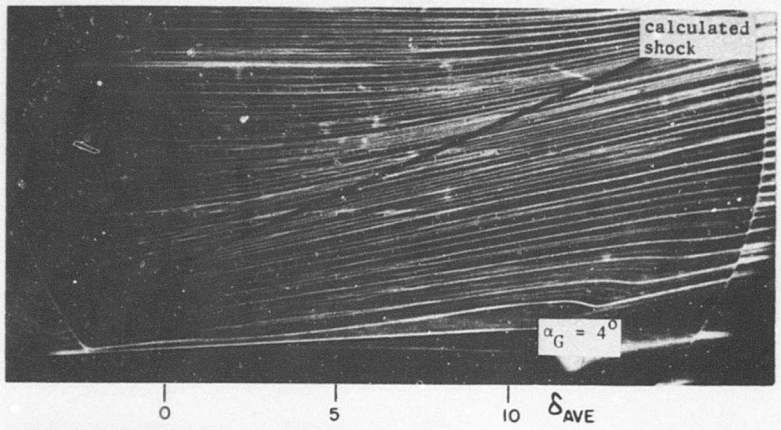

Fig. 7: Photograph of Oil Flow Pattern, $\alpha_G = 4^o$, Model 1

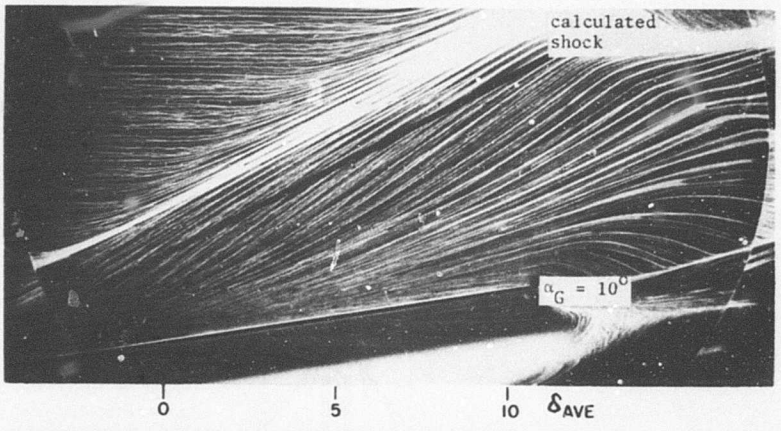

Fig. 8: Photograph of Oil Flow Pattern, $\alpha_G = 10^o$, Model 1

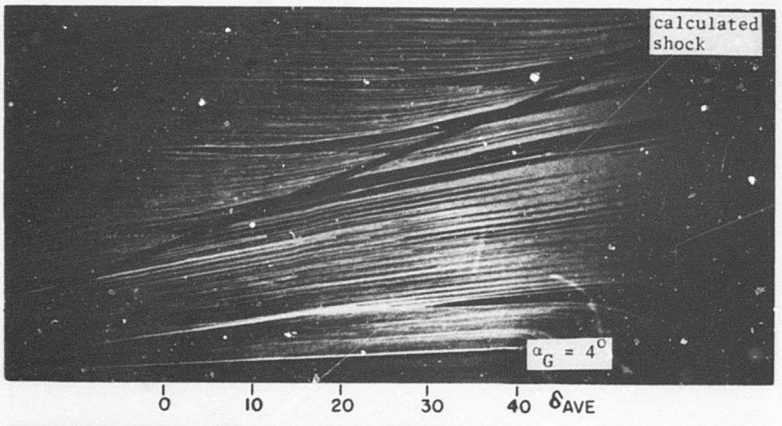

Fig. 9: Photograph of Oil Flow Pattern, $\alpha_G = 4^o$, Model 2

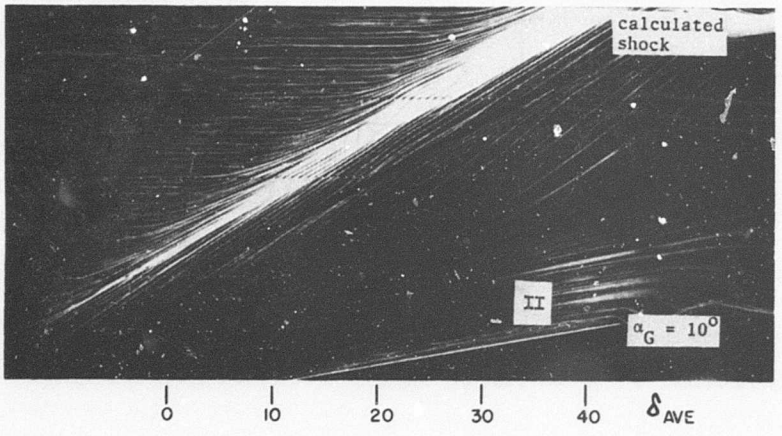

Fig. 10: Photograph of Oil Flow Pattern, $\alpha_G = 10^o$, Model 2

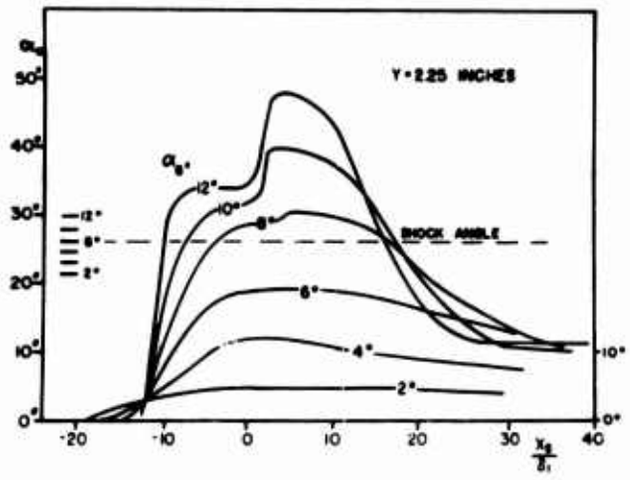

Fig. 11: Oil Line Angles, Y = 2.25 inches, Model 2

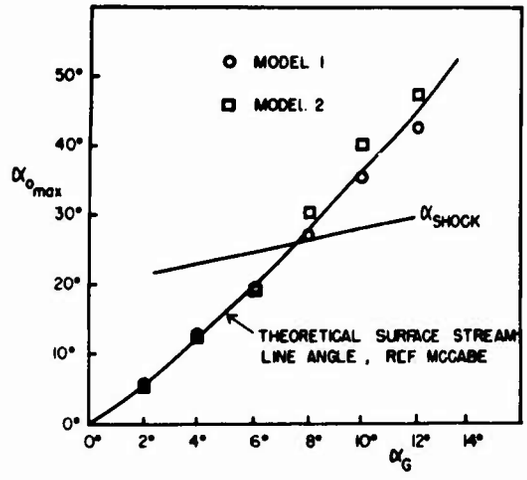

Fig. 12: Comparison with McCabe's Secondary Flow Theory

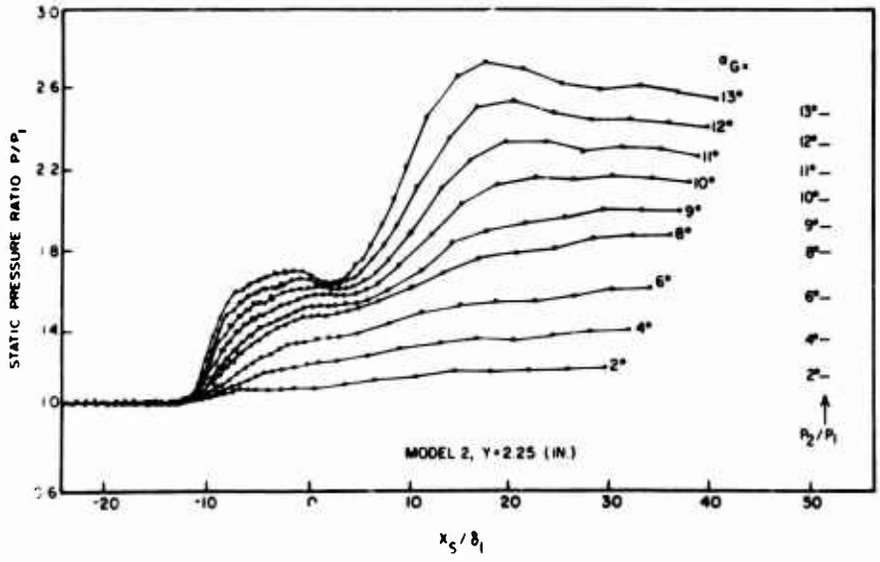

Fig. 13: Static Pressure Distributions, Y = 2.25 inches, Model 2

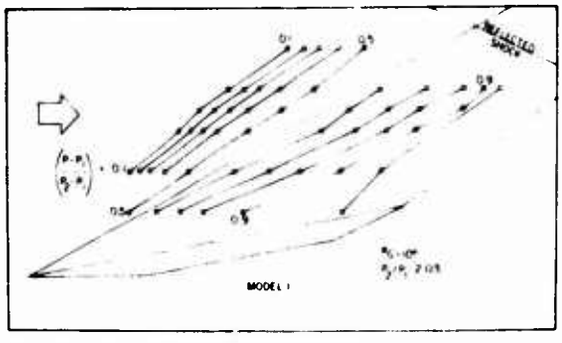

Fig. 14: Surface Isobar Pattern, $\alpha_G = 10^0$, Model 1

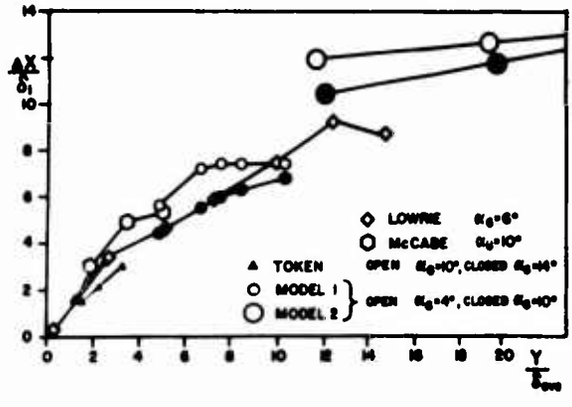

Fig. 15: Upstream Extent of Interaction Region

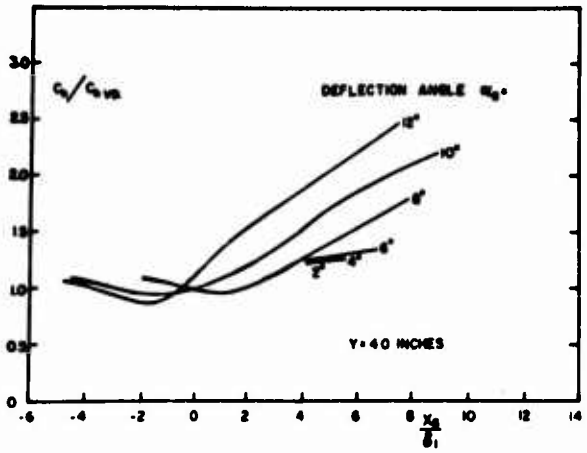

Fig. 16: Heat Transfer, Y = 4.0 inches, Model 1

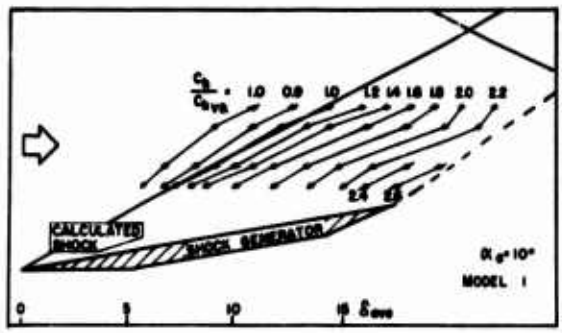

Fig. 17: Heat Transfer Pattern, $\alpha_G = 10^o$, Model 1

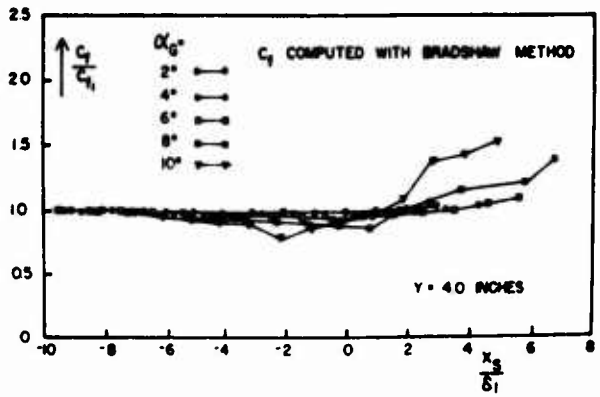

Fig. 18: Skin Friction, Y = 4.0 inches, Model 1

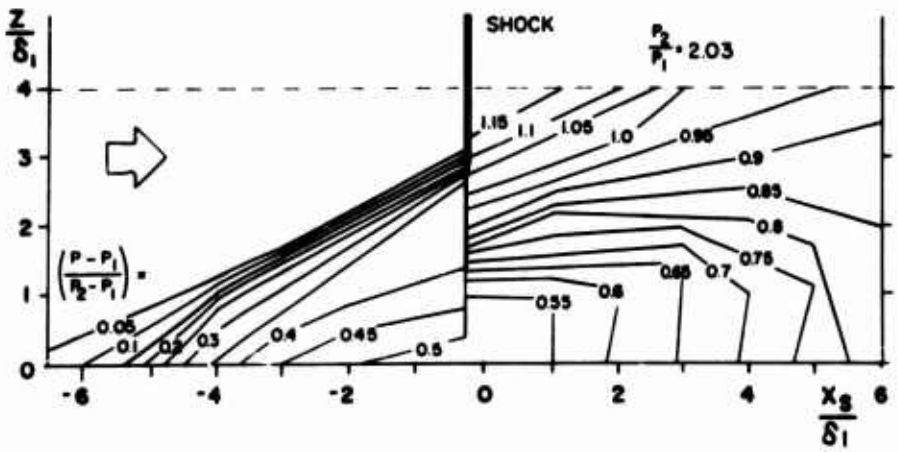

Fig. 19: Static Pressure Contour Plot in XZ-Plane, Y = 4.0 inches, $\alpha_G = 10^o$, Model 1

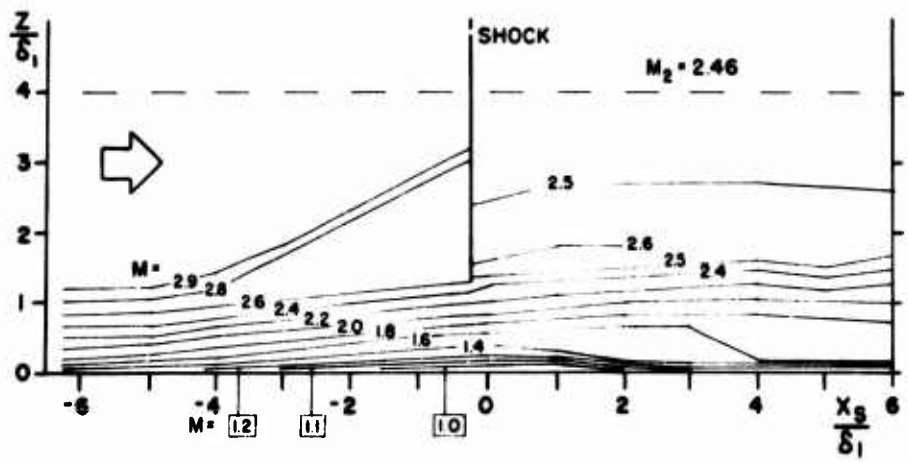

Fig. 20: Mach Number Contour Plot in XZ-Plane, Y = 4.0 inches $\alpha_G = 10^o$, Model 1

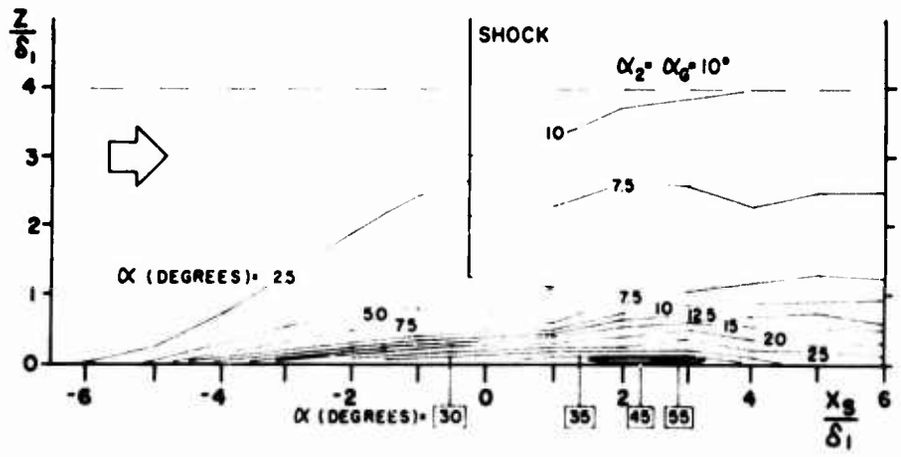

Fig. 21: Yaw Angle Contour Plot in XZ-Plane, Y = 4.0 inches, $\alpha_G = 10^o$, Model 1

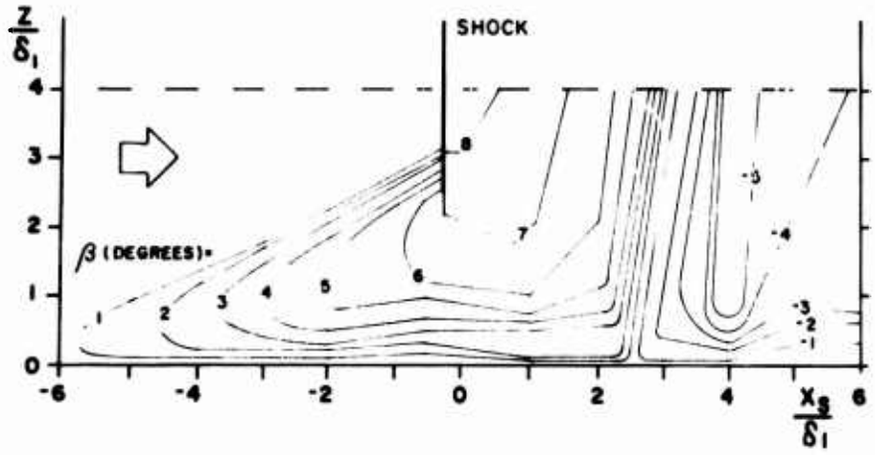

Fig. 22: Pitch Angle Contour Plot in XZ-Plane, Y = 4.0 inches, $\alpha_G = 10^o$, Model 1

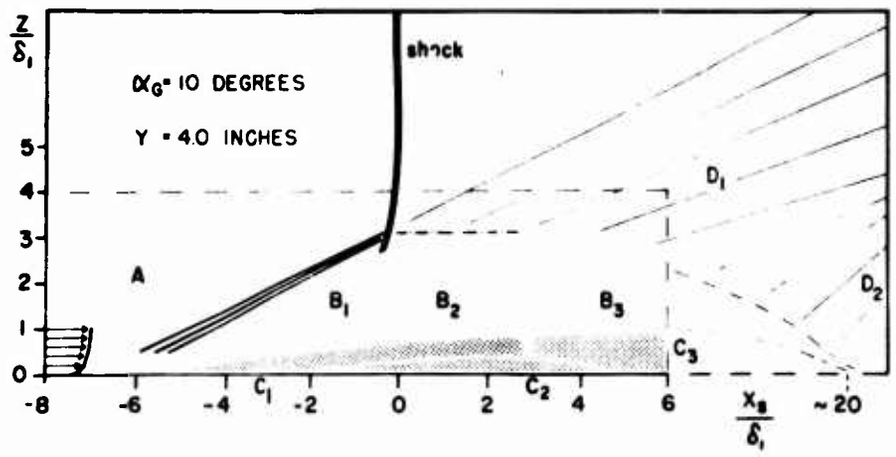

Fig. 23: Flow Model in XZ-Plane, $\alpha_G = 10^o$

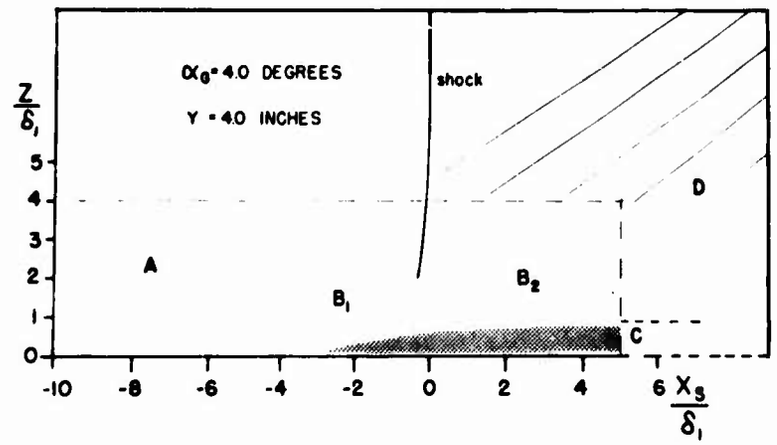

Fig. 24: Flow Model in XZ-Plane $\alpha_G = 4^o$

COMMENT ON PAPER 41

by

J.H.B.Smith
Royal Aircraft Establishment
Farnborough, Hants, UK

The Authors raise the question of whether or not the flow resulting from the interaction between the shock waves and the boundary layer is to be regarded as separated, and conclude that for $\alpha_G = 10°$ it is not, even for model 2. A conceptually useful criterion for deciding whether separation has taken place is provided by considering the limit of infinite Reynolds number. If the size of the disturbed region vanishes in this limit, the flow is attached: if the disturbed region remains of finite extent, the flow is separated. The Authors' analysis suggests that the extent of the interaction region measured parallel to the wall scales with the boundary layer thickness, as shown in Figure 15, and this is consistent with an attached flow. However no results are presented to indicate how the extent of the interaction region measured normal to the wall differs between models 1 and 2. It would help to resolve the question if adequate data could be obtained on the extent of the interaction region measured normal to the wall on model 2.

In my view, it is easier to interpret the oil-flow (Fig.10) and the static pressure distribution (Fig.13) on the basis that a shear layer separates ahead of the calculated shock position and rolls up into a vortex just downstream of the calculated shock; while further downstream an attachment line gives rise to fresh boundary layers, one flowing towards the calculated shock and the other parallel to the shock generator.

THE MANY FACETS OF 3D TRANSONIC SHOCK-INDUCED SEPARATION

H. Yoshihara
Engineering Staff Specialist
General Dynamics Convair Division
Mail Zone 620-02, P.O. Box 80847
San Diego, California 92138 USA

and

D. Zonars
Chief Scientist
USAF Flight Dynamics Laboratory (CA)
Wright-Patterson Air Force Base
Ohio 45433 USA

SUMMARY

Pressure distributions obtained in wind tunnel tests on several wing-fuselage configurations at high subsonic Mach numbers are used to illustrate several shock-induced separation scenarios that are essentially 3D in nature. Pearcey's Type B interactions, distinguished by prior history effects, appear in several different forms. The described results in general are characteristic primarily of aft-cambered airfoils.

1. INTRODUCTION

Shock-induced separation frequently plays the key role, not only in the cruise performance of aircraft, but in the maneuver performance when buffet limits the maneuver envelope.

The detailed nature of the many aspects of shock-induced separation in the planar case has been thoroughly investigated and clearly explained by the well-known early efforts of Pearcey of NPL, whose recent absence from transonic research has been a great loss. In the case of swept wings the efforts of Hall and Rogers of NPL and RAE, Küchemann of RAE, and Haines of ARA have set the stage for much of our present understanding of the complexities added by the third dimension.

In the present presentation we shall review some 3D features of shock-induced separation that were recently observed in wind tunnel tests on wing-fuselage configurations at high subsonic Mach numbers. The configurations were all high wing types having wing sweeps $\sim 25^{\circ}$ or 45° and aspect ratio of ~ 5. The wings incorporated an aft-cambered airfoil, and the results to be described are in large part peculiar to this type of airfoil. The wings were further twisted with a twist typically suggested by subcritical theory.

Introductory to the 3D results, we shall first present several relevant planar examples of shock-induced separation which will set the stage for the 3D cases and will serve in part to accentuate the 3D effects.

2. PLANAR EXAMPLES

In the present section we shall first present experimental pressure distributions for the planar airfoil case characterizing the flow in the mid-semispan region of the 25° wing-fuselage configurations. The concept of the Type B interaction due to Pearcey will then be reviewed, followed by a planar example having a counterpart occurring in one of the 3D examples.

2.1 PRESSURE DISTRIBUTIONS FOR AIRFOIL I

Tests on Airfoil I (10% thickness ratio) were carried out earlier in the NAE (Ottawa) 2D high Reynolds number wind tunnel (Ref. 1). The pressure distributions at $M_\infty \sim 0.76$ at various values of α are shown in Fig. 1. Here the value of $M_\infty \sim 0.76$ and the 10% thickness ratio correspond approximately to the values normal to the 25° sweep in the 3D case (Configuration A) to be discussed. The test Reynolds number was 30×10^6 inch chord.

The results of Fig. 1 show that even at the lowest α of 1° (below drag divergence) there is a shock-induced separation present on the upper surface (though of limited extent) which has reduced the pressure rise across the shock relative to the inviscid (normal shock) value shown by the dashed line. The reduced shock pressure rise here is caused by the modification of the normal shock at the surface in the inviscid case to a strong oblique shock as a result of the wedge-nosed viscous ramp effect that now appears aft of the shock due to the displacement effects of the shock-induced separation. The presence of the viscous ramp will alter the effective shape of the airfoil and will cause an upstream displacement of the shock relative to the inviscid flow location.

Clearly as the incidence is increased, the shock wave is strengthened, the interaction with the boundary layer worsened leading to an expanding viscous ramp, finally culminating in an increasing upstream shock displacement relative to the inviscid location. By this deteriorating shock-induced separation the orderly monotonic rearward movement of the shock with increasing incidence in the inviscid case is "decelerated" such that at a given state of the worsening interaction the rearward shock displacement is halted and then reversed to an upstream direction. Buffet onset

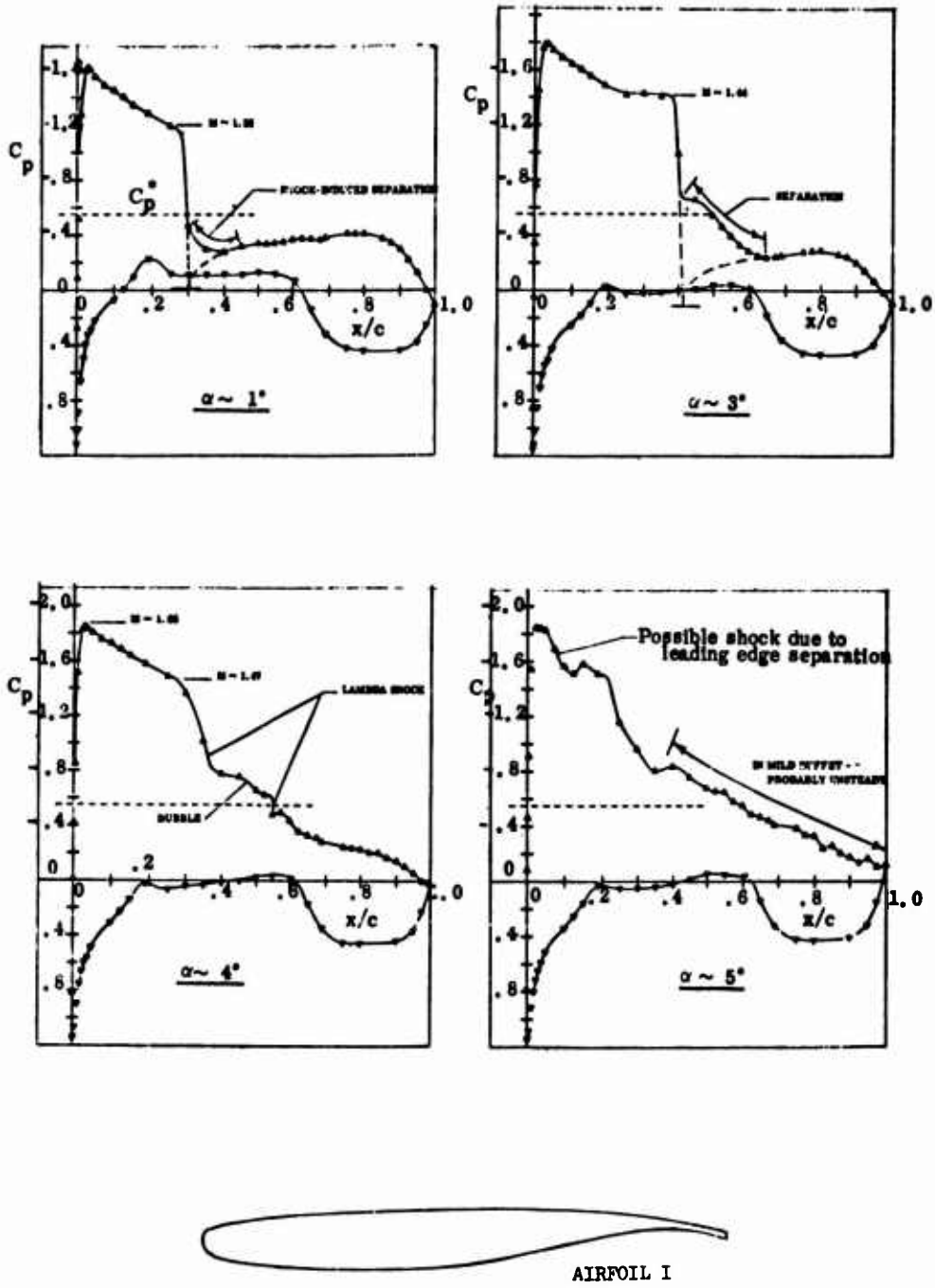

AIRFOIL I

Figure 1. Pressure Distributions on Airfoil I Obtained in the NAE 2D High Reynolds Wind Tunnel at M_∞ = 0.76 and Re. No. = 30 x 10^6/15 inch Chord.

appears to be closely related to the reversal stage of the shock movement.

For aft-cambered airfoils it is further seen in Fig. 1 that an abrupt adverse (subcritical) pressure gradient arises along the midchord region of the lower surface causing a separation further downstream. The effect of this separation is to reduce the aft overpressures by an order of $\Delta C_p \sim 0.15$ as determined by calculations.

In the case of aft-cambered airfoils there is further a more "global" effect of the aft separations affecting both the upper and lower surfaces - namely, that of reducing the plateau underpressures on the upper surface and the plateau overpressures on the lower surface by the resulting reduction of the effective aft camber. We shall see later that this effect will have a serious consequence in the 3D case.

2.2 A TYPE B INTERACTION

It is well known that the "well being" of a boundary layer to resist separation when encountering an adverse pressure gradient is measured by the "fullness" of the velocity profile. Thus when a boundary layer has suffered a loss of fullness in its prior history and then encounters an abrupt adverse gradient before it has fully recovered, it will be clearly less immune to separation. It is this situation Pearcey (Ref. 2) has labeled a Type B interaction.

In the classic experiments of Seddon (Ref. 3) where the interaction of a near-normal shock with the turbulent boundary layer along a flat plate was examined, one can see the qualitative nature of the degradation of the turbulent fullness by the shock-induced separation and its subsequent recovery. Thus in Fig. 2 we show the velocity profiles in the recovery zone measured by Seddon. Though the rate of recovery is most probably distorted by the influence of the wind tunnel sidewall boundary layers, one can see nevertheless how badly the profile fullness is degraded by the separation even after the boundary layer has reattached. Here the measure of the degree of "Type B ness" in a given case would be dependent upon the ratio (> 1) of the profile recovery length to the distance to the nearest downstream adverse pressure gradient of significance.

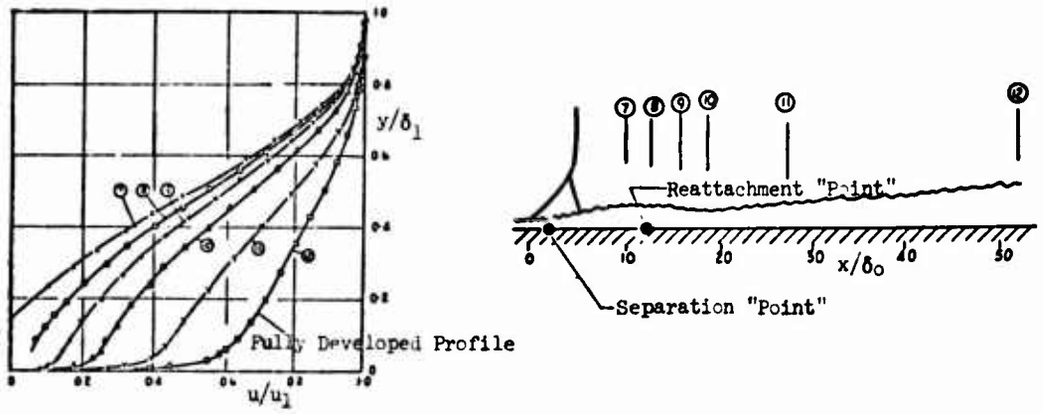

Figure 2. Velocity Profiles in the Recovery Zone Measured by Seddon.

In Fig. 3 we now show an interesting case for Airfoil I in buffet at the extreme conditions of $M_\infty = 0.90$ and $\alpha = 4^\circ$ at a Reynolds number of 3.1×10^6/6 inch chord where a Type B separation is triggered on the lower surface by a shock-induced separation on the upper surface.

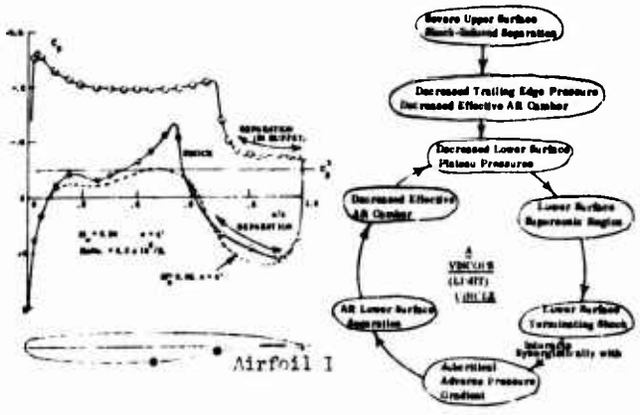

Figure 3.
A Feed-Back Type B Separation Phenomenon for Aft-Cambered Airfoils.

To delineate the chain of events leading to the above phenomenon let us start from a flow below buffet onset and increase M_∞ to the value of 0.9 of Fig. 3 keeping a fixed incidence of 4^o. An immediate change occurring is the strengthening of the upper surface shock and the consequent severe separation of the boundary layer. The C_p distribution over the lower surface during these initial moments will most probably remain unchanged as suggested by its observed invariance with M_∞ in steady state tests where severe aft separation is absent. (This initial invariant distribution (for $M_\infty = 0.85$; $\alpha = 4^o$) is shown by the dashed line in Fig. 3.)

With the severe aft upper surface separation the effective aft camber will be decreased, and the consequence of this will now propagate to reduce the lower surface plateau overpressures. This then will lead to low supersonic Mach numbers arising upstream of the pronounced convexity on the lower surface (between the circles • of Fig. 3) along which the flow will now expand further to higher Mach numbers. The resulting supersonic region will then be terminated by a lower surface shock; and this shock acting in conjunction with the "subcritical" adverse gradient already present will worsen the aft lower surface separation in an exaggerated Type B interaction. The worsened aft lower surface separation will now reduce further the effective aft camber triggering the chain of events shown in Fig. 3.

At the same time there is the countering effect that the decrease of the effective aft camber will also decrease the upper surface plateau Mach numbers tending to decrease the strength of the upper surface shock that initially triggered the described sequence of events.

In summary we have seen in Fig. 3 an example where an upper surface phenomenon has triggered the generation of a severe Type B interaction on the lower surface through the far reaching effects of the aft camber.

3. SOME 3D SHOCK-INDUCED SEPARATIONS

In wing-fuselage flows we encounter examples of shock-induced separations which are both quasi-planar in nature (as might occur in the wing mid-semispan region) and those which are essentially 3D in nature having no counterpart in planar flows. The latter arise simply because of the 3D nature of the shock configuration causing the separation and the 3D behavior of the boundary layer itself, particularly those which are badly separated. We shall give some examples of both types of interactions in the present section.

3.1 EXAMPLE I (25^o SWEEP) - TYPE B INTERACTION

In wing-fuselage configurations the shock pattern is complicated by the inviscid spanwise propagation effects. To illustrate the nature of this distortion of the shock configuration let us consider Configuration A at $M_\infty = 0.9$ at $\alpha = 3^o$. This configuration has a high wing with a quarter chord sweep of 25^o and incorporates the Airfoil I described earlier. The fuselage has an essentially rectangular cross-section.

The resulting shock pattern on the wing surface is shown in Fig. 4. On the upper surface it is seen that a forward shock has now appeared which may be attributed to the presence of the relatively low suctions over the glove region and on the upper surface of the fuselage. The effects of the latter have propagated laterally across the span along the Mach lines (bicharacteristics) to cause the forward shock.

The corresponding chordwise (streamwise) pressure distributions at selected spanwise stations are next shown in Fig. 5. Here the C_p is defined in terms of the free stream "dynamic" pressure, and $C_p^*(25^o)$ is the value corresponding to the local velocity whose component normal to the 25^o sweepline is sonic.

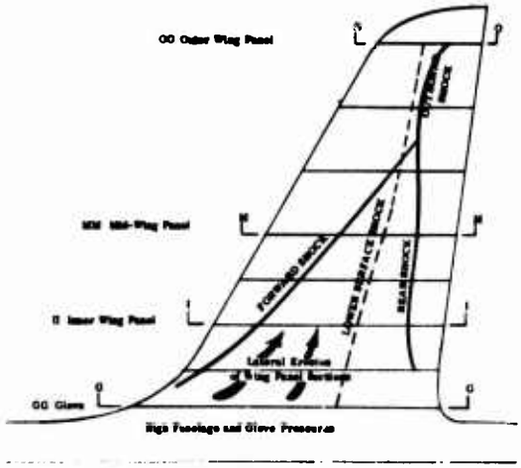

Figure 4. Shock Pattern for Configuration A at M_∞ = 0.90, $\alpha \sim 3^o$, and Re. No. $\sim 4 \times 10^6$/mean chord.

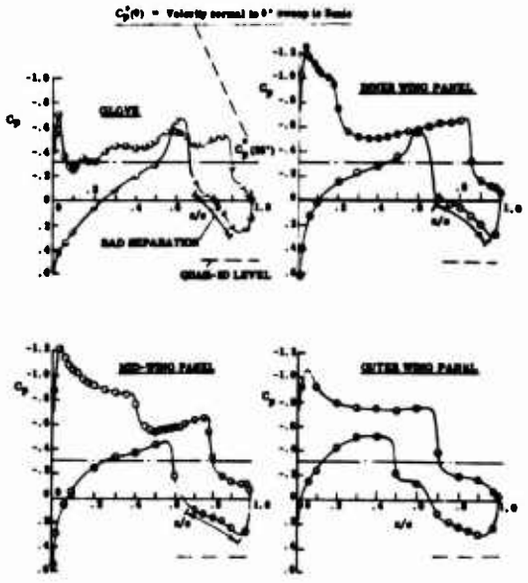

Figure 5. Corresponding Chordwise Pressure Distributions.

A comparison of the distributions of Fig. 5 with the planar distributions of Fig. 1 will give a qualitative picture of the 3D effects though the correspondence is somewhat clouded by the unknown induced incidence in the 3D case. Unquestionably the appearance of the foward shock has weakened and displaced rearward the primary terminating shock wave of the 2D case even in the mid-wing panel region.

The more interesting phenomenon of Figs. 4 and 5 is however the appearance of the lower surface shock. The appearance of such a shock is not triggered by severe upper surface separation as in the planar case of Fig. 3, but by the 3D inviscid lateral propagation effects from the uncontoured side surface of the fuselage. Here expansion waves are generated which propagate outboard onto the sensitive "throat" region of the lower surface creating the lower surface supersonic region and the terminating shock wave. The latter has been again unfortunately positioned in an undesirable juxtaposition with the abrupt subcritical adverse pressure gradient due to the aft camber causing a Type B worsening of the aft lower surface separation. The result of this separation destroys much of the aft overpressures that make aft cambering attractive. (The corresponding inviscid overpressure level being indicated by the dashed line in Fig. 5.) Finally the resulting reduction of the effective aft camber in turn feeds back to abet in the "strengthening" of the supersonic region as in Fig. 3.

3.2 EXAMPLE II (25° SWEEP) - AN ANOMOLOUS TRAILING EDGE PRESSURE DIVERGENCE

In the results for the second wing-fuselage configuration (Configuration B) many of the same features on the upper surface were exhibited. Configuration B also had a wing with a quarter chord sweep of $\sim 25^{\circ}$ mounted as a high wing on a fuselage of near-rectangular cross-section, but with a significantly larger glove. The airfoil section was similar to that of Configuration A.

An interesting phenomenon was found in the case of Configuration B at $M_\infty = 0.90$ relating to the behavior of the trailing edge pressure which sometimes is used (perhaps inadvisedly in the 3D case) to detect the onset of buffet. In Fig. 6 we have plotted the trailing edge pressure at the spanwise station $\eta = 0.75$ at both $M_\infty = 0.90$ and 0.80 at various values of α. (The Reynolds number here was approximately 7×10^6/mean chord). The behavior of the trailing edge pressure at $M_\infty = 0.80$ is the usual variation that one is accustomed to, but at $M_\infty = 0.90$ a premature humping has taken place at lower incidences. To determine the cause of the premature divergence we have plotted in Fig. 7 the pressure distributions at $\alpha = 0^{\circ}$ and 6° where higher trailing edge pressures prevail, and $\alpha = 4^{\circ}$ where a much lower "separated" pressure prevails.

An explanation of the above behavior of the trailing edge pressures can be seen in Fig. 8 where the flow patterns for the three incidences have been sketched based upon the surface pressures. Here the greatly depressed trailing edge pressure at $\alpha = 4^{\circ}$ appears to be caused by the simultaneous presence of significant shock-induced separations on both the upper and lower surfaces, both most probably of Type B, which are not both simultaneously present at $\alpha = 0^{\circ}$ and 6°.

At $\alpha = 0^{\circ}$ severe shock-induced separation is present only on the lower surface, while at 6° it is present only on the upper surface as a Type B interaction.

At $M_\infty = 0.8$ neither shock wave nor severe separation appears on the lower surface in the above incidence range.

3.3 EXAMPLE III (45° SWEEP) - A CASE WITH SEVERE SPANWISE CONTAMINATION

Finally we consider a wing-fuselage configuration where the high wing has a sweep of $\sim 45^{\circ}$. The airfoil section is aft cambered. In Fig. 9 we show the shock traces on the wing surface at $M_\infty = 0.95$ and $\alpha \sim 9^{\circ}$, while in Fig. 10 we give the corresponding chordwise pressure distributions at several span stations. (The Reynolds number was approximately 4×10^6/mean chord.)

For this high sweep case we see the consequences of the lateral contamination that arises on both the upper and lower surfaces of the wing due to the sweep effect. On the upper surface it is seen that the separated air formed in the inboard regions has been transported down the "sweep lines" contaminating and worsening the shock-induced separation further outboard. At the span station $\eta = 0.75$ the degree of contamination is indicated by the large extent of the separation bubble relative to the mild strength of the forward shock which has a Mach number normal to the shock of approximately 1.2. Further, in the outboard region the forward shock, which in an inviscid case would be configured topologically as in Fig. 3, has been displaced significantly upstream in the outer half of the wing, eliminating the outboard shock.

If we examine the lower surface pressure distributions in Fig. 10, we see that a comparable spanwise flow of the inboard separated air formed aft of the subcritical adverse gradient has occurred greatly increasing the dead air displacement effects in the outboard regions. The consequences have resulted in a near-halving of the aft overpressures at the span station $\eta = 0.9$ relative to those at $\eta = 0.3$.

4. CONCLUDING REMARKS

The several examples described herein suggest the wide variety of forms shock-induced separations can assume in the 3D case. The nature of such separations is of course dependent not only upon the 3D shock wave configuration itself, but upon prior history effects in the boundary layer effected through the weakening of the velocity profile by previous events (Type B), or by the spanwise contamination effects as by the spanwise flow of the separated air seen in Example III.

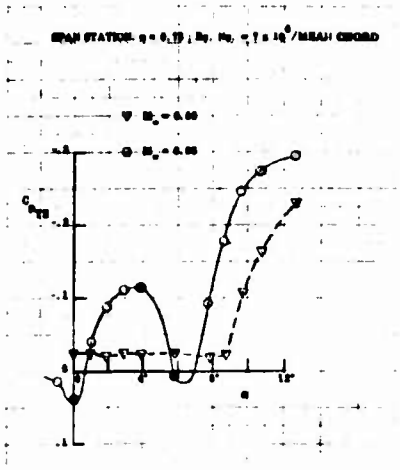

Figure 6. Trailing Edge Pressure Variation with α at Span Station $\eta = 0.75$ for Configuration B (25°) Sweep).

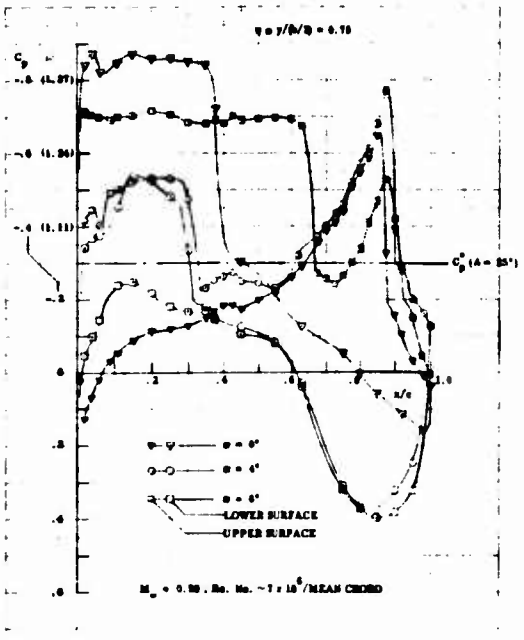

Figure 7. Chordwise Pressure Distributions for Various α at $\eta = 0.75$ for Configuration B (25° Sweep).

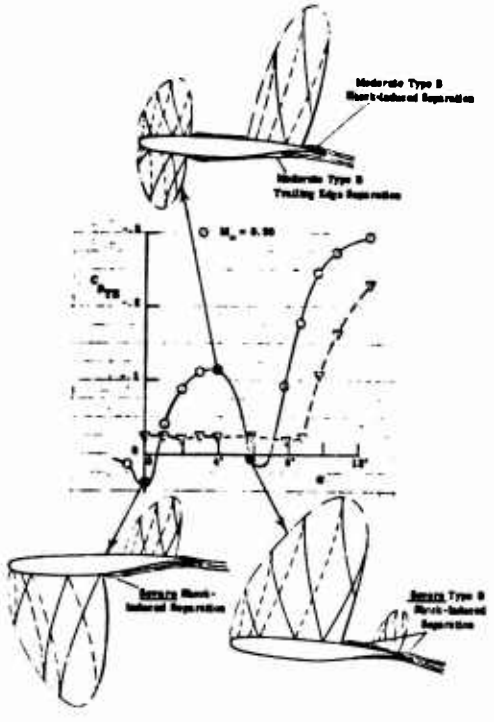

Figure 8. Suggested Associated Flow Patterns.

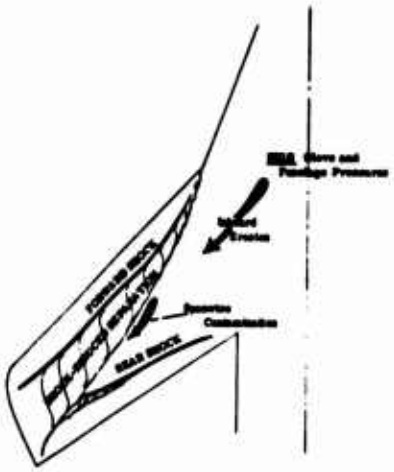

Figure 9. Shock and Separation Pattern at 45° Sweep, $M_\infty = 0.95$ and $\alpha = 9°$.

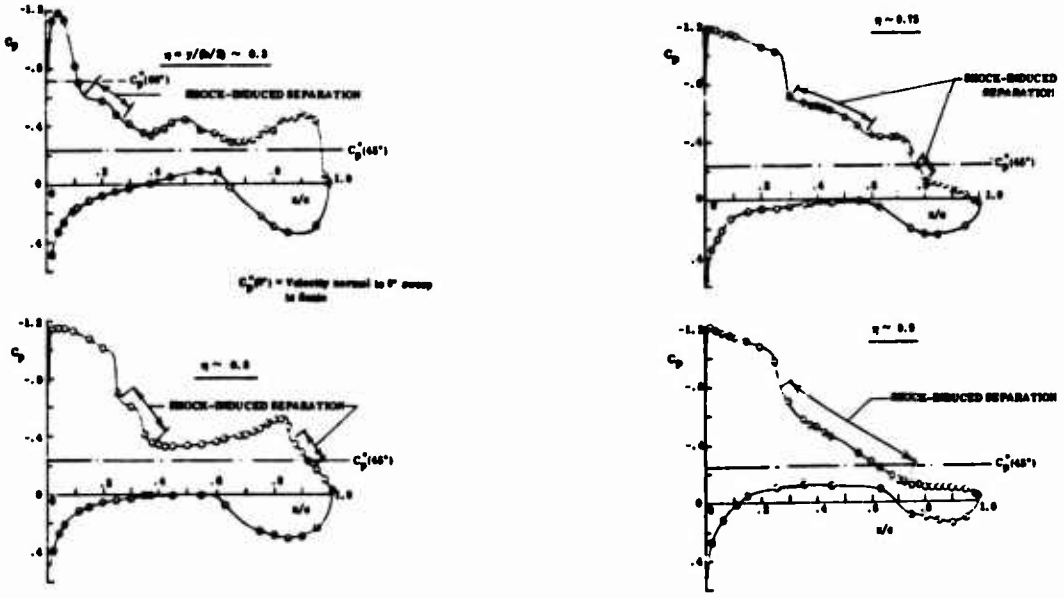

Figure 10. Pressure Distributions at Various Span Stations for $M_\infty = 0.95$, $\alpha = 9°$ and 45° Sweep.

In the highly sensitive arena of transonic flow the interactions as described between the inviscid and viscid flows continue to behave in the strong interaction mode.

The examples presented here mostly represent extreme cases. They have been presented to illustrate flow mechanisms that undoubtedly occur less spectacularly under design conditions. A fuller physical understanding of the many facets of shock-induced separation will enable one to diagnose more accurately wind tunnel results and to provide meaningful configuration improvements to prevent the appearance of the more severe forms of 3D shock-induced separations envolving type B interactions or spanwise contaminations.

5. REFERENCES

1. Peake, D., Yoshihara, H., etc., Transonic Lift Augmentation of Two-Dimensional Supercritical Aerofoils by means of Aft Camber, Slot Blowing, and Jet Flaps in High Reynolds Number Flow, presented at the meeting of the Ninth International Council of the Aeronautical Sciences at Haifa, Israel, 25-30 August 1974.

2. Pearcey, H., Haines, B., and Osborne, J., The Interaction Between Local Effects at the Shock and Rear Separation, AGARD CP No. 35, 1968.

3. Seddon, J., The Flow Produced by Interaction of a Turbulent Boundary Layer with a Normal Shock Wave of Strength Sufficient to cause Separation, R&M No. 3502, British ARC, 1960.

AN ADDED NOTE - Prospects for an Early Prediction Method

Boundary layers of practical concern are turbulent. As such we must not forget that we are confronted with an unsteady phenomenon. Thus, for example, at a separation "point" (which in fact may be a zone) reversed flow at the surface need not exist continually but only during a statistically dominant fraction of the time. In cases of well-behaved unseparated turbulent boundary layers, the "scale" of the unsteadiness is of sufficiently higher order than the characteristic scale of the (macroscopic) flow, that viable (time averaged) steady models of the turbulent transport could be postulated and definitized empirically in terms of a few parameters.

For the more complex cases envolving the milder forms of separation, for example, the low speed type rear separations on an airfoil, the above phenomenological procedure so far has been dismally inconsistent. The causes may be several fold - either the above time-averaging has been strained, or more likely the turbulent transport has been inadequately defined in terms of the proper macroscopic flow variables or their gradients. Undoubtedly such mundane matters as the quality of the tunnel air flow or that of the experimentors, or the fact that a "2D" separation may in fact be 3D also participate to muddle the situation.

In the present case of shock-induced separations there is little question that the usual coarse-graining comes a cropper since the characteristic scale of the turbulent transport clearly is no longer of higher order than the relevant macroscopic scale of the flow which in the present case is measured by the "thickness" of the shock pressure rise. It is this absence of local equilibrium of the turbulent transport that complicates the present situation. Indeed if we take the liberty of borrowing a concept from non-equilibrium chemically reacting flows, the concept of "frozen" turbulent transport might permit us to bridge the precipitous shock, if indeed such a concept is meaningful, but then a suitable non-equilibrium turbulent transport model must still be developed for the smoother relaxing recovery zone downstream of the shock.

Needless to say the prospects of acquiring a viable empirical non-equilibrium turbulent transport model within the meaningful future is bleak.

The applied aerodynamicist, at this stage, should be content with a procedure that will yield the pressure distribution in a real flow. Thus he need concern himself only with the displacement effects of the boundary layer. Thus as a near-term expedient it is suggested that the immediate effort be directed towards developing a model for the viscous ramping.

Such an approach was investigated in a preliminary fashion in the planar case. Here in a finite difference calculation empirical pressures were prescribed along the airfoil surface (downstream of severe adverse gradients) where significant viscous displacement effects are expected, while elsewhere the airfoil slopes were prescribed. The results of the calculation would then yield the effective shape of the airfoil (and hence the viscous ramping) that would directly yield the real pressure distribution including the correct shock location. In the above example the viscous ramp aft of the shock was found to be composed of a wedge nose section (conforming to the oblique shock pressure rise) followed by a section having the same curvature as the airfoil itself, with a final thickened displacement layer starting just upstream of the trailing edge. By carrying out a sequence of such calculations a viscous ramp model could itself be phenomenologically formulated, or on a more sophisticated level empirically-fitted "equilibrium" functions in the Head-Green procedure could be determined using the knowlege of the displacement thickness distributions. (Here the Head-Green procedure is an integral method embodying a non-equilibrium transport mechanism analogous to that suggested by Bradshaw.) The above procedure would require the static pressures to be reasonably invariant across the boundary layer, as was found by Seddon's measurements. The conditions directly below the shock impingement point are of course unknown, so that here the oblique shock relations via the shock polar must be assumed to be applicable. The suggested phenomenological modeling of the viscous ramp is primarily intended for Type A shock-induced separations that are quasi-2D in nature. The contemplation of extending the modeling to Type B interactions or to 3D separations with spanwise contamination as described earlier is indeed frightening, but on the other hand a proper configuration design would strive to avoid such occurences at least at the primary operating conditions, clearly making such extensions less urgent.

ROUND TABLE DISCUSSION

Professor Gersten: Ladies and Gentlemen, We will start the Round Table Discussion on Flow Separation. I would rather like to call it a general discussion instead of a Round Table Discussion because I have the feeling that we all should participate in a general discussion about the subject we were talking about this week. The procedure I have in mind is the following: to start our general discussion I asked a few experts to give their point of view about the outcome of the meeting so far. The idea is that we have first the summaries about the meeting and perhaps some thoughts about the future outlook and then we will start the general discussion. We will have all the brief reports from the experts first and afterwards the general discussion. If you agree on this procedure I have the great pleasure to introduce to you the experts here at the table: Professor Inger, US, who will give his views about the Laminar Separation Session; Professor Young, UK, will give his thoughts about Turbulent Two-Dimensional Separation; Mr Smith, UK, who gave already an excellent survey paper about the subject he is responsible for which is Three-Dimensional Turbulent Separation. Last but not least, I asked Professor Bogdonoff, US, to give a particular report on all the experimental difficulties in measuring at or close to separation or in a separation region. We should start by asking Professor Inger to give his views about laminar separation.

Professor Inger: I'd like to break my comments down into two major categories; one, analytical studies and two, numerical methods. Also interspersed will be a few side comments about experimental considerations.

First, let me summarize what we heard in the field of analytical work. In my view a major aspect of this conference was the emergence of matched asymptotic (or "multiple-deck") methods as a very potent new approach to understanding viscous-inviscid interaction and separation phenomena. This outgrowth of the ground- work of Stewartson and Messiter would seem to be the logical next step up from Prandtl's orginal boundary layer concept as an asymptotic approximation, and hence particularly appropriate to the conference theme laid down by Professor Schlichting in his opening Prandtl Memorial Lecture. In addition, these asymptotic treatments emphasize the ideas of proper scaling and order of magnitude analysis, both of which again originated with Prandtl.

I feel the asymptotic approach also provides some very important in-sights. First it exposes much of the underline physics and the "fine grain structure" of the flow. Secondly, it delineates the basic scaling of both the independent and the dependent variables and thus should prove very useful in guiding numerical studies of these type of problems. In fact we have seen some such usage occurring already. Thirdly, we learn how to deal with and eliminate local singularity phenomena, in particular the classical (and physically-unrealistic) separation point singularity can be very neatly disposed of by asymptotic analysis when viscous-inviscid interaction is taken into account. Finally, it is capable with some additional work of extension to turbulent flows as well as laminar and we can see the beginnings of this already.

Now let me make some critical comments on analytical studies. As Professor Schlichting reminded us in his opening lecture, theory must ultimately lead to predictions of experimentally verified facts and should be useful to engineers. In my view the laminar multiple-deck analyses are weak in this regard; there is need for some good basic lowspeed laminar flow experiments specifically designed to prove out these theories. The conference was notable for its lack of this type of experimentation (of course this can be done at high Mach numbers but then the several compressibility and dP/dy effects severely complicate the issue). A weakness of the theory which should be improved upon is that it tends to be rather esoteric and very limited as to the geometrical situations and the values of the basic parameters to which it is applicable (e.g., Reynolds numbers of 10^9 or larger). Burggraf's paper tended to suggest that asymptotic methods might in fact be used to suggest some approximate analytical approaches of a "layered" type that can yield engineering analysis tools valid over a much more practical range of flow conditions and configurations. For example, although perhaps not commonly appreciated, the very successful method of Stratford (which was referred to repeatedly at this conference) is in fact precisely such a method; if you re-read his original paper you will see that it is based on such a layered approach. I think we can go a lot further in this direction.

Now let me turn to some brief remarks on what we heard about numerical solutions. First, it has been firmly established that *provided* viscous-inviscid interaction is taken into account, the boundary layer equations provide accurate engineering solutions for flows including separation bubbles (for details on a very fine scale, Navier-Stokes terms must be included, but such detail is to my knowledge outside the realm of experimental detection). Over a very wide range of practical conditions for moderate Mach numbers, we may also neglect the lateral pressure gradient; however at high Mach numbers in regions of separation or reattachment we likely should include dP/dy to get a good prediction of the flow, but we can still do this with a boundary layer type of model if it includes the inviscid y-momentum equation. In cases where there are highly curved bodies we also may have to include either longitudinal or transverse curvature terms, but with these additions we can probably handle most of the configurations of practical

interest. Secondly, I personally was pleased to see that it has finally become generally accepted that the mathematical "singularity" at separation is eliminated by the inclusion of viscous-inviscid interaction (as Professor Schlichting mentioned, it sometimes takes a long time for an idea to catch on: the original paper by Catherall and Mangler which really demonstrated this elimination was published in 1966!). Incidentally, I think our colleagues in the unsteady boundary layer business should address this point more actively.

Another conclusion I draw is that there now seem to be some pretty good finite difference programs which can treat separation bubble-type problems and which will be cost-effective and superior to integral methods in being more flexible, more extendable to turbulent flow, and free from spurious super sub-critical jumps and saddle point singularities that are creatures of many integral methods. However, it appears that the success of many schemes *still* is very sensitive to the choice of suitable variables and coordinate systems for the particular problem and hence to the cleverness of the investigator. Moreover, it is not clear why some investigators seem to be doing very well indeed at very high Reynolds numbers even with Navier-Stokes problems where others experience severe problems in stability and so forth. Perhaps like experimental work we ought to start running each others computer programs to find out just what the realities are, how sensitive they are to the investigators doing the program, etc. Finally, it is worth stressing that the purely numerical approach works well only for problems which are already reasonably well understood. For new problem areas with new phenomenon in the foreseeable future, quite a bit of analysis and experiment will always be required before numerical analysis is either feasible or desirable.

Professor Gersten: Thank you very much for your very interesting comments. As I said before, I would like to proceed immediately to the next report by Professor Young on two-dimensional turbulent boundary-layer separation.

Professor Young: Thank you Mr Chairman. I must say that some of the points that Professor Inger made about problems of laminar separation could equally well be made with regard to turbulent boundary layer separation.

I recall that in Mr Smith's paper he pointed out that we study separation: (a) to understand it, and (b) to control it. Perhaps we should keep those objectives very much in mind in reviewing what has been discussed during the course of this meeting. If we ask ourselves what sort of problems we can solve we see that at least in the two-dimensional case they are the weak interaction problems where the boundary layer has a relatively small effect on the external flow. If therefore we consider problems in which the actual pressure distribution is given then it seems to me that we have adequate methods of calculation for determining the position of separation. Which method we care to choose is almost a matter of taste, there are both good integral and good differential methods available. However, in most cases we are dealing with situations where we do not know the final pressure distribution and the problem in general is a strong interaction one where the separation induces a large change in the external flow and consequently the external flow reacts back on the boundary layer in a way that cannot readily be predicted at the outset. It is for such problems that one notes relatively little by way of information or work that was reported at this meeting. Perhaps there is not really very much going on, it is a difficult area but I hope that it will be an area to which people will turn their attention increasingly, because in most practical situations involving separation the interaction is a strong one. One has only to think of problems of wing stalling or of the shock stall both in two and three dimensions. We need to be better supplied with experimental information as well as theoretical methods if we are to deal with those situations with any confidence.

Between the problem of the attached boundary layer and that of the fully separated boundary layer we have the small bubble situation of the kind which was envisaged in many of the papers on shock boundary layer interaction with reattachment of the boundary layer after a small region of separation. Here it seems that we are developing quite a number of methods involving variants of the boundary layer equations coupled with the external flow, variants of what some people referred to as the Navier-Stokes equations but in which the way in which the turbulence was modelled was perhaps the weakest feature. It seems to me that perhaps this problem of turbulence modelling is where we should direct much further research in the future. One is aware from experimental data that, for example, the entrainment in a turbulent boundary layer that is attached to the surface can be very different from the entrainment when it is separated, or indeed when it is reattaching. Generally when it is reattaching the turbulence level is extremely high and the entrainment rate is very high. These sort of changes in the structure of the turbulent boundary layer are not as far as I can see very readily reflected in those models which have so far been used and this seems to me a major area for further work both experimental and theoretical. We have seen (though with perhaps a degree of hind sight on the part of the people concerned) that by fiddling various constants and introducing lag terms etc. a degree of agreement between theory and experiment has been obtained which for many engineering purposes may be very acceptable. However, one hopes that some of the methods of which we heard will in fact be proven for cases other than those on which they have been based and therefore shown to be satisfactory in a general way.

The question has been raised by Dr Simpson of the possible importance of normal stresses in regions approaching separation and I agree that this needs further attention.

To sum up the overall picture, we seem to be dealing with the weak interaction case fairly effectively but there is a good deal more work to be done in modelling turbulence in shear layers and we are only just on the fringe of dealing with the more general problem of strong interaction.

I have also listed what I thought were some of the detailed problems that were thrown up during the course of our discussions on which we need more work, There is the question of static pressure variations across the boundary layer in regions of separation. I think that it was Professor Liepmann who said he thought that with the development of the laser anemometer we shall no longer have to worry about static pressure variations. I find myself less optimistic on that matter. It seems to me that we are interested in the static pressure distribution in its own right quite apart from getting our velocity profiles correct.

It also seems to me that the transonic problem in two and three dimensions is one that we do not really understand as well as we should not only because of the complexity of the shockwave patterns that can develop, as we heard about this morning, but because we are very unclear about the nature of the interaction between boundary layers and shocks and its dependance on the oncoming boundary layer. Indeed the whole of the argument that is currently going on as to how large a wind tunnel you need for this sort of work turns on the fact that we do not know whether by increase of Reynolds number the resulting decrease in thickness and change of profile of the boundary layer approaching the region of interaction can result in major changes in the final interaction pattern or not. It seems from the evidence in the highest Reynolds wind tunnels that we have that the changes with Reynolds number can still be quite large. Perhaps here is where some of the theories if they were adequately developed could be very helpful. I would like to see someone attempting fairly detailed parametric studies changing the oncoming boundary layer, particularly its thickness and its profile, and investigating the nature of the resulting interaction assuming that we can devise a theory which people will accept for the interaction itself. There was one paper which made a start in this direction, it seems to me that this is a field of work that could well be encouraged.

I was interested to see that there were two papers on trying to control separation. This is again an area which did not receive very much attention in the course of this meeting – perhaps it might be one that will turn up more strongly in a future meeting, I hope not at the 200th anniversary of Prandtl but before then! I believe that this is an area of experimental work that could well produce some very valuable dividends for the practising engineer in due course.

The question of steadiness of separated flows was touched on during the course of the meeting. The general question of unsteady aerodynamics is a major one, worthy of another symposium, but it cannot be ignored in the context of separation. Separation is a rather unsteady phenomenon and we need to examine more closely than we have in the past the nature of the unsteadiness; it is probably of low frequency in general and as such might be amenable to analysis.

Finally, a perennial plea that we perhaps ought not to rely too much on using the biggest and fastest computers that there are around, they are extremely costly. One gets the impression that people who have access to them tend to forget their basic initial cost or the cost of large program development but sometime or other the bill will have to be paid. I think that there is an increasing need to develop methods of calculation which are relatively quick and cheap for most engineering purposes. The very expensive program can be used for test cases of the cheaper methods but cannot remove the need for such methods. I think that covers all the points I want to make.

Professor Gersten: Thank you very much, Professor Young, for this excellent survey. We would like to go on with the report by Mr Smith.

Mr Smith: Thank you Professor Gersten. I wish that I could present as clear and tidy a picture as my predecessors have. I get the impression that in the three-dimensional field each paper we had practically stood by itself and as far as summarizing it goes I could do very little more than repeat the survey lecture that I gave you to start with. However I have been told not to do this but to be brief and a little provocative. I take it that means not wasting my time saying how much I enjoyed the meeting but I should like to say that I think it has been great fun and to thank whoever is responsible for the invitation.

Most of the things that I find I want to say are comments on what was missing,and, if I might, I should like to go straight outside the area I am supposed to talk about and come back to the triple deck solutions. What was missing for me was an assessment of the work of Sychev (Mekh. Zhid. Gaza, 3, pp.47-49, 1972), so, for the sake of getting something on the record, I should like to say just a few words about this, and if one of the experts in this field cares to demolish what I say I should be only too delighted. The mathematics I take it are quite correct and I don't wish to dispute the relevance of asymptotic series. However I had the impression that Sychev said rather more than this and the first thing that I thought he said was that two dimensional laminar separation is always provoked by a steep adverse pressure gradient immediately upstream of the separation point. And the second thing that I thought he said was that the position of the separation on the bluff body is close, that is, close in the asymptotic sense, to the point at which a constant pressure streamline can leave the body without a curvature singularity. In other words the location of separation on a bluff body is determined by an inviscid mechanism. Now, I don't believe either of those two things. I think that his results are valuable, as Professor Inger was saying, in that they give a local description of what is happening; but I don't think they give the sort of overall information which I understand that he claims.

Now the other thing that was missing, I thought, from the program, and this is not the fault of the participants but the fault of the planners, is the thing that Professor Young was referring to: the absence of unsteady separation from our considerations. As we know, many of the separations that are of practical interest and importance to aircraft designers are essentially unsteady separations, buffeting, helicopters, stall, there are dozens of problems. We know also that Professor Sears and his students have done something to add to our understanding of how unsteady separation takes place, at least in two dimensional flows, and I should have liked to explore these ideas and to see how much solid ground there is in this rather difficult area. Also like Professor Young, I was disappointed that so many papers concentrated on small scale separations, to the extent that we actually spent some time discussing who could see the smallest one! My own suspicion is that if a separation can be modelled by boundary layer theory then it is likely to be unimportant.

If I could try to draw together these two aspects of two-dimensional separated flow, the need to understand the unsteady flow and the need to model the larger scale flows, I should like to suggest that attempts to treat large scale separations as time dependent flows could well lead to an increase in our understanding. This ties in with the question of what we should use our big computers for, apart from developing engineering calculation methods. We should use them for numerical experiments because numerical experiments well carried out can lead to an increase in our understanding of the physical world. I should like to see numerical experiments trying to model large scale separations through an unsteady, essentially inviscid approach. If you don't have a big computer, you might try writing down the equations and boundary conditions that ought to be satisfied, because I don't think this has really been done either. Well, I hope that has been provocative at any rate.

The overall impression I get from the papers is not particularly cheerful: most people seem to be managing to keep their heads above the waves, but not very much more than this. I thought that there were two hopeful signs, though. One was the advent of laser anemometry as described to us by Professor Simpson. The other one was the continuing possibility of acquiring relevant and helpful information from relatively simple experiments as demonstrated by Professor Young. I thought his paper was a first class example of this, where in a fairly simple set up one could discover a flaw in what I regard as the best boundary-layer method we have, that of Bradshaw.

As far as the papers on three dimensional flows, which I am supposed to be talking about, are concerned I found the experimental ones most stimulating, particularly of course the flow visualization. These gave us all an enormous amount to think about. The results which Dr McCroskey presented on behalf of Sedney and Kitchens were really very beautiful and nicely supplemented by the results he was able to include from the German experiments and by the picture which Dr Sutton showed us. Now I was very surprised by the pictures of spirals originating from free stagnation points, because I always tend to think in terms of inviscid flows, and these did not look at all like vortex sheets embedded in irrotational inviscid flows. Are they in fact just phenomena of inviscid shear flows? In other words, if we accept that the flow is rotational but still inviscid, would we find the same curious separation pattern, with free stagnation points out in the flow? There are very few shear flow solutions for flows past obstacles and I think this is an area of considerable interest: at one extreme it interests the environmental aerodynamicists with their flows around buildings and at the other extreme it interests people who put probes in boundary layers and find unexpected large upstream influences. The topic of oblique shock-wave interactions is one which I missed out from my summary lecture. It is something which is only recently being taken up again and there was little to say about it then. There is clearly rather more to say about it now and I hope that we can perhaps talk about it a bit giving Professor Bogdonoff a chance.

Professor Gersten: Thank you very much, Mr Smith. I think your brief report was perfect and also provocative as requested. Before we go on I just want to mention the fact that we had the intention to have a session on unsteady separation and actually I approached Professor Sears to give a survey paper on this subject but unfortunately he was not able to come and do it. Moreover, it turned out that we had not enough papers on this subject to fill up a whole session on unsteady separation. Therefore we had to cancel it for this meeting because we had already enough papers on other subjects. This is the explanation why unsteadiness was perhaps not fully discussed here. Now let's go on with Professor Bogdonoff's remarks.

Professor Bogdonoff: I would like to give a view on this meeting from an obviously prejudiced point of view as an experimentalist. First, I was rather disappointed in the balance of the meeting between looking at things and essentially rubbing them finer as compared to looking at things where we don't even know the gross details. If I had to give a general opinion of the meeting it seems to me that we have put much less emphasis on the possible real value of much of our work by not concentrating more on three dimensional turbulent flows which are what the real world is mostly about.

Now the usual answer for this is that you work with laminar flows and do the easier job first. But it is not at all clear that studying laminar flows in great detail will always give you a great understanding of what is going to happen when it becomes turbulent. There are in many examples complete changes in order of magnitude of the effects when the flow becomes turbulent. I was impressed with the efforts that are going in to the very detailed computational methods and obviously the very powerful tool that the computer is, but I am still apalled as to what they use as the test points to prove that these massive programmes are correct. One assumption is that if you

include the full Navier-Stokes equations then you don't have to worry about it since with a fine enough mesh you come out with the right answer. However, there are still key questions about the detailed computations of the Navier-Stokes equations which have been covered in other conferences.

I think that we, as experimentalists, should try to provide a set of redundant experiments cross checked with Californian air, Princeton air, Canadian air and European air which can provide the real guidelines for the computational techniques. There is now so much being invested in these systems that the necessity is great for having some very well detailed and agreed upon correct experiments to use as the test points. I found very little of this being done in the compressible high speed area analogous to the effort at Stanford a few years ago.

In the other end of the affair I was disappointed in the lack of major activities which utilize new capabilities that clearly are very early in the design stage and perhaps will simply be reflected in time by changes in the kind of experiments. Mr Simpson gave us the only results of this meeting using a laser anemometer. There indeed has been a sort of revolution in experimental techniques in the last few years and hopefully this will be the base for a set of experiments which might provide much more than the usual sort of surface conditions which all of us are used to. I think that much of what we talk about in the way of three-dimensional flows are best described by that group of blind men examining an elephant. Mr Smith drew I think a very good set of remarks about three-dimensional flows but the fact of the matter is that there are many three-dimensional flows for which we do not even understand gross physical phenomena. I would like to simply pick on some of my colleagues who continually talk about vortices due to skewed shocks when I know of detailed experiments which have shown a vortex. I think that there are many of these complex three-dimensional flows which are strong interactions in Professor Young's category that are going to have to be predicted by the computational techniques. Much of what we have in three-dimensional flows in a way is sort of pre-conditioned by the fact that we have worked with two-dimensional flows for so long we have a tendency to skew it, put another parameter in, and draw our physics for that. It may not indeed be a useful technique or method of approach. From the experimental side the two things which I might say look to be most useful in the field that we are in is; one, this business of trying to provide very good models upon which we can base the analytical or computational studies that we are doing, and, the second is a concentration by all sorts of techniques, conventional and new, which are coming through non-intrusive instrumentation. These techniques will provide a model of three-dimensional flows to hopefully form a solid base upon which these massive two-dimensional calculations will be even more massive in three dimensions. They hopefully will provide some reality in what we are trying to compute to get closer to the kind of problems that are real, the kind of problems that Yoshihara talked about, the kind of problems which we face in the design of real fluid mechanical things where three-dimensional turbulent boundary layers are present.

I really think that this should be the driving function for much of our work. It means that the experimentalists and theoreticians will have to work a lot harder, but it seems to me the time has come for real, practical problems to be the main focus of our effort.

Professor Gersten: Thank you very much, Professor Bogdonoff. Now, we should start the general discussion. The subjects of the whole meeting and the brief reports given by the experts are now open for discussion. I would like to suggest that we try to have an order, in other words the laminar problems first and the turbulent ones next, but it is not necessary. The discussion is opened now.

Professor Liepmann: I should like to make a few remarks, not aimed at a specific presentation but concerning turbulent boundary layers, separation, and shock wave boundary layer interaction in general.

First of all it cannot be emphasized enough that separation is *not* a local boundary layer problem but a phenomenon which depends on the flow in the large. Boundary layer theory is, after all, a perturbation procedure to correct a potential flow for the comparatively small viscous effects. For flow past a flat plate, the inviscid potential problem is unique; for bluff bodies, transonic flow with shock waves, etc., the flow in the large and hence the pressure field are themselves dependent on the viscous or turbulent shear, and not given in advance. Consequently, the computation of the point of zero shearing stress on the basis of boundary layer theory, with a given pressure distribution, is not the essential part of the separation problem. Besides the flat plate at zero angle of attack, only in some cases, such as shock wave boundary layer interaction on a plane surface, does one have *a priori* an idea how the global pressure distribution looks and can treat the separation locally. In this respect I regret that comparatively little emphasis in this meeting was directed to ordinary subsonic separation from bluff bodies.

In a problem inherently as complex as separation it is clear that computational methods are very important. However, it seems to me worthwhile to stress two points: Computations of turbulent flow are still empirical and, to a large extent, interpolation procedures to bridge between sets of measurements. Any extension of such computations to cases where no good measurements yet exist is not safe and has to be approached with much caution.

The second point I would like to emphasize is the importance of overall physical and/or analytical ideas to provide some guidance for detailed and/or computational approaches. For example, before extending turbulent shear flow computations to high Mach numbers one should ask the question, does a turbulent boundary or shear layer exist for very large Mach number? The increasing acoustic radiation from turbulent flow with increasing

Mach number will eventually become a significant, and possibly dominant part of the turbulent energy balance. Hence, at sufficiently high Mach number, the turbulence must be modified and possibly this "radiation damping" at high M will shift transition and turbulence to higher and higher Re.

Similarly, the interplay between wave and wake drag is obviously of primary importance in shock wave boundary layer interaction problems. Here too, I miss the use of overall considerations: For example, consider a setup consisting of a wedge and a flat plate in supersonic flow, with the wedge shock impinging on the flat plate. For inviscid flow only the wedge experiences drag. For viscous flow, in the absence of interference the plate has wake drag, the wedge predominantly wave drag. With shock wave boundary layer interaction both the wave and wake resistance are modified. Is the net result an increase or decrease in the overall drag? The example is certainly somewhat academic but the problem of transonic drag due to shock waves and separation is rather similar in concept. It is by no means self-evident that separation *increases* the drag since the change in the effective shape weakens the shock and hence reduces the wave resistance. Indeed, I would expect an even trade off for weak waves in both cases.

Professor Gersten: Thank you, Professor Liepmann. I have a question to ask you about your first remark concerning the definition of separation which in your opinion has nothing to do with boundary layers. I was a little shocked by this remark because there is the problem of bubbles. Do you think bubbles have nothing to do with separation? For example there is this famous work by Maugler and Catherall and their boundary layer calculation, where they get separation and reattachment with a small bubble. Would you call this separation and reattachment or not?

Professor Liepmann: There is certainly a small part of the separation problem which involves local separation bubbles which can be handled with a sort of pseudo-boundary layer theory. The shear layers, the bubble and backflow can be computed in some cases neglecting the normal pressure gradient.

Professor Gertsen: So you would distinguish between a weak and a strong separation? Weak separation takes place within the boundary layer and strong outside the boundary layer.

Professor Liepmann: Yes, I think that one may distinguish between local separation and break-away. The former is more an exercise for the reader and the latter a real deep problem.

Mr Bore: I was very relieved to find in the last lecture that someone referred to an aeroplane: with wings! Dr Yoshihara referred to the case of swept shock waves where the boundary layer may cease moving in a direction normal to the shock wave, but nevertheless on a real wing the low-momentum flow can move spanwise parallel with the shock wave intersection. This is an interesting point that we come across quite frequently, of course, on wings.

I would like to register three thoughts. First (I think this one is worth a lot of money!), the spanwise movement of low momentum boundary layer along a shock wave can be interrupted deliberately, for example by a chordwise vortex from a leading edge fence or vortex generators. I have not heard any comments on this practically very important matter here. Secondly, on wings, aircraft designers are not much worried about separation bubbles of small extent. What we are worried about is not incipient or microscopic separation bubbles: we are worried by a boundary layer *failing to reattach before the trailing edge*. *Third point*: From a practical point of view the study of control of separation (or should I say perhaps arranging that the boundary layer reattaches before the trailing edge) by chordwise vortices should be very worth while. Maybe turbulent flow itself could be regarded as flow with a large number of vortices milling around, so to study closely the effect of one vortex (or a simple array of vortices) on the boundary layer could be very revealing as well as practically useful.

Dr Korkegi: I would like to make a comment on some of the differences between two-dimensional separation and separation due to skewed or glancing shocks which I don't think came out too clearly in the meeting and is extremely important. Specifically, turbulent boundary layers are much more prone to separate due to a skewed or glancing shock interaction than due to a two-dimensional interaction. I realize several of us are aware of this, but I don't believe it was really brought out to any extent in this meeting. It is extremely important from a practical stand point for supersonic flows in rectangular inlets or flows at the junctions of wings and bodies, control surfaces and wings, etc. In fact, just recently I had published a short note on a correlation for the prediction of incipient, three D turbulent flow separation which is ridiculously simple. It was based on an analysis of McCabe's published a few years ago and I noticed it was referenced in some of the papers presented this past week. Just to give you a result very simply, it states that the pressure rise beyond which a turbulent boundary layer will separate due to a skewed shock interaction is something like 1.5 (I believe that was mentioned this morning by Dr Peake) independent of Mach number, Reynolds number, or what have you. It has been borne out by recent experiments over a Mach number range of 2 to 6. Anyhow what is important is the order of magnitude. In other words a pressure rise greater than 1.5 due to a skewed shock is likely to cause turbulent boundary layer separation. If we now look at

the two-dimensional turbulent separation case we find that the pressure rise beyond which the turbulent boundary layer will separate is very large and increases with increasing Mach number. While I don't have specific numbers in mind I believe it is something like 10 for a Mach number of 4 or 5. Therefore, in rectangular ducts and similar type configurations we really don't have to worry about the two-dimensional separation problem but rather, the three-dimensional one. It's the one that occurs on the wall adjacent to the compression surface and can give rise to non-uniform conditions, loss of total head, etc., in rectangular inlets of airbreathing engines and other similar configurations. I felt it was needed to bring this out as I don't think it was really touched on to any great extent in this symposium.

Professor Bogdonoff: Well there is a basic area of disagreement but it points out that I think is a very key thing here. The work referred to by Dr Korkegi puts on the same plot something called three-dimensional separation and two-dimensional separation and it is my own strong feeling that you are comparing apples and oranges. Three-dimensional separation is completely different then two-dimensional separation, the results of three dimensional separation end up to be a completely different kind of flow phenomena. Two-dimensional separation with its reverse flow, a mixing mechanism and a dissipative mechanism is completely different from the so called three-dimensional separation. To refer to the paper presented by Mr Oskam, something called three-dimensional separation has been defined on surface flow conditions which at least as far as I am concerned has little to do with the dissipative mechanism and the kinds of losses which are usually associated with things called separation. I think there is a major difficulty in trying to compare words which we use in the same way. We keep using this word separation in three dimension as compared to two-dimension and I think this is one of my basic points that I tried to make; that is, carrying over from two-dimension to three-dimension phenomena which are quite different, and using the same words I think causes some problems.

Dr Korkegi: I do not agree with Prof. Bogdonoff. I accept that there is a difference between three-dimensional separation and two-dimensional separation; however, when one looks at the physics of the phenomena one can see certain elements of similarity. Clearly in two-dimensional separation one has reverse flow rather than a structure of vortices. However, whenever one has a sufficiently strong interaction of a shock that is skewed to a boundary layer one is going to have vortices produced and scavenging of the flow by these vortices. I don't think we want to have a hang up about the interpretation of what we mean by separation and reattachment in two-dimensional flow and three-dimensional flow. Classically we are used to thinking of separation and reattachment as being associated with the shear stress going to zero at the wall. But that is only an interpretation that is valid for two-dimensional flow. I think we can still, as Mr Smith and others have talked about, refer to the term separation in the three-dimensional case. Otherwise we are getting into an exercise in semantics. In rather simple terms, I view separation as a line along which the flow lifts off a surface regardless of what the shear is, and reattachment (or attachment . . .), one along which the flow impinges on the surface regardless what the shear is. If we keep that physical concept and don't get hung up on the classical interpretation we will develop a better understanding of what goes on. I disagree furthermore that one cannot draw some relationship between certain types (let me be cautious here) of three-dimensional "separation" and two-dimensional "separation". In fact I simply view many regions of three-dimensional boundary layer separation – or, rather, their projection in a plane normal to the lines of interaction – as similar to two-dimensional separation with cross-flow and mass transfer. All I am trying to point out is that one can draw some analogies without necessarily being too naive. With reference to my earlier comment, whether or not one wishes to refer to the phenomenon as "separation", it is nevertheless an experimentally verified fact that a turbulent boundary layer will separate much earlier due to its interaction with a skewed shock than with a two-dimensional one and, therefore, it is the former interaction which is of practical concern in supersonic inlets. I think I have said enough and probably I have used more time than Professor Bogdonoff did.

Professor Rom: I would like to make a comment about the weak and strong interactions, It should be noted that the multilayer method can treat only relatively weak interactions which are characterized by having a "slender" viscous interaction region. That is, the viscous thickness is small relative to the length of the interaction region. In this case the multilayer methods, which are based on extensions of the boundary layer concepts are applicable and give useful results. However, in cases of strong interactions, that is when the viscous thickness is large, the use of the boundary layer concepts breaks down. In my opinion, this is the realistic problem to which Prof. Liepmann referred when he spoke about the "real" separation regions obtained in flows over bluff bodies.

The difference between weak and strong interactions is clearly demonstrated when one uses the Reynolds number based on a single parameter, to correlate also results obtained for flows with strong interaction. It is my suggestion, that, in the case of strong interactions, one has to include an additional scaling length. In such a flow the viscous thickness is determined by an interaction parameter in addition to the Reynolds number which is determined by the free stream conditions and a characteristic length. This result can be demonstrated by evaluating the scaling laws appropriate to the Navier-Stokes equations for large Reynolds numbers. In this case two independent length parameters can be defined, one in the external inviscid region and another in the viscous region. The scaling relations are then obtained by defining the compatability relations for strong interaction on the boundary between these regions. The emergence of the requirement for this additional length parameter is well illustrated in the

investigation presented in this Symposium by Professor Burggraf. It is shown in Burggraf's analysis that in the case of low supersonic flow over a shallow ramp the multilayer method describes quite well the experimental data. However, for steep ramps there is a large difference between the multilayer theory prediction and the experimentally measured pressure distributions. It is found that in order to correlate the data the ramp angle must be included. This can be taken as an example of possible difficulties in using the boundary layer scaling to correlate results obtained in cases of strong interaction.

Professor Gersten: I have a question to you about this point of view. Think of the simple incompressible two dimensional flow around a circular cylinder. What do you think is the second parameter to describe the separated flow for high Reynolds numbers? The Reynolds number is one parameter. What is your suggestion for the second parameter in such a flow?

Professor Rom: In the case of the cylinder flow, there is the wake width which is dependent on the position of separation. As you well know, there are still difficulties in calculating this position, and correlating the available experimental data.

Professor Gersten: But take the Navier-Stokes equations, there is one parameter in the Navier-Stokes equations, namely the Reynolds number. Where is the other parameter? Where does this second parameter come into the picture? I don't see where it comes in.

Professor Rom: Well this is a very good point. However, numerical solutions of the Navier-Stokes equations for high Reynolds number flows over solid boundaries (i.e. cases which are treated in the limiting cases by the boundary layer theories) require use of different length scales for the grid mesh. A very fine mesh for the viscous region and a relatively coarse mesh in the external flow.

Professor Gersten: So you are saying that the Navier-Stokes equations are not sufficient to describe the flow problem?

Professor Rom: No, the Navier-Stokes equations are sufficient, to the best of our knowledge. But, their solution, in the case of high Reynolds number flows, introduce different characteristic length scales*, one in the region of large gradients ("viscous" zones) and another in the essentially inviscid external flow.

Professor Gersten: Perhaps its a mathematical problem, not a physical one.

Professor Rom: The physics of the problem are well brought out in the presently discussed solutions of the Navier-Stokes equations. However, one must be careful not to distort the mathematical model of the physical flow when approximations are introduced.

Professor Gersten: Could we perhaps interrupt for a moment and ask Professor Inger about his views on this particular problem. Professor Inger, are you prepared to give a comment on this particular point, that the Reynolds number is not sufficient and that a second parameter is necessary.

Professor Inger: I concur with your view, Professor Gersten.

Professor Gersten: Good. I felt that Sychev's work was perhaps not appreciated enough here. I found that Mr Smith was perhaps a little bit hard on him, at least from my point of view. Professor Inger, what do you think about Sychev's work as a basis for this particular problem?

Professor Inger: I feel that Sychev has used the asymptotic approach well to delineate the basic flow structure in the high Reynolds number limit. However, an even better expert would be Professor Messiter who has dealt with Sychev's work in great detail; if he is here I would like to hear his views. (Professor Messiter was not present.)

---

* Note added in proof: These characteristics "lengths" are analogous to the characteristics "time" scales, which are defined in the numerical solution of the time dependent Navier-Stokes equations. This was pointed out later in the discussion by Professor Ghia.

Professor Liepmann: The idea underlying the work of Sychev, was well as the earlier contribution of Roshko, are in my opinion similar in spirit to that of the Kutta condition. I.e., it is attempted to arrive at a specific potential flow problem through the use of some overall knowledge of the vortex wake.

Mr Smith: Sorry Professor Liepmann but I did not understand from what you said precisely which side of the argument you have come down on. At first I thought you were agreeing with me that it was a local solution, and then towards the end of your remarks I thought you said it was a way, like the Kutta condition, of determining the overall flow field from an essentially inviscid argument. Now are you saying that you believe in the deduction of the overall flow field from the inviscid argument?

Professor Liepmann: Yes I think I do - how shall I put it - It is not an argument which is derived fully but which I believe takes into account a certain global behaviour of the flow, and from it arrives at a local condition. In this sense I consider it similar to the Kutta condition.

Professor Gersten: There must be an asymptotic solution of the Navier-Stokes equations for very high Reynolds numbers for a circular cylinder which must be, except for certain thin local layers, essentially a global inviscid flow solution, because the Reynolds number goes to infinity.

Professor Liepmann: I *believe* that the solutions of the Navier-Stokes equations are unique. However, the potential solutions are not. For large Re *one* of these potential flows will be close to *the* Navier-Stokes solution. Furthermore, the solutions to the Navier-Stokes equations must be very sensitive to the initial conditions (to make the existence of turbulence understandable). For numerical schemes this sensitivity may pose a problem.

Dr Peake: I think that my remarks are addressed more, perhaps to Professor Bogdonoff than to the other Panel members, for I would challenge the statement that we know little about three-dimensional flow fields in general. There has been a large amount of work done particularly by the RAE and ONERA during the last twenty years, which is well documented, and which is not read nor referenced as often as it should be; perhaps I may also be allowed a "plug" for some of the investigations (mainly experimental) that we have done at NAE in Canada.

Secondly, much of the discussion about incipient separation is, perhaps, academic, for in the practical design case, we want to avoid a catastrophic situation produced by the separated flow. In some instances, flow conditions past incipient separation may well be tolerable and the flow field still usable.

Thirdly, to illustrate, for example, the type of large-scale (vortical) separated flow fields from shock induced separations, I would refer to Professor Rainbird's work on right-circular cones to Mach 4.25, where the external flow field measurements above the leeside of the cone, show clearly the large-scale rolled-up shear layers.

Professor Newman: I want to make three points. The first relating to Smith's question about whether rotation and an inviscid solution would give the flow pattern shown. This is a point which is well made and should be investigated. We should also remind ourselves that this type of study has gone on in great detail for turbo machinery and, in particular, I think in the work of Hallock and Hawthorne it's a very well developed subject. The second point I want to make is based on Liepmann's comment about turbulent solutions being interpolations between measurements, it is a perfectly correct observation I think. The problem that we have, and nobody on the Panel has brought it up, is that we do not know how to predict the Reynolds shear stress which Reynolds left us ($\bar{\rho}\, u'v'$) . The primitive attempts to do this by Prandtl, Von Kármán and G.O.Taylor who tried to relate this to the local field are obviously wrong, and Townsend did us a great service in focusing attention on the turbulent energy equation. Unfortunately, I think at the present time the relationship between the theoreticians in this area, or the numerical modeller, and the people who make the measurements, is far from happy. On the part of the people who make measurements, they are tending to make higher and higher order correlation measurements with and without time delays, or to study the present structures in flows such as jets and wakes. The people who are modelling the Reynold stresses are doing so almost without any help from the experimentor. In particular, there is a very great need to measure the local fluctuating pressure in order to be able to correlate it with the local fluctuating velocity and velocity gradient, and I mean now of course the fluctuating velocity. So if anybody has any bright idea as to how to measure local fluctuating pressure, this would be very valuable. In fact I would like to finish my remarks by opening up a real Pandora's box in suggesting to you that perhaps Reynolds misled us right at the very start in time averaging the Navier-Stokes equations. There probably is a much more appropriate way of handling turbulent flow with another sort of averaging and of course I am not in a position to suggest one.

Dr Korst: It has already been pointed out by other discussers that this conference has limited its scope to deal mainly with rather weak types of separation and relatively weak interactions. This is consistent with the preference to attack

or reattack such problems which are reasonably well understood and amenable to ever more refined analytical or numerical treatment. A radically different situation arises when we are called upon to cope with real problems for which new solutions must be found, and for which an understanding must first be sought. To illustrate my point, I wish to enumerate some areas of concern related to a typical mission profile of space shuttle operations, such as:

(1) Plume induced separation, base pressure, and base heating problems arising from Space Shuttle Main Engine (SSME) and Solid Rocket Booster (SRB) operation during full flight of the very complicated take-off configuration (Figs. 1, 2);

(2) Flow separation, local heat transfer peaks resulting from plume impingement on the fuselage as the Solid Rocket Motor (SRM) staging engines initiate External Tank (ET) jettisoning;

(3) Plume impingement during orbital maneuvers with the Reaction Control System (RCS) and later plume induced separation leading to aerodynamic heating and control problems during reentry and descent.

It is of interest to note that such problems have not been covered in our sessions even though we should be greatly concerned about them and aware of our need to know, particularly since earlier experience with the X-15 has clearly established the severity of heat transfer and control problems associated with large scale separations and jet mixing region impingement. Such problems are germane to fully separated flows and always correspond to strong inviscid-viscid interactions.

For fully separated flows, the wake closure conditions are of utmost importance. This can be easily shown by observing that the separation point of slipstreams can move upstream drastically as plumes of propulsive jets expand upon encountering lower ambient pressures; yet, the conditions consistent with free interaction concepts remain satisfied locally. Hence, it appears to me that closure conditions at the end of large separation wakes have not (except for comments given by Prof. Liepmann and the references made by Dr Sirieix in his review lecture) received the attention they deserve when dealing with the mechanisms controlling separated flows.

A second observation is related to critical remarks made earlier by Dr Bogdonoff concerning attempts to achieve a better understanding of separated flow problems by generating numerical experience, mainly by utilizing large computer systems. The often striking elegance of procedures can, however, mask the lack of insight into the essential physical features of interactive flow mechanisms controlling transitional and turbulent separated flows. We should be skeptical of accepting seemingly accurate solutions if they merely reflect the opportunistic introduction or use of a sufficient number of free parameters.

Systematic study of relevant – yet basic – flow components controlling separation and, especially, fully separated flows can, however, often be carried out with advantage by first order or second order analytical approximations. Careful delineation of components, their rational treatment by analysis and subsequent synthesis into overall flow models can only be achieved if the understanding of essential physical concepts retains priority over and furnishes guidance for strictly algebraic procedures. Only on this basis can problems of great complexity be attacked. This includes the cases of flow separation I have mentioned in connection with space shuttle missions.

Mrs Ghia: First of all, I would like to thank Professor Gersten and the Programme Committee for organizing such a successful meeting. Coming now to the technical comments, I think that, even in numerical analyses, we have to emphasize the importance of theoretical work because it is the suitable combination of the two together that makes a successful solution technique, not numerical analysis alone. Of course, one should always aim to check numerical results against experimental data; however, if no experimental data is available for a given problem, I think checking against analytical results for limiting cases or limiting solutions can serve the purpose. Secondly, in seeking boundary-layer-type modelling of Navier-Stokes equations, one can never over-emphasize the significance of proper coordinate systems and dependent variables in formulating these equations. This is because, when one makes an approximation in the Navier-Stokes equations, the vector properties of the equations are lost and the resulting solutions have to depend upon coordinate systems. This was the reason I was rather puzzled by the question that was raised earlier about using the transformed conformal coordinates, as compared to Cartesian coordinates, to study the flow past a cylinder. I would feel very uncomfortable using Cartesian coordinates to do the cylinder flow problem. If polar coordinates can be considered appropriate for the cylinder problem, I don't see why a more suitable coordinate system system is not more appropriate.

As regards to the difficulty of computing high Reynolds number flows using Navier-Stokes equations, I think the reason for that is mainly because there are two different time scales and two different length scales in the problem, one for the viscous region and another for the inviscid region. It is important to choose the relaxation factors in the iterative numerical scheme or the time steps in ADI schemes such that both the time scales are given proper representation simultaneously. For the matrix inversions associated with implicit schemes, one also has to be concerned about satisfying the condition for diagonal dominance of the matrix. For problems that are primarily of a boundary-layer nature, the solution for high Reynolds number flows should not be too difficult if one takes into account the boundary-layer nature of the flows in addition to the other factors just discussed.

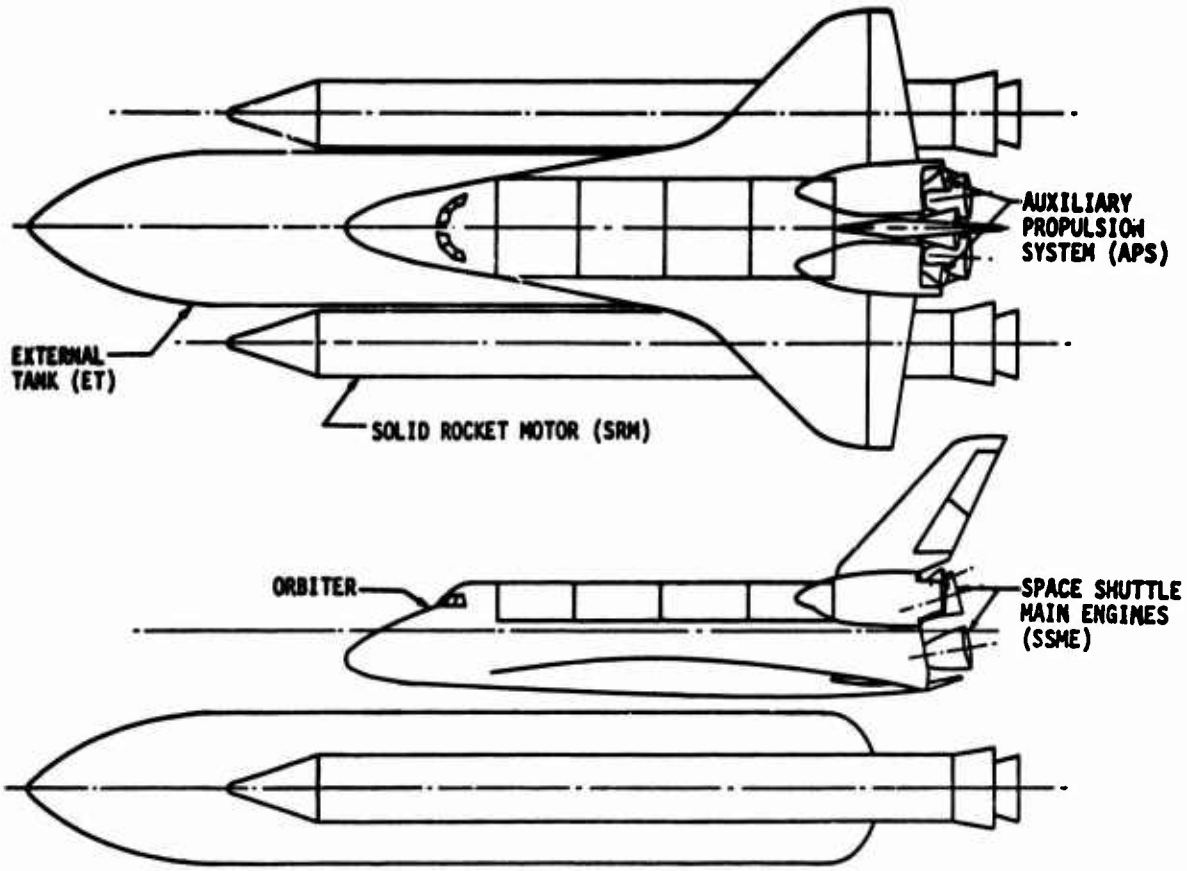

Fig.1 Space shuttle launch configuration

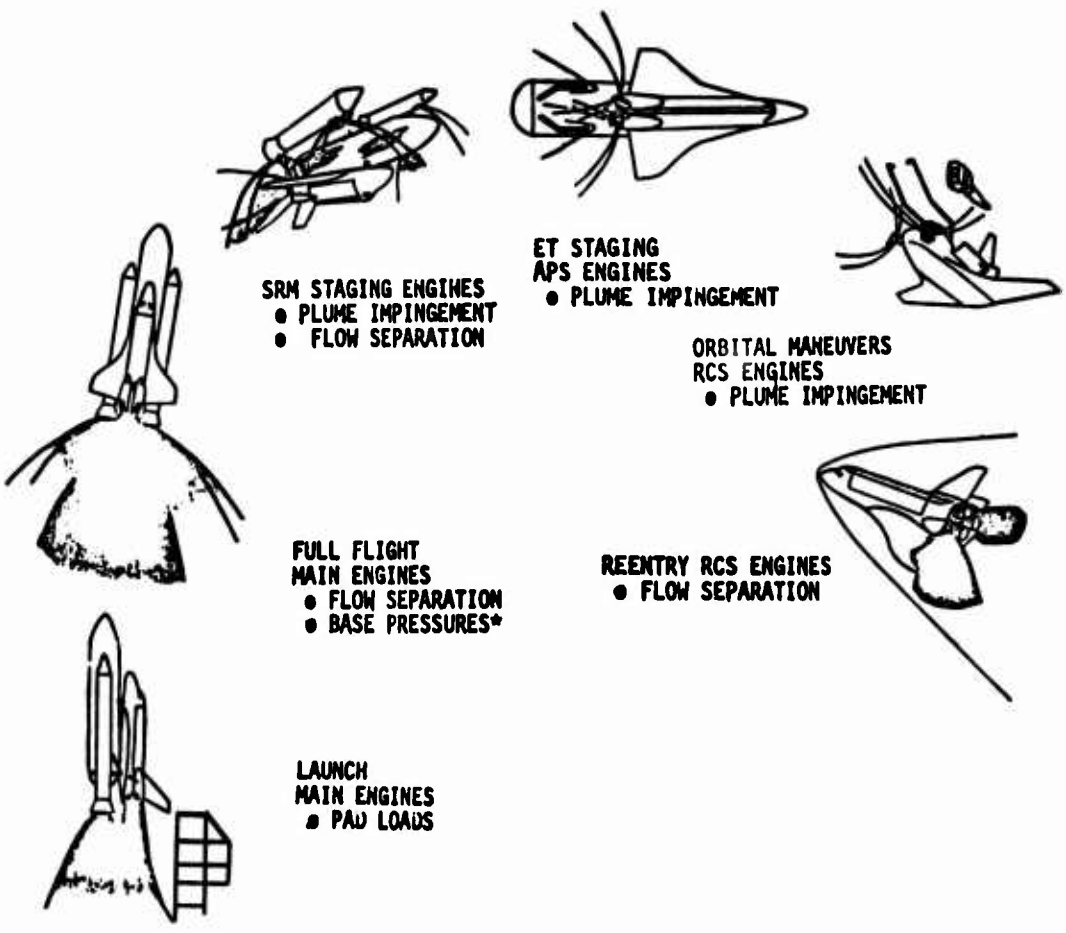

Fig.2 Mission profile illustrating rocket plumes associated with various shuttle operations

Again, I do agree with Professor Liepmann about the importance of eliminating the pressure as a primary variable for incompressible flows because it seriously retards the solution convergence rate. Even for three-dimensional flow problems, I think there are advantages to working with the vector potential and vorticity formation or a velocity-vorticity formulation, in spite of the fact that no reduction is achieved in the number of dependent variables with these approaches in the case of three-dimensional problems. Nevertheless, for three-dimensional problems with very complex geometrical configurations, one may have to give second thoughts to the various possible formulations and dependent variables.

Finally, a few words about the cylinder flow problem and the discussion which was just going on here. I too, have some apprehension about the success of a true boundary-layer model in studying this problem. This is the reason why we have tried to formulate those particular coordinates for the cylinder problem to determine a Navier-Stokes solution first, and then make certain approximations to the full equations to approach a boundary-layer-type model and see how well the approximate models work. If displacement thickness effects are properly taken into account, while also providing sufficient resolution for the viscous region, especially the wake region, then the approximate models should probably prove to be adequate. Thank you.

Professor Stollery: I enjoyed the Panel's words of wisdom, many of which I agree with. George Inger made a couple of points. he said that some more laminar experiments were needed and I should have thought that there were plenty of laminar experiments to keep the triple deck individuals happy for quite some time. He mentioned again this terrible red herring of sub- and super-critical flows. I would like to emphasize that the jump needed in super-critical flow is a means to an end. It may look unpleasant but it is practically very useful, I think it should be treated just in that light. Finally I would very much like to support Dr Peake and argue against Professor Liepmann, which is always dangerous, and suggest that incipient separation, far from being a word, is a very valuable concept indeed. It is the boundary between attached and well separated flows and this is precisely what the designer needs to know. Maybe we should interpret it with more clarity and a little more carefully but I think we do owe a debt to those people who probed it in great detail because they showed us some of the traps we can fall into. We must now think along the lines of significant departures in skin friction or heat transfer, the things we are interested in, when defining incipient separation.

Professor De Ponte: I will ask Professor Bogdonoff if, for a good experiment, he means only to measure, let's say, skin friction and so on and not to measure for example the shearing stresses, because we have seen here only one paper in which shearing stresses were measured and I think we need this for modelling turbulence. This is the first question. I think its important to have at least less accurate but more information on more parameters for checking computer programmes and the second question is you don't think that we need at least a better technique to know complex flows in the range between one meter per second and supersonic speed.

Professor Bogdonoff: I think the comment is a good one. I was trying to differentiate between two different kind of tests. We clearly need to support in the future, the kind of detailed information which we really have not spent much time with in the past simply because we are not sure of what drives the final results. There is now beginning a great deal of effort on obtaining detailed turbulent structure through boundary layers. It is going to take a long time to get enough of that information verified and checked and useful. It is the kind of information which is going to be necessary for the overall computer modelling, which, at the moment, is far ahead of the ability of the experimentalists to supply.

Many of the experiments we do are just for gross modelling and clearly we don't want to say that, for any boundary-layer experiment you want to make, you have to measure a turbulent shear stress. I mean that clearly would wipe out a great deal of activity. It seems to me that you have to have some perspective as to what is key in the problem you are looking at, and I think that we are going to have to if we are going to supply the details. Obtaining high quality, detailed experimental boundary-layer data will take a great deal of time and effort before you really believe it enough to go ahead and build theoretical models on it.

Professor Gersten: Thank you very much. I think it is now time to come to the end of this meeting. It is for me a great pleasure to express my sincere thanks to all the people who helped to make this meeting possible and, I hope, successful. I would like to thank the Mayor and people of the City of Göttingen for offering us this beautiful hall and for the reception. I would like to thank Professor Schlichting and the people in the AVA as they worked here as hosts. I would like to thank in particular the man who did most of the work here and this is Dr Meier the local coordinator. Of course I would like to thank Mr Lawford and Mel le Rivault. They worked most of the time behind the scene but nevertheless permanently. I would like to thank those individuals responsible for translation, projection, and sound acoustics Finally of course I would like to thank the session chairmen and the members of the Programme Committee and also the experts who took part in our final round table discussion. Many thanks to the authors and to all the people who contributed to the discussion. So, the meeting is now closed and we have to separate from Göttingen but hopefully perhaps we will somewhere and sometime reattach.